Yong-Whee Bahk

Combined Scintigraphic and Radiographic Diagnosis of Bone and Joint Diseases

Third Edition

Springer

Yong-Whee Bahk

Combined Scintigraphic and Radiographic Diagnosis of Bone and Joint Diseases

Yong-Whee Bahk

Combined Scintigraphic and Radiographic Diagnosis of Bone and Joint Diseases

Foreword by Henry N. Wagner, JR

3rd, revised and enlarged edition

With 692 Figures in 1329 Separate Illustrations

Springer

Yong-Whee Bahk, MD, PhD, Professor Emeritus
Department of Nuclear Medicine & Radiology
Sung Ae General Hospital
Seoul, 150-051 Korea

Library of Congress Control Number: 2006923239

ISBN 10	3-540-22880-2	Springer Berlin Heidelberg New York
ISBN 13	978-3-540-22880-6	Springer Berlin Heidelberg New York
ISBN 10	3-540-66424-6 2nd edition	Springer Berlin Heidelberg New York

Springer is a part of Springer Science+Business Media
springer.com

Editor: Dr. Ute Heilmann, Heidelberg
Desk editor: Dörthe Mennecke-Bühler, Heidelberg
Production editor: Nadja Kroke, Leipzig
Cover design: Frido Steinen-Broo, e-Studio Calamar, Spain
Production: LE-TeX Jelonek, Schmidt & Vöckler GbR, Leipzig
Typesetting: Arnold & Domnick, Leipzig
Printed on acid-free paper SPIN 11314073 21/3100/YL – 5 4 3 2 1 0

To those who suffer from skeletal disease
and those who heal and help the sufferers

Foreword to the third edition

In this refreshing 3rd edition of his classic book, Prof. Bahk has made further very important contribution to advancing bone and joint as well as soft-tissue imaging, among the most important and most widely used procedures in nuclear medicine. In his 25-year endeavor focusing on the scintigraphic imaging of the skeletal system, he has rightly emphasized the usefulness of the improved spatial resolution of bone scans obtained with the pinhole collimator. At the same time he has not forgotten to duly emphasize and illustrate the efficacy of 99mTc-HMPAO and 67Ga citrate scans and to discuss a recently introduced metabolic imaging technique, the 18F-FDG PET scan, in the diagnosis of bone and joint diseases.

The two previous editions have been thoroughly revised, rearranged, and expanded to include five new chapters on Normal Variants and Artifacts, Drug-induced Osteoporosis, Soft-tissue Tumors and Tumor-like Conditions, PET/CT in Bone and Joint Diseases, and A Genetic Consideration of the Skeletal Disorders with many new patient studies to realistically illustrate the immense value of all these new approaches. The diagnostic scope of some existing topical chapters on, for example, rheumatic skeletal disorders, benign and malignant bone tumors, and versatile traumatic injuries have also been broadened in depth and enriched by the addition of fresh cases.

Bone and joint and soft-tissue imaging reinforced with pinhole magnification have undeniably stood the test of time and have prosperously continued to improve in the solution of patients' problems on skeletal diseases, which are uncertain or nebulous in existence and character, often manifesting little or no sign on planar bone scintigraphs or images of other diagnostic modalities.

Professor Bahk's philosophy is that the combination of anatomical studies with high resolution biochemical imaging remains one of the best approaches to solving the problems in not only the bones and joints but also the entheses and soft tissues. His greatest contribution in this new edition is his fair emphasis on the irreplaceable advantages of pinhole imaging. The book is a must read for all practitioners and researchers of nuclear medicine as well as radiology, orthopedic surgery and pathology.

Baltimore, October 2006

Henry N. Wagner, Jr. M.D.
Johns Hopkins Medical Institutions
Baltimore, Maryland, USA

Preface to the third edition

As was remarked in the first preface the primary purpose of this humble book is aimed at introducing and establishing a more accurate, objective means of scintigraphic diagnosis of bone and joint diseases through a piecemeal analysis of scan findings: The tool is pinhole magnification (Fig. 1). Thus, endeavors have actually been made at further refining and enhancing the diagnostic yield of ^{99m}Tc-MDP pinhole bone scan using the anatomic and metabolic data thereof obtained along with that of collaterally performed radiography, ultrasonography, MRI or CT (Fig. 2). On the other hand, since this book was first brought out in 1995 a sizable volume of new knowledge has accumulated in the field of bone scan diagnosis through ever-increasing interest in and application of an array of scan methods that include SPECT, pinhole scintigraphy, 99mTc-HMPAO scan, immunoscintigraphy and most recently ^{18}F-FDG PET/CT in addition to already widely utilized three-phase bone scintigraphy, ^{67}Ga citrate scan and others.

It is due to the advent and wide spread use of those scan modalities and the compilation of harvested crops that this third edition is more or less thoroughly rewritten and enlarged. The revision is intended first to update the extended applicability and widened scope of the pinhole scintigraphic diagnosis of not only bone and joint diseases but also many soft tissue disorders in as much as they evolved during the last decade. Thus, in addition to former 18 chapters, current edition presents 5 new chapters to describe Normal Variants and Artifacts, Drug-Induced Osteoporosis, Soft-Tissue Tumors and Tumor-like Conditions, PET-CT in Bone and Joint Diseases and Bone Scintigraphic Consideration of Genetic Skeletal Disorders. In addition, the chapters on Rheumatic Skeletal Disorders, Malignant Tumors of Bone, Benign Tumors of Bone and Traumatic Diseases are completely rewritten and complemented by the addition of some 90 fresh cases. The second aim is to underscore the undisputed usefulness of pinhole scintigraphy (Fig. 3).

It is my conviction that even in this era of surging molecular imaging and burgeoning nanoscience techniques best possible grasping of macro-anatomy and fine visible chemical change continues to be the most essential orientation for well founded bone scintigraphic diagnosis and, on its extension, a more holistic understanding of bone and joint diseases. As we know high resolution and sensitivity are two important parameters that effectively enhance the diagnostic acumen of imaging study, and, fortunately, both can be attained to a significantly raised level when one properly uses the pinhole magnification technique.

Fig. 1. Pinhole scanner showing pinhole collimator inserted at the top of the cone shield assembly. The optimum aperture size is 4 mm

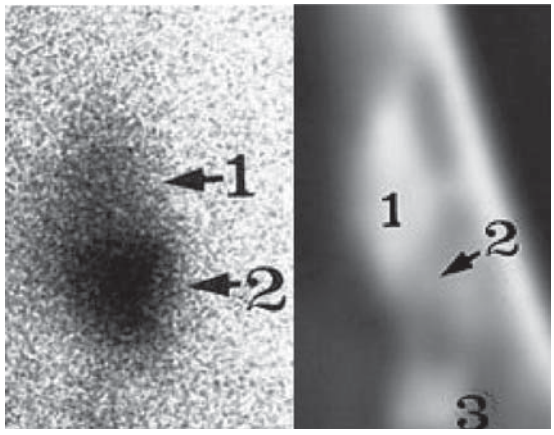

Fig.2. Anterior pinhole scan (left) and reconstructed coronal CT (right) of enchondromas in the left distal femur showing different 99mTc-MDP uptake according to the grade of mineralization. Tumors with advanced mineralization (1, 3) reveal low uptake and tumor with weak mineralization (2) reveals high uptake, reflecting different evolutional stages and metabolic activities of tumors

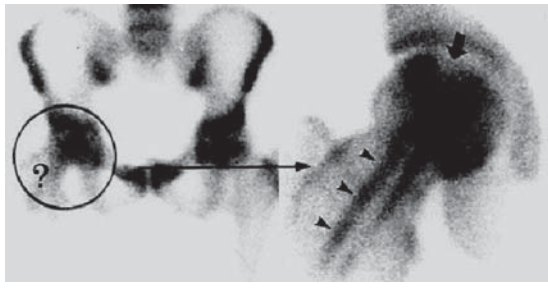

Fig. 3. Anterior planar (left) and pinhole (right) scan of the right hip with vascularized fibular graft implanted for avascular necrosis treatment. Note incredible improvement of both resolution and sensitivity. The graft is completely assimilated (arrowheads) with a small residual defect at the femoral capital top (arrow)

Acknowledgement

First of all, I am most grateful for many encouraging remarks and constructive opinions expressed by the reviewers in the United States, Germany, United Kingdom, Australia, Japan, Italy, Spain and Korea, my homeland, not to say the very generous acceptance of the earlier two editions of this book by anonymous readers and friends.

My very special thanks are due to Prof. Dr. Henry N. Wagner, Jr. who has graciously written the forewords on all three occasions. I am also deeply indebted to Dr. Yoon Kwang Kim, Chairman of the Sung-Ae Medical Foundation, Seoul, for his generous support. I wish to salute Mr. Tae Sung Choi, Mr. Kee Sup Chung and Mr. Dae Hee Moon, nuclear medicine technologists, for beautifully performing pinhole scintigraphy and Mr. Seun Mok Jeung, Mr. Pil Bok Wi and Miss Hyung Sook Hong for excellent photographic work.

Dr. Ute Heilmann and Ms. Dörthe Mennecke-Bühler and staff at the Springer-Verlag in Neuenheim, Heidelberg fully deserve my high admiration for their superb cooperation and fine editorial performance in creating this third edition.

Finally, I would like to pay a special and loving tribute to my wife, Rosa Yeun-Soo Cho, sons and daughter and grandchildren for everything that we have shared together during all these years.

Yong-Whee Bahk

Contents

1 Introduction and Fundamentals of Pinhole Scintigraphy

To those who acquired their anatomical knowledge of the skeleton with the aid of clean, dried bone specimens or a plastic mannequin it may appear as a mere inert weight-bearing scaffold of the human body. However, like all other organs, bone constantly undergoes remodeling and tubulation through the physiological and metabolic activities of osteoblasts and osteoclasts. The principal role played by these bone cells is the maintenance of bone integrity and calcium homeostasis by balancing between the ratio of bone collagen production and resorption and by governing mineralization processes. Collagen production is a histological property common to various connective tissues, but mineralization is unique to bone cells.

One of the first images of living human bone was a radiograph of the hand of the anatomist Kölliker taken by Wilhelm Conrad Röntgen at Würzburg University on 23 January 1896 (Fig. 1.1). Radiography then became the sole modality for visualizing the skeletal system in vivo, and it remained so until 1961 when Fleming and his coworkers produced the first

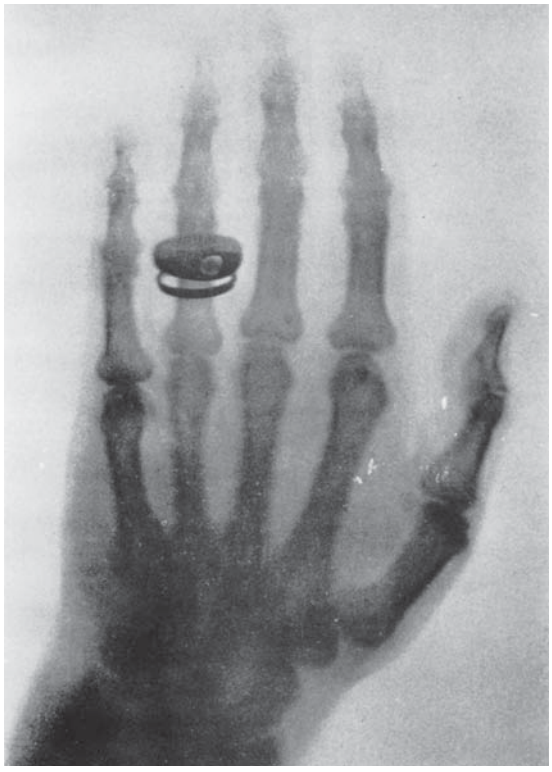

Fig. 1.1 One of the first radiographs of living human skeleton: anatomist Kolliker's hand, by Professor Röntgen in January 1896 at Würzburg University

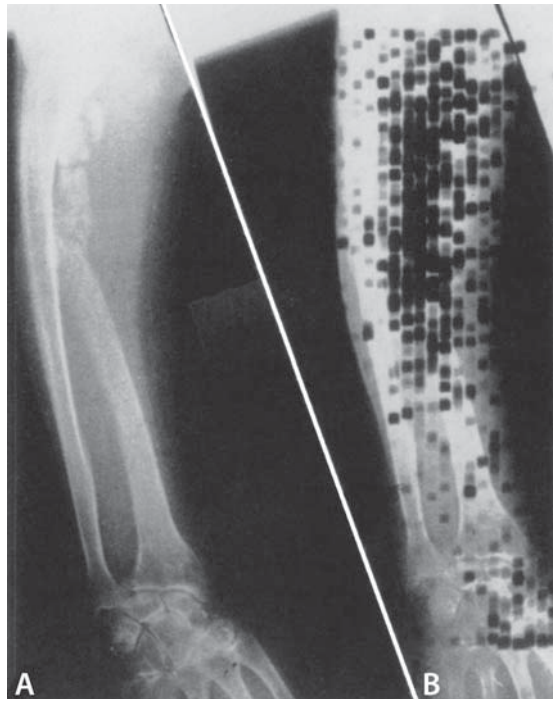

Fig. 1.2A, B One of the first bone scans made with ^{85}Sr. **A** Radiograph of forearm shows bone destruction due to metastasis in the proximal radius. **B** Dot photoscan reveals intense tracer uptake in the lesional area (from Fleming et al. 1961)

bone scintigraphic image using ^{85}Sr, a gamma ray-emitting radionuclide (Fig. 1.2). Using bone scintigraphy they successfully diagnosed bone metastasis and fracture. Historically, the event marked the beginning of the clinical use of bone scintigraphy for diagnosing skeletal disorders. During the development stage, bone scintigraphy suffered from many problems, particularly the limited image quality and consequent low diagnostic specificity. But with the wide availability of high-technology gamma camera systems furnished with efficient detector-amplifier assemblies, high-resolution collimators including fine pinhole, refined software, and ideal radiopharmaceuticals such as ^{99m}Tc-labeled methylene diphosphonate (MDP) and ^{99m}Tc-labeled hydroxydiphosphonate (HDP), bone scanning has long become established as an indispensable nuclear imaging procedure. Bone scanning is highly valued for two major reasons: exquisite sensitivity and unique ability to assess metabolic, chemical, or molecular profile of diseased bones, joints, and even soft-tissue structures. The usefulness of nuclear bone imaging modalities have most recently been enriched by the advent of bone marrow scintigraphy and positron emission tomography (PET) or PET-CT, further expanding the already wide scope of nuclear bone imaging science.

Indeed, bone scintigraphy is recognized for its sensitivity in detecting bone metastasis weeks before radiographic change is apparent and even ahead of clinical signs and symptoms. Its usefulness has also been thoroughly tested in the diagnosis of covert fracture, occult trauma with enthesitis, contusion, transient or rheumatoid synovitis, early osteomyelitis and pyogenic arthritis, avascular osteonecrosis, and a number of other bone and joint diseases. The introduction of single photon computed tomography (SPECT) has significantly enhanced lesion detectability by enhancing the image contrast through slicing complex structure of the pelvis, hip, spine and skull. In addition, ^{67}Ga citrate and ^{111}In- or ^{99m}Tc -labeled granulocyte scans have made important contributions to the diagnosis of infective bone diseases. As an adjunct the quantification of bone scan changes has been proposed (Pitt and Sharp 1985), and data are now automatically processed. This analytical approach is based on the calculation of the activity ratios of bone to soft tissue, bone to bone, and bone to lesion. Measurement of bone clearance of ^{99m}Tc-MDP, photon absorptiometry, and quantitative bone scan are used increasingly in the study of osteoporosis and osteomalacia. Most recently, ^{18}F FDG-PET has been shown to be a potent imaging method for the detection of not only the early primary cancers but also metastases to the bones, lymph nodes, and soft tissues (Abe et al. 2005; Buck et al. 2004).

In spite of unprecedented progress in computer technology, electronic engineering, and radiopharmaceuticals, the specificity of bone scintigraphic diagnosis has remained suboptimal and accordingly for more specific diagnosis of many bone and joint diseases additional information is still sought from radiography, CT, MRI and sonography, and finally such want has led to the hybridization of PET with CT. Silberstein and McAfee (1984) laboriously worked out a scintigraphic appraisal system to raise the specificity, but their success was partial. The factors counted on for scintigraphic diagnosis in the past were not specific morphological features that more or less directly reflected the pathological process in question, but included the following: increased or decreased tracer uptake, the number of lesions, unilaterality or bilaterality, homogeneity or not, and most problematically approximate anatomy. More essential determinants such as the size, shape, contour, accurate location, and internal texture of lesions cannot be portrayed by tracer uptake and distribution. Clearly, the reason for not analyzing more essential determinants was the relatively low resolution of the scan images made with multiple-hole collimators (O'Conner et al. 1991). This limitation remained unremedied even after the introduction of SPECT. While SPECT is very effective for the elimination of the overlap of neighboring bones and significantly enhances contrast, the resolution remains unimproved. PET, a tomographic modality like SPECT, can sensitively indicate

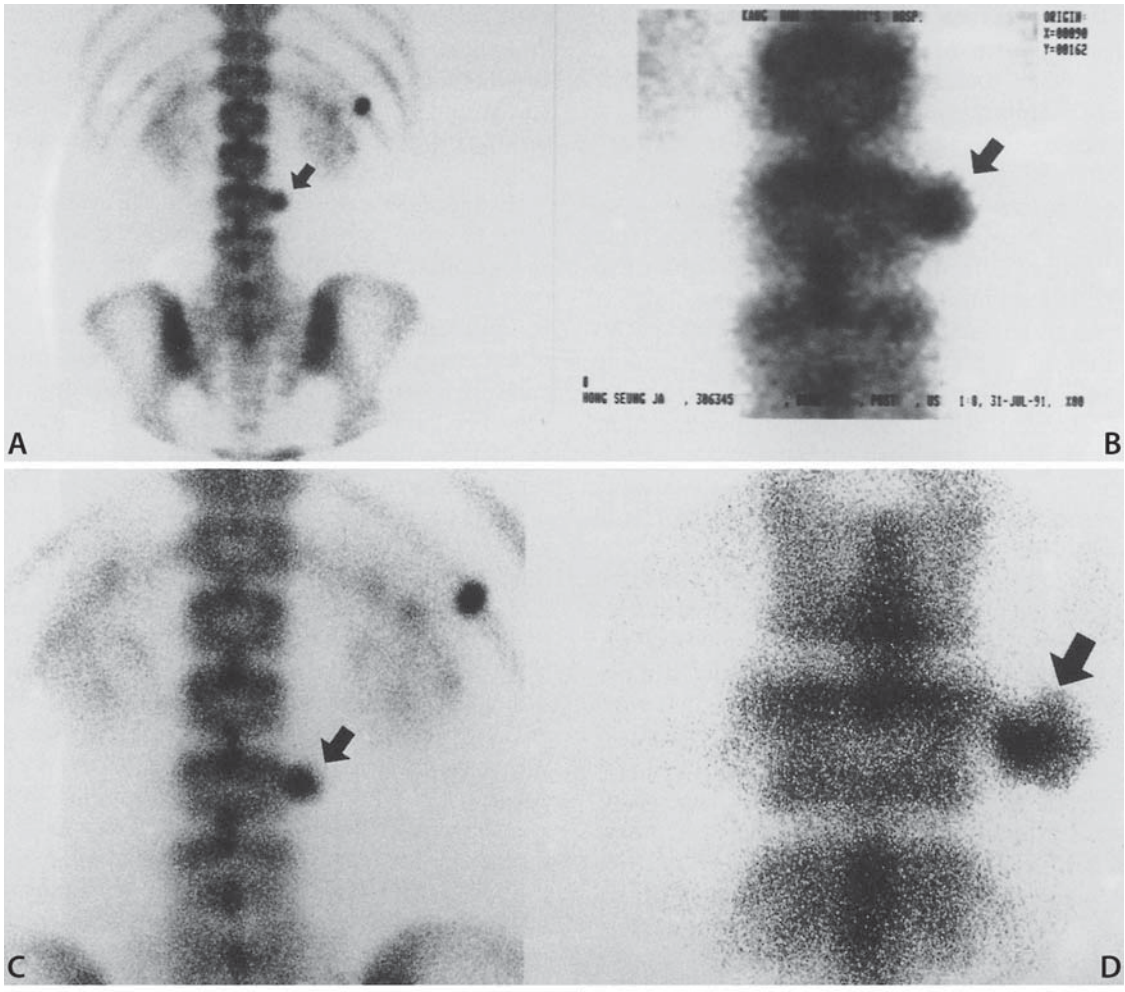

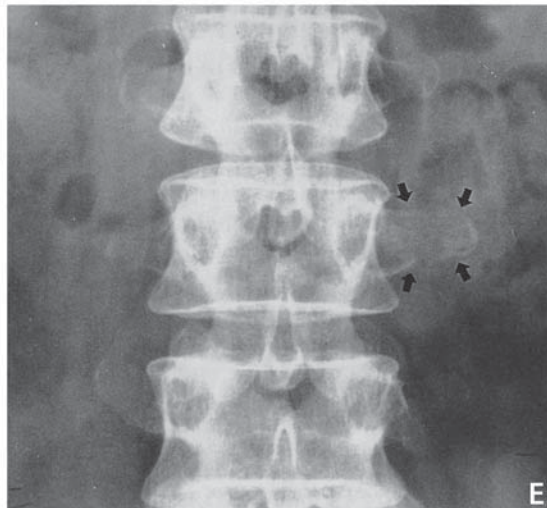

Fig. 1.3 Spot scintigraphs (**A–D**) showing the difference in the grade of resolution among four scanning methods used for displaying a metastasis (*arrows*) in the transverse process of L3 vertebra. **A** LEAP collimator. **B** Blowup or computer zooming. **C** Geometric enlargement. **D** Pinhole magnification. The lesion can be localized specifically in the transverse process only by pinhole scintigraphy (**D**). **E** Anteroposterior radiograph shows osteolysis in the transverse process of the L3 vertebra (*arrows*)

where increased amounts of FDG are deposited in the cytoplasm of, for example, cancer cells. A PET scan alone, however, cannot identify exact anatomy, needing the help of CT in the form of PET-CT hybridization. It is evident that on the whole the interpretation of scintigraphy has traditionally relied on nonspecific or indirect findings.

Fortunately, pinhole bone scintigraphy can in greater detail display pathological changes in the individual disease of bones and joints as well as the soft tissues through an optical magnification with highly improved resolution. It must be remembered that mere blow-up, computer zooming or multihole collimator magnification does not truly enhance spatial resolution (Fig. 1.3). Pinhole scintigraphy appears ideal for establishing an improved piecemeal interpretation system at least for skeletal disorders. The level of spatial resolution and image contrast attained by pinhole scintigraphy has been shown to be of an order that is practically comparable to that of radiography both in normal and many pathological conditions (Bahk 1982, 1985, 1988, 1992; Bahk et al. 1987). For example, the small anatomical parts of a vertebra in adults and a hip joint in children can be distinctly discerned using this method. In an adult vertebra the pedicles, apophyseal joints, neural arches, and spinous process are clearly portrayed and in a pediatric (growing) hip the acetabulum, triradiate cartilage, capital femoral epiphysis and physis, and trochanters are regularly discerned (Chap. 4).

Clinically, pinhole scanning permits differential diagnosis, for example, among metastases, compression fractures, and infections of the spine (Bahk et al. 1987). The "pansy flower" sign of costosternoclavicular hyperostosis, a pathognomonic "bumpy" appearance of the long bones in infantile cortical hyperostosis, and the "hotter spot within hot area" sign of the nidus of osteoid osteoma are just a few examples of diagnoses that can be made by observing characteristic or pathognomonic signs of the individual diseases (Bahk et al. 1992; Kim et al. 1992).

To summarize, it appears that, used along with the holistic physicochemical data derived from whole-body, triple-phase, and spot ^{99m}Tc-MDP bone scans, the detailed anatomicometabolic profiles of skeletal disorders portrayed by pinhole scintigraphy enormously enhance diagnostic feasibility. In addition, it is indeed worth reemphasizing that the diagnostic accuracy of pinhole scintigraphy can be greatly sharpened if the scintigraphs are read side-by-side with radiographs—the common royal road to all image interpretations (Fig. 1.3D, E).

1.1 A History of Nuclear Bone Imaging

Conceptually, the nuclear imaging of bone can be dated from the mid-1920s when the notion of bone-seeking elements evolved from the clinical observation of radium-related osteomyelitis and bone necrosis (Blum 1924; Hoffman 1925). Shortly following successful isolation by the Curies, radium was processed to produce self-luminous materials to be painted on watch dials and instrument panels. During the painting of such radioactive materials with small brushes, workers habitually pointed the brush tip between their lips, and this resulted in chronic ingestion and subsequent bone deposition of hazardous radioactive elements, eventually causing deleterious effects (Hoffman 1925). The initial theory was that bone deposition of radium was caused by phagocytosis of the reticuloendothelial cells in bone marrow, but soon it was found that bone itself actively accumulates radioelements (Martland 1926). This was later confirmed by Treadwell et al. (1942) who showed by radioautography that ^{89}Sr, a beta-emitting bone-seeking element, was laid down in both normal and sarcoma tissues.

Two decades elapsed until, with the advent of the γ-counter, γ-scanner, and γ-emitting bone-seekers such as ^{47}Ca and ^{85}Sr, a new era of nuclear bone imaging was opened. In 1961 Gynning et al. detected the spinal metastases of breast cancer by external counting of the in-vivo distribution of ^{85}Sr. The data were displayed in a profile graph so that increased radioactivities in diseased vertebrae were indicated by an acute spike. In the same year, the first photographic scintigraph of bone showing selective accumulation of ^{85}Sr at the site of metastasis with fracture in the radius was published (Fig.

1.2) (Fleming et al. 1961). On the other hand, Corey et al. (1961), using ^{47}Ca and ^{85}Sr, showed the possibility of detecting bone pathology by bone scanning before X-ray changes became manifest. However, the ^{47}Ca scan turned out to be impractical because of the high energy (1.31 MeV) of its principal gamma ray. Accordingly, ^{85}Sr was then held to be the radionuclide of choice for bone scanning, although it also has drawbacks of a long physical half-life (65 days) and a relatively high-energy gamma emission of 513 keV. Charkes (1969) suggested that ^{87}Sr might overcome these shortcomings. The physical half-life of ^{87}Sr is only 2.8 h, permitting safe administration of a larger dose with increased activity in bone. On the other hand, ^{18}F, another bone-seeking element, was already in use (Blau et al. 1962). This is a cyclotron product possessing a stronger avidity for bone than strontium, with about 50% of an injected dose incorporated into bone. It emits a positron that creates, by annihilation with an electron, two gamma rays having an energy of 511 keV that is suitable for external detection and scanning. Currently, ^{18}F in the form of ^{18}F-fluorodeoxyglucose (FDG) is globally used for PET in tumor and many other diseases. Once its high production cost and short physical half-life (1.83 h) prevented popularization, but these problems were solved with the development of an easily manageable, compact, economical cyclotron. The ready availability of ^{18}F-FDG and PET-CT is expected to make a significant contribution to nuclear imaging, especially in oncology.

In the meantime, technetium-^{99m} (^{99m}Tc) tagged compounds were introduced as potent bone scan agents by Subramanian and McAfee (1971). Technetium-^{99m} is an ideal radiotracer for most scintigraphy with a short physical half-life (6.02 h), a single gamma ray of optimal energy (140 keV), low production cost, and ready availability (Harper et al. 1965; Richards 1960). The first preparation was ^{99m}Tc-triphosphate salt but this was soon replaced successively by ^{99m}Tc-polyphosphate, ^{99m}Tc-pyrophosphate, ^{99m}Tc-diphosphonates, and finally ^{99m}Tc-methylene diphosphonate (MDP) (Castronovo and Callahan 1972; Subramanian et al. 1972, 1975; Citrin et al. 1975; Fogelman et al. 1977). With the integrated development of a family of ideal radiopharmaceuticals and high-technology gamma camera systems equipped with an efficient pinhole magnification device with software and SPECT, bone scintigraphy is now firmly established as the most frequently used and highly rewarding nuclear imaging method. Furthermore, bone marrow scan and the already mentioned ^{18}F FDG PET have been added to the existing large arrays of imaging modalities of the musculoskeletal system with almost unlimited diagnostic feasibility, which is thoroughly noninvasive.

Of various bone scintigraphic studies, this book mainly focuses on pinhole scintigraphy, a potent solution to the suboptimal specificity of ordinary bone scan, with commentary discussions on the SPECT, PET, and bone marrow scan. It is true that pinhole scintigraphy takes a longer time to perform than planar scintigraphy, but the longer time is more than compensated for by the richness of information. Actually, pinhole scan time is comparable to or even shorter than that of SPECT. As described in the technical section, the refined pinhole technique using an optimal aperture size of 4 mm, correct focusing, and ^{99m}Tc-MDP or -HDP, the time can now be reduced to as short as 15 min. The information generated by pinhole scanning is unique in many skeletal disorders (Bahk 1982, 1985; Bahk et al. 1987, 1992, 1994, 1995; Kim et al. 1992, 1993, 1999; Yang et al. 1994). Interestingly, historically the pinhole collimator was the first collimator used for gamma imaging by Anger and Rosenthall (1959). However, for reasons that are not apparent other than its tediousness, it has since largely been ignored and replaced by multihole collimators and planar SPECT. It seems that this has occurred within a short period of time without logical reasoning and thorough exploration into its utility. Nevertheless, restricted to the diagnosis of hip joint disease, pinhole scanning was enthusiastically used by Danigelis et al. (1975), Conway (1993), and Murray in Sydney (personal communication), and more re-

cently the Boston group extended its application to diseases of bone and joints other than the hip in the pediatric domain (Treves et al. 1995). As discussed in detail in Chap. 2, most recently dual-head planar pinhole scintigraphy (Bahk et al. 1998a) and pinhole bone SPECT (Bahk et al. 1998b) have been added to single-head planar pinhole scintigraphy. The former modification significantly shortens the scan time and solves the problem of the blind zone that is present on single-head pinhole scans, and the latter can further improve the resolution and contrast by the addition of slicing to magnification.

1.2 Histology and Physiology of Bone

Living bone is continuously renewed by production and resorption that are mediated through the bioactivities of the osteoblasts and osteoclasts, respectively. The bone turnover is well balanced and in a state of equilibrium unless disturbed by disease and/or disuse. When bone production is out-balanced by bone resorption or destruction, as in acute osteomyelitis, tumor, or immobilization, osteolysis or osteopenia may ensue. In a reverse condition, osteoblastic reaction predominates, resulting in osteosclerosis or increased bone density.

Histologically, five different types of bone cells are known to exist. They are osteoprogenitor cells, osteoblasts, osteocytes, osteoclasts, and bone-lining cells. Osteoprogenitor cells, also known as preosteoblasts, proliferate into osteoblasts at the osseous surface. Osteoblasts are the main bone-forming cells both in membranous and endochondral ossification. The osteoblast, a mononuclear cell, produces collagen and mucopolysaccharide that form osteoid. It is also closely associated with osteoid mineralization. The osteocytes are the posterity cells of osteoblasts entrapped within bone lacunae. Their main functions are the nutritional maintenance of the bone matrix and osteocytic osteolysis. Being multinucleated, osteoclasts are involved in bone resorption by osteoclasia. Formerly, the osteoclast and osteoblast were considered to stem from the same or at least related sources. New evidence, however, has indicated that the cell lines for these two cells are histogenetically different (Owen 1985). At present, it is widely held that osteoclasts originate from stromal cells of mesenchymal tissue via osteoprogenitor cells, while osteoblasts originate from the monocyte-phagocyte line of the hematopoietic system. Bone-lining cells are probably the inactivated form of osteoblasts. Like osteoblasts, these cells line the osseous surface. The cells are flat and elongated in shape with spindle-shaped nuclei. Although not established yet, their function is probably related to the maintenance of mineral homeostasis and the growth of bone crystals.

Osteogenesis is accomplished by mineralization of organic matrix or osteoid tissue, which is composed mainly of collagen (90%) and surrounding mucopolysaccharide. Mineralization starts with the deposition of inorganic calcium and phosphate along the longitudinal axis of collagen fibrils, a process referred to as nucleation. Nucleation is precipitated by a chemical milieu in which the local phosphate concentration is increased or conversely calcium salt solubility is decreased. After nucleation, salt exists in a crystalline form and grows in size as more calcium and phosphate precipitate. Crystallized salt has resemblance to hydroxyapatite [$Ca_{10}(PO_4)\cdot 6OH_2$].

Bone formation is stimulated by various factors including physical stress and strain and calcium regulatory hormones (parathormone, calcitonin), growth hormone, vitamins A and C, and calcium and phosphate ions. On the other hand, bone resorption occurs as bone matrix is denatured by the proteolytic action of collagenase secreted by osteoclasts. Factors that stimulate osteoclastic activity include bodily immobilization, hyperemia, parathormone, biochemically active metabolites of vitamin D, thyroid hormone, heparin, interleukin-1, and prostaglandin E.

The skeletal muscles are rich in actin and myosin, the interactions of which cause contraction. They are composed of a large number

of muscle fibers (cells). Muscle fibers, individually invested by the endomysium, are grouped in fascicles enveloped in successive connective tissue sheaths. Variable numbers of fascicles compose a skeletal muscle that is ensheathed by the epimysium. Tendon is a specialized connective tissue that unites with muscle belly forming the musculotendinous unit on one side and attaches to the periosteum, fibrous capsule of the joint, or directly to bone on the other side.

1.3 Mechanism of Bone Adsorption of ^{99m}Tc-Radiopharmaceuticals

The mechanism of ^{99m}Tc-labeled phosphate deposition in bone has not fully been clarified. However, it is known that the deposition is strongly influenced by factors such as metabolic activity, blood flow, surface bone area available to extracellular fluid, and calcium content of bone. For example, metabolically active and richly vascular metaphyses retain 1.6 times more ^{99m}Tc than less-active diaphyses of long bones (Silberstein et al. 1975), and such a metabolism- and vascularity-dependent biomechanism can be portrayed by scintigraphy of growing bone or highly vascular rachitic or pagetic bones. Another important factor is the nature of calcium phosphate in bone as indicated by the Ca/P molar ratio. Francis et al. (1980) experimentally demonstrated that diphosphonates are more avidly adsorbed to the immature amorphous calcium phosphate (Ca/P 1.35) than to the mature hydroxyapatite crystal (Ca/P 1.66). The low Ca/P salt typically exists in the rapidly calcifying front of osteoid matrix in the physes of growing long bones, whereas crystalline hydroxyapatite exists in the cortical bones.

Various theories have been proposed regarding the site of deposition. Jones et al. (1976) suggested that a small amount of phosphate chemisorbs at kink and dislocation sites on the surface of the hydroxyapatite crystal. On the other hand, the organic matrix is considered to be the site of calcium salt deposition (Rosenthall and Kaye 1975). Francis et al. (1981) have shown that the deposition of diphosphonate takes place almost exclusively on the surface of the inorganic calcium phosphate. Evidence in support of this finding has been provided by autoradiographic study (Guillermart et al. 1980).

1.4 Bone Imaging Radiopharmaceuticals

The advantageous properties of ^{99m}Tc were reported by Richards (1960) and Harper et al. (1965), but it was not until the introduction of triphosphate complex by Subramanian and McAfee (1971) that ^{99m}Tc became the most promising bone scan agent. Thus, this initial work on ^{99m}Tc-labeled phosphate compounds opened a path to the development of a series of novel bone scan agents. Within a short period of time, ^{99m}Tc-labeled polyphosphate, pyrophosphate, and diphosphonate were developed in series for general use. Chemically, phosphate compounds contain a plural number of phosphate residues (P–O–P), the simplest form being pyrophosphate with two residues. Phosphonate has P–C–P bonds instead of P–O–P bonds and diphosphonates are most widely used. Now these are available as ^{99m}Tc-labeled hydroxydiphosphonate (HDP) and ^{99m}Tc-labeled MDP. The phosphonate compounds have a strong avidity for hydroxyapatite crystal, especially at the sites where new bone is actively formed as in the physeal plates of growing long bones.

Following intravenous injection, ^{99m}Tc-phosphate and ^{99m}Tc-diphosphonate are rapidly distributed in the extracellular fluid space of the body, and about half of the injected tracer is fixed by bone and the remainder excreted in the urine by glomerular filtration (Alazraki 1988). According to Davis and Jones (1976), the amount of radiotracer accumulated in bone

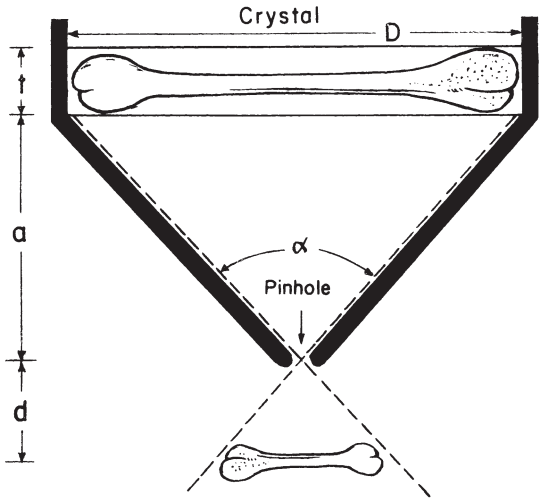

Fig. 1.4 Schematic diagram showing inversion and magnification of pinhole image. *D* Diameter of detector or crystal, *t* thickness of detector, *a* collimator length or detector-to-aperture distance, *d* aperture-to-object distance, *a* acceptance angle

1 h after injection is 58% with MDP, 48% with HEDP, and 47% with pyrophosphate. The latest form of the diphosphonate series is disodium-monohydroxy-methylene diphosphonate (oxidronate sodium, $CH_4Na_2O_7P_2$) marketed as TechneScan HDP. Its blood and nonosseous clearance is much faster than that of ^{99m}Tc-labeled MDP, and the blood level is about 10% of the injected dose at 30 min with a rapid fall thereafter, reaching 5%, 3%, 1.5%, and 1% at 1 h, 2 h, 3 h, and 4 h, respectively, after injection (Mallinckrodt 1996). An advantage of this preparation is that an optimum blood level is reached as early as at 1–2 h after injection; as a result the scan time is conveniently reduced without increasing the tracer dose.

1.5 Bone Marrow Scan Radiopharmaceuticals

^{99m}Tc-nanocolloid and ^{99m}Tc-anti-NCA95 antibody are two representative agents for bone marrow scanning. These agents image erythropoietic precursor cells, reticuloendothelial cells (REC), and granulopoietic cells. Phagocytosis is the mechanism by which ^{99m}Tc-colloids visualize REC. Unfortunately, red marrow uptake of currently available ^{99m}Tc-colloids is not large enough to produce marrow image of sufficient quality. In addition, disparity may occur between the locations of REC and hematopoietic cells in different hematological disorders. Theoretically, ^{52}Fe and ^{59}Fe can be used for the imaging of erythropoietic bone marrow, but their unsuitable physical characteristics prevent practical use. ^{111}In-chloride has been tested as an iron substitute, but has been found not to be satisfactory (Lilien et al. 1973). ^{111}In-chloride is an expensive agent.

1.6 Fundamentals of Pinhole Scintigraphy

This section considers the spatial resolution and sensitivity of the pinhole collimator as related to aperture size and aperture-to-target distance. In addition, the parameters that affect image quality are briefly discussed. For those interested in a mathematical presentation of this subject, a separate chapter is appended.

A scintigraphic image is the cumulative result of a number of physical parameters including (a) radionuclide, (b) amount of radioactivity, (c) collimator design, (d) detector efficiency, and (e) image display and recording devices. Other factors such as patient movement during scanning and various artifacts can also affect the spatial resolution, object contrast, and sensitivity, which all seriously affect lesion detectability (Appendix and Chap. 5).

The tracer must be localized to bone and deliver a low radiation dose while permitting a high count density in the target. In this respect, ^{99m}Tc with a half-life of 6.02 h and a monoenergetic gamma ray of 140 keV labeled to phosphates is ideally suited for bone scanning. As a rule, 740–925 MBq (20–25 mCi), or a slightly higher dose in the elderly who have

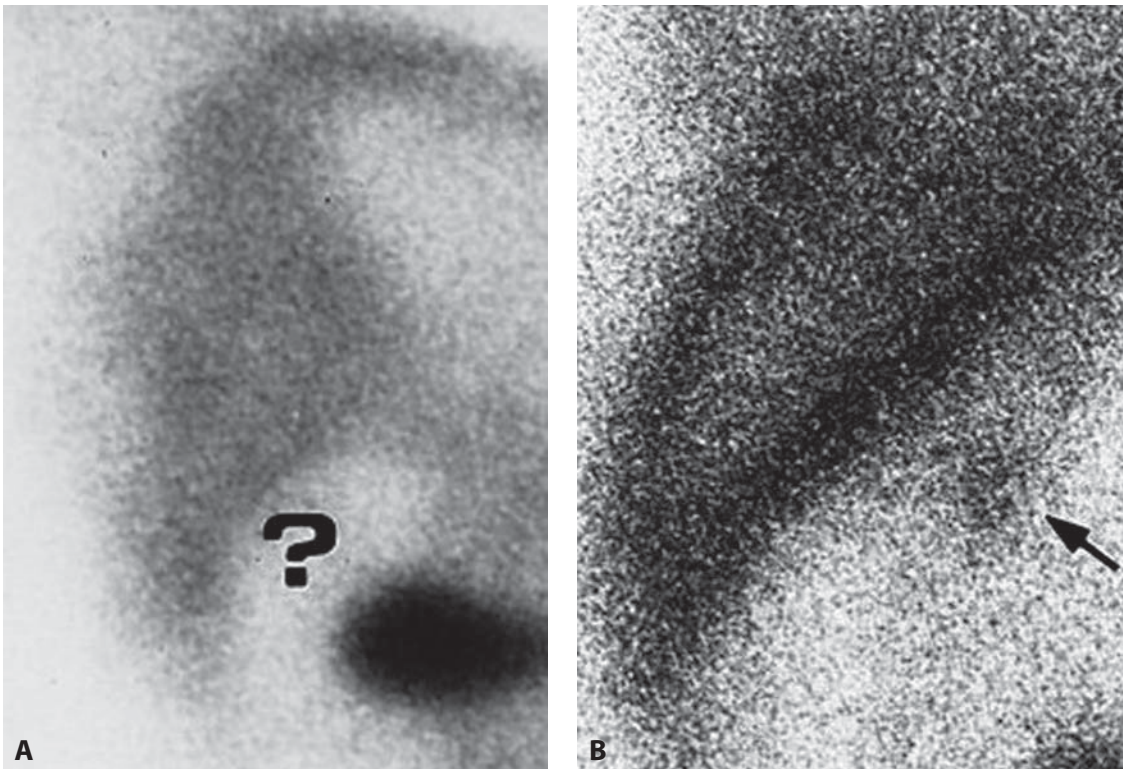

Fig. 1.5A, B Local recurrence of colon carcinoma. **A** Lateral planar bone scintigraph shows no abnormal tracer uptake (?). **B** Lateral pinhole scintigraph demonstrates minimal uptake in the presacral soft tissue, denoting recurrence (*arrow*)

reduced bone metabolic function, of ^{99m}Tc-MDP or ^{99m}Tc-HDP is injected with satisfactory results and an acceptably low radiation dose.

Basically, a gamma camera system consists of a scintillation detector with collimator, electronic devices, and image display and recording devices. Of these, the collimator is probably the most important variable that affects image resolution. The primary objective of a collimator is to direct the gamma rays emitted from a selected source to scintillation detector in a specifically desired manner. Four different types of collimators are used: pinhole collimator, and parallel-hole, converging and diverging multihole collimators.

The pinhole collimator is a cone-shaped heavy-metal shield that tapers into a small aperture perforated at the tip at a distance *a* from the detector face, which may be either circular or rectangular in shape (Fig. 1.4). The geometry of the pinhole is such that it optically creates an inverted image of the object on the crystal detector from the photons traveling through the small aperture. The design is based on aperture diameter, acceptance angle α, collimator length *a*, and collimator material.

The aperture diameter of a pinhole collimator is the most important and direct determinant of the system's resolution and sensitivity. Evidently, the collimator with a smaller aperture diameter can produce a scan image with a higher resolution, but at the expense of sensitivity, and vice versa. Therefore, optimization of the two contradicting parameters is necessary. In practice, a collimator with an aperture diameter of 3 or 4 mm is optimal. The magnification, resolution, and sensitivity of a pinhole collimator acutely change with the aperture-to-target distance. Thus, image magnification with a true gain in both resolution and sensitivity can be achieved by placing the collimator tip close to the target.

Fundamentally, the suitability of pinhole scintigraphy largely depends on the size or area of the target to be imaged. Relatively small structures or organs such as the appendiceal bones and joints and thyroid gland are perfectly suited. In the same context a small portion of large anatomical structures such as the skull, spine, chest, long bone, and pelvis can also be imaged satisfactorily with rich diagnostic information.

1.7 Rationale and Techniques of Pinhole Scintigraphy

Pinhole scintigraphy is indispensable when bone changes need to be visualized in greater detail than can be achieved by an ordinary scan for analytical interpretation. The information provided by the pinhole scan is often unique and decisive in making a specific diagnosis of bone and joint disorders (Bahk et al. 1987; Kim et al. 1999). Furthermore, this examination has been shown to be of immense value in detecting the lesions that are invisible on an ordinary scan due to low photon counts (Fig. 1.5).

Routinely bone scanning is started by taking both the anterior and posterior views of the whole skeleton for a panoramic viewing. The next step is spot imaging of the region of interest. The examination begins 2–3 h after injection of an ordinary dose of 20–15 mCi ^{99m}Tc-MDP or 1.5–2 h after injection of ^{99m}Tc-HDP at the same dose. The tracer dose might be increased to 1110 MBq (30 mCi) in the elderly to compensate for a physiologically reduced bone turnover rate. As the scrutiny of the preliminary scan dictates, the study may be augmented with the pinhole technique. It is advocated that as many apparently negative bone scans as possible be subjected to pinhole study as an extension of the already performed scanning, particularly when the region in question has symptoms such as pain, tenderness, or motion limitation. Quite commonly the pinhole scan discloses an entirely unexpected finding, leading to otherwise unattainable results (Fig. 1.6). The pinhole aper-

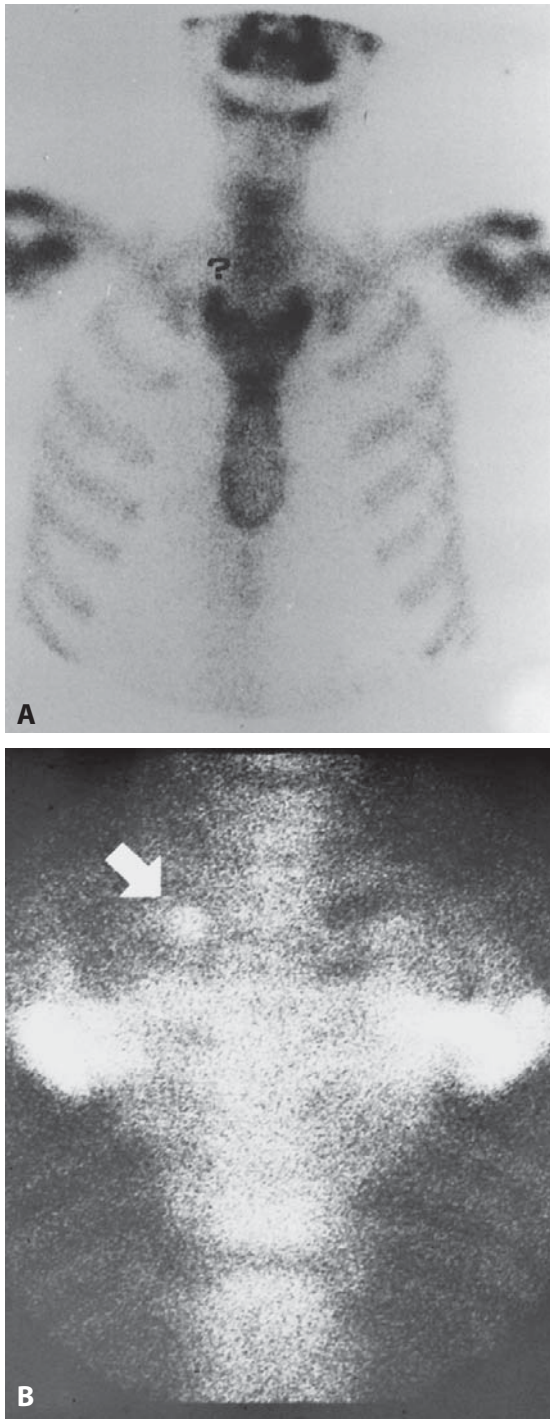

Fig. 1.6A, B Markedly enhanced lesion detectability of pinhole scintigraphy. **A** High resolution anterior planar bone scintigraph shows no abnormal tracer uptake (*?*). **B** Anterior pinhole scintigraph distinctly portrays small spotty uptake in the right transverse process of the T2 vertebra (*arrow*). The lesion was painful, and considered to represent metastasis

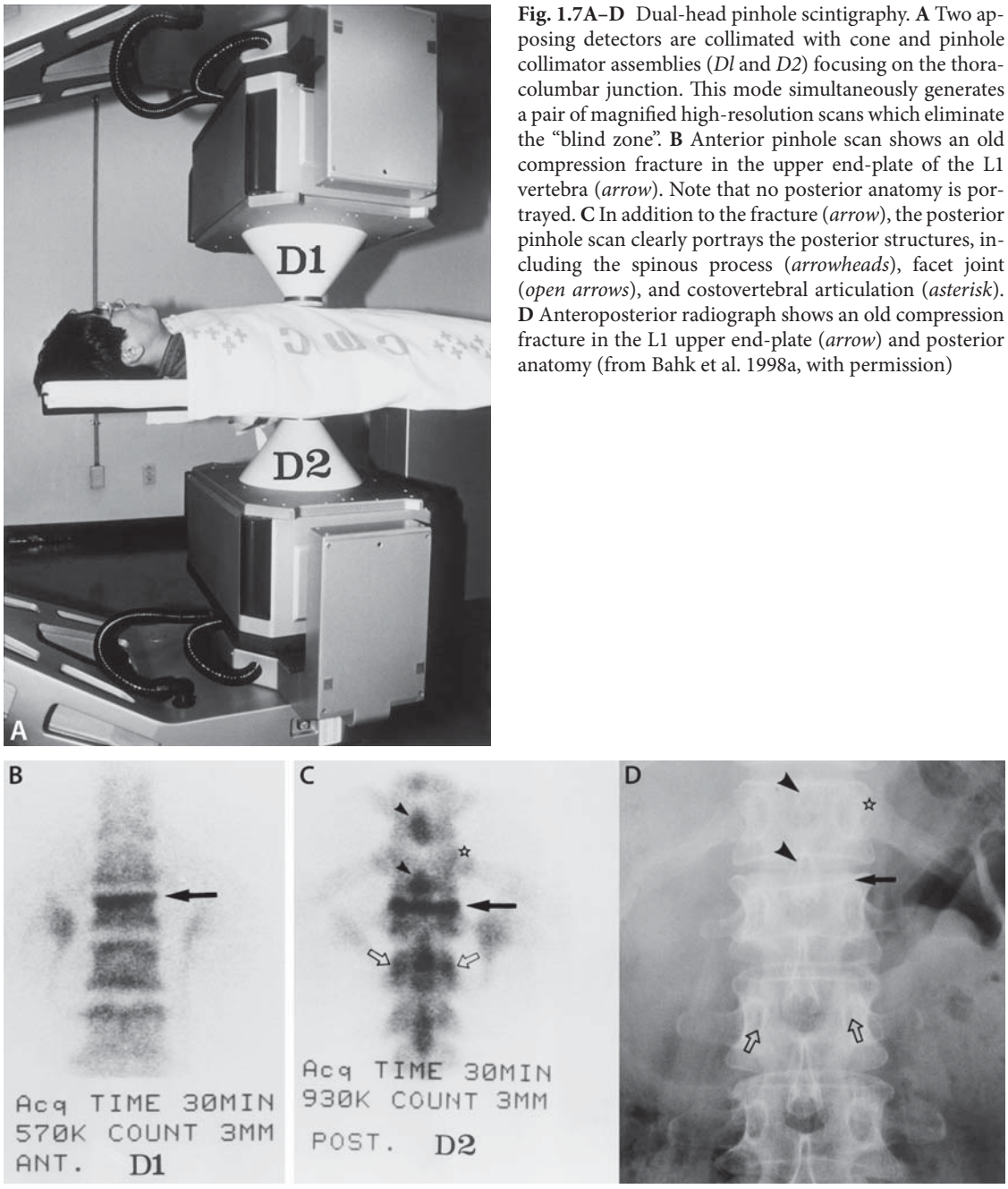

Fig. 1.7A–D Dual-head pinhole scintigraphy. **A** Two apposing detectors are collimated with cone and pinhole collimator assemblies (*Dl* and *D2*) focusing on the thoracolumbar junction. This mode simultaneously generates a pair of magnified high-resolution scans which eliminate the "blind zone". **B** Anterior pinhole scan shows an old compression fracture in the upper end-plate of the L1 vertebra (*arrow*). Note that no posterior anatomy is portrayed. **C** In addition to the fracture (*arrow*), the posterior pinhole scan clearly portrays the posterior structures, including the spinous process (*arrowheads*), facet joint (*open arrows*), and costovertebral articulation (*asterisk*). **D** Anteroposterior radiograph shows an old compression fracture in the L1 upper end-plate (*arrow*) and posterior anatomy (from Bahk et al. 1998a, with permission)

ture size is selected according to the count rate and scan time: when a target with high-count rates is studied, a small aperture can be used, producing a sharper image but at the expense of time. Empirically, it has been found that a pinhole collimator with an aperture size of 3 or 4 mm provides a good balance between image sharpness (resolution) and scan time (sensitivity). In general, pinhole scanning is efficiently performed with aperture-to-skin distance of 0–10 cm. For example, one vertebra or two with intervertebral disk, the hip or knee joint, fingers with small joints are imaged at no distance, while the whole cervical spine is imaged at a distance of about 10 cm. A total of 400–450 k-counts are accumulated over a period of 15–

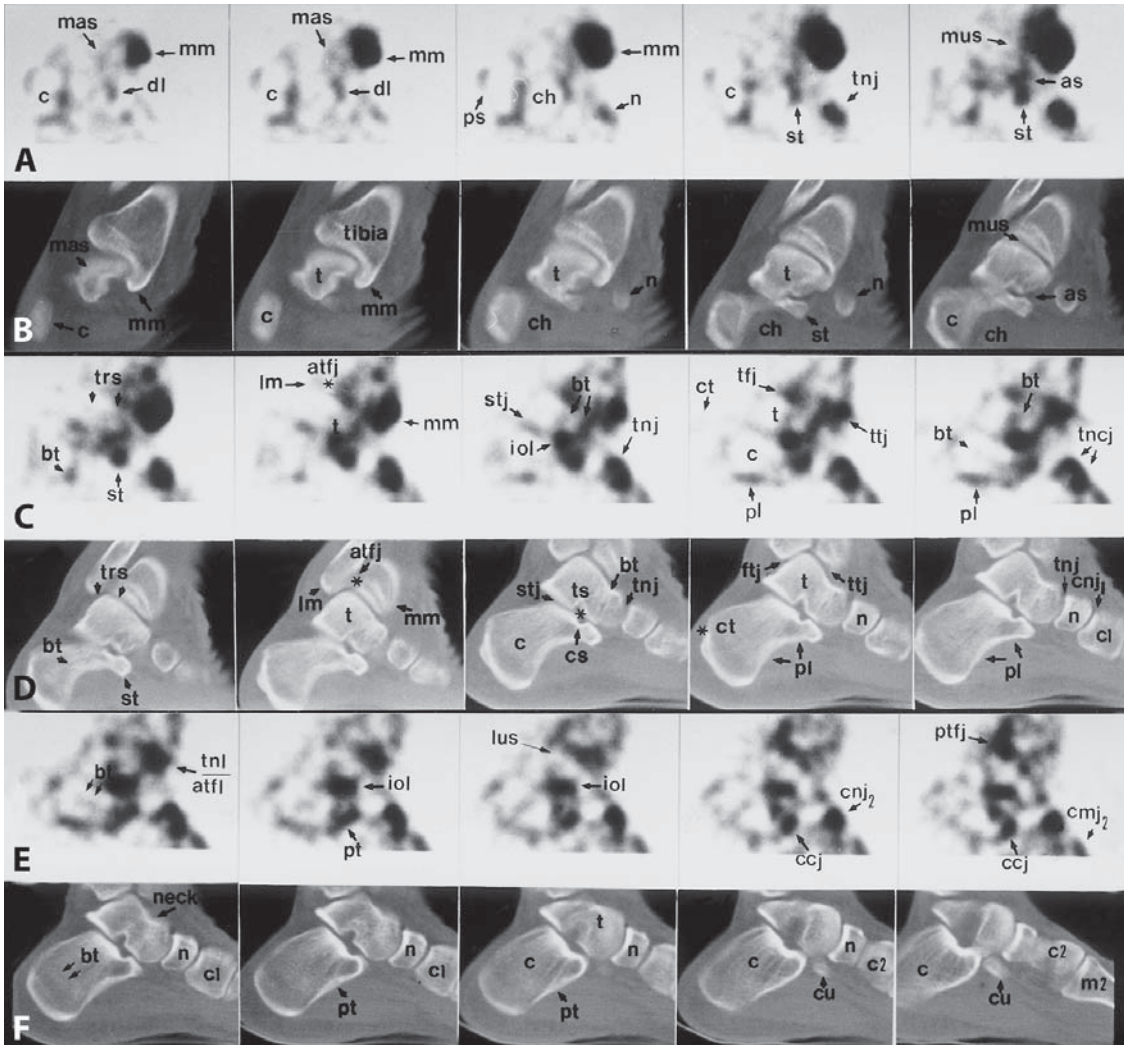

Fig. 1.8 Sagittal pinhole SPECT scans (**A, C, E**) and CT scans (**B, D, F**) of normal ankle and hindfoot. Note how well the resolution of the two modes compares. The slices were obtained continuously from the medial to lateral aspects of the ankle in both SPECT and CT scans. Slice thickness was 2.4 mm. *as* Articular surface, *atjj* anterior tibiofibular joint, *atfl* anterior talofibular ligament, *bt* bone trabeculae, condensed, *c* calcaneus, $C_{1,2}$ first, second cuneiform, *ccj* calcaneocuboid joint, *ch* calcanean hollow, *cl* cervical ligament, cmj_2 second cuneometatarsal joint, $cnj_{1,2}$ first, second cuneonavicular joint, *cs* calcanean sulcus, *ct* calcanean tendon, *cu* cuboid, *dl* deltoid ligament, *iol* interosseous ligament, *lm* lateral malleolus, *lus* lateral undersurface, m_2 second metatarsal, *mas* medial articular surface, *mm* medial malleolus, *mus* medial undersurface, *n* navicular, *pl* plantar ligament, *ps* posterior surface, *pt* peroneal tendon, *ptfj* posterior tibiofibular joint, *st* sustentaculum tali, *stj* subtalar joint, *t* talus, *tfj* talofibular joint, *tncj* talonaviculocuneiform joint, *tnj* talonavicular joint, *tnl* talonavicular ligament, *trs* trochlear surface, *ttj* tibiotalar joint (from Bahk et al. 1998b, with permission)

20 min. The scan time has been reduced from the previous 30–60 min by optimizing scan parameters and using ^{99m}Tc-HDP. It is worth pointed out that old analogue cameras produce far superior pinhole images than digital cameras. Unless critically ill, too old, or too young, patients willingly cooperate, knowing that such an examination is valuable. When clinical situation demands, patients may be calmed with mild sedation. Actually, the average time required for pinhole scanning of a bone or joint is shorter than that required for most imaging studies including SPECT except for simple radiography.

Dual-head pinhole scintigraphy, which makes use of two detectors at one time (Fig. 1.7A), generates a pair of high-resolution images (Bahk et al. 1998a) (Fig. 1.7B–D). This new technique clearly depicts objects in both the foreground and background, effectively eliminating the blind zone that limits the value of planar pinhole scanning. It also results in the reduction of scan time on average by half for each magnified image. In addition, pinhole bone SPECT has been introduced (Bahk et al. 1998b). This is a hybridization of SPECT and pinhole scintigraphy, and produces high-resolution sectional scans, for example, of the ankle, depicting anatomy and metabolic profile in greater detail. The resolution of pinhole SPECT is 2 linepairs/cm, which is roughly comparable to that of CT scanning (Fig. 1.8). Technically, pinhole SPECT can be done simply utilizing an ordinary single-head gamma camera that is capable of 360° rotation. The only modification necessary is to replace the parallel-hole collimator used for planar SPECT with a 4-mm aperture pinhole collimator. Magnified sectional images are reconstructed in exactly the same way as in planar SPECT by the use of the existing filtered back-projection algorithm and a Butterworth filter. As detailed in Chap. 2, pinhole SPECT can show characteristic topographic and metabolic changes in fracture, osteoarthrosis, rheumatoid arthritis, and sympathetic reflex dystrophy.

As routinely practiced in radiological diagnosis, standard anterior and posterior bone scans may be supplemented by lateral, oblique, or any angled view to disclose findings that are not visualized in other views. Commonly used special views include Water's view of the paranasal sinuses, Towne's view of the occiput, seated view of the sacrum and coccyx, butterfly view of the sacroiliac joint, frog-leg view of the hip joints, sunrise view of the patella, and tunnel view of the intercondylar notch of the distal femur (see respective figures in Chap. 4). Understandably, it is important to maintain the assured quality of individual scan parameters such as the patient's position, pinhole aperture size, aperture-to-target distance, and image processing. Experience indicates that too dark scans (excessive acquisition with a longer scan time) are almost as useless as those that are too light. The image blurring due to the motion of patient and/or machine or scan table is probably most undesirable. Proper use of immobilizing devices such as sand bags, a belt, or vacuum air-sand mattress are strongly encouraged.

References

Abe K, Sasaki M, Kuwabara Y, et al (2005) Comparison of ^{18}FDG-PET with ^{99m}Tc-HMDP scintigraphy for the detection of bone metastases in patients with breast cancer. Ann Nucl Med 19:573–579

Alazraki N (1988) Radionuclide techniques. In: Resnick D, Niwayama G (eds) Diagnosis of bone and joint disorders, 2nd edn. WB Saunders, Philadelphia

Anger HO, Rosenthall DJ (1959) Scintillation camera and positron camera. Medical Radioisotope Scanning. IAEA, Vienna

Bahk YW (1982) Usefulness of pinhole scintigraphy in bone and joint diseases (abstract). Jpn J Nucl Med 29:1307–1308

Bahk YW (1985) Usefulness of pinhole collimator scintigraphy in the study of bone and joint diseases (abstract). European Nuclear Medicine Congress. London, p 262

Bahk YW (1988) Pinhole scintigraphy as applied to bone and joint studies. In: Proceedings of Fourth Asia and Oceania Congress of Nuclear Medicine and Biology. Taipei, pp 93–95

Bahk YW (1992) Scintigraphic and radiographic imaging of inflammatory bone and joint diseases. Pre-Congress Teaching Course of Fifth Asia and Oceania Congress of Nuclear Medicine and Biology, Jakarta, pp 19–35

Bahk YW, Kim OH, Chung SK (1987) Pinhole collimator scintigraphy in differential diagnosis of metastasis, fracture, and infections of the spine. J Nucl Med 28:447–451

Bahk YW, Chung SK, Kim SH, et al (1992) Pinhole scintigraphic manifestations of sternocostoclavicular hyperostosis: report of a case. Korean J Nucl Med 26:155–159

Bahk YW, Park YH, Chung SK, et al (1994) Pinhole scintigraphic sign of chondromalacia patellae in older subjects: a prospective assessment with differential diagnosis. J Nucl Med 35:855–862

Bahk YW, Park YH, Chung SK, et al (1995) Bone pathologic correlation of multimodality imaging of Paget's disease. J Nucl Med 36:1421–1426

Bahk YW, Kim SH, Chung SK, et al (1998a) Dual-head pinhole bone scintigraphy. J Nucl Med 39:1444–1448

Bahk YW, Chung SK, Park YH, et al (1998b) Pinhole SPECT imaging in normal and morbid ankles. J Nucl Med 39:130–139

Blau M, Nagler W, Bender MA (1962) Fluorine-18: a new isotope for bone scanning. J Nucl Med 3:332–334

Blum T (1924) Osteomyelitis of the mandible and maxilla. Am J Dent Assoc 11:802–805

Buck AK, Glatting G, Reske SN (2004) Quantification of 18F-FDG uptake in non-small cell lung cancer: a feasible prognostic marker? J Nucl Med 45:1274–1276

Castronovo FP, Callahan RJ (1972) New bone scanning agent: ^{99m}Tc-labelled 1-hydroxy-ethyledene-1,1-sodium phosphate. J Nucl Med 13:823–827

Charkes ND (1969) Some differences between bone scans made with 87mSr and 85Sr. J Nucl Med 10:491–494

Citrin DL, Bessent RG, Tuohy JB, et al (1975) A comparison of phosphate bone-scanning agents in normal subjects and patients with malignant disease. Br J Radiol 48:118–121

Conway JJ (1993) A scintigraphic classification of Legg-Calvé-Perthes disease. Semin Nucl Med 33:274–295

Corey KR, Kenney O, Greenberg E, et al (1961) The use of calcium-47 in diagnostic studies of patients with bone lesions. AJR Am J Roentgenol 85:955–975

Danigelis JA, Fisher RL, Ozonoff MB, et al (1975) ^{99m}Tc-polyphosphate bone imaging in Legg-Perthes disease. Radiology 115:407–413

Davis MA, Jones AG (1976) Comparison of ^{99m}Tc labeled phosphate and phosphonate agents for skeletal imaging. Semin Nucl Med 6:19–31

Fleming WH, McIlraith ID, King R (1961) Photoscanning of bone lesions utilizing strontium 85. Radiology 77:635–636

Fogelman I, McKillop JH, Citrin DL (1977) A clinical comparison of ^{99m}Tc-hydroxyethylidene diphosphonate (HEDP) and ^{99m}Tc-pyrophosphate in the detection of bone metastases. Clin Nucl Med 2:364–367

Francis MD, Ferguson DL, Tofe AJ, et al (1980) Comparative evaluation of three diphosphonates: in vivo adsorption (C-14 labeled) and in vivo osteogenic uptake (Tc-^{99m} complexed). J Nucl Med 21:1185–1189

Francis MD, Horn PA, Tofe AJ (1981) Controversial mechanism of technetium-^{99m} deposition on bone (abstract). J Nucl Med 22:72

Guillermart A, Le Page A, Galy YG, et al (1980) Bone kinetics of calcium-45 and pyrophosphate labeled with technetium 96. An autoradiographic evaluation. J Nucl Med 21:466–470

Gynning I, Langeland P, Lindberg S, et al (1961) Localization with Sr-85 of spinal metastases in mammary cancer and changes in uptake after hormone and roentgen therapy. Acta Radiol 55:119–128

Harper PV, Lathrop KA, Jiminez F, et al (1965) Technetium ^{99m} as a scan agent. Radiology 85:101–109

Hoffman FL (1925) Radium (mesothorium) necrosis. JAMA 85:961–965

Jones AG, Francis MD, Davis MA (1976) Bone scanning: radionuclide reaction mechanisms. Semin Nucl Med 6:3–18

Kim JY, Chung SK, Park YH, et al (1992) Pinhole bone scan appearance of osteoid osteoma. Korean J Nucl Med 26:160–163

Kim SH, Chung SK, Bahk YW (1993) Photopenic metastases with septation from papillary thyroid carcinoma: a case report. Korean J Nucl Med 26:305–308

Kim SH, Chung SK, Bahk YW, et al (1999) Whole-body and pinhole bone scintigraphic manifestations of Reiter's syndrome: distribution patterns and early and characteristic signs. Eur J Nucl Med 26:163–170

Lilien DL, Berger HG, Anderson DP, Bennett LR (1973) 111In-chloride: a new agent for bone marrow imaging. J Nucl Med 14:184–186

Mallinckrodt (1996) TechneScan HDP kit for the preparation of technetium Tc-^{99m} oxidronate. Mallinckrodt, St. Louis, MO. http://imaging.mallinckrodt.com/_attachments/packageinserts/pi-n091.doc

Martland HS (1926) Microscopic changes of certain anemias due to radioactivity. Arch Pathol Lad Med 2:465–472

O'Conner MK, Brown ML, Hung JC, et al (1991) The art of bone scintigraphy – technical aspects. J Nucl Med 32:2332–2341

Owen M (1985) Lineage of osteogenic cells and their relationship to the stromal systems. In: Perk WA (ed) Bone and mineral research. Elsevier, Amsterdam

Pitt WR, Sharp PF (1985) Comparison of quantitative and visual detection of new focal bone lesions, J Nucl Med 26:230–236

Richards P (1960) A survey of the production at Brookhaven National Laboratory of radioisotopes for medical research. In: Congresso Nucleare, vol. 2. Comitato Nazionale Ricerche Nucleari, Rome

Rosenthall L, Kaye M (1975) Technetium-^{99m}-pyrophosphate kinetics and imaging in metabolic bone disease. J Nucl Med 16(1):33–39

Silberstein EB, McAfee JG (1984) Bone localization. In: Differential diagnosis in nuclear medicine. McGraw-Hill, New York

Silberstein EB, Francis MD, Tofe AJ, et al (1975) Distribution of ^{99m}Tc-Sn-diphosphaonate and free ^{99m}Tc-pertechnetate in selected soft and hard tissues. J Nucl Med 16:58–61

Subramanian G, McAfee JG (1971) A new complex of ^{99m}Tc for skeletal imaging. Radiology 99:192–196

Subramanian G, McAfee JG, Bell EG, et al (1972) ^{99m}Tc-labeled polyphosphate as a skeletal imaging agent. Radiology 102:701–704

Subramanian G, McAfee, Blair RJ, et al (1975) Technetium-^{99m}-methylene diphosphate – a superior agent for skeletal imaging: comparison with other technetium complexes. J Nucl Med 16:744–755

Treadwell A de G, Low-Beer BV, Friedell HL, Lawrence GH (1942) Metabolic studies on neoplasm of bone with the aid of radioactive strontium. Am J Med Sci 204:521–530

Treves ST, Connolly LP, Kirkpatrick AB, et al (1995) Bone. In: Treves ST (ed) Pediatric nuclear medicine, 2nd edn. Springer, New York Berlin Heidelberg

Yang WJ, Bahk YW, Chung SK, et al (1994) Pinhole skeletal scintigraphic manifestations of Tietze's disease. Eur J Nucl Med 21:947–952

2 Dual-Head Planar Pinhole Scintigraphy and Pinhole SPECT of Bone

2.1 Dual-Head Planar Pinhole Scintigraphy

The scope of bone diagnosis using pinhole scintigraphy has been expanded, and the efficacy has been improved with the latest introduction of dual-head planar pinhole bone scintigraphy (Bahk et al. 1998a) and pinhole bone SPECT (Bahk et al. 1998b).

Although single-head planar pinhole bone scintigraphy improves the resolution, a blind zone is inevitably created in the periphery of the field of view due to rapid radioactivity fall-off. The blind zone is typically observed in the periphery of the XY coordinate on the planar image and in the far background of the XZ coordinate if a pinhole collimator focuses on the foreground or midground of a scan object. Planar SPECT can solve the problem of the blind zone, but the resolution remains low, detracting from the value of SPECT. In order to solve the blind zone problem and to simultaneously enhance the image resolution, we developed dual-head pinhole scintigraphy by pinhole collimation of two detectors of a dual-head gamma camera (Fig. 1.7A). The method can produce a pair of magnified high-resolution images with eliminated blind zones (Fig. 2.1), and shorten the average scan time by half for each image.

Technically, a dual-head pinhole scan can be achieved by the collimation of two apposing detectors with pinholes of aperture 3–5 mm. Any dual-head gamma camera system can be used provided that the gantry has enough space to accommodate the patient after installing two cone-and-pinhole assemblies (Fig. 1.7A). The scanning is started, continued, and finished in exactly the same way as single-head pinhole scanning. Because the magnification and sensitivity of pinhole scintigraphy are inversely related to the distance between the pinhole and the object, the collimator should be positioned as close to the object as possible to secure the maximum effect. In addition, the distance between the collimator and the object (not the skin) for each of the two detectors should be kept as equal as possible in order to obtain a pair of scans of the same magnification. Figure 2.1 is an example of differing magnifications on the anterior and posterior scans of the same hip. The anterior scan was obtained with the detector in slight contact with the skin of the groin where virtually no muscle exists, whereas the posterior scan was obtained by placing the detector over the voluminous gluteal muscles. This resulted in a larger anterior image due to a shorter collimator-to-object distance and a smaller posterior image due to a longer distance. In most cases, such a difference between image sizes is not problematic. If, however, quantification is attempted the image sizes must be kept equal, which can be done either by maintaining the same distance or by utilizing an electronic zoom (Fig. 2.2).

The elimination of the background or foreground blind zone greatly enhances anatomical detail and the clarity of the metabolic profile, and hence, the diagnostic efficacy of bone scintigraphy. For example, important anatomical landmarks can be portrayed on a pair of anterior and posterior scans of the hip. The anterior scan visualizes the femoral head, acetabular so-

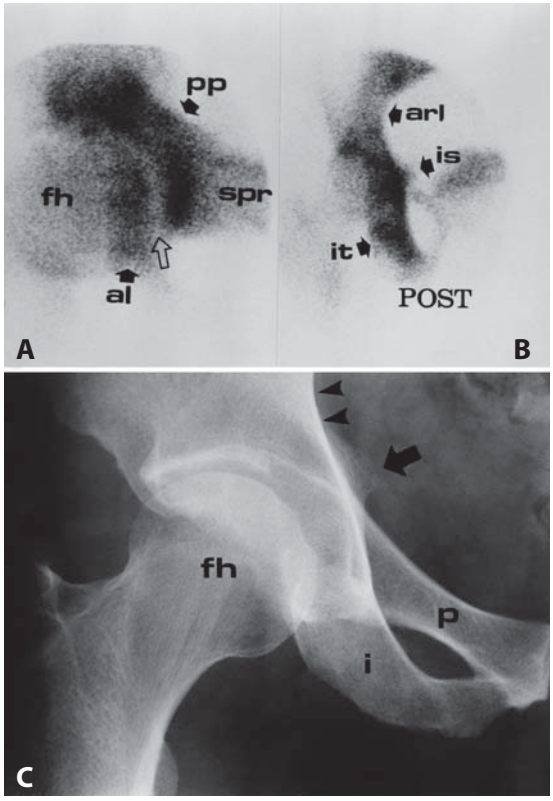

Fig. 2.1A–C Paired dual-head pinhole scans of a normal hip joint. **A** Anterior scan clearly showing the femoral head (*fh*), acetabular labrum (*al*), joint space (*open arrow*), acetabular socket, superior pubic ramus (*spr*), and pecten pubis (*pp*). **B** Posterior scan clearly delineating the ischial tuberosity (*it*), ischial spine (*is*), and arcuate line (*arl*). **C** Anteroposterior radiograph showing the femoral head (*fh*), ischium (*i*), pubis (*p*), ischial spine (*arrow*), and arcuate line (*arrowheads*) (from Bahk et al. 1998a, with permission)

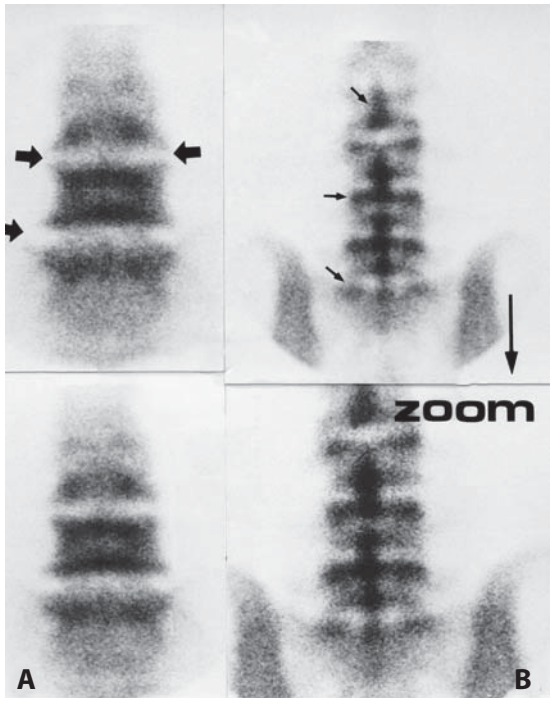

Fig. 2.2A, B Image size equalization by electronic zoom. **A** Anterior scans are equal in size (*left*). **B** Posterior scans are unequal in size (*right*). The original scan is small (*top*) but it can be made equal in size by zooming (*bottom*). Note that the anterior scans portray the anterior vertebral edges (*thick arrows*), whereas the posterior scans portray the spinous processes, posterior vertebral edges, and sacroiliac joints (*thin arrows*) (from Bahk et al. 1998a, with permission)

cket, articular space, and other landmarks (Fig. 2.1A) and the posterior scan provides a close-up view of the ischial tuberosity, ischial spine, and arcuate line (Fig. 2.1C). In the knee, the lateral pinhole image provides a close-up view of the lateral femoral and tibial condyles along with the quadriceps insertion at the anterior patellar surface (Fig. 2.3A), and the medial image provides a closes up view of the structures in the medial aspect of the knee (Fig. 2.3B).

Pathological information is also three-dimensional, remarkably detailed, and accurate. Thus, for example, in acute pyogenic synovitis of the ankle, paired medial and lateral pinhole scans permit an objective three-dimensional analysis of inflamed synovia in the anterior, posterior, medial, and lateral compartments of the ankle (Fig. 2.4A, B). At present, this is probably the best imaging examination of bone and joint diseases from the anatomical and metabolic points of view, but for the diagnosis of nonosseous pathology radiography is necessary (Fig. 2.4C).

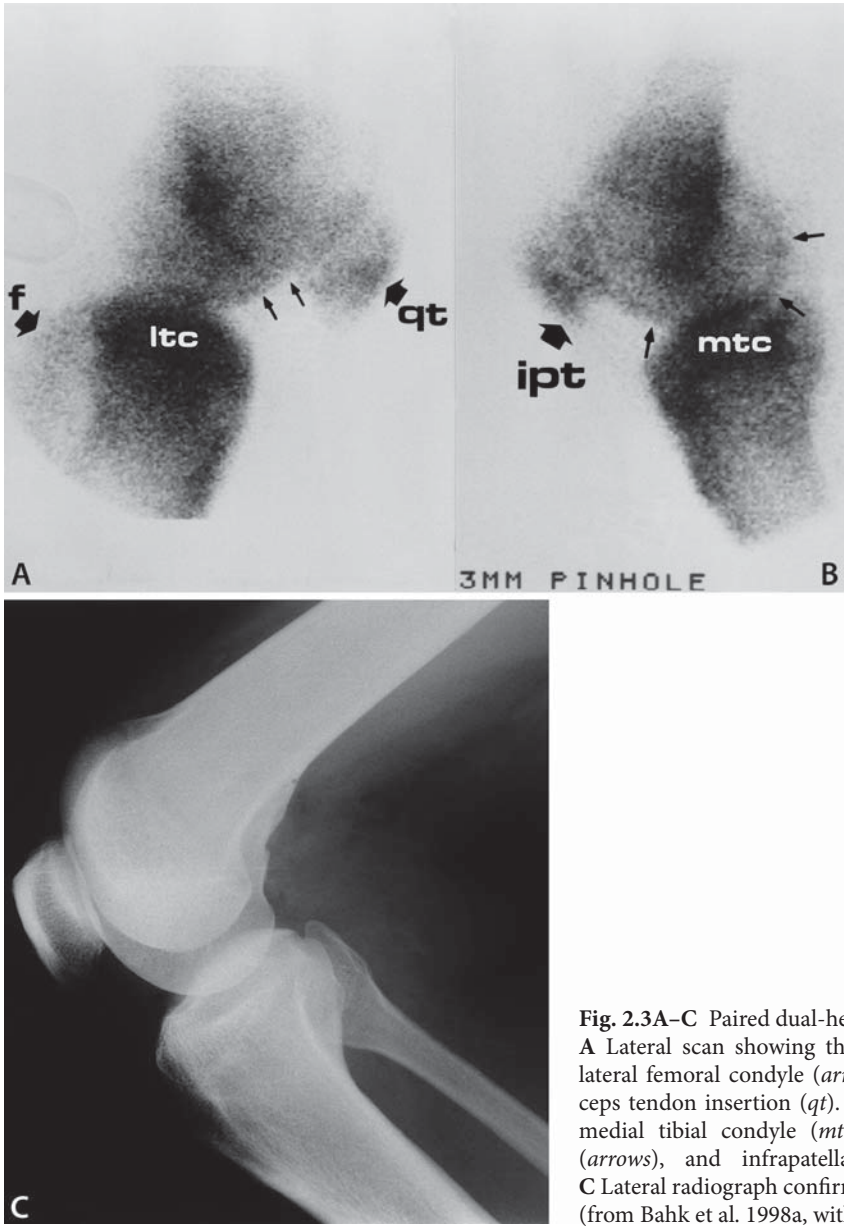

Fig. 2.3A–C Paired dual-head pinhole scans of the knee. **A** Lateral scan showing the lateral tibial condyle (*ltc*), lateral femoral condyle (*arrows*), fibula (*f*), and quadriceps tendon insertion (*qt*). **B** Medial scan revealing the medial tibial condyle (*mtc*), medial femoral condyle (*arrows*), and infrapatellar tendon insertion (*ipt*). **C** Lateral radiograph confirming the relevant topography (from Bahk et al. 1998a, with permission)

2.2 Pinhole SPECT of Bone

SPECT is basically an image separation technique, and currently two different modes, planar and pinhole, are available. The latter mode, pinhole bone SPECT, can efficiently separate the plane of interest from overlapping ones and simultaneously magnify the scan image optically. Conventional or planar SPECT was developed first by Kuhl and Edwards (1964) who used the technique for the sectional diagnosis of liver metastasis and brain tumors. Although prototypical, the image separation they obtained was already sufficient to attest to the usefulness of tomographic nuclear scanning. Since then, SPECT has undergone a series of continual modifications and refinements, and it can now generate sectioned scan images with doubled image contrast (Jaszczak et al. 1977). Basically, SPECT has two important functions: the separation of the plane of interest and con-

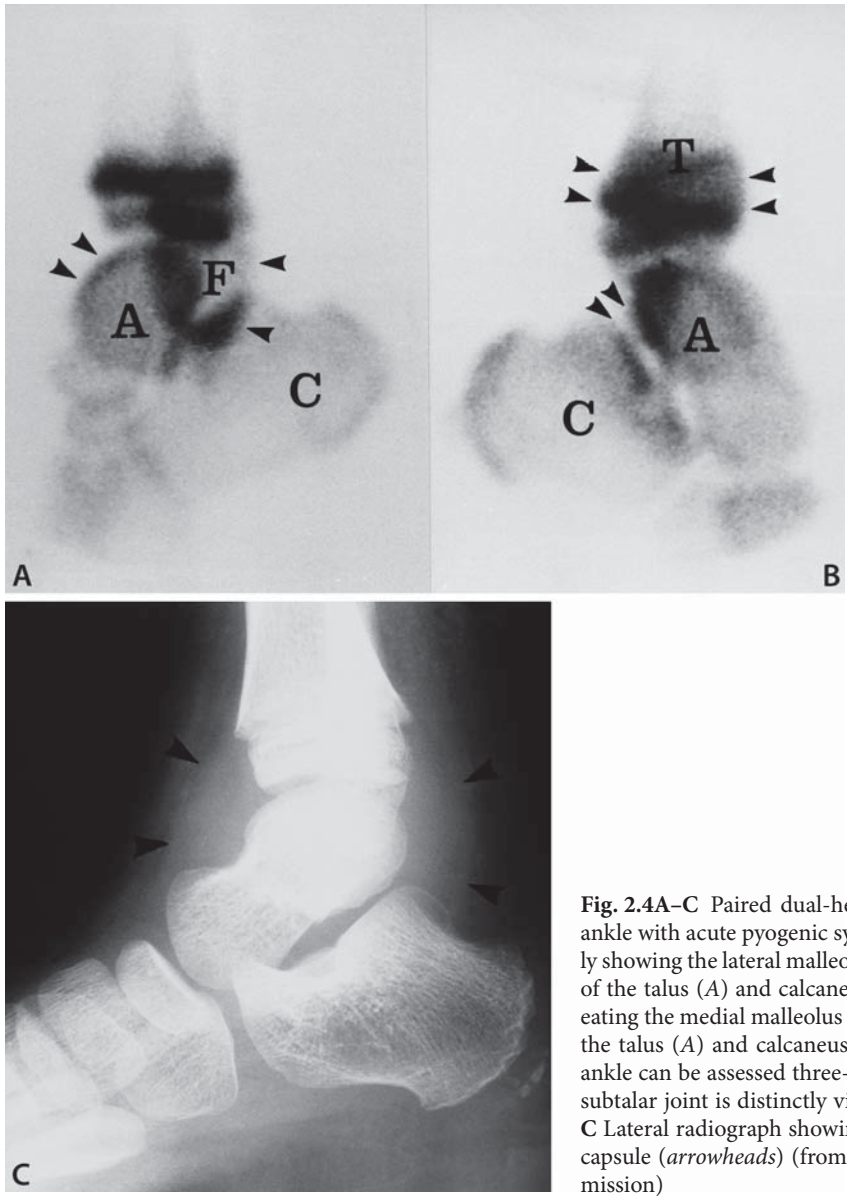

Fig. 2.4A–C Paired dual-head pinhole scans of the left ankle with acute pyogenic synovitis. **A** Lateral scan clearly showing the lateral malleolus (*F*) and the lateral aspects of the talus (*A*) and calcaneus (*C*). **B** Medial scan delineating the medial malleolus (*T*) and the medial aspects of the talus (*A*) and calcaneus (*C*). Note that the inflamed ankle can be assessed three-dimensionally. The posterior subtalar joint is distinctly visualized (*lower arrowheads*). **C** Lateral radiograph showing distension of the articular capsule (*arrowheads*) (from Bahk et al. 1998a, with permission)

trast enhancement. The resolution of planar SPECT, however, is not better (Groch et al. 1995) or rather is degraded compared to that of the planar scan (Collier 1989). The low resolution of SPECT is related to the optical design of the parallel-hole collimator, which primarily focuses on the enhancement of the system's sensitivity and not so much on the resolution. In addition, the resolution of a gamma camera system is impaired by a finite cut-off frequency of the reconstruction filter, limited interval of angular sampling, and restricted sizes of the display matrix. In general, planar SPECT images displayed on a small matrix naturally contain limited anatomical information, and this is especially true when the structure or lesion under study is small (Fig. 2.5).

The resolution of SPECT can be markedly improved by pinhole magnification, which is achievable simply by replacing the parallel-hole collimator with a pinhole collimator (Bahk et al. 1998b). Pinhole SPECT is carried out in exactly the same way as conventional planar SPECT. There is no need for any new software,

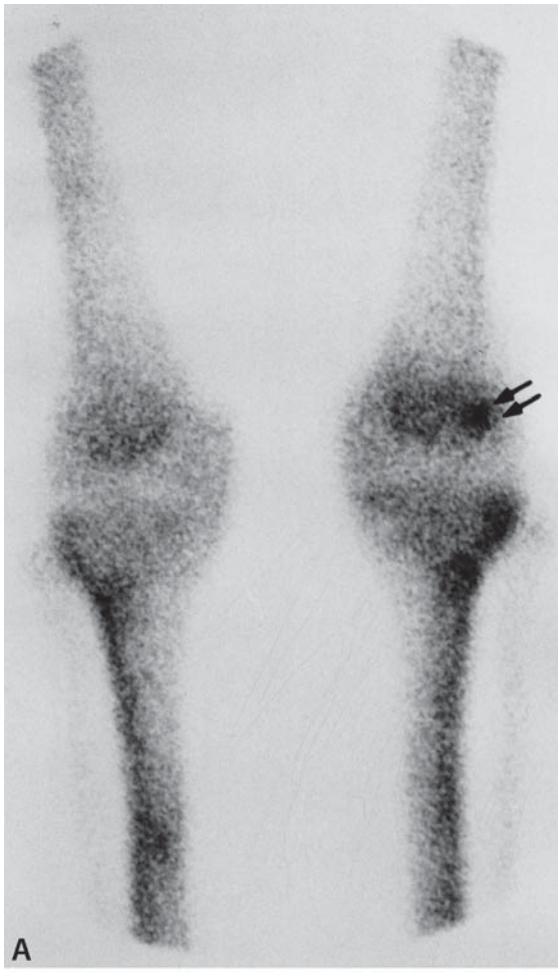

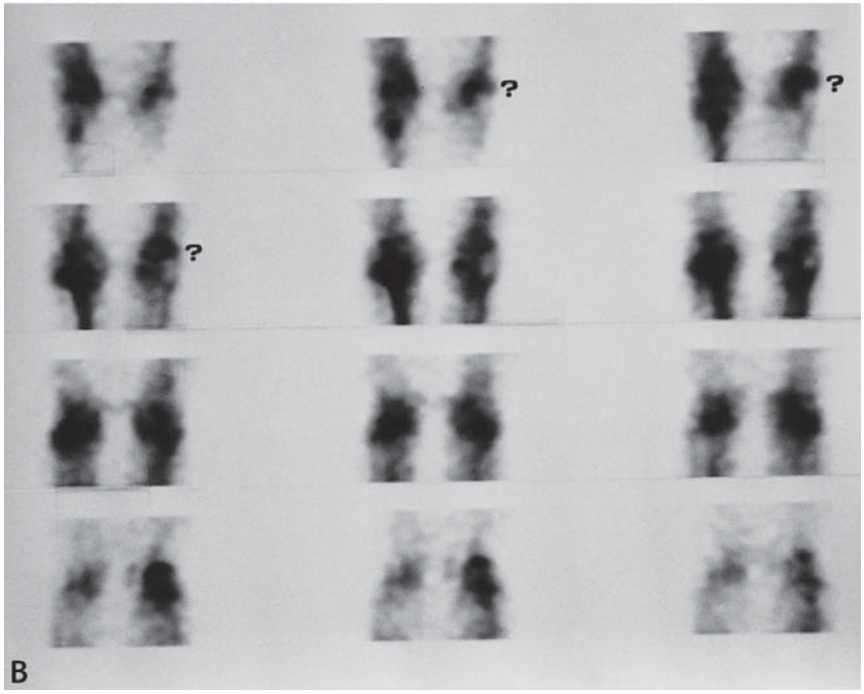

Fig. 2.5A, B Comparison of the resolution of a planar scan and a planar SPECT scan. **A** Anterior planar scan of both knees with cortical desmoid in the left lateral femoral condyle showing a small, ill-defined hot area (*arrows*). **B** The resolution of planar SPECT is lower, revealing many fallacious hot areas

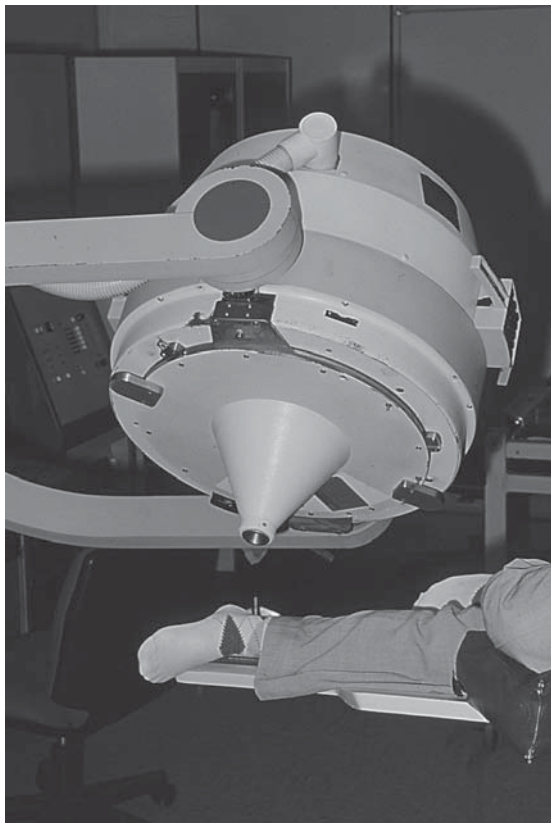

Fig. 2.6 Positioning of the pinhole collimator assembly for 360° rotation pinhole-SPECT of the ankle

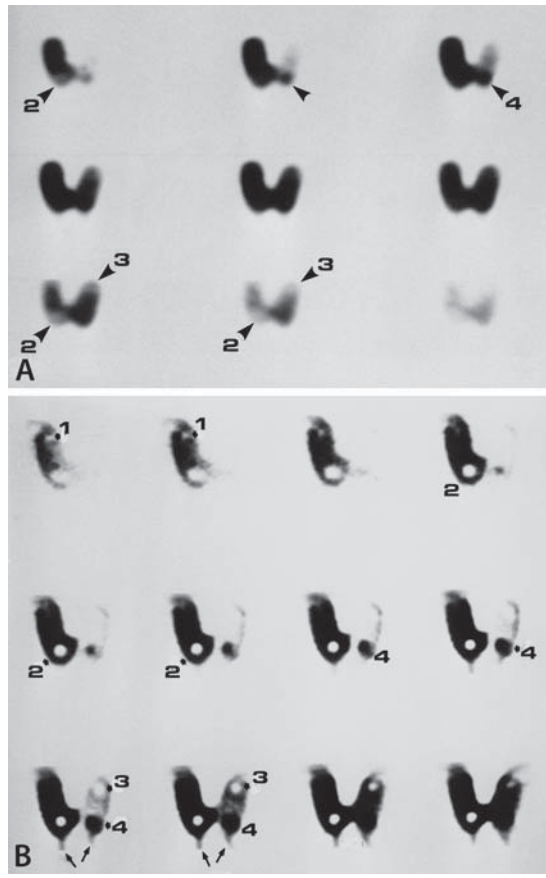

Fig. 2.7A, B Remarkable difference between the resolution of planar SPECT and pinhole SPECT. **A** Planar SPECT images of a thyroid phantom poorly delineating two cold lesions (*2, 3*) and one hot lesion (*4*). The cold lesion in the left upper pole is not visualized. **B** Pinhole SPECT images distinctly showing all three cold lesions (*1–3*), one hot lesion (*4*), and the injection tips (*arrows*) (from Bahk et al. 1998b, with permission)

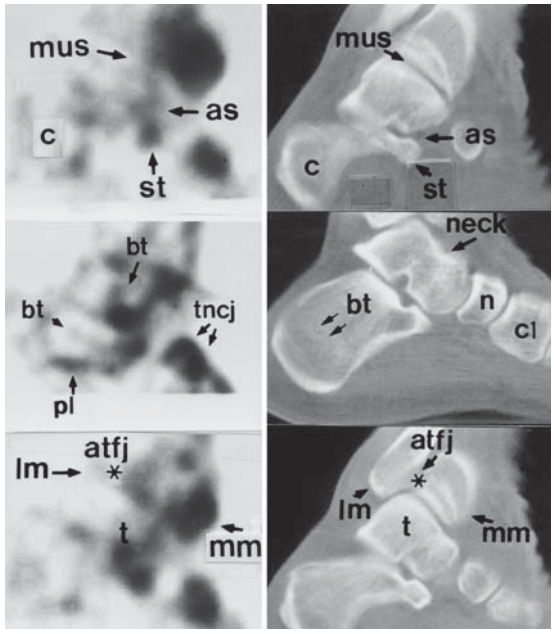

Fig. 2.8 Normal sagittal pinhole SPECT anatomy (*left*) of the ankle with CT validation (*right*). The *upper, middle,* and *lower* panels show the medial, middle, and lateral aspects of the ankle, respectively (*mus* medial under surface, *as* articular surface, *c* calcaneus, *bt* bone trabeculae condensed, *st* sustentaculum tali, *tncj* talonaviculocuneiform joint, *pi* plantar ligament, *atfj* anterior tibiofibular joint, *lm* lateral malleolus, *mm* medial malleolus, *t* talus)

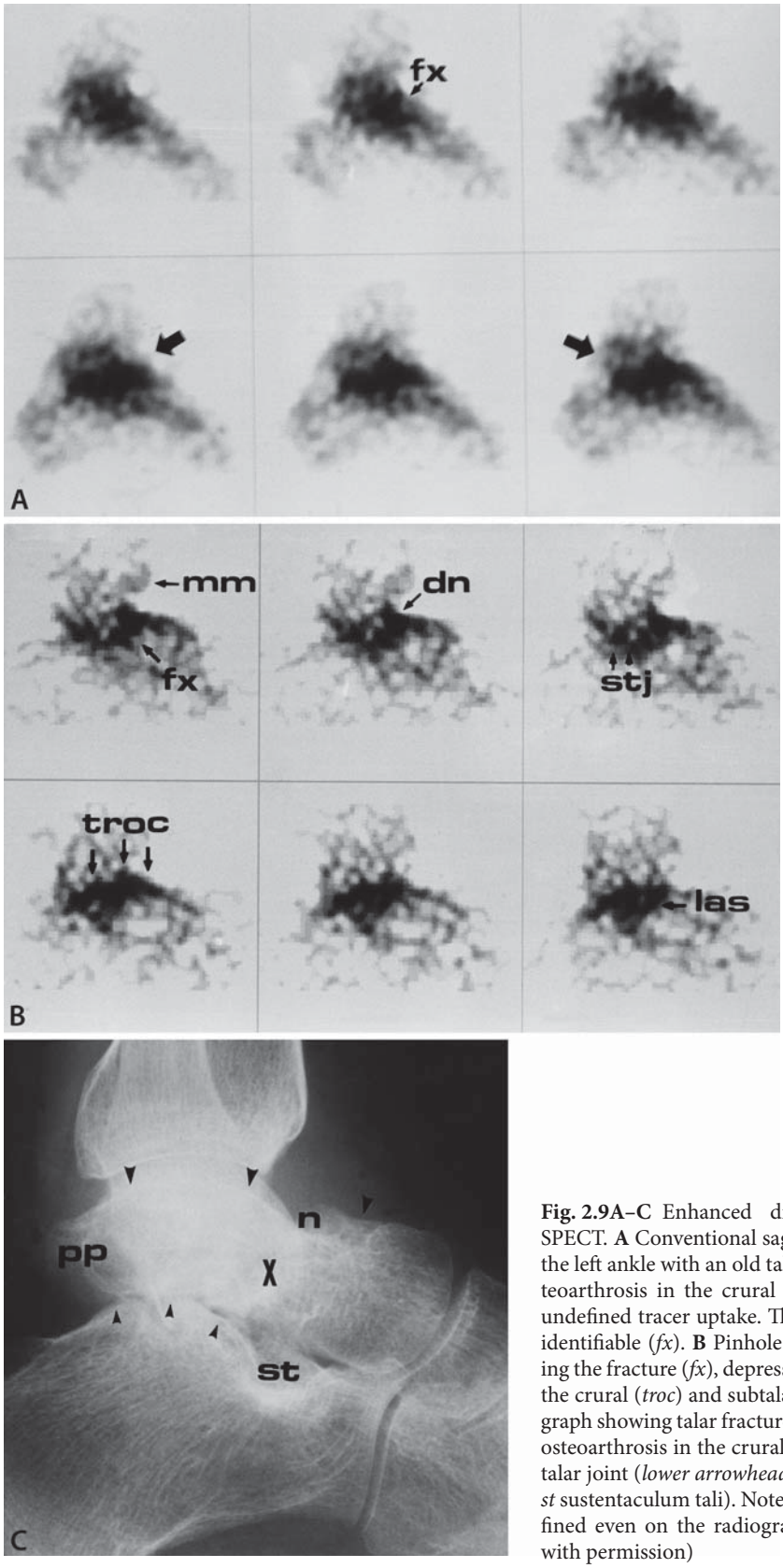

Fig. 2.9A–C Enhanced diagnostic value of pinhole SPECT. **A** Conventional sagittal planar SPECT images of the left ankle with an old talar fracture and secondary osteoarthrosis in the crural and subtalar joints revealing undefined tracer uptake. The fracture is marked, but not identifiable (*fx*). **B** Pinhole SPECT images clearly showing the fracture (*fx*), depressed neck (*dn*), and arthrosis in the crural (*troc*) and subtalar joints (*stj*). **C** Lateral radiograph showing talar fracture (*x*), neck depression (*n*), and osteoarthrosis in the crural (*upper arrowheads*) and subtalar joint (*lower arrowheads*) (*pp* posterior talar process, *st* sustentaculum tali). Note that the fracture is poorly defined even on the radiograph (from Bahk et al. 1998b, with permission)

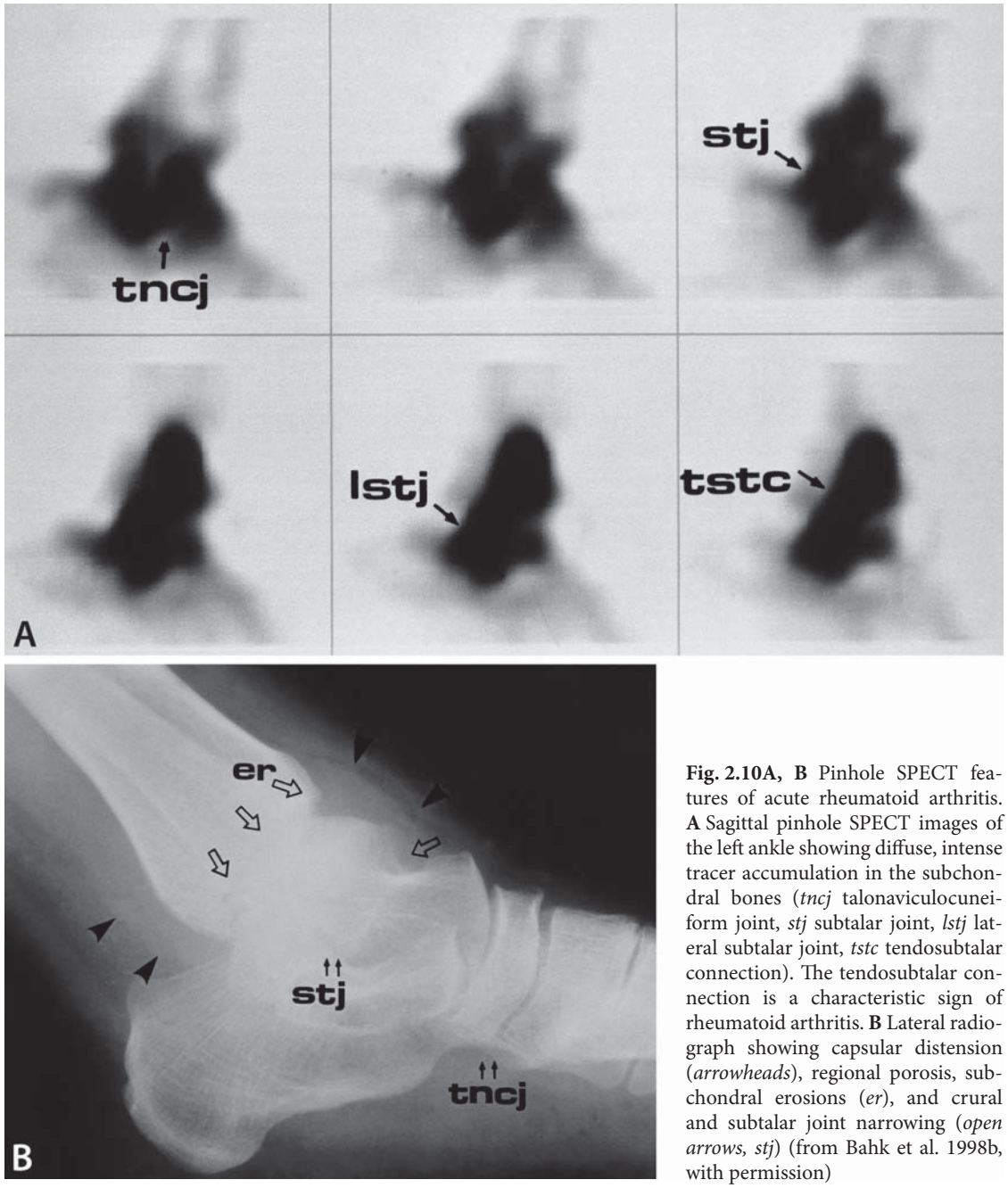

Fig. 2.10A, B Pinhole SPECT features of acute rheumatoid arthritis. **A** Sagittal pinhole SPECT images of the left ankle showing diffuse, intense tracer accumulation in the subchondral bones (*tncj* talonaviculocuneiform joint, *stj* subtalar joint, *lstj* lateral subtalar joint, *tstc* tendosubtalar connection). The tendosubtalar connection is a characteristic sign of rheumatoid arthritis. **B** Lateral radiograph showing capsular distension (*arrowheads*), regional porosis, subchondral erosions (*er*), and crural and subtalar joint narrowing (*open arrows, stj*) (from Bahk et al. 1998b, with permission)

revised reconstruction algorithm, or different filters. Unfortunately, however, currently available gamma camera systems have limitations to the range of circular motion of the pinhole-collimated detector. The range is such that the detector cannot rotate 360° around the trunk or larger appendicular bones and joints such as the hip and shoulder. Accordingly, pinhole SPECT is applicable only to the bones and joints in the ankle and wrist at present.

Pinhole SPECT is performed by the 360° rotation of a single detector collimated with a 4-mm pinhole and adapter cone (Fig. 2.6). The optimal distance between the pinhole and object is 13–15 cm, and accumulated radioactivities are 7.5–8 k-counts per acquisition. In 45 min

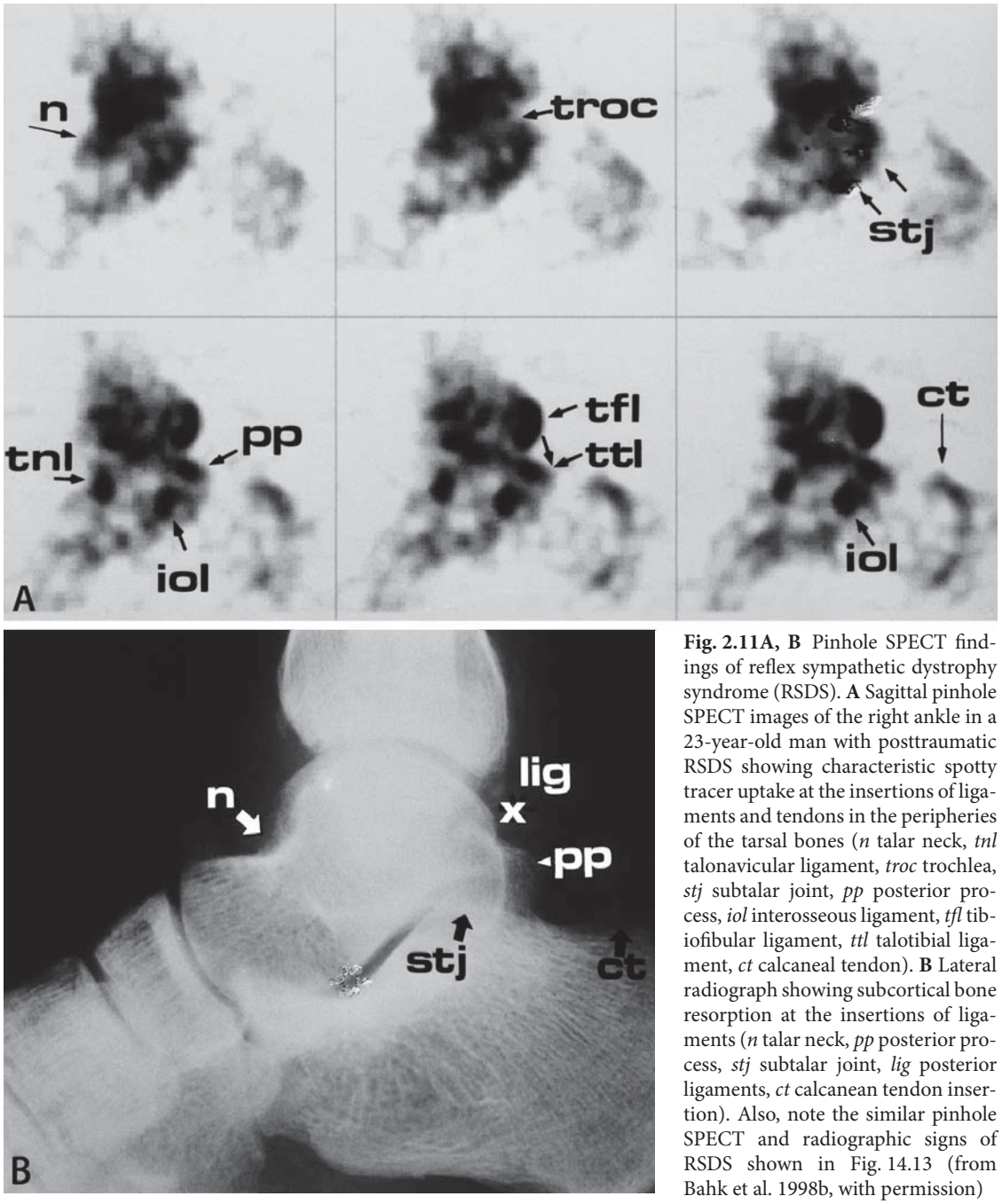

Fig. 2.11A, B Pinhole SPECT findings of reflex sympathetic dystrophy syndrome (RSDS). **A** Sagittal pinhole SPECT images of the right ankle in a 23-year-old man with posttraumatic RSDS showing characteristic spotty tracer uptake at the insertions of ligaments and tendons in the peripheries of the tarsal bones (*n* talar neck, *tnl* talonavicular ligament, *troc* trochlea, *stj* subtalar joint, *pp* posterior process, *iol* interosseous ligament, *tfl* tibiofibular ligament, *ttl* talotibial ligament, *ct* calcaneal tendon). **B** Lateral radiograph showing subcortical bone resorption at the insertions of ligaments (*n* talar neck, *pp* posterior process, *stj* subtalar joint, *lig* posterior ligaments, *ct* calcanean tendon insertion). Also, note the similar pinhole SPECT and radiographic signs of RSDS shown in Fig. 14.13 (from Bahk et al. 1998b, with permission)

64 acquisitions are made (40 s per scan and 2 min for relocation). For efficient imaging and better anatomical orientation, the sagittal view is preferred to the transaxial or coronal view because this particular view presents an object in a longitudinal array so that the dimension is longer and the congruency with neighboring bones and joints is better than in the other two views.

A thyroid phantom study has shown the resolution and contrast of a pinhole SPECT image to be far superior to those of planar SPECT images (Fig. 2.7). The hot and cold areas in the phantom are barely discernible on planar SPECT images, whereas all objects are clearly portrayed on pinhole SPECT images. The tiny injection tips are also clearly depicted.

A normal anatomical study with CT validation of the small bones and joints in the ankle and foot has confirmed plausible performance of pinhole SPECT (Fig. 2.8). It is able to depict most small landmarks in the tarsal bones and joints. For example, the bundles of condensed trabeculae in the weight-bearing axis of the talus and calcaneus can be imaged among the unstressed trabeculae.

Although the cases in which we have used pinhole SPECT are limited, the data obtained show that pinhole SPECT is useful and provides information of specific diagnostic value. The technique has been used to diagnose an old talar fracture and associated osteoarthritis, acute rheumatoid arthritis, and reflex sympathetic dystrophy syndrome (RSDS). Certain characteristic features were revealed in the individual diseases, leading to the specific diagnosis. Indeed, an old fracture in the talus was convincingly visualized on pinhole SPECT (Fig. 2.9B), but not on planar SPECT (Fig. 2.9A) or radiography (Fig. 2.9C). In addition, the talar neck compression and secondary osteoarthrosis in the crural and subtalar joints were appreciated. In acute rheumatoid arthritis, pinhole SPECT is able to depict diffuse and intense uptake in the synoviosubchondral bones of small intercommunicating articular compartments in the ankle (Fig. 2.10A). Interestingly, pinhole SPECT is able to depict the tendosubtalar connection sign, a specific radiographic sign of acute rheumatoid arthritis revealed by contrast synovioarthrography (Hug and Dixon 1977). On pinhole SPECT, the sign is visualized as intense bar-like tracer uptake in the calcaneofibular tendon that connects the fibular tip to the lateral surface of the calcaneus.

The third disease studied was RSDS (Chap. 14). Pinhole SPECT showed discrete spotty uptake peculiarly localized to the bone peripheries where tendons and ligaments insert (Fig. 2.11). The finding was interpreted to indicate dramatic bone resorption that is known to occur at the corticoperiosteal junctions in RSDS (Bahk et al. 1998b) (Fig. 2.11B). Such bone resorption has been shown to be mediated by vasoactive intestinal peptide released from sympathetic nerve fibers (Hohmann et al. 1986).

In summary, dual-head pinhole scintigraphy is an efficient means to eliminate the blind zones that are inevitably created in the peripheries of the field of view in the single-head planar pinhole scan, and can reduce the scan time by half. On the other hand, pinhole SPECT greatly enhances the contrast and resolution of bone scans, further enhancing diagnostic efficacy. With the future development of software programs for improved image processing and hardware for higher sensitivity and extended detector rotation, pinhole SPECT will make a valuable contribution to nuclear imaging science.

References

Bahk YW, Kim SH, Chung SK, et al (1998a) Dual-head pinhole bone scintigraphy. J Nucl Med 39:1444–1448

Bahk YW, Chung SK, Park YH, et al (1998b) Pinhole SPECT imaging in normal and morbid ankles. J Nucl Med 39:130–139

Collier BD (1989) Orthopaedic application of single photon computed tomographic bone scanning. In: Fogelman I (ed) Bone scanning in clinical practice. Springer, Berlin Heidelberg New York

Groch MW, Erwin WD, Bieszk JA (1995) Single photon computed tomography. In: Treves ST (ed) Pediatric nuclear medicine, 2nd edn. Springer, Berlin Heidelberg New York

Hohmann EL, Elde RP, Rysavy JA, et al (1986) Innervation of periosteums and bone by sympathetic vasoactive intestinal peptide-containing nerve fibers. Science 232:868–871

Hug G, Dixon STJ (1977) Ankle joint synoviography in rheumatoid arthritis. Ann Rheum Dis 36:532–539

Jaszczak RJ, Murphy PH, Huard D, Burdine JA (1977) Radionuclide emission computed tomography of the head with ^{99m}Tc and a scintillation camera. J Nucl Med 18:373–380

Kuhl DE, Edwards RQ (1964) Cylindrical and section radioisotope scanning of the liver and brain. Radiology 83:926–936

3 Clinical Applications

Understandably, the clinical use of bone scan was much restricted when first introduced in the early 1960s (Fleming et al. 1961). At that time bone scintigraphy was applied to the diagnosis of cancer metastasis (Fig. 1.2) and fracture (Fig. 3.1). Since then, its scope has been enormously expanded, indeed far beyond the scope originally envisaged. This expansion has been made possible basically by the availability of high-technology gamma camera systems and excellent radiopharmaceuticals, and developments in image interpretation science, which have led to ever-increasing clinical demands. Thus, bone scintigraphy has long been established as the most popular nuclear imaging modality, not only for the screening of acute and critical bone and joint disorders but also for standard diagnosis of most skeletal dis-

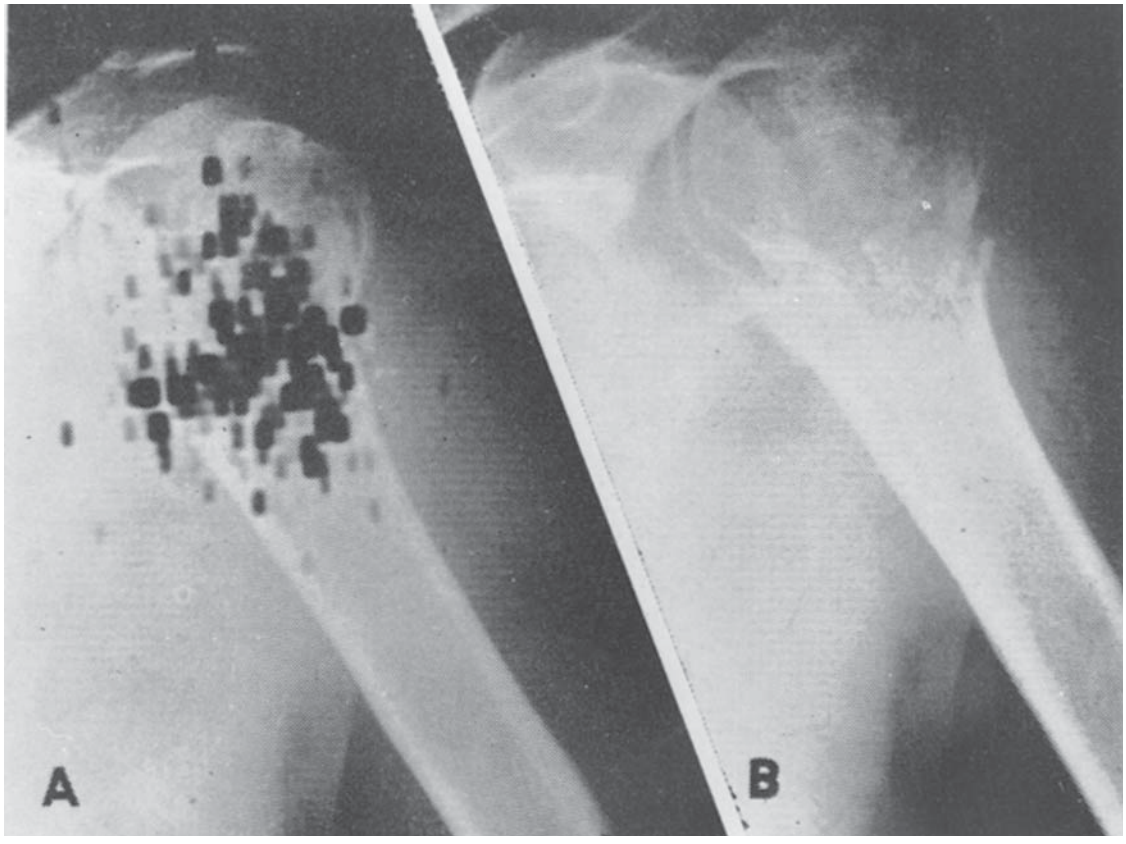

Fig. 3.1A, B One of the first bone scintigraphs made with ^{85}Sr. **A** Dot photoscan superimposed on the radiograph of the left humerus reveals increased tracer uptake in the proximal metaphysis at the site of cancer metastasis. **B** Radiograph shows irregular bone destruction (from Fleming et al. 1961)

Bone infections	Osteomyelitis, osteitis, periostitis, bone abscess
Noninfective osteitides	Osteitis condensans ilii, osteitis pubis, condensing osteitis of the clavicle, Paget's disease, costosternoclavicular hyperostosis
Transient synovitis	Initial diagnosis, posttherapeutic followup
Pyarthritis	Initial diagnosis, posttherapeutic followup
Osteoarthritis	Regional form, generalized form
Rheumatoid arthritis	
Seronegative spondyloarthropathies	Ankylosing spondylitis, Reiter's syndrome, psoriatic arthritis, enteropathic arthritis
Arthropathies related to specific conditions	Systemic lupus erythematosus, Sjögren's syndrome, gouty arthritis, Charcot's joint
Soft-tissue rheumatism disorders	Tendinitis, bursitis, plantar fasciitis, myositis ossificans
Osteochondroses	Legg-Calvé-Perthes disease, Köhler's disease, Friedrich's disease, Freiberg's infraction, Scheuermann's disease, Sever's disease
Osteochondritis dissecans	
Vascular bone disorders	Avascular necrosis, infarction, reflex sympathetic dystrophy, transient osteoporosis
Metabolic bone diseases	Senile and postmenopausal osteoporosis, primary and secondary hyperparathyroidism, rickets, iatrogenic portosis
Traumatic and sports injuries	Contusion, stress fracture, enthesopathy, covert fracture, pseudoarthrosis, fracture nonunion
Bone metastases	
Malignant and benign primary bone tumors	Osteosarcoma, chondrosarcoma, fibrosarcoma, Ewing's sarcoma, multiple myeloma and osteoid osteoma, enostosis, exostosis, fibrous cortical defect, and simple bone cyst

Table 3.1 Diseases diagnosable by pinhole scintigraphy

orders. Lately, the combined use of nuclear angiography, SPECT, and pinhole techniques has greatly increased its diagnostic potential in terms of both sensitivity and specificity.

Of particular interest, bone scintigraphy augmented with the pinhole technique has been shown to provide important and often unique information that can suggest or establish the specific diagnosis of many skeletal disorders (Bahk 1988, 1992; Bahk et al. 1987, 1992, 1994; Kim et al. 1992, 1993a, 1993b). Thus, pinhole scintigraphy seems a sine qua non in clinical practice and research of musculoskeletal disorders. A brief list of these disorders includes: (a) bone infections such as osteomyelitis; (b) noninfective osteitides such as osteitis condensans ilii and Paget's disease of bone; (c) transient synovitis; (d) pyarthritis; (e)

osteoarthritis; (f) rheumatoid arthritis; (g) seronegative spondyloarthropathies such as ankylosing spondylitis and Reiter's syndrome; (h) arthropathies related to specific conditions such as systemic lupus erythematosus and gouty arthritis; (i) soft-tissue rheumatism disorders such as tendonitis and bursitis; (j) osteochondroses such as Legg-Calvé-Perthes disease; (k) osteochondritis dissecans; (l) vascular bone disorders such as avascular necrosis and infarction; (m) metabolic bone diseases such as postmenopausal osteoporosis and hyperparathyroidism; (n) traumatic and sports injuries; (o) metastases; (p) malignant and benign primary bone tumors; and (q) many other skeletal disorders (Table 3.1). In general, pinhole scintigraphy has been shown to be a highly potent tool for the fine topographic study of diseases in complex anatomical units of the body such as the spine, head and neck, knee, and hip (Bahk et al. 1987).

It appears fully justified, therefore, to explore the utility of this easily and economically performable, yet immensely rewarding scan technique, for the diagnosis of the broad spectrum of skeletal disorders with the eventual goal of establishing a classic piecemeal interpretation system. This attempt might result in systematic upgrading of bone scintigraphic diagnosis through the mediation of an image transition. In this connection, it is fortunate that new pinhole collimators can be economically provided or may already be in available but just laid aside! It must be emphasized again that the time needed for pinhole scanning is, at most, comparable to that for SPECT. With the latest technical modification using ^{99m}Tc-labeled hydroxydiphosphonate (HDP) and optimized pinhole aperture and tracer acquisition, the vast majority of pinhole scans can now be completed in 15–20 min.

What is essential is to realize that the pinhole technique can truly improve the resolution, whereas simulated magnification or SPECT cannot. Basically, SPECT is a technique that deals with contrast and not with resolution. When SPECT is performed with pinhole collimation both the resolution and contrast are significantly enhanced. The resolution of pinhole SPECT is almost the same as that of CT. Practically, pinhole SPECT can portray most major anatomical landmarks, for example, in the ankle and hindfoot, including fine structures such as physiologically fortified trabeculae in the weight-bearing axes of the talus and calcaneus, the sites of tendinous and ligamentous insertion, and intertarsal and tarsometatarsal articulations (Fig. 2.8). It can also show characteristic pathological changes in various diseases as presented in Chap. 2.

3.1 Abnormal Bone Scan

Scintigraphic manifestations of bone and joint diseases can be described from four different view points: the morphology and number, the mode of tracer uptake, the tracer distribution pattern, and the vascularity and blood-pool pattern as revealed by nuclear angiography. More specifically, morphological changes can be expressed in terms of size, shape, contour, position, and texture; the number(s) may be solitary, multiple, or innumerable; the tracer uptake and vascularity may be increased, unaltered, or decreased; the uptake mode can be spotty, segmental, patchy, or diffuse or any combination thereof; and the distribution may be localized, diffuse, symmetrical, or otherwise. The great majority of bone lesions are indicated by increased tracer uptake or "hot" areas and a small fraction of cases manifest as photopenic or "cold" areas. It is to be noted, however, that the relative incidence of the photopenic presentation of bone and joint diseases definitely increases when the pinhole technique is used. Obviously, the lesions having unaltered uptake cannot be seen on scan. It is well known that avascular necrosis, myeloma, and renal cell carcinoma are characterized by a photopenic presentation. Any bone disease that causes significant bone destruction with deprived vascularity is considered to produce a photon defect.

3.2 Altered Biodistribution of Radiopharmaceutical

Significant dehydration, ascites, anasarca, and renal and/or hepatic failure cause increased soft-tissue uptake, resulting in a low bone-to-background ratio and degraded scan images. Unlabeled ^{99m}Tc-pertechnetate and oxidation of ^{99m}Tc-labeled phosphate complex may also increase the background activity, with undesirable tracer accumulation in the thyroid and liver as well as disturbance of alimentary tract excretion (see Chap. 5). On the other hand, the systemic administration of adjuvant chemotherapeutic agents, steroids, or iron is known to suppress bone uptake of tracer (Hladik et al. 1982). It is of interest that adjuvant chemotherapy may occasionally cause healing bone malignancies to flare up with increased tracer uptake so that they appear unresponsive to the treatment (Gillespie et al. 1975; see Chap. 17).

References

Bahk YW (1988) Pinhole scintigraphy as applied to bone and joint studies. In: Proceedings of Fourth Asia and Oceania Congress of Nuclear Medicine and Biology, Taipei, pp 93–95

Bahk YW (1992) Scintigraphic and radiographic imaging of inflammatory bone and joint diseases. Pre-Congress Teaching Course of Fifth Asia and Oceania Congress of Nuclear Medicine and Biology, Jakarta, pp 19–35

Bahk YW, Kim OH, Chung SK (1987) Pinhole collimator scintigraphy in differential diagnosis of metastasis, fracture, and infections of the spine. J Nucl Med 28:447–451

Bahk YW, Chung SK, Kim SH, et al (1992) Pinhole scintigraphic manifestations of sternocostoclavicular hyperostosis: report of a case. Korean J Nucl Med 26:155–159

Bahk YW, Park YH, Chung SK, et al (1994) Pinhole scintigraphic sign of chondromalacia patellae in older subjects: a prospective assessment with differential diagnosis. J Nucl Med 35:855–862

Fleming WH, KcIlraith ID, King R (1961) Photoscanning of bone lesions utilizing strontium 85. Radiology 77:635–636

Gillespie PJ, Alexander JL, Edelstyn GA (1975) Changes in 87mSr concentrations in skeletal metastases in patients responding to cyclical combination chemotherapy for advanced breast cancer. J Nucl Med 16:191–193

Hladik WB III, Nigg KK, Rhodes BA (1982) Drug-induced changes in the biologic distribution of radiopharmaceuticals. Semin Nucl Med 12:184–218

Kim JY, Chung SK, Park YH, et al (1992) Pinhole bone scan appearance of osteoid osteoma. Korean J Nucl Med 26:160–163

Kim SH, Bahk YW, Chung SK, et al (1993a) Pinhole scintigraphic appearance of infantile cortical hyperostosis: "Bumpy, segmental tracer uptake". Korean J Nucl Med 27:319–320

Kim SH, Chung SK, Bahk YW (1993b) Photopenic metastases with septation from papillary thyroid carcinoma: a case report. Korean J Nucl Med 26:305–308

4 Normal Pinhole Scintigraphic Anatomy of Bone and Joint

Yong-Whee Bahk and Soo-Kyo Chung

Pinhole bone scintigraphy can portray the anatomy of the skeletal system in much greater detail than ordinary planar scintigraphy. Its level of resolution in practice has been shown to be reasonably comparable to that of radiography as far as gross topography is concerned. This chapter systematically describes normal pinhole scintigraphic anatomy. It will be seen that the pinhole scan approach substantially enhances the recognition of anatomy compared to the conventional scan approach (Flanagan and Maisey 1985; Merrick 1987).

4.1 Skull and Face

A comparatively large amount of tracer accumulates in relation to the cranial tables and sutures, orbital walls, paranasal sinuses, nasal cavity, zygoma, sphenoidal ridge, and skull base including the temporomandibular and atlantooccipital joints (Fig. 4.1). Normally, the maxilla and mandible accumulate tracer in the premolar zones presumably due to major masticatory movement. The vertex view shows uptake in the sagittal and coronal sutures and occasional variants. The modified vertex view is

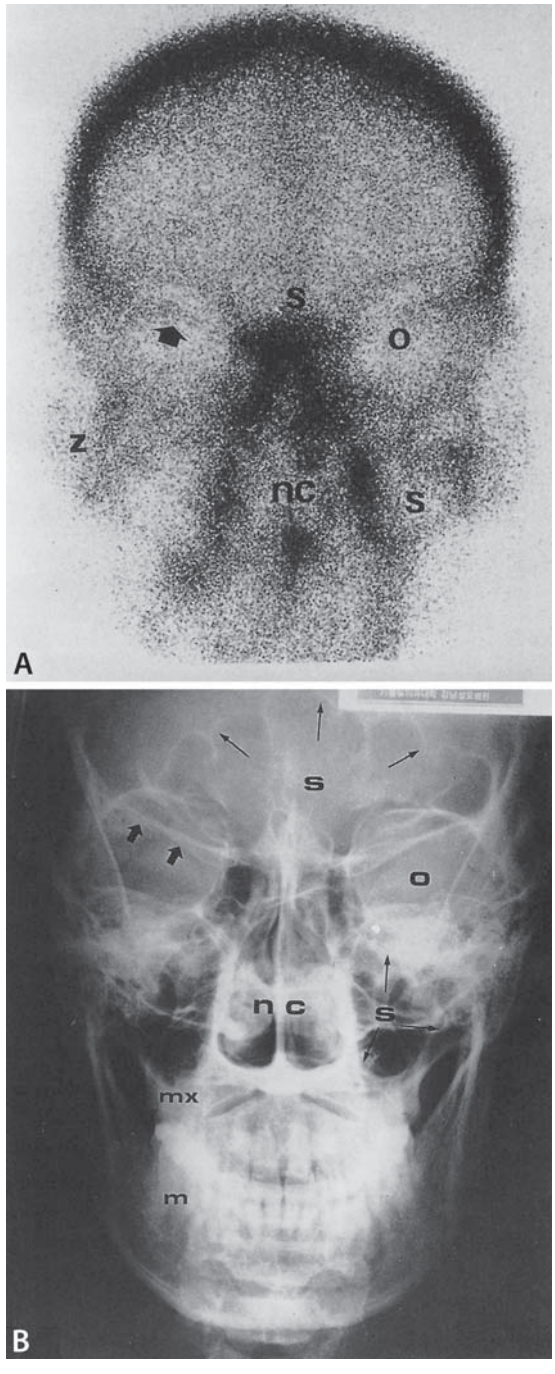

Fig. 4.1A, B Anterior view of the skull and facial bones. **A** Anterior pinhole scintigraph shows prominent tracer uptake in the cranium and nasal mucosal and paranasal mucoperiosteal membranes, clearly delineating the paranasal sinuses (*s*), nasal cavity with turbinates and septum (*nc*), zygomas (*z*), and orbits (*o*) (*arrow* sphenoidal ridge). **B** Posteroanterior radiograph identifies the maxillary and frontal sinuses (*s, thin arrows*), nasal cavity with turbinates and septum (*nc*), orbits (*o*), and sphenoidal ridges (*thick arrows*)

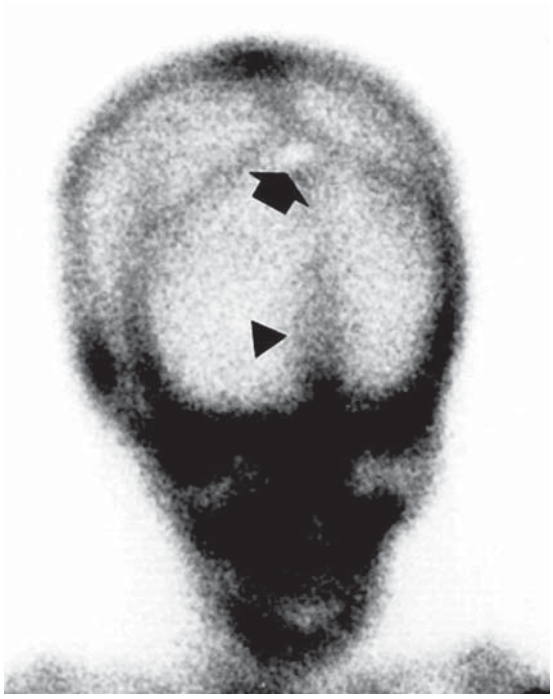

Fig. 4.2 Slightly tilted anterior scintigraph of the skull in a 2-year-old boy shows an open anterior fontanel at the intersection of the coronal and sagittal sutures (*arrow*). Note tracer uptake in the metopic suture (*arrowhead*)

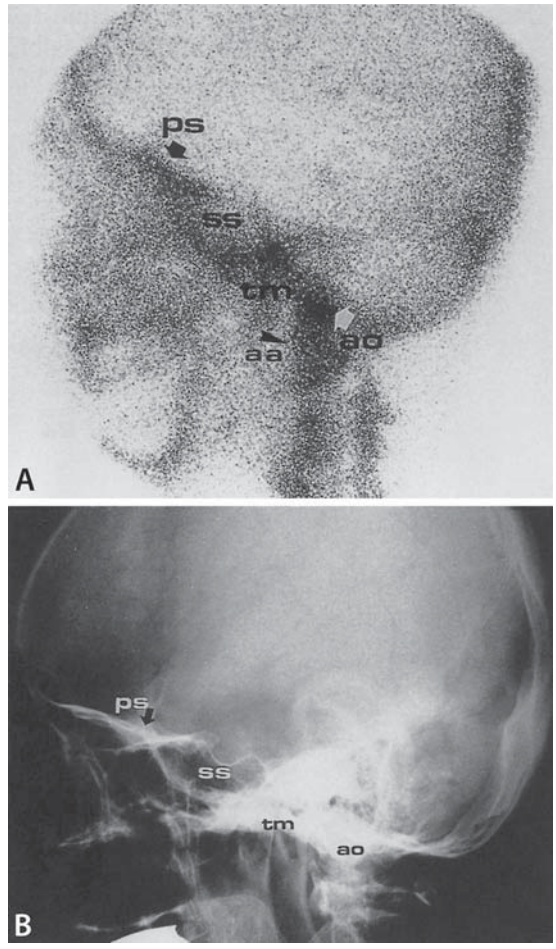

Fig. 4.3A, B Lateral view of the frontotemporal skull. **A** Lateral pinhole scintigraph of the skull shows intense tracer uptake in the atlantooccipital joint (*ao*), temporomandibular joint (*tm*), sphenoid sinus (*ss*), and planum sphenoidale (*ps*). **B** Lateral radiograph identifies the planum sphenoidale (*ps*), sphenoid sinus (*ss*), temporomandibular joint (*tm*), and atlantooccipital articulation (*ao*), atlantoaxial joint (*aa*)

particularly useful for the demonstration of the fontanelles in children (Fig. 4.2). The close-up lateral pinhole scintigraph of the temporal region reveals prominent tracer uptake in the sphenoparietal ridge, planum sphenoidale, and sphenoid sinus, and also the temporomandibular, atlantooccipital and atlantoaxial joints (Fig. 4.3). In children, the sphenooccipital synchondrosis occasionally accumulates tracer intensely.

The special views adopted from radiography are utilized for the demonstration of small structures of the skull, especially the face, in which diverse parts are superimposed upon each other in ordinary anterior or lateral scans. The Waters' view is useful for separate visualization of the individual paranasal sinuses including the maxillary and frontal sinuses and the nasal cavity with the nasal bone above, the septum in the midline, and the turbinates in between (Fig. 4.4). The zygomatic arches and occasionally the crista galli can be imaged in this view. It is to be noted that more intense uptake normally occurs in and around the nasal cavity, contrasting with the relatively low uptake in the orbit, zygoma, and paranasal sinuses. Prominent uptake in the premolar regions of the maxilla is well portrayed in this view. The Towne's view can be utilized to visualize the lambdoidal suture and the posterior sector of the sagittal suture that conjoin to form the lambda in the occiput (Fig. 4.5). The straight

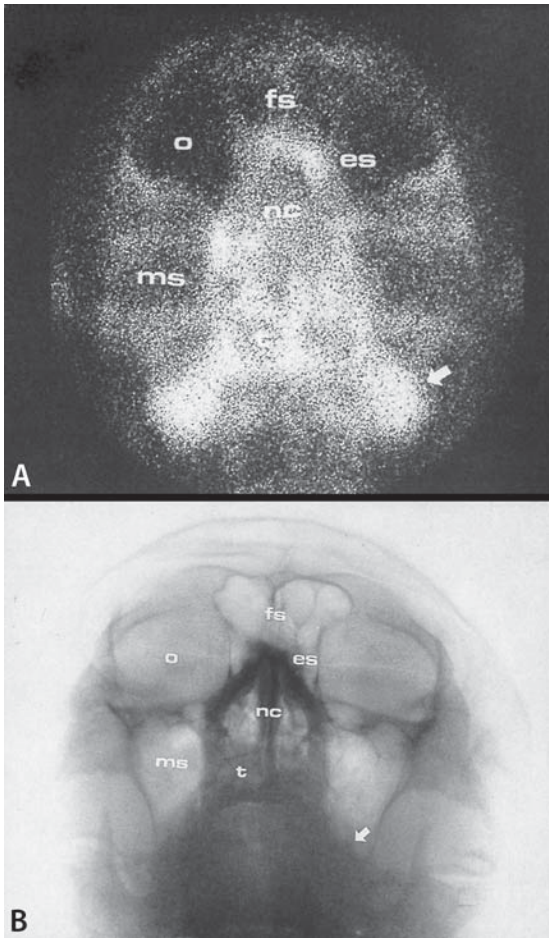

Fig. 4.4A, B Tilted anterior (Waters') view of the facial bones. **A** Pinhole scintigraph reveals the maxillary sinuses (*ms*), nasal cavity (*nc*) with turbinates (*t*), ethmoid sinuses (*es*), frontal sinus (*fs*), and orbits (*o*). Physiologically increased tracer uptake is noted in the premolar region of the maxilla due to mastication (*arrow*). Similar tracer uptake may also occur in the mandibular premolar region. **B** Tilted posteroanterior radiograph identifies the maxillary sinuses (*ms*), nasal cavity (*nc*) with turbinates (*t*), ethmoid sinus (*es*), frontal sinus (*fs*), and orbits (*o*) (*arrow* premolar region of the maxilla)

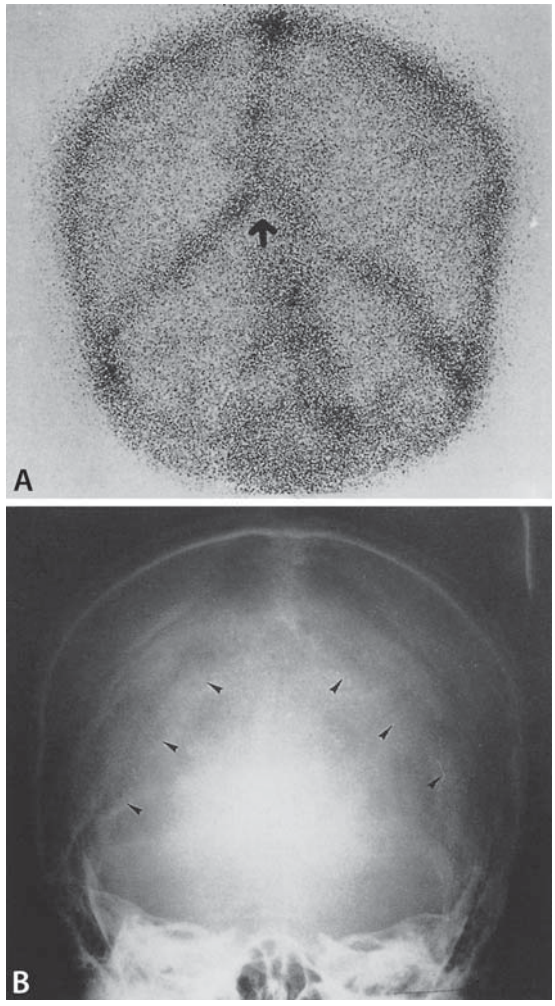

Fig. 4.5A, B Tilted posterior (Towne's) view of the occiput. **A** Tilted posterior pinhole scintigraph of the skull reveals tracer accumulation along the posterior sagittal and lambdoidal sutures (*arrow* Lambda). **B** Tilted anteroposterior radiograph identifies the posterior sagittal and lambdoidal sutures (*arrowheads*)

posterior view of the skull visualizes the torcular Herophili, lateral sinus, and often occipitoparietomastoid sutural junction (Fig. 4.6). Another special projection is the Stenvers or tilted tangential view of the mastoid, in which the temporomandibular joint, the osseous labyrinth of the inner ear, and the occipitoparietomastoid sutural junction can be regularly imaged due to their characteristic uptake. The aerated mastoid bone and relatively thin petrous ridge do not accumulate tracer visibly unless diseased (Fig. 4.7). A number of modified views are available and still others may be improvised for the study of the selected parts of the skull and facial bones as the clinical situation demands.

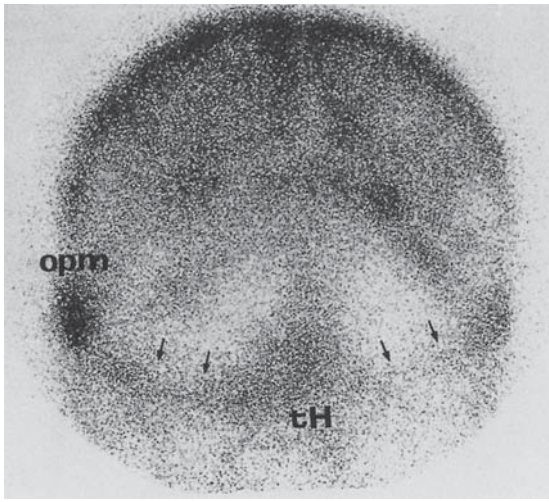

Fig. 4.6 Straight posterior view of the occiput. Posterior pinhole scintigraph of the skull delineates the torcular Herophili (*tH*), lateral sinus (*arrows*), and occipitoparietomastoid sutural junction (*opm*). The lambdoidal suture is also visualized

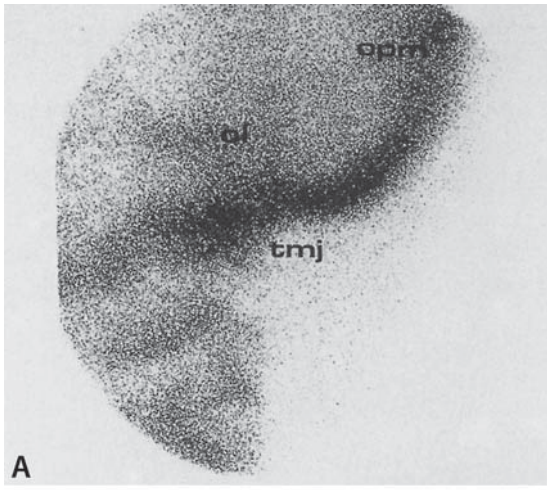

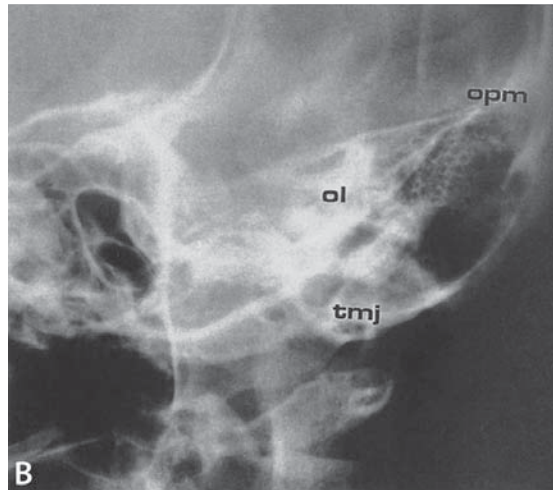

Fig. 4.7A, B Tangential (Stenvers) view of the mastoid. **A** Tangential pinhole scintigraph of the left mastoid demonstrates increased tracer uptake in the temporomandibular joint (*tmj*), osseous labyrinth (*ol*), and the occipitoparietomastoid sutural junction (*opm*). These landmarks surround the mastoid bone, which is relatively photopenic because of aeration. **B** Tangential radiograph identifies the temporomandibular joint (*tmj*), osseous labyrinth (*ol*), and the occipitoparietomastoid sutural junction (*opm*). The air cells in the mastoid are lucent

4.2 Neck

Pinhole scanning can be used to visualize the small parts of the individual cervical vertebrae, the hyoid bone, and the mineralized anterior neck cartilages. The spinous processes, laminae, and apophyseal joints are portrayed on the posterior view (Fig. 4.8) and the vertebral bodies with the endplates, pedicles, and apophyseal joints are visualized on the lateral view (Fig. 4.9). For the topographic study of the upper cervical spine and skull base a close-up pinhole scintigraphy is taken. Thus, the close-up posterior pinhole scan shows characteristic uptake in the dens in the midline sided bilaterally by photopenic median atlantoaxial articular spaces (Fig. 4.10). The lateral masses of the atlas, atlantooccipital joint, and paired lateral atlantoaxial joints are also visualized on this view. On the close-up lateral view, the disk spaces are presented as photopenic slits between "hot" vertebral bodies, whereas higher tracer uptake may be seen in the atlantooccipi-

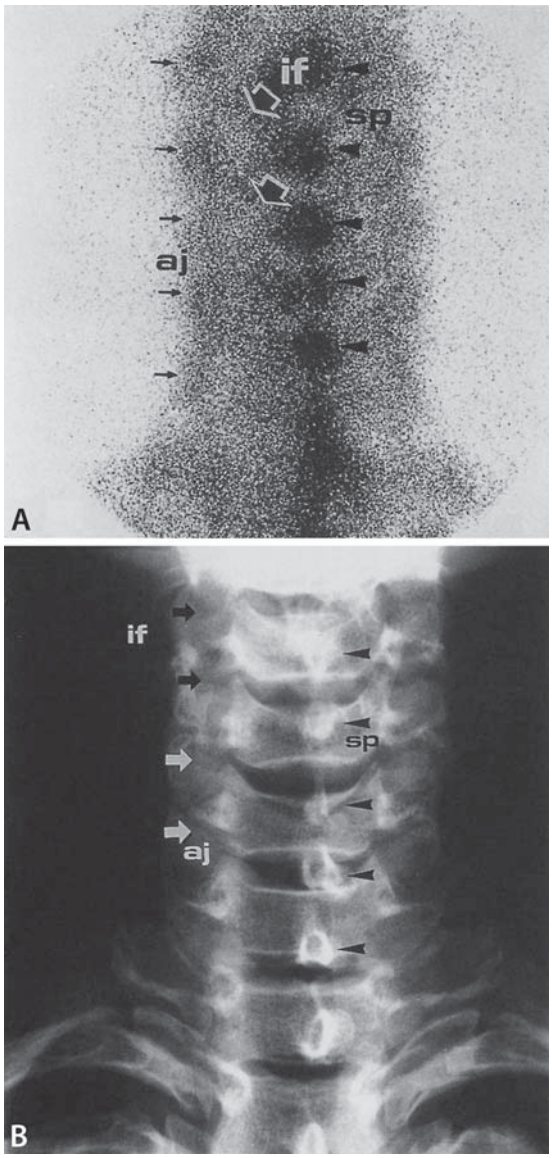

Fig. 4.8A, B Posterior view of the cervical spine. **A** Posterior pinhole scintigraph of the cervical spine shows increased tracer uptake in the spinous processes (*sp*) and apophyseal joints (*aj*). The intervertebral foramina (*if*) are demonstrated as photopenic areas lying between the spinous processes and apophyseal joints. **B** Anteroposterior radiograph identifies the spinous processes (*sp*), apophyseal joints (*aj*), and intervertebral foramina (*if*)

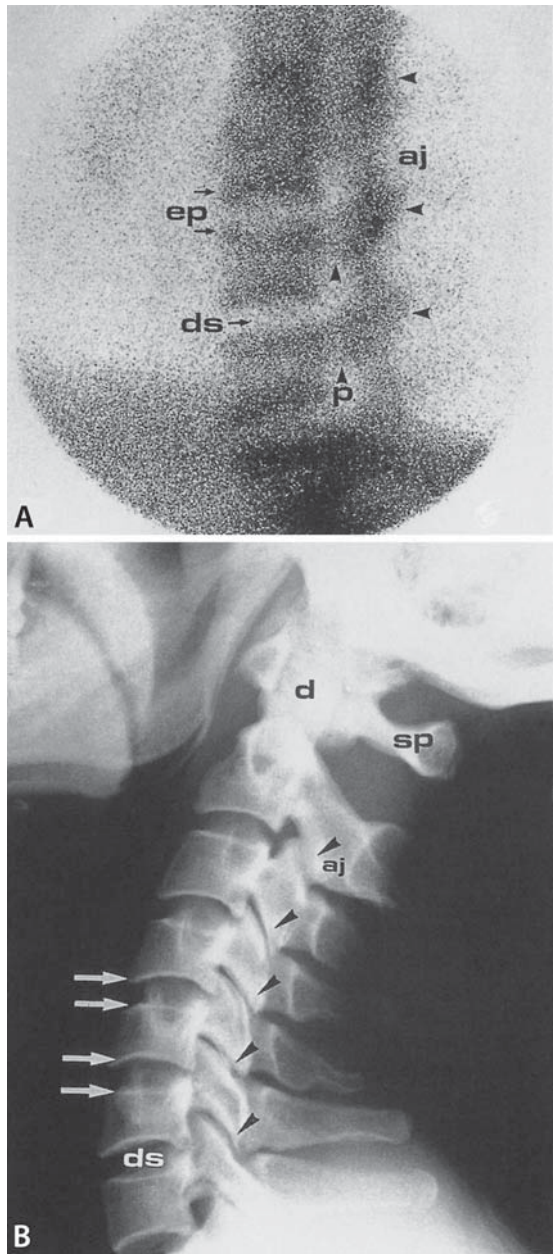

Fig. 4.9A, B Lateral view of the cervical spine. **A** Lateral pinhole scintigraph of the lower cervical spine shows minimally increased tracer uptake in the vertebral endplates (*ep*) and bodies, pedicles (*p*), and apophyseal joints (*aj*). The disk spaces and the intervertebral foramina are photopenic. **B** Lateral radiograph identifies the individual vertebrae with endplates (*arrows*) and disk spaces (*ds*), apophyseal joints (*aj*), and pedicles. The dens (*d*) and spinous process (*sp)* are also visualized

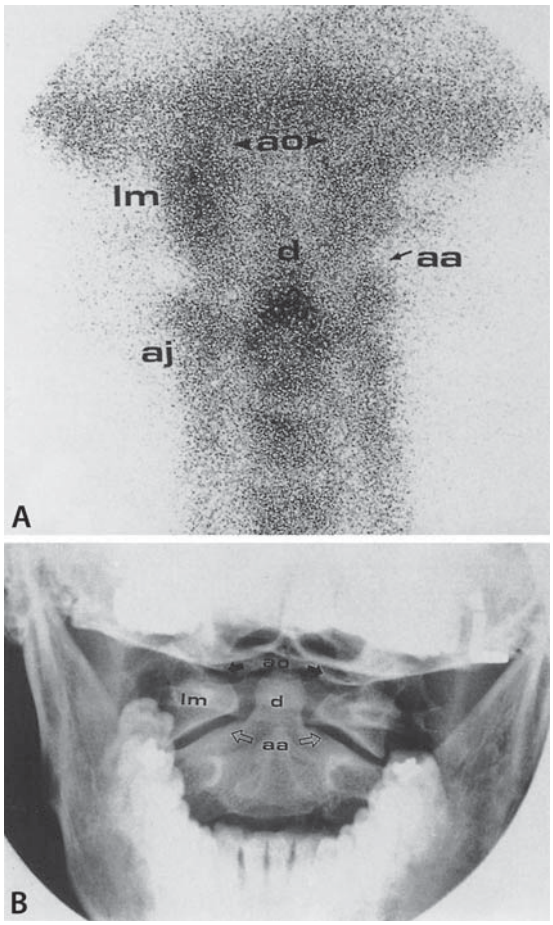

Fig. 4.10A, B Posterior view of the uppermost cervical spine and skull base. **A** Posterior pinhole scintigraph of the uppermost cervical spine and skull base reveals increased tracer uptake in the atlantooccipital joints (*ao*), lateral masses of the atlas (*lm*), the dens (*d*), and the apophyseal joints (*aj*). The atlantoaxial (*aa*) joints are relatively photopenic because they are larger than the other joints. **B** Open-mouth anteroposterior radiograph identifies the atlantooccipital joints (*ao*), lateral masses of the atlas (*lm*), the dens or odontoid process (*d*), and the atlantoaxial joints (*aa*)

tal joint, the median atlantoaxial joint, and the base of the dens. Generally, tracer uptake in the apophyseal joints and spinous processes tends to be moderate (Fig. 4.11). The os nuchae (calcification of the ligamentum nuchae), when not too small, can be visualized.

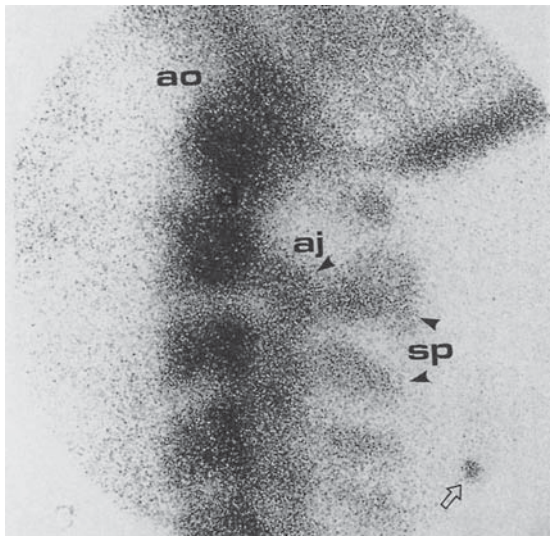

Fig. 4.11 Lateral view of the uppermost cervical spine. Lateral pinhole scintigraph of the upper cervical spine reveals increased tracer uptake in the atlantooccipital joint (*ao*), dens (*d*), apophyseal joints (*aj*), and spinous processes (*sp*) (*open arrow* faint tracer uptake in an os nuchae). The upper portion of Fig. 4.9B identifies the dens (*d*), apophyseal joints (*aj*) and spinous processes (*sp*)

4.3 Thoracic Cage

Various parts of the sternum including the sternoclavicular joints, the manubriosternal joints, and the first costosternal joints and the jugular notch can be distinctly imaged by pinhole scintigraphy (Fig. 4.12A). Normally, tracer uptake stands out in the sternoclavicular joints and the jugular notch where the sternocleidomastoid muscles are attached. The tracer uptake in the sternoclavicular joints is more often than not asymmetrical, and it is presumably related to handedness. The costosternal and xyphoid cartilages may concentrate tracer when mineralized (Fig. 4.12B). As a rare variant, the first two segments of the sternal body may form incomplete articulation and show prominent uptake, simulating a pathological process (Fig. 4.12C). It is to be interpreted with caution since the site also coincides with a persisting sternebra.

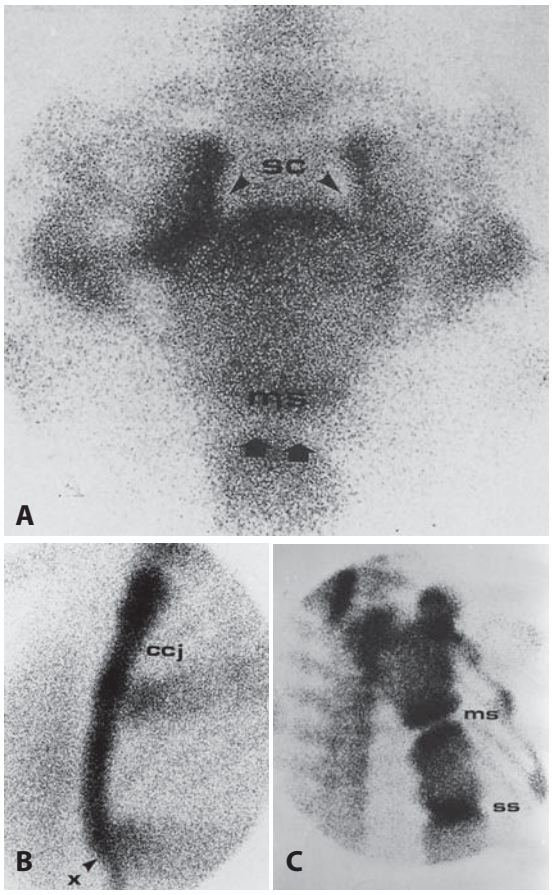

Fig. 4.12A–C Normal sternum in adults and children. **A** Anterior pinhole scintigraph of the manubrium sterni in a 42-year-old man shows tracer uptake in the sternoclavicular joints (*sc*), sternal notch, and manubriosternal junction (*ms*). Note increased tracer uptake in the right sternoclavicular joint due to right-handedness. **B** Lateral scintigraph in a woman shows physiological uptake in the costochondral junction (*ccj*) and retroverted xyphoid process (*x*). **C** Anterior scintigraph of the upper sternum in a child demonstrates prominent tracer uptake in the growing manubriosternal junction (*ms*) and proximal sternebra (*ss*)

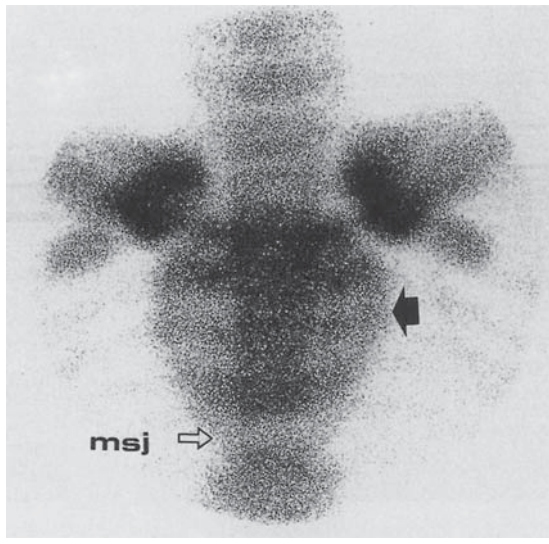

Fig. 4.13 Anterior view of the manubrium sterni in a child. Anterior pinhole scintigraph of the manubrium in an 11-year-old boy demonstrates a rounded, modest tracer uptake in the ossification center (*arrow*). The intense tracer uptake in the medial clavicular ends indicates active bone growth. The manubriosternal junction (*msj*) appears widened due to the relative abundance of cartilage at this age

An incompletely ossified sternum or sternal ossification center in children is typically discoid in appearance. At this stage, the medial clavicular ends and jugular notch avidly accumulate tracer due to brisk bone formation and the stress of the fortified ligaments (Fig. 4.13). Pinhole scintigraphically, the ribs and clavicles are shown as simple, bar-like structures with uniform tracer uptake of relatively low intensity. Understandably, however, the actively growing parts always accumulate tracer rather intensely.

4.4 Shoulder

Pinhole scintigraphy appears particularly suited for the study of the shoulder that contains the humeral head, the scapula, and the clavicle and the glenohumeral and acromioclavicular joints. The frontal view visualizes, in addition to the two above-mentioned joints, the glenoid, the acromion process, the coracoid process, the lateral end and conoid tubercle of the clavicle, and the head, neck, and tuberosities of the humerus (Fig. 4.14). Normally, tracer accumulates avidly in the glenohumeral and acromioclavicular joints on the handed side and the coracoid process: the former joints due to

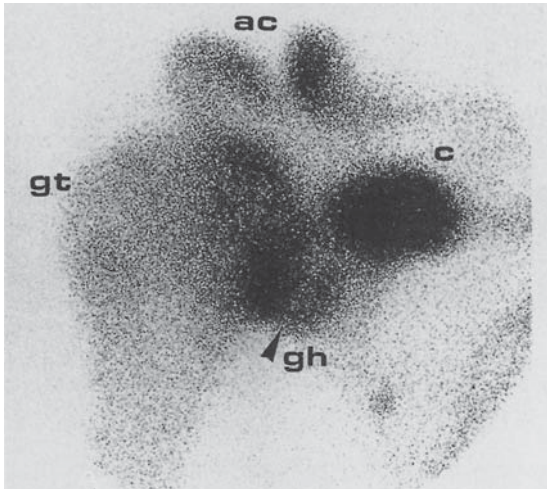

strenuous joint movement and the latter due to heavy attachments of the coracobrachialis, biceps, pectoralis minor, trapezoid, and conoid ligaments. As a whole tracer uptake in the acromioclavicular joints is moderate in intensity. In older children and adolescents with rapid bone development tracer is intensely accumulated in the growth plates (physes), process tips, and lateral clavicular ends (Fig. 4.15). The small anatomical parts of the scapula can be visualized in greater detail on both the anterior and tangential pinhole scans. In the latter view, the spine, angles and margins of the scapula, and the glenoid are clearly visualized, respectively, as stick-like, linear, and stumpy uptake. The infraspinatus fossa is shown as a large triangular photopenic area bordered superiorly by the scapular spine and at the sides by the scapular margins (Fig. 4.16). In addition, the acromion process is very distinctly portrayed.

Fig. 4.14 Anterior view of the shoulder. Anterior pinhole scintigraph of the shoulder in a 34-year-old man demonstrates high uptake in the tip of the coracoid process (*c*) and the bones about the glenohumeral joint (*gh*). The acromioclavicular joint (*ac*) and greater tuberosity (*gt*) are also demonstrated

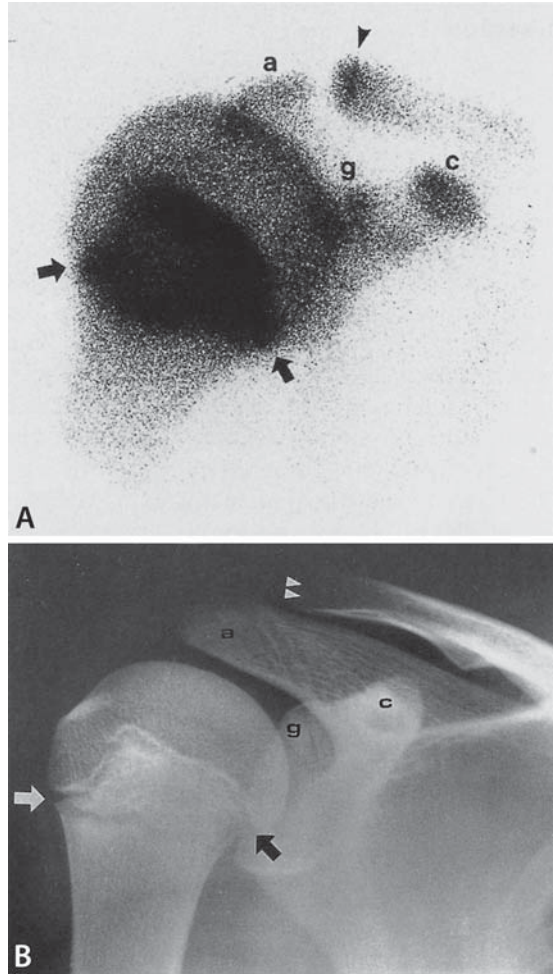

Fig. 4.15A, B Anterior view of the shoulder in a child. **A** Anterior pinhole scintigraph of the shoulder in a 10-year-old boy demonstrates intense tracer uptake in the physeal cartilage (ovoid appearance is due to obliquity; *arrows*) and less intense uptake in the acromion (*a*), glenoid (*g*) and coracoid (*c*) processes. Prominent uptake is also observed in the lateral end of the actively growing clavicle (*arrowhead*). **B** Posteroanterior radiograph identifies the wavy, radiolucent, physeal line across the humeral neck (*arrow*) and the acromion (*a*), glenoid (*g*) and coracoid (*c*) processes (*arrowheads* lateral end of the growing clavicle)

4.5 Thoracic and Lumbar Spine

Because of the larger size and widely spaced vertebrae in the lower spine, the small parts of the individual vertebrae are increasingly well delineated as one descends the spinal column toward the sacrum. For a baseline study, the

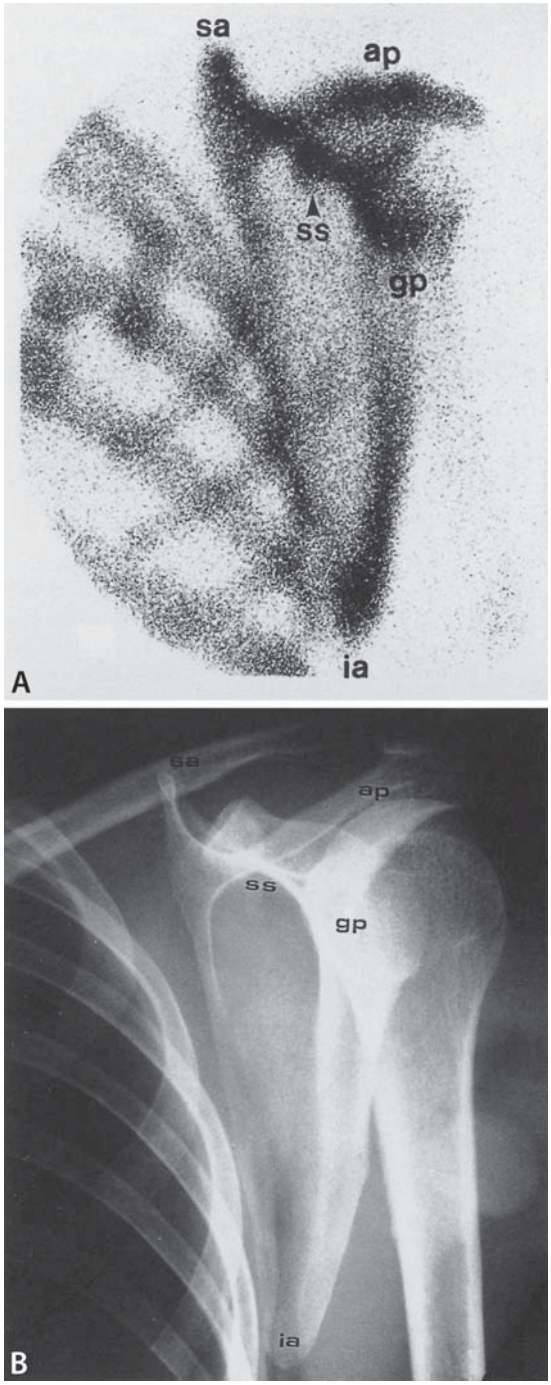

Fig. 4.16A, B Semilateral view of the scapula. **A** Near lateral pinhole scintigraph of the left scapula reveals intense tracer uptake in the spina scapularis (*ss*), glenoid process (*gp*), superior (*sa*) and inferior angles (*ia*), and the acromion process (*ap*). The scapular fossa is demonstrated as a large photopenic area below the spina. **B** Similarly rotated radiograph identifies the spina scapularis (*ss*), the superior (*sa*) and inferior scapular angles (*fa*), and the acromion (*ap*) and glenoid processes (*gp*)

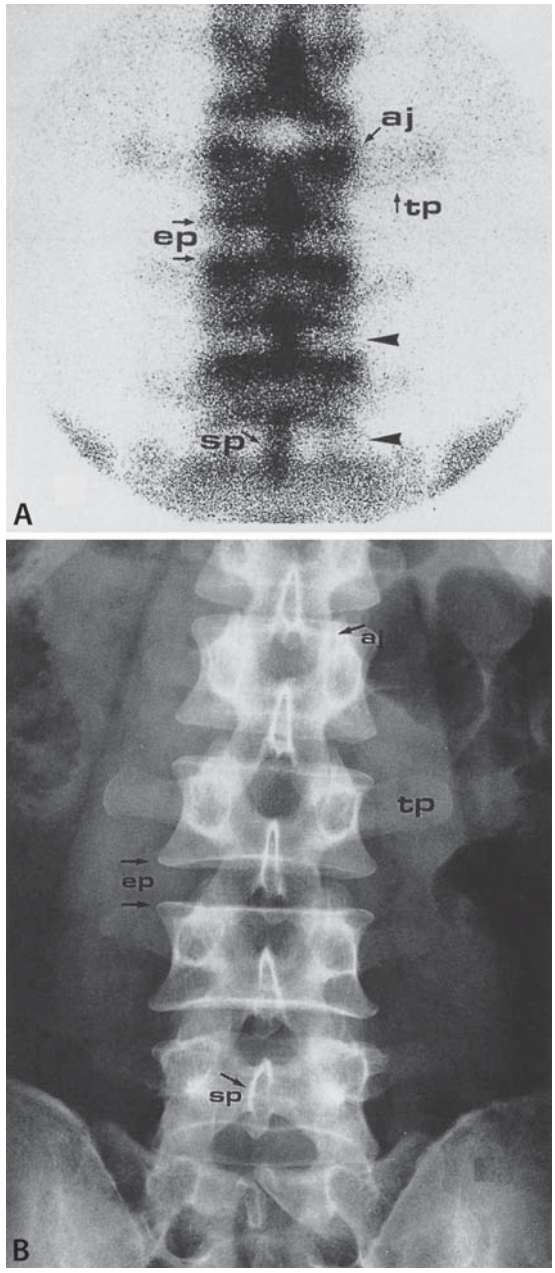

Fig. 4.17A, B Posterior view of the lumbar spine. **A** Posterior pinhole scintigraph of the lumbar spine demonstrates increased tracer uptake in the apophyseal joints (*aj*), spinous processes (*sp*), and vertebral endplates (*ep*). The intervertebral disk spaces are photopenic. **B** Anteroposterior radiograph identifies the apophyseal joints (*aj*), spinous processes (*sp*), transverse process (*tp*) and vertebral endplates (*ep*). The disk spaces appear lucent

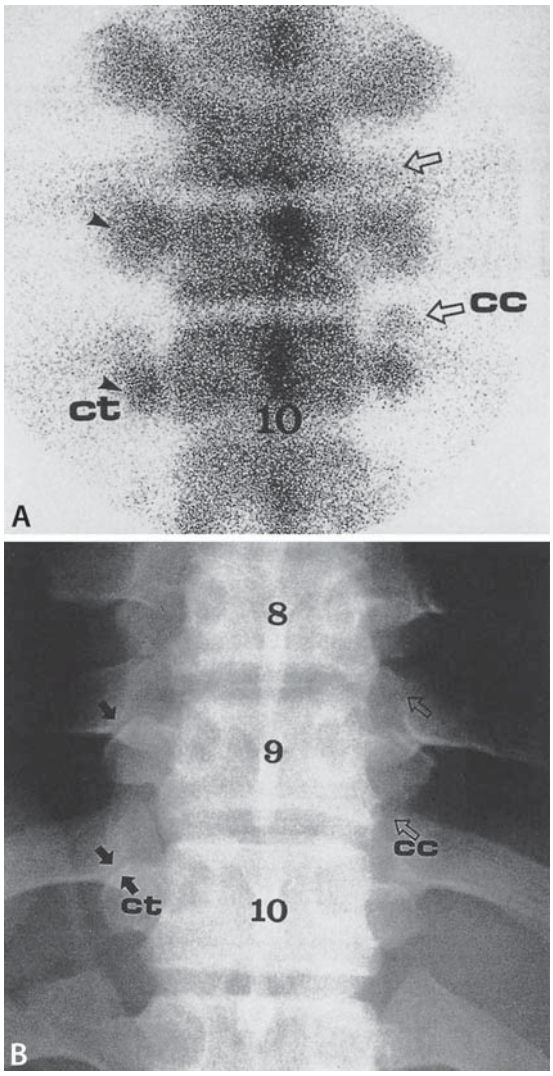

Fig. 4.18A, B Posterior view of the midthoracic spine. **A** Posterior pinhole scintigraph of the midthoracic spine demonstrates minimal, patchy tracer uptake in the costotransverse joints (*ct*), spinous processes, and vertebral endplates. On occasion the costocorporeal joints (*cc*) may be seen in the superomedial aspect of the costotransverse joints. **B** Anteroposterior radiograph identifies the costovertebral joints formed between the costal neck and the transverse process (*ct, arrow*) and the costal head and the vertebral articular facet (*cc*)

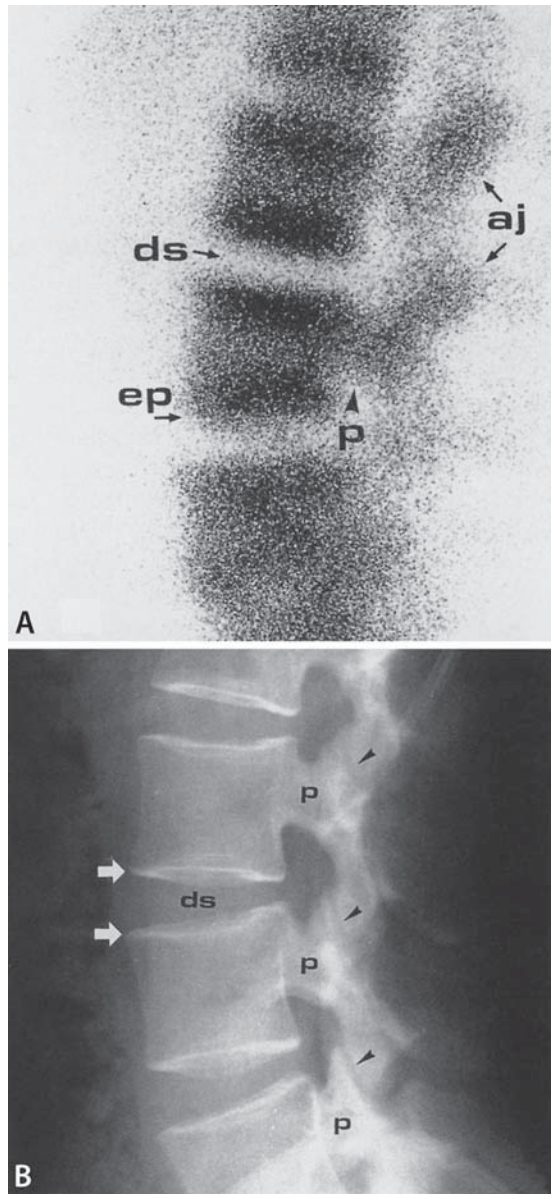

Fig. 4.19A, B Lateral view of the lumbar spine. **A** Lateral pinhole scintigraph of the lumbar spine demonstrates the apophyseal joints (*aj*), pedicles (*p*), vertebral endplates (*ep*) and disk spaces (*ds*). **B** Lateral radiograph identifies the apophyseal joints (*arrowheads*), pedicles (*p*), disk spaces (*ds*) and endplates (*arrows*)

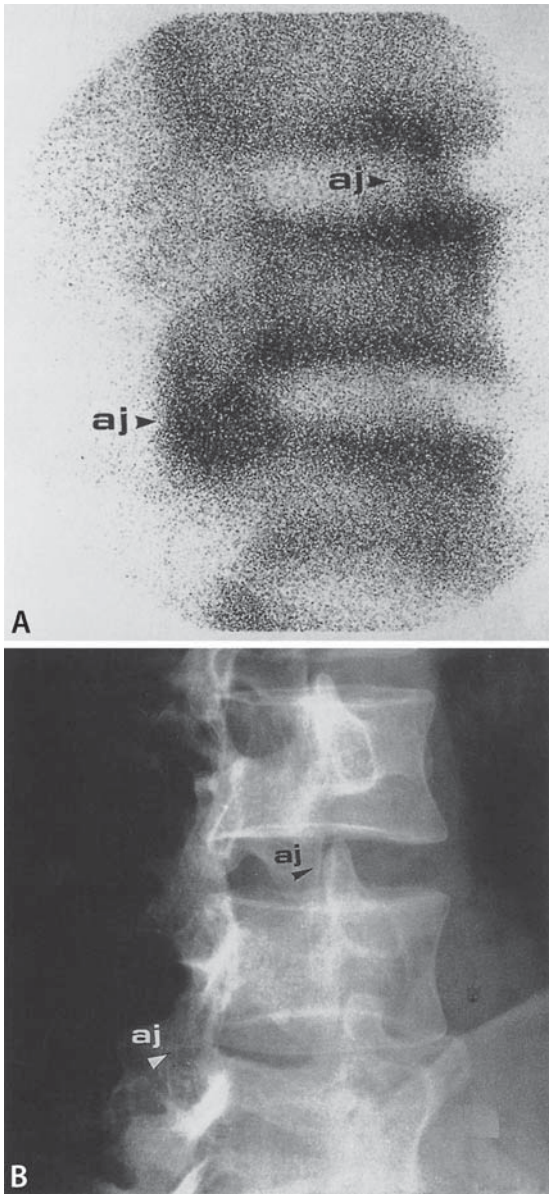

Fig. 4.20A, B Oblique view of the lumbar spine for demonstration of the apophyseal joints. **A** Oblique pinhole scintigraph of the lumbar spine delineates the apophyseal joints (*aj*) as a distinct structure of the vertebra. The joint located inferiorly is located nearer to the pinhole collimator, concentrating tracer more intensely than its counterpart further away. **B** Oblique radiograph identifies the apophyseal joints (*aj*)

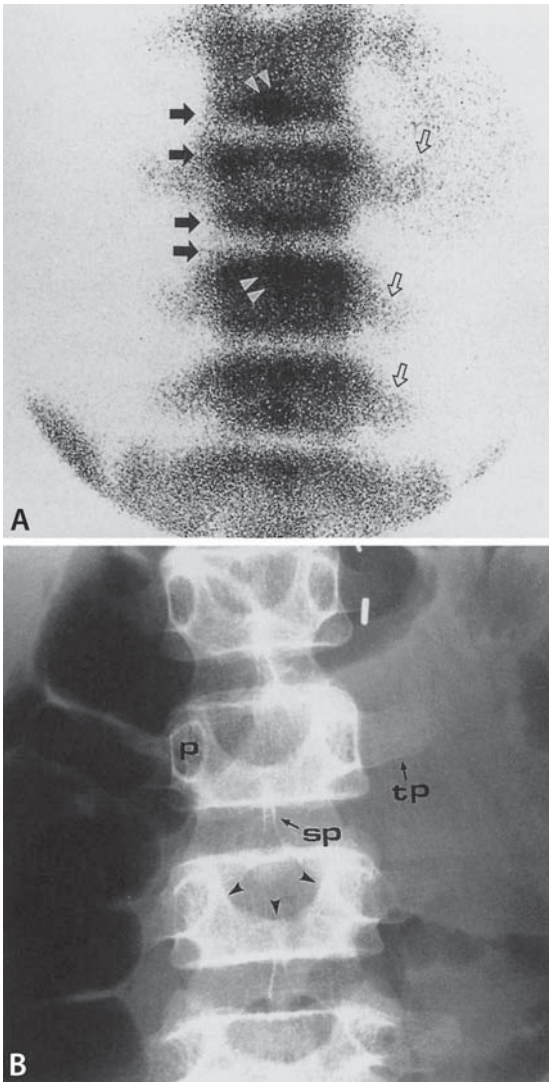

Fig. 4.21A, B Posterior view of the lumbar spine in a child. **A** Posterior pinhole scintigraph of the lumbar spine in a 12-year-old girl demonstrates intense tracer accumulation in the growing vertebral endplates (*arrows*) and spinous processes (*arrowheads*) and faintly also in the transverse processes (*open arrows*). The vertebral bodies in adolescence do not appear square as in adults (Fig. 4.17A) because ossification is still in progress. **B** Anteroposterior radiograph identifies the individual vertebrae with the pedicles (*p*), neural arch (*arrowheads*), transverse processes (*tp*) and spinous process (*sp*)

standard posterior scan suffices. In the posterior view the vertebral endplates, the disk spaces, and the spinous processes, and the apophyseal joints are all clearly portrayed (Fig. 4.17). In general the transverse processes accumulate tracer only faintly because they are small and thin. It is to be pointed out that the disk spaces are partly obscured by the spinous process in the midline and the facet joint in the sides. In the thoracic spine, the posterior scan additionally reveals the costovertebral and costotransverse joints (Fig. 4.18). The lateral view reveals the vertebral endplates, the intervertebral disk spaces, and the pedicles, and the apophyseal joints. On the lateral view the spinous processes are only faintly seen because they are thin in this projection. Typically, the intervertebral disk spaces are indicated by photon defects located between the endplates that concentrate tracer intensely (Fig. 4.19). For an unobstructed viewing of the facet joints, the oblique view is appropriate. The facet joints are distinctly visualized on this view because articular movement stimulates uptake (Fig. 4.20). The pinhole scintigraphic anatomy of pediatric vertebrae is characterized by the "not squared" tracer uptake in the growing endplates (Fig. 4.21).

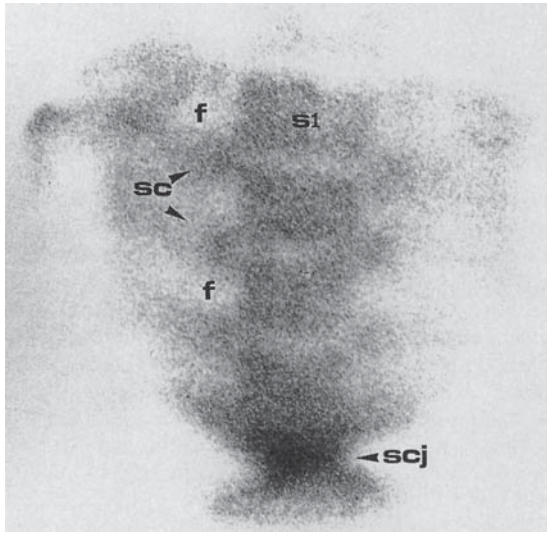

Fig. 4.22 Posterior view of the sacrum. Higher magnification posterior pinhole scintigraph of the sacrum demonstrates the individual sacral foramina (*f*) as ovoid photopenic areas surrounded by sacral crests (*sc*), which accumulate tracer minimally (*S1* first segment of the sacrum). The sacrococcygeal joint concentrates tracer modestly due to articular motion (*scj*)

4.6 Sacrum and Sacroiliac Joints

For the sake of integrity, the pinhole scan anatomy of the sacrum and the sacroiliac joints are described together. The posterior pinhole scintigraph of the sacrum taken at a relatively low magnification level reveals accumulation of tracer in the sacroiliac joints with mild uptake in the sacral body and lateral parts. The scan resolution at this magnification level is such that the small anatomical structures of the sacrum are not discerned. At a higher magnification levels, however, the intermediate and lateral sacral crests as well as the individual sacral foramina are portrayed (Fig. 4.22). Typically, the sacral foramina are presented as transversely ovoid photopenic areas. Occasionally, the sacrococcygeal joint stands out due to increased uptake caused by articular movement. Characteristically, the tracer uptake in the sacroiliac joints is more intense in the synovial lower compartment than in the ligamental upper compartment (Fig. 4.23A). The sacrum and ilia overlap at the sacroiliac joints in the straight posterior view, requiring the butterfly view for their separation (Fig. 4.23B, C). In this special view, the upper compartment is portrayed as a vertical, wedge-shaped photopenia between the tuberosities of the ilium and sacrum, whereas the lower compartment is only incompletely separated. Tracer is accumulated more intensely in the iliac auricular surface than in the sacral because greater articular movement occurs in the former. It is to be underscored that, contrary to the traditional description, the lower compartment more avidly accumulates tracer than the upper. The upper and lower compartments of the sacroiliac joints are separated from each other by an oblique

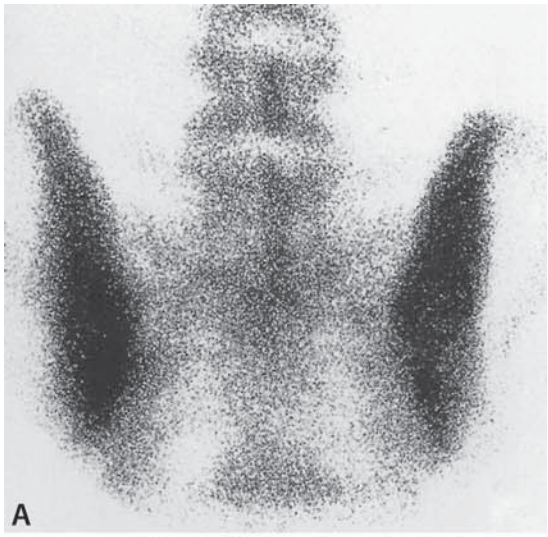

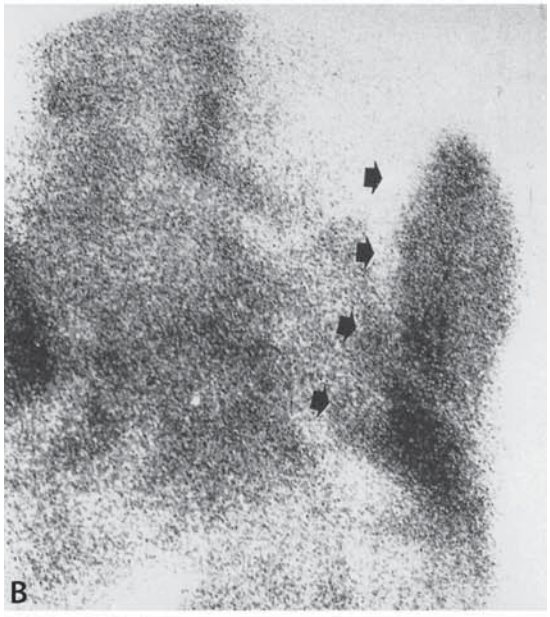

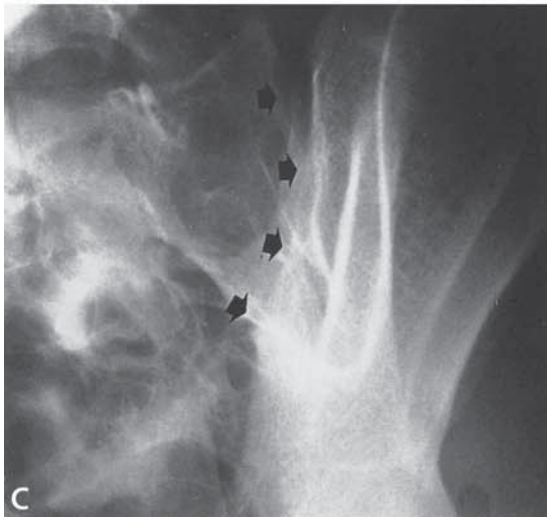

Fig. 4.23A–C Posterior view of the sacroiliac joints. **A** Lower magnification, posterior pinhole scintigraph of the sacrum portrays intense, triangular tracer uptake symmetrically in both sacroiliac joints. The uptake in the sacrum is relatively minimal, revealing no detail. **B** Posterior tangential or butterfly pinhole scintigraph of the right sacroiliac joint separates the joint space, which is wedge-shaped in the upper compartment (*arrows*). The separation is incomplete in the synovial, lower compartment and complete in the ligamentous, upper compartment. The prominent tracer uptake is localized on the iliac side. **C** Tangential radiograph identifies the joint space between the sacrum and ilium (*arrows*)

photopenic band, featuring increased uptake in the quadrilateral auricular surface of the lower compartment (Fig. 4.23B). The posterior iliac crest accumulates tracer only modestly.

4.7 Pelvis and Hip

The anterior view of the pelvis and the hip in the pediatric and juvenile age groups shows moderate tracer uptake in the acetabular fossa, triradiate growth cartilage, femoral head and neck, and trochanters, and intense uptake in the physeal plates (Fig. 4.24). The ilium, pubis, and ischium are portrayed as independent bones at this age. The ilium is indicated by horizontal "hot" plates and the ischium and pubis by vertical "hot" plates. In younger subjects the hip joint proper is totally free of tracer because the cartilaginous layers over the femoral head and acetabulum are relatively thick and the acetabular fossa is still shallow. Amazingly, pinhole scintigraphy can depict the tracer accumulated in the fovea capitis, to which the femoral capital ligament is attached (Fig. 4.24A). As bones cease to grow, tracer uptake in the fused physeal plates becomes sharply reduced and nearly completely vanishes when bones are fully mature. Thus, in adults, tracer intensely accumulates in the acetabular roof, supraacetabular bone, and iliac crest, whereas tracer uptake diminishes in the femur. The iliac fossa is shown as a large void. At higher magnification

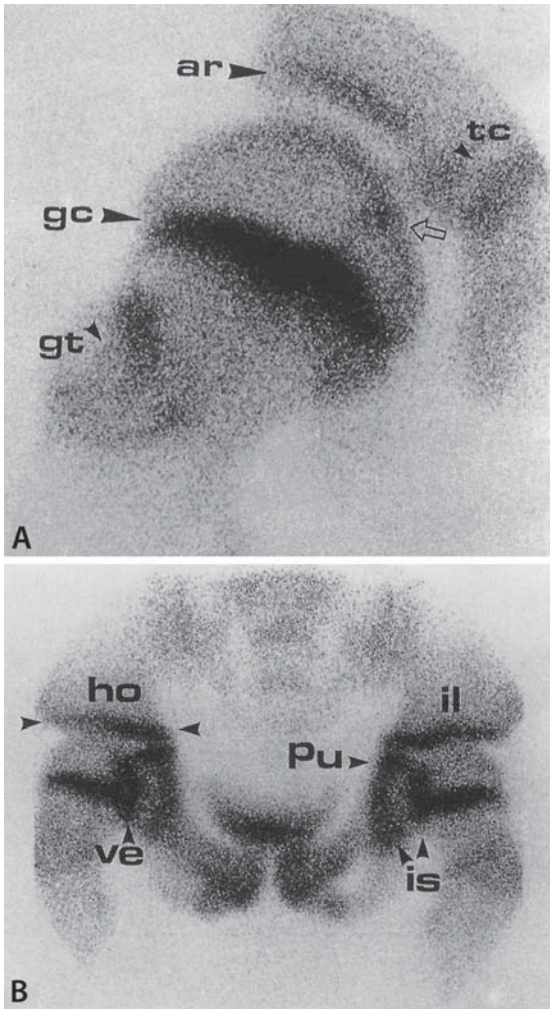

Fig. 4.24A, B Anterior views of the hip in children. **A** Higher magnification anterior pinhole scintigraph of the right hip in a 12-year-old boy reveals pronounced tracer uptake in the growth cartilage zone (*gc*) and slightly increased tracer uptake in the base of the greater trochanter (*gt*), the acetabular roof (*ar*), the triradiate cartilage (*tc*), and in the femoral head. Observe the increased uptake in the fovea where the femoral ligament inserts (*arrow*). **B** High magnification anterior pinhole scintigraph of the pelvis in a 9-year-old boy demonstrates intense tracer uptake in the growth cartilages of the ilium (*il*), pubis (*pu*), and ischium (*is*). Characteristically, the ilial cartilage is aligned horizontally (*ho*) and the pubis and ischial cartilages vertically (*ve*). Actually, the ischiopubic junction is shown en face as a vertically ovoid structure

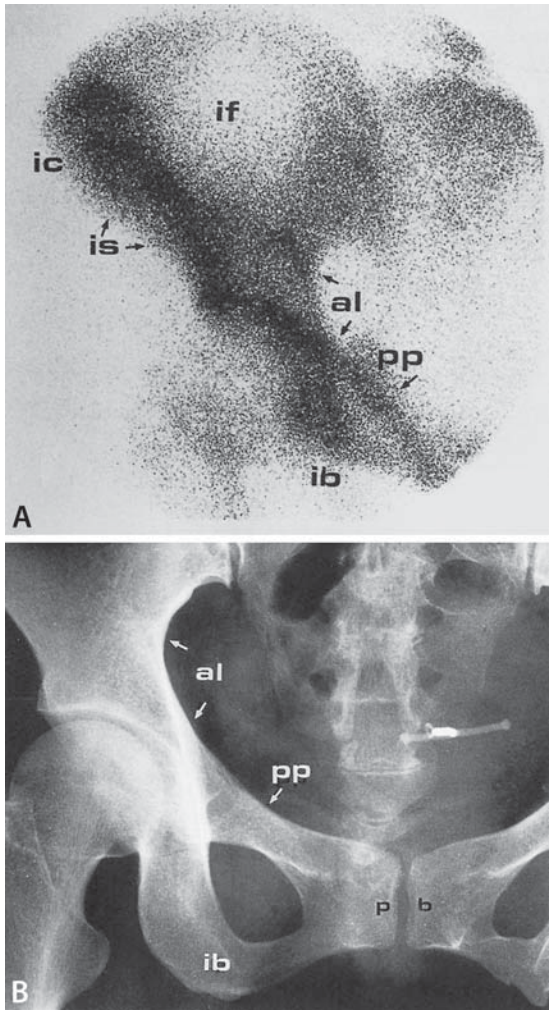

Fig. 4.25A, B Anterior view of the right hemipelvis and hip. **A** Anterior pinhole scintigraph of the right hemipelvis and hip reveals increased tracer uptake in the iliac crest (*ic*), iliac spines (*is*), arcuate line (*al*), pecten pubis (*pp*), ischial body (*ib*), and acetabular roof. The iliac fossa (*if*) is demonstrated as a photopenic area. In adults, as opposed to adolescents (Fig. 4.24), tracer accumulates mainly in the acetabular bones, which are involved in articular motion, and is reduced in the remaining bones because of decelerated bone turnover. **B** Anteroposterior radiograph identifies the arcuate line (*al*), pecten pubis (*pp*), ischium (*ib*), and pubis (*pb*) as well as the acetabular roof

levels, the anterior iliac spines, the arcuate line, the pecten pubis, and the ischial body are clearly visualized (Fig. 4.25). Unlike in younger subjects, the hip joints in adults become poorly defined because tracer uptake in the completely formed femoral head and well-deepened

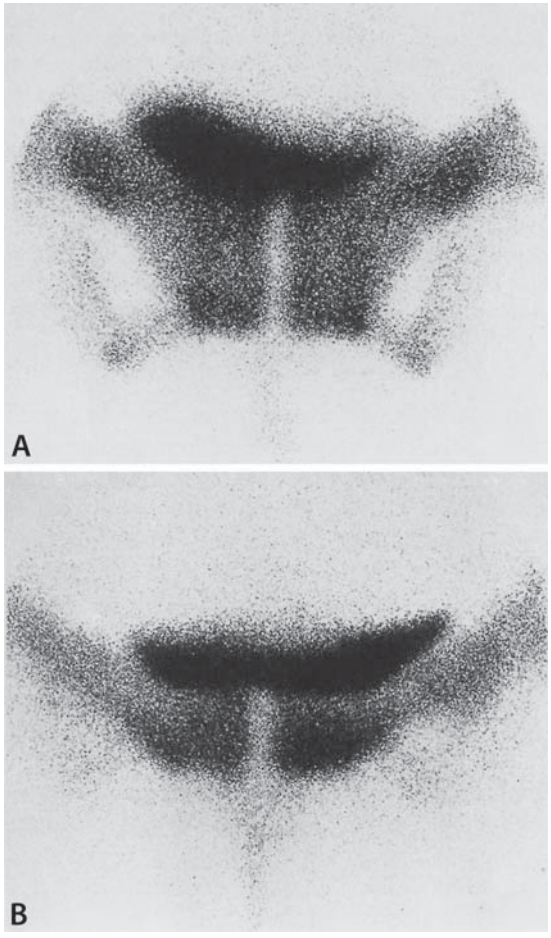

Fig. 4.26A, B Anterior view of the pubis. **A** Anterior pinhole scintigraph of the symphysis pubis reveals intense tracer uptake in the pubic bones about the symphysis and the articular space, which is photopenic. **B** Anterior pinhole scintigraph of the dorsally inclined pubis shows a drastic change in appearance. The same effect can be created by caudally tilting the long axis of pinhole collimator. Typically, tracer uptake in the pubic bone is uniform

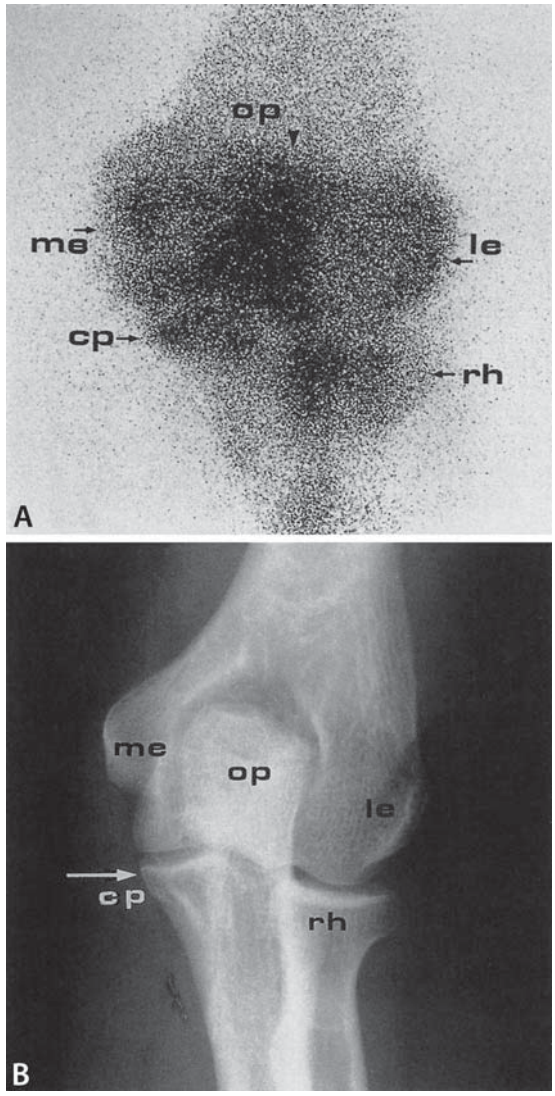

Fig. 4.27A, B Anterior view of the elbow. **A** Anterior pinhole scintigraph of the left elbow reveals increased tracer uptake in the olecranon process (*op*), medial (*me*) and lateral epicondyles (*le*), coronoid process (*cp*), and head of the radius (*rh*). **B** Anteroposterior radiograph identifies the olecranon process (*op*), medial and lateral epicondyles (*me, le*), coronoid process (*cp*) and the head of the radius (*rh*)

acetabular fossa overlaps. Tracer uptake in the pubic bones about the symphysis is rather conspicuous, especially in women of childbearing age. The pubic bone uptake gradually decreases with age. Otherwise, there are no sex or age differences in the pubic bone uptake pattern (Chung et al. 1992). Dorsal inclination of the pubic bone or obliquity of the pinhole collimator axis may result in a drastic change in appearance (Fig. 4.26). The iliac crests and auricular surfaces are visualized to advantage in the posterior scan.

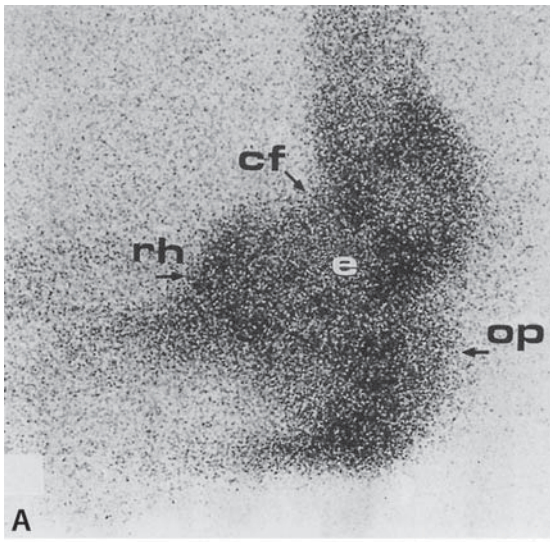

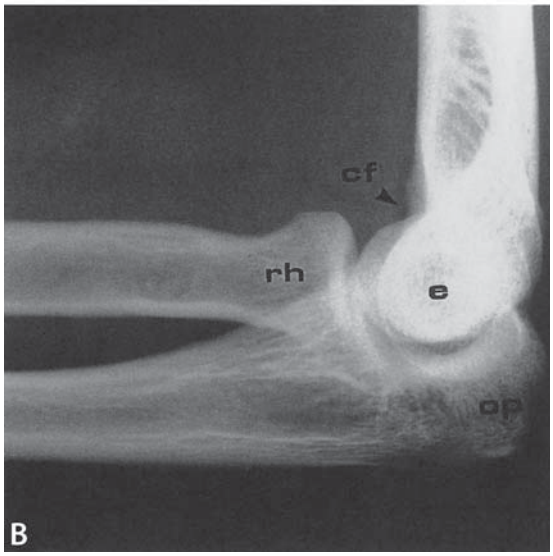

Fig. 4.28A, B Lateral view of the elbow. **A** Lateral pinhole scintigraph of the elbow demonstrates the coronoid fossa (*cf*), head of the radius (*rh*), epicondyles (*e*) and olecranon process (*op*). **B** Mediolateral radiograph identifies the coronoid fossa (*cf*), head of the radius (*rh*), epicondyles (*e*) and the olecranon process (*op*)

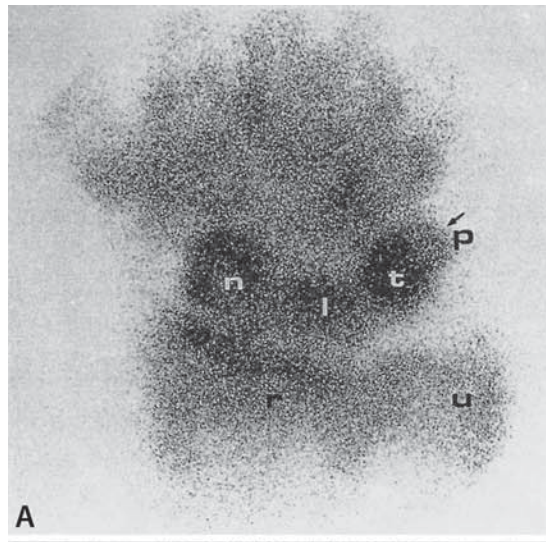

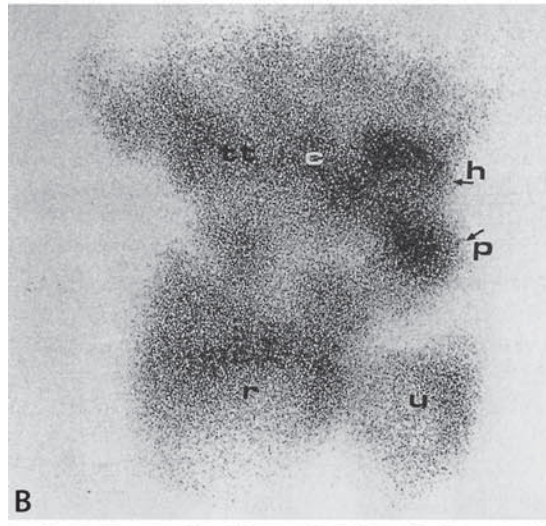

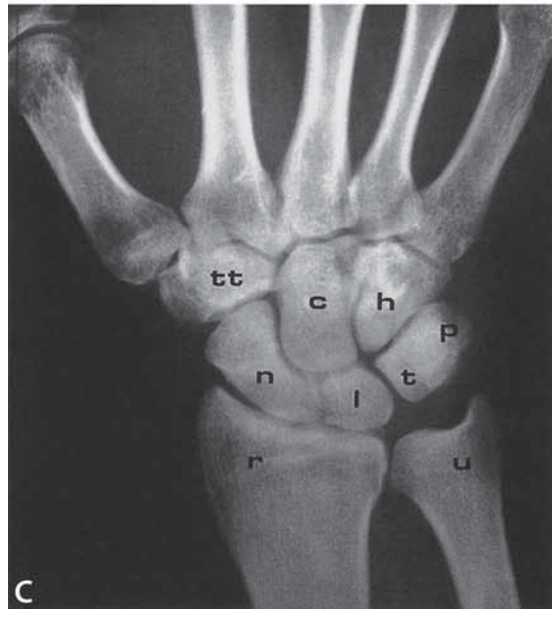

◁ **Fig. 4.29A–C** Dorsal and ventral views of the wrist. **A** Dorsal pinhole scintigraph of the right wrist demonstrates minimally increased tracer uptake in the distal ends of the radius (*r*) and ulna (*u*) and the four proximal carpal bones: the navicular (*n*), lunate (*l*), triquetral (*t*) and pisiform (*p*). **B** Ventral pinhole scintigraph shows minimal tracer uptake in the distal radius (*r*) and ulna (*u*) and the four distal carpal bones: the hamatum (*h*), capitatum (*c*), and trapezoid and trapezium (*tt*). The pisiform (*p*) is also visualized. Note the difference between the findings revealed by the dorsal and ventral views. **C** Dorsoventral radiograph identifies the distal radius (*r*) and ulna (*u*), the navicular (*n*), lunate (*l*), triquetral (*t*), pisiform (p), hamatum (*h*), capitatum (*c*) and trapezoid and trapezium (*tt*)

4.8 Limbs

On the whole, tracer is accumulated only minimally in the shafts of long bones, especially in adults, with higher uptake typically localizing to bone ends. Accordingly, pinhole scanning is more effective and informative in the periarticular bones of the limbs. A useful technical guideline for limb pinhole scintigraphy is to place the collimator as close as possible to the side or site of interest; for example, either the medial or lateral side in the ankle and anteriorly or posteriorly in the hip and knee. However, such technical caution may be waived if one uses dual-head pinhole scintigraphy.

4.8.1 Upper Limbs

The pinhole scintigraphic anatomy of the proximal humerus is discussed above in Section 4.4 Shoulder. Using magnification scanning, the topography of the elbows, wrists, and hands can also be efficiently detailed. The anterior scan of the elbow depicts the medial and lateral humeral condyles, the radial head, the olecranon process and fossa, the coronoid process, and articular spaces (Fig. 4.27). On the other hand, the medial or lateral views delineate the radial head, the olecranon process, and the coronoid process and fossa (Fig. 4.28). The dorsal structures of the elbow are better seen on the posterior view. In the elbow, the joint is usually not well defined because of its structural complexity and relative smallness. In the

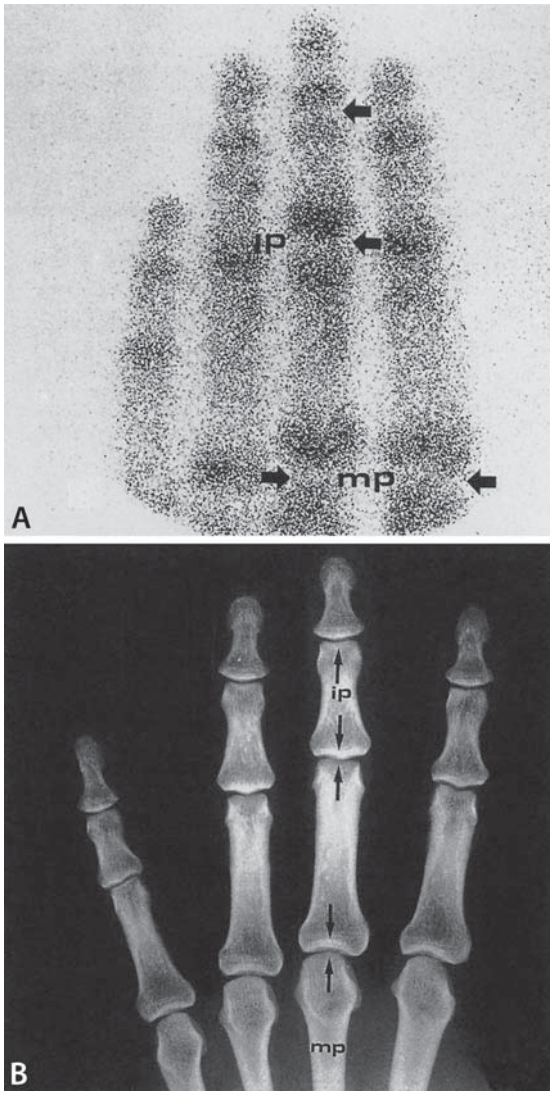

Fig. 4.30A, B Dorsal view of the distal hand. **A** Dorsal pinhole scintigraph of the left hand demonstrates the metacarpophalangeal (*mp*) and interphalangeal joints (*ip*). Tracer accumulates mainly in the bases and heads of the phalanges, delineating joints. **B** Dorsoventral radiograph of the same hand identifies the metacarpophalangeal (*mp*) and interphalangeal joints (*ip*)

wrist, each carpal bone can be imaged when proper views are chosen; however, the triquetrum and the pisiform cannot be separated as they are intimately superimposed upon one another (Fig. 4.29). Instead, the overlap of these two bones is represented scintigraphically by the "added tracer uptake" phenomenon. The hamate tends to accumulate tracer relatively more intensely than others. For a

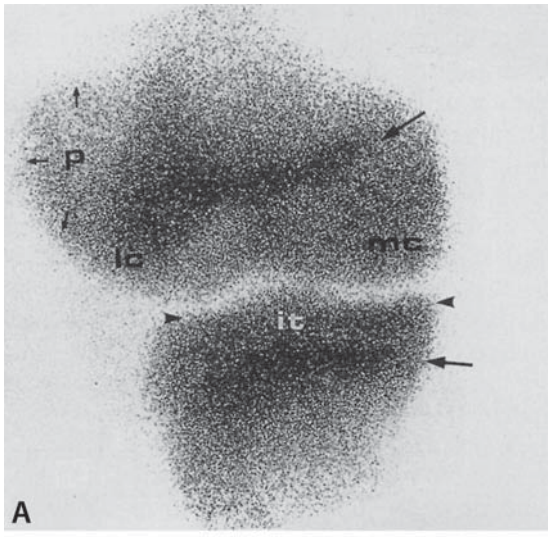

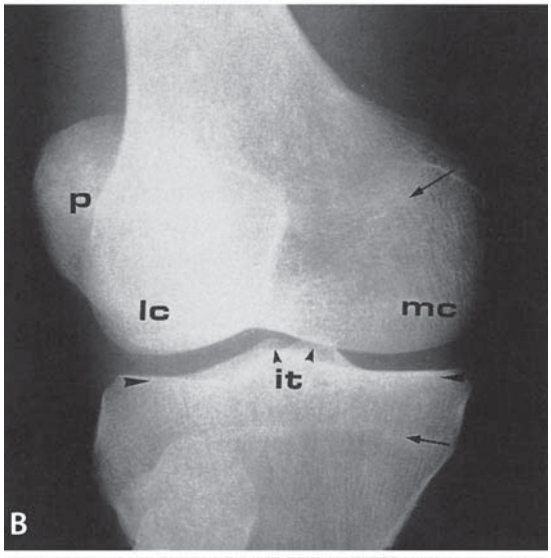

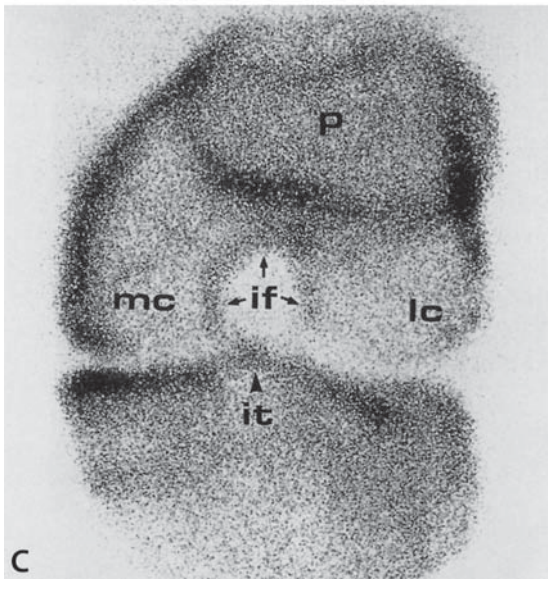

Fig. 4.31A–C Anterior and tunnel views of the knee. **A** Anterior pinhole scintigraph of the right knee demonstrates increased tracer uptake in the medial (*mc*) and lateral condyles (*lc*), patella (*p*), intercondylar tubercles of the tibia (*it*), and tibial plateaus (*arrowheads*). The closed physeal lines in the distal femur and proximal tibia are indicated by transverse, linear tracer uptake (*large arrows*). **B** Anteroposterior radiograph identifies the medial (*mc*) and lateral condyles (*lc*), intercondylar tubercles of the tibia (*it*), tibial plateaus (*arrowheads*), and patella (*p*). The closed physeal lines are faintly visible in the distal femur and proximal tibia (*arrows*). **C** Cranially tilted posterior pinhole scintigraph of the knee (tunnel view) provides a bone-free view of the medial (*mc*) and lateral condyles (*lc*), intercondylar fossa (*if*), tibial tubercle (*it*) and patella (*p*)

clearer portrayal of the proximal carpal bones the dorsal view is adequate (Fig. 4.29A), whereas the ventral view is more appropriate for the portrayal of the distal carpal bones (Fig. 4.29B); this is because the respective views are closer to the target carpal bones. In addition the dorsal view can advantageously portray the distal ends of the radius and ulna as well as the proximal carpal compartments (Fig. 4.29A). It is to be emphasized that the dorsal and ventral views must be utilized, respectively, for an optimal visualization of the proximal and distal carpal bones. (This is a typical situation in which both the inverse square law and rapidly diverging field of view in pinhole collimation seriously affect the image quality: the shorter the aperture-to-target distance, the more distinct is the image.) Pinhole scintigraphy is useful for the visualization of the individual phalanges and metacarpals, including their joints (Fig. 4.30). For the individualized observation of a single phalanx or interphalangeal joint, greater magnification may be obtained using the contact collimation technique.

4.8.2 Lower Limbs

Pinhole scintigraphic anatomy of the proximal femur is described in detail in Section 4.7 Pelvis and Hip. The knees, ankles, and feet are other major objectives of pinhole scintigraphy in the lower limbs. The anterior view of the knee depicts the medial and lateral femoral condyles, tibial plateau, intercondylar tuber-

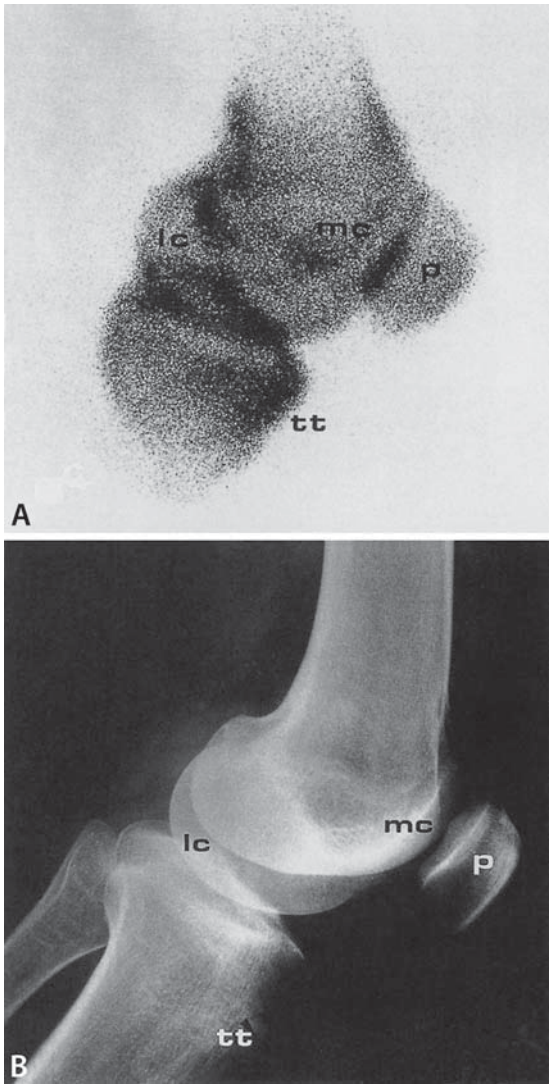

Fig. 4.32A, B Medial view of the knee. **A** Medial pinhole scintigraph of the left knee demonstrates increased tracer uptake in the medial (*mc*) and lateral condyles (*lc*), tibial tuberosity (*tt*) and patella (*p*). **B** Mediolateral radiograph identifies the medial (*mc*) and lateral condyles (*lc*), tibial tuberosity (*tt*) and patella (*p*)

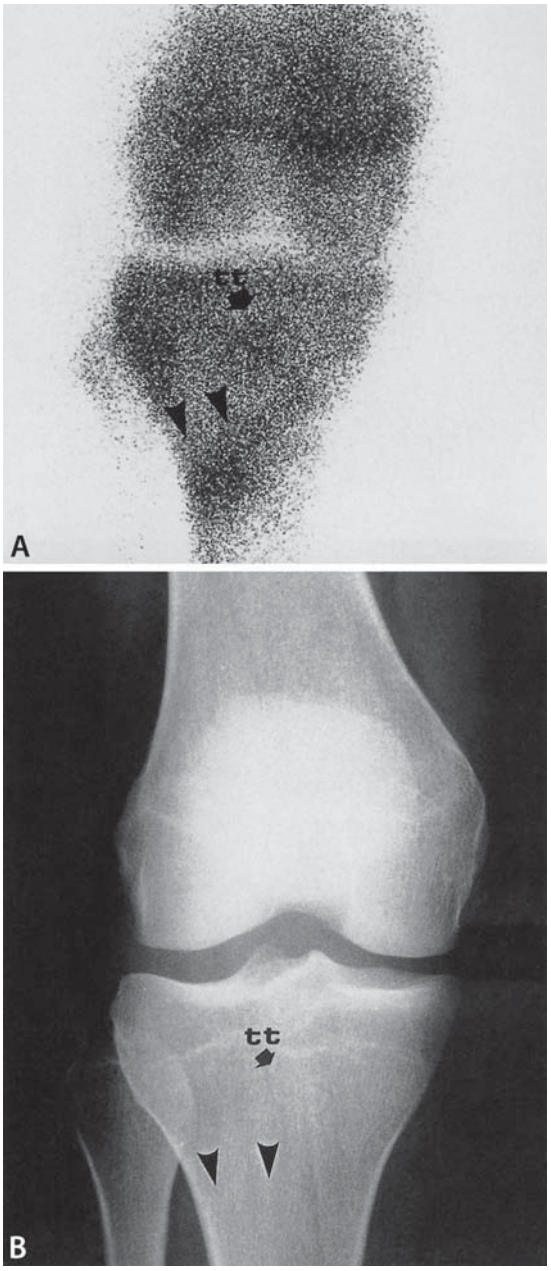

Fig. 4.33A, B Anterior view of the proximal tibia. **A** Anterior pinhole scintigraph of the proximal tibia demonstrates minimally increased tracer uptake in the tibial tuberosity (*tt*) and slightly distolaterally at the insertion site of the patellar ligament (*arrowheads*). **B** Anteroposterior radiograph identifies the tibial tuberosity (*tt*) and the insertion site of the patellar ligament (*arrowheads*)

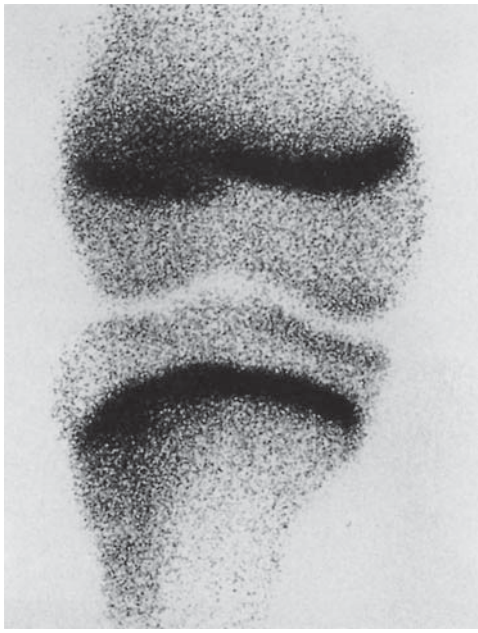

Fig. 4.34 Anterior view of the knee in a child. Anterior pinhole scintigraph of the knee in a 12-year-old boy shows prominent tracer uptake in the physes of the distal femur and the proximal tibia. The epiphyseal border of the intense physeal tracer uptake is well demarcated, whereas the metaphyseal border appears gradually to fade out toward the shaft, indicating that the ossification gradually becomes completed toward the diaphysis

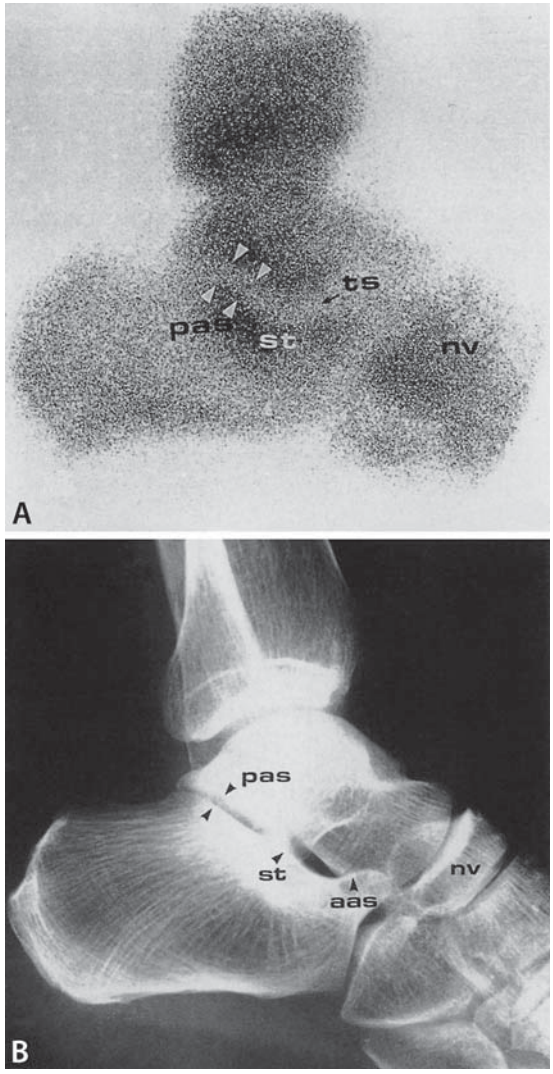

Fig. 4.35A, B Medial view of the ankle. **A** Medial pinhole scintigraph of the left ankle and hindfoot demonstrates minimal tracer uptake in the posterior articular surfaces of the talus and calcaneus (*pas, arrowheads*), the sustentaculum tali (*st*) and the tarsal sinus (*ts*). The tarsal navicular is also visualized distally to the talonavicular articulation (*nv*). Mainly demonstrated are the structures in the foreground, which is closer to the collimator. **B** Mediolateral radiograph identifies the posterior articular surfaces of the talus and calcaneus (*pas, arrowheads*), the sustentaculum tali (*st*), and the anterior articular surface of the calcaneus (*aas*). The tarsal sinus is shown as a bone-free slit between the talus and calcaneus

cles or tibial spines, and the patella en face (Fig. 4.31A, B). The relatively small fibular head is usually invisible because it is overshadowed by the thick tibia, and tracer uptake is minimal. Characteristically, the subchondral bones and physeal plates, either growing or recently closed, show higher tracer uptake. It is to be noted that, unlike in the elbow, the joint space in the knee is presented as a clear photopenic space on the anterior view because, as is well known, the joint is larger and simpler. For unobstructed, bone-free observation of the knee, which includes the femoral condyles and intercondylar fossa, the tibial condyles and plateaus, and the tibial tubercles, the tunnel view is ideal (Fig. 4.31C). In the medial or lateral view the femoral condyle that is nearer to the collimator is more magnified and vice versa (Fig. 4.32). The tibial tuberosity and tubercle and the patella are clearly depicted in profile. In the side views, the peripheries of the periarticular bones that overlap each other are indicated by curvilinear uptake, the additive effect of tracer uptake of two different structures. The anterior close-up pinhole view of the proximal tibia often portrays physiological tracer uptake

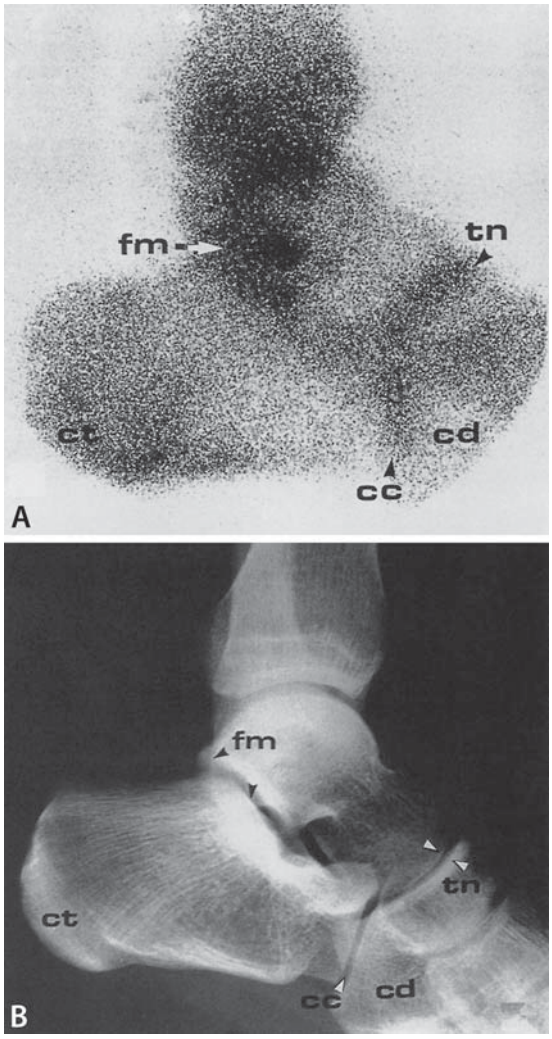

Fig. 4.36A, B Lateral view of the ankle. **A** Lateral pinhole scintigraph of the right ankle and hindfoot shows minimal tracer uptake in the fibular malleolus (*fm*), calcaneal tuberosity (*ct*), and talonavicular (*tn*) and calcaneocuboid joints (*cc*). The cuboid is delineated by virtue of periarticular tracer uptake (*cd*). Note that mainly the structures closer to the collimator are demonstrated. **B** Mediolateral radiograph identifies the fibular malleolus (*fm*), calcaneal tuberosity (*ct*), talonavicular (*tn*) and calcaneocuboid joints (*cc*) and the cuboid (*cd*)

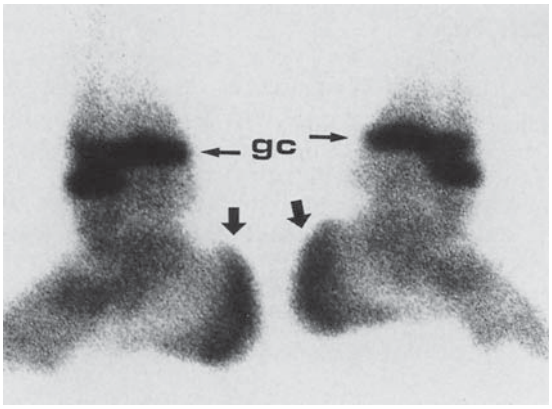

Fig. 4.37 Lateral views of both ankles in a child. Medial views of both ankles (simultaneous acquisition) in a 10-year-old boy reveal extremely intense tracer accumulation in the growth cartilages in the distal tibia and fibula (*gc*) as well as the calcaneal apophysis (*arrows*). In general, the joints are blurred due to the increased periarticular tracer accumulation

in the tibial tuberosity, and also distolaterally at the insertion of the patellar ligament (Fig. 4.33). As in any long bones, the physeal plates in the distal femurs and the proximal tibias and fibulas in growing children intensely accumulate tracer (Fig. 4.34). More often than not the proximal fibular physeal plate is obscured by the larger overlapping tibial plate. Characteristically, the tracer accumulated in the metaphyseal border of a "hot" physeal plate fades as it advances toward the diaphysis, reflecting gradual deceleration and completion of ossification.

For the study of the bones in the ankle and foot, both the medial and lateral views and a complementary dorsal view are necessary. The medial pinhole scan shows tracer uptake in the trochlea and posterior articular surface of the talus as well as the sustentaculum tali and the posterior articular surface of the calcaneus, which together form the subtalar joint or the tarsal sinus (Fig. 4.35). Increased uptake may also be present in the navicular and the cuboid of the midfoot as well as the tibial and fibular malleoli that articulate with the talus in the ankle. On the other hand, the lateral scan reveals notable tracer uptake in the bones about the talofibular, talocalcaneal, talonavicular, and calcaneocuboid joints as well as the calcaneal tuberosity (Fig. 4.36). In children and adolescents tracer accumulates intensely in the physeal plates of the distal tibia and fibula and the apophysis of the calcaneus (Fig. 4.37). Regardless of age, the intertarsal joints are not well portrayed because they are relatively small in size and the tarsal bones irregularly overlap. This is particularly true in actively growing

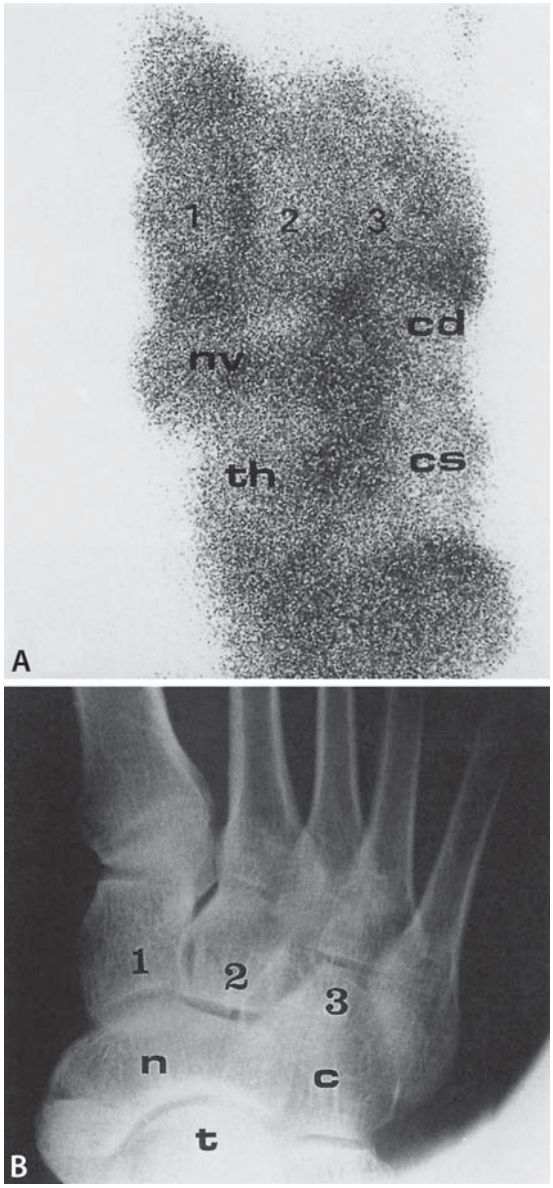

Fig. 4.38A, B Dorsal view of the foot. **A** Dorsal pinhole scintigraph of the right foot demonstrates tracer uptake in the talar head (*th*), articular surface of the calcaneus (*cs*), navicular (*nv*), and cuboid (*cd*). The first (*1*), second (*2*), and third (*3*) cuneiforms are also visualized. Note that the individual tarsal bones are rendered visible by the tracer accumulated in the periarticular bones. **B** Dorsoplantar radiograph identifies the talar head (*t*), articular surface of the calcaneus, navicular (*n*) and cuboid (*c*) (*1 2 3* three cuneiforms)

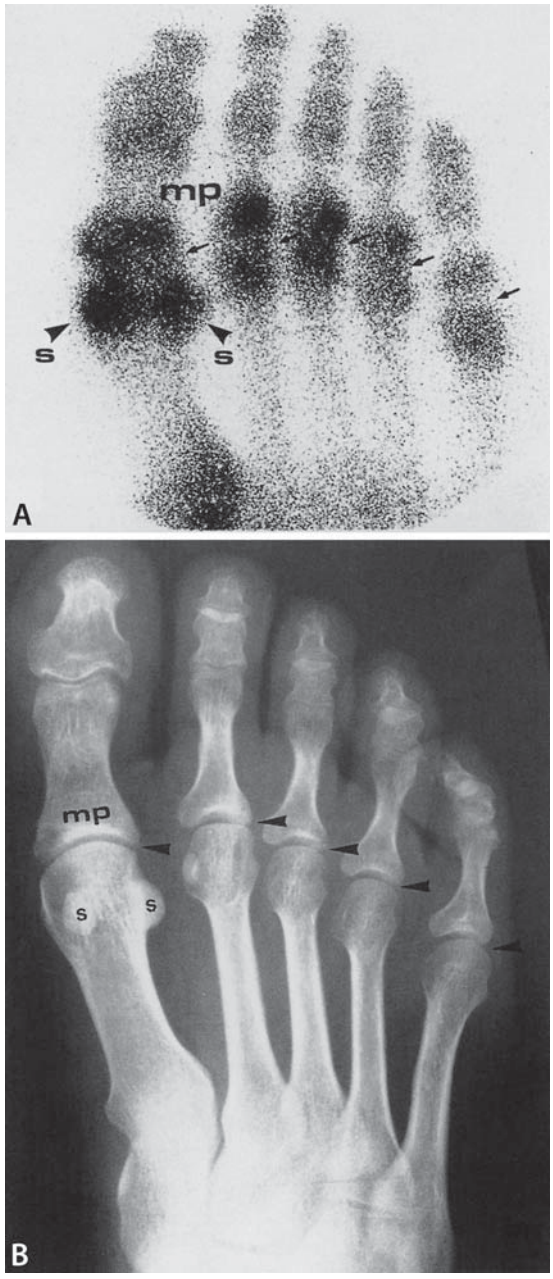

Fig. 4.39A, B Dorsal view of the forefoot. **A** Dorsal pinhole scintigraph of the right forefoot demonstrates the metatarsophalangeal joints in all five toes (*mp, arrows*). Tracer localizes more or less in the bases and heads of the metatarsals and phalanges. The two sesamoid bones of the first metatarsal head concentrate tracer intensely, reflecting their articular involvement (*arrowheads*). **B** Dorsoplantar radiograph identifies the metatarsophalangeal joints (*mp, arrowheads*) and the two first metatarsal sesamoids (*s*)

children, in whom the periarticular bones concentrate tracer intensely (Fig. 4.37). However, the dorsal scan visualizes every tarsal bone and intertarsal joint with acceptable clarity (Fig. 4.38). Finally, the metatarsophalangeal and interphalangeal joints are distinctly delineated by increased tracer uptake localized to the heads and bases of the metatarsals and phalanges, the equivalent of long bone ends where tendons and ligaments are attached (Fig. 4.39). The sesamoids at the plantar aspect of the first metatarsal head are shown as doubly enhanced tracer uptake due to articulation and the additive effect of tracer in the sesamoids and overlying first metatarsal head (Fig. 4.39).

References

Chung MH, Lee HJ, Kim SH, et al (1992) ^{99m}Tc-MDP uptake pattern of normal pubic bone. Korean J Nucl Med 26:333–337

Flanagan JJ, Maisey MN (1985) An atlas of normal skeletal scintigraphy. Wolfe Medical, London

Merrick MV (1987) The normal bone scan. In: Fogelman I (ed) Bone scanning in clinical practice. Springer, Berlin Heidelberg New York

5 Normal Variants and Artifacts

Myung-Hee Sohn and Yong-Whee Bahk

Recalling the expression "all is not gold that glitters", increased uptake is not necessarily pathological. Indeed, normal bone scintigraphs are often altered or modified by physiological or anatomical factors, imitating pathology (Howarth et al. 1996). For example, the tuberosity of the humerus and proximal tibia, to which the deltoid and quadriceps muscles are attached, respectively, may accumulate tracer intensely due to constant physical stress. Tracer uptake is normally increased in growing bones, either locally in the physes (Figs. 4.13 and 4.15) or generally in the entire skeleton, and also in anatomical variants. Modest tracer uptake may be observed in secondary ossification centers that have recently been fused (Fig. 4.31A).

A number of artifacts can be produced by various technical factors related to kit preparation or intravenous injection of radiopharmaceuticals, attenuation of gamma rays, or the function of the gamma camera and computer systems (Hung et al. 1996; Forstrom et al. 1996; O'Connor 1996).

Fortunately, artifacts possess characteristic features of their own so that their identification is straightforward in most instances. Conversely, however, it is also true that symptom-free bone lesions or congenital anomalies can exist, imposing diagnostic problems. As is well known, the tracer not accumulated by bone is excreted through the kidneys, occasionally disclosing unexpected renal or bladder diseases. It is not uncommon that the tracer retained in the renal calices, ureters, and bladder simulates a disease in bone. Radioactivity emitted from soft-tissue lesions is another source of mimicry of bone lesions (Gray and Krawnow 1996). Thus, many normal variants and artifacts can lead to erroneous diagnosis unless one becomes thoroughly familiar with them. This chapter describes some more common variants and artifacts that have a strong resemblance to real pathology. The artifacts related to the gamma camera and computer systems are beyond the scope of this book.

5.1 Normal Variants

5.1.1 Skull

The appearance and intensity of tracer uptake within the skull vary because the count rate is comparatively low and radioactivity distribution is usually uneven. A higher count rate is commonly observed in the peripheries of the skull due to curvature and perpendicular or tangential aligning of the scan detector. Accordingly, calvarial uptake may be diffusely or locally not uniform even in the absence of hyperostosis. Diffuse increased calvarial uptake related to postmenopausal osteoporosis is a rather common finding in elderly women (Senda and Itoh 1987) (Fig. 5.1A, B). Experience dictates that radiographic correlation is a necessity to accurately distinguish increased tracer uptake of simple cranial hyperostosis from pathological uptake of polycythemic cranial hyperostosis, iatrogenic osteoporosis, Paget's disease and renal osteodystrophy with osteomalacia (Fig. 5.1C, D).

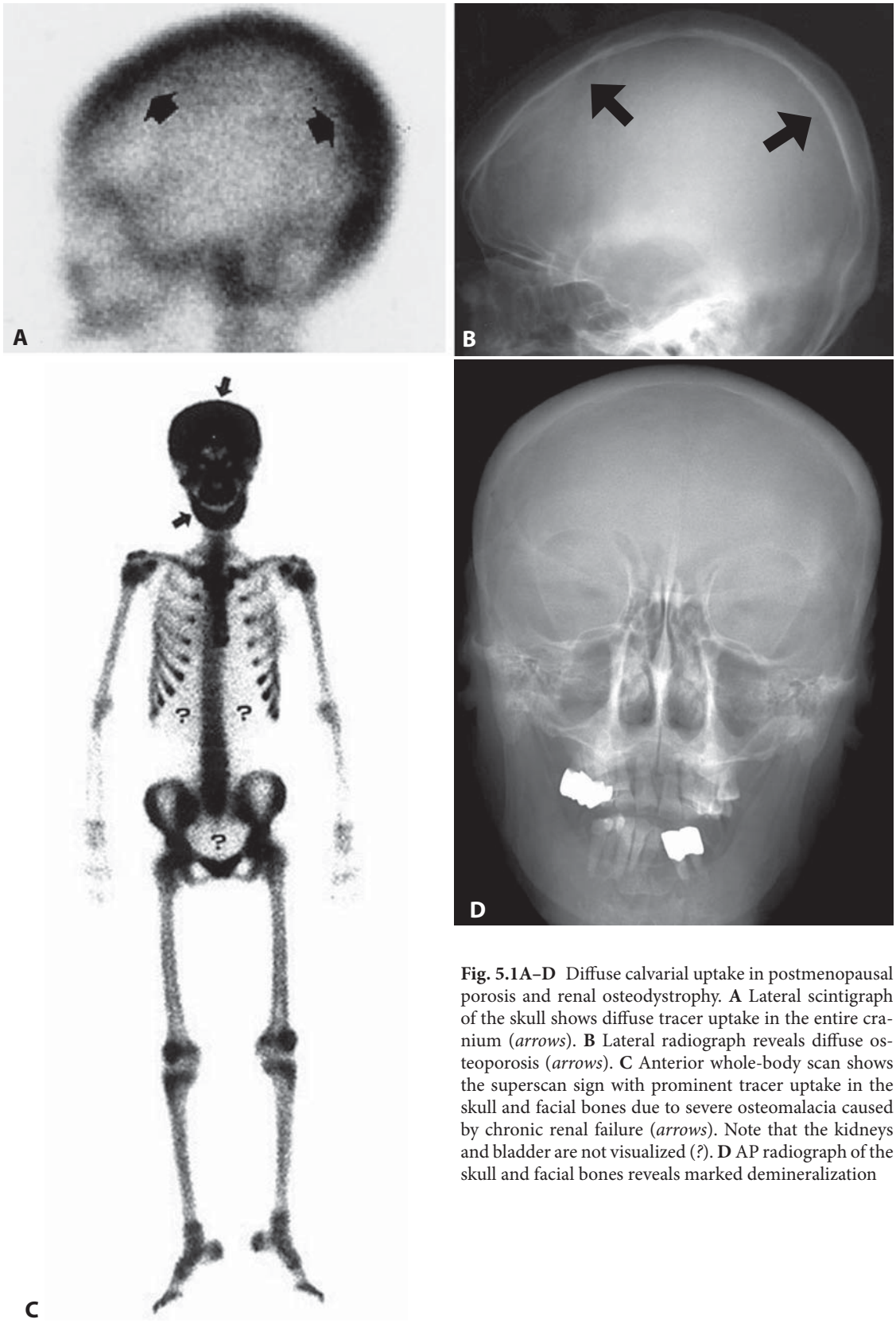

Fig. 5.1A–D Diffuse calvarial uptake in postmenopausal porosis and renal osteodystrophy. **A** Lateral scintigraph of the skull shows diffuse tracer uptake in the entire cranium (*arrows*). **B** Lateral radiograph reveals diffuse osteoporosis (*arrows*). **C** Anterior whole-body scan shows the superscan sign with prominent tracer uptake in the skull and facial bones due to severe osteomalacia caused by chronic renal failure (*arrows*). Note that the kidneys and bladder are not visualized (*?*). **D** AP radiograph of the skull and facial bones reveals marked demineralization

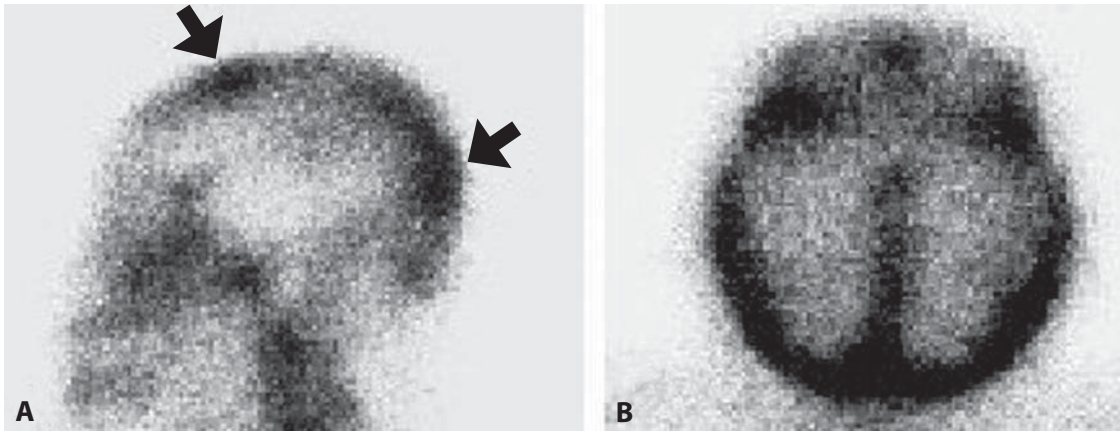

Fig. 5.2A, B Physiological sutural uptake. **A** Lateral scintigraph of the skull shows localized uptake in the coronal suture and the lambda (*arrows*). **B** Vertex view reveals cross-like uptake in the coronal and sagittal sutures

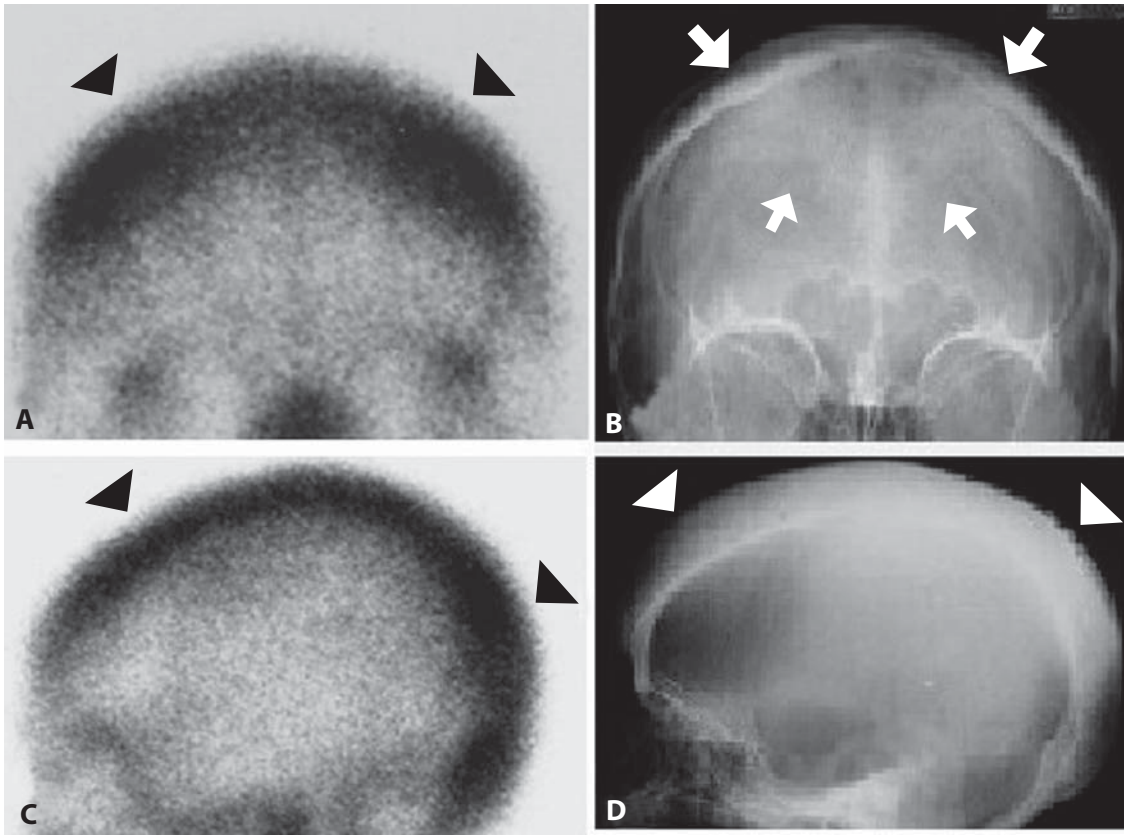

Fig. 5.3A–D Increased uptake in hyperostosis calvariae diffusa. **A** Anterior scintigraph of the skull shows symmetrical tracer uptake in both calvaria (*arrowheads*). **B** Anterior radiograph reveals diffuse inner table thickening (*arrows*). **C, D** Lateral scintigraph and radiograph show diffuse uptake and diploic thickening, respectively (*arrowheads*)

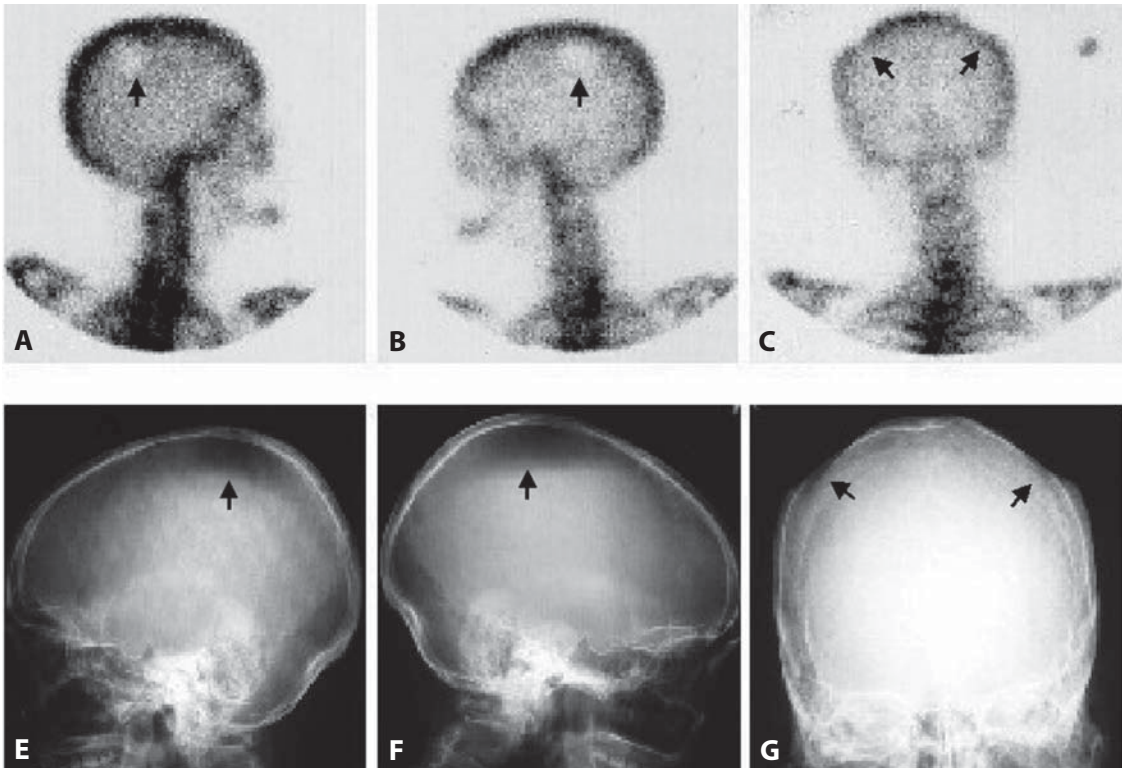

Fig. 5.4A–F Parietal bone thinning. **A, B** Right and left lateral scintigraphs of the skull show localized round photon defects in the parietal bones. **C** Semi-Towne's view scan shows symmetrical parietal photon defects. **D, E** Right and left lateral radiographs reveal lucent zones in both parietal bones. **F** Towne's view radiograph demonstrates typical scalloped appearance due to the absence of the outer table and diploë

Tracer uptake in normal sutures may simulate pathological uptake on the lateral view, but the vertex view can instantly solve the problem (Fig. 5.2). Hyperostosis frontoparietalis demonstrates symmetrical uptake in the thickened diploë of the frontal and parietal bones, typically in women (Fig. 5.3A, C). This has been speculated to result from raised levels of androgen and prolactin (Ceylan and Caner 2003). Radiography shows characteristic inner table thickening (Fig. 5.3B, D). New evolution of hyperostosis frontalis interna that was not present on previous scintigraphs has been reported to simulate metastasis in cancer patients receiving adjuvant chemotherapy. Conversely, parietal thinning causes symmetrical photopenia (Fig. 5.4A–C). This occurs in 0.25–2.37% of patients with a higher incidence in women (Rao and Lieberman 1980). The condition might be confused with myeloma or photopenic metastasis. Radiography reveals the absence of the outer table and diploë with the inner table remaining (Fig. 5.4D–F). Parietal foramina also produce photon defects in the parasagittal regions (Sty and Starshak 1983).

Foci of small spotty uptake in the skull are fairly common variants, occurring in 0.7% of 3000 bone scans (Harbert and Desai 1985). They are to be differentiated from benign lesions or even metastasis, especially in patients with known malignancy. The majority of such uptake occurs near or within a suture or parasagittal regions (Fig. 5.5 top). Radiography usually does not show changes to back-up scintigraphic findings. However, correlation with high-resolution CT may reveal anatomical bases such as vascular channels and sutural foramina (Fig. 5.5 bottom). Other etiologies are subradiographic cartilaginous rests and pachionian granulations. It is to be emphasized that seemingly trivial "hot"

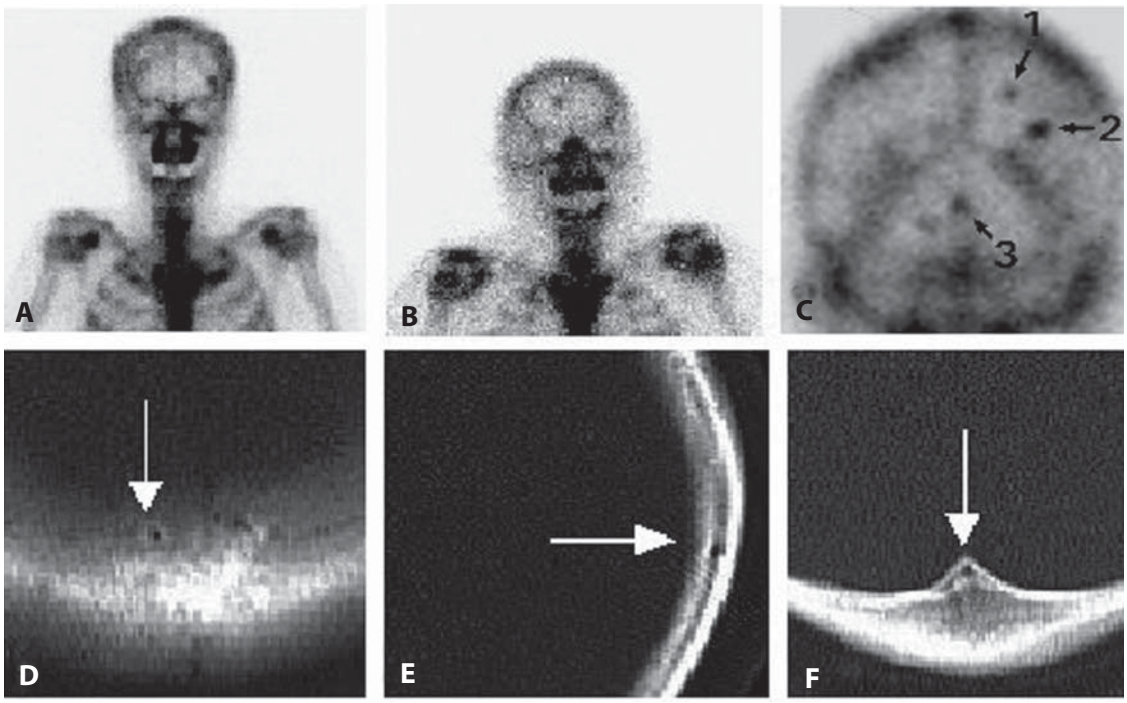

Fig. 5.5A–F Two different cases of a solitary spotty "hot" area and a case of multiple spotty "hot" areas in various parts of the skull. **A, B** The spotty hot area is shown in the left frontal bone and right parasagittal bone, respectively. **C** Two hot areas (*1, 2*) are located in the high and middle parietal regions and one (*3*) is in the posterior straight sinus. CT demonstrates vascular channels in *1* and *2* and a probable intrasutural cartilage defect in *3*. The foci in **A** and **B** had not changed in size on follow-up performed 1 year later. Skull radiographs were all negative (not shown here)

spots, especially those in the middle or lower cranial vaults, may represent true diseases such as osteoma, hemangioma, and even metastasis. As mentioned elsewhere, radiographic or CT correlation (Fig. 5.6A–D) and follow-up scanning at well-balanced intervals is the royal road (Fig. 5.6E, F). A shorter follow-up period is preferred to procrastination; for example, 3 months rather than 6 months especially when the primary tumor has a strong proclivity toward early metastasis. Not infrequently, prominent spotty uptake occurs in an "osteomatoid" variant of the frontal process of the maxillary bone (Fig. 5.6G, H). One survey in 200 consecutive patients of both sexes (male 58%, female 42%) revealed the "osteomatoid frontal process" in 6%. It occurred on the right and the left in 58% and 42%, respectively (Bahk 2005, unpublished data). All patients were free of symptoms.

The tracer uptake in the temporal bone due to malignant otitis or chronic mastoiditis may simulate metastasis (Hirano et al. 1998). Radiographic and clinical correlations are essential for differential diagnosis. Spotty areas of tracer uptake in the mandible and maxilla are common, and the majority are odontogenous in nature.

5.1.2 Neck

The atlantooccipital joint and the spinous process of C7 normally accumulate tracer, and increased uptake in the C2 spinous process is also a physiological finding (Murray and Frater 1994) (Fig. 5.7). However, in patients with known or suspected cervical trauma, such a finding must be interpreted with caution. The increased tracer uptake in the spinous processes of C2 and C7 may occur in those who strain the neck more or less regularly during sport or occupational activities. Differential diagnostic problem may arise when the neck is traumatically sprained (Figs. 16.14 and 16.15).

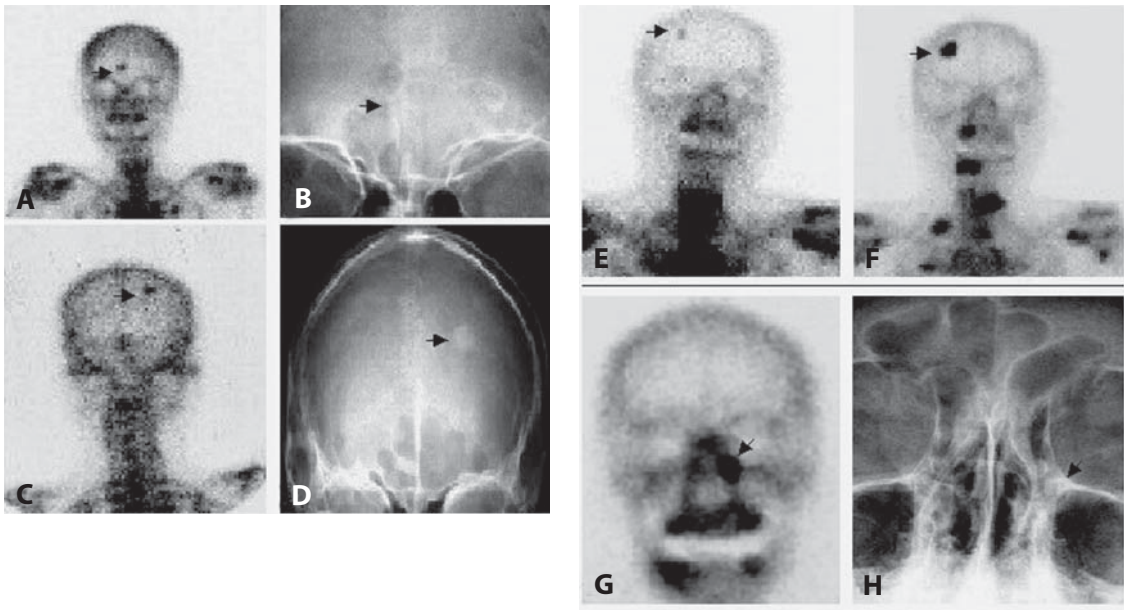

Fig. 5.6A–H Various diagnoses of solitary spotty "hot" areas in the skull. **A, B** Anterior scintigraph and radiograph, respectively, show a spotty hot area and osteoma in the right frontal sinus. **C, D** Posterior scintigraph and Towne's view radiograph, respectively, show hot area and sclerotic bone of osteoma in the left posterior parietal bone. **E, F** Serial anterior scans of the skull show insidious evolution of solitary metastasis from lung carcinoma in the right frontal bone over a period of 6 months. The initial scan shows a tiny uptake and the 6-month follow-up shows significant growth. **G, H** Anterior scintigraph and radiograph, respectively, show a small, spotty hot area and a small compact bone of "osteomatoid variant" in the frontal process of the left maxillary bone

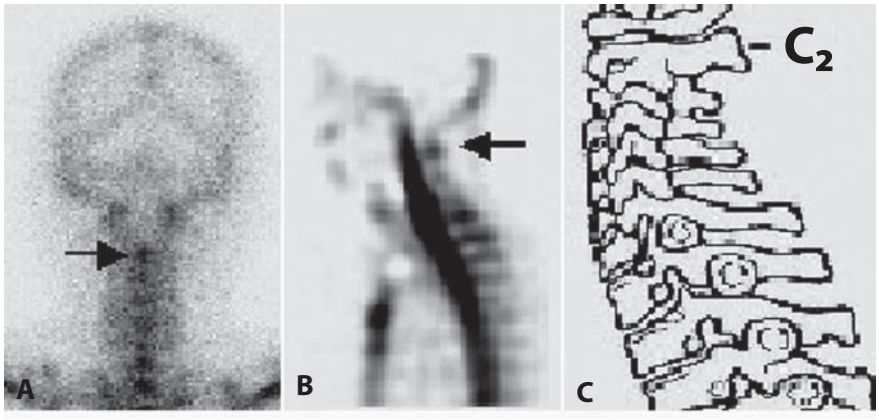

Fig. 5.7A, B, C Physiological prominence of the C2 spinous process. **A** Posterior scintigraph of the cervical spine shows focal uptake in the C2 spinous process (*arrow*). **B** Sagittal SPECT confirms spotty uptake to involve the C2 spinous process (*arrow*). **C** Schematic drawing of the cervical spine shows the prominent C2 spinous process

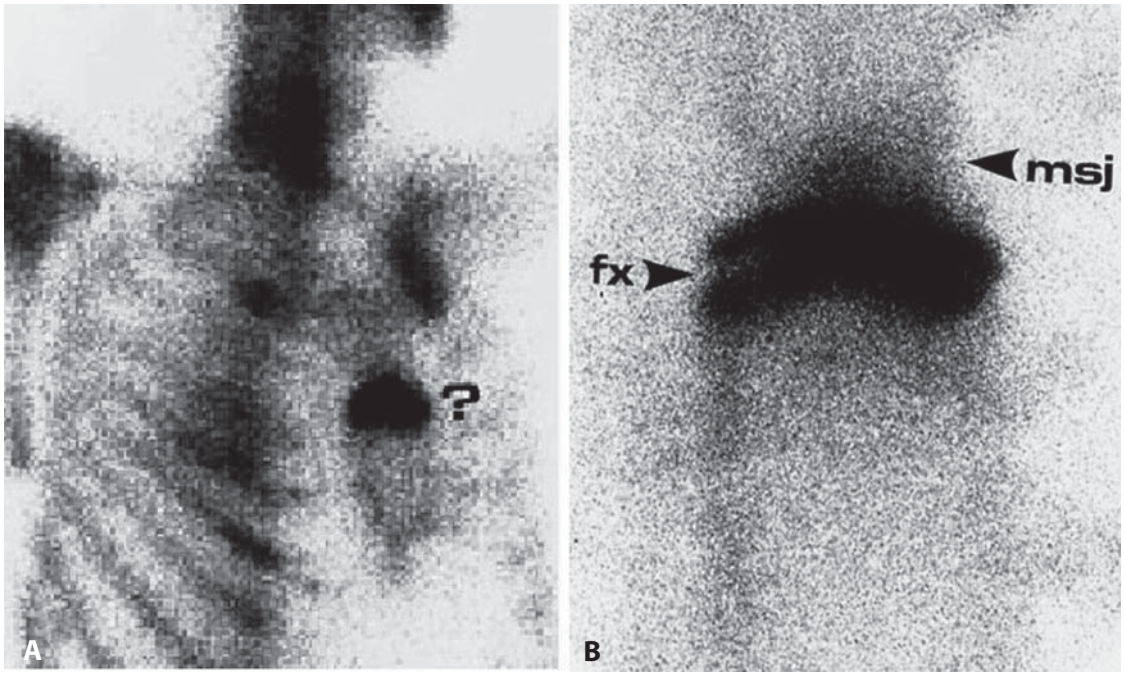

Fig. 5.8A, B Value of pinhole scintigraphy in studying the sternum. **A** Oblique planar scintigraph of the sternum with traumatic injury shows an ovoid uptake (*?*). **B** Pinhole scintigraph reveals fractures involving the upper edge of the body (*fx*) with a well-preserved manubriosternal joint (*msj*)

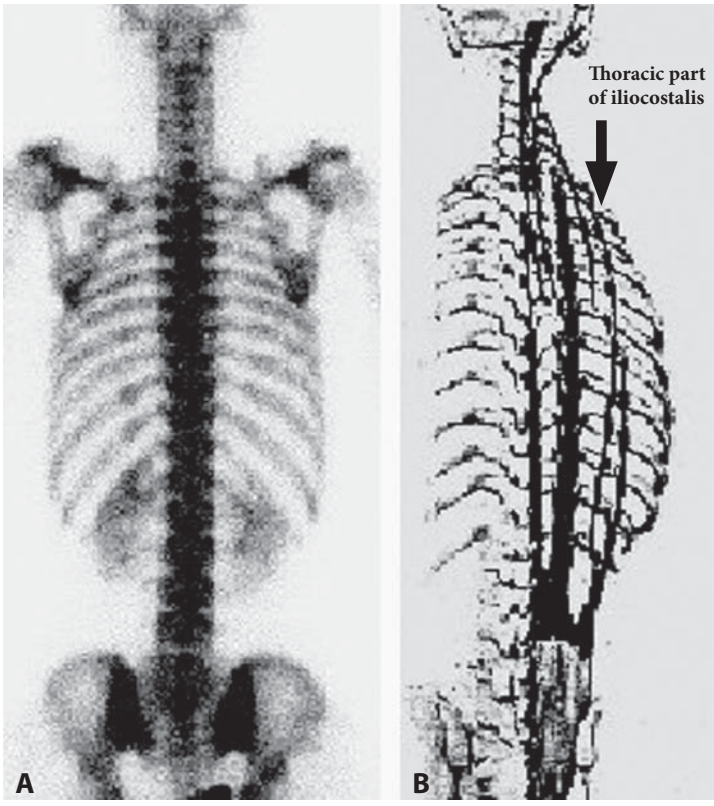

Fig. 5.9A, B Rib stippling. **A** Posterior scintigraph of the axial skeleton shows multiple longitudinal rosary-like spotty uptake in the posterior arcs of the ribs parallel to the spine bilaterally, indicating insertions of the iliocostalis portion of the erector spinae musculature. **B** Schematic drawing

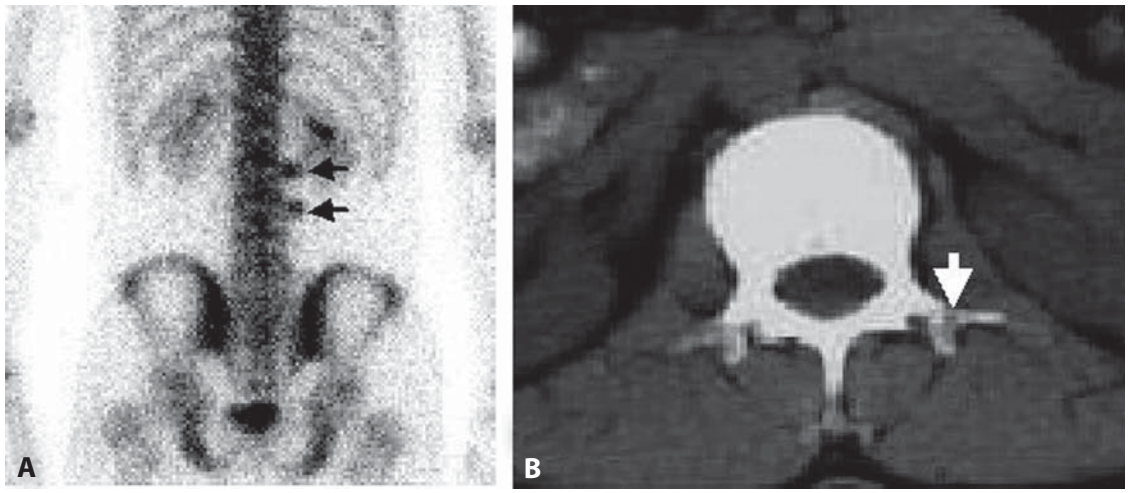

Fig. 5.10A, B Secondary ossification centers of the transverse processes seen in a 17-year-old male. **A** Posterior scintigraph of the lumbar spine shows two small spotty uptakes in the right transverse processes of L2 and L3. **B** Transverse CT image through L2 shows a small low density in the right transverse process (*arrowhead*). No history of trauma

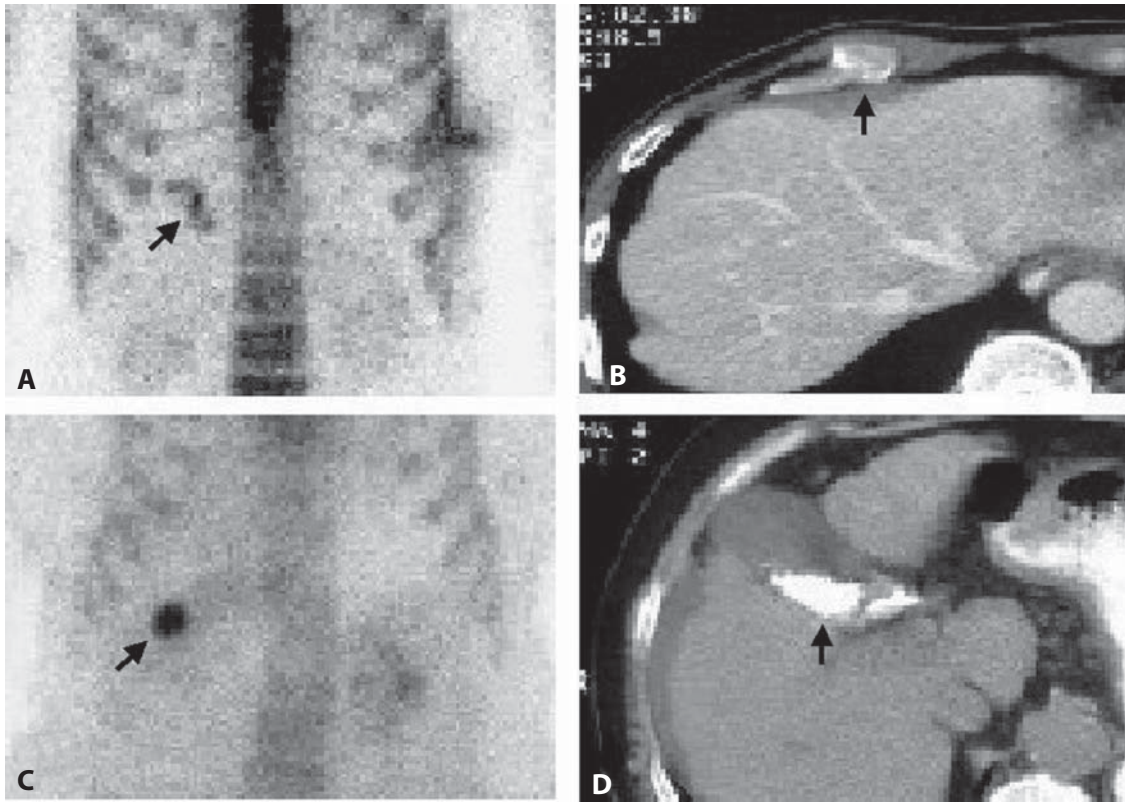

Fig. 5.11A–D Focal uptake in the right upper abdomen. **A, B** Anterior scintigraph of the abdomen and transverse CT of right rib 6, respectively, show spotty tracer uptake and physiological rib cartilage mineralization. **C, D** Anterior scintigraph of the abdomen and transverse CT of the gallbladder, respectively, show tracer uptake and a calcified stone

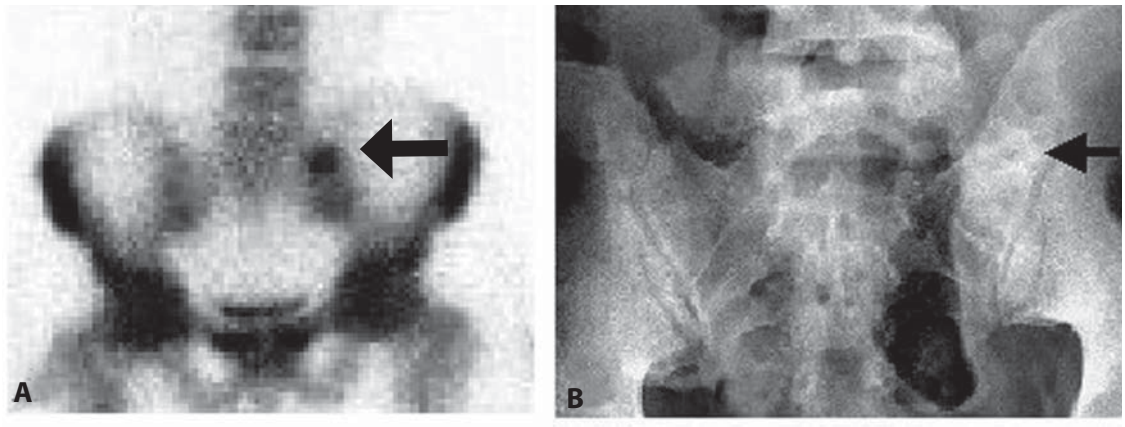

Fig. 5.12A, B Osteoarthritis of the transitional lumbosacral joint. **A** Anterior scintigraph shows a spotty uptake in upper part of the left sacroiliac joint (*arrow*). **B** AP radiograph confirms transitional joint with irregular sclerosis (*arrow*)

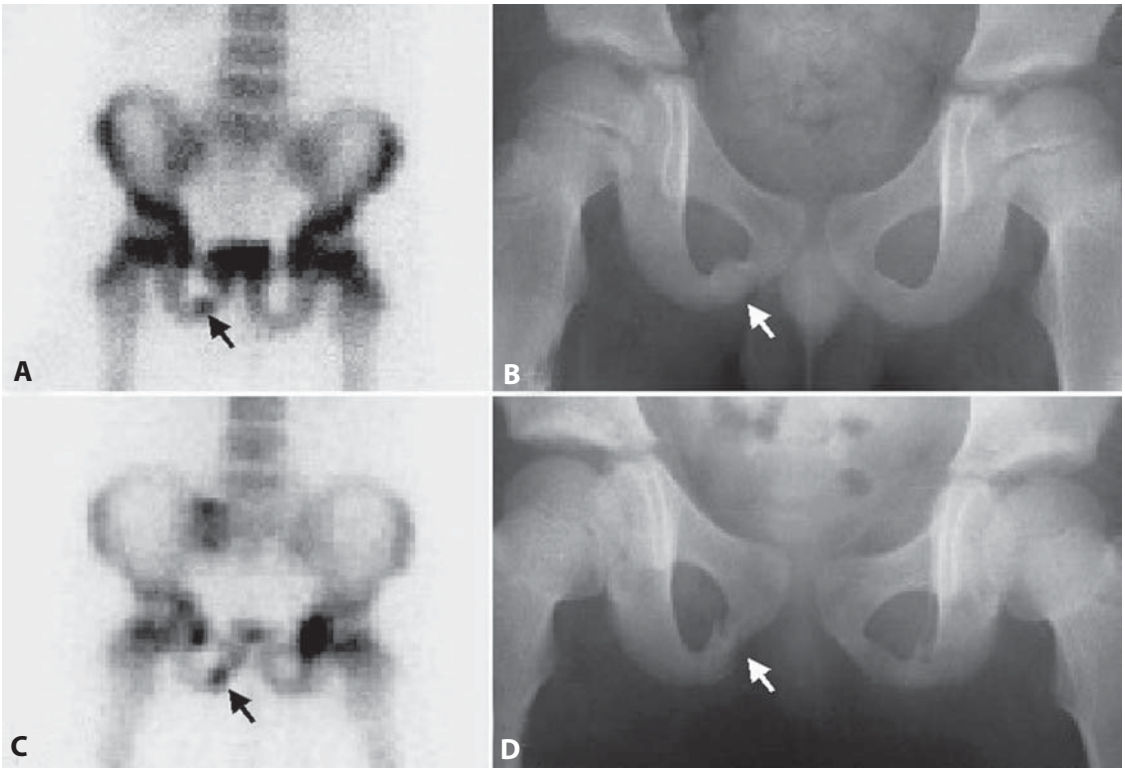

Fig. 5.13A–D Uptake in ischiopubic synchondrosis. **A, B** Anterior scintigraph and AP radiograph of the pelvis in a 7-year-old boy demonstrates physiological tracer uptake and cartilaginous remnant. **C, D** Anterior scintigraph and AP radiograph of the pelvis in a 5-year-old girl with fracture of the right inferior pubic ramus respectively show a hot area and fracture

5.1.3 Thorax

The size, shape, and tracer uptake of normal sternum vary greatly. The sternum develops and ossifies from six different ossification centers: one for the manubrium, four for the body, and one for the xiphoid process. Any of these centers may show locally increased uptake. The increased uptake in the manubriosternal junction is physiological. However, high or wayward uptake should not be misread as normal, especially in those who have a history of trauma or malignancy. It is not rare in these situations that pinhole scintigraphy plays a decisive role in arriving at a correct diagnosis (Fig. 5.8). Localized incomplete fusion of the sternal body creates a hole in the lower sternum, and conversely sternebrae show increased uptake. Rosary-like tracer uptake may appear where the iliocostalis thoracis portions of the erector spinae muscle group insert within the posterior angles of the ribs, unilaterally or bilaterally. This is called "rib stippling" (Fink-Bennet and Johnson 1986) (Fig. 5.9). The specific localization and characteristic appearance should suffice to avoid confusion.

5.1.4 Spine and Abdomen

Focal uptake can be caused in the transverse process of the spine by the persistence or incomplete fusion of the secondary ossification centers (Fig. 5.10). Ossification centers usually ossify at puberty and fuse with the primary centers by the age of 25 years. If fusion fails to occur at the scheduled time, they persist and show increased tracer uptake. The uptake, as in the growth plates of the long bones, is maximal at the time of the initiation of fusion and gradually reduces thereafter as fusion is completed. Such uptake can easily be mistaken for a fracture, especially when the patient is traumatized. Occasionally, calcified rib cartilages, gallstones, or hepatic tumors accumulate tracer, posing diagnostic problems (Fig. 5.11).

5.1.5 Pelvis

Blood-flow and blood-pool may be increased in the uterus in women of reproductive age during the early phase of nuclear angiography (Mandell et al. 1986). Its likely basis is endometrial hyperemia during the secretory phase and hemorrhage or necrosis during the menstrual phase. Early pregnancy produces uterine blushing due to myometrial hyperplasia, hyperemia, and edema (Lim et al. 2001b). Sanitary tampons in menstruating women are known to show radioactivity, mimicking bladder diverticulum or a calcified tumor. In men an area of increased blood flow appears in the pudendum due to penile erection. Focal uptake occurs in bone biopsy sites and the transitional lumbosacral joint with degenerative change (Fig. 5.12). Nonvisualization of the sacrum with severe osteoporosis is not uncommon in the elderly. It is well known that in children between the ages of 4 and 12 years, small spotty "hot" area(s) may appear in the inferior ischiopubic synchondrosis (Fig. 5.13A, B). In patients with a history of trauma and local pain, such uptake should be differentiated from fracture (Fig. 5.13C, D).

The anterolaterosuperior aspect of the femoral head is not covered by the acetabulum because the anterior rim is receding and shallow. Accordingly, the femoral heads may fallaciously appear photopenic on the anterior view but are visible on the posterior view. Tracer retained in an incompletely voided bladder can mimic a lesion of the pubic bone, and a modified angle of view can solve the problem (Fig. 5.14).

5.1.6 Limbs

Well-circumscribed tracer uptake, the "delta" sign, is seen within the proximal mid-shaft of the humerus in 7% (Fink-Bennet and Vicuna-Rios 1980). The uptake is either bilateral or unilateral, and mimics pathology (Fig. 5.15A, B). The finding reflects the presence of a well-developed deltoid tuberosity, to which the distal portion of the deltoid muscle is attached. Rarely, metastasis or myeloma can cause similar uptake (Lim et al. 2001a) (Fig. 5.15C, D). Like the deltoid tuberosity of the humerus, the tuberosity of the proximal tibia intensely accumulates tracer due to infrapatellar ligamental attachment (Eggli and Tulchinsky 1996) (Fig. 5.16). The herniation pits of the femoral

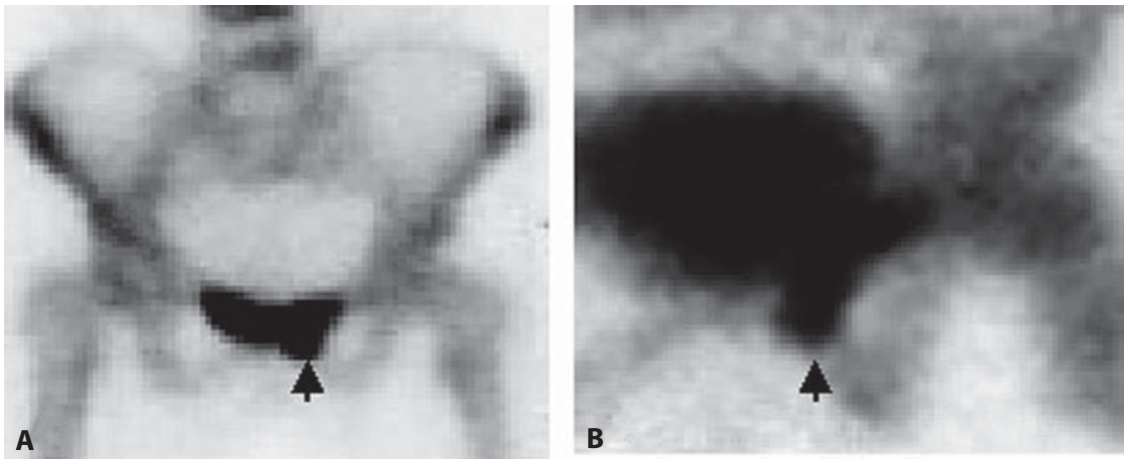

Fig. 5.14A, B Value of angled view in pelvic bone imaging. **A** Anterior scintigraph of the pelvis shows inferiorly protruding bladder activity (*arrow*). **B** Oblique scintigraph of the same patient shows the bladder to be completely separated from a bony lesion (*arrow*)

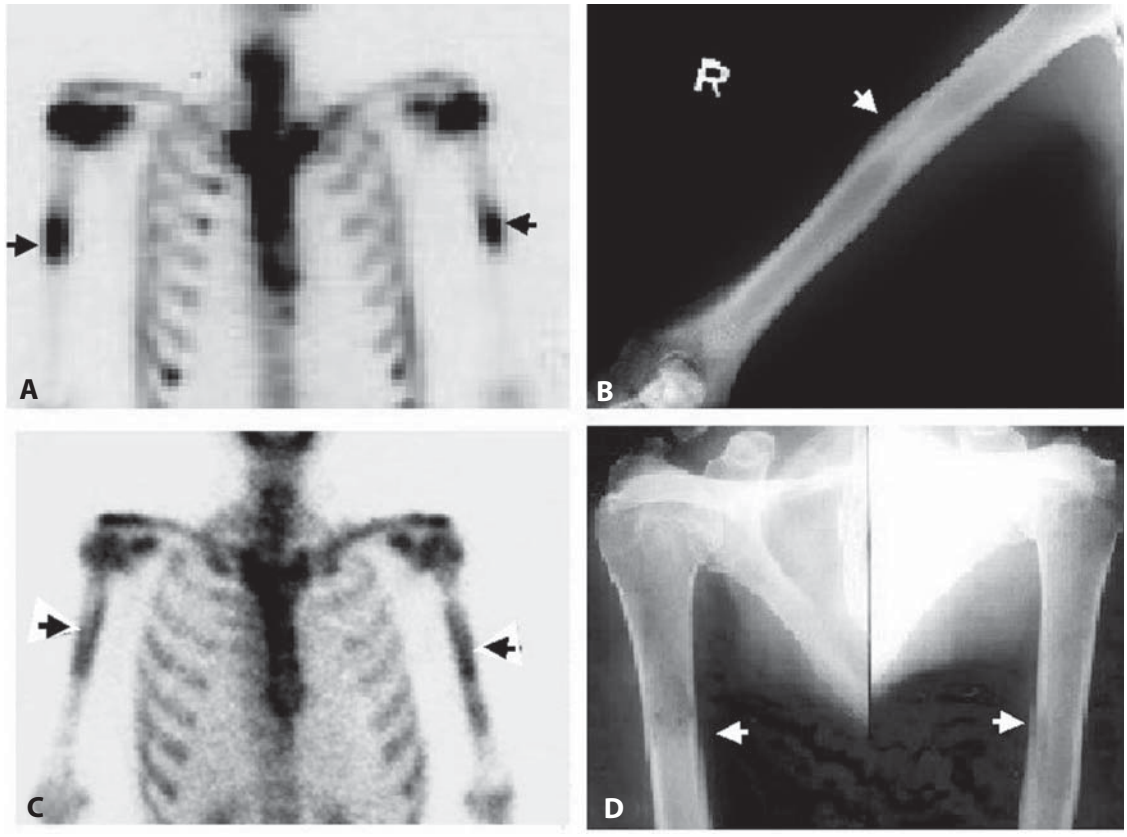

Fig. 5.15A–D The "delta" sign and metastasis. **A, B** Anterior scintigraph of both humeri and AP radiograph of the right humerus respectively show small segmental uptake in the midshafts and the deltoid tuberosity. These are physiological and referred to as the "delta" sign. **C, D** Anterior scintigraph and AP radiographs of both humeri respectively demonstrate symmetrical small segmental uptake and osteolysis in the midshafts, denoting cancer metastases (*arrowheads*). The findings in **C** and **D** are similar but are not the same patient

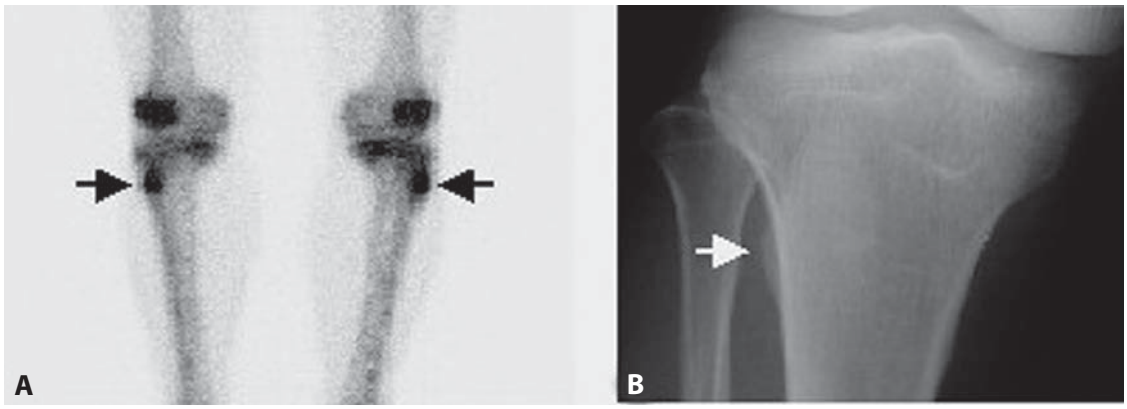

Fig. 5.16A, B Physiological uptake in the tibial tuberosities. **A** Anterior scintigraph of the knees shows increased uptake in the proximal tibia (*arrows*). **B** AP radiograph of the right knee shows prominent tuberosity (*arrow*)

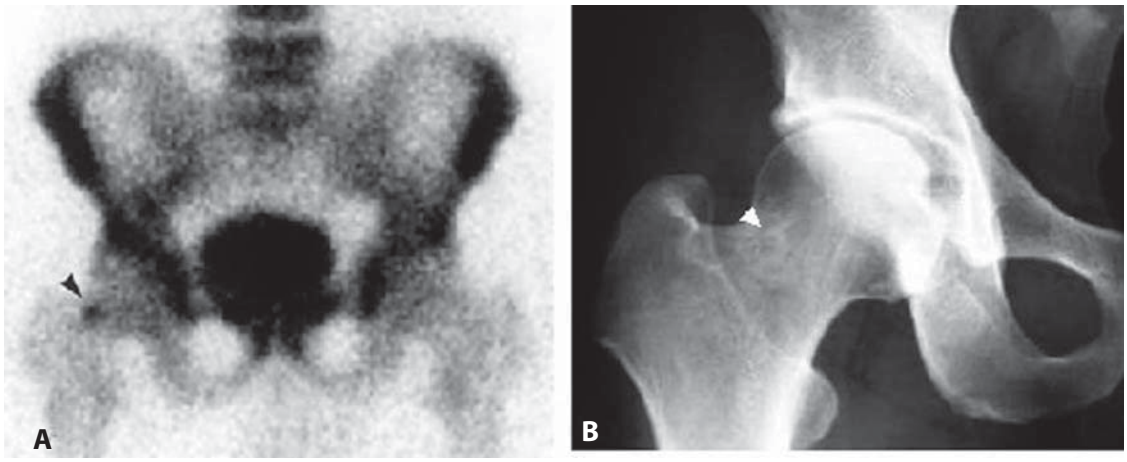

Fig. 5.17A, B "Hot" spotty uptake in herniation pit. **A** Anterior scintigraph of the pelvis shows spotty uptake in the right femoral neck (*arrowhead*). **B** AP radiograph reveals herniation pit with reactive sclerosis (*arrowhead*)

neck are fairly common, with prevalence of 4–5%. The pit is formed by the herniation of fibroconnective tissue and fluid through a cortical defect (Pitt et al. 1982). Occasionally, pits are painful, especially in athletes (Daenen et al. 1997). Most pits do not accumulate tracer visibly, but with stress they become visible (Fig. 5.17A). Caution must be used in their interpretation because metastasis or fracture occasionally creates a similar finding. Radiography is helpful in most cases (Fig. 5.17B). Increased tracer uptake in the patella (the "hot patella" sign) is common, occurring in 15% of 100 consecutive patients (Kipper et al. 1982). Like the herniation pit, the hot patella is not a normal variant in the strict sense, but may present without symptoms or etiology. The pathological hot patella can be observed in association with osteoarthritis (Fig. 9.15), chondromalacia (Fig. 9.18), metastasis (Fig. 17.35), fracture, and bursitis (Bahk et al. 1994).

Not uncommonly, long curvilinear uptake may appear within the muscles of the thighs medially to the femora in the elderly (Fig. 5.18A). In the great majority it is due to calcification of sclerotic arterial walls (Fig. 5.18B).

5.1.7 Accessory Navicular Bone

The navicular accessory bone is located at the medial aspect of the navicular bone proper. Its

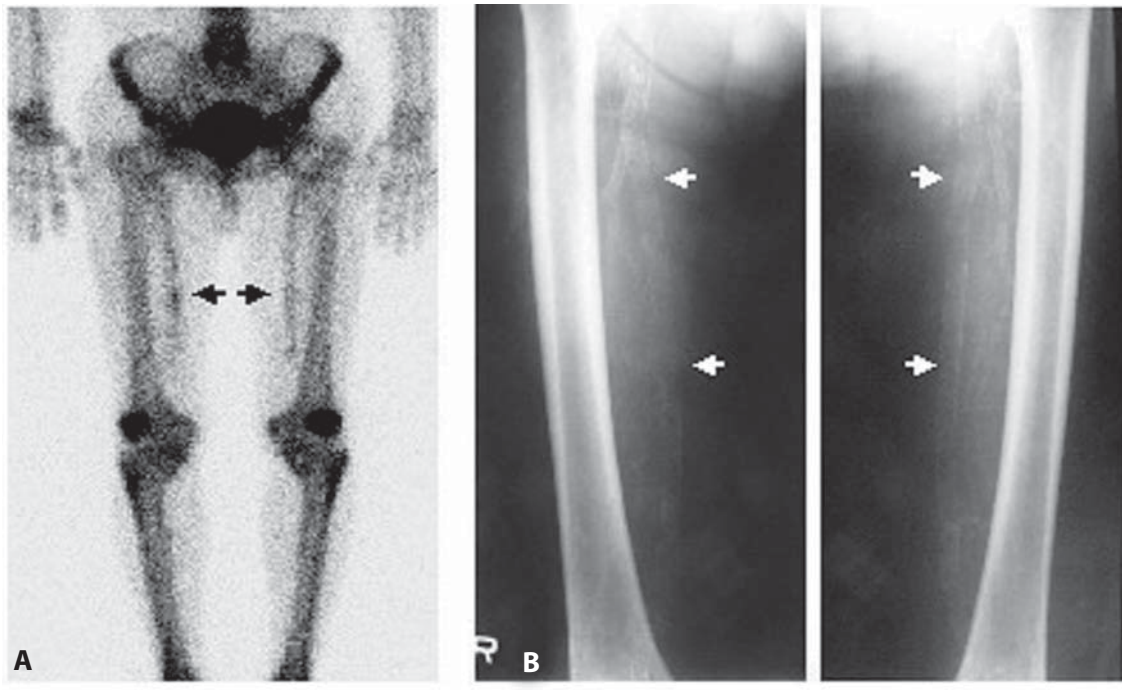

Fig. 5.18A, B Vertical linear uptake in calcified femoral arteries. **A** Anterior scintigraph of both thighs shows long linear uptake in the medial aspects of both thighs (*arrows*). **B** AP radiograph reveals diffusely calcified femoral arteries (*arrows*)

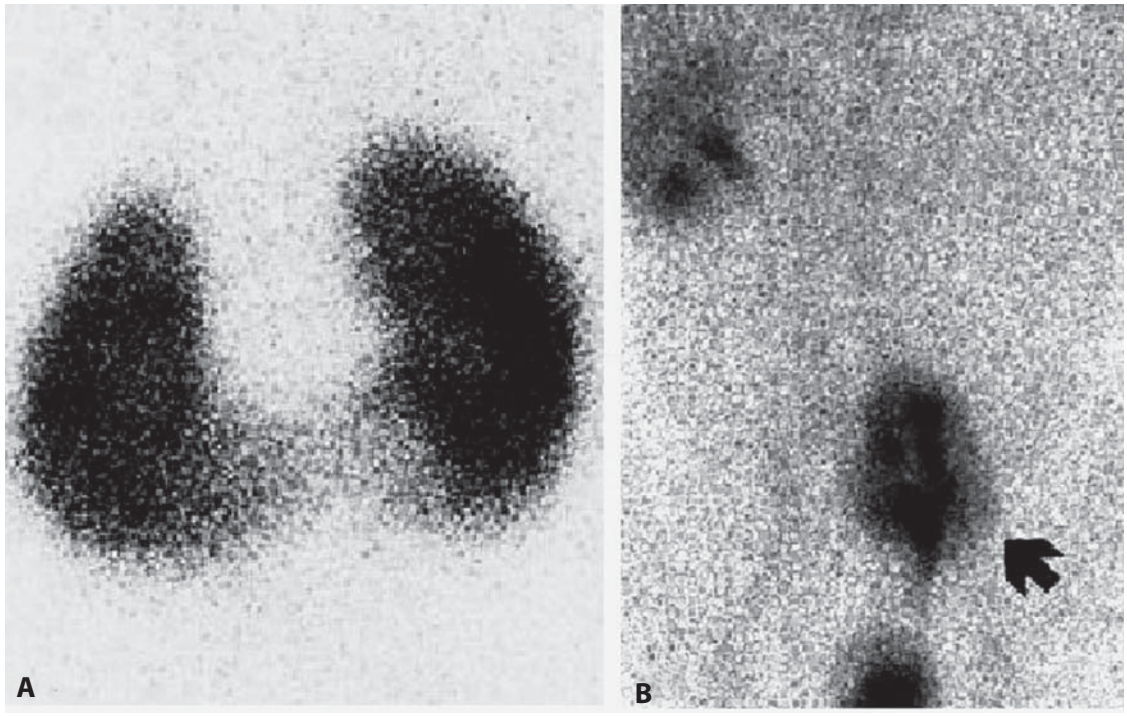

Fig. 5.19A, B Horseshoe kidney and ectopic kidney. **A** Posterior scintigraph of the abdomen shows horseshoeing of the kidney with fused isthmus. **B** Anterior scintigraph of the left lower abdomen reveals an ectopic kidney (*arrow*) and bladder connected by a short ureter

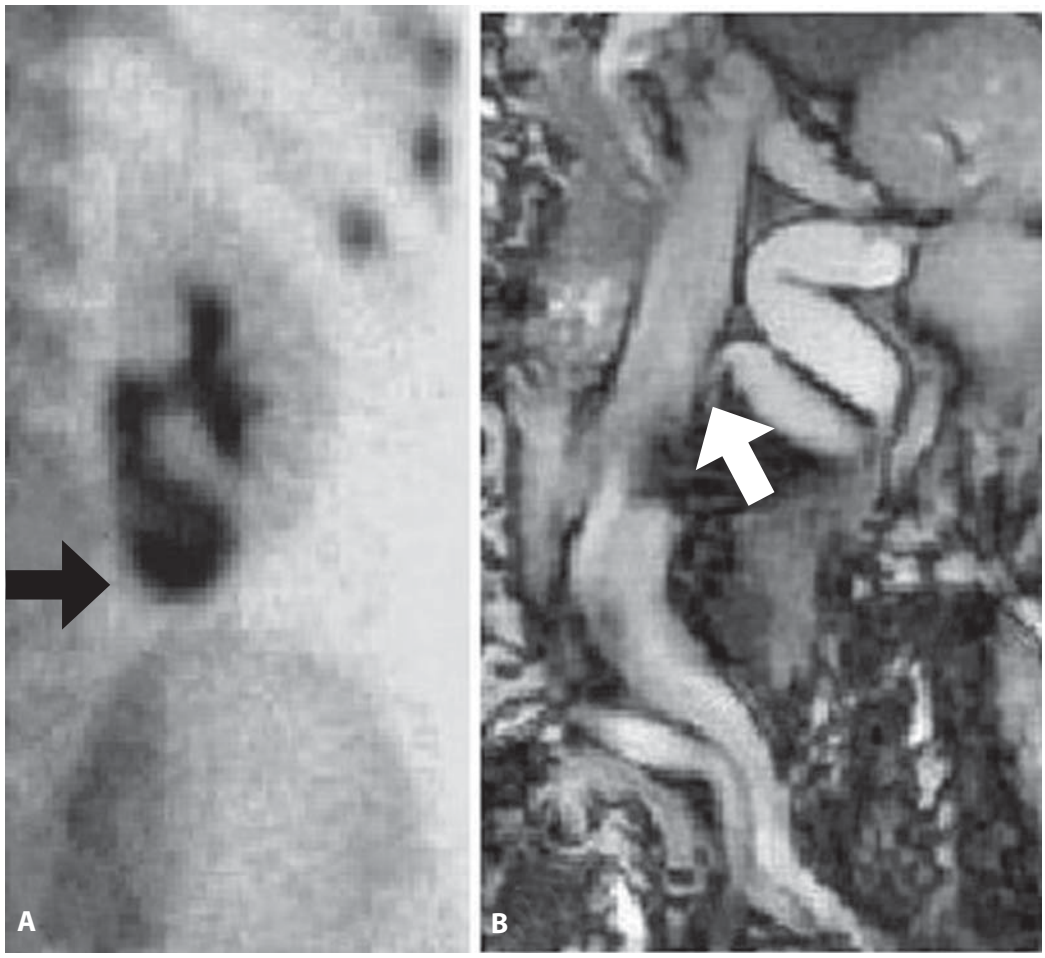

Fig. 5.20A, B Retrocaval ureter. **A** Posterior scintigraph of the abdomen shows moderate dilatation of the right renal calices, pelvis, and ureter due to ureteral obstruction at the L4-5 level (*arrow*). **B** MRI reveals compression of the right ureter by the inferior vena cava and dilated proximal ureter with kinking (*arrow*)

occurrence is either unilateral or bilateral (Lawson et al. 1984). Our recent scintigraphic study of 200 consecutive patients, 92 men and 108 women, with ages ranging from 20 to 68 years, showed the incidence of bilateral and unilateral accessory navicular bone(s) to be 0.5% and 3.5%, respectively, without gender predilection (Fig. 9.51).

5.1.8 Urogenital System

As mentioned earlier ^{99m}Tc-MDP excreted through the kidneys detects renal, ureteral, or bladder diseases of congenital or acquired origin. Horseshoe kidney (Fig. 5.19A), ectopic kidney (Fig. 5.19B), and retrocaval ureter (Fig. 5.20) belong to the former category and renal tumors, ureteral obstruction, vesicoureteral reflux (Fig. 5.21A), and ureterocele (Fig. 5.21B) belong to the latter.

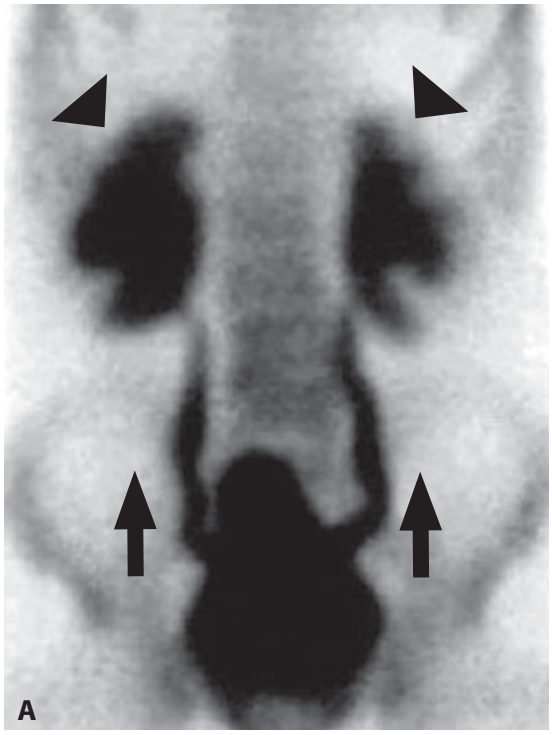

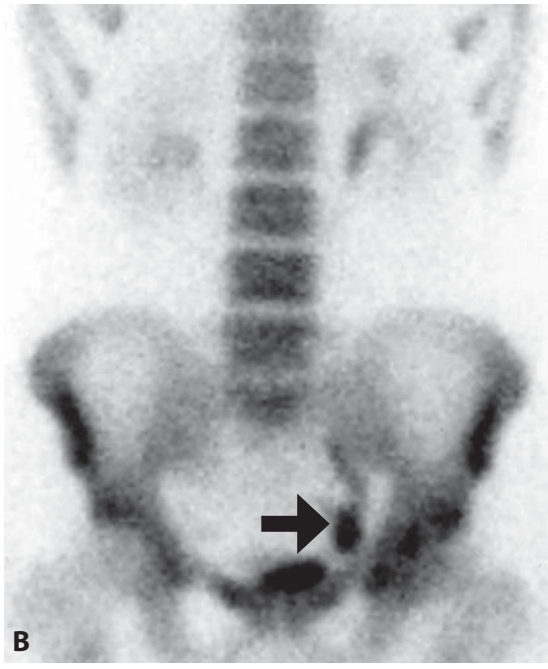

Fig. 5.21A, B Vesicoureteral reflux and ureterocele. **A** Anterior whole-body ^{99m}Tc-MDP bone scan in a 52-year-old male patient incidentally shows overt vesicoureteral reflux (*arrows*) with marked hydronephroses (*arrowheads*). **B** Anterior whole-body ^{99m}Tc-MDP bone scan in another 52-year-old male reveals the "cobra head" sign of ureterocele on the left (*arrow*). Note associated ureteral and calyceal dilatation

5.2 Artifacts

5.2.1 Radiopharmaceuticals and altered body chemistry and anatomy

Free 99mTc pertechnetate liberated in air-induced vial or delayed use of prepared kit may be deposited in the thyroid gland, salivary glands and gastric mucosa (Fig. 5.22 A). Altered body chemistry such as hypercalcemia causes extraosseous deposition of 99mTc-MDP in the lungs and stomach (Fig. 5.22 B). 99mTc-MIBI used a day before for cardiac scan is excreted via the liver at the time of bone scan and confusingly visualizes the bile ducts and bowel loops (Fig. 5.22 C) and bladder fistula also artifactually visualizes the intestine on bone scan (Tsai et al. 1999) (Fig. 5.22 D). Besides, the presence of aluminum ions or water in the kit leads to the formation of ^{99m}Tc-colloids that are phagocytosed by the reticuloendothelial cells, visualizing the liver and spleen. Visualization of the gallbladder has also been reported (Hung et al. 1996). When plural scintigraphic studies are performed in the same patient, the administration of the second agent before adequate clearance and decay of the first may create artifacts (Howarth et al. 1996). For example, ^{67}Ga citrate used for lymphoma can leave disturbing background activities behind on ^{99m}Tc-MDP scans. This is the result of significant down-scatter and septal penetration of medium-energy ^{67}Ga emission into the 140-keV energy window of ^{99m}Tc-MDP used for bone scanning.

5.2.2 Injection and Tourniquet Artifacts

Intravenous injection of tracer and release of a tourniquet may result in a sudden increase in blood flow in the limb distal to the tourniquet, causing the tourniquet effect during the blood-flow and blood-pool imaging of nuclear angiography (Desaia and Intenzo 1984) (Fig. 5.23). Delayed scintigraphy is usually little affected, but rarely undesirable change may occur when a tourniquet has been applied for a prolonged period of time, for example 15 minutes (Orzel et al. 1989). In order to prevent this occurring,

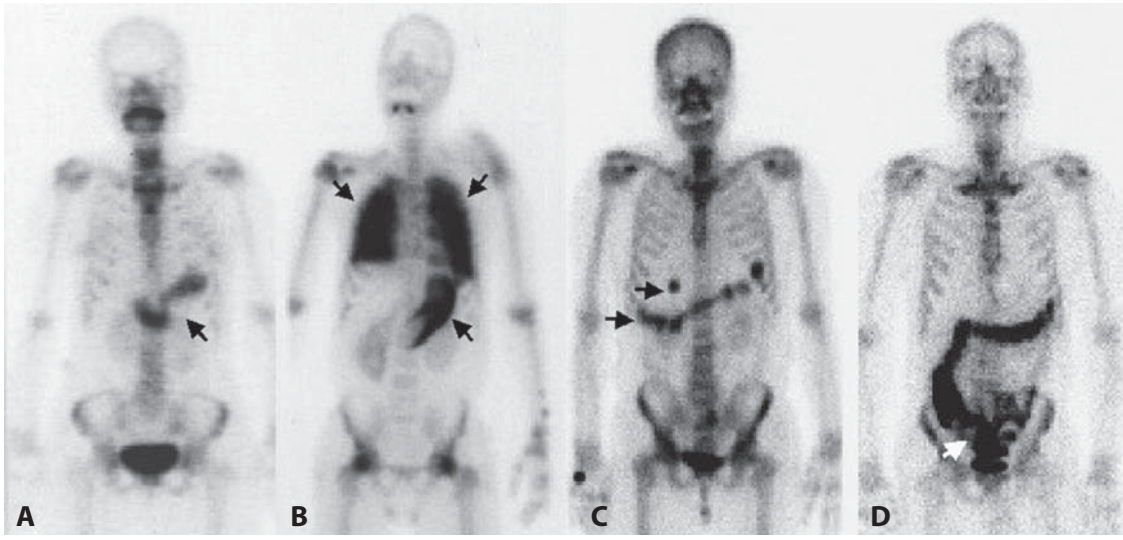

Fig. 5.22A–D Examples of various artifactual extraosseous uptake in ^{99m}Tc-MDP scans. **A** Anterior scan shows free pertechnetate in the stomach (*arrow*). **B** Diffuse tracer uptake in the lung (*upper arrows*) and stomach (*lower arrow*) due to hypercalcemia. **C** Normal ^{99m}Tc-MDP bone scan with confusing residual ^{99m}Tc-MIBI activities in the biliary tract (*upper arrow*) and colon (*lower arrow*) from MIBI cardiac scan performed 1 day before. **D** Tracer bypassed into the urinary bladder through a fistula between the bladder and colon (*arrow*)

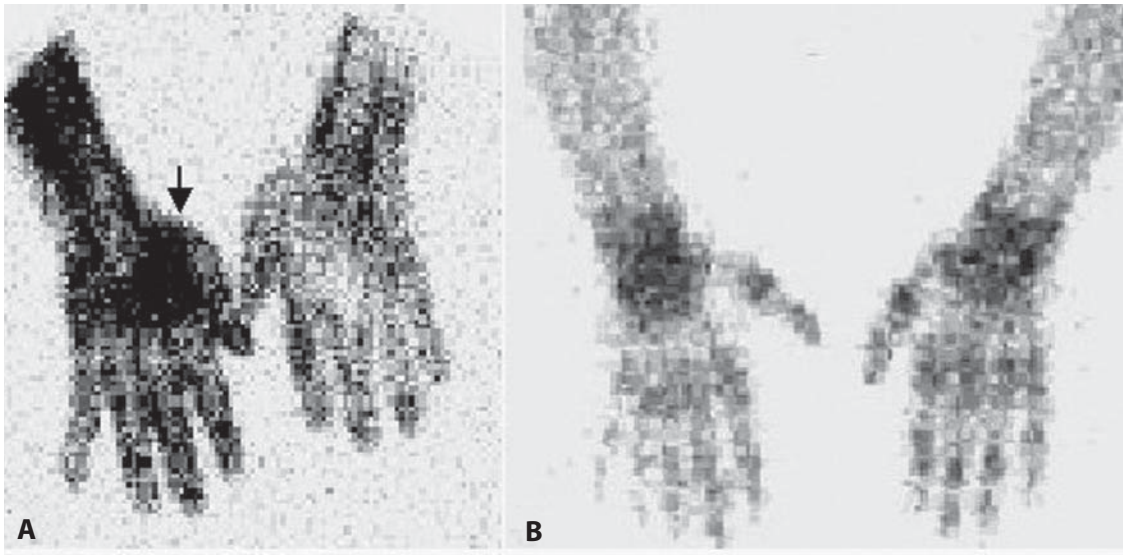

Fig. 5.23A, B Tourniquet effect. **A** Blood flow image after sudden release of tourniquet shows increased vascularity in the left forearm and palm (*arrow*). **B** Delayed image reveals passing of the transient hyperemia

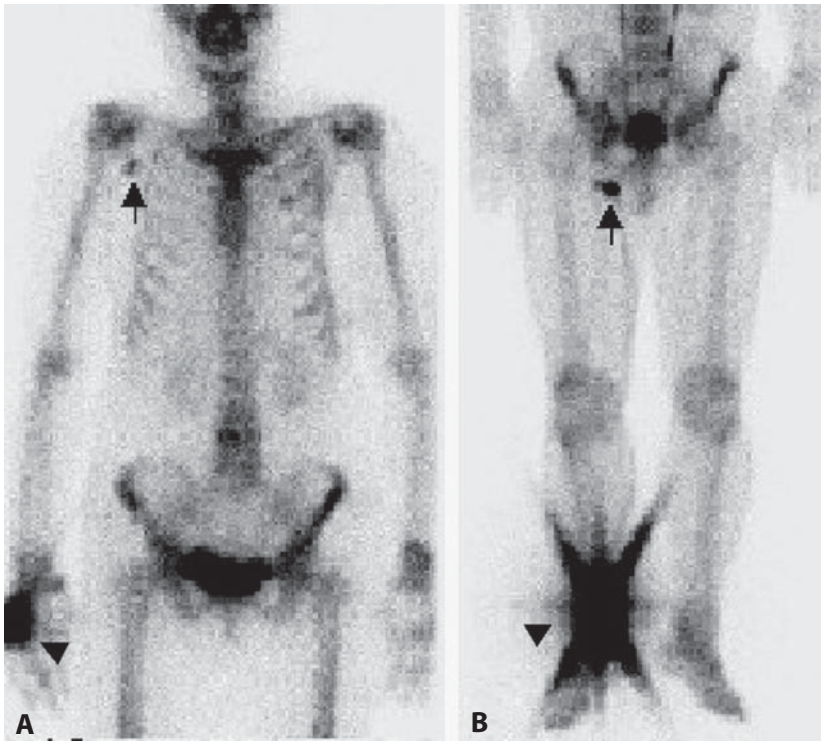

Fig. 5.24A, B Lymph node visualization by extravasated tracer in two different patients. **A** Anterior ^{99m}Tc-MDP bone scan of the trunk shows tracer accumulated in a small right axillary lymph node (*arrow*) after tracer leakage in the ipsilateral hand (*arrowheads*). **B** Anterior ^{99m}Tc-MDP bone scan of the lower limbs reveals tracer accumulated in a small right inguinal lymph node (*arrow*) following the trace leakage in the ipsilateral ankle (*arrowheads*)

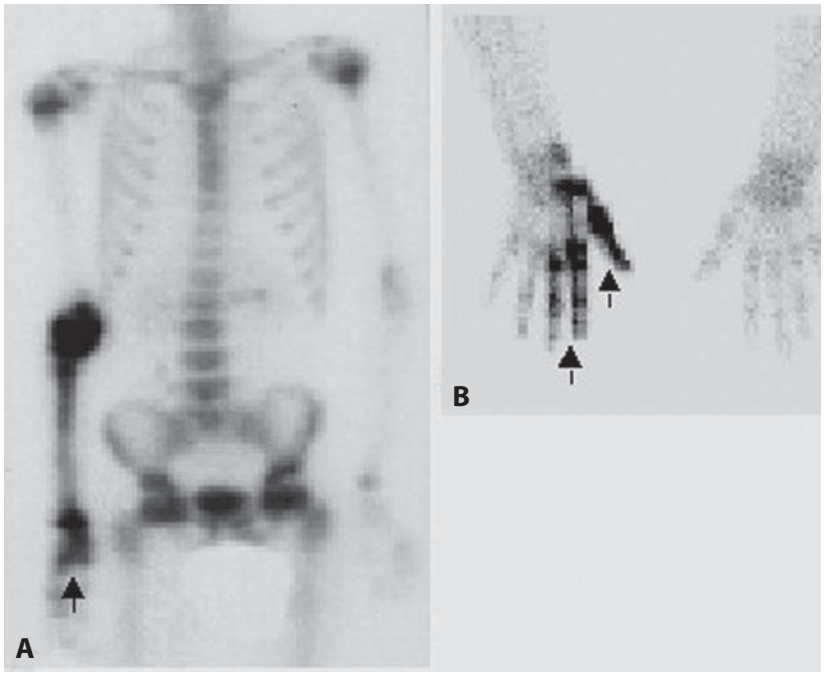

Fig. 5.25A, B Radioactive flushing due to inadvertent intraarterial injection of tracer. **A** Anterior scan of the right forearm shows diffusely increased activity (*arrow*) distal to the injection site at the antecubital fossa. **B** Dorsal scan of the right hand shows radioactive flushing of the first through third fingers (*arrows*)

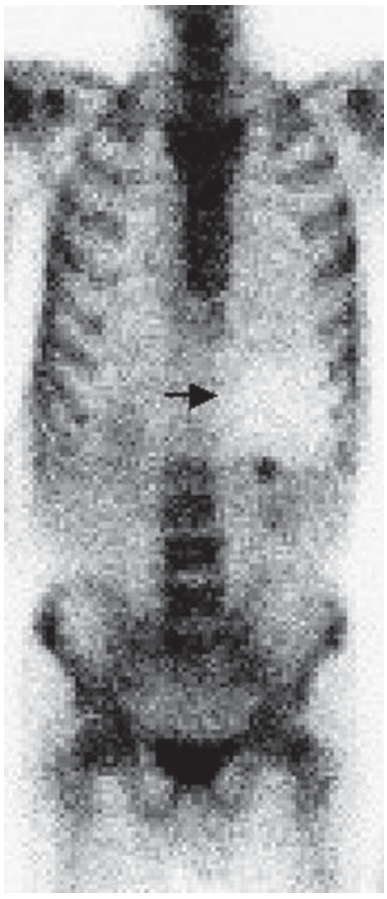

Fig. 5.26 Food photon defect in the stomach. Anterior scan shows a large photon defect the left upper abdomen due to food retained within the stomach (*arrow*)

non-tourniquet injection or, if a tourniquet is used, a wait of more than 5 minutes is needed for the reactive hyperemia to subside (Kirsh and Tepperman 1985).

When a large amount of tracer leaks into the subcutaneous tissues during injection, the ipsilateral regional lymph nodes are visualized as a result of lymphatic clearance of the escaped tracer (Howarth et al. 1996). Overlapping bone, this may mimic bone pathology (Fig. 5.24). Inadvertent arterial injection can cause diffusely increased activity in the distal upper extremity extending from the level of the injection site to the fingertips (Fig. 5.25) due to the delivery of a high concentration tracer to the soft tissue distal to the injection site, the "glove" phenomenon (Howarth et al. 1996).

5.2.3 Radioactivity Attenuation Artifacts

Gamma ray energy (140 keV) of ^{99m}Tc becomes attenuated when photons pass through matter losing over 50% of counts in 5 cm of soft tissue (Jaszczak and Coleman 1985). Photon defects produced by attenuation are very common, and they are due to external or internal objects with a high atomic number or a large volume. Internal attenuating objects include permanent cardiac pacemakers, joint prostheses, breast or penile implants, and foods in the stomach

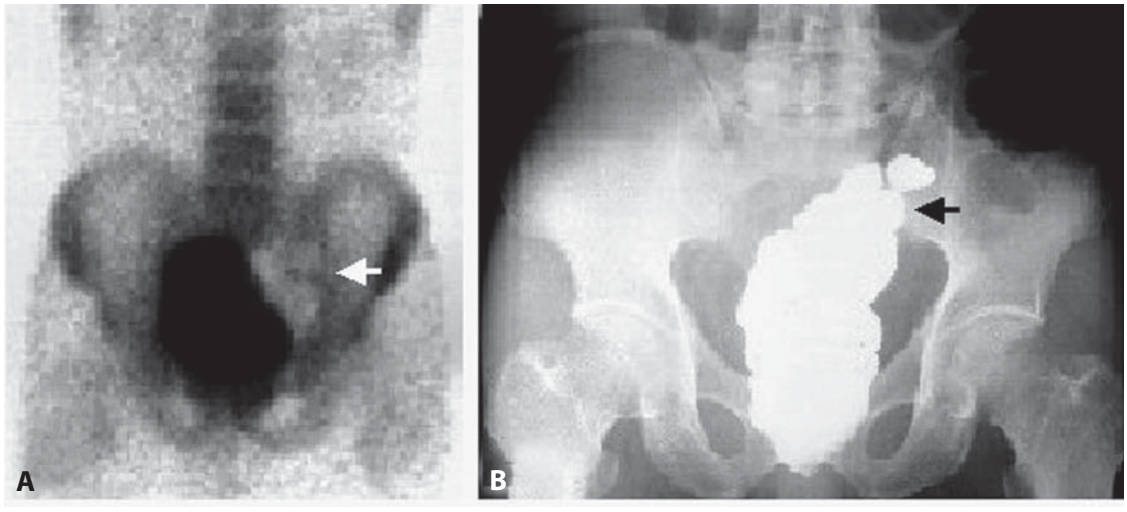

Fig. 5.27A, B False photon defect due to barium attenuation. **A** Anterior scan of the pelvis shows a photon defect in the left pelvic cavity (*arrow*). **B** Radiograph reveals barium retained in the rectum from a gastric barium study performed 3 days previously (*arrow*)

(Fig. 5.26), barium from gastrointestinal or colon study (Fig. 5.27), among others, and external objects include rings, earrings, necklaces, coins, keys, buttons, belt buckles, among others. Presenting on either the anterior or posterior view but not on both, they are easily identified by their characteristic shapes and locations. The appearance of such artifacts can be avoided by simply removing metallic objects. Rarely, an additional different angle scan or even radiography may be required to solve the question.

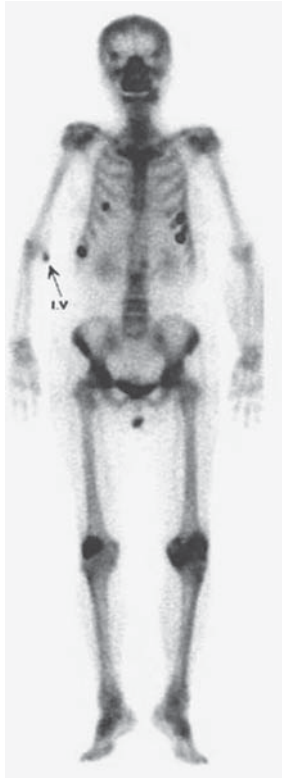

Fig. 5.28 Tracer contamination at injection site. Anterior whole-body scan shows small spotty uptake at an intravenous injection site in the right elbow. Proper marking is most helpful. Incidentally, there are multiple spotty uptake areas in rib fractures

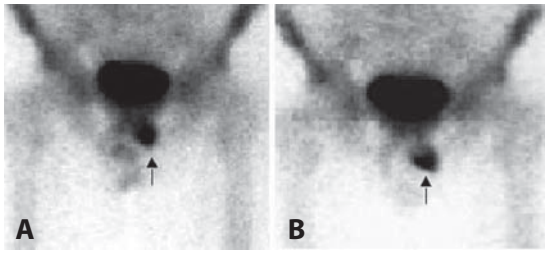

Fig. 5.29A, B Contaminated phimosis mimicking a pubic lesion. **A** Anterior scan of the pelvis shows small spotty uptake in the left pubic bone suggesting a bone lesion (*arrow*). **B** After removing clothes, thorough skin washing and bladder voiding the uptake remained, confirming phimosis. Close observation reveals cap-shaped balanus (*arrow*)

5.2.4 Soiling

One of the most disturbing and most common artifacts is soiling produced by radioactive contamination. Contamination is commonly seen at the injection site. Proper marking of the site is the best means to avoid confusion (Fig. 5.28). Soiling due to radioactive urine is the next most common artifact. Rechecking the gamma count after removal of the clothes and skin cleansing may confirm or dismiss contamination. At times, specially angled views prove useful for localizing soiled skin or clothes. On the other hand, since radioactivity cannot be removed by simple washing in certain body areas such as in phimosis, contamination must be interpreted with great caution (Fig. 5.29). It is also worth remembering that an artifact may be created by contaminated sweat in hyperhidrosis (Ajmani et al. 1977).

References

Ajmani SK, Lerner SR, Pircher FJ (1977) Bone scan artifact caused by hyperhidrosis: case report. J Nucl Med 18:801–802

Bahk YW, Park YH, Chung SK, et al (1994) Pinhole scintigraphic sign of chondromalacia patellae in older subjects: a prospective assessment with differential diagnosis. J Nucl Med 35:855–862

Ceylan E, Caner B (2003) Evolution of hyperostosis frontalis interna butterfly sign demonstrated by bone scan. Clin Nucl Med 28:78–79

Daenen B, Preidler KW, Padmanabhan S, et al (1997) Symptomatic herniation pits of the femoral neck: anatomic and clinical study. AJR Am J Roentgenol 168:149–153

Desaia A, Intenzo C (1984) The "tourniquet effect". J Nucl Med 25:697–699

Eggli DF, Tulchinsky M (1996) Normal planar bone scan. In: Collier BD, Fogelman I, Rosenthal L (eds) Skeletal nuclear medicine, 1st edn. Mosby-Year Books, St. Louis, pp 23–42

Fink-Bennett D, Johnson J (1986) Stippled ribs: a potential pitfall in bone scan interpretation. J Nucl Med 27:216–218

Fink-Bennett D, Vicuna-Rios J (1980) The deltoid tuberosity – a potential pitfall (the "delta" sign) in bone-scan interpretation: concise communication. J Nucl Med 21:211–212

Forstrom LA, Dunn WL, O'Connor MK, et al (1996) Technical pitfalls in image acquisition, processing, and display. Semin Nucl Med 26:278–294

Gray HW, Krawnow AZ (1996) Soft tissue uptake of bone agents. In: Collier BD, Fogelman I, Rosenthal L (eds) Skeletal nuclear medicine, 1st edn. Mosby-Year Books, St. Louis, pp 375–399

Harbert J, Desai R (1985) Small calvarial bone scan foci – normal variations. J Nucl Med 26:1144–1148

Hirano T, Otake H, Ichikawa K, et al (1998) Chronic mastoid sinusitis mimicking metastatic disease demonstrated by Tc-99m HMDP bone scintigraphy. Clin Nucl Med 23:327–328

Howarth DM, Forstrom LA, O'Connor MK, et al (1996) Patient-related pitfalls and artifacts in nuclear medicine imaging. Semin Nucl Med 26:295–307

Hung JC, Ponto JA, Hammes RJ (1996) Radiopharmaceutical-related pitfalls and artifacts. Semin Nucl Med 26:208–255

Jaszczak RJ, Coleman RE (1985) Single photon emission computed tomography (SPECT) principles and instrumentation. Invest Radiol 20:897–910

Kipper MS, Alaxraki NP, Feiglin DH (1982) The "hot" patella. Clin Nucl Med 71:28–32

Kirsh JC, Tepperman PS (1985) Assessment of hand blood flow: a modified technique. AJR Am J Roentgenol 144:781–783

Lawson JP, Ogden JA, Sella E, Barwick KW (1984) The painful accessory navicular. Skeletal Radiol 12:250–266

Lim ST, Sohn MH, Kwak JY, et al (2001a) Skeletal metastases mimicking bilateral "delta sign" on Tc-99m MDP bone scintigraphy. Clin Nucl Med 26:573–574

Lim ST, Sohn MH, Yim CY (2001b) Pregnancy-induced uterine blush detected incidentally by three-phase bone scintigraphy. Clin Nucl Med 26:654

Mandell GA, Harcke HT, Sharkey C, et al (1986) Uterine blush in multiphase bone imaging. J Nucl Med 27(1):51–55

Murray IP, Frater CJ (1994) Prominence of the C2 vertebra on SPECT. A normal variant. Clin Nucl Med 19:855–859

O'Connor MK (1996) Instrument- and computer-related problems and artifacts in nuclear medicine. Semin Nucl Med 26:256–277

Orzel JA, Rosenbaum DM, Weinberger E (1989) "Tourniquet effect" can alter delayed static bone scan. AJR Am J Roentgenol 152:896

Pitt MJ, Graham AR, Shipman JH, et al (1982) Herniation pit of the femoral neck. AJR Am J Roentgenol 138:1115–1121

Rao BK, Lieberman LM (1980) Parietal thinning: a cause for photopenia on bone scan. Clin Nucl Med 5:313

Senda K, Itoh S (1987) Evaluation of diffusely high uptake by the calvaria in bone scintigraphy. Ann Nucl Med 1:23–26

Sty JR, Starshak RJ (1983) Skull scintigraphy. Parietal foramina. Clin Nucl Med 8:87

Tsai SC, Kao CH, Lin WY, et al (1999) Intestinal accumulation of Tc-99m MDP on bone scan. Semin Nucl Med 29:80–81

6 Infective and Inflammatory Diseases of Bone

Bone infections and inflammations are among the most common and important indications for bone scintigraphy, the sensitivity of which has been firmly established (Duszynski et al. 1975; Gilday et al. 1975). Etiologically, the offending organisms are diverse, and the causes of nonspecific osteitides are obscure except for X- or γ-irradiation in radiation osteitis. For a scintigraphic description, bone infections may be categorized according to the site of initial affliction. Thus, pyogenic infection in bone marrow is termed osteomyelitis, and infections of the cortex, periosteum, and soft tissues are referred to, respectively, as infective osteitis or abscess, infective periostitis, and soft-tissue abscess. More often than not the three types of bone infection as well as soft-tissue infection become concurrent if the initial event is not brought under prompt control.

Clinically, bone infections may be classified into acute, subacute, and chronic, although attempts at sharp demarcation are for the most part unsuccessful and impracticable. Nonetheless, if well-isolated the acute bone infection is characterized by an abrupt, febrile, and painful onset with swelling, tenderness, and limited motion. In the chronic stage, symptoms and signs become poorly defined. Garré's sclerosing osteitis is a special form of chronic osteomyelitis. A group of inflammatory bone diseases of unknown cause are termed nonspecific osteitides. These include osteitis condensans ilii, osteitis pubis, condensing osteitis of the clavicle, Caffey's infantile cortical hyperostosis, and Paget's osteitis deformans. Bony proliferation and sclerosis are common features.

Before the advent of bone scintigraphy the imaging diagnosis of infective and inflammatory bone diseases was solely the domain of radiography. However, since Capitanio and Kirkpatrick in 1970 reported that acute osteomyelitis could be diagnosed by bone scintigraphy days earlier than by radiography, its usefulness has been systematically explored in infective bone diseases.

6.1 Acute Osteomyelitis

Osteomyelitis is primarily a disease of childhood and infancy, but a recent rise in its frequency is noted among the elderly (Waldvogel et al. 1970). The major offenders are *Staphylococcus aureus* in children, β-hemolytic streptococcus, *S. aureus* and *Escherichia coli* in neonates, and gram-negative bacilli in adults and drug abusers. One study of 348 adult patients with osteomyelitis by Waldvogel and Papageorgiou (1980) revealed that *S. aureus*, enteric species, and streptococcal organisms are causative in 60%, 29% and 8%, respectively. The organisms can reach bone by blood flow, by continuity from the infected soft-tissue focus, or by direct implantation through an open wound from needling, cutting, acupuncturing, or operation.

6.1.1 Pathogenesis

In the hematogenous form, the infective process classically starts in the metaphysis of long bone by the lodgment of organisms in endarteries, in which a slow blood flow facilitates their entrapment. As bone and bone marrow become the loci of bacterial proliferation, tissues

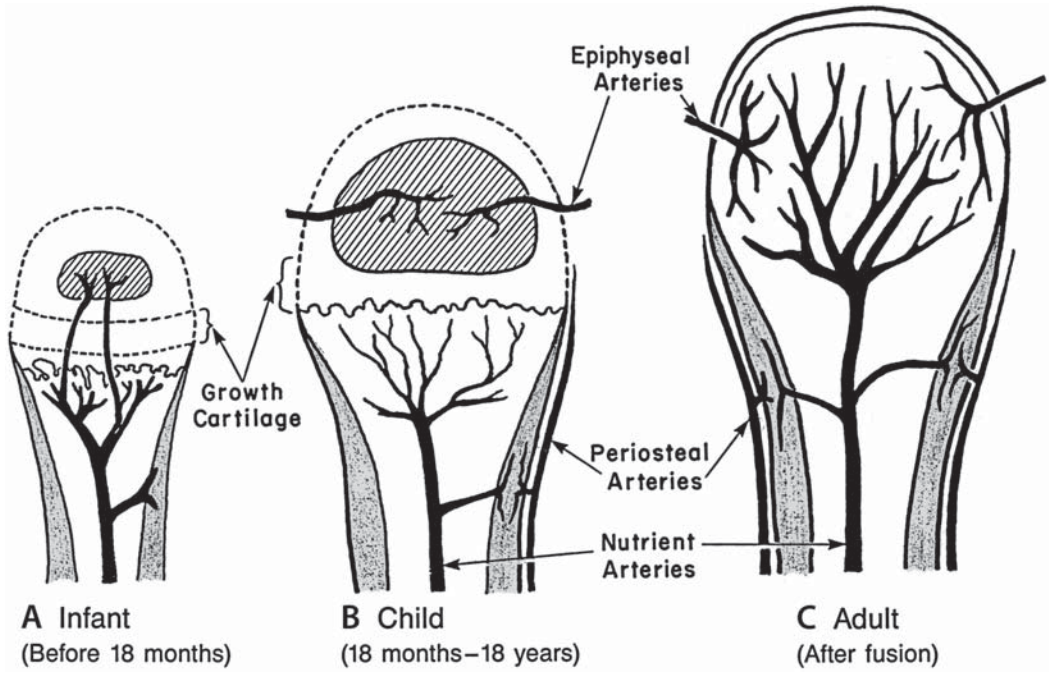

Fig. 6.1A–C Schematic presentation of changing vascular supplies in long bone according to the three different age groups. Basically, the main blood supply to long bone ends derives from the nutrient artery. **A** In an infant under the age of 18 months small arteries penetrate the growth cartilage to reach the epiphysis. **B** After 18 months, with the involution of the physeal vessels, the vascular supply in the epiphysis derives from the epiphyseal arteries and becomes separated from that in the metaphysis by the cartilaginous barrier. **C** Following physeal fusion the nutrient arterial branches joined by the epiphyseal branches distribute throughout the whole bone end. The blood supply in the cortex derives from the periosteal artery in the outer zone and from the nutrient artery in the inner zone (adapted from Rogers 1987)

react intensely with hyperemia, edema, cell infiltration, and suppuration, creating a milieu under pressure within the closed space of the bone marrow. Both the elevated intramedullary pressure and the proteolytic action of the offenders cause infective material to leak through the haversian and Volkmann's canals of the cortex out to the subperiosteal layer, to produce an abscess. As a result, the affected bone becomes necrotized and the periosteum reacts with brisk new bone formation. The former is known as sequestrum and the latter involucrum. As shown in Fig. 6.1, the metaphyseal vascular supply, periosteal attachment, and histological characteristics of the physis in the long bone differ among infants under 1 year of age, children aged up to 16 years, and adults after bone fusion. During infancy, some of the metaphyseal arteries penetrate the growth cartilage to enter the epiphysis, carrying bacteria to that part. In children, however, such a transchondral vasculature ceases to exist and, instead, more mature growth cartilage resists the bacterial spread from the metaphysis. This barrier delimits the infection to the metaphysis in the initial stage of an acute osteomyelitis (Fig. 6.2).

6.1.2 Radiographic Manifestations

The earliest but nonspecific radiographic change of acute osteomyelitis is soft-tissue swelling with the obliteration of the fat plane. It can be detected as early as 3 days after the sudden onset of disease. However, the direct sign of bone infection manifests more than a week later. The initial bone alterations are local osteopenia and osteolysis typically in the long bone metaphysis. With the rapid progress of the disease, infection spreads rampantly from cancellous bone to cortex and periosteum,

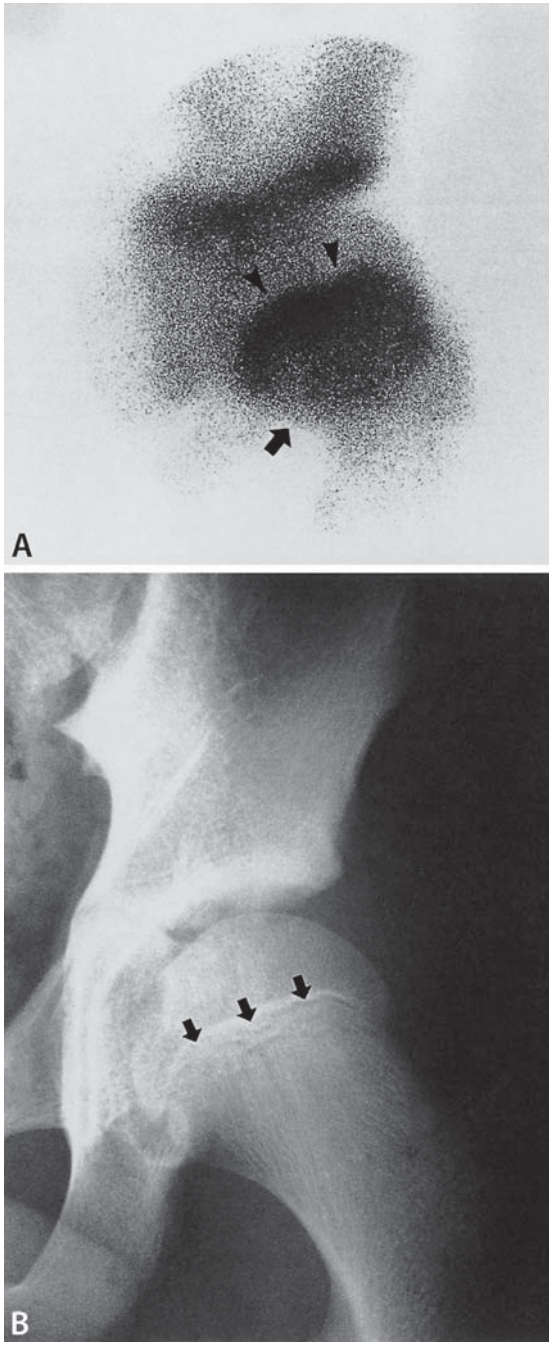

Fig. 6.2A, B Characteristic metaphyseal localization of acute osteomyelitis with the sharp delimitation by physeal cartilage. **A** Anterior pinhole scintigraph of the left proximal femur in a 15-year-old boy with acute osteomyelitis reveals intense tracer uptake localized in the metaphysis (*arrow*). Its upper border is sharply demarcated by the physis, which concentrates tracer intensely (*arrowheads*). **B** Anteroposterior radiograph shows as yet no radiographic alteration. The physeal barrier is represented by the wavy, linear lucency of cartilage (*arrows*)

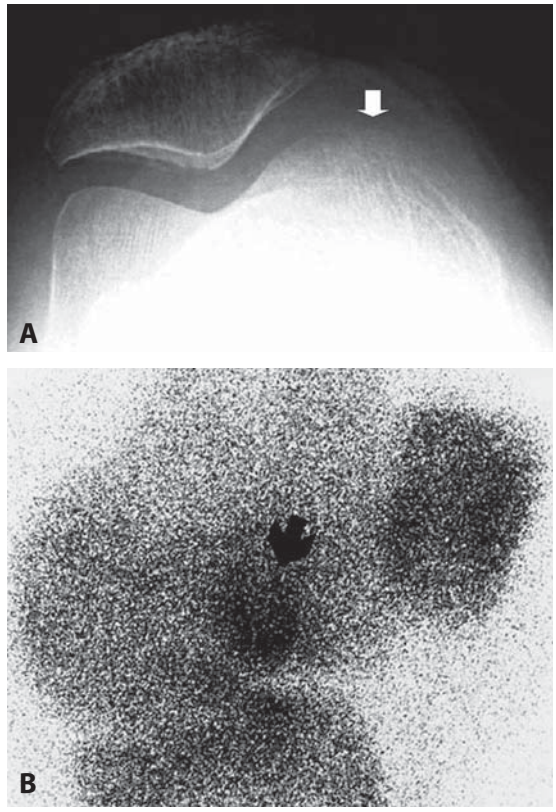

Fig. 6.3A, B Peripheral osteomyelitis with articular involvement in an adult. **A** Sunrise view radiograph of the right knee of a 65-year-old female with medial femoral condylar infection shows peripheral osteolysis with localized joint involvement (*arrow*). **B** Semilateral pinhole scan reveals an ill-defined patchy area of increased uptake in the medial femoral condyle (*arrow*)

showing permeation or frank destruction of bone and periosteal new bone formation. In infants the infection in the long-bone end may extend into the adjacent joint. On occasion, articular involvement may also occur in adults when the infective focus is located in the periarticular bone such as the femoral or tibial condyle (Fig. 6.3A). If diagnosis is delayed or the treatment instituted is inadequate, the disease may be transformed to the subacute and chronic type, creating sequestrum, involucrum, and cloaca. A sequestrum is denoted by bony condensation, an involucrum by sclerosis around the sequestrum, and a cloaca by an opening in the involucrum. A radiolucent rim

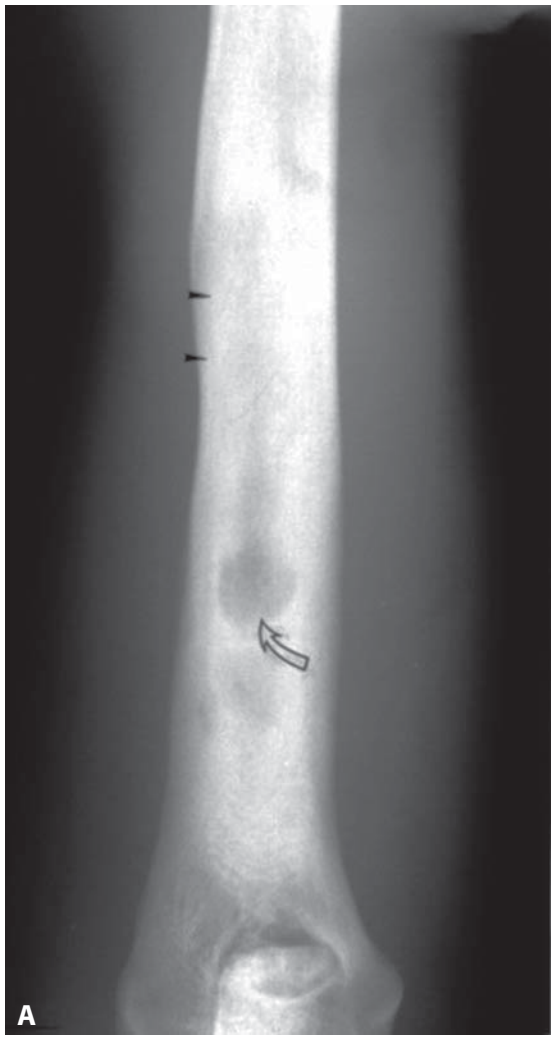

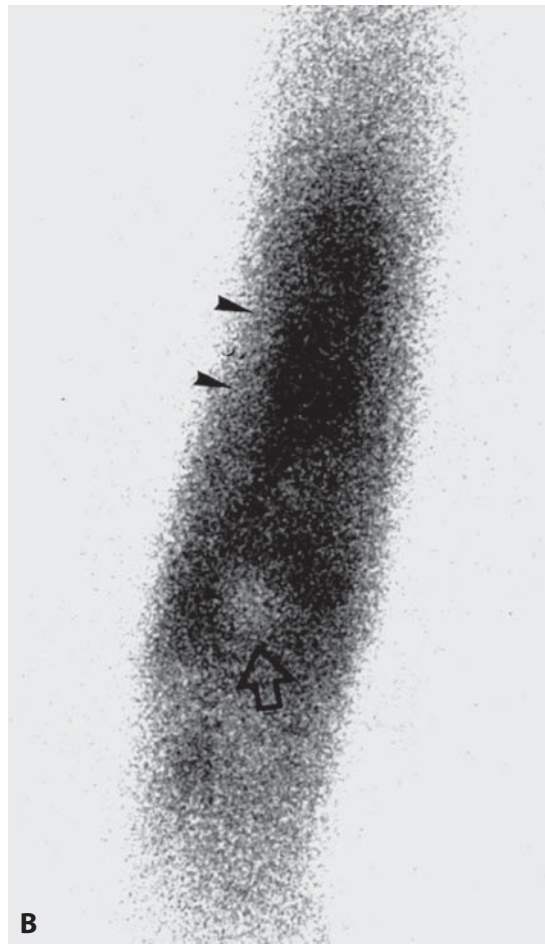

Fig. 6.4A, B Chronic osteomyelitis. **A** AP radiograph of the right humerus of a 24-year-old male with sclerotic marrow infection shows irregular thickening of the endosteum, cortex, periosteum, and trabecular bone (*arrowheads*) with bone defect (*open arrow*). **B** Pinhole scintigraph reveals intense tracer uptake confined to the medullary cavity with mild pancortical uptake (*arrowheads*) with a photopenic defect (*open arrow*)

of granulation may surround the sequestrum. When infection is protracted, sclerosing osteomyelitis may ensue. Chronic osteomyelitis is manifested as irregular thickening of the cortex, periosteum, and trabecular bone, frequently with bone defect and deformity (Fig. 6.4A).

6.1.3 Pinhole Scintigraphic Manifestations

As mentioned above, bone scanning is more sensitive and specific than radiography in detecting early osteomyelitis, particularly in the long bones. Thus, bone scan reinforced with the pinhole technique may show photopenia, which is the earliest scan sign that reflects the ischemia produced in the infective focus by the bacterial embolization in the arterial arcade and elevated intramedullary pressure. Experimentally, Rinsky et al. (1977) noted tracer uptake to be either normal or reduced in 21 out of 23 rabbits on day 3. One week later (day 10) 15 out of 19 rabbits showed positive change.

Once active osteolysis begins, tracer accumulates intensely in the lesional bone, which is

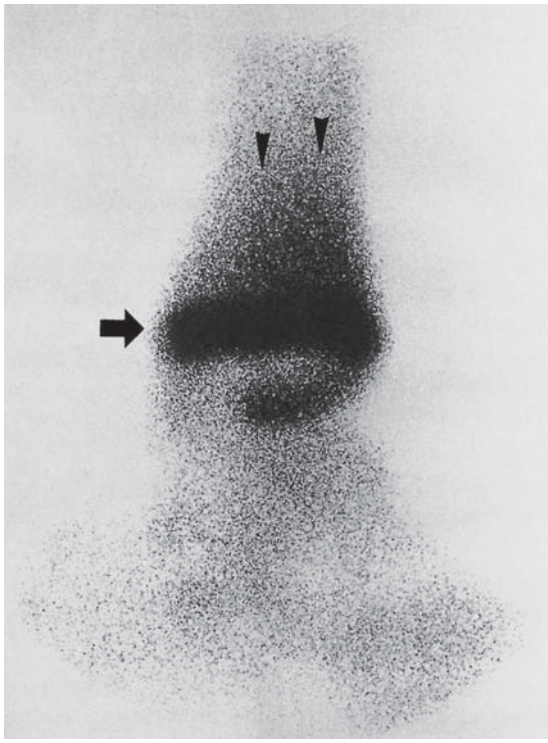

Fig. 6.5 Metadiaphyseal spread of osteomyelitis. Lateral pinhole scintigraph of the left ankle in another 15-year-old boy portrays diffusely increased tracer uptake in the distal tibial metaphysis with the imperceptibly fading upper border, indicating gradual shaftward spread of the inflammation (*arrowheads*). The physeal zone is moderately widened with extremely intense tracer uptake (*arrow*)

characteristically localized to the long-bone metaphysis (Fig. 6.2). Close observation may reveal the epiphyseal border of uptake to be sharply delimited by the "hot" physeal plate but the diaphyseal aspect to be blurred. The regional cortex is preserved at this stage. The tracer uptake is concentric and patchy. As disease progresses abnormal uptake spreads toward the diaphyseal side, forming an invasive front line (Fig. 6.5). With further progression of infection the cortex becomes lysed and subperiosteal abscess is formed, which are then followed by sequestration and new bone formation. At this stage, uptake spreads to the cortex, subperiosteum, and periosteum. Occasionally, a short segment of extremely intense uptake may appear in the cortex that flanks osteomyelitis in the metaphysis, reflecting rapid spread of infection to the cortex with abscess formation or infective osteitis (see below). Pinhole scintigraphy is useful for the diagnosis of evasive uptake in a small, initiating infection obscured by prominent physeal uptake on ordinary scans.

The usefulness of nuclear angiography in the diagnosis of acute osteomyelitis has been well documented (Duszynski et al. 1975; Gilday et al. 1975; Rosenthall et al. 1982; Maurer et al. 1981; Majd and Frankel 1976). Scintigangiography shows increased blood flow and blood pool in affected bone (Fig. 6.6). The angiography combined with pinhole scanning is indeed valuable for: (a) differential diagnosis of the infection of small bones such as sesamoids (Fig. 6.7), (b) assessment of the effect of antibiotic therapy with or without fenestration or drainage (Fig. 6.8), and (c) localization of the residual or reactivated infective focus (Fig. 6.9).

6.2 Subacute and Chronic Osteomyelitis

If not treated promptly and effectively by an antibiotic regimen and/or operative fenestration, the acute infection is transformed into the subacute or chronic forms. Pathologically, abscess, necrosis, bony proliferation, cortical and periosteal thickening, and deformity are seen. It is during this stage of disease that the sequestra and involucra develop. Abscesses may be produced by the coalescence of suppurative foci in subacute and chronic osteomyelitis. They are walled-off by a prominent bone reaction and usually accompanied by the thickening of the cortex and periosteum.

Radiographically, the chronic osteomyelitis manifests bizarre bone changes that include protean trabecular and cortical thickening, radiolucent defect, periosteal reaction, and deformity (Fig. 6.10A). The intramedullary localization, a hallmark of osteomyelitis, is well maintained regardless of the chronicity of the

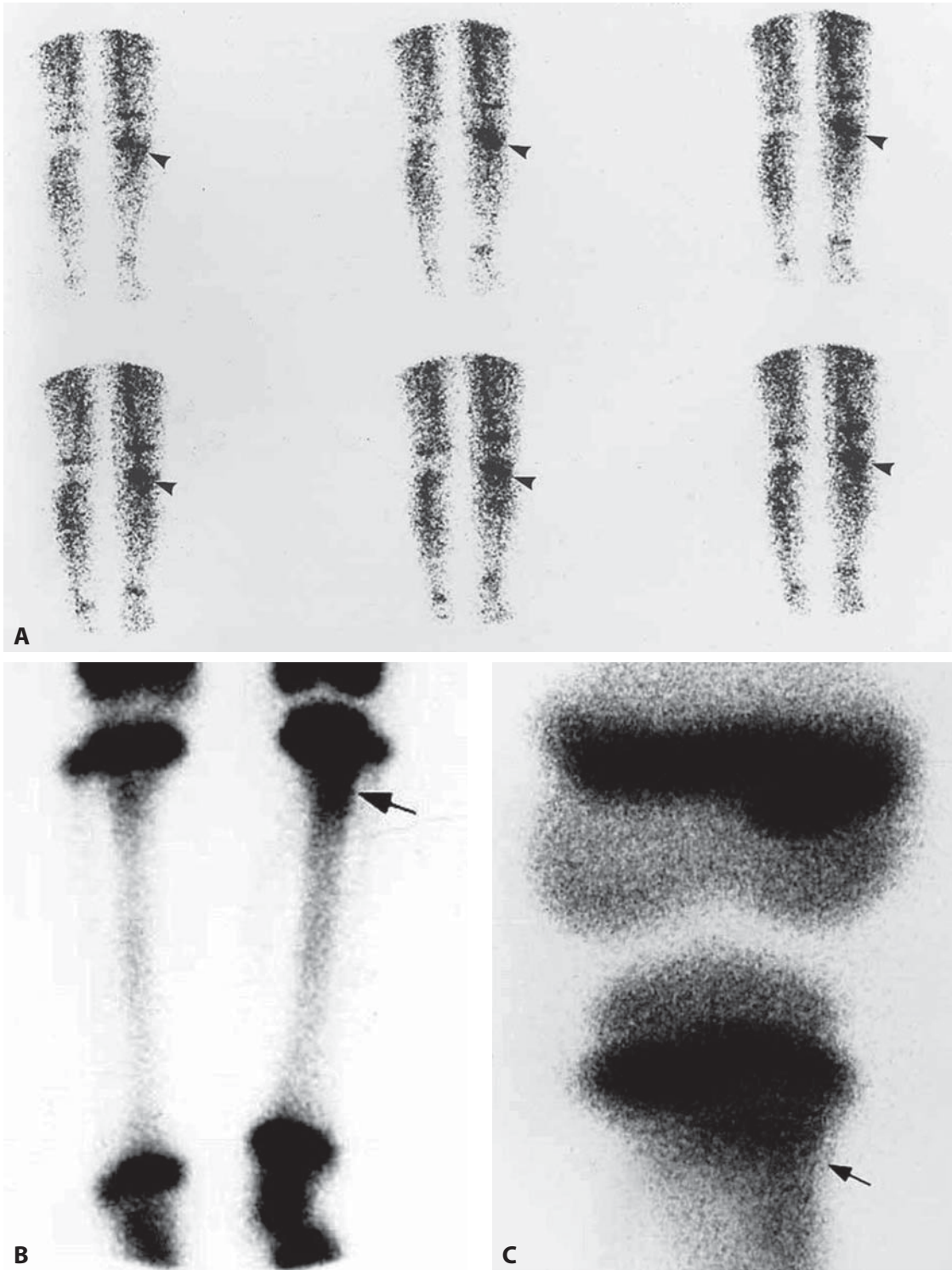

Fig. 6.6A–C Three-phase ^{99m}Tc-MDP bone scintigraphy in acute osteomyelitis. **A** Blood flow scan of both legs in a 5-year-old girl with pain and fever in the left knee shows increased vascularity in the left proximal tibial metaphysis (*arrowheads*). **B** Planar bone scintigraph shows increased uptake in the left proximal tibial metaphysis that is inseparable from the epiphyseal uptake (*arrow*). **C** Pinhole scintigraph clearly localizes pathological uptake to the metaphysis (*arrow*)

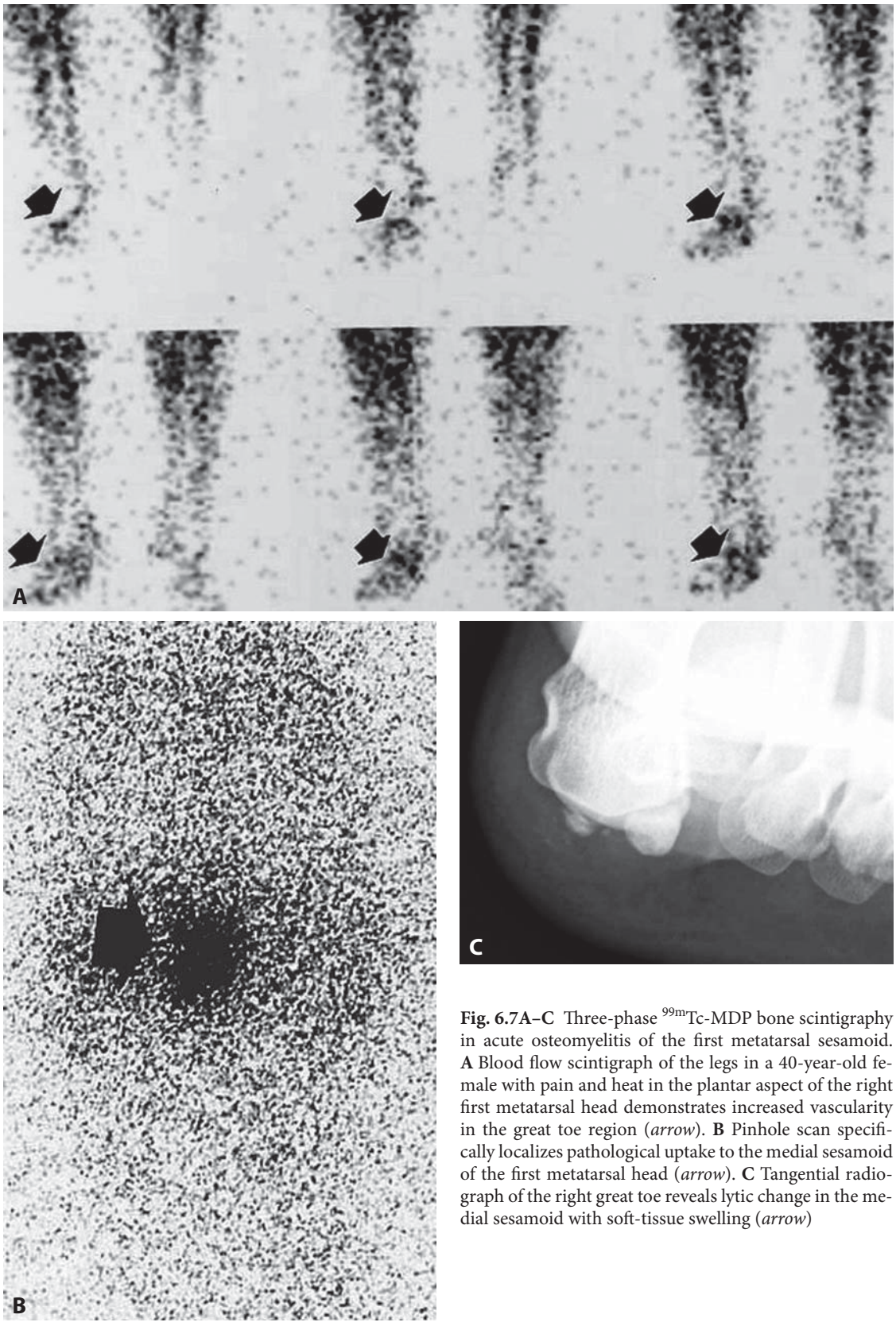

Fig. 6.7A–C Three-phase ^{99m}Tc-MDP bone scintigraphy in acute osteomyelitis of the first metatarsal sesamoid. **A** Blood flow scintigraph of the legs in a 40-year-old female with pain and heat in the plantar aspect of the right first metatarsal head demonstrates increased vascularity in the great toe region (*arrow*). **B** Pinhole scan specifically localizes pathological uptake to the medial sesamoid of the first metatarsal head (*arrow*). **C** Tangential radiograph of the right great toe reveals lytic change in the medial sesamoid with soft-tissue swelling (*arrow*)

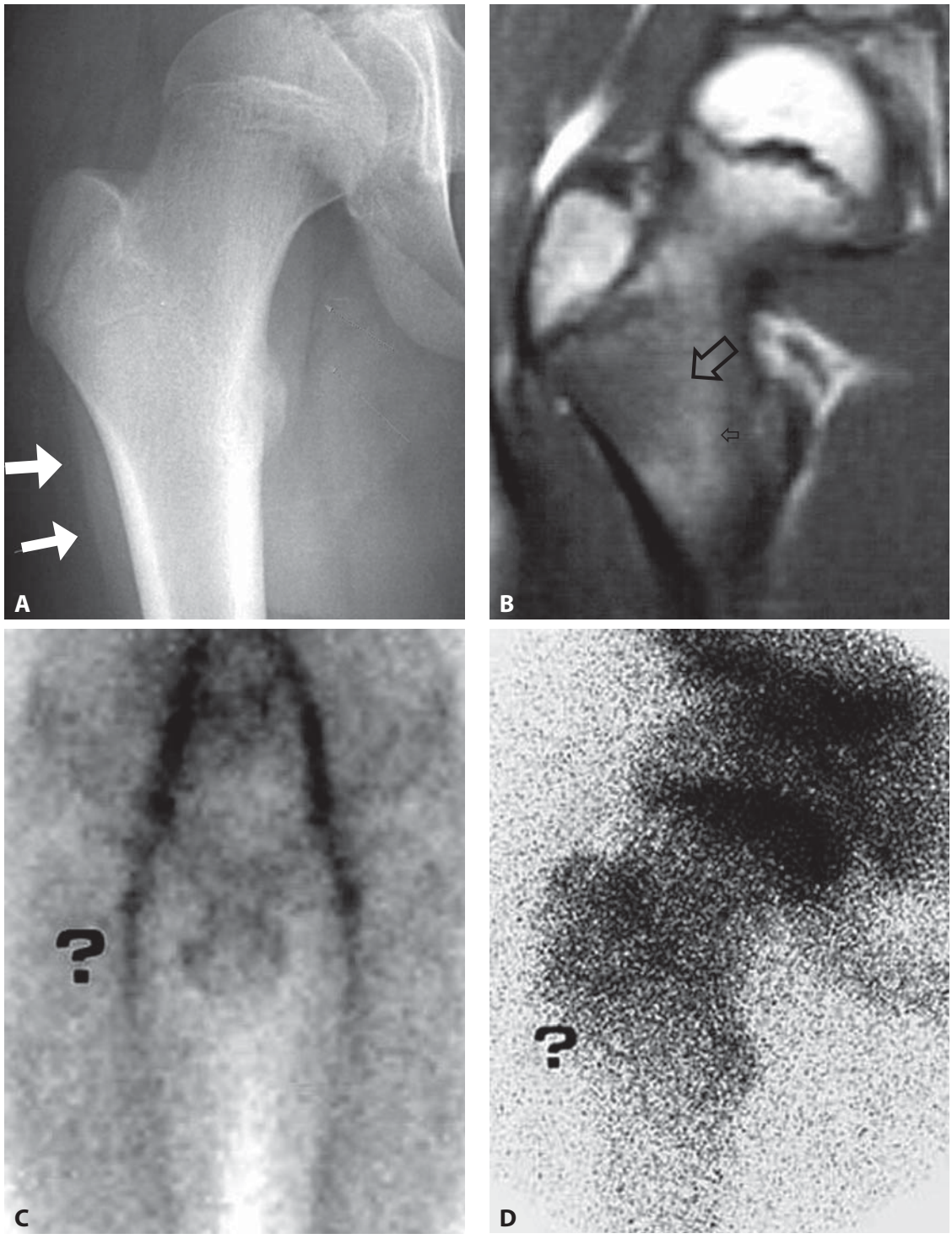

Fig. 6.8A–D Nuclear angiographic assessment of the effect of antibiotic therapy of early osteomyelitis. **A** Plain AP radiograph of the right proximal femur in an 11-year-old boy with high fever, local pain and leukocytosis shows periosteal reaction in the lateral aspect of the proximal femoral metaphysis (*arrows*). **B** T1-weighted MRI demonstrates low signal confirming infection in the bone marrow (open *arrow*). **C** Nuclear angiograph performed 10 days after cephalosporin therapy shows no abnormal vascularity, denoting the subsidence of infection (*?*). **D** Pinhole scintigraph shows no abnormal uptake either (*?*)

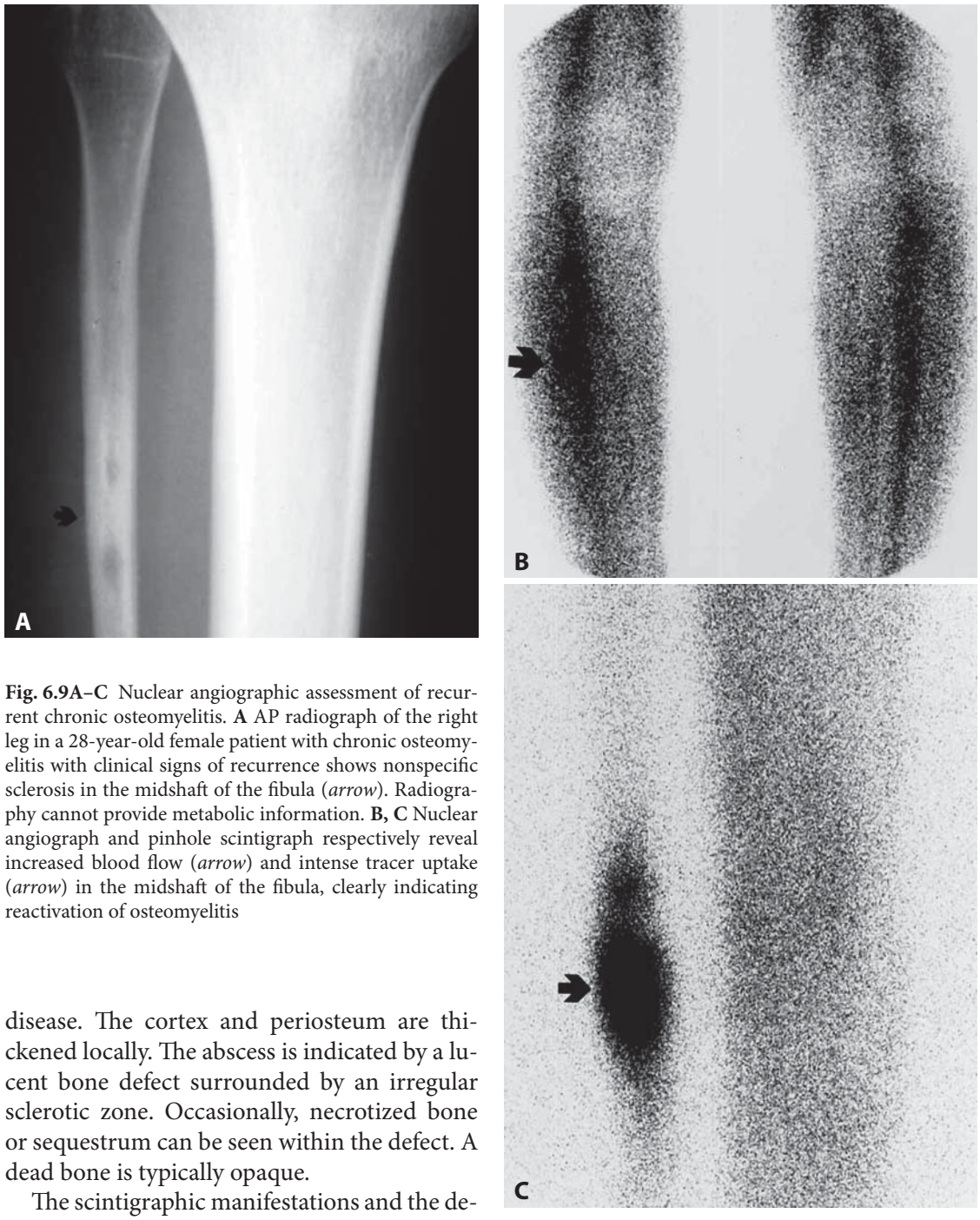

Fig. 6.9A–C Nuclear angiographic assessment of recurrent chronic osteomyelitis. **A** AP radiograph of the right leg in a 28-year-old female patient with chronic osteomyelitis with clinical signs of recurrence shows nonspecific sclerosis in the midshaft of the fibula (*arrow*). Radiography cannot provide metabolic information. **B, C** Nuclear angiograph and pinhole scintigraph respectively reveal increased blood flow (*arrow*) and intense tracer uptake (*arrow*) in the midshaft of the fibula, clearly indicating reactivation of osteomyelitis

disease. The cortex and periosteum are thickened locally. The abscess is indicated by a lucent bone defect surrounded by an irregular sclerotic zone. Occasionally, necrotized bone or sequestrum can be seen within the defect. A dead bone is typically opaque.

The scintigraphic manifestations and the demonstrability of subacute and chronic osteomyelitis as well as bone abscesses and osteitis depend upon the nature of bone pathology and the scintigraphic method applied. Understandably, ordinary bone scintigraphy provides less information than pinhole scintigraphy (Fig. 6.10B). This rule is particularly applicable to the assessment of the metaphyseal localization of osteomyelitis and the associated reactive change in the cortex. Pinhole scintigraphy can clearly resolve the apparently homogeneous "hot" area shown on an ordinary scintigraph into two or more different components: the main marrow space pathology and associated cortical change (Fig. 6.10C). In general,

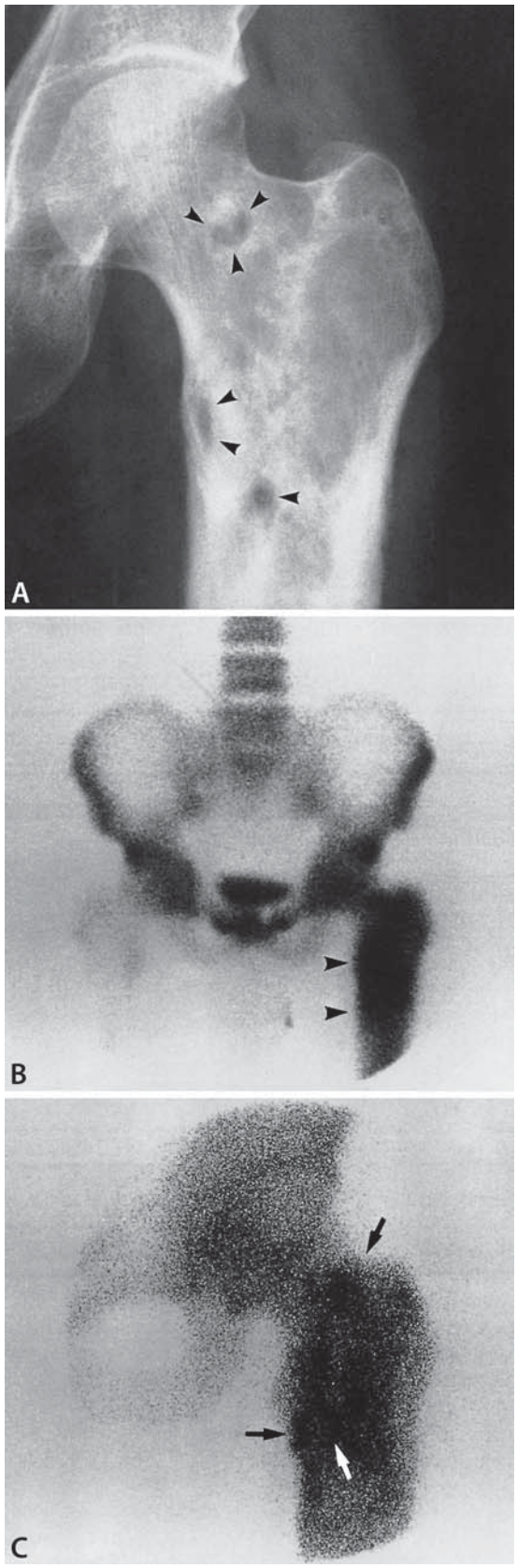

subacute or chronic osteomyelitis is indicated by a bizarre mixture of increased and decreased uptake representing, respectively, sclerotic and dead bone. The abscess or sequestrum larger in size than a finger tip can be shown as a "cold" defect surrounded by intense uptake; the demarcation is usually sharp. The smaller abscesses or involucra are indicated by a spotty "hot" area scattered within a large lesional area. Sequestra are not visualized because they are devitalized and unable to concentrate tracer. By the fusion of pinhole scan and radiography images after size-equalization, the tracer uptake and radiographic density can be correlated. Although our experience was limited it appeared that the area with increased uptake roughly corresponds to radiolucent or less sclerotic areas of chronic osteomyelitis and vice versa (Fig. 6.11). A possible implication of this observation is that the persistently active inflammatory foci in long-standing osteomyelitis likely remain in the radiographically lucent or less sclerotic area with increased tracer uptake than in the markedly sclerotic areas with little or no tracer uptake. Nuclear angiography can provide valuable objective information on the vascularity that increases in an active infective focus (Yang et al. 1988) (Fig. 6.9B).

Fig. 6.10A–C Radiographic and scintigraphic alterations in chronic osteomyelitis with involucra (abscesses), sclerosis, and cortical thickening. **A** Anteroposterior radiograph of the left proximal femur in a 31-year-old man with intractable osteomyelitis shows irregular osseous and cortical thickening, lucent involucra (*arrowheads*), and deformity. **B** Ordinary spot scintigraph reveals homogeneous tracer uptake without textural detail (*arrowheads*). **C** Anterior pinhole scan shows patchy areas of intense tracer uptake, representing the involucra, osteosclerosis, and cortical thickening

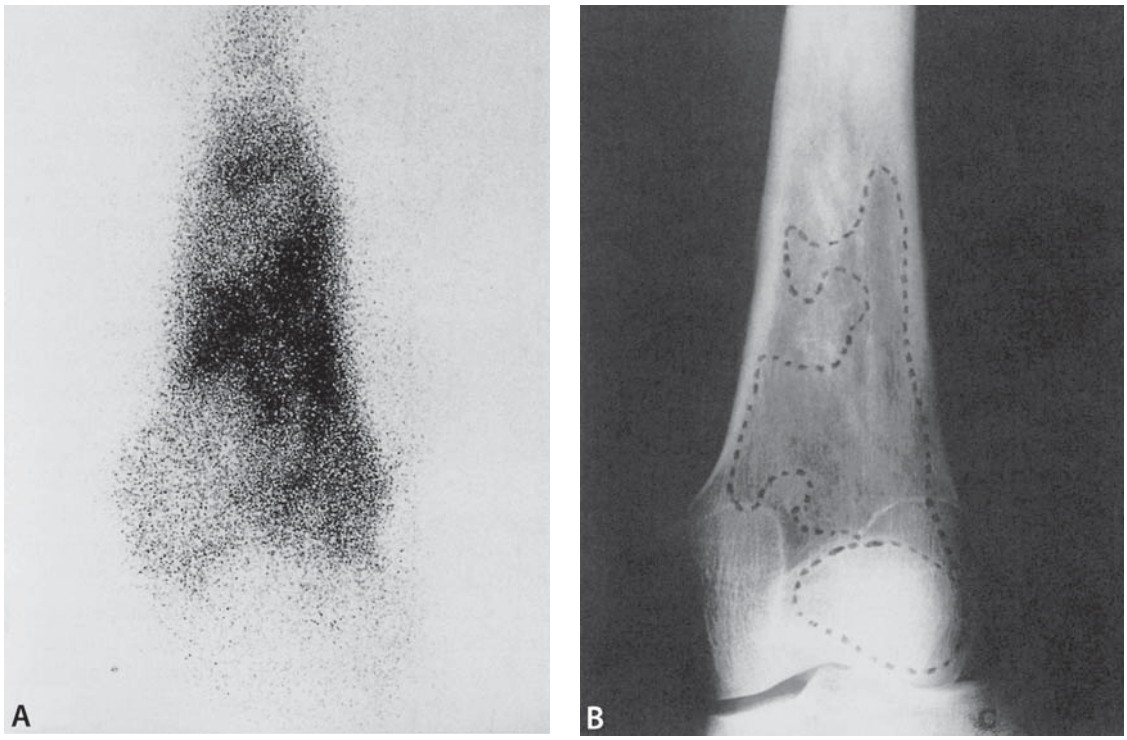

Fig. 6.11A, B Superimposition of a pinhole scintigraph on a radiograph in chronic osteomyelitis. **A** Anterior pinhole scintigraph of chronic osteomyelitis in the left distal femur shows mottled and patchy areas of increased tracer uptake. **B** Superimposition of transcribed scintigraphic alterations shown in **A** on the radiograph after image size equalization by photographic enlargement reveals more intense tracer uptake in radiographically less dense or lucent area, denoting the foci with residual inflammation (*dotted areas*). In contrast, the radiodense areas do not concentrate tracer detectably

6.3 Acute and Chronic Infective Osteitis and Cortical Abscess

Infective osteitis is suppurative infection of the cortical bone. It may be acute or chronic, and occurs either as an isolated disease (Fig. 6.12) or a concomitant process to osteomyelitis (Fig. 6.13). Pathologically, the process is characterized by cortical bone suppuration and abscess formation. The intracortical localization is characteristic, and such a peculiar localization has been accounted for by the presence of an anastomotic vascular network of the dual blood supply from both the nutrient and periosteal arteries. Being confined to the cortex, it is referred to as cortical abscess. It can leak out to infect the neighboring joint (Fig. 6.3) or soft tissue. Cortical abscess is different from Brodie's abscess, which is a chronic suppurative process of cancellous bones (see below).

Radiographically, acute infective osteitis manifests as permeative lysis of the cortex with erosion or disruption of the profile and periosteal reaction (Fig. 6.12A). Occasionally, cortical infection may occur in the epiphysis or the end of a long bone such as the femoral or tibial condyle, infecting the neighboring joint (Fig. 6.3A). The chronic infection in the irregular bones manifests as sclerosis in the cortical and subcortical zone. If pus leaks out into the neighboring soft tissue an abscess is formed, and the abscess presents as radiolucency (Fig. 6.14A).

Characteristic pinhole scintigraphic features include segmental uptake within the cortex of a long bone (Fig. 6.13B), a patchy "hot" area within the cortex of a long-bone epiphysis (Fig. 6.3B), or an irregular "hot" area in the cortex of a carpal and tarsal bone (Fig. 6.14B).

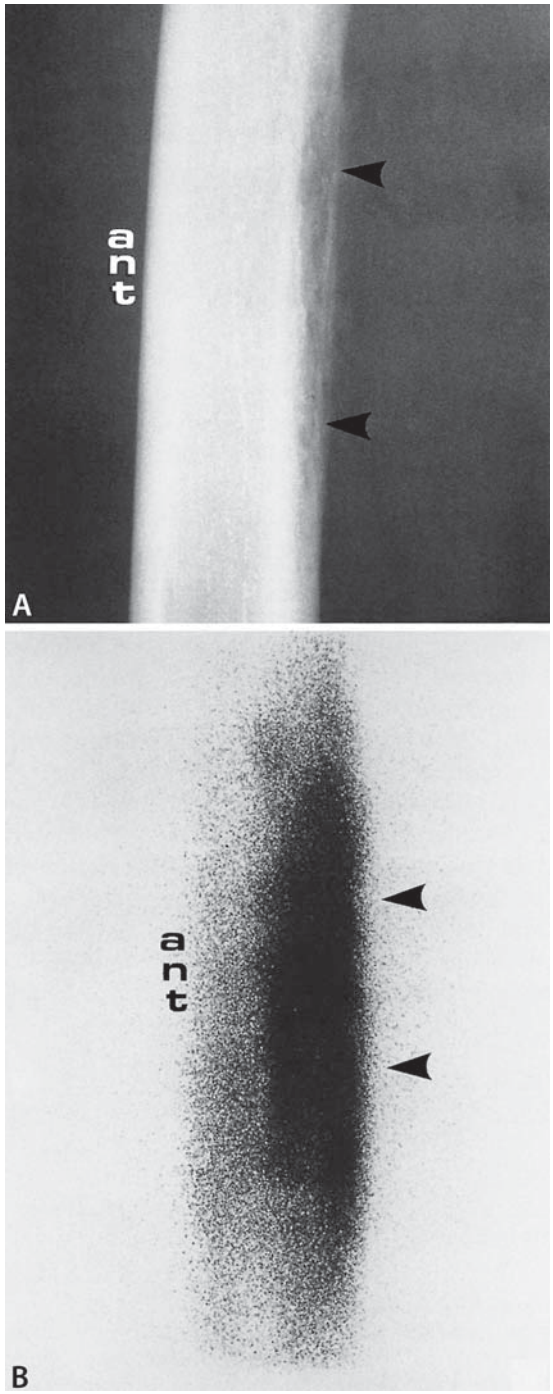

Fig. 6.12A, B Acute infective osteitis (cortical bone infection). **A** Lateral radiograph of the right femur in a 36-year-old man with gram-negative bacillary infection demonstrates cortical lysis and rupture with periosteal thickening in the posterior aspect of the midshaft (*arrowheads*). **B** Lateral pinhole scintigraph shows extremely intense tracer uptake eccentrically in the posterolateral aspect of the midshaft cortex (*arrowheads*). The involvement of bone marrow is minimal

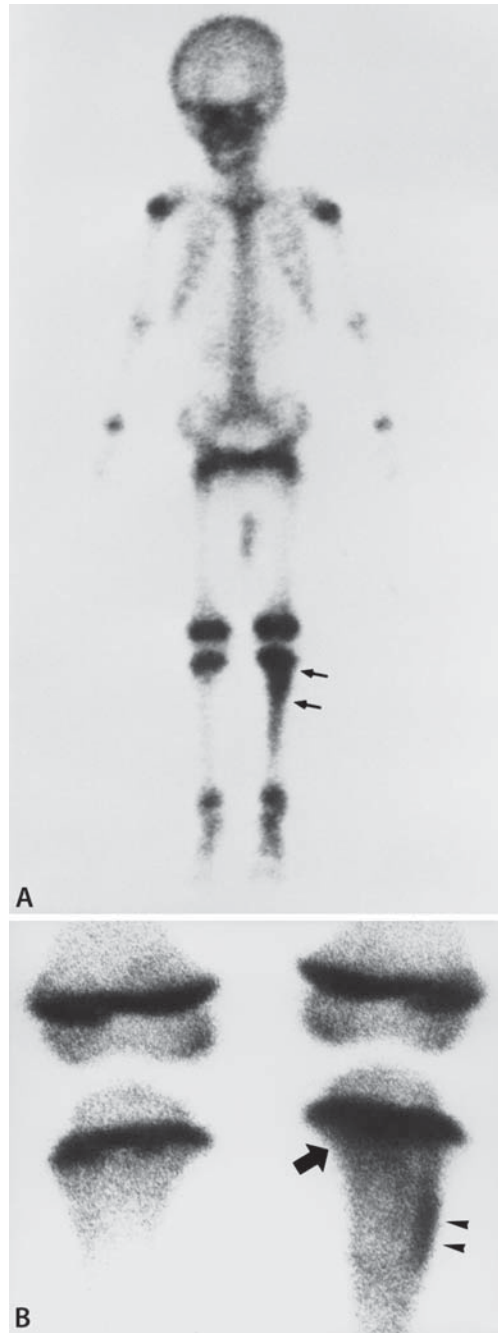

Fig. 6.13A, B Acute gram-negative bacillary osteomyelitis with concomitant infective osteitis. **A** Anterior whole-body planar scan in a 5-year-old boy shows ill-defined areas of intense tracer accumulation in the proximal left tibia (*arrows*). No anatomical details are shown. **B** Anterior pinhole scintigraph of both knees (simultaneous acquisition) shows intense tracer uptake in left proximal tibial metaphysis (*arrow*) and lateral cortex (*arrowheads*) clearly revealing and distinguishing osteomyelitis and concomitant osteitis, respectively. Also, note distinct delineation of the physeal plate!

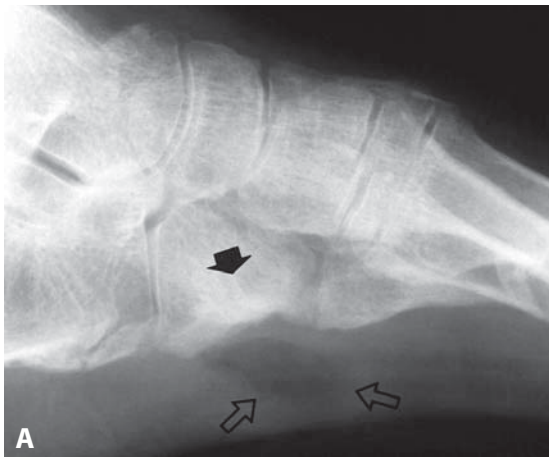

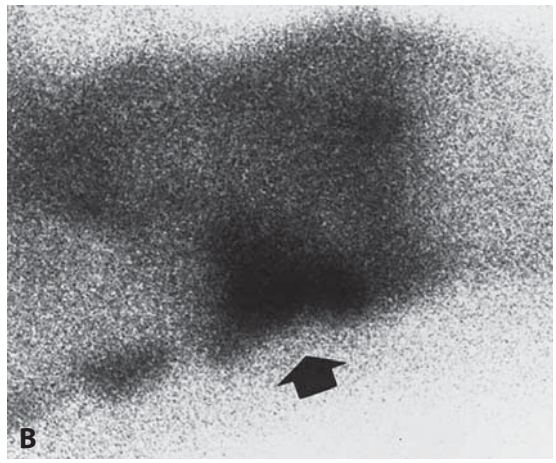

Fig. 6.14A, B Chronic osteomyelitis of irregular bone. **A** Lateral radiograph of the left cuboid in a 51-year-old male patient with chronic infection shows cortical defect with sclerosis (*arrow*). There is a flat ovoid lucency within the plantar soft tissue, denoting abscess formation (*open arrows*). **B** Lateral pinhole scintigraphy reveals intense uptake in the cortex and subcortical bones in the infected cuboid (*arrow*)

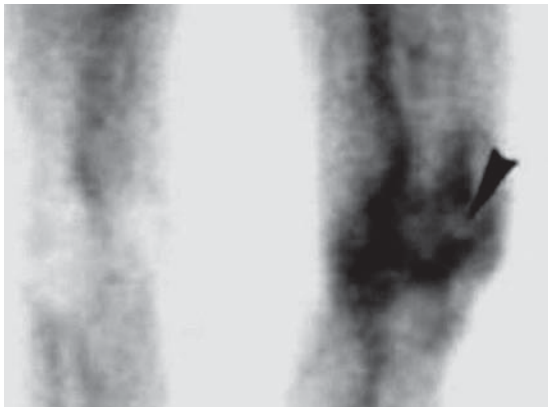

Fig. 6.15 Locally increased vascularity in osteitis. Anterior ^{99m}Tc-MDP angiograph shows irregular areas of increased blood flow and blood pool in the left knee with a localized area of intense bone uptake at the infective focus in the lateral femoral condyle (*arrowhead*)

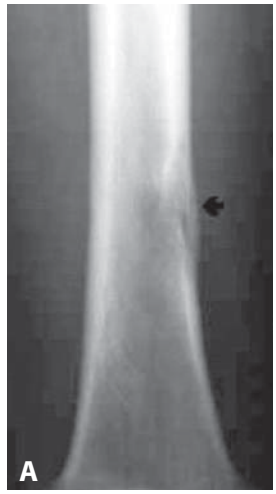

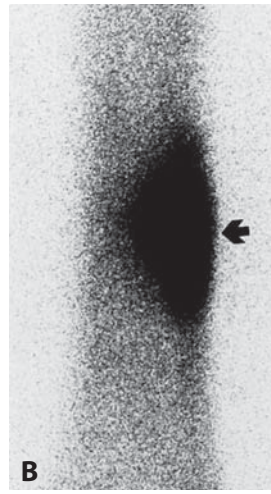

Fig. 6.16A, B Cancer metastasis to the long bone cortex simulating cortical osteitis. **A** Anterior pinhole scintigraphy of the right femoral shaft in a 57-year-old female patient with renal cell carcinoma shows irregular cortical thickening in the lateral cortex of the left lower femoral shaft (*arrow*). **B** Anterior pinhole scintigraph portrays discrete fusiform uptake in the cortex strongly simulating cortical infection (*arrow*)

The lesion may be either concomitant to osteomyelitis in the adjacent metaphysis (Fig. 6.13B) or isolated (Fig. 6.14). It remains eccentric in location unless the infection involves the whole circumference or an entire bone. Nuclear angiography may prove locally increased vascularity in the affected cortex (Fig. 6.15). Occasionally, carcinomas from the breast, lung, or kidney metastasize to the long bone cortex, scintigraphically resembling cortical infection. However, metastasis is typically focal and discrete (Fig. 6.16).

6.4 Acute Infective Periostitis

Acute infective periostitis is primary invasion of the periosteal cloak that covers the cortex. The infective products first accumulate beneath and raise the periosteum, subsequently spreading to the cortex and endosteum in succession. Radiographically, the raised and stimulated periosteum reacts with new bone formation (Fig. 6.17A). Ordinary bone scintigraphy shows intense uptake that is simply homogeneous without a textural pattern (Fig. 6.17B). However, pinhole scanning separates the seemingly homogeneous uptake into two different components: the outer faint uptake zone of periosteal thickening and the inner intense uptake zone of cortical reaction. Together these changes give rise to an irregularly striated appearance to the contour of the infected bone, contrasting with the intramedullary localization of the pathological uptake in osteomyelitis (Fig. 6.2A) and the eccentric uptake in cortical abscess (Fig. 6.12B). The specific localization and characteristic textural pattern of uptake in these three different diseases are pathognomonic of the individual diseases. On the other hand, nuclear angiography combined with pinhole scanning can play a unique role in assessing the aborted acute periostitis that is brought under control by early diagnosis and prompt institution of effective treatment (Fig. 6.8).

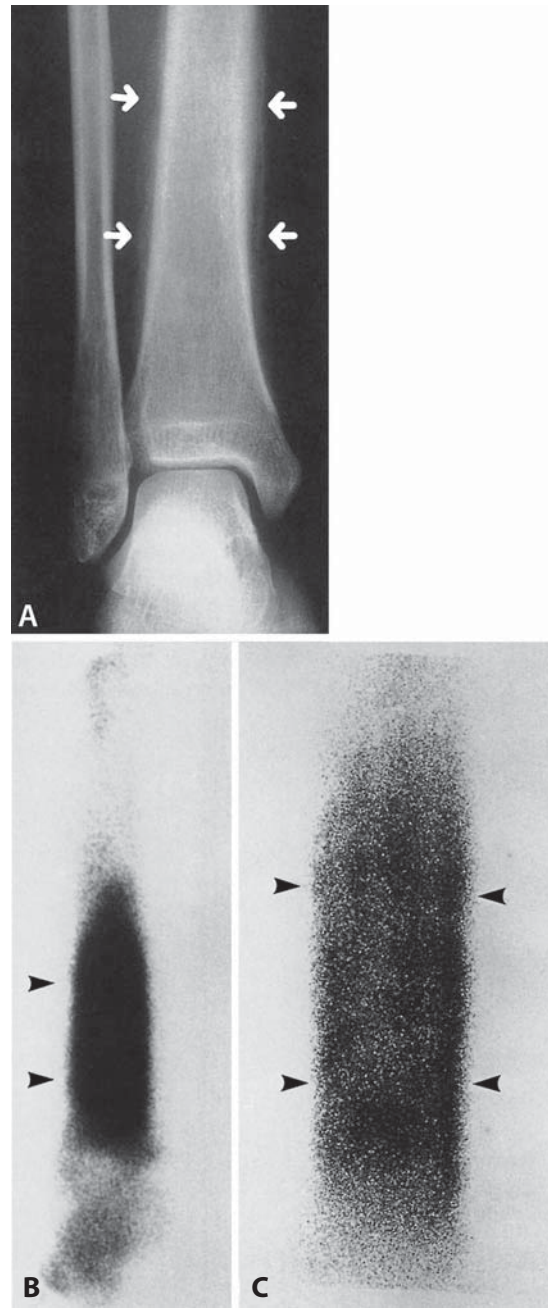

Fig. 6.17A–C Acute infective periostitis. **A** Anteroposterior radiograph of the right lower leg in an 18-year-old girl with multiple bone infections involving the right ulna, femur, and tibia demonstrates diffuse, lace-like periosteal thickening in the lower third of the right tibial shaft (*arrows*). **B** Anterior pinhole scan portrays modest tracer uptake in diffusely thickened periosteums (*arrowheads*). The uptake is irregular and typically peripheral in distribution, giving rise to a "striped wool-jersey" appearance. **C** Ordinary spot scintigraph shows very intense tracer uptake that is homogeneous without any differential features (*arrowheads*)

6.5 Special Forms of Osteomyelitis

6.5.1 Neonatal and Infantile Osteomyelitis

Osteomyelitis and pyarthrosis are not common in infants and children. Nevertheless, these constitute important causes of chronic illness and serious deformity that last a long time. The symptoms of infantile, especially neonatal, skeletal infections are peculiarly subtle, usually manifesting as pseudoparalysis of a limb at most and fever only in half of cases

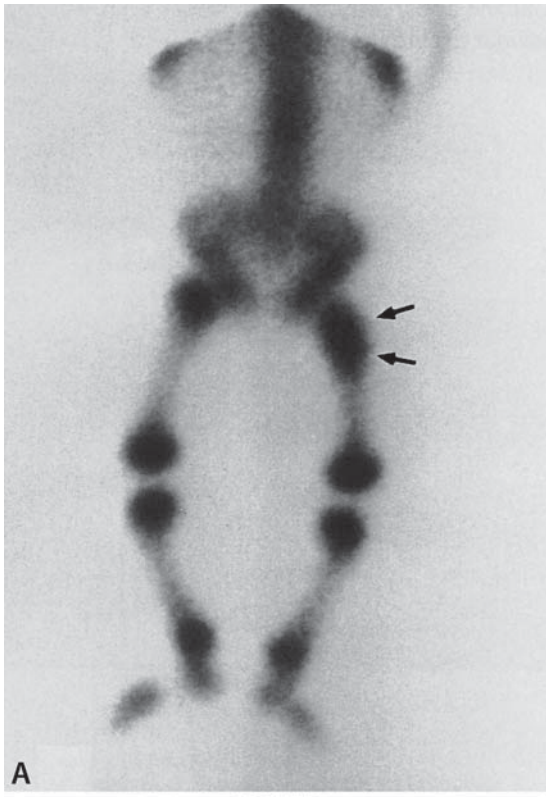

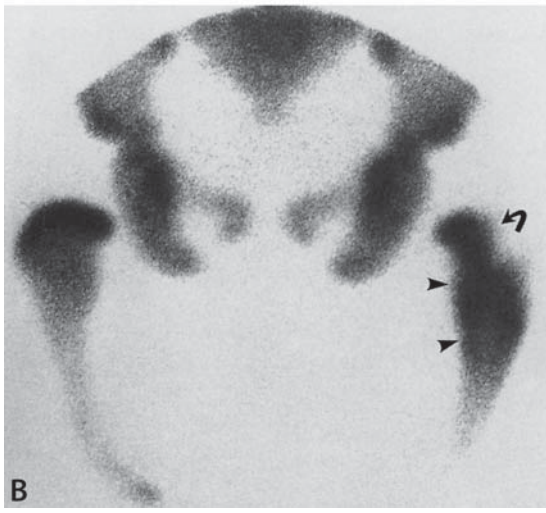

Fig. 6.18A, B Simultaneous demonstration of primary infective osseous focus and secondary pyarthrosis. **A** Anterior spot scintigraph of the pelvis and lower limbs in a 15-day-old baby girl running a high fever shows intense tracer uptake in the proximal left femur without detail (*arrows*). **B** Anterior pinhole scintigraph clearly localizes the abnormal uptake in the left proximal femur, establishing the diagnosis of osteomyelitis (*arrowheads*). The hip joint is subluxed with the adducted femoral neck due to secondary pyarthrosis (*curved* arrow). As yet no ossification centers have developed in the femoral heads

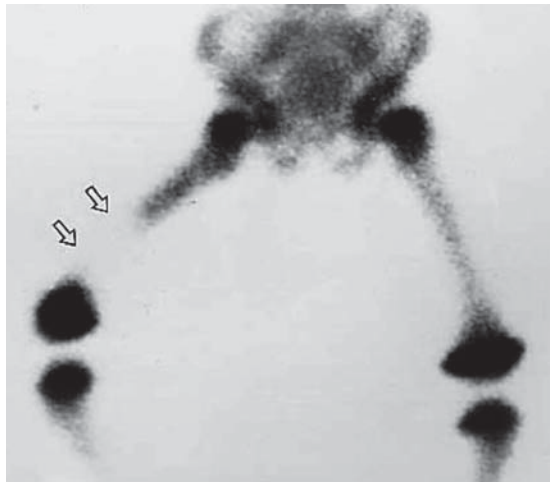

Fig. 6.19 "Cold" manifestation of acute osteomyelitis in an infant. Anterior bone scan of the lower limbs in a 1-year-old boy with acute osteomyelitis and subperiosteal abscess shows a large segmental photon defect in the right distal femoral shaft (*open arrows*) (courtesy of Drs. S.M. Lee, S.K. Bae, and M.R. Cho, 2000]

(Nelson 2000). Pathological features are distinctive with occasional subperiosteal abscess formation with local ischemia. As mentioned above, unlike in later life, the terminal branches of the nutrient arteries in the metaphysis in neonates penetrate the physeal cartilaginous barrier, permitting organisms to be easily carried to the epiphysis (Mok et al. 1982). Accordingly, in neonates, any part of a long bone including the epiphysis, metaphysis, and diaphysis can be the site of infection. Offending organisms, *S. aureus* in 80%, are often introduced by an infected umbilical cord. Commonly affected bones are the femur, tibia, and humerus, and their neighboring joints are involved in 50% of cases (Rogers 1987).

Radiography of an early osteomyelitis shows soft-tissue swelling with fat-line effacement without bony change (Fig. 6.8A), and subsequently lysis and periosteal new bone formation. When the adjacent joint is involved the capsule becomes distended.

Bone scintigraphy has been valued for the diagnosis of the neonatal or pediatric osteomyelitis because of its high sensitivity (Ash and

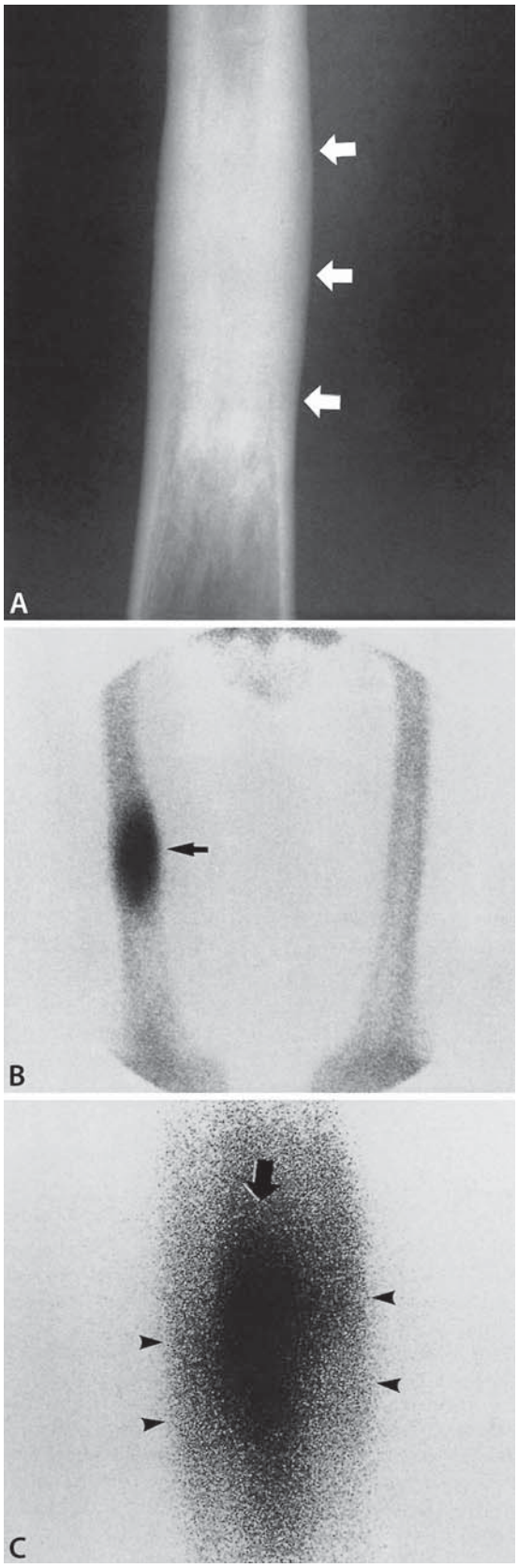

Gilday 1980). Pinhole scintigraphy greatly enhances the specificity. Generally, on scintigraphy the characteristic feature is intense tracer uptake specifically localized to the marrow space of the metaphysis and diaphysis (Fig. 6.18). The involvement of the neighboring joint manifests as widening and separation of the joint space with dislocation and rotation of the affected bone, for example, the proximal femur. Acute infantile osteomyelitis with subperiosteal abscess is occasionally shown as a "cold" lesion due to vascular interruption and raised intramedullary pressure (Jones and Cady 1981; Lee et al. 2000) (Fig. 6.19).

6.5.2 Sclerosing Osteomyelitis of Garré

This is a rare nonpurulent variant of subacute or chronic osteomyelitis. Pathologically, the condition is characterized by prominent proliferation and thickening of the periosteum and spongy trabeculae, but with little pus formation, necrosis, or granulation tissue. The mandible is the typical site of involvement. When a long bone is affected the diaphysis is the site of predilection, and this finding contrasts with the metaphyseal predilection of acute osteomyelitis.

Radiography shows diffuse thickening of the cortex, endosteum, and cancellous bones with resultant medullary space obliteration. It typically involves the mandible or the midshaft of a long bone (Fig. 6.20A).

Ordinary bone scintigraphy reveals intense void uptake in the middle portion of a long bone. The uptake is homogeneous without a particular feature (Fig. 6.20B). Pinhole scan, however, shows the homogeneous uptake to consist of two clearly separate zones: the more

Fig. 6.20A–C Intramedullary localization of tracer in sclerosing osteomyelitis of Garré. **A** Anteroposterior radiograph of the right femoral shaft in a 36-year-old man with a chronic bone infection shows marked bony sclerosis with minimal expansion (*arrows*). **B** Ordinary anterior spot scintigraph reveals intense tracer uptake without specific textural features (*arrow*). **C** Anterior pinhole scintigraph specifically localizes extremely intense tracer uptake of osteomyelitis in the marrow space (*arrow*) with much less intense uptake in the associated bone reaction in the cortex (*arrowheads*)

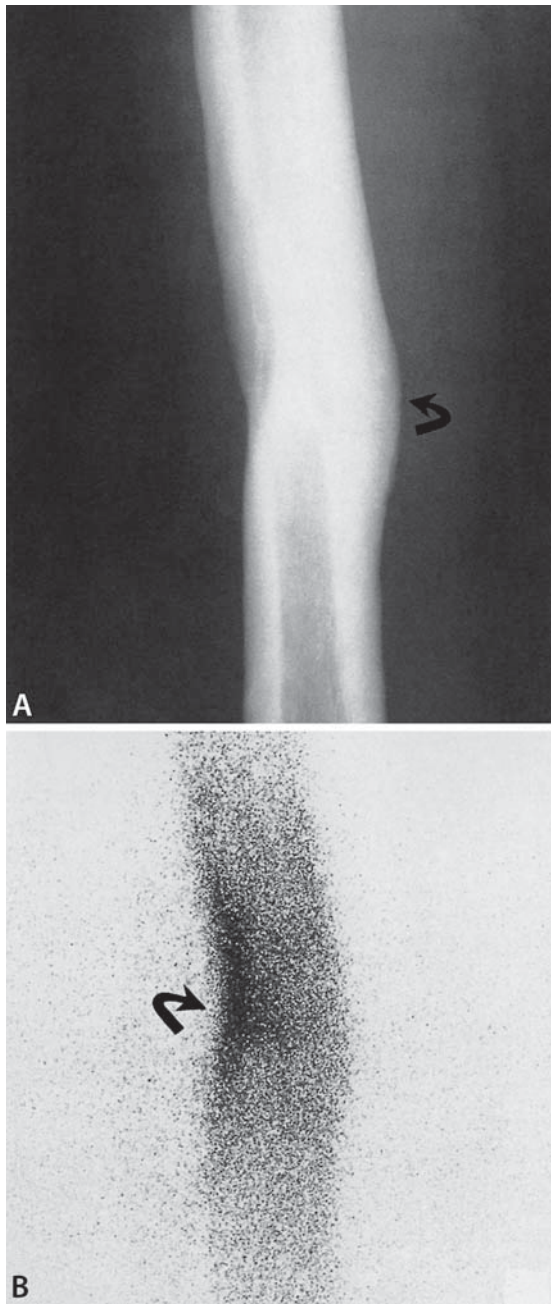

Fig. 6.21A, B Old osteomyelitis. **A** Anteroposterior radiograph of the right femur in a 31-year-old man with an ill-defined "pain" in an old osteomyelitis site reveals a thickened cortex with medial angulation (*curved arrow*). **B** Anterior pinhole scintigraph shows moderate tracer uptake in the concave lateral border of the affected area (*curved arrow*) but no abnormal tracer uptake in the thickened, convex medial border. The increased uptake in the lateral border may be related to increased bone turnover due to more stressful weight bearing (Wolff's law)

intense uptake in the medullary space and the less intense uptake in the thickened corticoperiosteal layer (Fig. 6.20C). The former represents the main chronic infective focus in the bone marrow and the latter the associated corticoperiosteal reaction. The medullary uptake is uniform and expansive. Tracer uptake in a longstanding, inactive osteomyelitis is reminiscent at most, but the radiographic sclerosis is prominent and persistent (Fig. 6.21). It is to be noted that, if present, the concave border of the angulated long-bone shaft may accumulate tracer intensely, reflecting undue stress carried by this deformed part (Wolff's law).

6.5.3 Brodie's Abscess

Brodie's abscess is another special form of chronic hematogenous osteomyelitis. It is a local disease and may be single or multiple. The causative agent in the vast majority of cases is staphylococcus. This form of abscess has been suggested to develop when an infective organism is low in virulence or the host has increased resistance to infection (Grieco 1972). Brodie's abscess is common in children, and the most common site of involvement is the distal or proximal tibia, and other tubular bones; flat and irregular bones are involved less frequently. Histologically, the abscess wall is marginated by inflammatory granulation tissue and spongy bone eburnation. Radiography shows irregular lucent area(s) surrounded by sclerosis. The lesion is usually located in the metaphysis, abutting the physeal plate (Fig. 6.22A).

Pinhole scintigraphy reveals an ill-defined area of intense uptake characteristically located in the diaphyseal marrow space, for example, of the distal femur (Fig. 6.22B). The principal lesion is surrounded by a reactive zone that accumulates uptake less intensely.

6.5.4 Osteomyelitis in Flat and Irregular Bones

The irregular bone most often affected with osteomyelitis in adults is the spine; this is discussed in detail below. The next most commonly affected bones are the pelvis, skull, and tarsal bones.

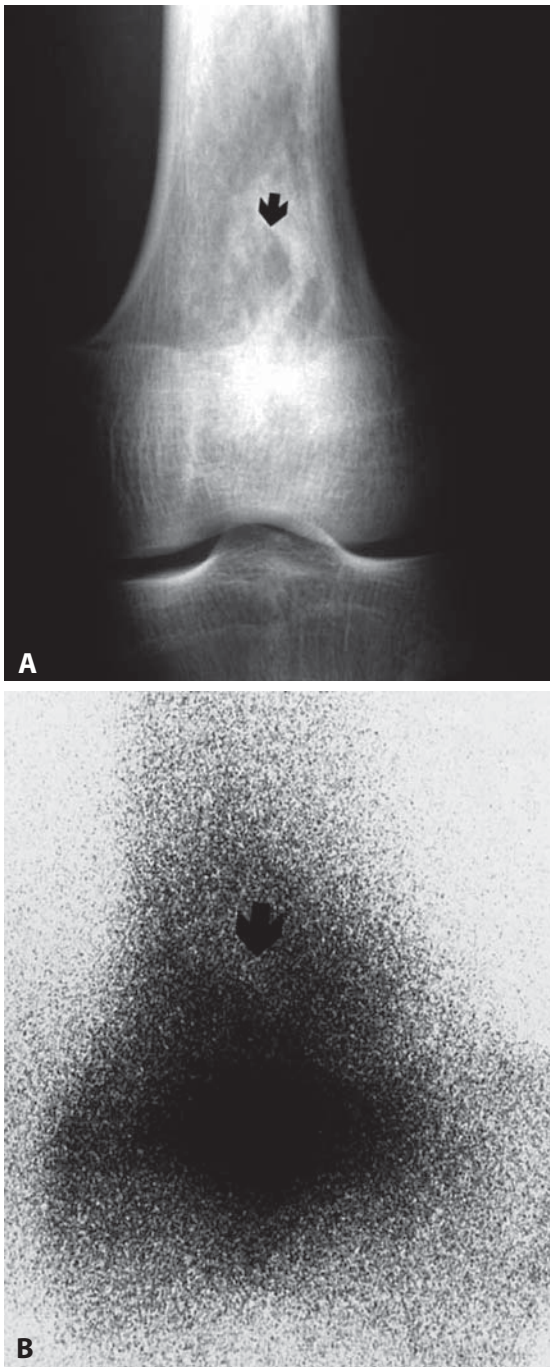

Fig. 6.22A, B Brodie's abscess. **A** AP radiograph of the right distal femoral metaphysis in a 31-year-old male patient with Brodie's abscess shows irregular lucent defects surrounded by diffuse sclerosis. The defects are created by saucerization. **B** Anterior pinhole scan of the same infective lesion shows an ill-defined area of intense uptake localized to the metaphyseal medullary space (*arrow*)

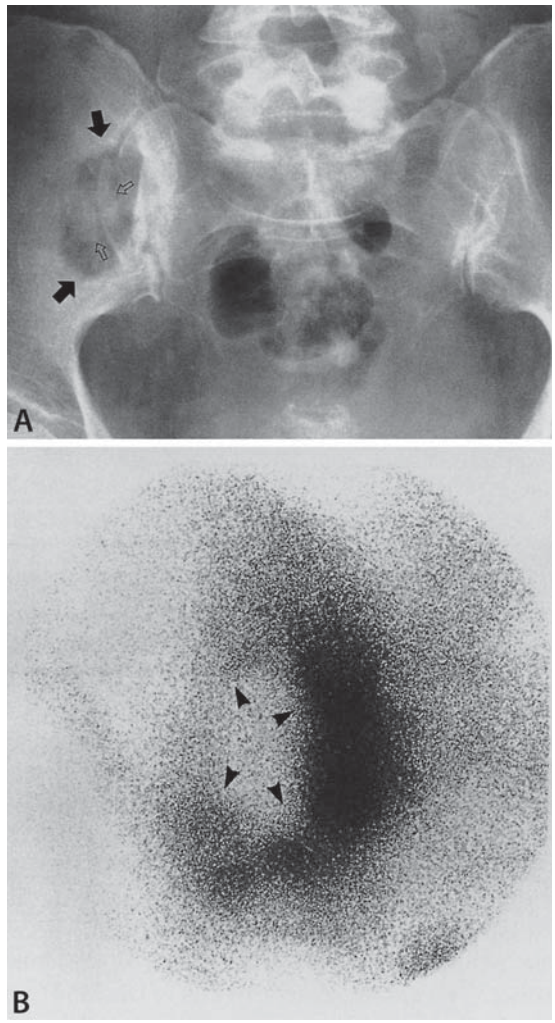

Fig. 6.23A, B Subacute osteomyelitis with bone abscess in the ilium. **A** Anteroposterior radiograph of the pelvis in a 53-year-old woman with postoperative pelvic bone infection shows large, ovoid bone destruction with surrounding sclerosis in the right ilium near the sacrum (*arrows*). A small dead bone is seen within the lesion (*open arrows*). The radiograph is printed with the right side to the left to match the pinhole scintigraph. **B** Posterior pinhole scintigraph shows a large, ovoid, photopenic defect surrounded by intense tracer uptake in the left ilium, indicating bone abscess formation (*arrowheads*). The dead bone is not visualized because it does not accumulate tracer

Radiographically, like the long bones, the flat and irregular bones show rapid osteolysis with abscess formation, producing a lucent bone defect surrounded by sclerosis (Fig. 6.23A). Un-

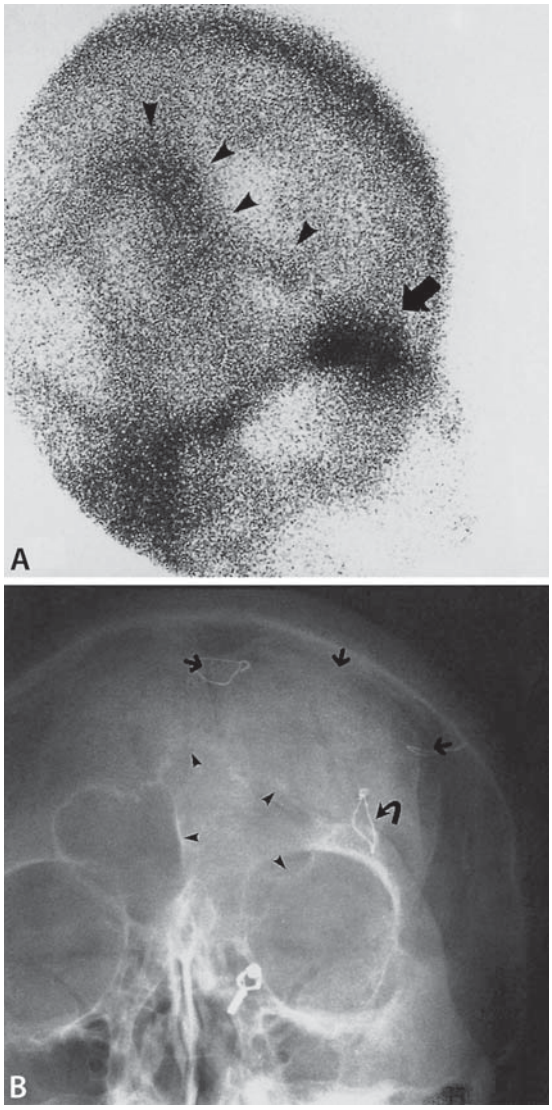

Fig. 6.24A, B Focal infection in a craniotomy defect. **A** Anterior pinhole scan of the left frontal skull shows intense tracer uptake localized in the immediate supraorbital region, indicating focal infection of a craniotomy defect (*arrow*). Uninfected craniotomy defects do not concentrate tracer. Incidentally, some tracer uptake is seen in the periphery of the left frontal sinus due to unrelated sinusitis (*arrowheads*). **B** Water's view radiograph reveals the craniotomy defect in the left frontal bone with scalp sutures (*arrows*) and clouding of the left frontal sinus (*arrowheads*). The infection in the left supraorbital bone is hardly recognizable (*curved arrow*)

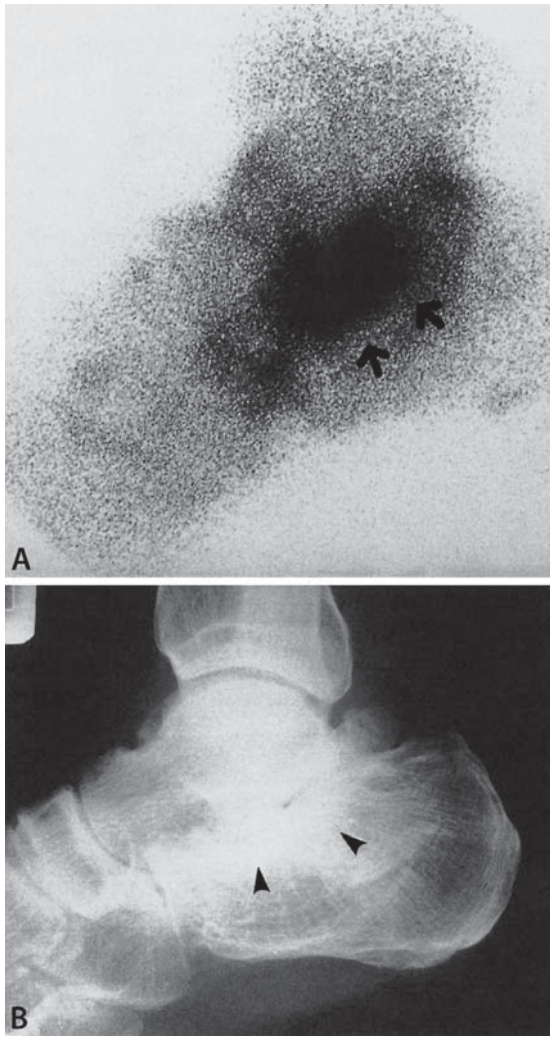

Fig. 6.25A, B Subarticular (the equivalent of long bone metaphysis) localization of osteomyelitis in irregular bones. **A** Medial pinhole scan of the right ankle in a 54-year-old male diabetic with chronic osteomyelitis induced by acupuncture shows extremely intense tracer uptake in the subarticular zones of the talus and calcaneus about the subtalar joint (*arrows*). **B** Mediolateral radiograph reveals the narrowing of the subtalar joint with marked eburnation in the periarticular bones (*arrowheads*)

less treated appropriately, sooner or later the adjacent joint may become involved.

Pinhole scintigraphy shows diffusely increased tracer uptake in osteomyelitis of the flat bone, and a photopenic area in the abscess, when formed (Fig. 6.23B). The infection of surgical defects in the skull, a flat bone, demonstrates a similar finding (Fig. 6.24A). Ge-

nerally, the intensity of tracer uptake varies according to the severity of the infection.

When the tarsal bones are infected, tracer typically accumulates in the periarticular or apophyseal cancellous bones, the equivalent of the metaphysis of the long bones. The chronic osteomyelitis in the hindfoot often shows prominent tracer uptake in eburnation. This is particularly true in the bones about the subtalar joint that constantly bears the body weight (Fig. 6.25).

6.5.5 Osteomyelitis in Diabetic Foot

Diabetic foot denotes a complex bone and joint disorder that involves the foot in patients with longstanding diabetes. Infection directly extends from either contiguous cellulitis or infected skin ulcers or is mediated by the combination of circulatory, neuropathic, and degenerative alterations. Arteriosclerosis and occlusion, and resultant osteonecrosis are common complications of diabetes mellitus. In diabetics it is often difficult to distinguish between primary and secondary osteomyelitis in the tarsal bones and toes, especially when the infection runs a protracted course with a concurrent skin infection.

Radiographically, diabetic tarsal bone infection is characterized by the combination of irregular lytic and sclerotic changes and joint space narrowing. Regardless of the primary site, bone and joint infection causes the diffuse swelling of the overlying soft tissues. Soft-tissue changes are most severe when gangrene is superimposed (Fig. 6.26A). Avascular necrosis and amputation of phalangeal bones are not rare in advanced diabetics (Fig. 6.26B).

The pinhole scintigraphic findings of osteomyelitis in diabetics are not dissimilar to those of osteomyelitis in non-diabetics. In the acute stage, tracer accumulates intensely in the subchondral or apophyseal cancellous bones with joint space narrowing if invaded. In the chronic stage, the joint space becomes further narrowed and eventually closed, and the periarticular bones show extremely intense uptake due to eburnation (Fig. 6.25A). Nuclear angiography is a useful means for differential diagnosis between osteomyelitis and cellulitis in the diabetic foot (Park et al. 1982). It also plays a unique role in diagnosing diabetic vasculopathy with gangrenous change and peripheral bone lesions (Fig. 6.26).

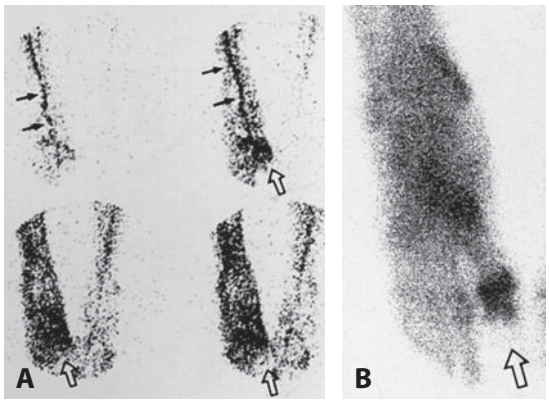

Fig. 6.26A, B Three-phase bone scintigraphy of diabetic digital gangrene. **A** Nuclear angiographs show markedly increased blood flow and blood pool in the right leg and foot (*arrows*) with vascular deprivation in the distal great toe (*open arrows*). **B** Pinhole scan reveals increased tracer uptake in the surviving proximal phalanx and avascular necrosis of the distal phalanx of the great toe (*open arrow*)

6.5.6 Osteomyelitis of the Spine

Osteomyelitis of the spine (pyogenic spondylitis) typically affects adults. The main causative agents include *S. aureus* and streptococcus, and rarely gram-negative bacilli and salmonella. Pyogenic spondylitis may result from the direct implantation of organisms at the time of operation. However, in the vast majority the infection is blood-borne. The organisms are introduced through the arterial rather than venous pathway, and the early foci are located in the subchondral zone or the endplate of the vertebral body, the area richly supplied with nutrient endarteries (the equivalent of the long bone metaphysis). Clinically, the infection starts in the subchondral zone of one of the midlumbar vertebrae and rapidly spreads to the apposing vertebra above or below across the disk. In the course of the spreading the disk is inescapably involved, producing infective (pyogenic) diskitis. Pyogenic spondylitis

almost always involves two neighboring vertebrae in a set, and in only less than 1% of cases is it confined to one vertebra and one disk.

Radiographically, acute infective spondylitis with diskitis is characterized by the osteolysis of apposing endplates with a narrowed intervertebral space (Fig. 6.27B). The early lytic focus in the anterior rim of the vertebral endzone may not be seen easily, and conventional or computed tomography is often required. Indeed, such a lesion is one of the most important indications for bone scintigraphy (see below). Later in the chronic or healed stage, osteosclerosis may ensue.

Ordinary scintigraphy shows simple block-like uptake in infective spondylitis, not distinguishing the individual components of the disease. Pinhole scintigraphy, however, can localize the abnormal uptake to the endplates of the affected vertebrae with visualization of the disk space in between. In the acute and subacute stages, tracer distribution is typically unequal between the two apposing endplates (Fig. 6.27A). Thus, the classic hematogenous form of spinal infection may indicate the sequence of infection: a dominant tracer uptake in the initially affected upper endplate of a caudally situated vertebra and less extensive uptake in the subsequently affected lower endplate of a cranially situated vertebra. At this stage, the disk space is invariably narrowed due to diskitis. The sequence of infection may be reversed in the direct implantation type, yet the basic features including the dominant initial focus, narrowed disk space, and less dominant secondary focus may remain the same (Fig. 6.28). When spondylitis is established, tracer accumulates in the entire span of the apposing endplates, giving rise to the sandwich-like appearance (Bahk et al. 1987). Old or long-standing lesions develop spurs at the vertebral edge, manifesting as horizontally aligned "hot" beaking. One condition that may resemble chronic pyogenic spondylitis with endplate sclerosis is spondylosis. However, the latter disorder strongly tends to involve the lower-most lumbar vertebrae and the sacrum, manifesting parallel band-like or arcuate uptake in the end-

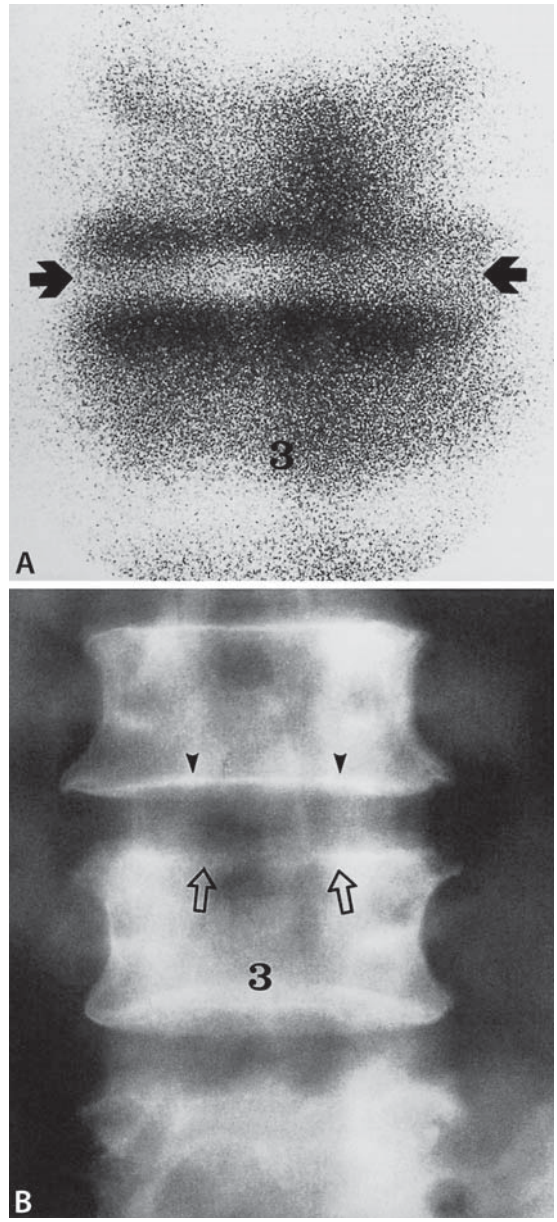

Fig. 6.27A, B Asymmetrical endplate involvement in acute, hematogenous, pyogenic spondylitis. **A** Posterior pinhole scintigraph of L2 and L3 vertebrae in a 53-year-old man with back pain reveals extensive area of intense tracer uptake in the dominant, initial infection in the upper half of the L3 vertebra and less intense change in the recessive, secondary focus in the lower endplate of the L2 vertebra. The disk space is narrowed (*arrows*). **B** Conventional anteroposterior X-ray tomogram shows lysis in the initial infection site of the L3 vertebra (*open arrows*) and mild shagginess in the secondarily involved L2 vertebra (*arrowheads*)

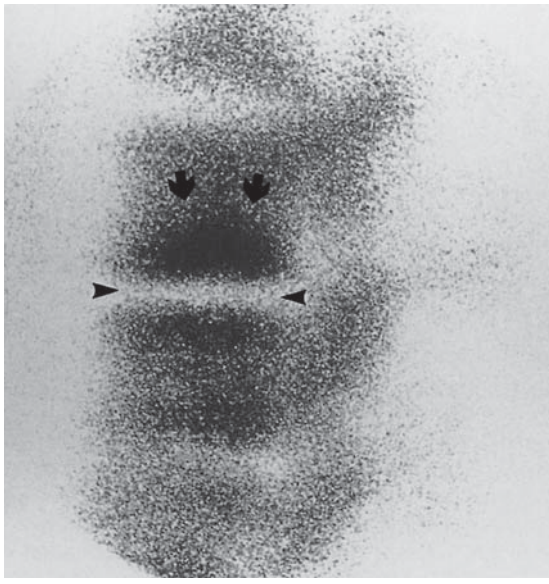

Fig. 6.28 Reversed asymmetry of the endplate involvement in postoperative spondylitis. Lateral pinhole scan of the midlumbar spine in a 20-year-old man with gram-negative bacillary spondylitis that started after laminectomy shows intense, semilunar tracer uptake in the initial focus in the lower L3 vertebral body (*arrows*) and less intense uptake in the upper endplate of the secondarily affected L4 vertebra. The disk space is narrowed (*arrowheads*)

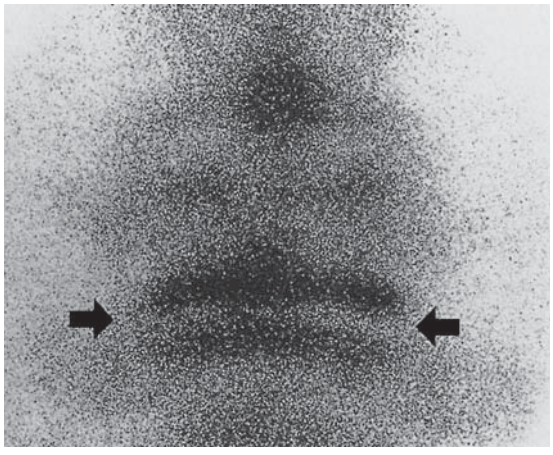

Fig. 6.29 Parallelism of the endplate involvement in spondylosis. Anterior pinhole scan of the lower lumbar spine in a 42-year-old woman with lumbago demonstrates parallel arcuate tracer uptake in the lower endplate of the L4 vertebra and the upper endplate of the L5 vertebra (*arrows*). The intervertebral disk space is narrowed due to disk degeneration

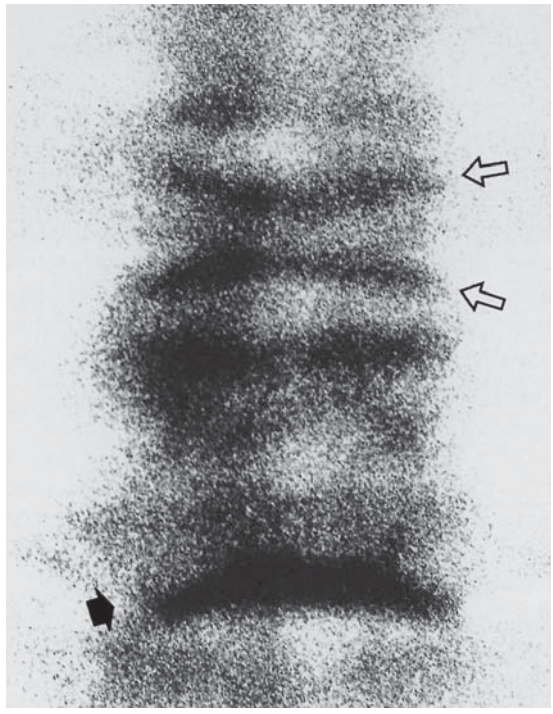

Fig. 6.30 (Uni)concave and biconcave endplate deformities in spinal compression fractures. Posterior pinhole scan of the lumbar spine in an elderly woman with marked osteoporosis shows biconcave deformity in the L2 vertebra (*open arrows*) and (uni)concave deformity in L4 due to compression fractures (*arrow*). The former fractures were older than the latter, and hence show less intense tracer uptake. Note that the disk spaces are not narrowed

plates with a narrowed disk space (Fig. 6.29). Another confusing condition is the "fish vertebra" deformity of porotic vertebrae, but the depressed or concave "hot" endplate with a widened disk space is pathognomonic (Fig. 6.30). The radiographic and scintigraphic manifestations of tuberculous spondylitis are essentially the same as those of acute pyogenic spondylitis except for a few minor differences, which are discussed in the following section.

6.6 Tuberculosis of Bone

Tuberculosis is the chronic infective disease caused by *Mycobacterium tuberculosis* or rarely by *M. bovis*, and is characterized pathologically by caseous necrosis and granuloma formation. In the majority of cases skeletal involvement is secondary to an extraosseous primary focus in the lung or urinary tract, and is hematogenous. Tuberculous spondylitis is mediated via Batson's paravertebral venous plexus, whereas the tuberculosis in the other bones is via the arterial route. Unlike pyogenic infection, tuberculosis affects the spine and ribs much more frequently than the long bones. Clinically, bone tuberculosis may present either as a localized abscess or osteomyelitis. The onset is slow and insidious and the course usually protracted. Rib affection is called caries. In infants and young children, the phalangeal bones are occasionally involved, causing dactylitis that has a puffed, expansile, spine-like appearance; hence, spina ventosa. As shown in Fig. 6.31, tuberculous dactylitis is also known to occur in adults (Feldman et al. 1971).

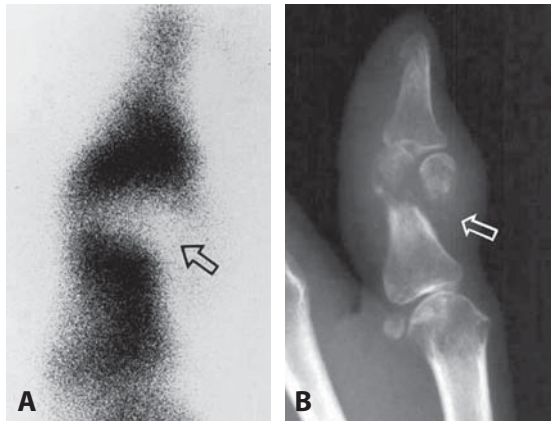

Fig. 6.31A, B Tuberculous dactylitis with the spina ventosa (puffed spine) sign in an adult. **A** AP pinhole scan of the left first finger in a 33-year-old female patient with digital tuberculosis shows increased tracer uptake in the head of the proximal phalanx and the base of the distal phalanx with a photon defect in the interphalangeal joint (*open arrow*). **B** Lateral radiograph reveals swollen soft tissue with osteolysis and pathological fracture involving the proximal phalangeal head (*arrow*)

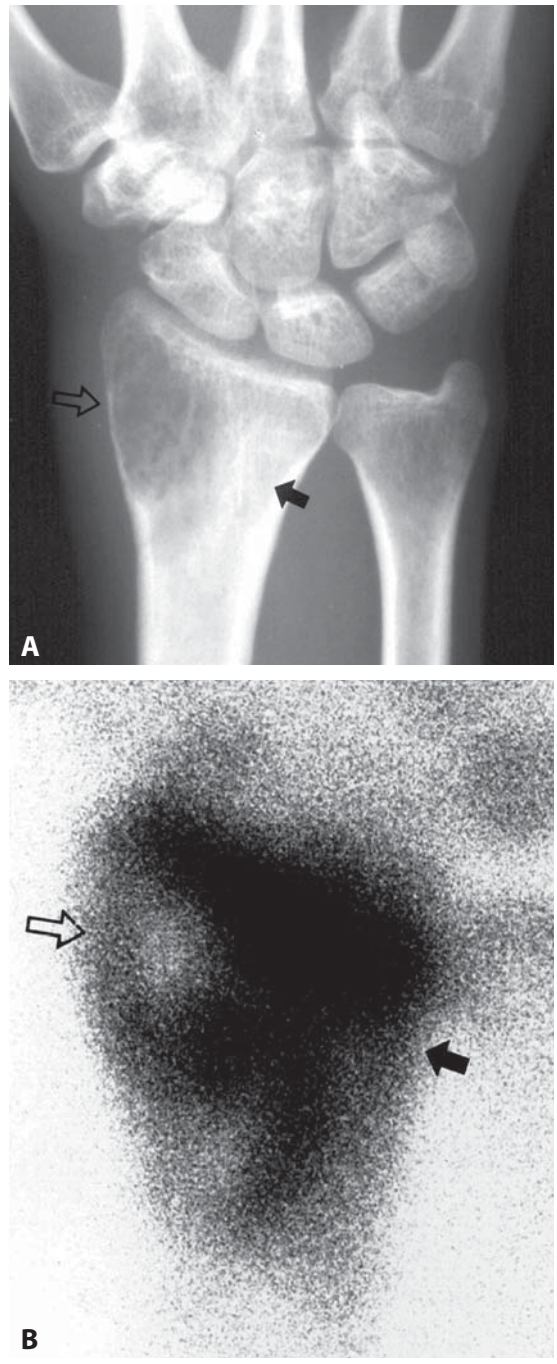

Fig. 6.32A, B Classic osteolytic manifestation of long bone tuberculosis with abscess and unimpressive reactive bone change. **A** Dorsoventral radiograph of a 41-year-old female with cystic tuberculosis in the right distal radius shows a poorly defined ovoid radiolucency (*open arrow*) with reactive sclerosis in the ulnar side (*solid arrow*). **B** Dorsal pinhole scan shows intense tracer uptake with a photon defect due to the abscess (*open arrow*). Intense uptake is mainly in the ulnar side of the lesion (*solid arrow*)

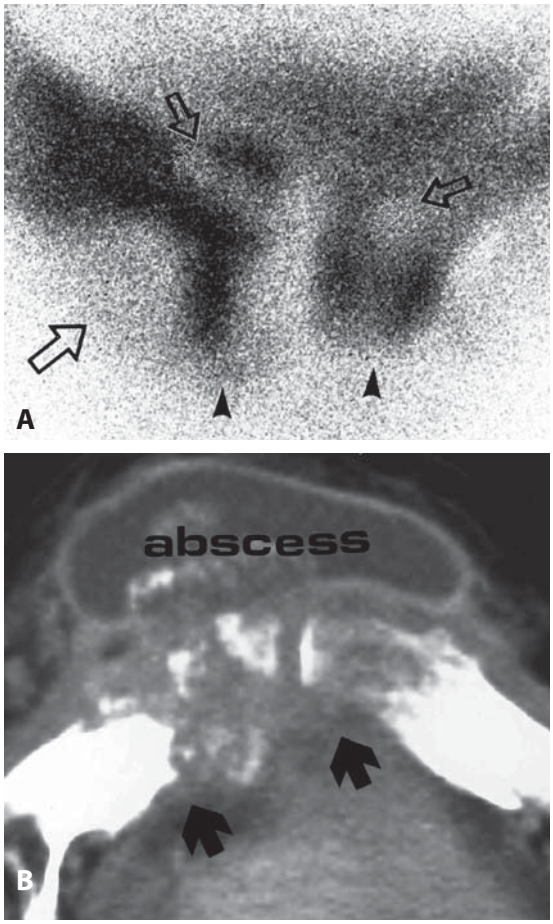

Fig. 6.33A, B Cyst-like manifestation of bone tuberculosis. **A** Anterior pinhole scan of the pubis in a 63-year-old female patient with tuberculosis shows multiple photon defects due to abscesses (*open arrows*) with prominent lesion uptake (*arrowheads*). **B** Transverse CT of the pubis reveals irregular lysis intermingled with residual bony fragments (*arrows*) and a large prepubic abscess formation (*abscess*)

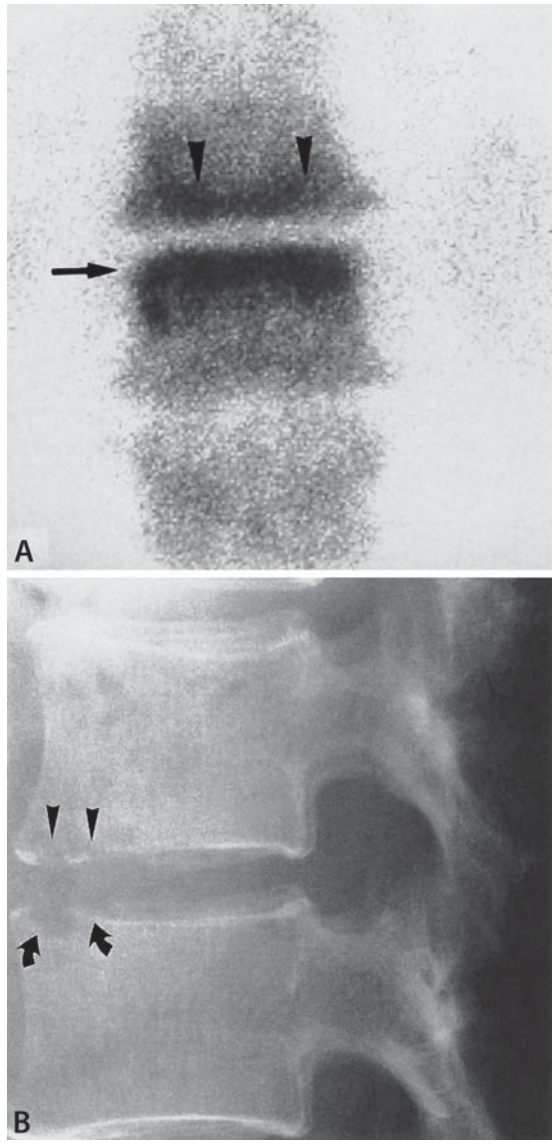

Fig. 6.34A, B Tuberculous spondylitis with asymmetrical "sandwich" sign. **A** Posterior pinhole scintigraph of the midlumbar spine in a 50-year-old man shows very intense, band-like tracer uptake in the initially infected upper endplate of the L3 vertebra (*arrow*) and less intense uptake in the secondarily affected lower endplate of the L2 vertebra (*arrowheads*). The disk space is narrowed. **B** Lateral radiograph shows lysis in the upper anterior edge of the L3 vertebra (*arrows*) and a subtle, spread lesion in the apposing endplate across the disk space, which is slightly narrowed (*arrowheads*). Essentially, the alterations are the same as those of pyogenic spondylitis shown in Figs. 6.27 and 6.28

Characteristic radiographic features include bone destruction with minimal bone proliferation (Fig. 6.32). Unlike in pyogenic infection, sequestration or significant periosteal reaction is uncommon. In dactylitis, however, sequestrum may occasionally be formed (Fig. 6.31). Abscess formation is a prominent feature of bone tuberculosis (Fig. 6.33). When the spine is involved, bone destruction typically starts in the anterior subchondral region of the vertebral body, gradually extending to the remaining part and transdiskally to the adjacent ver-

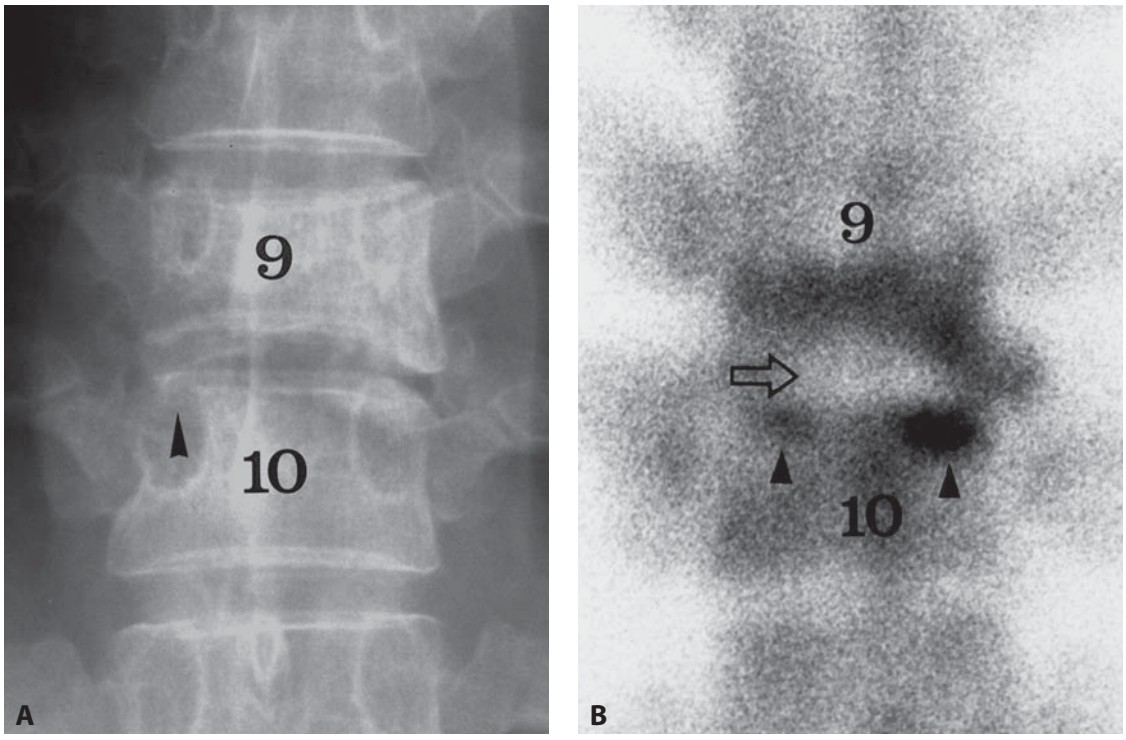

Fig. 6.35A, B Pathological fracture of tuberculous vertebra with apparent widening of subjacent disk space. **A** AP radiograph of the midthoracic spine of a 46-year-old female with tuberculous spondylitis shows moderate compression of the T9 vertebra (*arrow*). The disk space is narrowed with the central portion being seemingly preserved. Focal osteolysis is noted in the right edge of the T10 upper endplate, denoting transdiskal spread of tuberculosis (*arrowhead*). **B** Posterior pinhole scan shows diffuse tracer uptake in the collapsed T9 vertebra with segmental transdiskal spread to the T10 upper endplate (*arrowheads*). Note apparent disk space widening (*open arrow*), and side mismatch due to the different radiographic and scintigraphic projections

tebra (Fig. 6.34). Disk-space narrowing is the hallmark of diskitis, and tuberculous spondylitis is usually multivertebral. Pathological fracture is not uncommon, and, if it occurs the disk space may appear spuriously preserved (Fig. 6.35).

Characteristic pinhole scintigraphic features of long-bone tuberculosis include increased tracer uptake in the metaphysis (Figs. 6.32 and 6.36), an important feature of hematogenous infection in the long bones, as discussed in osteomyelitis (Fig. 6.2). In the same context the bone scan features of flat bone tuberculosis are not dissimilar to those of nontuberculous infection of the flat bones: a protean mixture of irregular increased and decreased tracer uptake. Sufficiently large tuberculous abscess or lytic focus is portrayed as a photopenic area surrounded by markedly increased tracer uptake in the perifocal sclerosis (Figs. 6.32 and 6.37). As in other infective spondylitides, the scintigraphic findings of tuberculous spondylitis vary according to the disease stage. In the early stage, the dominant tracer uptake occurs in the initial focus in one vertebral endplate (not in the two apposing endplates of the two neighboring vertebrae as seen in the later stage; Fig. 6.34). Even in this early stage the reduction of intervertebral distance may be evident. Nearly all cases reveal the involvement of the apposing endplate at this stage, although the change is mild. Importantly, sooner or later the unchecked initial lesion in the end-zone spreads to the center of the vertebra, manifesting as diffused uptake in a large area (Fig. 6.38). It is unusual to observe such a central spread in infective spondylitis, in which acute or subacute changes with intense uptake are still in the

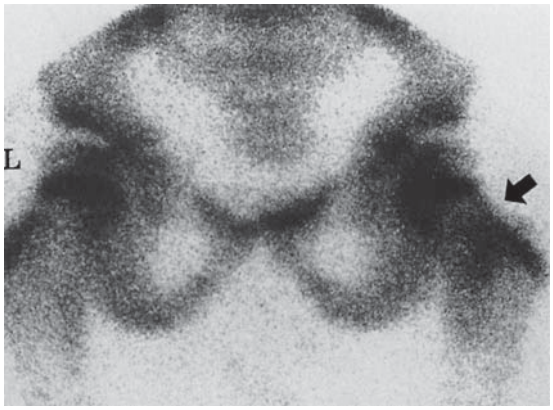

Fig. 6.36 Tuberculosis in long bone. Posterior pinhole scan of both hips in a 4-year-old boy shows increased tracer uptake in the proximal metaphysis of the right femur, denoting tuberculous osteomyelitis (*arrow*). Compare with the normal left hip (*L*). The finding is very similar to that of acute osteomyelitis, but the uptake is less intense

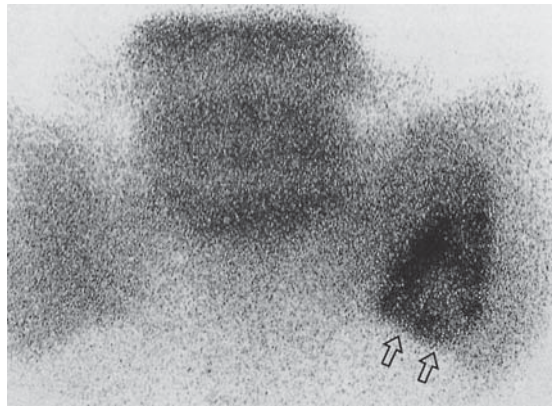

Fig. 6.37 Tuberculous bone abscess. Anterior pinhole scintigraph of the left sacroiliac joint shows diffusely increased tracer uptake in the lower aspect of the left sacroiliac joint. Irregular "cold" areas represent bone destruction (*open arrows*). Unlike in pyogenic infection, reactive bone formation is inconspicuous

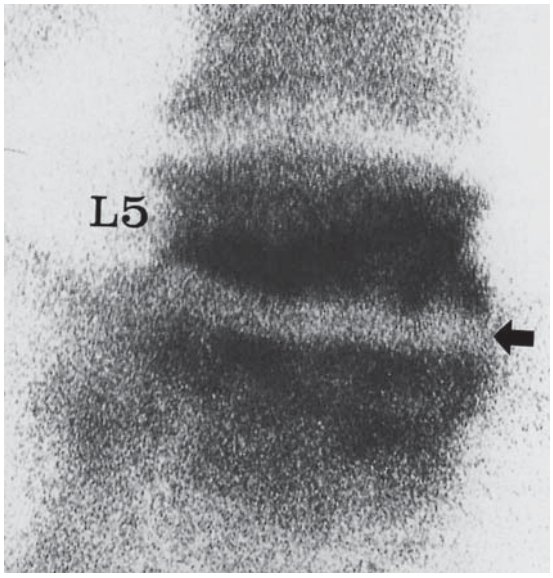

Fig. 6.38 Centripetal and transdiskal spread of initial endplate tuberculosis. Anterior pinhole scintigraph of L5 and S1 vertebrae in a 68-year-old man shows intense tracer uptake in nearly the entire L5 vertebral body and fairly extensive alteration in the S1 vertebra, indicating transdiskal spread from L5. The disk space is markedly narrowed (*arrow*)

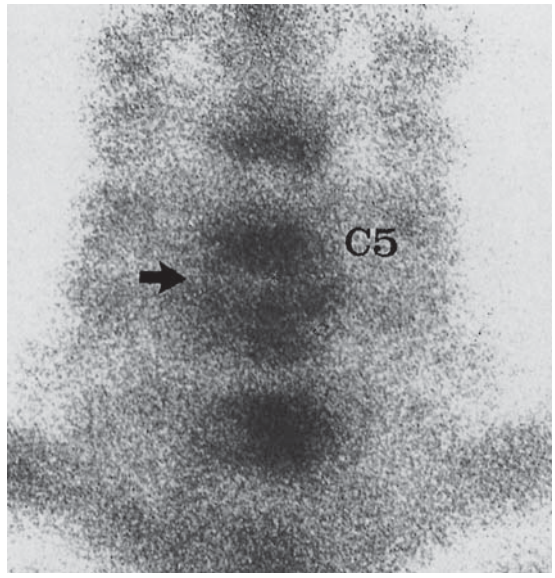

Fig. 6.39 Tuberculosis in the lower cervical spine. Posterior pinhole scintigraph of the lower cervical spine shows intense tracer uptake in C5 and C6 vertebrae with narrowing of the disk space (*arrow*). Note intense tracer uptake in the adjacent normal spinous processes, confusing the situation. However, disk space narrowing is the hallmark of infective spondylitis

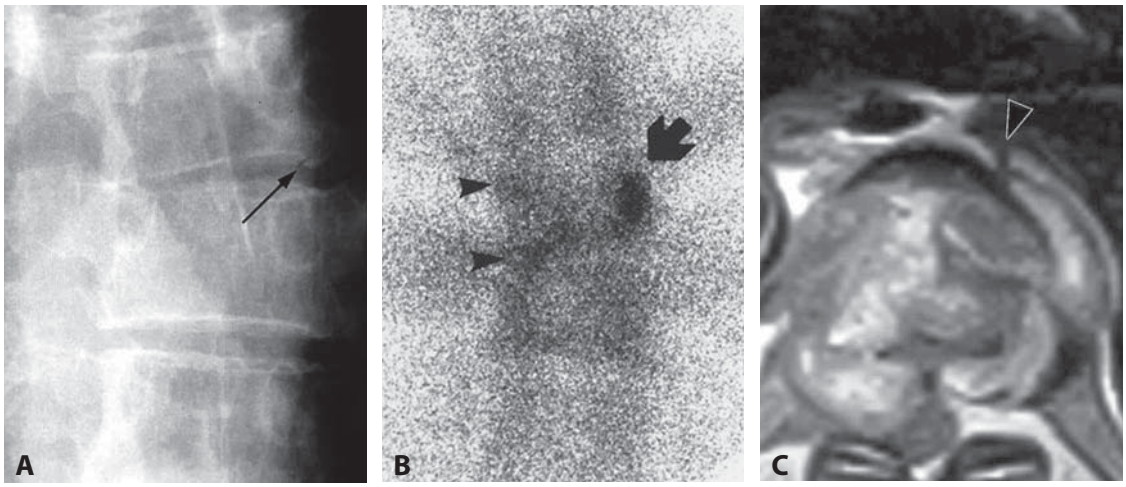

Fig. 6.40A–C Sensitivity of pinhole scan in the diagnosis of a pathological fracture of a tuberculous spine. **A** AP radiograph of the T5 and T6 vertebrae in a 75-year-old male with tuberculous spondylitis shows a barely discernible fracture in the anterior lower edge of T5 (*arrow*). The fracture was noticed after observing the pinhole scan. Note disk space narrowing due to tuberculous diskitis. **B** Posterior pinhole scan reveals prominent uptake in the fracture (*arrow*). Underlying tuberculous changes are indicated by increased uptake that frames the affected vertebrae (*arrowheads*). **C** T2-weighted MRI confirms the diagnosis (*arrowhead*)

end-zone (Figs. 6.27 and 6.28). Eventually, with protracted transdiskal spread of the infection, the neighboring vertebra becomes extensively involved, making the difference between the original and following lesions nearly unrecognizable (Fig. 6.38). Frequently, the affected vertebrae are collapsed at this stage. Tuberculous spondylitis in the lower cervical spine may impose a diagnostic problem because the normally intense tracer uptake in the vertebral bodies and spinous processes often simulates pathology. Nevertheless, the disk space narrowing in infective spondylitis is a highly reliable sign (Fig. 6.39). In advanced cases the disk space is completely obliterated, and two or more neighboring vertebrae may become fused to form a "block vertebra".

The vertebrae replaced with tuberculous necrosis and granulomatous tissues are fragile and prone to pathological fracture (Fig. 6.34), and small fractures defy radiographic detection, especially in the thoracic spine that is difficult to visualize radiographically without anatomical overlapping (Fig. 6.40A). However, pinhole scintigraphy can sensitively detect it (Fig. 6.40B). It is to be remembered that the necrosis, granulomas, and sequestrated bones of tuberculosis are not imaged positively because they do not accumulate tracer. Rib tuberculosis or caries manifests as mottled or homogeneous uptake with occasional fracture (Fig. 6.41).

6.7 ^{111}In- and ^{99m}Tc-Leukocyte and ^{67}Ga Citrate Scintigraphy in Skeletal Infections

Acute infection of bones and joints can be diagnosed using ^{99m}Tc-MDP scintigraphy reinforced with nuclear angiography and the pinhole technique. However, white blood cells labeled with ^{111}In or ^{99m}Tc are employed for more specific diagnosis of bone infection superimposed on fracture, operative wound, or prosthesis. One latest clinical study has confirmed the accuracy of ^{111}In-leukocyte scintigraphy in the diagnosis of posttraumatic and postoperative cranial and spinal infections (Medina et al. 2000). In order to replace expensive 111In with readily available ^{99m}Tc, leukocytes are labeled with hexamethyl-propylene

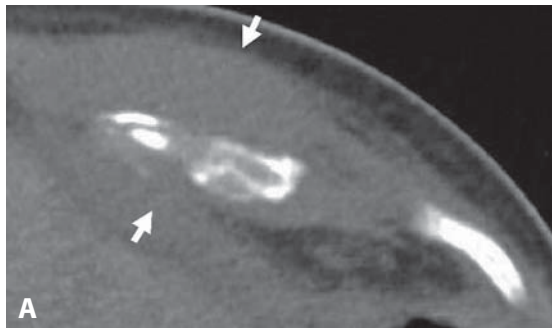

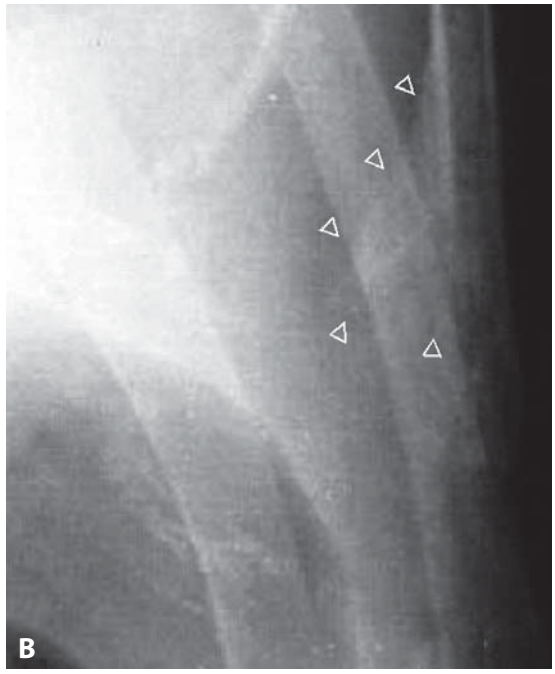

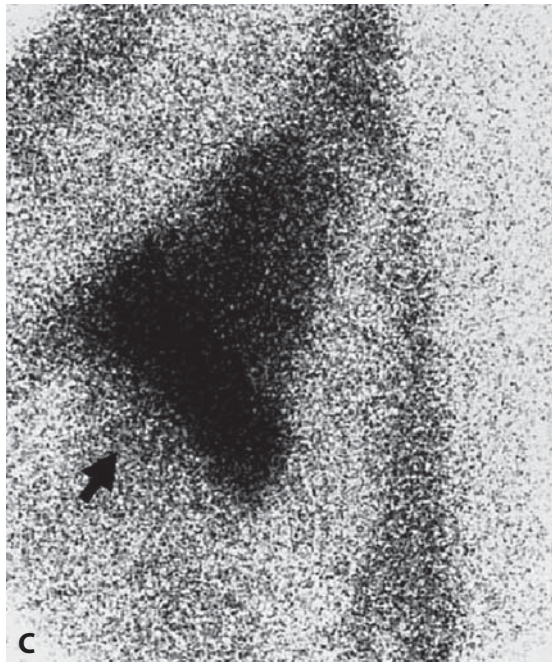

Fig. 6.41A–C Rib caries. **A** CT of the anterior portion of left rib 7 in a 66-year-old male with tuberculosis shows irregular osteolytic change with host bone fragmentation and soft-tissue abscess (*arrows*). **B** Tilted AP radiograph of the left lower chest demonstrates flaring and osteolysis in the anterior part of the left rib 7 (*arrow*). **C** Anterior pinhole scan reveals fan-shaped tracer uptake with the more intense uptake in the main infective focus at the costochondral junction, the site analogous to the long bone metaphysis

Fig. 6.42A, B Value of ^{67}Ga citrate scan in the diagnosis of infective focus. **A** ^{99m}Tc MDP whole-body bone scan shows intense uptake in the right tibia and fibula without indicating the infective focus (*?*). **B** ^{67}Ga scan shows tracer specifically accumulated in the infective focus in the right proximal tibia (*arrow*) ▷

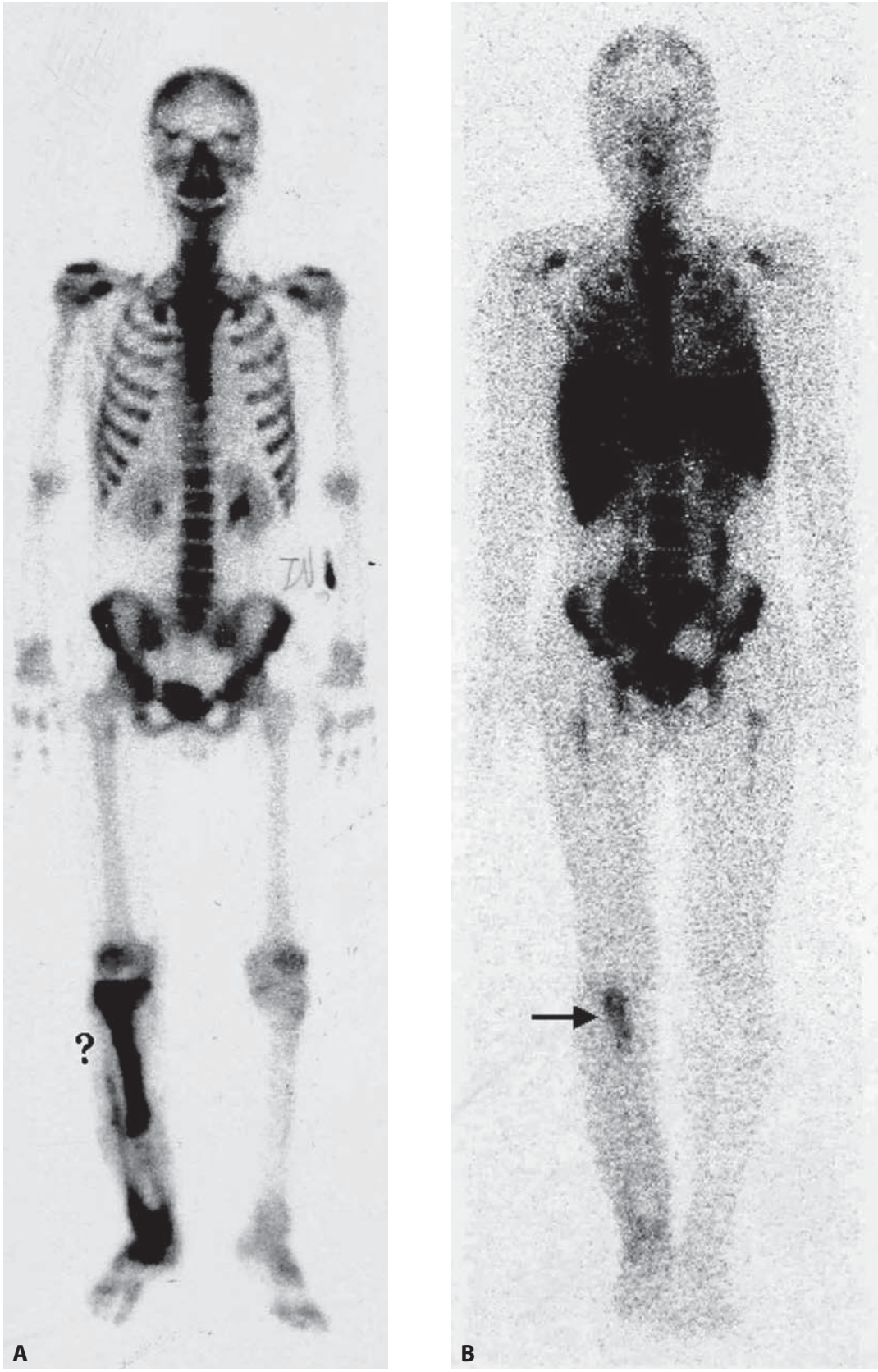
?
A
B

amine oxime (HMPAO). The image quality of ^{99m}Tc-HMPAO leukocyte scans is acceptable (Fig. 6.42), and has been shown to be superior to that of 111In-leukocyte scans (Peters 1994). Unfortunately, however, ^{99m}Tc-HMPAO avidly accumulates in the axial skeleton even in its normal state. In general, the ^{99m}Tc-HMPAO leukocyte scan is more suited to rapid screening of acute infection, whereas the ^{111}In-leukocyte scan is suited to chronic infection. Once ^{67}Ga citrate was used for the diagnosis of infective diseases but it indiscriminately accumulates in tumors. Some radioantibodies such as ^{99m}Tc-antigranulocyte antibodies have been tested but have been found to be neither reliable nor advantageous (Hotze et al. 1992; McAfee et al. 1991).

References

Ash JM, Gilday DL (1980) The futility of bone scanning in neonatal osteomyelitis. J Nucl Med 21:417–420

Bahk YW, Kim OH, Chung SK (1987) Pinhole collimator scintigraphy in differential diagnosis of metastasis, fracture, and infections of the spine. J Nucl Med 28:447–451

Capitanio MA, Kirkpatrick JA (1970) Early roentgen observations in acute osteomyelitis. Am J Roentgenol 108:488–496

Duszynski DO, Kuhn JP, Afshani E, et al (1975) Early radionuclide diagnosis of acute osteomyelitis. Radiology 117:337–340

Feldman F, Auerbach R, Johnston A (1971) Tuberculous dactylitis in the adult. AJR Am J Roentgenol 112:460–479

Gilday DL, Eng B, Paul DJ, et al (1975) Diagnosis of osteomyelitis in children by combined blood pool and bone imaging. Radiology 117:331–335

Grieco MH (1972) Pseudomonas arthritis and osteomyelitis. J Bone Joint Surg Am 54:1693–1704

Hotze AL, Briele B, Overbeck B, et al (1992) Technetium-99m-labeled anti-granulocyte antibodies in suspected bone infections. J Nucl Med 33:526–531

Jones DC, Cady RB (1981) "Cold" bone scans in acute osteomyelitis. J Bone Joint Surg Br 63:376–378

Lee SM, Bae SK, Cho MR (2000) Acute osteomyelitis shown as a cold lesion on bone scan. Korean J Nucl Med 34:516–520

McAfee JG, Gagne G, Subramanian G, Schneider RF (1991) The localization of indium-111-leukocytes, gallium-67-polyclonal IgG and other radioactive agents in acute focal inflammatory lesions. J Nucl Med 32:2126–2131

Majd M, Frankel RS (1976) Radionuclide imaging in skeletal inflammatory and ischemic disease in children. AJR Am J Roentgenol 126:832–841

Maurer AH, Chen DC, Camargo EE, et al (1981) Utility of three-phase skeletal scintigraphy in suspected osteomyelitis. J Nucl Med 22:941–949

Medina M, Viglietti AL, Gozzoli L, et al (2000) Indium-111 labelled white blood cells scintigraphy in cranial and spinal septic lesions. Eur J Nucl Med 27:1473–1480

Mok PM, Reilly BJ, Ash JM (1982) Osteomyelitis in neonate: clinical aspects and the role of radiography and scintigraphy in diagnosis and management. Radiology 145:677–682

Nelson JD (2000) Osteomyelitis and suppurative arthritis. In: Behrman RE, Kliegman RM, Jenson HB (eds) Textbook of pediatrics 16th edn. WB Saunders, Philadelphia

Park HM, Wheat LJ, Siddiqui AR, et al (1982) Scintigraphic evaluation of diabetic osteomyelitis. J Nucl Med 23:569–573

Peters AM (1994) The utility of [^{99m}Tc]HMPAO-leukocytes for imaging infection. Semin Nucl Med 24:110–127

Rinsky L, Goris ML, Schurman DJ, et al (1977) ^{99m}Technetium bone scanning in experimental osteomyelitis. Clin Orthop Rel Res 128:361–366

Rogers LF (1987) Infections and inflammations of bones. In: Juhl JH, Crummy AB (eds) Essentials of radiologic imaging, 5th edn. Lippincott, Philadelphia

Rosenthall L, Kloiber R, Damteu B, et al (1982) Sequential use of radiophosphate and radiogallium imaging in the differential diagnosis of bone, joint, and soft tissue infection: quantitative analysis. Diagn Imaging 51:249–258

Waldvogel FA, Papageorgiou PS (1980) Osteomyelitis: the past decade. N Engl J Med 303:360–370

Waldvogel FA, Medoff G, Swartz MN (1970) Osteomyelitis: a review of clinical features, therapeutic considerations and unusual aspects. N Engl J Med 282:198–206

Yang WJ, Chung SK, Bahk YW (1988) Three phase bone scintigraphy in active and inactive osteomyelitis. Korean J Nucl Med 39:209–213

7 Noninfective Osteitides

Noninfective osteitides are nonspecific inflammatory diseases of bone not caused by an infection. The causes are obscure and indeterminate except in radiation osteitis that results from ionizing radiation. Histologically, they are characterized by inflammatory bony proliferation and sclerosis. For the sake of scintigraphic description, the following diseases are dealt with under the heading of noninfective osteitides: osteitis condensans ilii, osteitis pubis, condensing osteitis of the clavicle, costosternoclavicular hyperostosis, Caffey's infantile cortical hyperostosis, Paget's disease of bone (osteitis deformans), and odontogenous osteitis. Radiation osteitis is also included in this category because it is also a nonspecific inflammatory disease with common radiographic and scintigraphic findings.

7.1 Osteitis Condensans Ilii

Osteitis condensans ilii is a nonspecific, self-limited inflammatory disease of the iliac bone in women more typically of childbearing age. This condition may be seen in older women, and even in men although rarely. One study revealed its incidence to be 1.6% (Numaguchi 1971). It is mostly bilateral and symmetrical, although unilateral cases are not rare. The cause is unknown, but, as with osteitis pubis, it has been related to abnormal stress of pregnancy and delivery, which cannot explain its occurrence in men.

The radiographic features of osteitis condensans ilii in the classic cases are simple yet unique, presenting triangular or spinnaker-like condensation of the ilia at the sacroiliac joints bilaterally and symmetrically (Fig. 7.1A). The condensation is localized to the lower anterior aspects of the ilia. Unlike in osteoarthritis, infective arthritis, or seronegative arthropathy, the sacroiliac joints in this condition are little affected and sacral involvement is minimal if any. The shape changes according to the degree of sacral inclination in relation to the radiographic projection (Fig. 7.2A). Regional osteophytic beaking is a common accompaniment.

Pinhole scintigraphy likewise shows symmetrical, club-shaped, or round areas of intense tracer uptake in the lower halves of both ilia along the sacroiliac joints (Figs. 7.1B and 7.2B). The shapes vary according to the sacral inclination. When the coronal plane of the sacrum is relatively flat the lesion looks like a spinnaker and when horizontally tilted the lesion appears round. In occasional cases, tracer uptake is asymmetrical and inhomogeneous, probably due to involutional change with age. It is well known that bilateral and more or less symmetrical tracer uptake may also occur in the lower sacroiliac joints in ankylosing spondylitis, but this is usually ill defined (see Ankylosing Spondylitis in Chapter 11) and mostly attended by the associated stigmata in the spine and other skeleton. It is to be remembered for differential diagnosis that unilateral sacroiliac joint uptake can occur in infection, trauma, metastasis, or seronegative spondyloarthropathies. Using pinhole scanning a more likely or specific diagnosis can frequently be indicated and the value of the tangential view in this situation cannot be overemphasized (Fig. 7.3).

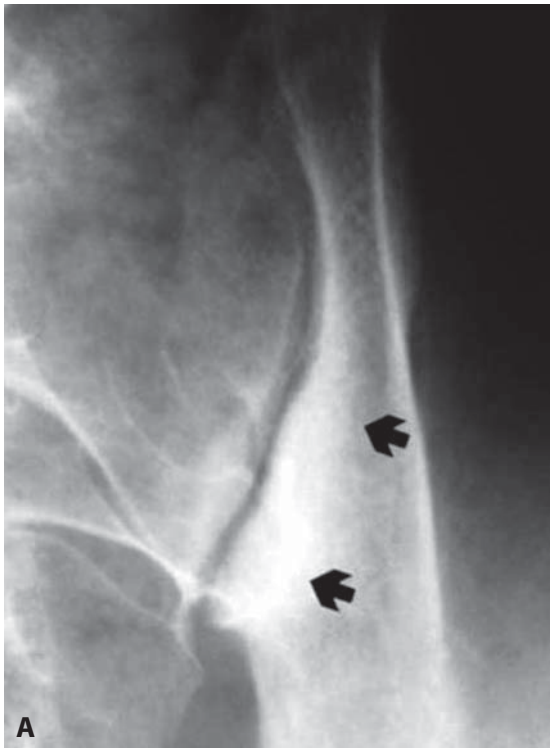

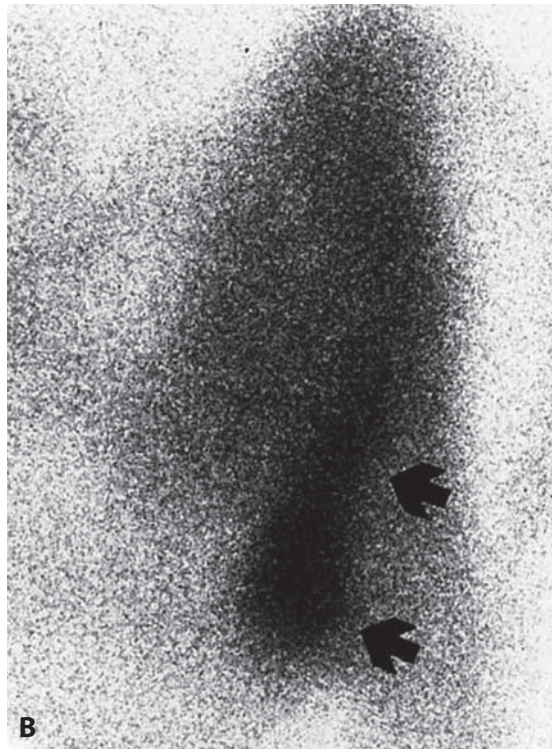

Fig. 7.1A, B Osteitis condensans ilii with the classic "spinnaker" sign. **A** AP radiograph of the left sacroiliac joint in a 32-year-old female shows long triangular bony condensation in the iliac side of the lower sacroiliac joint (*arrows*). Note preserved articular space. **B** Anterior pinhole scan reveals intense spinnaker uptake exactly corresponding to the radiographic condensation (*arrows*)

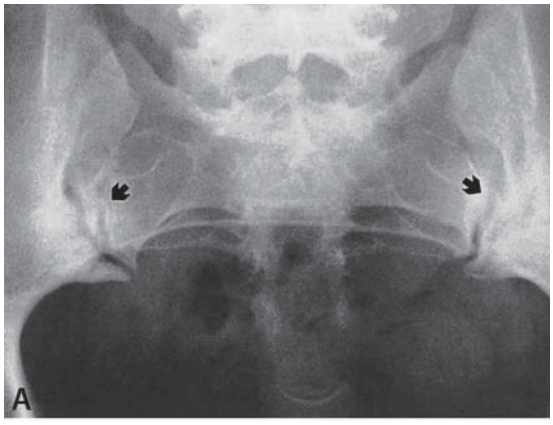

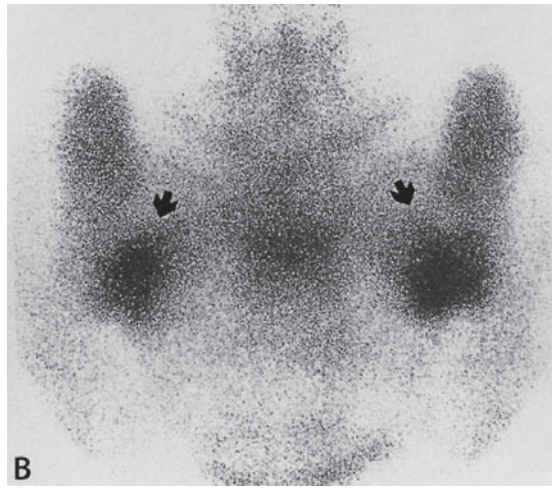

Fig. 7.2A, B Osteitis condensans ilii with modified round uptake in sacrum acutum. **A** AP radiograph of the pelvis with bilateral condensans ilii in posterocranially tilted sacrum in a 25-year-old female shows symmetrical roundish condensation (*arrows*). **B** Anterior pinhole scan shows well-matched round uptake (*arrows*). This finding is due to end-on (axial) viewing of the spinnaker

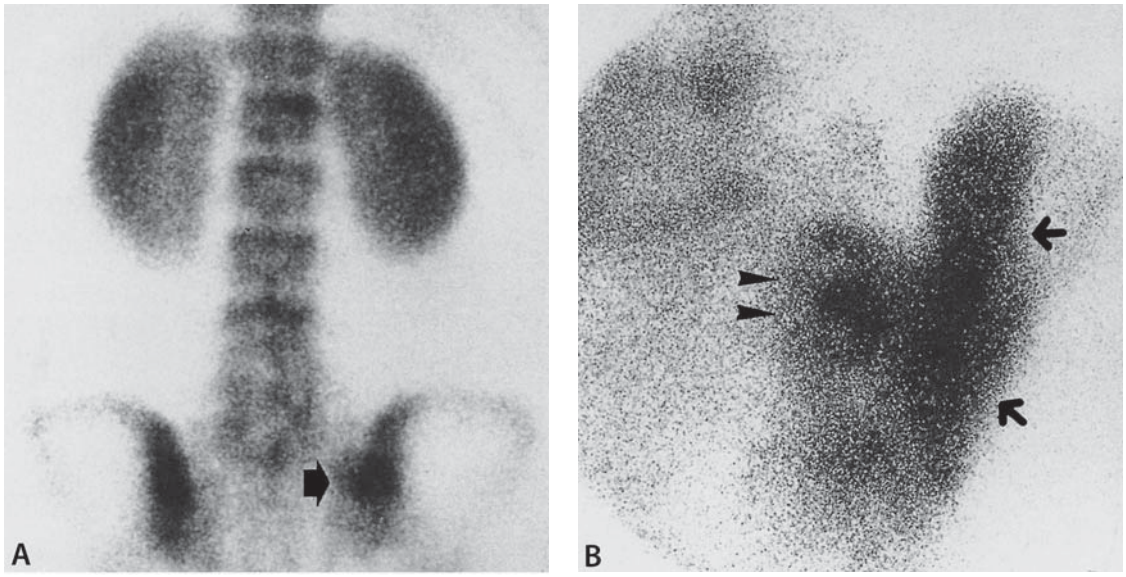

Fig. 7.3A, B Usefulness of pinhole scintigraphy in the study of the sacroiliac joints. **A** Posterior spot scintigraph shows a suspicious lesion in the right sacroiliac joint (*arrow*). **B** Tangential pinhole scan shows the intense tracer uptake to be localized in the mid-sacrum, a metastasis from lung cancer (*arrowheads*). Note the normal iliac tracer uptake (*arrows*)

7.2 Osteitis Pubis

Osteitis pubis is a nonspecific inflammatory disease of the symphysis pubis. The involvement is symmetrical, but the unilateral type is not rare. It develops after delivery and a pelvic operation such as prostatectomy or bladder surgery, although idiopathic occurrence in men or nulliparous women has been reported (Numaguchi 1971; Segal and Kellogg 1954). The histological feature is simple bony condensation (Rendich and Shapiro 1936). Clinically, the postoperative type is painful, whereas the postpartum type is usually asymptomatic. In many aspects osteitis pubis bears strong resemblance to osteitis condensans ilii, and both are considered related to physical stress. Indeed, the two conditions can occur simultaneously.
Radiographic features include cortical erosions, sclerosis, joint space narrowing, and rarely bony ankylosis (Fig. 7.4A), and vary according to the stage and duration of the disease.

Pinhole scintigraphy is useful in the study of osteitis pubis. Accurate judgment of abnormal uptake in the symphysis pubis in women of childbearing age is often difficult especially on ordinary scintigraphs because the pubic bone normally accumulates tracer significantly in this age group. However, pinhole scintigraphy shows the tracer uptake confined to the bones about the symphysis with narrowed joint (Fig. 7.4B). It is helpful to note that the physiological uptake is uniform and not localized to the cortex (Fig. 4.26). In a milder form, uptake may be subtle yet typically para-articular in location (Fig. 7.5B). Repeated pregnancies and deliveries may lead to recurrences, causing prominent uptake in the pubic bone that is deformed with a gaping symphysis (Fig. 7.6). In contrast and understandably, quiescent osteitis accumulates little tracer although radiographic changes remain (Fig. 7.7).

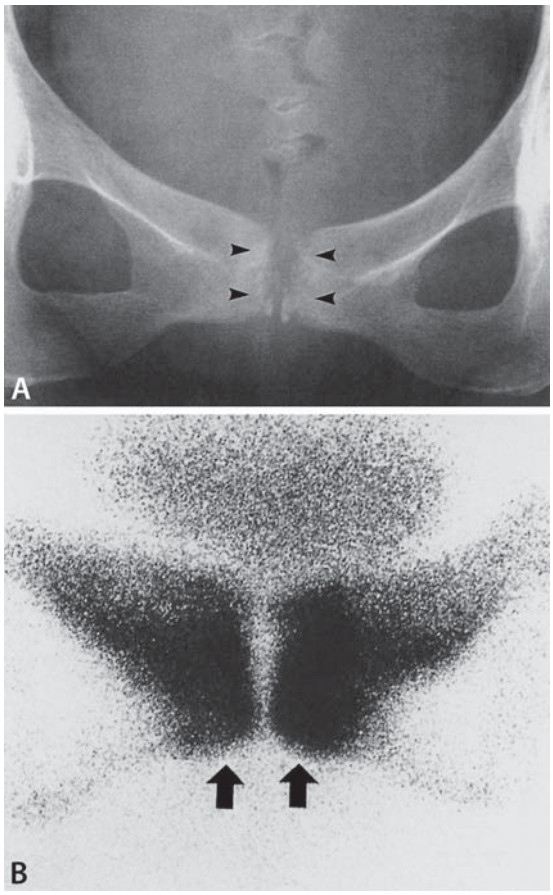

Fig. 7.4A, B Osteitis (condensans) pubis. **A** Anteroposterior radiograph of the pubis in a 25-year-old woman reveals irregular erosions and sclerosis in the para-articular bones of the symphysis (*arrowheads*). The lower joint space is narrowed, but the upper joint space appears falsely widened due to erosion (*arrowheads*). **B** Anterior pinhole scan localizes extremely intense tracer uptake in the para-articular pubic bones (*arrows*), distinguishing it from the less intense uptake in the normal areas. Such a crucial difference in tracer uptake cannot be demonstrated by ordinary scintigraphy. Here also the articular space is narrowed in the lower aspect but falsely widened in the upper

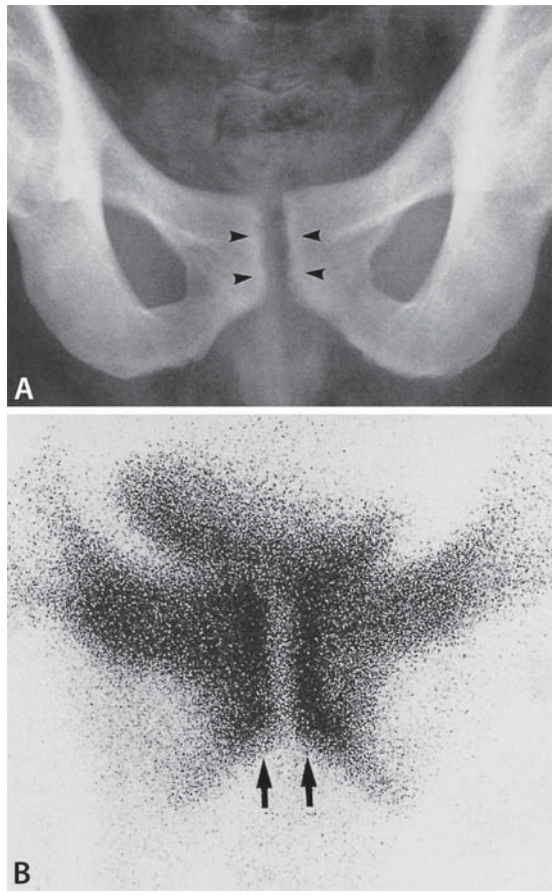

Fig. 7.5A, B Osteitis pubis in the early phase. **A** Anteroposterior radiograph of the pubis in 41-year-old man shows mild eburnation in the para-articular bones with contour irregularity (*arrowheads*). **B** Anterior pinhole scintigraph indeed shows subtle, abnormal tracer uptake in the immediate para-articular bones (*arrows*). The articular space is not narrowed. Compare with the tracer uptake in the normal pubic bones (Fig. 4.26)

7.3 Condensing Osteitis of the Clavicle

Originally described by Brower et al. (1974) as a clavicular version of osteitis condensans ilii and osteitis pubis, this entity is clinically characterized by painful swelling of the medial end of the clavicle again in young women of childbearing age. Undue stress to the clavicle appears to be the cause. Pathology is not related to infection, neoplasm, or avascular necrosis. The main histological changes include appositional trabecular thickening in the cancellous bone and periosteal reaction, which probably represent a response with bony proliferation to mechanical stress. Osteophytes are seen in some patients. Solovjev (1976) has recorded

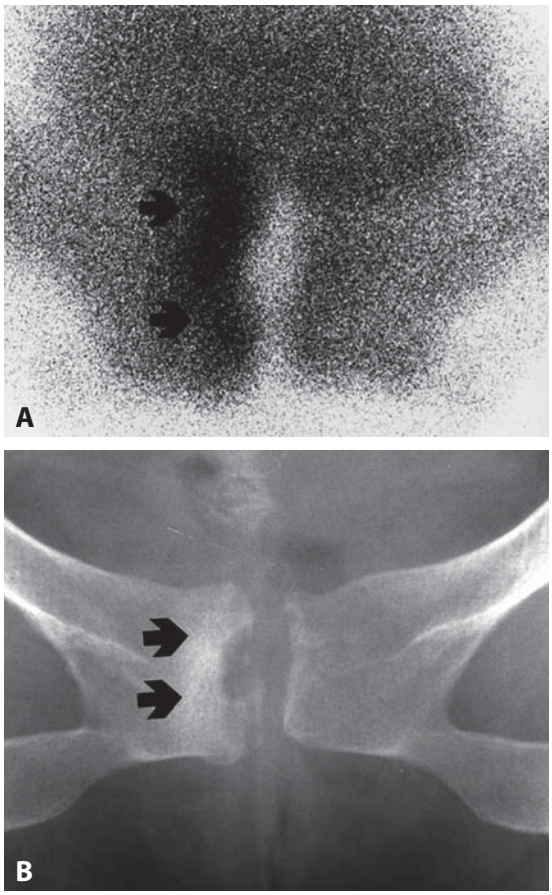

Fig. 7.6A, B Chronic osteitis pubis with increased tracer uptake. **A** Anterior pinhole scan of the pubis in a 28-year-old female with painful chronic osteitis in the right symphysis pubis shows increased para-articular uptake with apparent joint space widening (*arrows*). **B** AP radiograph reveals irregular para-articular sclerosis with bone defect (*arrows*). Patient had a history of marked dystocia

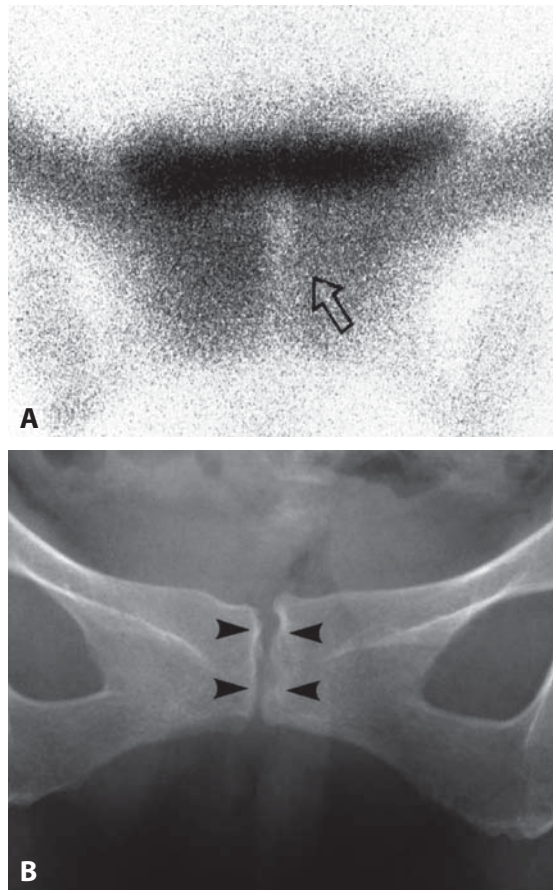

Fig. 7.7A, B Ancient osteitis pubis with decreased tracer uptake. **A** Anterior pinhole scan of the pubis in a 42-year-old female with old painless osteitis in the left symphysis pubis shows decreased para-articular uptake with minimal joint space widening (*open arrow*). **B** AP radiograph reveals reminiscent irregular para-articular sclerosis with bone defect (*arrowheads*). Decreased tracer uptake may reflect an atrophic state

the same disease under the term osteitis condensans claviculae.

Radiographic changes include irregular osteolysis and bony condensation in the lower aspect of the medial clavicular end with occasional spurring. Narrowing and subchondral cyst formation may be present in the adjacent sternoclavicular joint (Jurik et al. 1985). For the diagnosis of these changes, often not prominent, conventional X-ray tomography or CT is required (Fig. 7.8A).

Scintigraphically, the condition is characterized by intense tracer uptake (Teates et al. 1978). Pinhole scintigraphy reveals two different tracer uptake patterns: moderate uptake in the lower part of the medial clavicular end and rather conspicuous uptake in the sternoclavicular joint (Fig. 7.8B). The findings basically differ from those of Friedrich's disease (osteochondrosis of the clavicle), in which uptake is sharply localized to the aseptic necrosis of the medial clavicular end (Fig. 13.5).

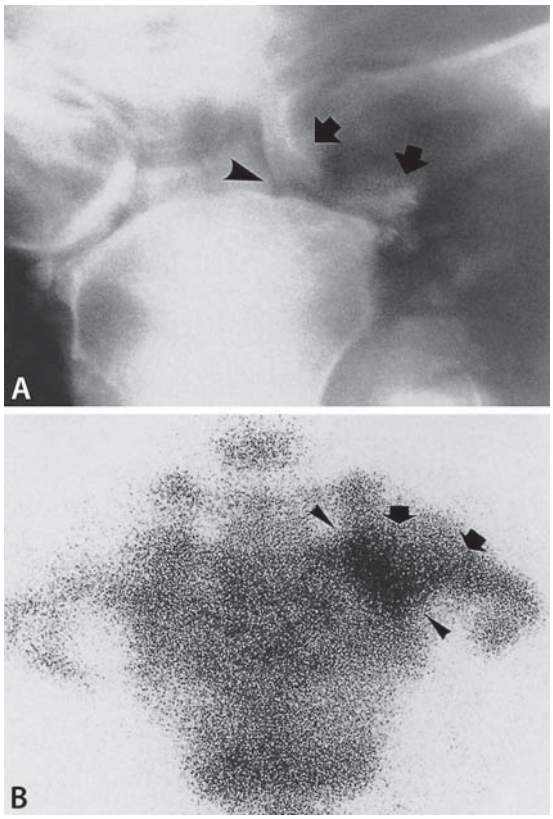

Fig. 7.8A, B Condensing osteitis of the clavicle. **A** Anterior conventional X-ray tomogram of the sternoclavicular joints in a 48-year-old woman reveals irregular lysis and sclerosis in the medial end of the left clavicle (*arrows*) with narrowing of the adjacent sternoclavicular joint (*arrowhead*). **B** Pinhole scan shows intense tracer uptake in the lower aspect of the medial clavicular end (*arrows*) with relatively more prominent uptake specifically in the sternoclavicular joint that is involved secondarily (*arrowheads*)

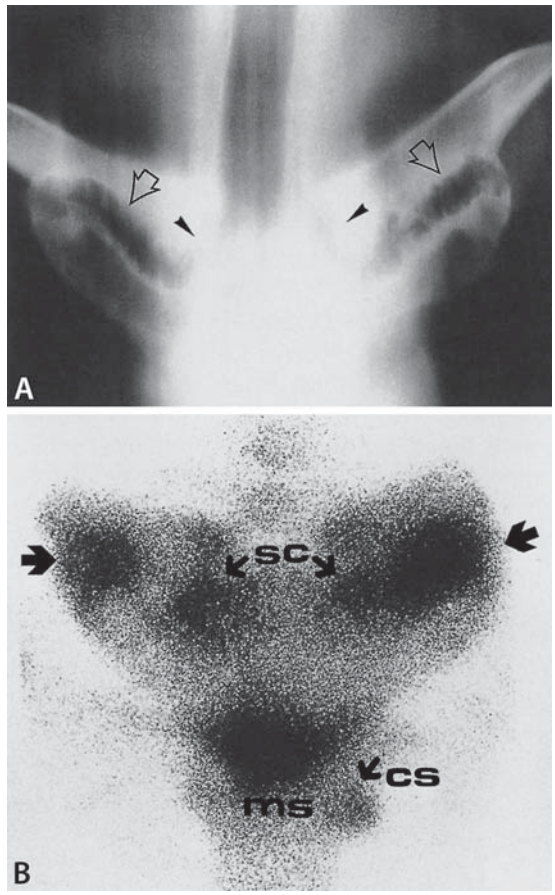

Fig. 7.9A, B Sternocostoclavicular hyperostosis. **A** Anterior conventional X-ray tomogram of the sternum in a 42-year-old man reveals a sawtooth-like synostosis between the medial ends of both clavicles and the first ribs (*open arrows*) and bony fusion of the sternoclavicular joints and the first costosternal junctions (*arrowheads*). The manubriosternal junction is also involved (not shown here). **B** Anterior pinhole scintigraph shows intense tracer uptake in the sternoclavicular (*sc*), costosternal (*cs*), and manubriosternal (*ms*) joints and their periarticular bones. The most conspicuous uptake is seen in the costoclavicular synostosis (*arrows*) and the fused manubriosternal junction (*ms*). The whole picture may well be likened to a "pansy flower"

7.4 Sternocostoclavicular Hyperostosis

Sternocostoclavicular hyperostosis (or intersternocostoclavicular ossification) is a painful, chronic, nonsuppurative inflammatory disease of the sternum. Pathologically, the condition is characterized by the prominent overgrowth of the sternum, clavicle, and upper anterior ribs with ossification of the adjacent soft tissue (Sonozaki et al. 1979). The condition, considered to be a manifestation of systemic reaction to a focal infection, responds to antibiotics and prostaglandin inhibitor treatment (Chigira et al. 1986). In contrast to osteitis of the ilium, pubis, and clavicle, this condition affects both genders equally. Bilateral and more or less symmetrical involvement is the rule.

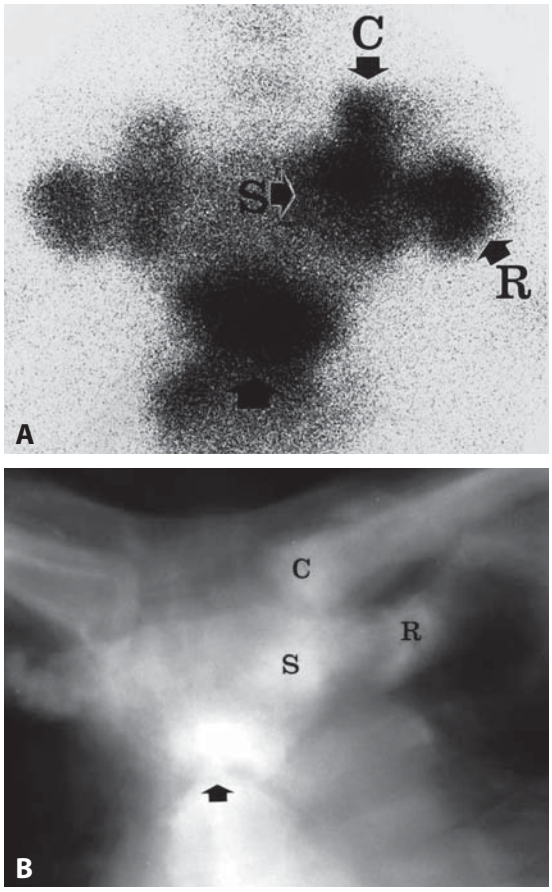

Fig. 7.10A, B Asymmetrical peristernal involvement in sternocostoclavicular hyperostosis. **A** Anterior pinhole scan of the sternum in a 38-year-old female shows patchy uptake in the left medial clavicular end (*C*), sternal end (*S*), and first rib (*R*), as well as the manubriosternal joint (*arrow*). **B** Conventional X-ray tomograph shows patchy areas of bony condensation in the respective anatomical parts about the manubrium

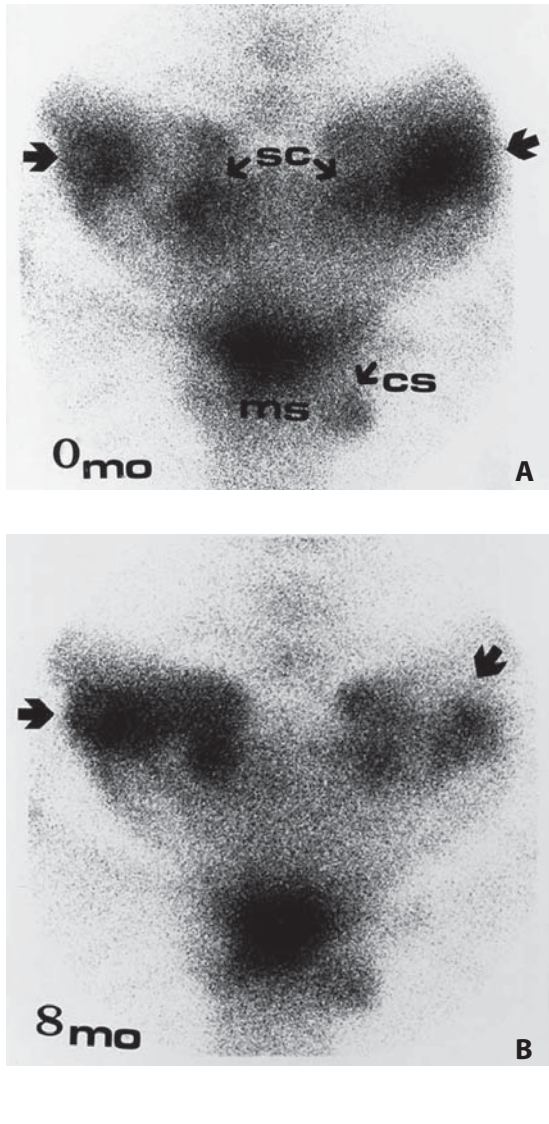

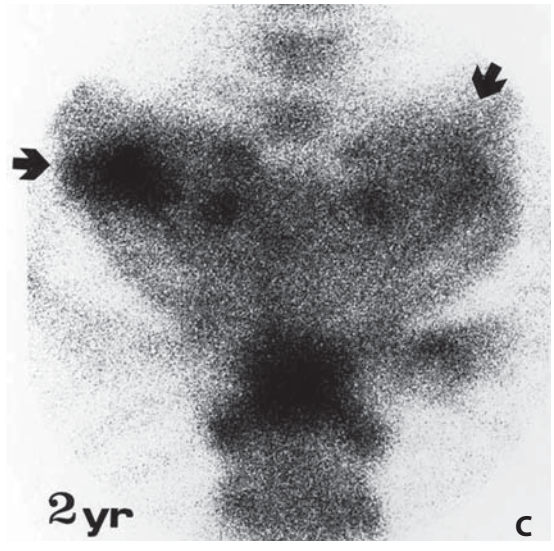

Fig. 7.11A–C Serial pinhole scans of sternocostoclavicular hyperostosis. **A** Initial scan of the sternum in a 44-year-old male with typical symmetrical disease shows patchy "hot" areas in the first costoclavicular syndesmoses (*arrows*), sternoclavicular joints (*sc*), and manubriosternal joint (*ms*), producing the "pansy flower" sign. **B** First follow-up performed 8 months later shows aggravation of the right lesion, amelioration of the left lesion, and unchanged lesion in the manubriosternal joint. **C** Further follow-up performed 2 years later shows improved uptake in the left costoclaimlar syndesmosis (left arrow)

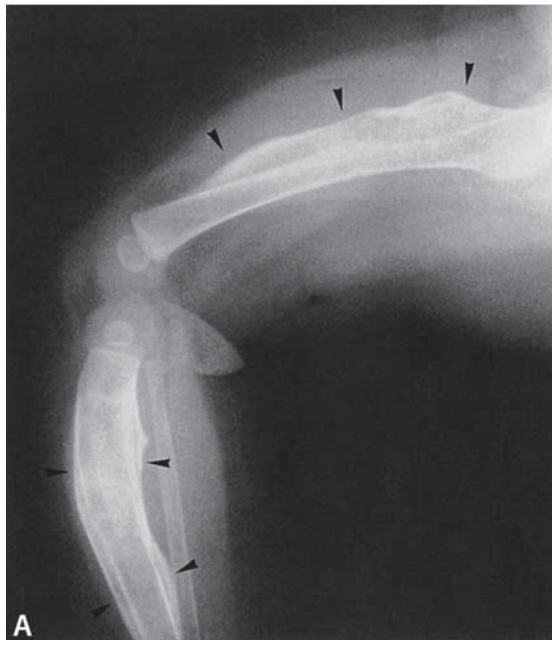

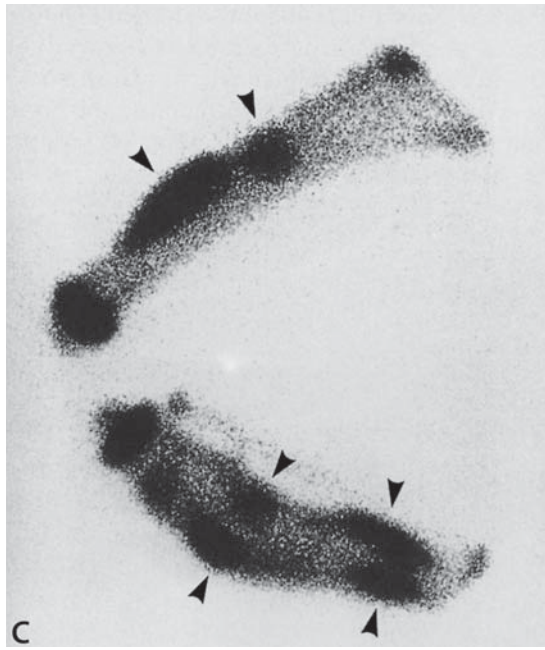

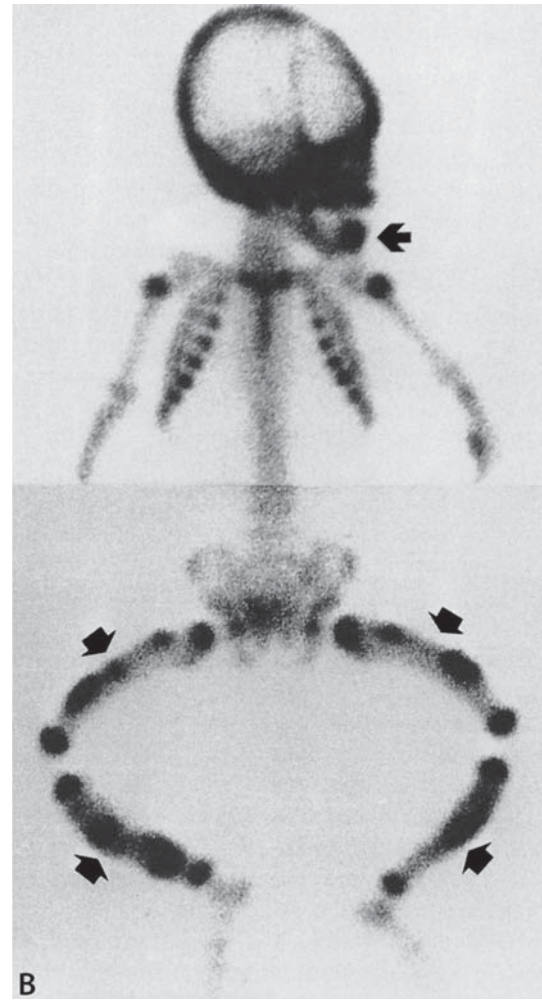

Fig. 7.12A–C Infantile cortical hyperostosis of Caffey. **A** Lateral radiograph of the right lower limb in a 1-year-old baby girl with multiple "bumpy" bones shows undulated periosteal thickening in the femur and tibia (*arrowheads*). **B** Composite whole-body anterior scan reveals multiple "hot" areas in the mandible, femora, and tibiae (*arrows*). **C** Pinhole scintigraph of the right lower limb delineates diffuse, wavy, intense tracer uptake in the cortices of the femur and tibia, producing a "bumpy bone" appearance; the scintigraphic version of the similar radiographic manifestations of infantile cortical hyperostosis (*arrowheads*)

Radiographically, the affected bones about the manubrium sterni show hyperostotic condensation and synostosis. The joints between the manubrium and the clavicle and the sternum and the ribs as well as the manubriosternal joint are irregularly narrowed and obliterated. Conventional X-ray tomography is ideal for the delineation of these changes (Fig. 7.9A).

Ordinary planar scintigraphy reveals increased tracer uptake in the medial ends of the clavicles and the anterior parts of the first ribs (Sartoris et al. 1986). Pinhole scanning shows intense uptake in the condensed bones and narrowed or fused joints around the manubrium. The uptake is more prominent in the synostosis of the clavicles and the first ribs and the manubrium and the body than in the sternocla-

vicular joints, producing the "pansy flower" sign (Bahk et al. 1992) (Fig. 7.9B). Peristernal involvement may be asymmetrical, but the basic scintigraphic features are the same as in the symmetrical type, showing intense uptake in the condensed bones (Fig. 7.10). Serial pinhole scans performed in one of our patients showed multiple areas of increased uptake of different intensities around the sternum at a time, reflecting the fact that the pathological changes are chronologically heterogeneous. Thus, while the tracer uptake (disease activity) in one lesion decreases, the uptake in the others increases on the serial follow-up scans (Fig. 7.11). With time bony condensation slowly progresses but tracer uptake becomes reduced over a course of years.

7.5 Infantile Cortical Hyperostosis (Caffey's Disease)

Infantile cortical hyperostosis is a rare disease of prenatal life and early infancy. Although a viral theory has been favored and there is a definite familial trait (Swischuk 1989; Bernstein and Zaleske 1995), the accurate etiology is yet to be established. A febrile episode, irritability, and accelerated erythrocyte sedimentation rate suggest an infection. The mandible is most commonly affected and the clavicles, ribs, ulna, radius, tibia, and fibula are rather regularly involved. No bone is exempt except the vertebrae and phalanges. The periosteums react with extensive new bone formation, which eventually blends into the underlying cortex. Corticosteroid has a dramatic effect on this disease.

Radiographic features include diffuse, undulating corticoperiosteal thickening and soft-tissue swelling (Fig. 7.12A). As discussed above, the mandible is most commonly involved so that the absence of its involvement makes the diagnosis questionable. The clavicles, ribs, long bone diaphyses, and scapula show undulating hyperostosis.

Whole-body bone scintigraphy is ideal in delineating the involved bones panoramically (Fig. 7.12B) and subsequent pinhole scanning permits individualized study of each lesion in greater detail (Fig. 7.12C). Ordinary bone scan shows mono- or polyostotic involvement often simulating osteomyelitis (Taillefer et al. 1983). However, pinhole scintigraphy clearly depicts the characteristic "bumpy" uptake in the thickened periosteums and cortices of the long-bone diaphyses (Fig. 7.12C). Although our study is limited in number it is tempting to comment that the tracer uptake in multiple foci of infantile cortical hyperostosis does not closely correlate with radiographic change presumably due to the fact that lesions seen at one time are in different stages of the disease (Bahk et al. 1993). A very similar finding is observed in sternocostoclavicular hyperosis (see above).

7.6 Osteitis Deformans (Paget's Disease of Bone)

Osteitis deformans is a relatively common inflammatory bone disease of unknown etiology. This is one of the most challenging diseases, whose clinical, radiographic, and scintigraphic manifestations are bizarre and protean. A full account of Paget's disease is presented in Chap. 18.

7.7 Odontogenous Osteitis of the Mandible (Periapical Abscess)

Inflammation or infection about the dental root apex is one of the most common conditions in the mandible that manifests as intense tracer uptake. The condition is also important clinically since it occasionally progresses to alveolar abscess, apical granuloma, and cyst formation. The process may be either sterile or septic with a septic source usually in the infected dental pulp.

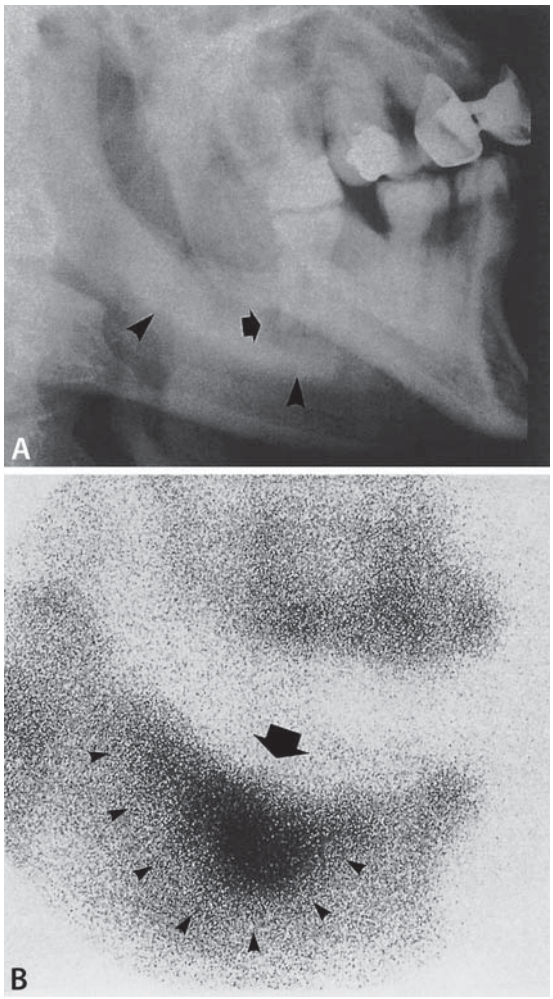

Fig. 7.13A, B Odontogenous osteitis related to periapical inflammation in the mandible. **A** Slightly tilted lateral radiograph of the right mandible in a 59-year-old man with mandibular dental pain shows bone resorption about the second molar roots (*arrow*) and in the extracted third molar alveolus and diffuse sclerosis (*arrowheads*), denoting the periapical abscess, erosions, and reactive eburnation, respectively. **B** Lateral pinhole scintigraph shows very intense tracer uptake focally in the molar alveolar bones (*arrow*) and less intense uptake around it (*arrowheads*). The presence of more intense tracer uptake in the periapical bone may represent infection, but infection is not a prerequisite to nonspecific, intense, mandibular tracer uptake. Indeed, frequently the painless. noninfective bone resorption is attended by intense tracer accumulation

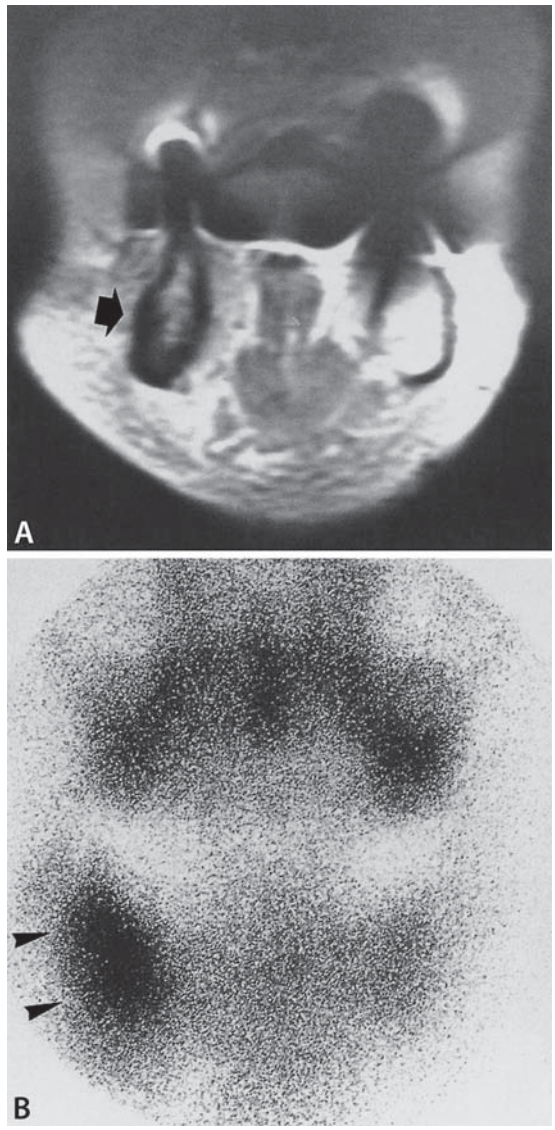

Fig. 7.14A, B Early radiation-induced osteitis in the mandible (2 months after 65 Gy irradiation with 6 MeV gamma-ray for right submandibular malignant lymphoma). **A** T1-weighted gadolinium DTPA-enhanced coronal MRI section through the premolar zone of the mandible in a 47-year-old woman with mandibular irradiation shows a modest volume decrease of the irradiated marrow with suppressed enhancement and regional cortical thickening, indicating marrow depletion with shrinkage and osteitis, respectively (*arrow*). **B** Anterior pinhole scintigraph shows diffusely increased uptake in the irradiated area due to an osseous reaction (*arrowheads*)

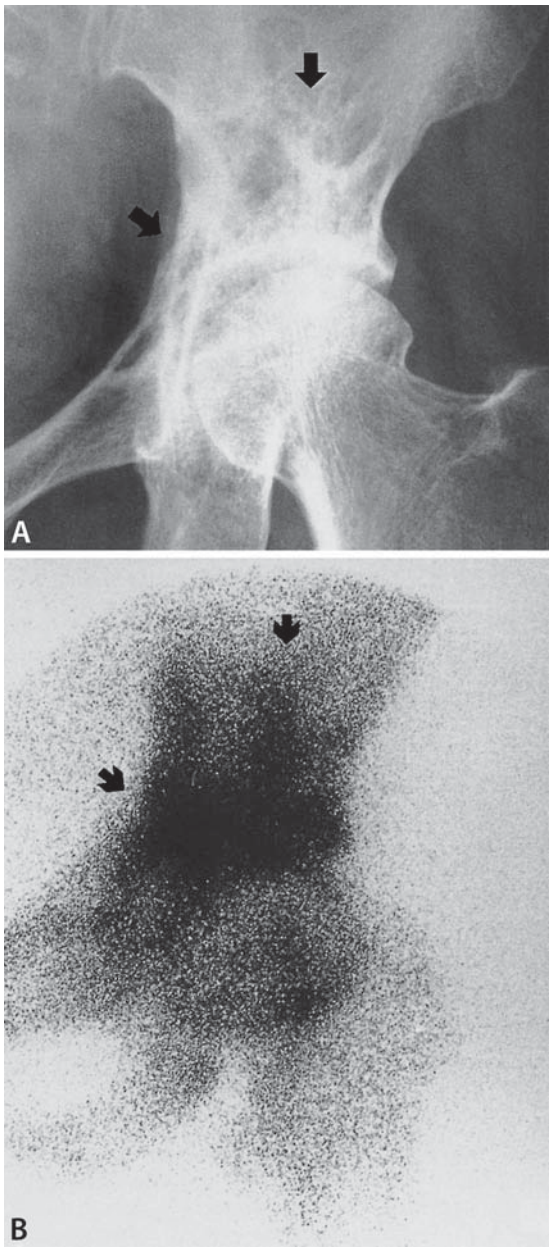

Fig. 7.15A, B Chronic radiation osteitis in the innominate bone (18 months after 47.50 Gy irradiation with 6 MeV gamma-ray for breast cancer metastasis). **A** Anteroposterior radiograph of the left hip in a 43-year-old woman with known breast cancer metastasis reveals irregular bone thickening with interspersed streaky and cystic lucencies in the irradiated left innominate bone (*arrow*). The femoral head was shielded, hence saved, preserving a normal trabecular pattern. **B** Anterior pinhole scan shows moderately increased, irregular tracer uptake roughly corresponding to radiographically sclerotic areas (*arrows*). Observe the normal tracer uptake in the shielded femoral head

Radiographically, the nonspecific chronic bone inflammation is represented by diffuse reactive osteosclerosis, whereas periapical abscess is represented by focal bone destruction (Fig. 7.13A). The characteristic pinhole scintigraphic feature of nonspecific sterile osteitis in the mandible is an ill-defined area of homogeneous tracer uptake in the molar and premolar regions, whereas the tracer uptake in periapical abscess is very intense, and usually surrounded by less intense, reactive uptake (Fig. 7.13B).

7.8 Radiation Osteitis (Osteonecrosis)

The term radiation osteitis was originally coined by Ewing (1926) to describe a series of pathological changes that occur in bone after irradiation. Irradiation of bone may result in immediate or delayed arrest of cell division, cell death with reduced matrix production, metaplasia, or neoplasia. The irradiated bones manifest ischemic necrosis, sclerosis, and occasional infection of radionecrosis. These changes occur as secondary reactions to the destruction of osteoblasts and microvascular occlusion (King et al. 1979). The radiation effects on bone are dose-dependent. The threshold radiation dose for the bone changes is estimated to be 30 Gy, and cell death occurs at 50 Gy (Bragg et al. 1970). In a study of 100 patients with radiation osteitis, Bragg and associates (1970) noted involvement in decreasing order of the mandible (32%), clavicle (18%), humeral head (14%), ribs (9%), and femur (9%). The mandible is more commonly affected than the maxilla because of the compactness of bone and poor blood supply (Guttenberg 1974) and is more vulnerable when the irradiated tumor is located close to it (Bedwinek et al. 1976) (Fig. 7.14). Unlike most radionecrosis the mandibular lesion starts early after the completion of irradiation.

Radiographically, altered bones are irregularly mottled due to the mixture of porosis, coarsened trabeculae, and sclerosis (DeSantos

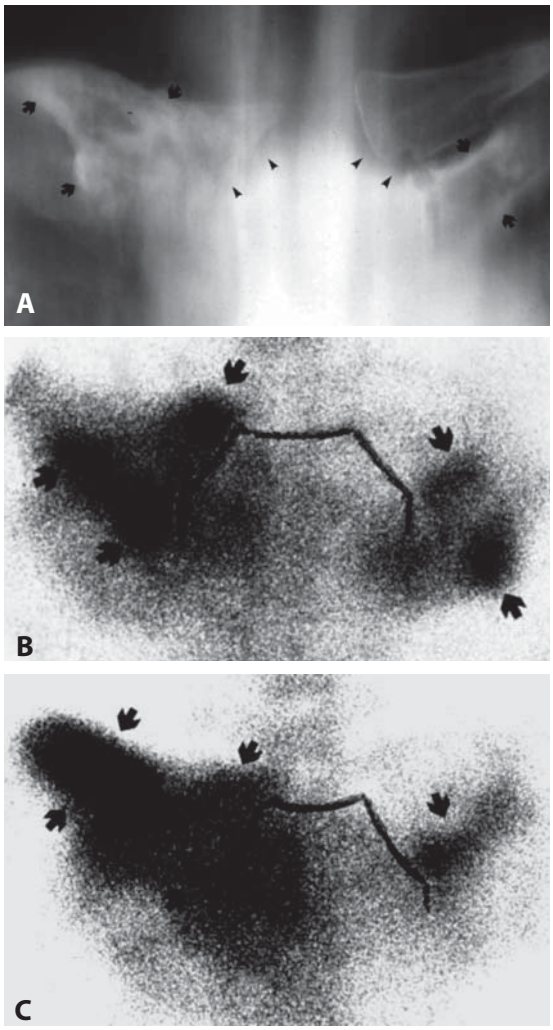

Fig. 7.16A–C Initial and follow-up radiation osteitis. **A** Conventional X-ray tomograph of the sternum taken in a 48-year-old female 1 year after completion of 50 Gy 6 MeV irradiation for sarcoma in the medial aspect of the right clavicle shows chronic radiation osteitis with irregular sclerosis and osteonecroses (*three arrows*) and left clavicle (*two arrows*) (*arrowheads* altered sternal notch and joints). **B** The initial pinhole scan taken at the same time as the tomograph shows intense uptake in the medial aspect of the right clavicle and also in the left clavicular end. **C** Follow-up pinhole scan taken 6 years later shows persistent uptake with further intensification in the right clavicle that bore the sarcoma and improved uptake in the left clavicle that did not bear the tumor

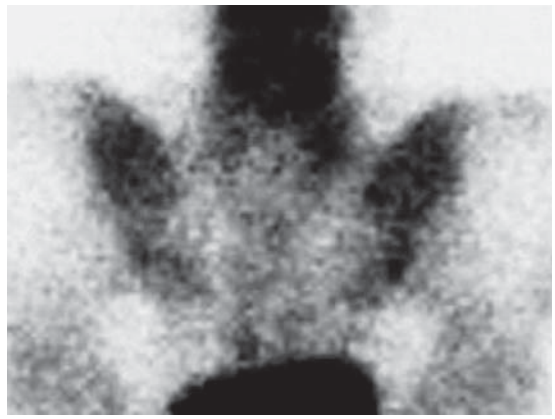

Fig. 7.17 Suppressed tracer uptake in irradiated adult bone. Posterior pinhole scan of the sacrum in a 56-year-old female irradiated 2 years previously for stage II cervical cancer after hysterectomy shows a large area of photopenia in the main body of the sacrum

and Libshitz 1979) (Fig. 7.15A). New bones gradually form, replacing irradiated bones in the course of years (Fig. 7.16). Computed or conventional tomography (Fig. 7.16A) and MRI (Fig. 7.14A) demonstrate osteosclerosis mixed with lucent areas of fibrosis as well as atrophied bone marrow at this stage.

Scintigraphy of radiation osteitis resulting from a large-dose irradiation (50 Gy or more) reveals intense uptake (Figs. 7.14B and 7.15B), contrasting with the well-known suppressed uptake in bones irradiated with a lower dose and without osteitis (Fig. 7.17). The uptake is typically uniform and well defined in the early phase, denoting subacute inflammation (Fig. 7.14B). However, it is gradually transfigured to a mottled pattern in the chronic phase due to irregular mixing of osteonecrosis, regeneration, and sclerosis (Fig. 7.15B and 7.16B), and eventually returning to a uniform appearance in the late reparative phase now due to extended new bone formation (Fig. 7.16C). On the other hand, avascular necrosis (Rosenthall 1987) and fibrous replacement are indicated by "cold" defects or photopenia when they are sufficiently large (Fig. 7.15).

References

Bahk YW, Chung SK, Kim SH, et al (1992) Pinhole scintigraphic manifestations of sternocostoclavicular hyperostosis: report of a case. Korean J Nucl Med 26:155–159

Bahk YW, Chung SK, Yang WJ (1993) "Bumpy" appearance of infantile cortical hyerostosis: pinhole scintigraphic sign. Korean J Nucl Med 27:319–320

Bedwinek JM, Shukovsky LJ, Fletcher GH, et al (1976) Osteonecrosis in patients treated with definitive radiotherapy for squamous cell carcinomas of the oral cavity and naso- and oro-pharynx. Radiology 119:665–668

Bernstein RM, Zaleske DJ (1995) Familial aspects of Caffey's disease. Am J Orthop 24:777–781

Bragg DG, Shidnia H, Chu FCH, et al (1970) The clinical and radiographic aspects of radiation osteitis. Radiology 97:103–111

Brower AC, Sweet DE, Keats TE (1974) Condensing osteitis of the clavicle: a new entity. AJR Am J Roentgenol 121:17–21

Chigira M, Maehara S, Nagase M, et al (1986) Sternocostoclavicular hyperostosis. A report of nineteen cases, with special reference to etiology and treatment. J Bone Joint Surg Am 68:103–112

DeSantos LA, Libshitz HI (1979) Adult bone. In: Libshitz HI (ed) Diagnostic roentgenology of radiotherapy change. Williams & Wilkins, Baltimore

Ewing J (1926) Radiation osteitis. Acta Radiol 6:399–412

Guttenberg SA (1974) Osteoradionecrosis of the jaw. Am J Surg 127:326–332

Jurik AG, de Carvalho A, Graudal H (1985) Sclerotic changes of the sternal end of the clavicle. Clin Radiol 36:23–25

King MA, Casarett GW, Weber DA (1979) A study of irradiated bone. I. Histopathologic and physiologic changes. J Nucl Med 20:1142–1149

Numaguchi Y (1971) Osteitis condensans ilii, including its resolution. Radiology 98:1–8

Rendich RA, Shapiro A (1936) Osteitis condensans ilii. Bone Joint Surg 18:899–908

Rosenthall L (1987) The bone scan in arthritis. In: Fogelman I (ed) Bone scanning in clinical practice. Springer, Berlin Heidelberg New York

Sartoris DJ, Schreiman JS, Kerr R, et al (1986) Sternocostoclavicular hyperostosis: a review and report of 11 cases. Radiology 158:125–128

Segal G, Kellogg DS (1954) Osteitis condensans ilii. Am J Roentgenol Radium Ther Nucl Med 71:643–649

Solovjev M (1976) Condensing osteitis of clavicle (in German). Rofo 125:375–376

Sonozaki H, Azuma A, Okai K, et al (1979) Clinical features of 22 cases with "inter-sterno-costo-clavicular ossification": a new rheumatic syndrome. Arch Orthop Trauma Surg 95:13–22

Swischuk LE (1989) Infantile cortical hyperostosis (Caffey's disease): In: Imaging of the new born, infant, and young child, 3rd edn. Baltimore: Williams & Wilkins

Taillefer R, Danais S, Marton D (1983) Scintigraphic aspect of infantile cortical hyperostosis (Caffey's disease) (in French). J Can Assoc Radiol 34(1):12–15

Teates CD, Brower AC, Williamson BR, et al (1978) Bone scans in condensing osteitis of the clavicle. South Med J 71:736–738

8 Diseases of Joints and Soft-Tissue Infections

The joints are the sites of a great variety of diseases of known and unknown etiology (Table 8.1). The joint diseases of ^{99m}Tc-MDP bone scintigraphic interest, pinhole scintigraphy in particular, include synovitis, infective arthritis, degenerative arthritis, rheumatoid arthritis, seronegative spondyloarthropathies, and metabolic articular disorders. Based on the histological characteristics, joints are divided into the fibrous, cartilaginous, and synovial types (Williams and Warwick 1989). In the respective joints, apposed bone surfaces are fastened by the connective and cartilaginous tissue and separated by the synovial lining and cavity. Table 8.2 shows typical joints that belong to each of these categories.

In general the pathological, radiographic, and scintigraphic manifestations of articular diseases may differ according to the histological characteristics of the joint involved in a given disease and among various diseases. Radiographically, articular diseases can be diagnosed by the analysis and summation of four basic features: (1) changes in the joint space, (2) periarticular bone abnormalities, (3) malalignment or deformity of the joint, and (4) periarticular soft-tissue alterations. This is a classic analysis-based, inductive, interpretational system, long developed and traditionally adopted in radiological diagnosis. Unfortunately, the system is not readily applicable to ordinary bone scanning simply because of relatively low resolution. Pinhole scintigraphy and nuclear angiography, however, can provide useful and often unique diagnostic information on both the morphology and the vascular and metabolic profiles in articular and periarticular pathologies (Fig. 8.1).

It is clear that the level of resolution of scintigraphy even after pinhole magnification is

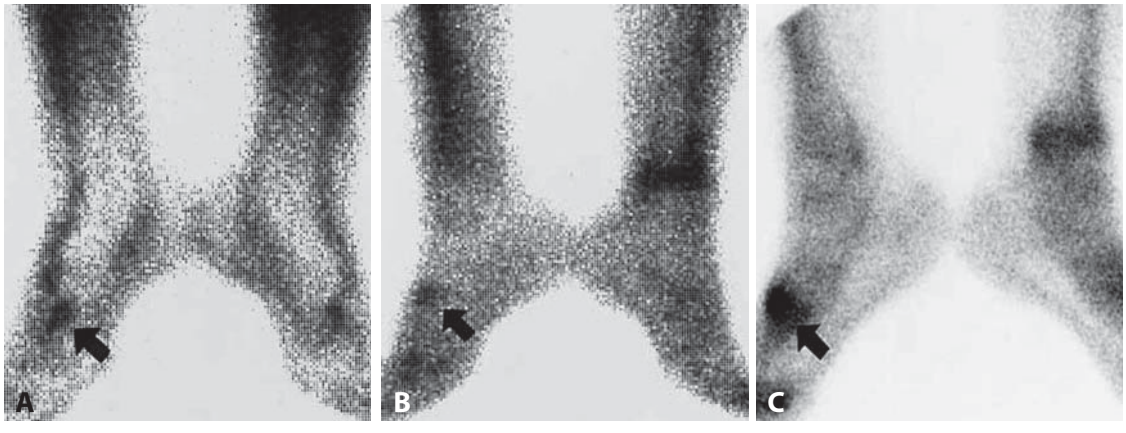

Fig. 8.1A–C Value of nuclear angiography in arthritis. **A** Blood-flow phase scan of the right foot in a 57-year-old male with infective arthritis of the second tarsometatarsal joint shows focally increased vascularity denoting active inflammation (*arrow*). **B** Blood-pool scan reveals mild stain (*arrow*). **C** Static bone scan shows intense focal bone uptake due to an infection (*arrow*)

Infective and related arthritides	Acute infective arthritides	Transient synovitis
		Sympathetic or sterile synovitis
		Pyogenic arthritis (pyarthrosis)
	Chronic infective arthritides	Tuberculous arthritis
		Chronic pyogenic arthritis
		Mycotic arthritis
		Others
Degenerative joint diseases (osteoarthritis)	Primary osteoarthritis	
	Secondary osteoarthritides	Posttraumatic osteoarthritis
		Postinfective osteoarthritis
		Diffuse idiopathic skeletal hyperostosis
Arthritis of collagen diseases	Rheumatoid arthritis	Seronegative spondyloarthropathies
		Ankylosing spondylitis
		Reiter's syndrome
		Psoriatic arthritis
		Enteropathic arthritis
	Connective tissue diseases	Systemic lupus erythematosus
		Dermatomyositis
		Scleroderma
		Mixed connective tissue disease
Metabolic joint diseases	Gout	
	Pseudogout (calcium pyrophosphate disease)	
	Hyperparathyroidism	
	Ochronosis	
	Others	
Neuropathic joint diseases (neuroarthropathies)	Primary neurological joint disease (Charcot's joints)	
	Diabetes	
Miscellaneous	Relapsing polychondritis	
	Hypertrophic pulmonary osteoarthropathy	

Table 8.1 A scintigraphic classification of arthritides

Fibrous joints	Sutures	Cranial sutures (coronal, sagittal, occipital, lambdoidal, squamosal)
	Syndesmoses	Radioulnar syndesmosis, tibiofibular syndesmosis, interspinous syndesmosis, supraspinous syndesmosis, intertransverse syndesmosis
Cartilaginous joints	Synchondrosis	Spheno-occipital synchondrosis, ischiopubic synchondrosis, femoral epiphyses
	Symphyses	Pubic symphysis, sacral symphyses, manubriosternal joint, intervertebral joints between bodies
Synovial joints	Hinge	Elbow, knee, ankle, interphalangeal joints
	Pivot	Proximal radioulnar joint, atlantoaxial joint
	Condyloid	Metacarpo[tarso]phalangeal (knuckle) joint
	Gliding	Acromioclavicular joint, vertebral apophyseal joints, joints between some carpal and tarsal bones
	Ball-and-socket	Shoulder joint, hip joint

Table 8.2 A scintigraphic classification of joints

not comparable to that of radiography (the limiting spatial resolution of screen/film radiography and pinhole bone scan is 5–10 line-pairs/mm (Huda and Slone 1995) and 1–5 line-pairs/cm, respectively. Nevertheless, the anatomical detail of pinhole scanning is comparable to that of radiography in so far as it is used as qualitative determinant.

Thus, pinhole scintigraphy in articular diseases reveals (a) obliteration, narrowing, or widening of the joint space, (b) increased, unaltered, or decreased tracer uptake in the periarticular bones, (c) alterations in the size, shape, and architecture of the periarticular bones, (d) dislocation or subluxation, and (e) angulation or other deformities. Analysis of the pattern of tracer uptake in terms of homogeneity or inhomogeneity is another important diagnostic feature of pinhole scintigraphy. Joint obliteration is indicated by the presence of increased tracer uptake in the articular space. Clinically, this may indicate either actual closure of the articular space due to cartilaginous destruction with fibrous or bony ankylosis or markedly increased periarticular bone turnover in response to congestion, inflammation, or infection with or without articular narrowing.

8.1 Sterile and Sympathetic Arthritis

8.1.1 Transient Synovitis of the Hip

Transient synovitis is a self-limited, nonspecific, inflammatory disease, typically affecting the hips in children aged between 3 and 10 years. Boys are affected much more commonly than girls. It occurs frequently after a respiratory tract infection. Erythrocyte sedimentation rate and white blood cell count are mostly normal. Other terms for the condition include irritable hip syndrome, observation hip, transitory arthritis, transitory coxitis, and simple serous coxitis. The etiology is not yet established, but a viral infection or hypersensitivity reaction to

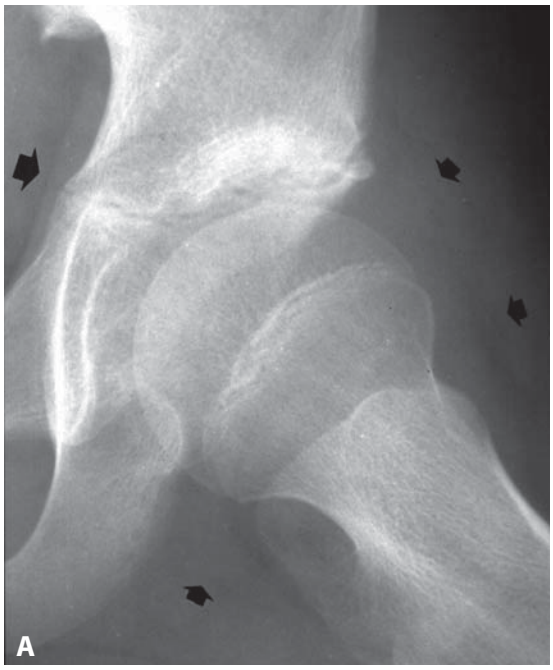

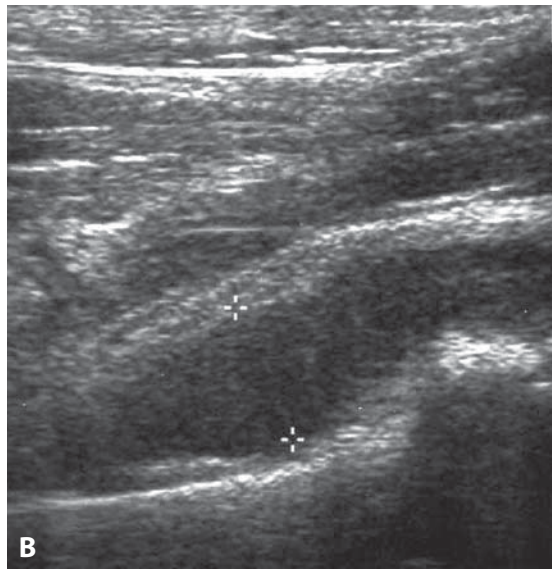

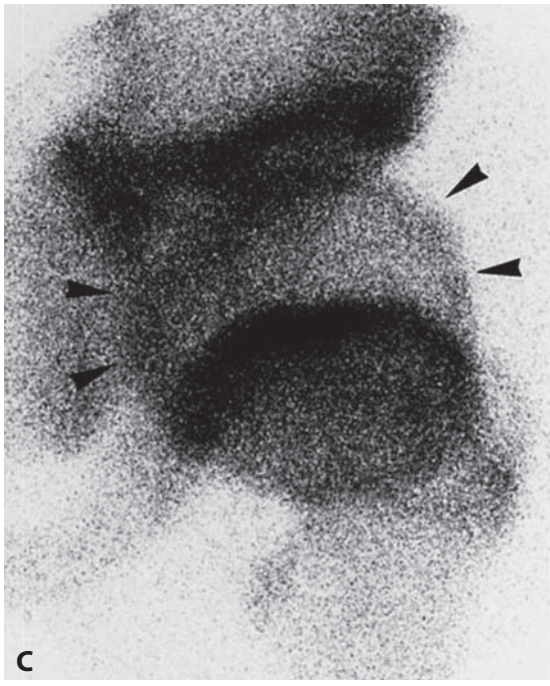

Fig. 8.2A–C Transient synovitis. **A** Anteroposterior radiograph of painful left hip in a 14-year-old boy shows distension of the joint capsule (*small arrows*) and thickening of the obturator muscle (*large arrow*). **B** Sonogram shows moderate widening of the joint space with effusion (*between crosses*). **C** Anterior pinhole scan portrays subtle but clearly defined tracer uptake in the subchondral zone of the femoral head denoting synovial inflammation (*arrowheads*)

infection elsewhere in the body is considered to be a likely cause.

The basic radiographic abnormality is capsular distension with the displacement of the capsular fat line (Fig. 8.2A). This sign is observed in only a fraction of patients; in the majority the study is not informative. Ultrasonography is readily available and extremely useful for the direct, real-time demonstration of synovial effusion (Fig. 8.2B).

The tracer uptake in transient synovitis is usually mild or moderate at most, barely delineating the femoral head and the acetabular fossa on ordinary scintigraphs. Pinhole scintigraphy, however, can detect even an extremely subtle increase in uptake. The detectability of the lesion can be further raised when the healthy hip is used as a reference. Increased subchondral bone uptake in synovitis is accounted for by increased blood flow through the anastomotic vascular channels induced by hyperemia in the inflamed synovium (Rosenthall 1987). Scintigraphic findings differ according to the amount of effusion present within the diseased joint. When the amount is small to moderate the subchondral bone in the femoral head accumulates tracer, giving rise to a capped appearance (Fig. 8.2C) and when the amount is large uptake may become reversed to photopenia due to the elevated intracapsular

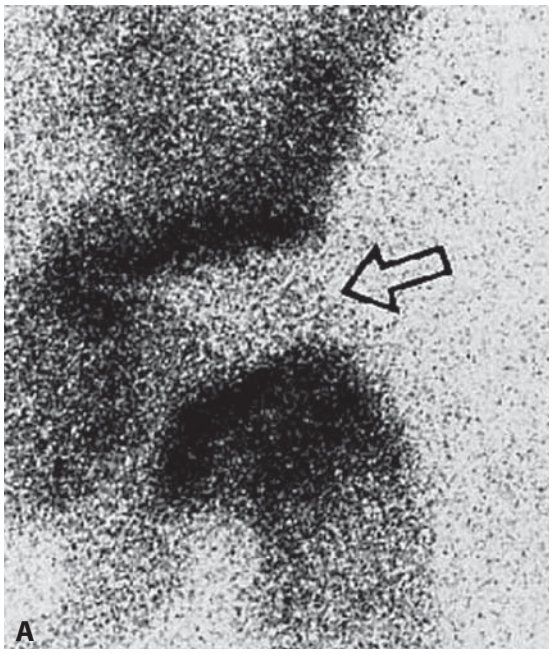

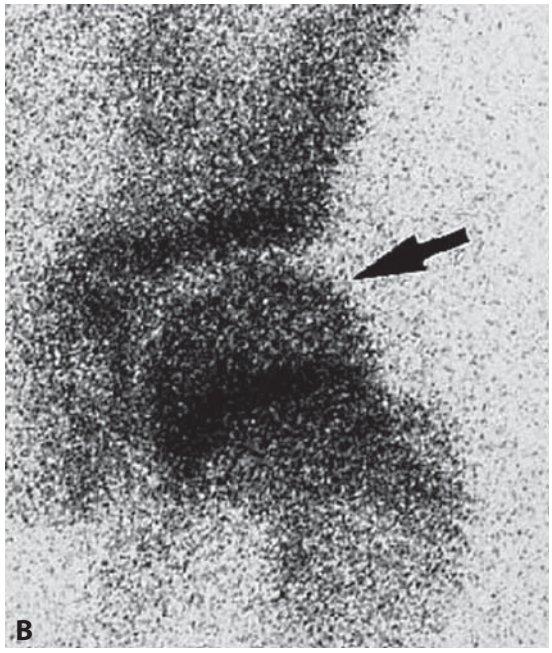

Fig. 8.3A, B Photopenic presentation of acute synovitis. **A** Anterior pinhole scan of painful left hip in a 10-year-old boy shows absence of tracer uptake in the femoral epiphysis due to elevated intracapsular pressure (*open arrow*). **B** Follow-up anterior pinhole scan taken after tapping shows instant return of uptake with increased subchondral uptake (*arrow*)

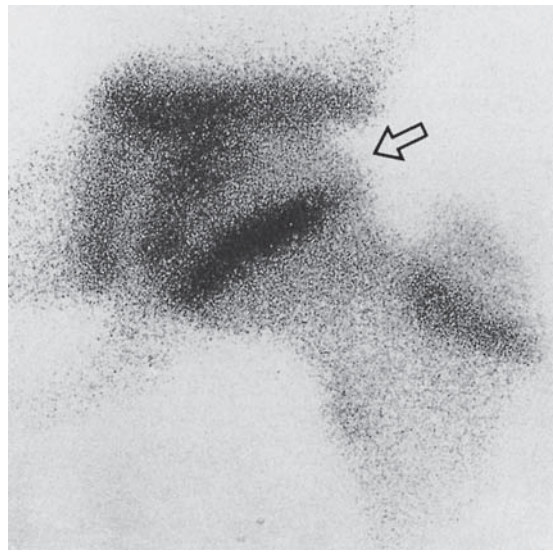

Fig. 8.4 Transient ischemia in synovitis. Anterior pinhole scan of the left hip in a 16-year-old boy with limping gait shows an ill-defined photopenia in the lateral aspect of the femoral head (*open arrow*), designating focal bone ischemia incidental to increased intracapsular pressure. Note increased uptake in the medial aspect

pressure (Fig. 8.3A). The photopenia can instantly revert to normal or be slightly increased by rebound after needle aspiration (Fig. 8.3B). Obviously, the extent of photopenia parallels the amount of effusion; the smaller the effusion the milder is the photopenia (Fig. 8.4). It is to be mentioned that the tracer uptake in transient synovitis is usually much less intense than in an infective arthritis (see Section 8.2.1). In the great majority of cases, simple bed rest brings recovery in a few days, and the recovery can be confirmed by pinhole scintigraphy or sonography.

8.1.2 Sympathetic Synovitis

Sterile sympathetic synovitis may be created in a joint in reaction to osteomyelitis in the juxtaarticular bone, for example, in the hip. This type of synovitis has also been known to be triggered by an infective organism growing in a distant site as a hypersensitivity response (Goldenberg 1983).

Radiography reveals joint capsular distension, occasionally with regional osteopenia. Pinhole scintigraphic features include diffusely

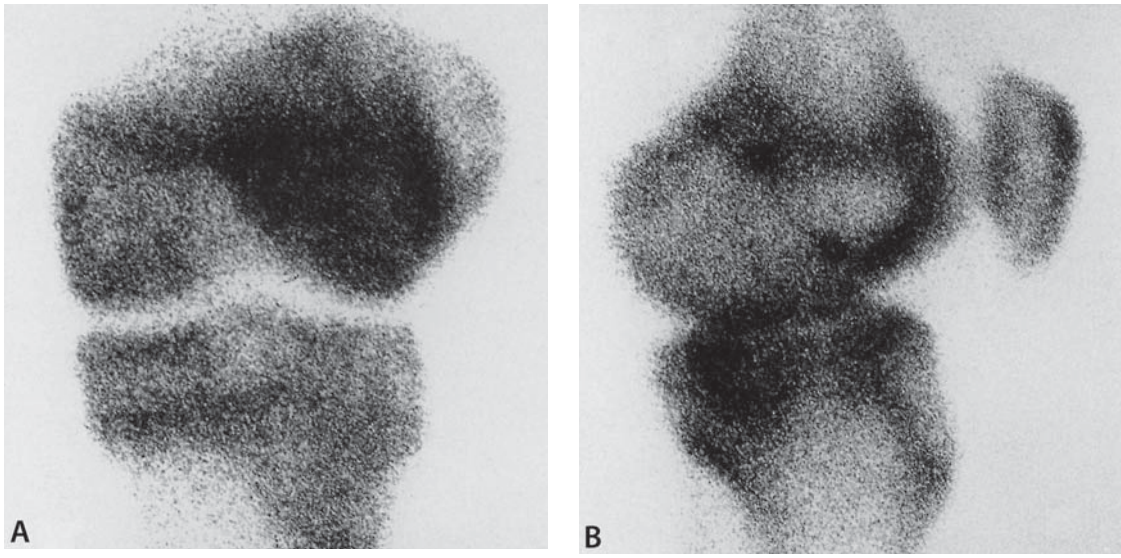

Fig. 8.5A, B "Wrapped bone" sign in acute, serous, sympathetic synovitis of the knee. **A** Anterior pinhole scintigraph of the right knee in a 22-year-old man with synovitis reveals moderately intense tracer uptake in all the periarticular bones including the patella, silhouetting the individual bones. **B** Lateral pinhole scan shows generalized subchondral tracer uptake more distinctly. The findings may be termed the "wrapped bone" sign

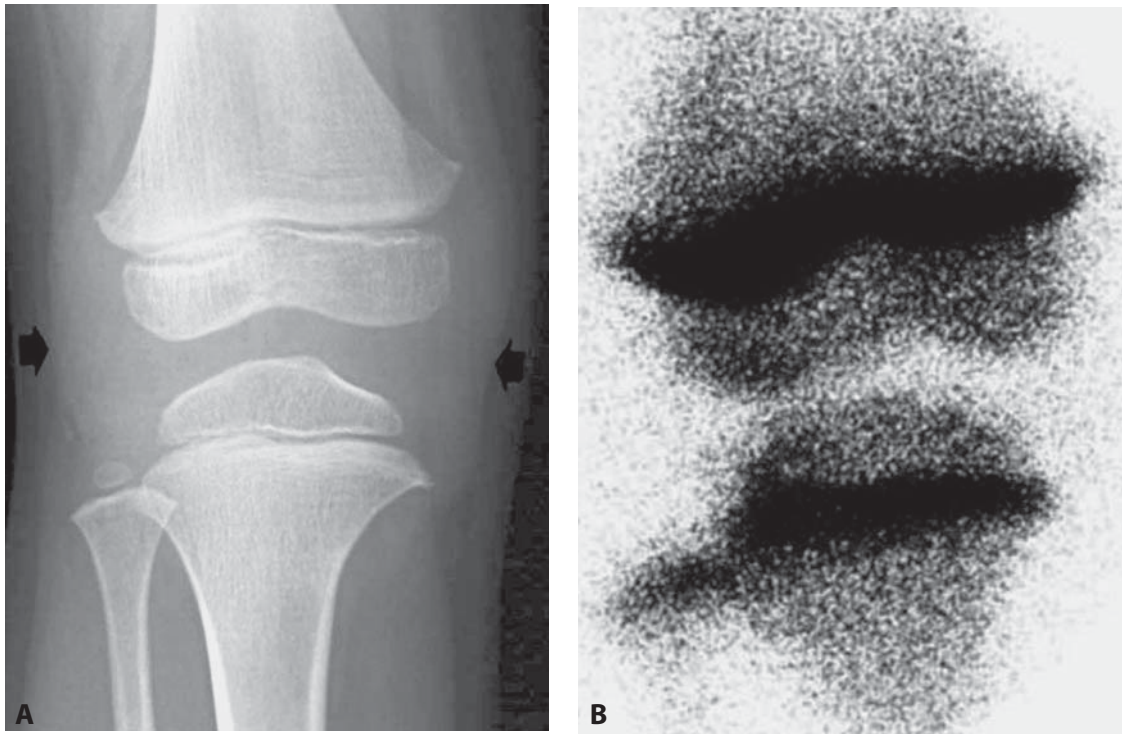

Fig. 8.6A, B Sterile traumatic synovitis. **A** Anteroposterior radiograph of the right knee in a 4-year-old boy with simple traumatic synovial effusion shows distension of the joint capsule bilaterally (*arrows*). **B** Anterior pinhole scan reveals no abnormal tracer uptake denoting the absence of significant inflammation

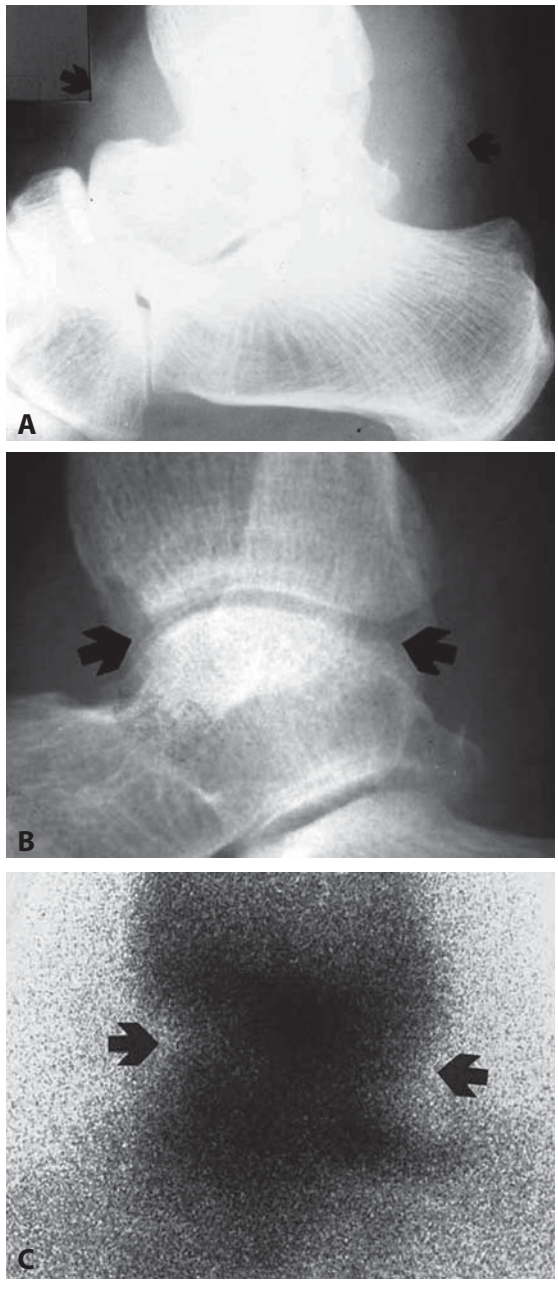

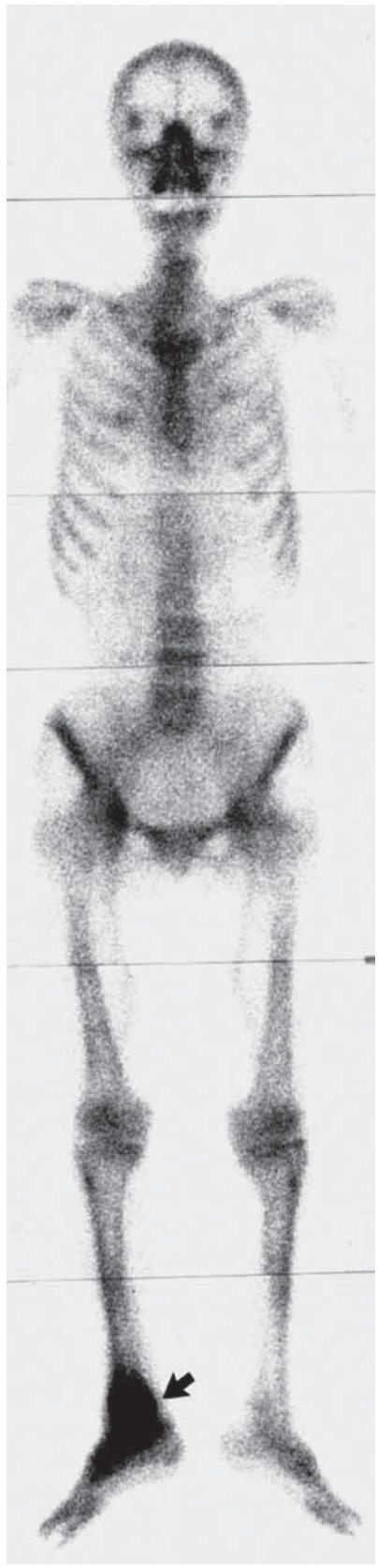

Fig. 8.7A–D Synovitis in prolonged hemodialysis. **A** Lateral soft-tissue radiograph of the right ankle in a 56-year-old female with acute recurrent synovitis after years of hemodialysis shows distension of the articular capsule and periarticular soft-tissue swelling (*arrows*). **B** Bone technique radiograph reveals articular narrowing with subchondral resorption in the trochlear surface (*arrows*). **C** Pinhole scan shows diffuse tracer accumulation in the joint (*arrows*). **D** Whole-body scan shows prominent tracer uptake in the right ankle with generally increased skeletal uptake reflecting systemic osteomalacia. Note that renal uptake is absent

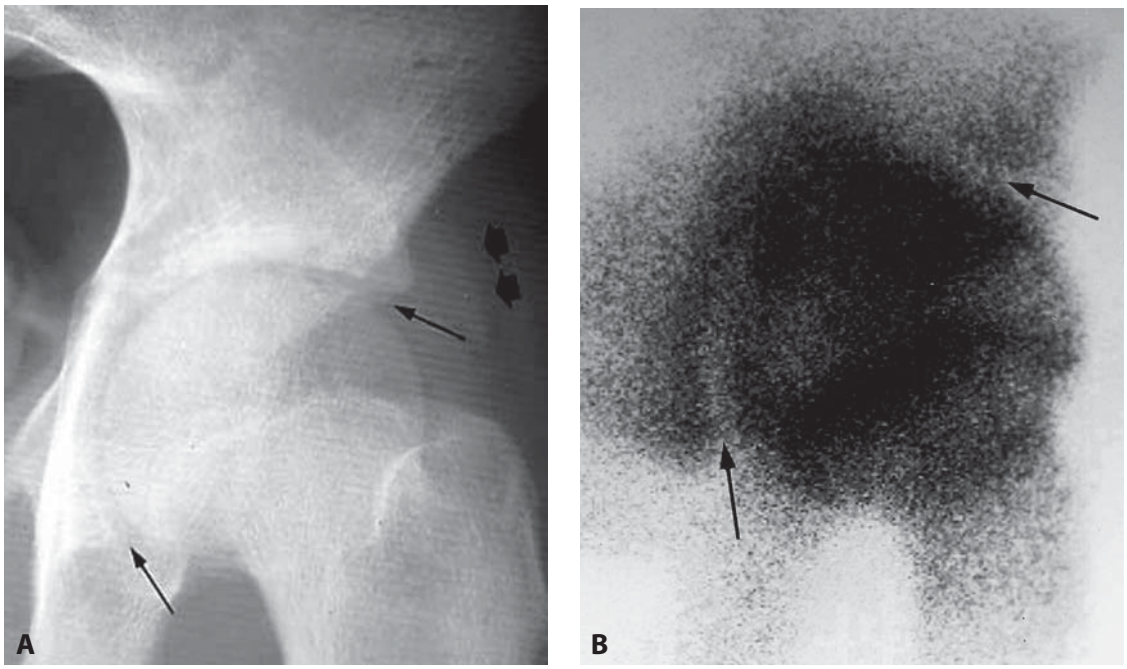

Fig. 8.8A, B Acute pyarthrosis with chondrolysis. **A** Anteroposterior radiograph of the left hip in a 13-year-old girl shows marked joint space narrowing with capsular distension (*arrows*). **B** Anterior pinhole scan reveals intense periarticular uptake with narrowed joint space (*arrows*)

increased tracer uptake in the subchondral bones of the joint. Essential findings are similar to those of transient synovitis. In some patients, the uptake tends to be diffused in the whole femoral head, giving rise to the "hot femoral head" sign. In those with an established primary infective focus in the juxtaarticular bone, for example, in the intracapsular portion of the femoral neck or head, both the primary focus and the secondary synovitis can be simultaneously portrayed by pinhole scintigraphy. Nuclear angiography and spot scans are as useful as pinhole scans for viewing the tracer accumulated in a diseased joint. When sterile synovitis involves the knee, tracer diffusely accumulates in the subchondral layers of all the component bones including the patella, rendering them distinctly silhouetted (Fig. 8.5). This is termed the "wrapped bone" sign.

8.1.3 Sterile Traumatic Synovitis

Following contusion or a sprain of a joint sterile synovitis may develop. Such a synovitis is caused by or associated with bone contusion, rupture of the anterior cruciate ligament, meniscal tear, or impingement of reparative tissue (Comin and Rodriguez-Merchan 1997; Huh et al. 2004). The traumatic synovitis produces sterile effusion of various amounts, which occasionally may result in fibrosis. Radiographic features include capsular distension and osteopenia of regional bones, and the signs of traumatic injuries such as fracture. Scintigraphy shows widening of the joint space when effusion is profuse. Characteristically, however, unlike in transient synovitis and reactive synovitis, the subchondral uptake is mild or absent unless infection supervenes (Fig. 8.6).

8.1.4 Synovitis in Renal Transplantation and Prolonged Hemodialysis

Following renal transplantation and during long repeated hemodialysis, acute or chronic synovitis may supervene as a complication (Bravo et al. 1967). Generally, the articular inflammation is simple, but occasional infection has been reported (Spencer 1986). The physical irritation of denatured and fragmented articu-

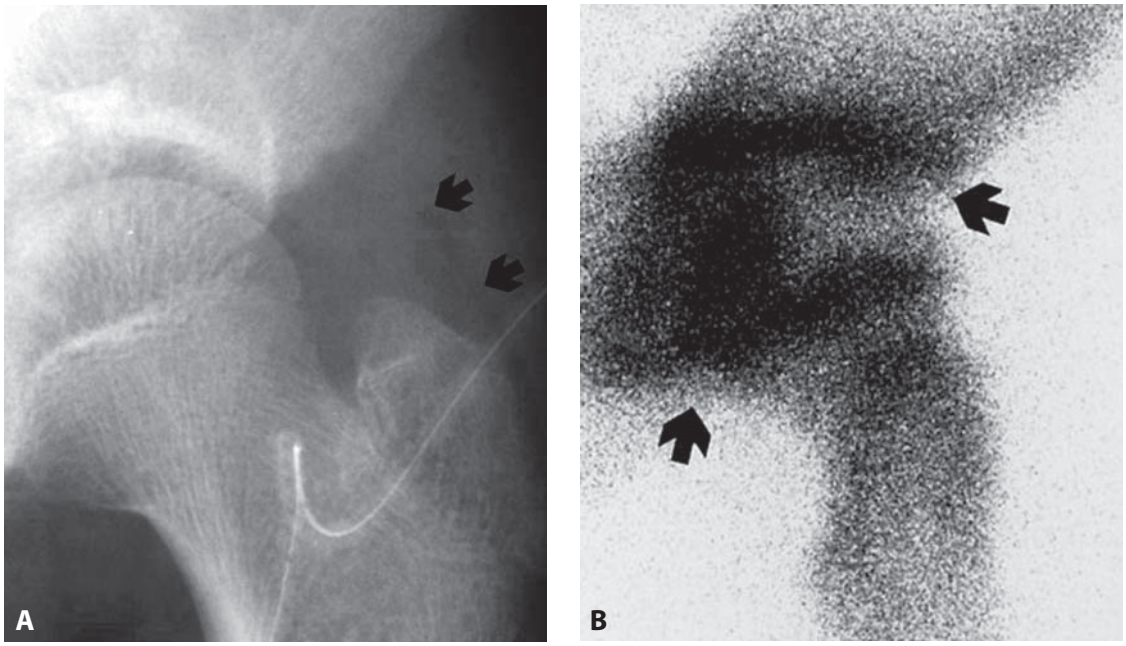

Fig. 8.9A, B Acute pyarthrosis with aborted chondrolysis following early treatment. **A** Anteroposterior radiograph of the left hip in another 13-year-old girl taken after aspiration of pus from the joint shows marked capsular distension (*arrows*) but with a well-preserved joint space. Note an indwelling drain. **B** Anterior pinhole scan reveals increased tracer uptake that is not as intense as in untreated case shown in Fig. 8.8B

lar cartilage has been held to be responsible in some instances.

Soft-tissue radiography shows distension of the articular capsule and periarticular soft-tissue swelling when the process has run a chronic course or in the presence of infection (Fig. 8.7A) and bone technique radiography demonstrates articular narrowing with diffuse periarticular osteopenia (Fig. 8.7B).

The pinhole scan features are similar to those seen in other types of synovitis, although they are mild unless complicated by an infection. Once infection is present, pyarthrosis manifests as extremely intense tracer uptake with a narrowed joint, which looks like a joint "in flame" (Fig. 8.7C). Interestingly, whole-body bone scintigraphy, a necessary imaging in bone scanning, demonstrates systemic low skeletal uptake with the absence of kidney uptake, denoting osteoarthropathy secondary to chronic renal failure (Fig. 8.7D).

8.2 Infective Arthritis

8.2.1 Pyogenic Arthritis (Pyarthrosis)

Pyogenic arthritis is a septic condition of a joint. As in acute osteomyelitis, acute pyarthrosis may result from: (a) hematogenous spread of bacteria with direct synovial lodgment, (b) transphyseal (across the growth cartilage) spread of a primary infective focus in the long-bone metaphysis, (c) contiguity, or (d) penetration or operation. The most common offenders are micrococci and gram-negative bacilli.

In children, pyarthrosis has a predisposition for the large joints of the limbs, whereas bacterial spondylitis and diskitis (equivalent to the infection of a diarthrosis joint) is more common in adults. Often, the sternoclavicular joint and sacroiliac joint are afflicted in drug abusers.

The acute pathological responses of the synovial membrane to bacterial invasion include edema, swelling, and hypertrophy with pus formation. After a few days the articular carti-

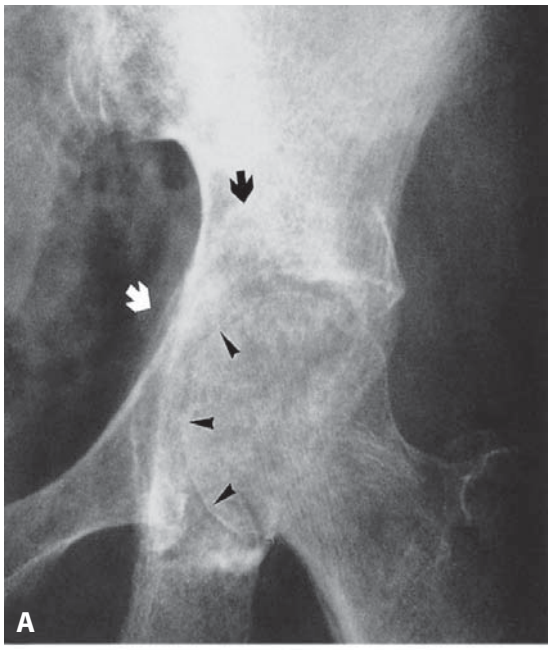

Fig. 8.10A, B Protrusio acetabuli complicating an advanced hip joint pyarthrosis and concurrent osteomyelitis in the innominate bone. **A** Anteroposterior radiograph reveals mottled lysis in the supra-acetabular bone with acetabular protrusion (*white arrow*). The articular space is completely closed at the centromedial aspect (*arrowheads*). **B** Anterior pinhole scintigraph of the left hip in a 60-year-old woman with pyarthrosis shows extremely intense tracer uptake in the hip joint and supra-acetabular bone (*arrows*). There is minimal bulging of the pelvic border, the sign of early acetabular protrusion or pathological fracture (*middle arrow*).

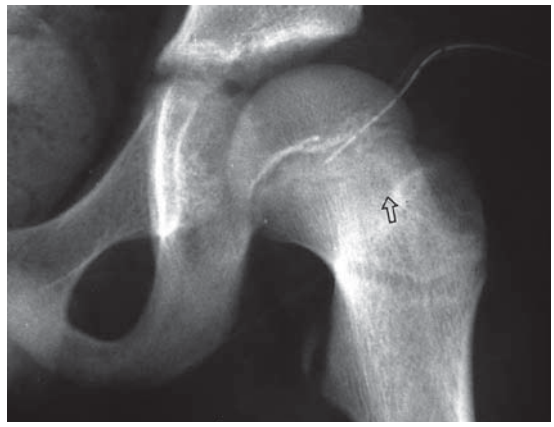

Fig. 8.11 Pediatric pyohip caused by direct extension of adjacent acute osteomyelitis (the same case as Fig. 8.15). Anteroposterior radiograph of the left hip in an 11-year-old girl after aspiration shows an infective focus in the ipsilateral femoral neck (*open arrow*)

lage begins to melt and lysis extends to the subchondral bone if the infection is uncontrolled. Without cartilage the joint is narrowed, collapsed, and eventually ankylosed.

Radiographically, the acute infected joint shows capsular distension, joint space narrowing, and periarticular bone erosions (Fig. 8.8A). The infective arthritis aborted by the early institution of proper treatment may also show similar findings but with a relatively well-preserved joint space (Fig. 8.9A). In the chronic phase the joint is deformed with eburnation and bony ankylosis may ensue (Fig. 8.10A). In children, pyohip can occur as an extension of acute osteomyelitis in the ipsilateral femoral neck, and both conditions can be diagnosed by radiography (Fig. 8.11).

Ordinary planar scintigraphy simply reveals intense tracer uptake in the joint. However, pinhole scintigraphy shows the intense uptake to be localized to markedly narrowed joint, reflecting the destruction of the articular cartilages and subchondral bones (Fig. 8.12). The articular narrowing tends to be conspicuous in the hips, the knees, and the spine that bear body weight. In contrast, the tracer uptake and articular narrowing are not so conspicuous in the glenohumeral joint (Fig. 8.13) and elbow, which are out of the main weight-bearing axis

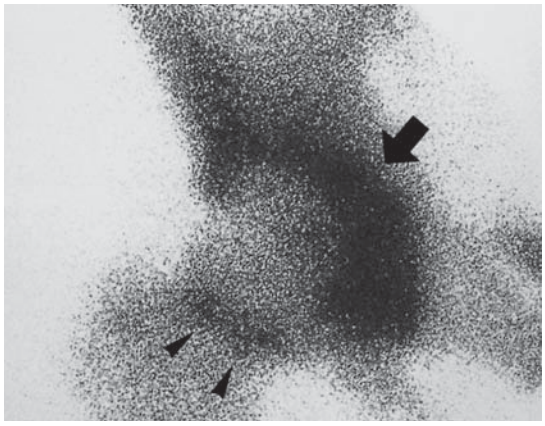

Fig. 8.12 Pyarthrosis of the hip. Anterior pinhole scintigraph of the right hip in a 25-year-old man shows extremely intense tracer uptake diffusely in the acetabular fossa and the femoral head with total obliteration of the joint (*arrow*). Some tracer uptake is seen also in the femoral neck, probably at the site of the subcapital capsular and synovial attachment (*arrowheads*)

of the body. In pyarthrosis of the hip, tracer accumulates more extensively in the acetabular fossa than in the femoral head (Fig. 8.12). The uptake is concentric and symmetrical, reflecting uniform chondrolysis. A similar change can be seen in rheumatoid arthritis that is attended by more or less generalized cartilage destruction by pannus (see Chap. 10). In inadequately managed patients, the acetabulum may become fractured, resulting in protrusio acetabuli that avidly accumulates tracer (Fig. 8.10B). Pyarthroses of the knee and the ankle manifest as prominent uptake in the entire joint so that all of the bones forming the respective joint are silhouetted (Fig. 8.14). Pathological uptake appears to conform to the synovial lining. Understandably, the tracer uptake in pyarthrosis is far more intense than in simple synovitis. The intensity of uptake in an infective arthritis seems to be related to the severity of infection. In pediatric pyarthrosis, pinhole scintigraphy can occasionally detect the primary focus of infection in the adjacent bone (Fig. 8.15).

Pinhole scintigraphy is a useful means for the study of acute infection in the irregular joints of the elbow (Fig. 8.16) and the small joints of the hand and foot (Fig. 8.17). Occasi-

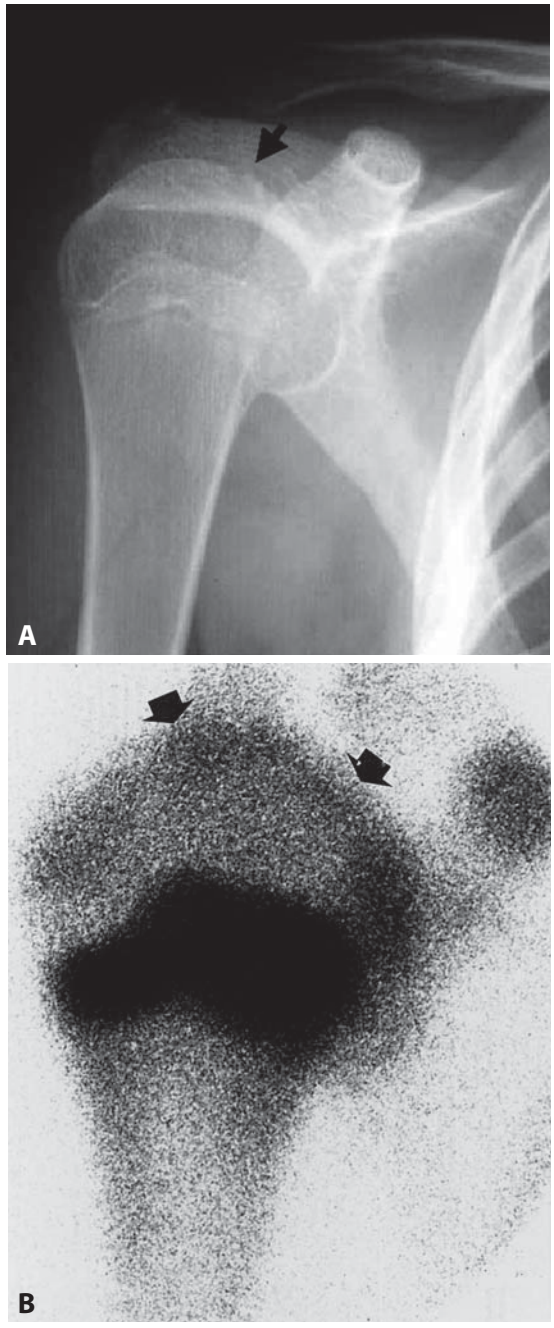

Fig. 8.13A, B Inconspicuous scan change in pyarthrosis of the glenohumeral joint. **A** Anteroposterior radiograph of the right shoulder in a 13-year-old girl with pyogenic arthritis of the shoulder joint shows minimal cortical erosion in the humeral head (*arrows*). **B** Anterior pinhole scan reveals increased tracer uptake in the subchondral zone (*arrows*). Note that the tracer uptake is not so intense

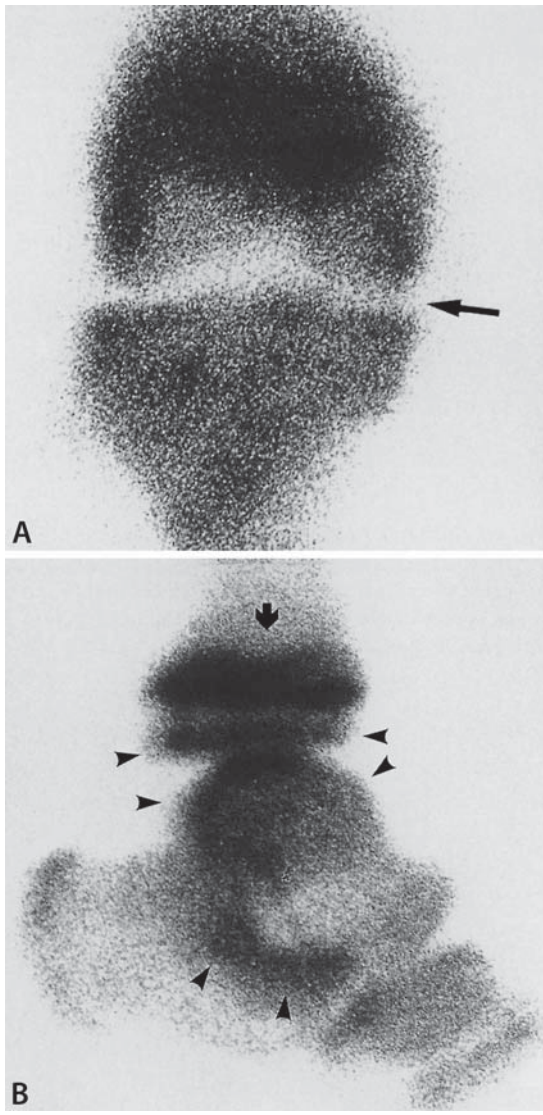

Fig. 8.14A, B Generalized intense tracer uptake in pyarthrosis in the knee and ankle with the "wrapped bone" sign. **A** Anterior pinhole scintigraph of the right knee in a 29-year-old woman with pyogenic arthritis shows intense tracer uptake in all of the bones about the knee joint, giving rise to the "wrapped bone" appearance. The joint space is narrowed (*arrow*). **B** Lateral pinhole scintigraph of the ankle in a young man with acute pyogenic infection shows tracer uptake in the subarticular zones of the distal tibia and fibula (*arrow*), the trochlea (*horizontal arrowheads*), and the bones of the subtalar joint (*lowermost arrowheads*). Note the broadening of the distal tibial physeal line and extremely intense tracer uptake in the adjacent metaphysis that represents acute osteomyelitis, the cause of pyarthrosis in this case (*arrow*)

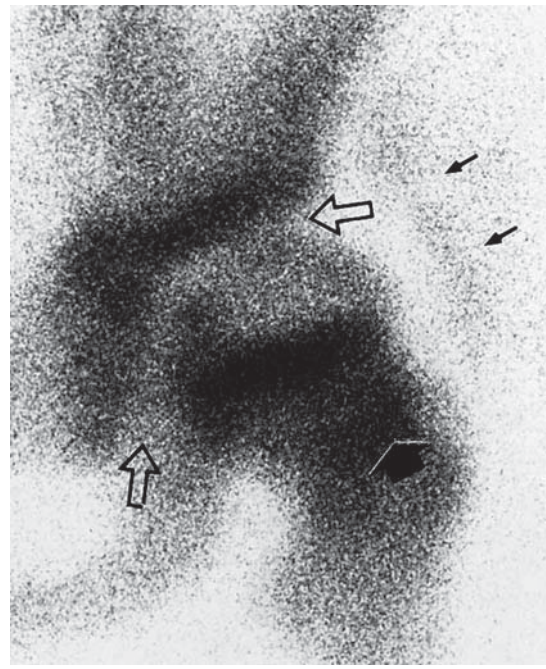

Fig. 8.15 Primary infective focus in pediatric pyarthrosis (the same case as Fig. 8.11). Anterior pinhole scan of the left hip in an 11-year-old girl with acute pyarthrosis (*open arrows*) caused by direct extension of infection from adjacent osteomyelitis in the femoral neck (*arrow*). Note tracer accumulated in soft-tissue bacterial seeding during aspiration (*small arrows*)

onally, soft-tissue infection caused by bacterial contamination during the aspiration of an infected joint can be diagnosed using bone scintigraphy (Fig. 8.15; same joint as shown radiographically in Fig. 8.11).

Pyarthrosis and regional osteoporosis of the hip may impose a diagnostic problem because of the great similarity of their symptoms and planar scan findings. With the aid of pinhole scintigraphy, however, tracer uptake in the regional osteoporosis can be clearly differentiated from that of pyarthrosis: the tracer uptake of pyarthrosis is in the joint (Fig. 8.12) and that of osteoporosis is in the femoral head (Fig. 8.18).

8.2.2 Pyarthrosis and Abscess of the Sacroiliac Joint

The sacroiliac joint may be infected through the hematogenous route, from a contiguous focus, or by direct bacterial implantation from

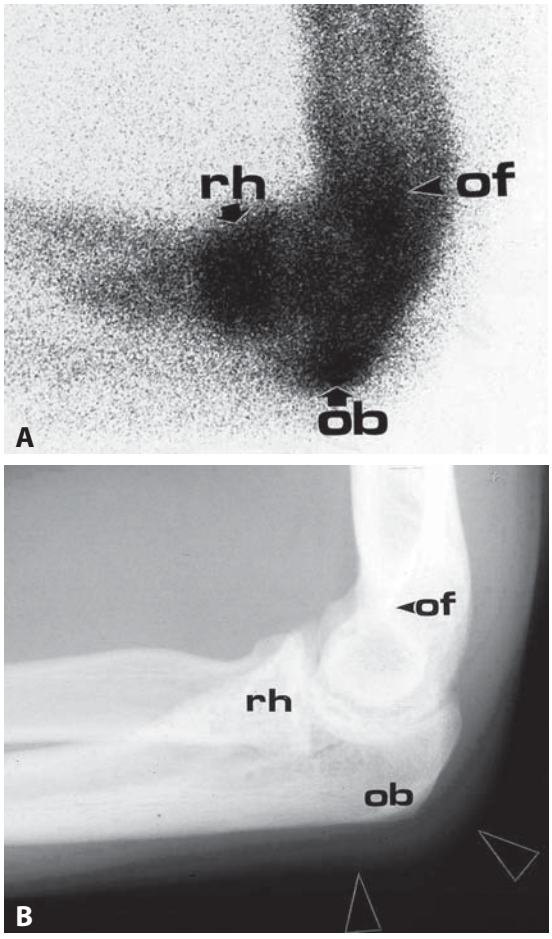

Fig. 8.16A, B Acute infective arthritis of the elbow. **A** Lateral pinhole scan of the right elbow in a 31-year-old male shows intense tracer uptake in the radial head (*rh*), olecranon base (*ob*), and olecranon fossa (*of*). **B** Lateral radiograph reveals diffuse blurring of the joint with thickening of the cubital soft tissue overlying the olecranon (*arrowheads*)

biopsy, surgery, or a traumatic wound. As in the endarteries of the long-bone ends, the subchondral blood circulation in the ilium is slow, facilitating bacterial lodgment in the synovium. The pyogenic infection of the sacroiliac joint is typically unilateral (Gordon and Kabins 1980). The infection rapidly spreads and dissolves the cartilages and bones, often causing apparent joint space widening. The destroyed joint is replaced by granulation tissue and fibrosis with marginal reactive sclerosis.

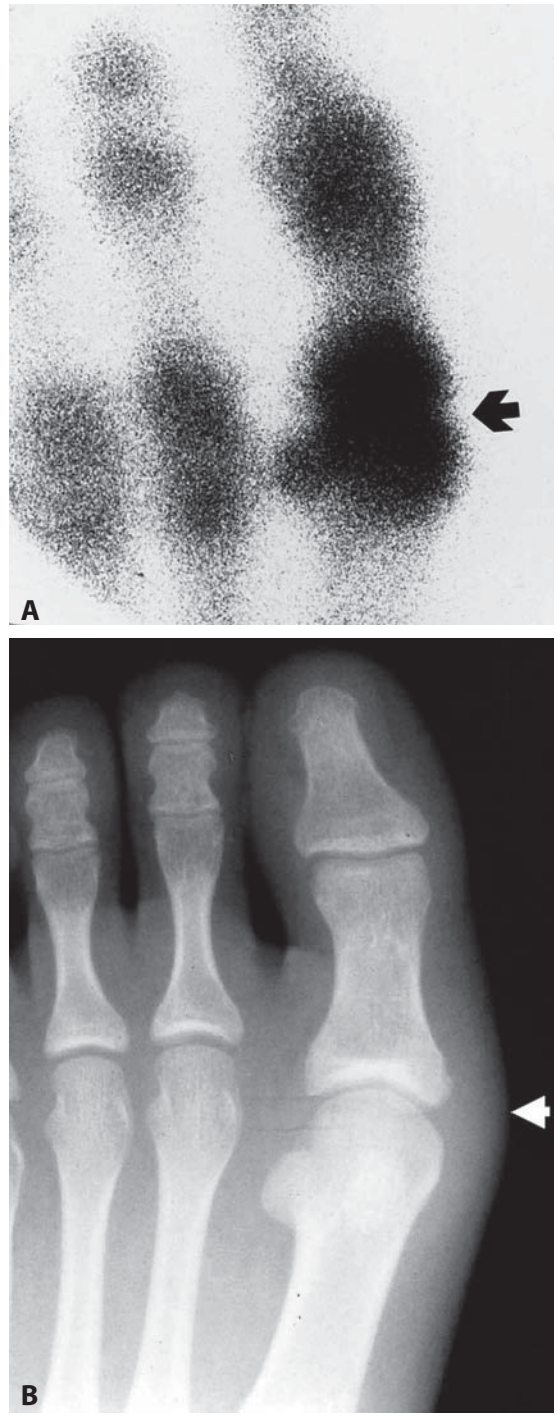

Fig. 8.17A, B Pyogenic arthritis of a small digital joint. **A** Dorsoplantar scan of the left foot in a 15-year-old girl with acute infection in the first toe shows marked tracer uptake in the bones around the metatarsophalangeal joint (*arrow*). **B** Radiograph reveals narrowed joint space with blurring and marked periarticular soft tissue thickening (*arrow*)

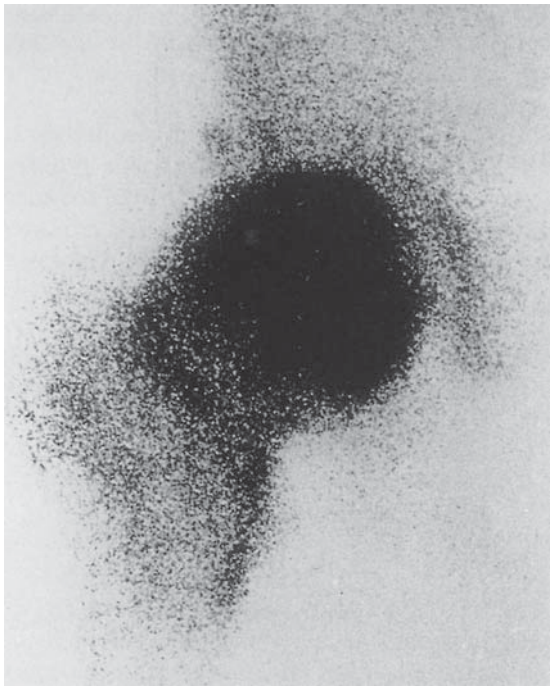

Fig. 8.18 Intense tracer uptake in the regional osteoporosis of the femoral head simulating pyogenic infection. Anterior pinhole scintigraph of the left hip in a 34-year-old woman with pain shows extremely intense tracer uptake in the femoral head. Importantly, unlike in infection, the tracer uptake is exclusively confined to the femoral head and other bones are completely free. Ordinary spot scintigraph did not provide such crucial information

Radiographically, the acute or subacute pyogenic infection of the sacroiliac joint manifests as either apparent widening of the joint space and blurring or erosion of the subchondral bones (Fig. 8.19A). If an abscess forms it presents as a bone defect surrounded by irregular sclerotic margin (Fig. 8.20A), strongly resembling tuberculosis (see Sect. 8.2.3).

Pinhole scan findings differ according to the disease stage. In the acute stage, spinnaker-like uptake appears in the lower synovial compartment (Figs. 8.19B) and in the chronic stage with abscess formation uptake becomes bizarre containing a photopenic defect (Fig. 8.20B). It is to be noted that the scintigraphic finding of acute pyarthrosis of the sacroiliac joint radically differs according to the sacral inclination relative to the coronal plane of the body. Thus,

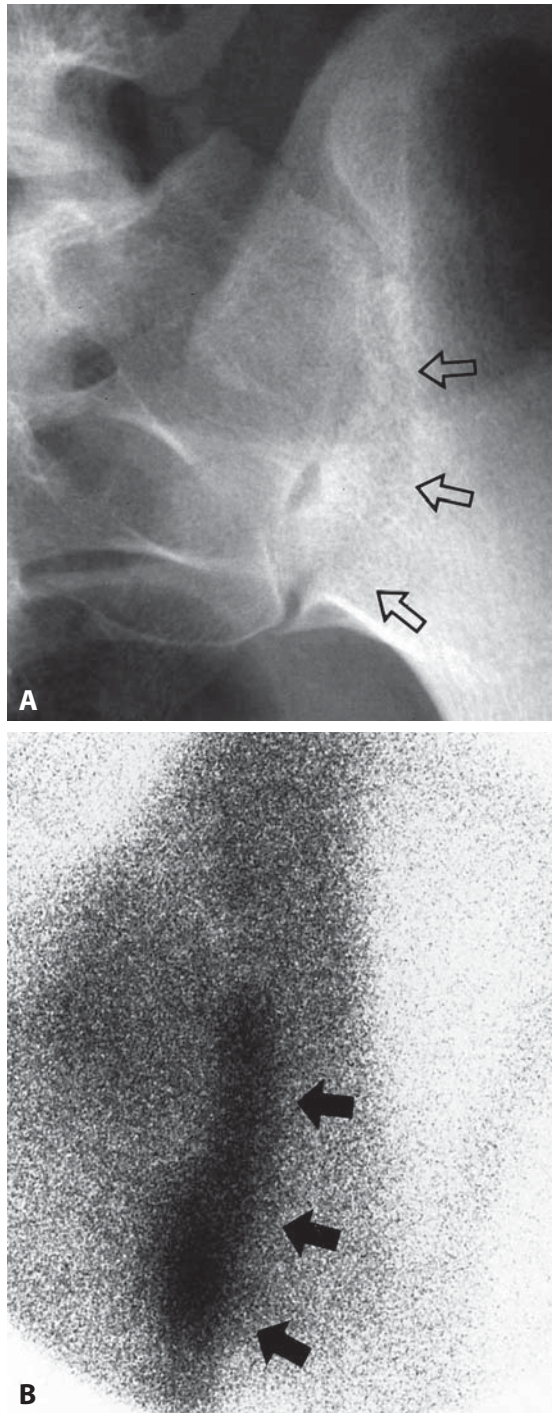

Fig. 8.19A, B Subacute pyogenic infection of the sacroiliac joint. **A** Anteroposterior radiograph of the left sacroiliac joint in a 19-year-old female shows apparent joint space widening with erosion and blurring of subchondral bones characteristically in the synovial lower compartment (*open arrows*). **B** Anterior pinhole scan reveals vertically aligned intense bar-like uptake of the synovial sacroiliac joint (*arrows*)

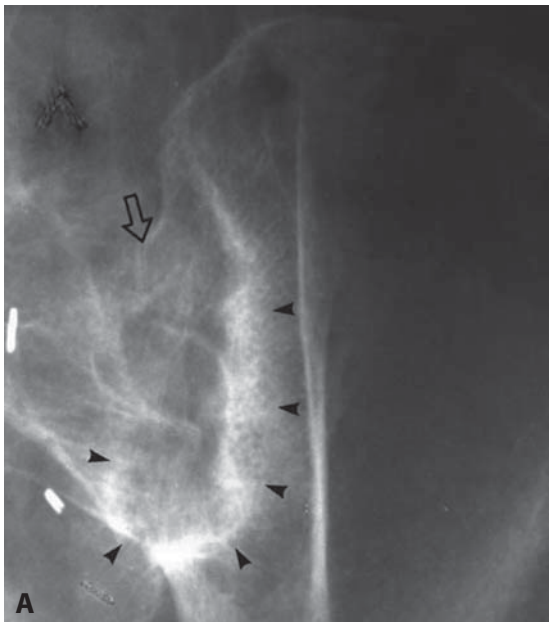

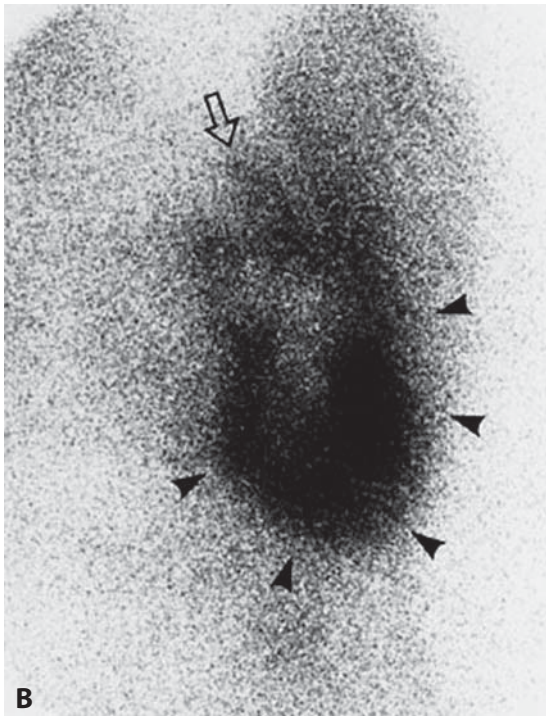

Fig. 8.20A, B Abscess formation in chronic pyogenic sacroiliitis. **A** Anteroposterior radiograph of the left sacroiliac joint in a 65-year-old female with a chronic infection developed after hysterectomy performed 4 months previously shows large irregular gaping bone destruction (*open arrow*) with prominent marginal reactive bone formation (*arrowheads*). Note two small metallic surgical clips. **B** Anterior pinhole scan reveals a photon defect due to an abscess (*open arrow*) surrounded by prominent tracer uptake in sclerosis (*arrowheads*)

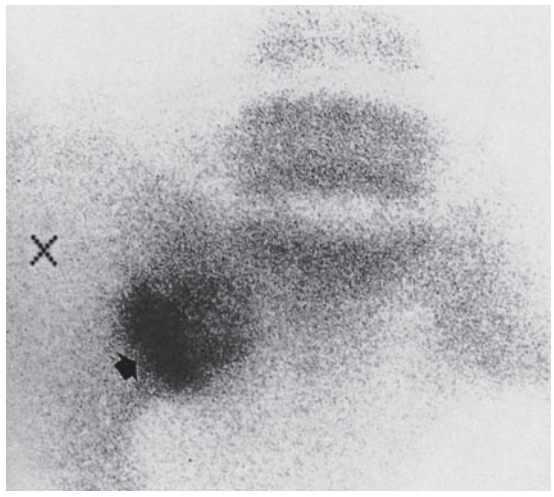

Fig. 8.21 Subacute pyogenic sacroiliitis. Anterior pinhole scan of the pelvis in a 33-year-old man with right pyogenic sacroiliitis shows intense tracer uptake in the lower aspect of the joint (*arrow*). Minimal reaction is also seen in the sacral border

when the sacrum is flat the uptake appears to be elongated club shaped (Fig. 8.19B), but if posteriorly tilted (sacrum acutum) the uptake becomes roundish in appearance (Fig. 8.21).

8.2.3 Tuberculous Arthritis of Peripheral Joints

Tuberculosis in the peripheral joints runs an insidious, chronic course as tuberculosis elsewhere. For the most part, the mode of infection of tuberculous arthritis is blood-borne with a primary focus usually in the lung. It may also arise from direct contamination with tuberculosis in the neighboring bone. Granulomatous tissue and pannus erode and dissolve articular cartilages and subchondral bones, causing irregular narrowing and disfiguring. Tuberculosis affects any joint (Enarson et al. 1979), but larger joints such as the hip, knee, and sacroiliac joint are sites of predilection (Lee et al. 1995; Campbell and Hoffman 1995). The sternoclavicular joint, glenohumeral joint, elbow, wrist, ankle, and joints of the hand and foot are less commonly affected. The occurrence is usually monarticular (Evanchick et al. 1986).

Radiographic features include osteopenia, subchondral erosions, periarticular bone des-

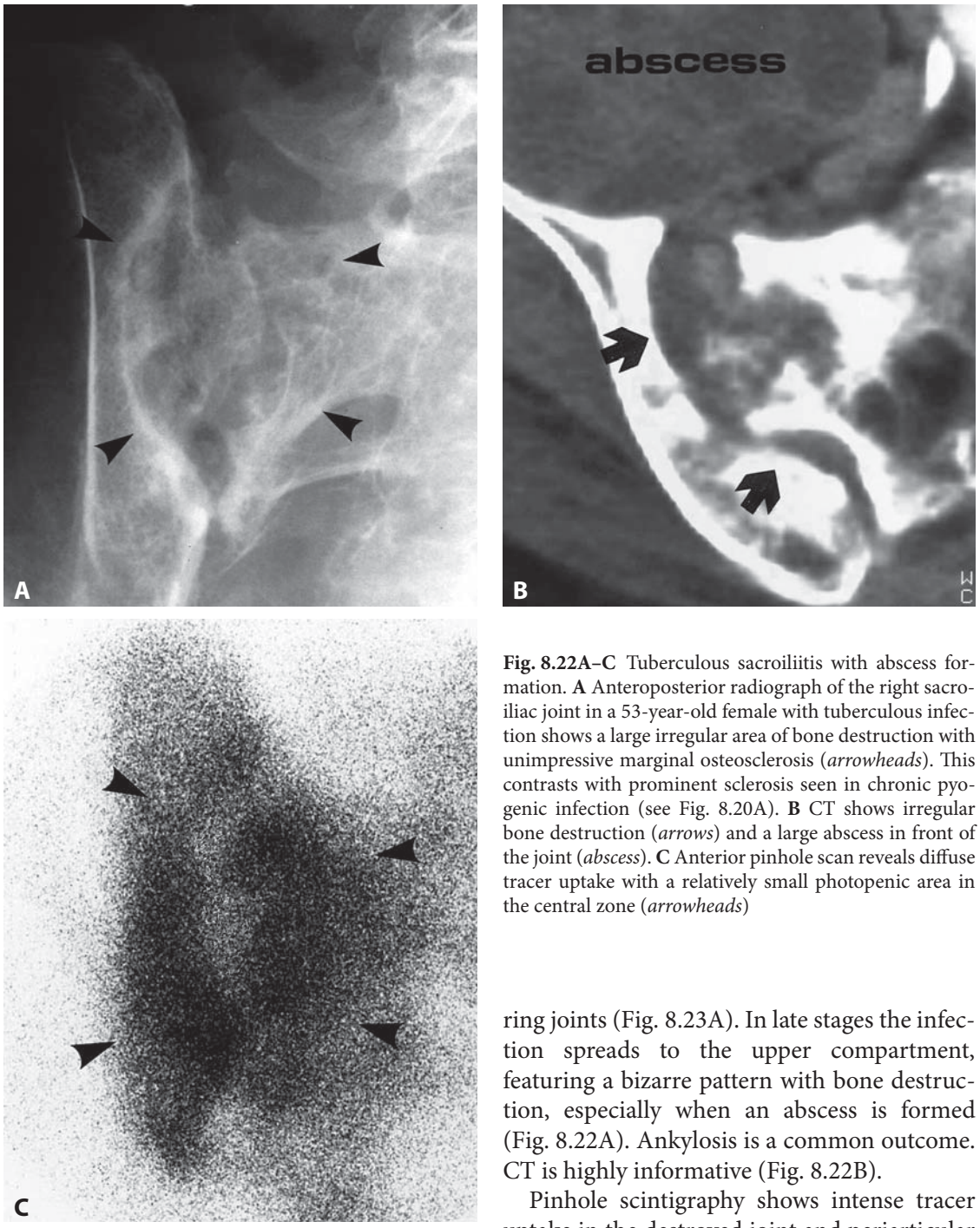

Fig. 8.22A–C Tuberculous sacroiliitis with abscess formation. **A** Anteroposterior radiograph of the right sacroiliac joint in a 53-year-old female with tuberculous infection shows a large irregular area of bone destruction with unimpressive marginal osteosclerosis (*arrowheads*). This contrasts with prominent sclerosis seen in chronic pyogenic infection (see Fig. 8.20A). **B** CT shows irregular bone destruction (*arrows*) and a large abscess in front of the joint (*abscess*). **C** Anterior pinhole scan reveals diffuse tracer uptake with a relatively small photopenic area in the central zone (*arrowheads*)

truction, articular narrowing, and soft-tissue swelling (Figs. 8.22A and 8.23A). Unlike in pyarthrosis or rheumatoid arthritis, the bone destruction tends to be eccentric in the noncontact or marginal areas of a joint, resulting in asymmetrical narrowing of the joint. The articular narrowing is severer in the weight-bearing joints (Fig. 8.23A). In late stages the infection spreads to the upper compartment, featuring a bizarre pattern with bone destruction, especially when an abscess is formed (Fig. 8.22A). Ankylosis is a common outcome. CT is highly informative (Fig. 8.22B).

Pinhole scintigraphy shows intense tracer uptake in the destroyed joint and periarticular bones (Figs. 8.22C and 8.23A). Articular narrowing is a constant feature, which is more severe in the weight-bearing joints of the spine, hip, knee, or ankle (Fig. 8.23) than in the non-weight-bearing glenohumeral or sternoclavicular joints (Fig. 8.24). The interphalangeal joints of the hand and foot are also affected as

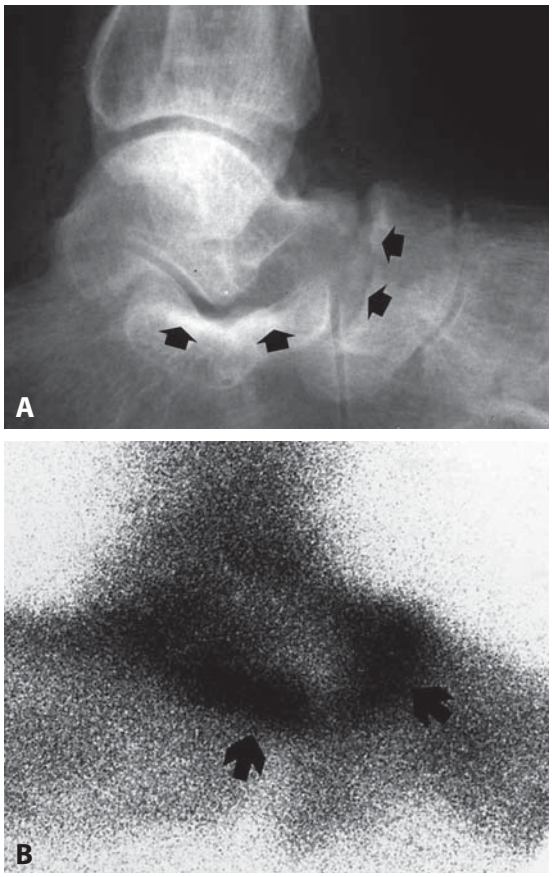

Fig. 8.23A, B Tuberculosis in the subtalar joint. **A** Lateral pinhole scan of the left ankle in a 37-year-old female shows intense tracer uptake in the subtalar and talonavicular joints with reduced height of the hindfoot bones (*arrows*). **B** Lateral radiograph reveals comparable arthritic changes with narrowed and flattened joint spaces (*arrows*) and diffuse porosis

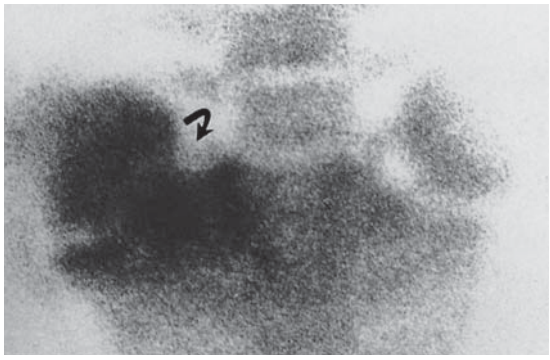

Fig. 8.24 Tuberculosis in the sternoclavicular joint. Anterior pinhole scintigraph of the sternum in a 33-year-old woman reveals intense tracer uptake in the medial end of the right clavicle and the apposing sternum. The articular space is irregularly narrowed (*curved arrow*)

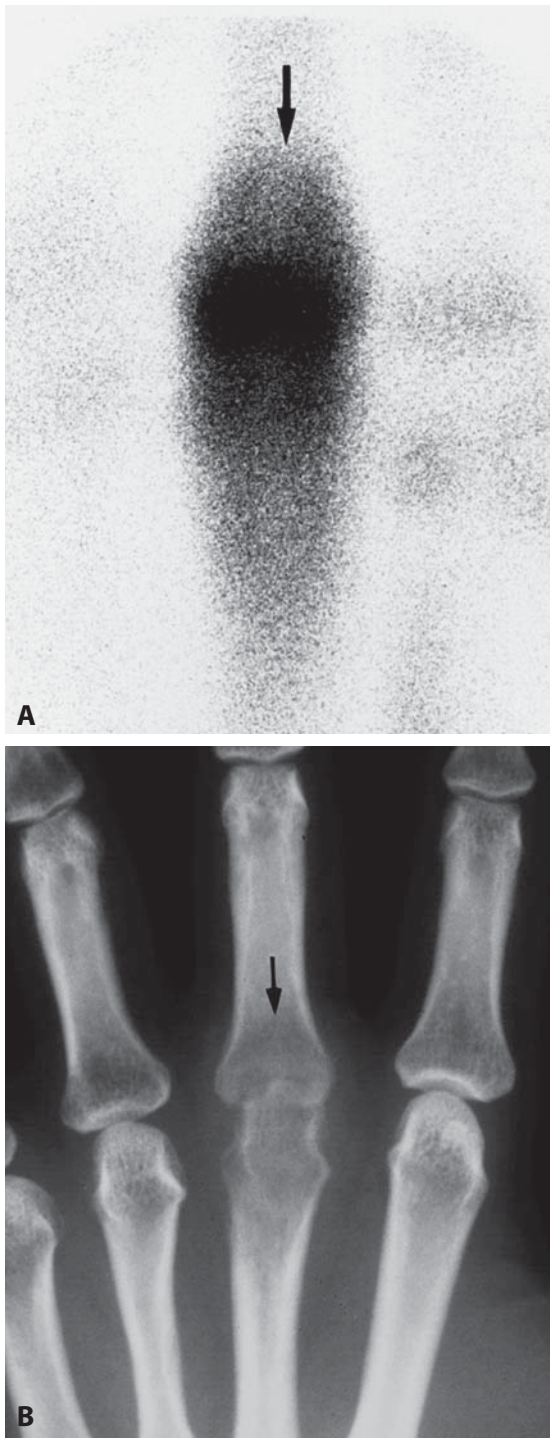

Fig. 8.25A, B Phalangeal tuberculosis. **A** Dorsopalmar pinhole scan of the right third metacarpophalangeal joint in a 35-year-old female shows intense tracer uptake in the narrowed joint sided by less intense watershed uptake (*arrow*). **B** Radiograph reveals complete articular narrowing with prominent osteopenia but without osteosclerosis (*arrow*)

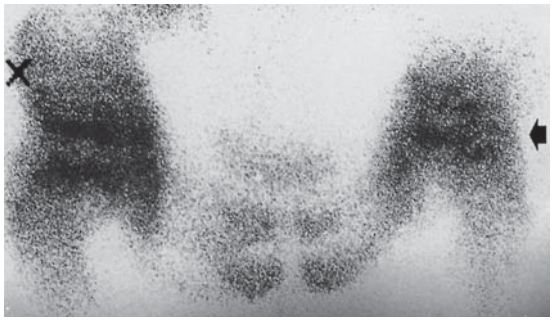

Fig. 8.26 Obscurity of the local anatomy and stunted growth in chronic tuberculous arthritis in a child. Anterior pinhole scan of the lower pelvis in a 6-year-old girl with known tuberculosis of the left hip reveals obliteration of the local anatomy with closed joint. The regional bones are small and slender due to atrophy and stunted growth which is indicated by the absence of tracer in the physis, the sign of arrested bone growth (*arrow*)

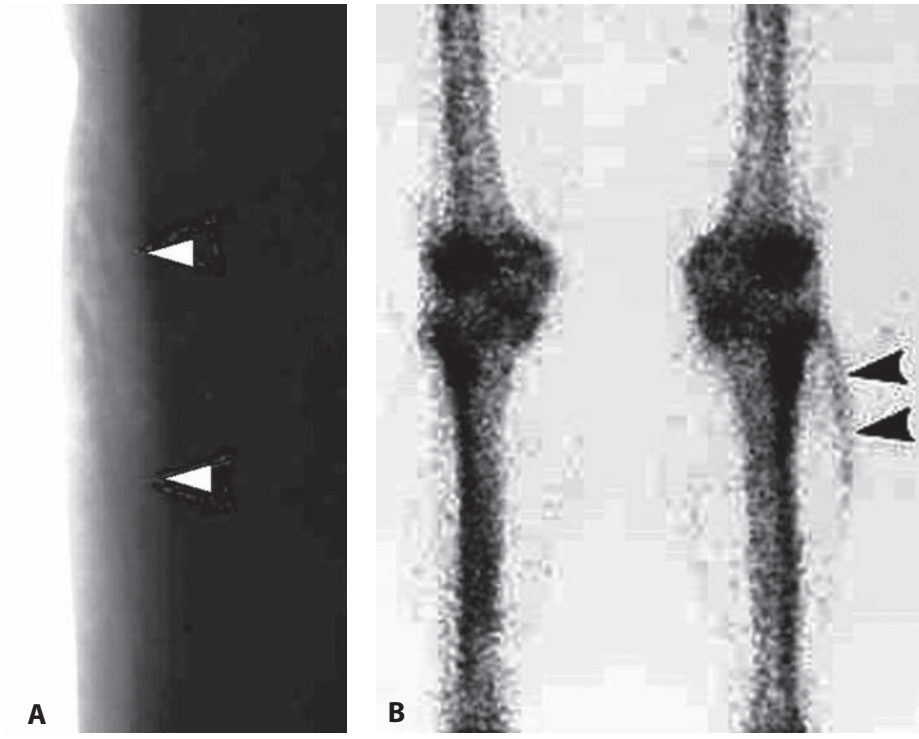

Fig. 8.27A, B Simple infective fasciitis. **A** Soft-tissue technique radiograph of the left leg in a 22-year-old male shows fish flesh-like derangement of subcutaneous tissue with blurred intermuscular fascial plane (*arrows*). **B** Bone scintigraphy reveals long curvilinear uptake in the fascial plane (*arrowheads*)

separate tuberculous arthritis. Unlike dactylitis with diffuse involvement of a digit in a child (spina ventosa), the tuberculous infection of an adult finger joint is limited to the joint and periarticular bones, causing fusiform uptake that is composed of more intense uptake in the joint with less intense watershed uptake to the side (Fig. 8.25).

In general, tuberculous joints tend to remain relatively preserved until the late stage compared to pyogenic joints, especially when the affected joint is non-weight-bearing (Fig. 8.24). With the progress of tuberculosis, the joint becomes obliterated or seemingly widened due to para-articular bone destruction (Fig. 8.22A) and the regional bones deformed. In children, the bones in the affected limb are reduced in size due to premature physeal fusion and hypoplasia with decreased uptake. Pinhole scintigraphy can clearly indicate the precocious closure of the physis by the absence of tracer uptake in the growth cartilage (Fig. 8.26).

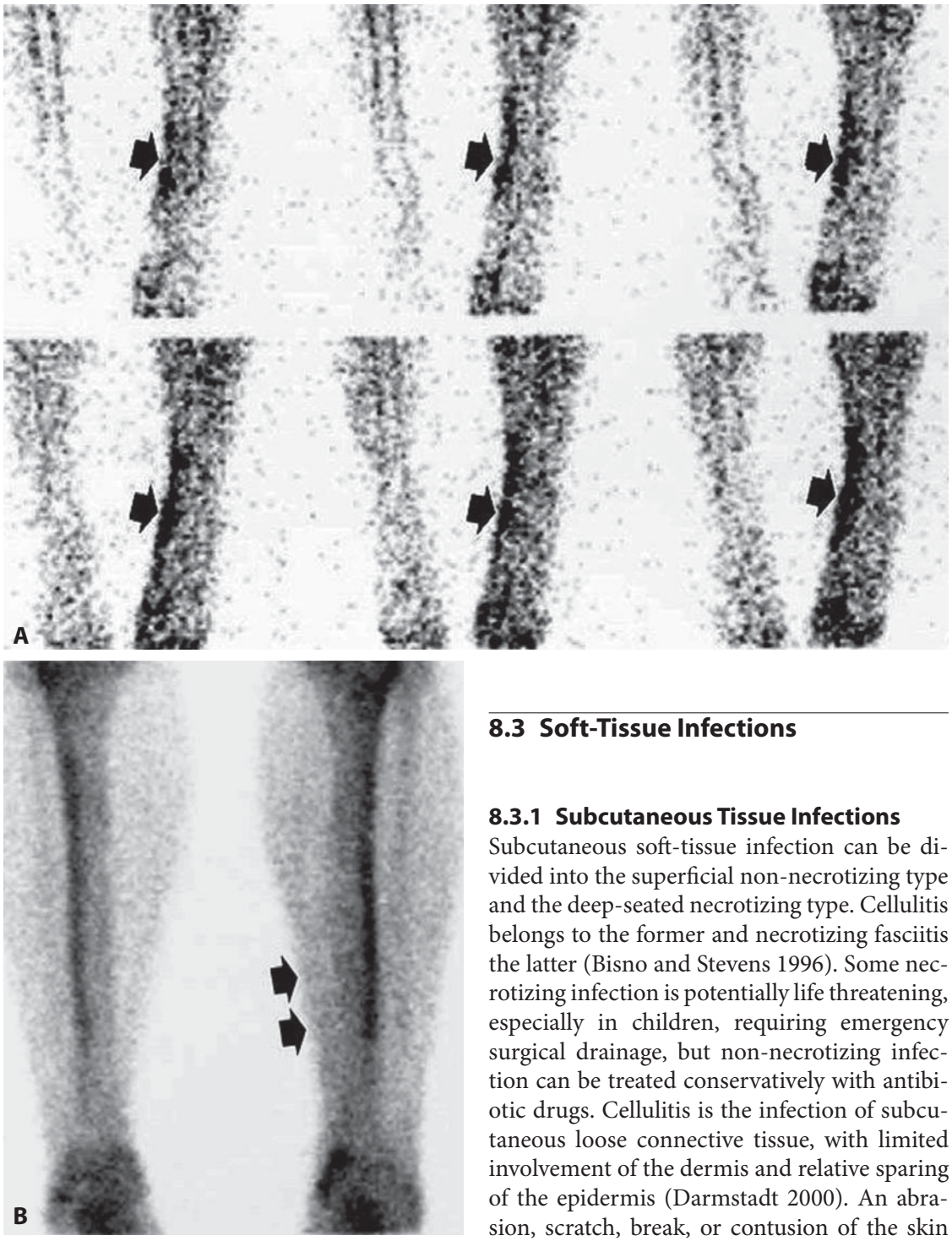

Fig. 8.28A, B Nuclear angiography in cellulitis. **A** Arterial phase angiography of the left leg in a 33-year-old male shows a segmental area of increased blood flow and blood pool in the subcutaneous layer (*arrows*). **B** Equilibrium phase scan reveals incomplete clearance of tracer but without bone uptake reflecting oosing (*arrows*)

8.3 Soft-Tissue Infections

8.3.1 Subcutaneous Tissue Infections

Subcutaneous soft-tissue infection can be divided into the superficial non-necrotizing type and the deep-seated necrotizing type. Cellulitis belongs to the former and necrotizing fasciitis the latter (Bisno and Stevens 1996). Some necrotizing infection is potentially life threatening, especially in children, requiring emergency surgical drainage, but non-necrotizing infection can be treated conservatively with antibiotic drugs. Cellulitis is the infection of subcutaneous loose connective tissue, with limited involvement of the dermis and relative sparing of the epidermis (Darmstadt 2000). An abrasion, scratch, break, or contusion of the skin predisposes to cellulitis. It more commonly occurs in patients with lymphedema or diabetes or in an immunosuppressive state. *Streptococcus pyogenes* and *S. aureus* are the main offenders. Necrotizing fasciitis is an infection of the deep layer of the fascia, usually sparing muscle.

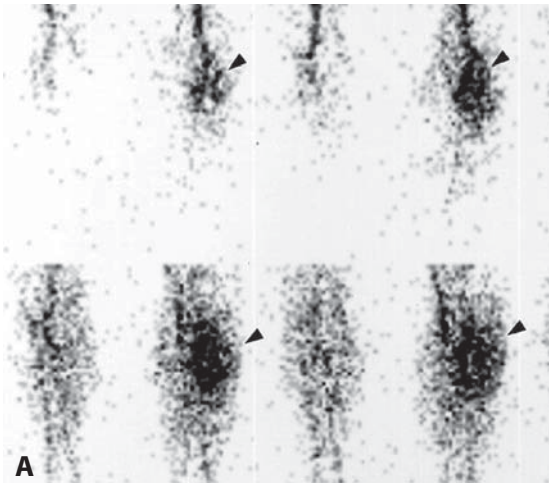

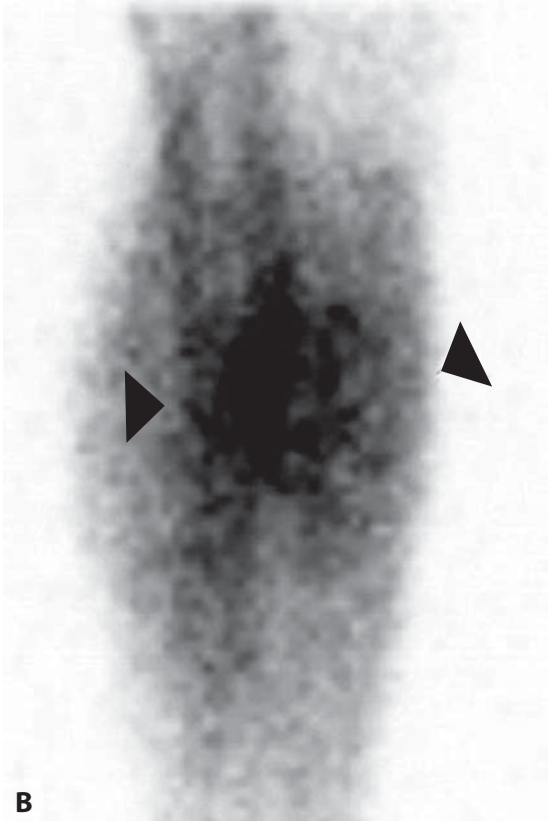

Fig. 8.29A–C Necrotizing fasciitis (*abscess*). **A** Arterial phase nuclear angiography of the left leg in a 43-year-old male with hemolytic streptococcal abscess shows an ill-defined area of increased blood flow in the deep soft-tissue layer (*arrowheads*). **B** Blood-pool scan reveals tracer uptake to be divided into an ill-defined central "hotter" zone and a peripheral "hot" zone (*arrowhead*). **C** Sonogram clearly demonstrates a vertically aligned spindle-shaped low-echo lesion surrounded by an incomplete echogenic capsule, denoting abscess and necrotized fascias, respectively (arrowheads)

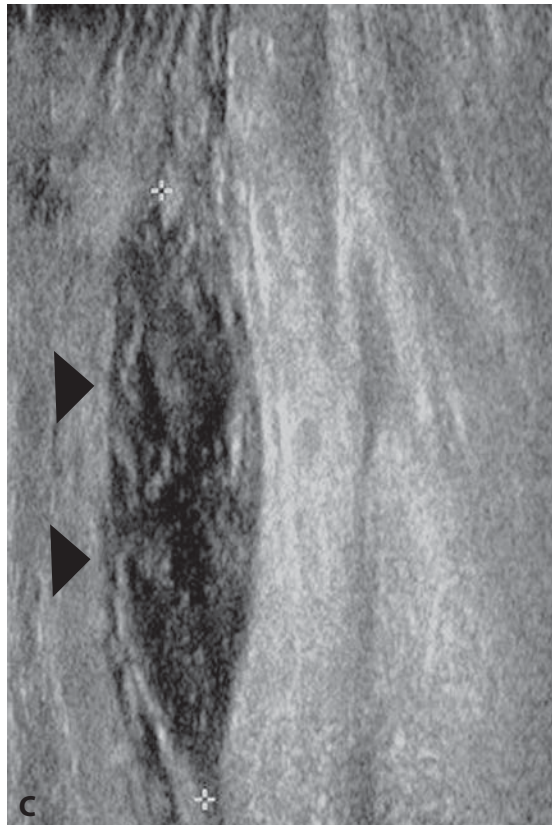

The extremities, the abdomen, and the perineal region are sites of predilection.

Radiography reveals fish flesh-like or irregular mottled densities of subcutaneous edema in the cellulitis, and soft-tissue swelling and blurring of intermuscular fascial plane in simple fasciitis (Fig. 8.27A). Bone scintigraphy reveals strip-like or diffused uptake in superficial soft tissues (Fig. 8.27B). Nuclear angiography is useful for the demonstration of increased vascularity in cellulitis, and occasional extravasation in the subcutaneous soft tissue (Fig. 8.28). Unlike in osteomyelitis or osteitis, the regional bone does not accumulate tracer. In addition, it is of great interest to note that the scan feature of necrotizing fasciitis (abscess) basically differs from that of simple fasciitis. Indeed, in necrotizing fasciitis nuclear angiography reveals hypervascularity and increased blood pool

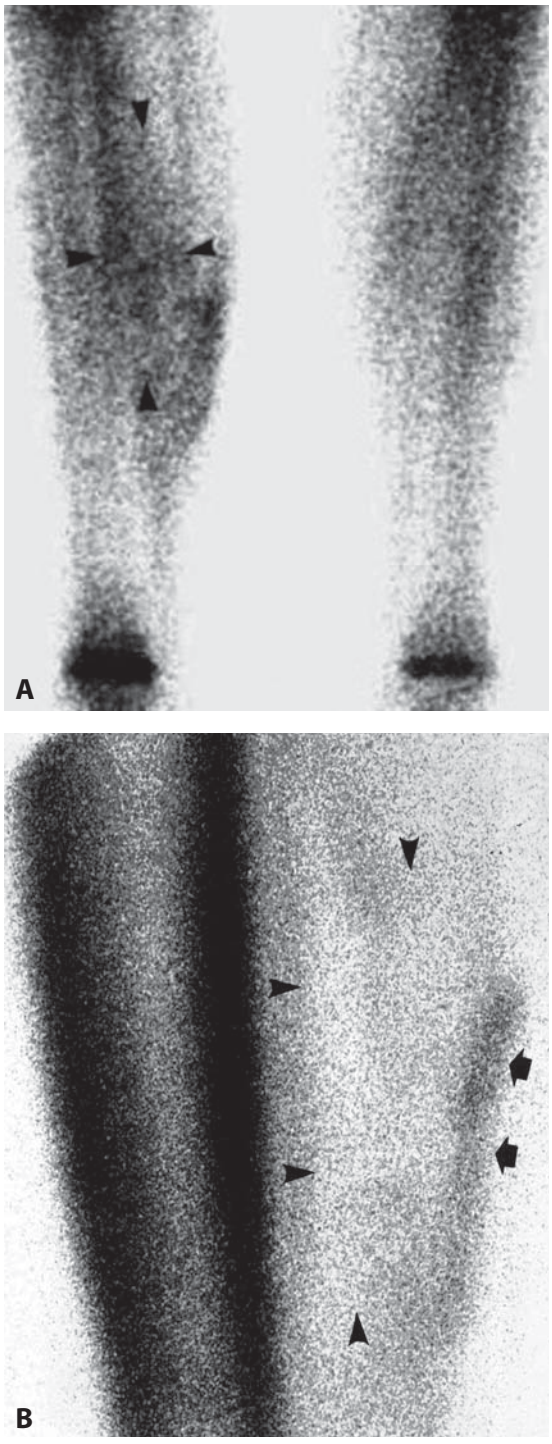

Fig. 8.30A, B Soft-tissue abscess. **A** Blood-pool scan of the right leg in a 12-year-old boy shows diffuse tracer stain in a sac formed in necrotic fascia (*arrowheads*). **B** Equilibrium scan reveals rapid clearing of tracer stain followed by photopenic replacement reflecting pus collection (*arrowheads*). Persistent subcutaneous uptake is in concurrent superficial cellulitis (*arrows*)

in and around the abscess formed in the deep muscle layer (Fig. 8.29A, B). Sonography is helpful in locating and confirming the abscess (Fig. 8.29C). In abscess with pus the blood pool scan shows diffuse tracer stain of a sac formed in the area of the necrotic fascia (Fig. 8.30A). However, such stain is rapidly washed out and replaced by photopenia on the equilibrium scan, suggesting that the stained material is either pus or necrotized tissue (Fig. 8.30B). As shown in this case, concurrent cellulitis is seen as lasting subcutaneous uptake rather than transient tracer stain.

8.3.2 Decubitus Ulcer (Bedsores)

Decubitus ulcers are the breakdown of soft tissue due to prolonged physical pressure in patients kept lying too still for a prolonged period of time. It most commonly occurs in paralyzed patients and the debilitated elderly. Although other sites such as the elbows, heels, and shoulders are involved, the great majority of ulcers develop over the sacrum, ischial tuberosities, and femoral trochanters and buttocks. Local soft-tissue infection and bacteremia are common accompaniments. *Staphylococcus aureus, Proteus mirabilis*, and *Escherichia coli* are the chief offenders. Superficial pressure sores that extend to the dermis but not into the subcutaneous fat layer may progress to deep sores after penetration of the fat layer, spreading to and contaminating the underlying bone (Hendrix et al. 1981). Frequently, a sinus tract is formed that communicates with the skin. The accurate diagnosis of osteitis that complicates pressure sores is difficult because a number of other conditions overlap in immobilized or paralyzed patients.

Radiography reveals pressure-related erosion and sclerosis in the bony prominences such as the femoral trochanters and ischial tuberosities. Generally, however, radiography is insensitive and nonspecific (Hendrix et al. 1981; Sugarman et al. 1983). CT is an excellent means to diagnose both soft-tissue and bone changes (Fig. 8.31A).

Pinhole scintigraphy shows irregular, patchy areas of increased tracer accumulation, deno-

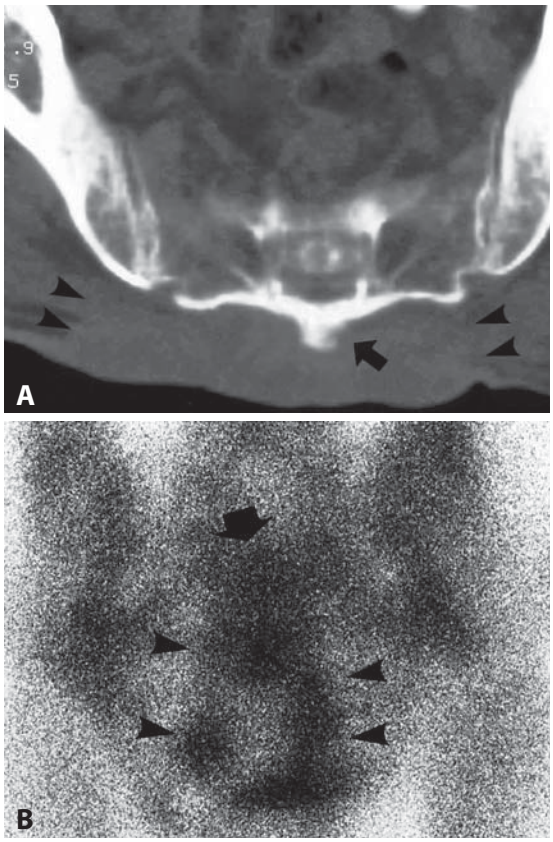

Fig. 8.31A, B Decubitus bone change with reactive sclerosis. **A** CT of the mid-sacrum in a 59-year-old male patient with decubitus ulcer shows diffuse thickening of the soft tissue over the sacrum (*arrowheads*). Local bones are sclerotic (*arrow*). **B** Posterior pinhole scan shows tracer uptake in the contact zone of the sacrum (*arrowheads*) including the spinous process (*arrow*)

ting active osteitis or nonspecific inflammatory reaction related to the overlying soft-tissue infection (Fig. 8.31B). Nonspecific reactive inflammation and actual infection are hard to distinguish, but the fact that tracer uptake tends to be more intense in the latter condition than in the former may be helpful.

References

Bisno AL, Stevens DL (1996) Streptococcal infections of skin and soft tissue. N Engl J Med 334:240–245

Bravo JF, Herman JH, Smith CH (1967) Musculoskeletal disorders after renal homotransplantations. Ann Intern Med 66:87–104

Campbell JB, Hoffman EB (1995) Tuberculosis of the hip in children. J Bone Joint Surg Br 77:319–326

Comin JA, Rodriguez-Merchan EC (1997) Arthroscopic synovectomy in the management of painful localized post-traumatic synovitis of the knee joint. Arthroscopy 13:606–608

Darmstadt GL (2000) The skin. In: Behrman RE, Kliegman RM, Jenson HB (eds) Nelson textbook of pediatrics, 16th edn. WB Saunders, Philadelphia, pp 1965–2054

Enarson DA, Fujii M, Nakielna EM, et al (1979) Bone and joint tuberculosis: a continuing problem. Can Med Assoc J 120:139–145

Evanchick CC, Davis DE, Harrington TM (1986) Tuberculosis of peripheral joints: an often missed diagnosis. J Rheumatol 13:187–189

Goldenberg DL (1983) "Postinfectious" arthritis. New look at an old concept with particular attention to a disseminated gonococcal infection. Am J Med 74:925–928

Gordon G, Kabins SA (1980) Pyogenic sacroiliitis. Am J Med 69:50–56

Hendrix RW, Calenoff L, Lederman RB, Nieman HL (1981) Radiology of pressure sores. Radiology 138:351–356

Huda W, Slone R (1995) Screen/film radiography. In: Review of radiologic physics. Williams & Wilkins, Baltimore, pp 63–78

Huh YM, Suh JS, Lee JW, Song HT (2004) Synovitis and soft tissue impingement of the ankle: assessment with enhanced three-dimensional FSPGR MR imaging. J Magn Reson Imaging 19:108–116

Lee AS, Campbell JA, Hoffman EB (1995) Tuberculosis of the knee in children. J Bone Joint Surg Br 77:313–318

Rosenthall L (1987) The bone scan in arthritis. In: Fogelman I (ed) Bone scanning in clinical practice. Springer, Berlin Heidelberg New York

Spencer JD (1986) Bone and joint infection in a renal unit. J Bone Joint Surg Br 68:489–493

Sugarman B, Hawes S, Musher DM, et al (1983) Osteomyelitis beneath pressure sores. Arch Intern Med 143:683–688

Williams PL, Warwick R, Dyson M, Bannister LH (1989) Gray's anatomy, 37th edn. Churchill Livingstone, Edinburgh London New York

9 Degenerative Joint Diseases

Osteoarthritis Degenerative joint diseases include osteoarthritis, osteoarthrosis, osteochondrosis and others, and are the most common joint disorders that gradually disable patients. These recently receive greater attention because of the unprecedented prolongation of life expectancy and the availability of efficient prosthetic therapy. The terms describing "degenerative joint diseases" are many and used more or less loosely and even interchangeably. Osteoarthritis and osteoarthosis designate degraded states of a synovial joint with and without significant inflammation, respectively. Osteoarthritis is classified into primary or idiopathic and secondary, and inflammatory when there is significant synovial involvement with effusion.

A number of factors have been implicated as causative, but mechanical wearing down of the articular cartilages and supportive structures due to aging and obesity appears most important. According to Mitchel and Cruess (1977), osteoarthritis results from an abnormal concentration of stress across a normal joint or conversely a normal concentration of stress across an abnormal joint with an altered cartilage or subchondral bone. On the other hand, a hereditable element of osteoarthritis has been demonstrated in 50% to 65% in a twin epidemiological study (Cicuttini and Spector 1997) and one most recent study has indicated the existence of vertical transmission of primary osteoarthritis (Spencer et al. 2005).

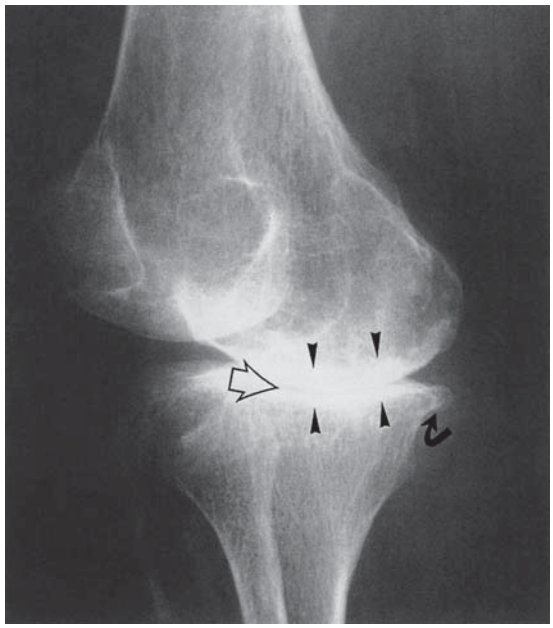

Fig. 9.1 Radiographic manifestations of osteoarthritis. Oblique radiograph of the right knee in a 51-year-old woman shows marked narrowing of the medial femorotibial compartment (*open arrow*) with subchondral eburnation (*arrowheads*) and a marginal osteophyte at the posterior tibial edge (*curved arrow*)

Pathology Osteoarthritis is initiated by either the enzymatic disruption of the cartilaginous matrix or microfractures in the subchondral bone trabeculae that are rendered vulnerable due to the thinning of the covering articular cartilage (Radin et al. 1977). Mild synovitis may develop after the appearance of histological alterations in the cartilage and bone as a result of the removal of the cartilage breakdown products through the synovial interstitium (Howell et al. 1976). Occasional cases show significant inflammation with effusion.

Radiographic Manifestations The radiographic features include: (a) narrowing of the joint space, (b) bone erosion, (c) eburnation in

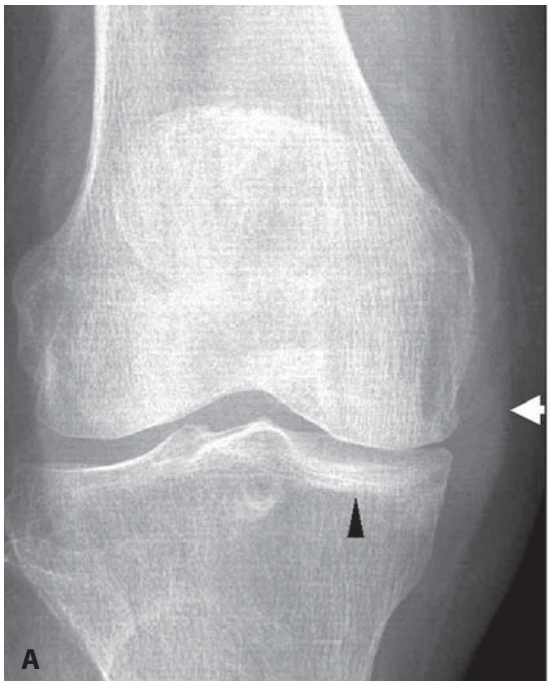

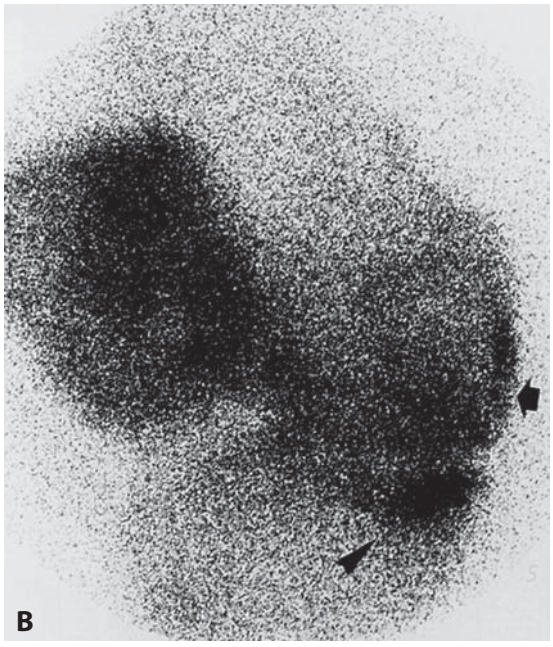

Fig. 9.2A, B Osteoarthritis with local synovitis. **A** Anteroposterior radiograph of the right knee in an 85-year-old female shows a narrowed medial articular compartment with a thickened capsule and collateral ligament (*arrow*) and sclerosis in the medial tibial plateau (*arrowhead*). **B** Anterior pinhole scan shows subchondral bone uptake with a narrowed joint space denoting synovitis with local bone reaction (*arrow*). Note focal sclerosis (*arrowhead*)

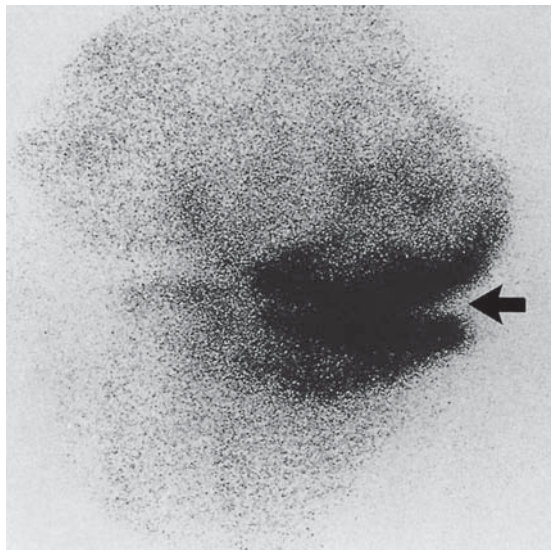

Fig. 9.3 Asymmetrical, discrete, periarticular segmental and spotty tracer uptake with articular narrowing in osteoarthritis in the knee. Anterior pinhole scan of the right knee in the same patient as in Fig. 9.1 shows irregular, asymmetrical, segmental intense tracer uptake in the medial femorotibial compartment and the distal femoral bone end with narrowed articular space (*arrow*)

the contact area, (d) osteophytosis in the noncontact area, and (e) cyst in the subarticular bone (Fig. 9.1). When osteoarthritis is attended by local synovitis that part of the joint becomes blurred with effusion, para-articular soft-tissue thickening, and bulging (Fig. 9.2A). An important differential diagnostic feature of osteoarthritis is that changes are asymmetrical and focal, and occur most typically in the area under stress and pressure. Such areas are in the lateral or medial aspect of the acetabular roof in the hip and in the medial, patellofemoral, or less frequently the lateral compartment, in the knee. Degeneration may occur both in the synovial and nonsynovial joints. The knee, the hip, the acromioclavicular joint, and the phalangeal joints belong to the former and the diskovertebral joints, the manubriosternal joints, and the symphysis pubis belong to the latter. The apophyseal and costovertebral joints of the spine are well-known seats of osteoarthritis.

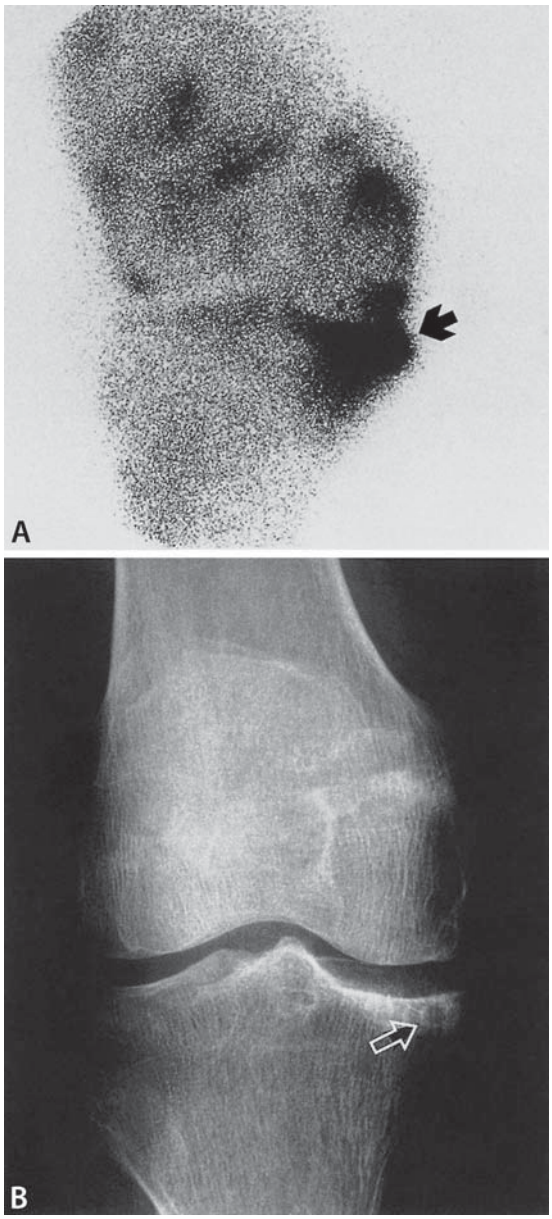

Fig. 9.4A, B Intense intraosseous tracer uptake in the cystic change of osteoarthritis. **A** Minimally rotated anterior pinhole scan of the right knee in a 74-year-old woman shows an extremely intense, triangular tracer uptake deep in the trabecular bone of the medial tibial condyle surrounded by less intense uptake (*arrow*). The joint is preserved and other asymmetrical, patchy tracer uptake can be seen in the femoral condyles. **B** Anteroposterior radiograph shows a small subcortical cyst and sclerosis in the medial tibial condyle (*arrow*)

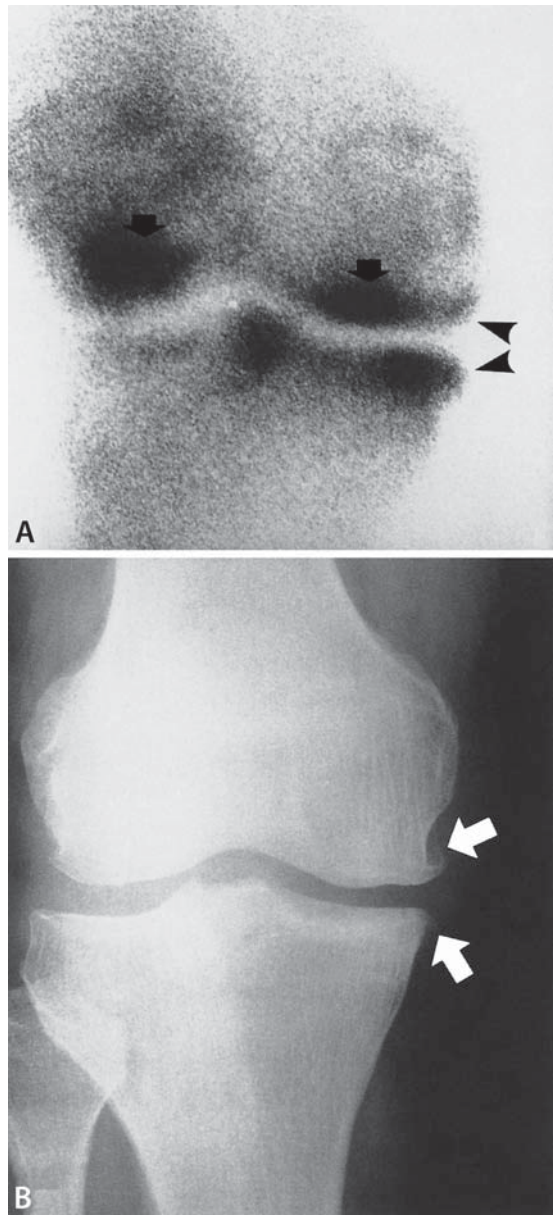

Fig. 9.5A, B Osteophytes in nonstress, marginal areas with little tracer uptake. **A** Anterior pinhole scintigraph of the right knee in a 72-year-old man shows insignificant tracer uptake in the osteophytes in the medial aspects (*arrowheads*). In contrast very intense uptake is seen in the articular surfaces of femoral condyles, medial plateau and tibial tubercle, all of which are radiographically unremarkable (*arrows*). These denote preradiographic change. **B** Anteroposterior radiograph shows mature osteophytes in medial aspect of the knee (*arrows*). Note that periarticular bones are normal despite very intense tracer uptake

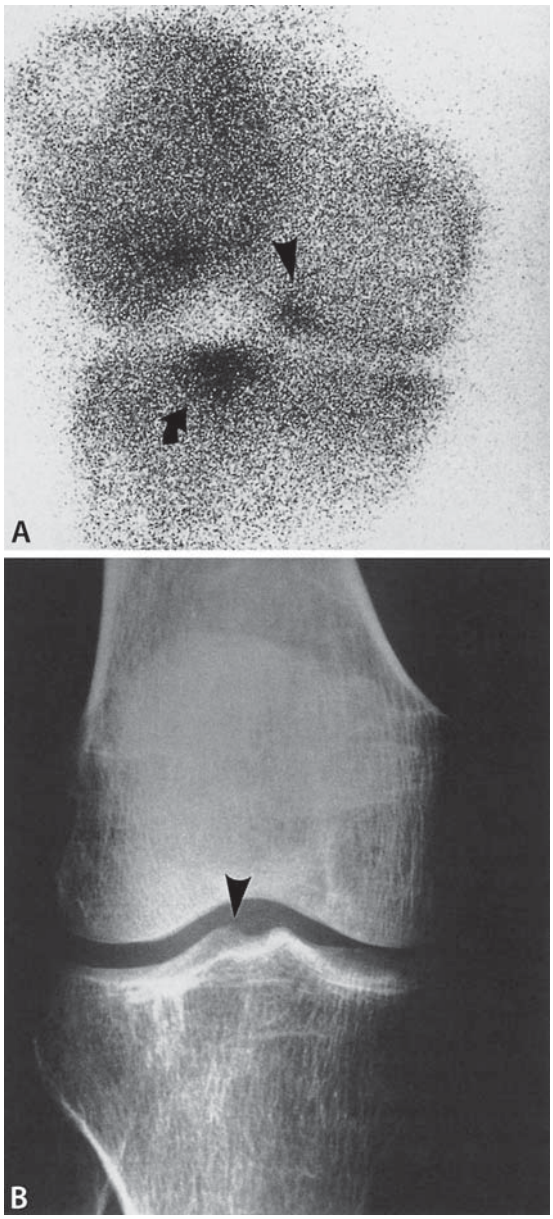

Fig. 9.6A, B Preradiographic manifestation of osteoarthritis and incipient osteophyte. **A** Slightly rotated pinhole scintigraph of the right knee in a 61-year-old woman with pain shows indeed subtle tracer uptake in the lateral aspect of the medial femoral condyle (*arrowhead*) and also in the lateral tibial tubercle (*arrow*). The medial femorotibial compartment is narrowed. **B** Anteroposterior radiograph appears normal, except for questionable pointing of the tip of the lateral tibial tubercle (*arrowhead*). The pointing may not have drawn enough attention if it had not been for the scan abnormality

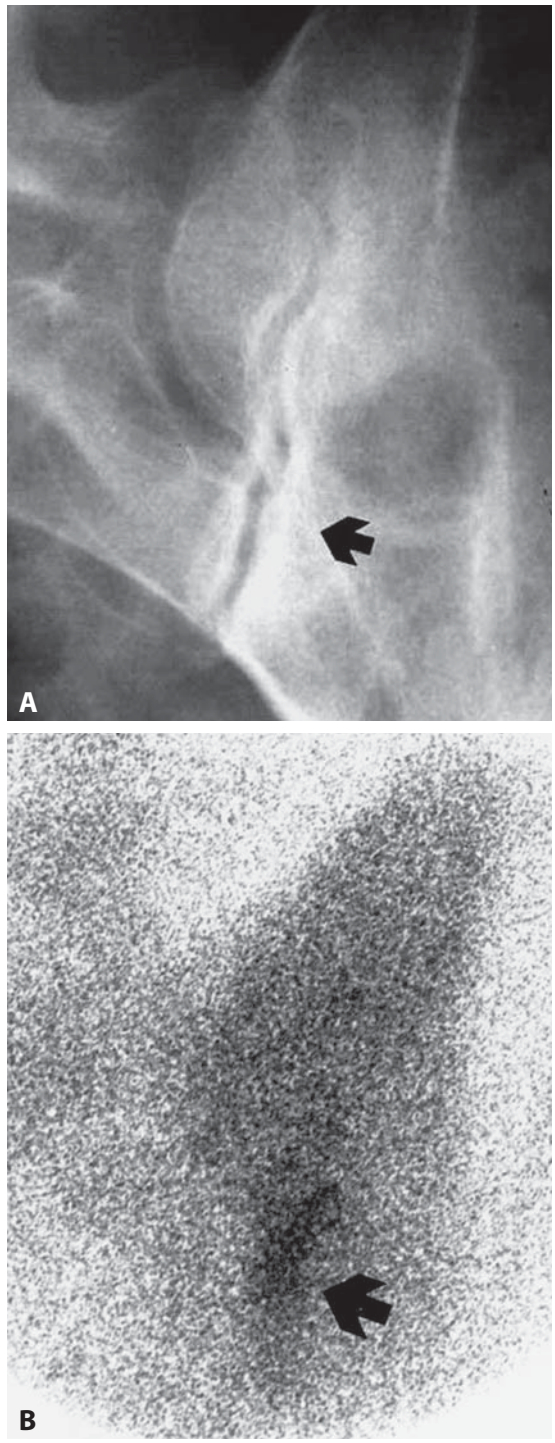

Fig. 9.7A, B Osteoarthritis in the sacroiliac joint. **A** Anteroposterior radiograph of the left sacroiliac joint in a 33-year-old male shows paraarticular sclerosis in the lower compartment (*arrow*). Note that sclerosis is more prominent on the iliac side than on the sacral side. **B** Anterior pinhole scan shows tracer uptake to be more intense in the iliac bone (*arrow*)

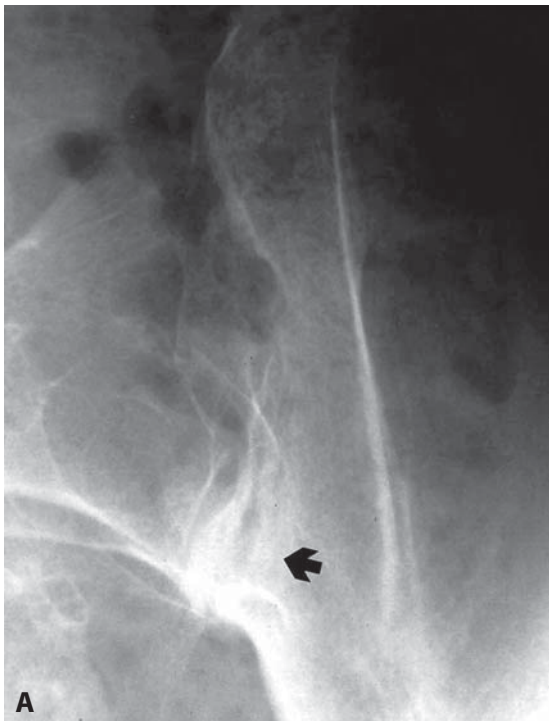

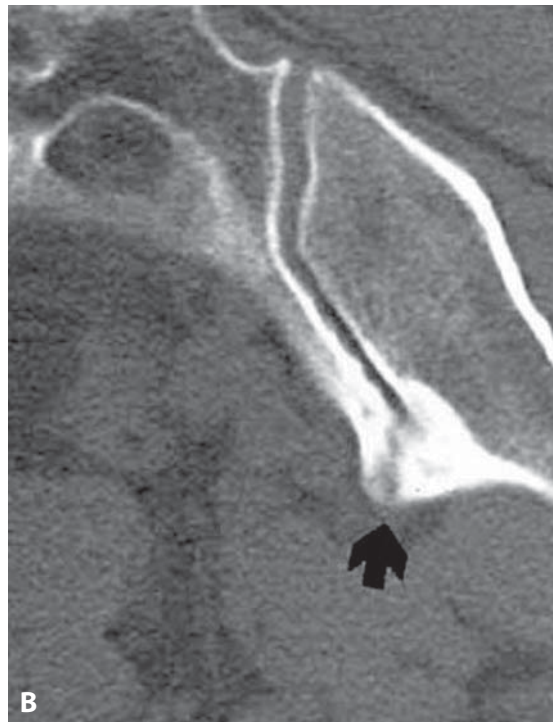

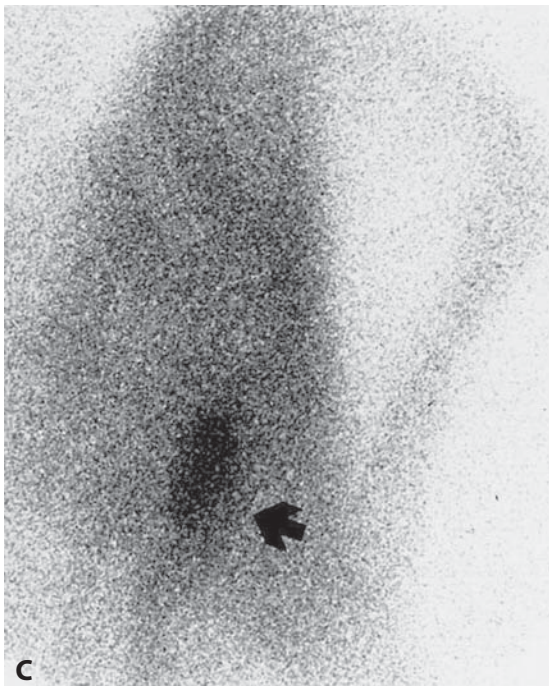

Fig. 9.8A–C Osteoarthritis in the sacroiliac joint with osteophytosis. **A** Anteroposterior radiograph of the left sacroiliac joint in a 49-year-old female shows sclerosis and articular obliteration in the lower articular compartment (*arrow*). **B** CT demonstrates anteriorly protruding hyperostosis with more prominent change occurring in the ilium (*arrow*). **C** Anterior pinhole scan shows tracer uptake in osteophytosis (*arrow*)

Pinhole Scintigraphic Manifestations Pinhole scan features include focal articular narrowing, segmental or patchy uptake, and malalignment or deformity (Fig. 9.3). Tracer uptake appears to closely correlate with cortical erosion, eburnation, and subchondral cystic change. It is to be noted that the cystic change in the cancellous bone beneath the cortex accumulates tracer more intensely than in eburnation or mature osteophytes (Fig. 9.4). On the other hand, the mature osteophytes found in the marginal, nonstress area of a joint accumulate tracer only minimally, indicating that they are metabolically inert (Fig. 9.5). Pinhole scintigraphy can often show area(s) of very subtle uptake in a painful yet radiographically normal joint (Fig. 9.6). Many such lesions are not visualized on ordinary scintigraphs.

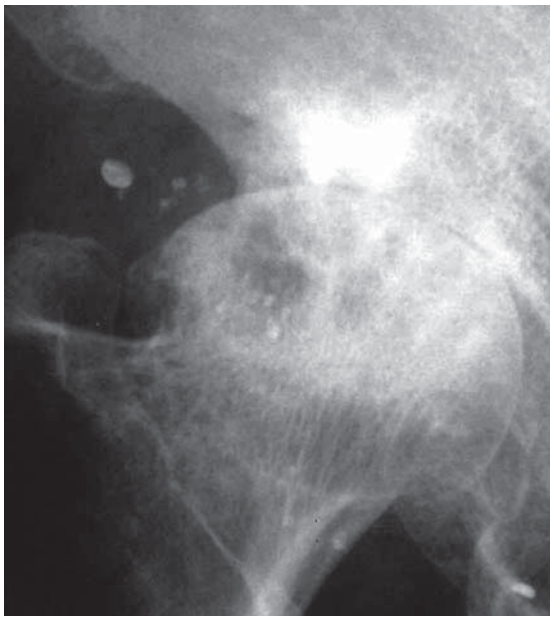

Fig. 9.9 Advanced osteoarthritis in the hip joint. Anteroposterior radiograph of the right hip in a 73-year-old female with longstanding arthritis shows articular narrowing, sclerosis, osteophytosis, subchondral cystic change, and osseous ankylosis (same patient as in Fig. 9.11)

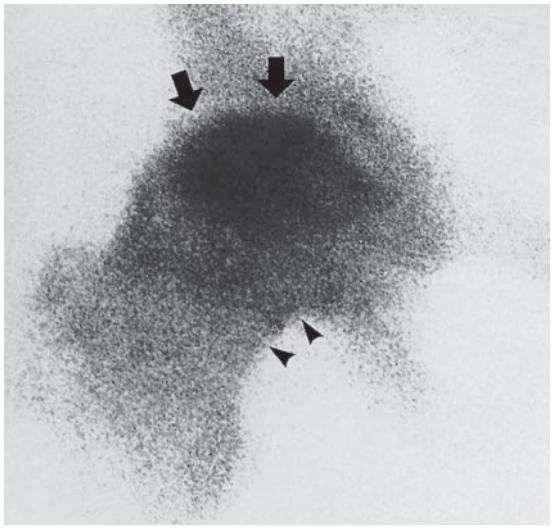

Fig. 9.10 Eccentric tracer uptake in the uppermost aspect of the femoral head in osteoarthritis. Anterior pinhole scintigraph of the right hip in a 62-year-old woman with advanced osteoarthritis shows intense tracer uptake localized eccentrically in the uppermost part of the femoral head (*arrows*) with narrowed joint. Modest tracer uptake can be seen also in the medial aspect of the neck, denoting buttress (*arrowheads*). The acetabulum shows little alteration. All these findings were validated by radiography (not shown here)

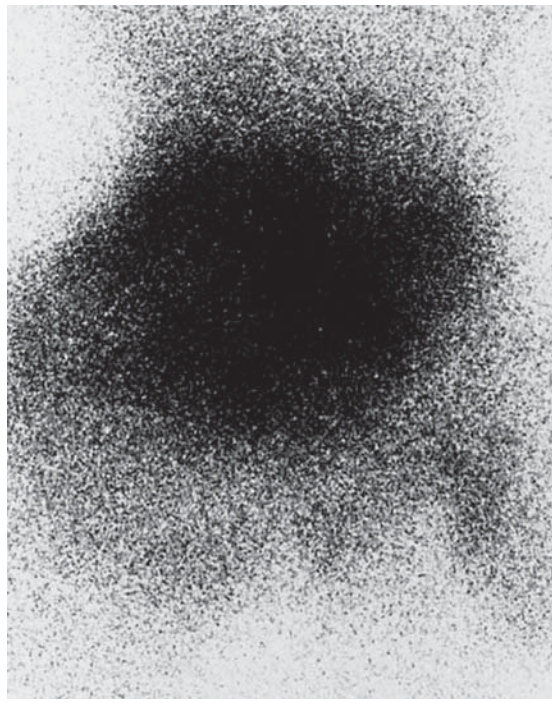

Fig. 9.11 Anterior pinhole scan of the right hip joint shows diffusely increased tracer uptake with dominant uptake involving the femoral head with extinct joint space due to ankylosis (same patient as in Fig. 9.9).

9.1 Sacroiliac Joint

This is the articulation between the sacral and iliac auricular surfaces that are reciprocally curved and roughened or sinuous. This curvature and roughness restricts joint movements and biomechanically contributes to the stability and strength of the joint so that it can efficiently transmit weight from the spine to the lower limbs. The articulation is divided into two parts: (1) the synovial joint in the anteroinferior half or two-thirds, and (2) the ligamentous (fibrous) joint in the remaining posterosuperior part (Brower 1988). The iliac surface is covered by thin hyaline cartilage (1 mm) and the iliac surface by thick fibrous cartilage (3–5 mm). The thinness of the cartilage in the iliac side explains why the disease

involves this side first and the sacral side next. The degenerative changes of the sacroiliac joint may develop before the age of 30 years and become prominent after middle age. Pathological sequences are cartilage fibrillation, erosion, necrosis, and denudation followed by fibrous ankylosis. Bony eburnation and osteophytosis are common findings of the disease in the late stage. The involvement may be either unilateral or bilateral.

Radiographic manifestations include irregular cortical erosion, subchondral sclerosis, articular narrowing, and osteophytosis (Fig. 9.7A). In general articular narrowing is not a prominent feature in the sacroiliac joint, and osteophytosis typically occurs in the lower anterior aspect of the joint with beaking. CT is extremely helpful in the analysis of all these features (Fig. 9.8B)

Pinhole scintigraphy demonstrates increased tracer uptake that is localized to the lower aspect of the joint in the early stages (Figs. 9.7B and 9.8C). Radiographic correlation reveals the uptake to specifically occur in the sclerotic bone that is in the iliac edge.

9.2 Hip

The hip is a ball-and-socket joint that permits multiaxial movement. It is surrounded by a dense, strong, fibrous capsule. Along with the knee, the hip joint is the most typical site of osteoarthritis. Clinical symptoms are rotation or extension difficulty and pain that may be referred to the buttock, thigh, groin, greater trochanteric region, and knee.

The radiographic features, as in all other joints, include articular narrowing, osteosclerosis, osteophytosis, subchondral cystic change, and ankylosis (Fig. 9.9). Rarely, osteochondral or loose bodies may be present. The articular narrowing is accompanied by asymmetrical migration of the femoral head with respect to the acetabulum. On anterior radiographs the migration is mostly superolateral or superome-

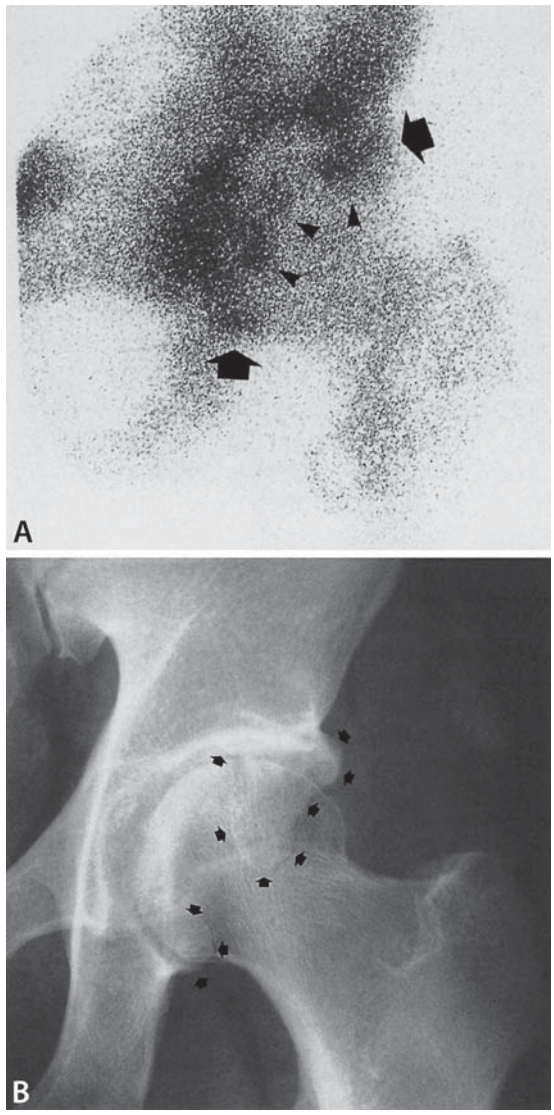

Fig. 9.12A, B Scintigraphic demonstration of the marginal osteophytes in osteoarthritis in the hip. **A** Anterior pinhole scintigraph of the left hip in a 33-year-old man with osteoarthritis secondary to dislocation reveals several beaded areas of increased tracer uptake along the acetabular brim as well as an eccentric, patchy uptake in the medial edge (*lower arrow*). Beaded lesions represent stalactic osteophytes; those at the lateral and medial edges are imaged in profile (*arrows*) and those at the anterior and posterior edges en face (*arrowheads*). The eccentricity of the patchy tracer uptake is characteristic of osteoarthritis. **B** Anteroposterior radiograph shows the stalactic bony excrescences along the acetabular brim (*arrows*)

dial, and infrequently axial or central. The finding contrasts with the concentric migration of the femoral head in infective arthritis (Fig 8.12) and rheumatoid arthritis (see Chap. 10).

Ordinary scintigraphy may show marked tracer uptake in the affected hip without topographic detail. In contrast, pinhole scintigraphy shows tracer uptake that is eccentric in location either in the uppermost (Fig. 9.10) or innermost aspect of the acetabulum, reflecting cranial or medial migration, respectively. On occasion, moderate uptake may also be observed in the medial aspect of the femoral neck due to buttressing (Fig. 9.10). It is important to note that the tracer uptake in the acetabular side of the joint is usually less intense than that in the femoral head unless the disease is advanced. The joint space becomes extinct when sealed by ankylosis (Fig. 9.11). Osteophytes may be indicated by ovoid tracer uptake hanging from the acetabulum like a necklace (Fig. 9.12). As mentioned above, differentiation from pyogenic arthritis or rheumatoid arthritis is possible by noting concentric narrowing of the joint space in these conditions. As elsewhere, the preradiographic or early change can be indicated by subtle uptake in the femoral head. The sign is reliable especially when it is eccentric in location. Frequently, such a small uptake may pass undetected on ordinary scintigraphs.

9.3 Knee

The knee is the most common site of osteoarthritis. The anatomy of the knee is compound, having two condylar joints between the femur and tibia, and the sellar joint between the patella and femur. The joint is provided internally with the menisci and the cruciate ligaments and externally with the bursae above, in front of, and below the patella. The causes for osteoarthritis in the femorotibial compartment (knee) and the patellofemoral compartment (patella) are many and varied. For example,

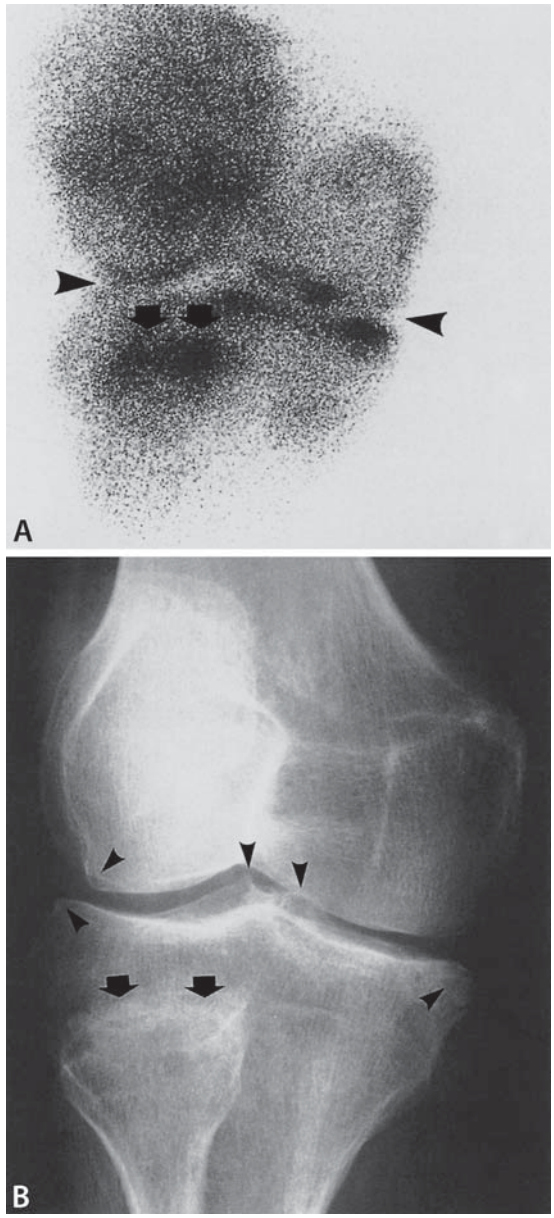

Fig. 9.13A, B Multicompartmental involvement in osteoarthritis in the knee. **A** Anterior pinhole scan of the right knee in a 35-year-old man shows multiple, asymmetrical areas of segmental, spotty, and patchy tracer uptake in the femorotibial compartments including the tibial tubercles and the proximal tibiofibular joint (*arrows*) with narrowed articular space (*arrowheads*). **B** Anteroposterior radiograph reveals minimal marginal osteophytes (*arrowheads*), the pointing of the tibial tubercles (*middle arrowheads*), and the narrowing of the joint. The proximal tibiofibular joint also shows periarticular sclerosis and articular obliteration (*arrows*)

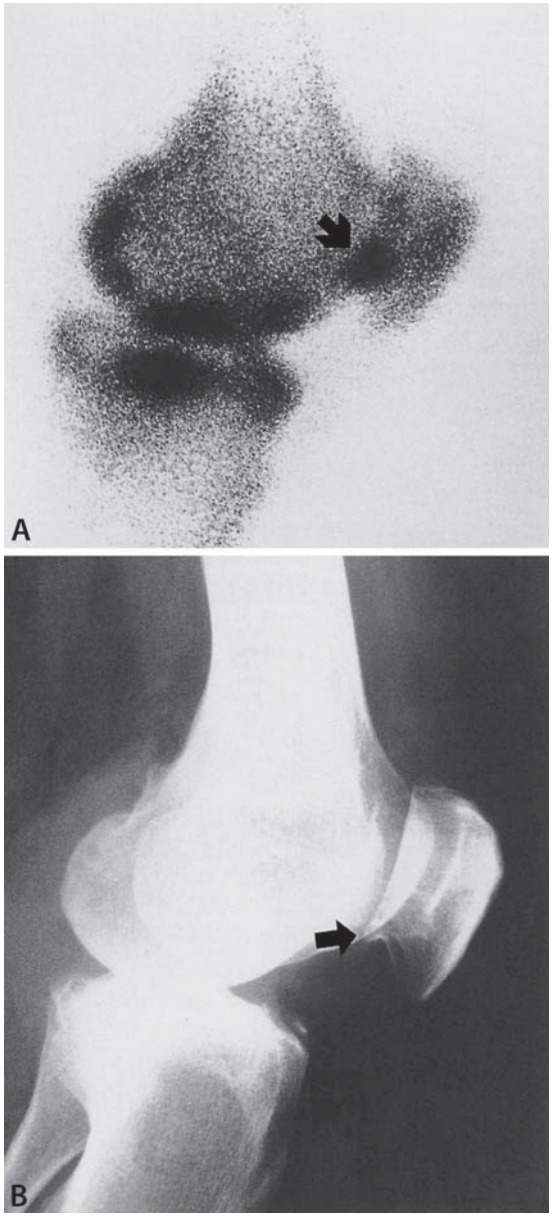

Fig. 9.14A, B Patellar involvement in osteoarthritis. **A** Medial pinhole scintigraph of the left knee in a 61-year-old woman shows a spotty "hot" area in the inferoposterior aspect of the patella (*arrow*) with associated spotty intense tracer uptake in the other periarticular bones. **B** Mediolateral radiograph demonstrates a small osteophyte in the inferoposterior aspect of the patella (*arrow*) and suspicious erosion in the apposing femoral cortex

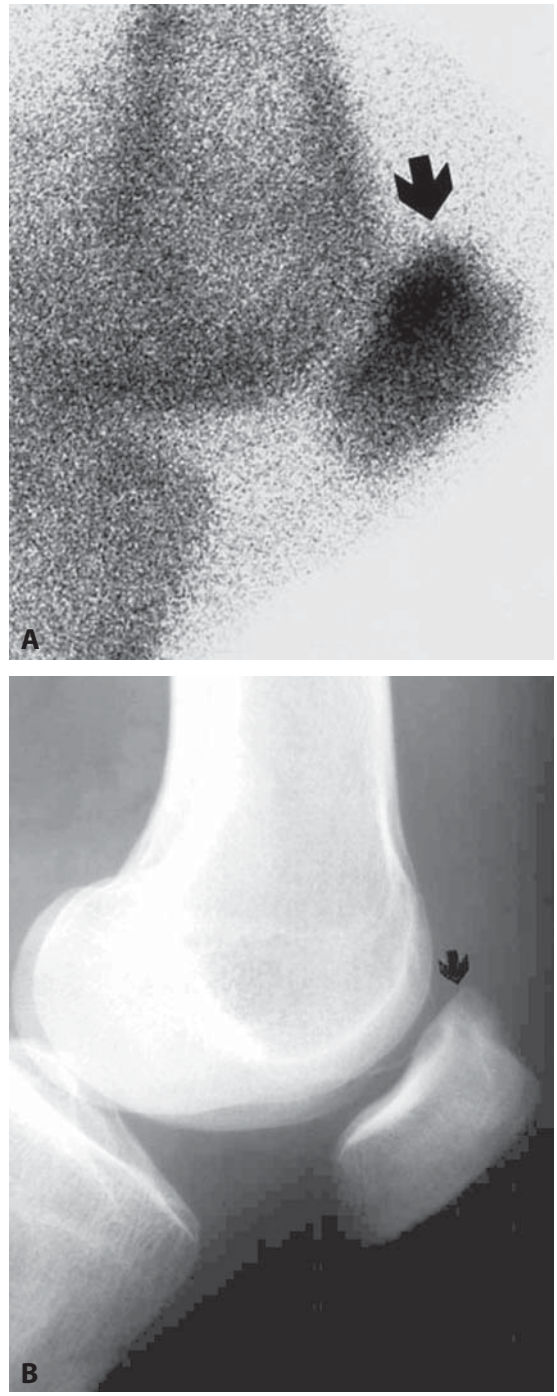

Fig. 9.15A, B Patellar osteoarthritis. **A** Lateral pinhole scan of the right patella in a 63-year-old male shows increased tracer uptake localized to the upper edge of the retropatellar facet (*arrow*). **B** Lateral radiograph reveals a small spur with sclerosis (*arrow*)

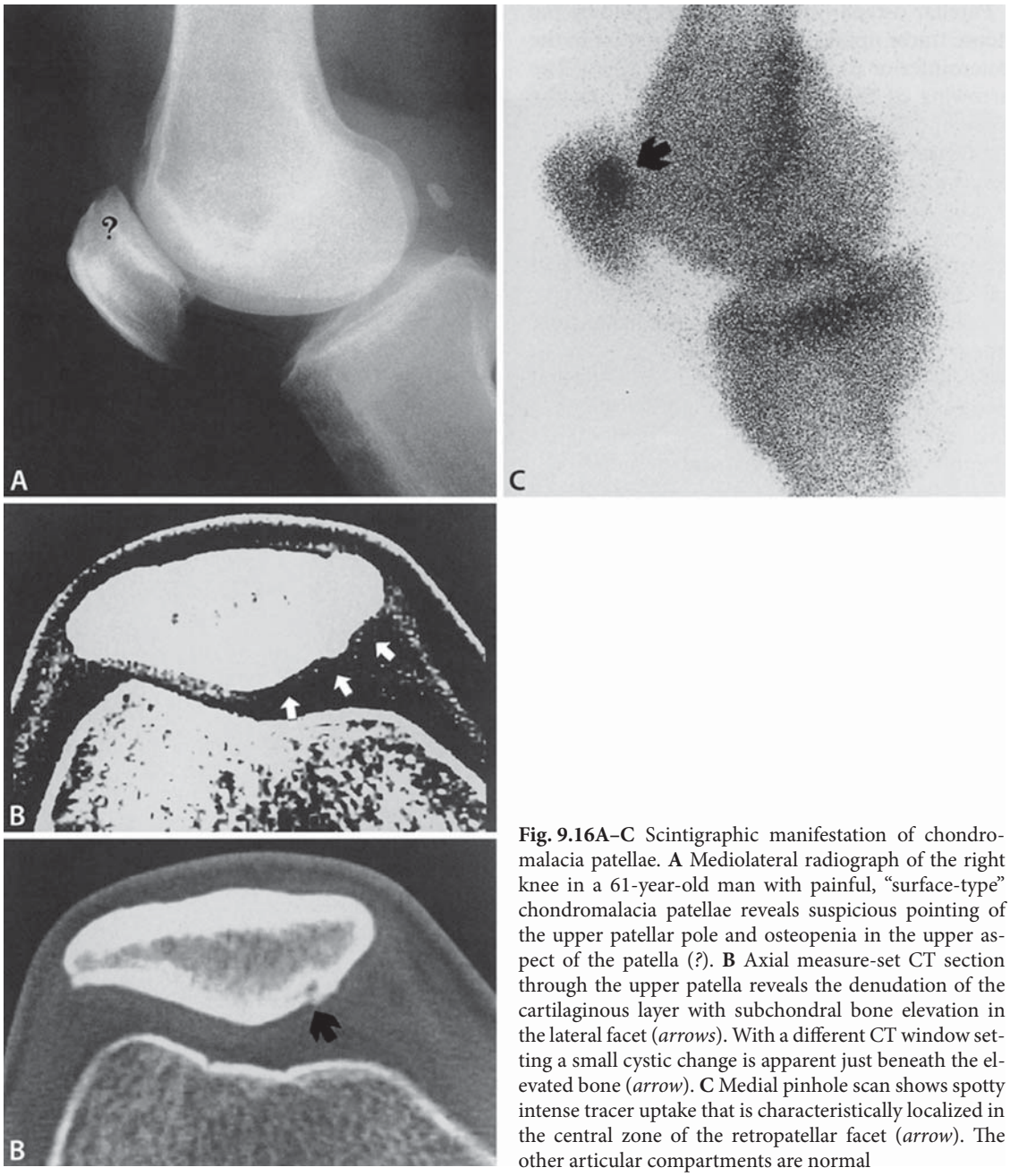

Fig. 9.16A–C Scintigraphic manifestation of chondromalacia patellae. **A** Mediolateral radiograph of the right knee in a 61-year-old man with painful, "surface-type" chondromalacia patellae reveals suspicious pointing of the upper patellar pole and osteopenia in the upper aspect of the patella (*?*). **B** Axial measure-set CT section through the upper patella reveals the denudation of the cartilaginous layer with subchondral bone elevation in the lateral facet (*arrows*). With a different CT window setting a small cystic change is apparent just beneath the elevated bone (*arrow*). **C** Medial pinhole scan shows spotty intense tracer uptake that is characteristically localized in the central zone of the retropatellar facet (*arrow*). The other articular compartments are normal

femorotibial osteoarthritis has been related to trauma, meniscus surgery, osteonecrosis, deformity and obesity, and femoropatellar osteoarthritis to trauma, deformity and chondromalacia patellae (Bahk et al. 1994; Resnick 2002). Symptoms may be surprisingly lacking during the early stage despite the presence of radiographic spurs or scintigraphic change, or conversely pain and limited motion may antedate the appearance of the radiographic or scintigraphic abnormality. Sooner or later, however, instability, awkward gait, limb deformity and subluxation may ensue with severe disablement. Radiographic features include articular narrowing of various grades, subchondral osteosclerosis, eburnation, cystic change, and

periarticular osteophytosis or spur formation. When acute synovitis supervenes the para-articular soft tissue becomes bulged due to effusion and synovial edema, and it occurs typically in the medial femorotibial compartment (Fig. 9.2A). Occasionally, vacuum shadow and loose bodies may be seen. Except for marginal spurs, most changes occur in the contact joint surfaces. In advanced cases, the joint becomes subluxed and sealed due to osseous ankylosis.

Pinhole scintigraphy in the earliest stage of osteoarthritis demonstrates spotty "hot" area(s) in the subchondral zones of the femorotibial compartment that is in close contact and weight bearing (Fig. 9.6). The degree of uptake varies widely from subtle to extreme, and the appearance may be spotty, mottled, patchy, or segmental. Tracer uptake and radiographic changes do not necessarily match each other, and a hot area may be seen where there is no radiographic change (Fig. 9.6). As the disease progresses focal uptake appears in the eburnation and spurs formed in the tibial plateaus, femoral condylar undersurfaces, and tibial tubercles (Fig. 9.13). The uptake is discrete and asymmetrical, mainly involving the medial and central femorotibial compartments (Figs. 9.4–9.6). When cystic change supervenes, uptake becomes markedly intensified. Cystic change is commonly observed in the medial tibial condylar edge, giving rise to the "hot edge" sign (Fig. 9.4). In occasional cases the whole knee joint compartments including the medial and lateral femorotibial compartments, the proximal tibiofibular compartment, and the patellofemoral compartment are involved (Fig. 9.13). The involvement of the tibial tubercles is indicated by uptake localized in the central elevation of the tibial head (Fig. 9.13).

In summary, unlike in infective arthritis and rheumatoid arthritis, the lesions in osteoarthritis are discrete and the joint is not completely affected. When acute synovitis supervenes uptake becomes diffuse, but is still confined to one side of the knee, more commonly the medial side. Subchondral cysts accumulate tracer most intensely, presenting the "hotter spot within hot area" sign. In contrast, mature osteophytes accumulate little or no tracer. Their location in the nonstress area keeps metabolism as inert and stable as that in the normal long bones (Fig. 9.5).

9.4 Patella

The patella, the largest sesamoid bone, is situated anterior to the knee. It is buried cranially in the rectus femoris muscle tendon and caudally in the infrapatellar tendon. The convex anterior surface, subcutaneous with a bursa between, is roughened to permit tendinous attachment, and the posterior or retropatellar facet is provided with a smooth articular surface divided by a vertical ridge. Along with the knee proper, the retropatellar facet is a notorious site of degenerative diseases including osteoarthritis and chondromalacia.

9.4.1 Patellar (Femoropatellar) Osteoarthritis

Patellar osteoarthritis is characterized by tracer uptake at the lower or upper edge of the retropatellar facet (Figs. 9.14 and 9.15). The narrowing of the patellofemoral joint and increased uptake in other articular compartments of the knee are important diagnostic features of osteoarthritis. Due to altered locomotion, osteoarthritis in genu valgum and genu varus tends to occur in the lateral and medial femorotibial compartment, respectively, whereas osteoarthritis in flexion deformity is prone to affect the posterior compartment. As discussed below chondromalacia patellae is not osteoarthritis in the strict sense, and, hence, usually not accompanied by osteoarthritis in other parts of the knee (Fig. 9.16).

9.4.2 Chondromalacia Patellae

Chondromalacia of the patella is a condition characterized by a series of degenerative changes that involve the cartilage and subchondral bone in the retropatellar facet. Clinically, two different types have been described on the basis

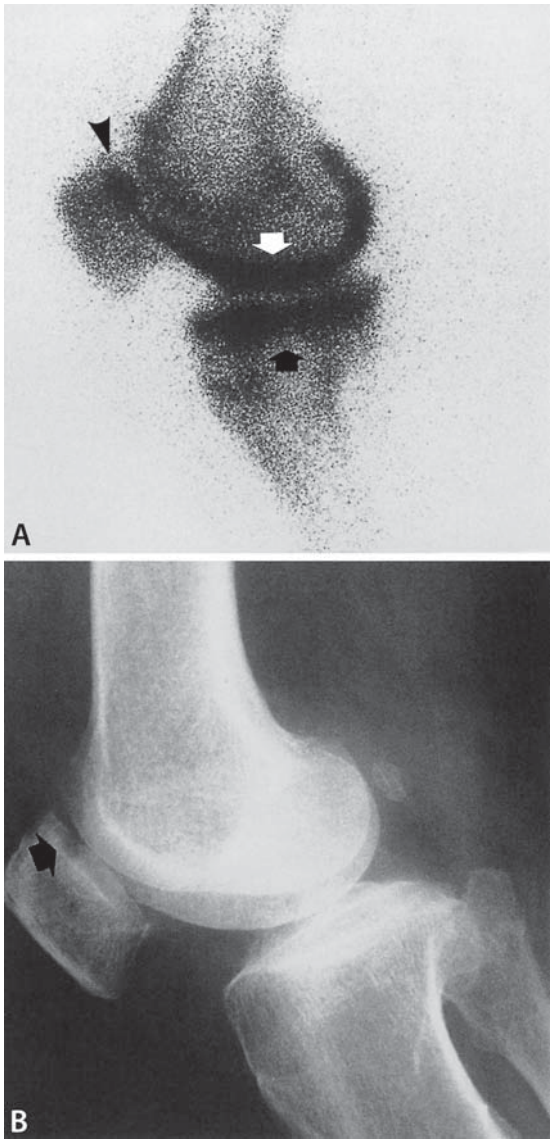

Fig. 9.17A, B Chondromalacia patellae associated with osteoarthritis. **A** Medial pinhole scan of the right knee in a 70-year-old woman shows spotty intense tracer uptake typically localized in the upper posterior aspect of the patella surrounded by less intense uptake (*arrowhead*). The patellofemoral and lateral femorotibial compartments accumulate tracer diffusely, designating associated osteoarthritis (*arrows*). **B** Mediolateral radiograph shows a small cystic change in the upper posterior aspect of the patella (*arrow*) and diffuse periarticular sclerosis in the patellofemoral and femorotibial compartments. CT scan confirmed roughened cartilage with subchondral cysts (not shown here)

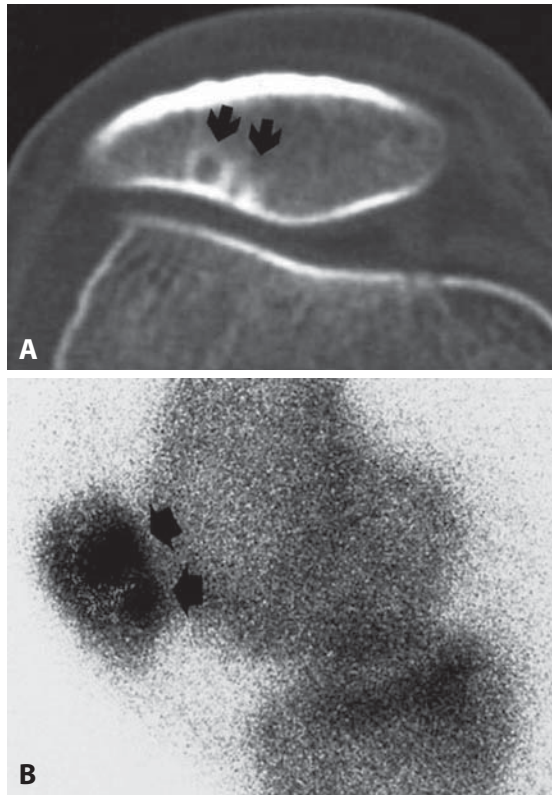

Fig. 9.18A, B Bone scintigraphic sign of chondromalacia patellae. **A** CT of the left patella in a 63-year-old male shows a small sharply defined subchondral cyst with sclerosis in the medial retropatellar facet (*arrow*). **B** Lateral pinhole scan reveals two spotty "hot" areas (*arrows*)

of the age and symptom. The first type, which is traditionally referred to as chondromalacia patellae, manifests as pain and crepitus over the patella in young adults and adolescents. The second type is a disease of older age. It is not necessarily associated with osteoarthritis in the femoropatellar joint.

Pathologically, in the initial stage the cartilage on the retropatellar facet undergoes softening and swelling, in the second and third stages fissuring and fibrillation with a "crab meat" appearance, and in the final stage thinning and ulceration. As a result, the subchondral bone becomes exposed (Wiles et al. 1956). According to Goodfellow et al. (1976), the changes in the

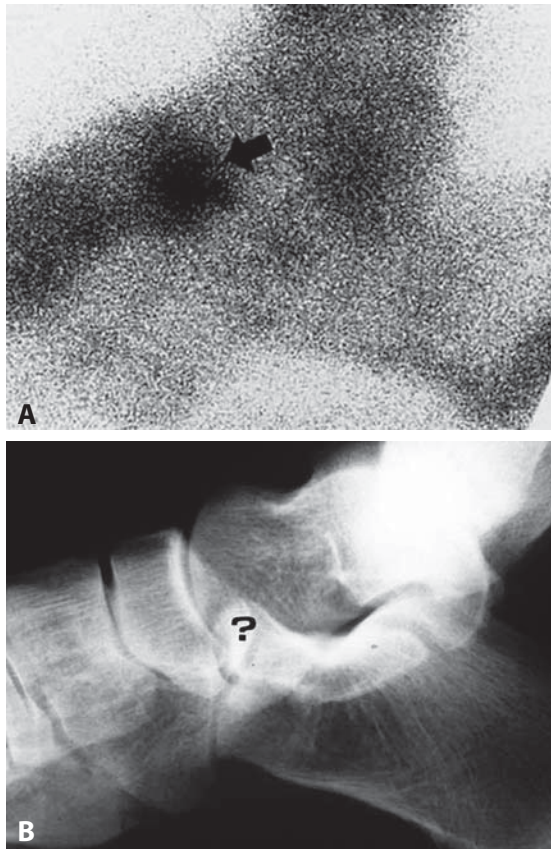

Fig. 9.19A, B Preradiographic manifestation of talar osteoarthritis. **A** Lateral pinhole scan of painful right ankle in a 31-year-old female shows spotty uptake in the anterior subtalar joint (*arrow*). **B** Lateral radiograph shows no abnormality (*?*)

articular cartilage of the patella may be categorized as the surface type or the basal type. The former is age-dependent, and its incidence increases precipitously with age, predisposing to osteoarthritis in later years, and the latter is a disease of young adults with more or less self-limited symptoms and clinical course.

Conventional radiography is of limited value in diagnosing this condition (Lund and Nilsson 1980), but arthrography and CT and MRI play a decisive role. Occasionally, simple radiography may reveal focal osteopenia in the retropatellar facet with or without subchondral bone changes (Figs. 9.16A and 9.17B). CT may reveal the roughening, thinning, or denudation of cartilage (Fig. 9.16B) and cystic change (Fig. 9.18A) in the subchondral bone. Concomitant degenerative change may occur, although this is not essential.

Scintigraphy reveals abnormal tracer uptake in 54% of patients with patellar pain (Dye and Boll 1986). Pinhole scintigraphy can reveal a specific sign (Bahk et al. 1994). This consists of small "hot" spotty uptake localized to the central retropatellar facet, denoting cartilage aberration and cystic change (Figs. 9.16C and 9.18B). Less intense reactive uptake may be present in the remaining patella. In the classic cases no associated lesions are present in other parts of the affected knee. The chondromalacia patellae associated with osteoarthritis can be readily recognized as such by pinhole scanning because, in addition to the characteristic retropatellar uptake, accompanying changes appear in the other articular compartments of the knee (Fig. 9.17A). Occasionally, the lesion may be doubled (Fig. 9.18). For differential diagnosis it is to be pointed out that osteoarthritis of the patella characteristically involves the lower or upper edge of the retropatellar facet with small osteophytosis (Figs. 9.14 and 9.15).

9.5 Ankle and Tarsal Joints

The ankle (talocrural joint) is uniaxial articulation between the lower tibial end together with the medial and lateral melleoli and the trochlear surface of the talus. Beneath the talus are the anterior, middle, and posterior subtalar joints and the talonavicular joint in front. The ankle is not a common site of osteoarthritis, and when involved it is usually the consequence of a significant trauma or the cumulative effects of repeated minor physical insults. In most cases, the talocrural joint and the subtalar and talonavicular joints are involved.

Radiographic manifestations of osteoarthritis of the ankle are inconspicuous in the early stage. As in any joint. However, established osteoarthritis manifests as articular narrowing,

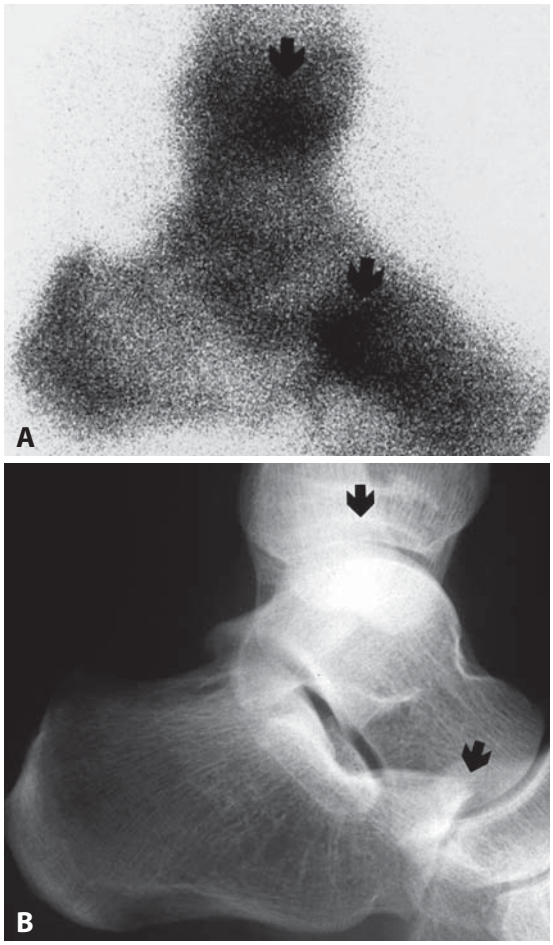

Fig. 9.20A, B Talocrural joint involvement in slightly advanced talar osteoarthritis. **A** Lateral pinhole scan of the left ankle in a 21-year-old male shows patchy areas of increased uptake in the anterior subtalar joint (*lower arrow*) and the talocrural joint (*upper arrow*). **B** Lateral radiograph demonstrates sclerosis in the anterior articular surface of the calcaneus (*lower arrow*) and talocrural articular narrowing and sclerosis (*upper arrow*)

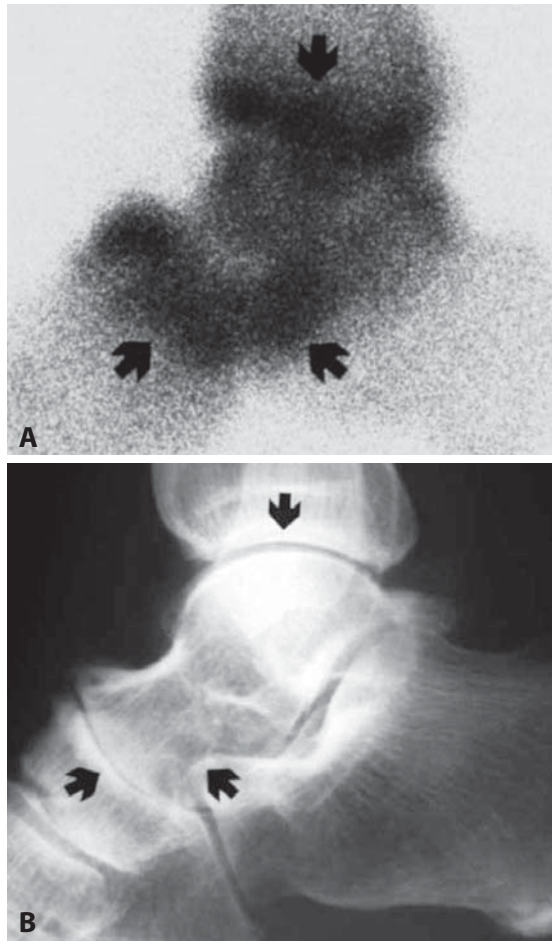

Fig. 9.21A, B Advanced talar osteoarthritis. **A** Lateral pinhole scan of the right ankle in a 36-year-old female shows diffuse tracer uptake in the subtalar and talonavicular joints (*lower arrows*) as well as the talocrural joint (*upper arrow*). **B** Lateral radiograph demonstrates sclerosis with marked articular narrowing (*arrows*)

subchondral sclerosis, and osteophytosis. Our limited observation has indicated that the change starts in the anterior subtalar joint followed by involvement of the talocrural joint, the middle and posterior subtalar joints, and the talonavicular joint seemingly in sequence.

The earliest change of talar osteoarthritis appears to start from the anterior subtalar joint of a painful ankle as a focal, spotty "hot" area (Fig. 9.19). Not infrequently, such a "hot" area is seen in the absence of radiographic change. As the disease progresses the talocrural joint becomes involved (Fig. 9.20) and then the subtalar and talonavicular joints (Fig. 9.21). The initial involvement of the anterior subtalar and talocrural joints is presumably related to the fact that these joints are constantly subjected to great stress and strain.

9.6 Shoulder

The shoulder has two articulations: the acromioclavicular joint and the glenohumeral joint. The former is a synovial joint formed between the medial acromial margin and the lateral clavicular end that are covered with fibrocartilage. It is completely surrounded by the fibrous capsule and provided with an articular disk in the upper part or rarely in the entire joint (de Palma 1957). The latter is a multiaxial joint formed between the roughly hemispherical humeral head and the shallow glenoid fossa of the scapula, possessing motion freedom but an insecure structure. The joint is deepened with the fibrocartilaginous rim, the glenoid labrum.

9.6.1 Acromioclavicular Joint

Degenerative change of this joint is primarily related to aging. The disease may start as early as the second decade of life, becoming severe by the fifth decade (de Palma 1957). The disease causes discomfort or pain that may be aggravated by motion, radiating to the upper arm.

Radiography in the early stage shows mild cortical thickening and subcortical osteopenia in the para-articular bones, giving rise to a pencil-line appearance and apparent articular widening (Fig. 9.22A). With the progress of pathological change the articulation becomes narrowed with prominent osteopenia (Fig. 9.23A). The articular change appears to be more prominent in the clavicular side than in the acromial side, and it is indeed peculiar to note that the acromion remains insignificantly affected on radiographs although tracer uptake is intense.

The pinhole scintigraphic findings are the mirror image of the radiographic findings with additional information on altered bone metabolism, featuring varied para-articular uptake and articular obliteration. The extent and intensity of tracer uptake appear to vary according to the severity of degenerative change and arthritic activity. Uptake is mild to moderate and predominantly localized to the clavicular end in the early phase when the articular space is relatively preserved (Fig. 9.22B). However, in the active chronic phase with advanced articular narrowing uptake becomes markedly intensified and spreads to the acromion with articular obliteration (Fig. 9.23B). Thus, pinhole scintigraphic analysis shows that degenerative arthritis in the acromioclavicular joint characteristically starts from the clavicular end, at least as far as bone metabolic change is concerned. On occasion, osteophytes are shown by increased tracer uptake. Increased uptake in acromioclavicular osteoarthritis is usually unilateral, and the side involved is related to the side of the hand used most.

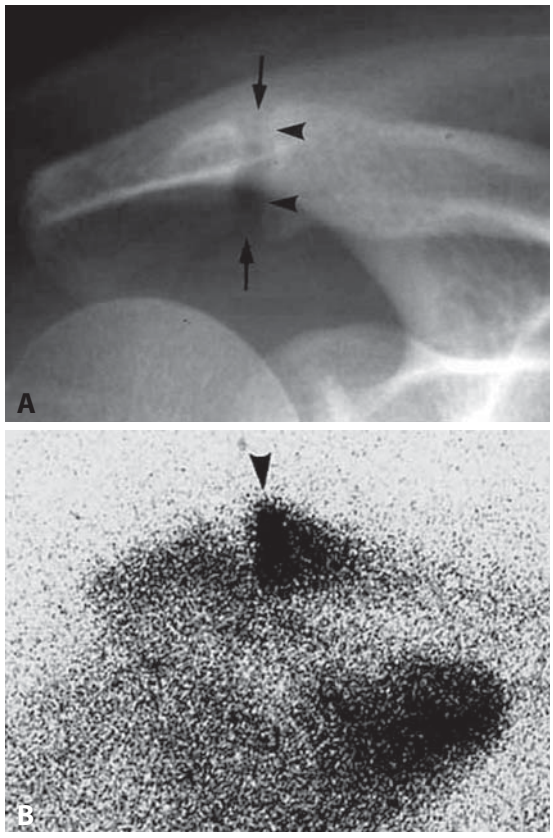

Fig. 9.22A, B Early acromioclavicular osteoarthritis. **A** Anteroposterior radiograph of a painful right shoulder in a 39-year-old female shows mild cortical thickening and osteopenia in the para-articular bones (*arrowheads*), producing the pencil-line sign with apparent articular widening (*arrows*). **B** Anterior pinhole scan reveals tracer to characteristically accumulate in the clavicular end (*arrowhead*) but not in the acromion

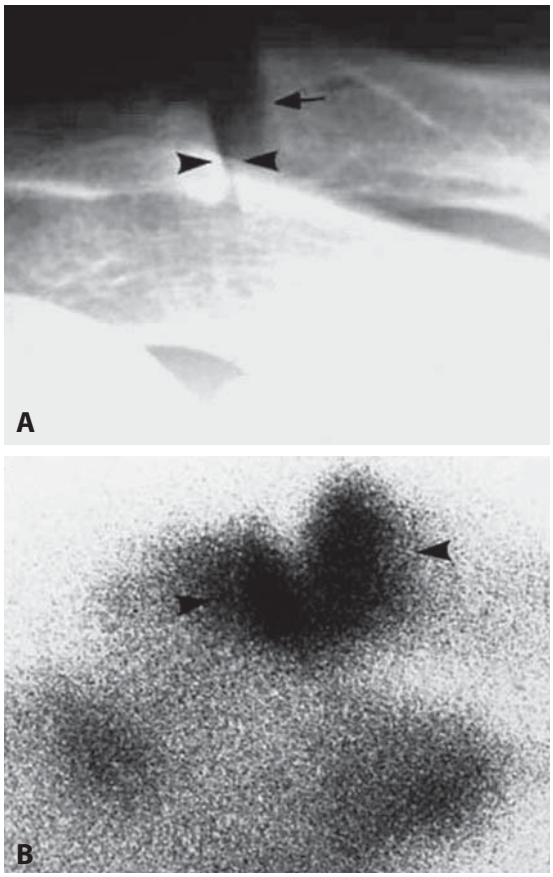

Fig. 9.23A, B Advanced acromioclavicular osteoarthritis. **A** Anteroposterior radiograph of a chronic painful right shoulder in a 22-year-old male shows marked narrowing of the lower articular space (*arrowheads*) with paradoxical widening of the upper compartment due to bony erosion (*arrow*). **B** Anterior pinhole scan reveals intense uptake now in both the clavicular end and the acromion (*arrowheads*)

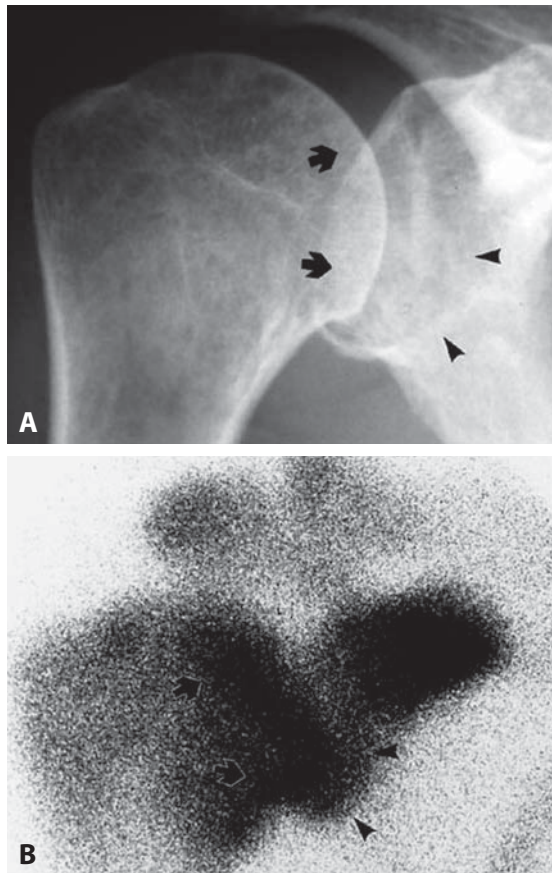

Fig. 9.24A, B Chronic osteoarthritis in the glenohumeral joint. **A** Anteroposterior radiograph of a painful right shoulder of several years duration in a 48-year-old female shows osteopenia and pencil-line cortex (*arrows*) in the humeral head and irregular erosion in the glenoid (*arrowheads*). **B** Anterior pinhole scan reveals intense uptake in the inferomedial aspect of the humeral head (*arrows*) and the apposing glenoid (*arrowheads*)

9.6.2 Glenohumeral Joint

Osteoarthritis of the glenohumeral joint may be associated with aging, occupation, sports, or accidental trauma. Bone diseases such as epiphyseal dysplasia, crystal deposition, hemophilia, or alkaptonuria may also cause osteoarthritis in this joint. The usual pathological sequence is chondrolysis with articular narrowing, hypertrophy with eburnation and osteophytosis, and cystic formation.

Radiography shows eburnation, marginal sclerosis, and cystic change with articular narrowing most typically in the anterior and inferior aspects of the joint. The inferomedial aspect of the humeral head and apposing rim of the glenoid fossa are also involved (Fig. 9.24). Glenohumeral osteoarthritis is often associated with the shoulder impingement syndrome (Fig. 9.25) and rarely complicated with subluxation (Fig. 9.26). When osteoarthritis is associated with impingement, cystic change may occur in the greater tuberosity at the site of the supraspinatus tendon attachment along with subacromial spur (Fig. 9.25). Our observation

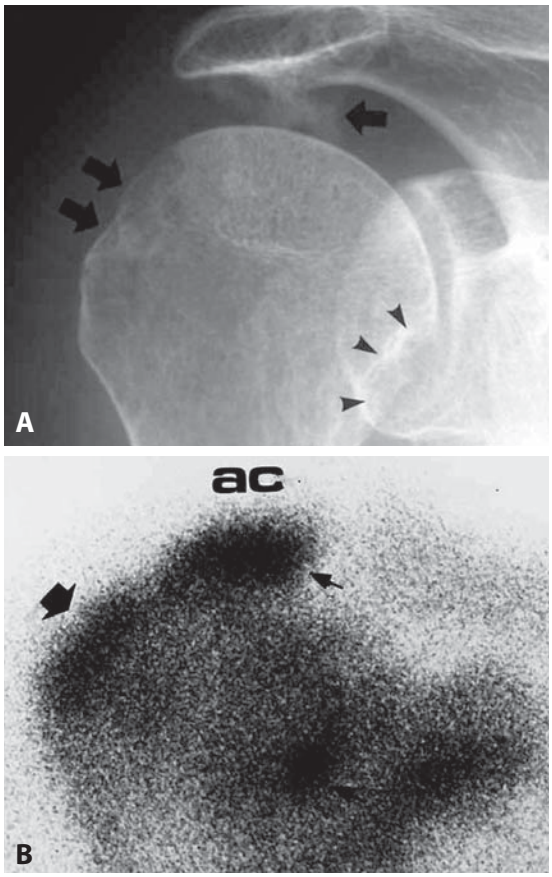

Fig. 9.25A, B Glenohumeral osteoarthritis associated with shoulder impingement syndrome. **A** Anteroposterior radiograph of a chronic painful right shoulder in an 82-year-old male shows marked narrowing of the lower glenohumeral articular compartment (*arrowheads*) and also osteopenia and cystic changes in the greater tuberosity (*pair of arrows*) and subacromial spur (*single arrow*). **B** Anterior pinhole scan reveals intense tracer uptake in the respective lesions including the greater tuberosity (*large arrow*) and the acromion (*ac*) where the supraspinatus tendon attaches (*small arrow*)

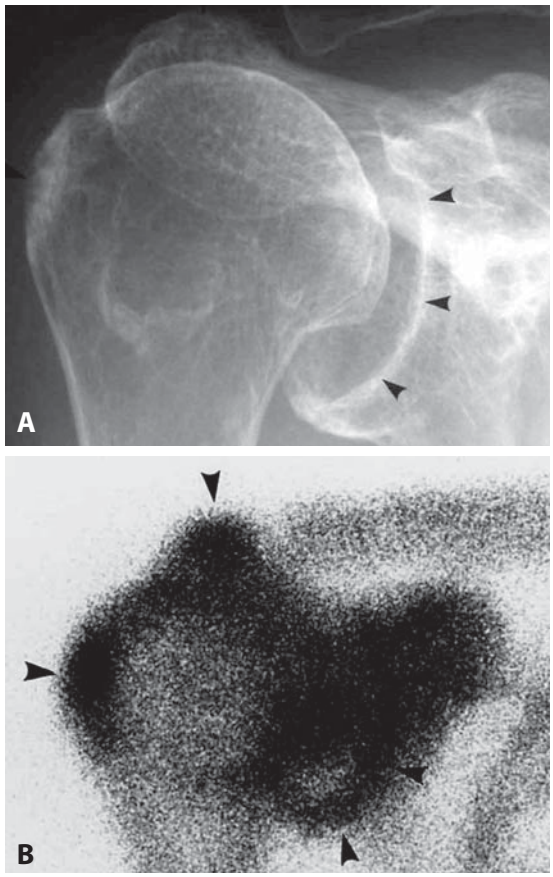

Fig. 9.26A, B Glenohumeral osteoarthritis complicated with subluxation. **A** Anteroposterior radiograph of the right shoulder in a 64-year-old female shows craniolateral displacement of the humeral head with widened articular space (*arrowheads*). Bones are markedly porotic with accentuated cortices. **B** Anterior pinhole scan reveals prominent tracer uptake in the widened glenohumeral joint (*lower arrowheads*). Note increased tracer uptake in the acromion (*top arrowhead*) and greater tuberosity (*left arrowhead*) suggesting impingement or rotator cuff syndrome

has indicated that the radiographic change in the humeral head is often less impressive than the scintigraphic change in the relatively early or active chronic stage of the disease when the metabolic activity is at its height (Fig. 9.27). Such a mismatch can be explained at least in part by disuse that can be diagnosed by osteopenia.

Pinhole scintigraphy shows increased tracer uptake in the articular surface of the glenoid fossa and humeral head (Fig. 9.24B). As mentioned above, the scintigraphic features often precede the radiographic change (Fig. 9.27). In moderately advanced cases the joint becomes diffusely obliterated and subcortical cyst, if formed, is indicated by "hotter area within hot area" (Fig. 9.25B). Subluxation is represented by the displacement of the humeral head and widened joint space (Fig. 9.26B).

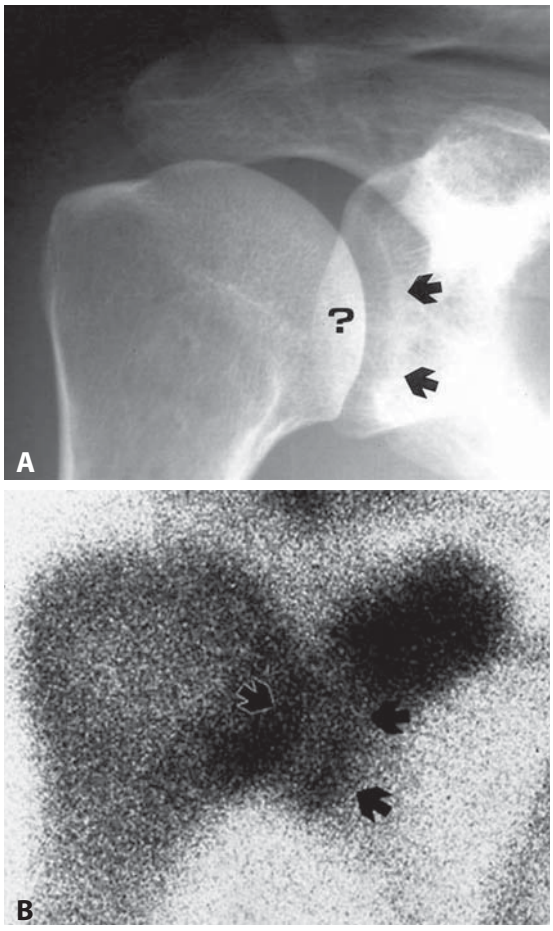

Fig. 9.27A, B Disparity between scintigraphic and radiographic osteoarthritic change in the early stage. **A** Anteroposterior radiograph of a painful right shoulder in a 56-year-old male shows no abnormality on the humeral side (*?*) and mild sclerosis in the lower glenoid (*arrows*). **B** In contrast, the anterior pinhole scan reveals prominent tracer uptake in both the humerus and the glenoid (*arrows*)

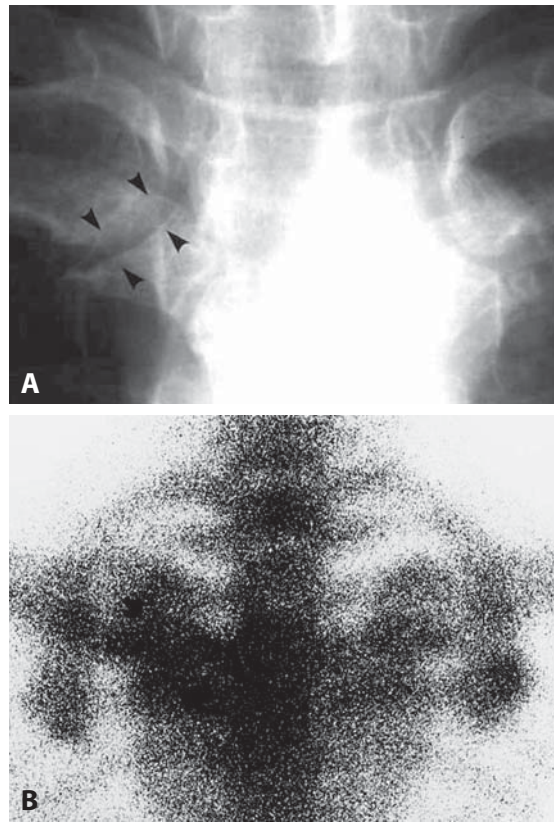

Fig. 9.28A, B Relatively early osteoarthritis in the sternoclavicular joint. **A** Plain anteroposterior radiograph of a painful right sternoclavicular joint in a 50-year-old female shows periarticular bone erosion, osteopenia and eburnation (*arrowheads*). Note false articular widening due to chondrolysis and osteopenia. **B** Anterior pinhole scan reveals slightly increased uptake in periarticular bones (*arrows*). The uptake is not impressive

9.7 Sternum

The sternum has two joints: the sternoclavicular joint and the manubriosternal joint. The former is the synovial joint and the latter is a symphysis.

9.7.1 Sternoclavicular Joint

The sternoclavicular joint is the synovial articulation between the medial end of the clavicle and the sternal clavicular notch, together with the upper part of the subjacent first costal cartilage. The movements and structures including the articular disk are much like those of the acromioclavicular joint. The fibrocartilaginous layer is much thicker on the clavicular surface than the sternal notch. This joint is also a common seat of osteoarthritis. Men are more frequently affected than women. Motion pain, local tenderness, and enlargement of the joint are the main presenting symptoms. The involvement is usually unilateral, but the bilateral type is not rare.

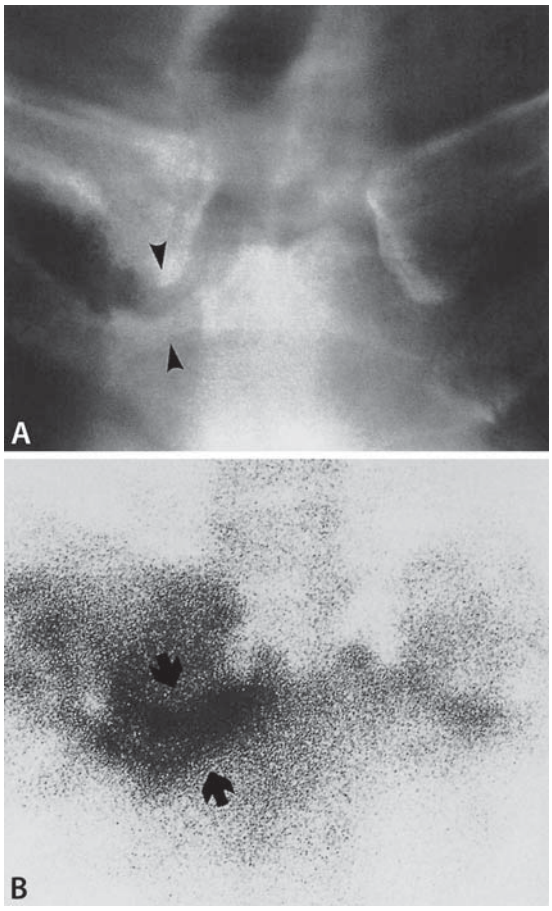

Fig. 9.29A, B Well-established osteoarthritis in the sternoclavicular joint. **A** Anteroposterior conventional X-ray tomogram of the sternum with a painful right sternoclavicular joint in a 49-year-old man reveals irregular subchondral erosions and sclerosis with small osteophytes in the bones about the joint (*arrowheads*). The joint is irregularly and eccentrically narrowed. **B** Anterior pinhole scan shows intense tracer uptake in the sternal margin (*lower arrow*) and the medial clavicular end (*upper arrow*) with eccentric articular narrowing. Note that the most intense tracer uptake is localized in the joint, the characteristic feature of osteoarthritis

Radiographic manifestations include periarticular bone erosions, joint space narrowing, eburnation, and osteophytosis. Understandably, these changes are mild or even dubious in the early stage (Fig. 9.28A). In general, the sternal facet is affected more prominently than the clavicular facet whose fibrocartilaginous layer is thicker. More often than not, chondrolysis and bone erosion may be disguised as joint space widening (Fig. 9.28A). Conventional tomography or CT is useful for the delineation of the true state of affairs (Fig. 9.29A).

Pinhole scintigraphy in the early stage shows an ill-defined area of minimally increased tracer uptake in the affected joint, vaguely denoting mild eburnation in the clavicular and sternal facets (Fig. 9.28B). With the progression of osteoarthritis, the articular space becomes obliterated and tracer uptake intensified. The uptake is typically more prominent at the sternal facet (Fig. 9.29B). Generally, the joint space is indiscernible even in the early stage and on a magnified scan, obviously due to the smallness of the joint and the ball-and-socket type of articular structure.

9.7.2 Manubriosternal Joint

Osteoarthritis also affects the manubriosternal joint, which is one of the largest fibrocartilaginous articulations. Degenerative arthritis mainly involves the central portion of the articular fibrocartilage with resultant articular narrowing and periarticular eburnation.

Radiographically, the manubriosternal joint shows diffuse or partial narrowing with irregular sclerosis of the subchondral bones. Occasionally, the joint may be totally closed (Fig. 9.30A). Conventional or computed tomography is extremely useful for a definitive demonstration of the joint. Pinhole scintigraphy shows intense tracer uptake that fills up the joint, spreading to the lower manubrium and upper gladiolus (Fig. 9.31). It is to be mentioned that the tracer uptake in manubriosternal osteoarthritis is maximal in the central portion of the joint (Figs. 9.30B and 9.31).

9.8 Elbow

The elbow joint is a compound synovial articulation that consists of two components: the humeroulnar joint and the humeroradial joint. The former is between the humeral trochlea and the ulnar trochlear notch and the latter be-

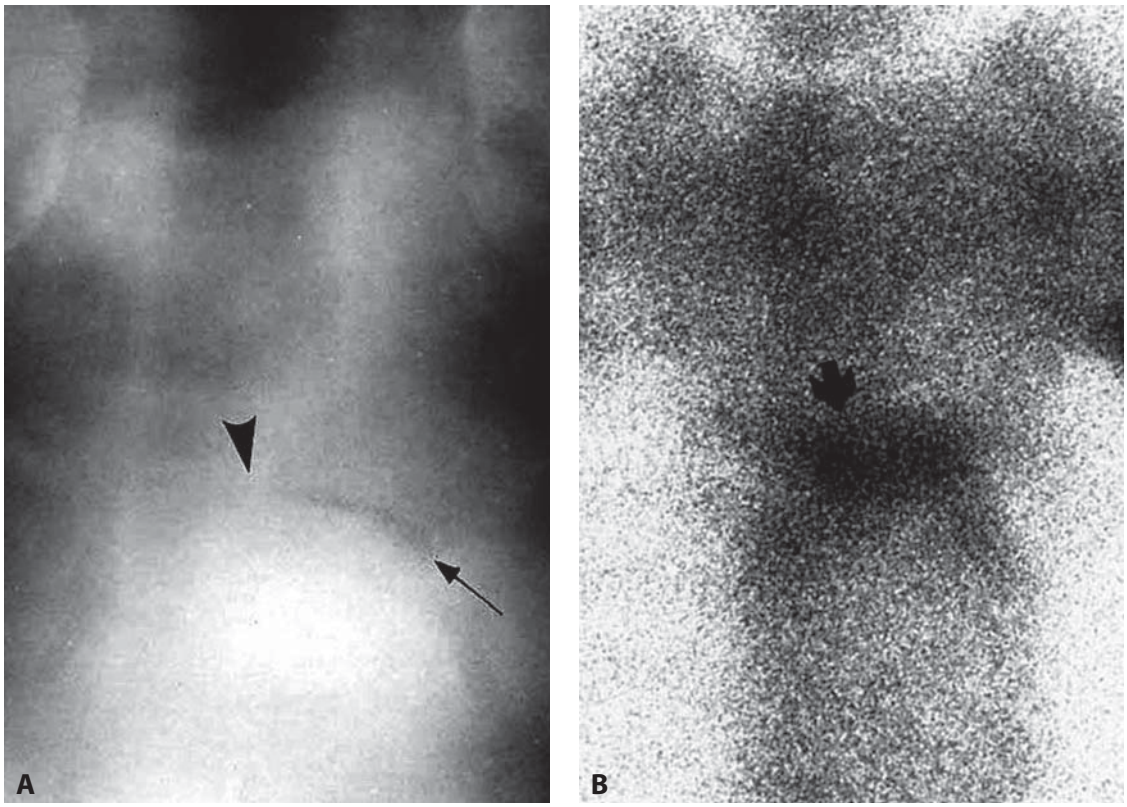

Fig. 9.30A, B Osteoarthritis in the manubriosternal joint. **A** Conventional X-ray tomography of the sternum in a 57-year-old male with chronic sternal pain shows curved linear lucency in the centro-left-lateral portion of the manubriosternal joint (*arrow*) with the obliteration of the right half (*arrowhead*). Plain radiography is not useful for the study of this thin and overshadowed joint. **B** Anterior pinhole scan shows a distinct band-like "hot" area in the centro-left-lateral portion of the joint denoting metabolically active arthritis (*arrow*). Planar bone scintigraphy cannot distinguish pathological uptake from physiological uptake in this joint

tween the humeral capitulum and the radial head. Osteoarthritis is relatively uncommon in the elbow, and it is generally secondary to trauma. The symptoms include limited motion, pain, and tender soft-tissue swelling.

Radiographic features include joint space narrowing and periarticular eburnation (Fig. 9.32A) and occasional enthesophytosis at the base of the olecranon. As elsewhere, on pinhole scintigraphy the alterations are characterized by the combination of extremely in-

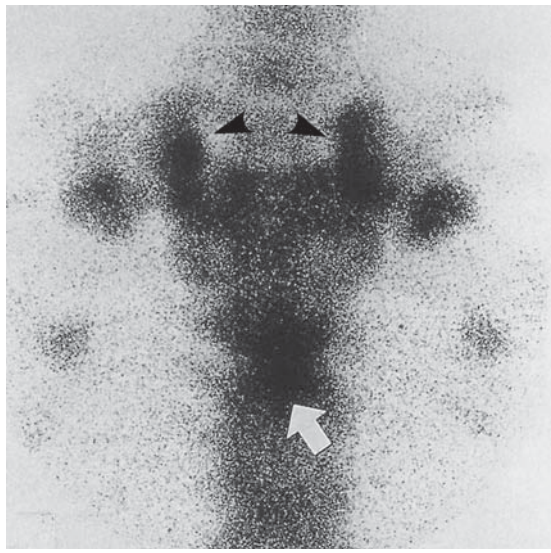

Fig. 9.31 Osteoarthritis in the manubriosternal joint. Anterior pinhole scan of the sternum with motion pain in the upper sternum in a 32-yearold woman shows very intense tracer uptake in the central aspect of the manubriosternal joint (*arrow*). Intense tracer uptake in the sternoclavicular joints (*arrowheads*) and the first costal cartilages is due to articular motion and ossification, respectively

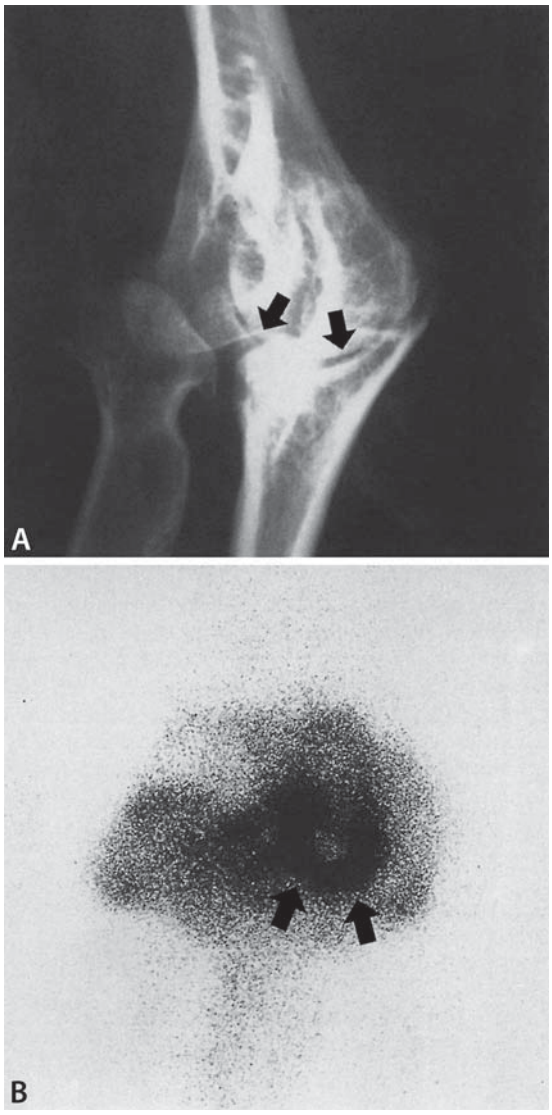

Fig. 9.32A, B Osteoarthritis in the elbow joint. **A** Oblique radiograph of the right elbow in a 47-year-old woman shows marked subarticular sclerosis with narrowing of the trochlear joint, producing a semilunar articular deformity (*arrows*). **B** Oblique pinhole scan reveals diffusely increased tracer uptake in the periarticular bones with the most intense uptake localized in the trochlear notch, creating the characteristic U-shaped appearance (*arrows*)

tense tracer uptake localized in the joint that is narrowed and moderately intense uptake in the surrounding periarticular bones. The trochlear notch is the site of involvement, producing the characteristic U-shaped uptake (Fig. 9.32B).

9.9 Wrist and Carpal Joints

The wrist (radiocarpal) joint is a biaxial and ellipsoid articulation formed between the distal end of the radius and the scaphoid, lunate, and triquetrum with triangular cartilage on the ulnar side. The joint is lined by synovium and surrounded by fibrous capsule and radiocarpal ligaments. In addition, there are complex intercarpal joints, interconnecting (a) the proximal carpal bones, (b) the distal carpal bones, and (c) the two carpal bone rows.

Osteoarthritis of the wrist predominantly affects the radial side with the most common sites being the trapeziometacarpal joint and the trapezioscaphoid joint (Fig. 9.33). The involvement of the radiocarpal joint, distal radiofibular joint, lunate–triquetal joint, and other intercarpal joints are not rare (Fig. 9.34). Causes are trauma in the majority of cases and calcium deposition disease in occasional cases. Symptoms include pain and tenderness, motion disturbance, and soft-tissue swelling. Osteoarthritis without an obvious or probable etiology is termed idiopathic, but its existence has been challenged.

Radiography is often not helpful in the early stage of the disease, but plays an important role in the intermediate and late stages. Radiographic changes include articular narrowing, sclerosis, osteophytosis, cystic change, bone collapse, and deformity. Characteristically, changes are limited to a single or few small joints of the wrist, and osteoporosis is not a significant feature (Fig. 9.33A). Typically, the osteoarthritis in the wrist occurs on the radial side (Fig. 9.33), but the posttraumatic type involves any joint (Fig. 9.34A). MRI and CT are extremely useful for the specific diagnosis of synovitis, cartilage destruction, and cystic change (Fig. 9.33B). Osteoarthritis of the hands in typists affects the trapeziometatarsal and trapezioscaphoid joints, causing radial subluxation and bayonet deformity in the late stage (Fig. 9.35A). The osteoarthritis secondary to rheumatoid arthritis may show localized sclerosis within diffusely porotic carpal bones (Fig. 9.36A).

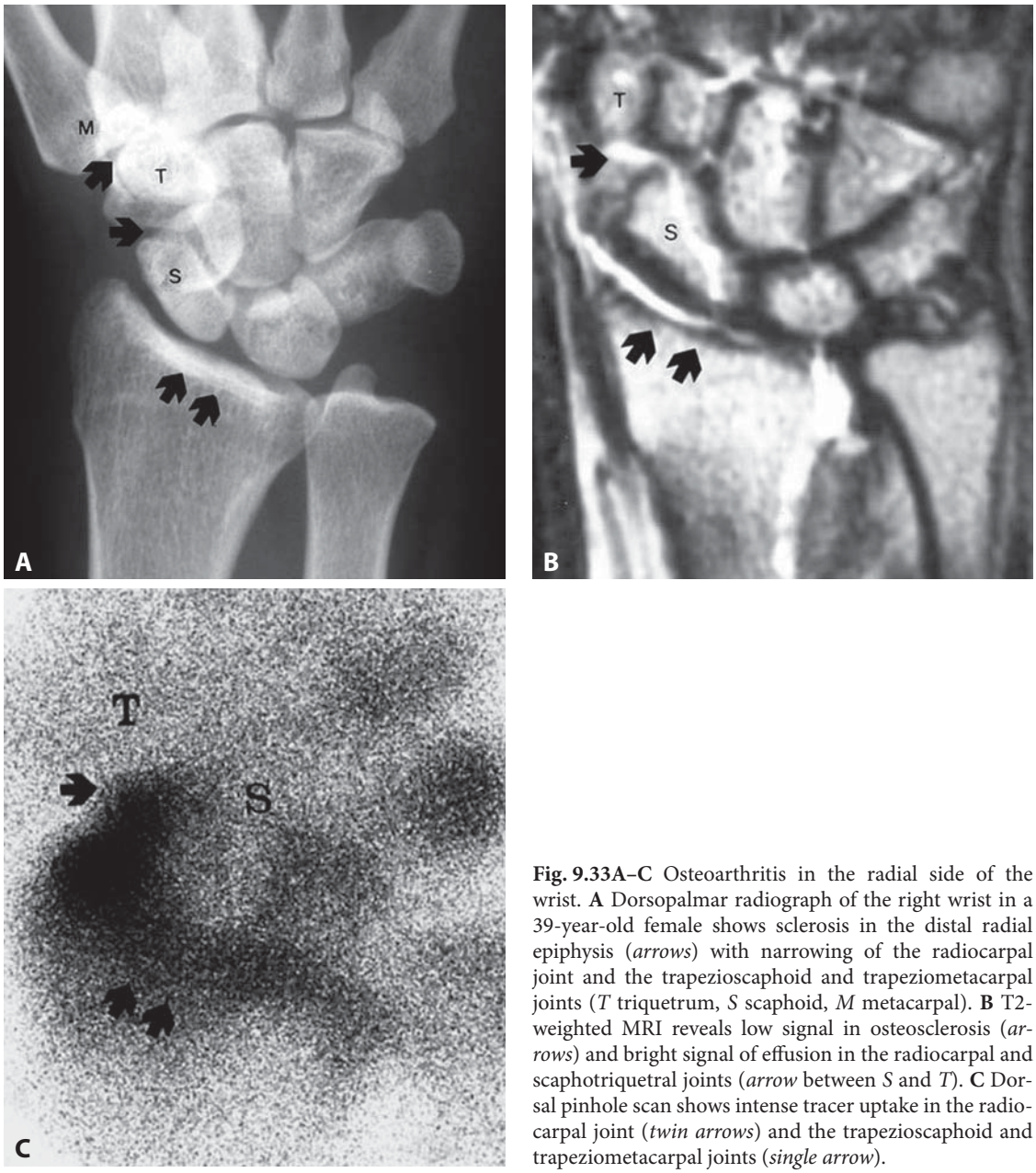

Fig. 9.33A–C Osteoarthritis in the radial side of the wrist. **A** Dorsopalmar radiograph of the right wrist in a 39-year-old female shows sclerosis in the distal radial epiphysis (*arrows*) with narrowing of the radiocarpal joint and the trapezioscaphoid and trapeziometacarpal joints (*T* triquetrum, *S* scaphoid, *M* metacarpal). **B** T2-weighted MRI reveals low signal in osteosclerosis (*arrows*) and bright signal of effusion in the radiocarpal and scaphotriquetral joints (*arrow* between *S* and *T*). **C** Dorsal pinhole scan shows intense tracer uptake in the radiocarpal joint (*twin arrows*) and the trapezioscaphoid and trapeziometacarpal joints (*single arrow*).

Pinhole scintigraphy plays an important role in the diagnosis of the early osteoarthritis with synovitis of the radiocarpal and trapeziometatarsal joints by showing tracer accumulated in the synovium and subchondral bones (Fig. 9.33C). Very subtle pathological changes localized to the proximal carpal bone can often be indicated by obvious uptake (Fig. 9.34B). Scintigraphy can also show the characteristic bayonet deformity produced by the radial subluxation of the trapeziometacarpal joint in the late stage (Fig. 9.35B). It is indeed interesting to note that the degree of tracer uptake parallels the degree of arthritic change: more intense

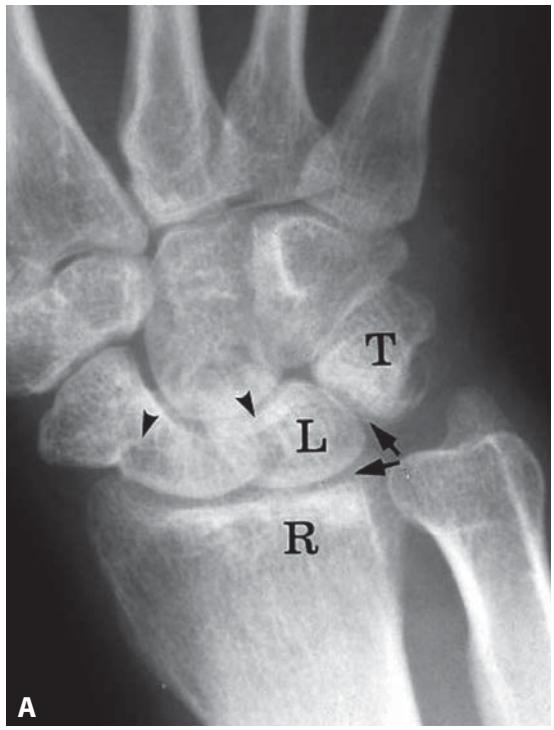

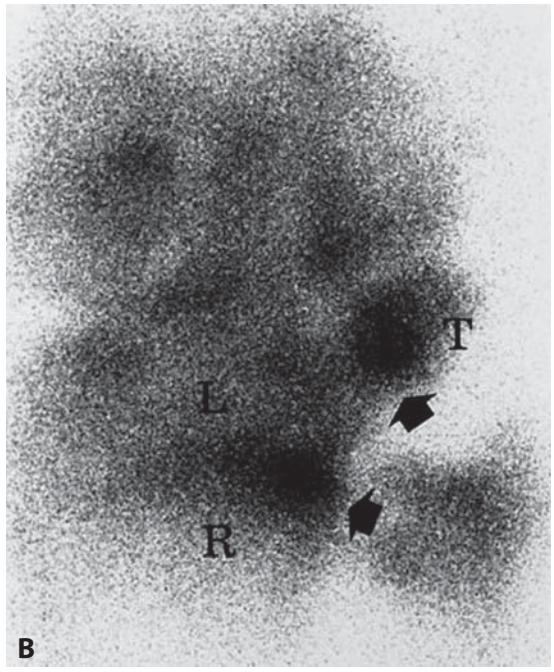

Fig. 9.34A, B Osteoarthritis in the ulnar side of the wrist. **A** Dorsopalmar radiograph of the right wrist in a 41-year-old female shows sclerosis in the distal radial epiphysis with narrowing of the radiocarpal joint and the lunate-triquetral joint (*R* radius, *L* lunate, *T* triquetrum). **B** Dorsal pinhole scan reveals intense tracer uptake in the radiocarpal joint (*lower arrow*) and the lunate-triquetral joint (*upper arrow*)

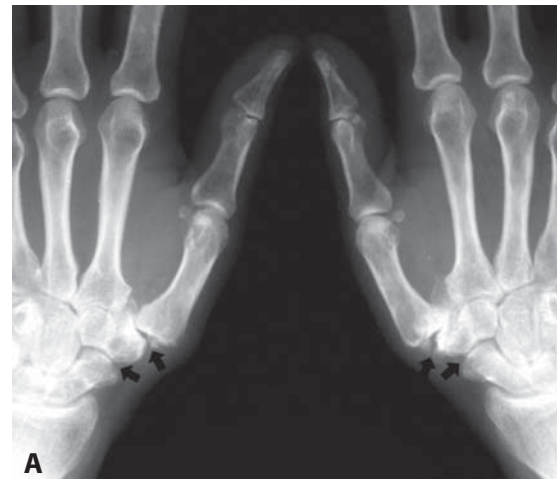

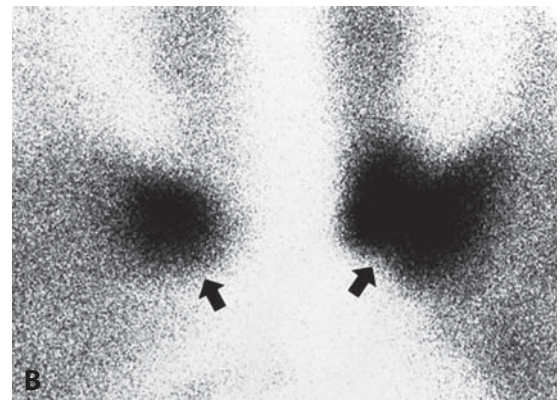

Fig. 9.35A, B Osteoarthritis of the hands in typists. **A** Dorsopalmar radiograph of both hands in a professional female typist shows osteoarthritis in the trapeziometatarsal and trapezioscaphoid joints of both hands with radial subluxation and bayonet deformity (*arrows*). **B** Dorsal pinhole scan reveals intense tracer uptake in classic bayonet deformity with squaring (*arrows*)

uptake in the joints with severer pathological change and vice versa (Fig. 9.35B). The osteoarthritis secondary to long-standing rheumatoid arthritis in the wrist radiographically indicated by osteosclerosis can easily be identified and diagnosed as such by prominent tracer uptake (Fig. 9.36B).

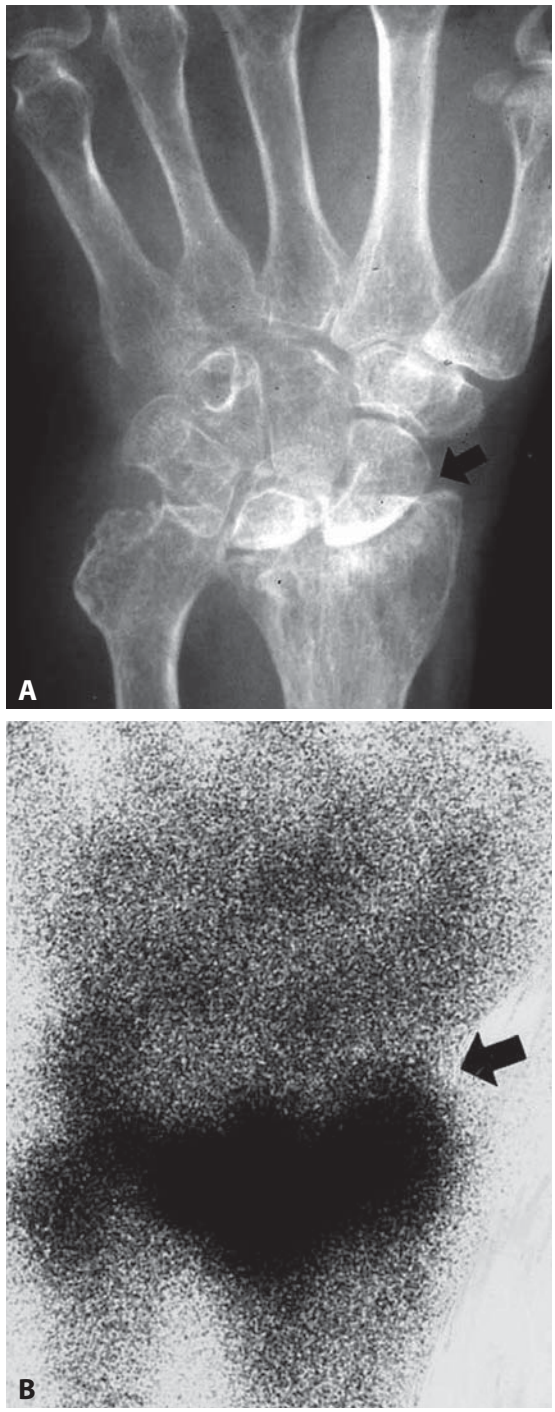

Fig. 9.36A, B Osteoarthritis secondary to rheumatoid arthritis. **A** Dorsopalmar radiograph of the left wrist in a 78-year-old female shows narrowing and obliteration of the entire carpal joints and osteoporosis, with the most prominent change occurring in the radiocarpal joint (*arrow*). **B** Dorsal pinhole scan reveals intense tracer uptake in the radiocarpal joint with the remaining carpal joints not accumulating tracer (*arrow*)

9.10 Spine

The spine has five different articulations: the diskovertebral and apophyseal joints in throughout the spine, the costotransverse and costocorporeal joints in the thoracic spine, and the uncovertebral joints in the cervical spine. Of these, the diskovertebral joint is fibrocartilaginous in type and others are synovial except for the uncovertebral joint that is mixed in type. Based on the principal site of involvement, diskovertebral degeneration can be divided into diskovertebral osteoarthritis and spondylosis deformans. The former osteoarthritis affects the nucleus pulposus with diffuse condensation of peridiskal bones (endplate-based sclerosis) of the lower lumbar and lumbosacral vertebrae and the latter the outer or Sharpey's fibers of the annulus fibrosus with osteophytosis. On the other hand, the degenerative change of the apophyseal and costovertebral joints is considered to be a classical osteoarthritis since these joints are synovial.

Radiographically, diskovertebral osteoarthritis manifests the narrowing of the intervertebral space, endplate sclerosis, and focal osteophytes, most typically in the L4, L5, and S1 vertebrae (Fig. 9.37A). Occasionally, compression fracture may be superimposed on an endplate that is already deformed by osteoarthritis, making the diagnosis extremely difficult (Fig. 9.38B). In contrast, spondylosis deformans is characterized by multiple osteophytes, often prominent, formed in the lateral and anterior edges of the endplates (Fig. 9.39A). The diskovertebral changes such as narrowing of the intervertebral spaces and endplate scleroses are usually inconspicuous.

Pinhole scintigraphic manifestations of diskovertebral osteoarthrosis include tracer uptake in the vertebral endplates and marginal spurs with significant diminution of the intervertebral space (Fig. 9.37B). The endplates are affected in pairs in a straight, parallel manner. Compression fractures resemble diskovertebral osteoarthritis, but fractures are rarely paired and not parallel when paired (Fig. 9.38B). Mo-

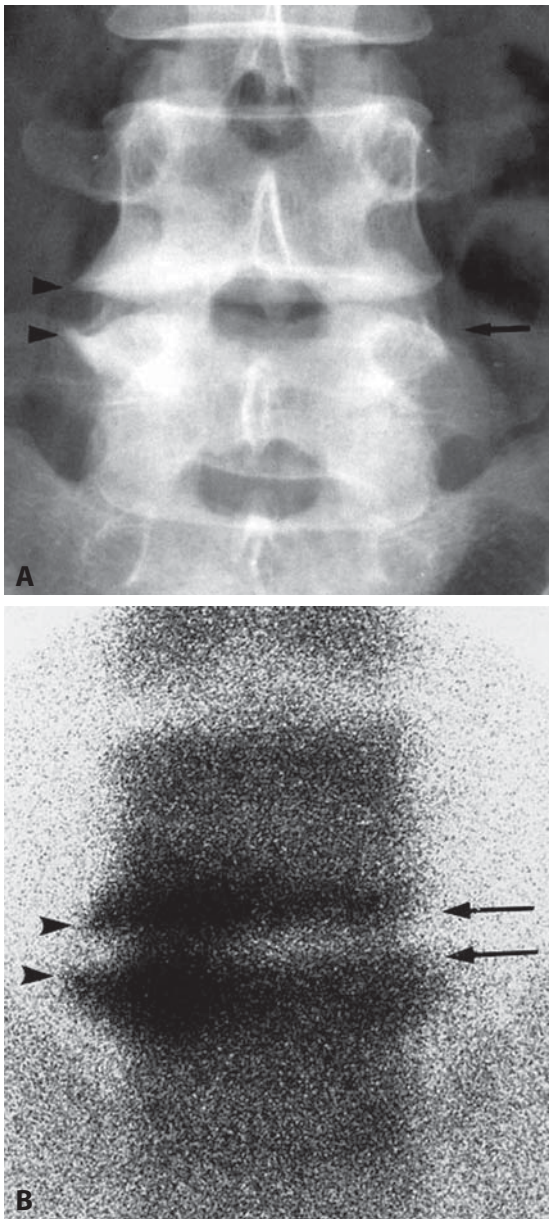

Fig. 9.37A, B Straightness of endplate sclerosis in intervertebral osteochondrosis in the lower lumbar spine. **A** Anteroposterior radiograph of the lower lumbar spine in a 37-year-old female shows typical endplate based sclerosis in the L4 lower and L5 upper endplates with narrowing of the disk space between (*arrow*). There are small claw-like spurs at the right lateral edges (*arrowheads*). **B** Anterior pinhole scan shows straight tracer uptake in the sclerosed endplates with disk space narrowing (*parallel arrows*) and spur uptake (*arrowheads*)

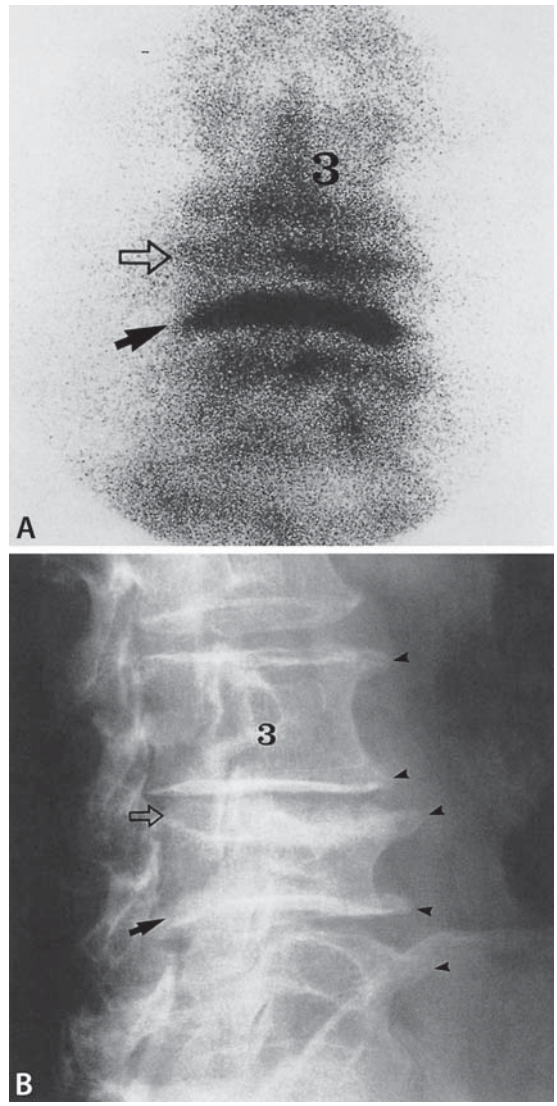

Fig. 9.38A,B Arcuate depression of the vertebral endplates in compression fractures of the spine. **A** Posterior pinhole scintigraph of the lower lumbar spine in a 67-year-old woman with old and new compression fractures of the L4 vertebra shows increased tracer uptake in the centrally depressed upper and lower endplates (*open* and *solid arrows*). Note that the tracer uptake is extremely intense in the fresh fracture of the lower endplate (*solid arrow*), whereas the uptake is minimal in the old fracture of the upper endplate (*open arrow*). **B** Near lateral radiograph of the same spine shows compression fractures in the upper and lower endplates of the L4 vertebra (*open* and *solid arrows*). Unlike in pinhole scintigraphy, the distinction between old and new fracture is often difficult in radiography. Note that the mature osteophytes in the nonstress areas do not concentrate tracer (*arrowheads*)

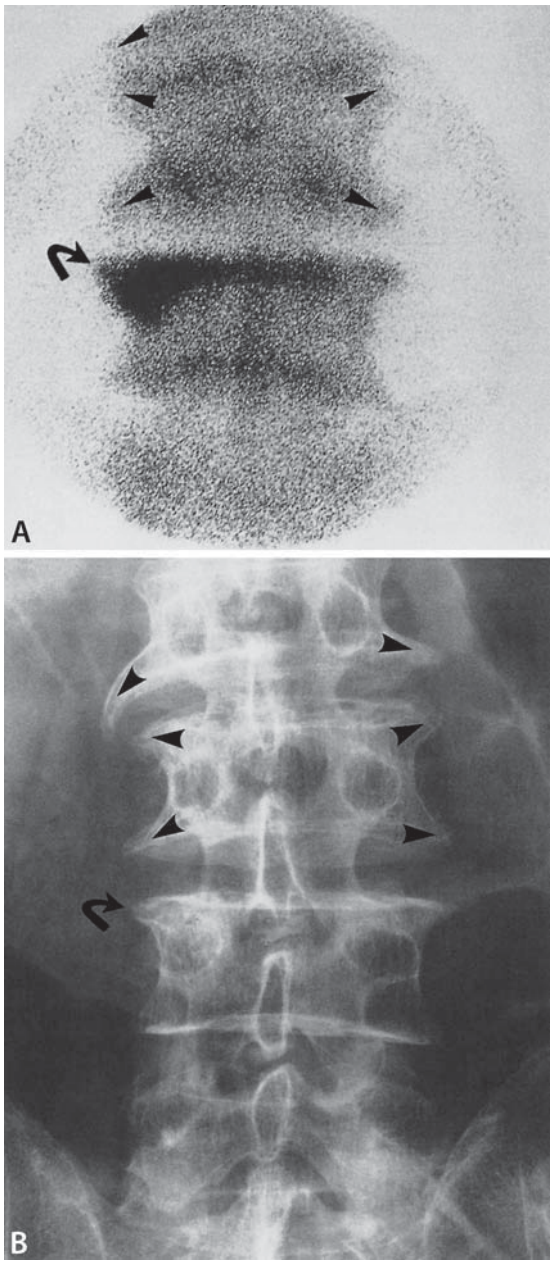

Fig. 9.39A, B Different intensities of tracer uptake in old and new osteophytes. **A** Anterior pinhole scan of the lower lumbar spine in an 80-year-old man with old and new osteophytes reveals little increase in tracer uptake in the prominent old osteophytes in the L2 and L3 vertebrae (*arrowheads*) but very intense tracer uptake in a "budding" osteophyte in the upper lateral aspect of the L4 vertebra (*curved arrow*). **B** Anteroposterior radiograph demonstrates prominent osteophytes in the L2 and L3 vertebrae (*arrowheads*) and an unimpressive osteophyte in the L4 vertebra (*curved arrow*)

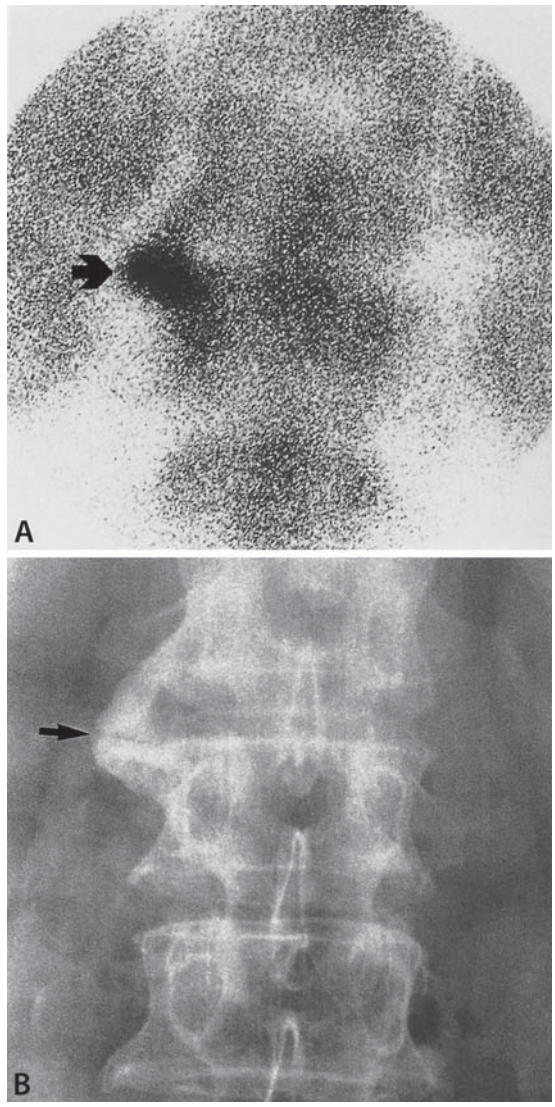

Fig. 9.40A, B Intense tracer uptake in abutting osteophytes. **A** Posterior pinhole scintigraph of the upper lumbar spine in a 72-year-old man with local pain reveals very intense trace uptake in a structure that protrudes outward from the L2–L3 vertebral junction (*arrow*). The most intense uptake occurs in the center where two osteophytes meet to fuse. **B** Anteroposterior radiograph shows a prominent paravertebral osteophyte formed by the two smaller, abutting osteophytes which arise separately from the lateral aspect of the lower endplate of the L1 vertebra and the upper endplate of the L2 vertebra (*arrow*). A narrow slit-like lucency at the center indicates the incompleteness of fusion (*arrow*) as confirmed by CT scan (not shown here)

reover, tracer uptake is markedly intensified and the disk space is preserved unless the disk is simultaneously involved in fracture. The osteophytes in spondylitis deformans are represented scintigraphically by beak-like uptake of various sizes and intensities at the lateral or anterior edges of the vertebral bodies (Fig. 9.39B). The tracer intensity in osteophytes appears to be related to age and location; the smaller and the less outgrowing the osteophyte, the more intense is the uptake and vice versa. Indeed, as in the knee (Fig. 9.5) and elsewhere, the mature osteophytes that lie in the lateral, nonstressed zones of the spine accumulate tracer only minimally, whereas the small, burgeoning spurs in the weight-bearing axis avidly concentrate tracer (Fig. 9.39B). Interestingly, old osteophytes appear imposing radiographically while fresh ones look unimpressive. Extremely intense uptake in one or two of many osteophytes and endplates occurs as the result of superimposed diseases such as fracture, infection, or metastasis. Thus, when fractured or abutted on another osteophyte, even a mature osteophyte conspicuously concentrates tracer (Fig. 9.40A).

The cervical spine is notorious for diskovertebral osteoarthritis, uncovertebral osteoarthritis, and apophyseal osteoarthritis. As in the lumbar and thoracic spine, diskovertebral osteoarthritis in the cervical spine is pinhole scintigraphically indicated by increased tracer upt-

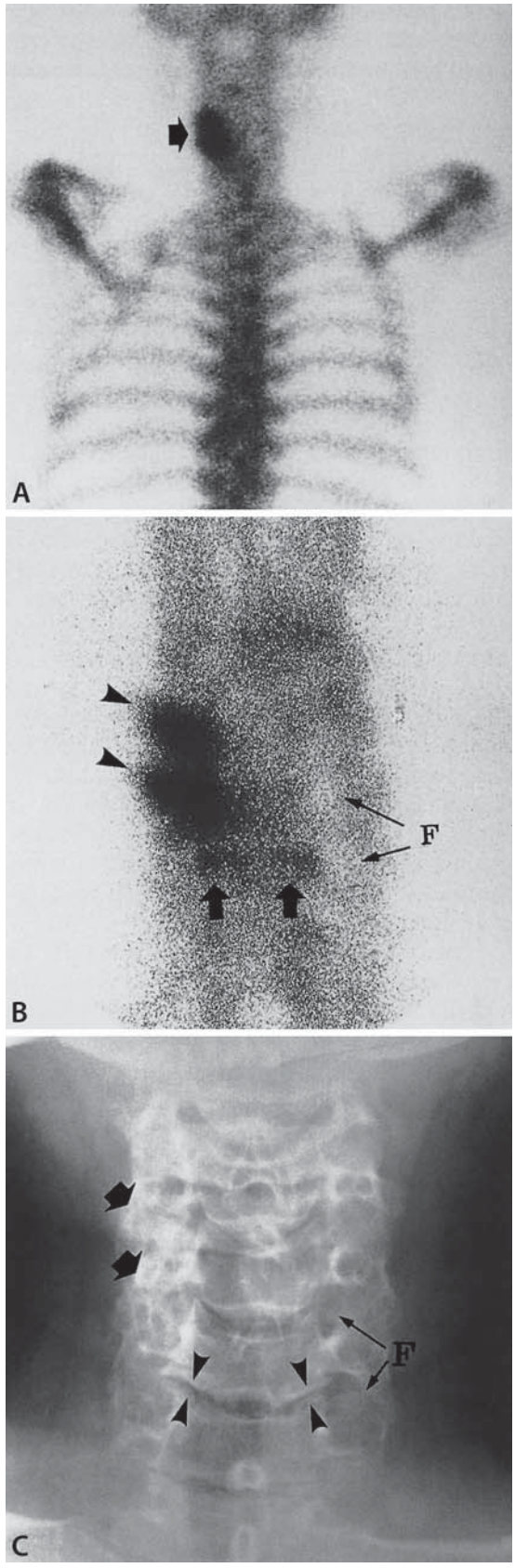

Fig. 9.41A-C Apophyseal and uncovertebral osteoarthritis of the cervical spine. **A** Posterior spot scintigraph of the cervical spine in a 62-year-old woman with posterior neck and left shoulder pain reveals intense tracer uptake in the left lateral aspect of the lower cervical spine (*arrow*). **B** Posterior pinhole scan shows intense tracer uptake in the apophyseal joints of C4–C6 vertebrae (*arrowheads*) and also modest tracer uptake in C6 and C7 uncovertebral joints (*arrows*). The latter joints can easily be located at the medial border of the intervertebral foramina (*F*). **C** Anteroposterior radiograph shows the obliteration with eburnation of the left apophyseal joints of C4–C6 vertebrae (*arrows*) and erosions in C6 and C7 uncovertebral joints (*arrowheads*). Observe the intimate positional relationship between the uncovertebral joints and the intervertebral foramina (*F*). The radiograph is printed with the right side on the left to match the scintigraph

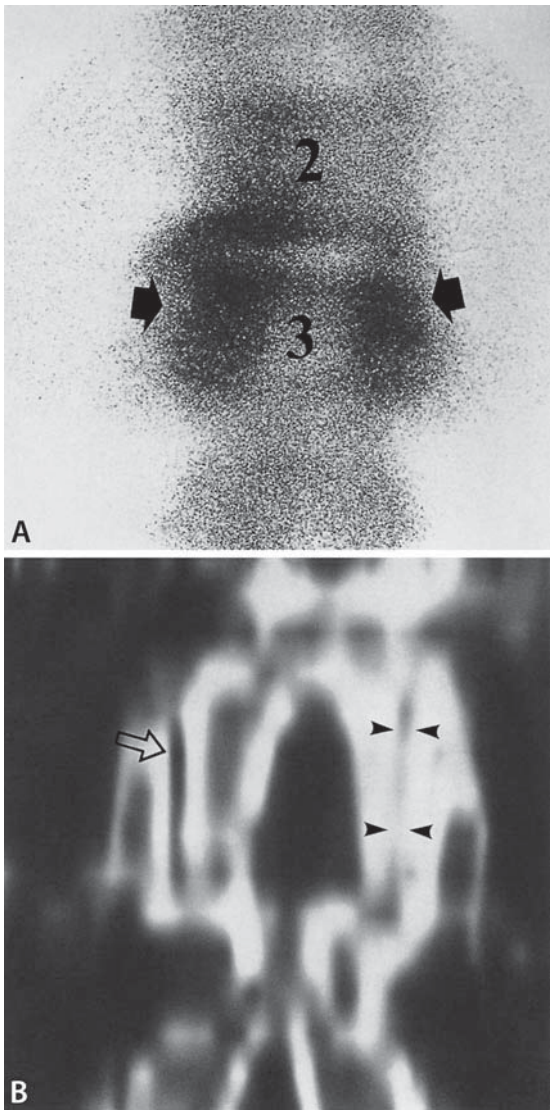

Fig. 9.42A, B Vertical alignment and half-astride position of the apophyseal joints in the lower lumbar spine. **A** Posterior pinhole scintigraph of the midlumbar spine in a 50-year-old woman with known apophyseal osteoarthritis shows intense tracer uptake in L2 and L3 apophyseal joints (*arrows*). Unlike horizontal alignment in the cervical spine (Fig. 9.41), the apophyseal joints in the lumbar spine are vertically aligned and astride in location. **B** Coronal CT section through the affected apophyseal joints reveals marked para-articular sclerosis with joint space narrowing on the right (*arrowheads*) and a vacuum on the left (*open arrow*). The CT image is printed with the right side on the left to match the scintigraph

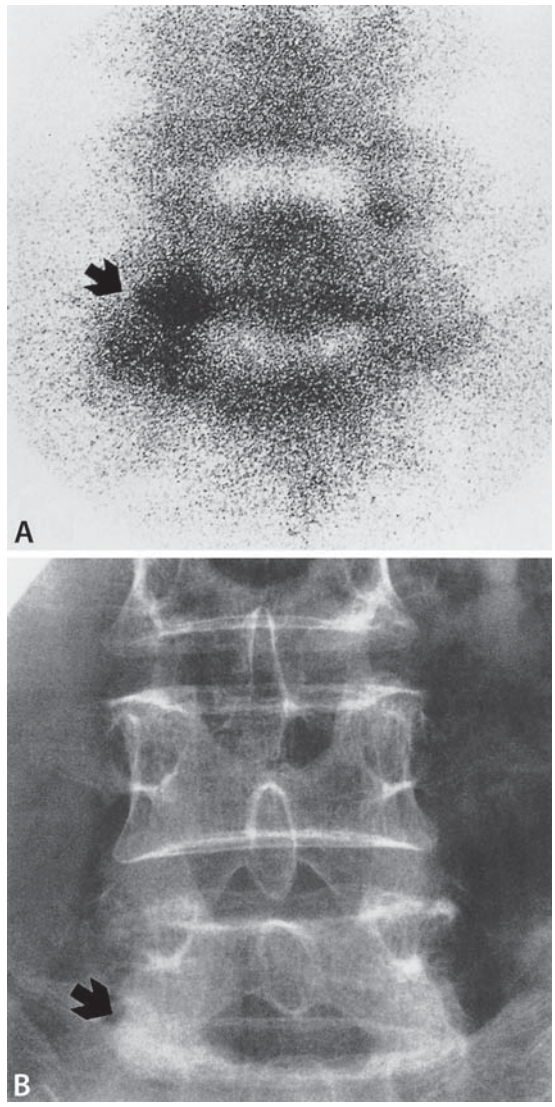

Fig. 9.43A, B Osteoarthritis in the lumbosacral apophyseal joint. **A** Posterior pinhole scintigraph of the lumbosacral region of the spine in a 59-year-old woman with local tenderness shows spotty tracer uptake in the left lumbosacral apophyseal joint (*arrow*). **B** Anteroposterior radiograph shows sclerosis in the left lumbosacral apophyseal joint (*arrow*). The radiograph is printed with the right side on the left to match the scintigraph

ake in the sclerosed endplates with narrowed disk space, and such findings are best appreciated on the lateral scan. It is to be noted that osteoarthritis can be confused with infective spondylitis, but radiographic findings basically differ between the two conditions: endplate sclerosis in osteoarthritis (Fig. 9.37A) and endplate lysis in infection (Fig. 6.37B).

The uncovertebral joint of Luschka is the articulation formed between the uncinate processes of the cervical vertebrae, and is found in all but the first two cervical vertebrae. Because this joint borders the medial aspect of the intervertebral foramina, their involvement is readily diagnosed by pinhole scintigraphy (Fig. 9.41B). As shown in this case, the simultaneous involvement of the uncovertebral and apophyseal joints is not uncommon.

Osteoarthritis of the apophyseal and costovertebral joints manifests as intense uptake in the respective joint. The uptake in apophyseal osteoarthritis is characterized by its lateral localization in the vertebral column on the posterior or anterior scan. It is laid more or less horizontally in the cervical and midthoracic regions (Fig. 9.41) and vertically in the lower thoracic and upper lumbar regions (Fig. 9.42). For unobstructed, viewing of individual apophyseal joints oblique pinhole scintigraphy is ideal. Apophyseal osteoarthritis may be either solitary or multiple, unilateral or bilateral. The lumbosacral apophyses are most commonly affected, manifesting as classic spotty uptake in the lateral edge(s) of the sacral base (Fig. 9.43). In occasional cases radiographic findings are inconclusive, but scintigraphic evidence is definitive. Indeed, the diagnosis of radiographically dubious osteoarthritis in the false joint between the broad transverse process of the lowermost lumbar vertebra and the lateral part of the transitionalized sacral base can be confirmed by pinhole scintigraphy (Fig. 9.44). It is to be emphasized that planar scan or often radiography is of limited diagnostic value in this condition.

The diagnosis of osteoarthritis of the costovertebral joints, both or either of the costotransverse and costocorporeal joints, can also be established by pinhole scintigraphic portrayal of increased uptake in the respective joints. To be exact anatomically, the costotransverse joint is located in the paraspinal region and the costocorporeal joint in the immediate juxtaspinal region; the former joints lie more laterally

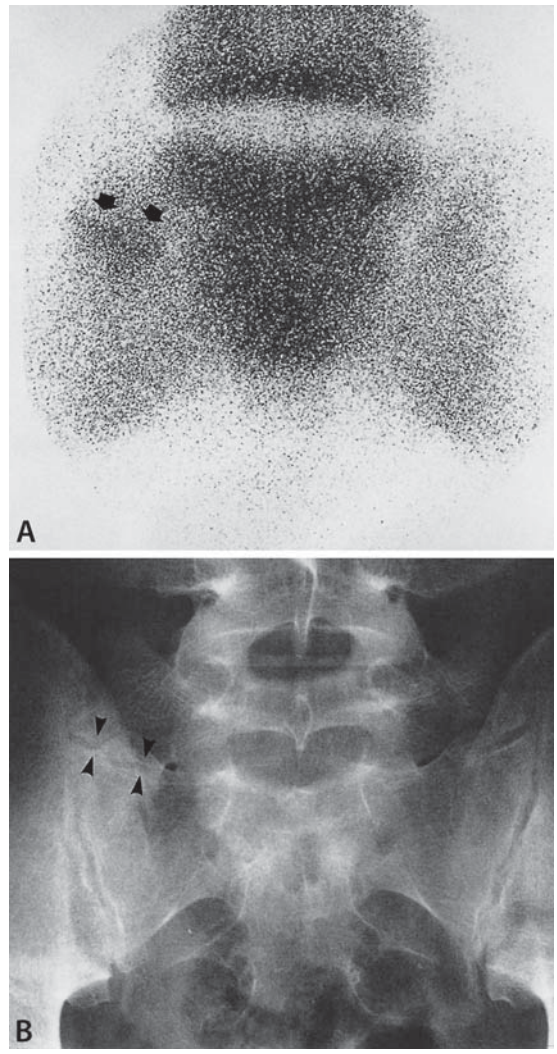

Fig. 9.44A, B Pinhole scintigraphic diagnosis of early osteoarthritis in transitionalized lumbosacral joint. **A** Anterior pinhole scan of the sacrum in a 22-year-old man with disturbing motion pain in the right lumbosacral region reveals indeed subtle tracer uptake in the anomalous lumbosacral joint (*arrows*). Ordinary scintigraph showed no abnormality (not shown here). **B** Anteroposterior radiograph reveals borderline paraarticular sclerosis in the anomalous joint formed in the transitionalized lumbosacral spine (*arrowheads*)

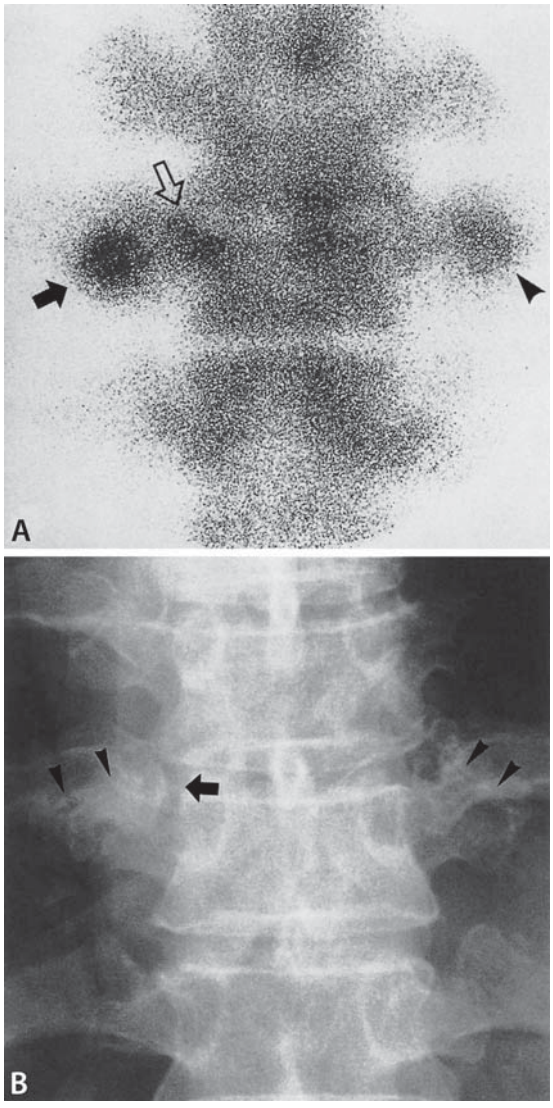

Fig. 9.45A, B Osteoarthritis in the costovertebral (costotransverse and costocorporeal) joints. **A** Posterior pinhole scintigraph of the lower thoracic spine in a 70-year-old man with local pain shows spotty tracer uptake in the left costotransverse (*solid arrow*) and costocorporeal (*open arrow)* joints of the T10 vertebra. The opposite costovertebral joint also shows minimally increased tracer uptake (*arrowhead*). **B** Anteroposterior radiograph shows articular narrowing and sclerosis in the costotransverse joints of the T10 vertebra on both sides (*arrowheads*). Note the more medially located costocorporeal joint with erosions (*arrow*). The radiograph is printed with the right side on the left to match the scintigraph

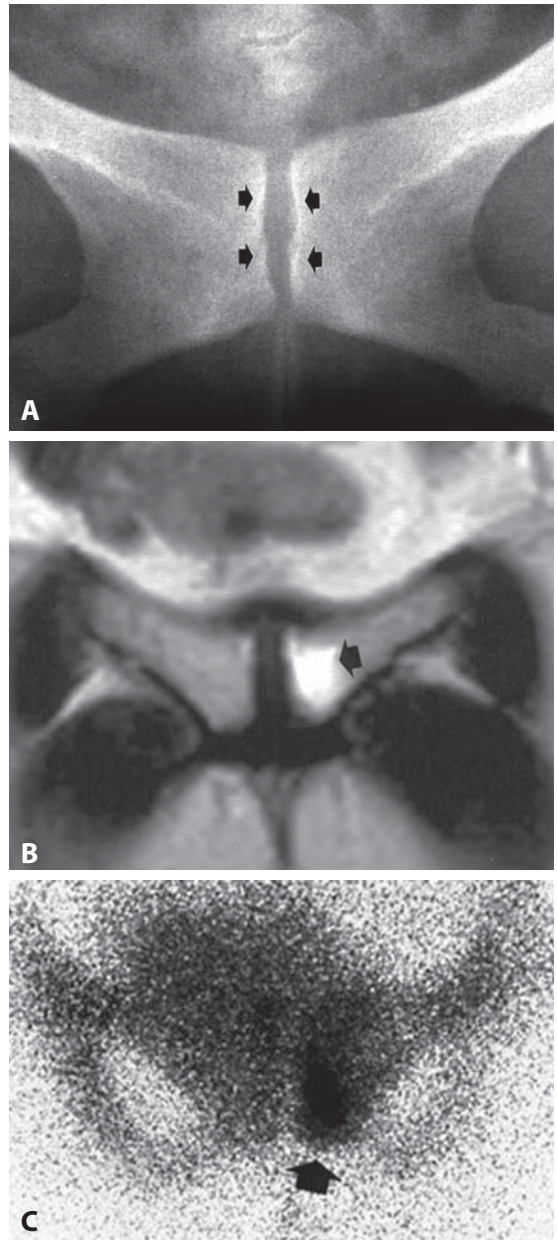

Fig. 9.46A–C Early osteoarthritis in the symphysis pubis. **A** Anteroposterior radiograph of painful pubic symphysis in a 61-year-old female shows local osteopenia and minimal eburnation with a preserved joint space (*arrows*). **B** Fat-suppressed T2-weighted MRI demonstrates subcortical edema in the left pubis (*arrow*). **C** Anterior pinhole scan shows intense tracer uptake specifically localized to the para-articular zone of the left pubic bone (*arrow*)

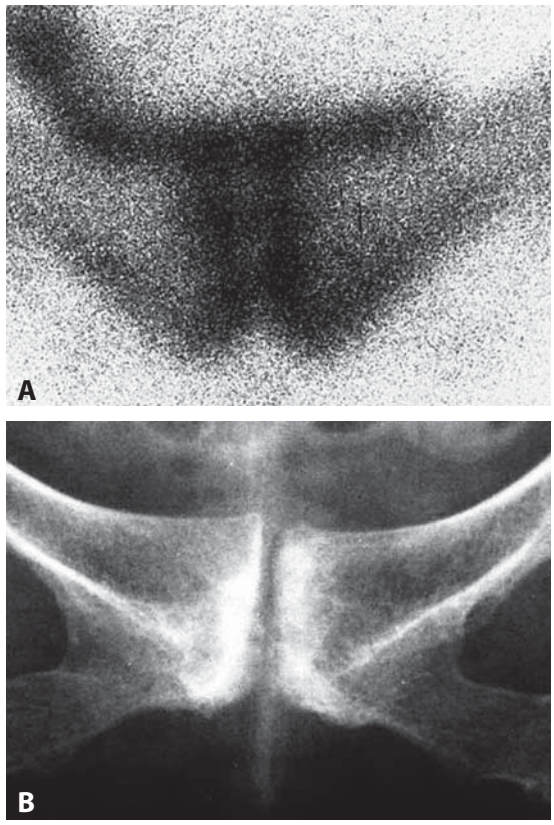

Fig. 9.47A, B Chronic osteoarthritis in the symphysis pubis. **A** Anteroposterior radiograph of painful pubic symphysis in a 72-year-old female shows local osteopenia and prominent eburnation with a narrowed joint space with vacuum shadow. **B** Anterior pinhole scan shows intense tracer uptake localized to the pubic bone cortices symmetrically, producing a collared neck appearance. This case suggests that the tracer uptake in pubic osteoarthritis may be linked not only to osteosclerosis but also to other causes such as osteopenia

than the latter (Fig. 9.45). As in the osteoarthritis of the apophyseal joints, the tracer uptake in costovertebral osteoarthritis is modest at most, and its occurrence is either monarticular or oligoarticular (Fig. 9.45) contrasting with multiple, intense, and usually lateralized tracer uptake in apophyseal joint fractures (Chap. 16). Apophyseal involvement in ankylosing spondylitis and other SNSA is for the most part multiple and symmetrical (Chap. 11).

9.11 Other Common Sites of Osteoarthritis

Osteoarthritis commonly affects the symphysis pubis, the interphalangeal joints of the hands and feet, and the sesamoidometatarsal joint of the great toe with hallux valgus (Resnick 2002) as well as the type II accessory bone of the navicular bone (Lawson et al. 1984). As elsewhere, common radiographic features include bone erosions, eburnation, articular narrowing, and cystic formation. Scintigraphy shows increased uptake and articular narrowing. Not infrequently, the scintigraphic changes appear more prominent and impressive than the radiographic changes, especially in the early stage.

9.11.1 Symphysis Pubis

Radiography reveals mild eburnation with preserved joint space in the early stage (Fig. 9.46A) and marked eburnation with joint-space narrowing in the late stage (Fig. 9.47). MRI demonstrates subcortical edema (Fig. 9.46B), which coincides with the site of intense tracer uptake. The changes may be unilateral or bilateral.

9.11.2 Metatarsosesamoidal Joints

Radiography shows lateral dislocation and rotation of the sesamoids, articular narrowing, eburnation in the medial metatarsal head, and soft-tissue thickening. Pinhole scintigraphy reveals prominent tracer uptake localized to the metatarsal sesamoids (Figs. 9.48B). Nuclear angiography demonstrates increased vascularity when the arthritis is attended by active inflammation (Fig. 9.49).

9.11.3 Navicular Accessory Joint

The characteristic radiographic features of osteoarthritis of the navicular accessory bone include irregular narrowing of the navicular and navicular-accessory synchondrosis or joint with the condensation of the accessory bone, mimicking avascular necrosis (Fig. 9.50A). The accessory bone avidly accumulates tracer, attesting to the fact that dense accessory bone is not due to necrosis but stimulated bone

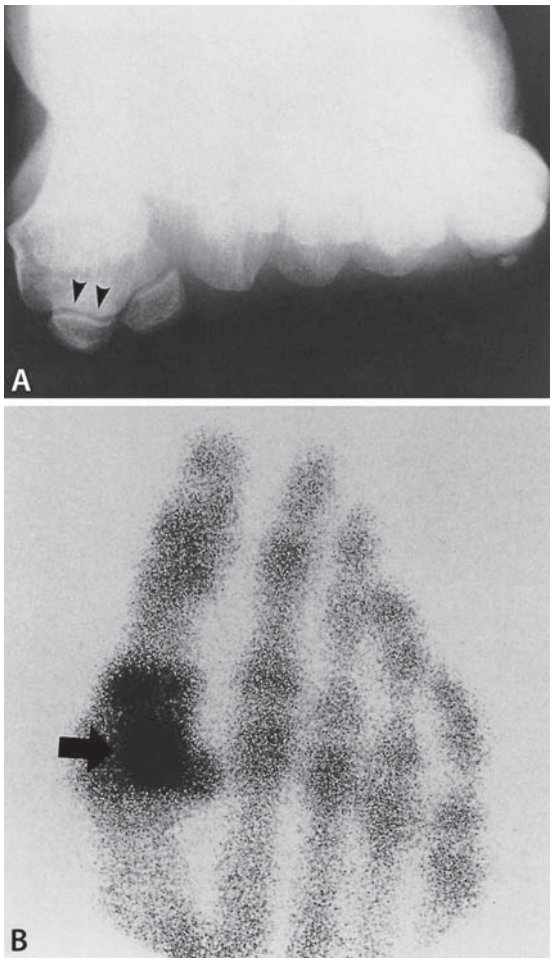

Fig. 9.48A, B Osteoarthritis in the "sesamoidal articulation" of the first metatarsal head. **A** Tangential radiograph (Lewis' view) of the plantar aspect of the painful right great toe in a 42-year-old woman shows minimal periarticular sclerosis and narrowing of the articulation formed between the medial sesamoid and the first metatarsal head (*arrowheads*). **B** Dorsal pinhole scan distinctly shows increased tracer uptake in the "enlarged" medial sesamoid (*arrow*) and the bones about the first metatarsophalangeal joint. Caution must be exercised not to over-read physiologically increased tracer uptake in the metatarsal sesamoids (Fig. 4.39)

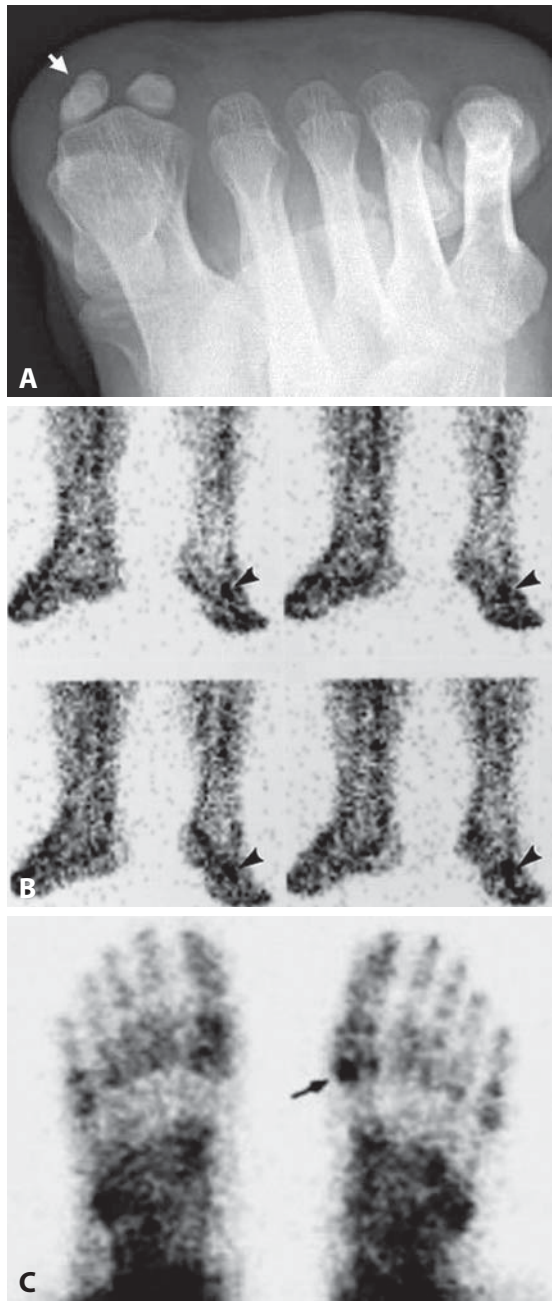

Fig. 9.49A–C Nuclear angiography in sesamoiditis. **A** Tangential view radiograph of painful left first metatarsal head sesamoids in a 35-year-old male shows mild sclerosis of the medial sesamoid bone (*arrow*). **B** Angiogram reveals increased blood flow and blood pool in the area in question (*arrowheads*). **C** Static planar bone scintigraphy shows tracer intensely accumulated in the medial sesamoid bone denoting degenerative sesamoiditis (*arrow*)

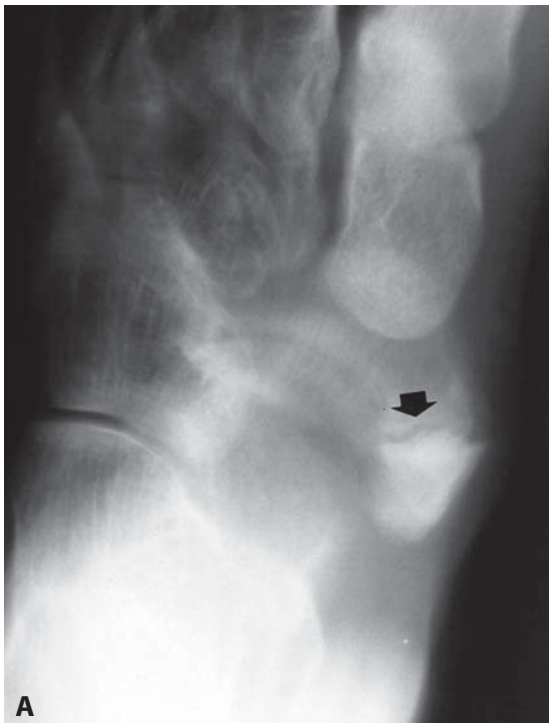

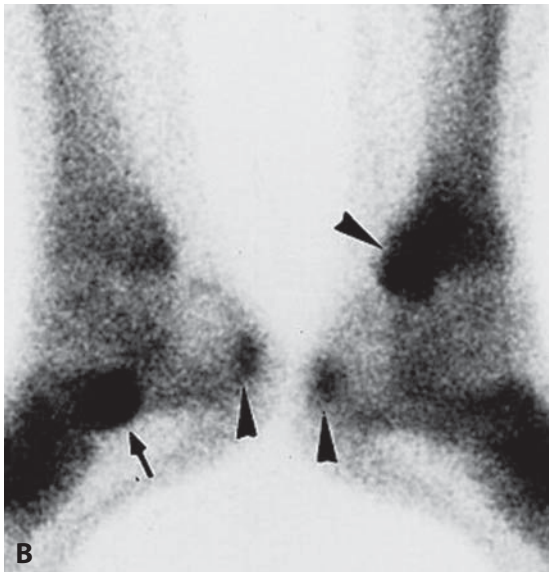

Fig. 9.50A, B Osteoarthritis of the navicular accessory joint. **A** Conventional X-ray tomogram of the right midfoot clearly demonstrates the condensed navicular accessory bone with articular formation (*arrow*). **B** Lateral bone scan of both feet reveals intense tracer uptake in pathological navicular accessory bone on the right (*arrow*). The tracer uptake seen in both retrocalcaneal surfaces and left posterior tibial malleolus are likely due to trauma in this sportswoman

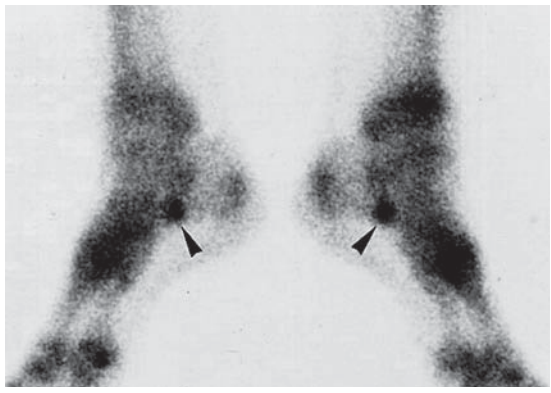

Fig. 9.51 Medial planar bone scan of both feet in a 31-year-old female incidentally shows tracer accumulated in navicular accessory bones that were symptomless

formation. Multiple "hot" areas may be seen in the neighboring or contralateral foot bones and joints in adolescents, athletes in particular, suggesting concurrent trauma. The occurrence of the navicular accessory bone is bilateral in occasional cases (Lawson et al. 1984) and if symptomatic accumulates tracer. Our recent study of 200 consecutive cases comprising 92 men and 108 women with ages ranging from 20 to 68 years showed the incidence of bilateral and unilateral "hot" navicular accessory bones to be 0.5% and 3.5%, respectively, without gender predilection (Fig. 9.51).

9.12 Generalized Osteoarthritis

Generalized osteoarthritis designates a multiarticular involvement pattern of five or more joints at one time with osteoarthritis. It is divided into primary and nodal type according to the absence or presence of Heberden's nodes. Kellgren et al. (1963) have reported high rates of its occurrence in both male relatives (36%) and female relatives (49%) compared to respec-

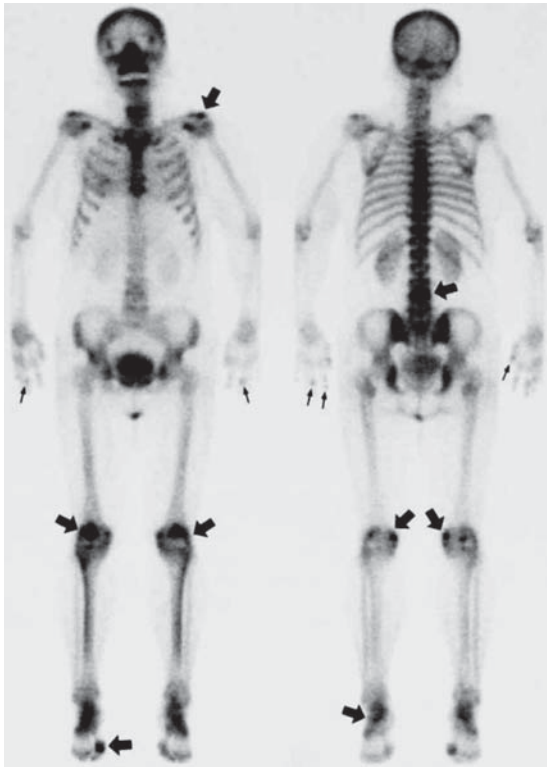

Fig. 9.52 Value of whole-body bone scintigraphy in the diagnosis of generalized osteoarthritis. Anterior (*left*) and posterior (*right*) whole-body bone scans in a 56-year-old female show asymmetrical multiarticular involvement including the lower lumbar spine

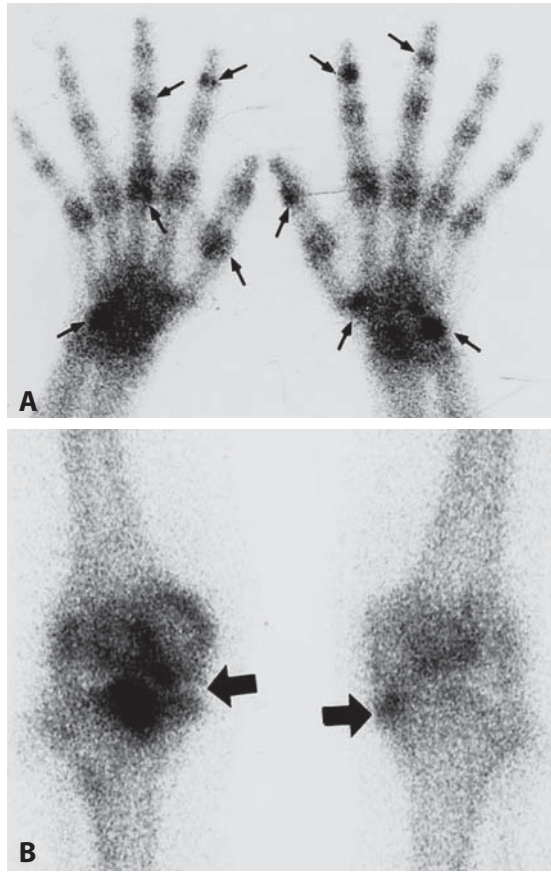

Fig. 9.53A, B Magnified scintigraphy can uniquely provide metabolic information on the individual osteoarthritis. **A** Dorsal scintigraph of both wrists and hands show tracer uptake to be more intense in sites of active osteoarthritis (*arrows*). **B** Anterior pinhole scan of both knees with osteoarthritis reveals different area sizes and uptake intensities between two joints reflecting difference of disease extent and intensity (*arrows*)

tive expected rates of 17% and 26%. Joints commonly involved include the apophyseal joints of the spine, the knees, the proximal interphalangeal joints of the finger, the first carpometacarpal joint, and the first tarsometatarsal joint (Kellgren and Moore 1952). The hips, wrists, and lateral metatarsophalangeal joints are also involved but less commonly.

For an efficient clinical investigation of this condition both radiography and scintigraphy are to be performed at the same time. Radiography is advantageous for the delineation of morphological changes such as bone erosion, sclerosis, and articular narrowing and the whole-body scintigraphy is the only available imaging method for panoramic observation of multiarticular disease (Fig. 9.52). In addition, pinhole scintigraphy can uniquely provide metabolic information on the individual osteoarthritis (Fig. 9.53).

Essential radiographic features are not dissimilar to those of osteoarthritis in other joints except for multiarticular involvement, and include articular narrowing, eburnation, cyst formation, and phalangeal joint osteophytosis with soft-tissue thickening. Periarticular osteophytic excrescences are termed Heberden's nodes when located on the distal interphalangeal joints and Bouchard's nodes when located on the proximal interphalangeal joints.

Whole-body scanning is ideally suited to the diagnosis of multiple joint involvement spread in the lumbar spine, knees, fingers, wrists, and ankles (Fig. 9.52). On the other hand, pinhole scintigraphy permits semiquantitative assessment of the extent and activity of individual arthritis by observing the intensity of tracer uptake in the individual arthritis (Fig. 9.53). Thus, arthritis in the active phase accumulates tracer intensely and in the dormant phase accumulates little tracer.

9.13 Degeneration-Related Disorders of the Spine

The disorders of this category include diffuse idiopathic skeletal hyperostosis (DISH), ossification of the posterior longitudinal ligament (OPPL), Schmorl's nodes, and limbus vertebra as well as spondylolysis and spondylolisthesis, and these constitute interesting objectives of bone scintigraphy that can simultaneously provide information on not only the anatomy but also the metabolic state of the individual conditions.

9.13.1 Diffuse Idiopathic Skeletal Hyperostosis

DISH, previously known as ankylosing hyperostosis of the spine and Forestier's disease, is characterized by bony proliferation at the site of tendon and ligament attachment to bone (entheses), calcification and ossification of the anterior longitudinal ligaments, and diskovertebral osteophytosis. This is a common but not insignificant disease of the spine and extraspinal skeleton. The etiology has not been established, but some investigators consider that it may be associated with degenerative process. There are three radiographic features proposed by Resnick and Niwayama (1976) as important prerequisites for the diagnosis of DISH (Figs. 9.54A and 9.55A). They include (1) the presence of flowing type calcification and ossification along the anterolateral aspects of four

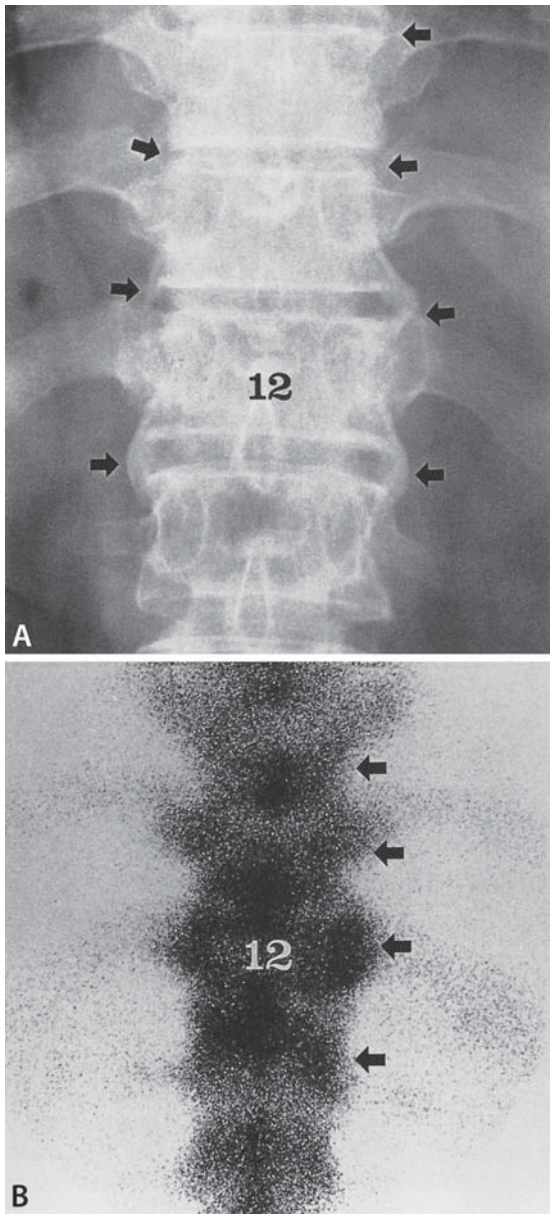

Fig. 9.54A, B Diffuse idiopathic skeletal hyperostosis (DISH). **A** Anteroposterior radiograph of the thoracolumbar spine in a 45-year-old man with DISH shows flowing ossification along the lateral aspects of T8–L1 vertebrae (*arrows*). Vertebral endplates and disk spaces appear preserved and the sacroiliac joints are not involved (not shown here). The radiograph is printed with the right side on the left to match the scintigraph. **B** Posterior pinhole scan shows intense tracer uptake in the costovertebral-apophyseal joints as well as the spinous processes of the thoracolumbar spine and less intense tracer uptake in the other vertebral elements (*arrows*). The individual vertebrae and disk spaces are not clearly discernible. Tracer uptake is disproportionately intense compared to relatively unimpressive radiographic changes (see Fig. 9.55)

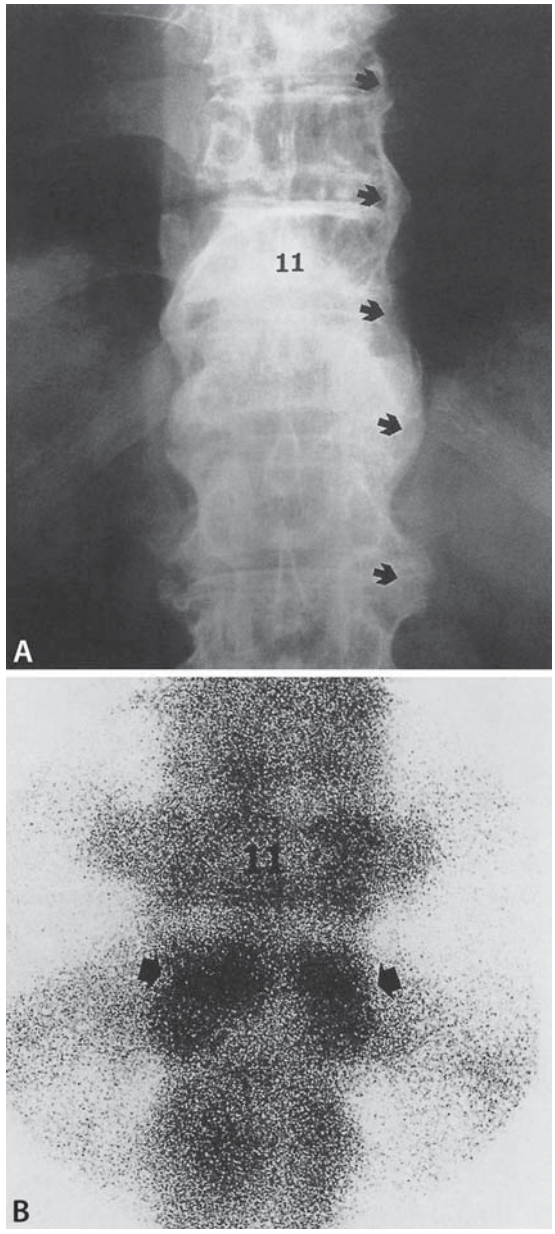

Fig. 9.55A, B Relatively low tracer uptake in more mature diffuse idiopathic skeletal hyperostosis (DISH). **A** Anteroposterior radiograph of the thoracolumbar spine in a 74-year-old man with DISH shows dense, flowing, paraspinal ossifications diffusely involving T9 through L2 vertebrae. The ossification is much more advanced than that of the case shown in Fig. 9.54. The radiograph is printed with the right side to the left to match the scintigraph. **B** Posterior pinhole scintigraph paradoxically shows generally reduced tracer uptake. The individual vertebrae and disk spaces are discernible. Isolated, intense tracer uptake in the costovertebral-apophyseal joints of T12 may denote the residual foci with an active pathology (*arrows*)

or more contiguous vertebral bodies with or without associated focal excrescences at the intervertebral level, (2) relatively preserved disk spaces without radiographic evidence of extensive disk degeneration such as the vacuum phenomenon or sclerosis, and (3) the absence of apophyseal and sacroiliac joint obliteration due to erosion, sclerosis, and bony fusion. The last feature distinguishes DISH from ankylosing spondylitis. In addition to the spine, the pelvis, trochanter, patella, calcaneus, and olecranon process are frequently involved. Osseous proliferation occurs at the entheses, producing the characteristic "whisker" sign.

Generally, scintigraphic manifestations of DISH are too subtle and complex to be recognized by ordinary scintigraphy (Paquin et al. 1983). With the aid of pinhole scintigraphy, however, DISH can be indicated more specifically by tracer uptake in the anterior and lateral aspects of vertebral bodies and disk spaces as well as the spinous processes, most commonly in the thoracic and lumbar spine. Interestingly, tracer accumulates relatively more intensely in the anterolateral aspect of the vertebral bodies than the disk spaces where radiographic hyperostosis with a bumpy contour occurs most prominently (Fig. 9.54B). Like hyperostoses elsewhere, anatomically unimpressive bony excrescences in DISH intensely accumulate tracer, obscuring the vertebral contour and disk spaces (Fig. 9.54), but larger ones accumulate little tracer rendering the spinal contour and disk spaces clearly portrayed (Fig. 9.55).

9.13.2 Ossification of the Posterior Longitudinal Ligament

Ossification of the posterior longitudinal ligament (OPLL) is an idiopathic disorder of the spine, in which calcification or ossification of various lengths occurs in the posterior longitudinal ligament. The middle cervical spine, T3 through T6, is most commonly affected. Pathologically, the condition is characterized by bony overgrowth of the ligament that is attached to the posterior surface of the vertebral body and intervertebral disk, compressing and flattening the spinal cord behind. The lesional bones are

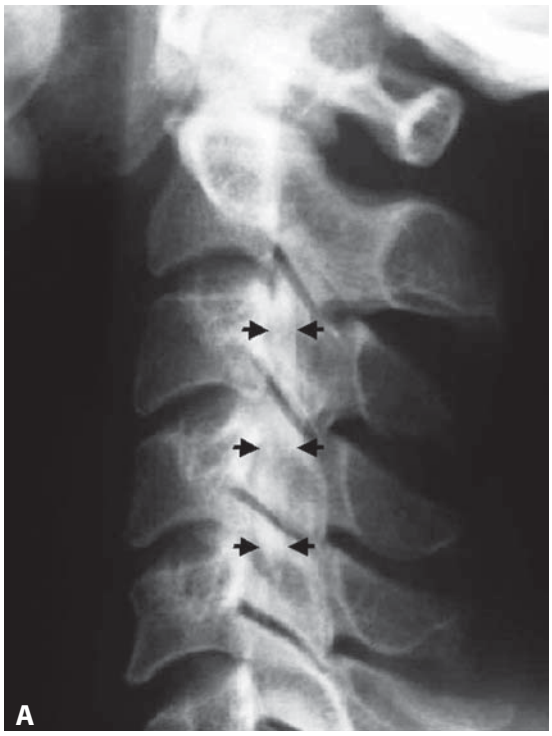

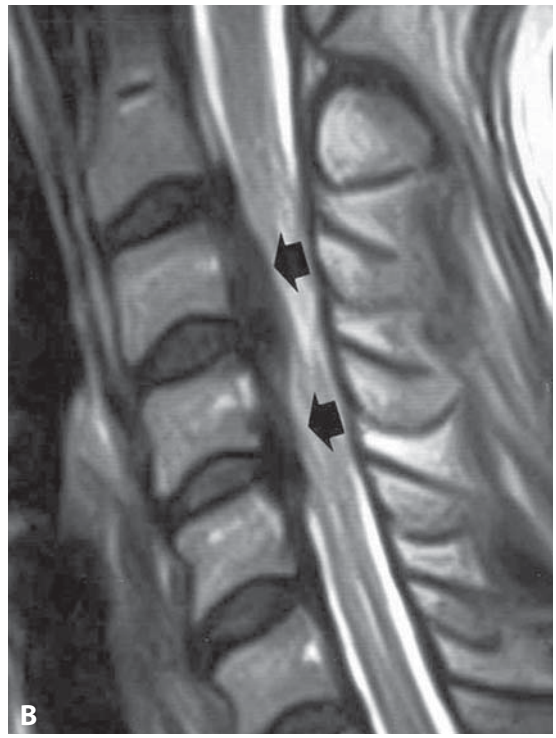

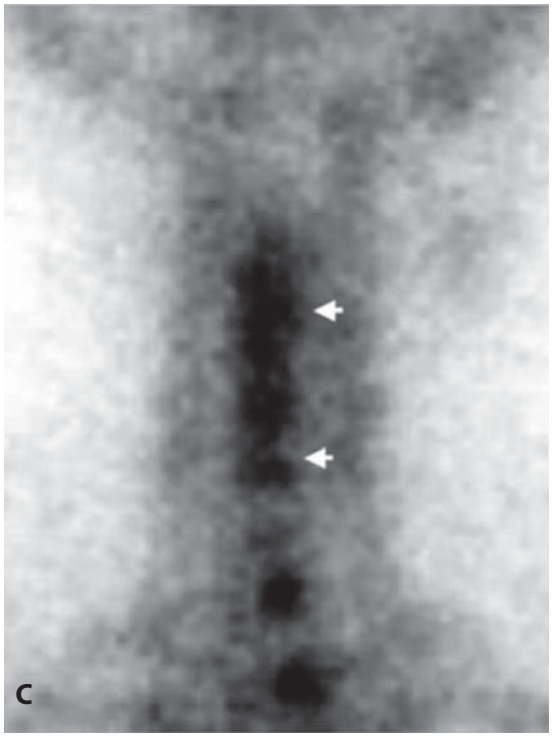

Fig. 9.56A–C Ossification of the posterior longitudinal ligament (OPLL). **A** Lateral radiograph of the cervical spine in a 46-year-old female shows vertical, plaque-like ossification attached to the posterior surface of the middle cervical vertebral bodies (*arrows*). **B** T2-weighted MRI reveals undulating low signal intensity of mineralized ligament posteriorly demarcated by bright signal of cerebrospinal fluid (*arrows*). C Posterior bone scan shows longitudinal tracer uptake in OPLL in the midline of the cervical spine (*arrows*)

lamellated with well-developed Haversian canals but poorly formed marrow (Ono et al. 1977). The most typical lesion occurs in the cervical spine, although other levels are not exempted. It is a fairly common disorder with prevalence rates of 2–4% in the middle-aged and older populations in Asian countries (Ogata and Kawaguchi 2004). The disorder may pass symptomlessly or cause numbness and tingling pain in the fingers, head and neck pain, and severe anesthesia of the trunk and lower extremities.

The characteristic radiographic features include vertical, plaque-like ossification that is either closely or loosely attached to the posterior surfaces of cervical vertebral bodies and disk spaces (Fig. 9.56A). T2-weighted MRI presents the calcified ligament as an undulating elonga-

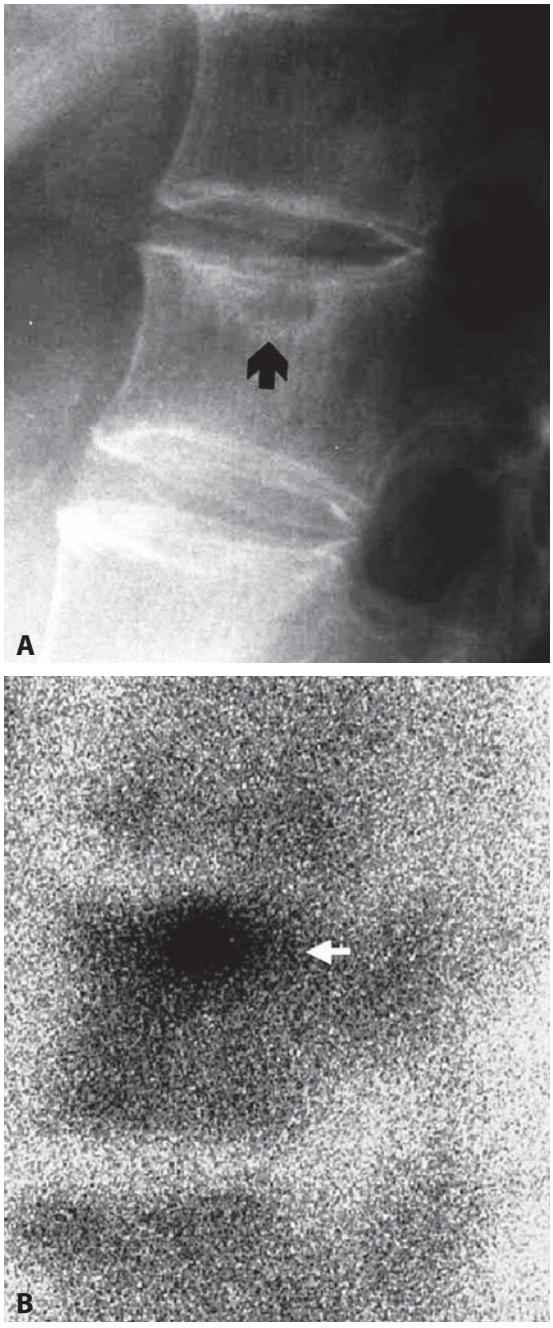

Fig. 9.57A, B Fresh Schmorl's node. **A** Lateral radiograph of L3 in a 60-year-old female with back pain shows an ill-defined ovoid bone defect within the vertebral body beneath slightly depressed endplate (*arrow*). **B** Lateral pinhole scan reveals an ovoid area of intense uptake, the border of which is unsharp (*arrow*)

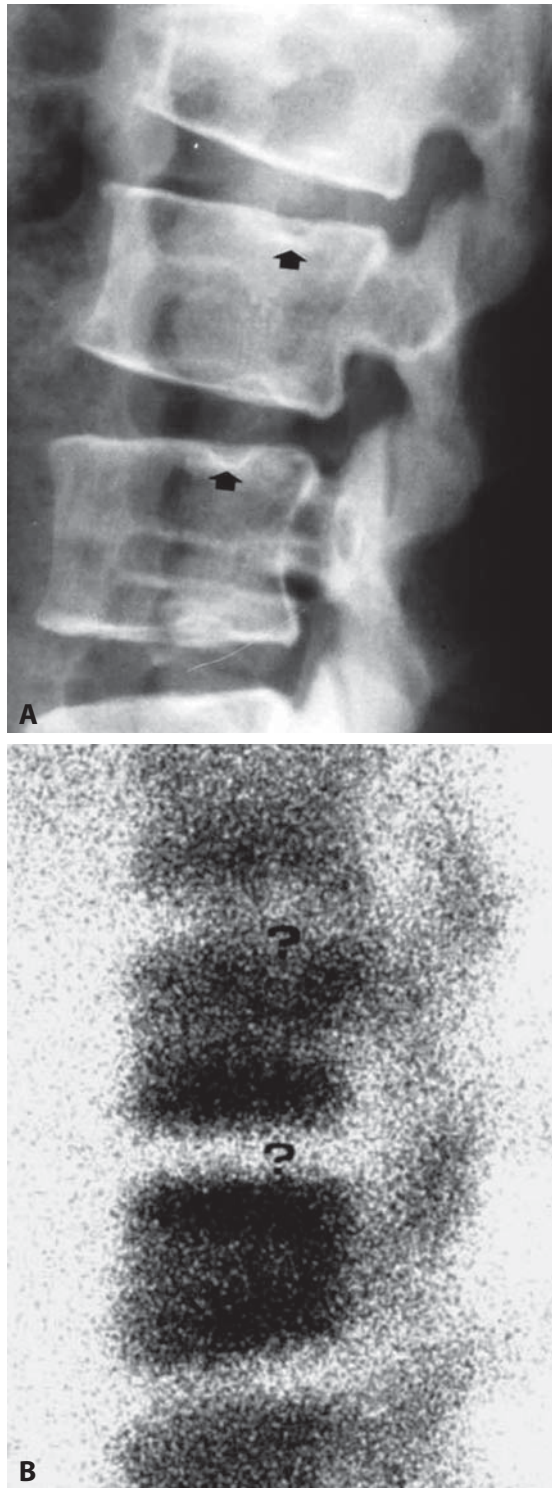

Fig. 9.58A, B Old Schmorl's nodes. **A** Lateral radiograph of the midlumbar spine in a 33-year-old female shows nail print-like sclerosis in the centroposterior parts of L3 and L4 vertebral endplates (*arrows*). **B** Lateral pinhole scan reveals abnormal tracer uptake (*?*)

ted plaque of low signal intensity demarcated by bright signal intensity of the surrounding cerebrospinal fluid (Fig. 9.56B). Posterior bone scintigraphy of the neck may reveal a longitudinal strip of increased tracer uptake in the midline of the cervical spine (Fig. 9.56C).

9.13.3 Schmorl's Cartilaginous Node

Schmorl's node is the dislocation of the denatured nucleus pulposus into vertebral cancellous bone through the weakened annulus fibrosus and diskovertebral junction, creating an intravertebral defect surrounded by eburnation. Nodes are often seen in association with diskovertebral osteochondrosis, trauma, osteoporosis, or Scheuermann's disease.

Radiographically, Schmorl's node presents as an ovoid or roundish defect within the vertebral body beneath the endplate. The outline is ill-defined and irregular when the lesion is relatively fresh (Figs. 9.57A) and sclerotic and well-defined when old (Fig. 9.58A). The disk spaces are narrowed and endplates are eroded and sclerotic. Pinhole scintigraphy shows disk space narrowing with increased endplate uptake. Schmorl's nodes are denoted by spotty or ovoid "hot" area (Figs. 9.57B and 9.59A). The intensity of tracer uptake appears to be related to the age and size of the node: large and poorly defined nodes tend to accumulate tracer intensely (Fig. 9.57B), whereas small, well-defined, sclerotic nodes accumulate little tracer (Fig. 9.58B). CT presents the node as a hypodense area within the cancellous bone surrounded by a hyperdense rim (Fig. 9.59B).

9.13.4 Limbus Vertebra

Limbus vertebra is the marginal dislocation of nucleus pulposus, another mode of disk herniation. It occurs typically in the anterior or posterior edge of the vertebral body, radiographically manifesting as the division of a small fragment with a cleavage (Fig. 9.60A). A fragment is not present in every case (Fig. 9.61A). Pinhole scintigraphically, the limbus with sclerosis is characterized by intense uptake localized to the anterior or posterior edge of an endplate, beaking outward when

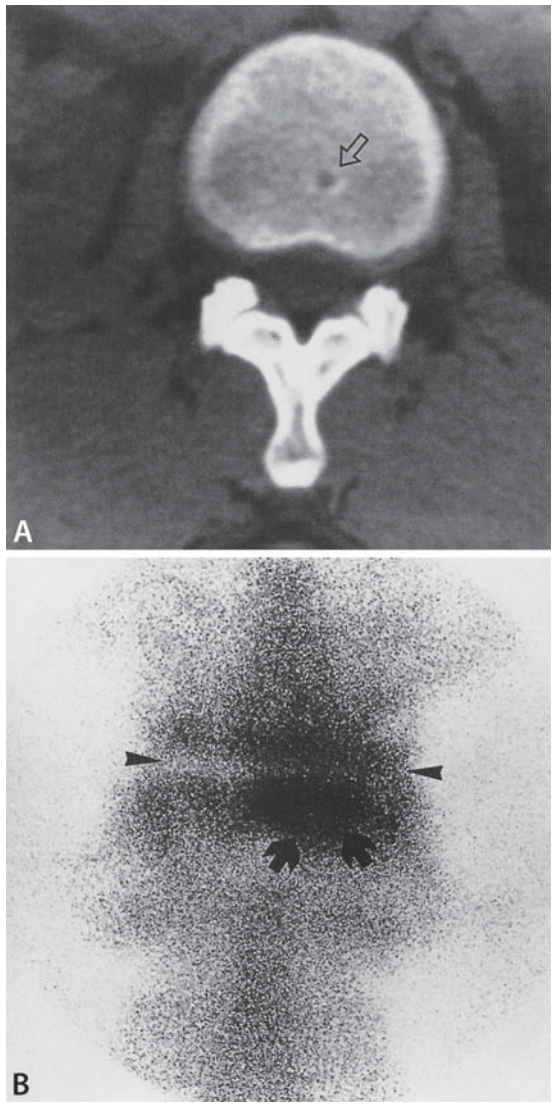

Fig. 9.59A, B Schmorl's node. **A** Axial CT scan through the upper part of the LI vertebra shows a small, round lucency surrounded by a sclerotic rim in the cancellous bone (*open arrow*). **B** Posterior pinhole scan shows very intense tracer uptake surrounded by less intense uptake zone in the right centrolateral aspect of the upper endplate of the LI vertebra, matching the CT scan defect (*arrows*). The disk space is moderately narrowed and the regional endplates concentrate tracer intensely due to associated osteochondrosis (*arrowheads*)

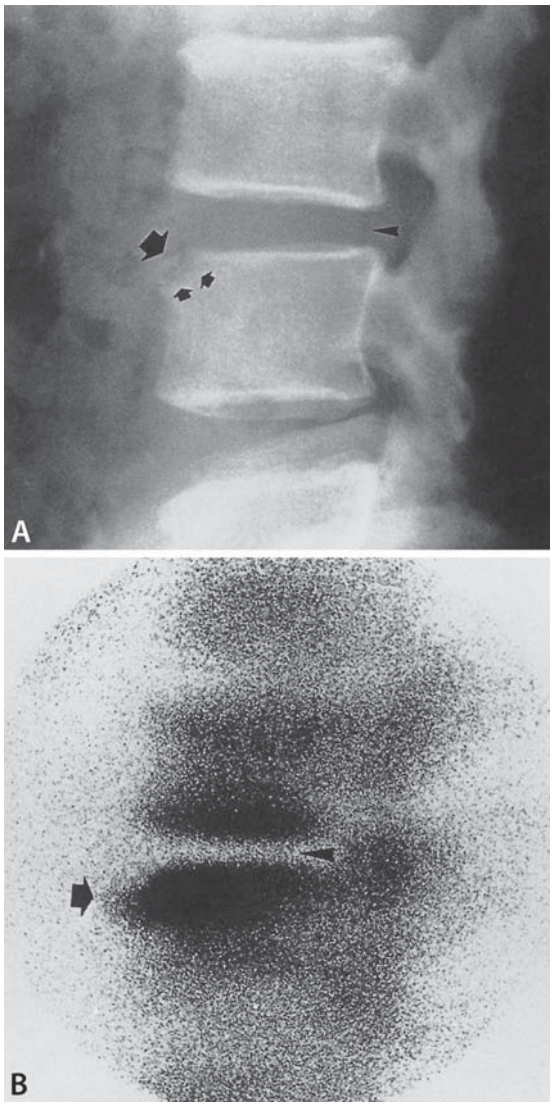

Fig. 9.60A, B Limbus vertebra. **A** Lateral radiograph of the L5 vertebra in a 53-year-old man with back pain reveals a small bone chip (*large arrow*) that is incompletely detached from the upper anterior edge with a lucent cleavage (*small arrows*). The disk space is slightly narrowed (*arrowhead*). **B** Lateral pinhole scintigraph shows very intense tracer uptake surrounded by less intense uptake in the area under study (*arrow*). The affected upper endplate of L5 and the apposing lower endplate of L4 concentrate tracer intensely with narrowed disk space between, indicating early osteochondrosis that may well be related to disk herniation (*arrowhead*)

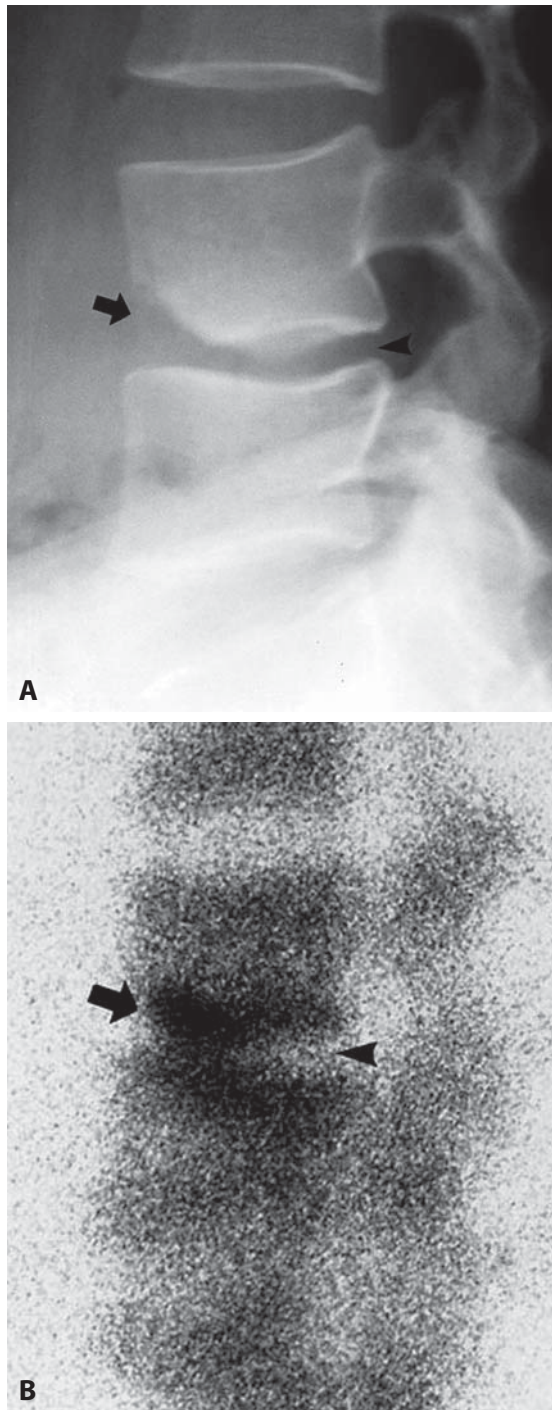

Fig. 9.61A, B Limbus vertebra with infraction. **A** Lateral radiograph of the lumbar spine in a 31-year-old female with low-back pain shows a triangular bone defect in the anterior edge of L4 lower endplate (*arrow*). The disk space is narrowed and the endplates sclerotic (*arrowhead*). **B** Lateral pinhole scan reveals intense tracer uptake in the triangular defect and sclerosed endplates with narrowing of the disk space (*arrowhead*)

fragmented (Fig. 9.60B). Apposing endplates show increased uptake and the disk space between is narrowed, reflecting diskovertebral osteochondrosis and disk degeneration.

9.13.5 Spondylolysis

Spondylolysis refers to the bone defect in the pars interarticularis. It is caused by repeated trauma or physical stress to the biomechanically vulnerable lamina between the superior and inferior articular facets. Spondylolysis divides a vertebra into the superior and inferior segment. The former segment includes the vertebral body, pedicles, transverse processes, and superior articular facet and the latter the inferior articular facet, laminae, and spinous process. Spondylolysis is an important disease that causes lasting low-back pain, especially in gymnasts (Jackson et al. 1976; Collier et al. 1985). The incidence ranges from 3% to 10%. A hereditary trait has been reported (Jackson et al. 1976).

Radiographic features vary according to disease stage: (a) osteopenic band in the early stage, (b) obvious bone defect across the lamina in the established stage, and (c) reactive sclerosis or callus formation and bony reunion in the late and cured stage (Fig. 9.62A). Spondylolysis, the bilateral form in particular, is frequently complicated by the anterior slippage or spondylolisthesis of the superior segment of the divided vertebra. CT is ideal for accurate anatomical investigation of spondylolysis and its associated lesions such as disk herniation, intervertebral foraminal narrowing, and neural canal indentation. MRI is another excellent modality for diagnosing bone defect, disk herniation, nerve compression, and soft-tissue changes.

Planar scintigraphy is not so helpful in defining bone defects because many fail to accumulate tracer visibly (Lusins et al. 1994). Furthermore, there is no predictable pattern of correlation between the radiographic and scintigraphic findings (Gelfand et al. 1981). Indeed, we performed pinhole scintigraphy in seven patients with proven spondylolysis, but none yielded a positive result (Fig. 9.62B).

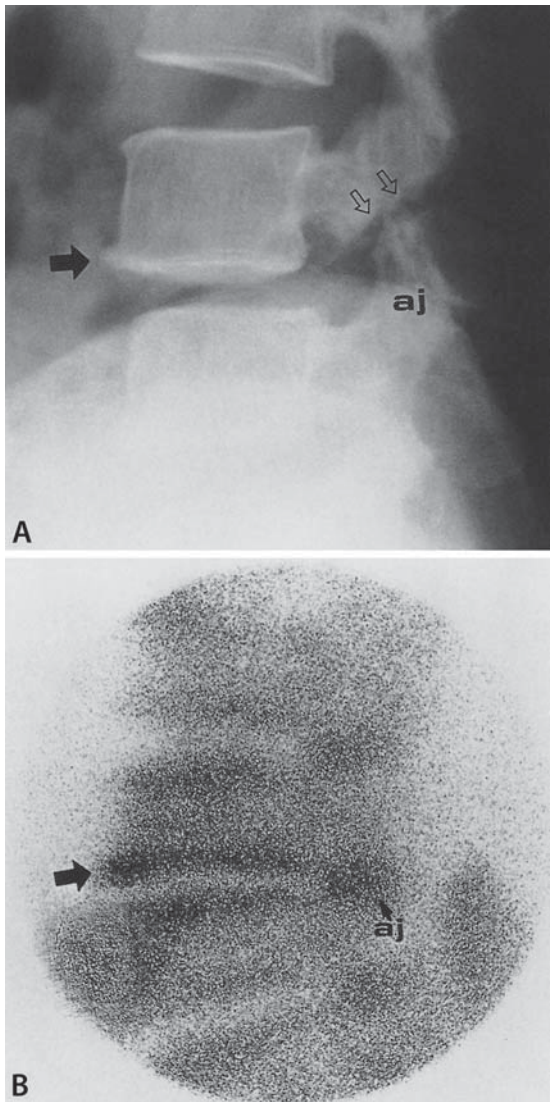

Fig. 9.62A, B Spondylolysis and spondylolisthesis. **A** Lateral radiograph of L4 and L5 vertebrae in a 45-year-old man with back pain shows a large bone defect involving the pars interarticularis of the L4 vertebra (*open arrows*) and mild anterior sliding. A small osteophyte is seen (*arrow*) (*aj* apophyseal joint). **B** Lateral pinhole scintigraph portrays no abnormal tracer uptake in the spondylolysis defect. However, the anterior sliding of the L4 vertebra is clearly delineated by virtue of increased tracer uptake in the osteophyte and lower endplate, the sign of the secondary osteochondrosis (*arrow*)

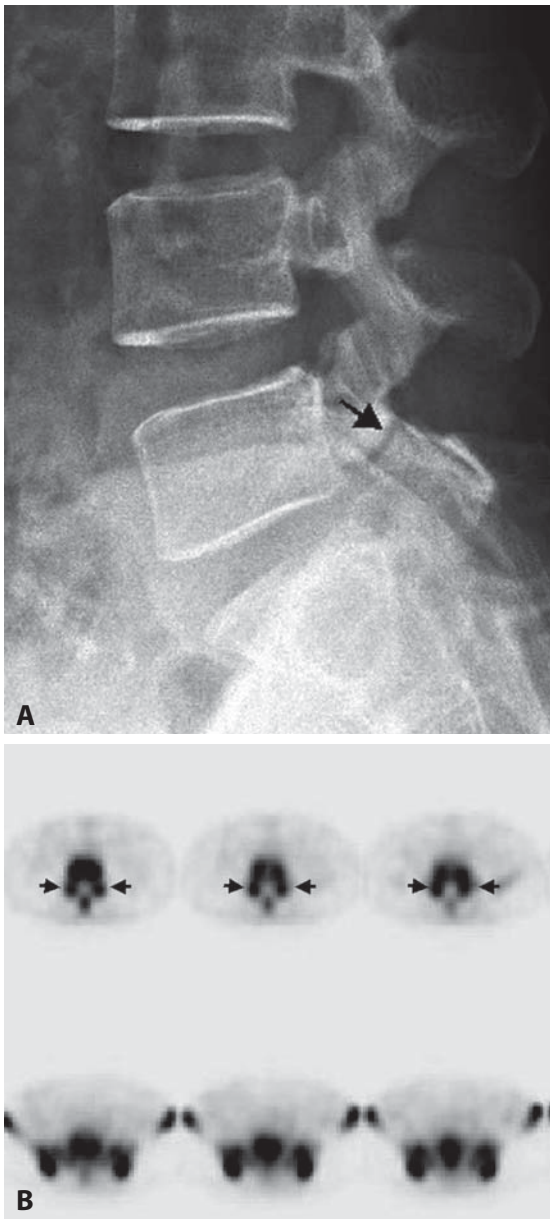

Fig. 9.63A, B High-resolution SPECT of acute spondylolysis. **A** Lateral radiograph of L5–S1 in a 41-year-old female with sudden back pain shows a band-like bone defect across the pars interarticularis (*arrow*). **B** High-resolution SPECT demonstrates small ovoid "hot" areas in the pars interarticularis bilaterally (*arrow*)

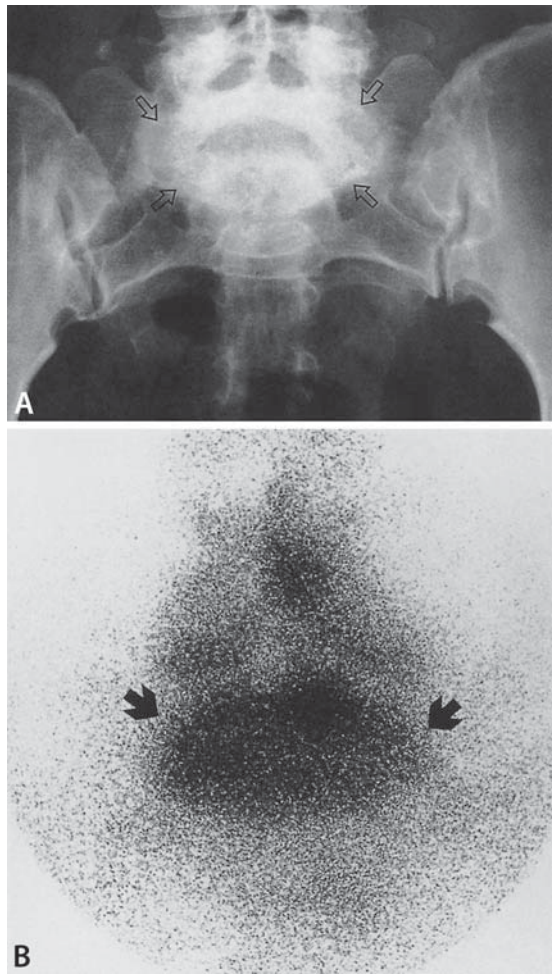

Fig. 9.64A, B Spondylolisthesis. **A** Anteroposterior radiograph of the lumbosacral spine in a 47-year-old man with disabling back pain demonstrates an ovoid "double bone density" overlapping the base of the sacrum (*open arrows*). **B** Anterior pinhole scintigraph shows the characteristic "ovoid vertebra" sign, indicating anterior and downward sliding of the L5 vertebra (*arrows*)

Spondylosis appears to be one of uncommon situations in which pinhole scintigraphy makes little contribution to the diagnosis. The likelier reasons are that the collimator-to-object distance is too great to image a small defect in the pars interarticularis and that old defects do not concentrate tracer visibly (Collier et al. 1985; Lusins et al. 1994). High-resolution SPECT can be recommended for acute spondylolysis as it can eliminate overlap, enhancing image contrast (Fig. 9.63). However, it is not useful for ancient or healed lesions (Collier et al. 1985; Lusins et al. 1994).

9.13.6 Spondylolisthesis

Spondylolisthesis denotes the sliding of one vertebra upon another either in the anterior or posterior direction (retrolisthesis). The sliding may be associated with spondylolysis or degenerative diseases such as apophyseal osteoarthritis and diskovertebral osteoarthritis. The latter type is aptly termed degenerative spondylolisthesis or spondylolisthesis with intact neural arch.

Radiographic features include vertebral slippage and endplate eburnation, most commonly in the two lowermost lumbar vertebrae and the lumbosacral joint (Figs. 9.62A and 9.64A). The anterior downward tilt of the displaced vertebral body seen on the lateral view is another diagnostic sign. On the anterior view the downward tilt is indicated by the change of quadrilateral shape of the vertebral body into ovoid shape, arbitrarily termed the "ovoid vertebra" sign. Interestingly, pinhole scintigraphy shows prominent uptake in the ovoid vertebra, which is densely sclerosed (Fig. 9.64B).

References

Bahk YW, Park YH, Chung SK, Kim SH, Shinn KS (1994) Pinhole scintigraphic sign of chondromalacia patellae in older subjects: a prospective assessment with differential diagnosis. J Nucl Med 35:855–862

Brower AC (1988) The sacroiliac joint. In: Arthritis in black and white. WB Saunders, Philadelphia, pp 103–120

Cicuttini FM, Spector TD (1997) What is the evidence that osteoarthritis is genetically determined? Bailieres Clin Rheumatol 11:657–669

Collier BD, Johnson RP, Carrera BF, et al (1985) Painful spondylolysis and spondylolisthesis studied by radiography and single photon emission tomography. Radiology 54:207–211

de Palma AF (1957) Degenerative change in sternoclavicular and acromioclavicular joints in various decades. Charles C Thomas, Springfield

Dye SF, Boll DA (1986) Radionuclide imaging of the patellofemoral joint in young adults with anterior knee pain. Orthop Clin North Am 17:249–262

Gelfand MJ, Strife JL, Kereiakes JG (1981) Radionuclide bone imaging in spondylolysis of the lumbar spine in children. Radiology 140:191–195

Goodfellow J, Hungerford DS, Woods C (1976) Patello-femoral joint mechanics and pathology: 2. Chondromalacia patellae. J Bone Joint Surg Br 58:291–299

Howell DS, Sapolsky AL, Pita JC, Woessner JF (1976) The pathogenesis of osteoarthritis. Semin Arthritis Rheum 4:365–383

Jackson DW, Wilste LL, Cirincoine RJ (1976) Spondylolysis in the female gymnast. Clin Orthop 117:68–73

Kellgren JH, Moore R (1952) Generalized osteoarthrosis and Heberden's nodes. Br Med J 1:181–187

Kellgren JH, Lawrence JS, Bier F (1963) Genetic factors in generalized osteoarthrosis. Ann Rheum Dis 22:237–255

Lawson JP, Ogden JA, Sella E, Barwick KW (1984) The painful accessory navicular. Skeletal Radiol 12:250–266

Lund F, Nilsson BE (1980) Radiologic evaluation of chondromalacia patellae. Acta Radiol Diagn 21:413–416

Lusins JO, Elting JJ, Cicoria AD, Goldsmith SJ (1994) SPECT evaluation of lumbar spondylolysis and spondylolisthesis. Spine 19:608–612

Mitchel NS, Cruess RL (1977) Classification of degenerative arthritis. Can Med Assoc J 117:763–765

Ogata N, Kawaguchi H (2004) Ossification of the posterior longitudinal ligament of spine (OPLL). Clin Calcium 14:42–48

Ono K, Ota H, Tada K, et al (1977) Ossification of the posterior longitudinal ligament. Spine 2:126–138

Paquin J, Rosenthall L, Esdaile J, et al (1983) Elevated uptake of ^{99m}technetium methylene diphosphonate in the axial skeleton in ankylosing spondylitis and Reiter's disease: implications for quantitative sacroiliac scintigraphy. Arthritis Rheum 26:217–220

Radin EL, Paul IL, Rose RM (1977) Current concepts of the etiology of idiopathic osteoarthrosis. Bull Hosp Joint Dis 31:117–120

Resnick D (2002) Degenerative disease of extraspinal locations. In: Resnick D. Diagnosis of bone and joint disorders, 4th edn. WB Saunders, Philadelphia, pp 1271–1381

Resnick D, Niwayama G (1976) Radiographic and pathologic features of spinal involvement in diffuse idiopathic skeletal hyperostosis (DISH). Radiology 119:559–568

Spencer JM, Loughlin J, Clipsham K, Carr AJ (2005) Genetic background increases the risk of hip osteoarthritis. Clin Orthop Relat Res 431:134–137

Wiles P, Andrews PS, Devas MB (1956) Chondromalacia of the patella. J Bone Joint Surg Br 38:95–113

10 Rheumatoid Arthritis

Rheumatoid arthritis is a fairly common systemic disease of multifarious and obscure etiologies, affecting primarily the synovial membranes of the joints in the appendicular and axial skeleton. It has a notorious predilection for the small joints of the hands and feet although the large joints of the wrists, knees, elbows, shoulders, and sternum are not exempted. The involvement is typically polyarticular and symmetrical. In the spine, the cervical vertebrae, particularly the atlantoaxial joint, are most commonly involved, and cervical involvement may or may not be accompanied by appendicular arthritis (Bland 1967). The prevalence rate estimated using the 1958 criteria of the American Rheumatism Association for definite rheumatoid arthritis varies from 0.3% to 1.5% (Wolfe 1968), and limited population studies performed in Europe and North America have indicated the incidence to range from 1% to 3%. A recent limited population study performed in Seoul has shown a prevalence rate of 1.5% (Bae SC, 2005, personal communication). Women are affected two to three times more frequently than men. Adults in any age may be affected, with the highest incidence occurring between the fifth and sixth decades of life.

The clinical diagnosis is based on seven criteria recommended by the American Rheumatism Association: (1) morning stiffness, (2) arthritis of three or more joints, (3) arthritis of hand joints, (4) symmetrical arthritis, (5) rheumatoid nodules, (6) serum rheumatoid factor, and (7) radiological alterations including erosions and/or periarticular osteoporosis in the hand and wrist joints (Arnett et al. 1988). Clinically, the involvement of the small joints in the hands and feet is essential for diagnosis. The next most commonly involved sites are the cervical spine, shoulders, elbows, wrists, hips, knees, and ankles. The sternum, temporomandibular joints, sacroiliac joints, and symphysis pubis are less regularly affected.

Pathology and Laboratory Tests Rheumatoid arthritis initiates as synovitis, which is pathologically characterized by edema, hyperemia, and exudation (Gibson 1955). Prominent cellular infiltration and proliferation of granulation tissue follow. With the progression of disease the synovia become thickened with the enlargement of villi, resulting in pannus formation in the perichondriums. By the action of hydrolytic enzymes, pannus erodes and tears the articular cartilage and subchondral bone at the unprotected marginal zones, and eventually the periarticular ligaments and tendons. In the late stage, disorganized articulations are replaced by fibrous and osseous ankylosis.

A number of laboratory tests are available for the clinical diagnosis of this disease. Accelerated erythrocyte sedimentation rate and increased C-reactive protein and rheumatoid factors are more reliable. The quantitative data are known to be well correlated with the clinical activities of rheumatoid arthritis.

Radiographic Manifestations Radiographic features vary according to the disease stage. In the early stage periarticular soft-tissue swelling and articular widening are observed, reflecting synovial edema and effusion. Periarticular osteopenia is an important finding, which is not regularly observed in osteoarthritis (Fig. 10.1A). Erosion and destruction of the articular carti-

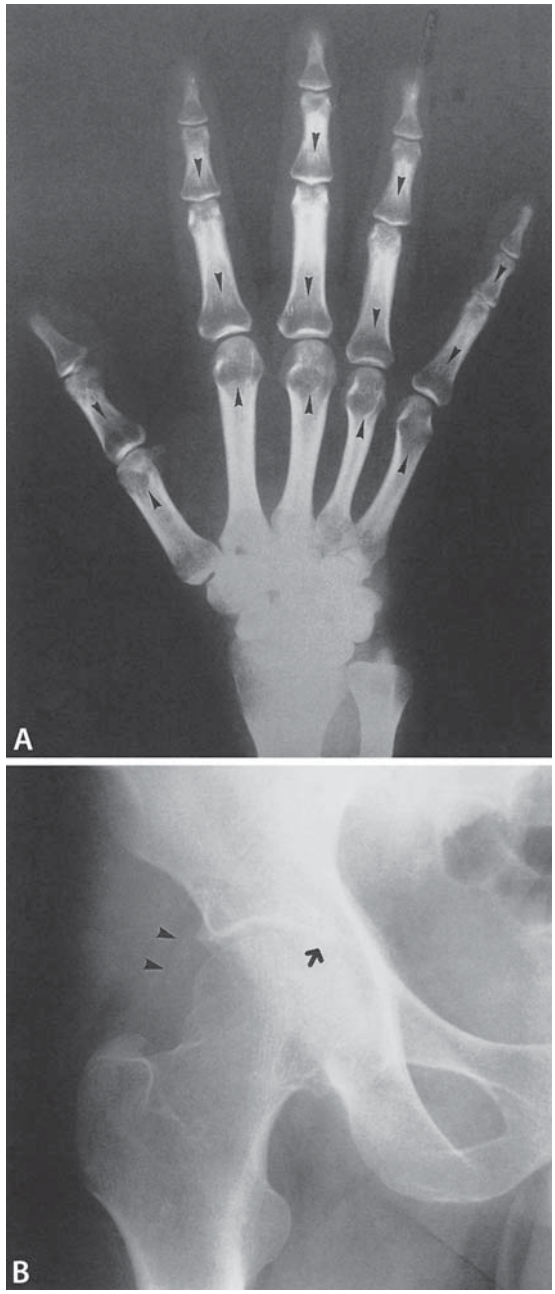

Fig. 10.1A, B Marked periarticular osteoporosis and symmetrical articular narrowing in rheumatoid arthritis. **A** Dorsoventral radiograph of the right hand in a 23-year-old woman with acutely exacerbating rheumatoid arthritis shows marked porosis in the periarticular bones of the proximal interphalangeal joints and metacarpophalangeal joints (*arrowheads*). **B** Anteroposterior radiograph of the right hip in a 44-year-old man with rheumatoid arthritis reveals concentric narrowing of the joint with axial shift of the femoral head (*arrow*). The regional bones are porotic and the articular capsule is distended (*arrowheads*)

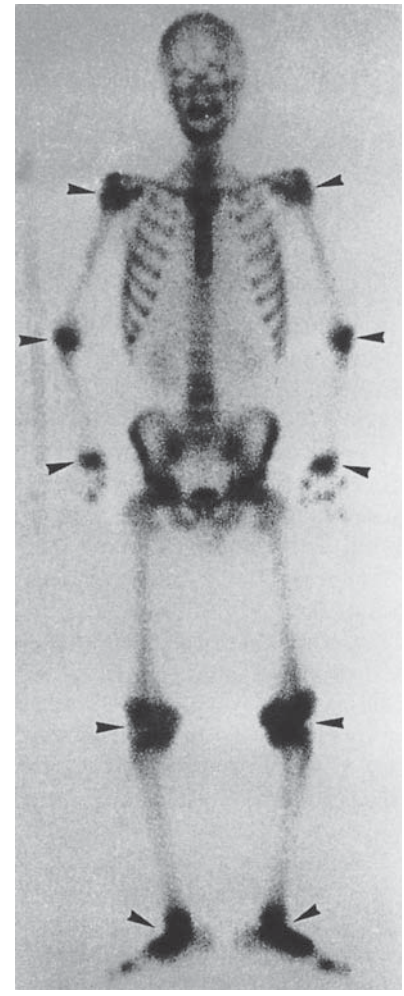

Fig. 10.2 Whole-body survey scintigraphy in polyarthritis. Anterior whole-body scintigraph delineates the classic, symmetrical, polyarticular nature of rheumatoid arthritis. All of the large and small joints in the upper and lower extremities are involved (*arrowheads*)

lage follow with resultant articular narrowing, which is typically concentric and symmetrical (Fig. 10.1B) as opposed to asymmetrical narrowing in osteoarthritis (Fig. 9.10). Erosion and destruction occur in the periphery and center of joints, but tend to more severely involve the peripheral bones that are not protected by cartilage (Fletcher and Rowly 1952). The subchondral bones exposed to pannus after cartilage disintegration are readily eroded and

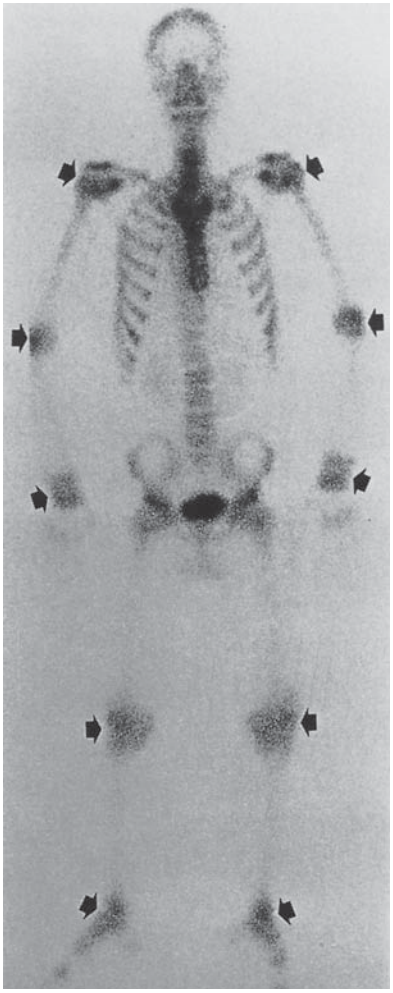

Fig. 10.3 Symmetrical, polyarticular tracer uptake in wheelchair-bound poliomyelitis patient. Anterior whole-body scintigraph in a 35-year-old polio patient confined to a wheelchair (affected at the age of 3 years) with sinewy arms and bust and atrophic lower limbs reveals increased tracer uptake in all extremity joints, strongly mimicking symmetrical, polyarticular uptake pattern of rheumatoid arthritis (*arrows*). Tracer accumulations in the upper limb joints are generally more intense and are attributable to the active, muscular exercise of propelling the wheelchair, whereas those in the lower limb joints are less intense and well attributable to the longstanding disuse in this polio patient. Radiographic studies confirmed the skeletal hypertrophy in the upper limbs and atrophy in the lower limbs (not shown here)

broken, and undergo cystic change. In the late stage the diseased joints are ankylosed with angulation, subluxation, and even dislocation.

Bone Scintigraphic Manifestations ^{99m}Tc-MDP bone scintigraphy is the method of choice for the study of rheumatoid arthritis because it can provide not only holistic information on symmetrical polyarthritic involvement by whole-body scanning but can also show the individual articular changes in great detail by pinhole scanning. Recently, the scintigraphic imaging techniques have been worked out in the form of guidelines (Sandrock et al. 2003).

The whole-body scan reveals increased uptake in all or many of the joints in the extremities (Fig. 10.2). Characteristically, the lesions are polyarticular and symmetrical on both sides of the body with the involvement of the small joints in the hands and feet. The high-resolution spot view or pinhole scan reveals further information, which is often specific. It is worth mentioning that rheumatoid polyarthritis may be strongly simulated on the whole-body scan by increased articular uptake in bed-ridden patients or those on crutches or in a wheelchair due to disuse or excessive use of the upper and lower limbs (Fig. 10.3).

On the other hand, pinhole scintigraphy in early rheumatoid arthritis reveals tracer uptake in the entire synovial cavity of the affected joints, denoting synovitis (Fig. 10.4A). The finding is similar to the "wrapped bone" sign of sympathetic synovitis (Fig. 8.5) or infective synovitis (Fig. 8.14). The articular space at this stage may be widened or unchanged. Periarticular osteopenia is clearly indicated by intense tracer uptake in the bones about the joints (Fig. 10.5). With the progress of the disease process articular cartilages and subchondral bones become disintegrated, resulting in articular narrowing. Rheumatoid erosions in the periarticular bones are shown as patchy or segmental areas of prominent uptake surrounded by a less intense uptake zone. The intensified uptake in the erosions is readily visualized in a large joint occasionally even with demonstration of inflamed para-articular tendons on the pinhole scan (Fig. 10.6). Bony ankylosis, the ultimate outcome of pannus and bone erosions, is indicated by tracer uptake of various intensities according to the age of ankylosis: mar-

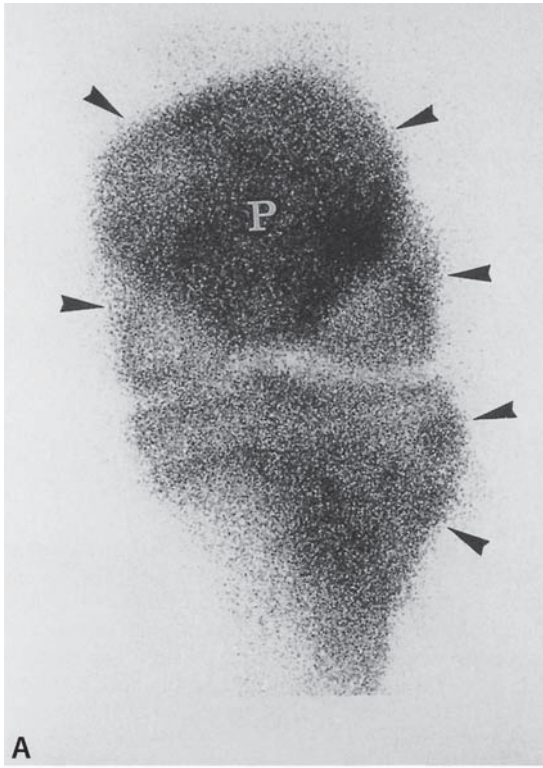

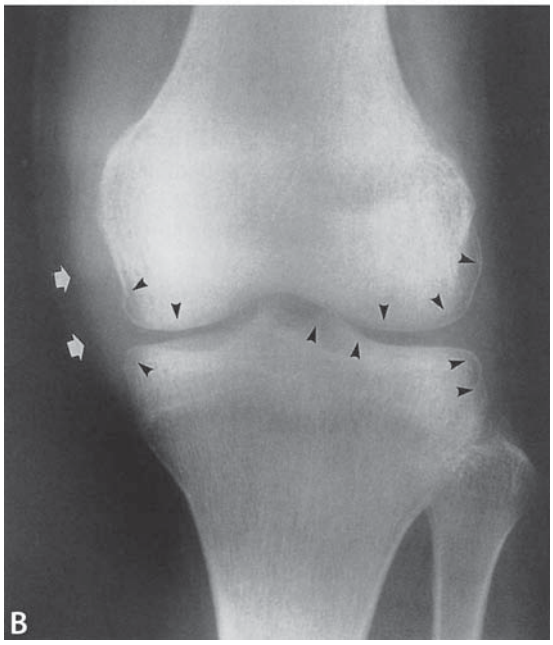

Fig. 10.4A, B Diffuse tracer uptake in the whole periarticular bones, producing a "wrapped bone" appearance in acute rheumatoid synovitis. **A** Anterior pinhole scintigraph of the left knee in an 18-year-old man shows generalized, linear tracer uptake in all periarticular bones (*arrowheads*) including the patella (*P*). The joint space is somewhat widened. **B** Anteroposterior radiograph shows periarticular soft-tissue swelling (*arrows*) and porosis with pencil-line bone profile (*arrowheads*)

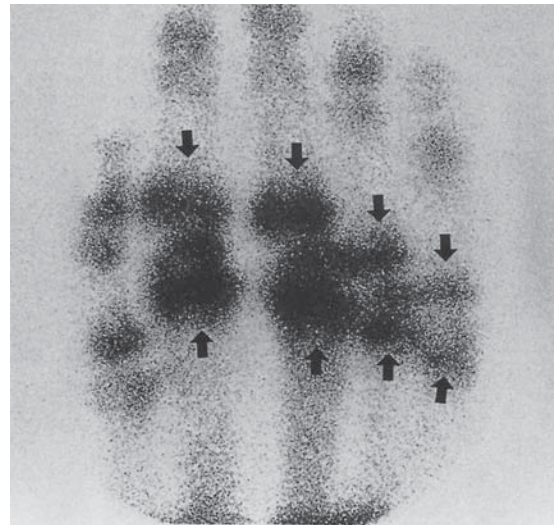

Fig. 10.5 Intense tracer uptake localized in the periarticular osteoporosis in rheumatoid arthritis. Dorsal pinhole scintigraph of the right hand with rheumatoid arthritis (the same patient as in Fig. 10.1A) shows intense tracer uptake localized in the bones about the metacarpophalangeal joints (*arrows*). Rapid diminution of bone size and tracer uptake in the periphery of the image is due to the characteristics of the pinhole geometry and the inverse square law, respectively. Note close correlation between the scintigraphic and radiographic findings

ked uptake in the active stage and mild uptake in the quiescent stage (Fig. 10.7). The traumatization or subluxation of an ankylosed joint results in intense tracer accumulation.

Nuclear angiography is very useful for dynamic assessment of vascular change that sensitively reflects the disease activity of rheumatoid arthritis (Hopfner et al. 2002, 2004) (Fig. 10.8). Recently, molecular nuclear imaging has also been added as a new diagnostic method in rheumatoid arthritis. The radiopharmaceuticals used for this include ^{99m}Tc-anti-E-selectin antibodies, ^{99m}Tc-IgG, radiolabeled cytokines, and somatostatin receptor. In addition, ^{18}F-FDG PET has been introduced as a novel imaging modality in rheumatoid arthritis (Beckers et al. 2004) (Fig. 10.9).

Fig. 10.6 Segmental or patchy tracer uptake in bone erosions and "faint" tracer uptake in tenosynovitis in rheumatoid arthritis. Anterior pinhole scintigraph of the left knee in a 35-year-old woman with established rheumatoid arthritis shows intense, segmental tracer uptake in the tibial plateaus and lateral femoral condyle (*arrows*). Faint but significant tracer uptake can be seen also in the distal biceps femoris tendon, denoting concurrent tenosynovitis (*arrowheads*). These findings were validated by radiography (not shown here)

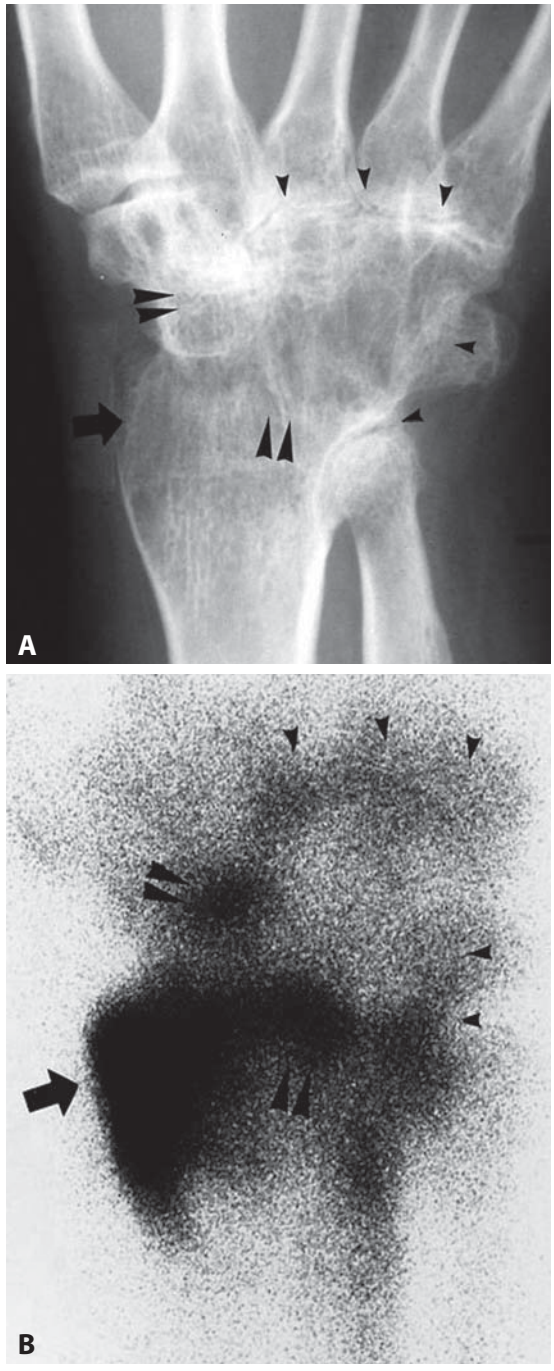

Fig. 10.7A, B Advanced bony ankylosis. **A** Dorsopalmar radiograph of the right wrist in a 39-year-old female shows diffuse sealing of the radiocarpal, intercarpal, and carpometacarpal joints due to bony ankylosis (*arrowheads*). The radial styloid reveals osteopenia with inflamed adjacent tendon (*arrow*). **B** Dorsal pinhole scan demonstrates increased tracer uptake of various intensities in ankylosed wrist joints (*arrowheads*) with conspicuous uptake occurring in the radial styloid that is the site of active inflammation (*arrow*)

10.1 Hand (Fingers)

The early alteration of rheumatoid arthritis has been described to initiate from the second and third metacarpophalangeal joints and the third proximal interphalangeal joint (Fig. 10.10A). As shown in this case, however, the synchronous involvement of the wrist is common. Indeed, wrist involvement is as characteristic and heralding as digital involvement, or is even predominant during the early stages of the disease (Hendrix et al. 1987). Radiography reveals erosion, articular narrowing, and marked po-

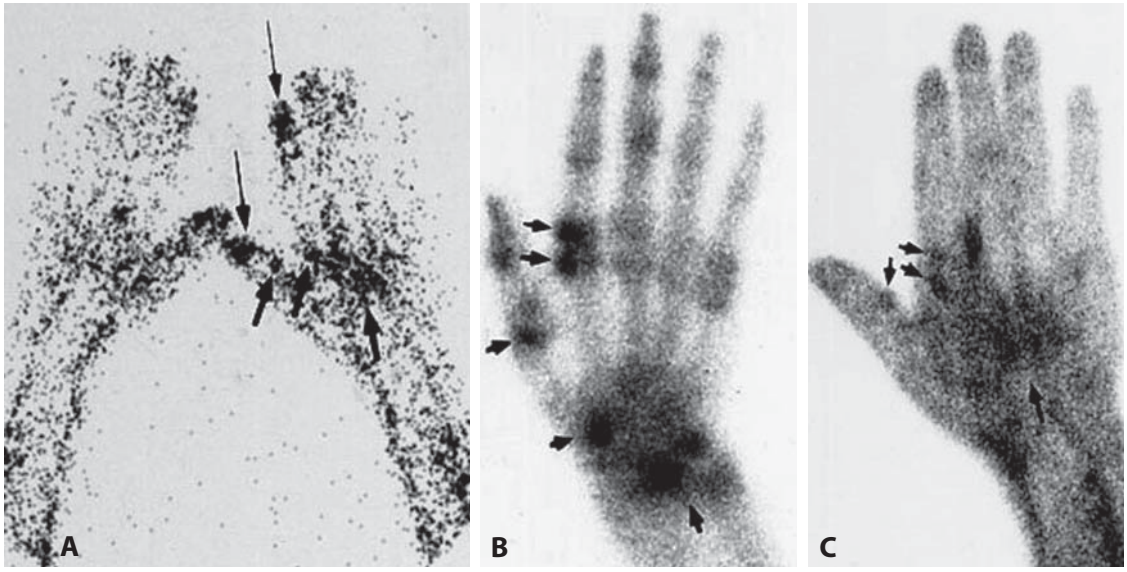

Fig. 10.8A–C Nuclear angiography in rheumatoid arthritis. **A** Blood flow scan of both hands in a 53-year-old male with rheumatoid arthritis shows blotchy areas of increased vascularity in the intercarpal and first through third carpometacarpal joints (*arrows*). **B** Equilibrium scan also reveals increased blood pool (*arrows*). **C** Static bone scan demonstrates increased uptake in the intercarpal and first and second metacarpophalangeal and interphalangeal joints (*arrows*)

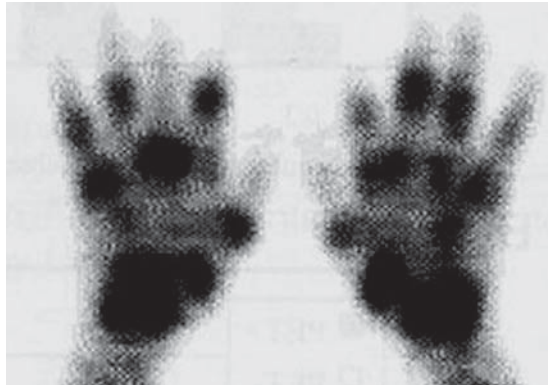

Fig. 10.9 ^{18}F-FDG PET for assessment of rheumatoid arthritis activity. Dorsal PET scans of both wrists and hands show prominent, symmetrical FDG uptake in the carpal and interphalangeal joints (Fig. 1D in Beckers et al. 2004)

rosis. Pinhole scanning shows intense tracer uptake characteristically in the juxta-articular bones, with the joint space being either widened or preserved (Fig. 10.5). The uptake tends to extend beyond the subchondral zones toward the phalangeal and metacarpal shafts, representing the watershed phenomenon. Radiographic correlation reveals that tracer is highly concentrated in the subchondral and periarticular bones, which are markedly osteopenic (Figs. 10.1A and 10.5). When the disease is moderately advanced the joints become narrowed and tracer uptake coalesces across the joints (Fig. 10.7). It is logical that the smaller joints between the phalanges are more readily closed than the larger metacarpophalangeal joints. The intensity of tracer uptake appears roughly parallel with that of pathological changes such as local osteopenia and periarticular swelling. Interestingly, deformity such as subluxation, dislocation, or flexion accumulates tracer most conspicuously, distinguishing it from inactivated ankylosis (Fig. 10.11).

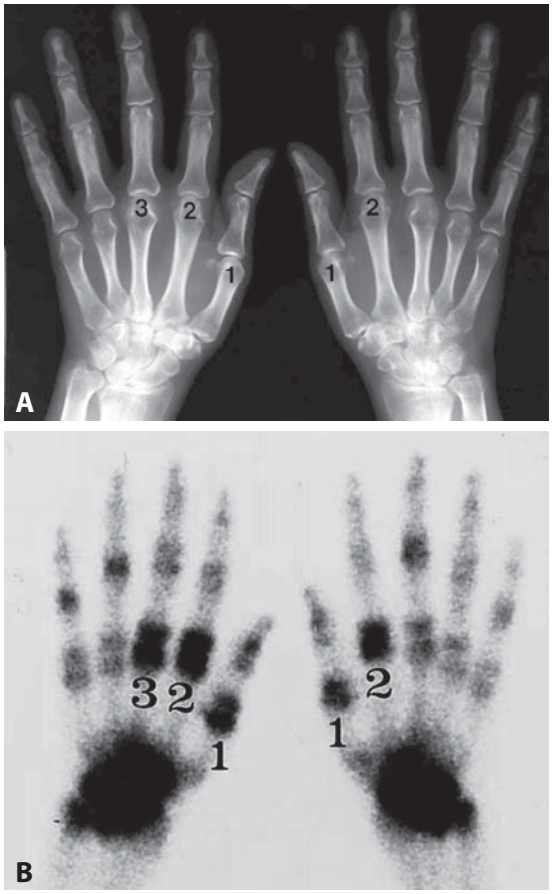

Fig. 10.10A, B Early manifestations of hand rheumatoid arthritis. **A** Dorsopalmar radiographs of hands show classic involvement of the first through third metacarpophalangeal joints (*1, 2, 3*). **B** Dorsal bone scan reveals intense tracer uptake in the diseased metacarpophalangeal joints (*1, 2, 3*)

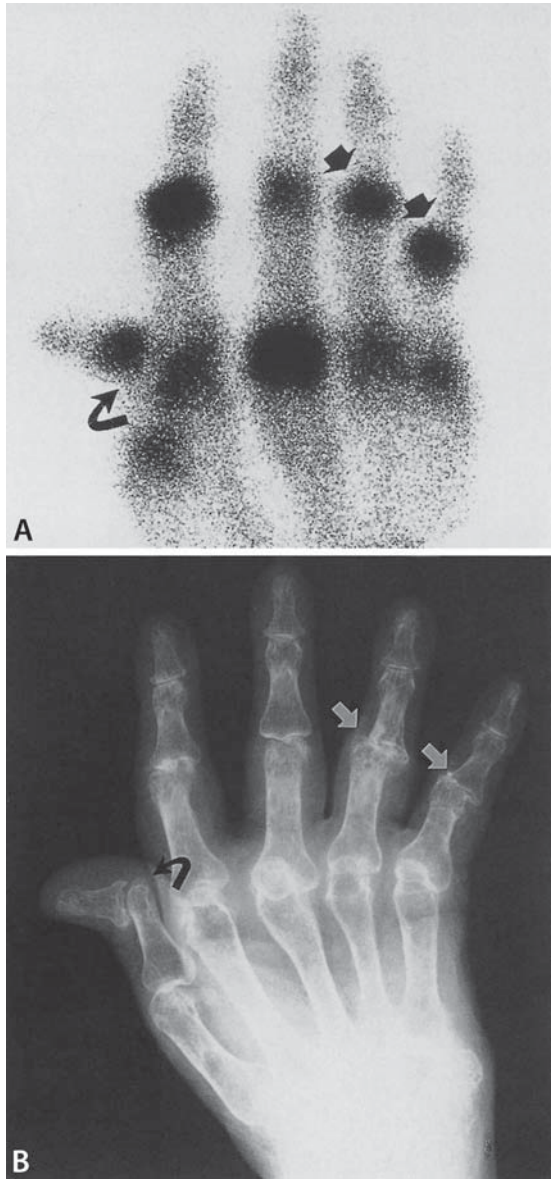

Fig. 10.11A, B Extremely intense tracer uptake in the subluxed, dislocated, and flexed finger joints in deforming rheumatoid arthritis. **A** Dorsal pinhole scan of the right hand in a 76-year-old woman with deforming rheumatoid arthritis reveals very intense tracer uptake in the proximal interphalangeal joints of the index, ring, and little fingers and the metacarpophalangeal joint of the middle finger (*arrows*). The interphalangeal joint of the thumb also concentrates tracer intensely (*curved arrow*). **B** Dorsoventral radiograph shows the subluxation of the proximal interphalangeal joints of the index, ring, and little fingers and the metacarpophalangeal joint of the middle finger (*arrows*) as well as the flexion deformity in the thumb (*curved arrow*)

10.2 Wrist

The involvement of the radiocarpal, distal radioulnar, and prestyloid compartments (Resnick 1974) and the pisiform–triquetral compartment (Resnick 1976) is characteristic of rheumatoid arthritis of the wrist in early stages. While pinhole scans demonstrate significant tracer uptake in the radiocarpal, distal radioulnar, and pisiform–triquetral compartments (Fig. 10.12A) radiographic alterations are subtle and occasionally doubtful (Fig. 10.12B). The

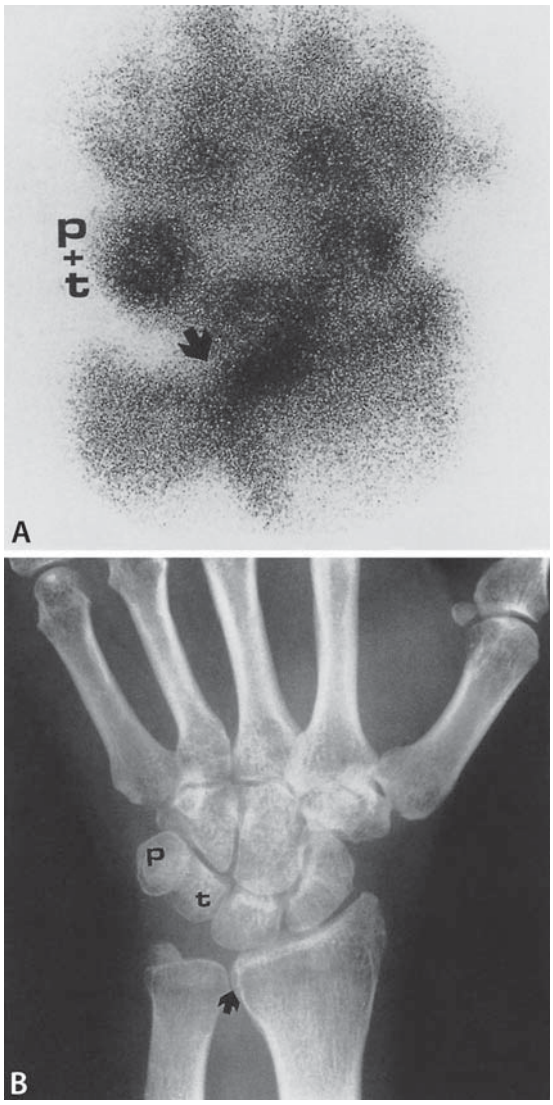

Fig. 10.12A, B Preferential tracer uptake in the distal radioulnar joint and the triquetral and pisiform in rheumatoid arthritis. **A** Dorsal pinhole scintigraph of the left hand in a 45-year-old woman with relatively early rheumatoid arthritis portrays intense tracer uptake in the distal radioulnar joint (*arrow*) and the triquetral and pisiform (*t*+*P*). **B** Dorsoventral radiograph shows diffuse porosis in the carpal bones, especially in the triquetral and pisiform(*P, t*) with narrowed radioulnar joint (*arrow*)

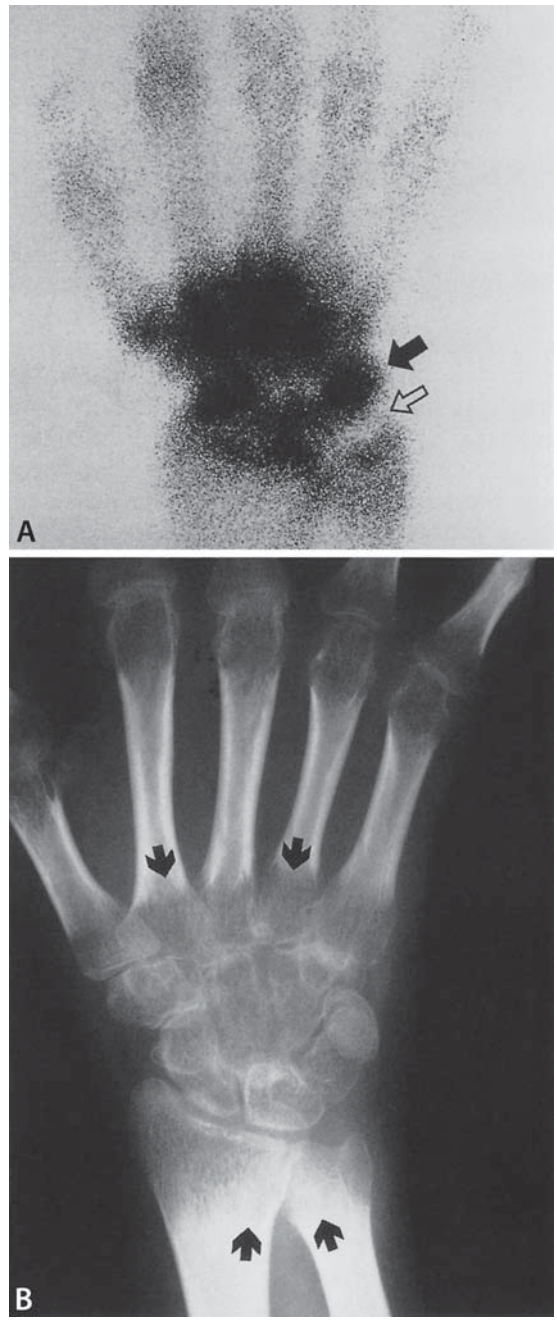

Fig. 10.13A, B Intense tracer uptake in porotic carpal bones. **A** Dorsal pinhole scintigraph of the right hand in a 52-year-old woman with acutely inflamed rheumatoid change attended by severe porosis in the carpus shows intense tracer uptake in the entire carpal bones and the distal radial end. The triquetral–pisiform uptake appears relatively more prominent (*black arrow*), and the prestyloid recess of the radiocarpal compartment is preserved (*open arrow*). **B** Dorsoventral radiograph shows severe porosis in the carpal bones and the distal radius and ulna (*arrows*). The digits are also porotic, but they do not appear "hot" because of rapid fall-off of the count rates in the image periphery

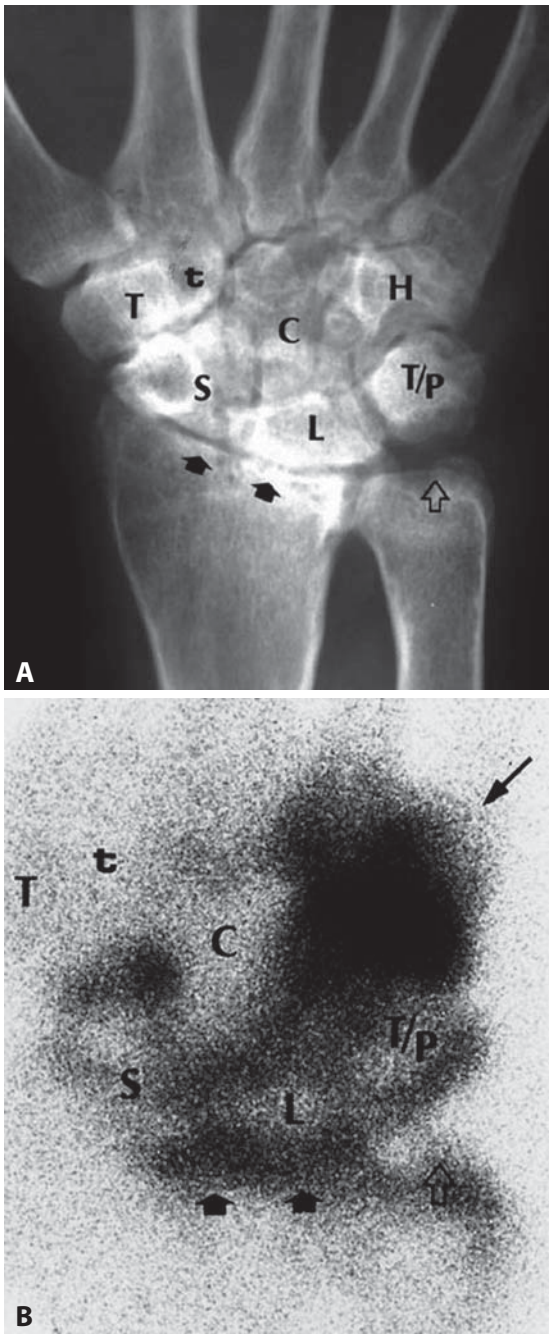

Fig. 10.14A, B Moderately advanced rheumatoid arthritis dominantly affecting the radiocarpal, ulnocarpal, intercarpal, and carpometacarpal joints. **A** Dorsopalmar radiograph of the right wrist in a 48-year-old male with advanced rheumatoid arthritis shows narrowing of the intercarpal joints and the radiocarpal and ulnocarpal joints (*arrows*) (*T* trapezium, *t* trapezoid, *C* capitate, *S* scaphoid, *L* lunate, *T/P* triquetrum/pisiform). **B** Dorsal pinhole scan reveals increased uptake localized to the carpal and wrist joints giving rise to a "Coke on the rocks" appearance. The hamate is buried in intense uptake denoting active inflammation (*arrow*)

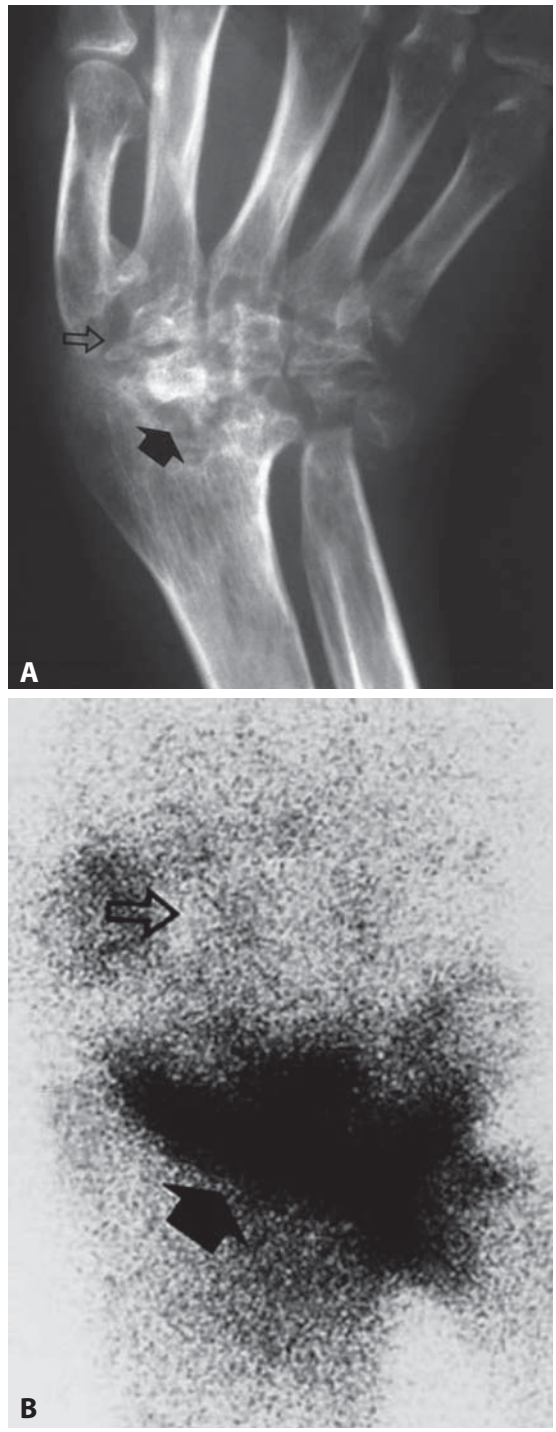

Fig. 10.15A, B Late rheumatoid arthritis. **A** Dorsopalmar radiograph of the right wrist in a 33-year-old female with disfiguring rheumatoid arthritis shows contraction of the entire carpal and carpometacarpal bones and joints with mutilating deformity (*arrows*). **B** Dorsal pinhole scan reveals markedly increased tracer uptake in the wrist joints (*black arrow*) but not in carpometacarpal joints (*open arrow*). The uptake difference reflects diseased activity that cannot be assessed by radiography

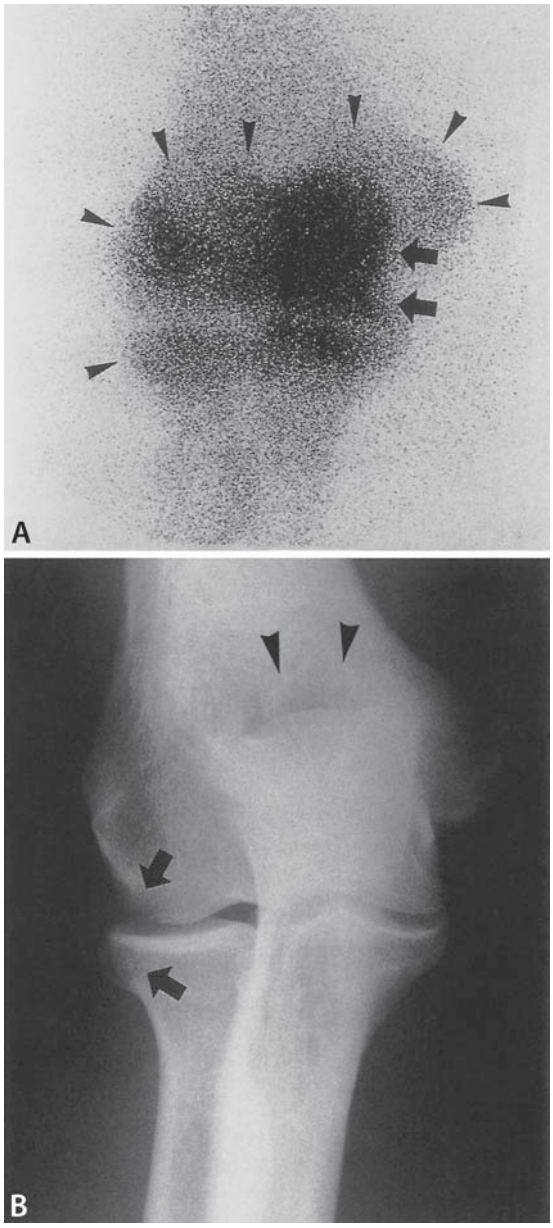

Fig. 10.16A, B Synovitis and periarticular porosis in early rheumatoid arthritis in the elbow. **A** Anterior pinhole scintigraph of the left elbow in a 51-year-old man with rheumatoid synovitis demonstrates diffusely increased tracer uptake in the periarticular bones and the synovial cavity with blurred joint space (*arrowheads*). The more prominent uptake is noted in the olecranon fossa and the trochlear notch, presumably due to the adding effect of synovitis and porosis in this comparatively large synovial joint (*arrows*). The joint space appears preserved. **B** Anteroposterior radiograph delineates prominent porosis in and about the olecranon fossa and trochlear notch (*arrowheads*) as well as in the other periarticular bones (*arrows*)

prestyloid recess, which contains meniscus, may appear unaltered in the early stage of disease. In the active phase of chronic rheumatoid arthritis tracer uptake becomes markedly intensified (Fig. 10.13A). As in the fingers, such prominent uptake is confined to pronounced osteopenia, diffusely darkening the entire wrist. Occasionally, moderately advanced rheumatoid arthritis may present in a different manner, with the radiocarpal, intercarpal, and carpometacarpal joints being clearly shown by increased uptake, giving rise to an appearance that may be likened to "Coke on the rocks" (Fig. 10.14A). The residual arthritic focus with acute inflammation is indicated by a patchy area of increased uptake.

In the much later disfiguring stage the wrist may be transformed into a shrunken block of bones (Fig. 10.15). Tracer uptake may be reminiscent or increased depending upon disease activity. Thus, the locus of acute exacerbation within once inactivated rheumatoid arthritis is indicated by area(s) of extremely intense uptake against the background of little tracer uptake of the contracted wrist (Fig. 10.15). In general, the inflammatory activity of rheumatoid arthritis is not related to the chronicity of the disease, and accordingly florid and dormant lesions can coexist side by side in a joint. It is to be underscored that pinhole scintigraphy can uniquely distinguish active from quiescent lesions of rheumatoid arthritis with accuracy.

10.3 Elbow

The reported incidence of elbow involvement in rheumatoid arthritis varies widely, ranging from 10% to 70%. A study by Freyberg (1968) showed the incidence to be 34%. Synovitis and erosion affect the humeroulnar joint (the olecranon fossa and trochlear notch) and humeroradial joint. Pinhole scans in the early stage show increased uptake localized to the humeroulnar joint and peripheral bones, which are

osteopenic (Fig. 10.16). The finding has a strong resemblance to similar change in early rheumatoid arthritis of the wrist (Fig. 10.12). Chronic active rheumatoid arthritis reveals diffuse tracer accumulation in the whole elbow including the olecranon fossa and notch, the coronoid fossa, the radial fossa, and the proximal radioulnar joint (Fig. 10.17). The eccentric uptake is considered to indicate erosions in the periarticular bones that are exposed by pannus with typical changes occurring in the radial head, the coronoid process, and the distal humerus (Foster et al. 1980).

10.4 Shoulder

The shoulder has three different joints: the glenohumeral joint, the acromioclavicular joint, and the coracoclavicular joint. The last of these is a variant joint between the coracoid process and conoid process of the clavicle. Furnished with a bursa it is the site of coracoclavicular ligament attachment, and its prevalence is 0.8% (Gumina et al. 2002).

Rheumatoid arthritis is common in the first two joints, but is rare in the last whose existence itself is rare (Lehtinen et al. 1999). Topographically, the superolateral aspect of the humeral head (Babini et al. 1992) and the region between the head and greater tuberosity of the humerus are the favorite sites of erosion and cystic formation. Pinhole scintigraphy provides useful diagnostic information, particularly in the early phase. Patients with acute synovitis show intense uptake in the periarticular bones that are osteopenic; for example, in the lateral end of the clavicle and the tip of the acromion when the acromioclavicular joint is affected (Fig. 10.18). The articular space appears widened or unchanged at this time. The severity of osteopenia strongly parallels the intensity of tracer uptake. In classical rheumatoid arthritis the acromioclavicular and glenohumeral joints are involved in symmetrical fashion (Fig. 10.19). More often than not the acromioclavicular

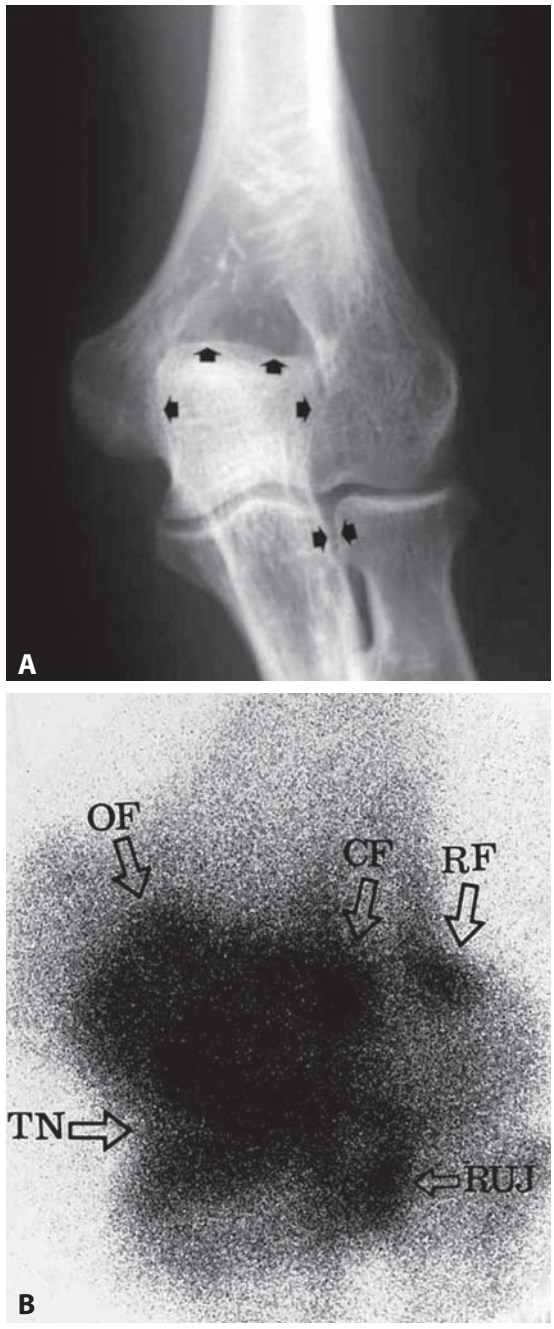

Fig. 10.17A, B Chronic active rheumatoid arthritis of the elbow. **A** Anteroposterior radiograph of the left elbow in a 67-year-old female shows diffuse osteoporosis with accentuated cortical lines (*upper four arrows* olecranon, *lower pair of arrows* radioulnar joint). **B** Anterior pinhole scan reveals tracer diffusely accumulated in the whole elbow including the olecranon fossa and notch (*OF*), coronoid fossa (*CF*), radial fossa (*RF*), trochlear notch (*TB*), and proximal radioulnar joint (*RUJ*). The eccentric uptake is considered to indicate erosions in the periarticular bones that are exposed by pannus

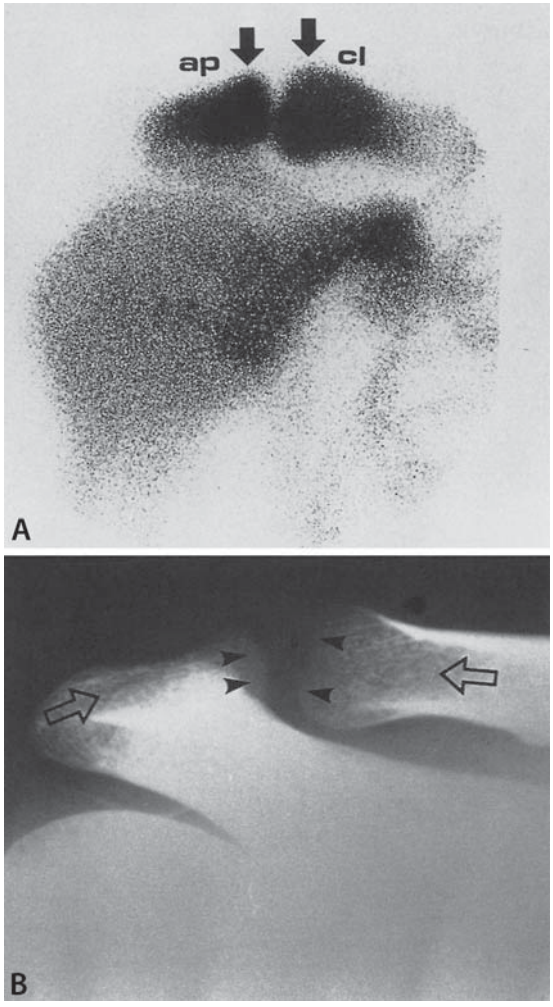

Fig. 10.18A, B Intense tracer uptake in the periarticular bones of the acromioclavicular joint in acute rheumatoid synovitis. **A** Anterior pinhole scintigraph of the right shoulder in a 29-year-old man with rheumatoid synovitis delineates extremely intense tracer uptake in the lateral clavicular end (*cl*) and the acromial tip (*ap*). The joint space appears fallaciously narrowed due to intense uptake (*arrows*). **B** Anteroposterior radiograph shows severe porosis in the bones about the acromioclavicular joint (*arrows*) and widening of the joint space due to effusion (*arrowheads*). Observe the intimate correlation between the scintigraphic and radiographic alterations of osteoporosis

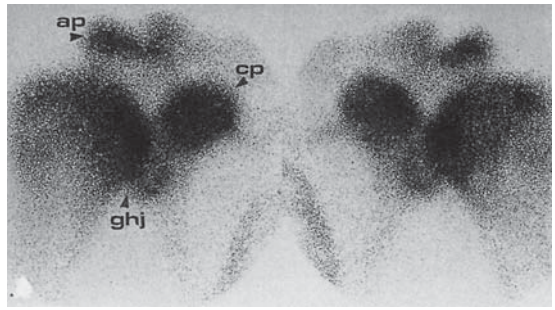

Fig. 10.19 Symmetrical involvement of both shoulders in rheumatoid arthritis. Anterior pinhole scintigraph of both shoulders (separate acquisitions) in a 55-year-old woman with established rheumatoid arthritis shows diffuse and patchy tracer uptake in the bones about the glenohumeral and acromioclavicular joints. Note nearly perfect symmetry (*ap* acromion process, *cp* coracoid process, *ghj* glenohumeral joint)

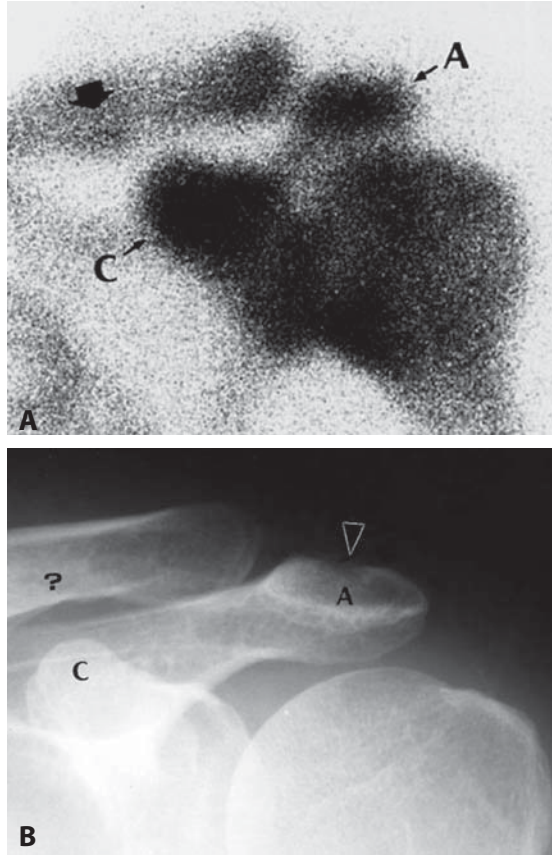

Fig. 10.20A, B Rheumatoid arthritis in the coracoid process and coracoclavicular joint. **A** Anterior pinhole scan of the left shoulder in a 51-year-old male shows increased tracer uptake in the coracoid process (*C*), conoid tubercle (*arrow*) and acromioclavicular joints (*A*). **B** Anteroposterior radiograph reveals regional osteoporosis and a small erosion in the acromion (*arrowhead*). No radiographic change is seen in the conoid tubercle (*?*)

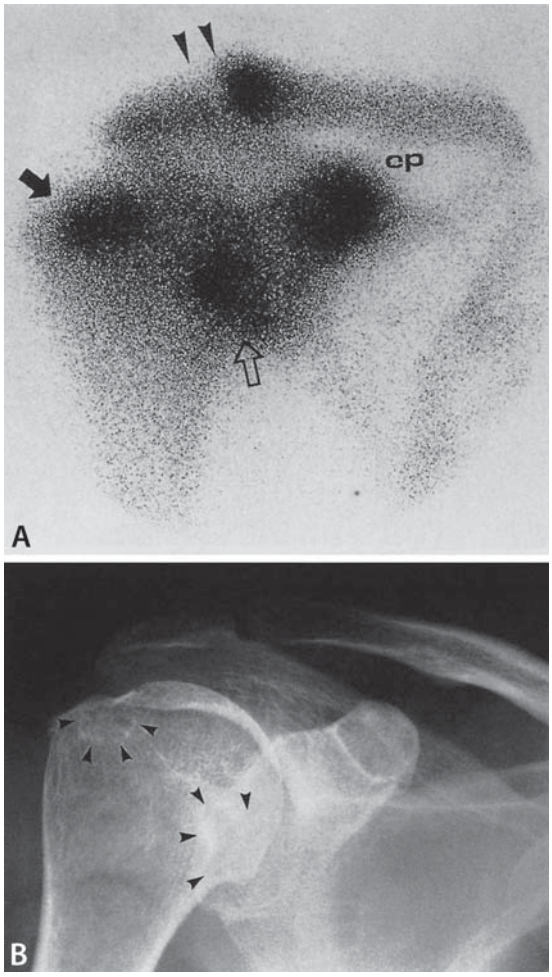

Fig. 10.21A, B Intense tracer uptake in rheumatoid subchondral cyst. **A** Anterior pinhole scintigraph of the right shoulder in a 53-year-old woman with rheumatoid intraosseous cysts in the humeral head shows patchy, intense tracer uptake in the base of the greater tuberosity (*black arrow*) and the inferomedial aspect of the humeral head (*open arrow*). The coracoid process (*cp*) and the lateral clavicular end (*arrowheads*) also concentrate some tracer. (Evaluation of the coracoid process uptake requires much caution because it concentrates tracer intensely in the normal state.) **B** Anteroposterior radiograph shows intraosseous cystic changes in the base of the greater tuberosity and the inferomedial aspect of the humeral head (*arrowheads*). The lateral end of the clavicle appears eroded

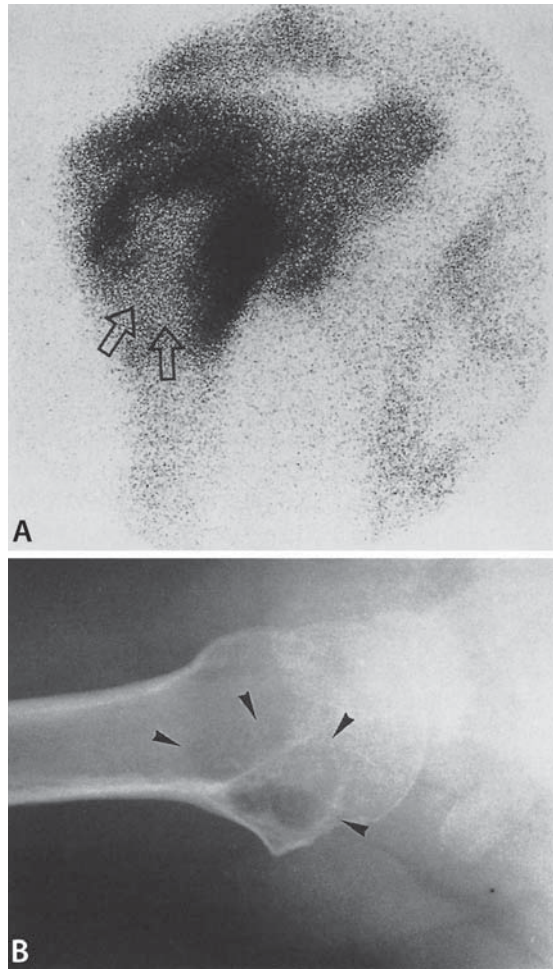

Fig. 10.22 Photopenic representation of large rheumatoid bone cyst. **A** Anterior pinhole scintigraph of the right humerus in a 43-year-old woman with a large intraosseous rheumatoid cyst shows a rectangular "cold" defect surrounded by markedly increased tracer uptake in the neck (*open arrows*). **B** Lateral radiograph demonstrates a cystic bone defect in the greater tuberosity (*arrowheads*)

joint and the coracoid process physiologically accumulate tracer, confusing the diagnosis. Therefore, it is mandatory to individually examine whether increased uptake is symptomatic or not. The case presented in Fig. 10.20 manifests as increased tracer uptake in the acromioclavicular joint, the conoid tubercle, and the coracoid process. All were painful and considered to be related to rheumatoid arthritis. Radiography showed focal erosion at the top of

the acromion with osteopenia in the regional bones.

With the destruction of articular cartilages and subchondral bones, the joints become narrowed and eventually closed with ankylosis. Small cysts are indicated by patchy uptake located within the subchondral cancellous bone (Fig. 10.21) and when a cyst is large enough it is shown as a photon defect (Fig. 10.22).

10.5 Sternum

The sternum is provided with three articulations: the paired sternoclavicular joints and the single manubriosternal joint. The former joints consist of the medial end of the clavicle and the clavicular notch along with the superior surface of the first costal cartilage and articular disk. The manubriosternal joint is mostly symphysis and partly synovial with cavitation created by disk absorption. The periarticular bony surfaces are covered by hyaline cartilage and connected by a fibrocartilage that may be ossified in the elderly.

The sternoclavicular joints are common sites of rheumatoid arthritis and involvement is usually bilateral, and the manubriosternal joint is affected in 30% to 70% of patients with rheumatoid arthritis (Resnick 2004). All three joints may occasionally be affected at the same time. Radiography reinforced by conventional or computed tomography is the diagnostic method of choice. As in other joints, the radiographic changes of rheumatoid arthritis of the sternum include bone erosions, widening or narrowing of the joint space, osteolysis, eburnation, and ankylosis (Fig. 10.23A). Pinhole scintigraphy shows diffusely increased tracer uptake, obliterating the joints symmetrically (Fig. 10.23B) or singly when the manubriosternal joint is the seat (Fig. 10.24). As in this case, isolated involvement of a single joint is not rare (Fig. 10.24). The manubriosternal joint may appear spuriously widened due to para-articular osteolysis (Fig. 10.25) and be rarely deformed due to subluxation. The tracer uptake in rheumatoid arthritis is diffuse and symmetrical, contrasting with discrete and asymmetrical uptake in tuberculous arthritis (Fig. 8.23) and osteoarthritis (Fig. 9.29). Costosternoclavicular hyperostosis clinically and radiographically resembles rheumatoid arthritis, but the "pansy flower" sign with the extra-articular involvement is pathognomonic of the former condition (Fig. 7.6).

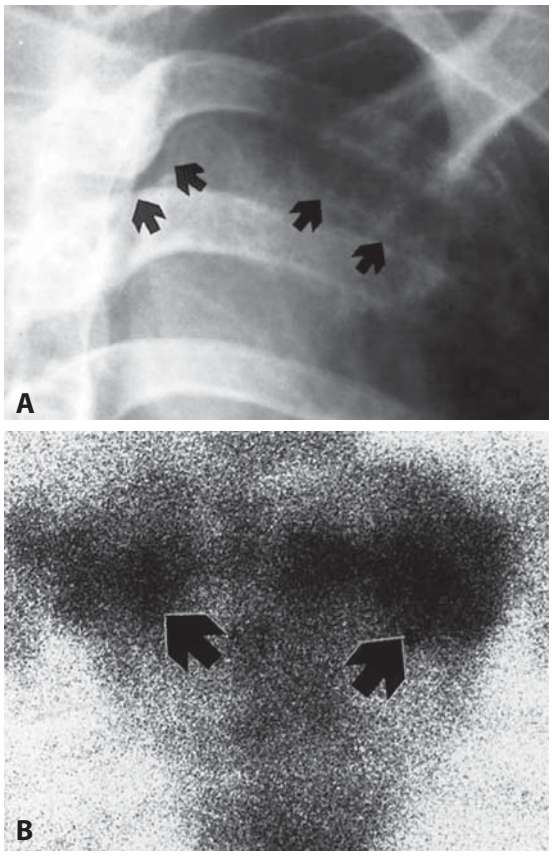

Fig. 10.23A, B Rheumatoid arthritis of the sternum. **A** Anteroposterior radiograph of the sternoclavicular joints in 42-year-old female shows subchondral erosions, articular narrowing and mild eburnation (*arrows*). **B** Anterior pinhole scan reveals diffusely increased tracer uptake in both sternoclavicular joints symmetrically (*arrows*)

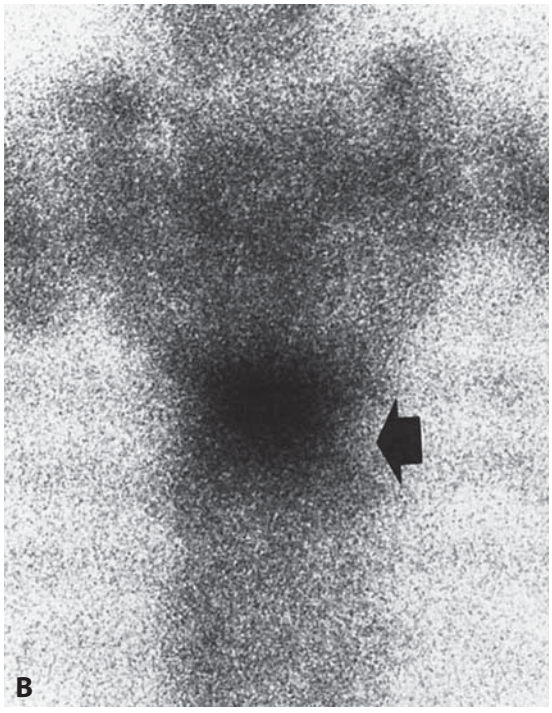

Fig. 10.24A, B Rheumatoid arthritis of the manubriosternal joint. **A** Lateral radiograph of the upper sternum shows blurring of the manubriosternal joint with soft-tissue swelling (*arrow*). The finding is inconclusive. **B** However, anterior pinhole scan reveals a patchy area of prominent tracer uptake in the manubriosternal joint (*arrow*)

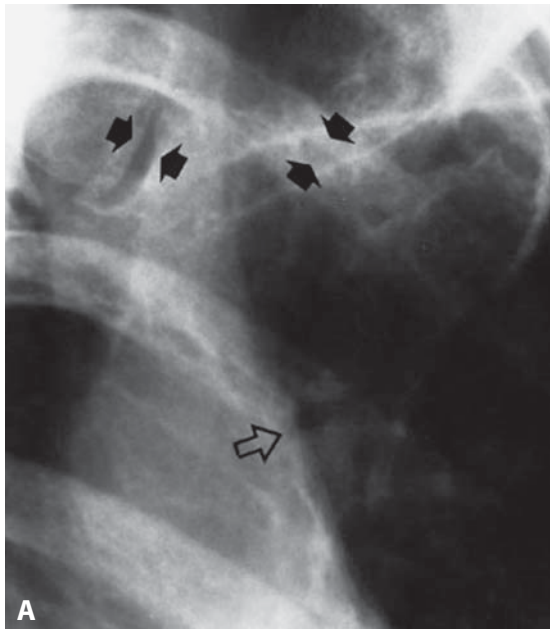

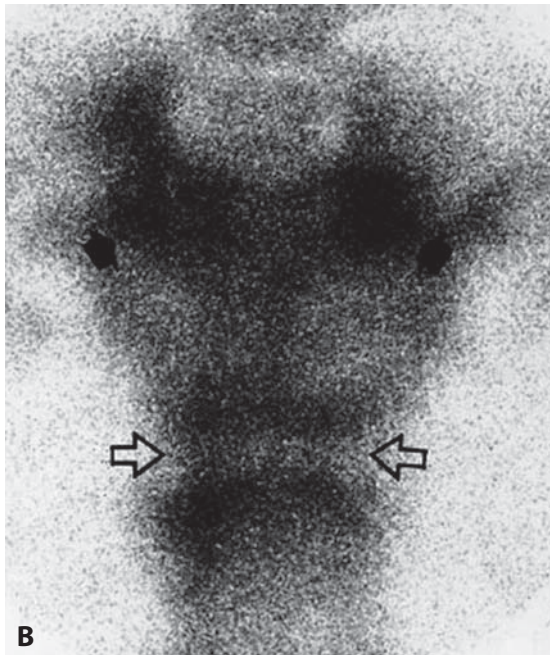

Fig. 10.25A, B Widening of the manubriosternal and sternoclavicular joints in rheumatoid arthritis. **A** Oblique radiograph of the upper sternum in a 41-year-female shows apparent widening of the manubriosternal joint (*open arrow*) and right sternoclavicular joint due to periarticular bone resorption and erosions (*pairs of arrows*). **B** Anterior pinhole scan reveals gaping of the manubriosternal joint (*open arrows*) and patchy uptake in the sternoclavicular joints (*solid arrows*)

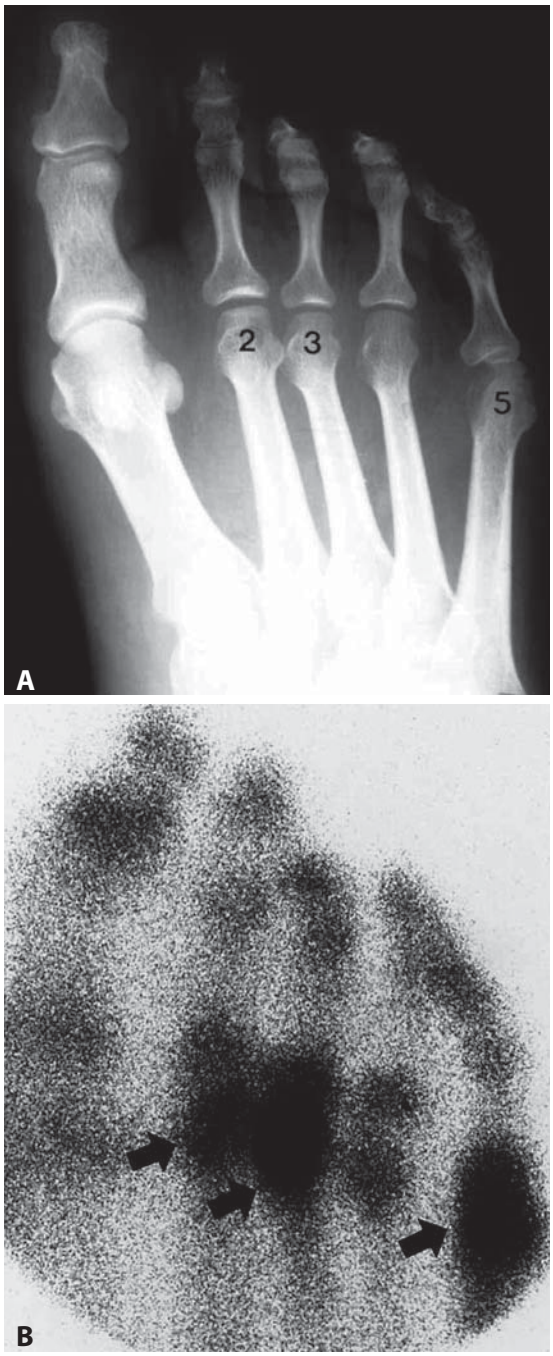

Fig. 10.26A, B Involvement of the second and third metatarsophalangeal and interphalangeal joints in rheumatoid arthritis. **A** Dorsoplantar radiograph of the right foot in a 33-year-old female shows regional osteopenia in the second through fifth toes with articular narrowing. **B** Dorsal pinhole scan reveals intense tracer uptake in the affected joints (*arrows*)

10.6 Foot

The metatarsophalangeal and interphalangeal joints of the second and third toes are most regularly involved in polyarthritic rheumatoid arthritis of the feet (Fig. 10.26). Of these joints, involvement of the metatarsophalangeal joint frequently heralds the disease. Pinhole scintigraphy is useful for first making the diagnosis and then assessing the individual pathological change in the toes. In the early stage, tracer accumulates conspicuously in and around the metatarsophalangeal joints, obscuring the articular spaces (Fig. 10.26). The tracer uptake appears expansive as opposed to the slender uptake of the normal digits (Fig. 4.39). In young patients the growth cartilages in the digits delimit rheumatoid change to the juxta-articular bones (Fig. 10.27). The sesamoid bones at the first metatarsal head are occasionally involved in rheumatoid arthritis, manifesting as characteristic "hot" nodule(s) (Fig. 10.27A). However, since the normal sesamoid bones also concentrate tracer due to articular movement (Fig. 4.39), their differentiation requires keen clinical judgment. It may be of help to remember that rheumatoid arthritis affects plural joints as opposed to the singular occurrence of the physiological uptake in the sesamoids. Following osteolysis and ankylosis joints become closed and articular malalignment, subluxation, and deformity may result. In the mutilating type, besides subluxation or dislocation, shortening or telescoping of digits may be seen.

10.7 Ankle and Tarsus

Rheumatoid arthritic involvement of the ankle and tarsus may be generalized or limited to one or a few joints. Normally, the larger joints of the ankle, the talus, and the calcaneus are readily discerned by radiography and pinhole scintigraphy (Chap. 4). These larger joints are also clearly visible in the early inflammatory phase

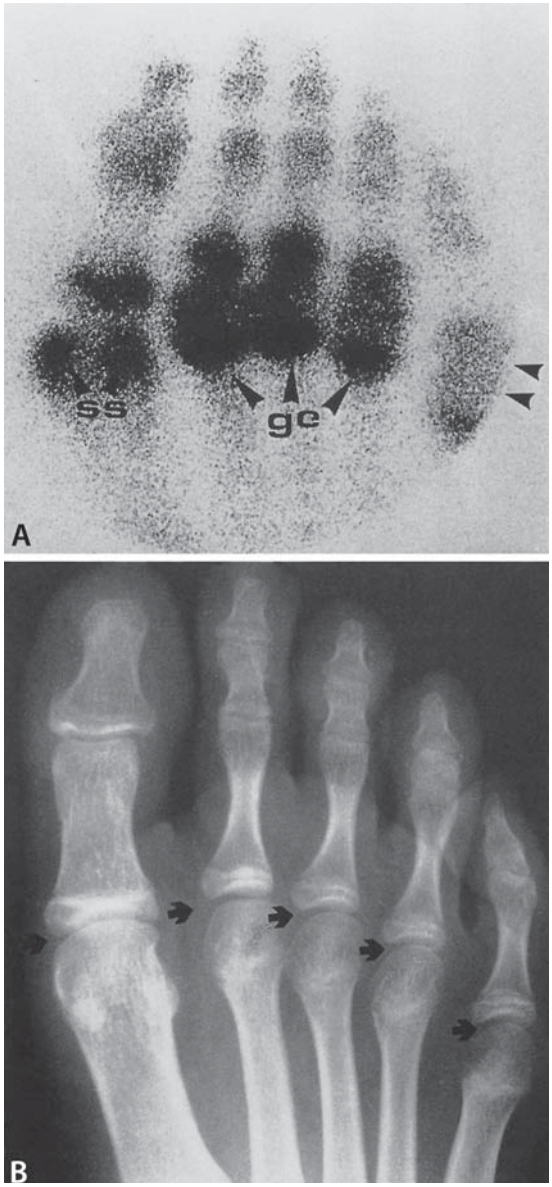

Fig. 10.27A, B Delimitation of tracer uptake by physeal cartilages in rheumatoid digits and sesamoidal rheumatoid arthritis. **A** Dorsal pinhole scintigraph of the right forefoot in a 14-year-old girl with juvenile rheumatoid arthritis reveals very intense, expansile tracer uptake in the periarticular bones of all five metatarsophalangeal joints, except for the fifth which was inadequately imaged due to its peripheral location (*arrowheads*). Physeal growth cartilages clearly delimit the abnormal tracer uptake in the metatarsal heads (*gc*), and the first metatarsal sesamoids reveal increased tracer uptake (*ss*). **B** Dorsoplantar radiograph reveals periarticular soft-tissue swelling, porosis, and joint space narrowing (*arrows*)

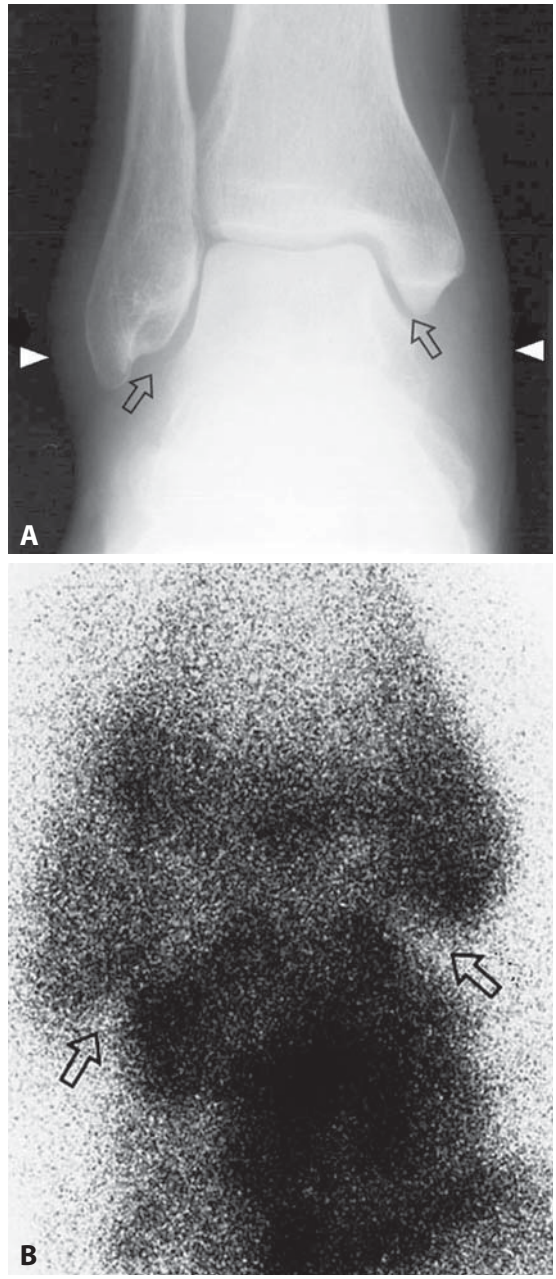

Fig. 10.28A, B Inflammatory rheumatoid arthritis in the ankle. **A** Anteroposterior radiograph of the right ankle in a 5-year-old female shows marked swelling of the periarticular soft tissues (*white arrows*) with well visualized articular space (*open arrows*). **B** Anterior pinhole scan reveals diffusely increased tracer uptake but with well-discernible articular space (*open arrows*)

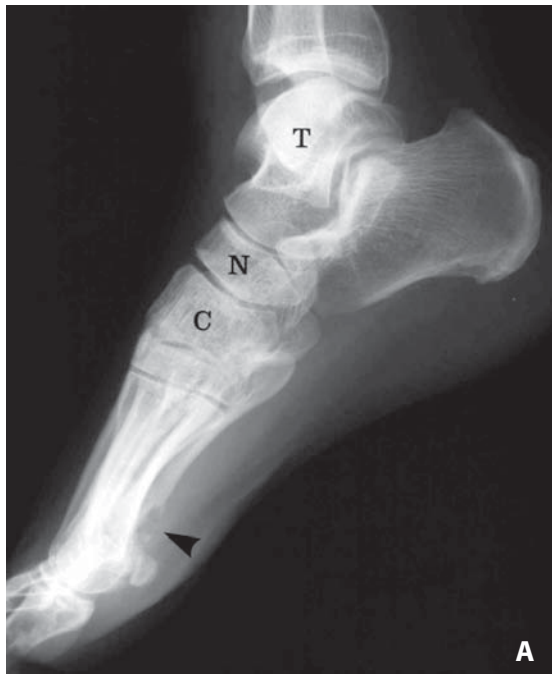

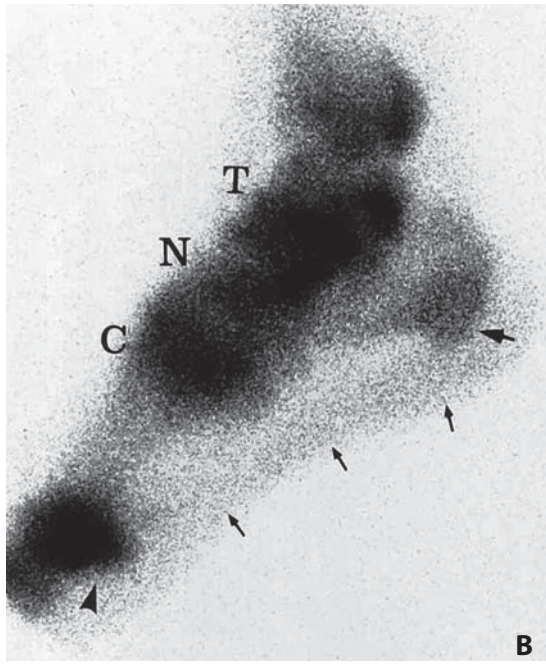

Fig. 10.29A, B Radiographically visible small joints become obliterated by tracer uptake in rheumatoid arthritis. **A** Lateral radiograph of the left foot shows diffuse porosis with narrowed intertarsal joints (*T* talus, *N* navicular, *C* cuboid). There is an erosion at the plantar aspect of fifth metatarsal (*arrowhead*). **B** Lateral pinhole scan reveals intense tracer uptake in the intertarsal joints and fifth metatarsal erosion (*arrowhead*). Note clear visualization of rheumatoid plantar fasciitis and associated edema in adiposofibrous tissue (*small arrows*) that are attached to the calcaneal tuberosity (*large arrow*)

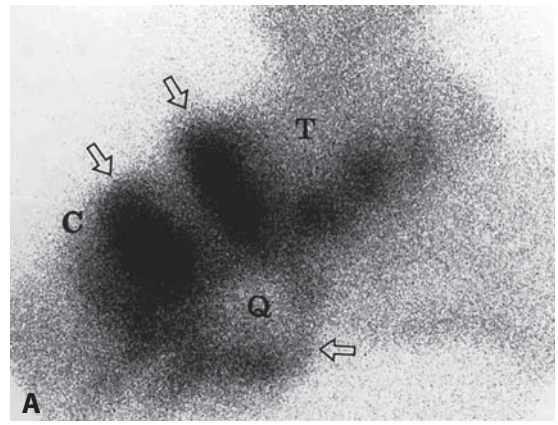

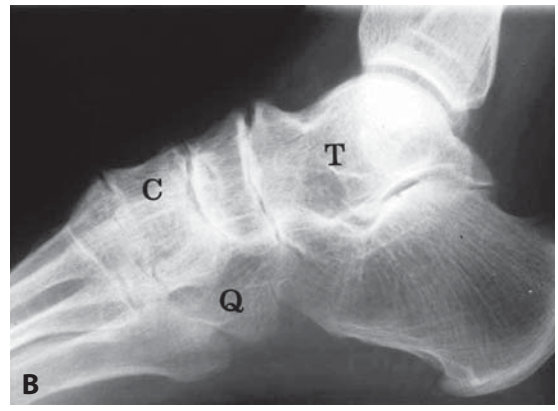

Fig. 10.30A, B Difference between pinhole scan features of rheumatoid arthritis and osteoarthritis. **A** Lateral pinhole scan of the left midfoot in a 57-year-old female shows intense tracer uptake diffusely obliterating the small narrowed intertarsal joints (*open arrows*) (*T* talus, *C* cuneiform, *Q* cuboid). **B** Lateral radiograph reveals markedly narrowed intertarsal articular spaces with eburnation and porosis

of rheumatoid arthritis (Fig. 10.28). However, the smaller intertarsal joints are visualized only on radiographs, and they are not visible on pinhole scans because tracer uptake easily obliterates inflamed joints (Fig. 10.29).

As pointed out by Calabro (1962), the midfoot rheumatoid arthritis characteristically involves the talocrural joint (Fig. 10.28) and the talocalcaneal and talonavicular joints (Fig. 10.29). Plantar fasciitis with the swelling of the adiposofibrous tissues may accompany tarsal rheumatoid arthritis, showing band-like uptake in the sole (Fig. 10.29B). Unlike seronegative spondyloarthropathies, rheumatoid arthritis affects the calcaneus less commonly. In

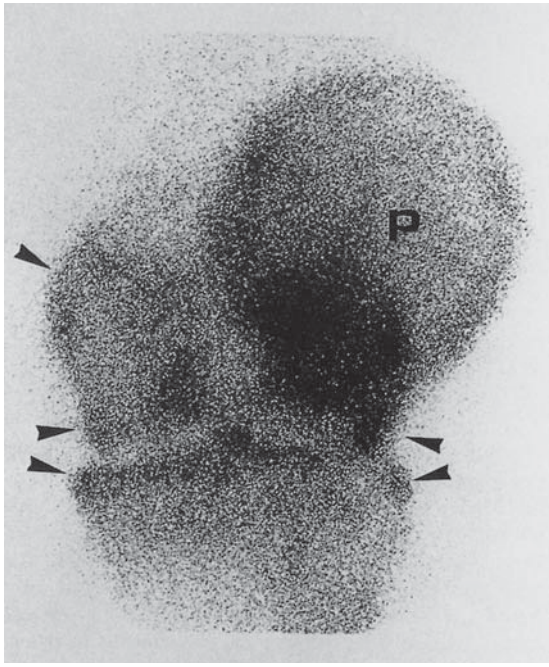

Fig. 10.31 "Wrapped bone" sign of acute rheumatoid synovitis in the knee. Anterior pinhole scintigraph of the left knee in a 35-year-old woman with acute rheumatoid synovitis delineates the classic linear tracer accumulation in the entire subchondral bones, giving rise to the "wrapped bone" sign (*arrowheads*). The patella (*P*) is also involved

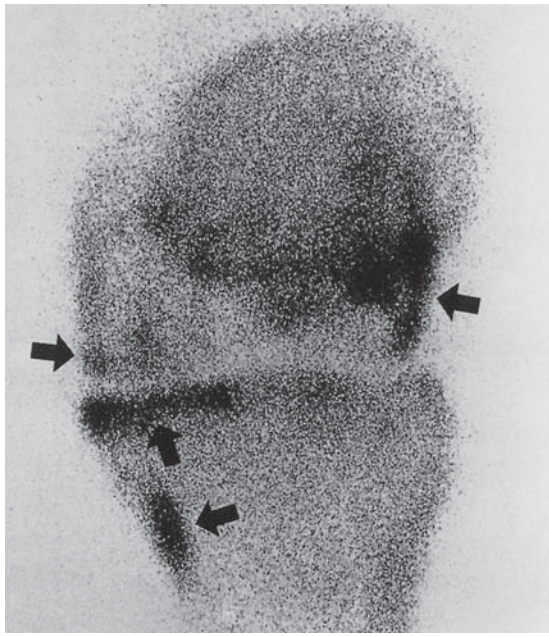

Fig. 10.32 Irregular, spotty tracer uptake in marginal rheumatoid bone erosions in the knee. Anterior pinhole scan of the left knee in a 26-year-old woman with relatively early rheumatoid arthritis shows small segmental and spotty areas of increased tracer uptake in the peripheries of the femoral condyles, the medial tibial plateau, and the medial proximal tibial metaphysis (*arrows*). The lesions are rather discrete and asymmetrical strongly resembling osteoarthritis (Figs. 9.3–9.6 and 9.13), but nevertheless are typically peripheral and attended by an associated symmetrical increase in the background uptake

the late stage the ankle and intertarsal and tarsometatarsal joints are closed due to ankylosis, forming a solid block of bones and joints with markedly increased tracer uptake.

Diagnostically, it is helpful to remember that the pinhole scintigraphic features of uncomplicated rheumatoid arthritis differ from those of osteoarthritis. Indeed, uptake is diffuse in the former (Figs. 10.29 and 10.30), whereas it is discrete in the latter (Figs. 9.4 and 9.5).

10.8 Knee

The knee is a common site of rheumatoid arthritis. It is the largest synovial joint, rendering the arthritic changes most clearly observable both on the radiograph and the pinhole scintigraph. Radiographic features include synovitis, chondrolysis, subchondral osteolysis, and cyst formation, more typically in the articular margins. In the late stage, ankylosis, crooking, and subluxation or dislocation may ensue. Pinhole scintigraphy can show most of these articular changes. Thus, synovitis is indicated by diffusely increased tracer uptake in the synoviosubchondral bones of the whole knee joint and the patella, giving rise to the "wrapped bone" appearance (Fig. 10.31). The subchondral bone erosions in the chronic stage are shown as spotty or segmental uptake (Fig. 10.32). These findings and nonstress area localization of spotty uptake are characteristic of rheumatoid arthritis in the early chronic stage. Sooner or later, the erosions spread to the stress area. As in other joints, the intraosseous rheumatoid cysts in the

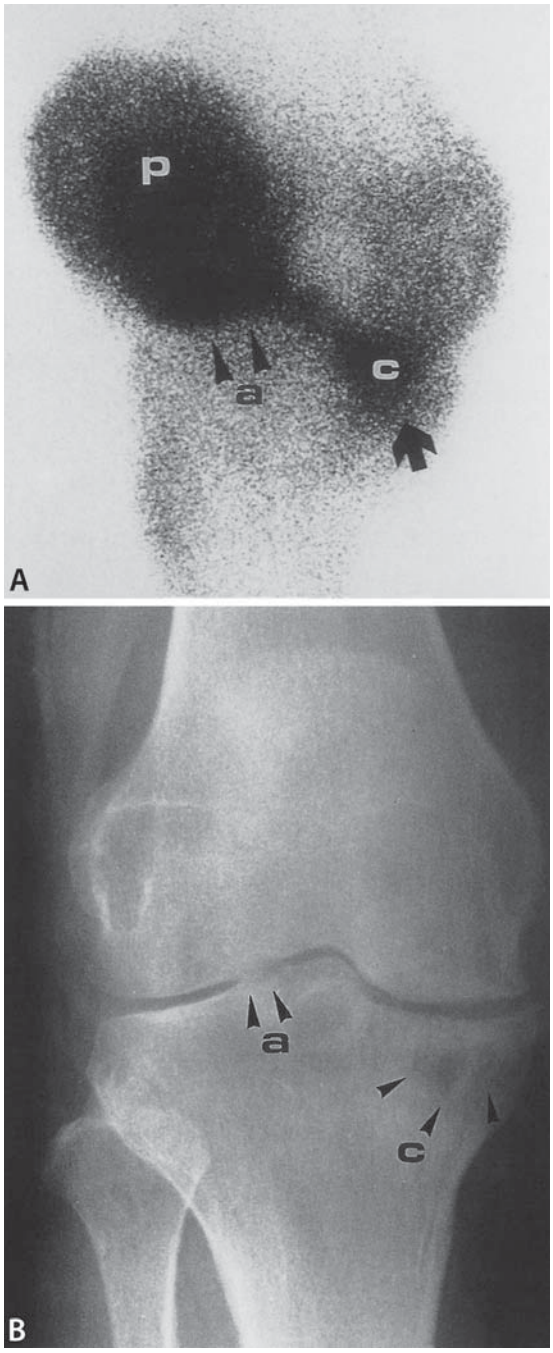

Fig. 10.33 Rheumatoid bone cyst and ankylosis in the knee. **A** Medial pinhole scintigraph of the right knee in a 25-year-old woman with longstanding juvenile rheumatoid arthritis portrays a small, very intense tracer uptake in a rheumatoid bone cyst in the posterior tibial condyle (*arrow*) (*P* patella, *c* cyst, *a* ankylosis. Another intense tracer accumulation is seen in the bony ankylosis in the anterior compartment (*arrowheads*). **B** Anteroposterior radiograph demonstrates the presence of twin cysts deep within the bony substance of the medial tibial condyle (*c*) and bony ankylosis in the lateral femorotibial compartment (*a*). Each of these lesions was confirmed by CT (not shown)

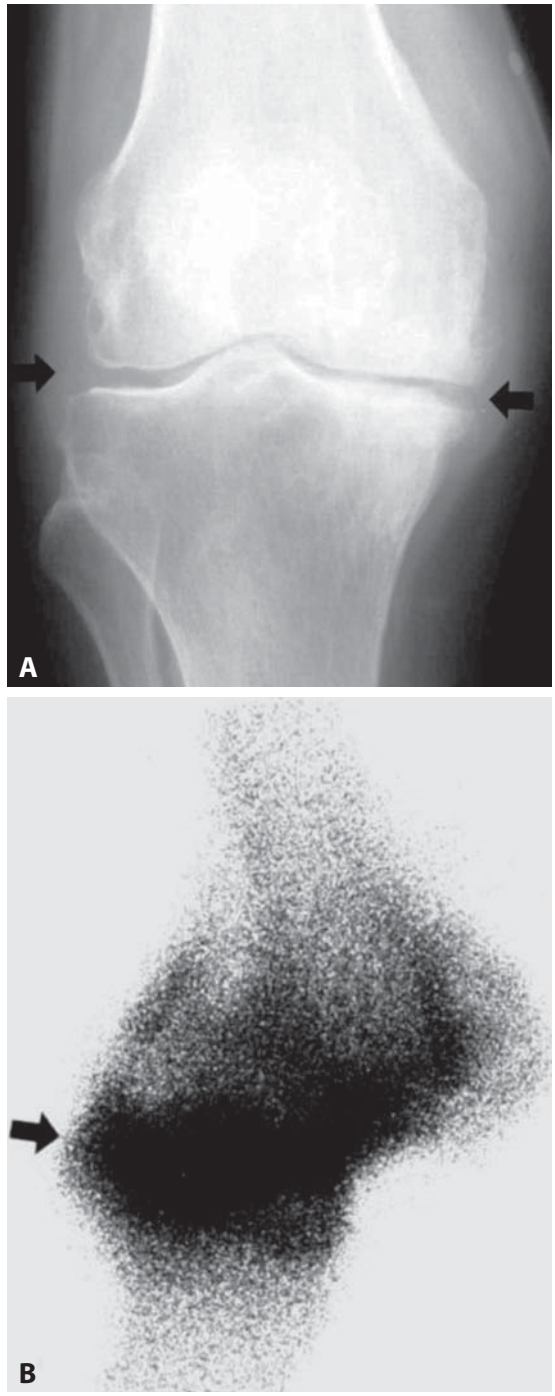

Fig. 10.34A, B Ankylosis with flexion deformity of the knee. **A** Anteroposterior radiograph of the right knee in a 69-year-ld female with malalignment and ankylosis of rheumatoid origin shows fusion and narrowing of the joint (*arrows*). **B** Lateral pinhole scan portrays extremely intense tracer uptake in the malaligned joint (*arrow*)

tibial head and distal femur accumulate tracer intensely, and fibrous or bony ankylosis is indicated by band-like uptake in the narrowed joint (Fig. 10.33). Articular narrowing occurs much earlier and is severer in rheumatoid arthritis than in osteoarthritis, in which the joint space remains not closed until the late stage (Fig. 9.13). Such difference can be attributed to the fact that the rheumatoid pannus with active proteolysis is wildly destructive while arid bone hypertrophy in osteoarthritis is relatively innocuous. Subluxation or flexion of the knee, a common sequela of long-standing rheumatoid arthritis, shows extremely intense tracer uptake in the malaligned joint (Fig. 10.34).

10.9 Hip

The hip is less commonly affected than the knee. The more classical changes are observed in patients with longstanding disease, especially those receiving corticosteroid therapy. Radiographic features include bone erosions, eburnation, and concentric articular narrowing. In addition, small cysts may be seen in sclerosed periarticular bones. With concentric narrowing of the joint, the femoral head migrates axially within the acetabular fossa (Fig. 10.35A). Rarely, the femoral head migrates eccentrically in the superolateral direction. In contrast to osteoarthritis, osteophytosis and buttressing in the femoral neck are not prominent in rheumatoid arthritis.

Pinhole scintigraphy shows tracer to accumulate intensely in the entire joint and periarticular bones, reflecting diffuse synovial inflammation with subchondral bone invasion (Fig. 10.35B). Articular narrowing is typically concentric and femoral migration is axial in direction as opposed to the eccentric narrowing and cranial or lateral dislocation in osteoarthritis (Fig. 9.10). As in the shoulder (Fig. 10.21A) and the knee (Fig. 10.33A), the cystic changes in the hip are indicated by intense tracer uptake (Fig. 10.36A).

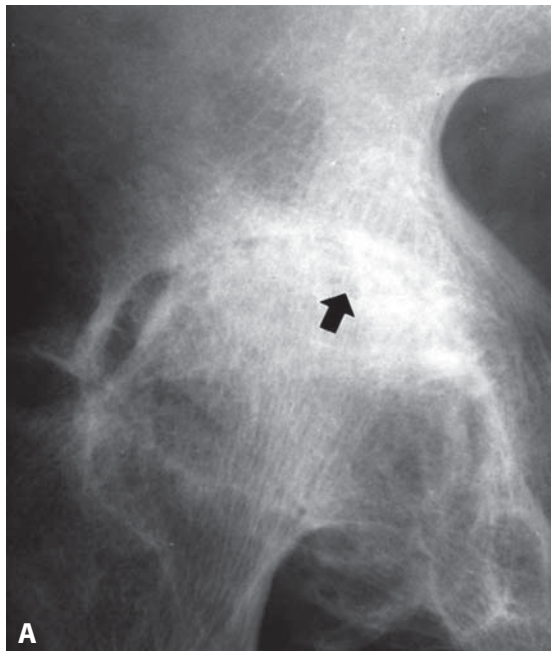

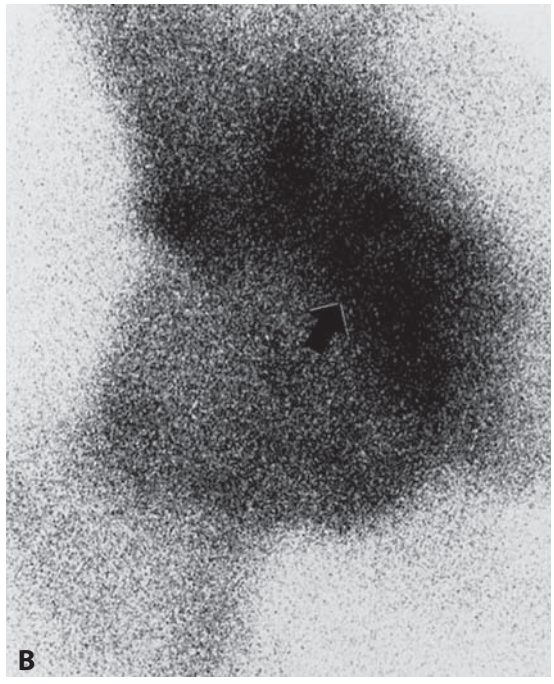

Fig. 10.35A, B Concentric hip joint narrowing with axial migration of the femoral head in advanced rheumatoid arthritis. **A** Anteroposterior radiograph of the right hip in a 44-year-old male shows typical concentric narrowing and axial femoral head migration (*arrow*). **B** Anterior pinhole scan reveals intense concentric tracer uptake with axial migration of the femoral head (*arrow*)

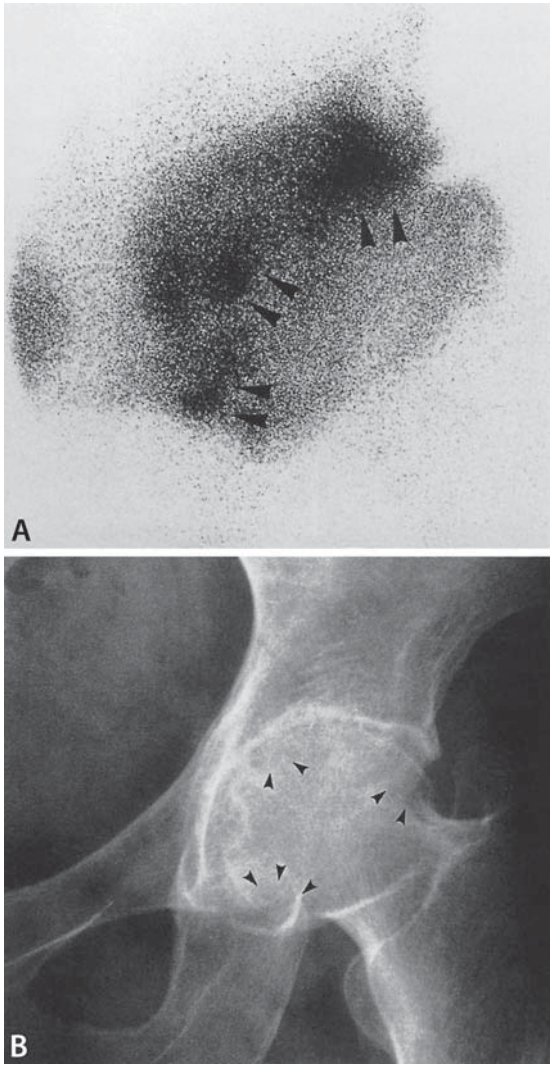

Fig. 10.36A, B Intense tracer uptake in rheumatoid bone cysts in the hip. **A** Anterior pinhole scintigraph of the left hip in a 40-year-old woman with multiple rheumatoid cysts reveals general increase in tracer uptake with patchy intense tracer uptake in the femoral head (*arrowheads*). The joint is concentrically narrowed and the femoral head is axially migrated. **B** Anteroposterior radiograph delineates multiple small bone cysts (*arrowheads*), joint space narrowing, axial femoral head migration, and porosis

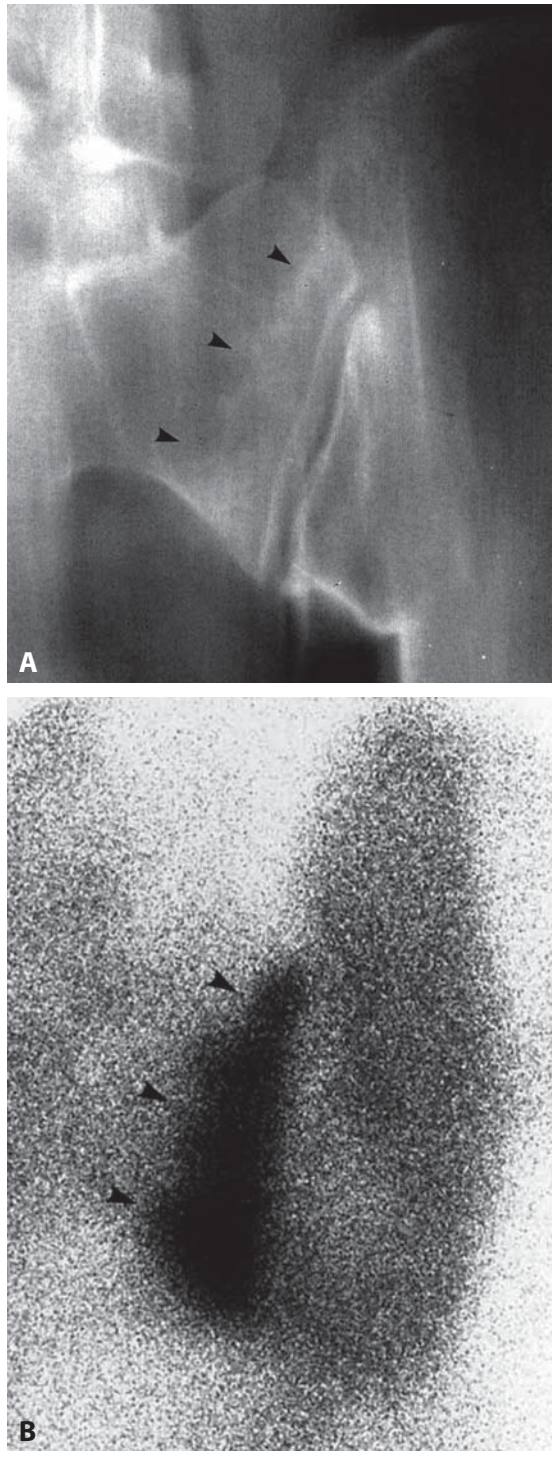

Fig. 10.37A, B Unilateral rheumatoid sacroiliitis. **A** Conventional tomogram of the left sacroiliac joint in a 53-year-old female shows sacral involvement of the disease with osteopenia and nebulous sclerosis in the sacral side (*arrowheads*). **B** Anterior pinhole scan reveals spinnaker-like tracer uptake in the sacral side (*arrowheads*)

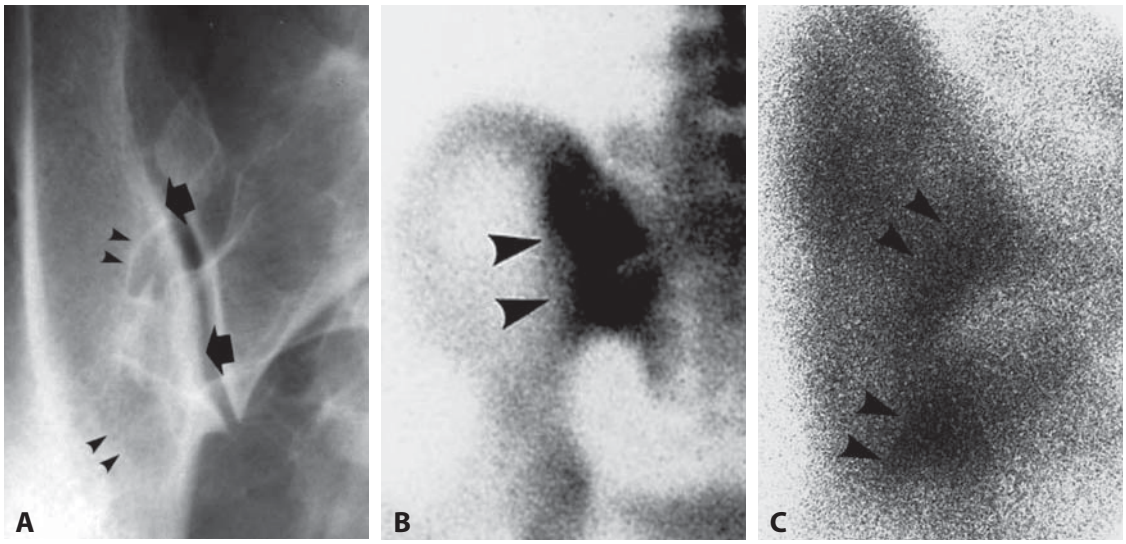

Fig. 10.38A–C Joint preservation in sacroiliac rheumatoid arthritis. **A** Anteroposterior radiograph of the right sacroiliac joint in a 59-year-old female shows iliac bone involvement of the disease with eburnation and a relatively well-preserved joint (*arrows*). Note characteristic cyst-like bone resorption and reactive sclerosis (*paired arrowheads*). **B** Anterior planar scan reveals simple homogeneous uptake without diagnostic features (*arrowheads*). **C** Pinhole scan shows increased uptake localized to cyst-like bone resorption (*paired arrowheads*)

10.10 Sacroiliac Joint

The involvement of the sacroiliac joints in rheumatoid arthritis is neither as common nor severe as in ankylosing spondylitis. The sacroiliac joints are affected more typically in patients with longstanding disease. The involvement may be bilateral or unilateral, and symmetry is not a regular feature. A strong proclivity toward iliac involvement has been described, but isolated sacral involvement appears not rare (Fig. 10.37). X-ray tomography shows para-articular osteopenia in the sacrum that is delimited by the pencil-lined cortex laterally and faint sclerosis medially. In contrast to the findings in rheumatoid arthritis of other weight-bearing joints, the narrowing of the joint space in sacroiliac rheumatoid arthritis is often not so prominent even in the presence of para-articular cystic change (Fig. 10.38A). Using conventional tomography, Elhabali et al. (1979) noted marked ankylosis and subchondral erosions in 38% of 72 patients with rheumatoid arthritis of the sacroiliac joint.

Planar ^{99m}Tc-MDP bone scintigraphy demonstrates simply homogenous uptake that completely obliterates joints (Fig. 10.38B). Pinhole scintigraphy, however, shows such uptake to be localized in the synovial compartment of the joint and cysts when present (Fig. 10.38C). It is interesting to note that rheumatoid arthritis in the ankylotic stage accumulates tracer not so intensely (Fig. 10.39) compared to that in the florid stage (Fig. 10.38C).

10.11 Spine

Rheumatoid arthritis is not common in the thoracic and lumbar spine. However, the high incidence in the cervical spine is well known. One of the most recent studies has indicated the radiographic prevalence rate of rheumatoid arthritis in the cervical spine to be 88.5% (Zikou et al. 2005). In contrast, a random sampling study showed rheumatoid arthritis to involve the lumbar spine in only 5% of men and 3% of women (Lawrence et al. 1964). Rheumatoid ar-

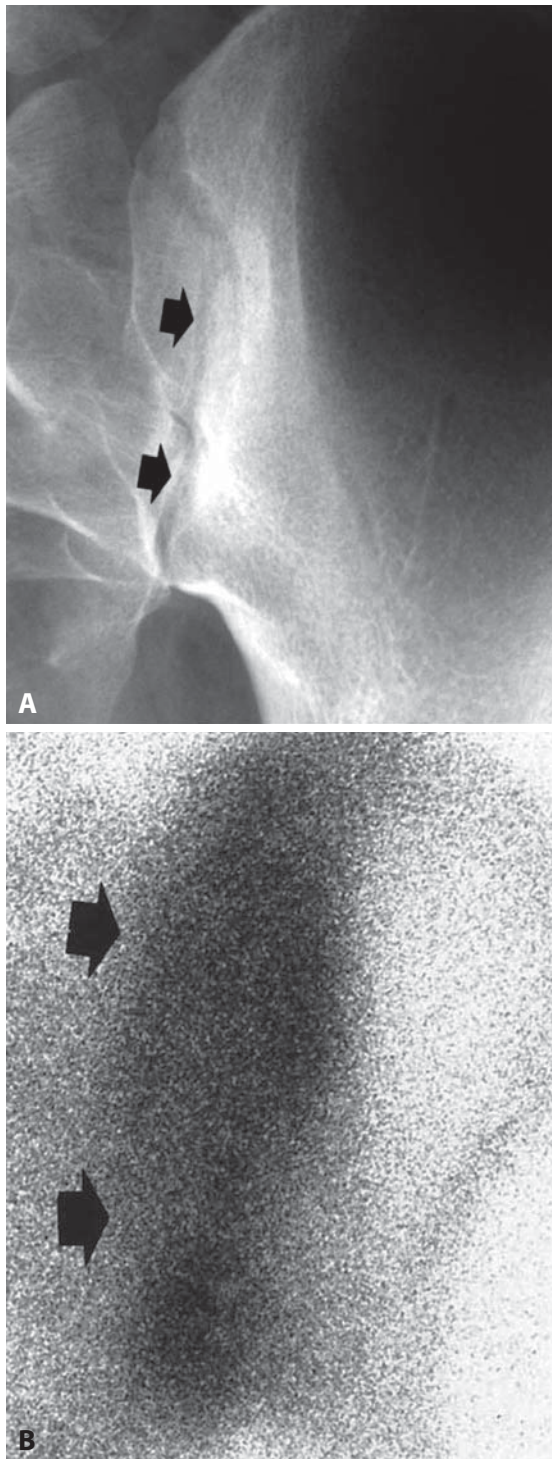

Fig. 10.39A, B Not so intense tracer uptake in ankylosed rheumatoid arthritis. **A** Posteroanterior radiograph of the right sacroiliac joint in a 23-year-old female shows diffuse iliac sclerosis and ankylosis (*arrows*). **B** Posterior pinhole scan reveals simply homogeneous tracer uptake of moderate grade with diffuse joint obliteration (*arrows*). Note that there is no differential uptake in this ankylotic arthritis as there is in florid arthritis (Fig. 10.37)

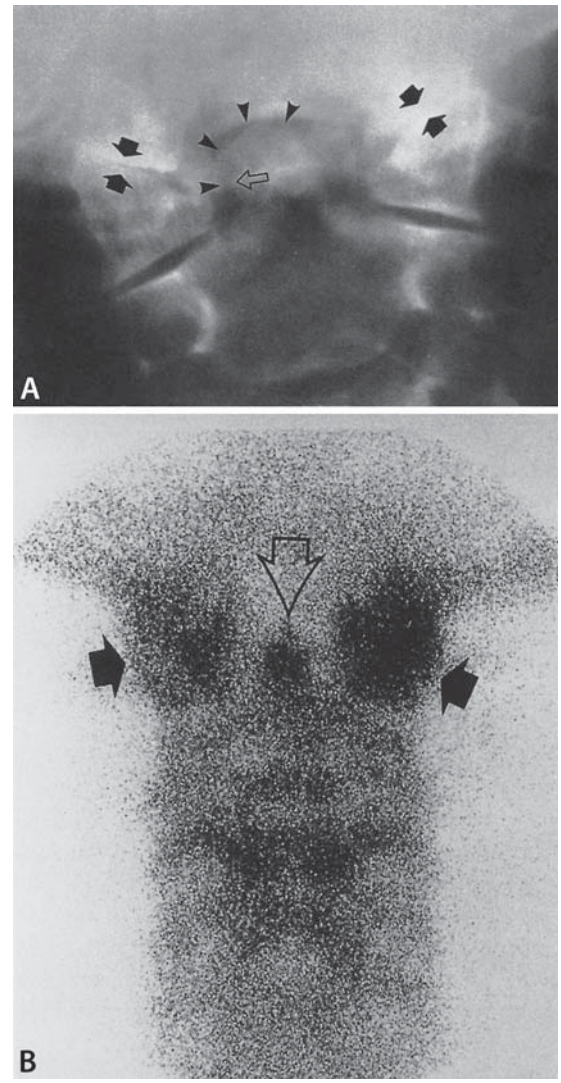

Fig. 10.40A, B Rheumatoid arthritis in the uppermost cervical spine and skull base. **A** Anteroposterior conventional X-ray tomogram of the uppermost cervical spine in a 70-year-old woman with rheumatoid spondylitis shows erosions involving the dens (*arrowheads*) with subluxation to the right (*open arrow*). The occipitoatlantal joints are markedly narrowed bilaterally (*arrows*). **B** Posterior pinhole scintigraph shows intense tracer uptake in both occipitoatlantal joints (*arrows*) as well as the dens (*open arrow*). Compare with the normal anatomy in Fig. 4.10

thritic involvement of the apophyseal joints has been emphasized (Sims-Williams et al. 1977). It is unquestioned that the more realistic incidence of spinal rheumatoid arthritis would be found to be higher if multiple radiographic

projections and bone scintigraphy, particularly pinhole scanning, were more regularly used.

Radiographically, the atlantoaxial rheumatoid arthritis reveals irregular erosion of the odontoid process, early widening and later narrowing of the atlantoaxial joints, and occasional subluxation (Fig. 10.40A). Involvement of the lateral masses and the facet joints of the axis and the occipitoatlantal joint is an important accompaniment. Rheumatoid apophysitis of the lumbar and thoracic spine is characterized by erosion, which may result in burring and narrowing or spurious widening of joint spaces (Fig. 10.41A). The oblique view is useful for a clearer presentation of apophysitis.

Pinhole scintigraphy of rheumatoid arthritis in the upper cervical spine shows tracer uptake in the lateral and median atlantoaxial joints around the odontoid process as well as the apophyseal joints and occipitoatlantal joint (Fig. 10.40B). The eroded dens also accumulates tracer. In the lumbar spine, the apophyseal and diskovertebral joints show increased uptake. To be anatomically specific, the apophyseal joint is not in the midline but in the lateral part of the intervertebral space on the posterior scan (Fig. 10.41B) and behind the vertebral body on the lateral scan (Fig. 10.42). Diskovertebral rheumatoid arthritis is indicated by increased uptake (Fig. 10.42). The disk spaces may or may not be narrowed. Lateral pinhole scintigraphy is a sensitive and reliable indicator of rheumatoid arthritis in the lumbar apophyseal joint (Fig. 10.42) and the median (anterior) atlantoaxial joint (Fig. 10.43).

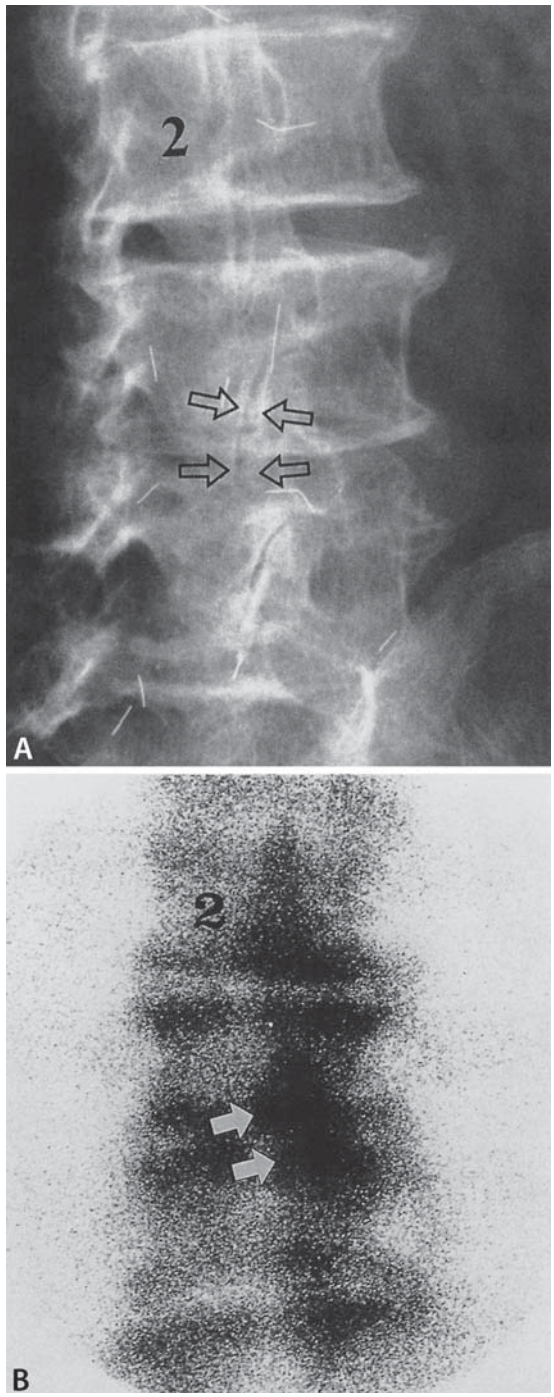

Fig. 10.41A, B Rheumatoid apophysitis in the lumbar spine. **A** Right posterior oblique radiograph of the lower lumbar spine in a 63-year-old woman with rheumatoid apophysitis of L3 and L4 vertebrae shows articular blurring and periarticular bone erosions (*open arrows*). **B** Posterior pinhole scintigraph reveals moderately increased tracer uptake in L3 and L4 apophyseal joint on the right (*arrows*). Note the typical astride position of the apophyseal joint at this level

10.12 Temporomandibular Joint

The temporomandibular joints are involved not infrequently in rheumatoid arthritis. Radiographic changes include osteopenia, subchondral bone erosions, narrowing or apparent widening of the mandibular fossa, locking or limited articular excursion, and ankylosis (Fig. 10.44A). Pinhole scintigraphically, the

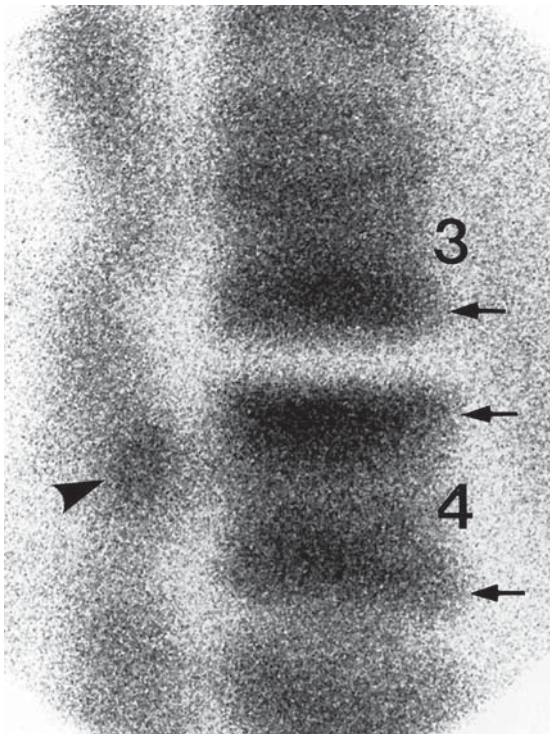

Fig. 10.42 Diskovertebral rheumatoid arthritis with apophyseal joint involvement. Lateral pinhole scan of the lumbar spine in a 27-year-old female shows increased uptake in the L3 lower and L4 upper and lower endplates (*arrows*). Apophyseal joint involvement is also indicated by posterior tracer uptake (*arrowhead*)

rheumatoid arthritis of the temporomandibular joint with remaining joint space and without ankylosis or sclerosis reveals intense tracer uptake that is well-confined to the joint. The area of uptake in a diseased joint is larger than in a normal joint, reflecting the ballooning of the eroded joint with reactive inflammation in the periarticular bones (Fig. 10.44B). When the joint is ankylotic with periarticular bone sclerosis, tracer uptake becomes decreased but diffusely spread with poor demarcation (Fig. 10.45). Such a finding is quite similar to that in ankylotic atlantoaxial rheumatoid arthritis (Fig. 10.43).

As in rheumatoid arthritis of other joints (Fig. 10.37), it is a general impression that relatively fresh temporomandibular rheumatoid arthritis with remaining joint space accumulates tracer rather intensely without diffusion

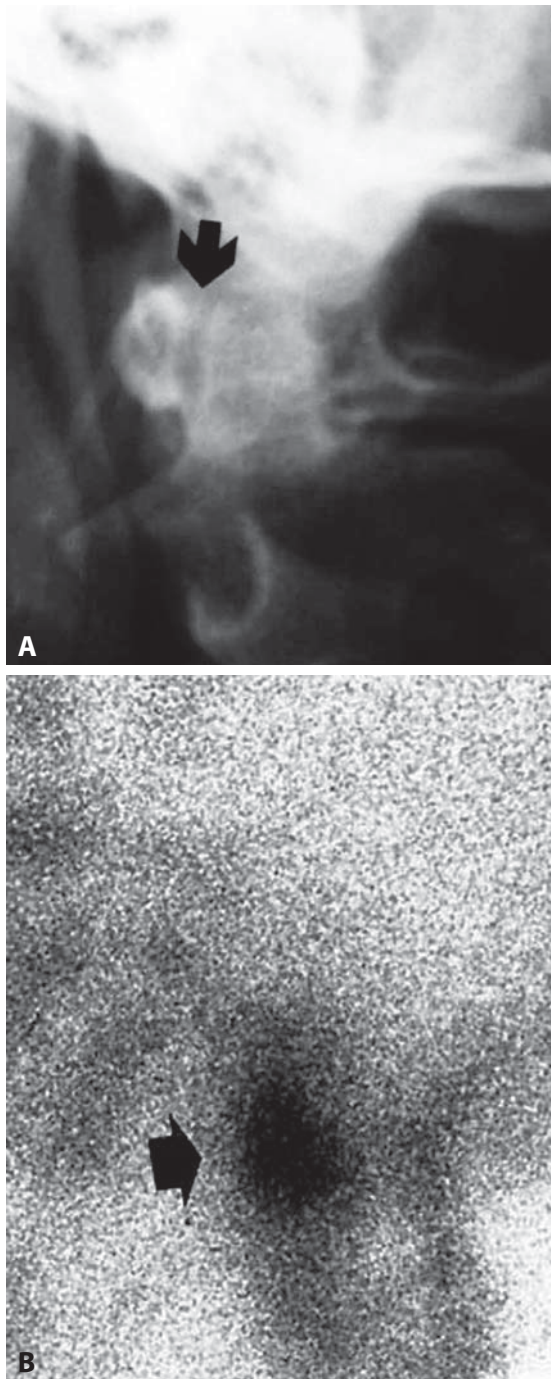

Fig. 10.43A, B Atlantoaxial rheumatoid arthritis. **A** Lateral radiograph of the upper cervical spine in a 33-year-old female shows blurring and apparent widening of the median atlantoaxial joint presumably due to erosion and fibrosis (*arrow*). **B** Lateral pinhole scan reveals poorly defined tracer uptake in diseased median atlantoaxial joint (*arrow*). Pinhole scan makes not only the diagnosis of specific joint involvement but also disease stage and activity

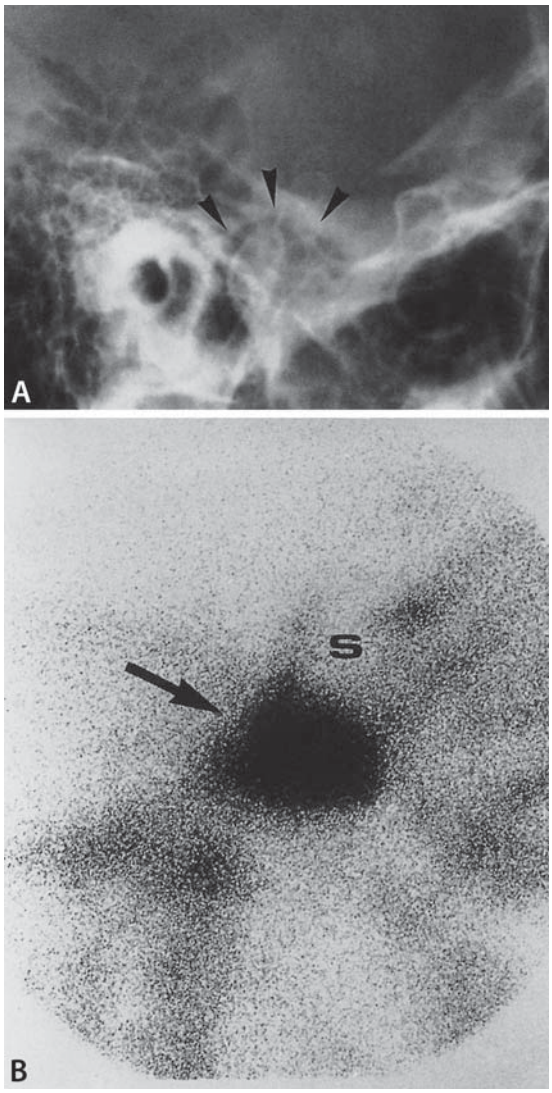

Fig. 10.44A, B Rheumatoid temporomandibular arthritis. **A** Oblique open-mouth radiograph of the right temporomandibular joint in a 51-year-old woman with established rheumatoid involvement reveals locking, articular narrowing and ballooning, and sclerosis and erosions (*arrowheads*). **B** Lateral pinhole scintigraph shows intense tracer uptake in the temporomandibular joint (*arrow*). The uptake is exaggerated reflecting the periarticular spread of inflammation and ballooning of the articular fossa. The sella turcica is presented as a "cold" fossa (*s*)

so that the diseased joint is well-defined (Fig. 10.44), whereas the less active lesions with joint space obliteration, ankylosis, and regional sclerosis accumulate tracer less intensely and diffusely so that the diseased joints are poorly defined (Figs. 10.35, 10.39, 10.43 and 10.45).

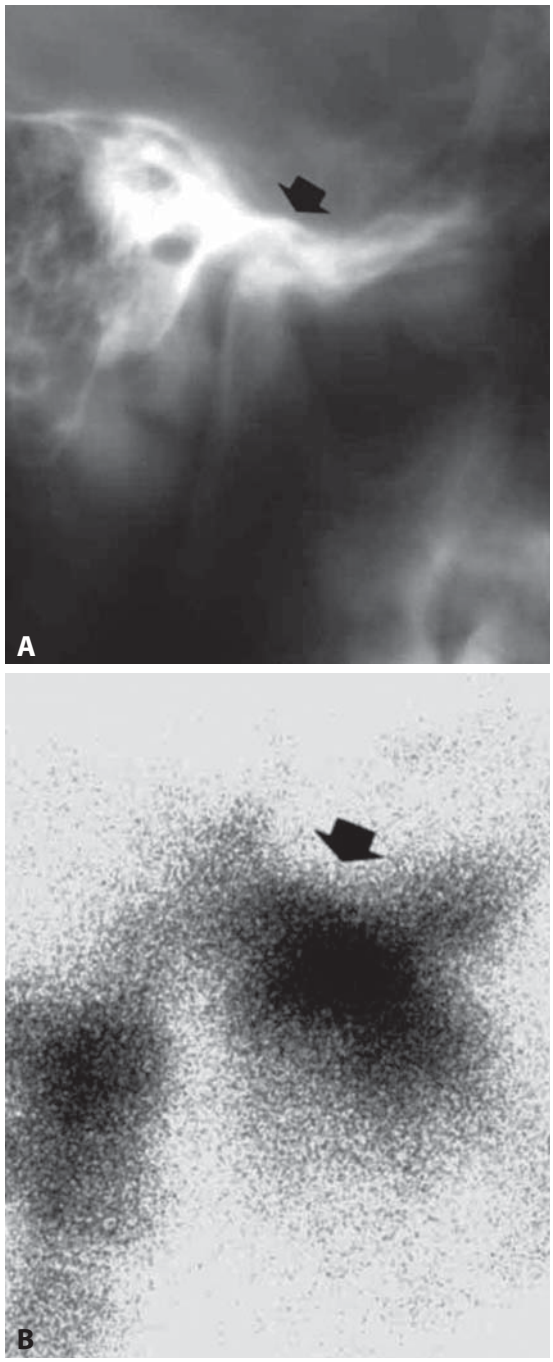

Fig. 10.45A, B Ankylotic rheumatoid arthritis of the temporomandibular joint with ill-defined and not-so-intense uptake. **A** Conventional tomogram of the right temporomandibular joint in a 26-year-old male shows ballooned fossa with erosion, ankylosis, and mandibular head lysis (*arrow*). **B** Lateral pinhole scan reveals increased tracer uptake with diffusely obliterated joint. The uptake is poorly defined and not as intense as the ankylotic type shown in Fig. 10.44

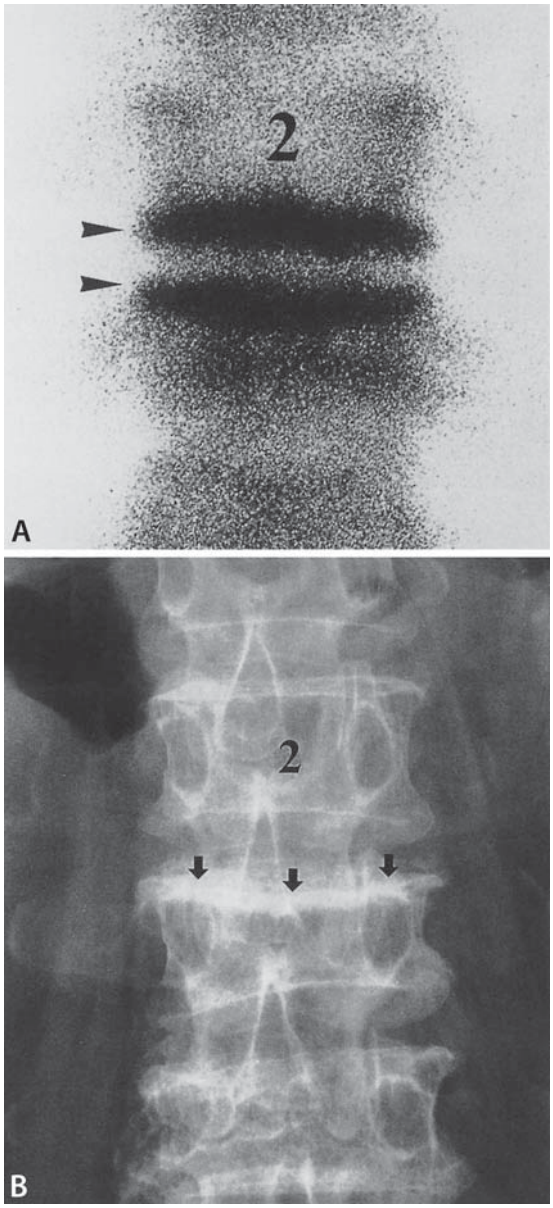

Fig. 10.46A, B Insufficiency spinal fracture in rheumatoid arthritis treated with corticosteroid. **A** Posterior pinhole scintigraph of the midlumbar spine in a 54-year-old woman shows minimally arcuate, very intense tracer uptake in the lower endplate of the L2 vertebra and the upper endplate of the L3 vertebra (*arrowheads*). **B** Anteroposterior radiograph reveals compression fracture with eburnation in the upper endplate of the L3 vertebra (*arrows*). The L2 vertebral fracture is not indicated radiographically

10.13 Insufficiency Fracture in Rheumatoid Arthritis

Patients receiving corticosteroid therapy often suffer from insufficiency fractures (trabecular disruption in nonlesional bones) of, for example, the spine, hip, and knee. Pathologically, osteopenia and osteonecrosis precede the fractures because they begin earlier as a result of microvascular occlusion and infraction. Radiographic manifestations include osteopenia, crescent or patchy lucency, and bone collapse and condensation due to impaction. In the spine, the vertebral bodies show condensation of the endplates with compressions of various grades (Fig. 10.46A). The femoral head and the tibial head are notorious sites for insufficiency fractures, showing a mixed pattern of mottled or patchy sclerosis and lucencies with volume loss of bone (Fig. 10.47A).

Pinhole scintigraphically, vertebral fractures are represented by extremely intense tracer uptake in endplates, which are depressed (Fig. 10.46B). Indeed, the depression is an essential feature of compression fractures. In uncomplicated cases, the disk space is either preserved or widened. On the other hand, insufficiency fractures in the femoral head and the tibial head are indicated by irregularly increased or decreased tracer uptake within the metaphyseal cancellous bones, reflecting fractures and avascular bone necrosis, respectively (Fig. 10.47B).

10.14 Juvenile Rheumatoid Arthritis

Juvenile rheumatoid arthritis is one of the most common pediatric rheumatic disorders and a major cause of chronic disability and occasional crippling deformity. The clinical manifestations include synovitis of the peripheral joints with effusion and periarticular soft-tissue swelling. Onset is before 16 years of age, and overall prevalence is estimated to be 113/100,000

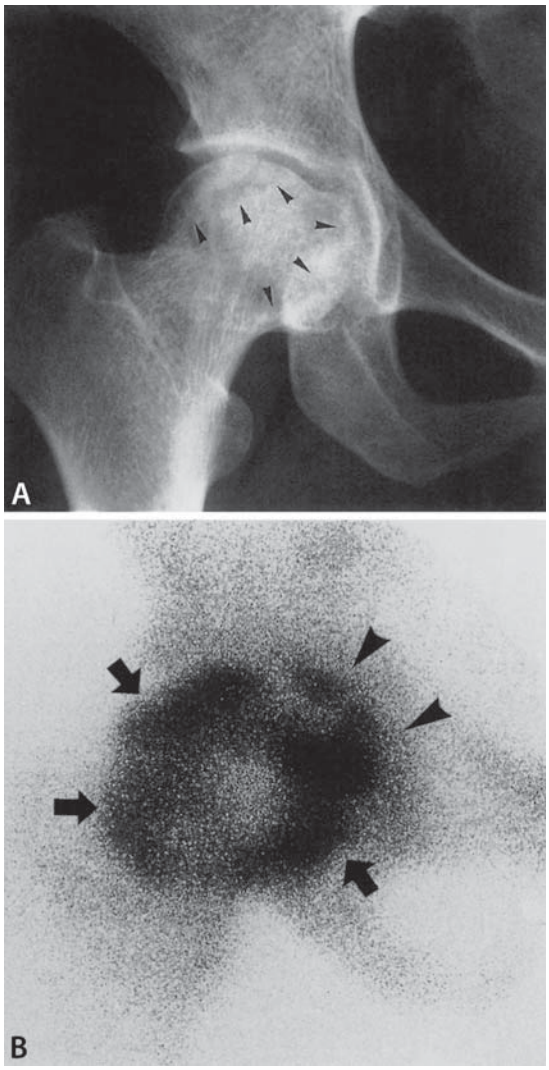

Fig. 10.47A, B Insufficiency fractures and avascular bone necrosis in rheumatoid arthritis treated with corticosteroids. **A** Anteroposterior radiograph of the right hip in a 34-year-old woman with rheumatoid arthritis shows peripheral sclerosis and central irregularity, suggesting microfractures and necrosis (*arrowheads*). Note that the volume of the femoral head is somewhat reduced. **B** Anterior pinhole scan reveals spotty "hot" areas in the periphery (*arrows*) and a "cold" area in the center of the femoral head, respectively denoting insufficiency fractures and avascular necrosis. Increased tracer uptake is also seen in the acetabulum with degenerative change (*arrowheads*)

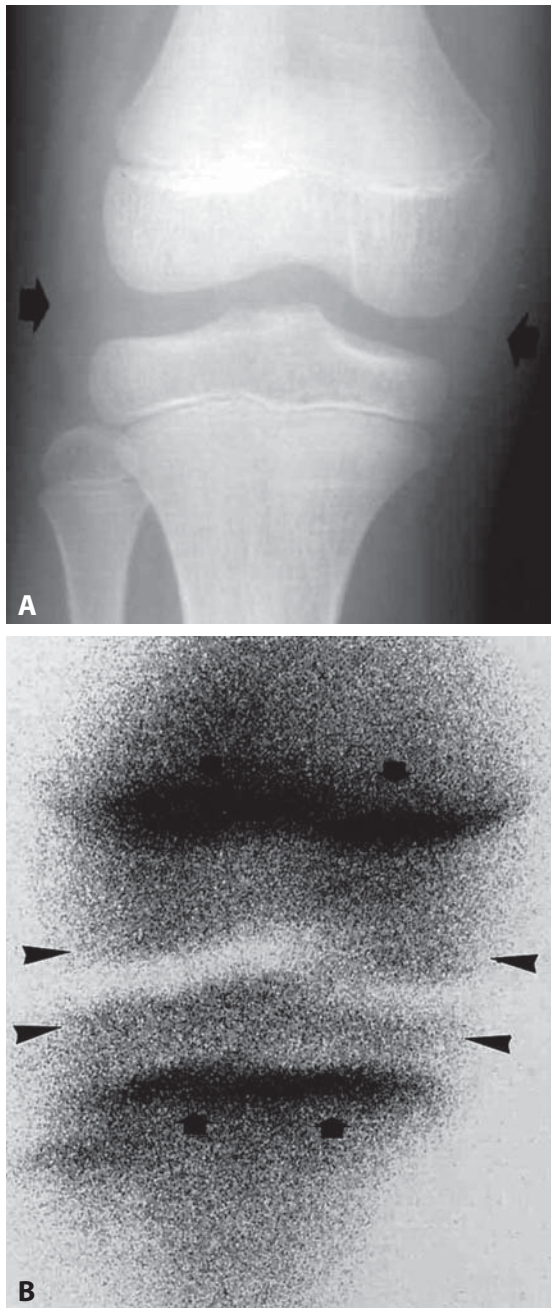

Fig. 10.48A, B Juvenile rheumatoid arthritis. **A** Anteroposterior radiograph of the right knee in a 14-year-old girl shows marked periarticular soft-tissue swelling and enlargement of the distal femoral and proximal tibial epiphyses with articular widening (*arrows*). **B** Anterior pinhole scan reveals increased tracer uptake showing enlarged articular bones (*arrowheads*) with intensified physeal activity (*arrows*) caused by hypervascularity

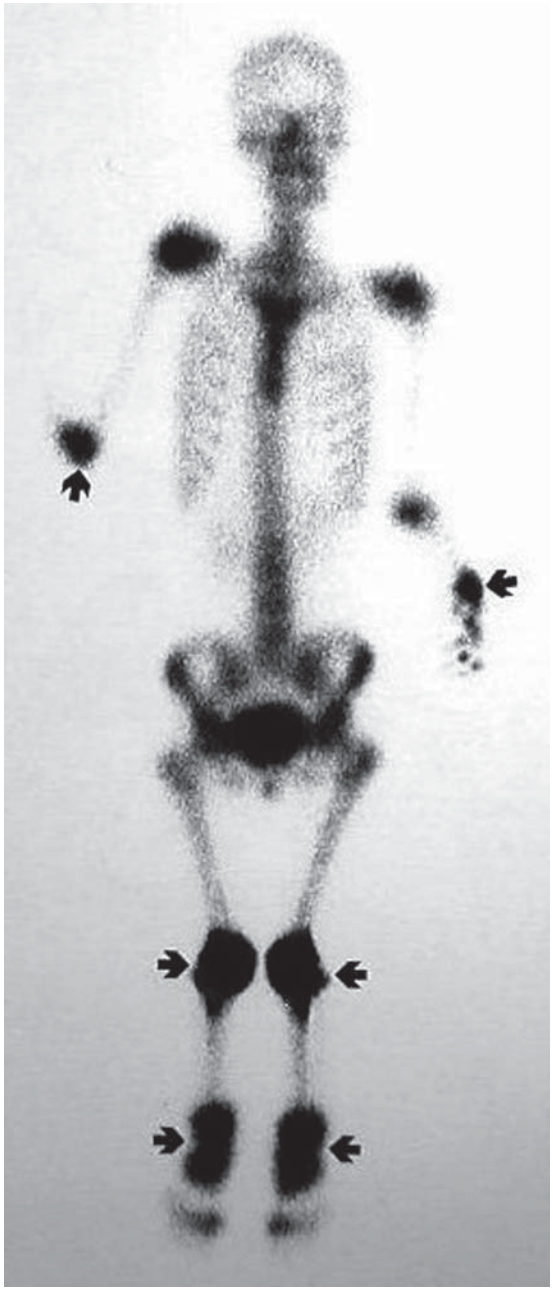

Fig. 10.49 Value of whole-body bone scintigraphy in the diagnosis of juvenile rheumatoid arthritis. Anterior whole-body bone scan in an 18-year-old female with polyarthritis clearly shows prominent symmetrical multiarticular tracer uptake (*arrows*)

(Miller and Cassidy 2004). Pathology is characterized by villous hypertrophy and hyperplasia with hyperemia and edema of subsynovial tissues. Pannus, an inflammatory exudate that covers the inner synovial lining, is a stigma of early rheumatoid arthritis. It gradually erodes the articular cartilages, invades contiguous bones, and finally results in ankylosis. Diagnosis is based on exclusions as well as on objective arthritis, classic intermittent fever, and rash.

Radiographic features include soft-tissue swelling and osteopenia and enlargement of the distal femoral and proximal tibial epiphyses with articular widening or narrowing (Fig. 10.48A). Cervical involvement is a heralding sign in 2% of patients (Ansell and Kent 1977). Detailed description on the scintigraphic features of juvenile rheumatoid arthritis is scanty (Jones et al. 1988). According to our limited experience, juvenile rheumatoid arthritis appears to be another excellent indication for bone scintigraphy reinforced with pinhole scintigraphy. Indeed, pinhole scintigraphy provides useful information on synovitis, erosion, and enlarged periarticular bones that are caused by hypervascularity (Fig. 10.48B). In addition, as in rheumatoid arthritis in adults, whole-body scanning is extremely valuable in juvenile rheumatoid arthritis for the holistic survey of monopauci-, or polyarticular involvement as well as bone contracture and deformity that may occur in the late stage (Fig. 10.49).

10.15 Nuclear Angiography in Rheumatoid Arthritis

Nuclear angiography is widely used for a dynamic assessment of vascular alteration in rheumatoid arthritis, especially in the early stage (Hopfner et al. 2002, 2004). As in any inflammatory or infective diseases of the skeleton, nuclear angiography provides unique information on the disease activity of rheumatoid arthritis using visual or quantitative analysis of the blood flow, blood pool, and tracer uptake

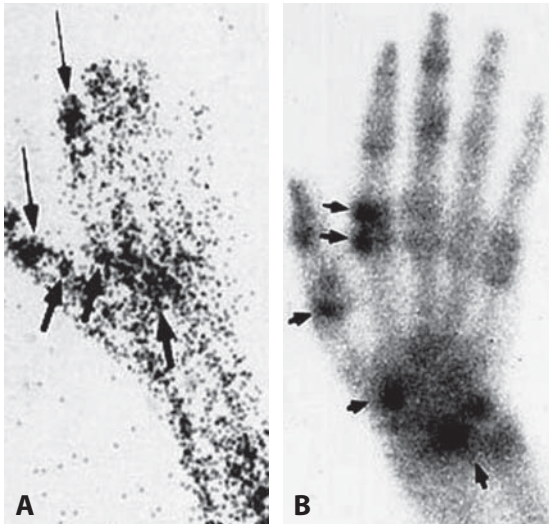

Fig. 10.50A, B Nuclear angiography in rheumatoid arthritis. **A** Nuclear arteriogram of the right hand with rheumatoid arthritis shows areas of increased vascularity in the intercarpal and first through third carpometacarpal joints (*arrows*). **B** Static bone scan reveals increased uptake in inflamed focus of rheumatoid arthritis (*arrows*)

both in the articular bones and the periarticular soft-tissue structures. Actually, synovitis with pannus is an ideal target of nuclear angiography since the synovial interface with the cartilage and bone is the primary "attack zone" for rheumatoid arthritis (Feldmann et al. 1990; de Bois et al. 1995).

Pathologically, synovial hypertrophy occurs following edema and blood vessel proliferation due to the coordinated action of vascular and cellular responses during the first weeks of rheumatoid arthritis (Cotran et al. 1989; Stevens et al. 1991). Indeed, nuclear angiography shows increased blood flow to and blood pool in the inflamed synovium and chondro-osseous zone on rheumatoid joints (Fig. 10.50A). The tips of the fingers may become flushed with increased blood flow. Such vasodilatation could be related to systemic microcirculatory compromise that has been known to occur in rheumatoid arthritis (Rothschild and Masi 1982), and more specifically to endothelial dysfunction (Vaudo et al. 2004). The equilibrium phase (static) bone scan reveals increased tracer uptake in inflamed focus of rheumatoid arthritis (Fig. 10.50B).

10.16 Molecular Imaging in Rheumatoid Arthritis

Molecular imaging can also provide information on rheumatoid activity. The radiopharmaceuticals developed for molecular imaging include ^{99m}Tc-anti-E-selectin antibodies, ^{99m}Tc-IgG, radiolabeled cytokines, and somatostatin receptor (de Bois et al. 1995; Jamar et al. 2002; Dalm et al. 2003). Scintigraphy using these agents has been shown to more sensitively visualize rheumatoid synovitis than ^{99m}Tc-HDP bone scintigraphy.

10.17 ^{99m}Tc-FDG PET-CT in Rheumatoid Arthritis

The fact that ^{18}F-FDG in inflamed joints was first reported by Yasuda et al. (1996) and, most recently, ^{18}F-FDG PET-CT has been used for the diagnosis of early rheumatoid arthritis (Beckers et al. 2004). ^{18}F-FDG PET-CT was systematically applied to the monitoring of disease activity by simultaneous multiarticular assessment. The knees and either the wrists and finger joints or the ankles and first metatarsophalangeal joints were evaluated individually and globally (Fig. 10.9). Parameters derived from PET-CT and clinical, biological, and sonographic parameters were correlated. This study has confirmed that metabolic activity is significantly increased in synovitis in active rheumatoid arthritic joints. The diagnostic use of ^{18}F-FDG PET-CT is expected for more effective treatment of early rheumatoid synovitis. Figure 10.51 shows an incidental finding of ^{18}F-FDG uptake in a patient with rheumatoid arthritis who developed diffuse large B-cell

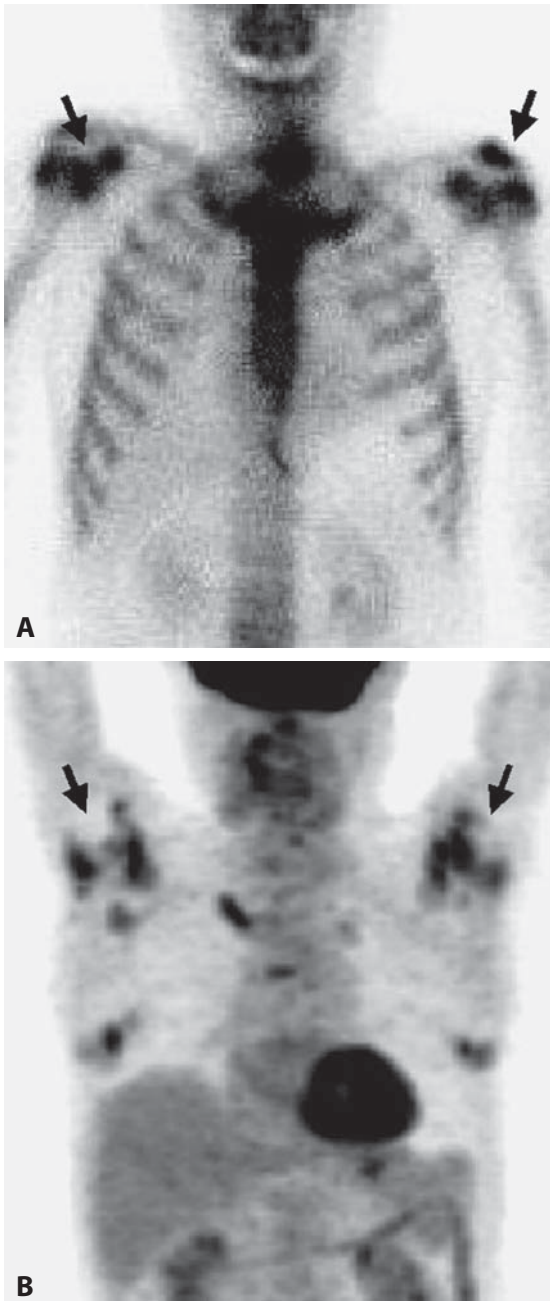

Fig. 10.51A, B ^{99m}Tc-MDP bone scan and ^{18}F-FDG PET in rheumatoid synovitis. **A** ^{99m}Tc-MDP bone scan shows mottled uptake in the shoulder joints denoting arthritis (*arrows*). **B** ^{18}F-FDG PET reveals exactly the same finding (*arrows*). Arthritis was incidentally diagnosed on PET performed for metastases that are indicated by scattered hot areas

lymphoma of the colon as a complication of prolonged administration of methotrexate and hydrocortisone for the treatment of rheumatoid arthritis.

References

Ansell BM, Kent PA (1977) Radiological changes in juvenile chronic arthritis. Skeletal Radiol 1:129–144

Arnett FC, Edworthy SM, Bloch DA, et al (1988) The American Rheumatism Association 1987 revised criteria for the classification of rheumatoid arthritis. Arthritis Rheum 31:315–324

Babini JC, Gusis SS, Babini SM, et al (1992) Superolateral erosions of the humeral head in chronic inflammatory arthropathies. Skeletal Radiol 21:515–517

Beckers C, Ribbens C, Andre B, et al (2004) Assessment of disease activity in rheumatoid arthritis with ^{18}F-FDG PET. J Nucl Med 45:956–964

Bland JH (1967) Rheumatoid arthritis of the cervical spine. Bull Rheum Dis 18:471–476

Calabro JJ (1962) A critical evaluation of the diagnostic features of the feet in rheumatoid arthritis. Arthritis Rheum 5:19–29

Cotran RS, Kuman V, Robbins SL (1989) Inflammation and repair. In: Cotran RS, Kuman V, Robbins SL (eds) Pathologic basis of disease. WB Saunders, Philadelphia, pp 39–86

Dalm VA, van Hagen PM, Krenning EP (2003) The role of octreotide scintigraphy in rheumatoid arthritis and sarcoidosis. Q J Nucl Med 47:270–278

de Bois MH, Pawels EK, Breedvelt FC (1995) New agents for scintigraphy in rheumatoid arthritis. Eur J Nucl Med 22:1339–1346

Elhabali M, Sherak O, Seidl G, et al (1979) Tomographic examinations of sacroiliac joints in adult patients with rheumatoid arthritis. J Rheumatol 6:417–425

Feldmanm M, Brennan FM, Chantry D, et al (1990) Cytokine production in the rheumatoid joint: implications for treatment. Ann Rheum Dis 49:480–486

Fletcher DE, Rowley KA (1952) The radiological features of rheumatoid arthritis. Br J Radiol 25:282–295

Foster DR, Park WM, McGall IW, Ward DJ (1980) The supinator notch sign in rheumatoid arthritis. Clin Radiol 31:195–199

Freyberg RH (1968) A study of time of onset of structural joint damage in rheumatoid arthritis (abstract). Arthritis Rheum 11:481

Gibson HJ (1955) Special pathology of rheumatoid arthritis. In: Copeman WSC (ed) Textbook of the rheumatic disease, 2nd edn. Churchill Livingstone, London

Gumina S, Salvatore M, De Santis R, et al (2002) Coracoclavicular joint: osteolytic study of 1020 human clavicles. J Anat 201:513–519

Hendrix RW, Urban MA, Schroeder JL, Rofer LF (1987) Carpal predominance in rheumatoid arthritis. Radiology 164:219–222

Hopfner S, Treitl M, Krolak C, et al (2002) Diagnosis of initial changes in the hand of patients with rheumatoid arthritis – comparison between low-field magnetic resonance imaging, 3-phase bone scintigraphy and conventional X-ray. Nuklearmedizin 41:135–142

Hopfner S, Treitl M, Becker-Gaab C, et al (2004) Diagnosis of initial changes in patients suffering from rheumatoid arthritis. Two years follow up control with a low-field magnetic resonance scanner, 3-phase bone scintigraphy and conventional X-ray. Nuklearmedizin 43:195–202

Jamar F, Houssiau FA, Devogelaer, et al (2002) Scintigraphy using a technetium ^{99m}-labeled anti-E-selectin Fab fragment in rheumatoid arthritis. Rheumatology (Oxford) 41:53–61

Jones MM, Moore WH, Brewer EK, et al (1988) Radionuclide bone/joint imaging in children with rheumatic complaints. Skeletal Radiol 17:1–7

Lawrence JS, Sharp J, Ball J, et al (1964) Rheumatoid arthritis of the lumbar spine. Ann Rheum Dis 23:205–217

Lehtinen JT, Kaarela K, Belt EA, et al (1999) Coracoclavicular involvement – an atypical manifestation in rheumatoid arthritis. Scand J Rheumatol 28:252–253

Miller ML, Cassidy JT (2004) Juvenile rheumatoid arthritis. In: Behrman RE, Kliegman RM, Jenson HL (eds) Nelson textbook of pediatrics, 17th edn. WB Saunders, Philadelphia, pp 799–805

Resnick D (1974) Rheumatoid arthritis of the wrist: why the ulnar styloid? Radiology 112:29–35

Resnick D (1976) Early abnormalities of pisiform and triquetrum in rheumatoid arthritis. Ann Rheum Dis 35:46–50

Resnick D (2004) Diagnosis of bone and joint disorders, 4th edn. WB Saunders, Philadelphia, pp 891–987

Rothschild BM, Masi AT (1982) Pathogenesis of rheumatoid arthritis: a vascular hypothesis. Semin Arthritis Rheum 12:11–31

Sandrock D, Backhaus M, Burmesten G, Munx DL (2003) Imaging technology in rheumatology: scintigraphy in rheumatoid arthritis. Z Rheumatol 62:476–480

Sims-Williams H, Jayson MIV, Baddeley H (1977) Rheumatoid involvement of the lumbar spine. Ann Rheum Dis 36:524–531

Stevens CR, Blake DR, Merry P, et al (1991) A comparison study by morphometry of microcirculation in normal and rheumatoid synovium. Arthritis Rheum 34:1508–1513

Vaudo G, Marchesi S, Gerli R, et al (2004) Endothelial dysfunction in young patients with rheumatoid arthritis and low disease activity. Ann Rheum Dis 63:31–35

Wolfe AM (1968) The epidemiology of rheumatoid arthritis: review. Bull Rheum Dis 19:518–523

Yasuda S, Shotsu A, Ide M, et al (1996) F-^{18} FDG accumulation in inflamed joints. Clin Nucl Med 21:740

Zikou AK, Alamanos Y, Argyropoulou MI, et al (2005) Radiological cervical spine involvement in patients with rheumatoid arthritis: a cross sectional study. J Rheumatol 32:801–806

11 Seronegative Spondyloarthropathies

Seronegative spondyloarthropathies (SNSA) affect genetically predisposed individuals and are triggered by environmental factors (Khan 2002). They consist of a group of closely related skeletal disorders characterized by the concurrence of arthritis and spondylitis, in which serological rheumatoid factor is absent, hence seronegative. SNSA include ankylosing spondylitis, Reiter's syndrome, psoriatic arthritis, arthritis associated with inflammatory bowel disease, and other rare forms of arthritides. The great majority of patients with one of these disorders demonstrate a positive test for HLA-B27, although in psoriatic arthritis the positivity rate is low. Two clinical features have been shown to be useful in distinguishing SNSA from rheumatoid arthritis. One is oligoarthropathy that is asymmetrical with a predilection for the peripheral joints and the other is enthesopathy (the enthesis is the bone insertion of ligament and tendon). In addition and fundamentally, SNSA can be differentiated from rheumatoid arthritis on genetic, immunological, pathological and radiological bases as well as by symptoms and signs. Radiography is helpful and ^{99m}Tc-MDP bone scintigraphy is highly sensitive but not specific (Hays and Green 1972; Desaulniers et al. 1974). Fortunately, however, a recent study by Kim et al. (1999) has shown that pinhole scintigraphy can provide specific information on SNSA, Reiter's syndrome in particular.

SNSA are ubiquitous, occurring worldwide in both sexes, and often present in a subclinical form, defying diagnosis. However, with a high index of suspicion and appropriately performed ^{99m}Tc-MDP bone scanning, the correct diagnosis can be reached without much difficulty. Actually, the whole-body bone scan portrays the characteristic distribution pattern of the affected spine and joints, and subsequently performed pinhole scan confirms the specific features of the individual arthritis and enthesopathy. In particular, plantar fasciitis and Achilles tendinitis in Reiter's syndrome, which are difficult to diagnose radiographically, can be sensitively detected by noting subtle tracer uptake in the characteristic sites (Kim et al. 1999). The pinhole scintigraphic features in the established cases closely correlate with those of radiography. In the following, the combined scintigraphic and radiographic manifestations of SNSA are discussed.

Pathology The basic pathological process that underlies the radiographic and scintigraphic manifestations of SNSA is enthesopathy. In addition, nonspecific inflammation and granulation attack the synovium and articular cartilage and bone. SNSA is expressed by fibrositis, ankylosis, ossification, and periarticular "whiskering". All these changes are relatively more mild in severity than in rheumatoid arthritis. Of particular interest in ankylosing spondylitis is the peculiar chondral type of ossification of fibrosed tissues, which have been transformed into cartilage, causing the "bamboo spine" deformity and the obliteration of the sacroiliac joints.

Radiographic Manifestations Radiographic manifestations may vary somewhat from disease to disease and also according to the stage of disease. On the whole, as opposed to rheumatoid arthritis, the periarticular osteopenia and subchondral erosions with articular nar-

rowing are not conspicuous features or may even be absent in SNSA. Instead, diffuse fibrosis, articular closure without narrowing, osteophytosis, whiskering, and spinal syndesmophytosis and ankylosis characterize the radiographic manifestations. Subchondral erosion may be a key feature in occasional sacroiliitis. Three radiographic features more or less common to ankylosing spondylitis, Reiter's syndrome, and psoriatic arthritis have been described. First, the numbers of joints affected in the appendicular skeleton are not many and asymmetrical with a predilection for the smaller limb joints (the lower limbs in ankylosing spondylitis and Reiter's syndrome and the distal phalanges in psoriatic arthritis). Second, the spine and sacroiliac joints are involved, especially in ankylosing spondylitis. Third, spinal syndesmophytosis ensues in ankylosis and the "bamboo" deformity and the enthesopathies in the pelvis and appendicular joints produce the "whiskering" sign.

The articulations regularly involved include the diskovertebral joints, sacroiliac joints, symphysis pubis, and parasternal joints and the entheses frequently affected include the tendon and ligament insertion sites of the pelvis, calcaneus, femoral trochanters, humeral tuberosities, and patella. The distribution pattern of affected joints in the individual SNSA is fairly typical. Thus, in ankylosing spondylitis the synovial joints and cartilaginous diskovertebral junctions and entheses of the spine are mainly affected. The median cartilaginous joints such as the manubriosternal joint and the symphysis pubis are also frequently involved (Bluestone 1979). The appendicular bones are less consistently and less severely affected. On the other hand, in Reiter's syndrome the lower limbs are more regularly involved, showing asymmetrical, spotty foci and calcaneal spur. Psoriasis affects many appendicular joints, including the distal interphalangeal joints.

Bone Scintigraphic Manifestations Bone scintigraphy reinforced with pinhole scanning is extremely useful in diagnosing the changes in the axial skeleton and peripheral joints in ankylosing spondylitis, Reiter's syndrome, and psoriatic arthritis. Whole-body scanning is ideal in providing a panoramic display of asymmetrical tracer uptake in the joints, bones, and entheses in the spine, sacroiliac joints, pelvis, and lower limbs (Fig. 11.1). Subsequent pinhole scanning of the region of interest greatly facilitates the in-depth analysis of the findings disclosed by whole-body scintigraphy, leading to specific diagnosis. As mentioned already, pinhole scintigraphy frequently helps detect preradiographic changes such as subtle and seemingly trivial tracer uptake in radiographically normal yet metabolically abnormal bone; for example, in the plantar aspect of the calcaneus in Reiter's syndrome (Fig. 11.2). In this situation, pinhole scintigraphy is clearly more sensitive and specific than any other diagnostic method. It is, however, beyond doubt that collateral radiography significantly enhances diagnostic accuracy and efficacy.

11.1 Ankylosing Spondylitis

Ankylosing spondylitis denotes nonspecific inflammatory or rheumatic disorder of the spine clinically characterized by stiffening, pain, fibrosis, and ankylosis. The disease typically affects the cartilaginous diskovertebral junctions and small accessory vertebral synovial joints, resulting in the "bamboo spine" deformity. The sacroiliac joint involvement is an essential constituent of the disease. The cause is obscure, but many recent studies have confirmed a strong association between this and other SNSA and the histocompatibility antigen HLA-B27. Spondylitis and sacroiliitis coexist in various degrees of severity, ranging from full-blown fibrosis with diffuse ankylosis to milder syndromes. This condition was once held to be rare, mainly affecting the male population, but is now recognized as a relatively common disease with Prevalence ranging from 0.5% to 1% of the population and a nearly equal sex distribution. Clinically, the initial chief complaint is back

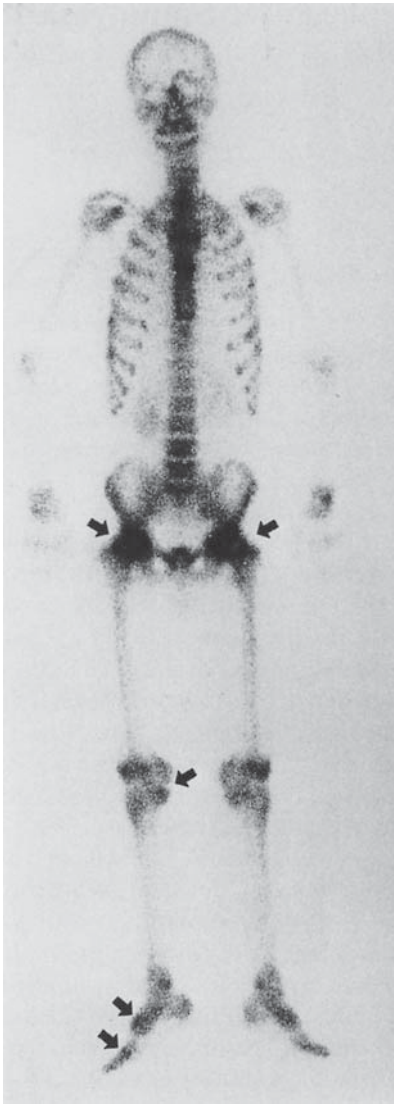

Fig. 11.1 Usefulness of whole-body scintigraphy in the study of the asymmetrical involvement of SNSA. Anterior whole-body scintigraph of a 37-year-old man with Reiter's syndrome reveals increased tracer uptake in both hips, the right knee, and the right foot (*arrows*). Note the asymmetrical and spotty distribution of the lesions in the lower limbs, an important feature of SNSA, particularly Reiter's syndrome

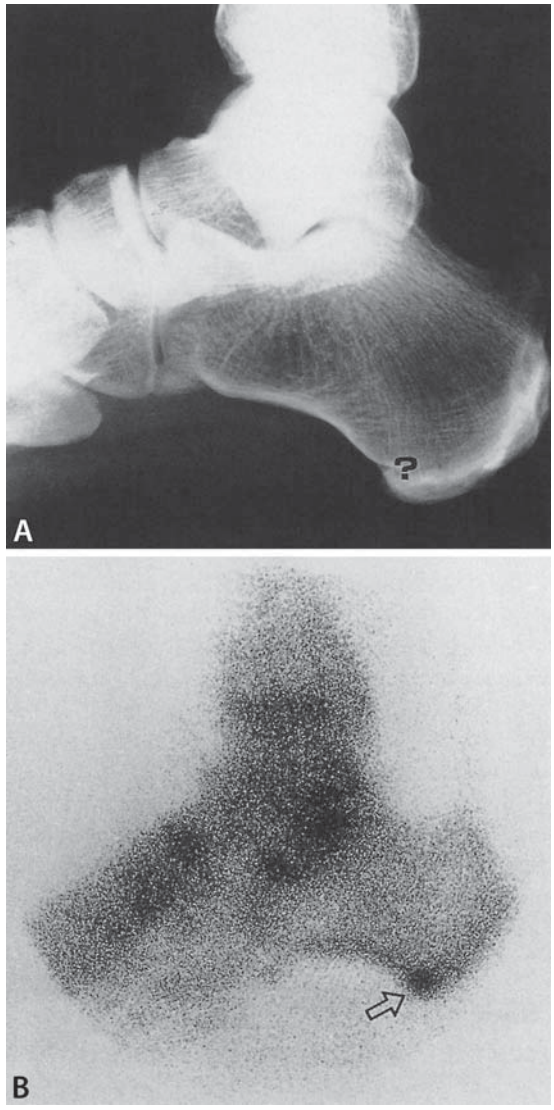

Fig. 11.2A, B Preradiographic diagnosis of Reiter's syndrome. **A** Mediolateral radiograph of the painful right heel in a 43-year-old man reveals no bony or soft-tissue abnormality (*?*). **B** Medial pinhole scintigraph shows very subtle tracer uptake in the posterior plantar aspect of the calcaneus, the sign of an early enthesopathic change in Reiter's syndrome (*open arrow*). The alteration could not be seen on an ordinary scintigraph (not shown)

pain with stiffening and limited motion of various degrees in about three-quarters of patients. Peripheral joint pain is complained of by 10% to 20% of patients (Sharp 1965) and chest tightness is an important symptom in some patients (Good 1963). The onset is insidious with the first symptom appearing between the ages of 15 and 35 years with the average in the mid-20s. The back pain is aggravated after rest and in the morning but improves after exercise. Sensory and motor symptoms are usually absent. In the early phase, the sacroiliac joint pain

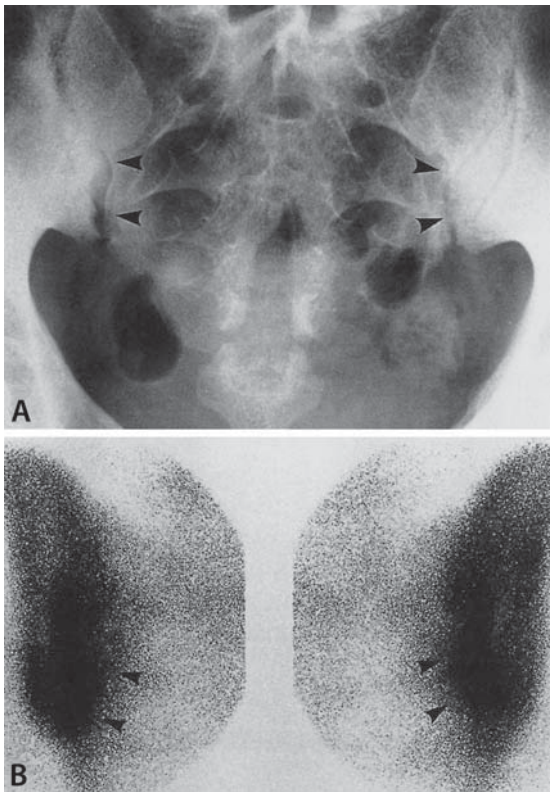

Fig. 11.3A, B Classic radiographic and scintigraphic manifestations of sacroiliitis in ankylosing spondylitis. **A** Anteroposterior radiograph of the sacroiliac joints in a 26-year-old man with ankylosing spondylitis reveals marginal blurring due to subchondral erosions and eburnation in the synovial lower compartment of both sacroiliac joints (*arrowheads*). Note nearly perfect symmetry of the pathology. **B** Minimally tilted posterior oblique pinhole scintigraphs of both sacroiliac joints (separate acquisitions) show increased tracer uptake localized in the synovial compartment of the joints symmetrically (*arrowheads*)

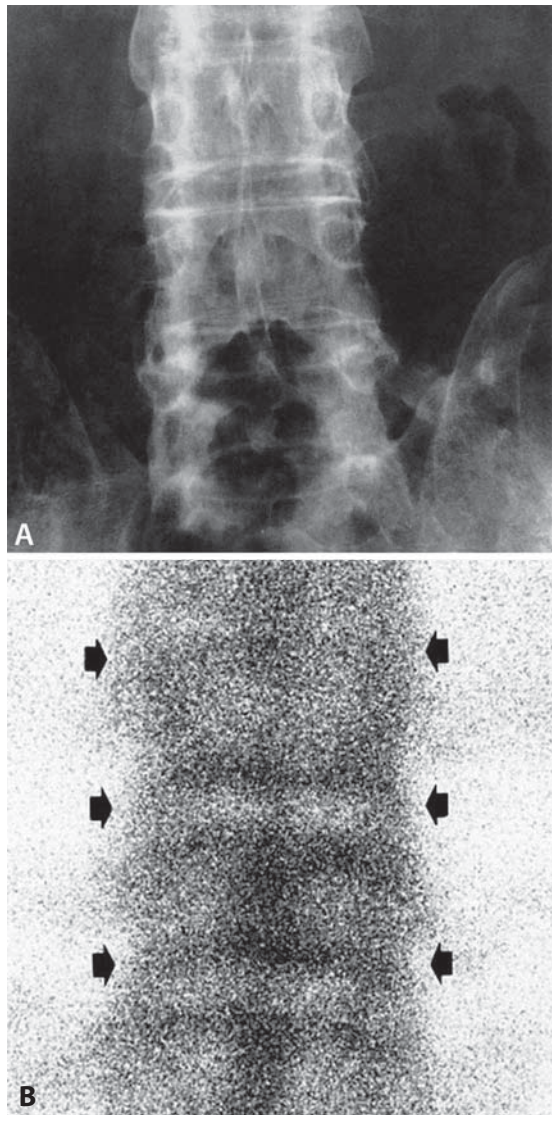

Fig. 11.4A, B Low tracer uptake in "bamboo spine" deformity of the advanced ankylosing spondylitis. **A** Anteroposterior radiograph of the lumbar spine with advanced ankylosing spondylitis in a 41-year-old man shows diffuse, osseous obliteration of the intervertebral spaces, small vertebral joints, and spinous processes, giving rise to the classic "bamboo spine" appearance. **B** Posterior pinhole scan shows a generalized decrease in tracer uptake due to quiescent metabolism in this stage of the disease. The spine appears "pale" with well-preserved disk spaces, a sign that the disks are not the main structures to be affected in this condition (*arrows*)

may be prominent. However, after ankylosis has been established it ameliorates and sometimes vanishes completely. Sciatica-like pain may be noted in about a half of patients at some stage of the disease (Ogryzlo 1972). The extraskeletal manifestations include iritis, spondylitic heart disease with cardiomegaly and pericarditis, tuberculosis-like fibrocavitary lung lesions, and intestinal inflammation or renal amyloidosis. It has been emphasized that the disease in a large number of patients with a milder form of the condition may pass undiagnosed.

Pathologically, as the term denotes, the inflammatory process initially involves the joints in the axial skeleton including the sacroiliac joints. In the spine the cartilaginous diskover-

tebral junctions and the synovial apophyseal, costovertebral, and neurocentral joints are affected. The most important feature in this and other SNSA is that, unlike in rheumatoid arthritis, the entheses and not the synovia are the main site of fibrositis (Ball 1971). Enthesopathy shows early lymphocytic and macrophage infiltration, suggesting its probable relationship to an immune-mediated pathogenesis. As the disease progresses, chondritis, osteitis, and periostitis may follow. In the final stage the bony ankylosis dominates.

Radiographically, the heralding alterations in the sacroiliac joints are characterized by a broad spectrum of findings, ranging from marginal blurring and bone erosions to eburnation and joint space narrowing. Sacroiliitis is typically bilateral (Fig. 11.3A). Classically, enthesopathy first moves from the sacroiliac joints cranially to the thoracolumbar and lumbosacral spine and then to the midlumbar, upper thoracic, and cervical level (Wilkinson and Bywaters 1958). The vertebral squaring, a characteristic sign of the condition, results from the syndesmophytosis of the annulus fibrosus and longitudinal ligaments. Eventually, the fibrosed ligaments become ossified, resulting in the "bamboo spine" deformity (Fig. 11.4A). With chronicity, the disease further moves down to the hindfoot, causing Achilles tendinitis and calcaneal spur or "whisker". In contrast to the symmetrical, polyarticular affection of rheumatoid arthritis, the peripheral enthesopathy and articular change in this disease are asymmetrical and sparse.

Scintigraphic alterations vary according to disease stage. In the early stage, bone scanning shows tracer uptake in the sacroiliac joints, typically, but not always, on both sides. Increased uptake has been described to occur characteristically in the central joints, which include the spinal apophyseal joints and the sternoclavicular, manubriosternal, and costosternal joints (Lin et al. 1980). Pinhole scanning of the sacroiliac joints demonstrates intense uptake symmetrically. The uptake is localized predominantly to the ilia, reflecting enthesopathy in the thick ventral and dorsal sacroiliac ligament as well as arthritis. The main lesions are clearly indicated by more intense uptake surrounded by less intense reactive uptake in the para-arti-

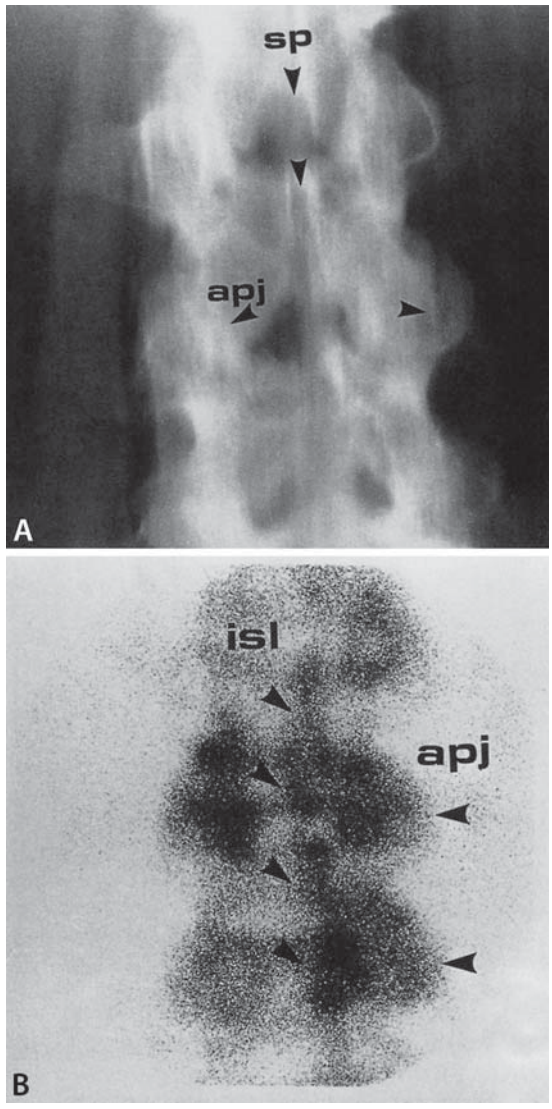

Fig. 11.5A, B Pinhole scintigraphic manifestations of the individual, vertebral structure involvement in ankylosing spondylitis. **A** Anteroposterior conventional X-ray tomogram of the midlumbar spine in a 30-year-old woman with ankylosing spondylitis shows narrowing and obliteration of the apophyseal joints (*apj*), fusion of the spinous processes (*sp*), and blurring of the vertebral contour. **B** Posterior pinhole scintigraph shows patchy, intense tracer uptake in the apophyseal joints (*apj, lateral arrowheads*), the vertebral endplates, the interspinous ligaments (*isl, midline arrowheads*), and the longitudinal ligaments

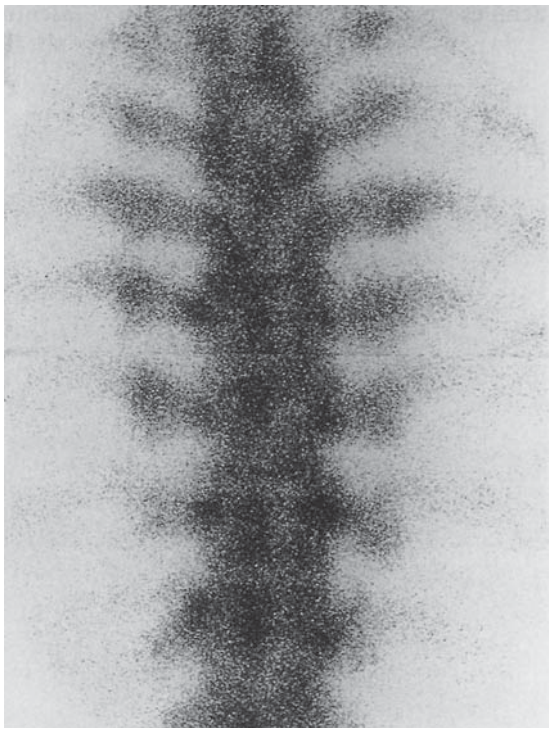

Fig. 11.6 "Centipede" sign of ankylosing spondylitis in the thoracic spine. Composite posterior pinhole scintigraph of the thoracic spine in a 22-year-old man with well-established ankylosing spondylitis shows diffuse tracer uptake in the longitudinal and interspinous ligaments, the synovial joints, and the diskovertebral junctions, producing the "centipede" appearance of generalized enthesopathic spondylitis. Compare with the normal thoracic spine (Fig. 4.18)

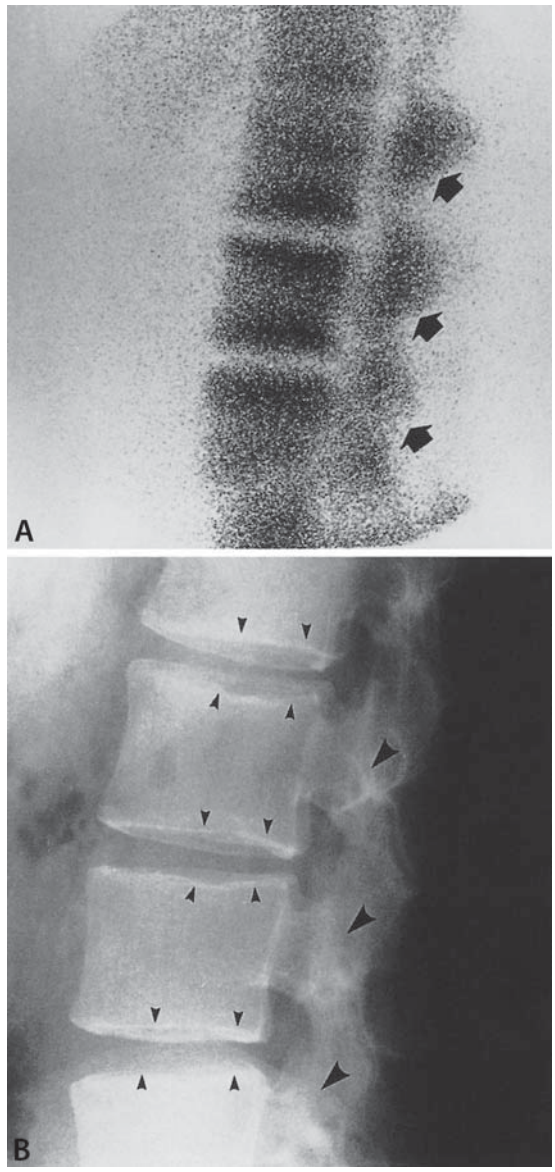

Fig. 11.7A, B Preradiographic demonstration of the vertebral squaring in ankylosing spondylitis. **A** Lateral pinhole scan of the lumbar spine in a 21-year-old man with ankylosing spondylitis shows the squaring of the L2–L5 vertebral bodies. The vertebral endplates and apophyseal joints also concentrate tracer significantly due to enthesopathy (*arrows*). **B** Lateral radiograph of the same lumbar spine demonstrates minimal disk space narrowing with endplate thinning (*small arrowheads*) and the obliteration of the apophyseal joints (*large arrowheads*), but no squaring of the vertebral bodies

cular bones (Fig. 11.3B). Associated spinal lesions may or may not be present at this stage. Later, as the spine becomes involved, pinhole scintigraphy shows (a) patchy uptake in the apophyseal joints, (b) horizontal band-like uptake in the diskovertebral junctions, and (c) midline uptake in the spinous processes and interspinous ligaments (Fig. 11.5). Diffuse involvement of the longitudinal ligaments along with the costovertebral joints, the spinous processes, and the interspinous ligaments of the thoracic spine gives rise to the characteristic "centipede" appearance (Fig. 11.6). It is important to note that the characteristic vertebral squaring may be often seen ahead of radiographic change (Fig. 11.7). As a whole, this and other already described scintigraphic features are in good accord with the classic radiographic findings. More classic squaring may be

seen in advanced cases. With further progression of the disease, the cervical spine becomes involved, presenting tracer uptake in the intervertebral and interarticular spaces as well as a narrowed atlantoaxial joint. Tracer uptake is markedly reduced in the late stage, reflecting the quieter metabolic state of the disease. As a result, the spine images "pale" and indistinct yet with well-preserved intervertebral spaces (Fig. 11.4B).

With chronicity, the peripheral joints become involved, particularly in females. The hip, sternal joints, glenohumeral joint, knee, hand, foot, and calcaneus are predisposed. The diffused pattern of tracer uptake in this disease is basically the same as that in rheumatoid arthritis, but the distribution is not symmetrical and the involvement is sparse. As mentioned earlier, the comparable alterations in osteoarthritis are usually discrete and focal (Fig. 9.5A).

11.2 Reiter's Syndrome

The classic type of the syndrome as described originally by Hans Reiter in 1916 (Reiter 1916) consists of a triad of urethritis, arthritis, and conjunctivitis. The disease mechanism is still obscure, but an interaction between several different infective organisms and a specific genetic background is now being seriously considered. As more clinical experience and laboratory data accumulate, the existence of various formes frustes of the syndrome have been noted. Further complicating the situation, the syndrome has been described under a number of different names such as sexually acquired reactive arthritis (Keat et al. 1978), incomplete Reiter's syndrome (Arnett et al. 1976), and even rheumatoid variants, creating semantic confusion. A more simple and practical criterion for definite Reiter's syndrome has been proposed by Willkens et al. (1981), who defined the syndrome as an episode of arthritis lasting longer than 1 month in association with urethritis or cervicitis. The syndrome may be associated with diarrheal disorder or a postvenereal complication. The prevalence of Reiter's syndrome is not easy to assess because of the difficulty in making a definite diagnosis. This is due mainly to the lack of absolute diagnostic criteria, the mobile community of young adults that constitutes the majority of patients, and the frequently suppressed history of venereal disease and forgotten features of diarrheal disorder. The

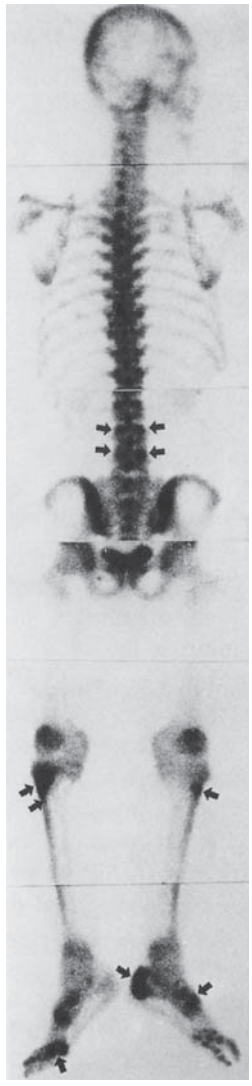

Fig. 11.8 Spotty asymmetrical polyarthritis and spondylitis in Reiter's syndrome. Composite whole-body spot scintigraph in a 26-year-old man with Reiter's syndrome panoramically delineates the lesions in the lower lumbar spin, both proximal tibiae, the right forefoot, and the left hind- and midfoot (*arrows*)

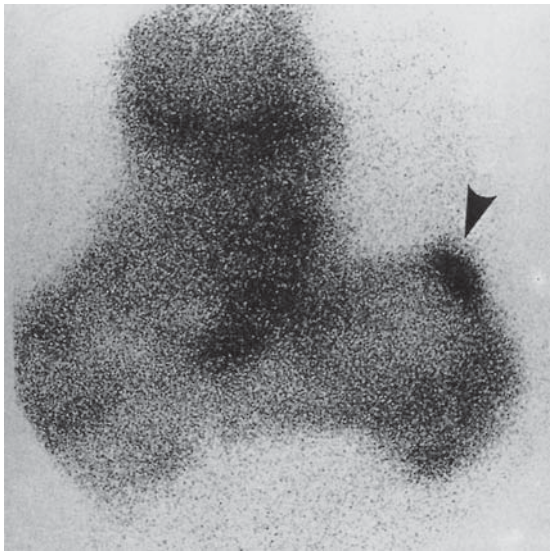

Fig. 11.9 Early pinhole scintigraphic diagnosis of Reiter's enthesopathy in the calcaneus. Medial pinhole scan of the right hindfoot in a 30-year-old man with focal osteoenthesopathy shows a small spotty tracer uptake in the upper posterior aspect of the calcaneus (*arrowhead*)

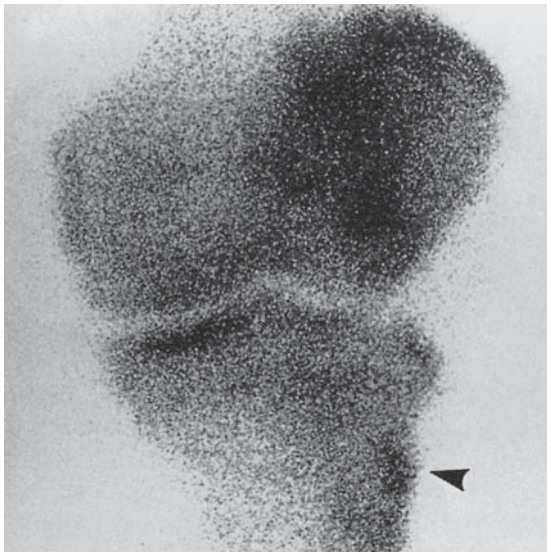

Fig. 11.10 Preradiographic diagnosis of early Reiter's enthesopathy in the knee. Anterior pinhole scintigraph of the left knee in a 48-year-old man with fibular head pain shows faint tracer uptake in the fibular ligament insertion site (*arrowhead*). The anatomical location was confirmed by radiography, which did not reveal comparable alteration (not shown). An ordinary scintigraph also failed to reveal abnormality even in retrospective observation

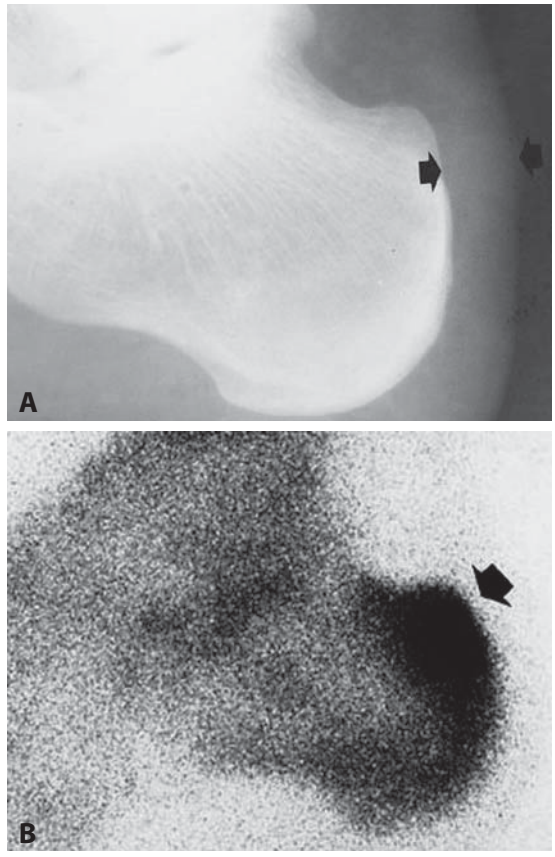

Fig. 11.11A, B Progression of scintigraphic change of upper retrocalcaneal enthesitis in Reiter's syndrome. **A** Lateral radiograph of the right calcaneus in a 26-year-old man shows thickening of the distal Achilles tendon at the calcaneal insertion (*arrow*). **B** Lateral pinhole scintigraph reveals intense reactive uptake at the Achilles insertion (*arrow*)

gender distribution has been reported as an overwhelming male preponderance, but a study by Fox et al. (1979) indicated a high prevalence of 15% in women. The highest incidence of the syndrome occurs in the third decade of life, but no age is immune.

Important clinical features are persistent or recurrent joint pain and pauciarticular involvement of the weight-bearing joints. Dactylitis, popularly known as the "sausage digit", is a characteristic digital manifestation. Tendinitis and fasciitis with extrasynovial swelling and enthesopathic spinal inflammation are other diagnostic stigmata. Urethritis or cervicitis and ocular lesions including conjunctivitis, iritis,

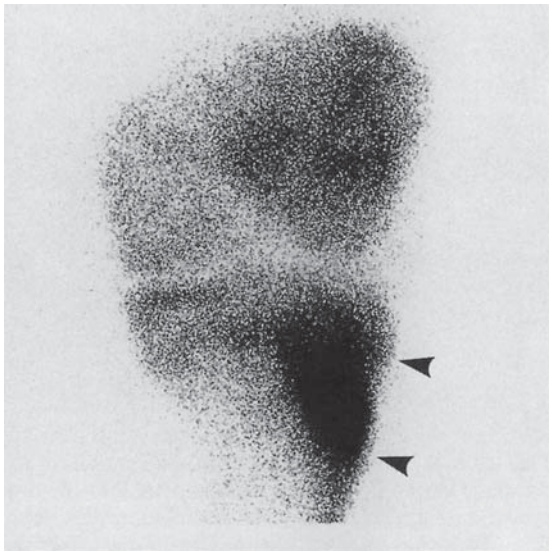

Fig. 11.12 (154). Progression of scintigraphic change of Reiter's osteoenthesopathy in the knee. Anterior pinhole scintigraph of the left knee in 26-year-old man with well-established Reiter's syndrome (the same patient as in Fig. 11.8) demonstrates extremely intense, triangular tracer uptake in the lateral aspect of the proximal tibia at the fibular ligament insertion site and the proximal tibiofibular articulation (*arrowheads*)

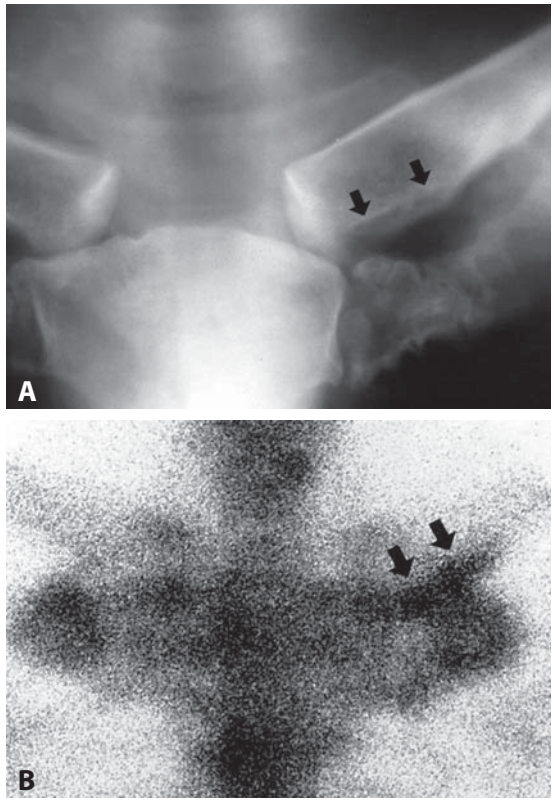

Fig. 11.13A, B Para-articular enthesitis of the sternoclavicular joint in Reiter's syndrome. **A** Conventional tomogram of the left sternoclavicular joint in a 43-year-old man shows erosions in the undersurface of the medial part of the clavicle and upper border of the subjacent ossified first rib cartilage (*arrows*). Note that the pathology is not in the joint but in the enthesis. **B** Anterior pinhole scintigraph reveals tracer uptake specifically localized to enthesis (*arrows*)

and uveitis may constitute important extraskeletal clinical manifestations.

Pathologically, the most characteristic change is observed in the entheses in the form of inflammatory enthesopathies that sharply contrasts with overwhelming involvement of the synovia in rheumatoid arthritis. Typical enthesopathies include Achilles tendinitis, calcanean plantar fasciitis, sausage digit, and the whiskering of the iliac crest, ischiopubic bone, trochanter, and spine. No radiographic change is present in the early stage. The first signs to manifest in the joints include periarticular soft-tissue swelling, articular narrowing, and bone erosions in the absence of significant osteopenia. Tendinitis, fasciitis, periosteal thickening, and whiskering follow. Spurs in the plantar and posterior portions of the calcaneus and sausage-like deformity of the toes are important features. Not infrequently unilateral or bilateral sacroiliitis occurs mimicking ankylosing spondylitis, and when the spine is involved radiographic findings become indistinguishable.

Bone scintigraphy is the method of choice for the panoramic mapping of asymmetrical foci of polyarthritis and spondylopathy of Reiter's syndrome (Fig. 11.8). When augmented with the pinhole technique, bone scintigraphy is more sensitive and often more specific than radiography, revealing early enthesopathies in the heel and knee (Kim et al. 1999). During the very early stage of the disease painful enthesopathies in the heel or knee may not be detected by radiography, but pinhole scintigraphy can portray subtle uptake as early as at

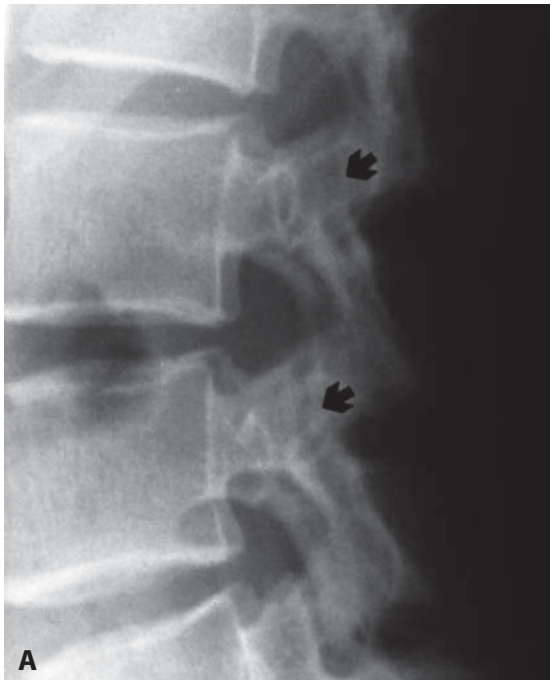

Fig. 11.14A, B Apophyseal joint involvement in spinal Reiter's syndrome. **A** Lateral radiograph of the lumbar spine in a 16-year-old male shows blurring and narrowing of the apophyseal joints of L2–3 (*upper arrow*) and L3–4 (l*ower arrow*). **B** Lateral pinhole scintigraph reveals increased tracer uptake in the affected apophyseal joints and also in L3 lower and L4 upper endplates denoting diskovertebral joint involvement, which is not shown on the radiograph

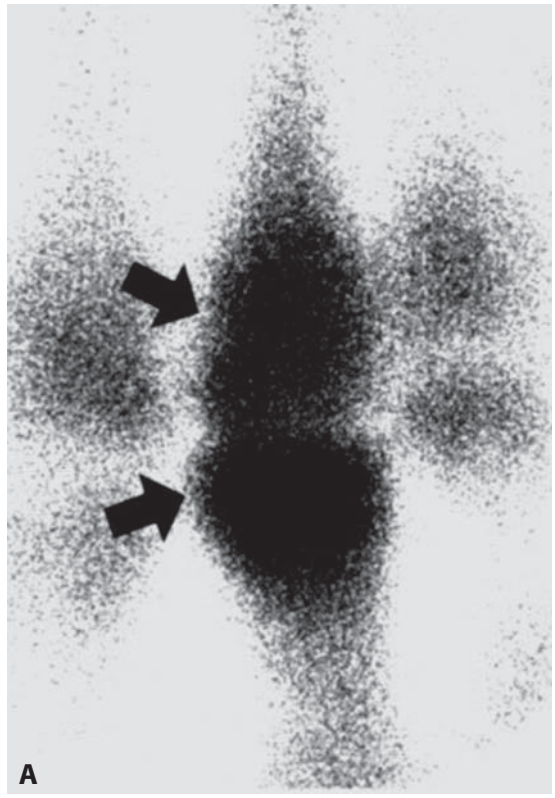

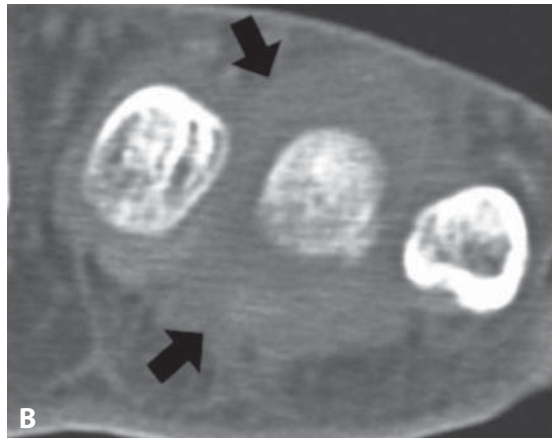

Fig. 11.15A, B The "sausage digit" sign. **A** Dorsal pinhole scan of the metatarsophalangeal joint of the right middle toe in a 30-year-old man with Reiter's syndrome shows fusiform tracer uptake resembling a sausage (*arrows*). **B** CT reveals edematous obliteration of the bone marrow with soft-tissue thickening or enthesitis (*arrows*)

this stage of the disease (Figs. 11.9 and 11.10). Even more importantly, many such extremely subtle yet significant tracer uptakes may pass undetected by ordinary bone scintigraphy. To be specific, the subtle uptake occurs in the superior posterior edge or the plantar aspect of the calcaneus in the heel (Figs. 11.2 and 11.9) and the fibular ligament insertion at the proximal tibia (Fig. 11.10). No corresponding radiographic change can be observed in many of these early cases. With progress of disease, the calcaneal tendon becomes involved, showing prominent tracer uptake in the upper and middle retrocalcaneal surface, whereas radiographically the enthesic or tendinous lesion is barely discernible (Fig. 11.11). Progressive change of enthesitis can also be observed in the proximal tibiofibular lesions (Fig. 11.12).

Pinhole scintigraphy provides unique information on the specific anatomical sites of involvement, the enthesis and synovial joint, by Reiter's disease in the hip, knee, hindfoot, finger, spine, and sternum. For example, in sternal Reiter's disease, characteristic tracer uptake occurs at the insertion of the costoclavicular ligament (Fig. 11.13) or both the anterior sternoclavicular ligament and the costoclavicular ligament, but usually not in the sternoclavicular joint. In the spine, the disease affects the apophyseal joints, manifesting characteristic tracer uptake that is localized to the joints (Fig. 11.14). On the other hand, the whole-body scan is indispensable for obtaining information on systemic distribution of SNSA. In addition, both the enthesopathy and arthropathy in Reiter's syndrome strongly tend to affect the lumbar spine and lower limb joints (Fig. 11.8), helping distinguish it from ankylosing spondylitis and psoriasis in which the lower limb joints are rather sparingly affected.

With regard to specific signs, pinhole scintigraphy can demonstrate both the anatomical

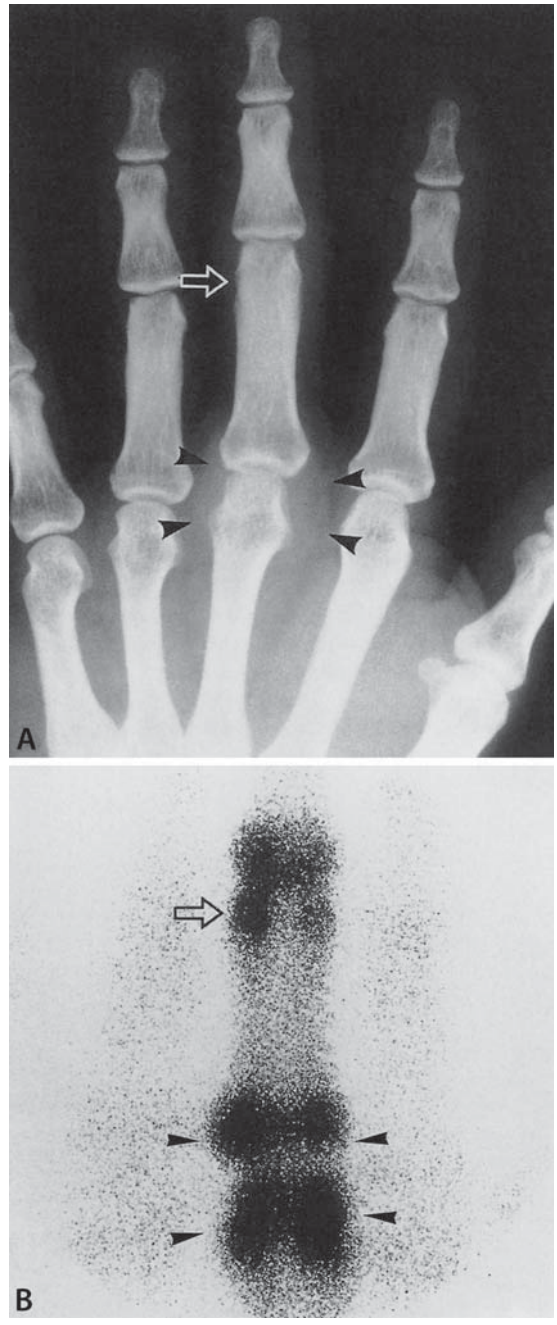

Fig. 11.16A, B Anatomical and metabolic alterations of the "sausage digit" in Reiter's syndrome. **A** Dorsoventral radiograph of the diffusely thickened right middle finger in a 25-year-old man with Reiter's syndrome shows fusiform soft-tissue swelling about the metacarpophalangeal (*arrowheads*) and proximal interphalangeal (*arrow*) joints with periarticular erosions and articular narrowing. **B** Dorsal pinhole scintigraph shows very intense tracer uptake sharply localized in the periarticular bones of the metacarpophalangeal (*arrowheads*) and proximal interphalangeal joint (*open arrow*). Note that the abnormal tracer uptake is confined to the knuckled regions of the heads and bases of the digital bones with preserved articular spaces, producing a "knuckle bone" appearance

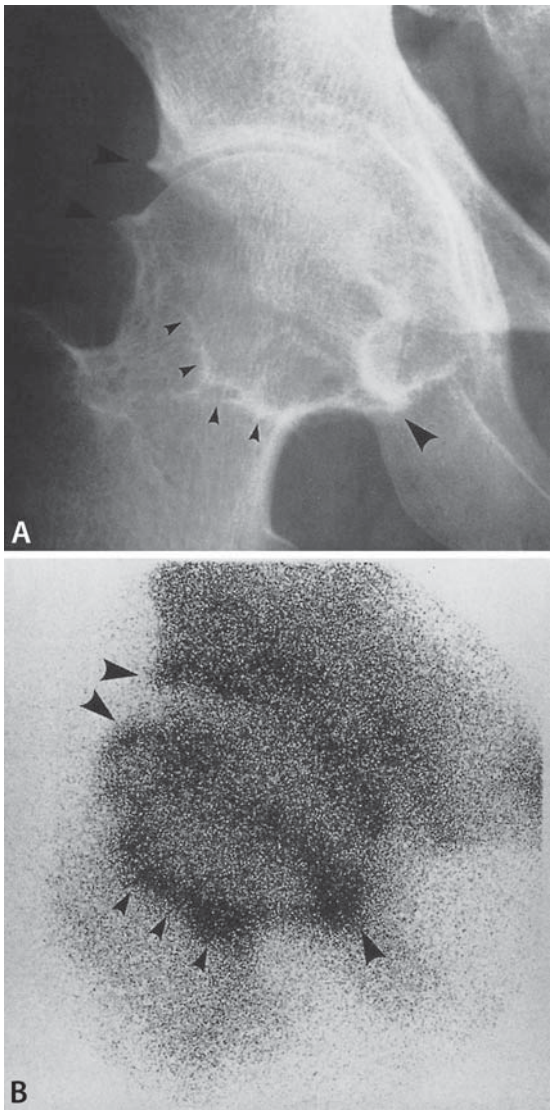

Fig. 11.17A, B Osteophytes or "whiskers" in the hip joint in Reiter's syndrome. **A** Anteroposterior radiograph of the right hip in a 28-year-old man with Reiter's syndrome shows shaggy bone excrescences in the femoral neck and the acetabular margin (*arrowheads*). Bone trabeculae appear coarsened and the joint space is moderately narrowed. **B** Anterior pinhole scintigraph shows necklace-like tracer uptake in the femoral neck and the acetabular margin (*arrowheads*)

and metabolic profiles of the sausage digit of Reiter's syndrome (Willkens et al. 1981). The sausage digit uptake reflects soft-tissue swelling resulting from effusion, periarticular edema, and bursal and tendinous inflammation or enthesopathy (Fig. 11.15). It may also be associated with erosions, periostitis, and whiskering (Fig. 11.16). Thus, pinhole scintigraphy shows expansive tracer uptake that is confined to the periarticular bones, especially the hallucis and digital muscles in the foot and the pollicis and digital muscles in the hand. The bones involved in this process consist of the base of the distally placed phalanx and the head of the proximally placed phalanx or metatarsal or metacarpal. When uptake is discrete it may be termed the "knuckle bone" appearance (Fig. 11.16B). To distinguish from rheumatoid arthritis, it appears helpful to observe that, except in rare early cases (Fig. 10.5), the tracer uptake in rheumatoid arthritis is diffuse and concentric, and not eccentric as in Reiter's syndrome. Such differences may reflect generalized synovitis in rheumatoid joints and eccentric enthesopathy in Reiter's syndrome (Fig. 11.16). The whiskers in the femoral head are indicated by spiky uptake and those in the neck by necklace-like uptake (Fig. 11.17).

Another sign is the asymmetrical, paravertebral "tear-drop" ossification that bridges the disk space in the thoracolumbar spine (Sundaram and Patton 1975). It is seen in 14% of cases, and antedates more widely recognized sacroiliac and peripheral articular involvement. Pinhole scintigraphically, this peculiar ossification is represented by roundish tracer uptake, bulging laterally from the margin of the disk space (Fig. 11.18). Occasionally, the uptake is exaggerated and larger in size than the radiographic "tear-drop" when apophysitis of the neighboring joint is superimposed (Fig. 11.19).

Bone scintigraphy is useful for the observation and follow-up of the inflammatory process in Reiter's disease after the initial diagnosis has been made and treatment instituted. Follow-up pinhole scanning performed 6 months after NSAID treatment with apparent amelioration of symptoms in one of our patients showed the spread of the inflammatory lesion from an initial single toe to three toes (Fig. 11.20). As an adjunct, nuclear angiography may be performed in Reiter's disease for the assessment of inflammatory change in terms of vascularity

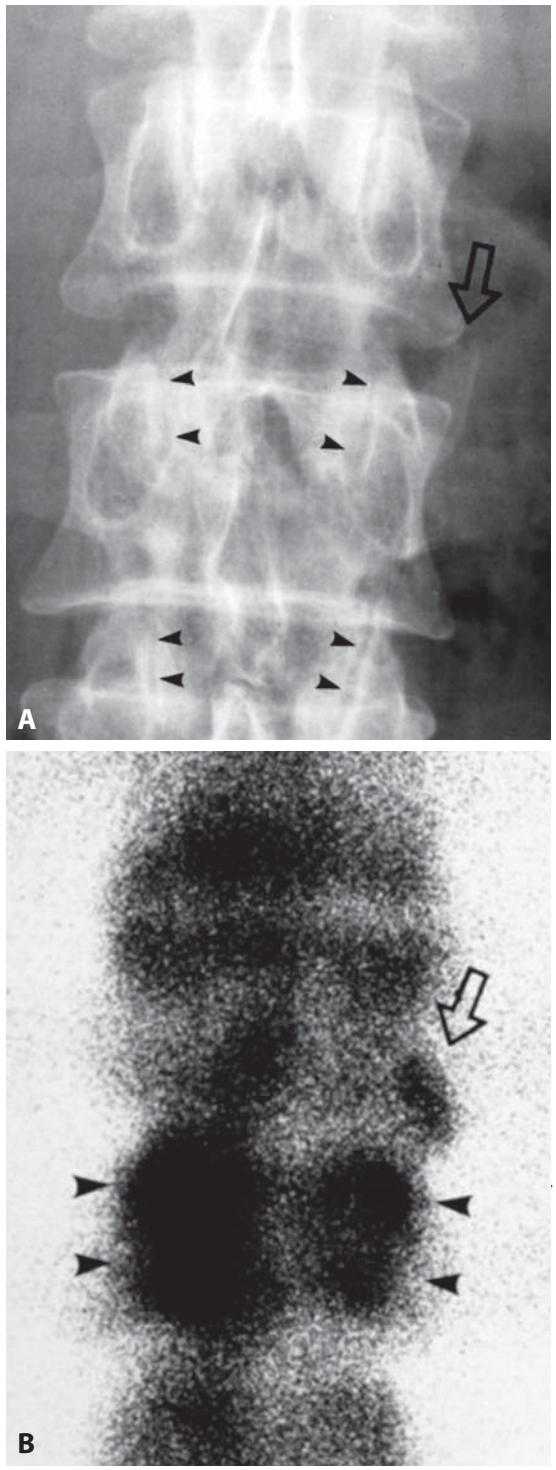

Fig. 11.18A, B The "tear-drop" sign in Reiter's syndrome. **A** Posteroanterior radiograph of the lumbar spine shows a vertically aligned ovoid bone bulging out at the L2–3 disk space level (*open arrow*). Apophyseal joints are narrowed due to apophysitis (*arrowheads*). **B** Posterior pinhole scintigraph reveals increased uptake in the "tear-drop" (*open arrow*) and apophysitis (*arrowheads*)

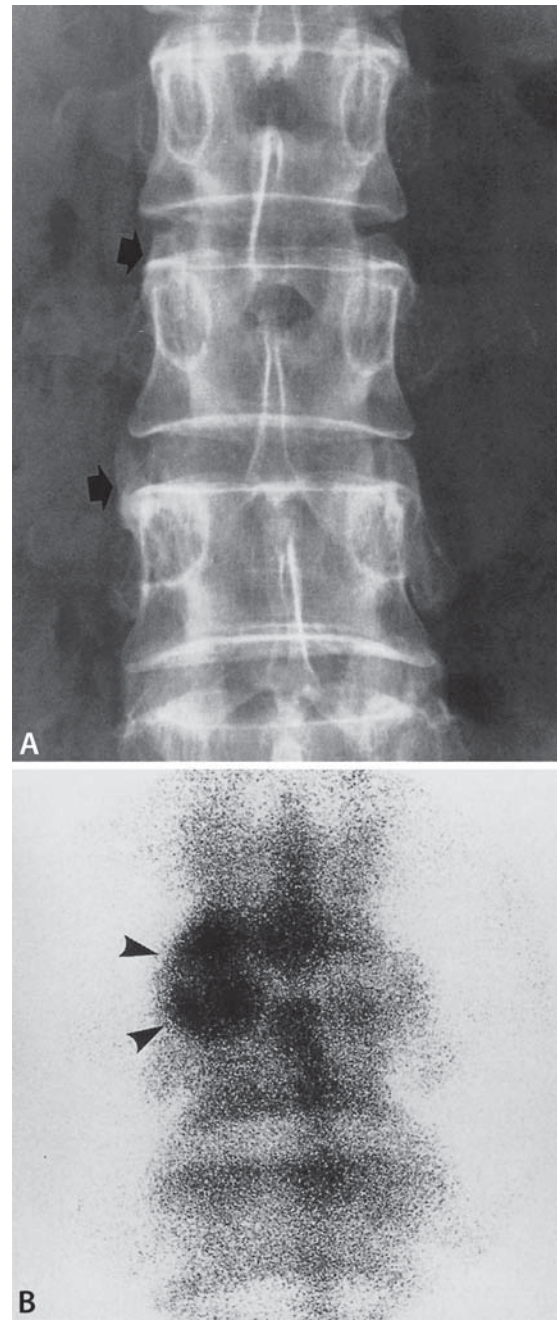

Fig. 11.19A, B Scintigraphic version of the "tear-drop" sign of the paravertebral ossification in Reiter's syndrome. **A** Anteroposterior radiograph of the lumbar spine in a 42-year-old woman with Reiter's syndrome reveals two small paravertebral ossifications in the upper right lateral aspects of L2 and L3 vertebrae (*arrows*). **B** Anterior pinhole scan of the L3 vertebra shows "tear-drop" shaped intense tracer uptake in the right paravertebral region, bridging the L2 and L3 vertebrae (*arrowheads*). The lesion in the L2 vertebra was not included because of the closest approximation of the collimator to the spine (contact imaging)

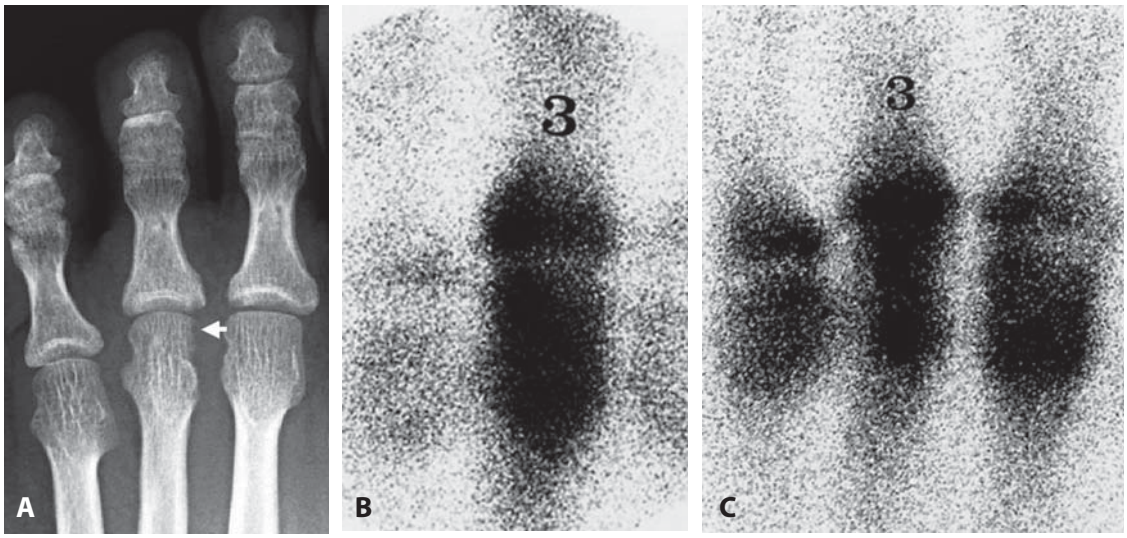

Fig. 11.20A–C Serial bone scans in Reiter's disease in the toes. **A** Initial dorsoplantar radiograph of the second through fourth toes of the left foot in a 29-year-old male with Reiter's syndrome shows minimal erosion in the head of the third metatarsal bone (*arrows*). **B** Initial bone scan reveals fusiform tracer uptake (*3*). **C** Follow-up scan 6 months after NSAID treatment shows spread of the lesion to two neighboring toes. This occurred with apparent amelioration of symptoms

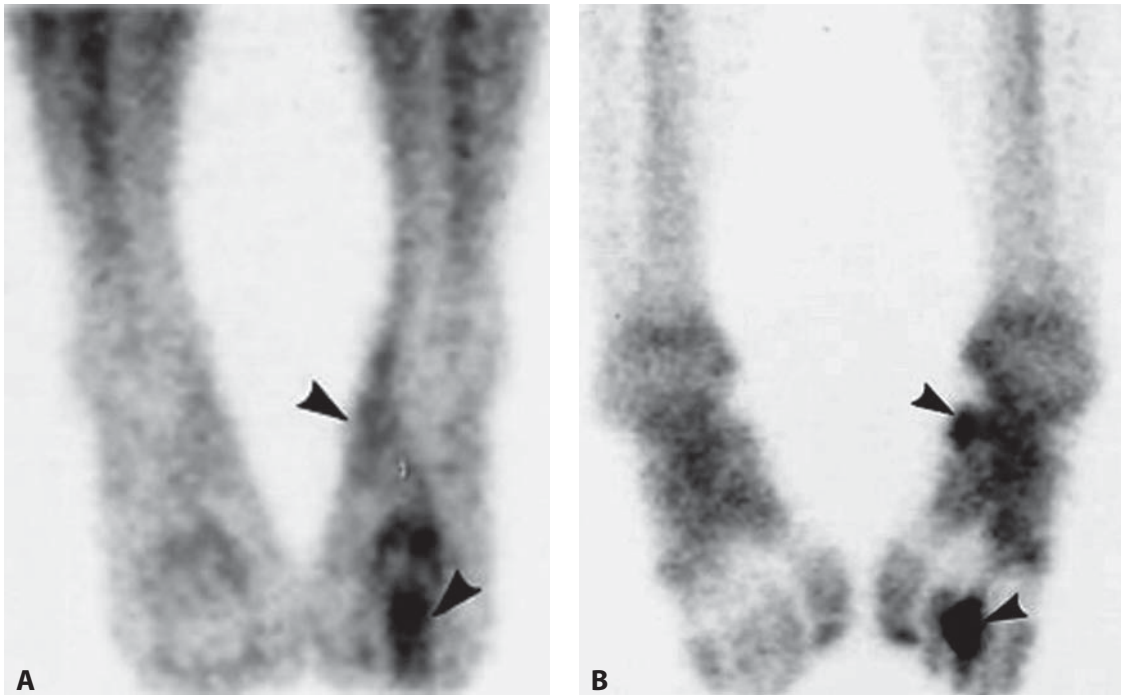

Fig. 11.21A, B Nuclear angiography in Reiter's syndrome. **A** Nuclear angiogram of the left ankle and foot in a 29-year-old male with Reiter's syndrome shows increased blood flow and blood pool (*arrowheads*). **B** Equilibrium scintigraph reveals bone uptake denoting both enthesopathy and bone reaction (*arrowheads*)

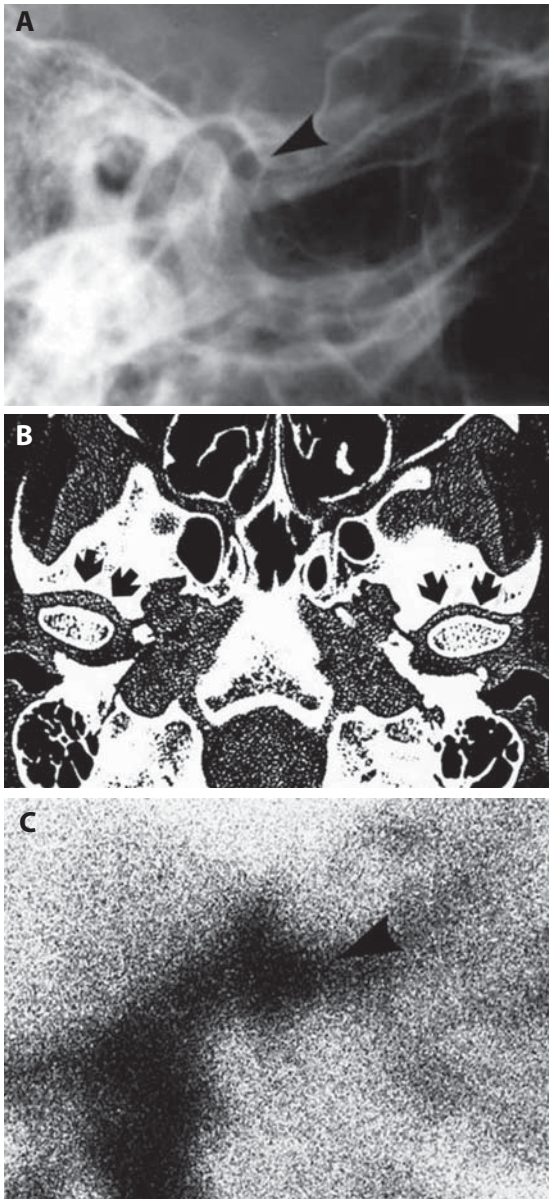

Fig. 11.22A–C Early changes of Reiter's syndrome in the temporomandibular joint. **A** Lateral radiograph of the right temporomandibular joint in a 38-year-old female shows articular widening (*arrowhead*). **B** Measure-set (W=264, C=115) CT reveals lysis of the joint disk with widened space (*left pair of arrows*). Note clearly visualized disk in the normal temporomandibular joint (*right pair of arrows*). **C** Lateral pinhole scintigraph shows patchy uptake (*arrowhead*)

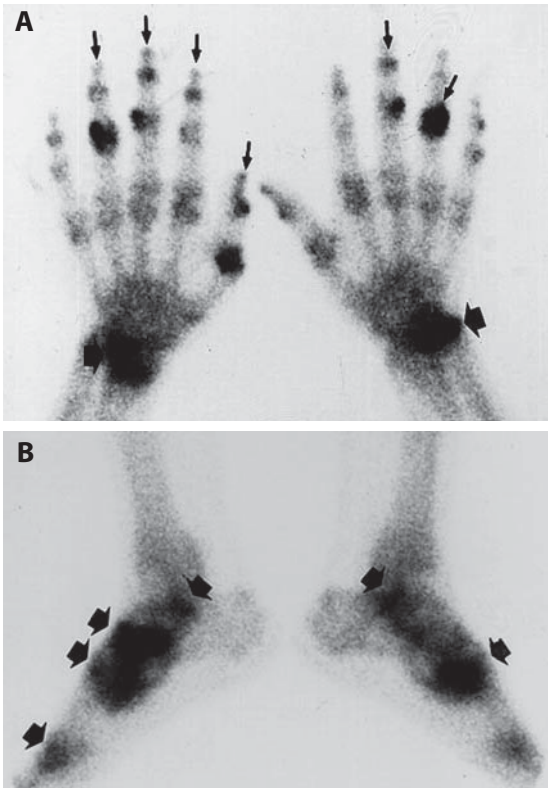

Fig. 11.23A, B Symmetrical polyarthritis in psoriasis. **A** Dorsoventral scintigraphs of hands and wrists show multiple joint involvement on both sides of the body strongly simulating rheumatoid arthritis (*arrows*). Note distal interphalangeal joint involvement. **B** Lateral scintigraphs of ankles and feet of the same patient reveal a similar polyarthritic manifestation of psoriatic arthritis (*arrows*)

that may increase in the active florid phase of the disease (Fig. 11.21). Reiter's syndrome of the temporomandibular joint radiographically manifests as articular widening and scintigraphically as patchy uptake in the early phase (Fig. 11.22). The differentiation between Reiter's syndrome and rheumatoid arthritis of the temporomandibular joint is impracticable simply because basically the same inflammatory process underlies both conditions.

11.3 Psoriatic Arthritis

The association of psoriasis with a specific type of arthritis is well established. Psoriatic arthritis may co-occur with, but is not related to, rheumatoid arthritis, and can be differentiated

on the basis of asymmetrical spotty distribution, positive HLA-B27 antigen test, negative rheumatoid factor, and the radiographic and scintigraphic findings. Occasionally, however, a symmetrical polyarthritic form may be encountered, strongly mimicking rheumatoid arthritis (Fig. 11.23). Psoriatic arthritis is relatively uncommon with a prevalence of probably no more than 5% (Hellgren 1969). The positivity for HLA-B27 antigen in psoriasis ranges from 46% to 78%, which is relatively low compared to Reiter's syndrome and ankylosing spondyloarthropathy.

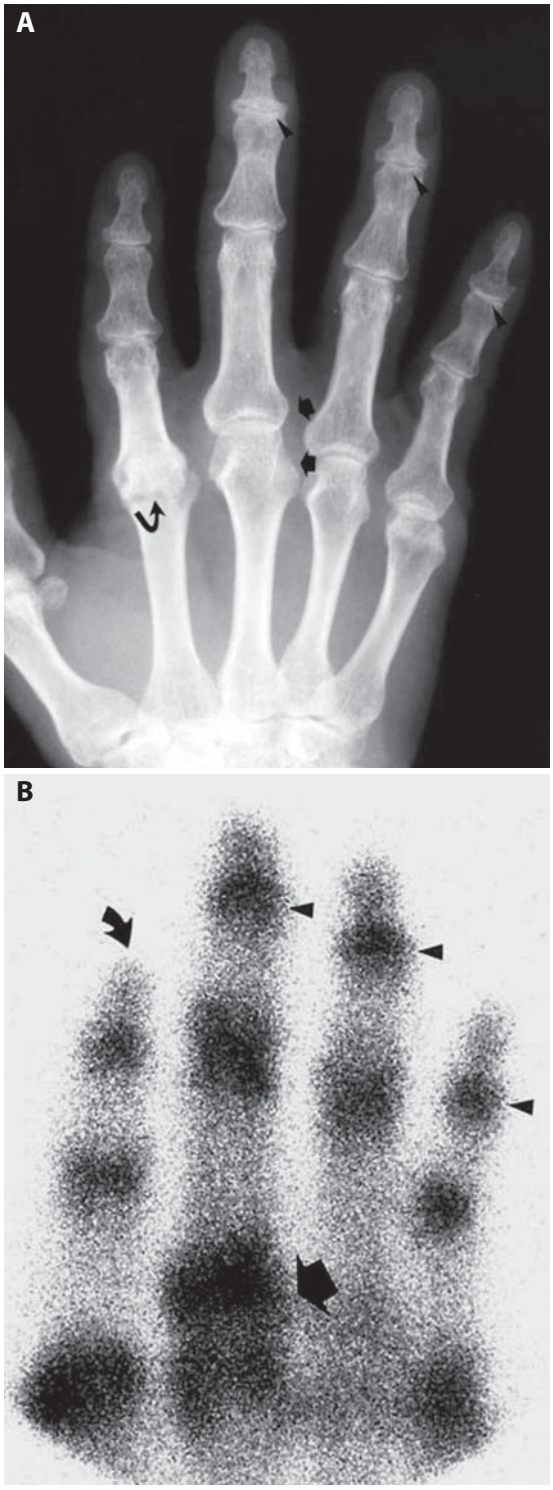

The clinical onset is insidious in most cases, but in about one-third it may present with acute manifestation. Psoriatic arthritis affects both sexes nearly equally, with the peak incidence occurring between the mid-30s and mid-40s of life. The strong proclivity for the involvement of the distal interphalangeal joints of the hands and feet is an important, but not a sine qua non, finding (Resnick and Niwayama 1988). The interphalangeal joints, metacarpophalangeal joints, and metatarsophalangeal joints are most commonly affected. The ankles, knees, wrists, and spine are not exempt, but significant change is unusual in the shoulders and hips. The distribution is characteristically asymmetrical and oligoarticular as in Reiter's syndrome, but symmetrical and polyarticular involvement may also occur (Fig. 11.23).

The fundamental pathology in peripheral psoriatic arthritis is synovitis, which is characterized by villous hypertrophy, lymphocytic infiltration, proliferating fibroblasts, and vascular necrosis. In the late stage the distal interphalangeal joints may become destroyed, subluxed, and disfigured with marginal bony

Fig. 11.24A, B Typical distal interphalangeal joint involvement in psoriatic arthritis. **A** Dorsoventral radiograph of the right hand in a 64-year-old male with long-standing psoriasis shows marked narrowing and eburnation of the distal and proximal interphalangeal joints as well as the metacarpophalangeal joint. The second finger is foreshortened due to flexure contracture and telescoping of the metacarpophalangeal joint (*curved arrow*). The third metacarpophalangeal joint shows the "knuckle" sign (*arrows*). **B** Dorsal pinhole scintigraph reveals intense tracer uptake in the distal interphalangeal joints (*arrowheads*) and foreshortening of the second finger (*curved arrow*) and the "knuckle" sign of the third finger (*arrow*)

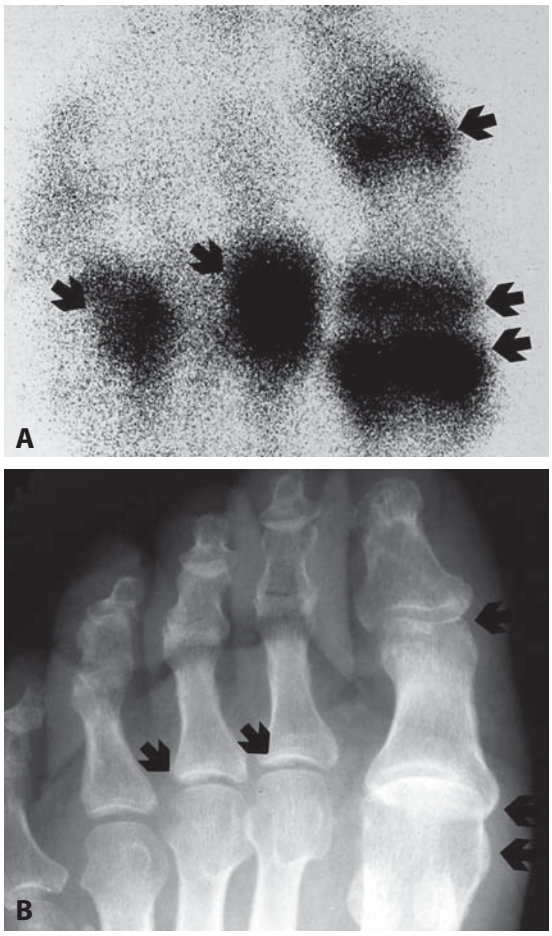

Fig. 11.25A, B Psoriatic arthritis in the foot. **A** Dorsoplantar radiograph of the left foot in a 37-year-old male with psoriasis shows narrowing and blurring of the first through third metatarsophalangeal joints as well as the first interphalangeal joint (*arrows*). **B** Dorsal pinhole scintigraph reveals intense tracer uptake in the affected joints with the "knuckle" sign in the great toe (*twin arrows*)

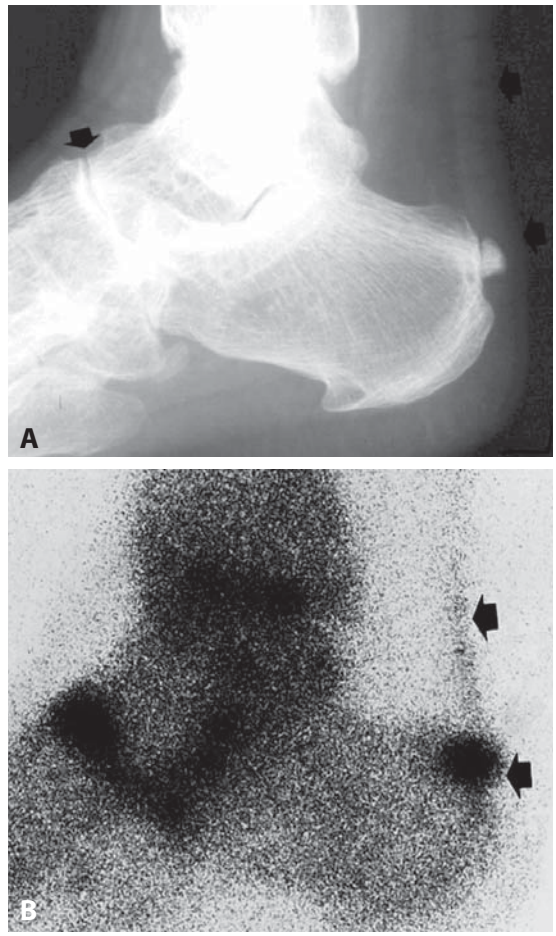

Fig. 11.26A, B Achilles tendoenthesitis in psoriasis. **A** Lateral radiograph of the right hindfoot in a 64-year-old male with psoriasis shows very subtle thickening of the distal Achilles tendon (*right upper arrow*) with a fractured new bone formed at the calcaneal insertion (*right lower arrow*). The talocrural, talonavicular, and subtalar joints are all diffusely narrowed (*single arrow*). **B** Lateral pinhole scintigraph reveals tracer uptake in the distal Achilles tendon and fractured new bone (*arrows*) as well as peritalar joints. Note especially intense uptake in newly formed bone that is fractured

excrescences due to enthesopathy. Lesions are asymmetrical and sparse and even unilateral in occasional cases, more regularly affecting the upper extremity including the fingers. In about 5% of cases the distal phalanx melts away completely, resulting in arthritis mutilans.

Radiographic manifestations are periarticular swelling, articular narrowing, subchondral bone erosions, and bony excrescence, and "whiskering". Both the distal and proximal interphalangeal joints are more regularly involved than other joints in the hands and feet (Figs. 11.23 and 11.24A). Resorption or lysis of the tufts, the "pencil and cup" appearance of the digits, subluxation, ankylosis, and telescoping may occur in severe cases. The individual articular changes are often indistinguishable from those of rheumatoid arthritis, but bony excrescences and mild or absent osteopenia deserve recognition as differential points.

Pinhole scintigraphic manifestations of the large and small joints of the limbs are essentially the same as in Reiter's syndrome and ankylosing spondylitis when disease is protracted. Articular psoriasis is indicated by marked tracer uptake, typically in the distal interphalangeal joints of the hands and feet (Fig. 11.23). Dwarfing and subluxation of fingers may occur in advanced cases (Fig. 11.24B). The scintigraphic features of toe involvement are not dissimilar to those of Reiter's syndrome (Fig. 11.25). In occasional cases pinhole scintigraphy can detect tendinitis or enthesitis by showing subtle tracer uptake, which is difficult to appreciate on ordinary planar scintigraphs (Fig. 11. 26).

11.4 Enteropathic Arthropathies

Enteropathic arthropathies are arthritides that are associated with either nonspecific or infective inflammatory diseases of the intestine. Nonspecific enteropathies include ulcerative colitis, Crohn's disease, and Whipple's disease, and common infective enteritides are salmonellosis, shigellosis, and yersiniasis. The exact cause-and-effect relationship between arthritis and inflammatory intestinal diseases is not fully clarified, although both immune mechanism and articular infection either primary or secondary to intestinal infection have been implicated. In recent years the importance of a genetic role in the evolution of enteropathic arthropathies has been discussed. In this connection, it is worth noting that approximately 90% of patients with ulcerative colitis or Crohn's

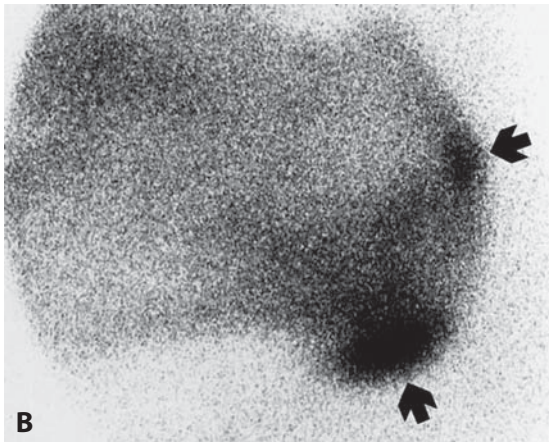

Fig. 11.27A, B Usefulness of ^{99m}Tc-MDP bone scintigraphy in psoriatic arthritis. **A** Whole-body bone scan in an 18-year-old male shows panoramic display of asymmetrical involvement of the joints in the lower extremities and the pelvis (arrows). **B** Lateral pinhole scintigraph of the right calcaneus reveals areas of increased tracer uptake in the retrocalcaneal and plantar aspects denoting enthesopathy (*arrows*)

disease with spondylitis and sacroiliitis have HLA-B27 antigen. It has been speculated that this antigen enhances susceptibility to infection or is linked to the generation of a pathogenetic immune response. The most common radiographic changes include periarticular soft-tissue swelling and osteopenia. In addition, as in Reiter's syndrome, subchondral bone erosions, articular narrowing, and cyst formation may occur although these changes are comparatively mild. Occasionally, the spine and sacroiliac joints are affected, resembling ankylosing spondylitis.

Scintigraphy demonstrates intense tracer uptake in the sacroiliac joints, knees, and ankles as well as the calcanei as in other SNSA. In essence, the findings are not dissimilar to those of other SNSA. Whole-body scintigraphy is ideal for grasping asymmetrical, oligoarticular involvement (Fig. 11.27A) and pinhole scintigraphy is most useful for the characterization of arthritis and enthesopathy in the individual joint and bone, the knee and calcaneus in particular (Fig. 11.27B).

References

Arnett FC, McClusky E, Schacter BZ, et al (1976) Incomplete Reiter's syndrome: discriminating features and HL-A W27 in diagnosis. Ann Intern Med 84:8–12

Ball GV (1971) Enthesopathy of rheumatoid and ankylosing spondylitis. Ann Rheum Dis 30:213–223

Bluestone R (1979) Ankylosing spondylitis. In: McCarty DJ (ed) Arthritis and allied conditions, 9th edn. Lea & Febiger, Philadelphia

Desaulniers M, Fuks A, Hawkins D, et al (1974) Radiotechnetium polyphosphate joint scanning. J Nucl Med 15:417–423

Fox R, Calin A, Gerber RC, et al (1979) The chronicity of the symptoms and disability in Reiter's syndrome: an analysis of 131 consecutive patients. Ann Intern Med 91:190–193

Good AE (1963) The chest pain of ankylosing spondylitis. Its place in the differential diagnosis of heart pain. Ann Intern Med 58:926–937

Hays MT, Green FA (1972) The pertechnetate joint scan: clinical correlations. Ann Rheum Dis 31:278–281

Hellgren L (1969) Association between rheumatoid arthritis and psoriasis in total populations. Acta Rheumatol Scand 15:316–326

Keat AC, Maini RN, Nkwazi GC, et al (1978) Role of *Chlamydia trachomatis* and HLA B27 in sexually acquired reactive arthritis. Br Med J 6113:605–607

Khan MA (2002) Update of spondyloarthropathies. Ann Intern Med 136:896–907

Kim SH, Chung SK, Bahk YW, et al (1999) Wholebody and pinhole bone scintigraphic manifestations of Reiter's syndrome: distribution patterns and early and characteristic signs. Eur J Nucl Med 26:163–170

Lin MS, Fawcett HD, Goodwin DA (1980) Bone scintigraphy demonstrating arthropathy of central joints in ankylosing spondylitis. Clin Nucl Med 5:364–366

Ogryzlo MA (1972) Ankylosing spondylitis. In: Hollander JL, McCarty DR Jr (eds) Arthritis and allied conditions, 8th edn. Lee & Febiger, Philadelphia

Reiter H (1916) Über eine bisher unerkannte Spirochäteninfektion (Spirochaetosis arthritica). Dtsch Med Wochenschr 42:1535

Resnick D, Niwayama G (1988) Psoriatic arthritis. In: Resnick D, Niwayama G (eds) Diagnosis of bone and joint disorders, 2nd edn. Saunders, Philadelphia

Sharp J (1965) Ankylosing spondylitis – a review. In: Dixon AS (ed) Progress in clinical rheumatology. Churchill Livingstone, London

Sundaram M, Patton JT (1975) Paravertebral ossification in psoriasis and Reiter's disease. Br J Radiol 48:628–633

Wilkinson M, Bywaters EGL (1958) Clinical features and course of ankylosing spondylitis as seen in a follow up of 222 hospital referred cases. Ann Rheum Dis 17:209–228

Willkens RF, Arnett FC, Bitter T, et al (1981) Reiter's syndrome: evaluation of preliminary criteria for definite disease. Arthritis Rheum 24:844–849

12 Other Rheumatic Osteoarthropathies and Soft-Tissue Rheumatism Syndromes

From among a larger group of rheumatic and similar osteoarthropathies, Sjögren's syndrome, Behçet's syndrome, systemic lupus erythematosus (SLE), tophaceous gouty arthritis, Charcot's joint, and secondary hypertrophic osteoarthropathy deserve appropriate descriptions since these disorders show ^{99m}Tc-MDP bone scintigraphic changes that suggest or often indicate the diagnosis. This is especially true in Sjögren's syndrome, Behçet's syndrome, SLE, and gouty arthritis, in which radiography often fails to yield a specific diagnostic sign in the early phase of disease.

The early radiographic manifestation of rheumatic osteoarthropathies is articular blurring with periarticular soft-tissue swelling, which is not specific (Fig. 12.1). Then, subchondral bone erosions, articular narrowing, cystic change, ankylosis, and deformity may follow in the later stage, which are also nonspecific. However, tophi with tophaceous bone erosions in gouty arthritis, bizarre disfiguring bone and joint changes in Charcot's joint, and lamellar periosteal thickening in secondary hypertrophic osteoarthritis are characteristic. On the other hand, both radiographic and scintigraphic manifestations overlap when a rheumatic arthritis, Sjögren's syndrome in particular, is combined with rheumatoid arthritis.

As is well known whole-body scanning is useful for grasping the pattern of involvement of rheumatic arthritides, which is typically pauciarticular, focal, and asymmetrical (Fig. 12.2A). If combined with rheumatoid arthritis, however, the involvement becomes symmetrical and polyarticular (Fig. 12.2B). Pinhole scintigraphy can sensitively detect the early arthritic change

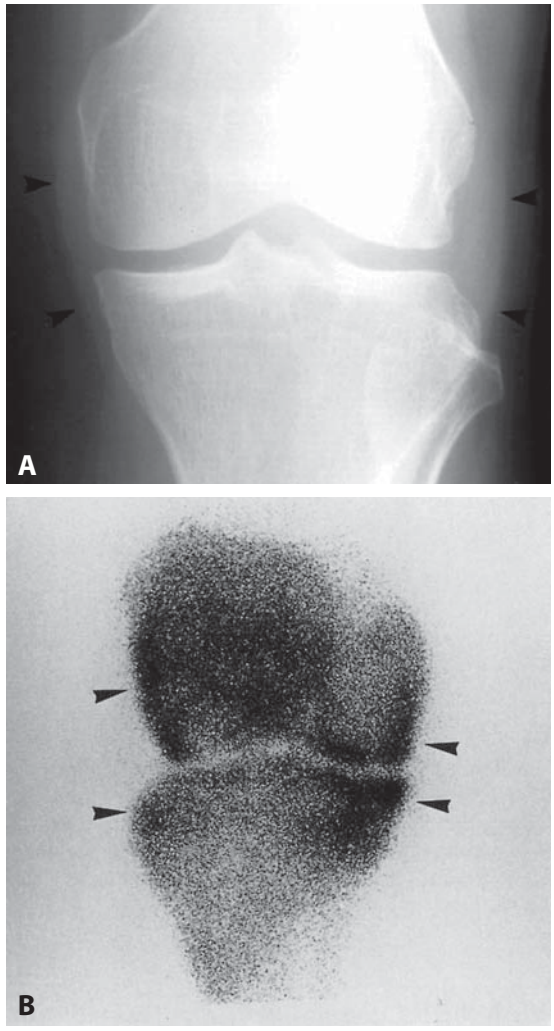

Fig. 12.1 A, B The "wrapped bone" sign seen in Sjögren's syndrome synovitis on bone scintigraph. **A** Anteroposterior radiograph of the right knee in a 41-year-old woman with Sjögren's syndrome reveals diffuse para-articular soft-tissue swelling with a blurred joint (*arrowheads*). **B** Anterior pinhole scintigraph shows diffusely increased tracer uptake in the entire periarticular bones with the more prominent uptake in the peripheries (*arrowheads*)

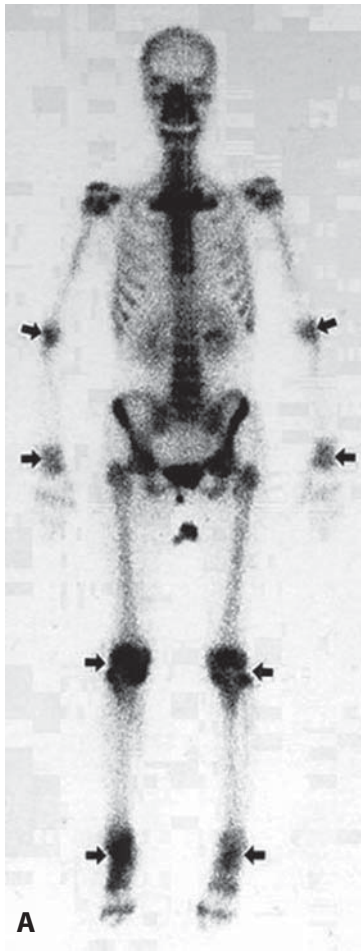

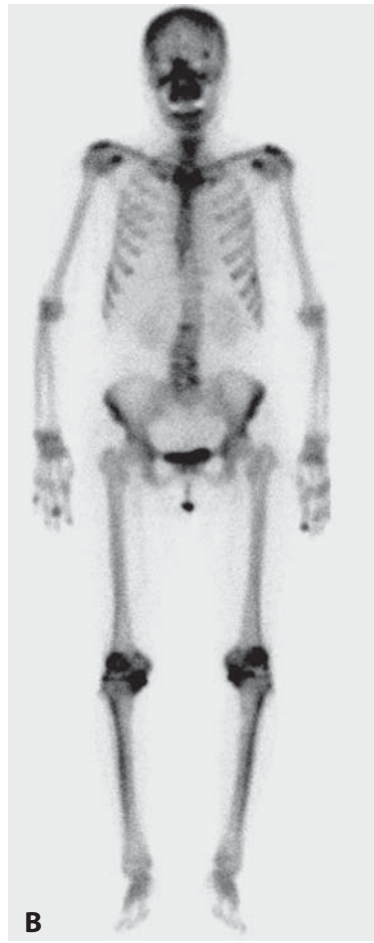

Fig. 12.2 A, B Whole-body bone scintigraphy for grasping involvement pattern of rheumatic arthritis. **A** Anterior whole-body bone scintigraph in Sjögren's syndrome combined with rheumatoid arthritis demonstrates symmetrical polyarthritis (*arrows*). **B** Anterior whole-body bone scintigraph in a 61-year-old woman with psoriasis of the hands reveals asymmetrical pauciarticular involvement of the finger joints (*arrows*). Knee joint changes are due to osteoarthritis unrelated to psoriasis (*arrowheads*)

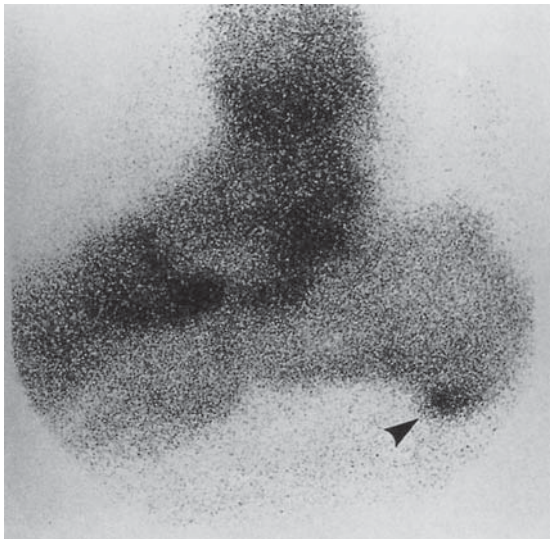

Fig. 12.3 Preradiographic demonstration of plantar fasciitis in Behçet's disease. Medial pinhole scintigraph of the painful right heel in a 32-year-old woman with known Behçet's disease shows a subtle, spotty tracer uptake in the medial process of the calcaneal tuberosity (*arrowhead*). Radiography was unremarkable (not shown)

characterized by diffuse synovial uptake with marginal accentuation (Fig. 12.1B). Similar findings may be seen in rheumatoid arthritis (Fig. 10.4) and acute infective arthritis (Fig. 8.5). Rheumatic-like disorders such as Behçet's syndrome may occasionally show spotty uptake in the knees and the plantar aspect of the calcaneus (Fig. 12.3), strongly resembling Reiter's enthesopathy (Fig. 11.9) or psoriatic plantar fasciitis (Fig. 11.27), and such uptake frequently heralds the disease before radiographic changes appear.

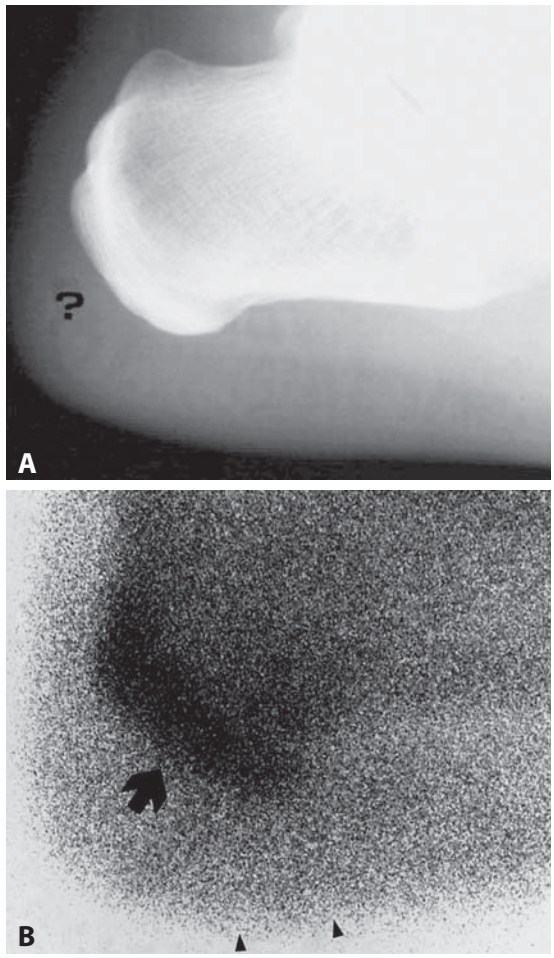

Fig. 12.4A, B Usefulness of bone scintigraphy in Behçet's syndrome. **A** Lateral radiograph of the left calcaneus in a 29-year-old woman shows suspicious soft-tissue thickening in the heel pad (*?*) without local bone change. **B** Lateral pinhole scintigraph reveals diffuse reactive tracer uptake in the lower retrocalcaneal surface (*arrow*) with diffuse extension to the heel pad denoting mild inflammation (*arrowheads*)

12.1 Sjögren's Syndrome

Sjögren's syndrome consists of keratoconjunctivitis sicca, xerostomia, and rheumatoid arthritis, and is considered to be a generalized autoimmune exocrinopathy (Strand and Talal 1980). Like most autoimmune diseases, Sjögren's syndrome occurs predominantly in women in fourth to seventh decades of life. The syndrome may be either primary or secondary to rheumatoid arthritis and less commonly SLE. Arthritic involvement may or may not be present, and when obvious it is almost always due to rheumatoid arthritis, manifesting as periarticular soft-tissue swelling in the early stage (Fig. 12.1) and erosions, articular narrowing, and subchondral intraosseous cyst in the chronic stage. Bone scintigraphy of Sjögren's syndrome complicated with rheumatoid arthritis demonstrates symmetrical tracer uptake in both large and small joints of the limbs and digits (Fig. 12.2A). To be exact, such polyarthritic manifestation is not due to Sjögren's syndrome but rheumatoid arthritis. Pinhole scintigraphy shows the typical "wrapped bone" sign with marginal uptake that may also be due to early rheumatoid synovitis (Fig. 12.1B). On the other hand, pinhole scintigraphy can diagnose retrocalcaneal enthesitis with heel pad swelling (Fig. 12.4A), which is extremely subtle and difficult to detect by radiography (Fig. 12.4B).

12.2 Behçet's Syndrome

Behçet's syndrome is a chronic relapsing disease, basically manifesting as painful oral ulceration, genital ulceration, and uveitis. Peculiarly, the prevalence is not uniform in global distribution: the majority of cases have been reported from the eastern Mediterranean countries, Korea, and Japan. The mean age of onset is between 25 and 30 years with men be-

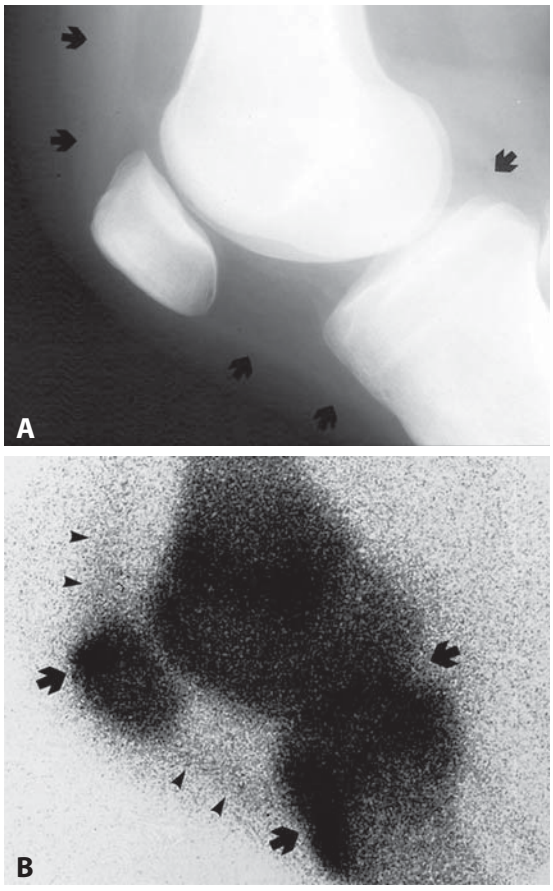

Fig. 12.5A, B Radiographic and scintigraphic features of acute Behçet's disease. **A** Lateral radiograph of the right knee in a 22-year-old woman with acute Behçet's disease shows diffuse articular distension denoting synovitis and periarticular soft-tissue swelling (*arrows*). **B** Lateral pinhole scintigraph reveals periarticular tracer uptake (*arrows*) with extremely subtle uptake in inflamed tendons (*arrowheads*). Note particularly intense uptake at the suprapatellar (*left upper arrow*) and infrapatellar (*lower arrow*) tendon insertions, the characteristic sign of enthesitis

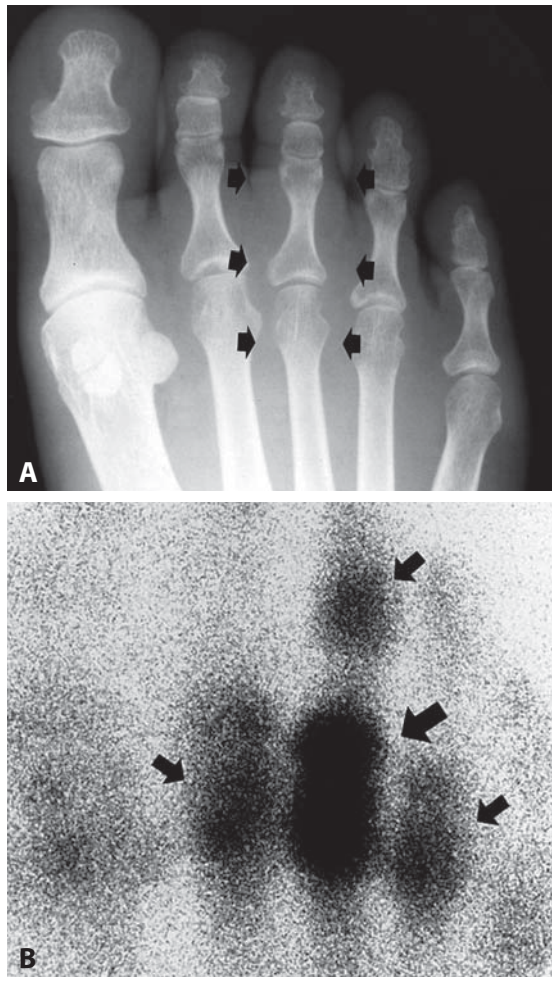

Fig. 12.6A, B The "sausage digit" in acute Behçet's dactylitis. **A** Dorsoplantar radiograph of the right foot shows diffuse periarticular soft-tissue swelling around the third toe metatarsophalangeal and proximal interphalangeal joints (*arrows*). **B** Dorsal pinhole scintigraph reveals diffuse sausage-like tracer uptake (*large arrow*). Note that dubious radiographic changes in the second and fourth toes are distinctly shown on the scintigraph (*small arrows*)

ing affected more commonly than women. A number of immunological abnormalities have been detected in patients with Behçet's disease, including antibodies to human mucosal cells, lymphotoxicity to heterologous oral epithelial cells, and blast transformation of patient's lymphocytes by human oral epithelial cells. HLA-B5 has been found to be increased fourfold in this disease in Korean, Japanese, and Turkish, but not in northern European, patients. Joints are involved in more than 50% of patients, and the involvement is mostly monoarticular or oligoarticular (Yurdakul et al. 1983). The knees, ankles, and wrists are the most common sites of affliction. The feet are occasionally involved and may produce the "sausage digit" sign and pseudopodagra (Giacomello et al. 1981).

Radiographic features in the acute stage include diffuse articular distension, denoting synovitis and periarticular soft-tissue swelling

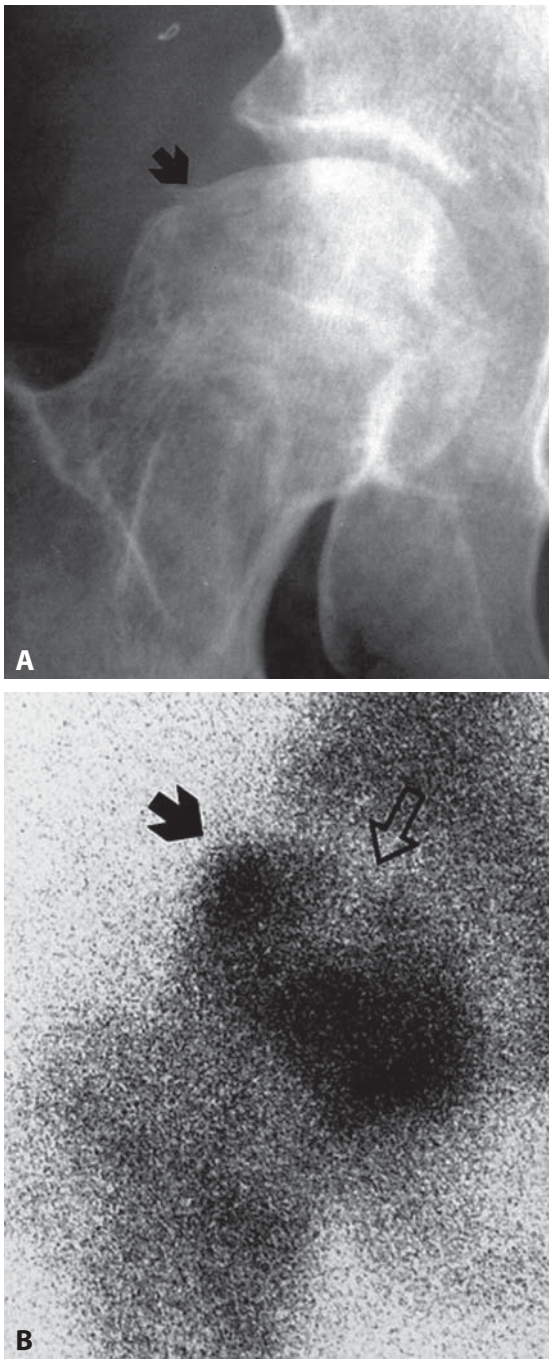

Fig. 12.7A, B Iatrogenic osteonecrosis in Behçet's disease treated with corticosteroid. **A** Anteroposterior radiograph of the right hip in a 29-year-old woman receiving corticosteroid shows mottled areas of increased bone density and osteopenia in the femoral head due to bone reaction and necrosis (*arrow*). **B** Anterior pinhole scintigraph reveals a small photon defect at the center of the femoral head with increased tracer uptake, respectively reflecting osteonecrosis (*open arrow*) and reactive and new bone formation (*solid arrow*)

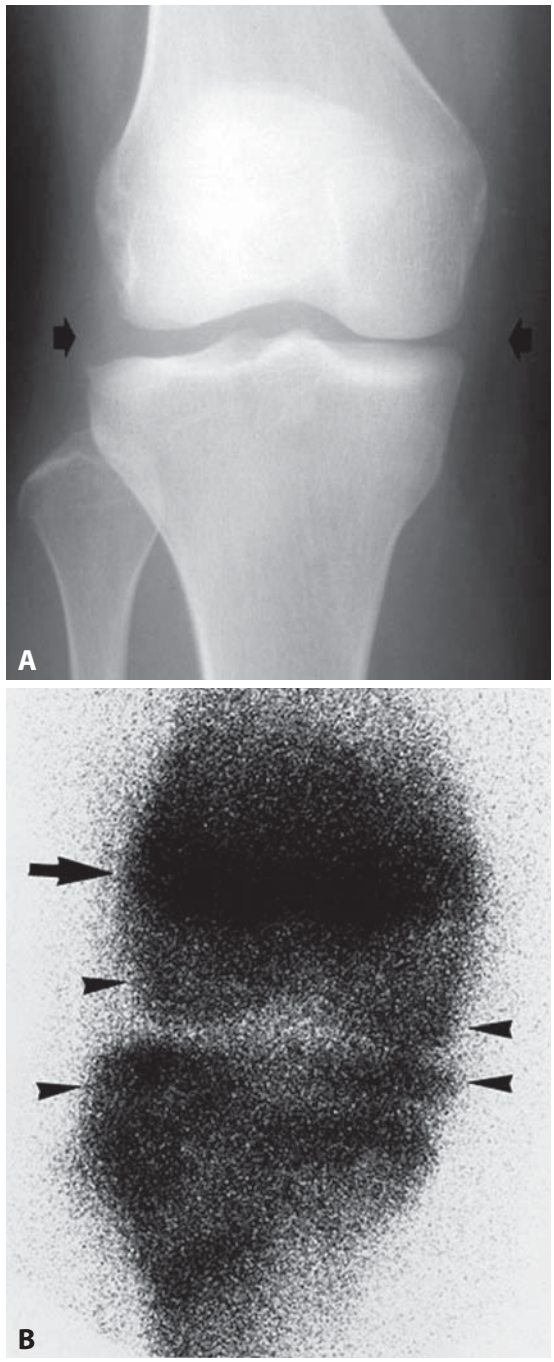

Fig. 12.8A, B Early changes of SLE. **A** Anteroposterior radiograph of the right knee in a 22-year-old woman shows articular widening and periarticular soft-tissue swelling (*arrows*). **B** Anterior pinhole scintigraph reveals diffusely increased tracer uptake in periarticular bones and soft-tissue structures (*arrowheads*). Note peculiar accentuated uptake in the distal femoral metaphysis that is sharply demarcated by the physeal line (*arrow*)

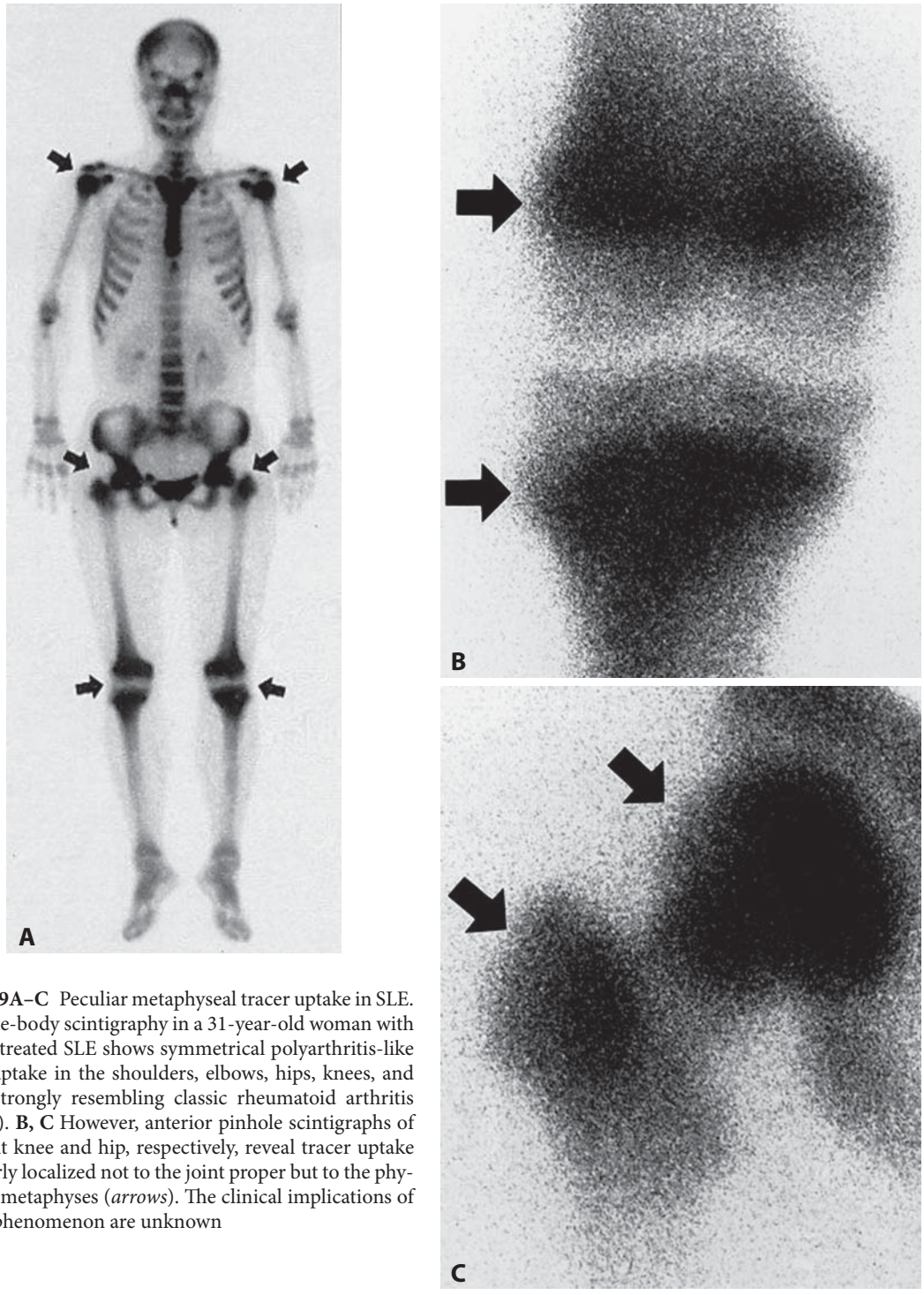

Fig. 12.9A–C Peculiar metaphyseal tracer uptake in SLE. **A** Whole-body scintigraphy in a 31-year-old woman with steroid-treated SLE shows symmetrical polyarthritis-like tracer uptake in the shoulders, elbows, hips, knees, and spine, strongly resembling classic rheumatoid arthritis (*arrows*). **B, C** However, anterior pinhole scintigraphs of the right knee and hip, respectively, reveal tracer uptake peculiarly localized not to the joint proper but to the physes and metaphyses (*arrows*). The clinical implications of such a phenomenon are unknown

(Fig. 12.5A). Osteopenia, articular narrowing, and bone erosions are usually inconspicuous, and, if conspicuous, they resemble rheumatoid arthritis. The "sausage digit" sign is another important feature, denoting soft-tissue swelling in and around the metatarsophalangeal joint (Fig. 12.6A). Whole-body bone scintigraphy reveals monoarticular or oligoarticular arthritis, and pinhole scintigraphy demonstrates diffuse periarticular tracer uptake occasionally

with subtle uptake in inflamed tendons (Fig. 12.5B). The "sausage digit" sign and other articular changes are efficiently diagnosed using this method (Fig. 12.6B). It is probably the best available means to accurately diagnose plantar fasciitis of Behçet's disease in its early phase (Fig. 12.3) and also iatrogenic osteonecrosis that frequently develop in patients with this disease under glucocorticoid treatment (Fig. 12.7).

12.3 Systemic Lupus Erythematosus

SLE is a relatively common chronic disorder of an inflammatory nature of unknown etiology. SLE affects multiple organ systems of the body including the skin, joints, entheses, kidneys, lungs, serous membranes, nervous system, and others. SLE may cause immunological changes and abnormalities, especially antinuclear antibodies. The clinical course is characterized by remission and acute relapse, and long-term steroid administration may result in osteoporosis, avascular necrosis, and microfractures, especially in the weight-bearing joints of the hips and knees. As in rheumatoid arthritis, articular involvement is multiple and symmetrical, but deformity is not a prominent feature unless complicated by osteonecrosis.

Radiographic changes include articular widening and periarticular soft-tissue swelling, and are observed more typically in steroid-naive patients. Although infrequent, articular narrowing, osteonecrosis, deformity, soft-tissue calcification, and acrosclerosis or acrolysis may be seen in patients with longstanding disease. Whole-body scintigraphy demonstrates sym-

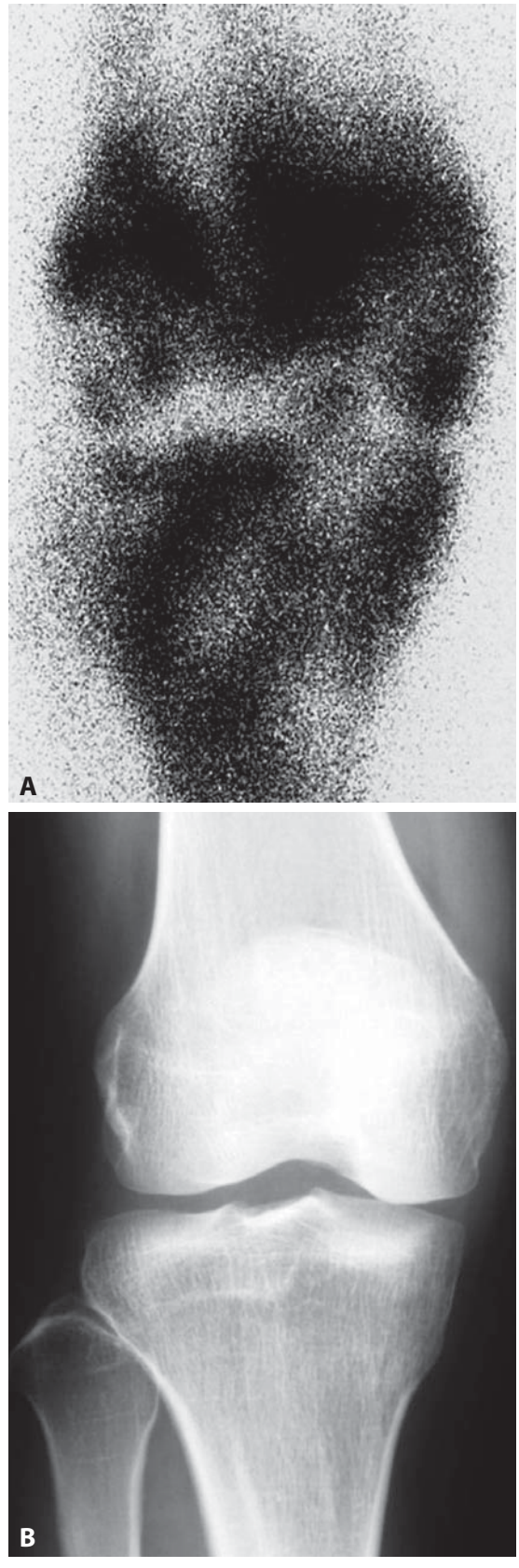

Fig. 12.10A, B Admixture of "cold" and "hot" areas in SLE. **A** Anterior pinhole scintigraph of the right knee in a 25-year-old woman with SLE treated with steroid for 3 months shows multiple photon defect irregularly mixed with increased tracer uptake reflecting avascular necrosis and microfractures, respectively. **B** Anteroposterior radiograph is surprisingly normal

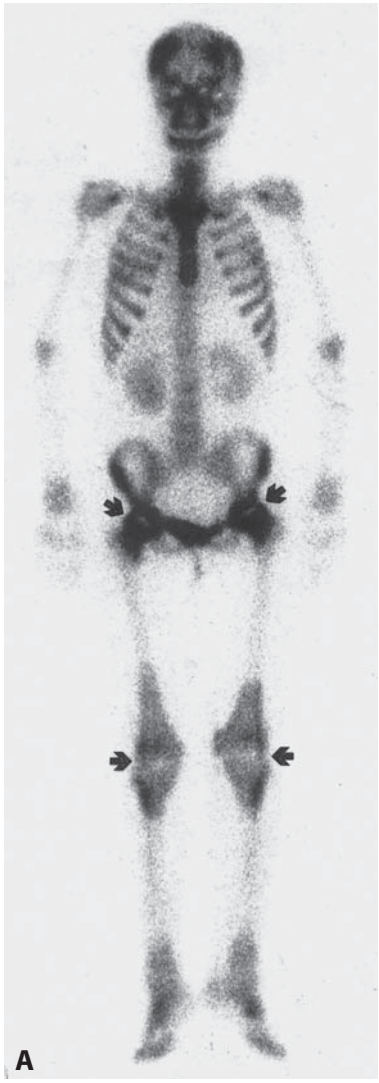

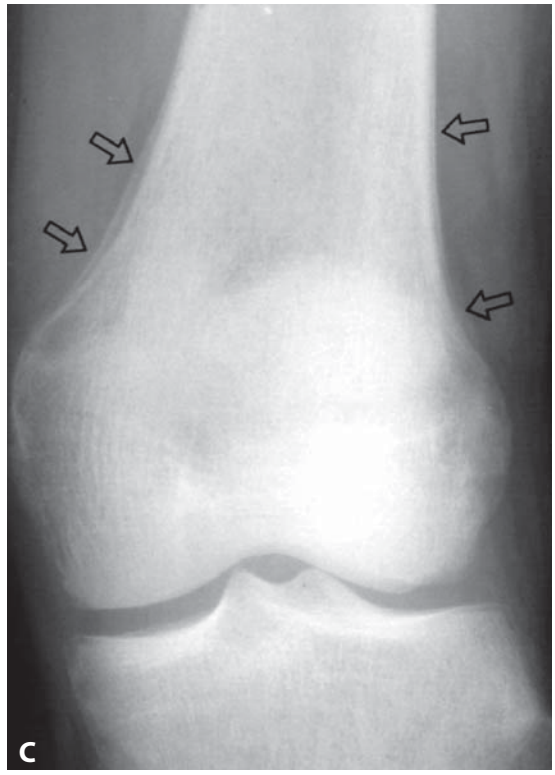

Fig. 12.11A–C SLE accompanied by hypertrophic osteoarthropathy. **A** Whole-body scan in a 24-year-old woman with steroid-treated SLE shows bone uptake in the hips and knees (*arrows*). **B** Composite anterior pinhole scan shows a mixture of photopenia in necrotized bones in the intercondylar region (*open arrows*) and diffusely increased uptake in hypertrophic osteoarthropathy in the distal femur (*arrows*). **C** Anteroposterior radiograph shows periosteal thickening in the distal femur (*open arrows*). Note that osteonecrosis and bone reaction are not visualized radiographically

metrical polyarthritis in the shoulders, elbows, hips, knees, and spine resembling classic rheumatoid arthritis (Fig. 12.9A). However, pinhole scintigraphy in relatively early or steroid-treated cases may reveal prominent tracer uptake that is peculiarly localized to the physes and metaphyses (Figs. 12.8B and 12.9B). Articular uptake may (Fig. 12.8B) or may not (Fig. 12.8B) coexist. The implication of such findings is not clear. In still other cases, the periarticular bone uptake is inhomogeneous with photopenic and photodense areas, probably representing avascular necrosis and microfractures, respectively (Fig. 12.10). Radiography may not be abnormal (Fig. 12.10B).

On occasion, SLE may become complicated with, in addition to osteonecrosis, hypertrophic osteoarthropathy, and both can be diagnosed accurately using pinhole scanning. Whole-body scans show irregular uptake of osteonecrosis in the hips and knees (Fig. 12.11A), and magnified scans show osteonecrosis as photopenia and osteoarthropathy as characteristic cortical uptake (Fig. 12.11B). Although rare, SLE may involve the costovertebral and costotransverse joints of the thoracic spine (Fig. 12.12), giving rise to a "centipede" appearance that is also observed in ankylosing spondylitis (Fig. 11.6).

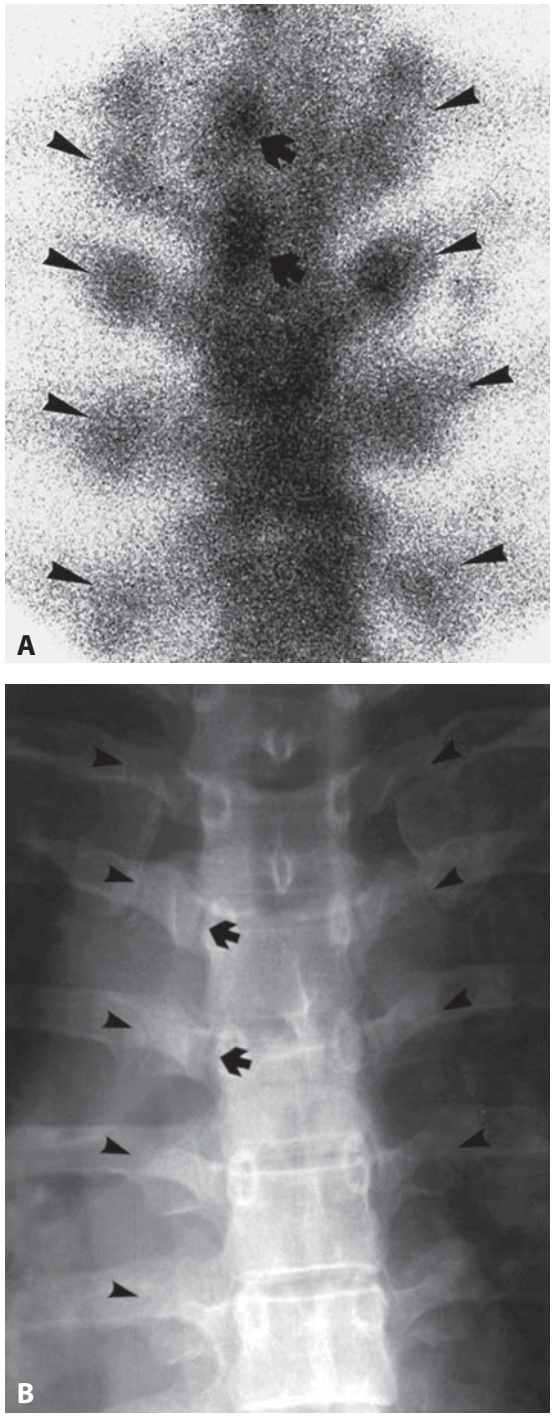

Fig. 12.12A, B The "centipede" sign of the costovertebral joint involvement in SLE. **A** Posterior pinhole scan of the mid-thoracic spine shows diffuse tracer uptake in the vertebrae along with visualization of the costovertebral joints (*arrows*) and costotransverse joints (*arrowheads*) creating the "centipede" appearance. **B** Anteroposterior radiograph reveals blurring and narrowing of the costovertebral joints (*arrows*) and costotransverse joints (*arrowheads*)

12.4 Gouty Arthritis

Gouty arthritis is caused by the aggregated presence of monosodium urate crystals in the limb joints or their deposition in the periarticular soft-tissue structures as foreign bodies. It is categorized into (a) acute gouty arthritis, (b) intercritical gout, and (c) chronic tophaceous gout. Of these, acute gouty arthritis and chronic tophaceous gout are discussed because the combined use of scintigraphy and radiography in these two diseases synergistically enhances diagnostic accuracy. Initial or relapsing acute gouty arthritis is characterized by exquisite pain, requiring urgent treatment. Attack occurs

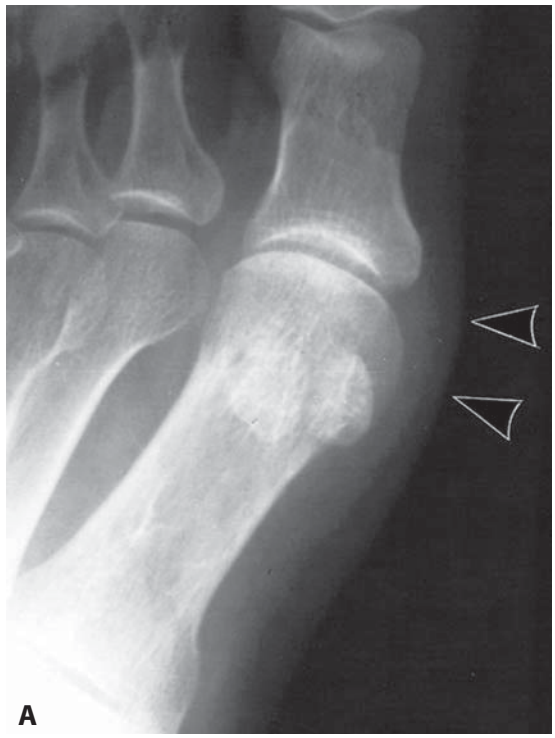

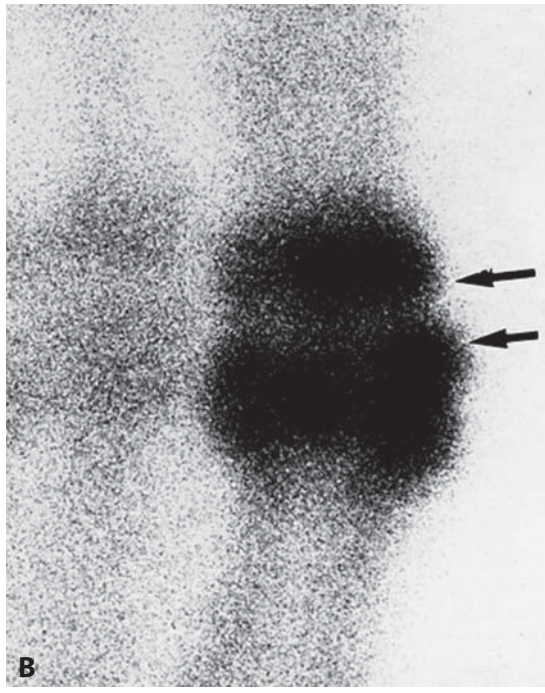

Fig. 12.13A, B Gouty arthritis in the great toe. **A** Dorsoplantar radiograph of the left great toe in a 63-year-old man with acute gouty arthritis shows swelling of the local soft tissue around the metatarsophalangeal joint (*arrowheads*). **B** Dorsal pinhole scintigraph reveals prominent tracer uptake in the head of the metatarsal and the base of the phalanx (*arrows*). Note that radiography does not show detectable bony change in this early stage

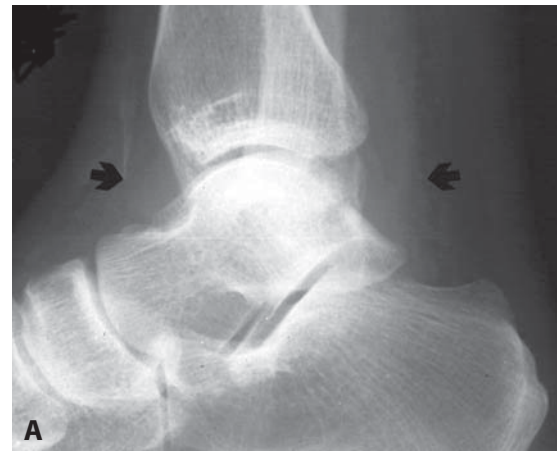

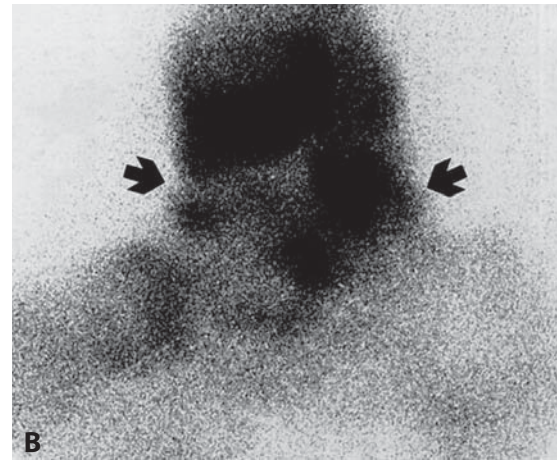

Fig. 12.14A, B Gouty arthritis in the ankle. **A** Lateral radiograph of the right ankle in a 41-year-old man shows diffuse swelling of the periarticular soft tissue without evidence of definite articular or bone change (*arrows*). **B** Lateral pinhole scintigraph reveals intense tracer uptake in the talocrural and posterior talocalcaneal joint (*arrows*). Note higher diagnostic sensitivity of pinhole scintigraphy

usually in a single joint in early phases and multiple joints in chronic phases. Urate crystals that show strong negative birefringence under polarized light, present in synovial fluid along with leukocytes during an attack. The basic pathology is nonspecific inflammatory reaction of the synovium with polymorphonuclear leukocytic infiltration. Although yet not accepted generally, the needle-shaped and rod-like crystals may be responsible for acute gouty synovitis and chronic gouty synovitis, respectively.

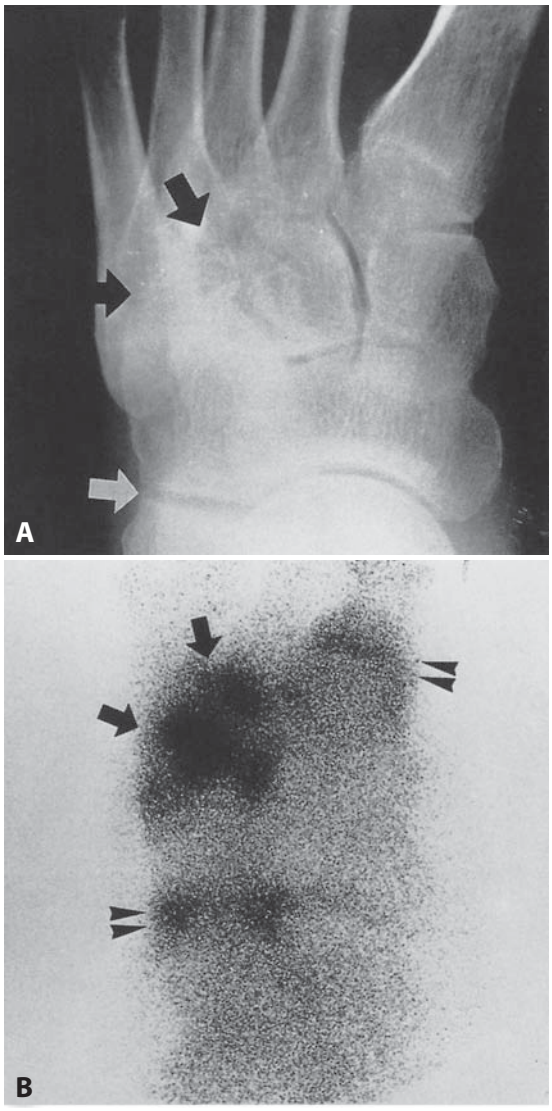

Fig. 12.15A, B Tophaceous gouty arthritis. **A** Dorsal pinhole scintigraph of the left foot in a 46-year-old man with chronic gouty arthritis reveals intense tracer uptake in the lateral tarsometatarsal joints (*arrows*) and also in some other joints but of less intensity (*arrowheads*). **B** Dorsoplantar radiograph shows erosion, porosis, and articular narrowing in the lateral tarsometatarsal joints (*black arrows*). The talocuboid joint is obscured due to inflammation and erosions (*white arrow*)

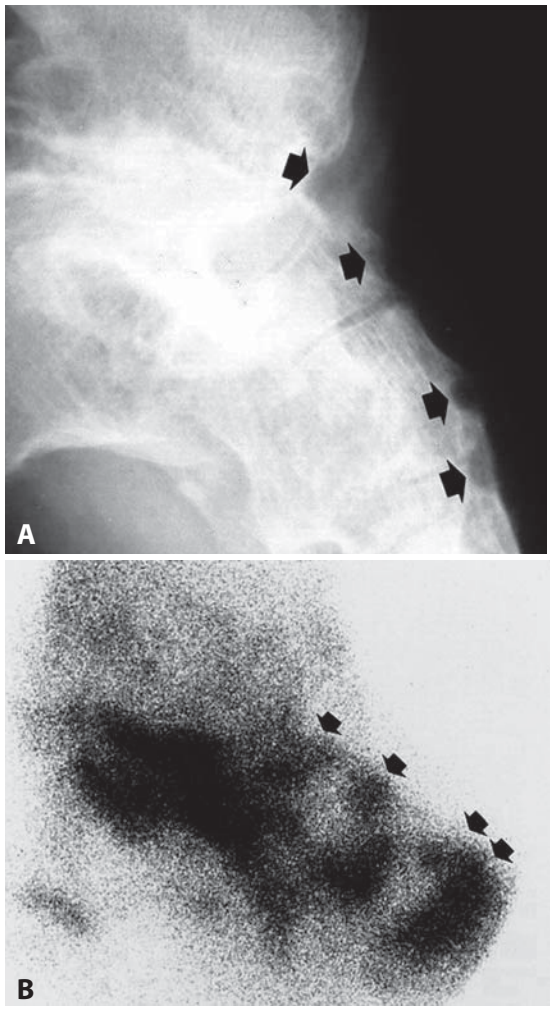

Fig. 12.16A, B Gouty arthritis with tophi in the midfoot. **A** Lateral radiograph of the left foot in a 41-year-old man with chronic gouty arthritis and tophi shows articular narrowing of the intertarsal and metatarsophalangeal joints with multiple punched-out tophaceous defects at the dorsal aspects of the tarsal bones (*arrows*). **B** Lateral pinhole scintigraph reveals tracer uptake in the subtalar and talonavicular joints and the intertarsal joints as well as punched-out defects (*arrows*)

Radiographic alterations are usually unimpressive during the first few years even in the presence of repeated acute attacks. Initiating changes are mild to moderate thickening of the synovium and periarticular soft tissue with focal osteopenia, for example, in the great toe (Fig. 12.13A), foot and ankle (Fig. 12.14A), but most typically in the great toe and the metatarsophalangeal and intertarsal joints (Fig. 12.15A). In contrast, patients with long-standing disease show joint space narrowing with subchondral cystic change (Fig. 12.16A). Generally, however, joint space narrowing is not a prominent feature in gouty arthritis. A

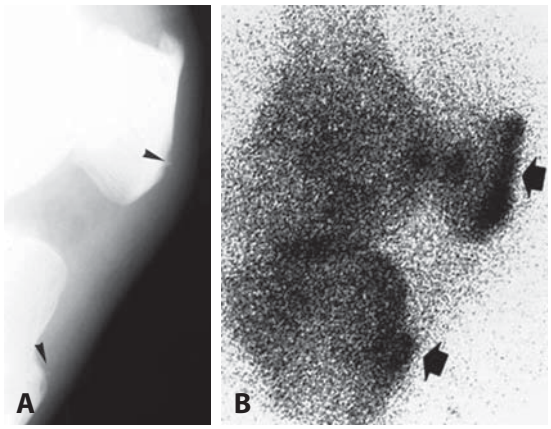

Fig. 12.17A, B Prepatellar bursitis and infrapatellar ligamental enthesitis with tiny calcified tophi. **A** Lateral soft-tissue radiograph of the right knee in a 47-year-old man with gouty enthesitis shows diffuse thickening of the prepatellar and infrapatellar ligaments and soft tissue (*arrows*). Note tiny calcium deposits (*arrowheads*). **B** Lateral pinhole scintigraph reveals intense tracer uptake in ligamental attachments at the prepatellar surface and tibial tuberosity (*arrows*)

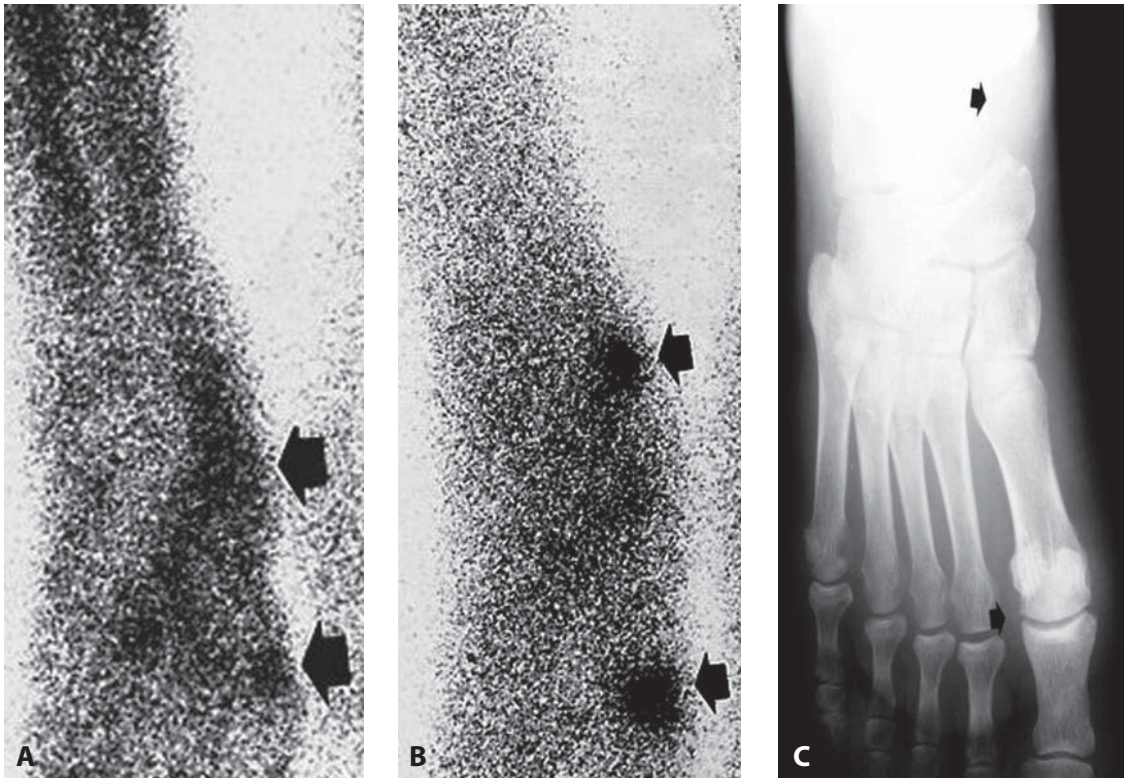

Fig. 12.18A–C Nuclear angiography in gouty arthritis. **A, B** Arteriogram and blood-pool scan of the right ankle in another 47-year-old man with gouty arthritis shows increased blood flow and blood pool focally at the medial aspect of the talonavicular joint (*upper arrow)* and the lateral aspect of the first metatarsophalangeal joint (*lower arrow*). **C** Dorsoplantar radiograph reveals diffuse soft-tissue swelling in the respective affected joints (*arrows*)

pathognomonic sign is calcium deposition in the tophi.

Scintigraphy shows marked tracer uptake in gouty arthritis from the early stage of the disease, often predating radiographic change. Pinhole scintigraphy is useful for the early and specific diagnosis of acute gouty synovitis. The magnified view of painful joints with acute gouty arthritis reveals prominent periarticular bone tracer uptake (Figs. 12.13B and 12.14B).

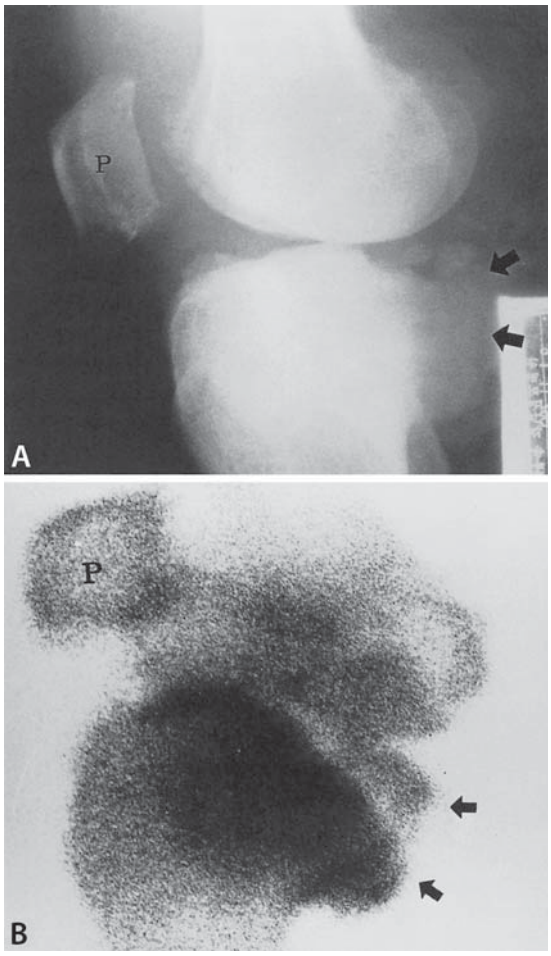

Fig. 12.19A, B Charcot's joint. **A** Mediolateral radiograph of the right knee in a 31-year-old man with advanced neuroarthropathy reveals bizarre bone destruction with exophytic bones (*arrows*), sclerosis, irregular joint space narrowing, subluxation, and soft-tissue swelling. **B** Medial pinhole scintigraph shows intense tracer uptake in the collapsed, subluxed tibial head and the exophytic bones (*arrows*). The joint is irregularly narrowed and deformed. Less intense tracer uptake can be seen in all the periarticular bones including the patella (*P*), producing the "wrapped bone" sign of synovitis

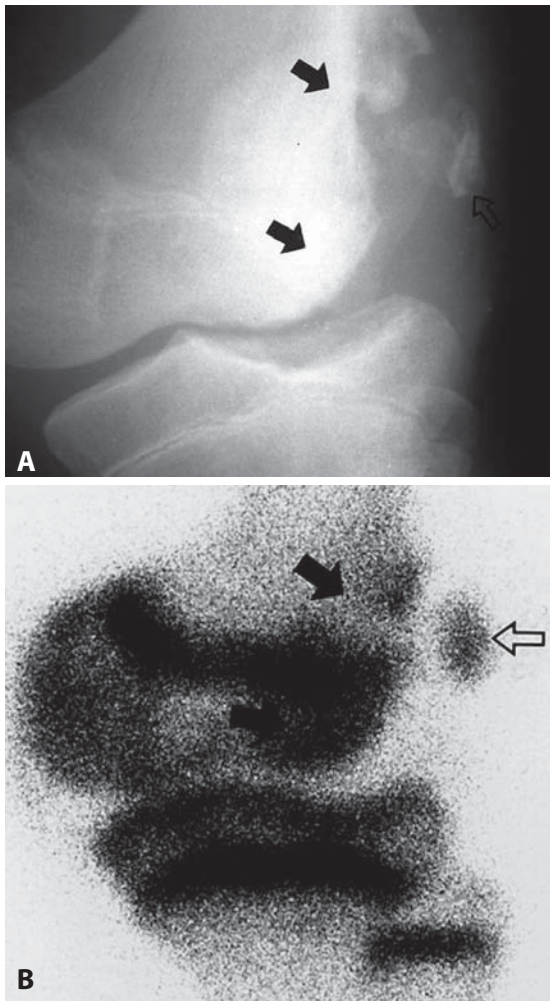

Fig. 12.20A, B Detached bones in Charcot's joint. **A** Anteroposterior radiograph of the left knee in a 13-year-old boy with poliomyelitis demonstrates subluxation and multiple fracture fragments liberated from the lateral femoral condyle (*arrows*). **B** Anterior pinhole scintigraph reveals diffusely increased tracer uptake in the subluxed joint and one of the detached bones (*open arrow*). Other detached bones do not accumulate tracer due to devascularization

The articular space may or may not be involved. Chronic tophaceous gouty arthritis with repeated attacks manifests as articular narrowing with patchy tracer uptake (Fig. 12.15). Occasional patients with longstanding disease may reveal discrete "hot" areas in the punched-out bone defects produced by tophi (Fig. 12.16B). One of our patients with prepatellar bursitis and infrapatellar ligamental enthesitis with calcified tophi showed very intense uptake in the prepatellar bone surface and ligamental insertion in the tibia (Fig. 12.17). Whole-body scanning is unique in globally grasping the affected joints in a single panoramic view. It is worth noting that nuclear angiography provides useful information about the activity of inflammation in gouty arthritis by showing increased blood flow and blood pool (Fig. 12.18).

12.5 Charcot's Joint or Neuroarthropathy

Charcot's joint involves virtually any joints under physical stress. As the term neuroarthropathy denotes destructive arthropathy of Charcot's joint is caused by a number of diseases that affect the central or peripheral sensory nerve fibers, rendering patients insensitive to pain and vulnerable to trauma. Causes include tabes dorsalis, syringomyelia, spinal injury, hemiplegia, poliomyelitis, and diabetes mellitus. Pathologically, the condition is characterized by chondrolysis, fracture and collapse, synovial and capsular hypertrophy, and disorganization of the joint; for example, soft-tissue thickening and resolution of the anterior cruciate ligament in the knee.

Radiography reveals soft-tissue swelling, articular narrowing, subluxation, slanting deformity, bony condensation and destruction, and exophytes (Fig. 12.19A). Occasionally, detached bones are visualized (Fig. 12.20A). Scintigraphy shows bizarre tracer uptake in crooked bones in and about diseased joints as well as exophytes and fragmented bones. The joint is narrowed, subluxed, and often grossly disfigured (Figs. 12.19B). Furthermore, it is important to note that bone scintigraphy has the ability to distinguish live from dead bones in Charcot's joint (Fig. 12.20B).

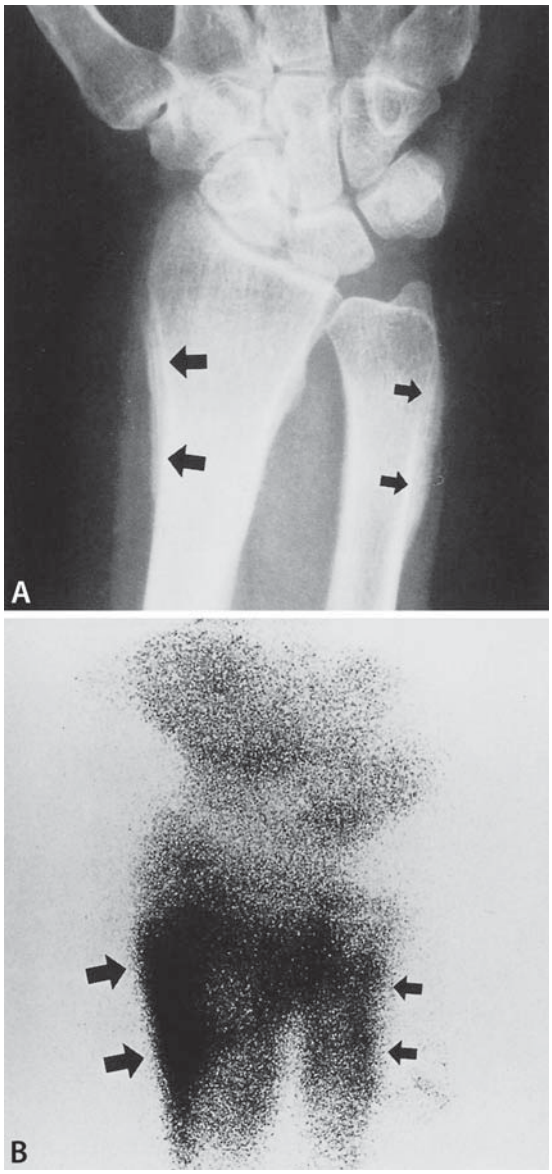

Fig. 12.21A, B Secondary hypertrophic osteoarthropathy. **A** Dorsoventral radiograph of the left wrist in a 65-year-old woman with known bronchogenic carcinoma shows lamellated and amorphous periosteal thickening respectively in the distal radius (*large arrows*) and distal ulna (*small arrows*). **B** Ventral pinhole scan portrays more intense tracer uptake in the lateral aspect of the distal radius (*large arrows*) and less intense uptake in the distal ulna (*small arrows*). Correlation with radiographic alterations reveals the more intense uptake to be related to the lamellated periosteal thickening and the less intense uptake to the amorphous thickening

12.6 Secondary Hypertrophic Osteoarthropathy

Secondary hypertrophic osteoarthropathy may be caused by a variety of pulmonary, pleural, abdominal, and cardiac diseases and other conditions such as SLE. Principal pathological alteration is periostitis with new bone deposition and intense overgrowth of vascular connective tissue that surrounds the tendon, bone, and joint. Synovitis is not uncommon, but usually mild. Hypertrophy may improve or even

vanish when the causative disease has been successfully treated.

The main radiographic feature is single-layered or lamellated periosteal thickening typically in the shafts of the long bones, clavicles, and phalanges. Involvement of the metaphysis and epiphysis is not prominent in the early stage but they eventually become involved along with the joints (Figs. 12.11 and 12.21). Initially, thickened periosteum appears loosely attached to the underlying cortex, but with time it becomes tightly incorporated into the cortex.

^{99m}Tc-MDP bone scintigraphy is a sensitive indicator of periosteal change, displaying the "double stripe" or "parallel track" sign along the shafts of the long bones. In occasional cases pinhole scanning separates periosteal new bone deposition from underlying cortex. Interestingly, the magnified scan permits correlation between radiographic periosteal thickening as assessed in terms of lamellation and amorphous deposition and the intensity of tracer uptake (Figs. 12.21 and 12.22). Thus, it appears that tightly stratified thickening occurs in the cortex of weight-bearing bone such as the distal femur (Fig. 12.11) and proximal tibia (Fig. 12.22), and accumulates tracer more intensely than loose thickening does. It seems that lamellation may be the way that newly formed bone more effectively bears physical stress; hence more bone turnover and tracer uptake. Bone scanning is particularly useful for (a) the diagnosis of hypertrophic osteoarthropathy, (b) the monitoring of therapeutic effect or etiological diseases, and (c) archiving healing or conversely aggravation. The most typical example is osteoarthropathy secondary to pulmonary carcinoma. When the causative primary malignancy is brought under control follow-up scanning may reveal resolution of the osteoarthropathic changes (Fig. 12.23), but when treatment fails scintigraphic changes conversely become aggravated with the extension of the lesion (Fig. 12.24).

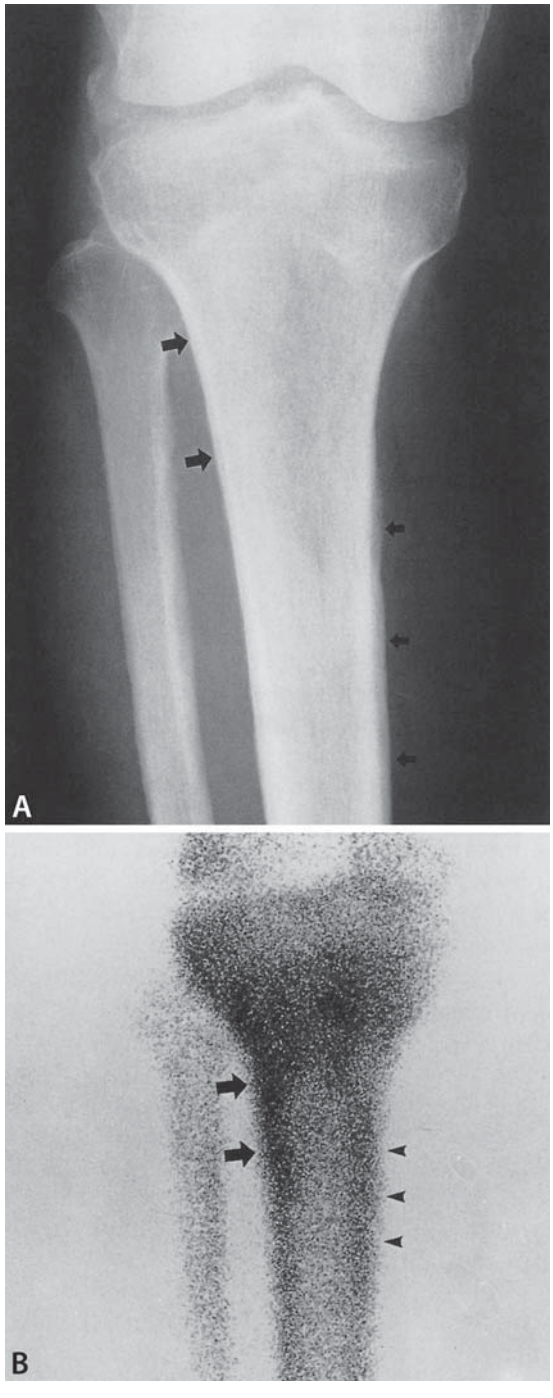

Fig. 12.22A, B Relatively more intense tracer uptake in the tightly lamellated periosteal thickening than in the loosely amorphous thickening. **A** Anteroposterior radiograph of the right proximal tibia in a 75-year-old man with bronchogenic carcinoma reveals dense single-layer periosteal thickening in the lateral aspect of the proximal tibia (*large arrows*) and amorphous thickening in the medial aspect (*small arrows*). Some exophytic bones are noted in the knee joint. **B** Anterior pinhole scintigraph shows the tracer uptake in the dense periosteal thickening (*arrows*) to be more intense than that in the amorphous thickening (*arrowheads*)

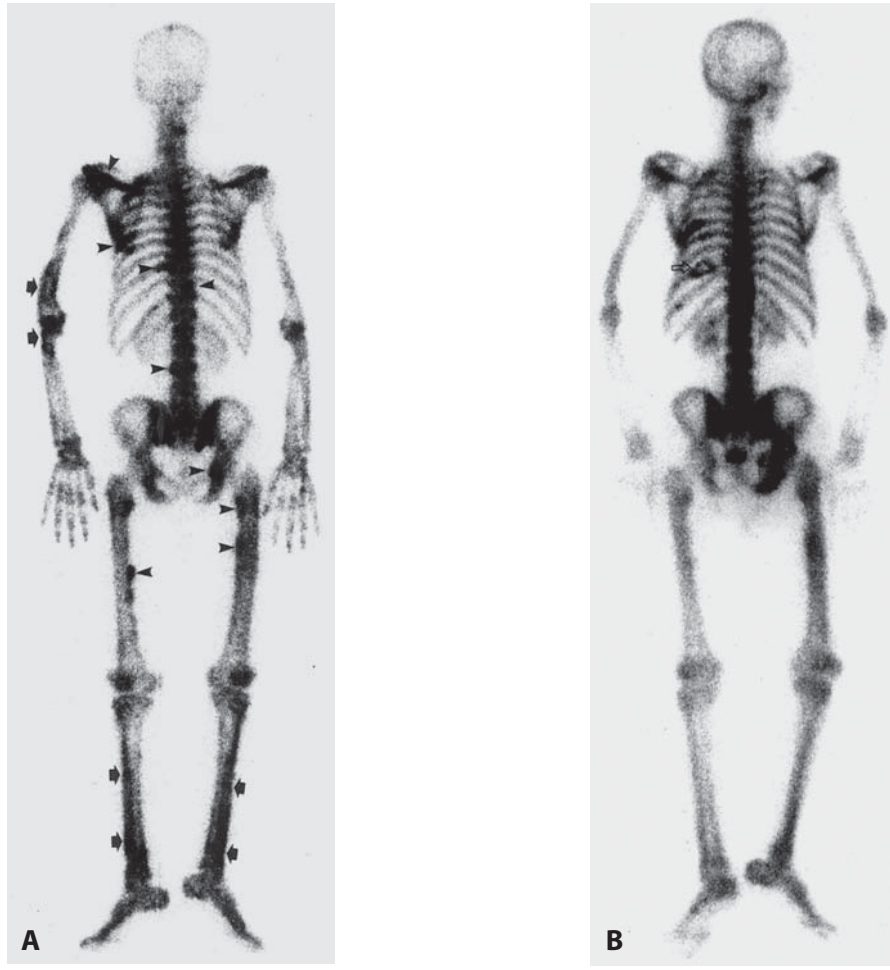

Fig. 12.23A, B Effect of neoadjuvant therapy on secondary osteoarthropathy. **A** Posterior whole-body bone scintigraph in a 59-year-old man with pulmonary carcinoma shows intense tracer uptake in multiple lesions of osteoarthropathy (*arrows*) and metastases (*arrowheads*). **B** Follow-up scan 8 months after chemotherapy reveals resolution of osteoarthropathy and most metastases. Note a newly developed osteolytic metastasis in left rib 9 (*open arrow*)

12.7 Periarticular Soft-Tissue Rheumatism Syndromes

Soft-tissue rheumatism syndromes are common inflammatory conditions clinically characterized by pain. For a bone scintigraphic discussion, the syndromes are arbitrarily categorized into (a) the periarticular soft-tissue rheumatism syndromes, and (b) the muscular and musculotendinous rheumatism syndromes. The former group includes bursitis, tenosynovitis, and enthesitis and the latter includes myositis ossificans, rhabdomyolysis, musculotendinous unit injuries (Baker 1984), and distal femoral cortical desmoids (Kimmelstiel and Rapp 1951). The diseases that belong to the latter group are described in the next section.

The symptoms of periarticular soft-tissue rheumatism syndromes are pain, tenderness, and swelling in the bursa, tendon sheath, and enthesis. The most common positive laboratory test is an elevated erythrocyte sedimentation rate. Individual lesions manifest as bursitis, tenosynovitis, capsulitis, fibrositis, or calcium deposition disease. Etiologically, trauma and repeated physical stress are likely causes in

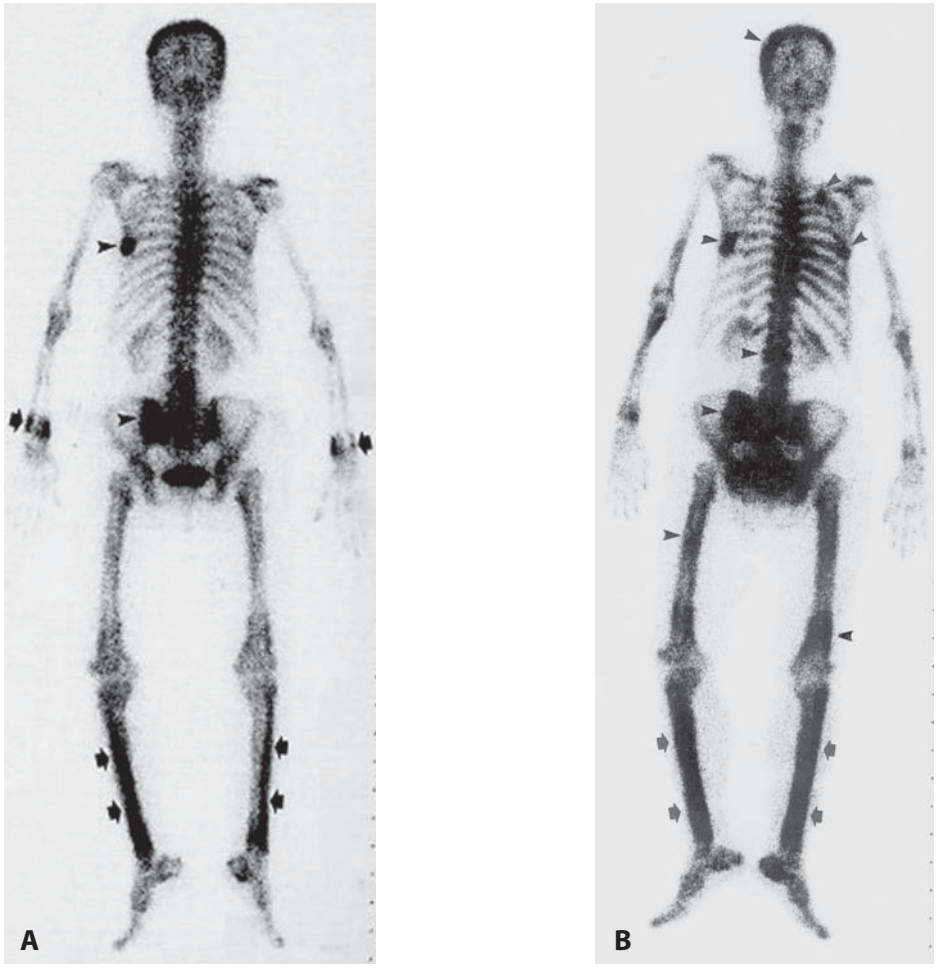

Fig. 12.24A, B Aggravation of osteoarthropathy in failed chemotherapy. **A** Posterior whole-body bone scintigraph in a 65-year-old woman with breast carcinoma shows intense tracer uptake in multiple lesions of osteoarthropathy (*arrows*) and metastases (*arrowheads*). **B** Follow-up whole-body scan 6 months after chemotherapy reveals worsening of both osteoarthropathy and metastases

most patients, but in occasional patients actual tear and rupture of fibrous aponeurosis and enthesis are responsible (see "Musculotendinous Unit Injuries" below). Cases without etiology are not rare. These disorders often mimic rheumatic arthropathy and even gouty arthritis, but no essential relationship has been found with any rheumatic articular diseases (Bluestone 1988). From among the many soft-tissue rheumatism syndromes, calcific bursitis, tenosynovitis, adhesive capsulitis of the shoulder, and plantar fasciitis clinically deserve detailed description from the combined radiographic and scintigraphic point of view.

Plain radiography, aided by the soft-tissue technique, plays a useful role in the diagnosis of most cases of tenosynovitis, bursitis, and plantar fasciitis. The presence of amorphous calcification in a bursa is a pathognomonic sign of calcific bursitis (Figs. 12.25A and 12.26A), and tendinitis is indicated by thickened tendon with occasional mineralization (Fig. 12.27A). In addition, erosion with osteosclerosis (Fig. 12.28A) or erosion alone (Figs. 12.29A) may occur in the bones in contact with or in close approximation to an inflamed bursa or tendon. The plain radiographic diagnosis of tenosynovitis in the wrist (Fig. 12.30A), **adhesive capsulitis** in the shoulder (Fig. 12.31A), and plantar fasciitis in the

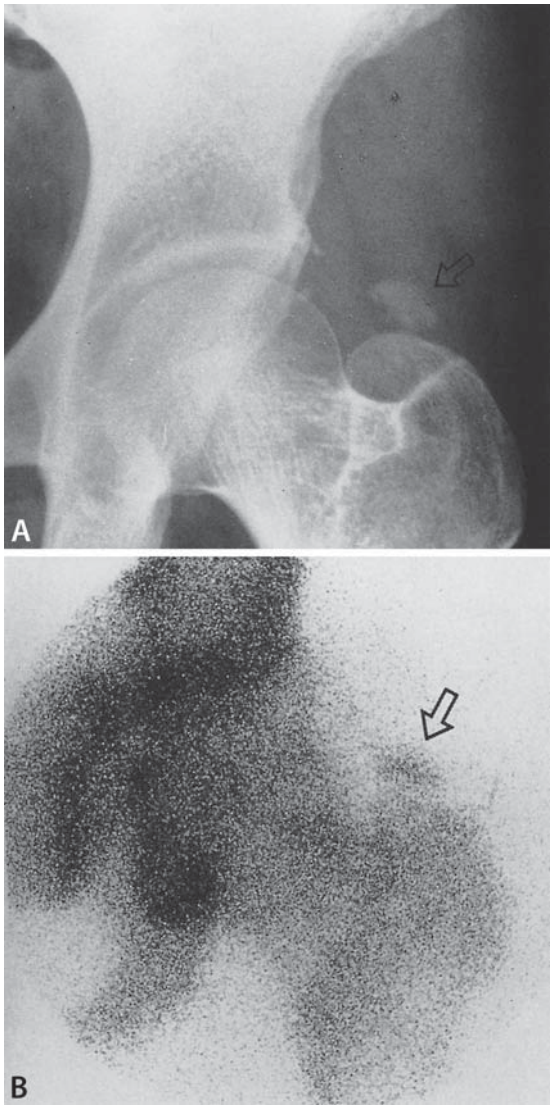

Fig. 12.25A, B Calcareous trochanteric bursitis (periarticular crystal deposition). **A** Anteroposterior soft-tissue radiograph of an aching left hip in a 46-year-old woman reveals a bean-sized, calcareous deposit in the supratrochanteric region (*open arrow*). **B** Anterior pinhole scan shows very subtle tracer uptake in the calcareous deposit (*open arrow*). This was not detected on ordinary scintigraph

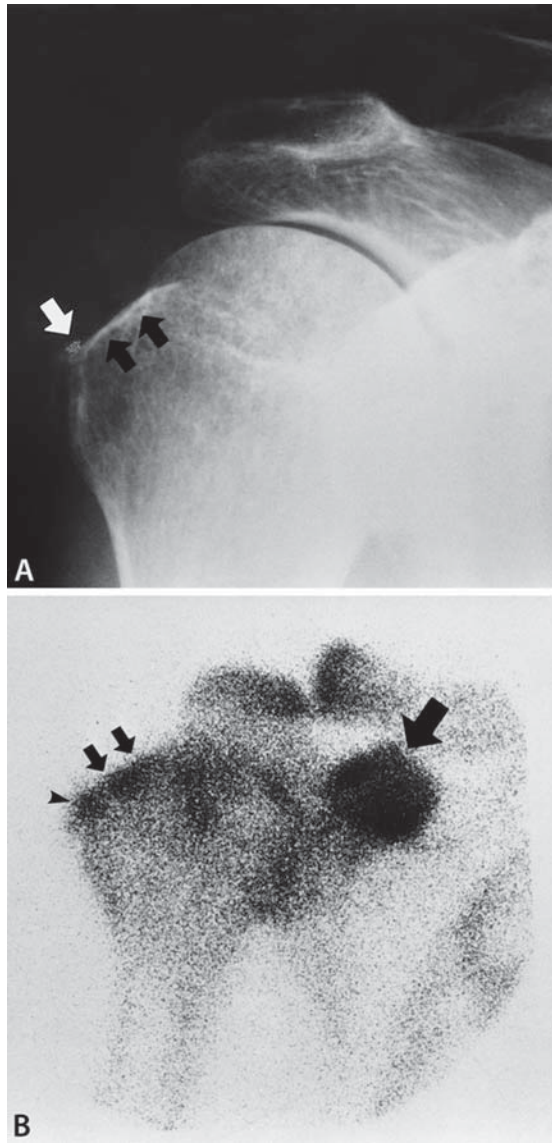

Fig. 12.26A, B Calcific subdeltoid and coracoid bursitis. **A** Anteroposterior radiograph of a painful right shoulder in a 59-year-old man shows calcium deposits in the subdeltoid bursa (*white arrow*) and coracoid bursa (*open arrows*). There is sclerosis localized in the upper aspect of humeral neck (*black arrows*). **B** Anterior pinhole scan shows tracer uptake in a calcific subdeltoid bursa (*arrowhead*) and associated sclerosis (*double arrows*) as well as in a calcific coracoid bursa (*single arrow*)

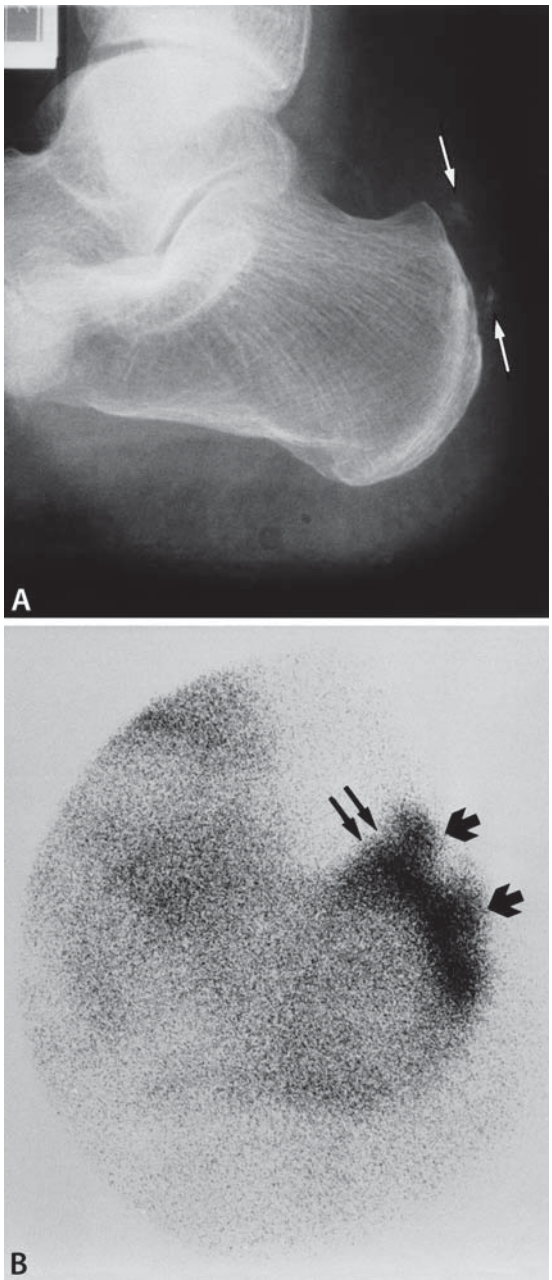

Fig. 12.27A, B Calcific Achilles tendinitis. **A** Lateral radiograph of a painful right hindfoot in a 63-year-old woman shows calcifications in the Achilles tendon which is thickened (*between arrows*). **B** Lateral pinhole scan reveals two small nodular hot spots in the posterior aspect of the calcaneus, indicating calcified tendinitis (*thick arrows*). Upper retrocalcaneal tracer uptake denotes osteitis associated with tendinitis (*thin arrows*)

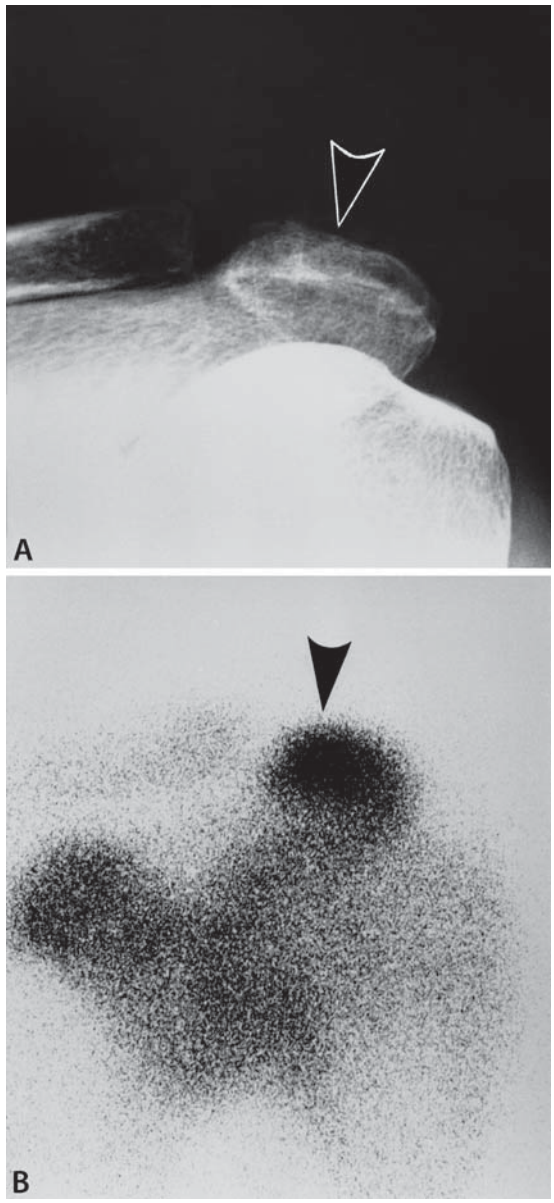

Fig. 12.28A, B Supra-acromial bursitis with regional bone erosions. **A** Anteroposterior radiograph of a painful left shoulder in a 43-year-old woman reveals irregular erosions in the upper aspect of the acromion (*arrowhead*). **B** Anterior pinhole scan shows intense tracer uptake in the corresponding area of the acromion (*arrowhead*)

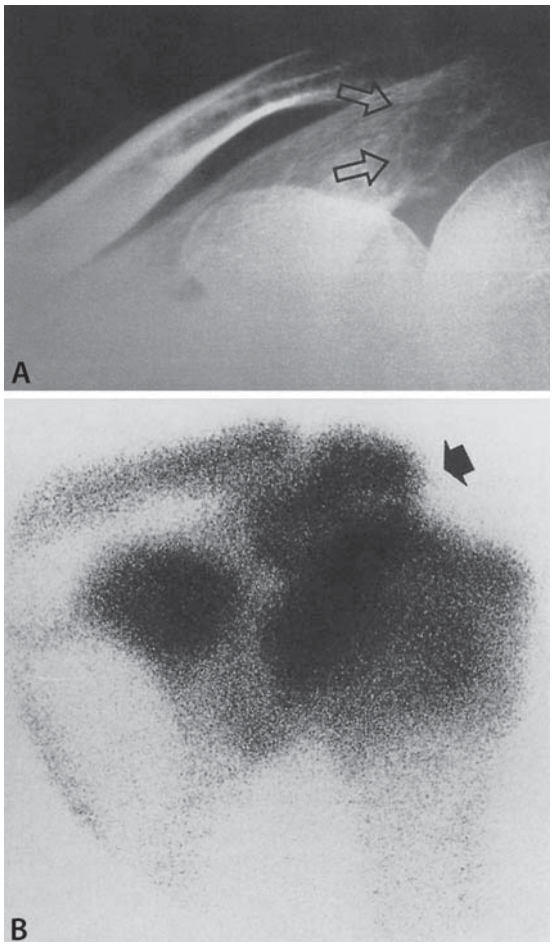

Fig. 12.29A, B Subacromial bursitis with regional bone erosions. **A** Anteroposterior radiograph of a painful left shoulder in a 63-year-old woman shows prominent osteoporosis in the acromion process, particularly in the undersurface, where modest cortical erosions are present (*open arrows*). **B** Anterior pinhole scan shows intense tracer uptake in the altered bones, with the most prominent uptake in the subacromial aspect (*arrow*)

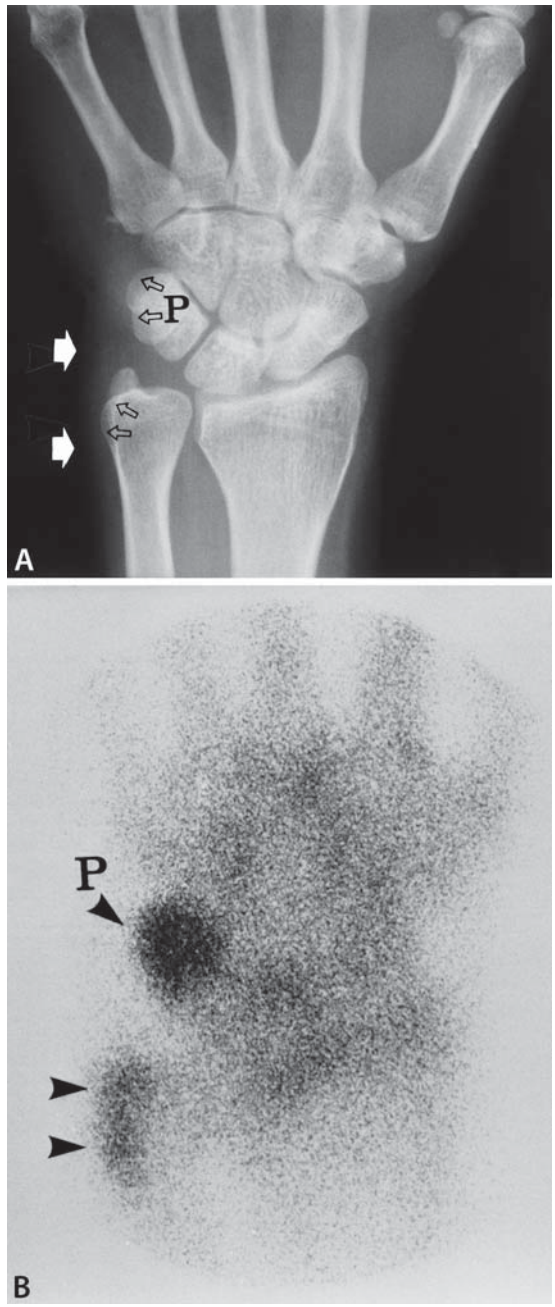

Fig. 12.30A, B Tenosynovitis of the flexor carpi ulnaris tendon. **A** Dorsoventral radiograph of a painful left wrist in a 48-year-old woman reveals swelling of the flexor carpi ulnaris tendon (*white arrows*) (*open arrows* tendinous insertions in the distal ulna and pisiform, *P*). **B** Dorsal pinhole scan shows increased tracer uptake in the ulnar (*pair of arrowheads*) and pisiform (*P, single arrowhead*) insertions of the flexor carpi ulnaris tendon

heel pad (Fig. 12.32A) is difficult if not associated with a bone change, whereas pinhole scintigraphy can specifically indicate their diagnosis by showing tracer uptake at the site in question even in the absence of radiographic change (Figs. 12.30B, 12.31B and 12.32B). Established plantar fasciitis always reveals a characteristic calcaneal spur (Fig. 12.33A). MRI may demonstrate edema in acute tenosynovitis

(Fig. 12.34A), and contrast arthrography is helpful in the diagnosis of adhesive capsulitis.

^{99m}Tc-MDP bone scintigraphy is a valuable imaging modality for the clinical investigation of various nonspecific inflammatory disorders of the periarticular soft-tissue structures, the entheses in particular. Thus, the planar scan shows increased uptake in bursitis, tendonitis, and enthesitis, but, as is well known, the mere tracer uptake is usually inadequate for making a specific diagnosis. Fortunately, pinhole scintigraphy provides accurate anatomical information, permitting the diagnosis of, for example, **bursitis** and tenosynovitis (Figs. 12.25B, 12.28B and 12.30B). In addition, pinhole scanning significantly enhances lesion detectability. As mentioned above, in bursitis and tenosynovitis, bone scanning reveals increased uptake in the erosions, reactive osteitis, or sclerosis in adjacent bone. Such secondary bone changes are typically observed in subdeltoid bursitis (Fig. 12.26), supra-acromial bursitis (Fig. 12.28), subacromial bursitis (Fig. 12.29), trochanteric bursitis, subachilles tenosynovitis (Fig. 12.27), and plantar fasciitis (Fig. 12.32).

12.7.1 Plantar Fasciitis

Plantar fasciitis or calcaneal periostitis, a common cause of painful heel pad, occurs either in isolation or as part of seronegative spondyloarthropathies or Behçet's disease. The usefulness of bone scan for the diagnosis of plantar fasciitis was first described by Sewell et al. (1980), and pinhole scintigraphy is known to indicate the diagnosis even in the absence of radiographic change by showing uptake, which is

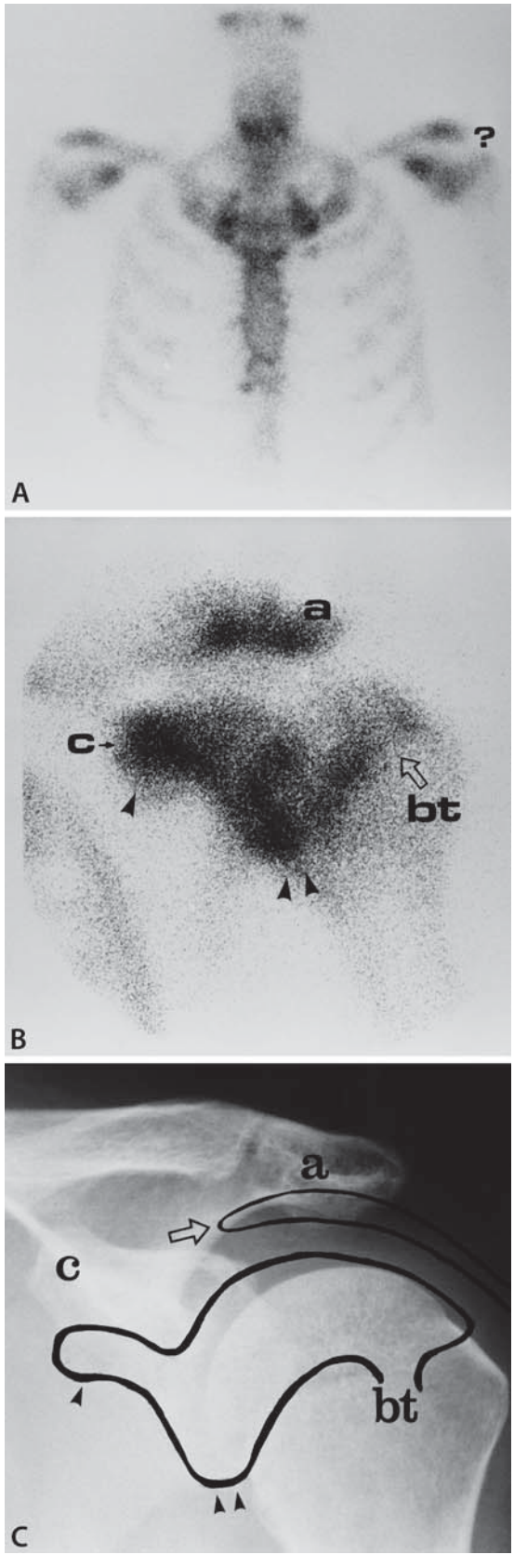

Fig. 12.31A–C Adhesive capsulitis of the shoulder. **A** Anterior planar scan of the left shoulder with pain and limited motion in a 33-year-old man shows no abnormality (*?*). **B** Anterior pinhole scan, however, shows the characteristic tracer accumulation in the acromion (*a*), coracoid (*c*), subcapsular recess (*single arrowhead*), and axillary pouch (*pair of arrowheads*) (*bt* biceps tendon). **C** Topography of the left shoulder showing relevant landmarks, including the acromion (*a*), coracoid (*c*), and biceps tendon (*bt*). The subacromial bursa (*open arrow*), subcapsular recess (*single arrowhead)*, and axillary pouch (*pair of arrowheads*) are also indicated

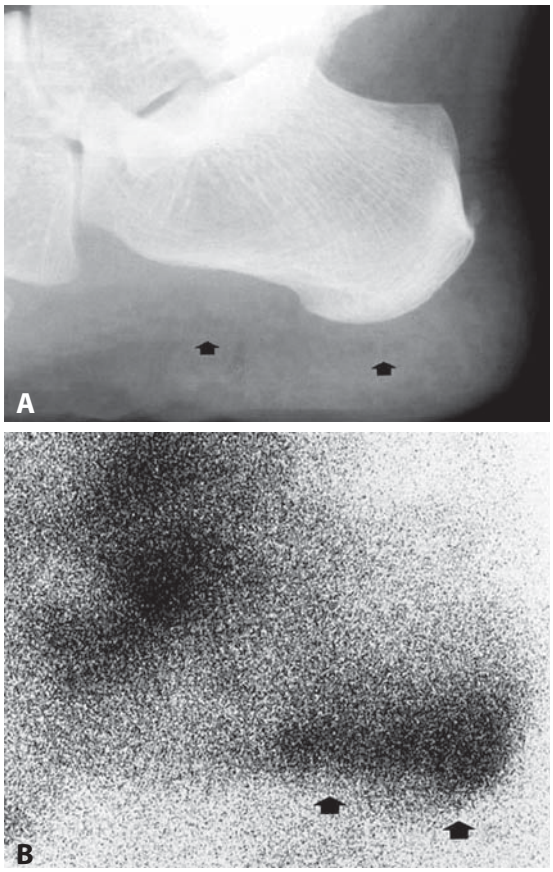

Fig. 12.32A, B Acute plantar fasciitis without calcaneal spur. **A** Lateral radiograph of the right hindfoot in a 51-year-old woman with a painful heel pad showing thickening of the plantar soft tissues (*arrows*) without regional bone abnormality. **B** Lateral pinhole scan shows subtle tracer uptake in the plantar aspect of the calcaneus at the long plantar tendon insertion (*arrows*). This uptake could not be appreciated on the plantar scan (not shown)

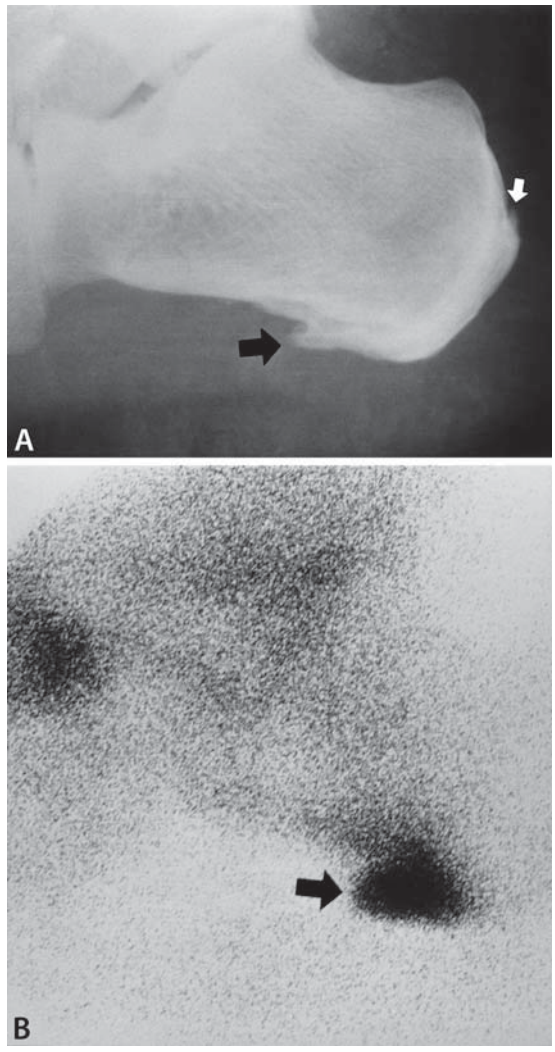

Fig. 12.33A, B Chronic plantar fasciitis with calcaneal spur. **A** Lateral radiograph of the right hindfoot in a 51-year-old woman with a painful heel pad reveals a plantar calcaneal spur (*black arrow*) with the incidental finding of a small, asymptomatic retrocalcaneal spur (*white arrow*). **B** Lateral pinhole scan shows the plantar spur concentrating tracer intensely (*arrow*), but the retrocalcaneal spur not doing so

often extremely subtle, in the calcaneal base and the plantar aponeurosis (Fig. 12.32). An ordinary planar scan is often inefficient for the diagnosis of such lesions. The soft-tissue rheumatism syndromes are local or focal in occurrence, and, hence, it is diagnostically imperative to exclude a possible association with systemic diseases such as rheumatoid arthritis, seronegative spondyloarthropathies, Sjögren's syndrome, Behçet's disease, and SLE. In this context, the important roles played by whole-body scanning and pinhole magnification scanning are to be underscored (Kim et al. 1999).

12.7.2 Degenerative Rheumatic Enthesopathy

Degenerative rheumatic enthesopathy is a common disorder in the elderly population. It affects any tendinous and ligamentous attachments to bones, causing pain (LaCava 1959; Cooper and Misol 1970). The sites of predilection include the tuberosity of the humerus, ulnar olecranon, patella, ischial tuberosity, tro-

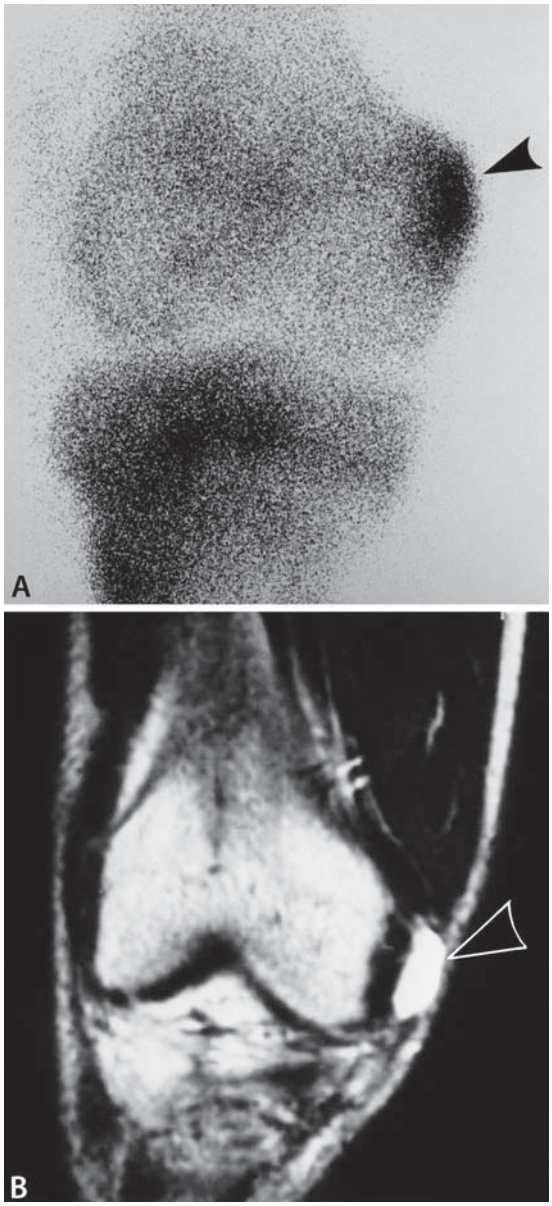

Fig. 12.34A, B Collateral ligament enthesitis. **A** Anterior pinhole scan of the painful left knee in a 21-year-old man shows intense tracer uptake localized to the lateral femoral epicondyle (*arrowhead*). **B** Coronal T2-weighted MRI demonstrates bright signal intensity, denoting edema in the lateral epicondyle where the fibular collateral ligament inserts (*arrowhead*)

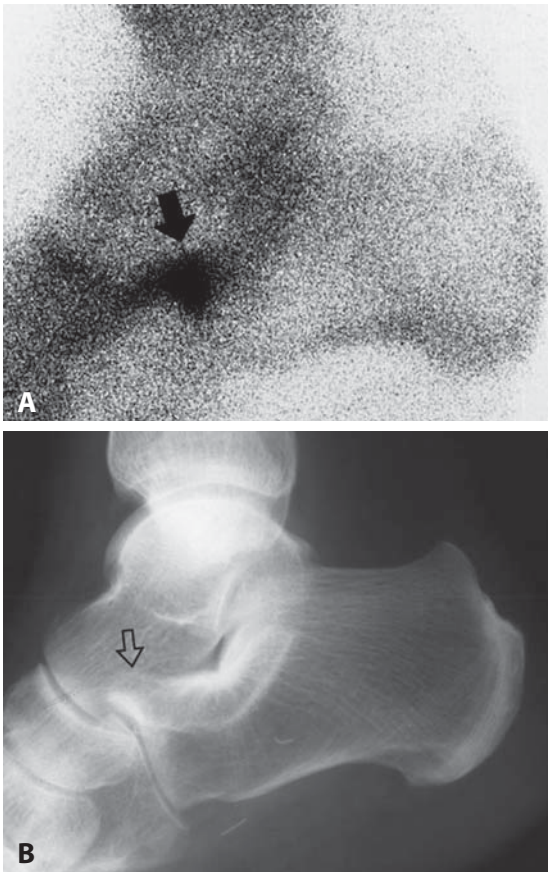

Fig. 12.35A, B Early focal rheumatic enthesopathy in the calcaneus. **A** Lateral pinhole scintigraph of the left ankle in a 57-year-old woman with local pain shows a small "hot" area in the anterior subtalar joint (*arrow*). **B** Lateral radiograph reveals a small area of barely recognizable bone resorption at the anterior articular surface of the calcaneal head (*open arrow*). Clinically, the radiographic change was first overlooked, then found and confirmed retrospectively after pinhole examination

chanters, talus, and calcaneus. Radiography reveals bony erosion in the early stage (Fig. 12.35A) and hyperostosis or bony excrescence in the late stage (Fig. 12.33A). Scintigraphy is highly sensitive, showing intense uptake specifically localized to the affected enthesis even in the early phase when radiography is negative or dubious (Fig. 12.35B). As shown in this case, subtle erosions present on a radiograph can frequently be confirmed at a second look after first seeing obvious tracer uptake on scintigraph. Enthesopathic hyperostoses intensely accumulate tracer when they are in an active phase with inflammation (Fig. 12.33B). Another factor for this intense tracer uptake is physical stress to the heel that is hard to avoid. Contusion, strain, and sports injuries may

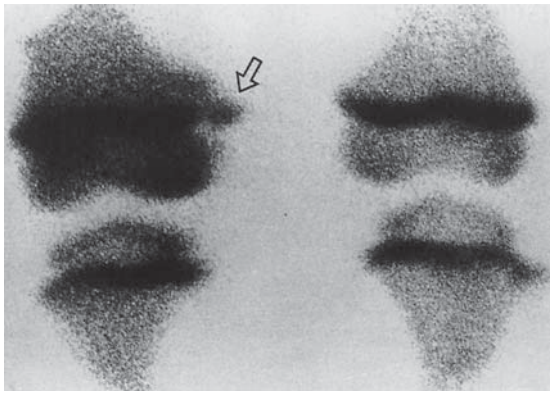

Fig. 12.36 Posttraumatic calcification of the medial collateral ligament of the knee (Pellegrini-Stieda syndrome). Anterior pinhole scintigraphs of both knees (simultaneous acquisition) in a 5-year-old girl shows small, spotty tracer uptake in the medial aspect of the right distal femoral epimetaphysis (*open arrow*). Radiographically, the uptake was located in the calcified lesion of the collateral ligament (not shown)

cause ligamental or tendinous inflammation with ectopic calcification in occasional cases. Such lesions may be visible on soft-tissue radiography if changes are considerable in extent and mineralized. MRI is useful for the demonstration of bone edema that is undetectable radiographically (Fig. 12.34A). When mineralization takes place in the medial collateral ligament of the knee, the condition is referred to as Pellegrini-Stieda disease (Fig. 12.36). Pinhole scintigraphy is a highly sensitive imaging method of soft-tissue mineralization, and can simultaneously provide information on the metabolic state of the disease. For example, painful calcified bursitis accumulates tracer avidly, but the quiescent form with calcification does not. Indeed, the calcific bursitis of the great trochanter presented in Fig. 12.25B was painful and did accumulate tracer. However, the calcific bursitis shown in Fig. 12.45 was an incidental finding and did not accumulate tracer; it was an inert and silent lesion.

We had the opportunity to perform pinhole scintigraphy in a patient with **chondrocalcinosis** of the knee joint. Interestingly, chondrocalcinosis in this particular case did not accumulate tracer (Fig. 12.37). This was considered to reflect the fact that chondrocalcinosis of this sort has little or no vascular supply, at least during certain stages of its evolution.

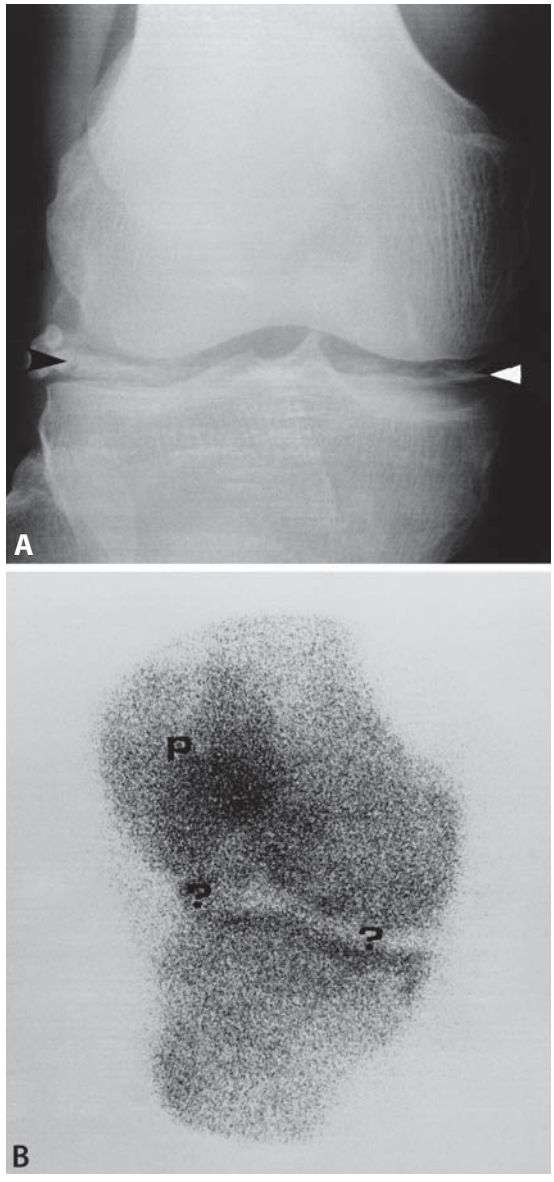

Fig. 12.37A, B Absence of tracer uptake in chondrocalcinosis. **A** Anteroposterior radiograph of the right knee in a 52-year-old man with an advanced chondrocalcinosis shows marked linear calcification in the articular cartilage (*arrowheads*). **B** Slightly tilted anterior pinhole scan shows no tracer accumulation in chondrocalcinosis (*?*) (*P* patella)

12.8 Muscular and Musculotendinous Rheumatism Syndromes

Muscular and musculotendinous rheumatism syndromes of both scintigraphic and radiographic interest include myositis ossificans, rhabdomyolysis, musculotendinous unit injuries, and distal femoral cortical desmoid.

12.8.1 Myositis Ossificans

Myositis ossificans denotes a condition in which the skeletal muscle is heterotopically ossified. The ossifying myositis caused by trauma is referred to as myositis ossificans traumatica and that unrelated to trauma is called myositis ossificans nontraumatica or pseudomalignant osseous tumor of soft tissue. According to Soule (1945), this condition is noninflammatory in nature and due to the alteration of perimysial connective tissue (fascia) and not the myocytes (muscle). It is generally accepted that the perimysial tissue, which induces the osteoprogenitor cells, is the source of heterotopic ossification (Friedenstein 1973). The causes include trauma and surgical damage in myositis ossificans traumatica and burns, paraplegia (Miller and O'Neill 1949), and autosomal mutation in myositis ossificans nontraumatica. The third type is myositis ossificans progressiva. This is a rare inflammatory disease of mesodermal tissue; hence, it also referred to as fibrodysplasia ossificans progressiva.

The radiographic features of muscular and musculotendinous ossification are similar regardless of etiology (Figs. 12.38A and 12.39A). However, the ossification in myositis ossificans progressiva is basically different from that of the other two types of myositis ossificans, and is characterized by diffuse sheet-like ossification that often connects different parts of the body such as the shoulder, rib cage, and pelvis.

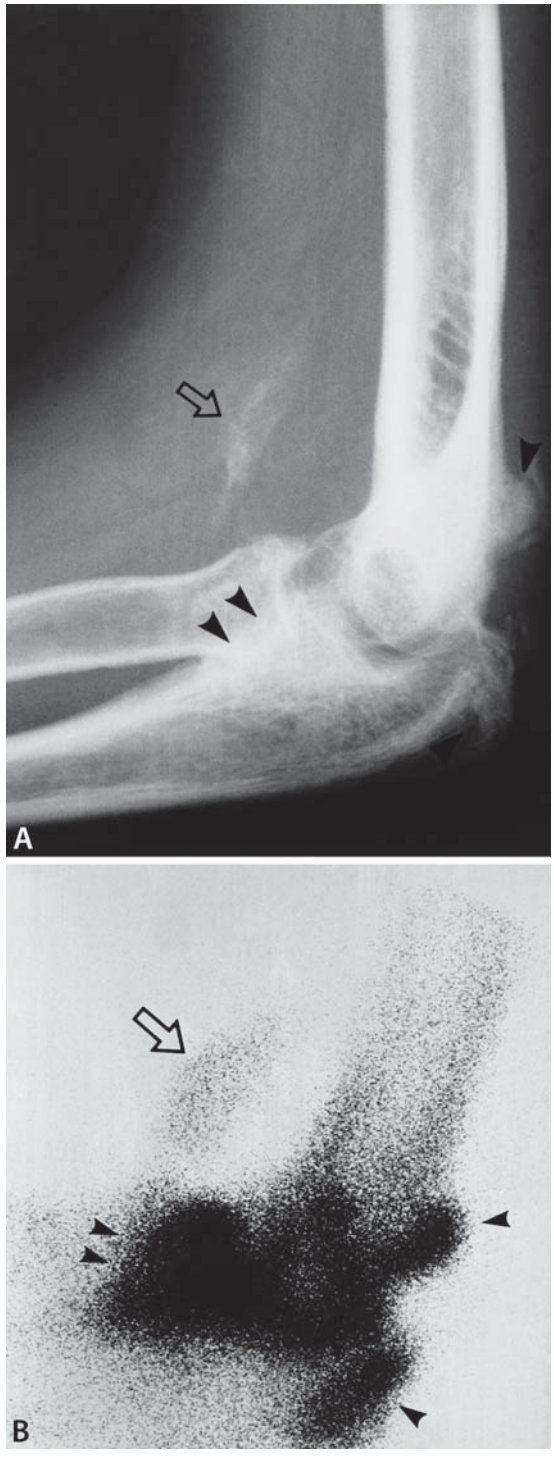

Fig. 12.38A, B Old myositis ossificans traumatica. **A** Lateral radiograph of the right elbow in a 15-year-old boy with myositis ossificans of the biceps muscle shows fusiform ossification in the antecubital fossa (*open arrow*). Fracture had occurred 9 months previously. The proximal ulna and distal humerus are the sites of old fractures with deformity and osteophytes (*arrowheads*). **B** Lateral pinhole scan shows mild tracer uptake in myositis (*open arrow*). Note marked tracer uptake in fractures and osteophytes (*arrowheads*)

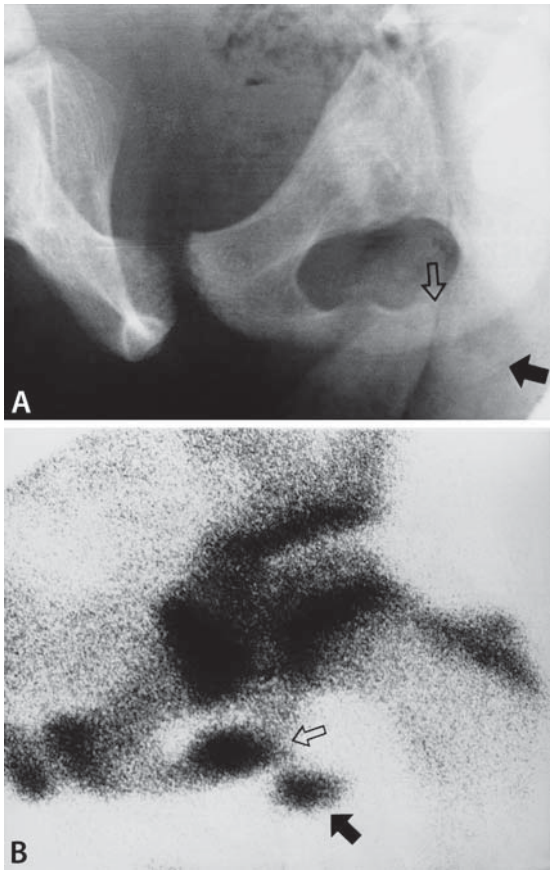

Fig. 12.39A, B Fresh myositis ossificans traumatica. **A** Oblique radiograph of the left ischium in a 9-year-old girl reveals barely visible amorphous calcification in the muscle below the ischium (*solid arrow*). Fracture is also faintly visualized with minimal callus formation (*open arrow*). **B** Oblique pinhole scan shows intense tracer uptake in both fracture (*open arrow*) and myositis (*solid arrow*). Note that tracer uptake in this fresh myositis ossificans is far more intense than that in the old myositis shown in Fig. 12.38B

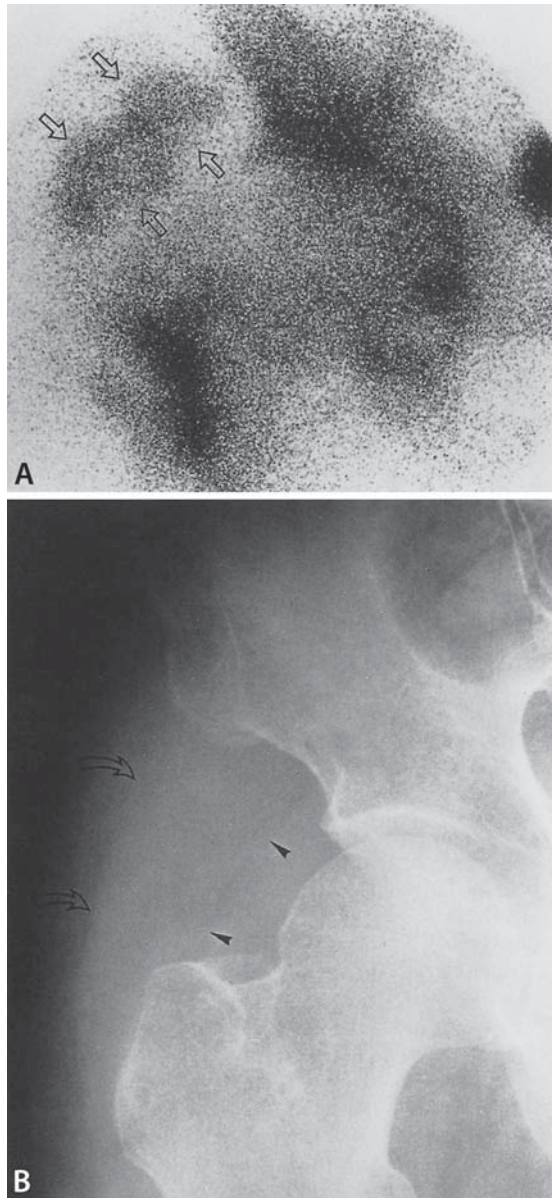

Fig. 12.40A, B Myositis ossificans without radiographic alteration. **A** Anterior pinhole scan of the right hip in a 66-year-old paraplegic man shows tracer uptake in the gluteus muscle (*open arrows*). The lesion was an incidental finding on a bone scan performed for another purpose. The lesions were bilateral and confirmed by CT scan. **B** Anteroposterior radiograph showing no calcific density in the muscle (*arrows, arrowheads*)

Like any diseases that involve heterotopic ossification, the bones formed in myositis ossificans avidly accumulate tracer especially in an active phase so that the diagnosis can easily be suggested or made by ^{99m}Tc MDP scintigraphy. Thus, as described by Suzuki et al. (1974) and presented in Fig. 12.40, bone scintigraphy can very efficiently diagnose myositis ossificans even in the absence of radiographic evidence. Pinhole scanning is extremely sensitive, often showing subtle lesions that are not shown on ordinary planar scintigraphs. It can identify an individual muscle or muscle group affected (Figs. 12.38B and 12.39B). A further and unique advantage of this examination is that it can provide information on the metabolic acti-

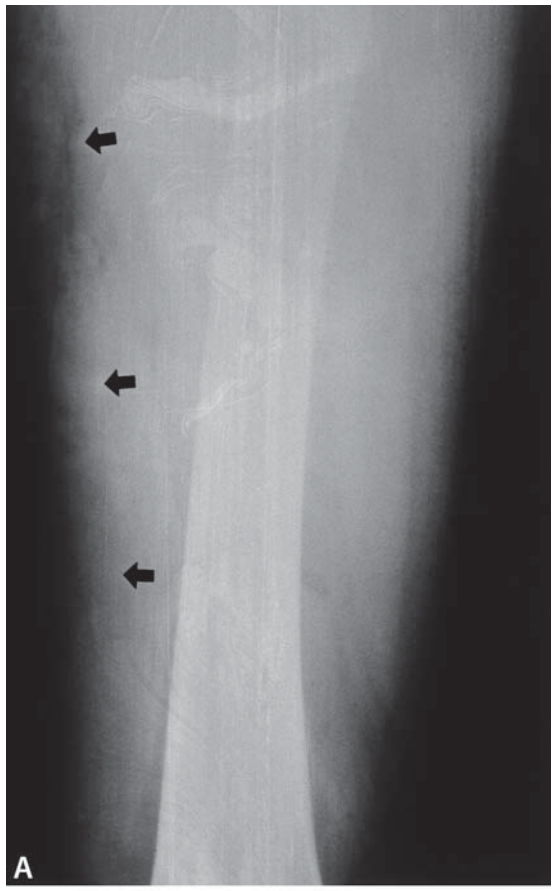

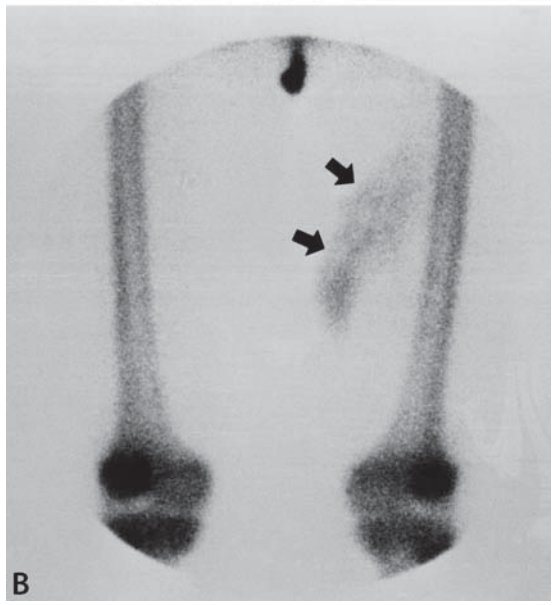

Fig. 12.41A, B Postincisional myositis ossificans. **A** Anteroposterior radiograph of the left thigh in a 37-year-old woman shows derangement of the adductor muscle shadow due to surgical incision (*arrows*). No calcification is seen. **B** Anterior planar scan shows large fusiform tracer uptake indicating myositis in the adductor muscles (*arrows*)

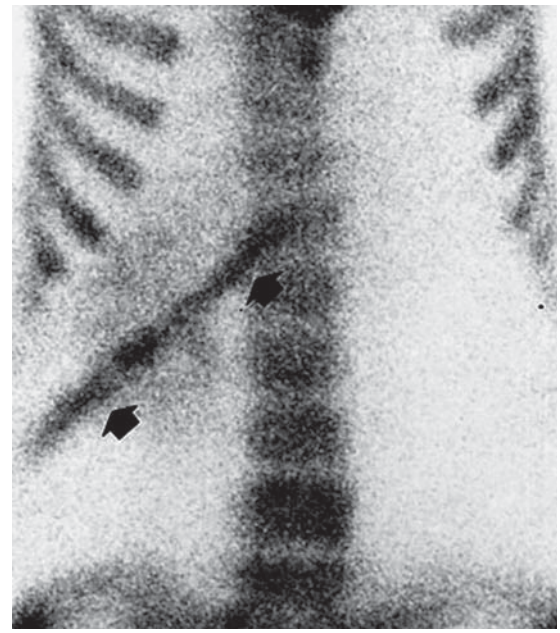

Fig. 12.42 Tracer uptake in a fresh incisional skin wound. Anterior bone scintigraph of the abdomen in a 69-year-old woman shows prominent linear uptake in a scar formed after laparotomy performed 6 days previously for gallbladder stone removal (*arrows*)

vity of a calcifying lesion in its evolutionary stage. Understandably, fresh lesions accumulate tracer far more avidly than old ones (Figs. 12.38B and 12.39B). Myositis ossificans may result from a surgical incision or an operative injury of skeletal muscles (Fig. 12.41). Incisional soft-tissue wounds accumulate tracer well within a week following an operation (Fig. 12.42), and mineralized foci may be presented as areas of discrete uptake of ^{99m}Tc-MDP within a few weeks (Fig. 12.43). Nuclear angiography and equilibrium phase scintigraphy are ideal for noninvasive dynamic assessment of activity of myositis ossificans in terms of mineralization or calcification (Fig. 12.44).

12.8.2 Rhabdomyolysis

Also known as myonecrosis, this condition is characterized by diffuse skeletal muscular injury with the release of muscle cell contents into the blood plasma. A review of the condition has revealed that it is not an uncommon

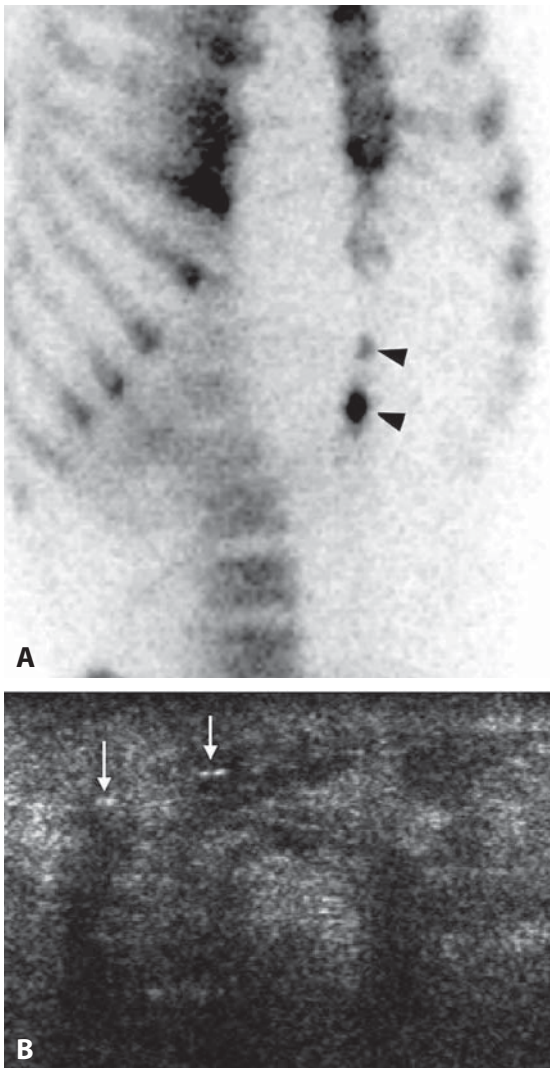

Fig. 12.43A, B Discrete tracer uptake in mineralized incisional scars. **A** Oblique bone scintigraph of the upper abdomen in a 46-year-old man shows two small spotty "hot" areas in a focally calcified scar formed after a laparotomy performed 3 weeks previously for the treatment of traumatic hemoperitoneum (*arrowheads*). **B** Sonogram demonstrates small plaque-like calcium deposits with acoustic shadows (*arrows*)

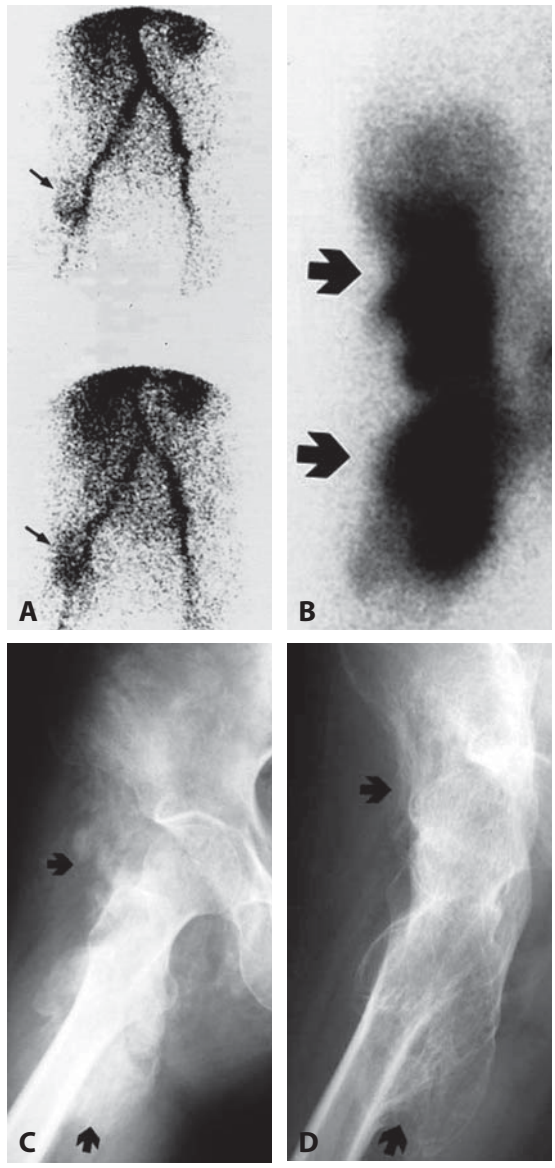

Fig. 12.44A–D Nuclear angiography for disease activity assay of myositis ossificans. **A** Arteriography of the pelvis and hips in a 55-year-old hemiplegic woman with myositis ossificans nontraumatica of the right gluteus muscles and fascias bridging the right ilium and femur shows increased blood flow (*arrow*). **B** Equilibrium pinhole scan reveals prominent tracer uptake in the gluteus and fascias denoting actively progressive mineralization (*arrows*). **C** Anteroposterior radiograph demonstrates large ill-defined areas of nebulous mineralization covering the right iliofemoral region (*arrows*). **D** Anteroposterior radiograph taken 2 years later shows fully mature heterotopic bones with trabeculation (*arrows*)

disorder (Gabow et al. 1982). The etiologies are many and varied (Lamminen 1996). The more common etiologies are excessive muscular activity (Matin et al. 1983; Valk 1984), direct muscular injury, ischemia, external compression, and ethanol intoxication (Koffler et al. 1976; Silberstein and Bove 1979). Pathology is characterized by swelling, hyalinization, de-

generation, and regeneration of muscle fibers (Armbrustmacher 1988). When muscle fibers disrupt, myoglobin escapes into the extracellular fluid and plasma, resulting in myoglobinemia, frequently causing acute renal failure. Plasma creatine kinase is elevated. In contrast to myositis ossificans, in which perimysial connective damage prevails, myocytes are mainly affected in rhabdomyolysis. Clinically, half of the cases are indolent, and in the majority of cases objective symptoms and signs are absent (Gabow 1982).

Radiography is not helpful in the diagnosis of rhabdomyolysis, although it can be utilized to exclude inflammatory and calcifying muscular disorder (Fig. 12.45). CT is characterized by low attenuation in affected muscles (Fig. 12.45B) and MRI reveals streaky or mottled high-intensity edema in necrotized muscles on T2-weighted images (Fig. 12.46C).

^{99m}Tc-MDP bone scanning has been widely used for the diagnosis of rhabdomyolysis since the first reports of Haseman and Kriss (1985) and Patel and Mishkin (1986). It is a highly reliable and sensitive examination. Procedures include whole-body scintigraphy for systemic survey (Fig. 12.46A) and pinhole scintigraphy for the identification of a specific muscle or muscle group (Figs. 12.45A and 12.46B).

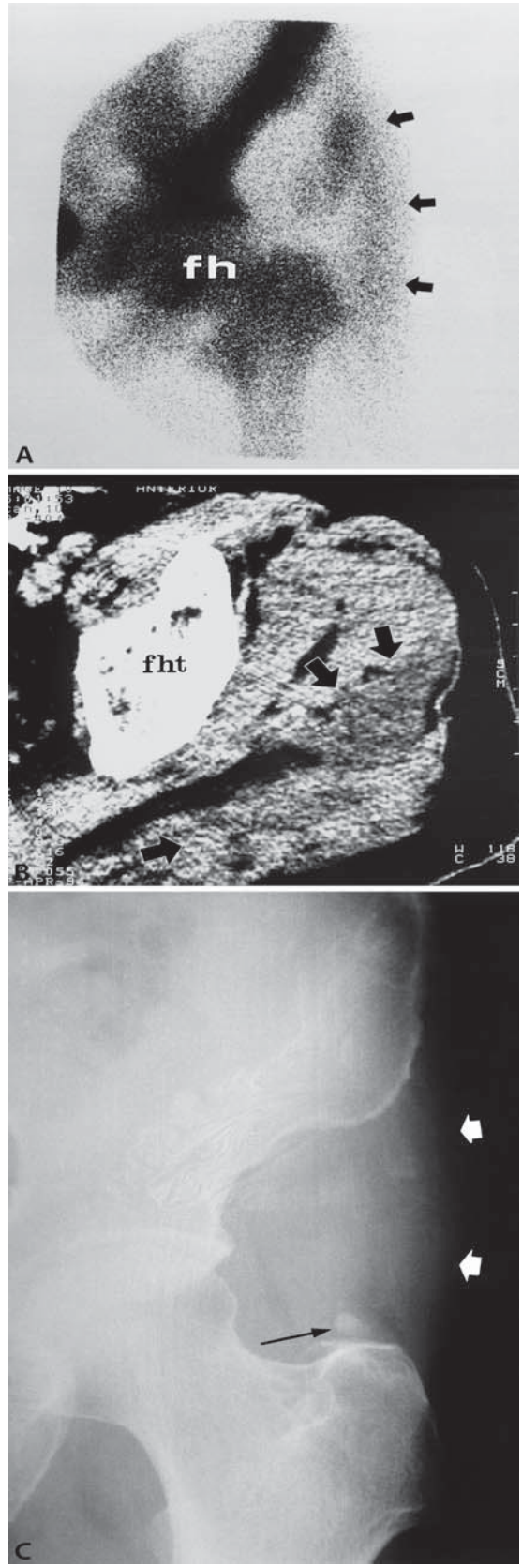

Fig. 12.45A–C Compression rhabdomyolysis. **A** Anterior pinhole scan of the left hip in a 69-year old bed-ridden man with lung cancer reveals fusiform tracer uptake in the gluteus medius muscle (*arrows*) (*fh* femoral head). **B** Transaxial CT scan at the level of the femoral head top (*fht*) reveals low attenuation with hypodense foci in the gluteus medius muscle (*pair of arrows*) and gluteus maximus muscle (single arrow), denoting edema and necrosis. **C** Anteroposterior radiograph of the hip shows the gluteal muscles in question to be unremarkable (*white arrows*). Incidentally, there is calcific trochanteric bursitis (*long arrow*), which does not concentrate tracer. The lesion was asymptomatic

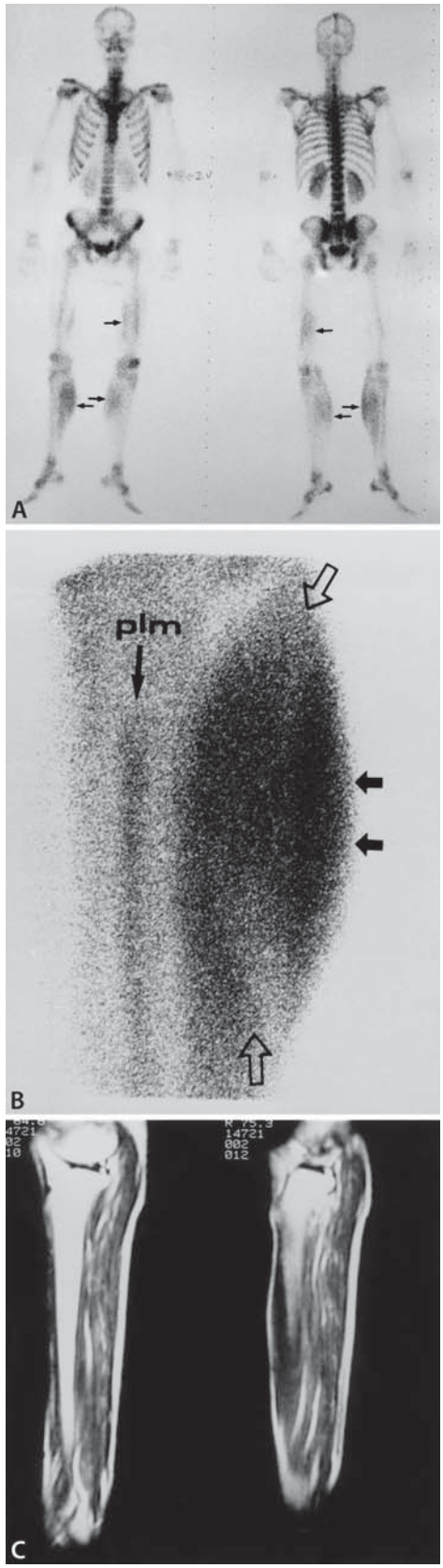

12.8.3 Musculotendinous Unit Strain or Injuries

The musculotendinous unit is the portion of a muscle attached to a tendon, tendinous insertion, or enthesis, and strain is defined as a stretching or tearing of the musculotendinous unit (Baker 1984). According to the nature and extent of damage a strain can be graded as first, second, or third degree. The first grade indicates minimal stretching of the musculotendinous unit without permanent injury, the second grade partial tearing, and the third grade complete disruption of a portion of the unit. Among a number of musculotendinous injuries, rotator cuff syndrome, strain of the biceps muscle or triceps muscle, tennis elbow, De Quervain's tenosynovitis, and strain of the quadriceps femoris muscle and the gastrocnemius-soleus muscle are well known.

Soft-tissue radiography may be used to diagnose injuries in the musculotendinous unit. However, diagnostic yields are generally low and information is not specific except for calcification. Contrast arthrography can accurately delineate musculotendinous injuries and tendon rupture, especially in the shoulder, whose anatomy is complex. MRI, a noninvasive modality, is extremely useful for the investigation of soft-tissue anatomy and pathology (McNamara and Greco 1996) and sonography is increasingly used for the same purpose. ^{99m}Tc MDP bone scanning is another noninvasive method. It can sensitively detect injured muscle and tendon. Unless injuries are negligible, pinhole magnification can nearly always show increased uptake of various degrees, identifying the specific muscle or muscle group damaged (Fig. 12.47).

Fig. 12.46A–C Rhabdomyolysis in the lower extremities. **A** Anterior and posterior whole-body bone scans in a 34-year-old bed-ridden man with cervical fracture and quadriplegia show diffuse tracer uptake in the muscles in the thighs and lower legs (*arrows*). **B** Lateral pinhole scintigraph of the right lower leg distinctly visualizes and distinguishes the medial (*between open arrows*) and lateral head of the gastrocnemius muscle (*solid arrows*) and peroneus longus muscle (*plm*). **C** T2-weighted sagittal MRI shows longitudinal striations of high signal intensity, denoting muscular edema. Note that the muscles are diffusely wasted and thin

12.8.4 Distal Femoral Cortical Irregularity

Distal femoral cortical irregularity, also known as cortical or periosteal desmoid, is characterized by concave, convex, or divergent irregularity of the cortex in the popliteal surface of the distal femur and the epicondyle. One of the first descriptions is due to Kimmelstiel and Rapp (1951). Typical sites of involvement are the attachment of the gastrocnemius muscle head, mostly the medial one (Suh et al. 1996) or adductor magnus muscle. It is not a neoplasm but a traumatic lesion of the musculotendinous unit (Resnick and Greenway 1982), and is considered by some investigators as a variation of ossifying periostitis (Mirra 1989). Pathologically, the condition is characterized by fibrin with mineralization, suggesting a reparative process. In one recent series, the average age of the patients was 34 years, ranging from 4 to 64 years (Suh et al. 1996). The lesions may cause pain in occasional cases.

Radiography shows cortical irregularity that is usually subtle and unimpressive (Fig. 12.48A). However, MRI can clearly show convex or concave aberration or the combination of both. To be exact, MRI of the concave type reveals a well-defined area of low signal intensity on T1-weighted images, which becomes enhanced with administration of gadolinium DTPA (Fig. 12.49A, B). We have performed pinhole bone scans in three patients with this condition: one patient showed ill-defined patchy uptake in the popliteal surface of the distal femur (Fig. 12.48B), and two patients showed well-defined roundish uptake (Fig. 12.49).

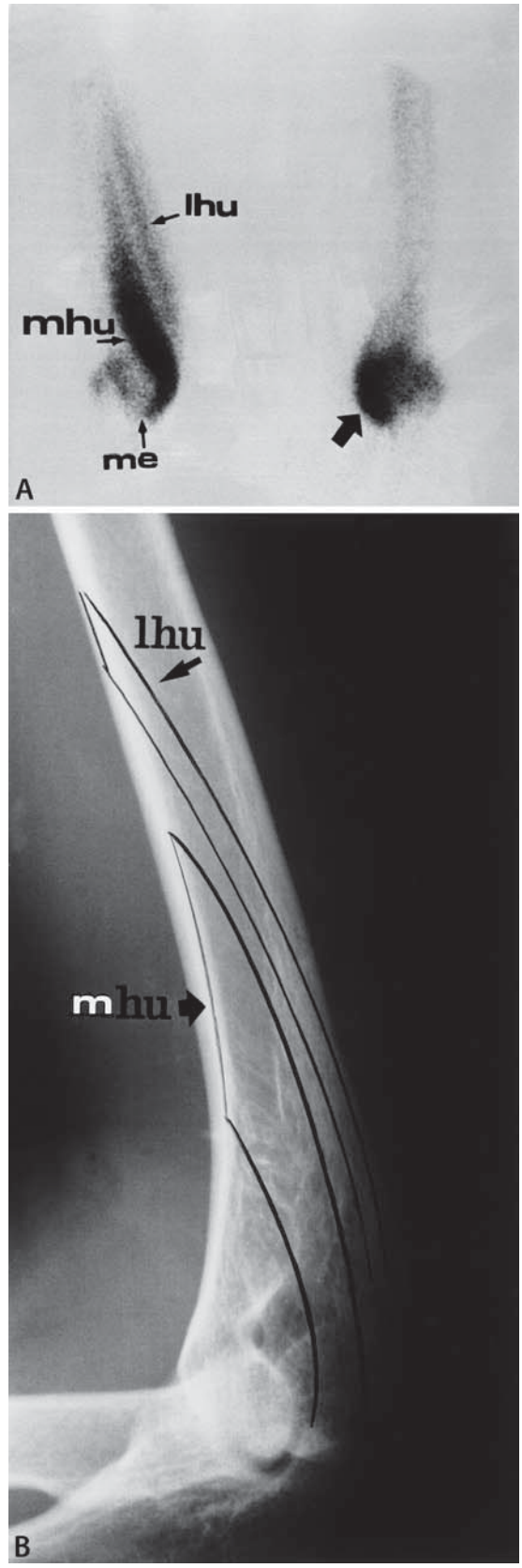

Fig. 12.47A, B Musculotendinous strain. **A** Oblique planar scans of both upper arms in a 26-year-old man who used dumb-bells show peculiar bundle-like tracer uptake in the musculotendinous units of the left upper arm muscles. The medial head unit (*mhu*) and lateral head unit (*lhu*) of the triceps are clearly delineate (*me* medial epicondyle of the humerus where the triceps muscles insert). There is an intense tracer uptake in the right medial epicondyle (*thick arrow*) representing epicondylitis (reverse tennis elbow). **B** Lateral radiograph of the distal humerus showing musculotendinous units of the medial head (*mhu*) and lateral head (*lhu*) of the triceps muscles

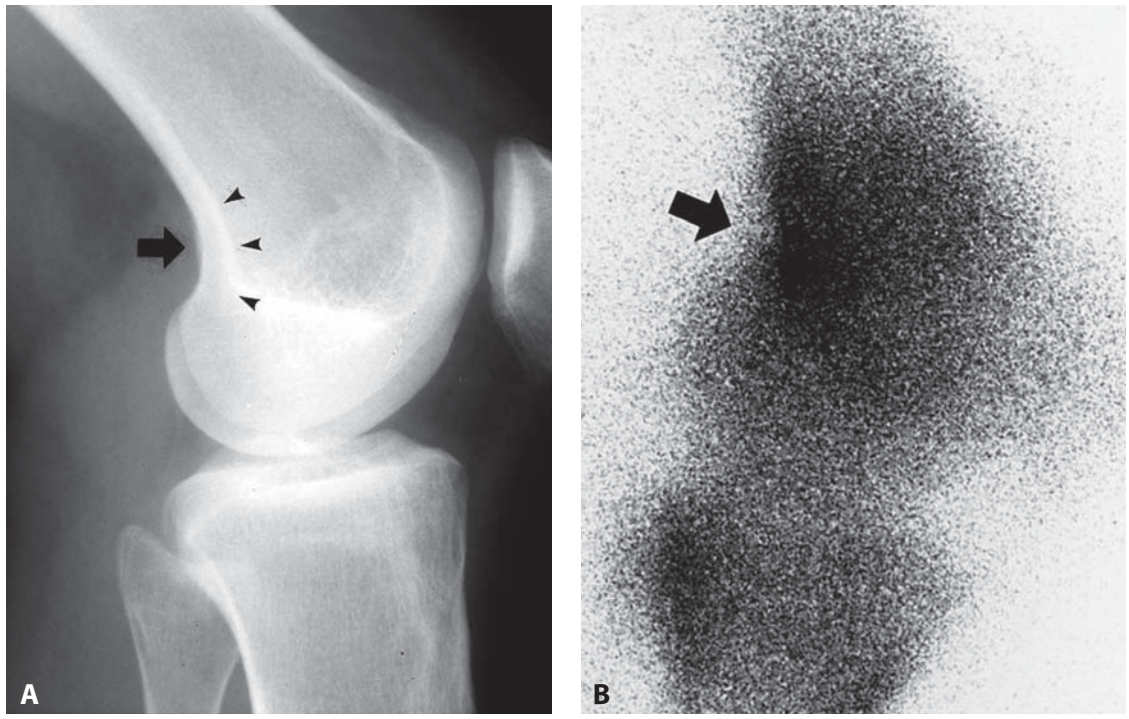

Fig. 12.48A, B Distal femoral cortical desmoid. **A** Lateral radiograph of the left distal femur in a 31-year-old woman with focal pain shows concave cortical irregularity in the posterior aspect of the distal femur (*arrow* and *arrowheads*). **B** Lateral pinhole scintigraph reveals an ill-defined area of intense tracer uptake surrounded by a less intense zone denoting main and reactive lesions, respectively (*arrow*)

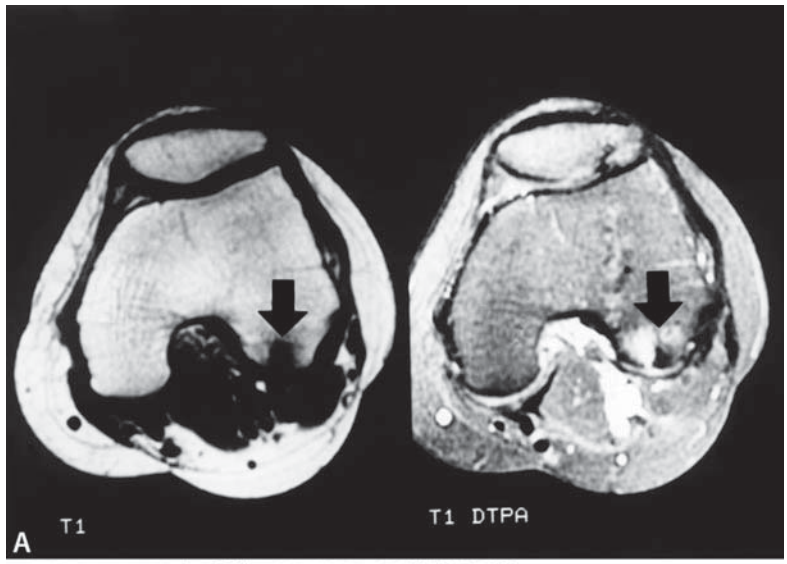

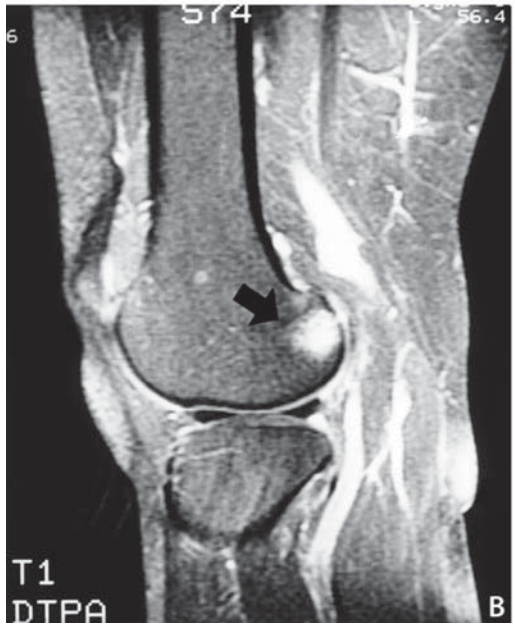

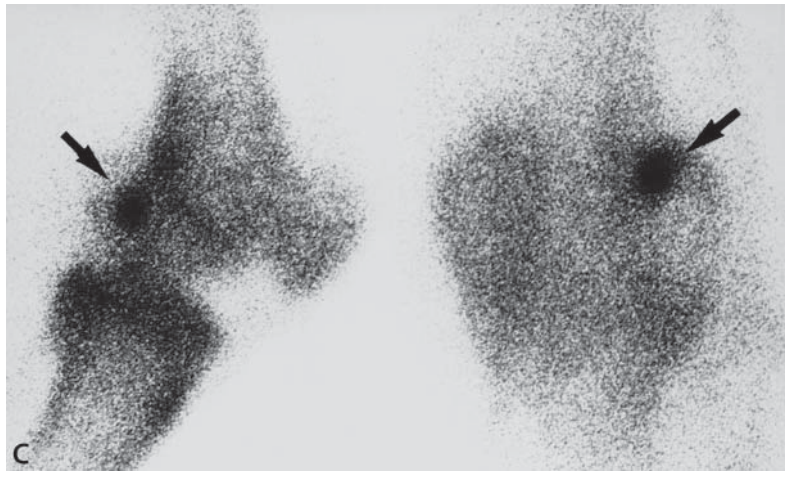

Fig. 12.49A–C Cortical desmoid in the lateral femoral condyle. **A** Transaxial T1-weighted MRI of the left femoral condyle in a 54-year-old woman with regional pain shows a small roundish area of low signal intensity in the posterior aspect of the lateral femoral condyle (*left, arrow*). The lesion is enhanced after gadolinium infusion (*right, arrow*). **B** Sagittal T1-weighted MRI shows a sharply defined small, roundish lesion with enhancement (*arrow*). **C** Lateral (*left*) and anterior (*right*) pinhole scans show a characteristic small, roundish hot area in the upper posterior aspect of the lateral femoral condyle (*arrow*). Note that the lesion in this particular case is not in the medial femoral condyle, but in the lateral condyle

References

Armbrustmacher VW (1988) Skeletal muscle. In: Rubin E, Farber JL (eds) Pathology. Lippincott, Philadelphia, pp 1394–1415

Baker BE (1984) Current concepts in the diagnosis and treatment of musculotendinous injuries. Med Sci Sports Exerc 16:323–327

Bluestone R (1988) Symptoms and signs of articular disease. In: Resnick D, Niwayama G (eds) Diagnosis of bone and joint disorders, 2nd edn. Saunders, Philadelphia, pp 822–843

Cooper RR, Misol S (1970) Tendon and ligament insertion. A light and electron microscopic study. J Bone Joint Surg Am 52:1–20

Friedenstein AJ (1973) Determined and inducible osteogenic precursor cells. In: Sognaes R, Vaughan J (eds) Hard tissue growth, repair and remineralization. Ciba Foundation Symposium II, New York. Elsevier, Amsterdam, pp 169–181

Gabow PA, Kaehny WD, Kelleher SP (1982) The spectrum of rhabdomyolysis. Medicine 61:141–152

Giacomello A, Sorgi ML, Zappini A (1981) Pseudopodagra in Behçet's syndrome. Arthritis Rheum 24:750

Haseman MK, Kriss JP (1985) Selective, symmetric, skeletal muscle uptake of Tc-99m pyrophosphate in rhabdomyolysis. Clin Nucl Med 10:180–183

Kim SH, Chung SK, Bahk YW, et al (1999) Whole-body and pinhole bone scintigraphic manifestations of Reiter's syndrome: distribution patterns and early and characteristic signs. Eur J Nucl Med 26:163–170

Kimmelstiel P, Rapp I (1951) Cortical defect due to periosteal desmoids. Bull Hosp Joint Dis 12:286–297

Koffler A, Fiedler RM, Massry SG (1976) Acute renal failure due to nontraumatic rhabdomyolysis. Ann Intern Med 85:23–28

LaCava G (1959) Enthesitis – traumatic disease of insertions. JAMA 169:254–255

Lamminen A (1996) Rhabdomyolysis. In: Fleckenstein JL, Crues JV III, Reimers CD (eds) Muscle imaging in health and disease. Springer, Berlin Heidelberg New York, pp 343–348

Matin P, Lang G, Carretta R, Simon G (1983) Scintigraphic evaluation of muscle damage following extreme exercise: concise communication. J Nucl Med 24:308–311

McNamara MT, Greco A (1996) Miscellaneous muscle lesions. In: Fleckenstein JL, Crues JV III, Reimers CD (eds) Muscle imaging in health and disease. Springer, Berlin Heidelberg New York, pp 325–449

Miller LF, O'Neill CJ (1949) Myositis ossificans in paraplegics. J Bone Joint Surg Am 31:283–294

Mirra JM (1989) Parosteal tumors. In: Mirra J (ed) Bone tumors. Lea and Febiger, Philadelphia, pp 1605–1610

Patel R, Mishkin FS (1986) Technetium-99m pyrophosphate imaging in acute renal failure associated with nontraumatic rhabdomyolysis. AJR Am J Roentgenol 147:815–817

Resnick D, Greenway G (1982) Distal femoral cortical defects, irregularities, and excavations. Radiology 143:345–354

Sewell JR, Black CN, Chapman AH, et al (1980) Quantitative scintigraphy in diagnosis and management of plantar fasciitis. J Nucl Med 21:633–636

Silberstein EB, Bove KE (1979) Visualization of alcohol-induced rhabdomyolysis: a correlative radiotracer, histochemical, and electron microscopic study. J Nucl Med 20:127–129

Soule AB Jr (1945) Neurogenic ossifying fibromyopathies. A preliminary report. J Neurosurg 2:485–497

Strand V, Talal N (1980) Advances in the diagnosis and concept of Sjögren's syndrome (autoimmune exocrinopathy). Bull Rheum Dis 30:1046–1052

Suh JS, Cho JH, Shin KH, et al (1996) MR appearance of distal femoral cortical irregularity (cortical desmoid). J Comput Assist Tomogr 20:328–332

Suzuki Y, Hisada K, Takeda M (1974) Demonstration of myositis ossificans by ^{99m}Tc pyrophosphate bone scanning. Radiology 111:663–664

Valk P (1984) Muscle localization of Tc-99m MDP after exertion. Clin Nucl Med 9:493–494

Yurdakul S, Yazici H, Tuzun Y, et al (1983) The arthritis in Behçet's disease: a prospective study. Ann Rheum Dis 42:505–515

13 Osteochondroses and Related Diseases

Contrary to the initial unitary concept of primary avascular osteonecrosis, the osteochondroses are now recognized as a group of heterogeneous pathological conditions. In fact, this disease group embraces the conditions variously characterized by primary avascular osteonecrosis as in Legg-Calvé-Perthes disease, by the absence of osteonecrosis as in Scheuermann's disease, and by the osteonecrosis due to fractures as in Kienböck's disease. It is of interest that the actual existence of Sever's disease, or calcaneal apophysis, was once challenged and even denied by many authors, but it has become an established entity (Madden and Mellion 1996; Volpon and de Calvalho 2002). The clinical features are local pain and tenderness with athletic activity and habitual exposure to or frequent history of trauma. Most osteochondroses affect actively growing bones predominantly in boys in the first and second decades of life, but Friedrich's disease and Freiberg's disease more commonly occur in young adult women.

Radiographic manifestations include bony fissuring, fragmentation, rarefaction, condensation, collapse and flattening, and irregularity of bone contour and osteochondral junction. With recovery, affected bone(s) may resume a normal texture, shape, and contour, although bony deformity or secondary degenerative osteoarthritis is not uncommon. Basically, radiographic changes are similar to those of the diseases characterized by avascular necrosis as in Legg-Calvé-Perthes disease and by microfractures as in Freiberg's disease.

Importantly, however, scintigraphic features differ according to the underlying pathology. Thus, on the one hand ischemic bone is represented by photopenia, and on the other microfractures and infraction are indicated by intense tracer uptake. Pinhole scintigraphy provides useful anatomical information on the contour, shape, and texture of the osteochondral zone and the adjacent bones, often leading to a specific diagnosis.

13.1 Legg-Calvé-Perthes Disease (Capital Femoral Epiphysis)

This is the most common osteochondrosis, affecting predominantly boys with a peak age of incidence from 6 to 10 years. The involvement is for the most part unilateral, with a bilateral incidence of about 10%. The presenting clinical symptoms are limp, limited joint motion, and pain. The etiology is not established, but traumatic insult to the vulnerable retinacular arteries, which mainly nourish the femoral head during the active growth stage, seems plausible. The vascular injury with subsequent ischemia may restrict the blood supply with resultant avascular bone necrosis. Characteristically, the articular cartilage is preserved or hypertrophied to compensate for the collapsing epiphysis.

Early radiographic changes include distension of the joint capsule and a small ossification center or epiphysis with slightly increased bone density. The decrease in size is often extremely subtle so that it can easily be overlooked at first and retrospectively realized only after scintigraphic diagnosis (Fig. 13.1). A diminutive ossification center is considered to be related to

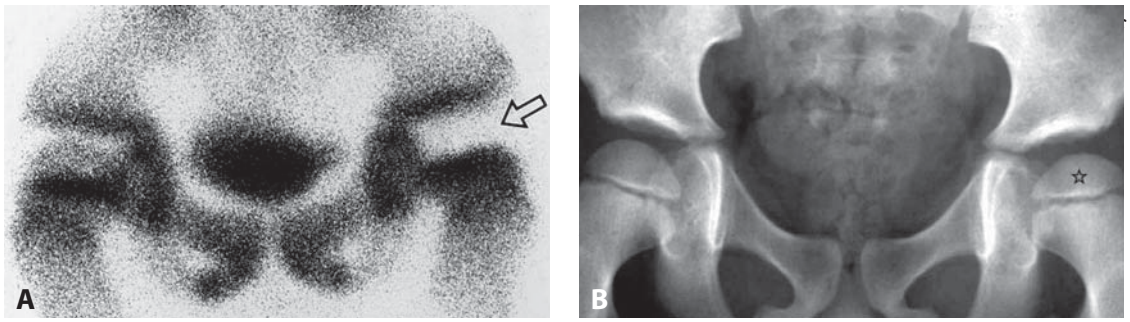

Fig. 13.1A, B High sensitivity of bone scintigraphy in the diagnosis of early Legg-Calvé-Perthes disease. **A** Anterior pinhole scintigraph of the pelvis in a 5-year-old boy with left hip pain shows obvious photopenia in the left femoral head (*open arrow*). **B** Anteroposterior radiograph of the pelvis reveals a barely discernible decrease in epiphyseal size (*star*)

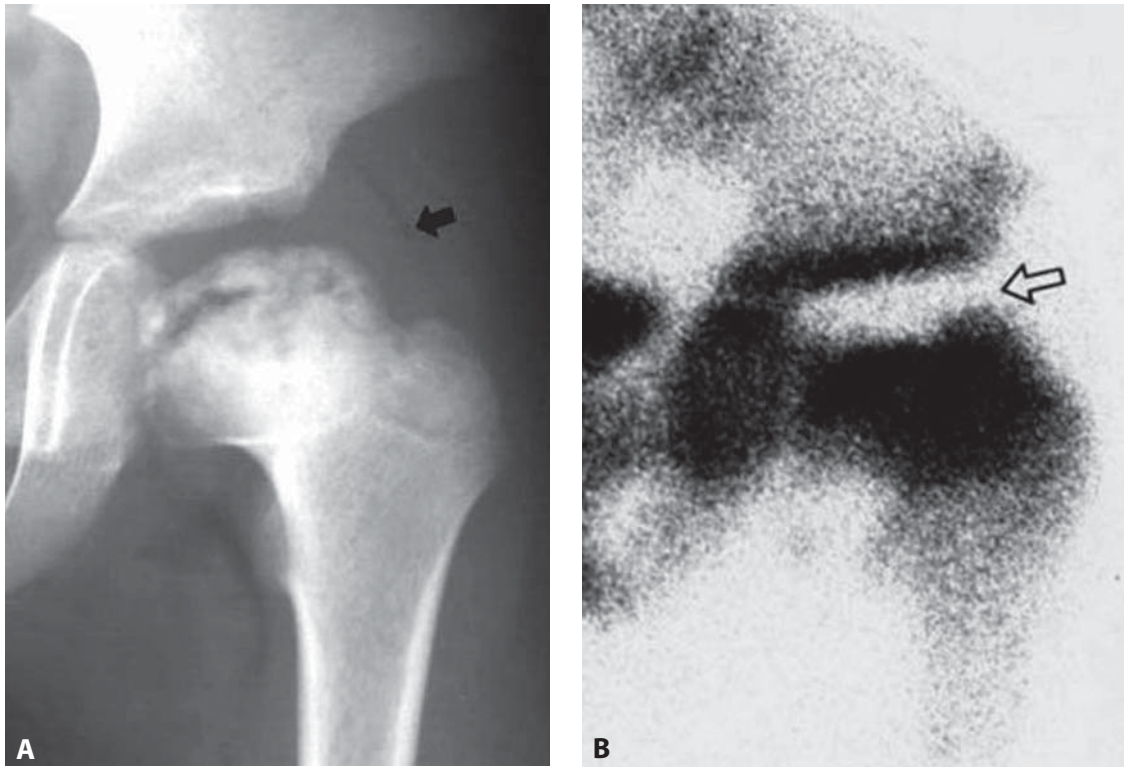

Fig. 13.2A, B Flattening, fragmentation, and condensation in advanced Legg-Calvé-Perthes disease. **A** Anteroposterior radiograph of the left hip in an 8-year-old boy with advanced bone change shows flattening of the epiphysis with irregular fragmentation as well as sclerosis (*arrow*). Note widening of the joint space. **B** Anterior pinhole scintigraph reveals photon defect (*open arrow*) with intense tracer uptake in broadened femoral neck where active sclerosis is in progress

retarded bone growth rather than compression. With progression of the disease, fissuring, fragmentation, fracture, flattening, and condensation follow (Fig. 13.2A). The joint is wi-

Bone scintigraphy is useful for both the initial diagnosis and follow-up of the clinical course (Fisher et al. 1980). Legg-Calvé-Perthes disease has traditionally been quoted as the best model

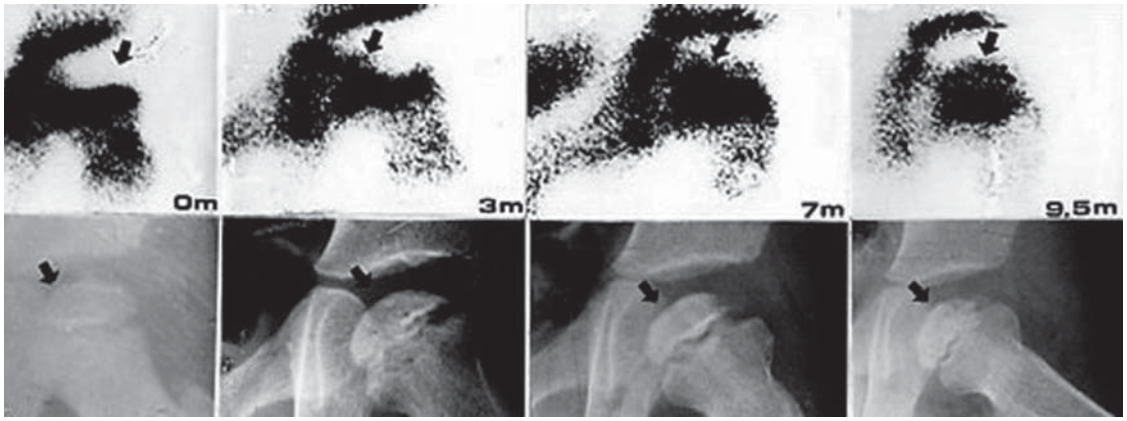

Fig. 13.3 Serial semiquantitative assessment of revascularization during the healing phase of Legg-Calvé-Perthes disease. *Top row* Serial pinhole scintigraphs of the left hip shows initial total photon defect followed by gradual restoration with revascularization that starts from the medial column. *Bottom row* Equivalent serial radiographs reveal initial decrease in epiphyseal height gradually followed by restoration

to illustrate the diagnostic benefit of pinhole scintigraphy (Danigelis 1976). Indeed, pinhole scintigraphy can detect photopenia in the earliest stage of disease. Thus, an obvious photon defect may be seen while radiographic change is absent or dubious (Fig. 13.1). As widely practiced, pinhole scanning is useful for a serial semiquantitative assessment of revascularization during the healing phase (Fig. 13.3). Early repair is denoted by the characteristic uptake in the lateral margin of the capital femoral epiphysis, the "spur" sign (Conway 1993) (Fig. 13.4). The broadening and shortening of the femoral neck are important sequelae. These sequelar changes and collapsed ossification center accumulate tracer intensely to form a block with a preserved cartilaginous space above (Fig. 13.2B).

13.2 Friedrich's Disease (Medial Clavicular End)

This disease is considered to be rare. It mostly affects adult women, and less commonly men. The presenting symptoms are local swelling and tenderness. Involvement is typically unilateral. Etiology is not established, but physical stress with changed clavicular motion and resultant microfractures and ischemic necrosis seems a plausible explanation (Jurik et al. 1985). According to these authors, Friedrich's disease is related to condensing osteitis of the clavicle. However, the latter condition lacks aseptic necrosis, and instead is associated with an increased number and thickness of trabeculae (Brower et al. 1974) (Fig. 13.5). Pinhole scintigraphic study of a case of Friedrich's disease by us showed findings that were consistent with ischemic osteonecrosis. As indicated in the original description, the pathogenesis of Friedrich's disease appears similar to that of Legg-Calvé-Perthes disease in so far as the scintigraphic changes are concerned (Fig. 13.1A).

Radiographically, this disease reveals an irregular radiolucent defect in the medial clavicular end with apparent widening of the adjacent sternoclavicular joint. The lateral margin of the defect is scalloped with sclerosis (Fig. 13.5A). The growth of the affected clavicular end is impeded with resultant local undergrowth.

Pinhole scan findings are similar to those of radiography, and include an irregular photon defect in the hypoplastic clavicular end that is bordered laterally by the "hot" scalloped margin (Fig. 13.5B). The basic scintigraphic pattern has strong resemblance to that of Legg-

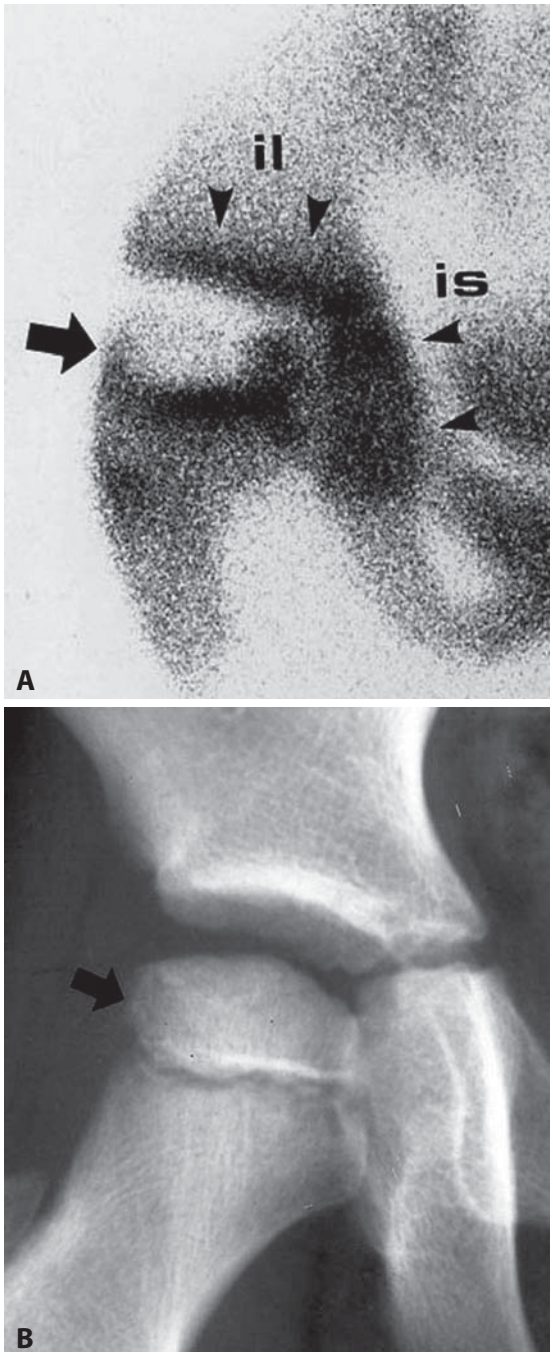

Fig. 13.4A, B The "spur" sign of early healing. **A** Anterior pinhole scintigraph of the right hip in a 7-year-old boy shows characteristic tracer uptake in the lateral margin of the capital femoral epiphysis (*arrow*) (*il* ilium, *is* ischium; synchondrosis in between). **B** Anteroposterior radiograph reveals the fullness of the lateral portion of the epiphysis denoting early recovery (*arrow*). Note broadening and shortening of the femoral neck

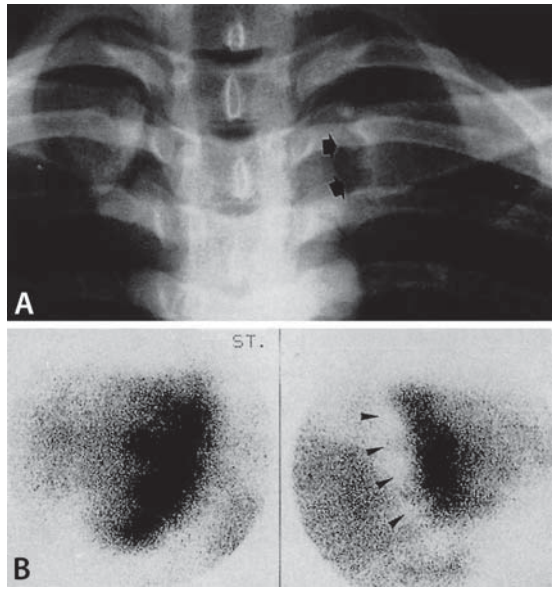

Fig. 13.5A, B Friedrich's disease. **A** Anteroposterior radiograph of the left clavicle in a 19-year-old man with local pain, tenderness, and bulging reveals scalloped bony defect with sclerotic margin in the medial clavicular end (*arrows*). **B** Anterior pinhole scintigraph shows scalloped photon defect involving the medial end of the left clavicle (*arrowheads*)

Calvé-Perthes disease. As described in Chapter 7, pinhole scintigraphy appears to be a valuable adjunct in the differential diagnosis between this condition and condensing osteitis of the clavicle, a similar but completely different entity (Fig. 7.8).

13.3 Freiberg's Infraction (Metatarsal Head)

This condition belongs to the osteochondrosis group. It mainly affects girls during adolescence. Trauma has been considered to be causative. Local pain, tenderness, limitation of motion, and soft-tissue swelling are presenting symptoms. The second metatarsal head is most typically involved with occasional involvement of the third and fourth metatarsal heads. Pathological features include early trabecular necrosis followed by comminution and micro-

fractures of subchondral bones resulting in subarticular bone collapse and the depression and flaring of the articular surface.

Radiographic features include irregular collapse, condensation, and dwarfing of the metatarsal head (Fig. 13.6A). The adjacent joint may be widened with periarticular osteophytosis. Pinhole scintigraphically, Freiberg's infraction demonstrates prominent tracer uptake denoting microfractures involved in active repair. This finding contrasts with photopenic osteonecrosis observed in Legg-Calvé-Perthes disease and Friedrich's disease. The tracer uptake is localized to the metatarsal head and obliterates the adjacent metatarsophalangeal joint (Fig. 13.6B). All or most of the tarsometatarsal, metatarsophalangeal, and interphalangeal joints of the diseased foot reveal increased tracer uptake, presumably due to disuse.

Theoretically, it is anticipated that Köhler's disease of the tarsal navicular bone and Kienböck's disease of the carpal lunate bone may also accumulate tracer intensely, since both diseases are commonly related to traumatic etiologies and resultant fracture and osteonecrosis.

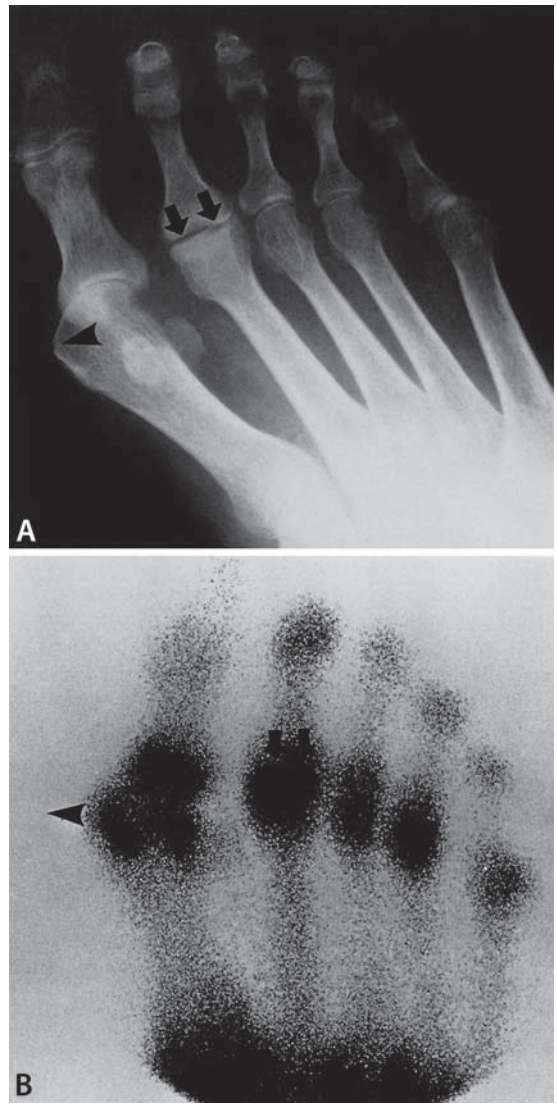

Fig. 13.6A, B Freiberg's infraction of the second metatarsal head. **A** Dorsoplantar radiograph of the right forefoot in a 24-year-old woman delineates irregular flattening and widening with eburnation of the second metatarsal head (*arrows*). Note the hallux valgus deformity (*arrowhead*). **B** Dorsal pinhole scintigraph reveals very intense tracer uptake in the second metatarsal head that is flattened and widened (*arrows*). Intense tracer uptake can be seen also in the deformed great toe (*arrowhead*)

13.4 Osteonecrosis of the First Metatarsal Sesamoid

The first metatarsal sesamoid can be the seat of osteochondrosis or sesamoiditis. Renander first described this condition in 1924 (Renander 1924). His two cases involved the medial sesamoid of the first metatarsal. Clinically, the lesion is painful and often disabling. It may be related to trauma or sports injury or may be idiopathic (Ogata et al. 1986). Microscopic findings are osteonecrosis and proliferative granulation tissue, which are similar to those seen in idiopathic osteonecrosis of the femoral head. When complicated with fracture inflammation may become accentuated.

Radiographic findings include fuzzy bone contour, fragmentation, and condensation (Fig. 13.7A). Pinhole scintigraphy shows round tracer uptake that is confined to the diseased sesamoid bone. Reactive uptake may be seen in the neighboring lateral sesamoid that is not directly affected (Fig. 13.7B).

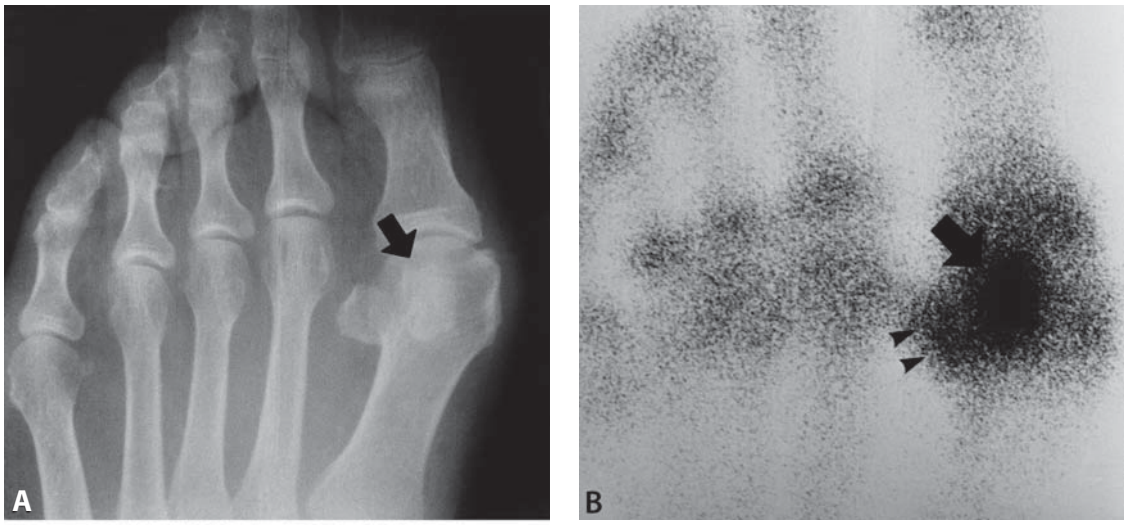

Fig. 13.7A, B Osteonecrosis of the first medial metatarsal sesamoid. **A** Dorsoplantar radiograph of the left forefoot in a 48-year-old woman with local tenderness and pain showing blurring and sclerosis of the first medial metatarsal sesamoid (*arrow*) and hallux valgus. **B** Dorsal pinhole scintigraph showing intense tracer accumulation in the affected sesamoid (*arrow*). Note sympathetic tracer uptake in the lateral sesamoid (*arrowheads*)

13.5 Scheuermann's Disease (Vertebral Secondary Ossification Center)

Scheuermann's disease (juvenile idiopathic kyphosis) is characterized by nonflexible dorsolumbar kyphosis due to the weakening of secondary ring ossification centers through which intravertebral dislocation of denatured intervertebral disks occur. This is not a rare condition with the reported prevalence ranging from 0.4% to 8% of the general population (Ali et al. 1999). Lesions are usually multiple, and cause undulant endplate defects, occasional anterior disk prolapse, and limbus vertebra. The middle and lower thoracic spine is most commonly affected. Histology reveals abnormal vertebral and growth plate cartilage with defective ossification (Ippolito and Ponseti 1981), and weakened cartilages predispose to disk dislocation during periods of excessive physical activity. Osteonecrosis is absent; hence this is not an osteochondrosis in the true sense as originally stated by Scheuermann.

Radiographic features include irregular undulation of the endplates with radiolucent defects surrounded by sclerotic rim, disk space narrowing, and anterior wedging (Fig. 13.8A). Infraction or limbus vertebra is another important feature. Lesions are typically multiple.

Pinhole scintigraphy reveals tracer uptake to be increased in the affected vertebral endplates with typical anterior wedging and scalloping (Fig. 13.8B). Interestingly, the tracer uptake in the endplates affected with this disease appears increased compared to that of normal endplates, the tracer uptake of which is reduced due to decelerated or ceased growth of the adolescent spine. Phenomenally, the increased tracer uptake in Scheuermann's disease might be accounted for by pathologically enhanced bone metabolism in congenitally fragile vertebral endplates, in which the biosynthesis of collagen and ground substance is disturbed (Aufdermauer and Spycher 1986).

13.6 Sever's Disease (Calcaneal Apophysis)

The existence of Sever's disease, or calcaneal apophysitis, as a clinical entity was once ques-

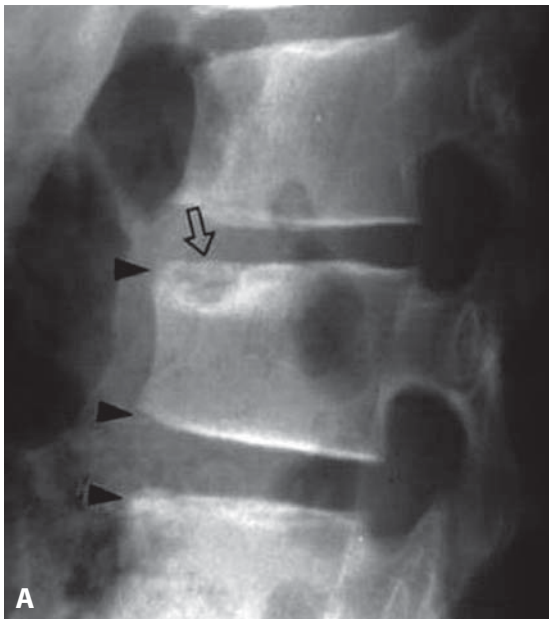

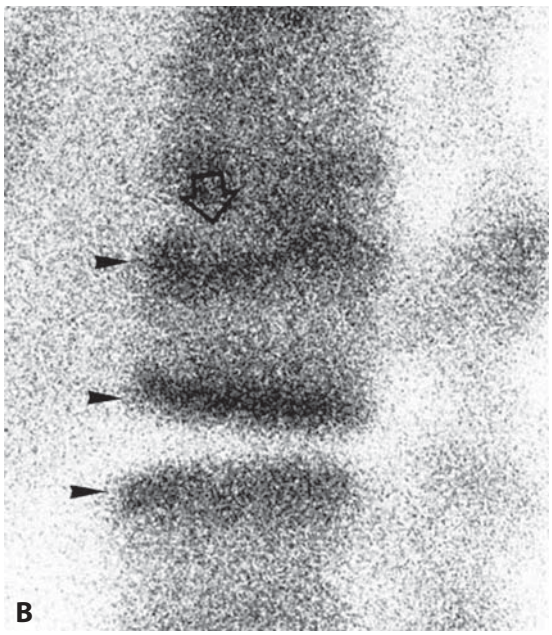

Fig. 13.8A, B Scheuermann's disease. **A** Lateral radiograph of the lumbar spine in a 14-year-old girl with back pain shows a notched bone defect with sclerosis in the anterior aspect of the L3 upper endplate with narrowing of the suprajacent intervertebral disk space (*open arrow*) and minimal sclerosis in the L2 and L4 upper endplates. Note anterior wedging of L3 due to disturbed growth and endplate sclerosis in L3 and L4 (*arrowheads*). **B** Lateral pinhole scintigraph shows anterior wedging with a shallow photon defect of Schmorl's node involving L2 (*open arrow*). The affected endplate reveals diffuse increased tracer uptake (*top arrowhead*). The other weakened and stressed endplates also intensely accumulate tracer (*middle and bottom arrowheads*)

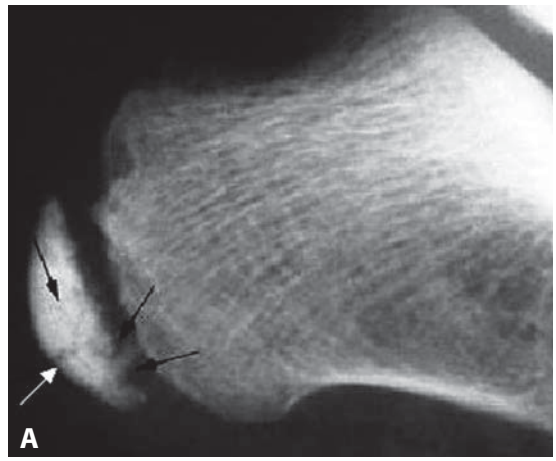

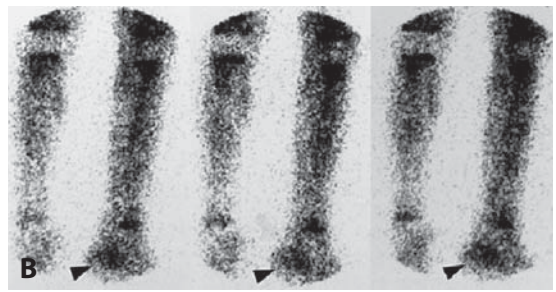

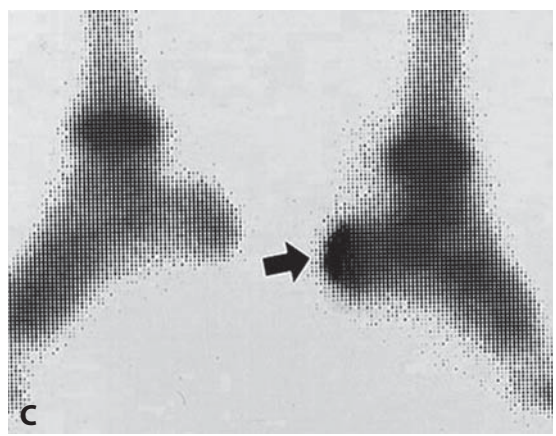

Fig. 13.9A–C Fine fissures within condensed apophysis and nuclear angiography in Sever's disease. **A** Lateral radiograph of painful left calcaneus in a 14-year-old boy shows fine fissures and marginal fragmentations in condensed apophysis (*arrows*). **B** Nuclear arteriogram reveals increased blood flow and pool in the retrocalcaneal surface (*arrowheads*). **C** Equilibrium bone scan demonstrates increased uptake in the apophysis (*arrow*)

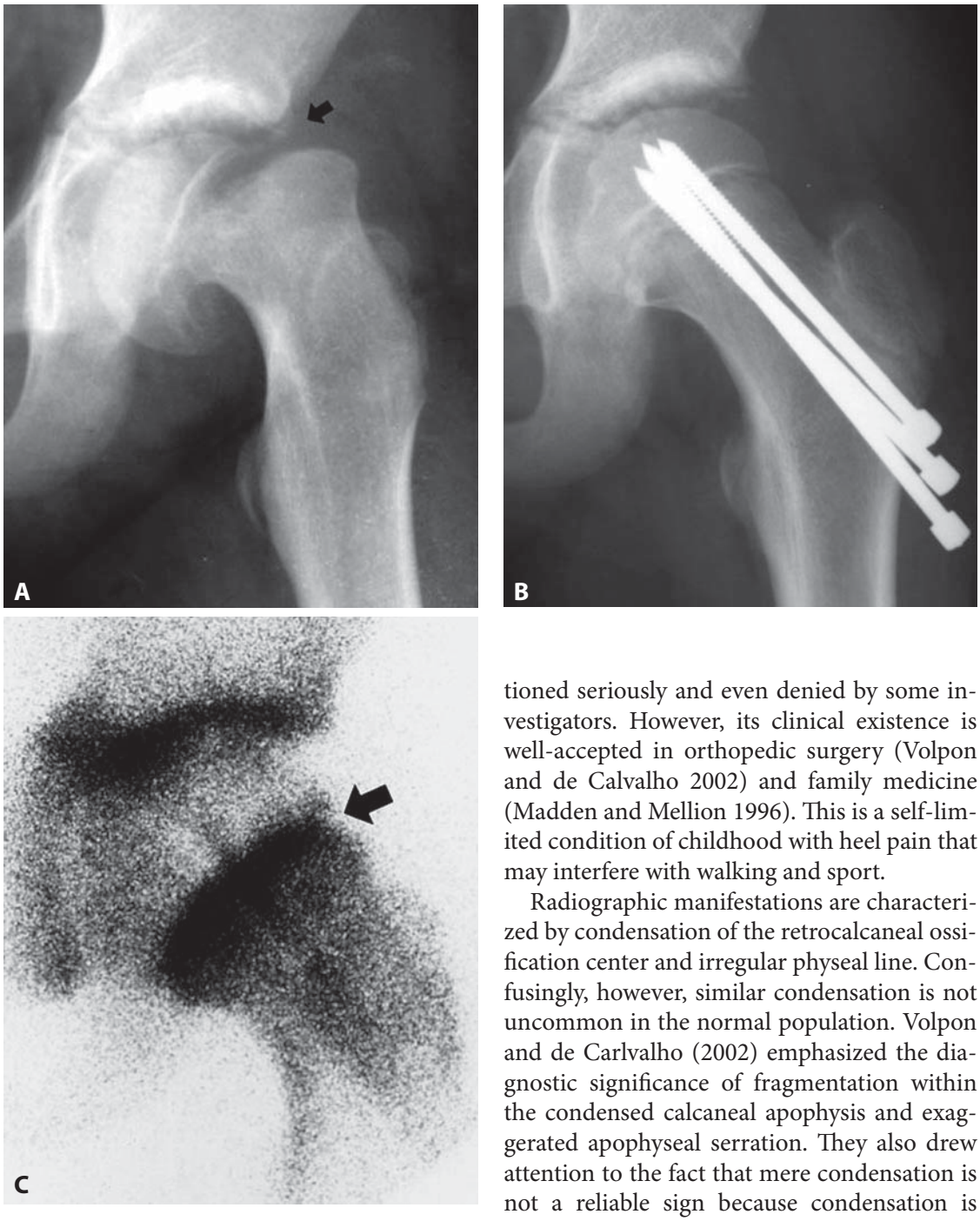

Fig. 13.10A–C Craniolateral slippage of the proximal femoral metaphysis. **A** Anteroposterior radiograph of the left hip in a 14-year-old boy with slipped femoral epiphysis shows typical craniolateral metaphyseal displacement (*arrow*). **B** Post-reduction radiograph reveals metaphyseal position satisfactorily restored with fixation nails. **C** Anterior postoperative pinhole scintigraph reveals restored slippage with intense physeal uptake denoting injury (*arrow*)

tioned seriously and even denied by some investigators. However, its clinical existence is well-accepted in orthopedic surgery (Volpon and de Calvalho 2002) and family medicine (Madden and Mellion 1996). This is a self-limited condition of childhood with heel pain that may interfere with walking and sport.

Radiographic manifestations are characterized by condensation of the retrocalcaneal ossification center and irregular physeal line. Confusingly, however, similar condensation is not uncommon in the normal population. Volpon and de Carlvalho (2002) emphasized the diagnostic significance of fragmentation within the condensed calcaneal apophysis and exaggerated apophyseal serration. They also drew attention to the fact that mere condensation is not a reliable sign because condensation is more prominent in normal individuals than in those with the disease. In one patient, we have seen fine fissures within the condensed apophysis with marginal fragmentation and irregular physeal line (Fig. 13.9A). Madden and Mellion (1996) stressed that a positive squeeze test and tight heel cord (attachment of tendo-Achilli) are more reliable than radiography.

Scintigraphy demonstrates intense tracer accumulation in the condensed calcaneal apophysis (Fig. 13.9B). Nuclear angiography performed in one of our patients with a painful sclerosed calcaneus showed increased blood flow and blood pool (Fig. 13.9C). Obviously, our experience is limited; nevertheless it is tempting to speculate that at least a fraction of patients with Sever's disease with a radiographically dense and scintigraphically "hot" calcaneus with pain may have increased vascularity with altered bone metabolism.

13.7 Slipped Capital Femoral Epiphysis

This condition involves the medial and posterior slippage of the capital femoral epiphysis along the physeal line. A slipped capital femoral epiphysis has been associated with a high incidence of genetic markers. In one study (Mullaji et al. 1993) the HLA-B27 antigen was positive in 20% of patients with this disorder. This is a disease of childhood and adolescence, with the peak in the early second decade. Involvement is unilateral in the great majority and bilateral in about 20%. Trauma, growth spurt, obesity, and excessive physical activity are suggested as contributing factors. Histologically, the main changes are observed in the hypertrophied chondrocytic zone of the growing physeal plate.

Radiographic diagnosis is obvious when slippage is more than moderate in grade (Fig. 13.10A). However, in milder cases the interpretation is not always easy, requiring multiple projections including the frog-leg view. The most characteristic sign is the craniolateral displacement of the proximal femoral metaphysis or the medioposterior dislocation of the capital femoral epiphysis. The displacement remains incompletely corrected after surgery in rare instances (Fig. 13.11A). Other radiographic signs include osteoporosis with a widened physeal line and an irregular metaphyseal margin. Im-

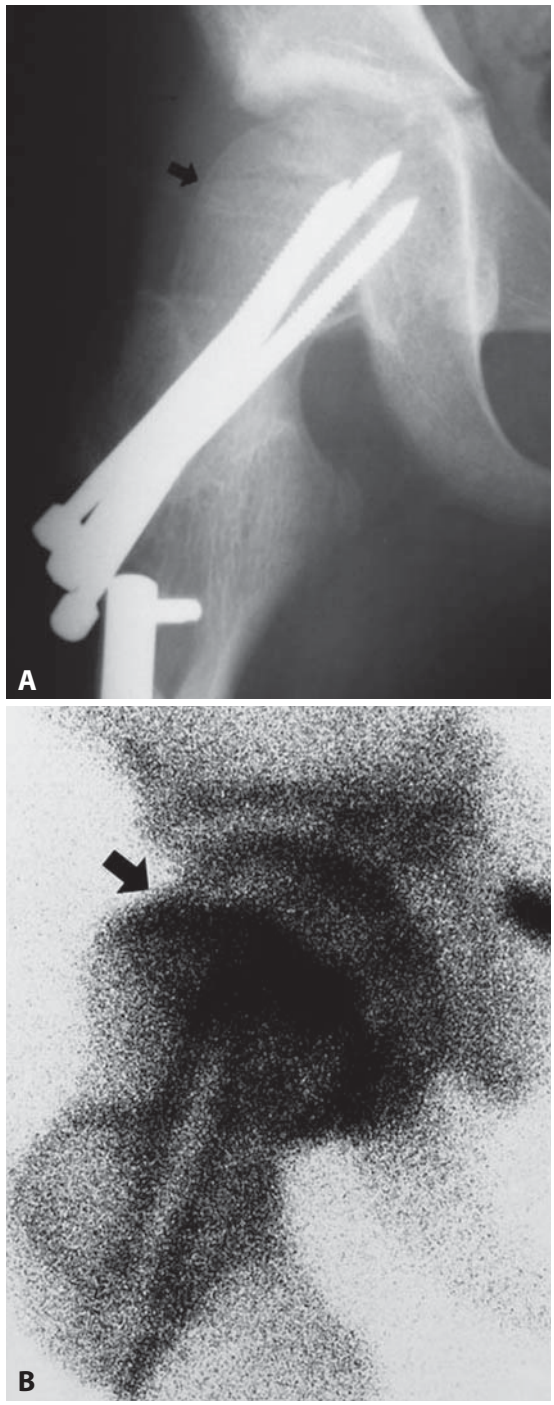

Fig. 13.11A, B Incomplete correction with mild residual protrusion. **A** Postoperative anteroposterior radiograph of the right hip in a 16-year-old boy with slipped femoral epiphysis treated with Knowle's pins shows restoration with minimal protrusion deformity (*arrow*). **B** Anterior pinhole scintigraph reveals mild protrusion with intense physeal tracer uptake without evidence of vascular compromise (*arrow*). Note well positioned nails with tracer uptake in creeping new bone formation

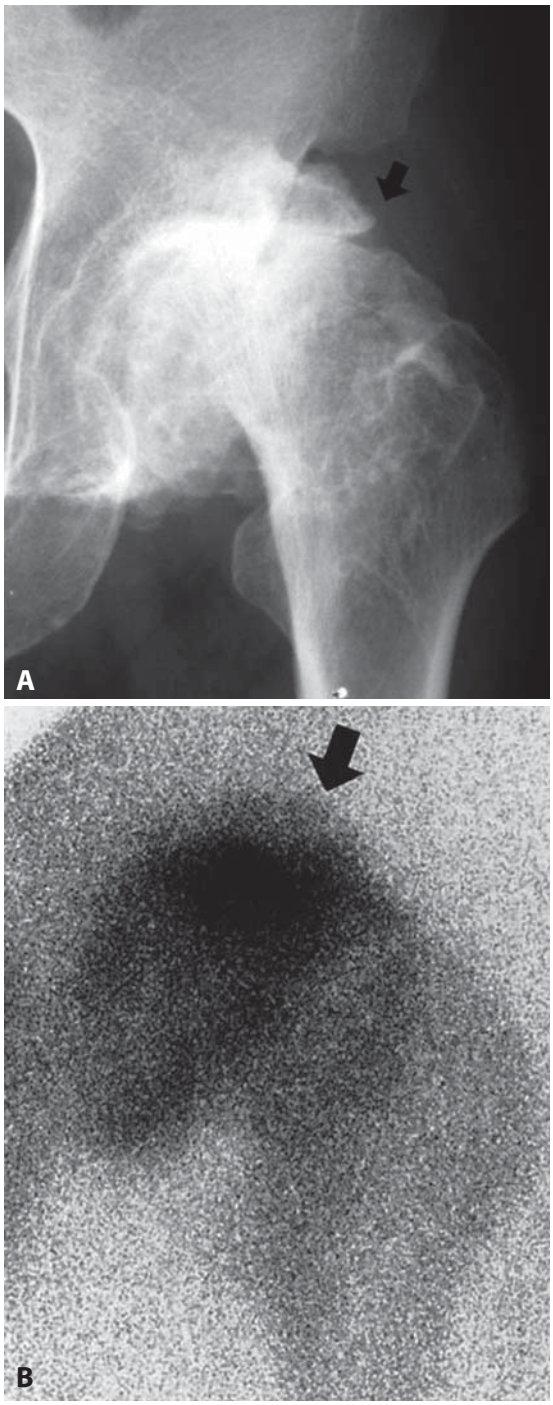

Fig. 13.12A, B Late consequences of improperly treated slipped femoral epiphysis. **A** Anteroposterior radiograph of the left hip in a 59-year-old man with untreated slippage shows coxa vara deformity with flattened femoral head, widened neck, articular narrowing, and bizarre acetabular hyperostosis (*arrow*). **B** Anterior pinhole scintigraph reveals findings of advanced secondary osteoarthritis with intense tracer accumulated in the closed joint and axial dislocation of the crooked femoral neck (*arrow*)

mediate or earliest possible surgical restoration is most desirable to prevent disabling deformity that may last for life. When left untreated or inadequately handled, coxa vara deformity with flattened femoral head, widened neck, articular narrowing, and bizarre acetabular hyperostosis become unavoidable (Fig. 13.12A).

^{99m}Tc-MDP bone scintigraphy is almost always performed after surgical reduction and refixation. Naturally, the scan shows increased tracer uptake in the repositioned physeal line, reflecting slippage, operative injury, and repair (Fig. 13.10C). Occasional patients, however, may present with residual craniolateral buckling of the proximal femoral metaphysis (Fig. 13.11B). Scintigraphy is an ideal means to obtain information on vascularity and anatomy following surgery and pinning (Figs. 13.10 and 13.11). Bone scanning is ideal for an integrated assessment of the anatomy, vascularization, metabolic profile, and complication of the capital femoral slippage both treated and untreated (Fig. 13.12).

13.8 Osteochondritis Dissecans

In essence, osteochondritis dissecans is the transchondral fracture of articular bones. It may cause fragmentation or avulsion of a some of the articular bones, with or without separation. This is a disorder of adolescence, and most frequently affects the medial femoral condyle. In contrast the humeral capitellum and the talus are sites of predilection in young children (Clarke et al. 1983; Newberg 1979). Although genetic factors or growth disturbances were suggested as causative, the condition is now generally believed to result from twisted or malaligned impaction forces applied to joints. Rarely, osteosarcoma can be associated with osteochondritis dissecans (Bahk et al. 1997).

The radiographic features are characterized by the presence of a small bone fragment demarcated with a fine radiolucent rind in the articular surface of the affected bone. Occasio-

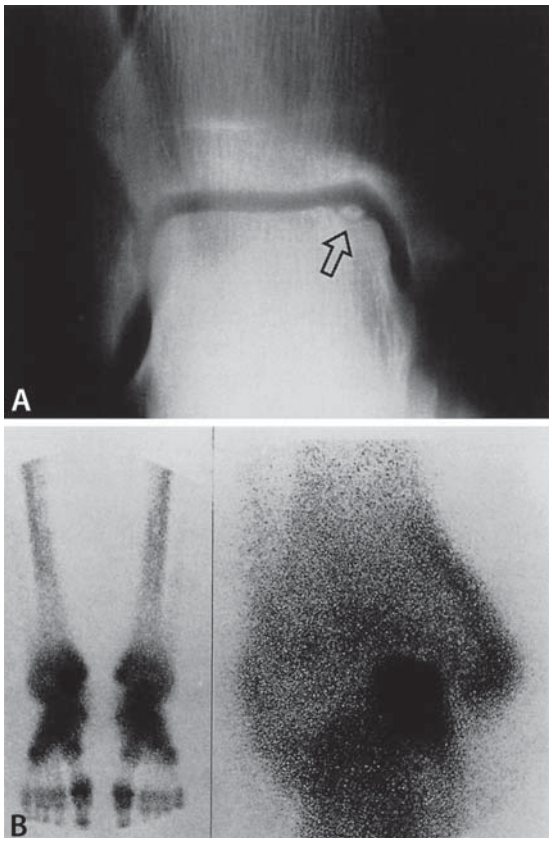

Fig. 13.13A, B Osteochondritis dissecans. **A** Anteroposterior conventional X-ray tomogram of the right ankle in a 52-year-old man reveals a small, ovoid, condensed bone fragment with a lucent rim in the medial edge of the trochlear surface of the talus (*open arrow*). **B** Anterior pinhole scintigraph demonstrates roundish intense tracer uptake in the medial aspect of the trochlear surface. The area of tracer uptake is much larger than the size of the bone defect, indicating the extended regional bone reaction. Note inadequate resolution of the planar image (*right*)

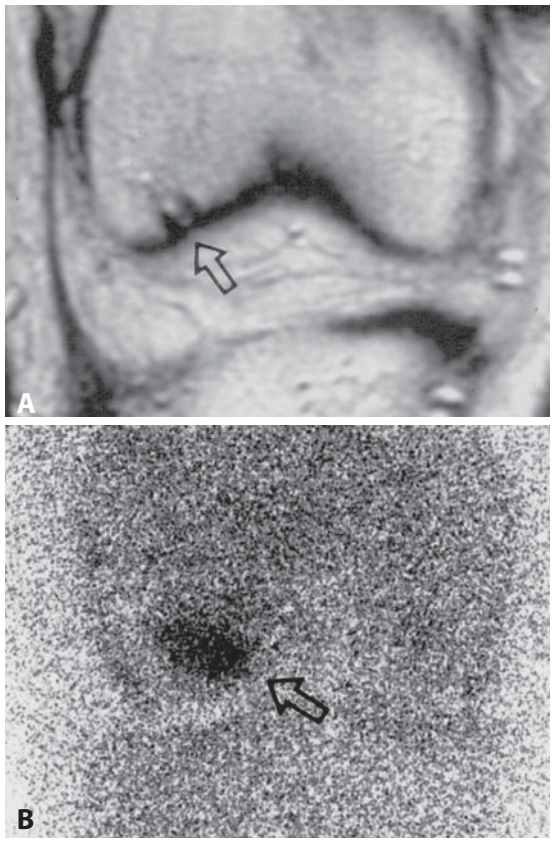

Fig. 13.14A–C Osteochondritis dissecans. **A** T2-weighted MRI of the left knee in a 49-year-old woman with local pain shows a small low signal with central high signal lesion at the medial femoral undersurface (*arrow*). **B** Anterior pinhole scintigraph reveals a small well-defined ovoid area of minimally increased tracer uptake (*arrow*). **C** Anteroposterior radiograph fails to show an abnormal finding (*?*)

nally, small lesions defy plain radiographic diagnosis, requiring computed or conventional tomography (Fig. 13.13A) or MRI (Fig. 13.14A). In rare instances, plain radiography may appear completely negative (Fig. 13.14A). If detached from the host bone the fragment may migrate into the joint cavity, becoming a joint mouse.

Planar bone scintigraphy is highly sensitive but not specific. Fortunately, however, pinhole scintigraphy can portray a spotty "hot" area that is characteristically localized to the subchondral portion of the periarticular bone, for example, the trochlear surface of the talus (Fig. 13.13B) or the undersurface of the medial femoral condyle (Fig. 13.14B). It is of interest to note that such uptake is usually larger in size than the bone fragment shown radiographically, probably reflecting an active reparative reaction or the watershed phenomenon.

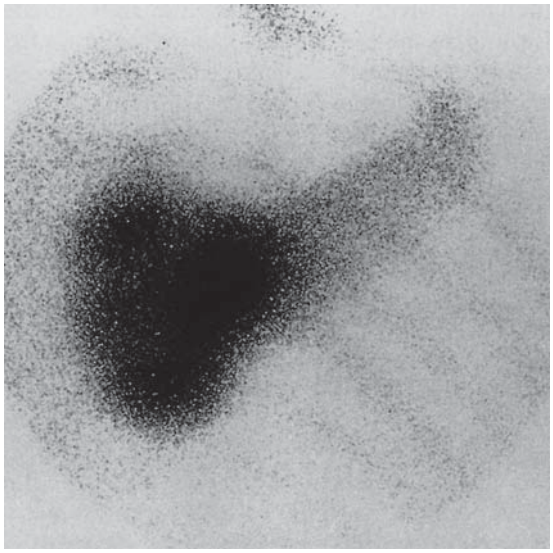

Fig. 13.15 Tietze's disease in the acute phase. Anterior pinhole scintigraph of the costal cartilage and medial end of the left first rib in a 24-year-old woman with local tenderness and swelling shows drumstick-like, intense tracer uptake in the costochondral junction and cartilage, reflecting expansile inflammation. Radiography was unremarkable (not shown here)

13.9 Tietze's Disease

Tietze's disease is a nonspecific, self-limited, inflammatory condition of the costochondral junctions (Tietze 1921). The disease is also referred to as costochondritis and costosternal syndrome, and predominantly affects the younger population. Although trauma and infection are considered to be causative and related, the accurate etiology remains obscure. Presenting symptoms include local tenderness, swelling, and occasional pain. The second rib is most commonly affected, but no ribs are immune. The prevalence is not low, and an epidemic-like presentation in six patients has been reported (Gill 1977). Pathological features include increased vascularity, degeneration with cleft formation, and calcification (Cameron and Fornasier 1974).

The radiographic manifestations are usually unimpressive and include occasional calcifica-

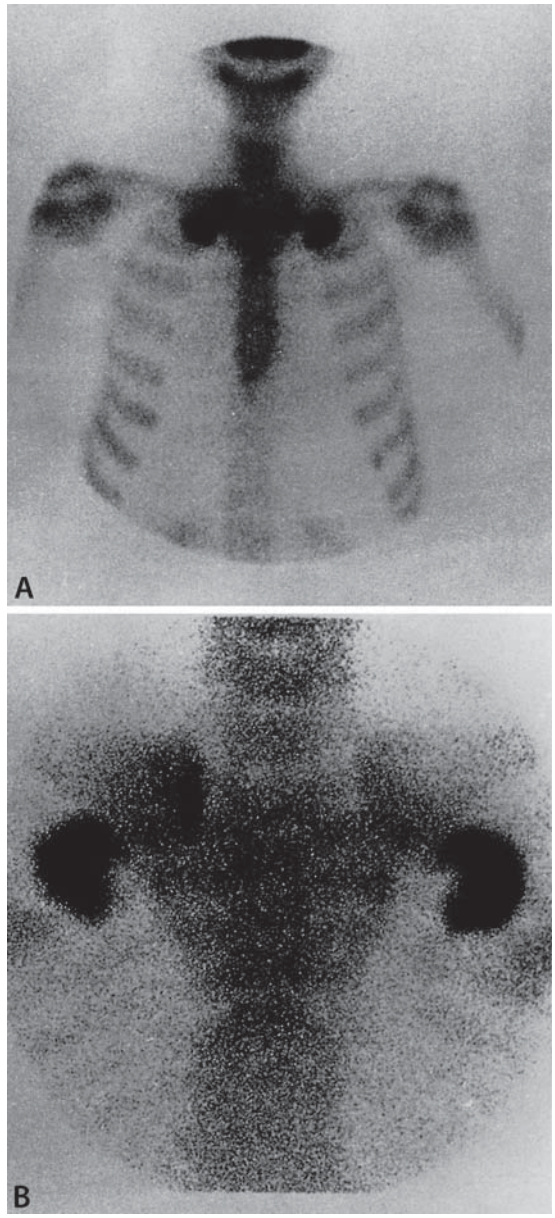

Fig. 13.16A, B Tietze's disease in the chronic phase. **A** Anterior planar scintigraph of the sternum in another 65-year-old woman with anterior chest pain reveals intense tracer uptake in the medial ends of both first ribs without textural detail. **B** Anterior pinhole scintigraph shows characteristic "comma" sign localized in the costochondral junctions. Unlike the expansile inflammatory reaction noted in the acute case (Fig. 13.15), the uptake in this chronic case tends to be localized in the costochondral junctions which are only minimally enlarged

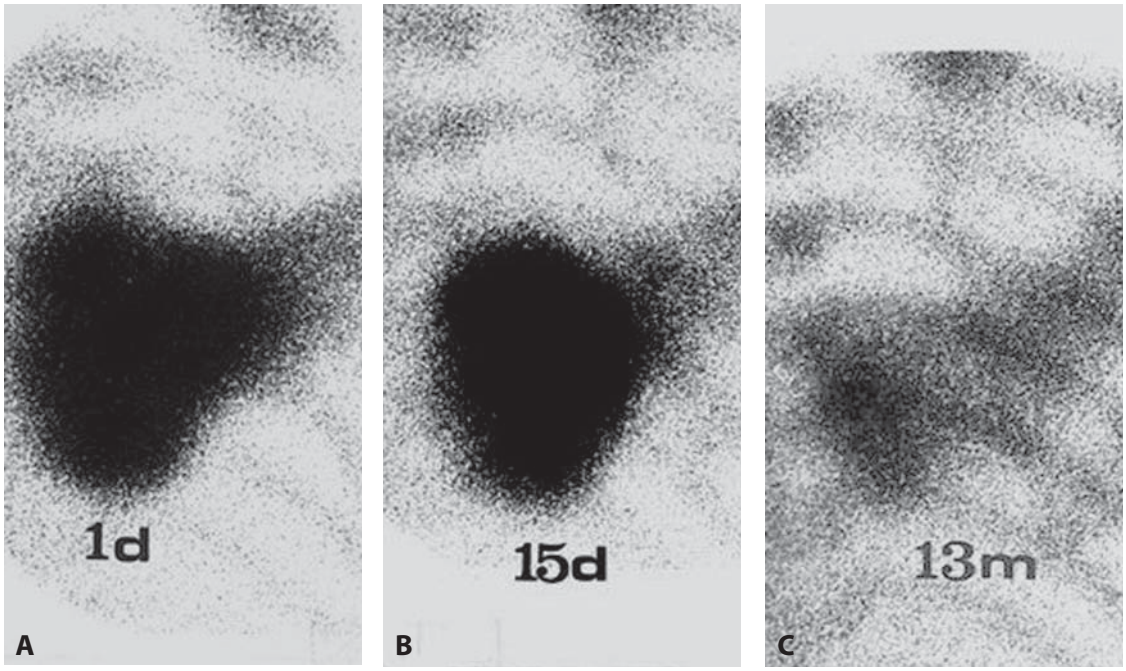

Fig. 13.17A–C Serial bone scintigraphy in Tietze's disease. **A** Initial anterior pinhole scintigraph of the painful left first rib in a 24-year-old woman shows prominent tracer uptake at the costochondral junction that is markedly enlarged. **B** Follow-up scintigraph obtained 15 days later reveals a partial subsidence of the enlargement but with persistent prominent uptake. **C** Further follow-up 13 months later demonstrates nearly normalized rib appearance and uptake

tion, sclerosis, and periostitis. Ordinary bone scintigraphy shows only increased tracer uptake (Sain 1978), but pinhole scintigraphy shows characteristic features (Yang et al. 1993). During the florid stage, intense uptake occurs in the whole costochondral junction that is enlarged, giving rise to a "drum stick" appearance (Fig. 13.15). With the subsidence of inflammation in the chronic stage, the uptake gradually reduces in size and shrinks with lessened intensity, producing the "comma" or "inverted comma" sign (Fig. 13.16). The pathological uptake may become reminiscent or return to normal over a period of a year or more (Fig. 13.17).

References

Ali RM, Green DW, Patel TC (1999) Scheuermann's kyphosis. Curr Opin Pediatr 11:70–75

Aufdermauer M, Spycher M (1986) Pathogenesis of osteochondrosis juvenile Scheuermann. J Orthop Res 4:452–457

Bahk WJ, Brien EW, Mirra JM (1997) Osteosarcomas associated with osteochondroma dissecans. J Bone Joint Surg Am 79:849–1853

Brower AC, Sweet DE, Keats TE (1974) Condensing osteitis of the clavicle: a new entity. AJR Am J Roentgenol 121:17–21

Cameron HU, Fornasier VL (1974) Tietze's disease. J Clin Pathol 27:960–962

Clarke NMP, Blakemore ME, Thompson AG (1983) Osteochondritis of the trochlear epiphysis. J Pediatr Orthop 3:601–604

Conway J (1993) A scintigraphic classification of Legg-Calvé-Perthes disease. Semin Nucl Med 23:274–295

Danigelis JA (1976) Pinhole imaging in Legg-Perthes disease: further observations. Semin Nucl Med 6:69–82

Fisher RL, Roderique JW, Brown DC, et al (1980) The relationship of isotopic image finding to prognosis of Legg-Perthes disease. Clin Orthop Rel Res 150:23–29

Gill GV (1977) Epidemic of Tietze's syndrome. Br Med J 2:499

Ippolito E, Ponseti IV (1981) Juvenile kyphosis: histological and histochemical studies. J Bone Joint Surg Am 63:175–182

Jurik AG, de Carvalho A, Graudal H (1985) Sclerotic changes of the sternal end of the clavicle. Clin Radiol 36:23–25

Madden CC, Mellion MB (1996) Sever's disease and other causes of heel pain in adolescents. Am Fam Physician 54:1995–2000

Mullaji AB, Emery RJH, Joysey VC, et al (1993) HLA and slipped capital femoral epiphysis. J Orthop Rheumatol 6:167–169

Newberg AH (1979) Osteochondral fractures of the dome of the talus. Br J Radiol 52:105–109

Ogata K, Sugioka MD, Urano Y, Chikama H (1986) Idiopathic osteonecrosis of the first metatarsal sesamoid. Skeletal Radiol 15:141–145

Renander A (1924) Two cases of typical osteochondropathy of the medial sesamoid bone of the first metatarsal. Acta Radiol 2:521–527

Sain AK (1978) Bone scan in Tietze's syndrome. Clin Nucl Med 3:470–471

Tietze A (1921) Über eine eigenartige Haufung von Fällen mit Dystrophie der Rippenknorpel. Berl Klin Wochenschr 58:829–831

Volpon JB, de Carvalho Filho G (2002) Calcaneal apophysitis: a quantitative radiographic evaluation of the secondary ossification center. Arch Orhop Traum Surg 122:338–341

Yang WJ, Bahk YW, Chung SK, et al. (1994) Pinhole scintigraphic manifestations of Tietze's disease. Eur J Nucl Med 21:947–952

14 Vascular Bone Disorders

Vascularity-related bone disorders of scintigraphic interest include avascular necrosis, infarction, dysbaric necrosis, hyperemic or congestive osteoporosis, congestive periostitis, and periostitis in Bürger's disease. ^{99m}Tc-MDP bone scintigraphy augmented with nuclear angiography and pinhole scanning appears to be the method of choice for dynamic biochemical study of these vascularity-related bone disorders because it is not only sensitive and often specific but also noninvasive, holistic, and easily repeatable in a day or two if necessary. In particular, pinhole bone scanning is highly valued for its ability to detect avascularity before radiography, and to subsequently assess the clinical course to revascularization (Fig. 14.1). On the other hand, nuclear angiography can diagnose regional osteoporosis or osteopenia that is related to hyperperfusion, hypoxia periostitis in Bürger's disease, and chronic venous congestion.

14.1 Avascular Osteonecrosis and Bone Infarction

Pathologically, osteonecrosis may be defined as the devitalization of osteocytes and cellular bone marrow elements. A single decisive factor that may lead to osteonecrosis is vascular deprivation with resultant ischemia. The causes vary, but they can be divided into definite and probable associations (Ficat and Arlet 1980). The definite causes include trauma, fracture, irradiation, sickling, electrical damage, freezing damage, and caisson disease. Although debatable, trivial trauma, alcohol indulgence, chemotherapeutic agents, corticosteroids, gout, rheumatoid arthritis, and connective tissue disorders are considered the probable causes. Avascular osteonecrosis associated with Legg-Calvé-Perthes disease and some other osteochondroses constitutes the third distinct group as discussed under the respective entries. Of many causes mentioned, femoral neck fracture, steroid-induced osteonecrosis, and osteonecrosis related with renal transplantation are probably most common. Osteonecrosis due to alcoholism, which typically affects the femoral head, is also common (Jones 1971; Jones 2001).

Both anatomical and radiographic studies have indicated avascular osteonecrosis and bone infarction to occur almost invariably within the fatty bone marrow of adult long bones (Resnick and Niwayama 1988). Avascular necrosis has a strong predilection for the long bone epiphysis and is painful in the acute phase, whereas bone infarction predominantly affects the meta-diaphysis of long bones and is easily transformed into the chronic form, which is silent. The femoral head is the most frequently affected site of avascular necrosis and the femoral condyles and small rounded bones in the wrist and ankle are also frequently affected. Bone infarction is typically multifocal, involving many long bones on both sides of the body and is rarely transformed into sarcoma with a prevalence rate of less than 1%.

Radiography is not regularly used in the early or preclinical stage of avascular bone necrosis and infarction. In established cases, however, plain radiography plays a decisive role, often needing no further diagnostic tests. Avas-

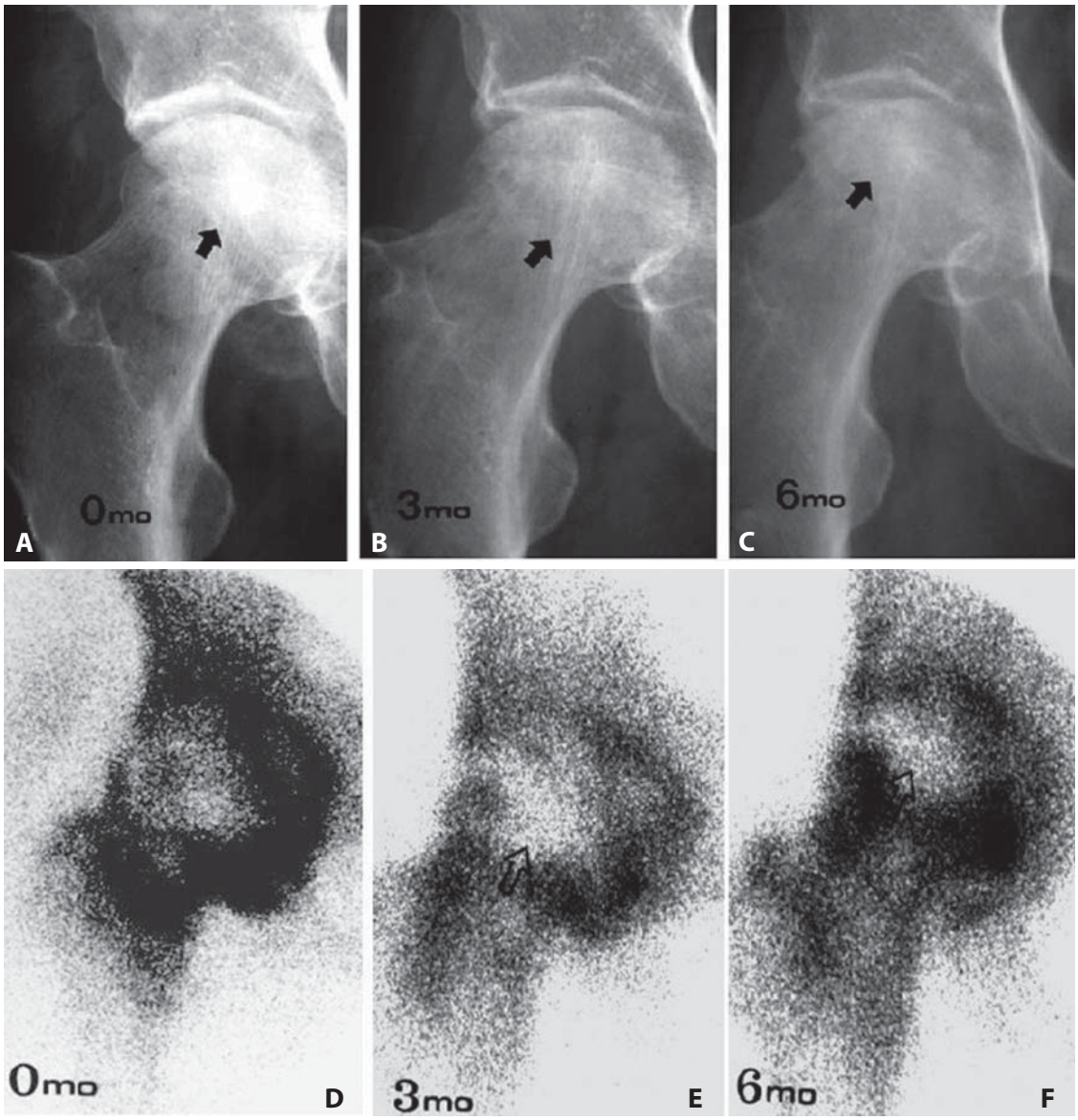

Fig. 14.1A–F Sensitive and specific diagnosis of avascularity and revascularization in avascular osteonecrosis. **A–C** Serial anteroposterior radiographs of the right hip in a 60-year-old male alcoholic with osteonecrosis show slowly progressive flattening and bony condensation over a period of 6 months (*arrows*). **D–F** Serial anterior pinhole scintigraphs show initial photon defect and reactive hypervascularity in the femoral head followed by gradual revascularization (*open arrows*)

cular necrosis manifests as subchondral crescent lucency, an admixture of irregular lucency and sclerosis, and bone flattening or collapse, which are virtually pathognomonic (Fig. 14.2A). The adjacent articulation is usually unaltered unless attended by secondary or preexisting osteoarthritis, and the "sagging rope" sign appears in occasional cases (Apley and Wientroub 1981; Clarke et al. 1983). In contrast, bone infarctions, seen most typically in dysbaric necrosis in the metadiaphyses of the long bones, manifest as irregular mottled, curly, or smoke-like mineralization (Figs. 14.3A and 14.4A). Idiopathic infarctions show basically the same radiographic changes in the long-bone metadiaphyses. When bone infarction is transformed to sarcoma, geographic osteolysis occurs with ballooning and cortical disruption (Fig. 14.5A).

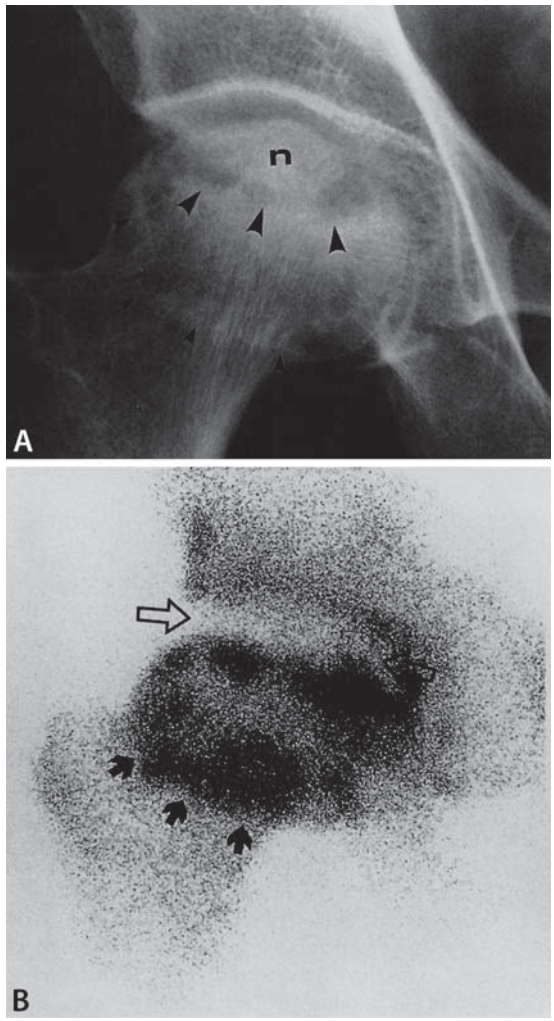

Fig. 14.2A, B Ischemic bone necrosis. **A** Anteroposterior radiograph of the right hip in a 55-year-old man with Chandler's disease reveals an ovoid, condensed bone in the femoral head top (*n*) bordered by a crescent lucent zone (*large arrowheads*), sclerosis, the collapse and flattening of the head, and a linear density in the head's base ("sagging rope" sign; *small arrowheads*). **B** Anterior pinhole scan shows a photopenic defect in the condensed bone of the femoral head top bordered by intense tracer uptake (*open arrows*), the collapse of the head, and band-like tracer uptake across the head's base. The last-mentioned is the scintigraphic version of the radiographic "sagging rope" sign that is the projection of the drooping head (*arrows*)

The concurrence of other mineralized infarctions in the adjacent bones, often across the joint, is an extremely helpful finding.

Scintigraphically, avascular osteonecrosis is indicated by a photon defect. As mentioned above, bone scintigraphy is not only specific but also highly sensitive in diagnosing avascular necrosis. Actually, it is not rare that an obvious photon defect can be shown in the absence of radiographic change (Fig. 14.6). Typically, such a photon defect is sharply demarcated caudally by intense uptake in the reparative and reactive zone that extends to the neck. It is of differential diagnostic interest to note that, unlike the poor caudal definition of reparative uptake, the demarcation of neck fracture uptake is very sharp so that it can clearly be distinguished from accompanying avascular necrosis in the femoral head (Fig. 14.7). In chronic avascular osteonecrosis, pinhole scintigraphy reveals the combination of four different findings: a "cold" area in the top of collapsed head, intense uptake along the lower border of the cold area in the top, mottled uptake in the remainder of the head, and lace-like uptake across the neck, the "sagging rope" sign (Fig. 14.2B). These four scan signs appear to be roughly correlated, respectively, with avascular osteonecrosis, reparative bone interface, reactive hyperemia, and bone reinforcement or microfractures of the overhanging anterior lateral edge of the femoral head that is drooping.

On the other hand, bone infarctions intensely accumulate tracer when the lesions are relatively fresh and mineralization is partial and modest (Figs. 14.3B and 14.4B). It appears that relatively fresh infarctions with active osteogenesis avidly accumulate tracer while densely calcified, aged infarctions accumulate little or no tracer. Sarcomatous transformation is indicated by bubbly photon defects with ballooning and irregular tracer uptake in ruptured or actively invaded borders (Fig. 14.5B).

14.2 Avascular Necrosis in Chronic Alcoholism

The existence of a close cause-and-effect relationship between alcoholism and avascular osteonecrosis has long been noted, most typically

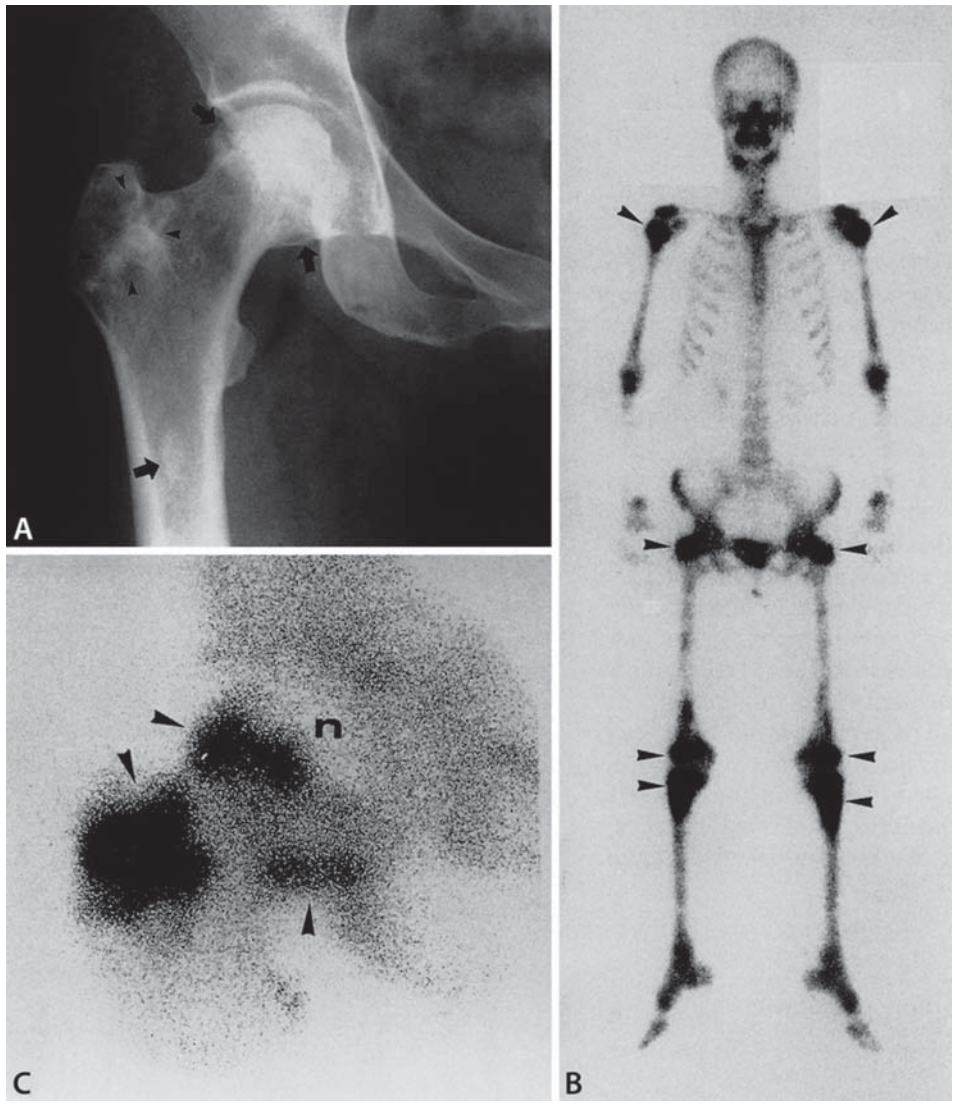

Fig. 14.3A–C Bone infarctions. **A** Anteroposterior radiograph of the right hip in a 55-year-old woman with multiple, idiopathic bone infarctions reveals irregularly mottled and ring-like densities in the head and proximal metadiaphysis of the right femur (*arrows, arrowheads*). The lesion in the greater trochanteric region has the classic serpiginous contour (*arrowheads*). **B** Anterior whole-body scan shows multiple infarctions with intense tracer uptake in the proximal humeri, the proximal and distal femora, and the proximal tibiae (*arrowheads*). **C** Anterior pinhole scintigraph of the right hip demonstrates intense tracer uptake in the old, calcified lesions in the base of the femoral head and the greater trochanter (*arrowheads*), whereas a fresh, uncalcified ischemic necrosis in the top of the head is photopenic (*n*). Scintigraphy is clearly more informative than radiography in revealing the infarctions that are not calcified

in the femoral head (Patterson et al. 1964). In a recent review Jones (2001) again emphasized the importance of alcohol-induced fatty liver as a major source of continuous or intermittent fat embolism that creates avascular necrosis. Radiographically detectable osteonecrosis was observed in the femoral head or the humeral head in all 30 chronic alcoholism patients he studied. The diagnosis was histologically confirmed in 19 patients. The mechanism was explained on the basis of endarterial occlusion created by repeated shower of fat emboli.

Radiographic and scintigraphic features are similar to those of avascular osteonecrosis with other etiologies such as corticosteroids. Thus,

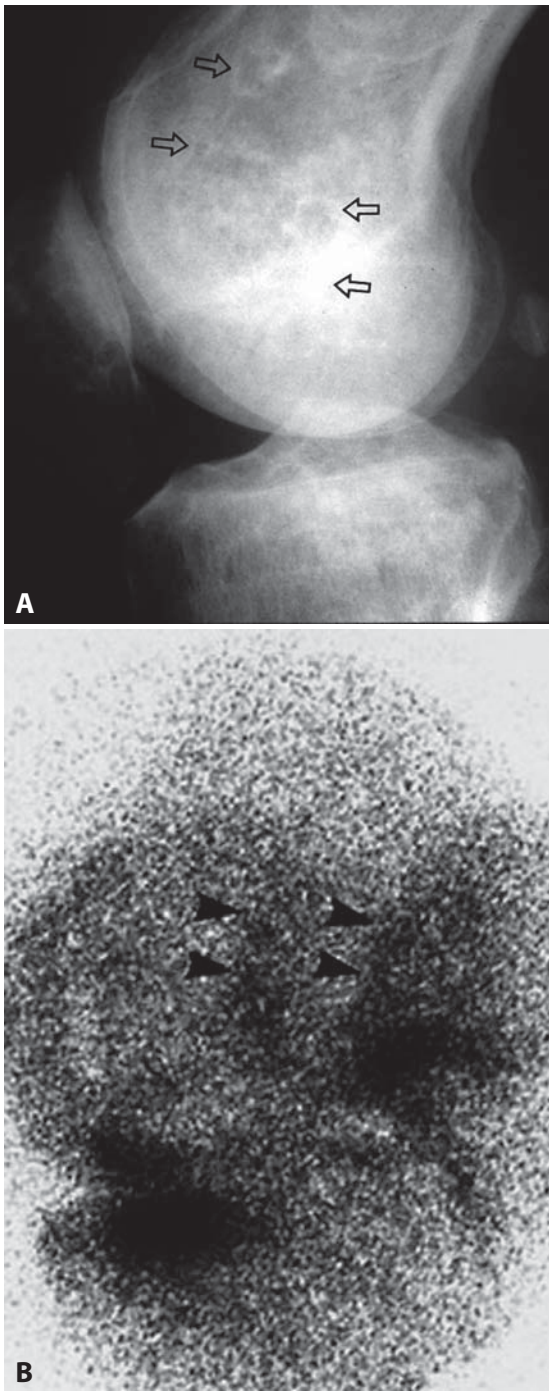

Fig. 14.4A, B Dysbaric bone infarctions. **A** Lateral radiograph of the right distal femoral metaphysis in a 58-year-old man with caisson disease shows irregular curly and smoke-like mineralization (*open arrows*). **B** Lateral pinhole scintigraph reveals irregular mottled and smoke-like tracer uptake (*arrowheads*)

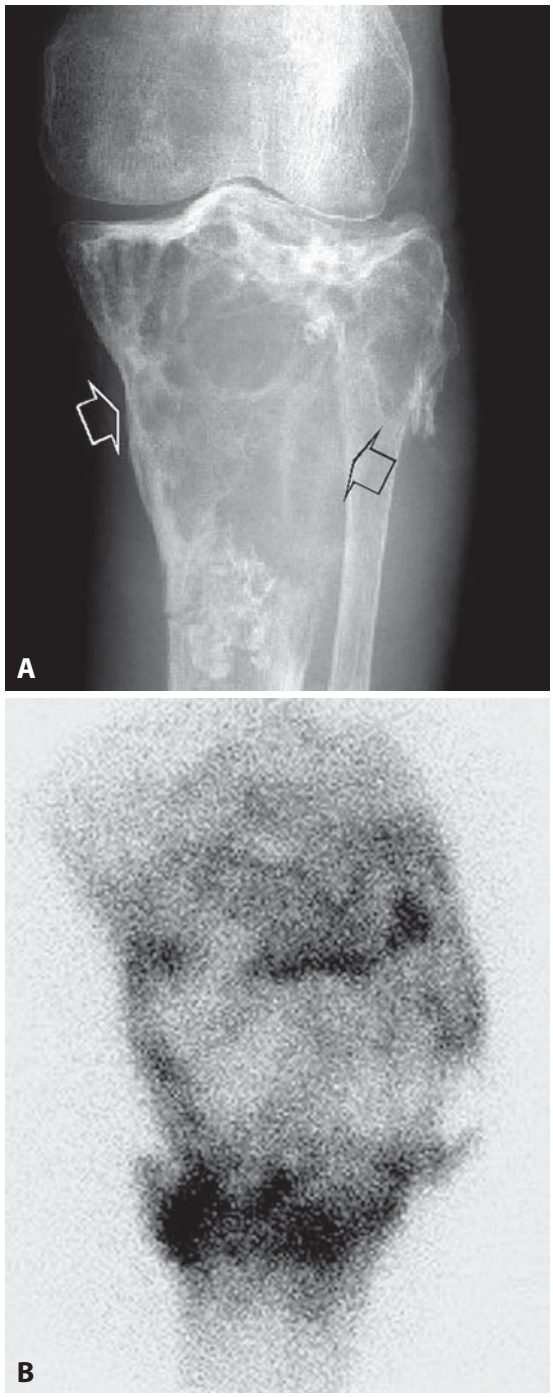

Fig. 14.5A, B Sarcomatous transformation of bone infarction. **A** Anteroposterior radiograph of the right proximal tibia in a 56-year-old man with a rapidly expanding tumor shows typical geographic osteolysis with ballooning and cortical disruption (*open arrows*). **B** Anterior pinhole scintigraph reveals a readily comparable ballooning bone lesion (courtesy of Prof. Won-Jong Bahk, M.D., Department of Orthopaedic Surgery, Euijongboo St. Mary's Hospital, Catholic University of Korea)

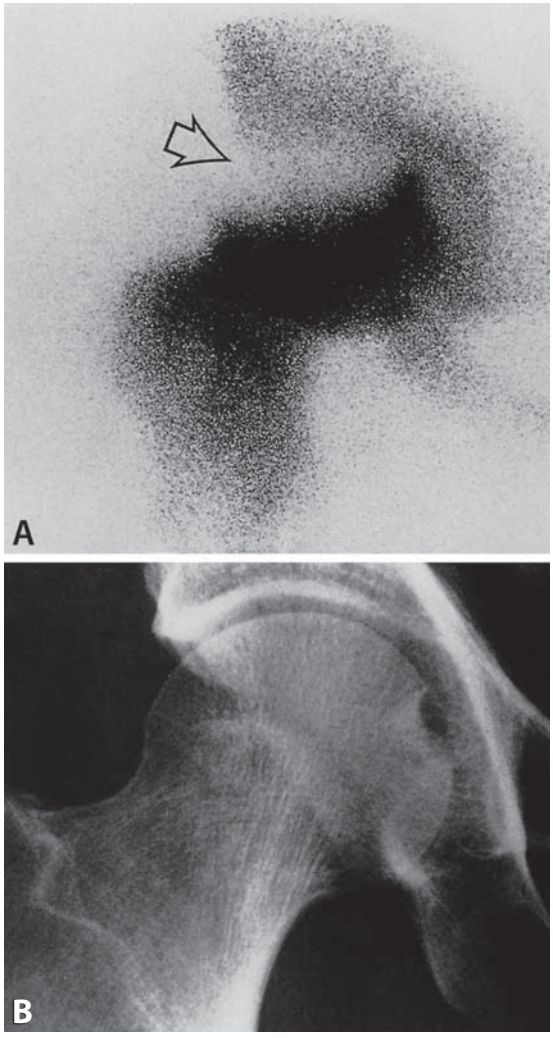

Fig. 14.6A, B Preradiographic detection of avascular osteonecrosis. **A** Anterior pinhole scintigraph of the painful right hip in a 46-year-old man reveals an obvious photon defect in the femoral head, denoting osteonecrosis (*open arrow*). Observe the diffuse tracer uptake in reactive bone of the surviving head and the adjacent neck. **B** Anteroposterior radiograph shows no definite abnormality

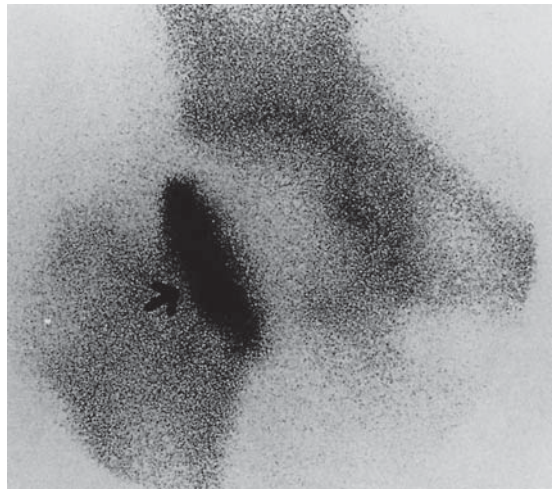

Fig. 14.7 Avascular femoral head osteonecrosis secondary to femoral neck fracture. Anterior pinhole scintigraph of the right hip in an adult man shows a large photon defect involving the whole femoral head and a sharply defined, extremely intense, band-like tracer uptake across the neck, denoting avascular necrosis and the causative fracture, respectively. The tracer uptake in the fracture is absolutely sharp in demarcation, contrasting with the diffuse uptake in the reactive bone of primary osteonecrosis (Fig. 14.6A)

radiography shows trabecular fractures and bony condensation, collapse, and deformity (Fig. 14.8A) and scintigraphic findings include the combination of irregular photopenia and intense uptake and bone and joint deformation (Fig. 14.8B).

14.3 Vascularity-Related Osteoporosis

Vascularity-related osteoporosis is arbitrarily assigned to include disuse (immobilization) osteoporosis, reflex sympathetic dystrophy (RSD), transient painful regional osteoporosis with hypervascularity, and nonspecific marrow edema. Osteoporosis and osteopenia is a condition in which bone mass is reduced with resultant increase in porosity. The former term emphasizes porosity and the latter reduced bone mass. The pathophysiology and precipitating factors are not fully clarified except disuse, hyperemia, congestion, and the "internuncial" theory of RSD. The distribution pattern of

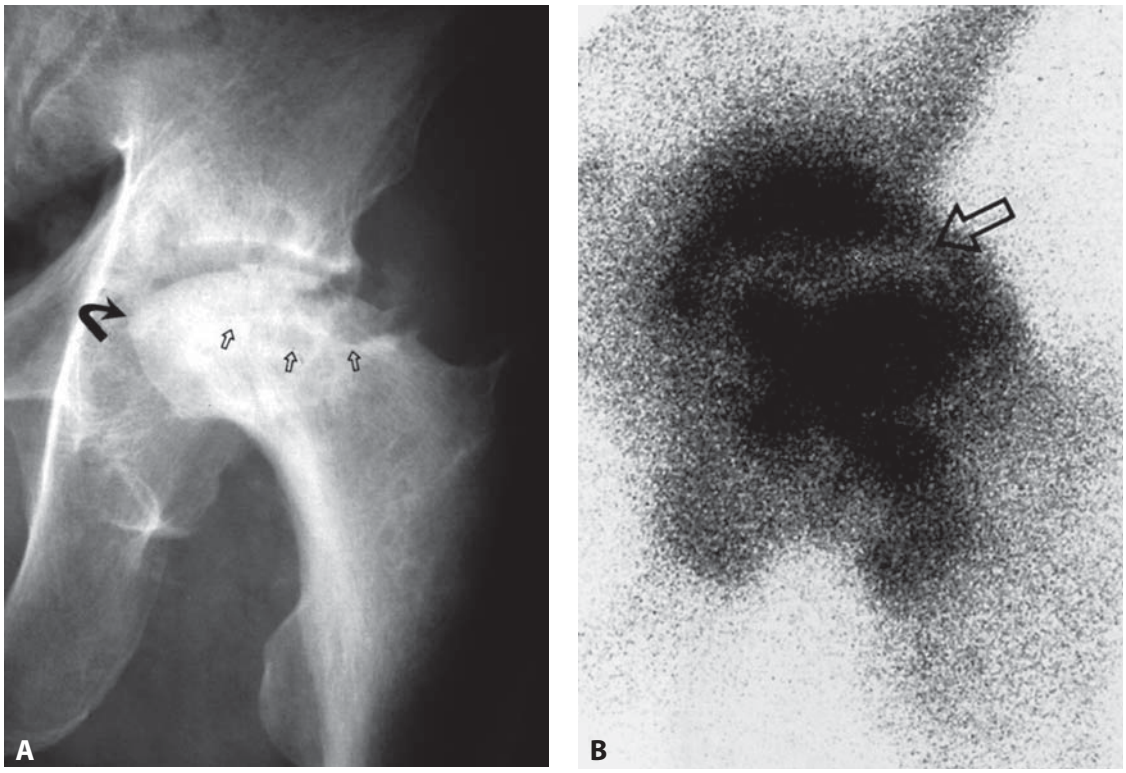

Fig. 14.8A, B Avascular osteonecrosis in alcoholics. **A** Anteroposterior radiograph of the left hip in a 36-year-old man with chronic alcoholism shows admixture of irregular bony condensation and lucency, deformity (*curved arrow*), and marked flattening of the head (*open arrows*). The hip joint is narrowed and the acetabular fossa deepened due to advanced secondary osteoarthritis. **B** Anterior pinhole scintigraph reveals intense tracer uptake in the femoral neck and narrowed joint with markedly collapsed head (*open arrow*)

osteoporosis may be classified as generalized, regional, or focal, and the clinical presentation as acute, subacute, or chronic. Patients with RSD and transient regional osteoporosis may complain of pain, tenderness, and soft-tissue swelling. Disuse porosis, however, is symptomless, unless complicated by fracture. From the view point of pathogenesis and scintigraphic description, osteoporosis can be divided into that with vascularity problems and that with metabolic or hormonal disturbances. Of these, vascularity-related osteoporosis is discussed here and the others are described in Chap. 15.

Plain radiography was the primary means of visually assessing osteoporosis. However, because of inadequate sensitivity it has been gradually replaced by radiographic bone densitometry, which can quantitatively measure bone mineral densities in the spine and femoral neck. Indeed, plain radiography can recognize positive change only after 30–50% loss of bone calcium. General radiographic features of osteoporosis include increased radiolucency, scarcity or absence of trabeculae, and thinning, scalloping, blurring, or tunneling of the cortex. Painful regional osteoporosis manifests as patchy areas of radiolucency due to paucity or apparent absence of trabeculae (Fig. 14.9A). On the other hand, the osteoporosis in disuse or RSD is characterized by regional involvement, manifesting as speckled, mottled, and patchy radiolucencies. RSD typically occurs in the carpal and tarsal bones. In severe RSD marked zonal lucencies may appear, for example, in the distal ends of the radius and ulna in addition to intense osteoporosis in the all carpal bones (Fig. 14.10A).

Bone scintigraphy shows conspicuous tracer uptake in transient regional porosis (Fig. 14.9B)

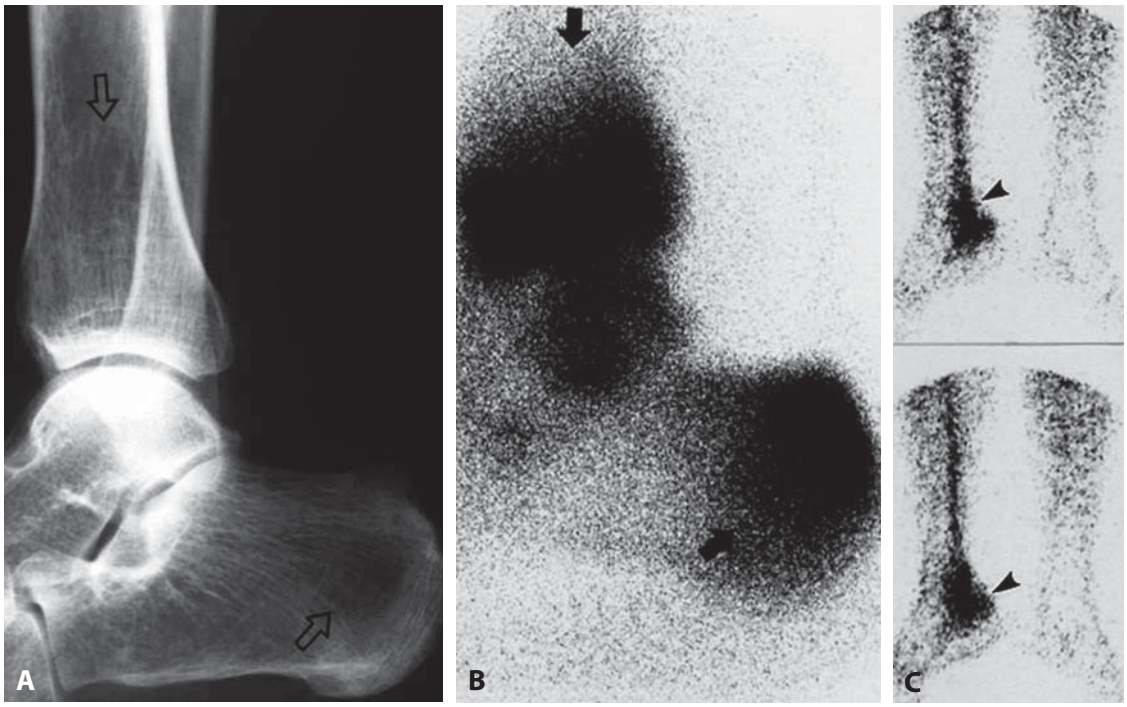

Fig. 14.9A–C Painful transient regional osteoporosis. **A** Lateral radiograph of the painful right hindfoot in a 40-year-old woman shows focal osteopenia in the posterior calcaneus (*lower arrow*) and distal tibial shaft (*upper arrow*). **B** Lateral pinhole scintigraph shows intense tracer uptake localized to the posterior calcaneus (*lower arrow*) as well as the distal tibia and talus (*upper arrow*). **C** Nuclear angiograph reveals regionally increased blood flow (*arrowheads*)

and mild to moderate uptake in RSD (Fig. 14.10C) and disuse porosis. In general the prominent regional tracer uptake in these conditions contrasts with systemic low uptake in postmenopausal, senescent, and metabolic osteoporosis. Nuclear angiography in transient regional osteoporosis (Fig. 14.9C) and RSD (Fig. 14.10B) demonstrates increased vascularity, permitting their distinction from disuse osteoporosis, which is not attended by hyperperfusion. It is of interest to note that the pinhole scintigraphic uptake pattern varies somewhat between these three conditions, probably reflecting difference in the modes of osteoporosis. Thus, tracer uptake appears typically patchy and homogeneous in transient regional osteoporosis (Fig. 14.9B), band-like and mottled in RSD (Fig. 14.10C), speckled or coarsely granular in disuse porosis (Fig. 14.11), and diffusely homogeneous in regional osteoporosis of the hip (Fig. 14.15).

14.4 Reflex Sympathetic Dystrophy

RSD is not rare. It is a rheumatic disorder of clinical importance and academic interest. Involvement is usually regional and diffuse, but can be segmental and small in rare cases (Helms et al. 1980). The condition is also referred to as causalgia, Sudeck's atrophy, posttraumatic osteoporosis and angiospasm, reflex neurovascular dystrophy, and the shoulder–hand syndrome. Common symptoms include pain, swelling, stiffness, tenderness, vasomotor and sensory disturbances, hyperesthesia, disability, and skin atrophy, and other trophic skin alterations such as hypertrichosis and hyperhidrosis. The pathogenesis is yet not clarified, although the theory of internuncial pool proposed by Lorente (1938) is widely supported. The theory assumes that painful impulses created by a peripheral injury travel via the afferent pathways to the spinal cord, where a series of reflexes originate. Reflex-

es then spread through the interconnecting pool of neurons to stimulate the lateral and anterior tracts, provoking the efferent pathways that travel to the peripheral nerves and finally causing neurovascular and bone-periosteal alterations of RSD. The identification of "sympathetic vasoactive intestinal peptide-containing nerve fibers" innervated at the cortical bone and bone-periosteal junction has provided a biochemical basis for the theory (Hohmann et al. 1986). Vasoactive intestinal peptide released from such sympathetic nerve fibers has been shown to cause hyperemia and dramatic bone resorption as in RSD. As described below, our recent pinhole SPECT study demonstrated that the spotty uptake in RSD is peculiarly localized to the peripheries of the tarsal bones. The areas appear to correspond to patchy bone erosions shown radiographically in the corticoperiosteal junctions (Bahk et al. 1998).

The diagnosis of RSD largely depends upon symptoms and radiographic and scintigraphic findings. Radiographic manifestations include confluent patchy osteopenia, subperiosteal bone resorption, and subcortical erosions of the carpal bones (Genant et al. 1975) (Figs. 14.10A and 14.12A) or tarsal bones (Figs. 14.13B and 14.14B). Band-like porosis is seen in the distal ends of the radius and ulna, and also the metacarpal bases when the wrist is involved (Figs. 14.10A and 14.12A). The osteoporosis in RSD may be diffuse (Fig. 14.10A) or peripheral and focal (Fig. 14.12A). Nuclear angiography is useful for the study of RSD, and shows hyperperfusion (Kozin et al. 1981) (Fig. 14.10B). Planar pinhole scanning shows mottled and band-

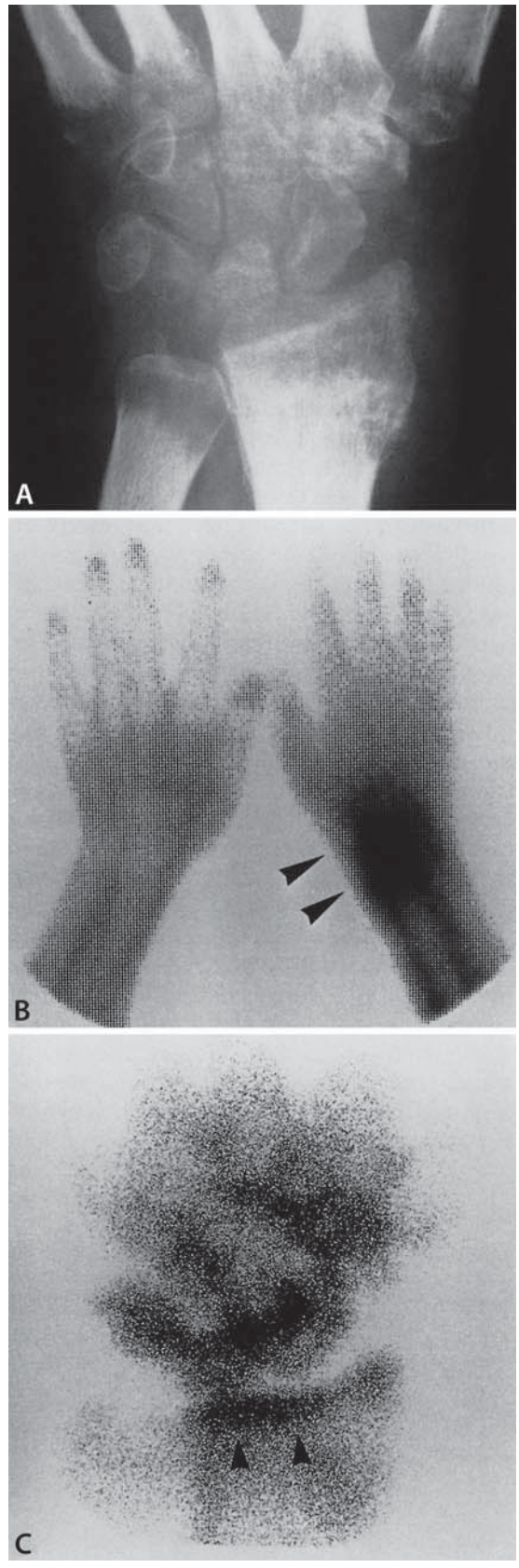

Fig. 14.10A–C Reflex sympathetic dystrophy syndrome (RSDS). **A** Dorsoventral radiograph of the left wrist in a 31-year-old man with severe wrist pain and skin discoloration shows marked porosis in the entire wrist bones. Minimal erosions are noted in the distal radius. **B** Scintiangiogram reveals increased blood pool in the wrist (*arrowheads*). **C** Pinhole scintigraph shows discrete linear and mottled tracer uptake in the radial end and the carpal bones. Note that tracer uptake is peripheral in location and does not necessarily correspond to the radiographic porosis

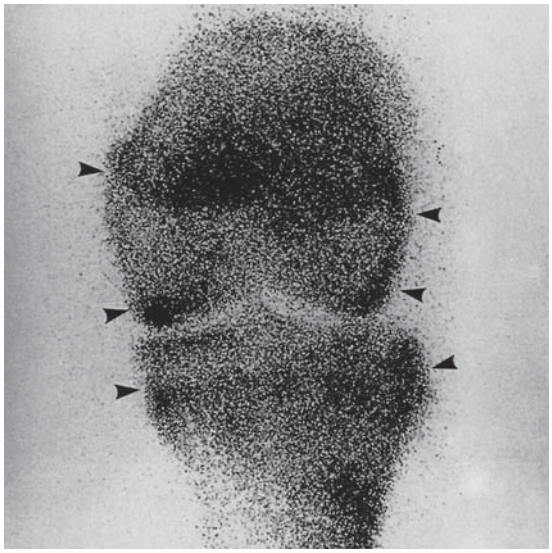

Fig. 14.11 Speckled and coarsely granular tracer uptake in disuse osteoporosis. Anterior pinholes scintigraph of the left knee in a 23-year-old woman with a disused left lower limb due to foot pain shows coarsely granular and irregularly mottled tracer uptake in the bones about the knee. More intense tracer uptake tends to occur in the peripheries (*arrowheads*)

like areas of intense uptake that is characteristically situated in the carpal bone peripheries, the distal ends of the radius and ulna, and the metatarsal bases when the wrist is involved (Figs. 14.10C and 14.12B). Similar tracer uptake may occur in the tarsal bones when the ankle is affected (Figs. 14.13A and 14.14A). There is the impression that patchy uptake in RSD does not correlate with radiographic osteoporosis. Such a discordance, which is typically observed in the distal ends of the radius and ulna in our limited cases, would imply that not all radiographic porosis is accompanied by active bone turnover. Interestingly, using pinhole SPECT, we have been able to localize spotty "hot" areas to the ligamentous and tendinous insertions (Figs. 14.13A and 14.14A). Such a peculiar localization is interpreted to point the sites where "the dramatic bone resorption mediated by the vasoactive intestinal peptide released from the sympathetic nerve fibers in RSD" (Hohmann et al. 1986) is seen most typically (Bahk et al. 1998; Kim et al. 2003).

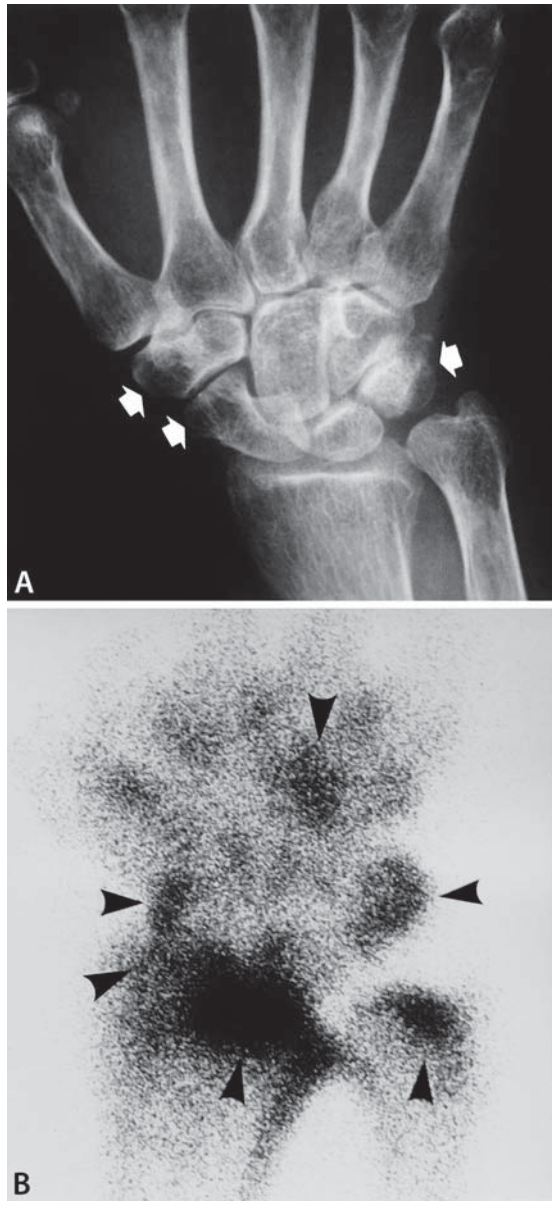

Fig. 14.12A, B The characteristic peripheral tracer distribution in reflex sympathetic dystrophy syndrome (RSDS). **A** Dorsoventral radiograph of the right wrist in a 34-year-old man with RSDS showing blotchy and mottled porosis in some of the wrist bones (*arrows*). There are no bone alterations in the distal radius or ulna. **B** Dorsal pinhole scan showing blotchy tracer uptake characteristically in the peripheries of the navicular and pisiform and in the distal radius and ulna (*arrowheads*). Note that tracer uptake does not necessarily correspond to radiographic porosis as in Fig. 14.10

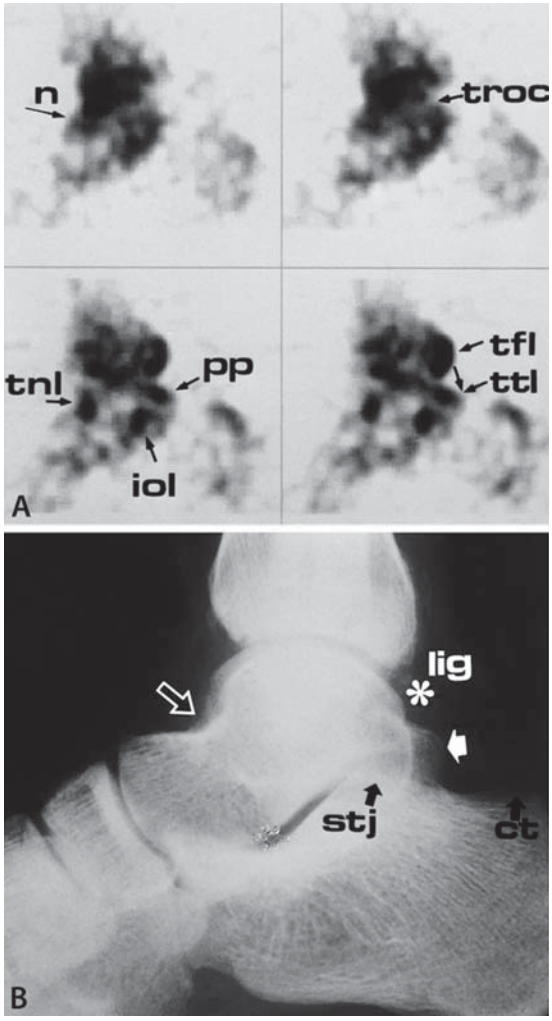

Fig. 14.13A, B Pinhole SPECT findings of reflex sympathetic dystrophy syndrome (RSDS). **A** Sagittal pinhole SPECT images of the right ankle in a 29-year-old man with posttraumatic RSDS shows spotty hot areas at the ligamentous and tendinous insertions of the bones in the ankle and hindfoot (*n* talar neck, *troc* trochlea, *stj* subtalar joint, *tnl* talonavicular ligament, *iol* interosseous ligament, *pp* posterior process of the talus, *tfl* talofibular ligament, *ttl* tibiotalar ligament, *ct* calcanean tendon). **B** Lateral radiograph shows subcortical bone erosions at ligamentous and tendinous insertions, including the talar neck (*open arrow*), posterior talar process (*solid arrow*), and insertions of talotibial ligament (*lig*), subtalar joint (*stj*), and calcanean ligament (*ct*)

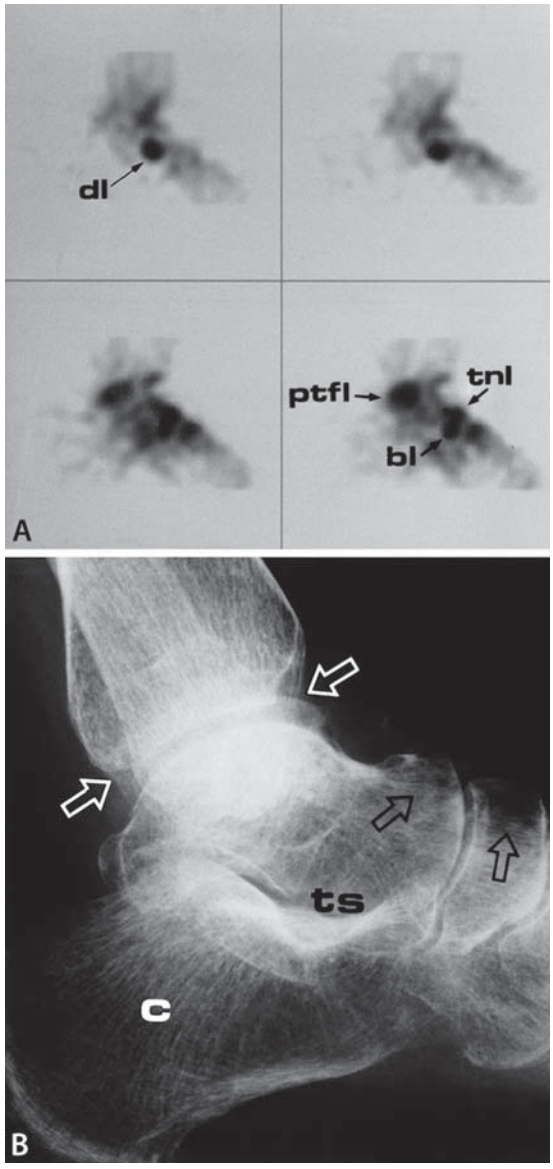

Fig. 14.14A, B Pinhole SPECT findings of reflex sympathetic dystrophy syndrome (RSDS). **A** Sagittal pinhole SPECT images of the left ankle in a 59-year-old woman with posttraumatic RSDS shows characteristic spotty hot areas at the insertions of the deltoid ligament (*dl*), tibiocalcaneal ligament in the subtalar joint (*stj*), posterior tibiofibular ligament (*ptfl*), talonavicular ligament (*tnl*), bifurcated ligament (*bl*), and dorsal cuneonavicular ligaments (*dcnl*). **B** Lateral radiograph shows blotchy subcortical bone resorption at the insertions of ligaments in the peripheries of the malleoli and tarsal bones (*open arrows*) (*ts* talar sulcus, *c* calcaneus)

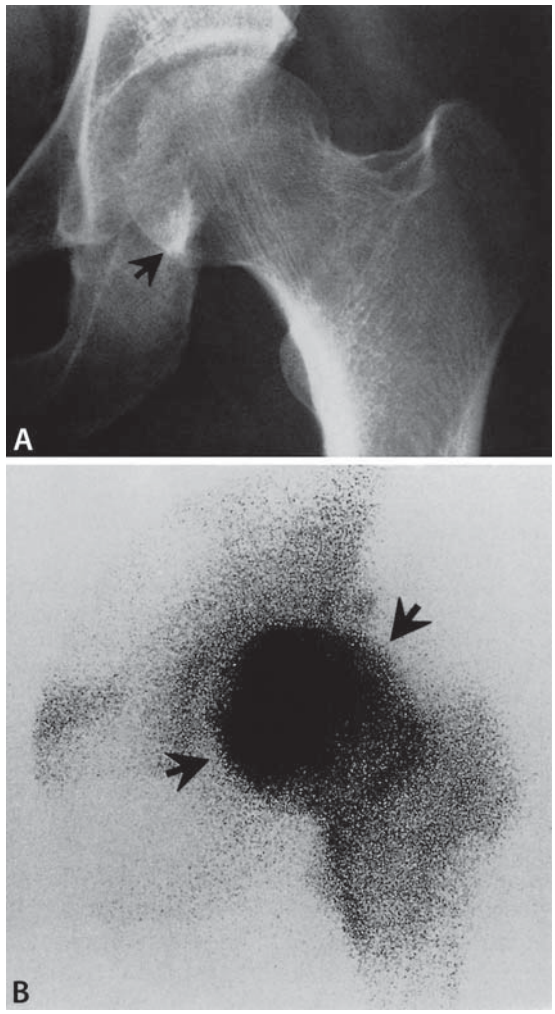

Fig. 14.15A, B Homogeneous tracer uptake in regional osteoporosis of the hip. **A** Anteroposterior radiograph of the painful left hip in a 30-year-old woman shows minimal osteopenia with trabecular coarsening in the femoral head (*arrow*). **B** Anterior pinhole scintigraph demonstrates extremely intense tracer uptake in the entire femoral head (*arrows*). Note well-preserved joint space and intact acetabulum

14.5 Transient Regional Osteoporosis

Two closely related types of transient regional osteoporosis have been described: transient osteoporosis of the hip and regional migratory osteoporosis. Classically, these two conditions have been dealt with as separate entities because of the difference between the involved site and the migratory nature of the latter disease. On the whole, however, the clinical, radiographic, and scintigraphic manifestations of these two diseases largely overlap, and their close kinship has been stressed (Naides et al. 1985). It therefore seems appropriate to discuss them together.

Clinically, both diseases show rapidly developing, painful osteoporosis in periarticular bones, without definite precipitating causes such as trauma or immobilization. The disease is self-limited and resolves spontaneously over a period from months to a year. Transient osteoporosis of the hip is usually unilateral, affecting men and women equally, with a predilection for the young and middle-aged. The onset is either abrupt or gradual, and pain becomes worse on weight bearing. On the other hand, regional migratory osteoporosis occurs in the periarticular bones of the knee, ankle, and foot and the humerus. As the term indicates, the painful lesions move from bone to bone. More than one bone may be involved at one time. This is also a disease of middle-age, and affects men more often than women.

Radiographically, transient osteoporosis of the hip shows progressive osteoporosis in the femoral head. Porosis is diffuse or zonal, the adjacent joint is uninvolved, and the subchondral bone plate is intact other than minimal thinning (Fig. 14.15A). The basic radiographic feature of regional migratory osteoporosis is identical with that of transient osteoporosis of the hip. The affliction is characteristically zonal (Fig. 14.16A), and MRI may demonstrate edema that coincides with porosis (Fig. 14.16B). The latter finding suggests the existence of a cause-and-effect relationship between bone marrow edema and transient or migratory osteoporosis as discussed below.

Pinhole scintigraphy is most suited for assessing the presence and extent of regional osteoporosis by observing tracer uptake, which is intense and homogeneous. The condition may be localized to the proximal humerus (Fig. 14.16C), proximal femur (Fig. 14.15B) or distal femur, and the proximal tibia or distal tibia (Fig. 14.9 C). Radiographically ambiguous

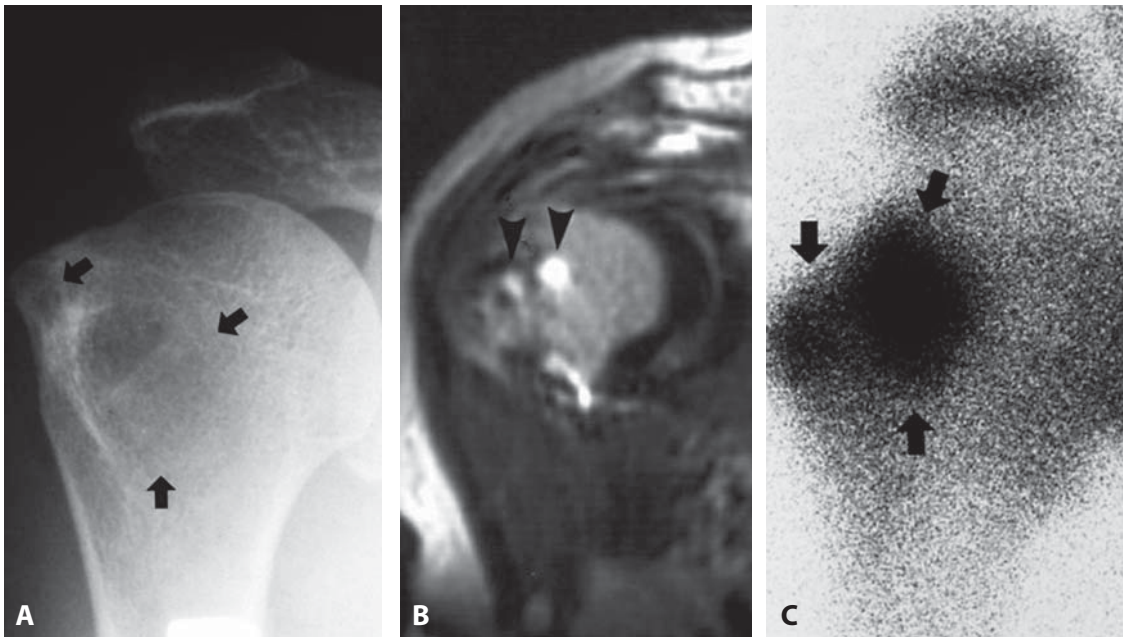

Fig. 14.16A–C Regional migratory osteoporosis. **A** Anteroposterior radiograph of the right shoulder with painful migratory porosis in a 55-year-old woman shows a roundish area of osteopenia localized to the humeral neck (*arrows*). **B** T2-weighted MRI reveals spotty areas of high signal intermixed with low signal marrow denoting edema (*arrowheads*). **C** Anterior pinhole scintigraph shows prominent tracer uptake exactly corresponding to the area of radiographic osteopenia (*arrows*)

focal osteoporosis, for example in the femoral neck, can also be sensitively detected by pinhole scanning (Fig. 14.17).

14.6 Transient Osteoporosis with Bone Marrow Edema

This condition has been proposed as a syndrome that is associated with osteoporosis (Wilson et al. 1988). These authors reported ten patients with hip or knee pain whose radiographs were either normal or minimally osteopenic at the diseased site. Bone scintigraphy showed increased tracer uptake, and MRI demonstrated decreased signal intensity on T1-weighted images and increased signal intensity on T2-weighted images, denoting hyperemia and edema. Clinical symptoms slowly resolved over a period of months and did not recur. In one case, intense uptake in the right femoral head returned to a near-normal state after 8 months. Marrow edema might be a coincidental process, but its association with regional osteoporosis cannot be denied. In essence, edema is a nonspecific response of marrow tissue to a variety of physical stresses or injuries (Moore et al. 1991), and is associated with an increased amount of extracellular water as a result of hyperperfusion (Wilson et al. 1988). Etiologically, bone edema has been related to a number of clinical conditions such as osteoporosis, RSD (Murphy and Totty 1986), and Legg-Calvé-Perthes disease (Bleumm et al. 1985). The other likely causes include contusion, infection, and primary or metastatic neoplastic disease (Moore et al. 1991).

Our experience indicates that pinhole scintigraphy is a valuable adjunct to the clinical study of this condition, displaying not only ominous lesions (Fig. 14.16) but also extremely subtle changes, which are radiographically invisible (Fig. 14.17). The tracer accumulated in this condition appears to be divided into two different components: the more intense central

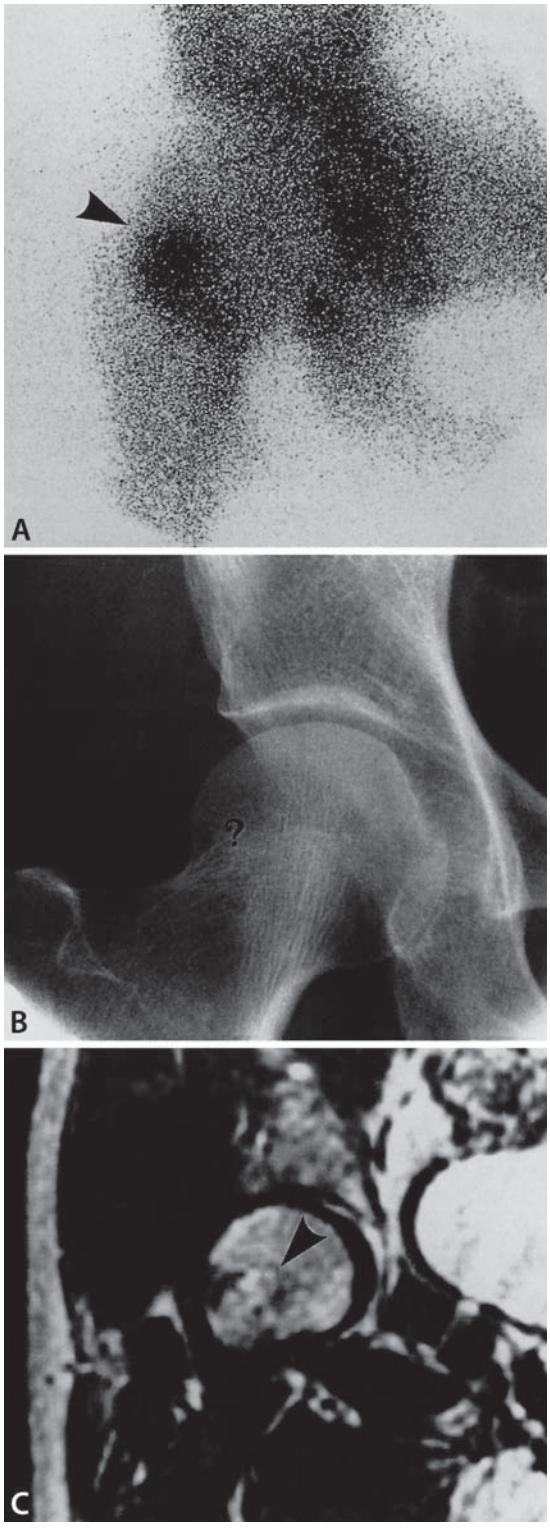

Fig. 14.17A–C Transient osteoporosis of the hip. **A** Anterior pinhole scintigraph of the painful right hip in a 57-year-old woman shows patchy, intense tracer uptake in the lateral aspect of the femoral neck (*arrowhead*). **B** Anteroposterior radiograph shows only equivocal osteopenia in the area in question (*?*). **C** T2-weighted coronal MRI reveals high signal intensity with a low-intensity rim in the base of the femoral head, corresponding to the scintigraphically "hot" area (*arrowhead*). On T1-weighted MRI the signal intensity of the lesion was low, denoting edema (not shown here)

uptake and the less intense peripheral or background uptake. Interestingly, our MRI correlation has indicated that the more intense uptake at the lesional center corresponds to edema that is represented by a bright signal on T2-weighted images while the less intense uptake in the periphery corresponds to extended reaction or the watershed phenomenon (Fig. 14.16).

14.7 Transient Indolent Bone Tracer Uptake

It is not uncommon to incidentally encounter prominent tracer uptake in the periarticular bones of the knee (Fig. 14.18), ankle, calcaneus (Fig. 14.19), and wrist (Fig. 14.20) on scintigraphs obtained for some other unrelated clinical reason. Such ominous uptake occurs without comparable radiographic alteration. Characteristically, the condition is asymptomatic or, if present, the symptoms may be trivial or unrelated. It seems transitory, probably appearing one day and disappearing over the next weeks or months. The nature and implication of this painless but often prominent uptake are not clear, although the possibility of either inherent vascular change or a focal response to unnoticed or trivial trauma might be a possibility.

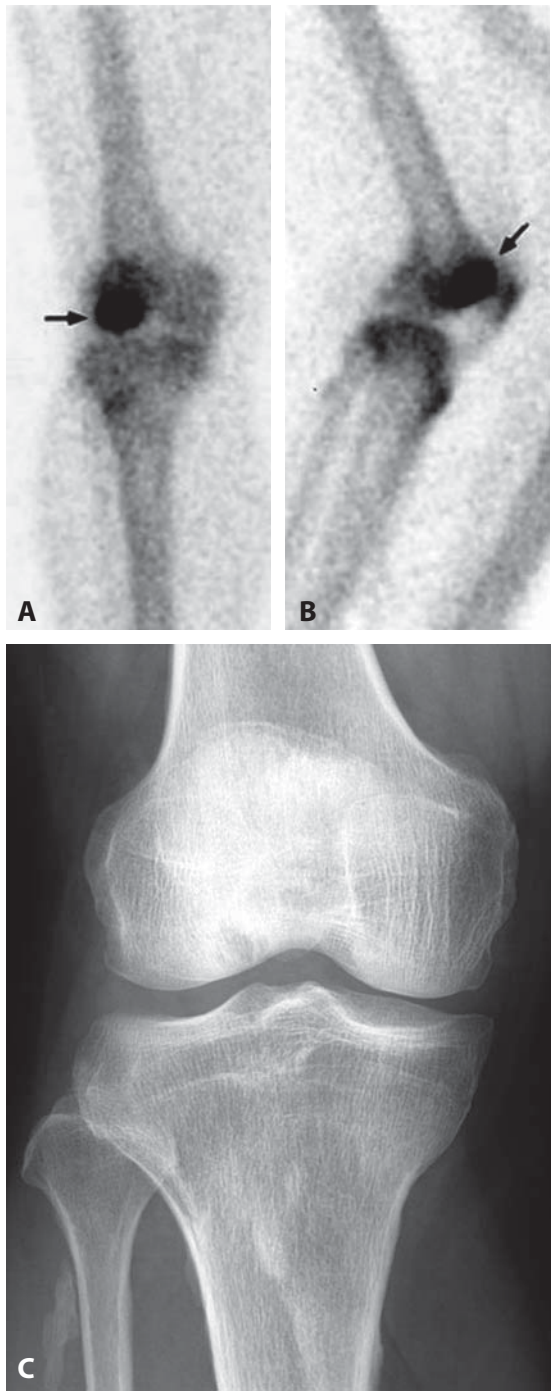

Fig. 14.18A–C Transient indolent bone tracer uptake in the knee. **A**, **B** Anterior and lateral scintigraphs of the right knee in a 76-year-old man show prominent tracer uptake confined to the lateral femoral condyle (*arrow*). The uptake was found incidentally during examination for a rib fracture and was completely asymptomatic. **C** Anteroposterior radiograph reveals no abnormality

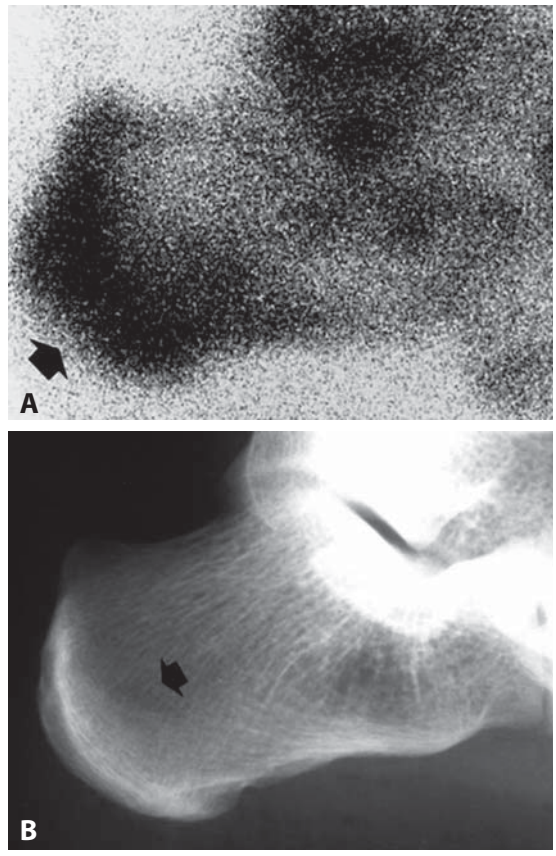

Fig. 14.19A, B Transient indolent tracer uptake in the calcaneus. **A** Lateral pinhole scintigraph of the left foot in a 31-year-old woman shows prominent tracer uptake in the retrocalcaneal surface (*arrow*). The uptake was found incidentally during examination for joint disease and was completely asymptomatic. **B** Lateral radiograph reveals no abnormality

14.8 Periostitis in Vascular Insufficiency

The periosteal bony proliferation associated with chronic vascular insufficiency in the lower limb is well known in radiology, and its scintigraphic version has been described (Gensburg et al. 1988). Pathogenetically, the phenomenon has been explained on the basis of hypoxia caused by venous congestion or arterial insufficiency (Lovell and Scott 1956). Some authors hold the infection in the concurrent trophic

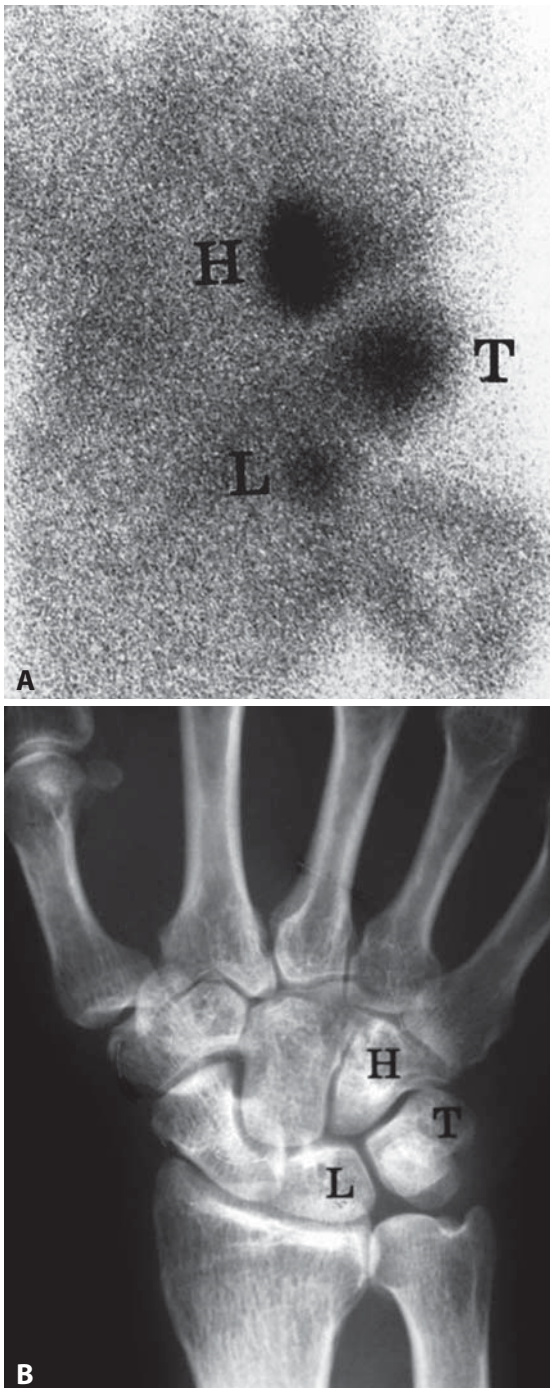

Fig. 14.20A, B Transient indolent tracer uptake in the carpal bones. **A** Dorsocarpal pinhole scintigraph of the right wrist in a 67-year-old man shows prominent tracer uptake in the hamate (*H*), triquetral (*T*), and lunate (*L*) bones. The uptake was found incidentally during examination of another part of the body and was completely asymptomatic. **B** Dorsocarpal radiograph reveals no abnormality (*H* hamate, *T* triquetral, *L* lunate)

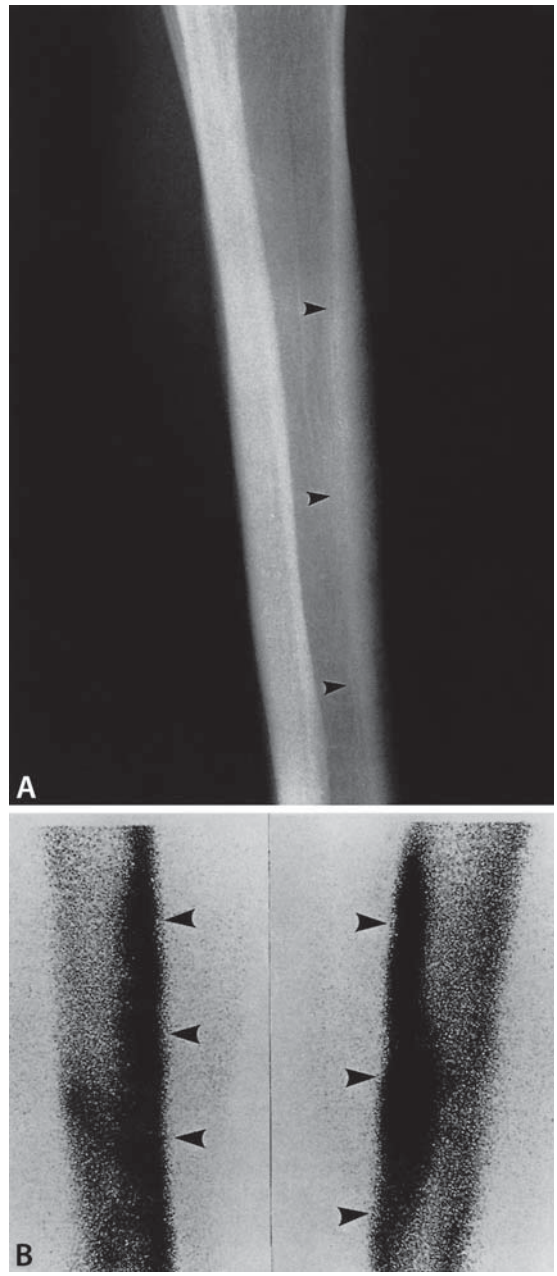

Fig. 14.21A, B Periostitis in Burger's disease. **A** Anteroposterior radiograph of the right tibial shaft in a 24-year-old man with longstanding Burger's disease reveals diffusely thickened cortex with blurred endosteal border (*arrowheads*). **B** Anterior pinhole scintigraphs of both midtibial shafts (separate acquisitions) show band-like intense tracer uptake in the medial aspect (*arrowheads*). The uptake encroaches upon the marrow space, denoting endosteal involvement in addition to periostitis

cutaneous ulceration to be responsible, but it is not essential. We have been able to document a case of diffuse periostitis in both tibiae in a patient with longstanding Bürger's disease (arteritis obliterans). The skin was entirely free of pathology in this case, supporting the view that the periostitis of this sort is not necessarily preceded by a skin lesion but is more likely associated with hypoxia from arterial obliteration.

The radiographic features are characterized by diffuse periosteal new bone formation along the shafts of the tibia and fibula. Periosteal ossification may be lamellated, lacy, or undulating, and eventually blends imperceptibly into the underlying cortex (Fig. 14.21A), and such findings are basically not dissimilar to those observed in secondary hypertrophic osteoarthropathy (Fig. 12.24).

Scintigraphy reveals diffusely increased tracer uptake in the shafts of the tibias and fibulas. The involvement is bilateral and symmetrical. Pinhole scintigraphy localizes the uptake specifically to the thickened periosteums. The endosteums are also involved, showing prominent tracer uptake that encroaches upon the marrow space (Fig. 14.19B).

References

Apley AG, Wientroub S (1981) The sagging rope sign in Perthes' disease and allied disorders. J Bone Joint Surg Br 63:43–47

Bahk YW, Chung SK, Park YH, et al (1998) Pinhole SPECT imaging in normal and morbid ankles. J Nucl Med 39:130–139

Bleumm RG, Flake THM, Ziedes des Plantes, et al (1985) Early Legg-Perthes disease (ischemic necrosis of the femoral head) demonstrated by MRI. Skeletal Radiol 14:95–98

Clarke NMP, Harrison MHM, Keret D (1983) The sagging rope sign: a critical appraisal. J Bone Joint Surg Br 65:285–287

Ficat RP, Arlet J (1980) Ischemia and bone necrosis. Williams & Wilkins, Baltimore

Genant HK, Kozin E, Beckerman C, et al (1975) The reflex sympathetic dystrophy syndrome. A comprehensive analysis using fine-detail radiography, photon absorptiometry and bone and joint scintigraphy. Radiology 117:21–32

Gensburg RS, Kawashima A, Sandler CM (1988) Scintigraphic demonstration of lower extremity periostitis secondary to venous insufficiency. J Nucl Med 29:1279–1282

Helms CA, O'Brien ET, Katzberg RW (1980) Segmental reflex sympathetic dystrophy syndrome. Radiology 135:67–68

Hohmann EL, Elde RP, Rysavy JA, et al (1986) Innervation of periosteums and bone by sympathetic vasoactive intestinal peptide-containing nerve fibers. Science 232:868–871

Jones JP (1971) Alcoholism, hypercortisonism, fat embolism and osseous avascular necrosis. In: Zim WM (ed) Idiopathic ischemic necrosis of the femoral head in adults. Georg Thieme, Stuttgart, pp 112–132

Jones JP Jr (2001) Alcoholism, hypercortisonism, fat embolism and osseous avascular necrosis. Clin Orthop Relat Res 393:4–12

Kim SH, Chung SK, Bahk YW, et al (2003) ^{99m}Tc-HDP pinhole SPECT findings of foot reflex sympathetic dystrophy: radiographic and MRI correlation and a speculation about subperiosteal bone resorption. J Korean Med Sci 18:707–714

Kozin E, Soin JS, Ryan LM, et al (1981) Bone scintigraphy in the reflex sympathetic dystrophy syndrome. Radiology 138:437–443

Lorente de No R (1938) Analysis of the activity of the chains of internuncial neurons. J Neurophysiol 1:207–244

Lovell RPH, Scott GBD (1956) Hypertrophic osteoarthropathy in polyarteritis. Ann Rheum Dis 15:46–50

Moore SG, Bisset GS III, Siegel MJ, et al (1991) Pediatric musculo-skeletal MR imaging. Radiology 179:345–360

Murphy WA, Totty WG (1986) Musculoskeletal magnetic resonance imaging. In: Kressel HY (ed) Magnetic resonance annual. Raven, New York

Naides SJ, Resnick D, Zvaifler NJ (1985) Idiopathic regional osteoporosis: a clinical spectrum. J Rheumatol 12:763–768

Patterson RJ, Bickel WH, Dahlin DC (1964) Idiopathic avascular necrosis of the head of the femur. J Bone Joint Surg Am 46:267–282

Resnick D, Niwayama G (1988) Pathogenesis of osteonecrosis. In: Resnick D, Niwayama G (eds) Diagnosis of bone and joint disorders, 2nd edn. Saunders, Philadelphia

Wilson AJ, Murphy WA, Hardy DC, et al (1988) Transient osteoporosis: transient bone marrow edema? Radiology 167:757–760

15 Metabolic Bone Diseases and Drug-Induced Osteoporosis

Bone scintigraphy has traditionally been considered to be not as useful as radiography in the study of metabolic bone diseases including senile or postmenopausal osteoporosis, osteodystrophy, drug-induced osteoporosis, and rickets and osteomalacia. However, aided by the pinhole technique, ^{99m}Tc-MDP bone scintigraphy has been shown to be able to portray characteristic features in systemic and local osteoporosis or osteopenia, which is defined as a state of reduced bone mass with increased cavity. Rickets and osteomalacia, a state of deficient formation of inadequately mineralized osteoid, can also be efficiently diagnosed by bone scintigraphy. Indeed, it is well known that bone scintigraphy is highly sensitive and reli-

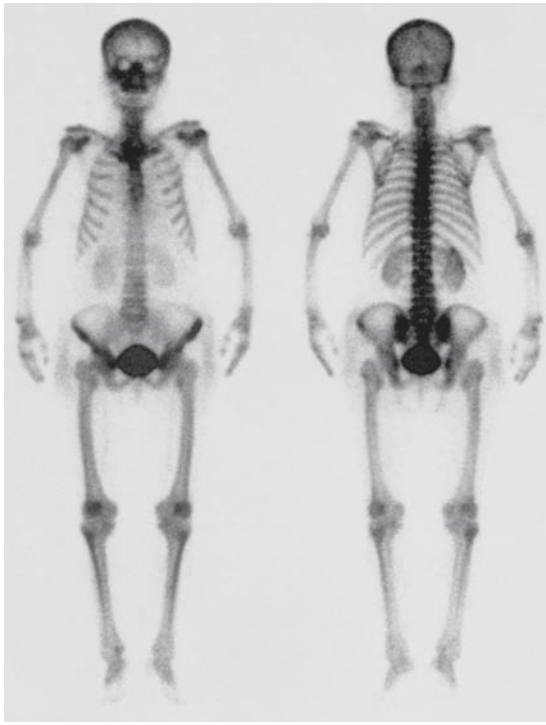

Fig. 15.1 Usefulness of whole-body bone scintigraphy in the study of systemic osteoporosis. Anterior (*left*) and posterior (*right*) whole-body scans in a 78-year-old woman with advanced osteoporosis show generally diminished skeletal uptake

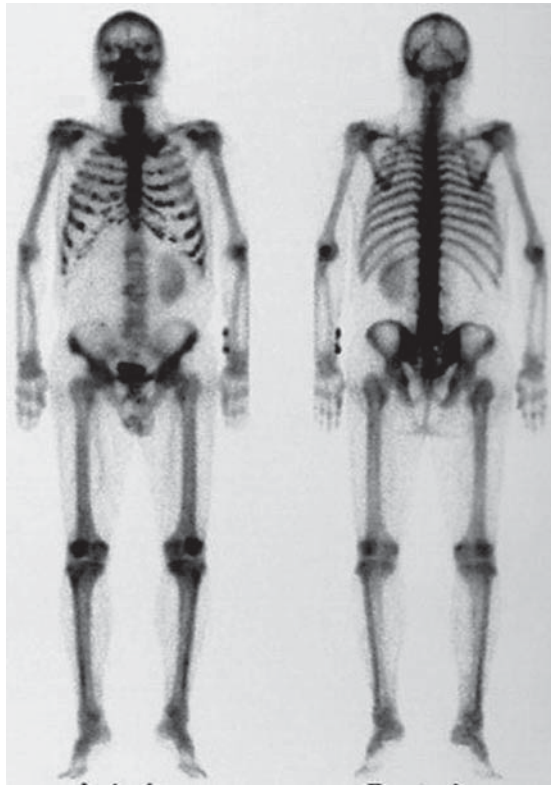

Fig. 15.2 Usefulness of whole-body bone scintigraphy in osteomalacia. Anterior (*left*) and posterior (*right*) whole-body scans in a 77-year-old man with primary hyperparathyroidism show generally increased skeletal uptake due to osteodystrophy with avaricious tracer uptake. Note well-functioning left kidney

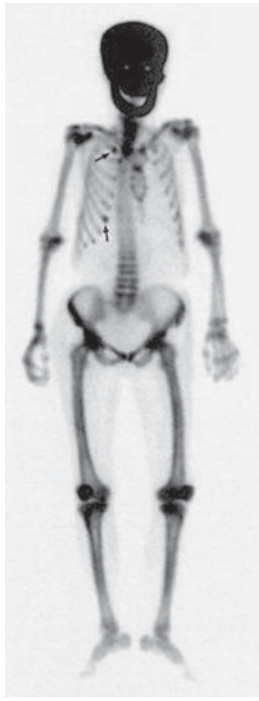

Fig. 15.3 Renal osteodystrophy. Anterior whole-body bone scintigraphy in a 73-year-old woman with end-stage renal failure and congestive heart failure shows generally increased tracer uptake with the most prominent uptake occurring in the skull. Note that both kidneys are not visualized and ribs are fractured (*arrows*)

able for detecting fractures and infractions in porosis and Looser's zone (pseudofracture, osteoid seam) in osteomalacia, which often defy radiographic diagnosis when pathological changes are extensive. In addition and importantly, refined whole-body scintigraphy can uniquely demonstrate systemic involvement pattern of porosis and malacia. For example, whole-body scintigraphy shows generally decreased bone uptake in postmenopausal and senile osteoporosis (Fig. 15.1), increased tracer uptake in osteodystrophy of primary hyperparathyroidism with visualized kidneys (Fig. 15.2), increased tracer uptake in renal osteodystrophy without visualized kidneys (Fig. 15.3), and decreased tracer uptake in hepatic osteodystrophy (Fig. 15.4). Such valuable information can easily be extracted from a pair of anterior and posterior views, which are routinely obtainable at no additional expense.

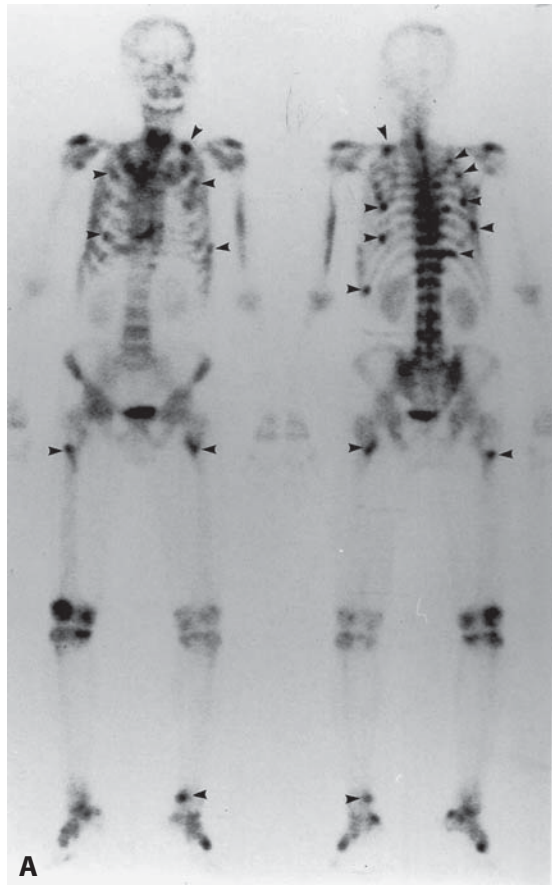

Fig. 15.4A, B Hepatic osteodystrophy with systemic osteoporosis. **A** Anterior (*left*) and posterior (*right*) whole-body bone scans in a 60-year-old man with alcoholic hepatopathy shows generalized low uptake with numerous bone infractions (*arrowheads*). **B** Anterior radiograph of the pelvis reveals a typical infraction in the lateral cortex of the right proximal femoral shaft (courtesy of Dr. H. Ohta, Department of Radiology, Osaka Medical School, Japan)

Metabolic bone diseases result from a number of etiologies including endocrine disorders, renal and hepatic failure, disturbed calcium-phosphorus metabolism, and vitamin C and D deficiency or D excess, and general under nourishment. The clinical entities of metabolic bone diseases are diverse, and symptoms and signs are complex. The present discussion is confined to (a) the involutional (senile and postmenopausal) osteoporosis, (b) disuse and immobilization osteoporosis, (c) osteodystrophy associated with primary and secondary hyperparathoidism, (d) drug-induced osteoporosis, and (e) osteomalacia and rickets since these conditions are considered to be more common and can be easily approached diagnostically by radiography and scintigraphy. Regional osteoporosis related to hypervascularity and disuse have already been given full and partial accounts in the foregoing sections.

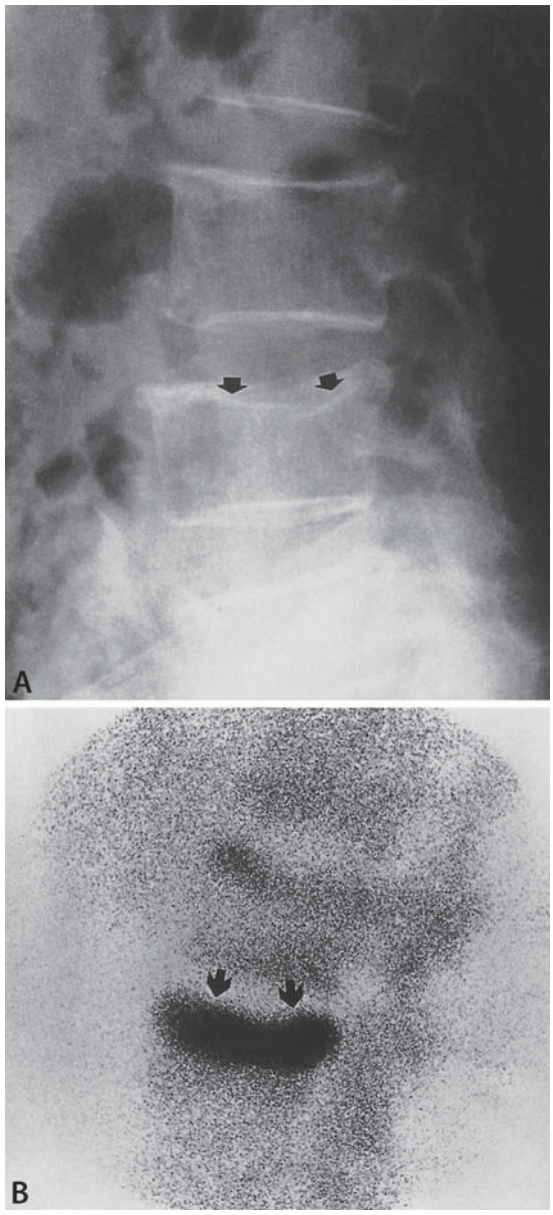

Fig. 15.5A, B Involutional osteoporosis. **A** Lateral radiograph of the midlumbar spine in a 55-year-old woman reveals generalized porosis and the classic "pencil line" vertebral contour and compression fracture in the upper endplate of the L3 vertebra (*arrows*). **B** Lateral pinhole scintigraph portrays arcuate, intense tracer uptake in the upper endplate of the L3 vertebra (*arrows*). Observe the generalized low tracer uptake in the porotic spine, producing the "pale vertebra" sign

15.1 Involutional Osteoporosis

Involutional osteoporosis includes senile osteoporosis and postmenopausal osteoporosis. The reported incidences vary according to the diagnostic method used and the population studied. One radiographic study of spinal osteoporosis in a series of ambulatory women aged between 45 and 79 years recorded an incidence of 29% (Smith et al. 1960). Most recent studies have indicated a prevalence of 50% in women and 20% in men in their late seventies (Fujiwara 2004) and 11.4% in women of 50 years or older and 1.6% in men of the same age group (Yang et al. 2006).

Osteoporosis reflects the state of bone mass reduction that makes the bone brittle and fragile. Postmenopausal osteoporosis typically affects women in the sixth and seventh decades of life. In addition to reduced estrogen level, lowered physical activity and nutritional state are related to this condition. Histologically, involutional osteoporosis is characterized by a disproportionate reduction of the trabecular bone mass compared to cortical bone mass, whereas senile osteoporosis shows a proportionate reduction of both the cortical and trabe-

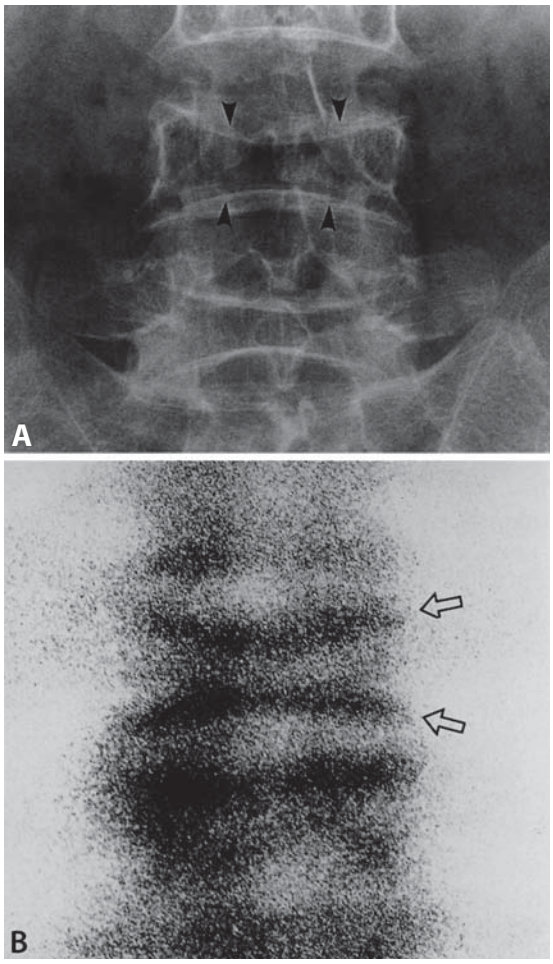

Fig. 15.6A, B Spinal osteoporosis with "fish vertebra" deformity and compression fracture. **A** Anteroposterior radiograph of the lower lumbar spine in a chronically bedridden 35-year-old woman shows generalized porosis and "fish vertebra" deformity in the L4 and L5 vertebrae (*arrowheads*). **B** Posterior pinhole scan of the midlumbar spine in another elderly woman with a similar porosis and "fish vertebra" deformity shows minimally increased tracer uptake in "fish vertebra" deformity of the L3 vertebra (*open arrows*)

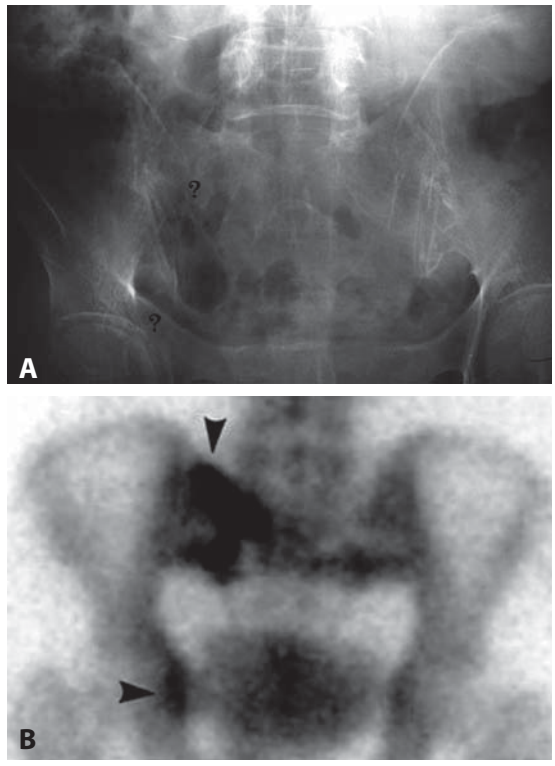

Fig. 15.7A, B Cryptic fractures in severe osteoporosis. **A** Anteroposterior radiograph of the pelvis in a 75-year-old woman with marked osteoporosis and fractures shows "blackening" of bones preventing the diagnosis of fractures (*?*). **B** Posterior bone scintigraph reveals low bone uptake due to porosis, and two localized areas of intense uptake in the left sacroiliac joint and ischial tuberosity denoting fractures (*arrowheads*)

cular bone. The most common and problematic complication of involutional osteoporosis is the spinal and distal radial fractures. The femoral neck, proximal humerus, tibia, and pelvis are other common sites.

Radiographically, osteoporosis manifests as increased radiolucency and graying of bone which shows thin, sparse trabeculae and slim, deficient cortices. In the spine, the porotic vertebrae may present the characteristic "pencil-line contour" sign (Fig. 15.5A) and frequently the "fish vertebra" deformity (Fig. 15.6A). Compression fracture with kyphosis is a hallmark of menopausal osteoporosis.

Scintigraphically, unlike markedly increased tracer uptake in transient osteoporosis, senile or postmenopausal osteoporosis is characterized by decreased uptake due to sharply reduced bone turnover (Fig. 15.1). Understandably, the subjective visual assessment of osteoporosis is inaccurate. More often than not, however, pinhole scintigraphy reveals the thinned cortices of long bones and vertebrae to be indistinct. This finding, arbitrarily termed the "pale bone"

sign, reflects deficient tracer uptake in osteopenia (Fig. 15.5B). When a porotic vertebral endplate is fractured tracer uptake becomes markedly intensified, distinctly standing out against the pale bones behind. The porotic lumbar vertebrae with either concave or biconcave endplates, the "fish vertebra" deformity, may also accumulate tracer, but the uptake is usually not so intense (Fig. 15.6B). Indeed, the intensity of tracer uptake in these two radiographically similar conditions clearly differs so that bone scintigraphy can discriminate one condition form the other. In general, fractures in the porotic bones and infractions (Looser's zone) in the malacic bones such as the spine and pelvis are extremely difficult to detect by radiographic examination, but such a problem can easily be solved with the use of bone scintigraphy (Figs. 15.4, 15.7).

15.2 Disuse and Immobilization Osteoporosis

Bone is not a mere lazy weight-bearing or protective scaffold for the body, but is day and night engaged with modeling and remodeling through the active physicochemical and metabolic activities of osteoblasts and osteoclasts. Appropriate physical stress and strain are essential for maintaining such homeostatic functions in an orderly state. Thus, disuse and immobilization may result in mobilization of the calcium stored in bone, leading to osteoporosis due to a negative balance with its level in the serum and urine sensitively changing. Osteoporosis may appear before 5–7 weeks in those under the age of 20 years and those over 50 years, and more commonly after 8 weeks of immobilization (Jones 1969). The pathogenetic basis for decreased bone production and increased bone resorption have been debated, although Heaney (1962) demonstrated in a radiocalcium study that both bone resorption and formation are increased, but with more resorption than formation.

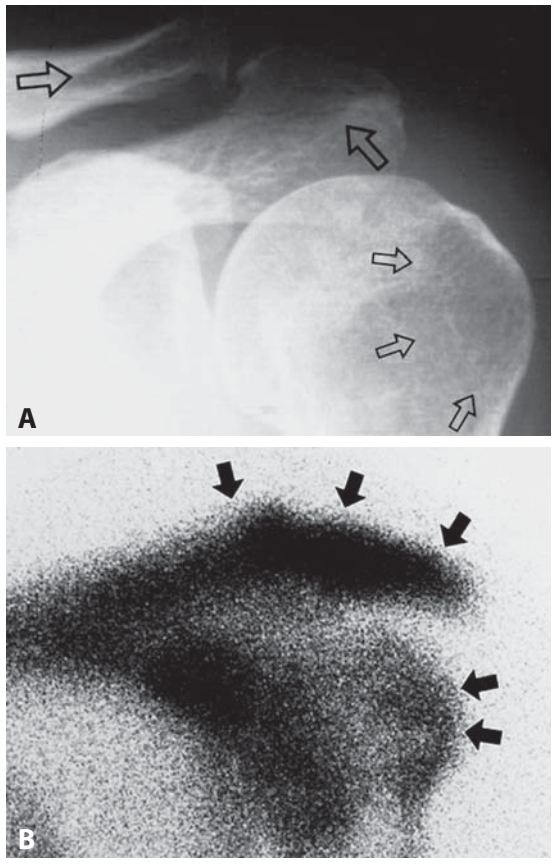

Fig. 15.8A, B Immobilization osteoporosis. **A** Anteroposterior radiograph of the left shoulder girdle in a 48-year-old woman with disuse after mastectomy for breast cancer shows diffusely "washed out" regional bones (*open arrows*). **B** Anterior pinhole scintigraph reveals intense tracer uptake in porotic bones (*arrows*)

Radiographically, osteoporosis is characterized by graying of bone which has a washed-out appearance that is generalized, diffuse, regional, or local in occurrence (Fig. 15.8A), and its pattern is homogeneous, band-like, or streaky and speckled. The trabeculae are coarsened and the cortex becomes pencil-lined, lamellated, or scalloped (Fig. 15.9A).

Scintigraphic findings vary according to the duration, severity, extent, and type of osteoporosis and the age of the patient, and this diversity seems to reflect the varied nature of the pathogenesis. Generally, however, senile or postmenopausal porosis (Fig. 15.1) and long-standing immobilization porosis (Fig. 15.9B)

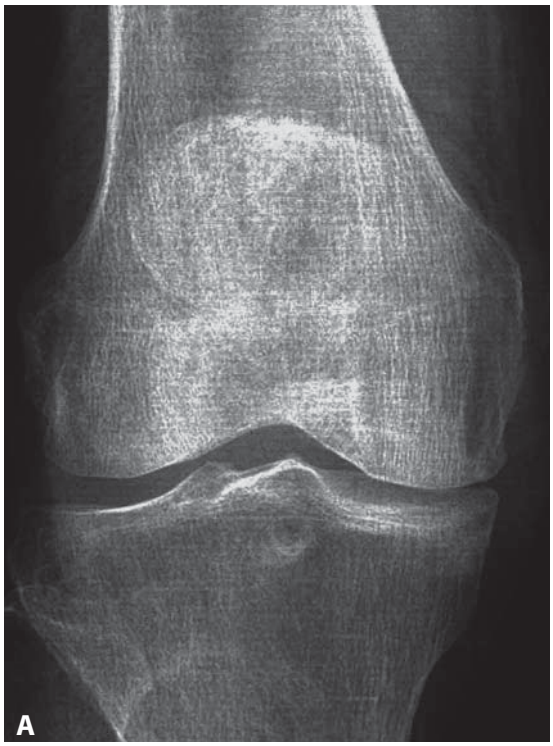

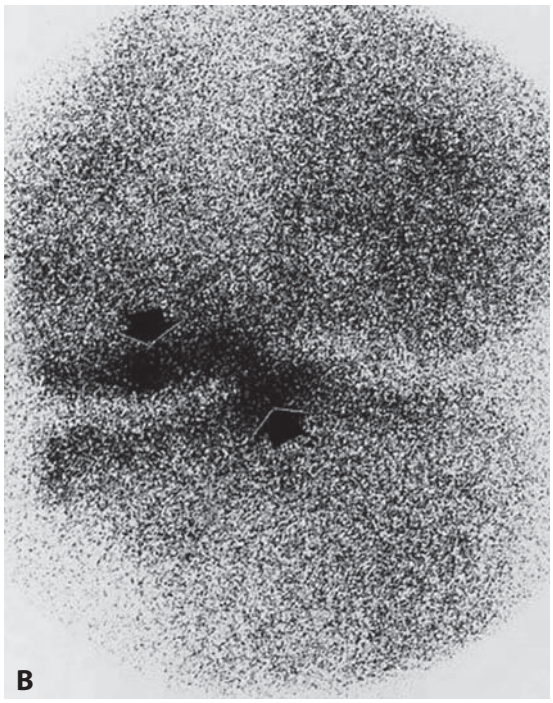

Fig. 15.9A, B Disuse osteoporosis. **A** Anteroposterior radiograph of the immobilized right knee in a 48-year-old woman due to osteoarthritis shows porosis with coarsened trabeculae and pencil-line cortex. No radiographic arthritic change is seen. **B** Anterior pinhole scintigraph reveals coarse speckled tracer uptake of porosis and zonal uptake of early osteoarthritis (*arrows*)

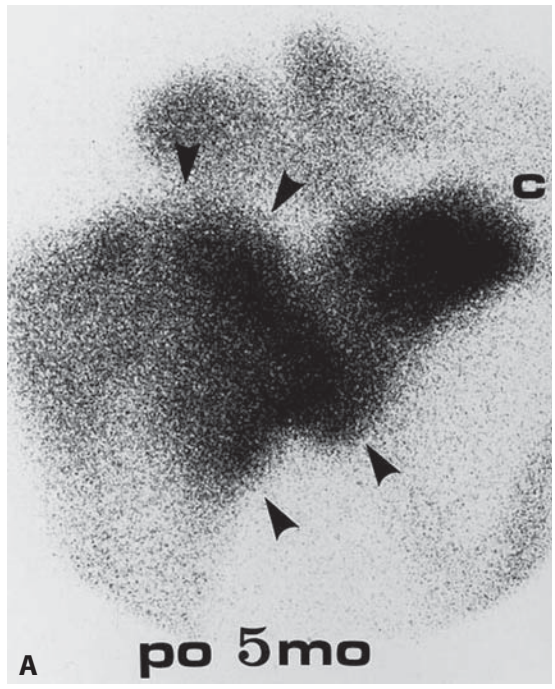

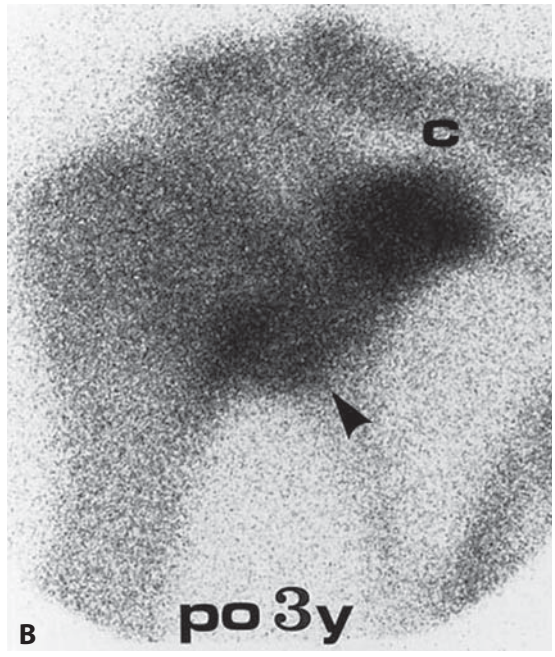

Fig. 15.10A, B Normal return of tracer uptake in disuse osteoporosis. **A** Initial anterior pinhole scintigraph of the right shoulder in a 48-year-old woman with local porosis caused by months of immobilization following ipsilateral mastectomy shows intense tracer uptake in the glenohumeral joint bones (*arrowheads*). **B** Follow-up scintigraph taken 3 years later reveals nearly normalized bone uptake (*arrowhead*) (*c* coracoid process)

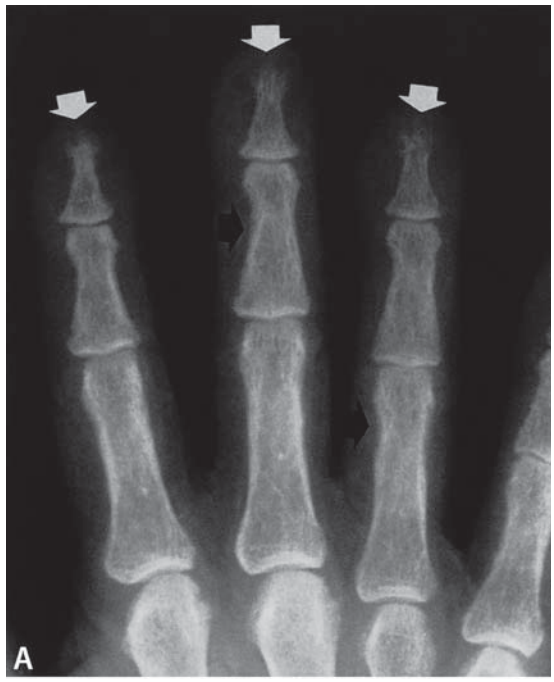

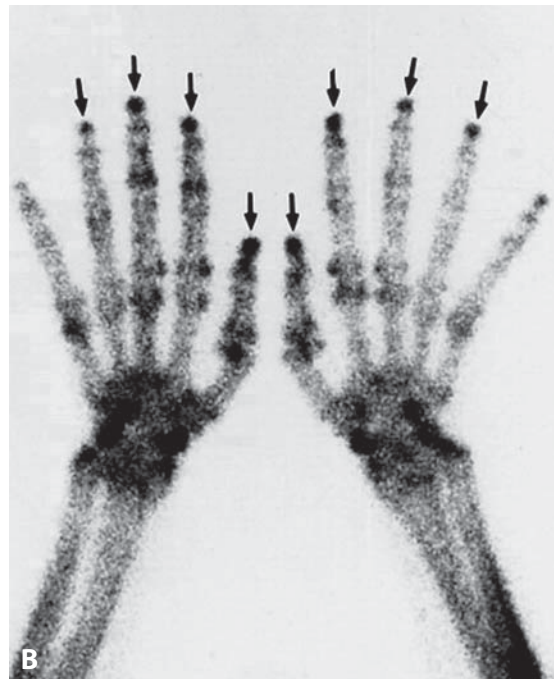

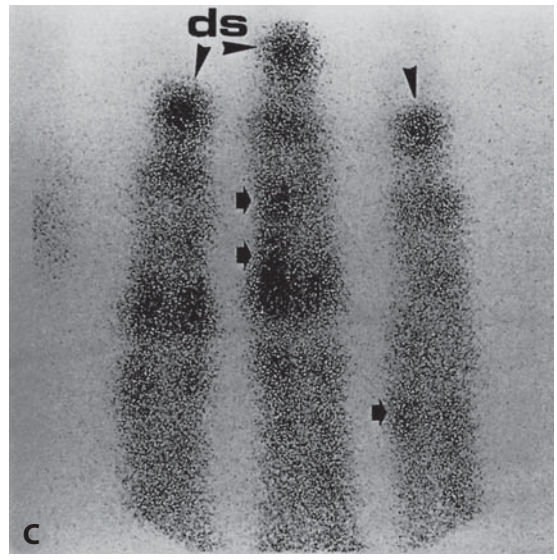

Fig. 15.11A–C Acrolysis and subperiosteal bone resorption in hyperparathyroidism. **A** Dorsopalmar radiograph of the right hand in a 56-year-old man with parathyroid adenoma shows generalized osteopenia with acrolysis (*white arrows*) and lacy subperiosteal bone resorption (*black arrows*). **B** High-resolution planar scintigraph of the hands demonstrates prominent tracer uptake in lysed tufts (*arrows*) and diffusely increased granular bone uptake in the phalangeal shafts. **C** Dorsal pinhole scintigraph shows diffuse granular uptake in phalangeal bones with peculiar uptake in the tufts (*arrowheads*) and subperiosteums (*arrows*). The tufts are clubbed giving rise to a "drumstick" appearance (*ds*)

do not intensely accumulate tracer and, conversely, relatively acute and localized porosis observed in young and middle-aged patients shows prominent tracer uptake (Fig. 15.8B). The increased tracer uptake in regional or localized disuse porosis may slowly return to normal with active reuse (Fig. 15.10).

15.3 Osteodystrophy Associated with Hyperparathyroidism and Brown Tumor

Osteodystrophy associated with hyperparathyroidism is a well-established clinicopathological entity of radiographic and scintigraphic interest. Hyperparathyroidism may be classified into the primary, secondary, or tertiary form. The primary type results from increased parathormone production with resultant excessive bone calcium mobilization. The etiology includes adenoma (75%), hyperplasia, and carcinoma. This is a disease of middle-age and older, and women are affected twice as frequently as men. The common clinical symptoms are primarily due to hypercalcemia, including

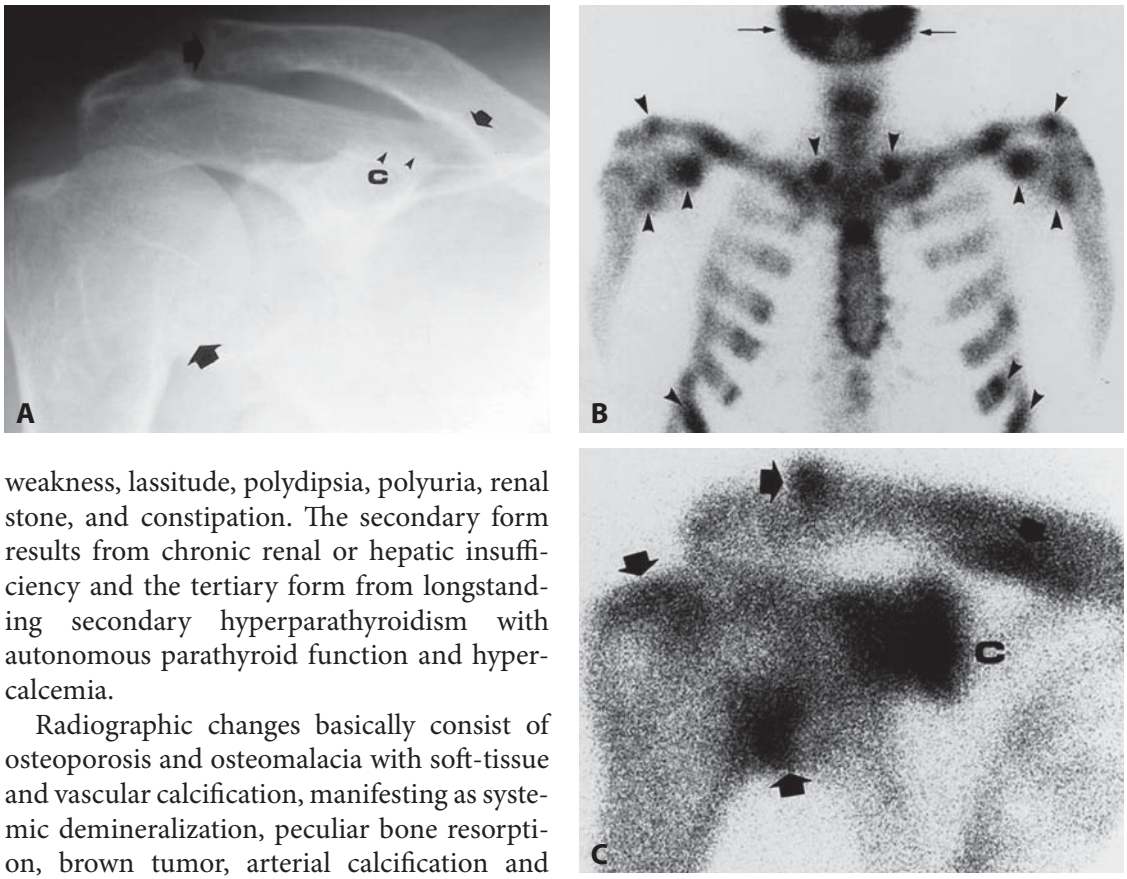

Fig. 15.12A–C Subchondral and subligamental bone resorption in hyperparathyroidism. **A** Anteroposterior radiograph of the right shoulder girdle in a 50-year-old man with primary hyperparathyroidism shows areas of subchondral bone resorptions in the acromioclavicular joint (*upper arrow*), medial glenohumeral joint (*lower arrow*) and coracoclavicular ligament (*c*). **B** Anterior planar scintigraph reveals areas of increased tracer uptake in the mandible, clavicles, coracoid processes, glenohumeral joints, and ribs bilaterally (*arrowheads*). The "hot" areas in the lower ribs represent infraction. **C** Anterior pinhole scintigraph shows tracer uptake in the lateral clavicular end, conoid ligament attachment (*upper arrow*), greater tuberosity, glenohumeral joint (*lower arrow*) and coracoid process (*c*)

weakness, lassitude, polydipsia, polyuria, renal stone, and constipation. The secondary form results from chronic renal or hepatic insufficiency and the tertiary form from longstanding secondary hyperparathyroidism with autonomous parathyroid function and hypercalcemia.

Radiographic changes basically consist of osteoporosis and osteomalacia with soft-tissue and vascular calcification, manifesting as systemic demineralization, peculiar bone resorption, brown tumor, arterial calcification and chondrocalcinosis. Bone resorption occurs in the subperiosteums, cortices, endosteums, and trabeculae and underneath the articular cartilages and ligaments. Of these, subperiosteal bone resorption with a lace-like change in the long bone is pathognomonic. Osteopenia, quantitatively assessed using bone densitometry, may widely vary in grade according to the severity and duration of the illness. Mild to moderate osteopenia in the early stage is difficult to diagnose by radiography, but advanced osteopenia manifests as a generalized decrease in bone mineral density with ground-glass-like change and the "salt-and-pepper" sign in the cranium. Subperiosteal bone resorption occurs most typically in the radial aspect of the phalangeal shafts as well as the tufts (Fig. 15.11A) and the tibia. Intracortical bone resorption creates small ovoid or cigar-shaped lucencies. Subchondral bone resorption may occur in the sacroiliac joints, symphysis pubis, diskovertebral joints, acromioclavicular joints, sternoclavicular joints, and glenohumeral joints (Fig. 15.12A). Another important feature is subligamentous bone resorption in the trochanters, ischial and humeral tuberosities, and coracoclavicular ligamentous insertion (Fig. 15.13A).

Brown tumors may occur both in primary and secondary hyperparathyroidism. Histolo-

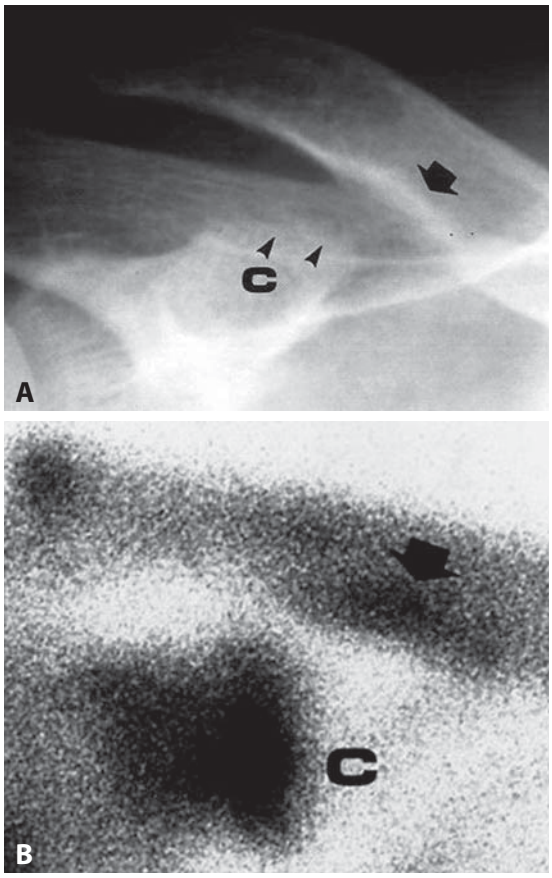

Fig. 15.13A, B Typical subligamental bone resorption in hyperparathyroidism. **A** Close-up radiograph of the right coracoconoid ligament attachments shown Fig. 13.12 shows areas of subligamental bone resorption at the conoid tubercle (*arrow*) and the coracoid process (*c*). **B** Close-up pinhole scintigraph reveals well-defined areas of conspicuous tracer uptake at the conoid tubercle (*arrow*) and the coracoid process (*c*)

gically, the tumors consist of osteoclasts, fibrosis, and giant cells, and are prone to involve the facial bones, ribs, femora, and pelvic bones. We have documented a case of multiple brown tumors in a patient on chronic hemodialysis with renal osteodystrophy. The cystic tumors were seen in the proximal femur and inferior ischial ramus (Gomez et al. 2003) (Fig. 15.14A). The loss of the lamina dura is also an important finding, although not specific.

Scintigraphically, the intensity of tracer uptake in primary hyperparathyroidism appears

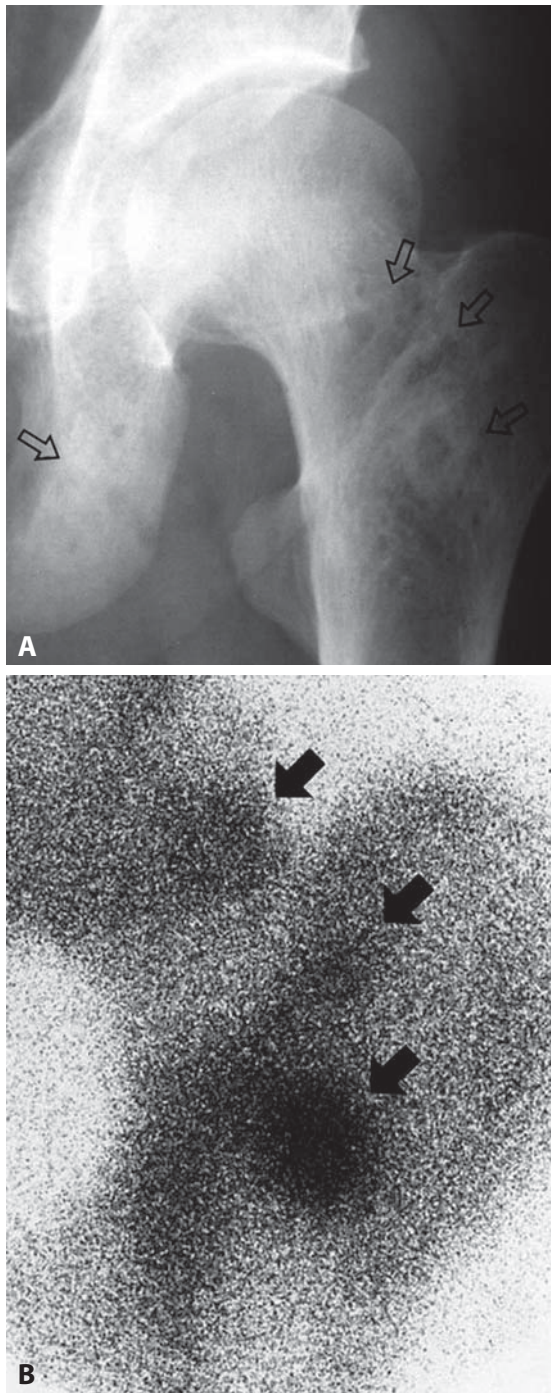

Fig. 15.14A, B Combined cystic brown tumors and sclerosis in hyperparathyroidism. **A** Anteroposterior radiograph of the left hip in a 49-year-old woman with hyperparathyroidism secondary to chronic renal failure shows multiple cystic brown tumors (*right open arrows*) and sclerosis (*left open arrow*). **B** Anterior pinhole scintigraph reveals multiple areas of intense uptake (*arrows*)

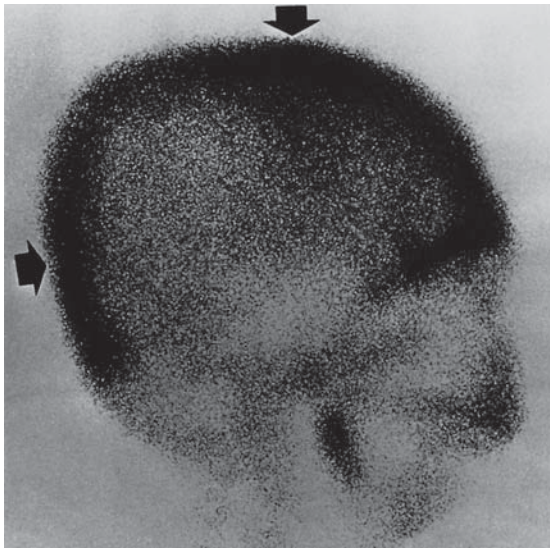

Fig. 15.15 Scintigraphic manifestation of the "salt-and-pepper" sign of the skull in hyperparathyroidism. Lateral pinhole scintigraph of the skull of the same patient as in Fig. 15.11 shows coarsely granular, increased tracer uptake throughout the whole cranium (*arrows*). Compare with the normal skull (Fig. 4.3A)

to correlate with the severity of radiographic bone change, ranging from apparently normal to intense uptake. High-resolution scintigraphy may reveal the drum-stick sign in the acrolysis of the fingers (Fig. 15.11B) and plaque-like uptake in subperiosteal bone resorption, typically in the radial aspect of the phalangeal shafts (Fig. 15.11C); these two findings are pathognomonic of hyperparathyroidism osteodystrophy. The calvaria, mandible, sternum, and shoulder bones show increased uptake (Sy 1974) (Fig. 15.12B, C). Another important change is subligamentous bone resorption indicated by tracer accumulation, for example, in the under surface of the lateral part of the clavicle and the tip of the coracoid process, which are the insertion sites of the coracoclavicular ligament (Fig. 15.13B). Brown tumors show increased tracer uptake, the intensity of which appears to vary according to the type of tumor: the radiographically lucent cystic type accumulates tracer less intensely than the partially mineralized one does (Fig. 15.14B). On the other hand, the magnified scan resolves the cranial uptake into two different components: intense uptake in the periphery of the skull scanned in profile and coarsely granular uptake spread diffusely in the central area of the skull scanned en face (Fig. 15.15). The latter finding appears to be the scintigraphic mirror image of the well-known radiographic "salt-and-pepper" sign.

15.4 Drug-Induced Osteoporosis

Steroids, heparin, and methotrexate are well-known osteoporosis-inducing drugs. Of these, steroids cause osteoporosis by decreasing bone formation through the inhibition of osteoblast formation and by increasing bone resorption through either direct stimulation of osteoclasts or increasing parathormone release (Sambrook and Jones 1995). The hypercortisonism of Cushing's disease (endogenous and exogenous) also causes systemic osteoporosis. The daily administration of heparin in doses larger than 15,000 units has been reported to lead to osteoporosis in patients with myocardial infarction, thrombophlebitis, pulmonary emboli, or cerebral thrombosis (Griffith et al. 1965). A pathological study of biopsied bone from heparin-induced osteoporosis by Megard et al. (1982) demonstrated severe osteoporosis with rarefied spongy bone and increased osteoclasts and decreased osteoblasts. Unfractionated heparin causes symptomatic spinal fractures in up to 3% of patients on long-term treatment and osteopenia in 30% (Hawkins and Evans 2005). In addition, these authors reported that low molecular weight heparin reduces the risk of osteoporosis and spinal fractures. Methotrexate is another medicine that may lead to iatrogenic osteoporosis (Mazanec and Grisanti 1989). It is used for the therapy of a wide variety of diseases including breast carcinoma, acute lymphocytic leukemia in children (Schwartz and Leonidas 1984), rheumatoid arthritis (Maenaut et al. 1997), systemic lupus erythematosus, psoriasis, and scleroderma (Singwe et al. 1998).

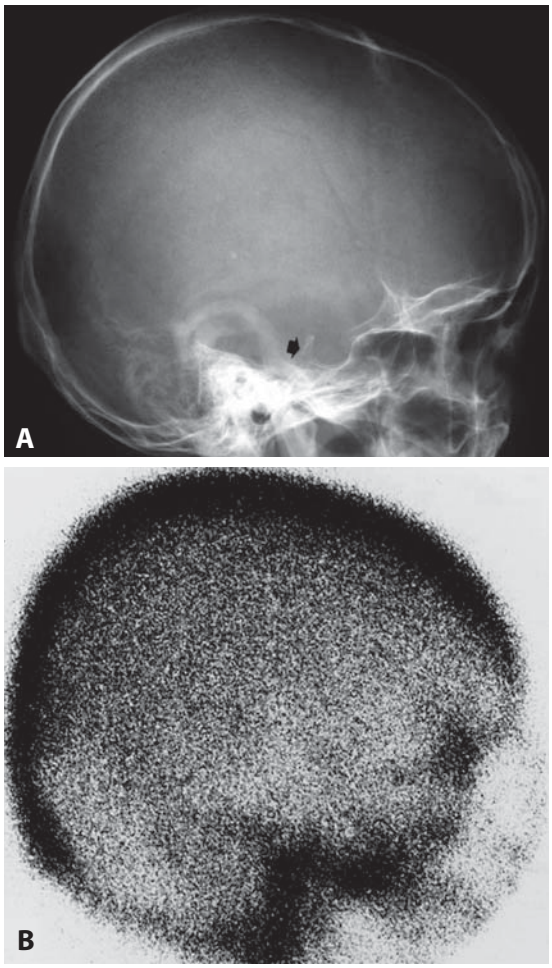

Fig. 15.16A, B Methotrexate-induced osteoporosis. **A** Lateral radiograph of the skull in a 50-year-old woman postoperatively treated with methotrexate for breast cancer shows diffuse porosis with white pencil-line cranial tables and washed-out sella (*arrow*). **B** Lateral pinhole scintigraph reveals diffusely increased tracer accumulation in the cranium and skull base with the salt-and-pepper sign

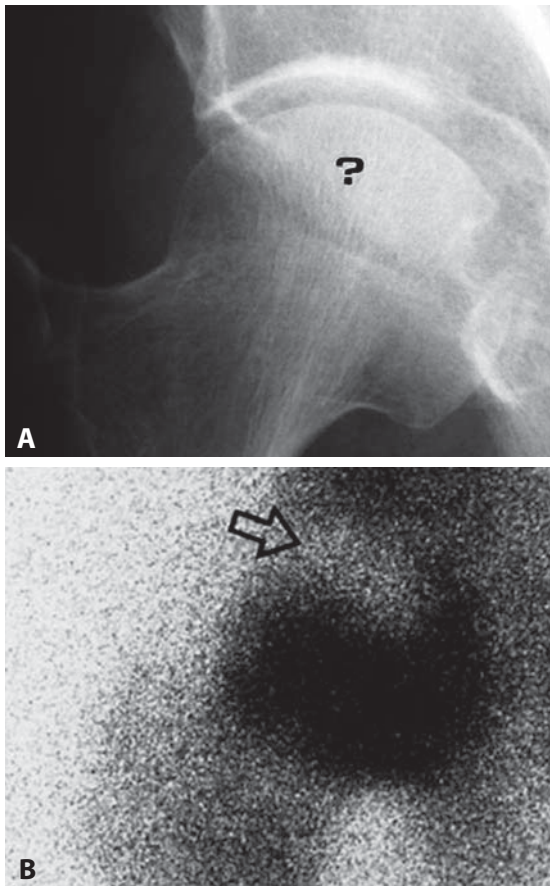

Fig. 15.17A, B Steroid-induced porosis and avascular osteonecrosis. **A** Anteroposterior radiograph of the right hip in a 62-year-old man treated with steroids for Wegener's granuloma of the nose shows no abnormality (*?*). **B** Anterior pinhole scintigraph reveals intense tracer uptake in the femoral head with an ovoid photon defect denoting avascular necrosis (*open arrow*)

Radiographic changes of drug-induced osteoporosis are not dissimilar to those of osteoporosis of other etiologies. Thus, the fundamental feature is generalized graying of cancellous bones with cortical accentuation. The skull presents the pencil-line sign of the thinned outer and inner tables with graying of the squamosal portions (Fig. 15.16A). The hip is one of the most common sites of steroid-induced osteoporosis and avascular osteonecrosis, showing coarsened trabeculae (Fig. 15.17A). Insufficiency fractures of the spine and sacrum and infractions of the ribs are other important features. Frequently, fractures and infractions are not detected because of profound osteopenia. Calluses in insufficiency fractures tend to be extensive, clearly standing out against gray bones in the background.

Scintigraphic features include a generalized increase in bone uptake, especially in young patients, with more intense tracer uptake in fractures and infractions. In the skull, drug-in-

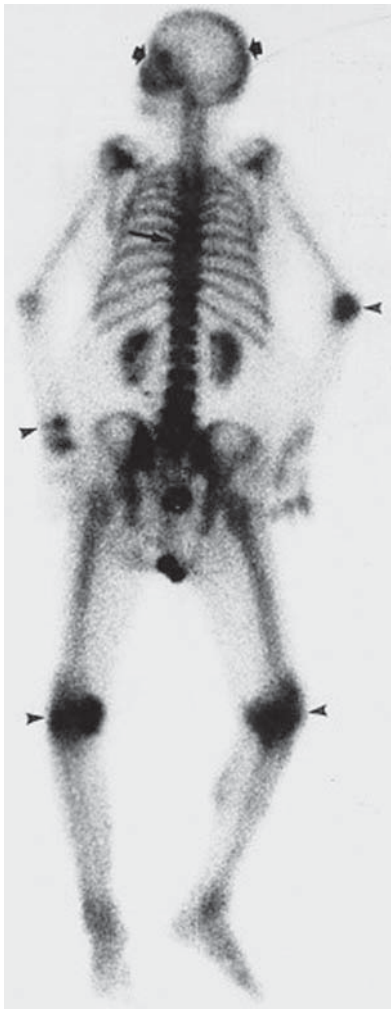

Fig. 15.18 Exogenous Cushing's disease. Posterior whole-body bone scintigraphy in a 68-year-old woman under long-term treatment with steroids for rheumatoid arthritis shows tracer uptake in the skull, facial bones, ribs, spine, and pelvis (*arrows*) as well as polyarthritis (*arrowheads*)

duced osteoporosis is indicated by markedly increased uptake in the entire cranial vault seen tangentially and by coarse granular uptake in the squamosal portion seen en face (Fig. 15.16B). Bone scanning is extremely useful for detecting avascular necrosis, which often accompanies steroid-induced osteoporosis (Fig. 15.17B). Osteonecrosis is painful, but may often pass undetected by radiography in the early stages (Fig. 15.17A). Exogenous Cushing's disease manifests as increased tracer uptake in the skull, facial bones, ribs, spine, and pelvis as well as arthropathy for which steroids are prescribed (Kingsley and Hickling 1986) (Fig. 15.18).

15.5 Rickets and Osteomalacia

As mentioned above, rickets and osteomalacia are due to deficient formation of inadequately mineralized osteoid. The basic difference between the two closely related conditions is that the former occurs in actively growing bones and the latter in mature bones. Etiological factors include deficiency of vitamin D and its active hormonal form 1,25-dihydroxyvitamin D3 and disturbed calcium–phosphorus metabolism. The functions of the vitamin D series include the homeostatic maintenance of calcium and phosphorus as well as bone mineralization. The active from of vitamin D acts on the intestine and bone as well as the kidneys and parathyroid glands. In the intestine it helps absorb calcium and phosphorus and in bone it mediates mobilization and redeposition of both ions. Hence, malabsorption syndromes, chronic renal failure with secondary hyperparathyroidism, and renal tubular disorder with acidosis may create osteomalacia.

Radiographically, rickets is characterized by, in addition to graying and a washed-out appearance of the entire skeleton, absence of the provisional calcification zones, widening and blurring of the physes, fraying and cupping of the metaphyses, and dwarfed deossified ossification centers (Fig. 15.19A). Osteomalacia also manifests as diffuse graying of bones with a washed-out appearance because of poor mineralization. While rickets typically involves the long bone ends and costochondral junctions in children, osteomalacia is characterized by Umbauzone or infractions in the stressed sites of the scapula, lower rib cage, pubic rami, and proximal femora in adults (Fig. 15.20).

Bone scintigraphic manifestations of rickets and osteomalacia can be divided into systemic

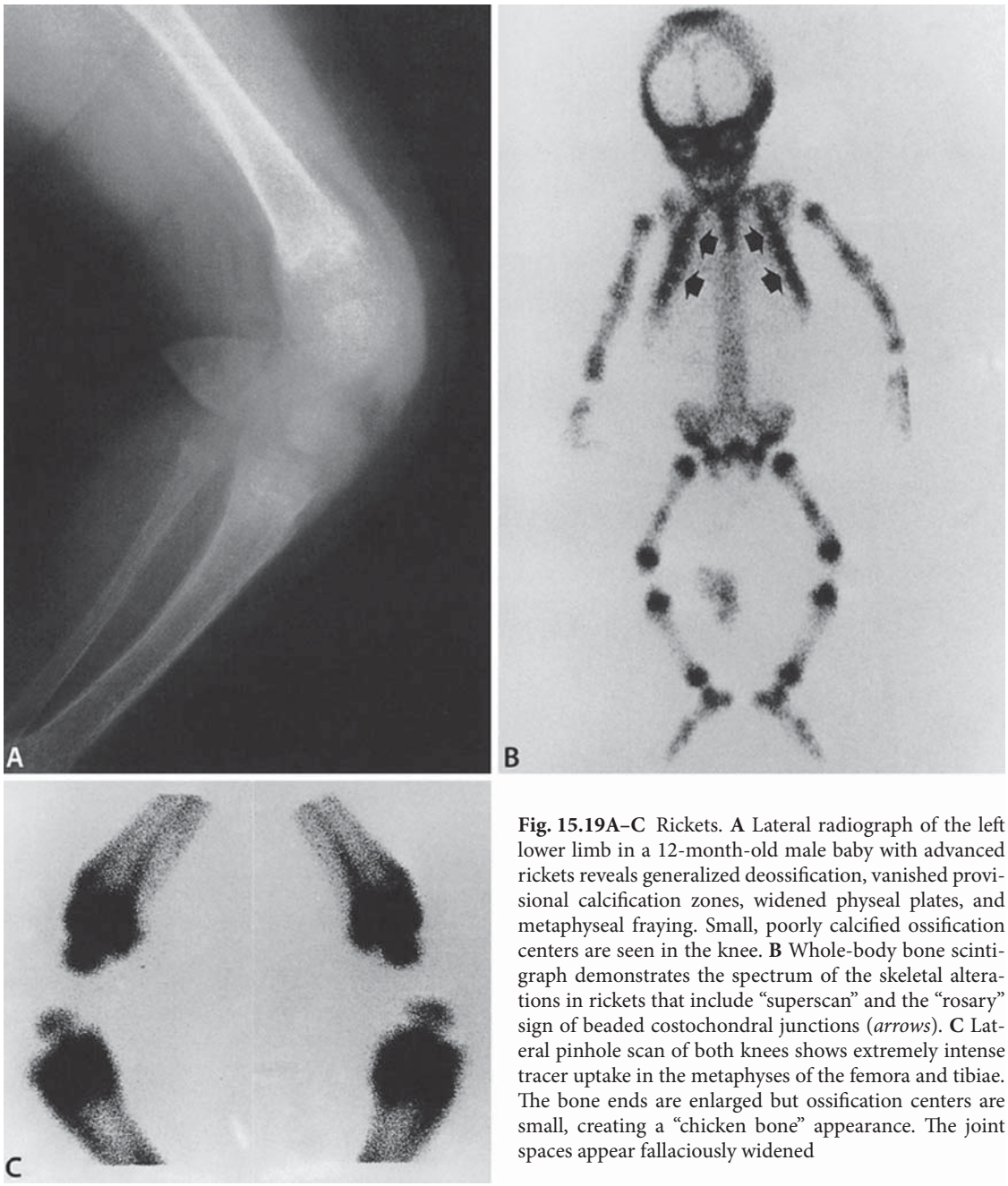

Fig. 15.19A–C Rickets. **A** Lateral radiograph of the left lower limb in a 12-month-old male baby with advanced rickets reveals generalized deossification, vanished provisional calcification zones, widened physeal plates, and metaphyseal fraying. Small, poorly calcified ossification centers are seen in the knee. **B** Whole-body bone scintigraph demonstrates the spectrum of the skeletal alterations in rickets that include "superscan" and the "rosary" sign of beaded costochondral junctions (*arrows*). **C** Lateral pinhole scan of both knees shows extremely intense tracer uptake in the metaphyses of the femora and tibiae. The bone ends are enlarged but ossification centers are small, creating a "chicken bone" appearance. The joint spaces appear fallaciously widened

and regional. For the observation of systemic changes a whole-body image is suitable and for the visualization of the individual lesions, pinhole scintigraphy is ideal. Whole-body scintigraphy shows increased tracer uptake in the entire skeleton, making it sharply contrasted with the background (Fig. 15.18B). Sy and Mittel (1975) called such a finding "superscan", and it is a sensitive indicator of altered bone metabolism. The kidneys show little or no tracer uptake because of renal dysfunction or drainage of available bone tracer by avaricious bones of malacia. This phenomenon occurs more typically in the osteomalacia of renal osteodystrophy (Fig. 15.3). Small spotty "hot" areas in the infractions in the peripheries of stressed

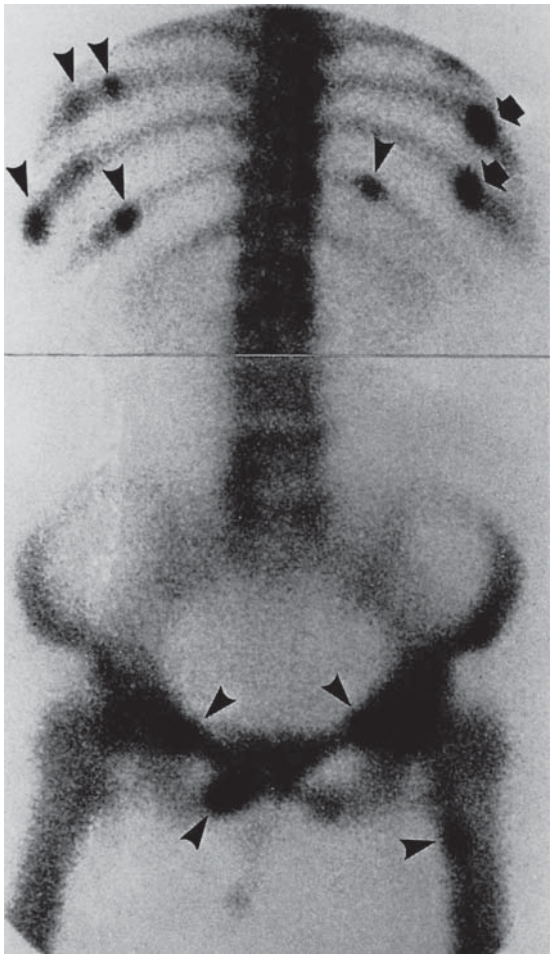

Fig. 15.20 Multiple hot spots of infractions and "superscan" in hyperparathyroidism. A composite scintigraph of the trunk (posterior view) and the pelvis (anterior view) in a 76-year-old woman with hyperparathyroidism shows multiple hot spots in the lower rib cage, the pelvic bones, and the left proximal femur (*arrowheads*). Typically, infractions are aligned vertically in the rib cage. The two larger hot spots in the right lower rib cage represent actual fractures (*arrows*)

bones such as the lower ribs (Fig. 15.12 B) and the pubic bones and proximal femora with the "superscan" sign are pathognomonic (Fogelman et al. 1977) (Fig. 15.20). Pinhole scanning of rickets shows intense uptake in the flared metaphyses and dwarfed epiphyseal ossification centers of the long bones, producing the "chicken bone" sign (Fig. 15.19C). The articular spaces appear spuriously widened due to dystrophic ossification centers (epiphyses) and bulky cartilages. On the other hand, the osteomalacia of primary hyperparathyroidism (Fig. 15.2) and renal osteodystrophy (Fig. 15.3) manifests as increased tracer uptake in the axial skeleton including the calvaria, mandible, rib cage, and sternum.

Other scintigraphic findings of osteodystrophy include the "tie sternum" sign, the "striped tie" sign, and costochondral beading or the "rosary" sign (Fig. 15.19B). The "hot patella" sign is not specific, occurring in many diverse conditions such as chondromalacia patellae, metastasis, and disuse porosis (Fogelman et al. 1983; Bahk et al. 1994). Pinhole scintigraphy is very useful for studying and archiving increased bone turnover focally in infraction or diffusely in the malacic skeleton. Its use is encouraged for the study of subtle subperiosteal bone resorption (Fig. 15.11), subchondral bone resorption (Fig. 15.12C), subtendinous bone resorption (Fig. 15.13B), and brown tumors or cystic change (Fig. 15.14B).

References

Bahk YW, Park YH, Chung SK, Kim SH, Shinn KS (1994) Pinhole scintigraphic sign of chondromalacia patellae in older subjects: a prospective assessment with differential diagnosis. J Nucl Med 35:855–862

Fogelman I, McKillop JH, Greig WR, et al (1977) Pseudofracture of the ribs detected by bone scanning. J Nucl Med 18:1236–1237

Fogelman I, McKillop JH, Gray HW (1983) The "hot patella" sign: is it of any clinical significance? J Nucl Med 24:312–315

Fujiwara S (2004) Epidemiology of osteoporosis and fracture (in Japanese). Clin Calcium 14:13–18

Gomez MC, Riquelme P, Sirandoni G, et al (2003) Brown tumors in multiple locations: manifestation of severe renal osteodystrophy. Case report (in Spanish). Rev Med Chil 131:1183–1187

Griffith CC, Nichols G, Asher JD, et al (1965) Heparin osteoporosis. JAMA 193:91–94

Hawkins D, Evans J (2005) Minimising the risk of heparin-induced osteoporosis during pregnancy. Expert Opin Drug Saf 4:583–590

Heaney RP (1962) Radiocalcium metabolism in disuse osteoporosis in man. Am J Med 33:188–200

Jones G (1969) Radiological appearance of disuse osteoporosis. Clin Radiol 20:249–253

Kingsley GH, Hickling P (1986) Polyarthropathy associated with Cushing's disease. Br Med J (Clin Res Ed) 292(6532):1363

Maenaut K, Westhovens R, Dequeker J (1997) Methotrexate osteopathy, does it exist? J Rheumatol 23:2156–2159

Mazanec DJ, Grisanti JM (1989) Drug-induced osteoporosis. Cleve Clin J Med 56:297–303

Megard M, Cuche M, Grapeloux A, et al (1982) Heparin osteoporosis: histomorphometric analysis of bone biopsy. One case (in French). Nouv Presse Med 11:261–264

Sambrook PN, Jones G (1995) Corticosteroid osteoporosis. Br J Rheumatol 34:8–12

Schwartz AM, Leonidas JC (1984) Methotrexate osteopathy. Skeletal Radiol 11:13–16

Singwe N, De Gars L, Karneff A, et al (1998) Multiple stress fractures in a scleroderma patient on methotrexate therapy. Rev Rheum Engl Ed 65:508–510

Smith RW Jr, Eyler WR, Mellinger RC (1960) On the incidence of senile osteoporosis. Ann Intern Med 25:855–862

Sy WM (1974) Bone scan in primary hyperparathyroidism. J Nucl Med 15:1089–1091

Sy WM, Mittal AK (1975) Bone scan in chronic dialysis patients with evidence of secondary hyperparathyroidism and renal osteodystrophy. Br J Radiol 48:878–884

Yang NP, Deng CY, Chou YJ, et al (2006) Estimated prevalence of osteoporosis from a Nationwide Health Insurance database in Taiwan. Health Policy 75:329–337

16 Traumatic, Surgical, and Sports Injuries of the Skeleton

The high sensitivity and reliability of bone scintigraphy in the diagnosis of fractures, sports injuries, and operative lesions of bone are well known. ^{99m}Tc-MDP bone scintigraphy aided by pinhole scanning is particularly useful for the diagnosis of covert fractures in complex anatomical sites and small bones, bone contusion, stress fracture, and traumatic enthesopathy. Many of these conditions are elusory or even invisible not only on ordinary radiographs but also on CT scans that uses slices in which not every small anatomical part is included. Retractor rib injuries such as periosteal stripping, contusion, fracture, and costovertebral articular severance constitute another important indication for bone scintigraphy. Pinhole scintigraphy appears to be the method of choice for detecting these seemingly trivial yet clinically worrisome injuries. This technique has also been shown to be extremely useful for noninvasive anatomical and biochemical assessment of traumatized articulations, muscles, tendons, and entheses, and even blood vessels. Furthermore, bone scintigraphy uniquely and often decisively provides real-time information on the vascularity and viability of fractured bone fragments and implanted bones as well as the existence, progress and quality of callus, and associated periosteal or adjacent soft-tissue mineralization.

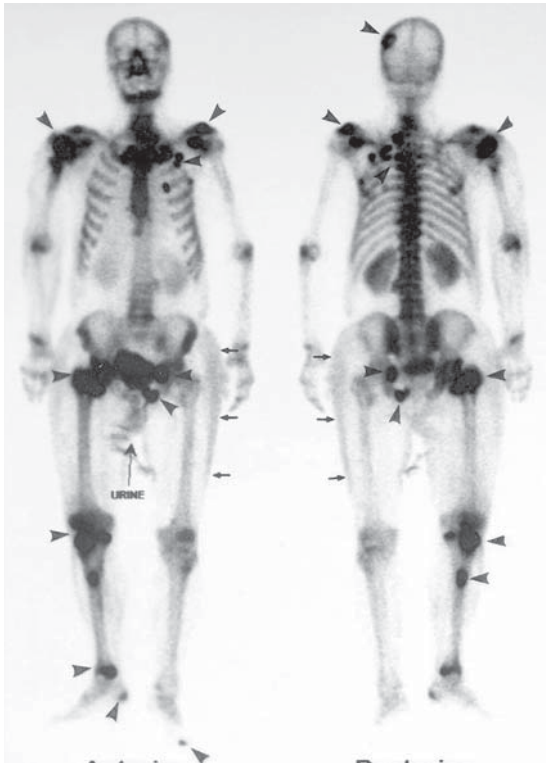

Fig. 16.1 Usefulness of whole-body scintigraphy in multiple bone and soft-tissue traumas. Anterior (*left*) and posterior (*right*) whole-body scintigraphs in a 64-year-old male who had suffered a fall show widely scattered fractures throughout the entire skeleton from the skull to the ankle (*arrowheads*). Note additional contusion to the soft tissues at the lateral aspect of the left buttock and lower extremity (*arrows*)

16.1 Bone Fractures

^{99m}Tc-MDP bone scintigraphy has two distinct advantages over other imaging modalities: one is its unique ability to diagnose fractures from the vertex to the toe tips using a pair of the whole-body scintigraphs (Fig. 16.1) and the other is the detection of radiographically and tomographically (conventional and CT) elusive fractures. Such fractures occur in (a) complex anatomy such as the atlantooccipital and

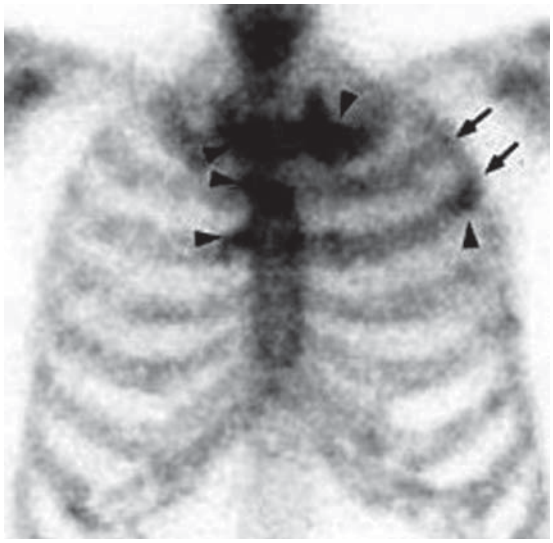

Fig. 16.2 Motor vehicle accident involving contact with the steering wheel. Anterior planar scintigraph of the chest in a 76-year-old male who had had steering-wheel injury 3 days previously shows patchy tracer uptake in the upper sternum and costosternal and sternoclavicular junctions (*arrowheads*). Note also diffuse tracer uptake in the associated rib injuries of the left upper chest (*arrows*)

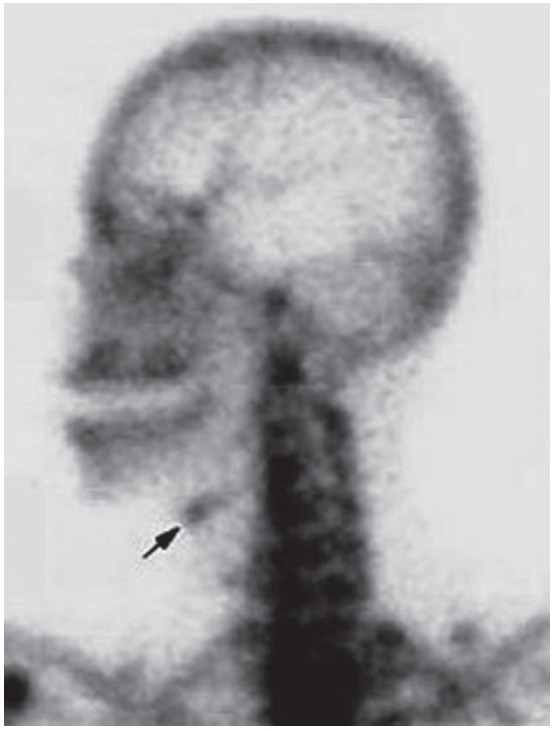

Fig. 16.3 Hyoid bone fracture. Left lateral planar scintigraph of the neck in a 26-year-old male who had been assaulted by a claw-hand in the anterior neck shows a small spotty tracer uptake at the lesser cornua of the hyoid denoting fracture (*arrow*)

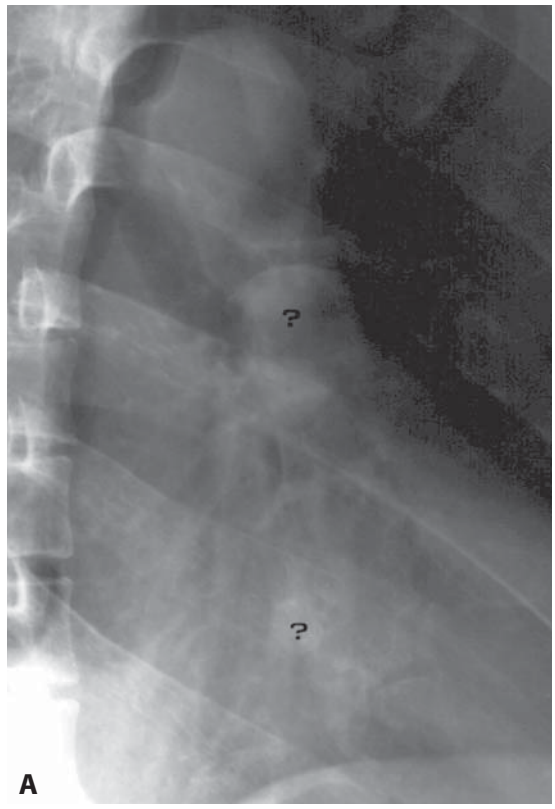

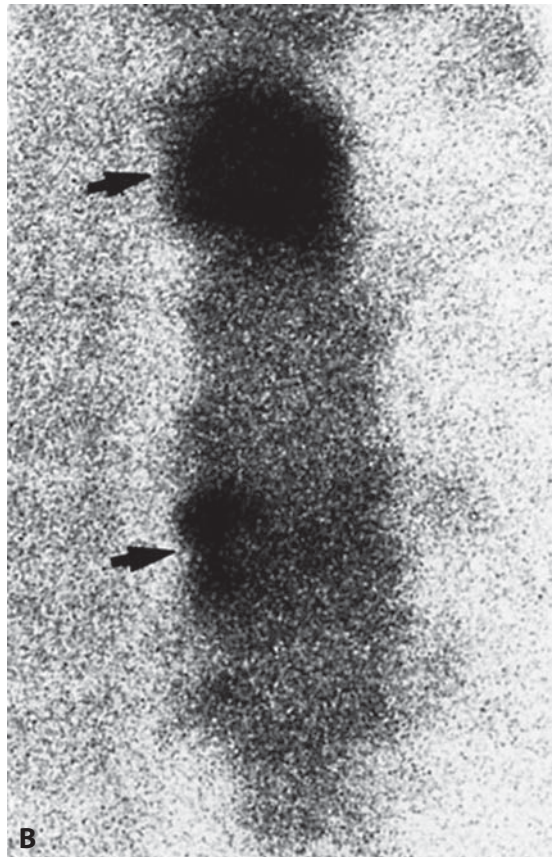

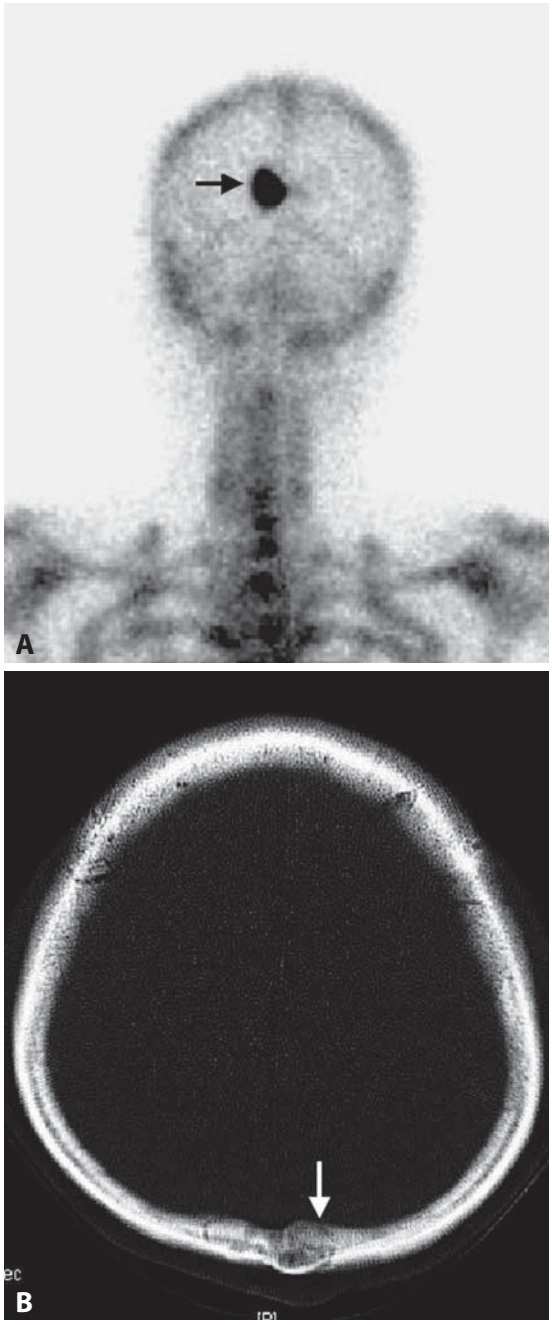

Fig. 16.5A, B Cranial vault fracture. **A** Posterior planar scintigraph of the skull in a 48-year-old male shows a spotty tracer uptake in the left posterior parietal bone near the lambda (*arrow*). **B** CT reveals fracture in the left posterior parietal bone near the lambda (*arrows*)

◁ **Fig. 16.4A, B** Sternal fractures. **A** Bone-free oblique radiograph of the sternum in a 37-year-old male with sternal trauma shows no definite abnormality (*?*). **B** Oblique pinhole scintigraph of the sternum reveals patchy tracer uptake in the upper end and the right lower lateral border of the sternum representing fractures (*arrows*)

atlantoaxial articulations and unclosed physis, (b) small accessory bones such as the hyoid and appendicular bones of the vertebra, (c) inseparable bones such as the facial bones, sternum, and sacroiliococcygeal bones, and (d) barely discernible porotic bone such as the ribs, vertebrae, and pelvis in the elderly. In not a small number of such fractures, plain radiography and even conventional or CT tomography are useless, often being diagnostically misleading. As mentioned above, bone scintigraphy is also useful for the study of traumatic injuries to the soft-tissue structures and entheses (Fig. 16.1).

Rib or sternal fractures in motor vehicle accidents involving the steering wheel (Fig. 16.2) and fractures of the hyoid bone (Fig. 16.3), upper and lower sternal body (Fig. 16.4), cranial vault (Fig. 16.5) and transverse or spinous process of the vertebrae (Fig. 16.6) are typical examples of fractures whose radiographic diagnosis is most difficult if not impossible. Importantly, as demonstrated in these example cases, not only radiography but also ordinary bone scintigraphy often fails to detect such fractures, necessitating magnification scintigraphy. It is also true that pinhole scintigraphy is not only more sensitive but also more accurate, and often enables one to differentiate fractures from bone metastasis (Harbert et al. 1981). Thus, for example, the tracer uptake in an uncomplicated rib fracture is vertically aligned to the long axis of the rib with more intense central uptake sided by less intense reactive uptake (Fig. 16.7 A) while the uptake in rib metastasis has a transverse orientation and is uniform (Fig. 16.7 B).

The diagnosis of fractures in the manubriosternal junction and/or its neighboring bones (Fig. 16.8), sacrum and sacroiliac joints (Fig. 16.9), coccyx (Fig. 16.10), unclosed physis (Fig. 16.11), and porotic bone (Fig. 16.12) is

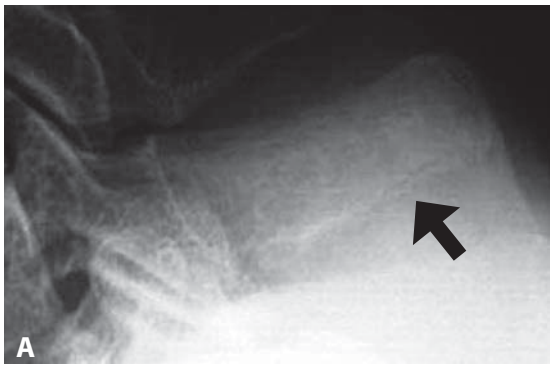

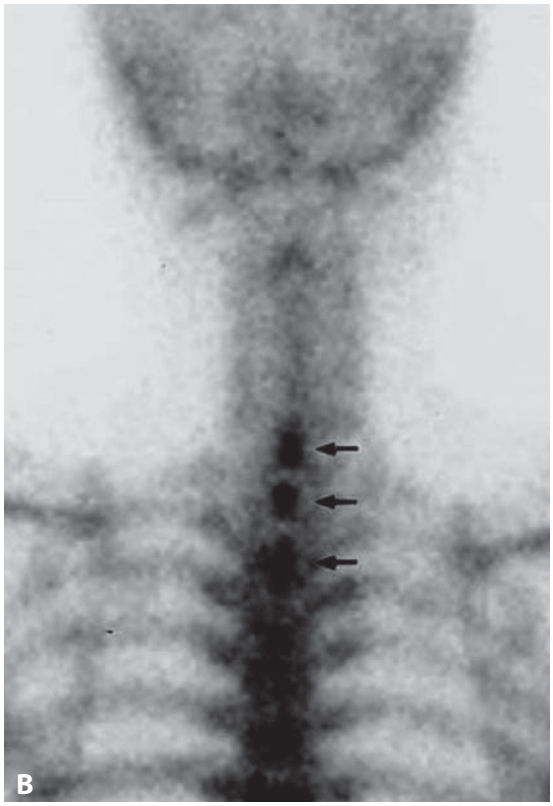

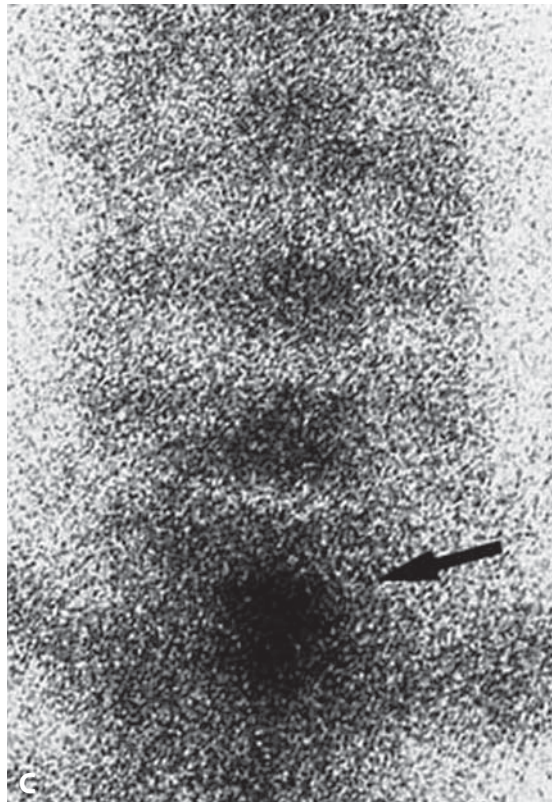

Fig. 16.6A–C Sensitivity of pinhole scanning in the diagnosis of cryptic fracture in the spinous process. **A** Lateral radiograph of the C7 spinous process in a 35-year-old male with neck injury shows barely discernible linear fracture (*arrow*). The fracture was made visible on PACS monitor only after seeing positive tracer uptake on scintigraphs. **B** Planar scintigraph reveals tracer uptake in the C6, C7 and T1 spinous processes (*arrows*). **C** Pinhole scintigraph localizes significant uptake specifically to the fracture of the C7 process (*arrow*)

greatly facilitated by pinhole scintigraphy. Small fractures in the facial bones, spine, hip, and knee (Fig. 16.13) are the other important objectives of pinhole scintigraphy. Retractor injuries to the ribs and costotransverse joints produced during open-heart or lung surgery are difficult to detect radiographically. Baisden et al. (1984) could not find rib fractures on chest radiographs in 36 consecutive patients who underwent open-heart operations through a median sternotomy incision using a conventional Ankeney retractor. Surprisingly, however, bone scintigraphy showed 44 rib fractures. Scintigraphy can diagnose not only fractures but also periosteal ripping (see Section 16.4 Operative Bone Injuries).

16.2 Joint Sprain

Sprain, a very common condition, is defined as a joint injury in which some of the fibers of a ligament or musculotendinous unit are ruptured but its continuity remains preserved.

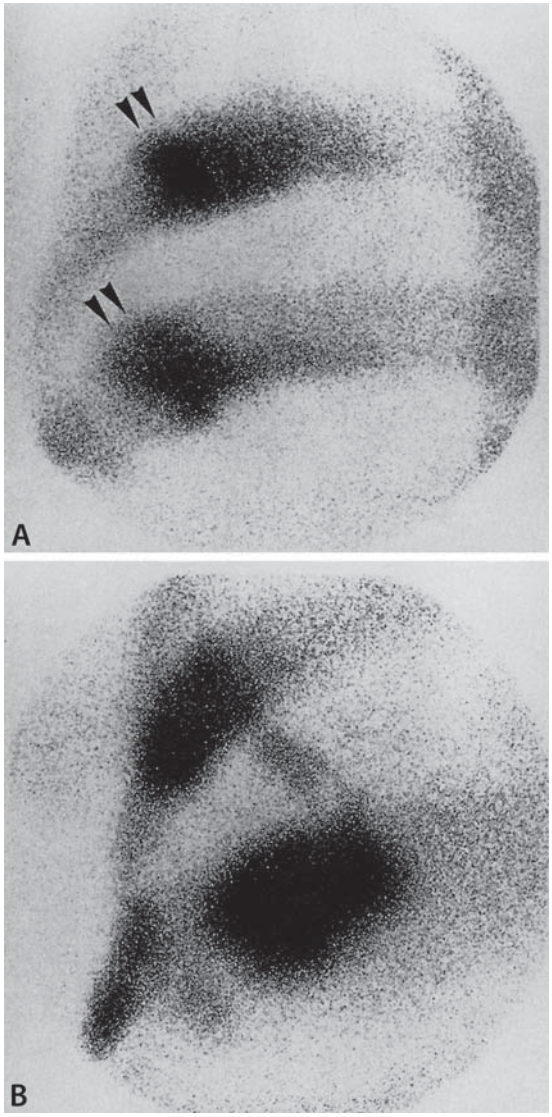

Fig. 16.7A, B Fracture versus metastasis in the rib. **A** Posterior pinhole scintigraph of the left middle rib cage in a 66-year-old man with fractures reveals two spotty "hot" areas. Characteristically, the lesions consist of the central, more intense tracer uptake that is sided by gradually fading, less intense uptake (*arrowheads*). The intense central uptake is vertically aligned. **B** Posterior pinhole scintigraph of the left middle rib cage in another 65-year-old man with known colon cancer metastases also shows two similar spotty "hot" areas. However, the tracer uptake in this case is uniform and transversely aligned

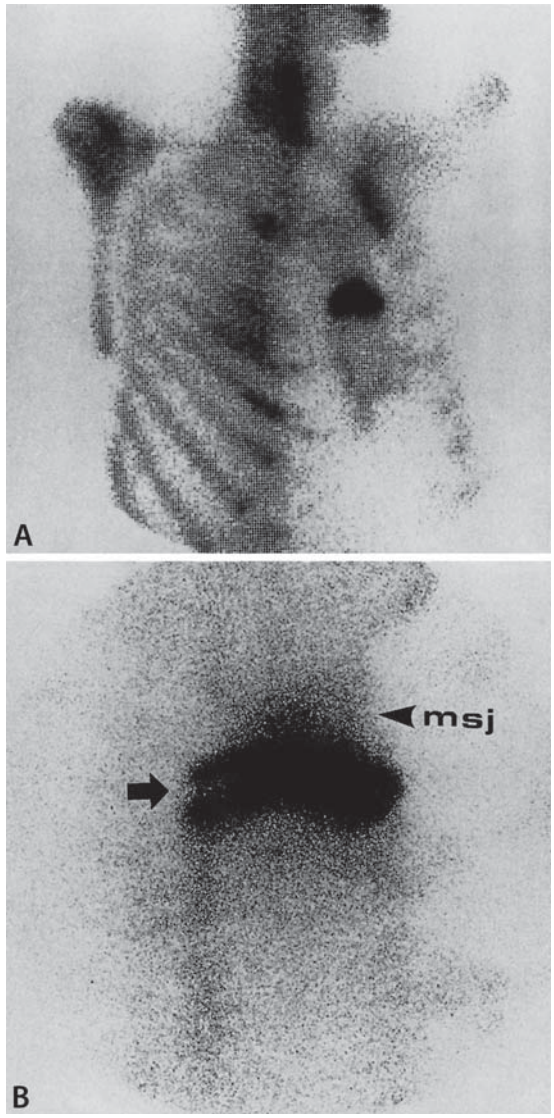

Fig. 16.8A, B Separation of juxta-articular sternal fracture from the manubriosternal joint. **A** Anterior oblique spot scintigraph of the sternum of a 35-year-old woman who was hit in the anterior chest with a fist shows intense tracer uptake in the region of the manubriosternal junction. Its anatomical relationship to the manubriosternal joint is not clear. **B** Anterior pinhole scintigraph of the area in question distinctly separates an obvious fracture (*arrow*) from the neighboring manubriosternal joint that is unhurt (*msj*)

Sprain affects any joint including those of the cervical and thoracolumbar spine and the upper and lower limbs. Because pathology involves nonosseous tissues, sprain is only indirectly recognizable on radiographs by noting subtle changes in alignment or anatomy of the spine and the soft-tissue structures about the joints. Unfortunately, such changes may easily

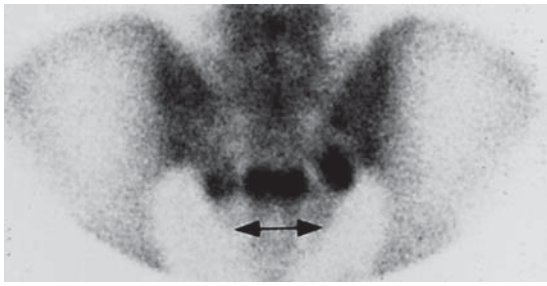

Fig. 16.9 The "H" sign in sacral fracture. Anterior planar scintigraph of the sacrum in a 33-year-old female with sacral fracture shows typical H-shape uptake (*double headed arrow*)

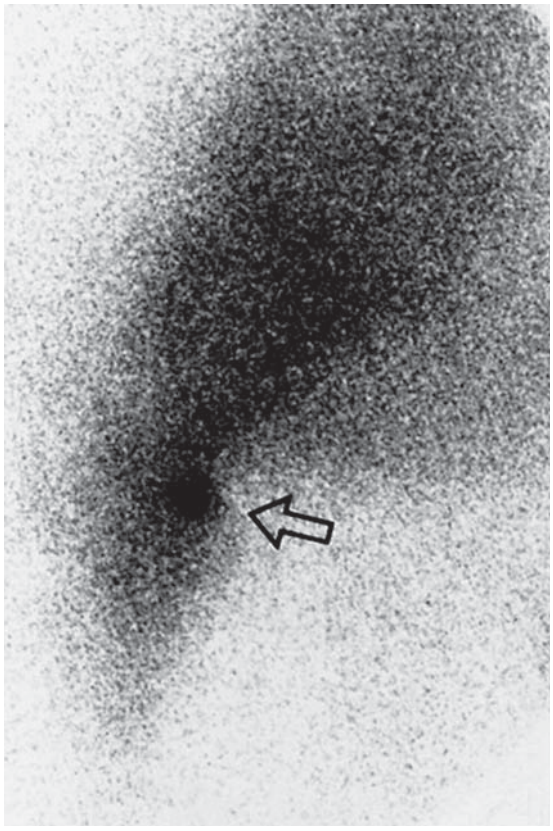

Fig. 16.10 Cryptic sacral fracture diagnosed by pinhole scintigraphy. Lateral pinhole scintigraph of the sacrum in a 46-year-old female with sacral trauma shows a small spotty area of slightly increased tracer uptake at the ventral aspect of the lower sacrum denoting fracture (*open arrow*). It was not detected on a planar scan (not shown here)

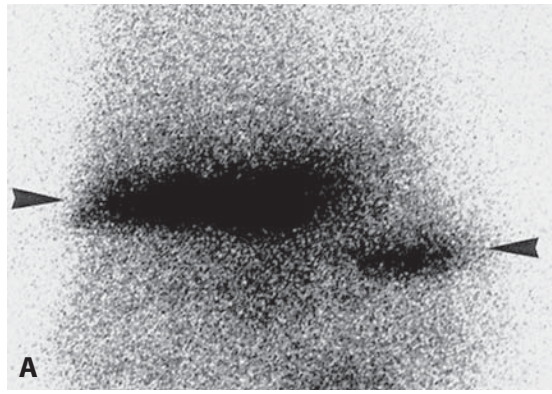

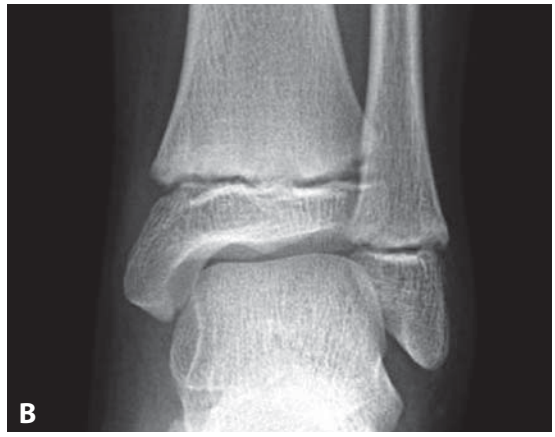

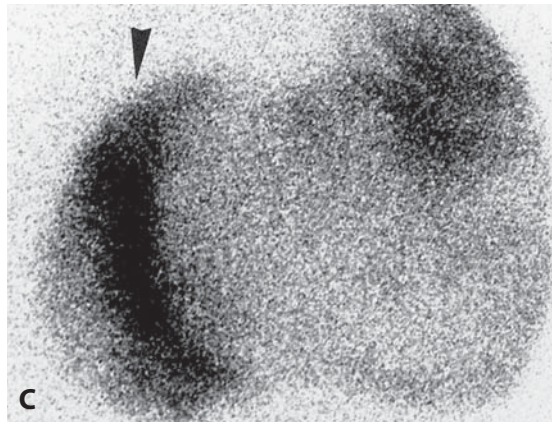

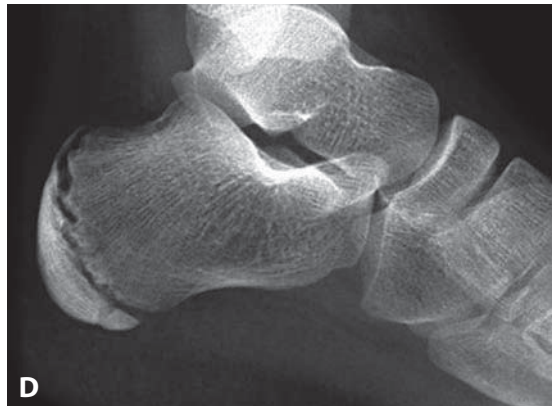

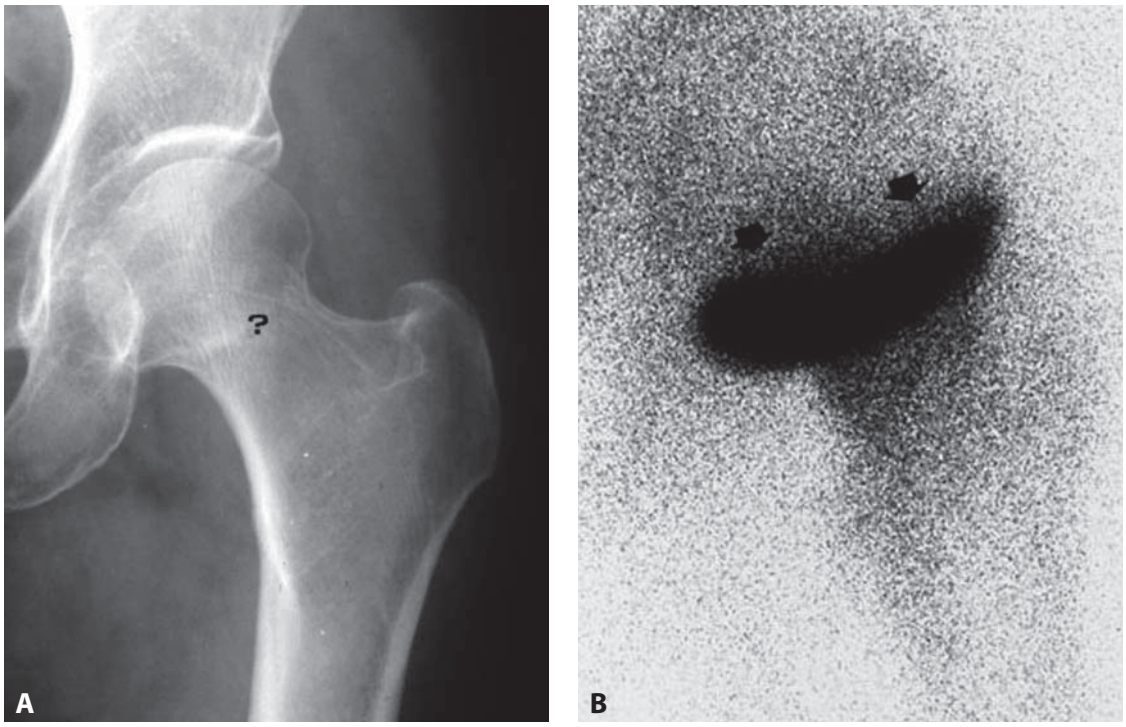

Fig. 16.12A, B Value of scintigraphy in the study of the painful hip. **A** Anteroposterior radiograph of the left hip in a 63-year-old female with pain shows a small linear intraosseous sclerosis of questionable significance at the neck (*?*). **B** Anterior pinhole scintigraph reveals prominent necklace-like tracer uptake at the junction of the femoral head and neck denoting stress fracture (*arrows*)

pass unnoticed or the findings, if detected, have limited diagnostic value.

The radiographic features of the spinal sprain include an increase in the distance between spinous processes, mild subluxation, asymmetrical widening of the apophyseal joint, and narrowing of the anterior disk space or widened disk space in hyperextension injury (Cintron et al. 1981). Traumatic injuries to the upper cervical spine including the atlantooccipital and atlantoaxial joints are often serious and fatal, but relatively mild injuries such as momentary subluxation or strain may occur in accidents involving sudden acceleration or deceleration. Sprain in the thoracolumbar spine has been assessed either on the basis of misalignment of the anterior and posterior columns (Holdsworth 1970) or the anterior, middle, and posterior columns (Denis 1983). In the sprain of the shoulder, knee, and ankle, bulging or periarticular soft-tissue thickening may be seen in the articular capsule that is not specific.

In contrast, however, bone scintigraphy shows findings that denote sprain. Thus, a magnified view (not necessarily pinhole scintigraphy) shows tracer that is characteristically accumulated in strained or momentarily subluxed joints and stretched ligamental attachments. Such findings appear specific. For example, when the upper cervical spine is hyperflexed with a abrupt distracting force applied to the skull, sprain or momentary subluxation may occur in the atlantoaxial joint and atlantooccipital joints and tracer may accumulate in the

◁ **Fig. 16.11A–D** Pinhole scanning in the diagnosis of physeal fractures. **A** Anterior pinhole scintigraph of the left ankle in an 11-year-old boy with ankle trauma shows increased tracer uptake in the distal tibial physis with a broadened lateral half. **B** Lateral radiograph reveals questionable lateral physeal separation. **C** Lateral pinhole scintigraph of the calcaneus of the same patient shows broadening of the upper retrocalcaneal apophysis due to separation (*arrowhead*). **D** Lateral radiograph reveals mild separation of the upper apophysis

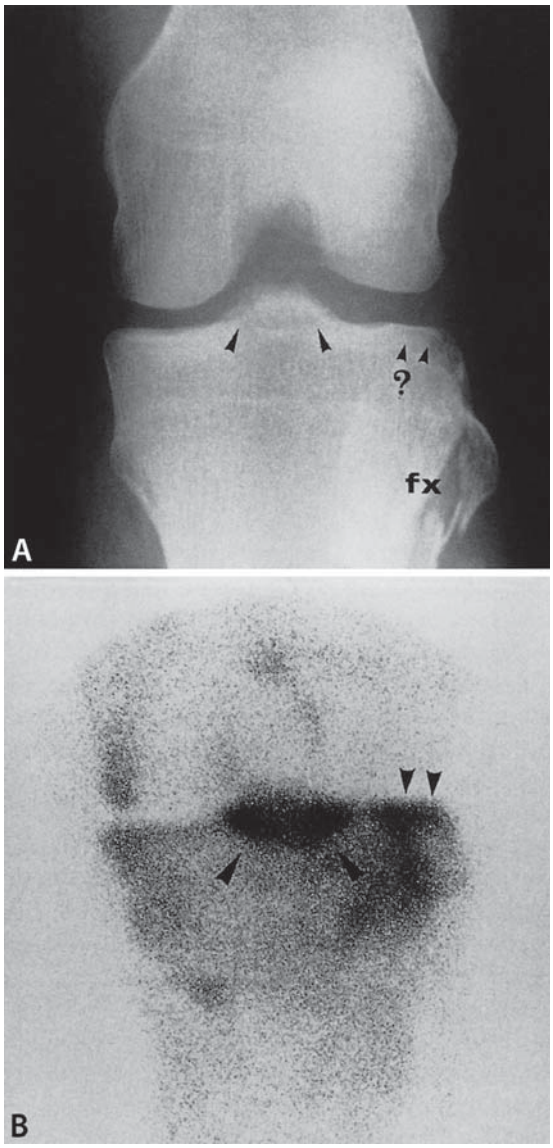

Fig. 16.13A, B Usefulness of pinhole scintigraphy in the detection of covert fracture. **A** Anteroposterior radiograph of the left knee in a 33-year-old man with knee injury shows fractures in the fibular neck (*fx*) and the base of the tibial tubercles (*arrowheads*). A fracture is hidden in the lateral tibial plateau (*?*). **B** Anterior pinhole scintigraph shows intense tracer uptake in the fractures of the tibial tubercles (*arrowheads*) and the fibular neck. In addition, a third lesion is shown in the lateral tibial edge (*pair of arrowheads*). After this study the knee was rescanned applying varus stress, confirming the hidden fracture in the lateral tibial plateau (not shown here)

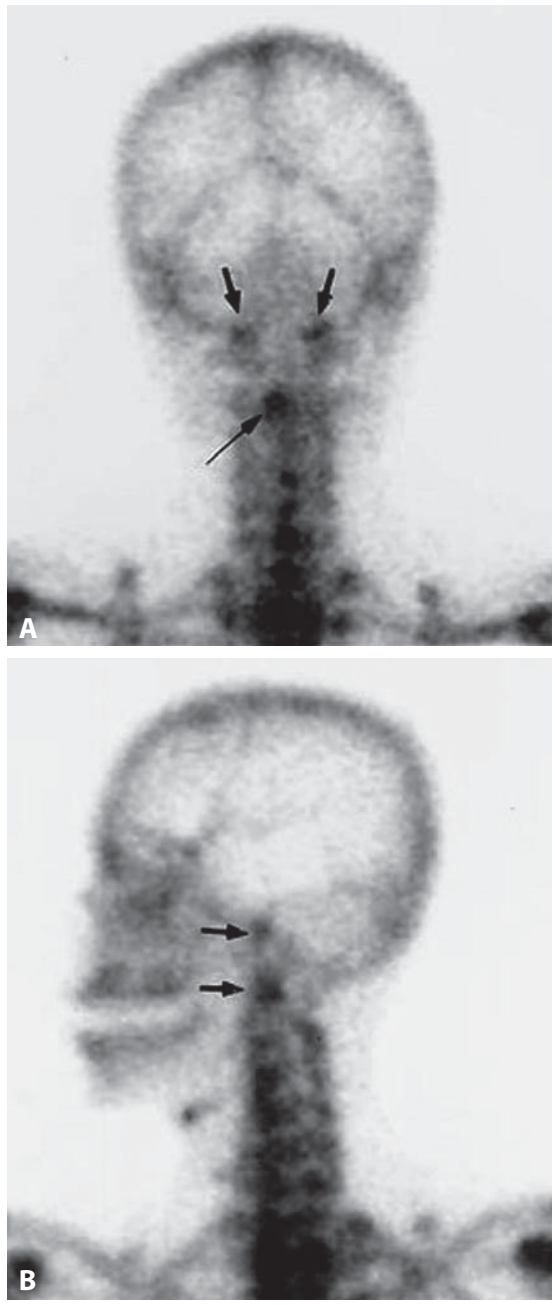

Fig. 16.14A, B Momentary subluxation of the atlantoaxial and atlantooccipital joints. **A** Posterior planar scintigraph of the skull base in a 26-year-old male with a abrupt neck injury shows small spotty tracer uptake in the atlantooccipital joints and atlantoaxial joint, producing an "inverted triangular spot" appearance (*arrows*). **B** Lateral scintigraph reveals tracer uptake in the atlantooccipital joints (*upper arrow*) and atlantoaxial joint (*lower arrow*)

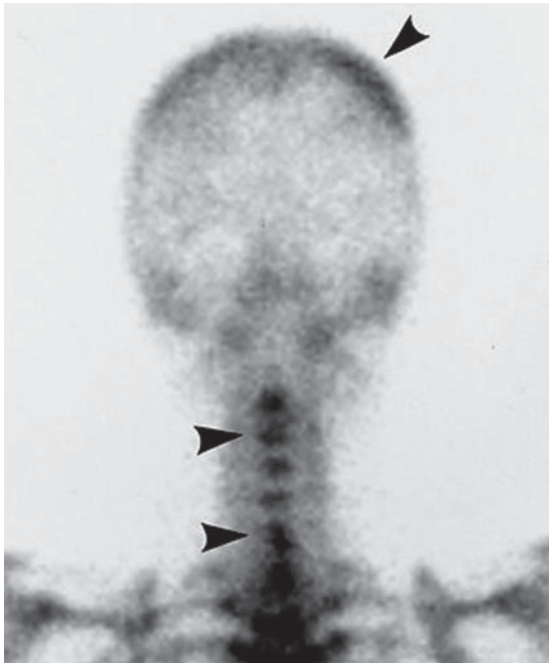

Fig. 16.15 Neck sprain. Posterior planar scintigraph of the cervical spine in a 22-year-old female with a neck injury shows discrete spotty tracer uptake in the entire cervical spinous processes except for C1 (*arrowheads*). Note incidental finding of right parietal bone uptake denoting contusion (*top arrowhead*)

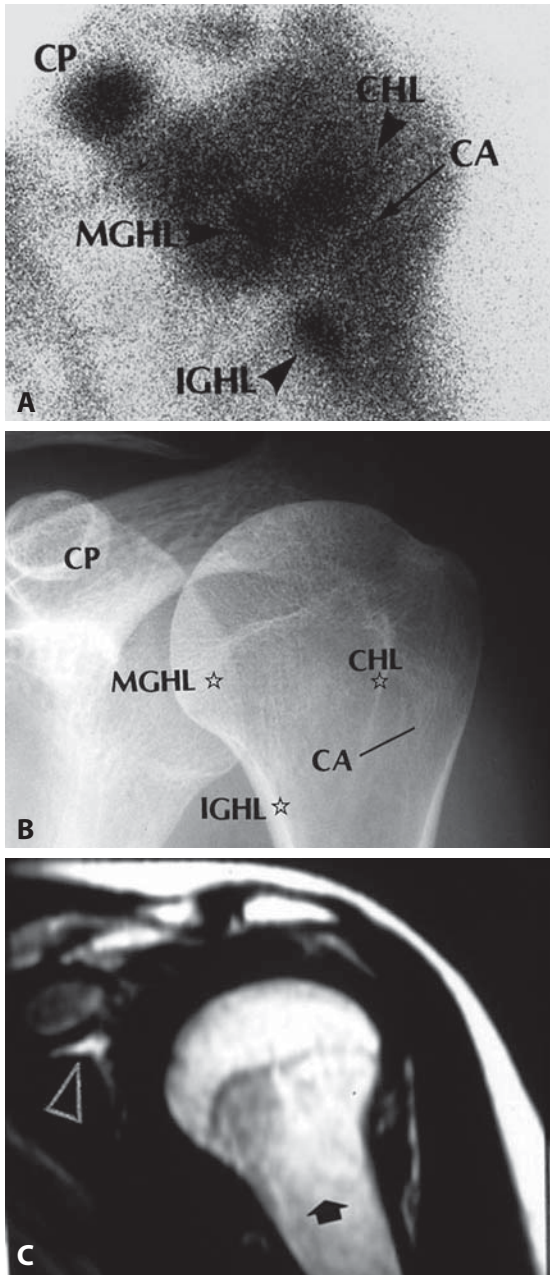

Fig. 16.16A–C Shoulder sprain. **A** Anterior pinhole scintigraph of the left shoulder in a 38-year-old female shows areas of increased tracer uptake at attachments of the medial glenohumeral ligament (*MGHL*), inferior glenohumeral ligament (*IGHL*), and coracohumeral ligament (*CHL*) (*CP* coracoid process, *CA* joint capsular attachment). **B** Anteroposterior radiograph of the same shoulder for the identification of the individual anatomical sites. **C** T2-weighted MRI demonstrates marrow edema in the humeral neck (*arrow*) and effusion in the coracoid bursa (*arrowhead*)

respective joint, giving rise to an "inverted triangular hot spot" appearance on the posterior view (Fig. 16.14A). The lateral view accurately identifies spotty uptake to be in the atlantoaxial joint and atlantooccipital joints located anteriorly to the foramen magnum (Fig. 16.14 B). The sprain of the atlantoaxial and atlantooccipital joints in this patient was clinically quite unique in that the head was flexed with a jerk as his throat was suddenly grasped and pushed by a hawk-claw hand during street fighting. The hyoid bone fracture shown in Fig. 16.3 was thus created in the same patient. In contrast, a whiplash injury with hyperextension may cause tracer to accumulate in the tips of the spinous processes of all cervical vertebrae, characteristically skipping that of the atlas (Fig. 16.15). The skip can be explained on the basis that the C1 vertebra receives an anchoring support of the ligament of the minor rec-

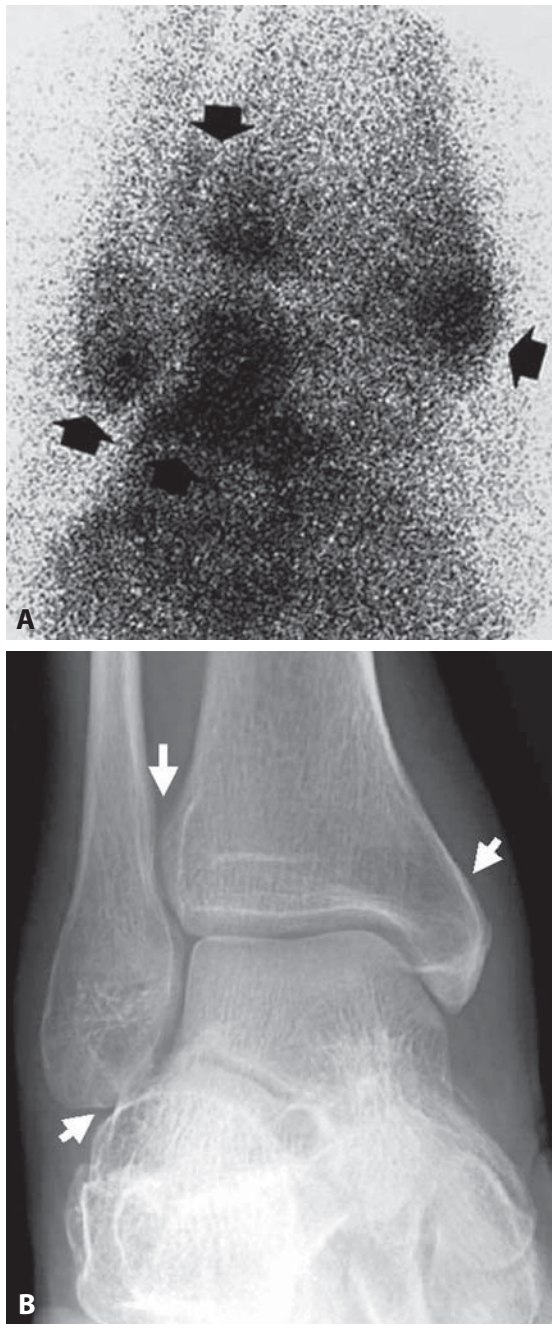

Fig. 16.17A, B Ankle sprain. **A** Anterior pinhole scintigraph of the right ankle in a 54-year-old male shows multiple areas of patchy tracer uptake at the attachments of the interosseous tibiofibular syndesmosis ligament (*upper arrow*), talofibular ligament (*left lateral arrow*), talocalcaneal ligament (*left medial arrow*) and deltoid ligament (*right arrow*). **B** Anteroposterior radiograph reveals osteopenia and para-articular soft-tissue swelling (*arrows*)

tus capitis posterior muscle that is separated from the interspinous ligament of the C2 and lower vertebrae. Similarly, sprain of the thoracolumbar spine causes increased uptake in the spinous processes and costovertebral joints.

When the major limb joints such as the shoulder, elbow, hip, knee, and ankle are sprained the injured ligamentous entheses accumulate increased tracer at their bony attachments. In the shoulder, for example, injured sites include the insertions of the coracoacromial ligament at the coracoid process, the middle glenohumeral ligament at the medial aspect of the humeral head, the inferior glenohumeral ligament at the medial aspect of the proximal humeral metaphysis, and the coracohumeral ligament at the tuberosity accumulate increased tracer (Fig. 16.16). On the other hand, in the ankle sprain manifests patchy "hot" areas in the attachments of the deltoid ligament, the anterior talofibular ligament, the talocalcaneal ligament, and the talofibular ligament (Fig. 16.17).

16.3 Bone Contusion (Occult Intraosseous Fracture)

The term contusion was originally used for the description of a skin injury characterized by subcutaneous hemorrhage without a skin break. It is also called bruise. Bone contusion is not a generally accepted concept, and no direct pathological evidence has been provided for it. However, it seems reasonable to employ this term clinically to describe the situation produced by a direct blow to bone with resultant local bone pain, tenderness, and soft-tissue swelling but without radiographic evidence of bone damage. Yao and Lee (1988) conducted an MRI study in eight patients with direct knee trauma with normal bone radiography. In the contused bone they observed high signal intensity on T2-weighted images, suggesting hemorrhage or edema. The bone scan showed increased uptake, the area of which was larger

than that of the MRI change. Based on of these observations, they considered the possibility of a linkage between hemorrhage and edema and microvascular injury and microfractures.

Theoretically, bone contusion cannot be diagnosed by radiography because the presence of obvious bone lesions such as trabecular change and fracture is inconsistent with the concept of contusion (Fig. 16.18A). However, like MRI, bone scintigraphy demonstrates bony alteration in the form of increased tracer uptake, which may reflect edema and/or hemorrhage with underlying trabecular damage in the acute stage and additional reparative bone reaction in later stages (Fig. 16.18B). Thus, pinhole scanning can provide objective evidence of osseous derangement in bone contusion. There appear to be two different patterns of tracer uptake: the one is simple homogeneous uptake and the other a composite of more intense uptake in the major lesion and less intense uptake in surrounding reactive change. The homogeneous tracer uptake in the first type pattern is considered to more realistically denote "bone contusion with edema and/or hemorrhage" (Fig. 16.18B) and the more intense uptake in the composite pattern is considered to represent microfractures. The composite injuries involve most typically the posteroinferior aspect of the calcaneal bone obliquely (Fig. 16.19). It is to be mentioned that no radiographic abnormality is detected in either pattern. Pinhole scintigraphy of 3-month-old microfractures in the posteroinferior portion of the calcaneus sustained in a fall showed exactly the same uptake pattern as the second type of bone contusion: more intense major uptake sided by less intense reactive uptake (Fig. 16.20A). Radiography revealed trabecular fractures with condensation (Fig. 16.20B). Interestingly, condensed small fractures in this case are sharply demarcated by local osteopenia in the calcaneal body. Probably, the initial radiography did not visualize condensed microfractures as clearly as now because osteopenia is usually a late development. The stress fracture of the calcaneus may resemble contusion. However, the former condition tends to affect the *superior*

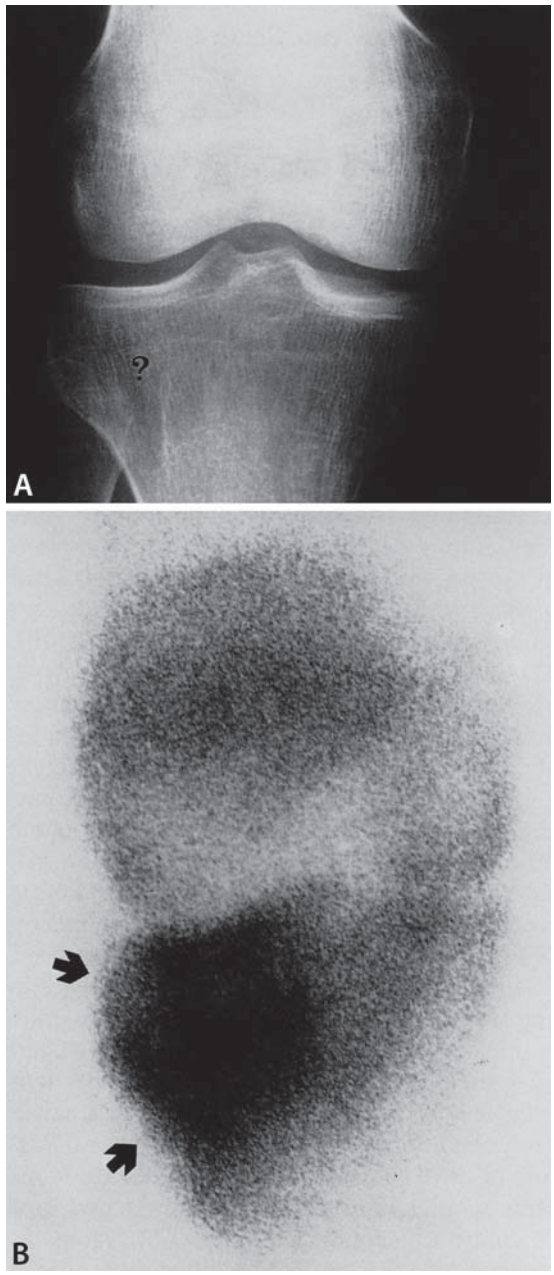

Fig. 16.18A, B Bone contusion. **A** Anteroposterior radiograph of the right knee in a 57-year-old man with local bruise shows no abnormal finding (*?*). **B** Anterior pinhole scan taken on the same day reveals intense tracer uptake localized in the bruised lateral tibial condyle (*arrows*)

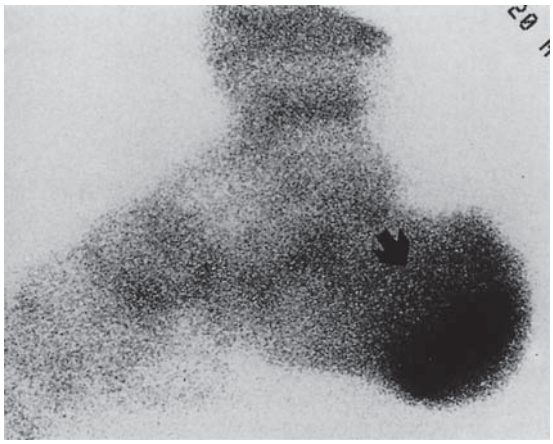

Fig. 16.19 Main and accompanying tracer uptake in bone contusion. Medial pinhole scintigraph of the right hindfoot in a 15-year-old young man who had fallen on the heel reveals a band-like area of extremely intense tracer uptake localized obliquely in the posteroinferior aspect of the calcaneus. The main tracer uptake is accompanied by less intense peripheral uptake (*arrow*). Radiography showed no evidence of fracture (not shown here)

aspect of the posterior calcaneus vertically and not the *inferior* aspect obliquely as in contusion (see Resnick and Niwayama 1988; Fig. 74.32).

Contusion of the humeral head, tibial head, femur, calcaneus, and sacrum and coccyx are among a list of more common indications for pinhole scintigraphy. In regard to the MRI manifestations, T2-weighted or fat-suppressed gradient echo images of bone contusion reveal high signal intensity (Fig. 16.21A), the area of which is smaller than that of tracer uptake (Yao and Lee 1988).

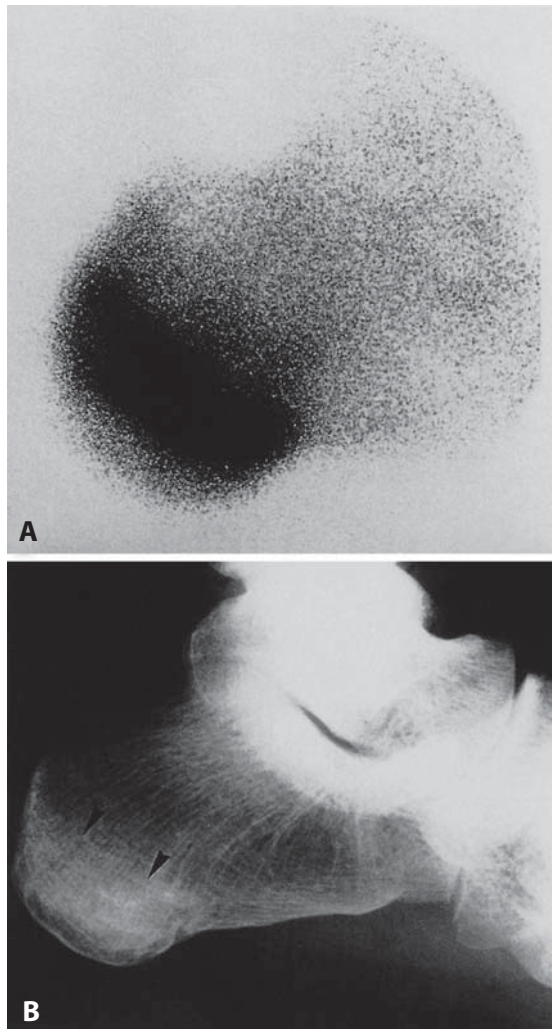

Fig. 16.20A, B Intraosseous fracture in the posteroinferior aspect of the calcaneus. **A** Medial pinhole scan of the left calcaneus in a 62-year-old man who had fallen on the heel 3 months previously shows extremely intense tracer uptake accompanied by less intense uptake in the posteroinferior aspect of the calcaneus. Note the characteristic oblique alignment of the lesion and the similarity to the alterations seen in Fig. 16.19. **B** Mediolateral radiograph shows definite intraosseous sclerosis, indicating microfractures with compressed trabeculae (*arrowheads*). The bone is markedly porotic. The finding in the initial radiograph was equivocal (not shown here)

16.4 Stress Fractures and Related Peri- and Endosteal Reaction

Stress fracture is also known as fatigue fracture or march fracture. As the term indicates, this condition results from undue physical loading or repeated or cyclic stress on a normal bone. The insufficiency fractures in the porotic, malacic, and other abnormal bones may also be included in this category, but the present discussion is limited to stress fractures in the narrow sense. Radiographically, early stress fractures manifest as periosteal, cortical, and/or endosteal reaction without bony breakage (Fig. 16.22A). With further physical loading,

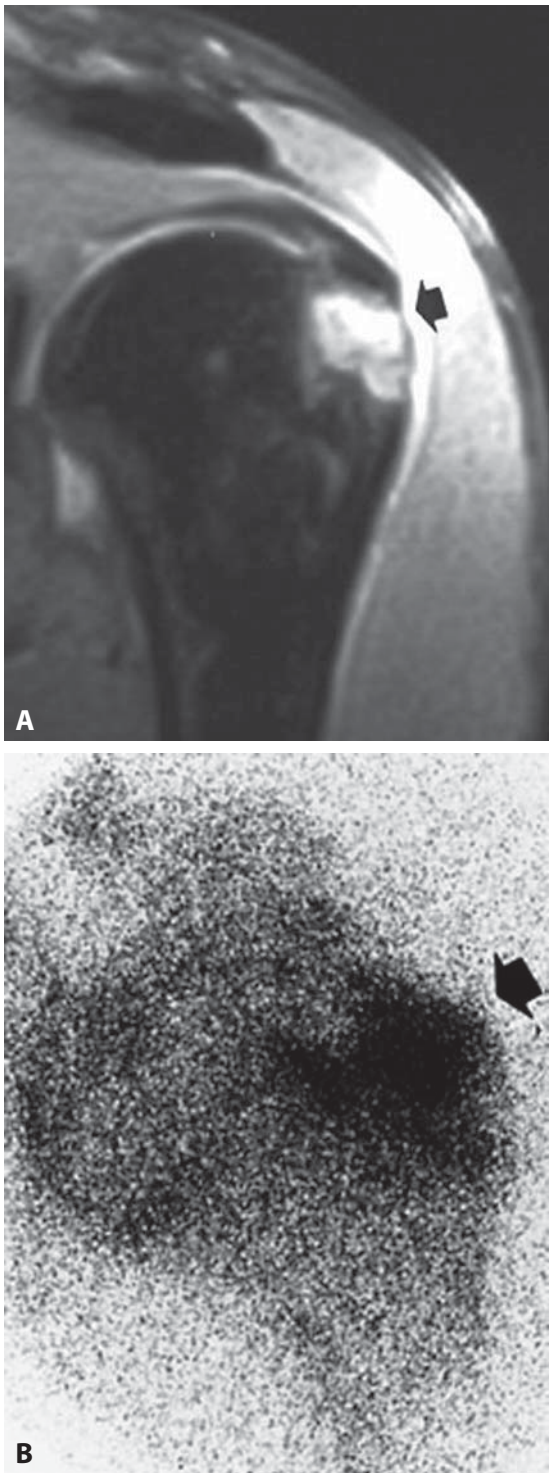

Fig. 16.21A, B Shoulder contusion. **A** Fat-suppressed MRI of the left shoulder in a 40-year-old male who had had a bicycle accident 2 days previously reveals bright signal of edema in the greater tuberosity bone marrow (*arrow*). **B** Anterior pinhole scintigraph reveals intense tracer uptake accurately corresponding to MRI change (*arrow*)

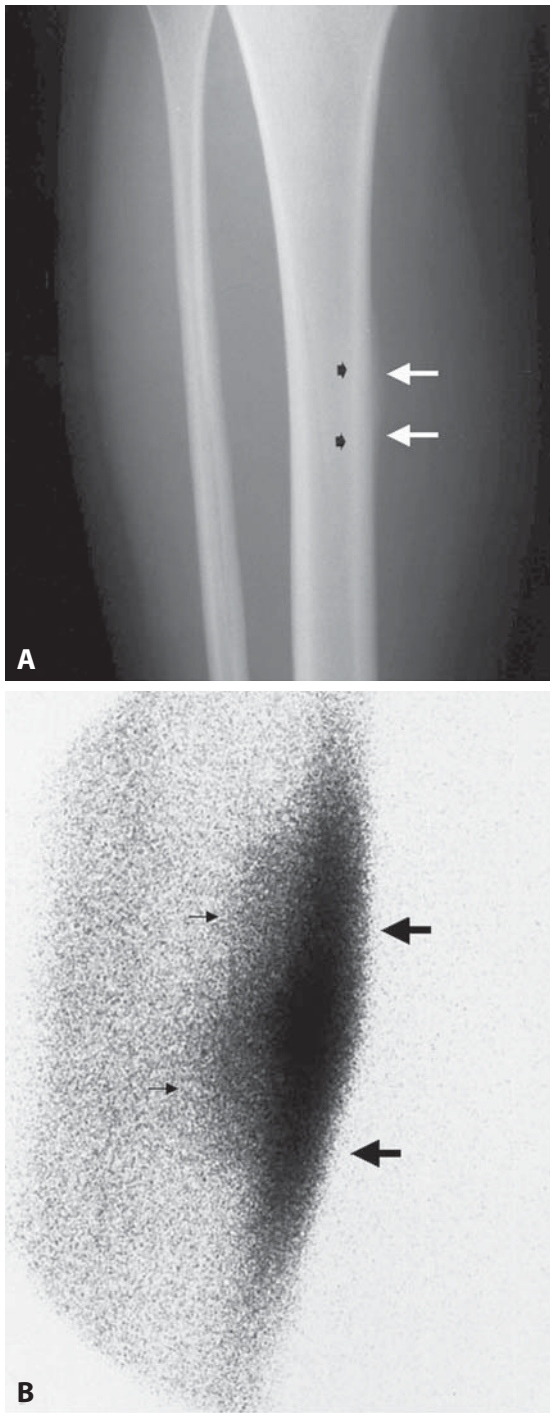

Fig. 16.22A, B Simultaneous involvement of the periosteum and endosteum in stress fracture. **A** Anteroposterior radiograph of the right tibia in a 15-year-old girl student with severe leg pain after sudden, strenuous running shows diffuse, reactive mineralization in the periosteum (*large arrows*) and endosteum (*small arrows*). **B** Anterior pinhole scintigraph reveals intense fusiform uptake in the medial cortex of the middle tibial shaft accompanied by less intense uptake in the endosteum (*small arrows*)

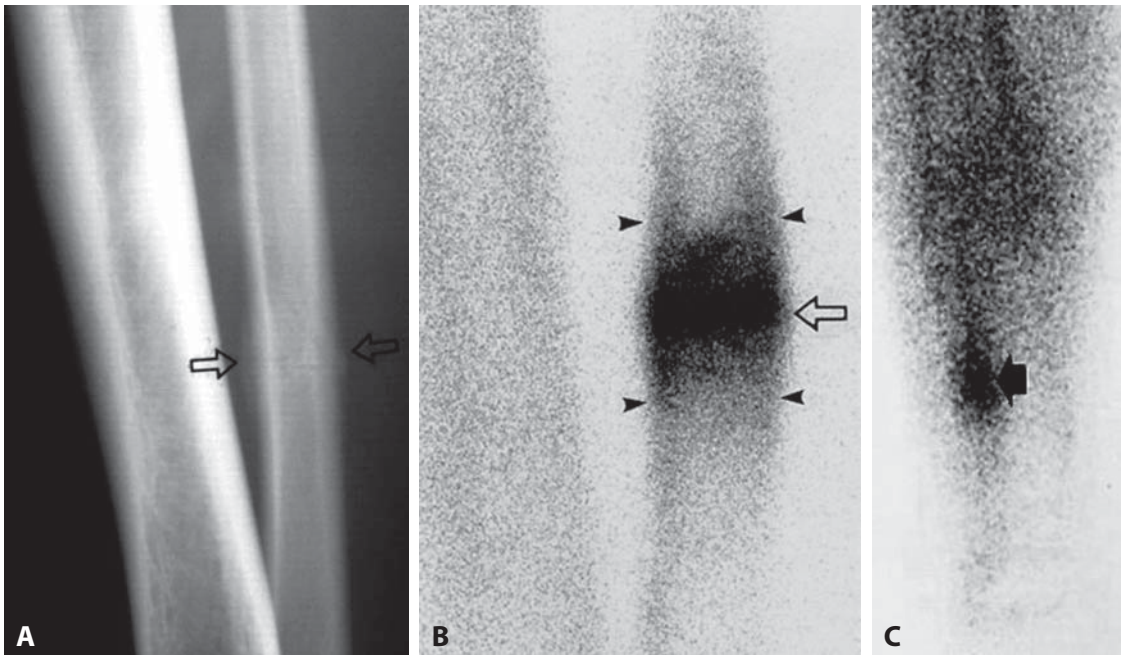

Fig. 16.23A–C Pinhole scan and nuclear angiography in the diagnosis of early stress fracture. **A** Anteroposterior radiograph of the left leg in a 13-year-old boy jogger shows subtle periosteal reaction in the midshaft of the fibula (*open arrows*). No fracture is seen. **B** Anterior pinhole scintigraph reveals a band-like zone of tracer uptake across the fibular midshaft sided by local periosteal uptake (*arrowheads*) denoting transverse fracture and periosteal reaction, respectively. **C** Nuclear angiogram shows increased blood flow in the fracture site (*arrow*)

microfractures or obvious fractures may develop due to the failure of periosteal reinforcement (Sweet and Allman 1971), presenting transverse linear lucent shadow (Fig. 16.23A) or band-like intraosseous sclerosis (Fig. 16.24A). On the whole, the radiographic manifestations are subtle and unimpressive (Figs. 16.22A, 16.23A and 16.24A) but tracer uptake is rather ominous (Figs. 16.22B, 16.23C and 16.24B). High sensitivity of bone scintigraphy of the periosteal change in stress fracture is well documented (Geslin et al. 1976; Roub et al. 1979), and bone scintigraphy can clearly distinguish periosteal from endosteal reaction in stress fractures (Sweet and Allman 1971). Pinhole scintigraphy is particularly useful in this situation (Figs. 16.22B and 16.23B), and nuclear angiography has been shown to be of great help in the early detection of stress fractures (Rupani et al. 1985) (Fig. 16.23C). A useful classification of the bone scan features of stress fracture has been proposed by Zwas et al. (1987).

Shin Splints Shin splints is a painful, stress-induced enthesopathy, the disease mechanism of which is basically similar to that of stress fracture. The periosteal disruption and reactive bone formation in shin splints are considered to be caused by the rupture of the Sharpey fibers that extend from muscle into the cortex through the periosteum (Rupani et al. 1985). The condition has been related to undue focal pull of the flexor digitorum longus muscle on the periosteum. It produces pain in the posterior medial aspect of the tibia. A histological correlation with bone scan has shown that the periosteal uptake occurs in new bone formation (Michael and Holder 1985).

Radiographic features include the thickening of the cortex, periosteum, and endosteum at the posteromedial part of the tibial shaft (Fig. 16.25A). In general, these changes are inconspicuous, and, hence, may occasionally pass unnoticed. In contrast the change on pinhole scans is distinct, presenting vertical tracer

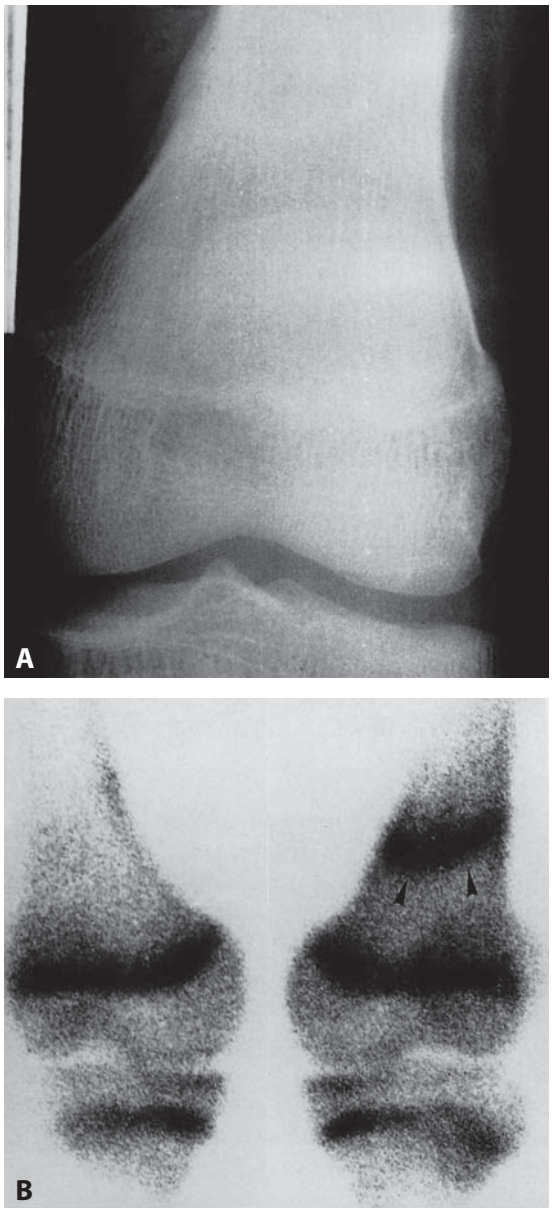

Fig. 16.24A, B Transverse tracer uptake in a long bone stress fracture. **A** Anteroposterior radiograph in a 16-year-old girl shows a barely discernible, transverse band-like density across the left distal femoral shaft (too dim to be reproduced). The regional periosteums are thickened but do not concentrate tracer significantly. **B** Anterior pinhole scans of both femora (simultaneous acquisitions) reveal transverse band-like tracer uptake across the left distal femoral shaft in stress fracture (*arrowheads*)

uptake in the cortex and endosteum (Fig. 16.25B). The pinhole scintigraphic findings of shin splints and stress fractures are basically different, readily permitting their differentiation: The uptake in the former condition is oriented vertically and tends to be less intense (Fig. 16.25B), whereas the uptake in the latter is transversely oriented and more intense (Fig. 16.23B and 16.24B). When a stress fracture involves a segment of the cortex longitudinally, which is not rare, tracer uptake is naturally oriented vertically (Fig. 16.22B). MRI of shin splints reveals vertical linear low signal with branching, which is considered to represent reactive bone thickening (Fig. 16.25C).

16.5 Surgical Bone Injuries

The bone injuries sustained during an operative procedure include contusion, fracture, and articular severance or dislocation. As is well known the thoracic cage is the most common site of operation-related bone injuries because open-heart or lung surgery requires forceful spreading of the intercostal or dissected sternal space for a wider operative field. Rib and sternal transection or resection can readily be detected by radiography. However, the contusion, microfractures, or covert fractures of the ribs, periosteal stripping, and severance or separation of the costocorporeal and costotransverse joints are extremely difficult to diagnose by plain radiography and often even by CT because the alterations are inconspicuous and many patients under postoperative care are unable or unwilling to cooperate in a radiographic room. In particular, rib contusion and periosteal stripping cannot be diagnosed unless substantial reparative or reactive bone has been formed. Fortunately, however, pinhole scintigraphy can sensitively detect these injuries as well as microfractures and costovertebral articular severance a few days after surgery by clearly portraying tracer uptake that is characteristic of each individual injury. Actually, contusion or microfractures created by a rib spreader are indicated by spotty uptake and periosteal injury by linear uptake typically

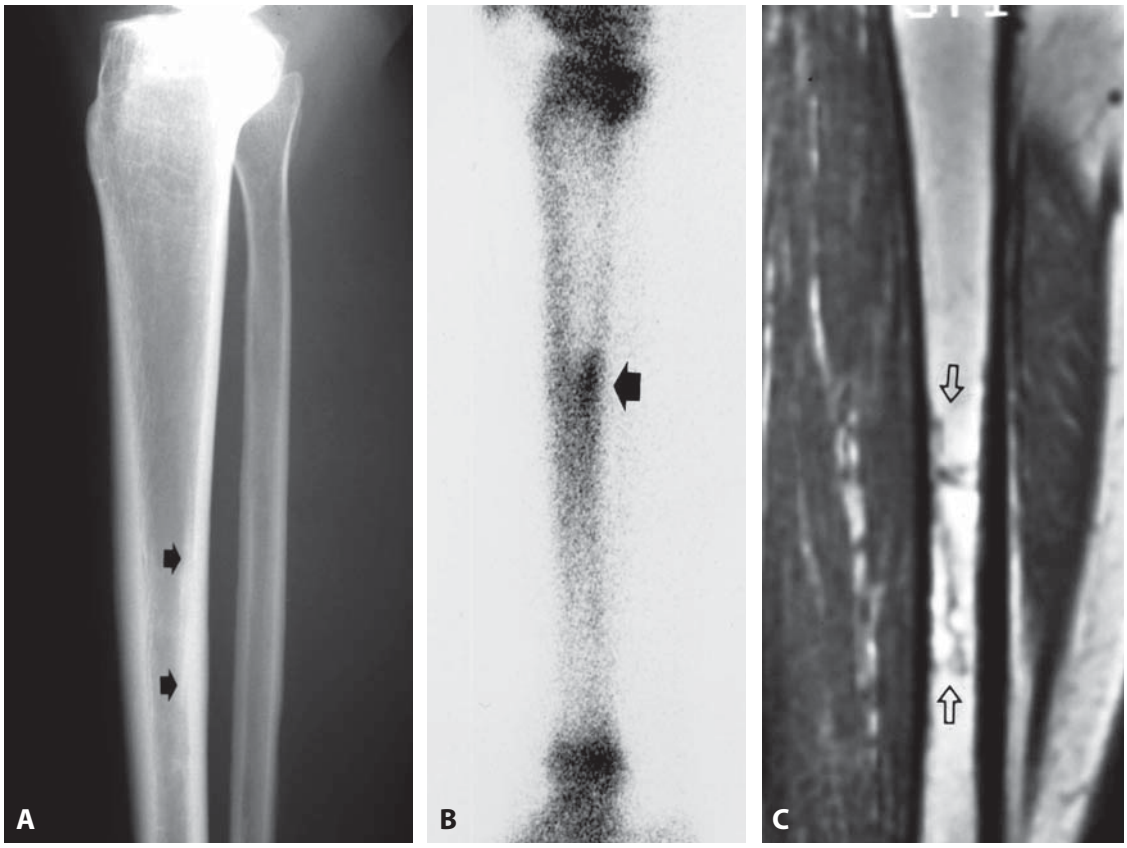

Fig. 16.25A–C Shin splints. **A** Lateral radiograph of the right leg in a 38-year-old female with pain shows diffuse corticoendosteal thickening in the posterior aspect of the tibial shaft (*arrows*). **B** Lateral planar scintigraph reveals vertical tracer uptake in the posterior cortex of the tibial shaft (*arrow*). **C** T1-weighted MRI demonstrates vertically aligned serpiginous low signal denoting linear bony thickening (*open arrows*)

along the cortical layer (Fig. 16.26A). The severed costocorporeal and costotransverse joints are portrayed on pinhole scan as small, vertically oriented, elongated uptake in the juxtaspinal and paraspinal regions, respectively (Fig. 16.26B). The former joint is formed between the vertebral articular facet and costal head and the latter between the articular facet of the transverse process and articular tubercles of the rib. The bone injuries produced at the site of biopsy, craniectomy or trephination, or at the donor site of graft can be detected with ease since they tend to accumulate tracer significantly. It is to be noted that such tracer uptake becomes intensified when the surgical defect contracts infection (Fig. 16.27).

16.6 Postreduction Changes of Joint Subluxation and Dislocation

The dislocation and subluxation of a joint can be efficiently diagnosed by radiography, and the state of reduction can also be assessed by radiography. However, the histological changes that may remain in the synovial capsule, joint, ligament, tendon, and bone after the reduction, especially nonsurgical, of a subluxation or dislocation are important object of pinhole scintigraphy. The most typical examples are reduced dislocations in the hip and shoulder.
The common injuries of scintigraphic interest are diffuse synovial inflammation and a sudden pull on the capsular attachment, for exam-

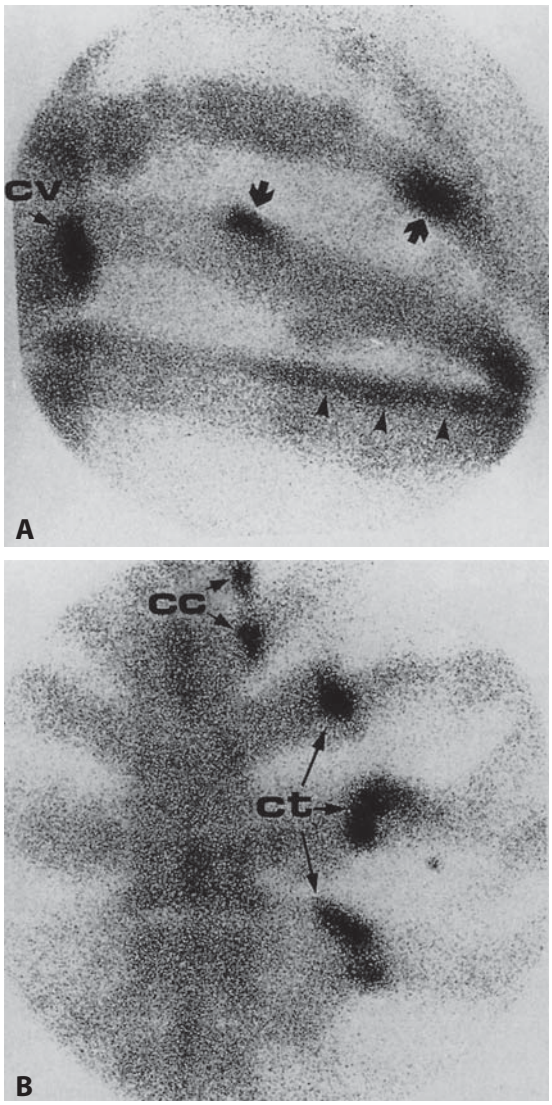

Fig. 16.26A, B Value of pinhole scan in traumatic injuries of the rib cage. **A** Various rib injuries produced by a surgical spreader. Posterior pinhole scintigraph of the right middle rib cage in a 49-year-old man who had undergone esophageal tumor surgery 14 weeks previously shows spotty tracer uptake in the occult rib fractures (*arrows*), linear uptake in the stripped periosteum (*arrowheads*), and vertically aligned, segmental tracer uptake in the severed costovertebral joint (*cv*). **B** Distinction between the injuries of the costotransverse (*ct*) and costocorporeal (*cc*) joints. Posterior pinhole scintigraph of the left middle rib cage in a 52-year-old man who had undergone esophageal cancer surgery 2 weeks previously reveals more or less vertically aligned, short segmental, very intense tracer uptake involving the costotransverse and costocorporeal joints which have been severed and subluxed. The former joints are located more laterally than the latter

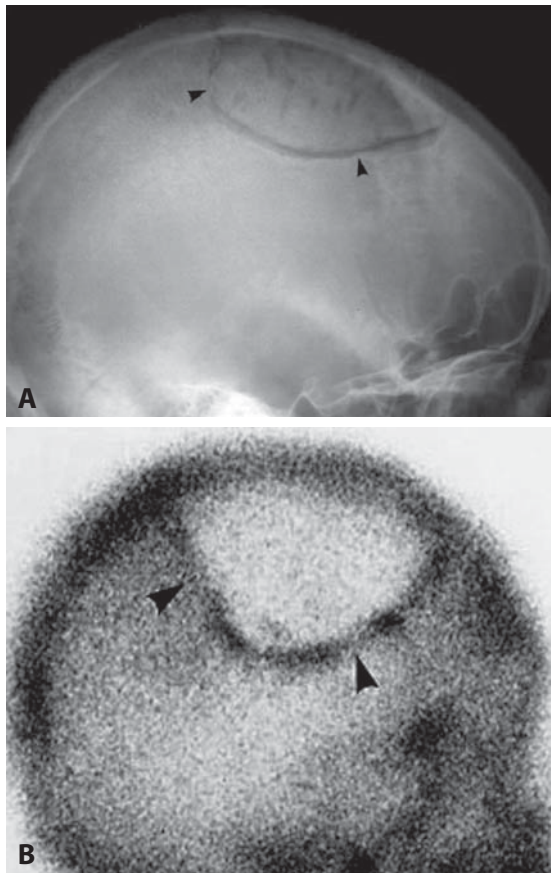

Fig. 16.27A, B Prominent tracer uptake in infected craniectomy. **A** Lateral radiograph of the skull in a 24-year-old man with an infected craniectomy wound in the right parietal bone shows an ovoid lucent surgical defect (*arrowheads*). **B** Lateral pinhole scintigraph reveals a large ovoid photon defect in the devitalized bone flap surrounded by increased tracer uptake in the craniectomy wound whose vascularity is preserved (*arrowheads*)

ple, at the zona orbicularis in the femoral neck with a widened joint space that is often asymmetrical (Fig. 16.28A). In the inferior dislocation or subluxation of the glenohumeral joint, a downward force is applied to the capsular and ligamentous attachments at the coracoid process, intertubercular sulcus, through which the synovium-lined biceps tendon passes, and glenoid labrum (Fig. 16.29A). As anticipated from the nature of the injuries in subluxation or dislocation in the hip and shoulder, pinhole scintigraphy shows characteristic tracer uptake in the capsular attachment of the femoral neck

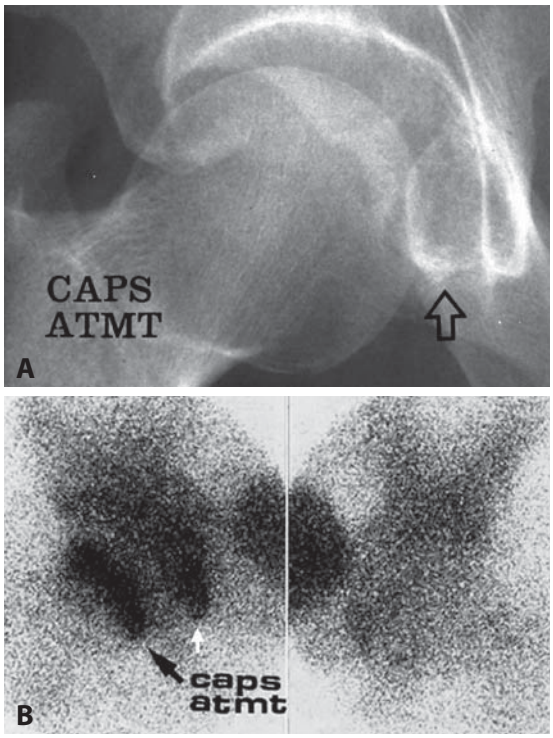

Fig. 16.28A, B Reduced hip dislocation. **A** Anteroposterior radiograph of the right hip in a 37-year-old man with a restored dislocation shows asymmetrical residual widening of the medial joint space (*open arrow*) (*CAPS ATMT* site of joint capsular attachment). **B** Anterior pinhole scintigraphs of both hips reveal intense uptake at the medial compartment of the right hip joint (*white arrow*) and at the joint capsular attachment (*caps atmt*). The latter uptake reflects the force of the pull on the capsule at the time of dislocation. Note that no abnormal tracer uptake is seen in the healthy left hip joint

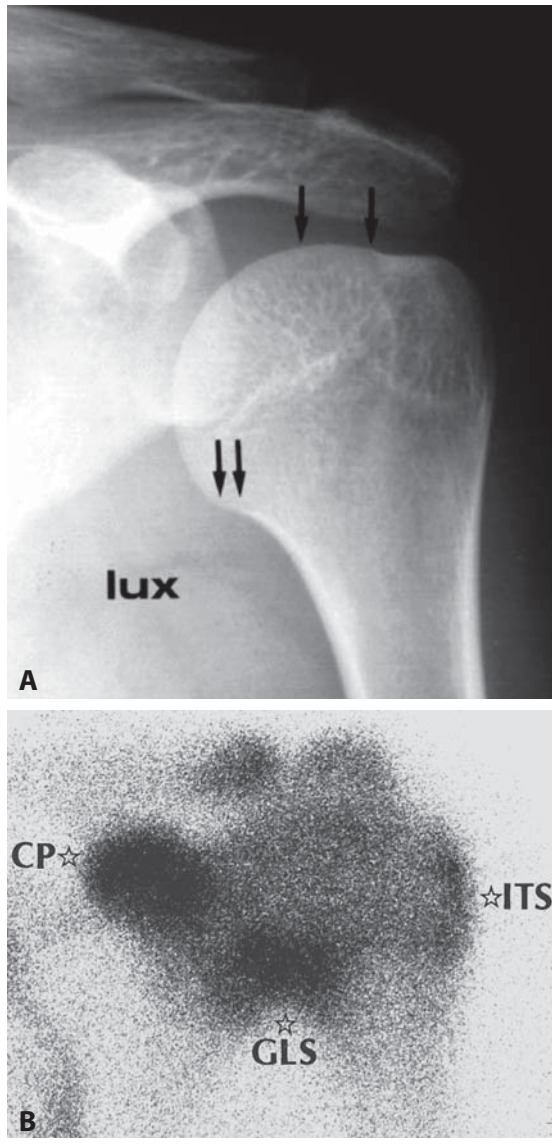

Fig. 16.29A, B Subluxation of the glenohumeral joint. **A** Anteroposterior radiograph of the left shoulder in a 24-year-old female with subluxation shows caudal displacement of the humerus out of the glenoid (*lower arrows*) with separation of the subacromial space (*upper arrows*). **B** Anterior pinhole scintigraph reveals patchy tracer uptake in the coracoid process (*CP*), glenoid labrum synovium (*GLS*), and intertubercular sulcus (*ITS*) in which the synovium sheathed biceps tendon lies

(Fig. 16.28B) and the glenoid labrum synovium in the shoulder (Fig. 16.29B). The former tracer uptake is arbitrarily termed the "collar" sign and the latter the "axillary saddle" sign. In addition, patchy tracer uptake may be seen in the medial aspect of the hip joint that remains widened with an inflamed synovium after reduction and also in the coracoid process and intertubercular sulcus of the humerus where the biceps tendon sheath with inflammation is located (Fig. 16.29B). Postreduction scintigraphy of fracture-dislocation of the femoral head shows the composite feature of, in addition to the "collar" sign of pull on the capsular attachment at the zona orbicularis, hip joint synovitis, and fracture, respectively, as band-like, diffuse, and focal uptake in the femoral neck, hip joint, and femoral head (Fig. 16.30).

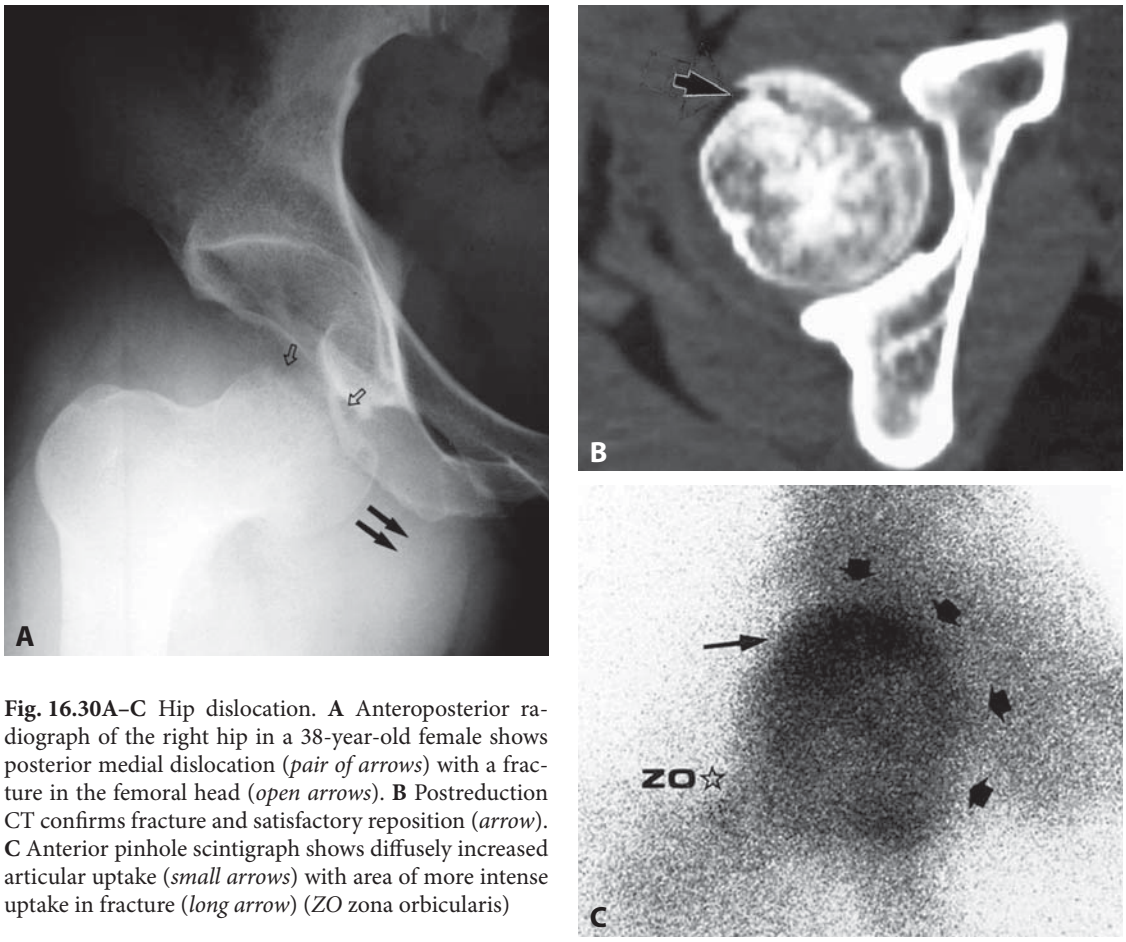

Fig. 16.30A–C Hip dislocation. **A** Anteroposterior radiograph of the right hip in a 38-year-old female shows posterior medial dislocation (*pair of arrows*) with a fracture in the femoral head (*open arrows*). **B** Postreduction CT confirms fracture and satisfactory reposition (*arrow*). **C** Anterior pinhole scintigraph shows diffusely increased articular uptake (*small arrows*) with area of more intense uptake in fracture (*long arrow*) (*ZO* zona orbicularis)

16.7 Arthroplasties and Fixation Devices

The scintigraphic diagnosis of bone or joint defects created by arthroplasties or fixation devices such as total hip replacements, intramedullary pins and nails, and screwed compression plates is self-explanatory unless complicated by distortion, breakage, or infection. In general, the shape and location of arthroplasties and fixation devices are readily shown by pinhole scintigraphy, because the majority of these devices are sufficiently large in size and made of photon-absorbing metallic materials, creating obvious photon defects with a shape that is specific for each device. For example, bipolar endoprostheses create a cup-like photon defect in the acetabular fossa, a rounded defect in the femoral head, and an elongated rod-like defect in the femoral neck and medullary cavity (Fig. 16.31). Likewise, widely used lumbar fixation devices with transpedicular screwing produce a characteristic lattice-like photon defect. It consists of vertical uptake in the lateral aspects of the spinal column denoting bone reaction and new bone formation, and multiple photopenic holes in between due to metallic screws (Fig. 16.32A). However, it is hardly possible to detect small metallic fixing devices such as screws and wires. In certain patients large intramedullary nails having remained in the bone marrow space for months and years may elicit new bone formation so that they present as long intramedullary uptake (Fig. 16.33), while in others intramedullary nails on removal leave behind tracks with increased uptake on pinhole scintigraphs (Fig. 16.34).

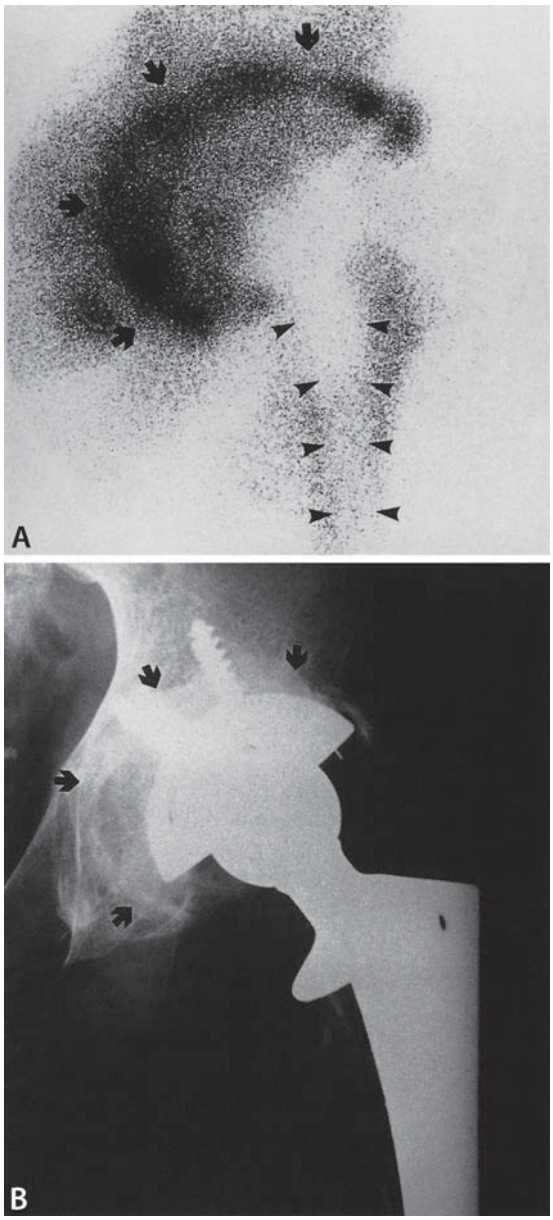

Fig. 16.31A, B Metallic arthroplasty. **A** Anterior pinhole scintigraph of the left hip in a 37-year-oldman with total arthroplasty reveals a cup-shaped photopenic defect in the acetabulum (*arrows*) and a long intramedullary defect in the proximal femoral shaft (*arrowheads*). The extremely intense tracer uptake seen in the acetabulum denotes severe osteoarthritis that necessitated the arthroplasty (*arrows*). **B** Anteroposterior radiograph reveals the total hip prosthesis as well as the sclerotic change of advanced acetabular osteoarthritis, which necessitated surgery (*arrows*)

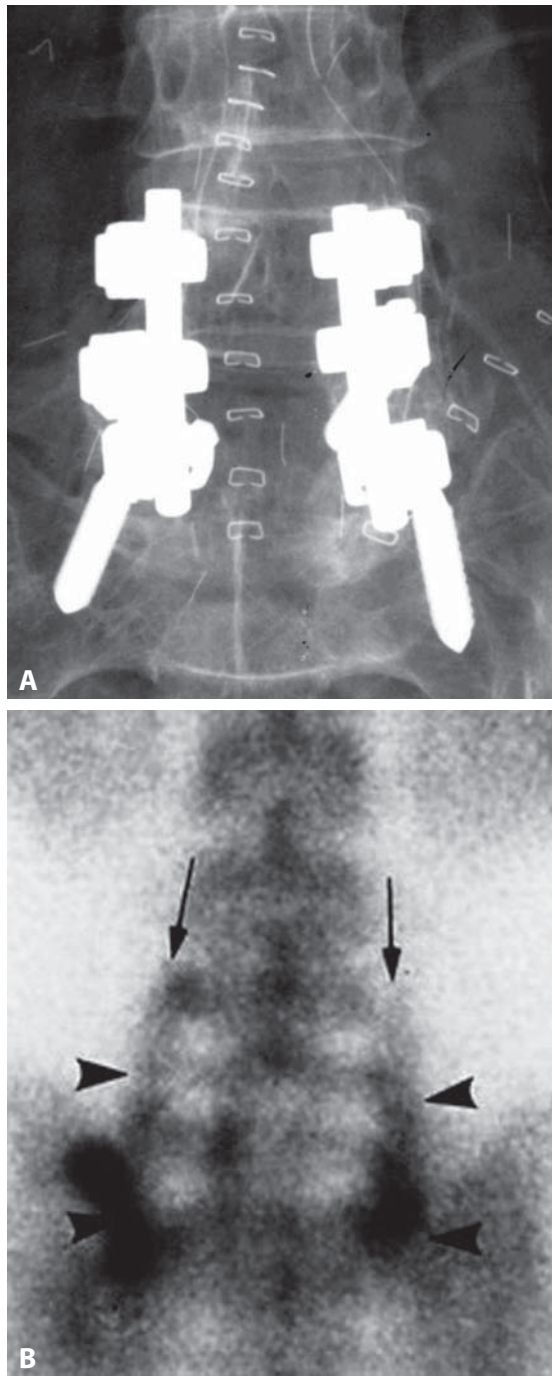

Fig. 16.32A, B Transpedicular metallic screw fixation. **A** Posteroanterior radiograph of the lower lumbar spine in a 67-year-old female with pedicular screwing shows a ladder-like metallic device and screws applied to the lower lumbar spine and sacral base. **B** Posterior pinhole scintigraph reveals lattice-like tracer uptake denoting reaction and new bone formation (*arrows*) and metallic devices tracts (*arrowheads*)

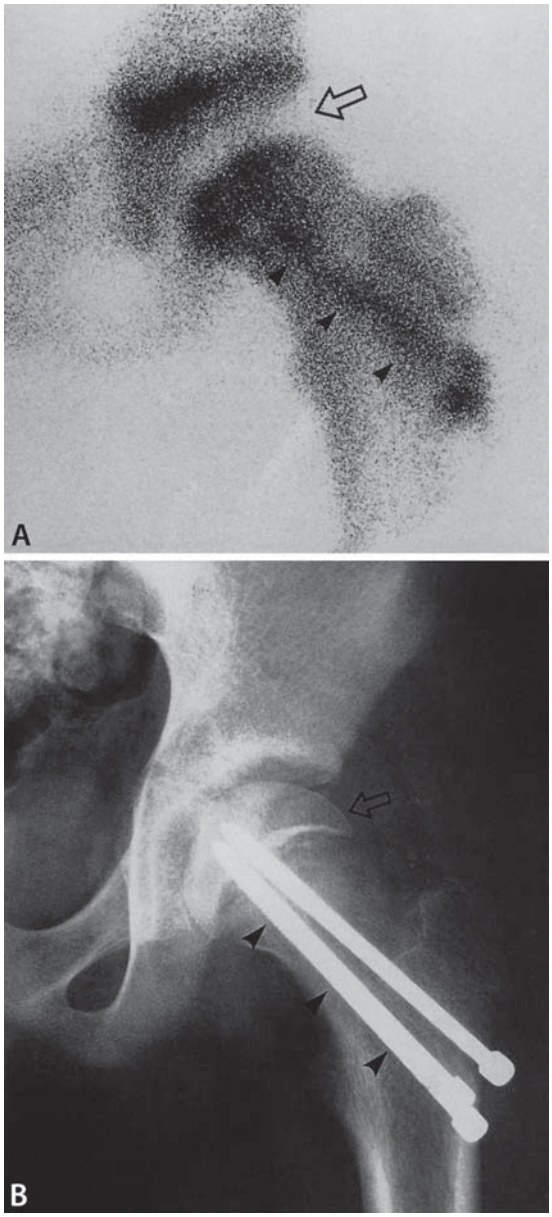

Fig. 16.33A, B Nonspecific bone reaction induced by intramedullary pinning. **A** Anterior pinhole scintigraph of the left hip in an 11-year-old girl with a slipped capital femoral epiphysis immobilized with Knowle's pins shows intense tracer uptake along the pin tracks (*arrowheads*). The metaphysis likewise concentrates tracer intensely due to the attempted repair. The epiphysis is totally "cold", denoting avascular bone necrosis (*open arrow*). **B** Anteroposterior radiograph shows three pins placed in the neck (*arrowheads*) and a flat femoral head with a widened physeal line (*open arrow*)

It is not clear how and why such different uptake patterns are created. One of the advantages of pinhole scanning is the feasibility of observing and archiving the etiological disease for which the arthroplasty or screwing was instituted. Common underlying diseases in the hip include degenerative arthritis (Fig. 16.31) and fracture or epiphysiolysis in the femoral neck (Fig. 16.33). A loosened or inflamed arthroplasty or fixation device within the medullary space, cortex, and periosteum can be diagnosed by this means because it accumulates tracer intensely (Fig. 16.35). Pinhole scintigraphy is likewise suited to the evaluation of early socle formation that supports the tip of the arthroplasty stem inserted deep into the midfemoral shaft, frequently before a radiographic change is manifest (Fig. 16.36). Tracer uptake is indeed subtle so that it may not be seen on ordinary scintigraphs. Socle formation is known to result from the stress shielding effect of the total hip prosthesis, and radiographically it can first be recognized in the chronic stage that spans from 6 to 18 months after implantation.

16.8 Healing of Bone Fracture

Bone scintigraphy is an efficient and reliable means of assessing fracture healing. Scintigraphic manifestations of fractures vary according to clinical stage (Matin 1979) and many other factors such as type, extent, location, patient's age, nutritional state, complications, and so forth. Generally, however, it is accepted that tracer uptake is rapid, intense, and diffuse in the acute stage (Fig. 16.37A) and becomes further intensified and localized in the subacute stage (8–12 weeks after injury; Fig. 16.37B). Thereafter, tracer uptake slowly diminishes and returns to normal over a period of a year or more (Fig. 16.38). Pinhole scintigraphy shows some characteristics of fracture healing in greater detail with enhanced information. The tracer uptake in acute fractures of normal ribs is charac-

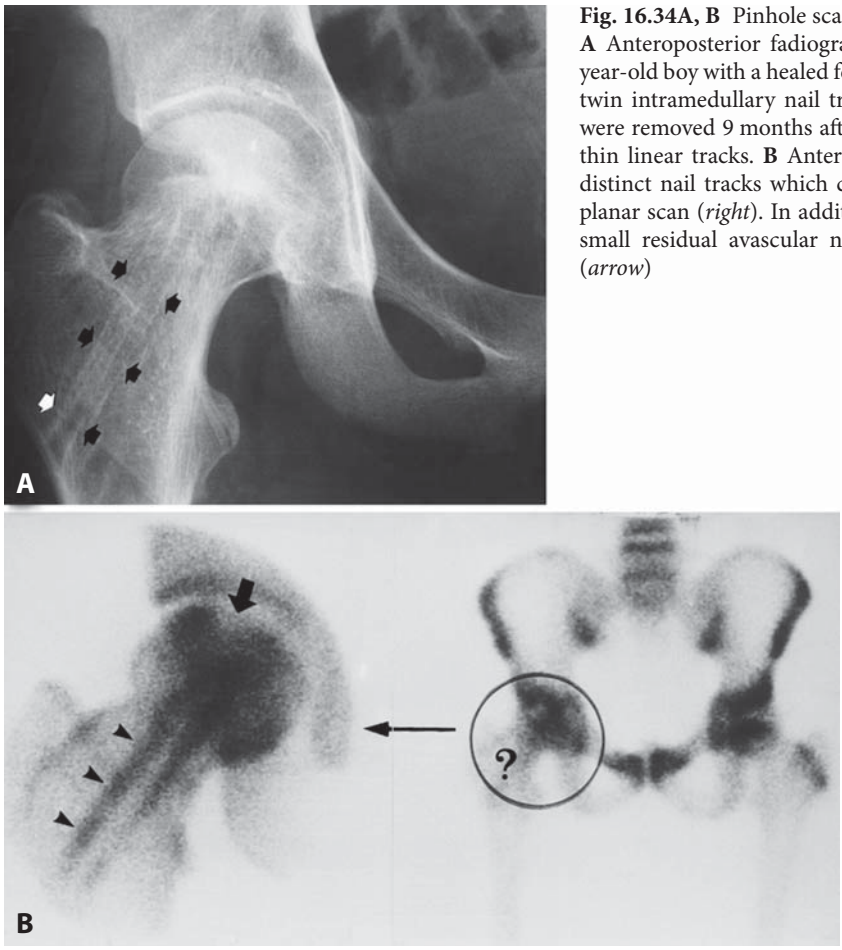

Fig. 16.34A, B Pinhole scan demonstration of nail tract. **A** Anteroposterior fadiogram of the right hip in a 15-year-old boy with a healed femoral neck fracture showing twin intramedullary nail tracks (*between arrows*). Nails were removed 9 months after placement, leaving behind thin linear tracks. **B** Anterior pinhole scan (*left*) shows distinct nail tracks which cannot be appreciated on the planar scan (*right*). In addition, the pinhole scan reveals small residual avascular necrosis in the femoral head (*arrow*)

terized by more intense main tracer uptake sided bilaterally by less intense reactive uptake, reflecting fracture and local hemorrhage or hyperemia, respectively (Fig. 16.37A; these fractures were 16 days old at the time of scintigraphy). In the subacute stage more intense uptake in the central region becomes narrowly limited to the fracture as reactive uptake subsides (Fig. 16.37B; these fractures were 8 weeks old). With the further passage of time, intense uptake slowly fades, with eventual return to normal within a year (Fig. 16.38). We have observed the complete healing of a compression fracture of the T9 vertebra in a 67-year-old male patient in 15 months as far as clinical and scintigraphic findings are concerned (Fig. 16.39) while a 40-year-old ancient fracture of the midshaft of the right femur in a male patient aged 80 years persistently accumulated tracer (Fig. 16.40). Such persistent uptake in the femoral shaft appears at least in part to be related to the force of weight bearing. In another femoral neck fracture in a female treated with intramedullary pinning, complete healing occurred in less than 25 months (Fig. 16.41). She was 64 years of age when last examined. In contrast to uniform tracer uptake in simple fresh fractures, fractures complicated by nonunion, dead bone, or infection present irregular photon defects within large uniform uptake of well-healed fracture with new bone formation and/or mineralized hematoma (Fig. 16.42).

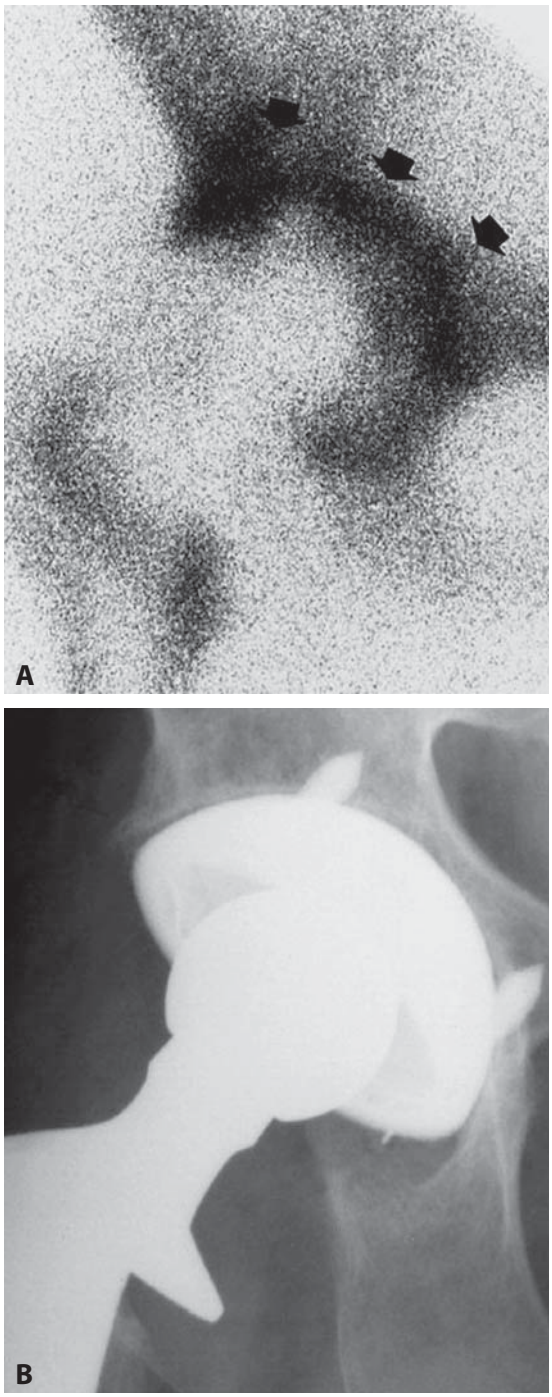

Fig. 16.35A, B Arthroplasty with inflammation. **A** Anterior pinhole scintigraph of the right hip in a 58-year-old female with total prosthetic hip replacement shows intense tracer uptake in the acetabulum with large photon defects of the prosthesis (*arrows*). **B** Anteroposterior radiograph reveals the cup-and-ball with handle of the prosthesis

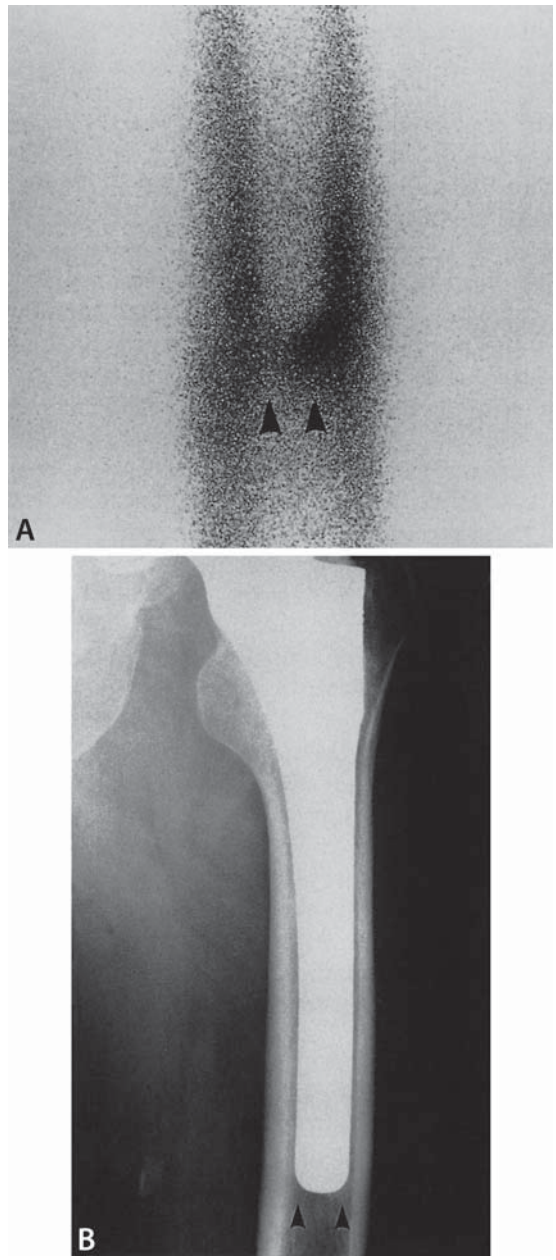

Fig. 16.36A, B Preradiographic detection of early socle formation in a femoral endoprosthesis. **A** Anterior pinhole scintigraph of the proximal left femoral shaft in a 68-year-old man with a bipolar endoprosthesis reveals minimally increased tracer uptake about the stem tip (*arrowheads*), indicating early socle formation with enhanced bone turnover. **B** Anteroposterior radiograph shows the stem tip. No bone reaction is seen at this stage (*arrowheads*)

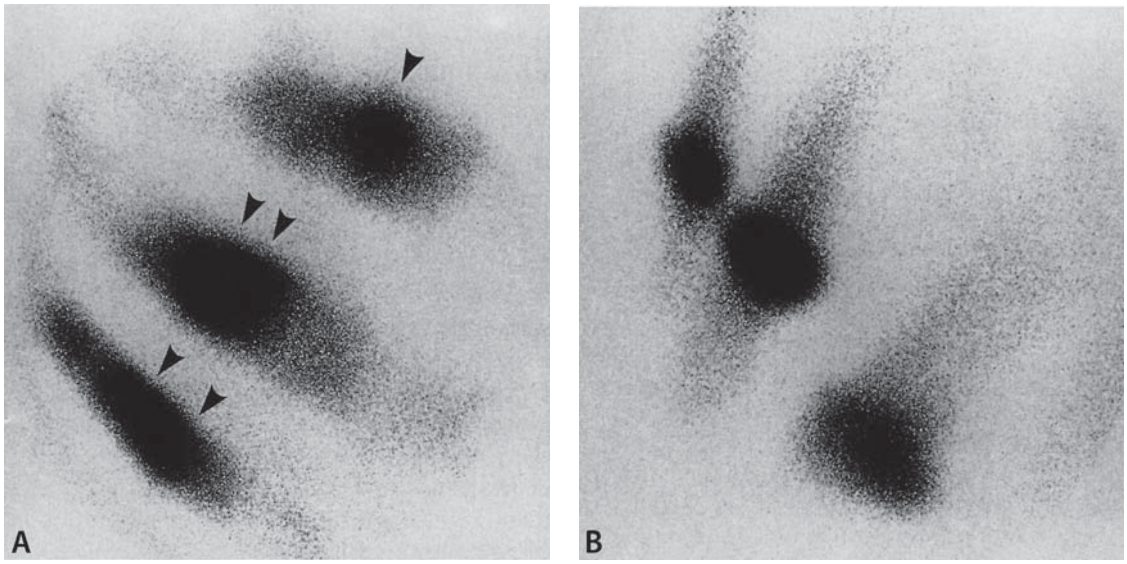

Fig. 16.37A, B Healing of rib fractures. **A** Anterior pinhole scan of the right middle rib cage in a 76-year-old man with 16-day-old fractures in the anterior axillary lines of ribs 5–7 shows intense tracer uptake in the center attended by less intense uptake on the side (*arrowheads*). The main uptake is vertically aligned. **B** Posterior pinhole scintigraph of the left lower rib cage in another 65-year-old man with 8-week-old fractures in the posterior axillary lines of ribs 8–10 shows well-defined, vertically aligned, discrete tracer uptake in each rib

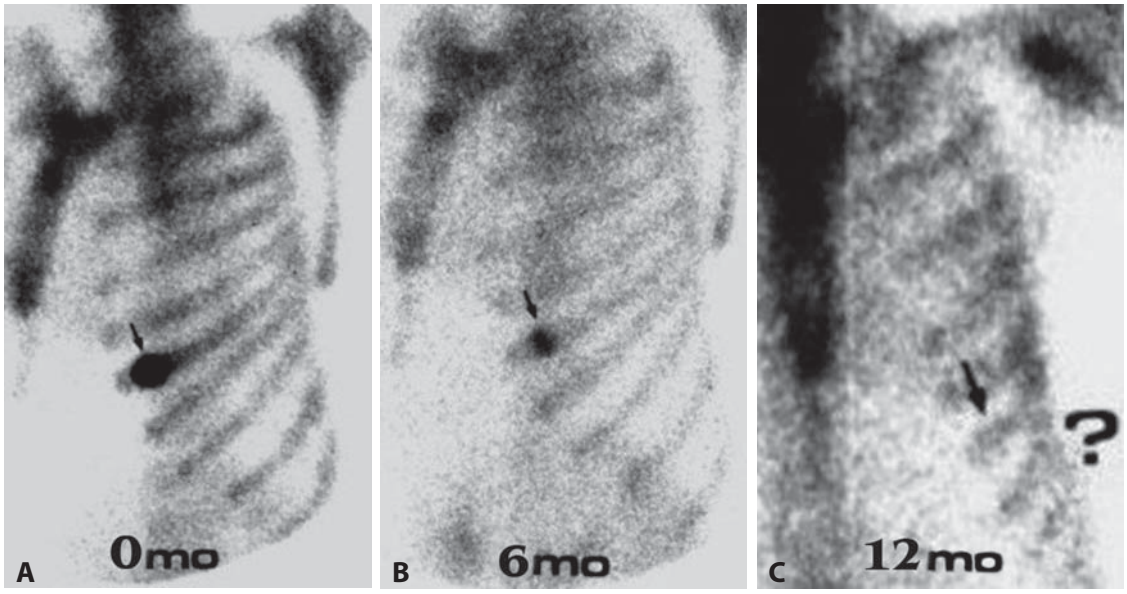

Fig. 16.38A–C Healing of rib fracture. **A** Initial anterior planar scintigraph of the left rib cage in a 50-year-old female with a fresh fracture in the anterior end of left bony rib 6 shows intense uptake (*arrow*). **B, C** Follow-up scintigraphs taken 6 and 12 months later, respectively, show gradual subsidence of tracer uptake return to normal within a year

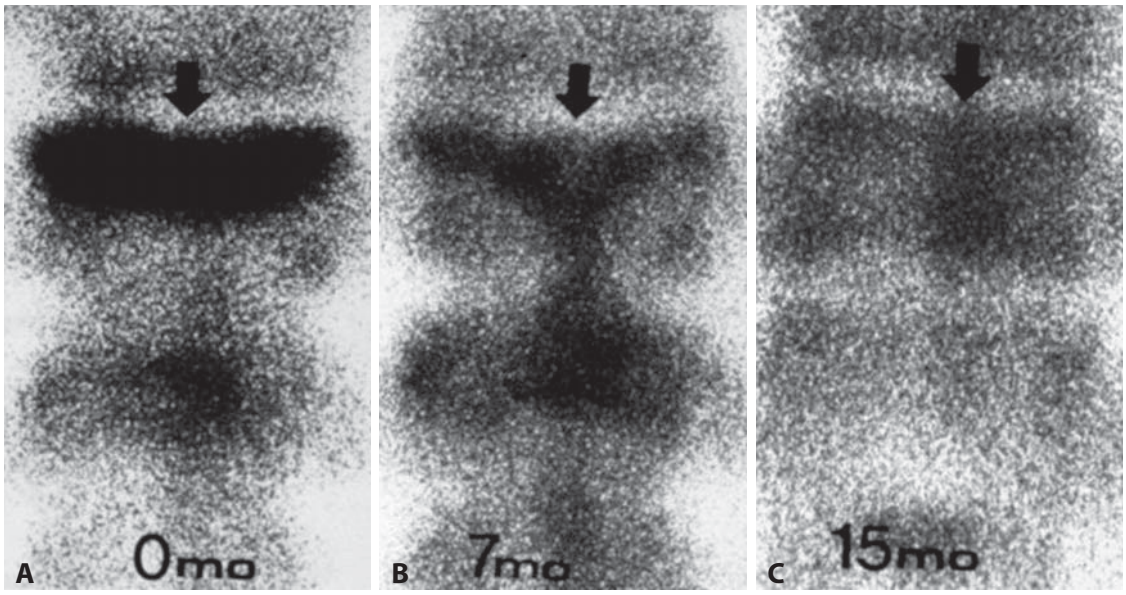

Fig. 16.39A–C Healing of compression fracture of the vertebra. **A** Initial posterior pinhole scintigraph of the L2 vertebra in a 67-year-old man with a fresh compression fracture in the upper endplate shows intense tracer uptake (*arrow*). **B, C** Follow-up scintigraphs taken 6 and 15 months later, respectively, show gradual subsidence of tracer uptake and an eventual return to normal. Note residual compression deformity (*arrow*)

16.9 Assessment of Vascularized Bone Grafts

Bone grafts can be vascularized autogenous grafts, conventional autogenous grafts, or free nonvascularized periosteal grafts. With the introduction of fine microvascular techniques, free vascularized autogenous grafts have become widely used (Taylor 1983). Donor sites are mostly the fibula, iliac crest, or rib. The main clinical indications for bone grafts include long-bone defects resulting from compound fractures, tumor ablation, malunion or pseudoarthrosis, avascular necrosis, and congenital malformations. The viability assessment is probably the most important examination after bone grafting, and revascularization is to be confirmed as early as possible. ^{99m}Tc-MDP bone scintigraphy combined with plain radiography is considered the most efficient modality for assessing graft viability and documenting the anatomical state, and early bone scintigraphy is performed between 1 and 2 weeks after surgery (Soost et al. 1999; Lauer et al. 2000).

Radiography is essential for the documentation and serial observation of the morphology of bone grafts. However, it cannot reliably evaluate viability in the early postoperative phase (Fig. 16.43A). For the study of graft viability, ^{99m}Tc-MDP bone scanning has long been used since the pioneering studies published in the early 1980s (Lisbona et al. 1980; Dee et al. 1981; Berggren et al. 1982). The bone scans for this purpose are obtained mostly using conventional planar scintigraphy. As is well known, however, the resolution of planar scintigraphy and SPECT is such that revascularization and surface bone formation of a graft are extremely difficult to assess (Fig. 16.43B). Fortunately, pinhole scintigraphy can produce scintigraphs with great detail, clearly depicting both the anatomical and metabolic state of a graft for reliable analysis of the viability and morphological fitness (Fig. 16.43C). Indeed, pinhole scintigraphy can demonstrate even creeping ossification on the graft surface and helps de-

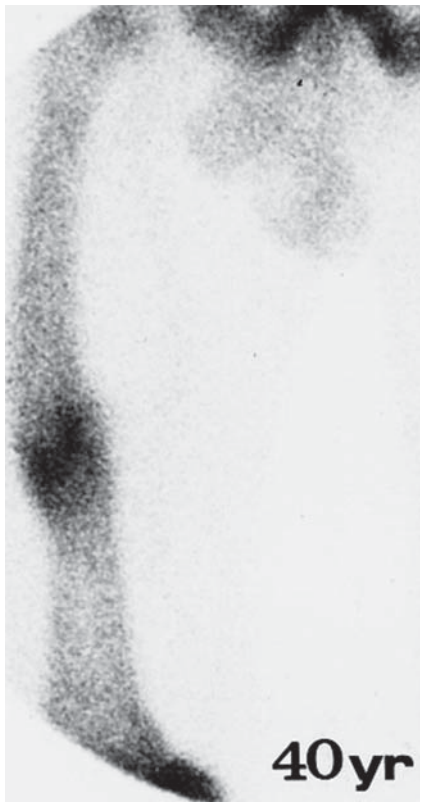

Fig. 16.40 Persistence of tracer uptake in an ancient fracture. Anterior planar scintigraph of the right femur in an 88-year-old man shows increased tracer uptake at the site of a 40-year-old fracture with a mild deformity

Fig. 16.41A, B Healing of femoral neck fracture with nailing. **A** Anterior pinhole scintigraph of the right hip in a 64-year-old female with femoral neck fracture treated by intramedullary nailing shows diffusely increased tracer uptake with especially intense uptake in the fracture (*single arrow*) and nail tract (*pair of arrows*). **B** Follow-up scintigraph taken 25 months later reveals good healing and complete resolution of abnormal uptake

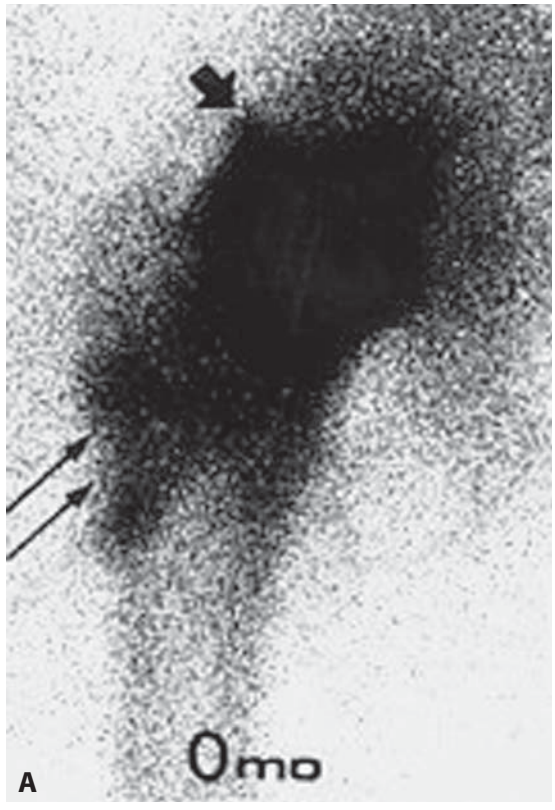

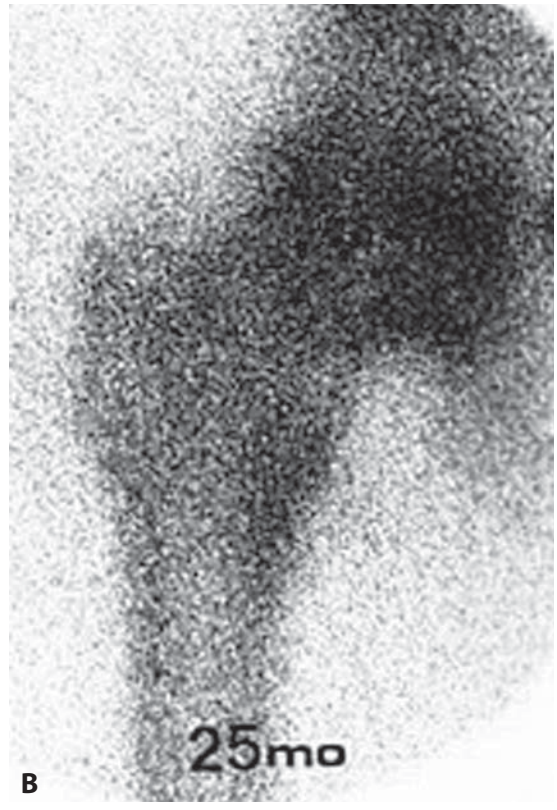

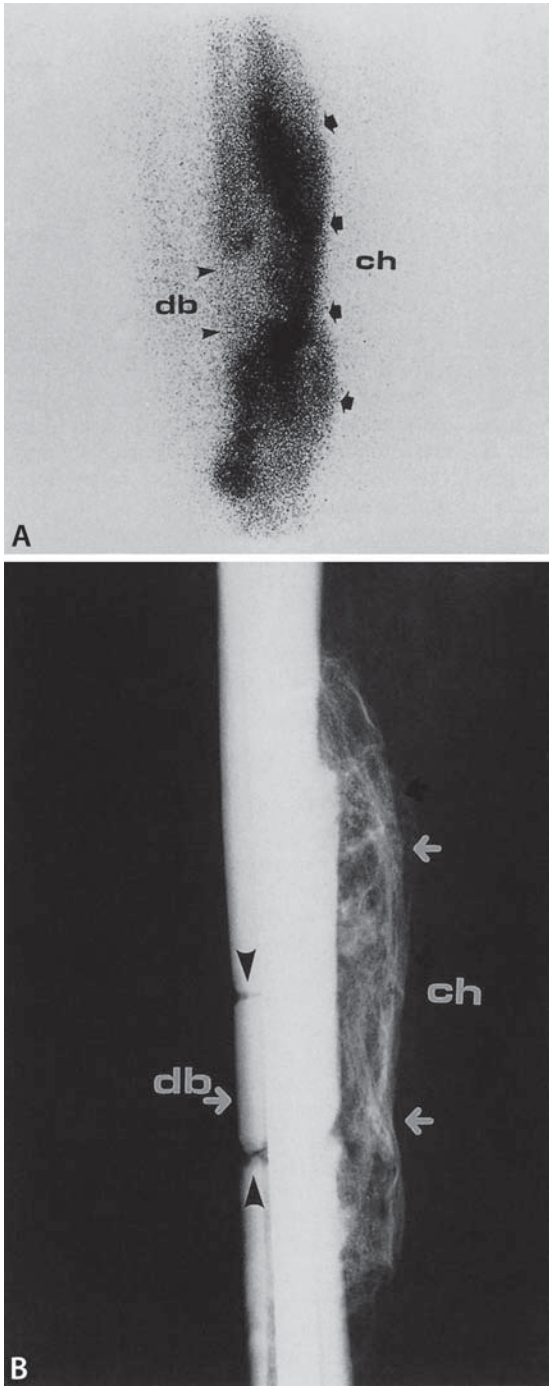

Fig. 16.42A, B Devitalized bone in comminuted fractures. **A** Anterior pinhole scintigraph of the right midfemoral shaft in a 22-year-old woman with comminuted fractures treated with a Küntscher's nail shows irregularly increased tracer uptake in the fracture site with a "cold" defect of the dead bone that is interposed in the lateral cortex (*db, arrowheads*). The prominent tracer uptake with a scalloped border in the medial aspect is calcified periosteal hematoma (*ch, arrows*). **B** Anteroposterior radiograph reveals a small, isolated bone fragment in the lateral cortex, corresponding to the "cold" defect (*arrowheads*). Note the extensive ossification in the periosteal hematoma formed along the medial cortex (*arrows*)

termine whether an implanted bone has been incorporated into and naturalized by the host bone. An additional advantage is that scintigraphy obtained for the observation of grafted bone often provides useful information on the condition that has necessitated the grafting. Actually, the disease treated in the particular patient shown in Fig. 16.43 was avascular osteonecrosis of the femoral head, and follow-up scintigraphy taken 6 months later showed partial revascularization (Fig. 16.43D). Figure 16.44 shows an example of a devitalized fibular graft that had been implanted to replace a necrotized tibial midshaft. This case clearly demonstrates that bone does not accumulate tracer when devascularized.

16.10 Complications of Traumatic Bone Injuries

The complications of fractures of scintigraphic interest include nonunion, pseudoarthrosis, avascular necrosis, devitalized bone fragments, displaced fragments, premature physeal closure, and myositis ossificans. Nonunion may be defined as the failure of fracture to heal and reunite completely during a period of 6–9 months following an injury, and include pseudoarthrosis (Cruess and Dumont 1975). It is most common in the femoral and tibial fractures, and radiographically indicated by a radiolucent bone defect that is not sealed with bone (Fig. 16.45A). Pinhole scintigraphy can depict a band-like photon defect between the fragments whose borders accumulate tracer intensely (Fig. 16.45B).

On the other hand, a typical pseudojoint consists of the pointed end of one fragment and concave adaptor of the other fragment (Fig. 16.46A). Radiographically, the fragments

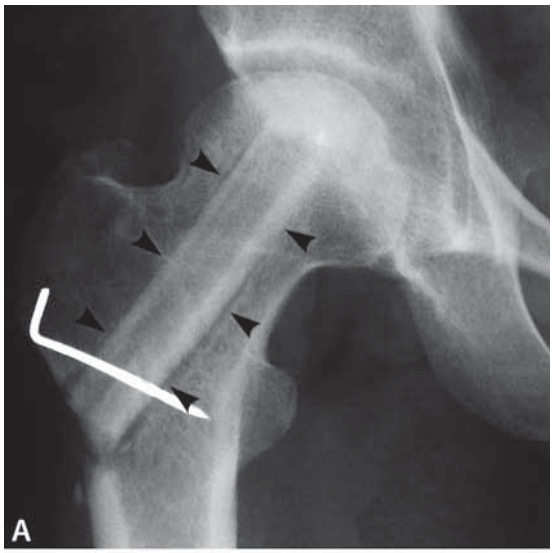

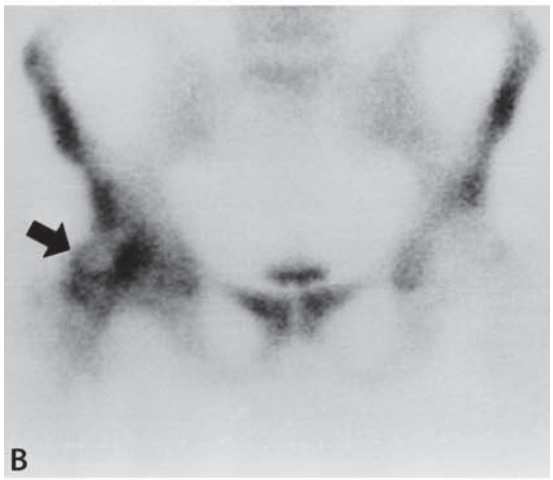

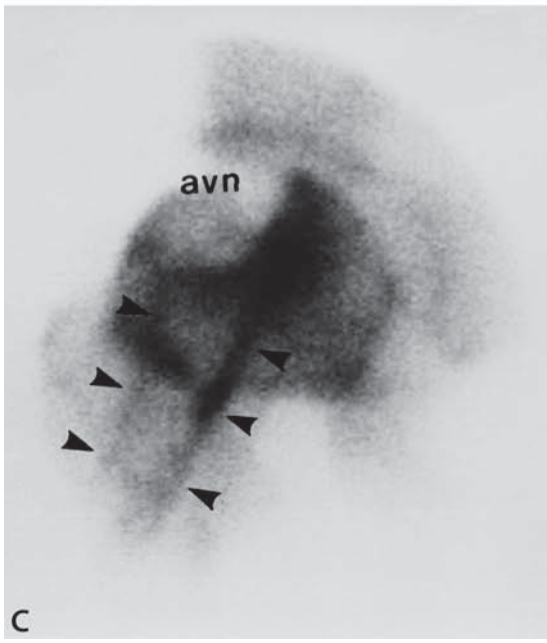

Fig. 16.43A–D Radiographic and scintigraphic assessment of vascularized bone graft. **A** Anteroposterior radiograph of the right hip in 29-year-old man with a free vascularized fibular graft performed 10 days previously to treat avascular necrosis in the femoral head. The graft is clearly shown to be located in the drilled lucent tunnel (*arrowheads*) along with an L-shaped pin. Note that aseptic necrosis is not clearly shown on the radiograph. **B** Anterior planar scan shows an ill-defined mixture pattern of irregular cold and hot areas (*arrow*). Neither the implant nor the hip joint anatomy can be discerned. **C** Anterior pinhole scan distinctly shows rich revascularization of the implant (*arrowheads*). Avascular bone necrosis in the femoral head (*avn*) is also well-visualized. **D** Anterior pinhole scan showing nearly complete metabolic incorporation or naturalization of the graft. Note that aseptic necrosis is also partially filled (*arrow*)

Fig. 16.44A, B Devitalization of fibular graft. **A** Anteroposterior radiograph of the left leg in a 28-year-old man with vascularized bone implanted for a large posttraumatic tibial defect shows a well-positioned fibular graft (*arrowheads*). **B** Anterior pinhole scintigraph reveals total absence of uptake in the implant indicating unsuccessful vascularization (*arrowheads*). Note positive bone uptake in survived tibia (*arrows*) and fibular fachture (XX) ▷

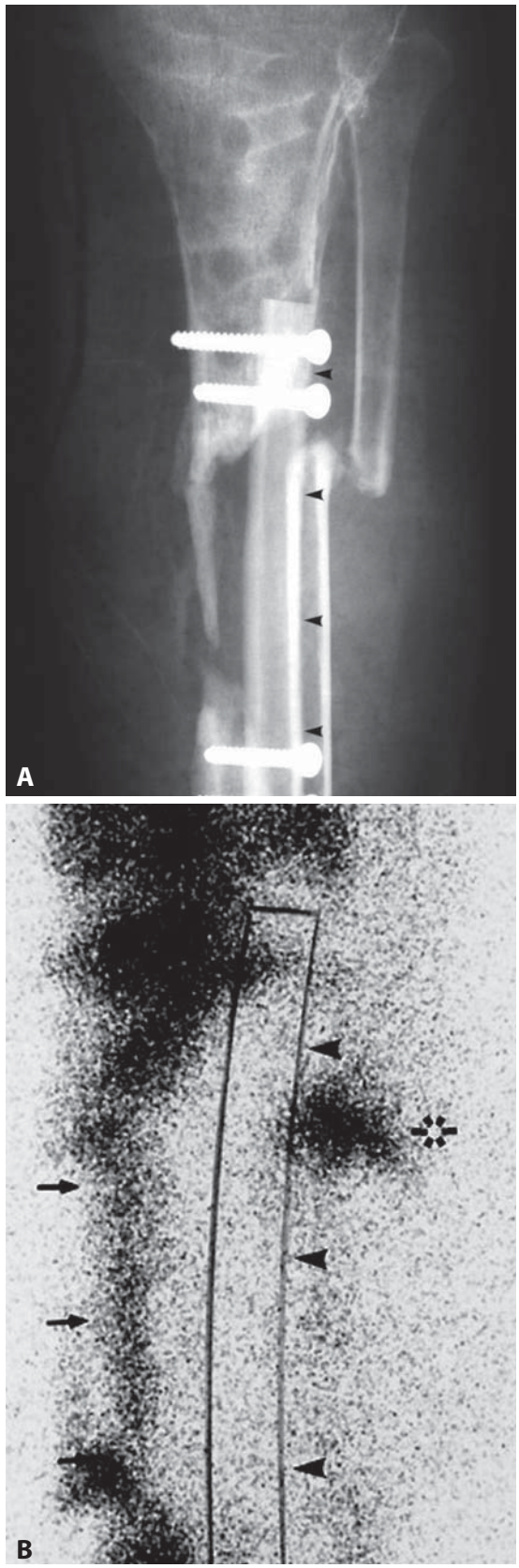

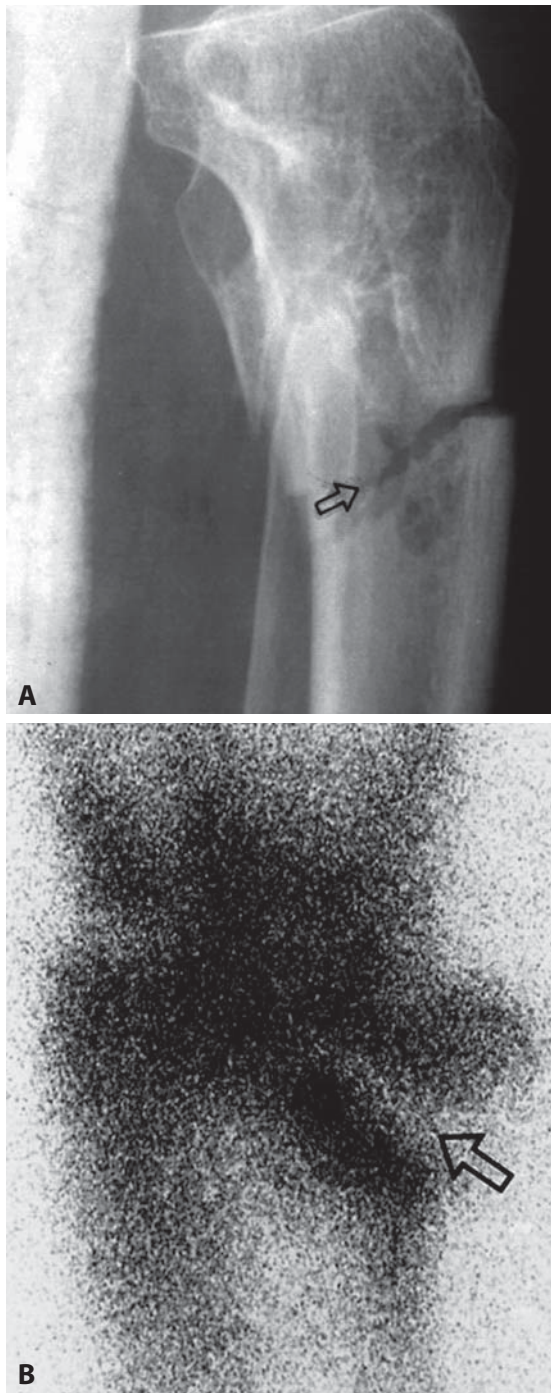

Fig. 16.45A, B Nonunion of fracture. **A** Lateral radiograph of the right tibia in a 59-year-old female with fracture nonunion shows an oblique linear radiolucent bone defect not in-filled with callus (*arrow*). **B** Anterior pinhole scintigraph reveals band-like photopenia with locally increased tracer uptake in the lateral aspect of the tibial shaft representing fracture nonunion (*arrow*). Note exuberant bony outgrowth with increased tracer uptake of inefficient callus formation above the arrow

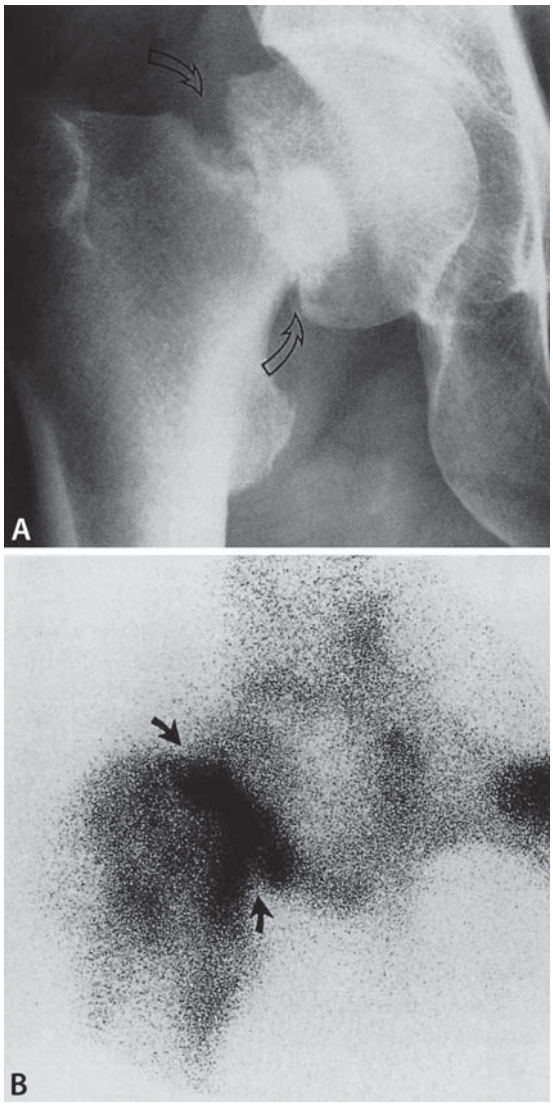

Fig. 16.46A, B Pseudoarthrosis. **A** Anteroposterior radiograph of the right hip in a 49-year-old man with complicated fracture of the right femoral neck shows the pointed, sclerotic end of the distal fragment and an irregularly widened fracture line (*open arrows*). **B** Anterior pinhole scintigraph shows very intense tracer uptake in the fracture ends with a widened fracture line (*arrows*)

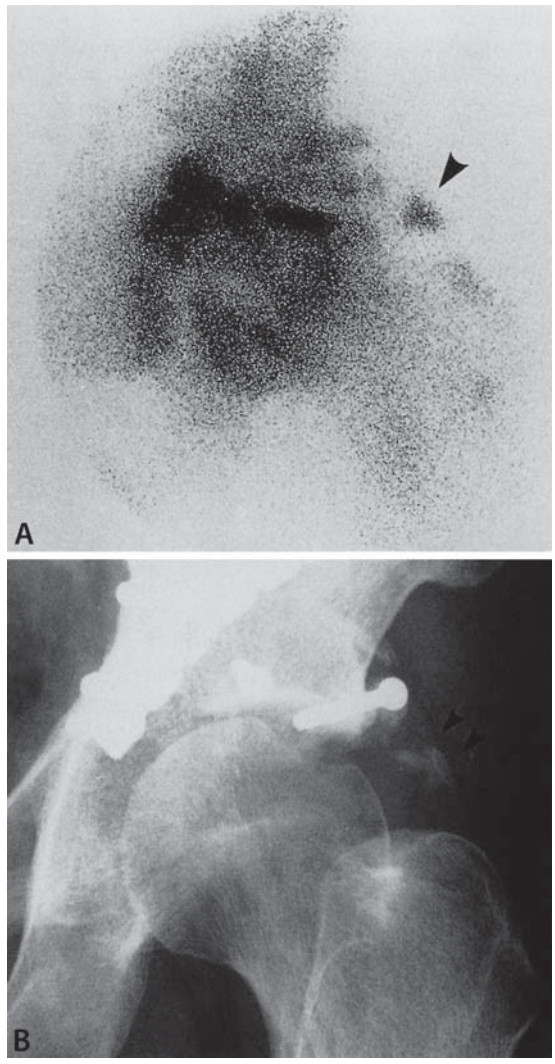

Fig. 16.47A, B Vascularization in the displaced fracture fragment. **A** Anterior pinhole scintigraph of the left hip in a 38-year-old man with 6-month-old surgically treated comminuted fractures in the left acetabulum shows small spotty tracer uptake in the lateral aspect of the hip (*arrowhead*) as well as moderate tracer uptake in the injured acetabular roof. **B** Anteroposterior radiograph shows a small displaced bone fragment in the soft tissue lateral to the hip joint (*arrowheads*). The fractures in the acetabulum are held with an AO reconstruction plate and screws

are sclerotic due to improper articulation. In contras to the findings in nonunion, pseudoarthrosis is characterized by increased tracer uptake, reflecting false articular motion and new bone formation (Fig. 16.46B). Often the devitalization of a fractured bone poses problems in clinical management of the disease. Deprived of a blood supply, bone is devitalized, and appears radiographically opaque (Figs. 16.42B). In an early stage, however, the radiographic recognition of devitalized bone is not easy because osseous changes are too subtle or absent (Fig. 13.1B). Bone scintigraphy can play a decisive role in this situation (Fig. 13.1A). It is well

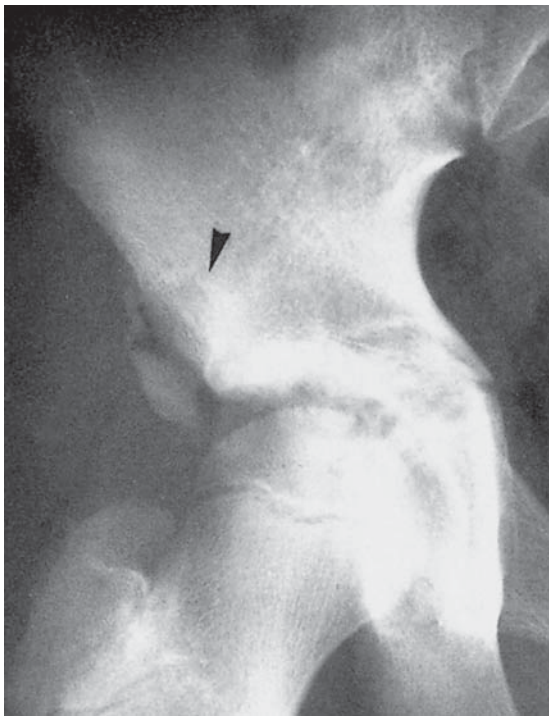

Fig. 16.48 Athletic avulsion fracture. Anteroposterior radiograph of the right hip in a 17-year-old soccer player shows ripping away of a small portion of bone from the anterior inferior iliac spine (Rossi and Gragoni 2001; with permission of Springer-Verlag)

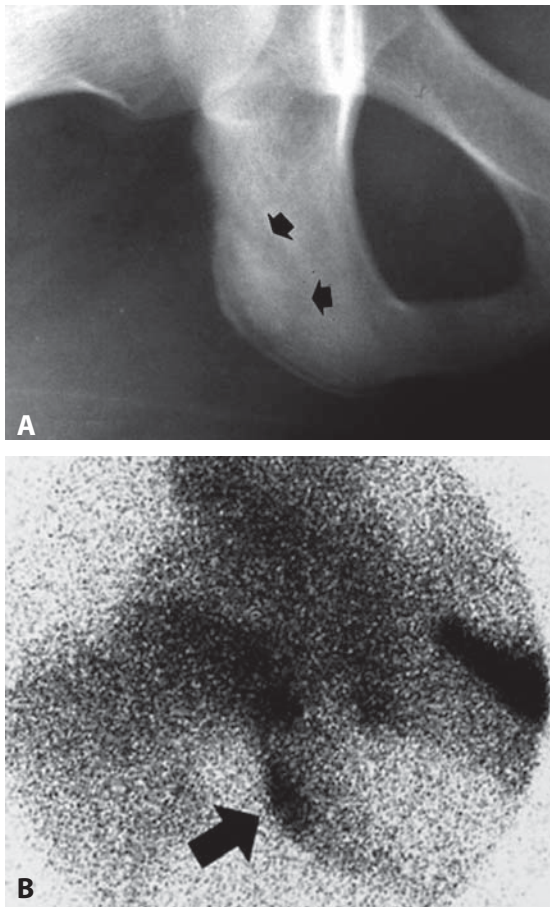

Fig. 16.49A, B Minimally detached avulsion fracture. **A** Anteroposterior radiograph of the right ischial tuberosity in a 14-year-old female short-track runner shows an avulsion fracture without ripping off (*arrows*). **B** Anterior pinhole scintigraph reveals a well-defined ovoid uptake (*arrow*)

known that bone scintigraphy can sensitively and selectively detect avascular bone soon after the vascular deprivation and frequently in the absence of radiographic changes. Dead bone is presented as a photon defect within live bone, which accumulates tracer (Fig. 16.44). Mineralized subperiosteal and parosteal hematomas (Fig. 16.42A) and myositis ossificans avidly accumulate tracer. Detached bony fragments of a fracture accumulate tracer as far as vascular supply is maintained (Fig. 16.47).

16.11 Sports Injuries to Bone

Sports injuries may be classified clinically as acute and chronic, and etiologically as excessive use and traumatic. The acute group includes bone fracture and contusion, joint dislocation and subluxation, and muscle, tendon, and ligament injuries. The chronic group includes stress fracture, shin splints, strain, osteitis or periostitis, and apophysitis (Brukner and Khan 1993). Full accounts of most of these acute and chronic injuries are given in the foregoing sections and Chapter 12. Therefore, the current discussion is limited to sports-related avulsion fractures that present interesting radiographic and scintigraphic findings.

Avulsion fracture may involve any bone at the attachment of ligament. A recent study on the prevalence, location, and sports distributi-

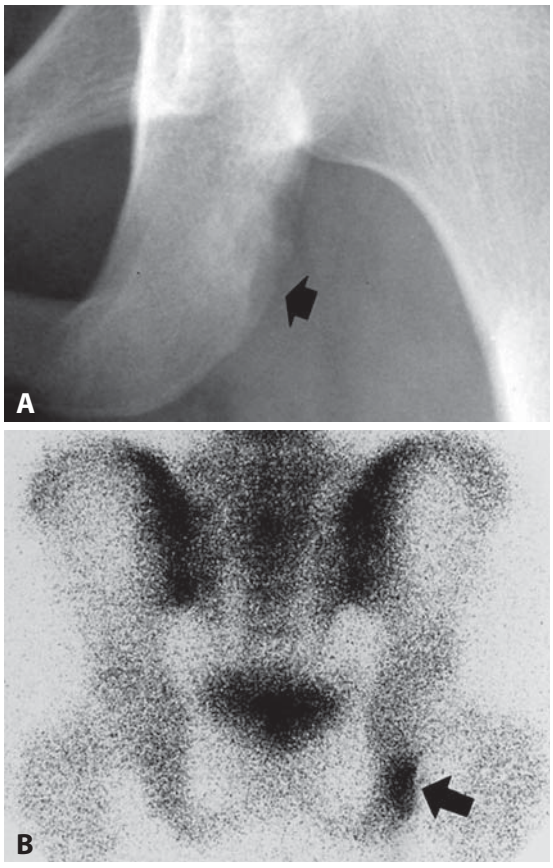

Fig. 16.50A, B Healed avulsion fracture. **A** Anteroposterior radiograph of the left ischium in a 17-year-old male *tae kwon do* participant shows a healed avulsion fracture and fracture bed (*arrow*). **B** Anterior pinhole scintigraph reveals poorly defined ovoid tracer uptake in the ischial tuberosity indicating that the fracture is healed (*arrow*)

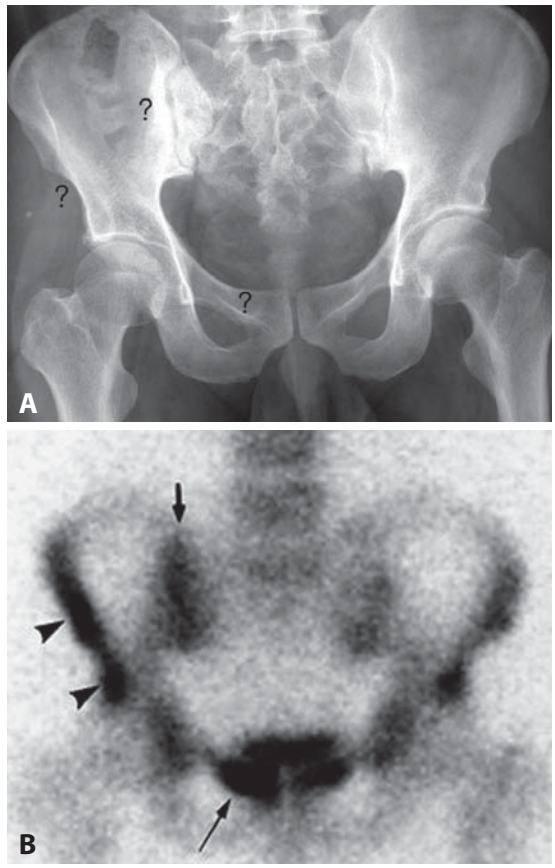

Fig. 16.51A, B Cryptic fractures and injuries diagnosed by bone scintigraphy. **A** Anteroposterior radiograph of the pelvis in a 42-year-old soccer player with multifocal pain in the right pelvis and hip 2 days after traumatization shows sclerosis in the right sacroiliac joint (*arrow*) and iliacus-sartorius muscle (*arrowheads*) (*??*painful sites). **B** Anterior planar scintigraph reveals areas of tracer uptake in the right sacroiliac joint (*upper arrow*), anterior iliac spines (*arrowheads*), and right upper pubic ramus (*lower arrow)*

on of avulsion fractures of the pelvic bone in 203 athletes revealed that the ischial tuberosity and the anterior iliac spines were involved in 53.7% and 41.4%, respectively (Rossi and Dragoni 2001). The ischial tuberosity and the anterior superior iliac spine are the sites of the sacrotuberous ligament and inguinal ligament. According to these authors the fractures, caused by sudden, forceful muscle contractions, occurred most commonly in soccer players and gymnasts. It has been reported that the avulsion fracture of the ischium may strongly simulate malignant bone-forming tumor such as Ewing's sarcoma, osteosarcoma, or lymphoma (Brander et al. 1995; Bahk et al. 2000).

Radiographically, avulsion fracture manifests as the ripping away of a small portion of a bone. The fracture is represented by a displaced bone fragment and the radiolucent bed from which it has arisen. The fragment may be separated from the bed (Fig. 16.48) or overlie it (Fig. 16.49A). For example, most of the fragments in ischial tuberosity avulsions lie parallel to the bed (Fig. 16.48), but some over-

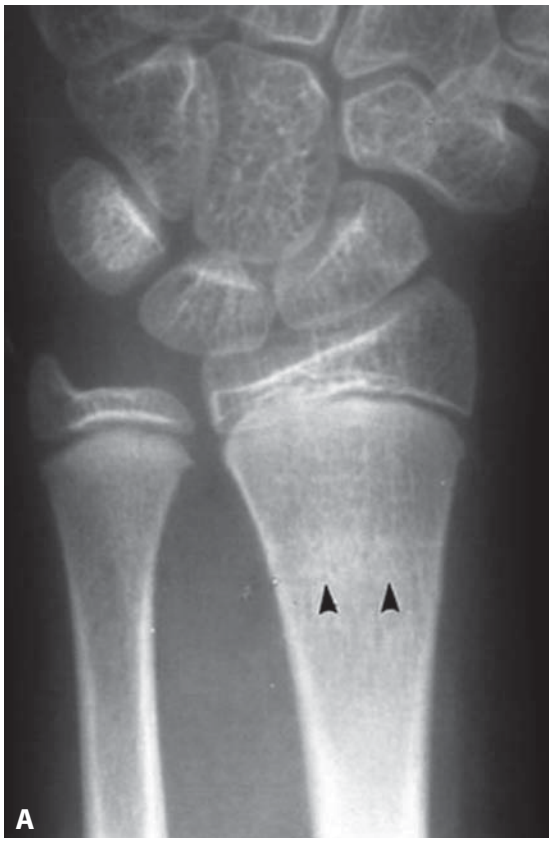

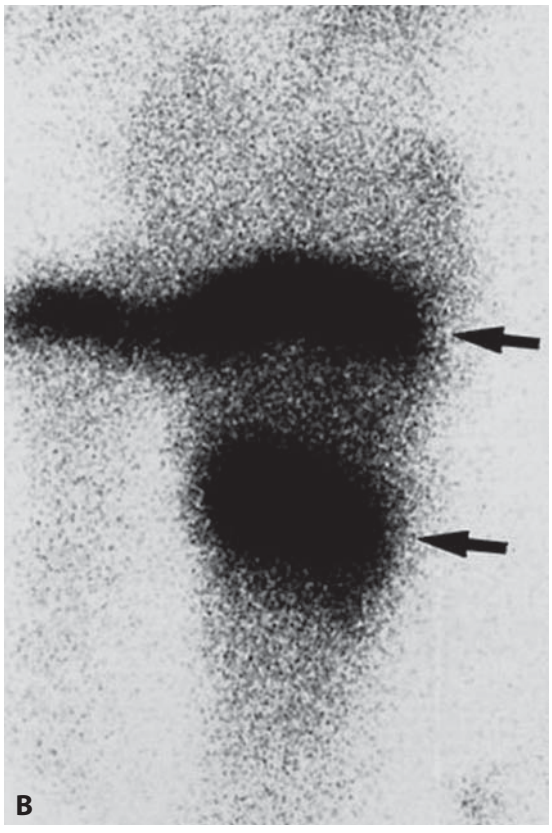

Fig. 16.52A, B Horizontal bar fractures. **A** Dorsoventral radiograph of the left wrist in a 12-year-old female horizontal-bar athlete shows a band-like area of faint intraosseous sclerosis (*arrowheads*). **B** Dorsal pinhole scintigraph reveals band-like areas of prominent tracer uptake not only in the distal radial metadiaphysis (*lower arrow*) but also in the physis (*upper arrow*) indicating double fracture. Note that radiography shows no abnormality in the physis

lie the bed (Fig. 16.50A). This difference appears to be related to the dissimilar attachment sites and directions of contraction of the biceps femoris-semimembranosus-semitendinosus muscles and the quadratus femoris muscle that pull the tuberosity from below and side, respectively. Accordingly, pinhole scintigraphy shows ovoid bean-shaped uptake around the tuberosity marginally (Figs. 16.49B and 16.50B). Theoretically, it is conceivable that the avulsed fragment may become photopenic when devitalized.

Bone scintigraphy is extremely useful in the assessment of acute periosteal avulsion without bony detachment. This condition cannot be diagnosed in the early stage by radiography unless significant periosteal new bone has been formed in the chronic stage. The injury, however, can be sensitively detected by bone scan because the injured corticoperiosteal zone intensely accumulates tracer within a few days of the traumatic event, for example, in the anterior iliac spines in soccer players (Fig. 16.51). Other sports-related injuries of scintigraphic interest comprise stress fractures in horizontal-bar gymnasts (Fig. 16.52) and those participating in aerobics (Fig. 16.53).

16.12 Sports and Traumatic Injuries to Soft-Tissue Structures

Soft-tissue structures traumatized during sports and accidents comprise the muscle, ligament, tendon, bursa, blood vessels, nerves, and skin, and the injuries can be divided into contusion, sprain, tear, or cut. Among these, (1) contusion

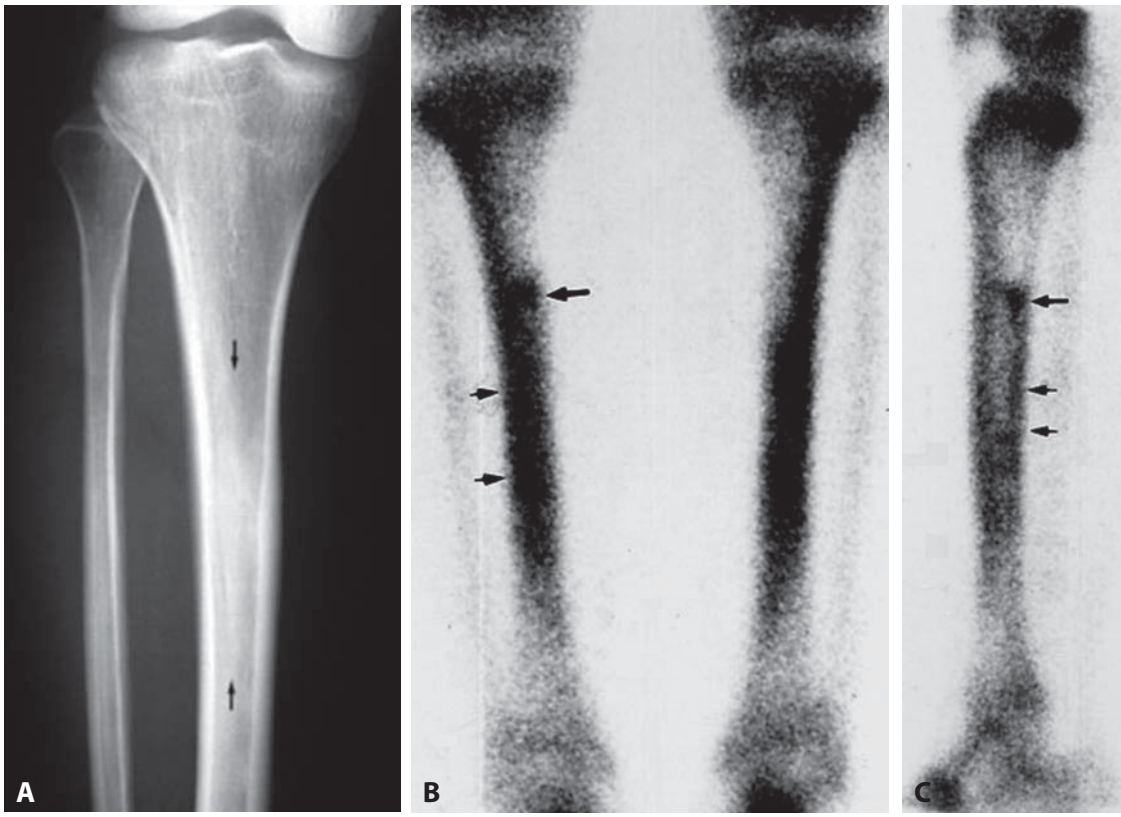

Fig. 16.53A–C Fracture in an aerobics participant. **A** Anteroposterior radiograph of the right leg in a 41-year-old female aerobics participant shows diffusely increased bone density in the tibial midshaft (*arrows*). **B** Anterior planar scintigraph of both legs reveals diffusely increased tracer uptake in the tibial shafts bilaterally. Fracture is indicated by the *large arrow*. **C** Lateral planar scintigraph of the right leg shows typical linear uptake with a fracture (*large arrow*) in the posterior cortex

to and sprain of the muscle and the tendon and ligament, (2) blood vessel contusion, and (3) skin injuries are discussed in this section.

Muscle strain and contusion are the most common sports or accidental injuries. Muscles are either strained or torn when the muscle fibers fail to withstand an excessive physical force such as sudden acceleration or deceleration and contusion is caused by a direct blow. Of the numerous muscles, the hamstrings, the quadriceps, and the gastrocnemius are more vulnerable. The most common site of muscle contusion is the front of the thigh in the quadriceps muscle. Muscle strain and contusion are extremely common among soccer and hockey players who are constantly exposed to bodily collision during the game. Tendon rupture is a form of severe traumatic injury that may occur in a player who suddenly starts playing without first warming up or in an older player. The Achilles and supraspinatus tendons are the most common sites of rupture. Skin injuries include abrasion, laceration, piercing, and degloving with damage of various grades to the underlying structures.

In general, radiography is of limited value in the diagnosis of soft-tissue injuries. However, it can sensitively detect and precisely localize metallic or high-density nonmetallic foreign bodies and mineralized lesions such as calcified subperiosteal or muscular hematoma (Fig. 16.54). Distorted anatomy and thickened soft-tissue structure can be clearly visualized using the soft-tissue technique, and the information obtained therefrom can be used to guide further investigation (Fig. 16.55). Degloving wound of the skin can also be diagnosed before and after repair (Fig. 16.56A).

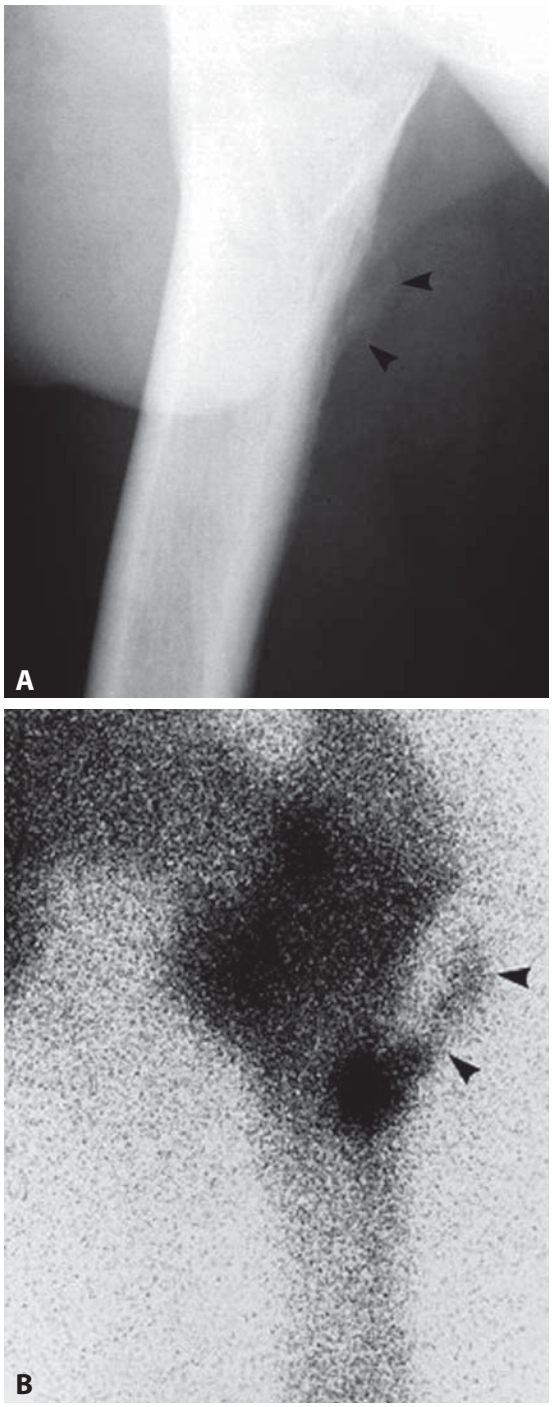

Fig. 16.54A, B Subperiosteal and fascial hematoma with mineralization. **A** Oblique radiograph of the right upper femur in a 54-year-old male shows a roughened corticoperiosteum with local soft-tissue mineralization in the lateroposterior aspect of the upper femoral shaft (*arrowheads*). **B** Anterior pinhole scintigraph reveals a roundish area of intense tracer uptake within the cortex with winglike extension laterally into adjacent soft tissues (*arrowheads*)

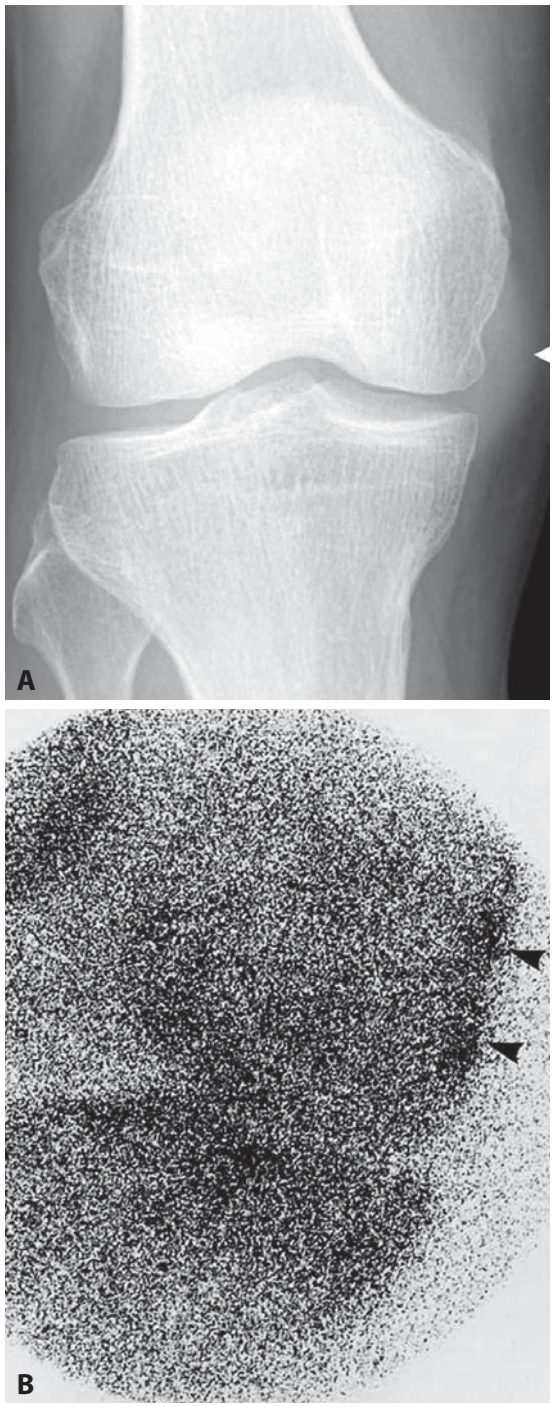

Fig. 16.55A, B Contusion to soft tissues about the knee. **A** Anteroposterior soft-tissue technique radiograph of the right knee in a 56-year-old man with knee contusion shows thickening of the medial articular capsule and collateral ligament (*arrowheads*). **B** Anterior pinhole scintigraph reveals extremely subtle tracer uptake in the medial femoral condylar surface denoting mild contusion (*arrowheads*). Such a lesion is often not detected by planar scintigraphy

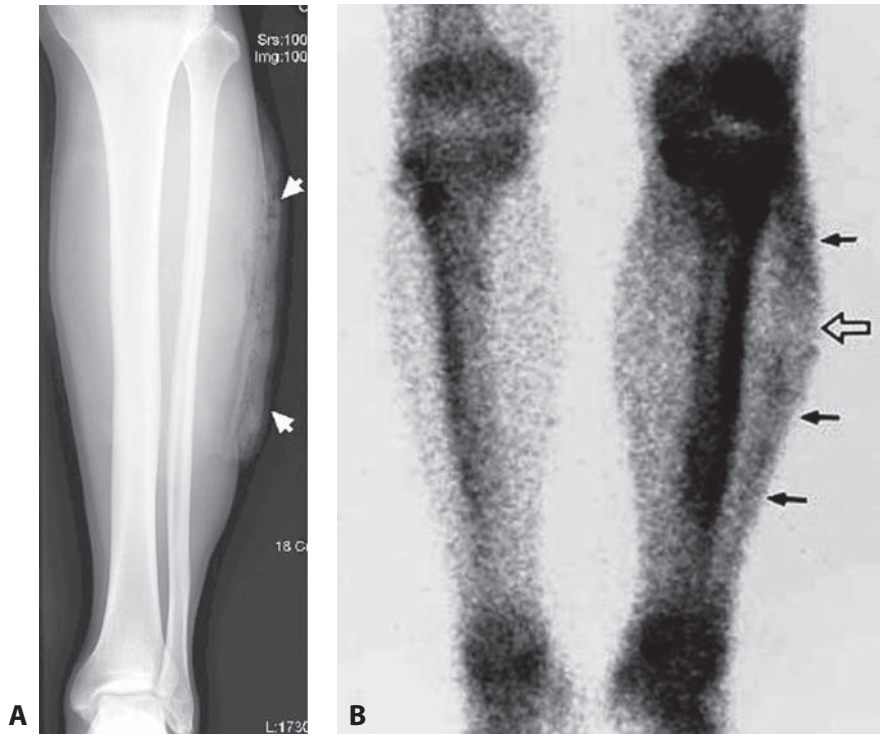

Fig. 16.56A, B Repaired degloving wound of the skin. **A** Anteroposterior soft-tissue radiograph of the left leg in a 23-year-old man with a repaired degloving wound of the lateral skin shows irregular derangement of the skin and subcutaneous soft tissues (*arrows*). **B** Anterior planar scintigraph of the legs reveals diffusely increased soft-tissue tracer uptake in the repaired damaged skin and subcutaneous soft tissues (*solid arrows*). Note a small photon defect at the suture site of the repaired degloving (*open arrow*)

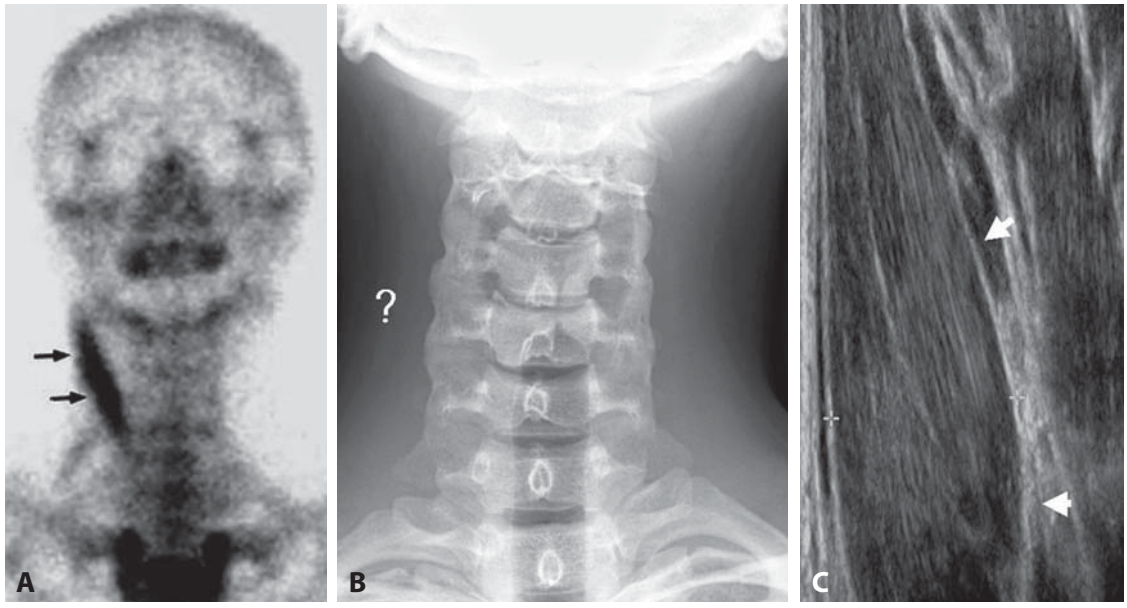

Fig. 16.57A–C Neck soft-tissue contusion. **A** Anterior planar scintigraph of the neck in a 23-year-old man who had sustained contusion 2 weeks previously to the right lateral neck shows prominent tracer uptake in the sternocleidomastoid muscle that is thickened (*arrows*). **B** Anteroposterior radiograph reveals no detectable abnormality except for blurred soft tissue (*?*). **C** Sonogram shows diffuse swelling of the sternocleidomastoid muscle with increased echoes in the perimysiums, epimysiums and fascias (*arrows*)

Fig. 16.58 Tensa fascia lata contusion. Anterior pinhole scintigraph of the right hip shows diffusely increased tracer uptake in the tensa fascia lata (*single arrow*). Note intense tracer uptake in the femoral neck fracture (*long arrows*)

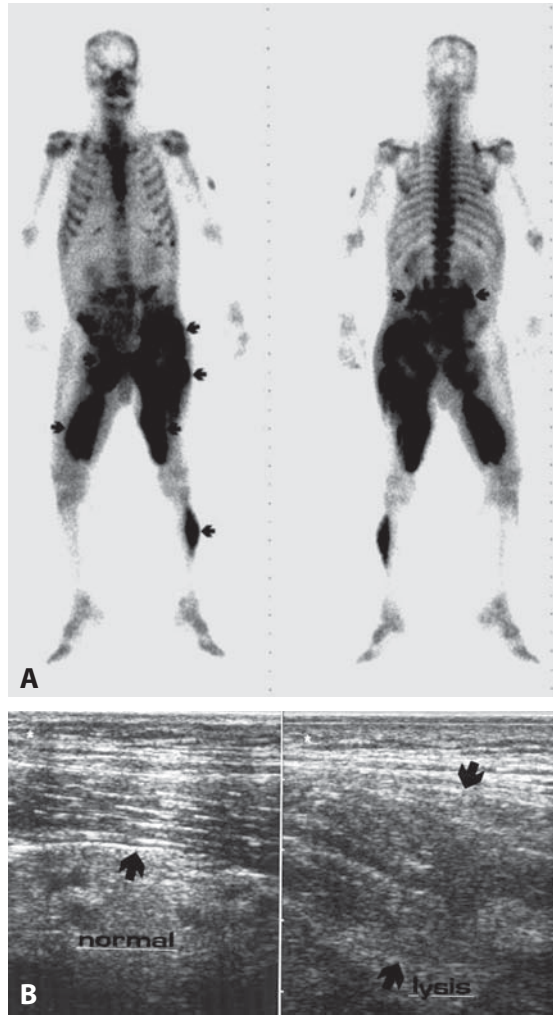

Fig. 16.59A, B Extensive posttraumatic rhabdomyolysis. **A** Anterior and posterior whole-body bone scintigraphs in a 48-year-old man who fell from a height show bizarre tracer uptake in the muscles of the pelvis, thighs and left leg denoting extensive myolysis (*arrows*). **B** *Right* sonogram of traumatized right thigh shows marked swelling of the muscles with echolucency denoting myolysis (*arrows*). *Left* normal control sonogram of a healthy thigh (*arrow*) reveals orderly muscular layering with fascial planes

Bone scintigraphy is generally used as a second-line investigation of soft-tissue injuries (Dayanandan and Ho 2005). Our experience, however, indicates that the scope of ^{99m}Tc-MDP bone scanning aided by the pinhole technique for the study of soft-tissue trauma is much wider than has traditionally been thought. Indeed, its extended use for the diagnosis of traumatic or sports injuries to the soft tissues has yielded a rich harvest. Clinically, the most beneficial condition appears to be soft-tissue contusion. ^{99m}Tc-MDP scan finding of contusion to the muscles (Fig. 16.57A) and fascias (Fig. 16.58) is sufficiently specific for no further investigation to be required. Radiography provides little information in most cases (Fig. 16.57B), but sonography is extremely helpful, often showing the pathognomonic sign (Fig. 16.57C). The pinhole scintigraphic sign of fascial contusion is characterized by tracer uptake localized to the fibrous sheet that invests muscle (Fig. 16.58). Increased tracer uptake in muscular and fascial contusion can be explained on the basis of myolysis as in myocardial infarction. The role played by whole-body scintigraphy in the diagnosis of multiple

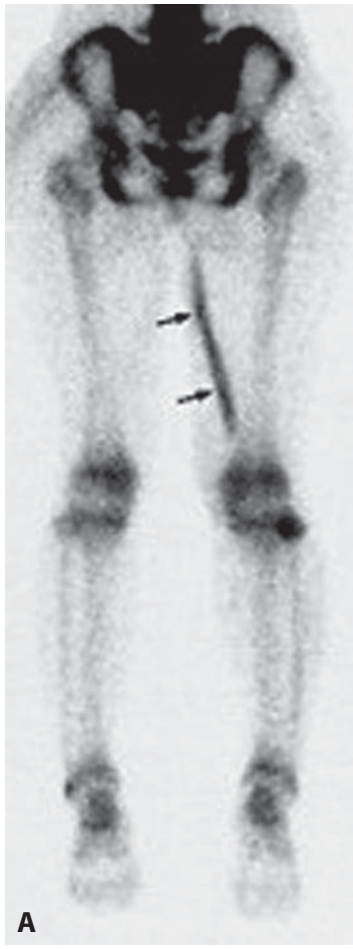

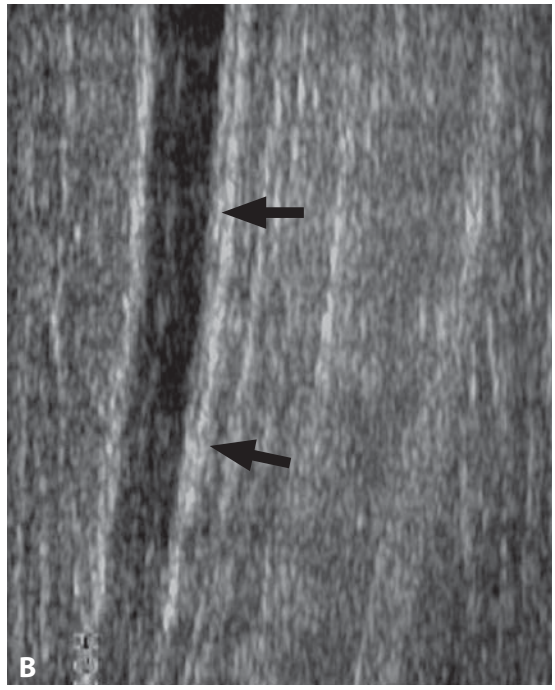

Fig. 16.60A, B Blunt traumatic phlebitis. **A** Posterior ^{99m}Tc-MDP bone scintigraph of the lower extremities in a 28-year-old female who 3 days previously had sustained a trauma to the left medial thigh shows long linear tracer uptake within the muscles (*arrows*). **B** Instant sonogram reveals diffuse thickening of the greater saphenous vein walls (*arrows*)

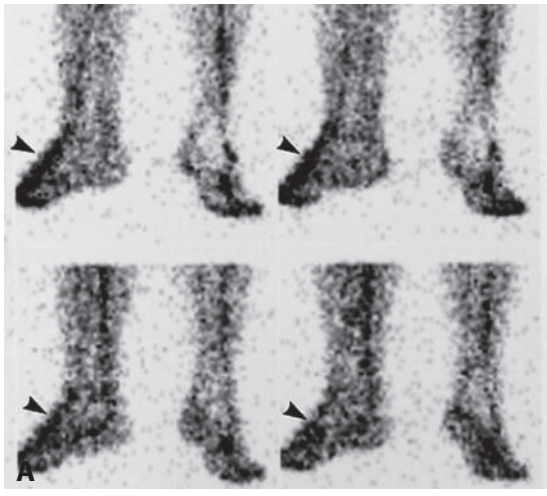

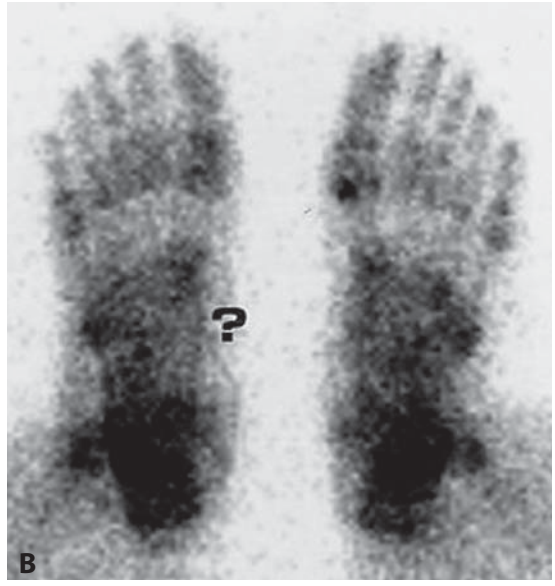

Fig. 16.61A, B Traumatic arteritis. **A** Oblique ^{99m}Tc-MDP angiogram of both legs in a 35-year-old male with recent trauma and subsequent mild cellulitis shows increased blood flow in the right pedis dorsalis artery (*arrowhead*). **B** An equilibrium phase scintigraph reveals no vascular stain or abnormal bony uptake (*?*). Such rapidly passing arterial tracer uptake is considered to be related to contusion and arteritis

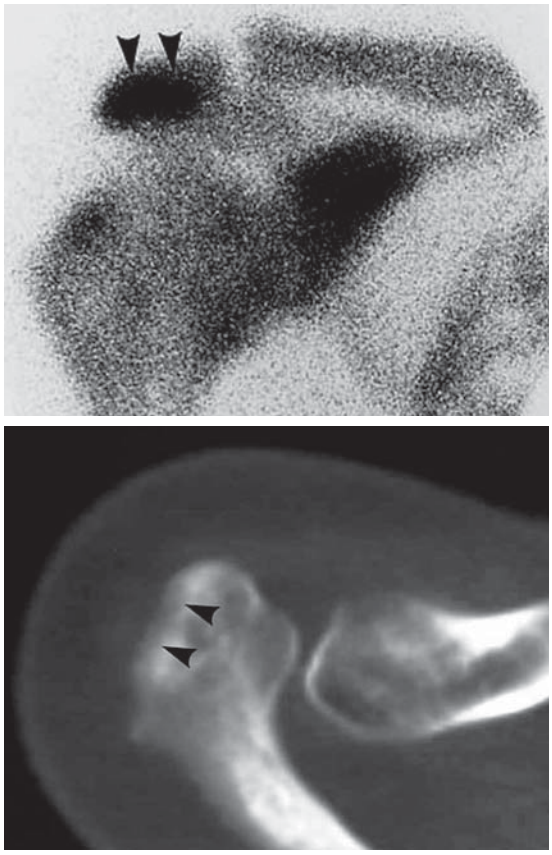

Fig. 16.62A, B Posttraumatic deltoid enthesitis. **A** Anterior pinhole scintigraph of the right shoulder girdle in a 54-year-old female who developed lasting pain after contusion shows marked tracer uptake localized to the acromion at the site of the deltoid attachment (*arrowheads*). Note that there is no other tracer uptake except in the coracoid process that is physiological. **B** CT performed the next day reveals sclerosis with erosion at the site in question denoting enthesitis (*arrowheads*). Radiography was negative

traumas is great in that it uniquely permits panoramic screening of the entire musculoskeletal system. The lesions detected by this means comprise muscle contusion, rhabdomyolysis, and bone fractures (Fig. 16.59). It deserves mention in passing that bone scintigraphy occasionally shows the devascularization of the damaged skin as photon defects, for example, in degloving after repair (Fig. 16.56B).

^{99m}Tc-MDP bone scintigraphy has also been found to be a powerful tool for the diagnosis of traumatic phlebitis (Fig. 16.60A). The scintigraphy in the 28-year-old female patient presented in this figure was performed to evaluate possible bone injury to her left thigh 3 days after a blunt trauma. Scintigraphically, the bone was unremarkable. Instead, the examination quite unexpectedly revealed linear tracer uptake within the muscles of the medial thigh. The instantly performed sonography showed diffuse thickening of the wall of the great saphenous vein, confirming phlebitis (Fig. 16.60B). No thrombus was present. Local traumatic phlebitis at intravenous injection sites is common (Rivas Doblado et al. 2004), but acute Sdiffuse phlebitis due to blunt trauma seems to have not been previously described. In this connection, it is also worth documenting that ^{99m}Tc-MDP angiography is able to reveal peculiar transient hypervascularity in the pedis dorsalis artery in infected skin contusion, which is considered to be a posttraumatic arteritis (Fig. 16.61). Finally, traumatic enthesitis can be diagnosed by pinhole bone scintigraphy (Fig. 16.62A) and CT (Fig. 16.62B), but not by radiography.

References

Bahk WJ, Brien EW, Luck JV Jr, JM Mirra (2000) Avulsion of the ischial tuberosity simulating neoplasm – a report of 2 cases. Acta Orthop Scand 71:211–214

Baisden CE, Greenwald LV, Symbas PN (1984) Occult rib fractures and brachial plexus injury following median sternotomy for open-heart operations. Ann Thorac Surg 38:192–194

Berggren A, Weiland AJ, Ostrup LT (1982) Bone scintigraphy in evaluating the viability of composite bone grafts revascularized by microvascular anastomoses, conventional autogenous bone grafts, and free nonrevascularized periosteal grafts. J Bone Joint Surg Am. 64:799–809

Brander VA, Hinderer SR, Alpiner N, Oh TH (1995) Rehabilitation in joint and connective tissue diseases. 3. Limb disorders. Arch Phys Med Rehabil 76(5 Spec No):S47–56

Brukner P, Khan K (1993) Clinical sports medicine. McGraw-Hill, Sydney

Cintron E, Gilula LA, Murphy WA, Gehweiler JA (1981) The widened disc space: a sign of cervical hyperextension injury. Radiology 141:639–644

Cruess RL, Dumont J (1975) Healing of bone, tendon and ligament. In: Rockwood CA Jr, Green DP (eds) Fractures. Lippincott, Philadelphia

Dayanandan A, Ho YY (2005) Bone scintigraphy appearances of incidentally diagnosed soft tissue disorders in musculoskeletal imaging. Australas Radiol 49:1–7

Dee P, Lambruschi PG, Hiebert JM (1981) The use of Tc-99m MDP bone scanning in the study of vascularized bone implants. J Nucl Med 22:522–525

Denis F (1983) The three column spine and its significance in the classification of acute thoracolumbar spine injuries. Spine 8:817–831

Geslin GE, Thrall JH, Espinosa JL, et al (1976) Early detection of stress fractures using Tc-99m polyphosphate. Radiology 121:683–687

Harbert JC, George FH, Kerner ML (1981) Differentiation of rib fractures from metastases by bone scanning. Clin Nucl Med 6:359–361

Holdsworth F (1970) Fractures, dislocations, and fracture-dislocations of the spine. J Bone Joint Surg Am 52:1534–1551

Lauer I, Czech N, Zieron J, et al (2000) Assessment of the viability of microvascularized bone grafts after mandibular reconstruction by means of bone SPET and semiquantitative analysis. Eur J Nucl Med 27:1552–1556

Lisbona A, Rennie WRJ, Daniel RK (1980) Radionuclide evaluation of free vascularized bone graft viability. AJR Am J Roentgenol 134:387–388

Matin P (1979) Appearance of bone scans following fractures including immediate and long-term studies. J Nucl Med 20:1227–1331

Michael RH, Holder LE (1985) The soleus syndrome. A cause of medial tibia stress (shin splints). Am J Sports Med 13:87–94

Resnick D, Niwayama G (eds) (1988) Diagnosis of bone and joint disorders, 2nd edn. WB Saunders, Philadelphia

Rivas Doblado JS, Artes Leon JL, Arjona Barcia J, et al (2004) How to reduce the incidence of traumatic phlebitis (in Spanish). Rev Enferm 27:42–46

Rossi F, Dragoni S (2001) Acute avulsion fractures of the pelvis in adolescent competitive athletes: prevalence, location and sports distribution of 203 cases collected. Skeletal Radiol 30:127–131

Roub LW, Gumerman LW, Hanley EN Jr, et al (1979) Bone stress: a radionuclide imaging prospective. Radiology 132:431–438

Rupani HD, Holder LE, Espinola DA, Engin SI (1985) Three-phase radionuclide bone imaging in sports medicine. Radiology 156:187–196

Soost F, Ivancevic V, Stoll C, Prochno T (1999) 3-phase bone scintigraphy of microsurgically attached bone transplants as early graft survival assessment (in German). Handchir Mikrochir Plast Chir 31:42–46

Sweet DE, Allman RM (1971) Stress fracture. RPC of the month from the AFIP. Radiology 99:687–692

Taylor GA (1983) The current status of free vascularized bone grafts. Clin Plast Surg 10:185–208

Yao L, Lee JK (1988) Occult intraosseous fracture: detection with MR imaging. Radiology 167:749–751

Zwas ST, Elkanovitch R, Frank G (1987) Interpretation and classification of bone scintigraphic findings in stress fractures. J Nucl Med 28:452–457

17 Malignant Tumors of Bone

Yong-Whee Bahk and Won-Jong Bahk

Malignant bone tumors are either primary or metastatic in nature. The high sensitivity and accuracy of ^{99m}Tc-MDP bone scintigraphy in diagnosing bone metastasis were established as long ago as 1961 (Fleming et al. 1961) (Fig. 1.2). In contrast, its usefulness in the investigation of primary bone tumors, both malignant and benign, appears not to be fully appreciated. The main reason is the low diagnostic yield of conventional planar bone scintigraphy; this is true. However, recognizing the fact that the magnified images of pinhole scintigraphy can depict anatomy in amazing detail along with unique metabolic information, a number of primary tumors and tumor-like diseases of bone have become among the most important and challenging indications for bone scanning.

In actuality ^{99m}Tc-MDP bone scintigraphy reinforced with the pinhole magnification technique and nuclear angiography has been demonstrated to be helpful in the diagnosis of primary bone tumors. The malignant tumors so far studied by this means include skeletal metastases and primary osteosarcoma, fibrosarcoma, Ewing's sarcoma, multiple myeloma, leukemia, and lymphoma and the benign tumors comprise osteoid osteoma, enchondroma, osteochondroma, simple bone cyst, and giant cell tumor (Bahk 1996; Bahk 1998; Kim et al. 1992). The method has also been applied to (a) the mapping of the multiple lesions in polyostotic diseases such as enchondromatosis or Ollier's disease, familial exostosis, fibrous dysplasia, and histiocytosis X (Kirchner and Simon 1981), (b) preoperative localization of the nidus in osteoid osteoma in flat or irregular bones in particular (Lisbona and Rosenthall 1979), (c) detection of the intramedullary skip metastasis in osteosarcoma and giant cell tumor (Levine et al. 1984), (d) assessment of regional tumor extent, (e) evaluation of tumors with ambiguous radiographic and histological findings, (f) distinction among osteosarcoma, Ewing's sarcoma, and chondrosarcoma (McLean and Murray 1984) and between bone cyst and cystic bone lesions (Hudson 1984), and (g) unexplained bone pains.

The use of gallium-67 citrate, thallium-201 chloride, ^{99m}Tc-MIBI, and other agents for bone tumors is not considered in this chapter since these radiopharmaceuticals have fully been described in numerous publications including standard nuclear medicine textbooks and a number of excellent review articles (Nadel and Rossleigh 1995; Neumann et al. 1995; Waxman 1995; Focacci et al. 1998; Pinkas et al. 2001).

17.1 Metastasis

Radiography plays a relatively less crucial role in bone metastases in the early phase when bone changes are minimal or undetectable. It is also true that radiography is less suitable for the diagnosis of metastases in anatomically complex and thickly overshadowed bones, or conversely in small or thin bones such as the cervical and thoracic vertebrae, the sternum, the ribs, the lumbosacral junction, and the sacroiliac joints. The reason is simply that osteolysis or neoplastic osteogenesis in those bones and structures is easily hidden unless the change is overt. Severe porosis in elderly and

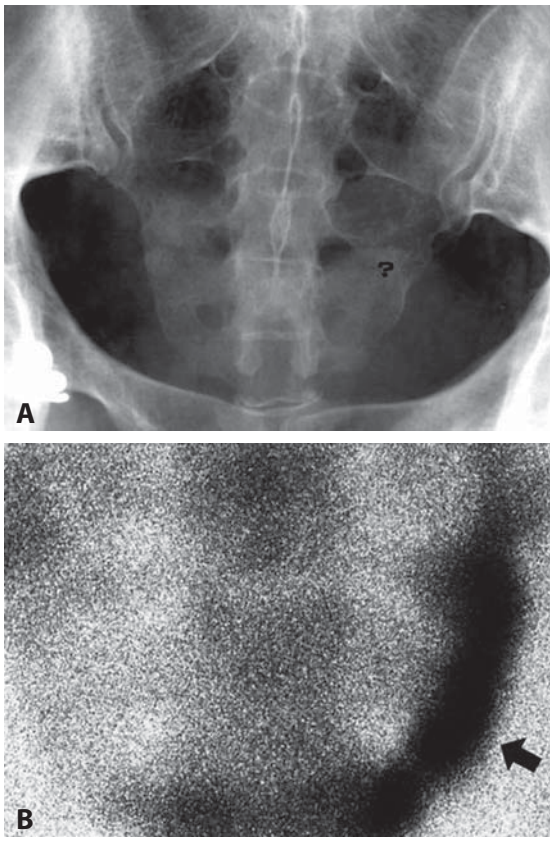

Fig. 17.1A, B Usefulness of bone scintigraphy in the diagnosis of metastasis. **A** Anteroposterior radiograph of the sacrum in a 37-year-old female with known primary breast cancer and left sacral pain shows no abnormality (*?*). **B** Anterior pinhole scintigraph reveals prominent tracer uptake along the left lateral sacral border representing metastasis (*arrow*)

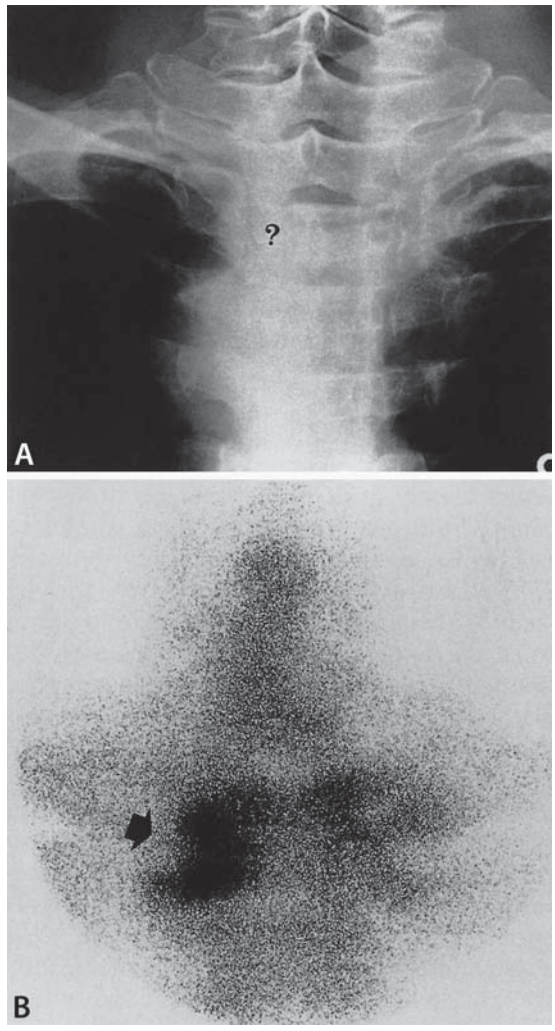

Fig. 17.2A, B Advantage of pinhole scintigraphy in the study of the diseases hidden in the overlapping structures of the thoracic cage and mediastinum. **A** Posteroanterior radiograph of the chest in a 63-year-old man with known bronchogenic carcinoma with a pain in the upper thoracic spine reveals no pathology (*?*). The radiograph is printed with the right side on the left to match the scintigraph. **B** Posterior pinhole scintigraph of the area in question reveals patchy tracer uptake in the left lateral aspect of the T3 vertebra, indicating metastasis (*arrow*)

bed-ridden patients prevents radiographic detection of metastases and often makes conventional or computed tomography powerless. Not infrequently, however, ^{99m}Tc-MDP bone scintigraphy diagnoses radiographically invisible or uncertain metastases because they accumulate tracer emitting enough γ-rays from within porotic or thin bones (Fig. 17.1) or through thick or superimposed bones (Fig. 17.2). In addition, whole-body scanning advantageously permits scrutiny of the entire skeleton so that it can cover the technical shortcomings of radiography that examines a restricted portion of the body in one session. For

Fig. 17.3A, B Value of whole-body bone scintigraphy in ▷ bone tumor. **A** Lateral radiograph of the skull in an 8-year-old girl with a mass in the cranium shows diploic space widening and erosions in both the outer and inner tables (*arrows*). Differential diagnoses included meningioma which was considered most likely. **B** Anterior whole-body scintigraph clearly indicates that the cranial lesion is just one of many such lesions in the skeleton (*arrows*) and also the right kidney is caudally displaced (*nb*), correctly indicating the diagnosis of neuroblastoma with multiple skeletal metastases

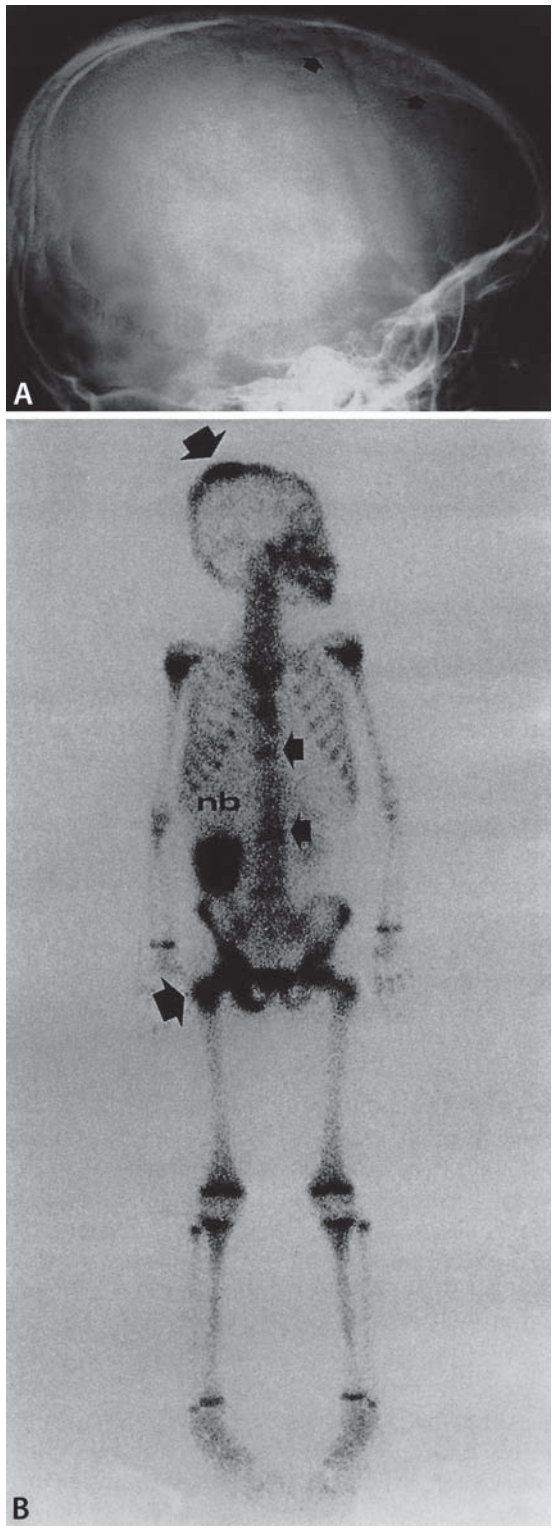

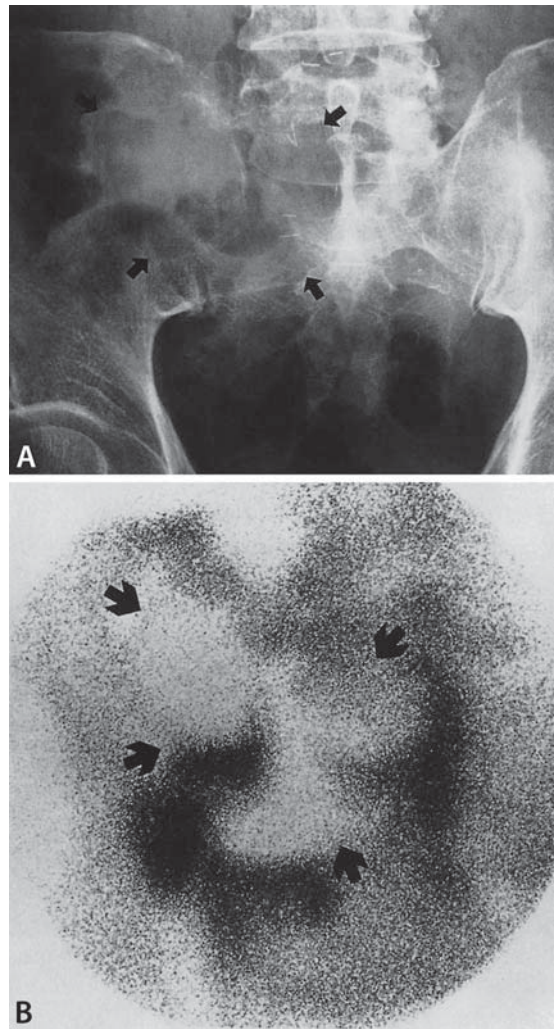

Fig. 17.4A, B Solitary osteolytic and photopenic metastasis in renal cell carcinoma. **A** Anteroposterior radiograph of the left iliac bone in a 48-year-old man with known renal cell carcinoma shows a large, irregularly shaped lysis in the left ilium and the neighboring sacrum (*arrows*). The radiograph is printed with the right side on the left to match the scintigraph. **B** Posterior pinhole scan shows a large, lobulated photon defect surrounded by intense tracer uptake in the left ilium and the neighboring sacrum (*arrows*)

example, if only the skull is radiographed for local swelling on the forehead, the true state of affairs may be disguised as a local pathology while the cranial lesion is just one of multiple metastases (Fig. 17.3).

Three basic radiographic changes of malignant metastases are osteolysis, osteogenesis, or a combination. The individual bone change is not specific by itself, but certain features or patterns are of diagnostic value. For example,

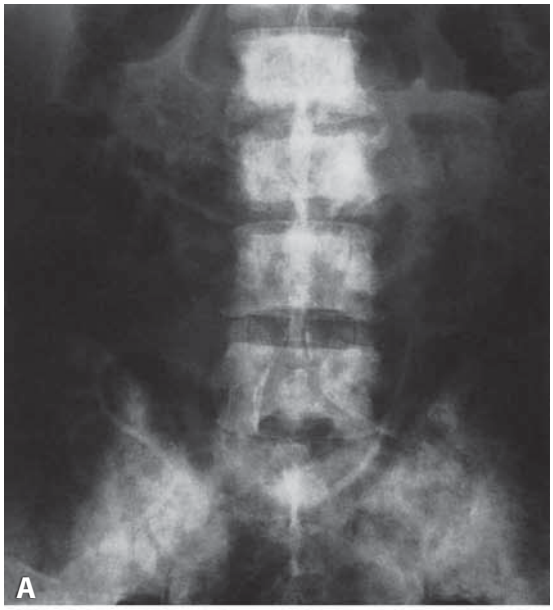

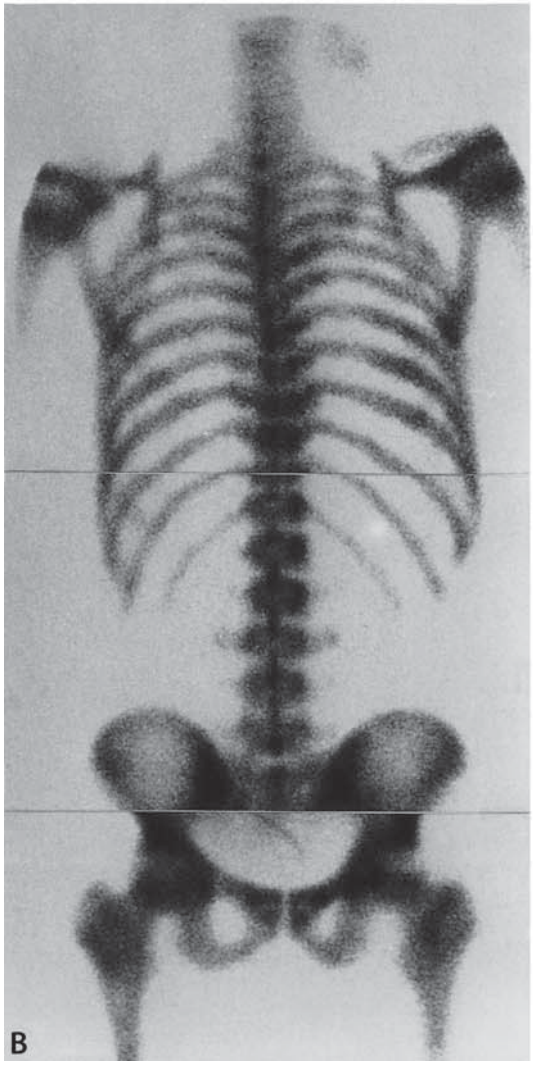

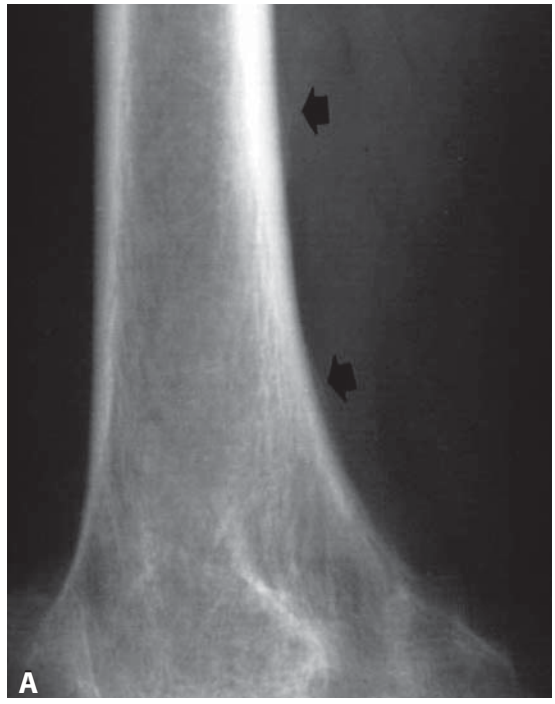

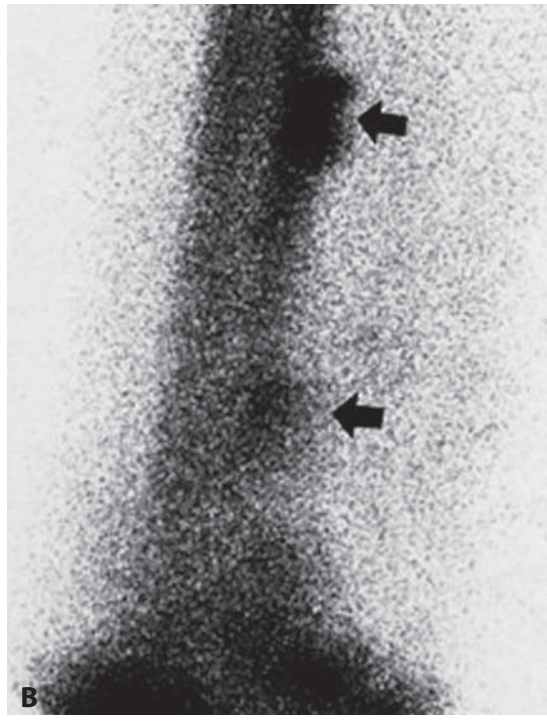

◁ **Fig. 17.5A, B** Diffuse osteoblastic and "hot" metastases in prostatic carcinoma. **A** Anteroposterior radiograph of the lumbosacral region in 75-year-old man with prostatic cancer metastases shows widely disseminated patchy opacities involving the lumbar vertebrae, the sacrum, and the iliac bones. **B** Composite posterior scintigraph of the axial skeleton reveals a generalized increase in tracer uptake, producing the "superscan" appearance

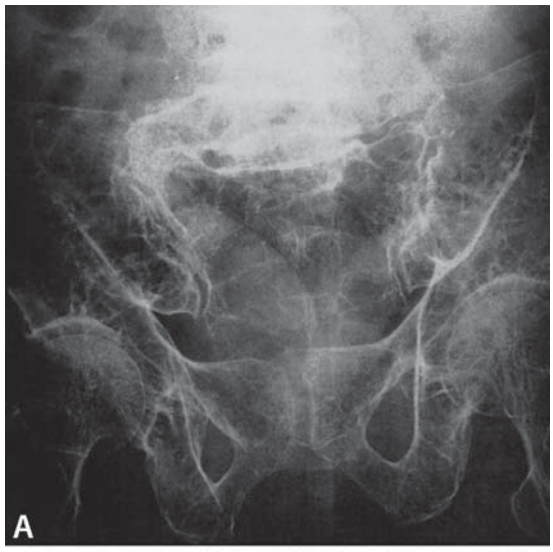

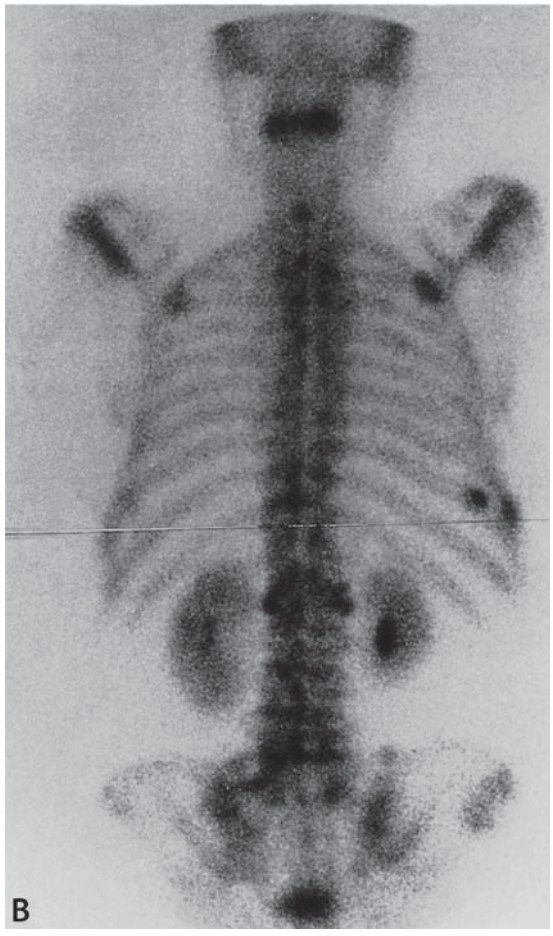

◁ **Fig. 17.6A, B** Corticoperiosteal metastasis of bronchogenic carcinoma. **A** Lateral radiograph of the right distal femur in a 65-year-old male shows barely discernible periosteal thickening (*arrows*). **B** Lateral pinhole scintigraph reveals areas of intense tracer uptake localized to the distal femoral corticoperiosteum (*arrows*). Radiographic changes were discovered retrospectively

the metastasis from renal cell carcinoma is often lytic and solitary (Fig. 17.4A) and the metastases from prostate carcinoma are usually osteoblastic and multiple or diffuse (Fig. 17.5A). It is also worth remembering that bronchogenic carcinomas, the squamous cell variety in particular (Greenspan and Norman 1988) (Fig. 17.6A), strongly tend to eccentrically metastasize to the cortex (Deutch and Resnick 1980) and multiple myeloma produces characteristic punched-out or soap-bubble-like lytic lesions in the skull, spine, pelvis, and proximal limb bones (Fig. 17.7A).

^{99m}Tc-MDP bone scanning is highly regarded for its ability to diagnose metastases, especially when the primary tumor has a great propensity toward early dissemination (Pistenma et al. 1975; Kirchner and Simon 1981). Its usefulness in detecting both distant and local intramedullary spread of a malignancy is well appreciated, making the study a sine qua non in the staging and managing of many malignant tumors (Fogelman and McKillop 1991) (Fig. 17.8). It should also be emphasized that ordinary scintigraphy has three pitfalls: relatively high false-negative results, ambiguous photopenic manifestation, and the lack of specificity in the majority of individual lesions. Previously, the incidence of false-negative bone scintigraphy in metastases was reported to be as high as 3% (Pistenma et al. 1975; Citrin and McKillop 1978). Publications also indicated that in a small percentage of patients radiography could detect metastases that were not visualized on scintigraph. The main reasons are the

Fig. 17.7A, B Diffuse cystic and photopenic lesions in myelomatosis. **A** Anteroposterior radiograph of the pelvis in a 59-year-old woman shows extensive cystic bone destruction, producing a "soap bubble" appearance. **B** Composite posterior scintigraph of the axial skeleton and rib cage shows extensive, ill-defined photopenic defects in the spine, pelvis, and rib cage, producing a "pale" skeleton. The scattered "hot" spots in the rib cage and lumbar spine represent fractures complicating myelomatosis

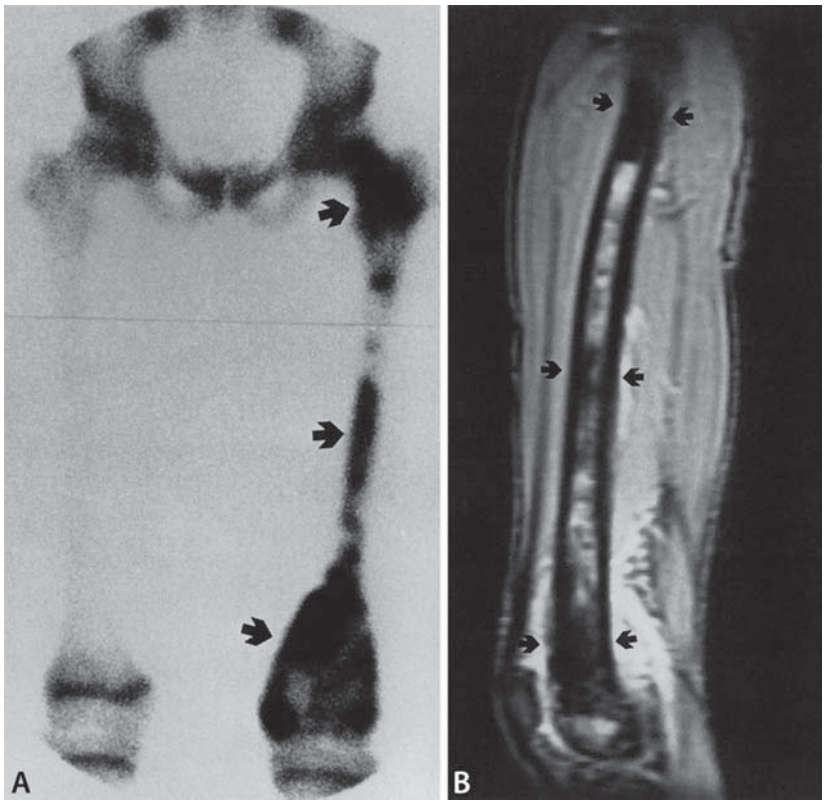

Fig. 17.8A, B Usefulness of scintigraphy in the detection of local intramedullary metastasis. **A** Composite anterior scintigraph of the pelvis and left femur in a 17-year-old man with a large primary osteosarcoma in the distal epimetaphysis reveals expansile, patchy intense tracer uptake (*bottom arrow*). In addition, two other "hot" areas are seen in the proximal and middle aspects (*middle and top arrows*), representing intramedullary metastases. **B** T1-weighted sagittal MRI reveals irregularly diminished signal intensity in the primary tumor (*bottom arrows*) as well as in the other two local metastases (*middle and top arrows*)

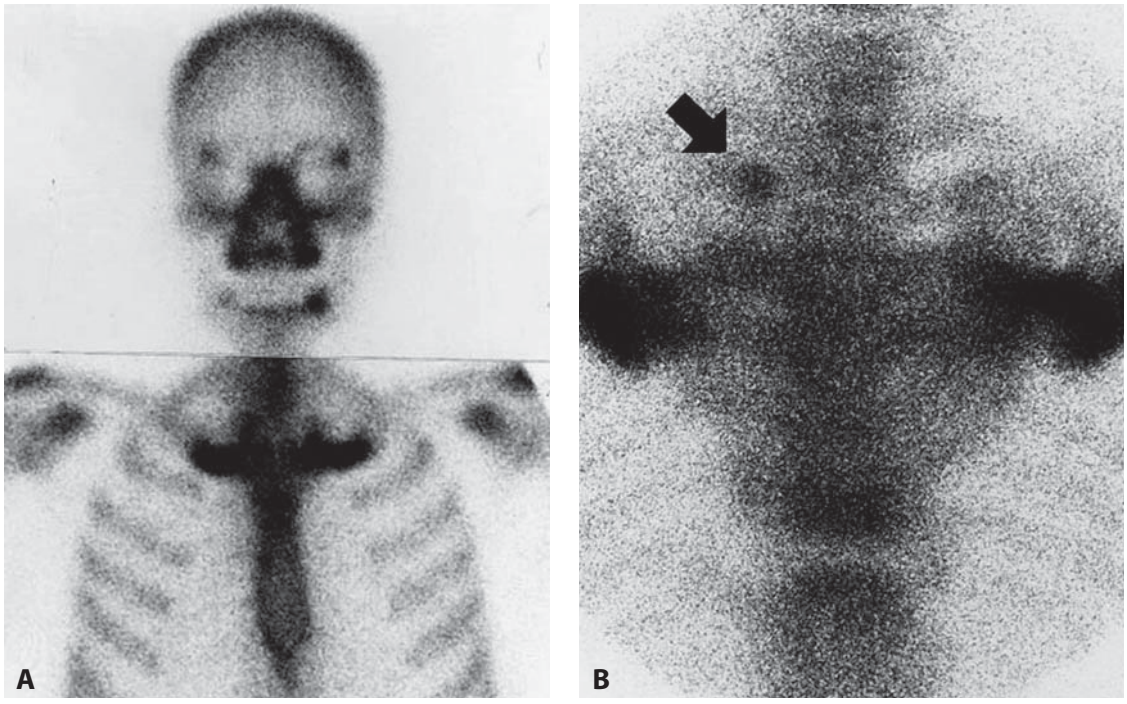

Fig. 17.9A, B False negativity of planar scintigraphy. **A** High-resolution anterior planar scan of the chest shows no abnormality. **B** Anterior pinhole scintigraph, however, reveals a small spotty uptake in the right second costovertebral junction indicating metastasis (*arrow*). The costosternal and manubriosternal joint uptake is physiological

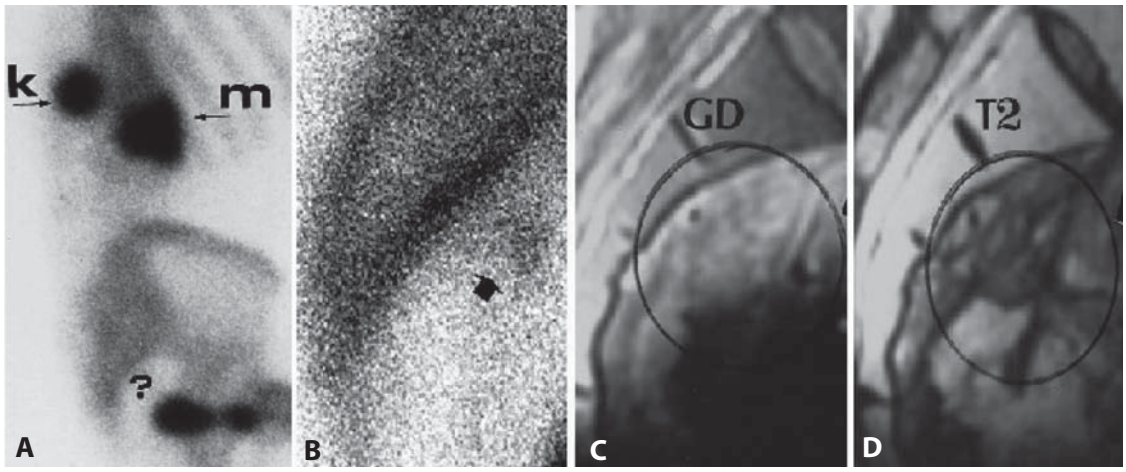

Fig. 17-10 A-D. Enhanced lesion detectability of pinhole scan. **A** Lateral planar scintigram of the sacrum taken as a part of metastasis series following colectomy for rectal carcinoma in a 42-year-old male shows no abnormal finding (*?*). *k* and *m* denote kidney and metastasis to the spine, respectively. **B** Lateral pinhole scintigram portrays increased uptake in the presacral recurrence *(arrow)*. **C** Gadolinium enhanced sagittal MRI reveals an area of high signal intensity in the upper presacral soft tissue metastasis *(circle)*. **D** T2 weighted sagittal MRI shows low signal intensity *(circle)*

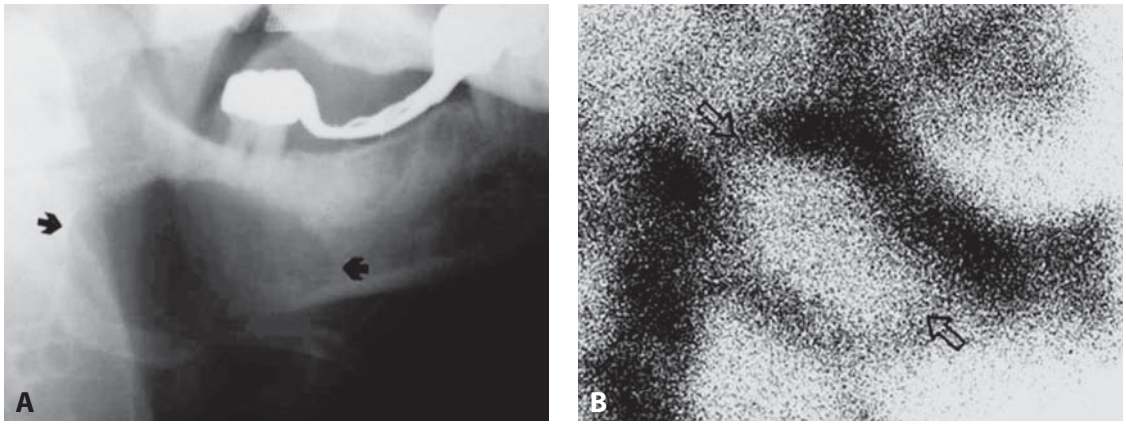

Fig. 17.11A, B Photopenic metastasis of renal carcinoma. **A** Lateral radiograph of the right mandible in a 61-year-old man shows a large osteolytic lesion (*arrows*). **B** Lateral pinhole scintigraph reveals typical photopenic presentation of renal cell carcinoma metastasis (*open arrows*)

smallness and photopenic presentation. However, many such lesions can correctly be diagnosed by properly using pinhole scintigraphy (the closer the detector to the objects, the higher the resolution and the greater the sensitivity), dramatically reducing the incidence of false-negative scans. Indeed, magnified scintigraphy can visualize not only tiny bone metastases (Fig. 17.9) but also soft-tissue invasion when richly vascularized or mineralized (Fig. 17.10).

On the other hand, elusive photopenic metastases can be identified as such by noting reactive tracer uptake in the periphery of the lesion on the pinhole scintigraph (Fig. 17.11). Among the primary malignancies whose metastatic lesions are often photopenic, carcinomas of the kidney (Kim et al. 1983) (Figs. 17.4 and 17.11), stomach (Fig. 17.12A), breast

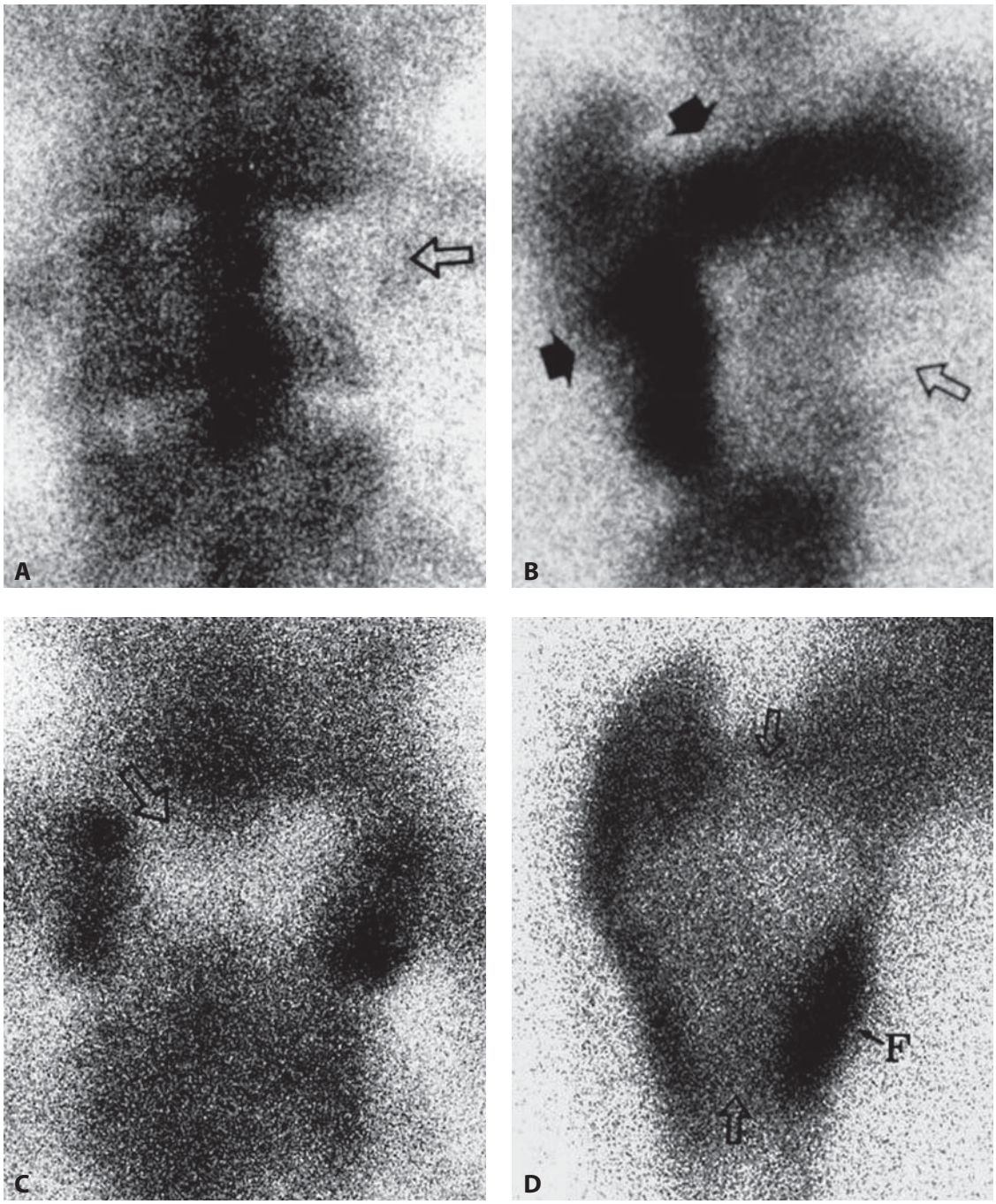

Fig. 17.12A–D Photopenic metastases from various primary carcinomas. Anterior pinhole scintigraphs of (**A**) L1 vertebra (*open arrow*), (**B**) manubrium sterni (*open arrow*), (**C**) T12 vertebra (*open arrow*), and (**D**) right femur show photopenic metastases (*open arrows*), respectively, from gastric carcinoma, breast carcinoma, laryngeal carcinoma, and cholangiocarcinoma, respectively (**D** *F* pathological fracture)

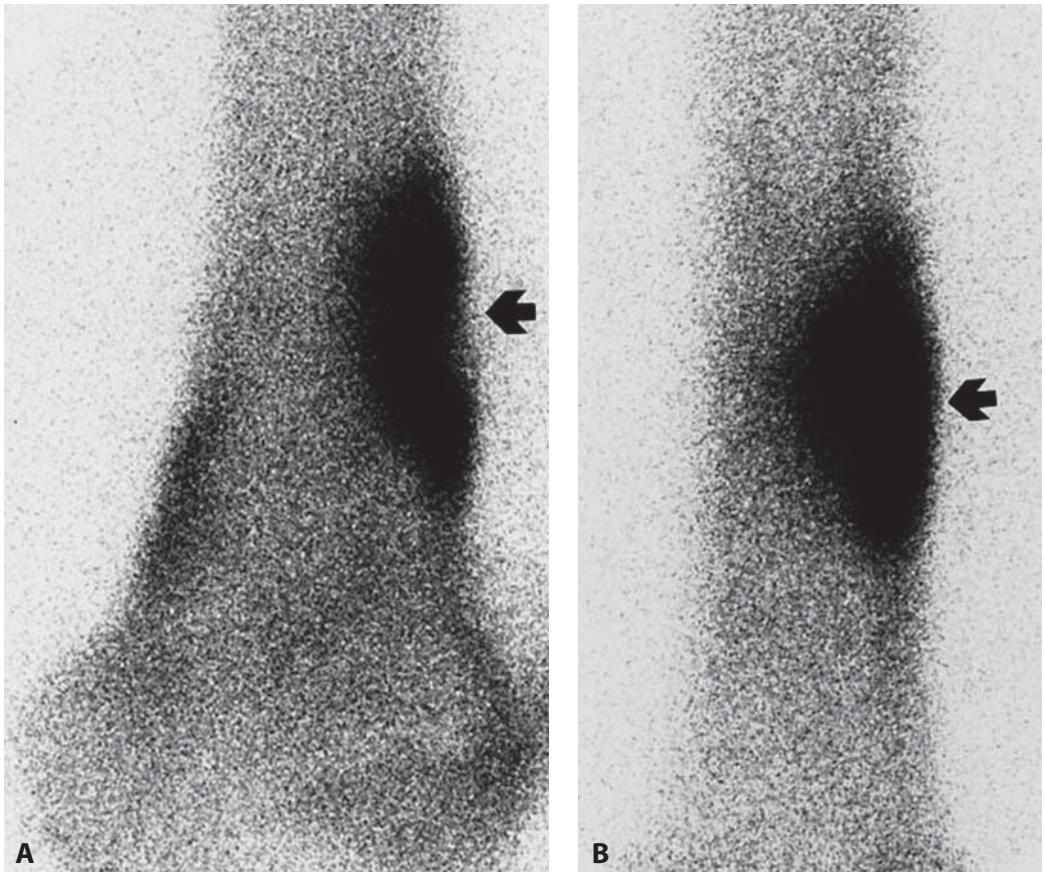

Fig. 17.13A, B Indistinguishable femoral cortical metastasis from carcinomas of the lung and kidney. **A** Anterior pinhole scan of the left distal femur in a 53-year-old female with lung cancer metastasis shows well-defined intracortical tracer uptake (*arrow*). **B** Anterior pinhole scintigraph of the left distal femur in a 57-year-old female with renal cell carcinoma metastasis shows exactly the same intracortical uptake (*arrow*)

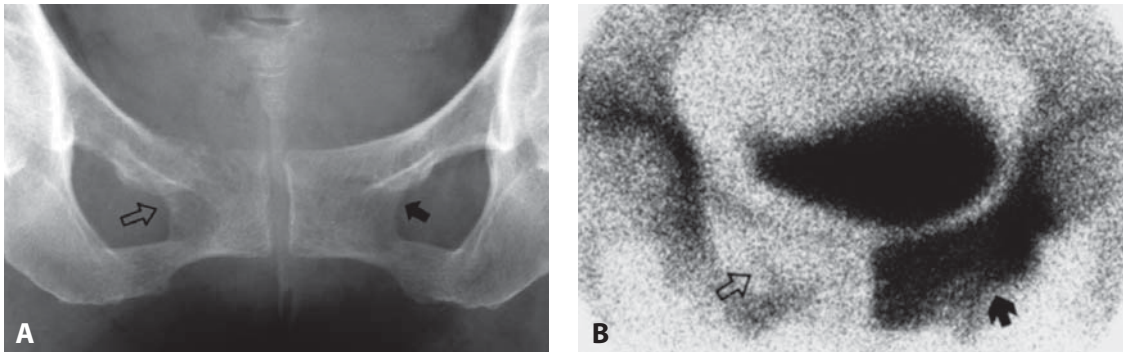

Fig. 17.14A, B Concurrence of photopenic metastasis in one pubic bone and photodense metastasis in the other pubic bone from gastric carcinoma. **A** Anteroposterior radiograph of the pubis in a 64-year-old female shows geographic osteolytic metastases in the right and left pubic bones (*arrows*). **B** Anterior pinhole scintigraph, however, reveals a photon defect in the right pubic bone (*open arrow*) and intense uptake in the left pubic bone (*solid arrow*)

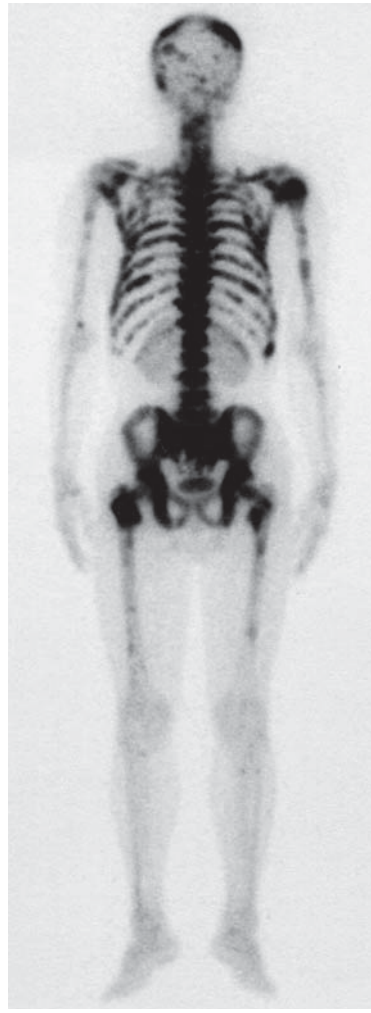

Fig. 17.16 Diffuse metastasis in hematopoietically active marrows. Posterior whole-body scintigraph in a 56-year-old man with gastric carcinoma metastases shows randomly spread tracer uptake with heavier involvement of the axial skeleton

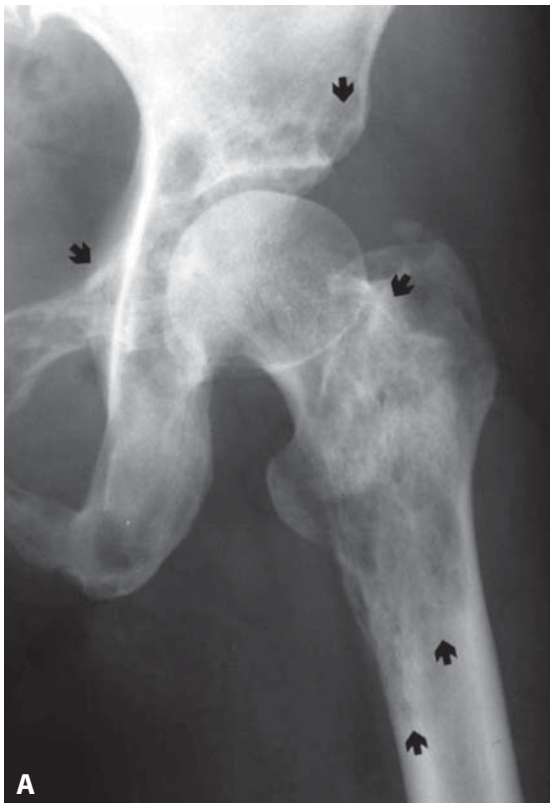

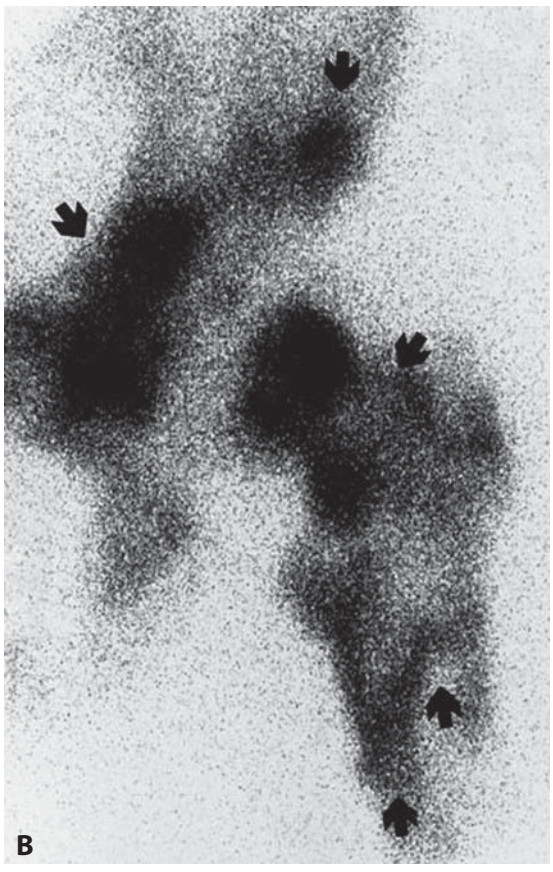

◁ **Fig. 17.15A, B** Mixed metastasis from breast carcinoma. **A** Anteroposterior radiograph of the left hip and proximal femur in a 51-year-old female with breast carcinoma metastases shows irregular osteolytic and osteoblastic lesions (*arrows*). **B** Anterior pinhole scintigraph reveals a mixture of photopenic and photodense lesions (*arrows*). There is no uniform correlation between radiographic and scintigraphic changes

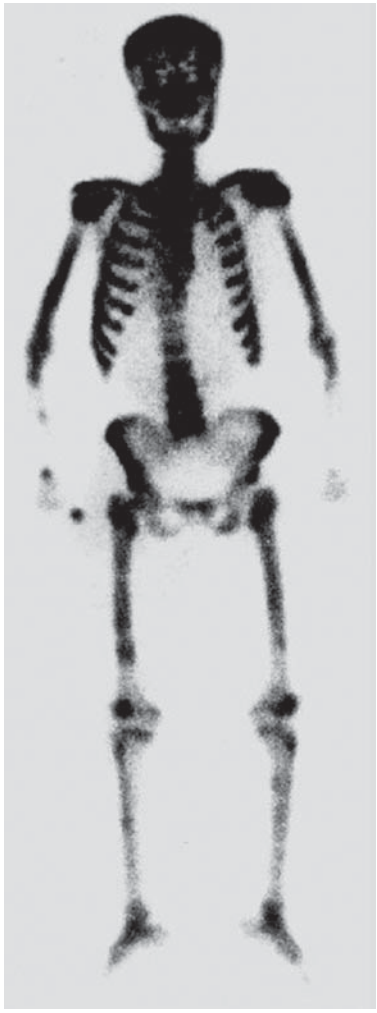

Fig. 17.17 The "superscan" sign produced by extensive skeletal metastases. Anterior whole-body scintigraph in a 59-year-old female with breast carcinoma metastases shows generalized skeletal uptake involving from the skull through the axis to the appendicular bones

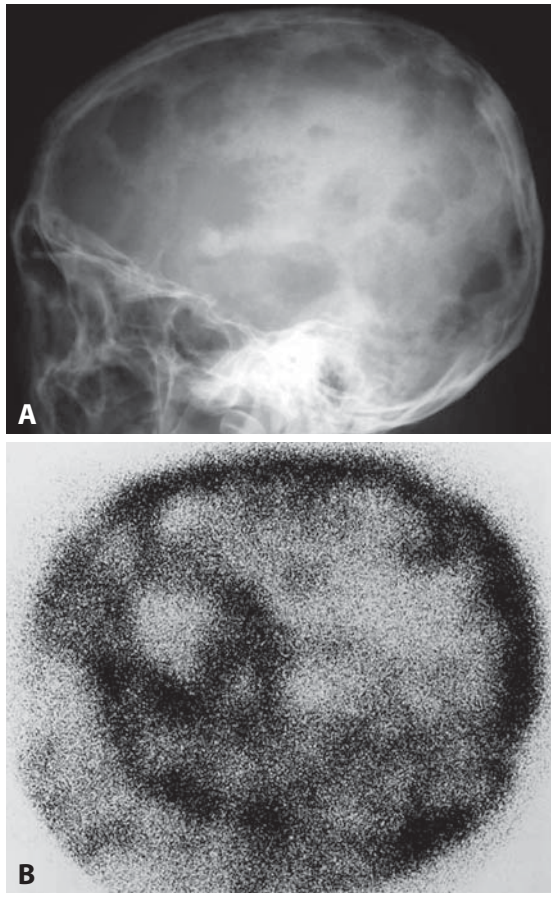

Fig. 17.18A, B Multiple bubbly cranial metastases from esophageal carcinoma. **A** Lateral radiograph of the skull in a 58-year-old male with esophageal carcinoma shows multiple round geographic lesions. **B** Lateral pinhole scintigraph reveals numerous photon defects with peripheral tracer uptake corresponding to lytic lesions

(Fig. 17.12B), larynx (Fig. 17.12C), and biliary tract (Fig. 17.12D) deserve mention. In addition, the involvement of certain bones has been related to malignant metastases. Examples are the "hot" areas in the calvaria, the scapula, the sternum, the pelvis, the vertebra, and the long-bone shaft (Kirchner and Simon 1981). Generally, however, no tumor-specific pattern of bone metastases has been recognized because the metastatic behavior of malignant tumors is so diverse and unpredictable. As shown in Fig. 17.13, different carcinomas can cause metastasis that shows exactly the same scintigraphic sign such as fusiform intracortical tracer uptake: The primary tumors were bronchogenic carcinoma in Fig. 17.13A and renal cell carcinoma in Fig. 17.13B. Conversely, it is also true that the same primary carcinomas create metastases of different types in two different bones at the same time (Fig. 17.14) or simultaneous mixed-type metastasis in the same bone (Fig. 17.15).

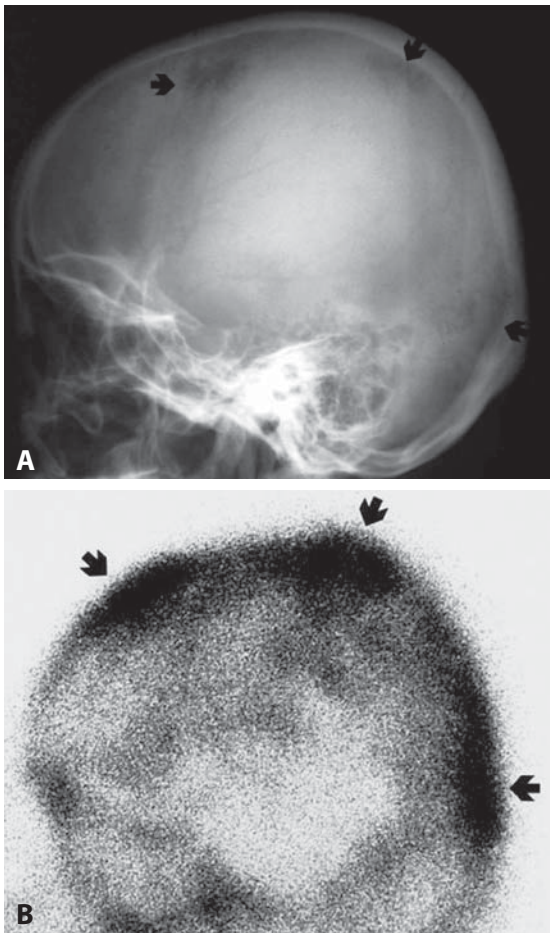

Fig. 17.19A, B Mixed type cranial metastases from breast carcinoma. **A** Lateral radiograph of the skull in a 39-year-old female with breast carcinoma shows coexistence of patchy lysis and osteoblastic lesions (*arrows*). **B** Lateral pinhole scintigraph reveals patchy tracer uptake in lytic lesions (*arrows*) and less intense uptake in blastic lesions

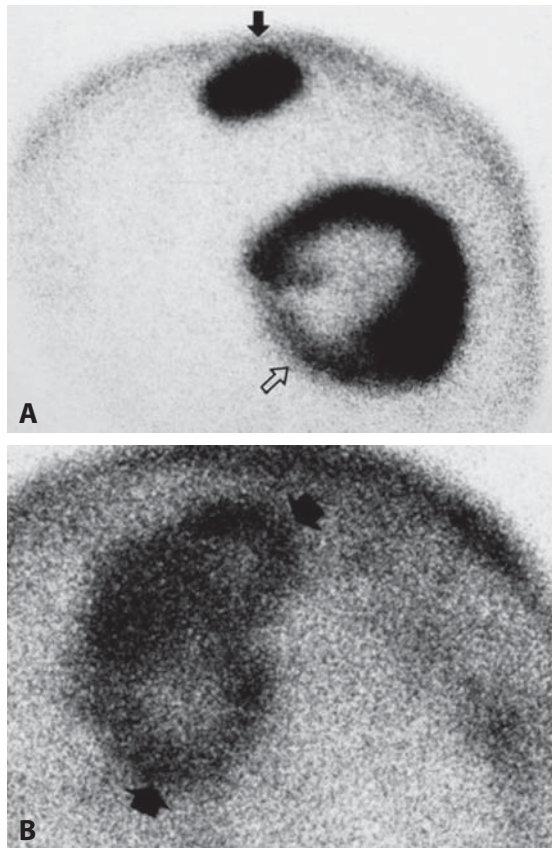

Fig. 17.20A, B Ring-like cranial metastasis from lung and breast carcinomas. **A** Lateral pinhole scintigraph of the skull in a 49-year-old female with lung carcinoma shows a ring-like metastasis (*open arrow*). A smaller daughter lesion is seen in the vertex (*solid arrow*). **B** Oblique pinhole scintigraph of the skull in a 37-year-old female with breast carcinoma shows a twin ring-like metastasis in the posterior parietal bone (*arrows*)

The multiplicity is a distinctive feature of metastasis. Indeed, the diagnosis becomes likelier if lesions are scattered randomly with the heavier involvement of the bones containing active hematopoietic marrow (Fig. 17.16). Metastases are called the "superscan" when diffuse and extensive (Fig. 17.17). Cranial spread of carcinoma may be considered as a modified expression of widespread metastasis that is not yet systemic. The number of bone metastases may vary from a few to numerous and even innumerable, and the scintigraphic expression may be either "hot" or "cold". Radiographic changes are predominantly osteolytic, mixed or osteoblastic. Figure 17.18 demonstrates innumerable radiographically geographic and scintigraphically photopenic cranial metastases from esophageal carcinoma and Fig. 17.19 is an example of scanty mixed-type cranial metastases from breast carcinoma.

As in certain primary bone tumors (McLean and Murray 1984; Goodgold et al. 1984; Hudson 1984), the characteristics of metastasis can be analyzed scintigraphically by the pinhole technique (Bahk et al. 1987). As predicted by McKillop (1987), it is not uncommon that pin-

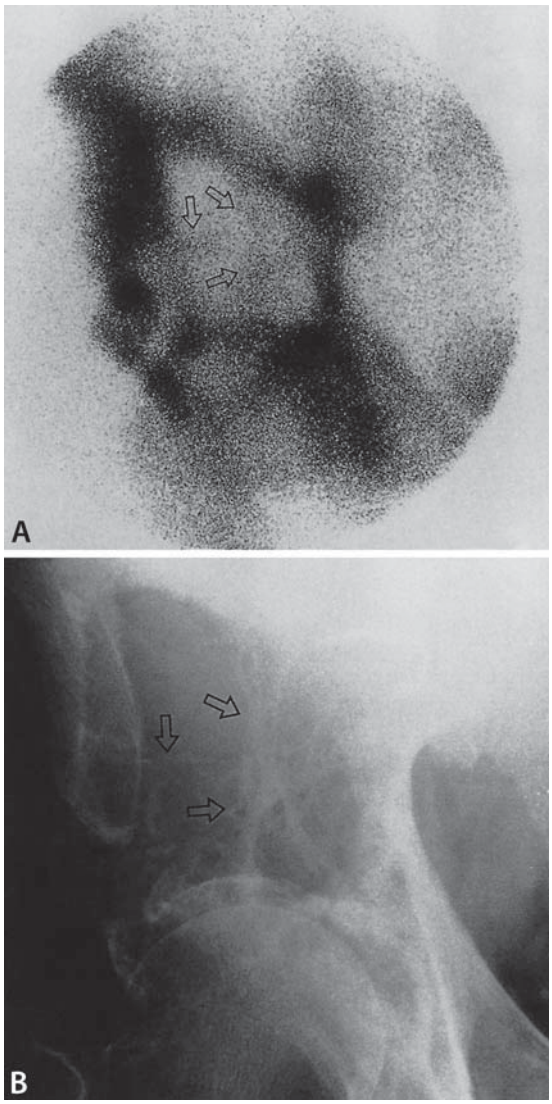

Fig. 17.21A, B Septated photopenic metastasis in follicular thyroid carcinoma. **A** Anterior pinhole scintigraph of the right innominate bone reveals a large, irregular photopenic defect surrounded by intense tracer uptake. Also linear tracer uptake can be seen within the defect, representing "septation" (*open arrows*). **B** Anteroposterior radiograph demonstrates a large area of bone destruction with "septation" (*open arrows*)

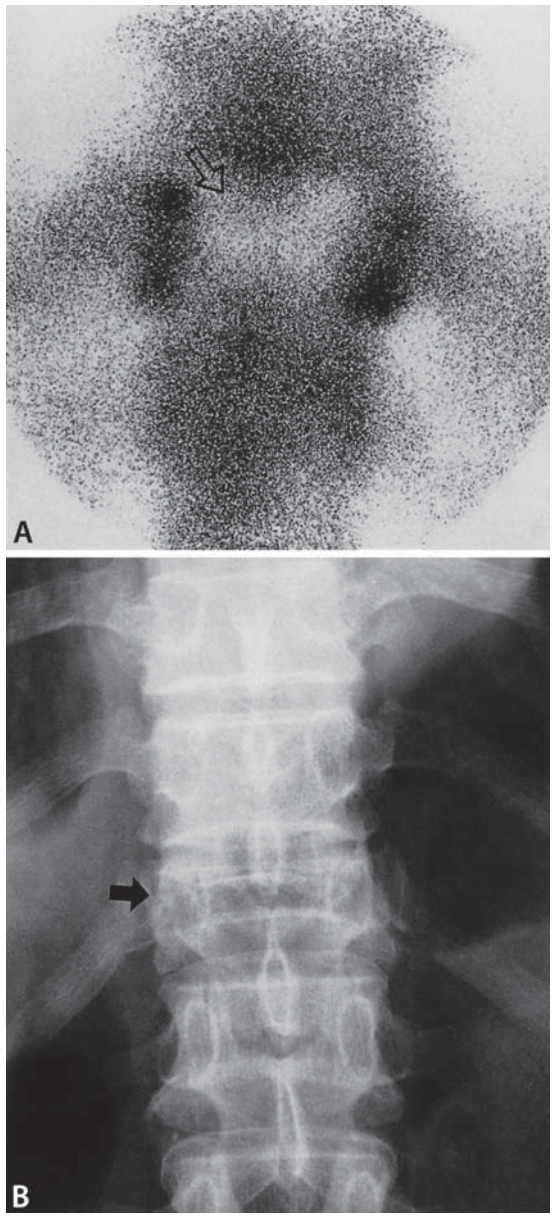

Fig. 17.22A, B Photopenic metastasis from laryngeal carcinoma. **A** Posterior pinhole scintigraph of the T12 vertebra in a 58-year-old man with squamous cell carcinoma of the larynx shows a large photopenic defect involving the whole vertebral body (*arrow*). The defect is bilaterally sided by the pedicles which are spared and concentrate tracer intensely. **B** Anteroposterior radiograph reveals osteolysis with moderate collapse. The pedicles are preserved (*arrow*)

hole scintigraphy depicts a photopenic component within apparently "hot" lesions shown on an ordinary scintigraph, giving rise to a ring-like or picture-frame-like appearance. Pathologically, photopenia is related to osteonecrosis, hypovascularity, and aggressive invasion, and is typically seen in metastases from carcinoma of the lung (Fig. 17.20A), breast (Fig. 17.20B), stomach, and kidney. The "ring" may be single or double and simple or signet shaped. Con-

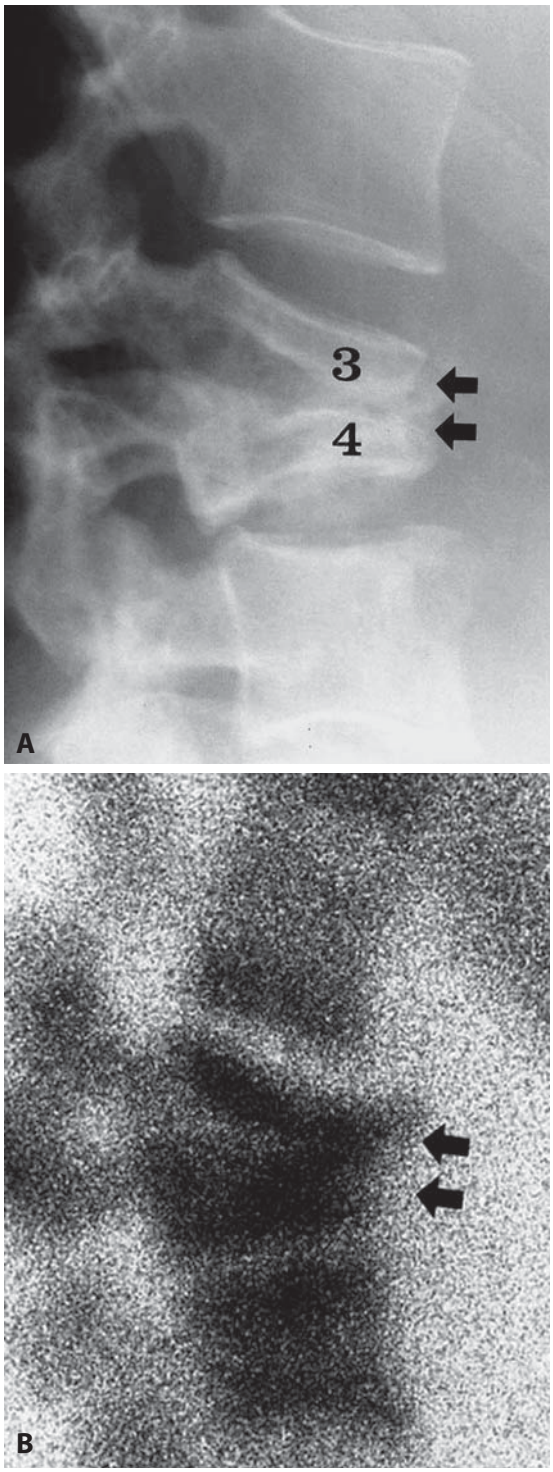

Fig. 17.23A, B Pinhole scan of tuberculous spondylitis. **A** Lateral radiograph of L3 and L4 in a 29-year-old female with advanced tuberculosis shows vertebral collapse with narrowed disk space (*arrows*). **B** Lateral pinhole scintigraph reveals intense tracer uptake in collapsed vertebrae with narrowed disk space (*arrows*)

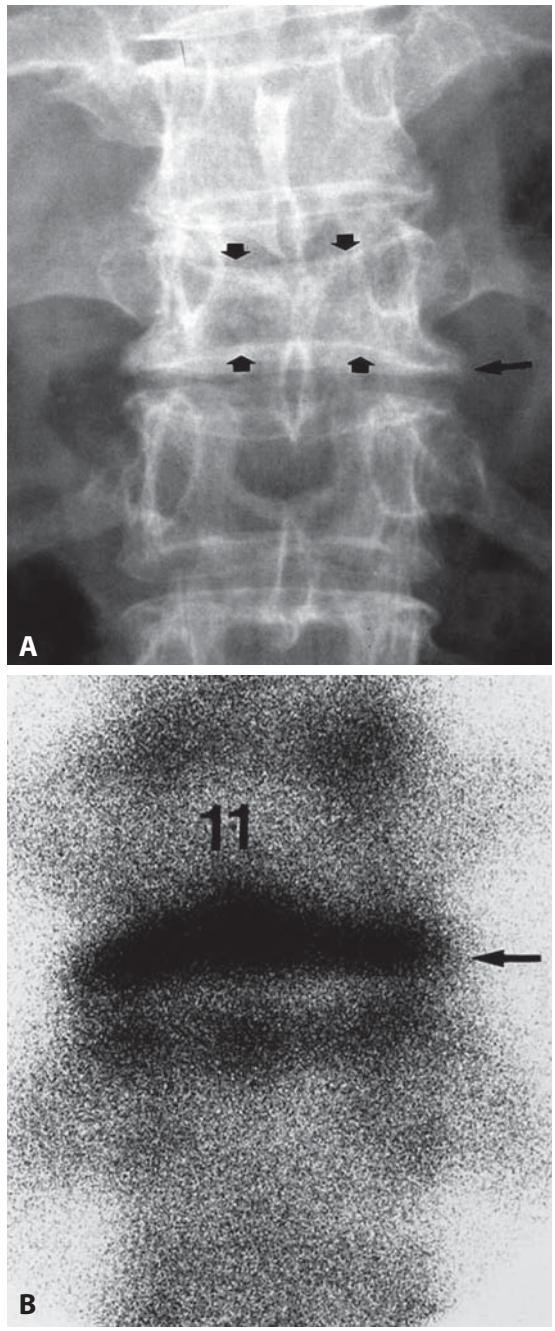

Fig. 17.24A, B Pinhole scan of spinal compression fracture. **A** Anteroposterior radiograph of T11 in a 64-year-old female shows compression of both the upper and lower endplates (*arrows*). There is preexisting hypertrophic change with spurs (*large arrow*). **B** Anterior pinhole scintigraph, however, reveals tracer uptake only in the lower endplate and not in the upper endplate indicating that the fresh fracture is in the lower endplate and that the upper endplate compression is due to an ancient fracture

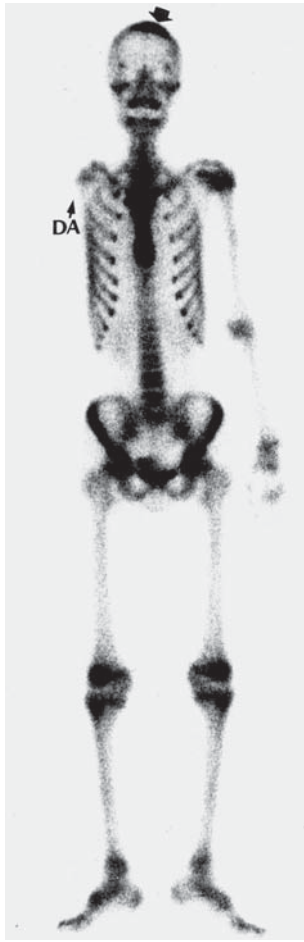

Fig. 17.25 Simultaneous demonstration of metastasis and primary tumor site. Anterior whole-body scan in a 20-year-old male with osteosarcoma treated by right upper-limb disarticulation (DA) shows a single metastasis in the skull (*arrow*)

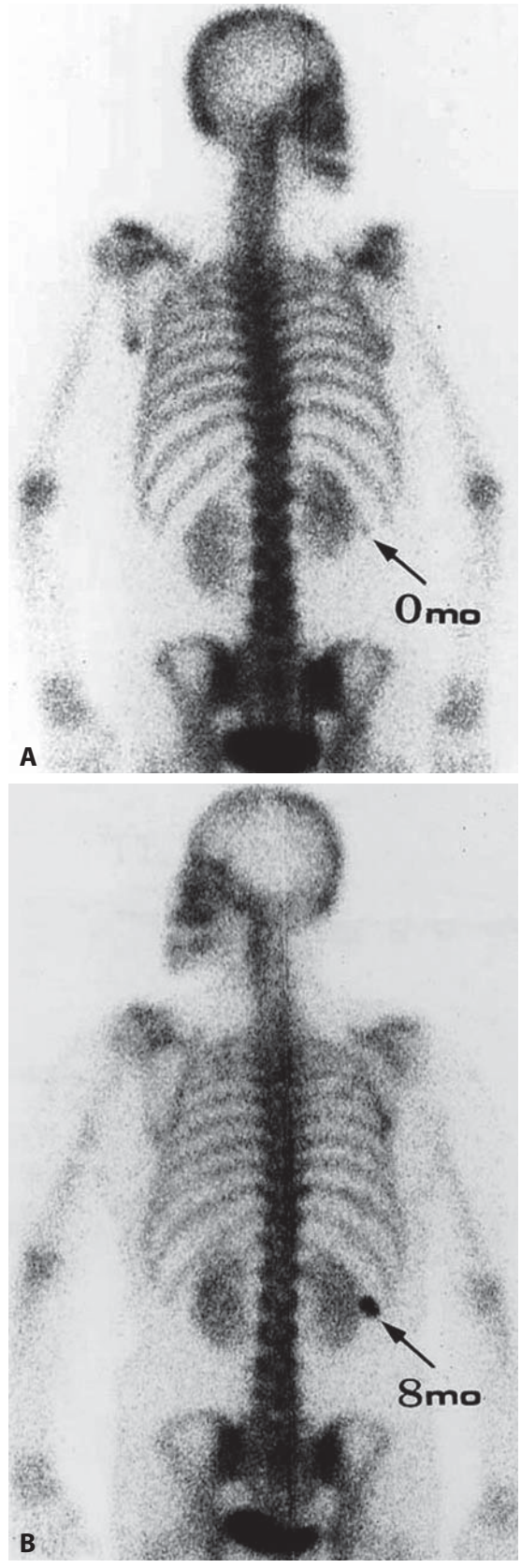

Fig. 17.26A, B High index of suspicion helps diagnose early metastasis. **A** Posterior planar scan of the axial skeleton in a 47-year-old female with breast carcinoma shows questionable uptake in the lateral edge of the right 12th rib (*arrow*). **B** Follow-up scan 8 months later reveals unmistakable metastasis (*arrow*)

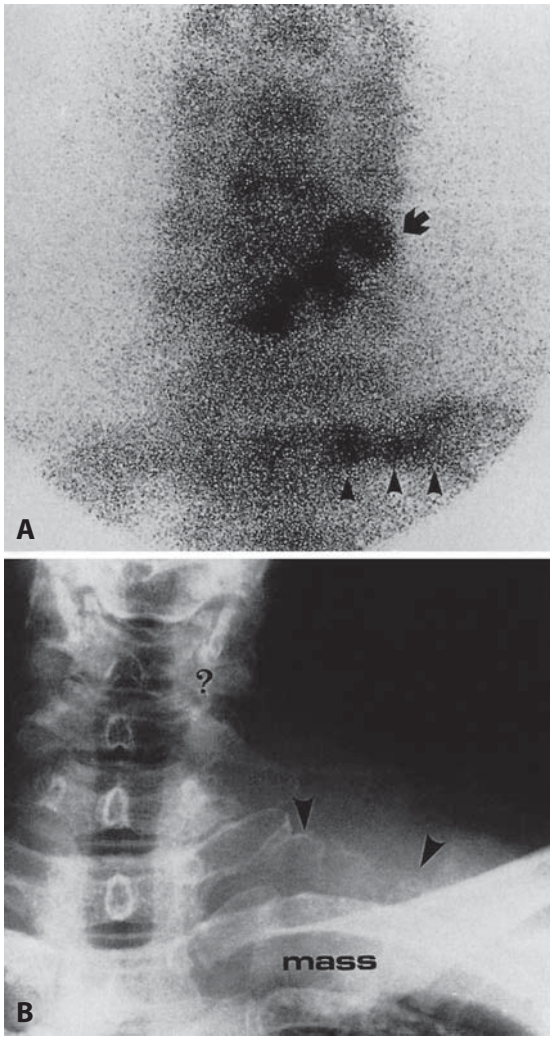

Fig. 17.27A, B Direct rib invasion by thoracic inlet (Pancoast's) tumor and incidental distant metastases. **A** Posterior pinhole scintigraph of the left thoracic inlet in a 50-year-old woman with Pancoast's tumor shows subtle tracer uptake in the first rib near the spine, indicating direct cancer invasion (*arrowheads*). Incidentally, the lower cervical spine shows patchy tracer uptake in the metastases (*arrow*). The scintigraph is printed with the right side on the left to match the radiograph. **B** Anteroposterior radiograph reveals lysis in the posterior first rib near the spine (*arrowheads*) and the primary tumor in the thoracic inlet (*mass*). The metastases in the lower cervical spine clearly shown by scintigraphy is not certain radiographically (*?*)

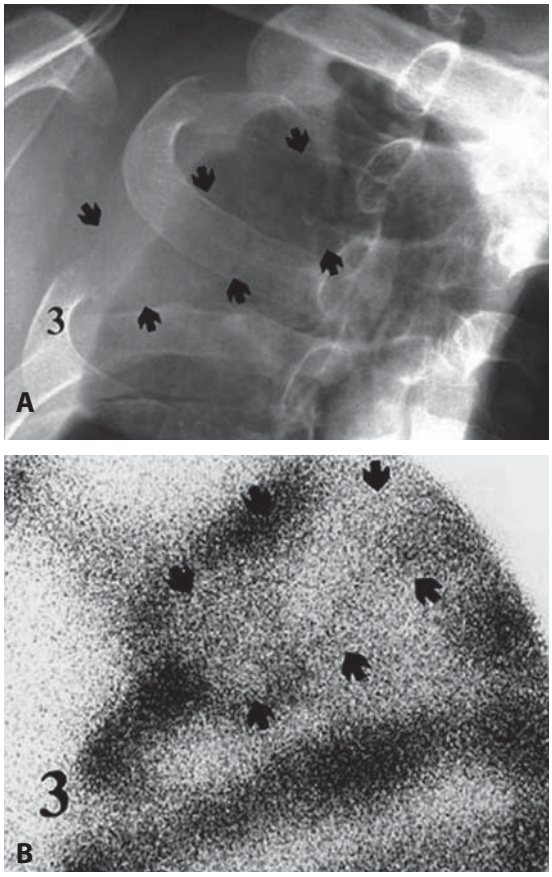

Fig. 17.28A, B Contiguous rib invasion by peripheral bronchogenic carcinoma. **A** Anteroposterior radiograph of the right upper chest in a 42-year-old male shows lysis of the posterior portion of the third rib (*arrows*). Tumor is not seen because of the high penetration technique. **B** Posterior pinhole scintigraph reveals concordant photon defect (*arrows*) with reactive rib uptake (*3*)

versely, the pinhole scan occasionally discloses septum-like or mottled areas of tracer uptake within photopenic metastases. The bone metastasis from follicular thyroid carcinoma is a typical example (Kim et al. 1993) (Fig. 17.21). As discussed above, photopenic changes are encountered more commonly in metastases from renal cell carcinoma and occasionally in those from carcinomas of the lung, stomach, breast, and head and neck.

Pinhole scintigraphy plays a decisive role in discriminating vertebral metastasis (Fig. 17.22) from infection (Fig. 17.23) and fracture (Fig. 17.24), all of which radiographically manifest as bone destruction (Bahk et al. 1987). Pinhole scanning is also extremely valuable in the staging of malignant tumors and searching for distant metastases since the entire skeleton

can be scrutinized (Fig. 17.25). In the investigation of an early metastasis, a high index of suspicion and keen judgment cannot be overemphasized. However trifling a lesion may appear at first scanning, it should not be dismissed at once but rather be closely followed up with great concern preferably in 3 months at first, particularly when the primary tumor has a strong proclivity toward early and high-rate bone metastasis (Tanaka et al. 1991). One notorious tumor of this kind is breast carcinoma. The case presented in Fig. 17.26 was a 47-year-old female patient with well-differentiated invasive ductal adenocarcinoma of the right breast with positive axillary nodes. The first follow-up scintigraph was taken 10 months after mastectomy. There was a tiny, ambiguous uptake in the lateral edge of the right 11th rib. The second follow-up was 8 months later and showed unmistakable metastasis. Fortunately, the lesion had remained solitary.

Direct invasion of local bone is another mode of metastasis. Well-known examples are Pancoast's tumor of the thoracic inlet (Fig. 17.27) and peripherally located lung carcinomas with contiguous invasion of the local rib (Fig. 17.28), rectal carcinoma with spread to the sacrum, and nasopharyngeal cancer with neighboring bone invasion (see "Nasopharyngeal Cancer" in Chapter 20). The direct rib invasion may (Fig. 17.27) or may not show tracer uptake (Fig. 17.28), requiring pinhole scintigraphy for accurate diagnosis (Fig. 17.27). Pinhole scintigraphy is very useful for the separate delineation of individual metastatic lesions that are closely positioned on the planar scintigraph (Fig. 17.29).

Cortical bone metastases occur as the result of hematogenous dissemination of tumor cells from almost any kind of carcinoma (Coerkamp and Kroon 1988). Extended application of the pinhole technique by us to the analysis of long bone metastases has been shown to be highly rewarding. Indeed, pinhole scanning distinguishes selective involvement of the cortex (Fig. 17.30), periosteum (Fig. 17.6), endosteum (Fig. 17.31), panosteum or all bone layers (Fig. 17.32), and medullary space (Fig. 17.33).

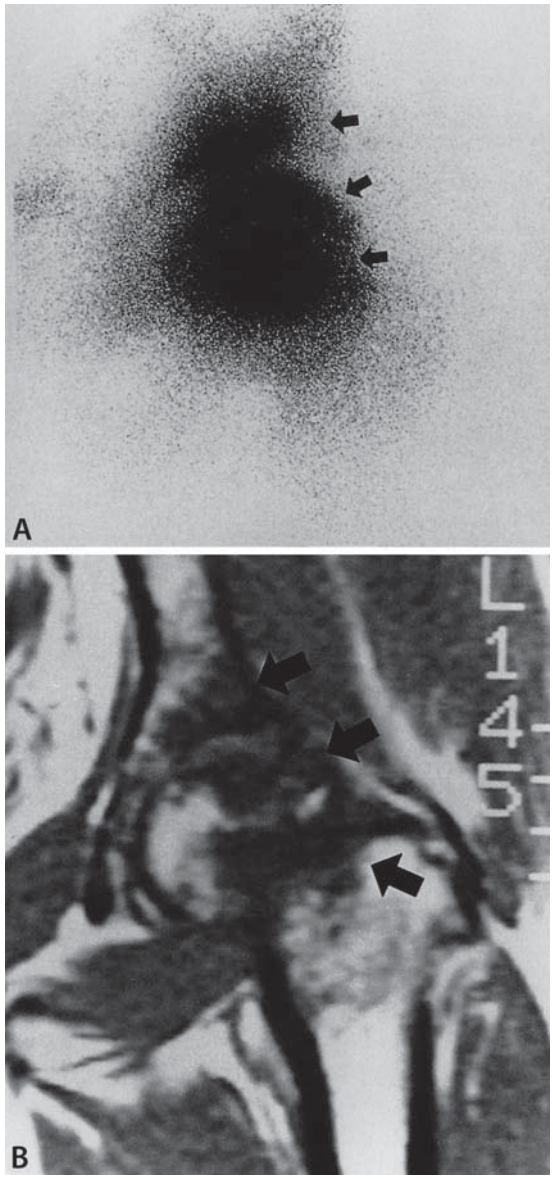

Fig. 17.29A, B Discreteness of the multiple individual lesions that are close to each other, a differential point in favor of metastasis. **A** Anterior pinhole scintigraph of the left hip in a 45-year-old woman with breast cancer shows discrete tracer uptake in the acetabulum (*top arrow*) and femoral head (*lower arrows*) across the clear joint, favoring the diagnosis of metastases at two different sites. The lesions were presented as a single pathology of the hip joint on ordinary scintigraph, raising the possibility of coxitis (not shown here). Also observe that the more intense tracer uptake occurs centrally in the tumor and the less intense uptake peripherally in the watershed. **B** T1-weighted coronal MRI shows decreased signal intensity in metastases in both the acetabulum (*top arrow*) and femoral head (*lower arrows*)

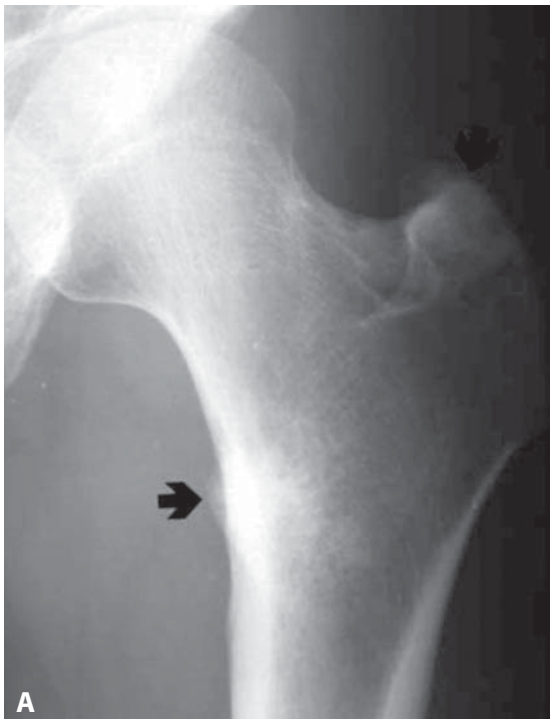

Fig. 17.30A, B Trochanteric metastasis. **A** Anteroposterior radiograph of the left proximal femur in a 26-year-old male with thymoma shows osteoblastic metastases to the greater and lesser trochanters (*arrows*). **B** Anterior pinhole scan reveals concordant tracer uptake (*arrows*)

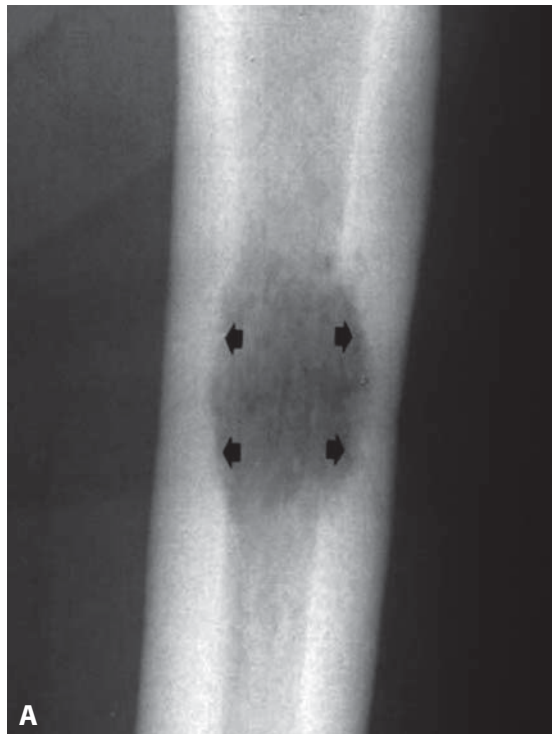

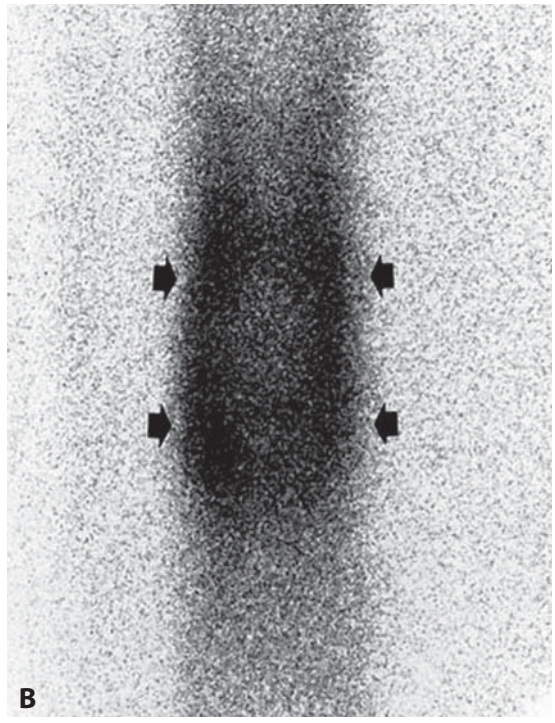

Fig. 17.31A, B Endosteal metastatic invasion. A Anterior pinhole scintigraph of the right femoral shaft in a 54-year-old male with pancreas cancer metastasis shows increased tracer uptake localized to endosteums (arriws). B Anteroposterior radiograph reveals an expansive osteolytic lesion invading endosteums

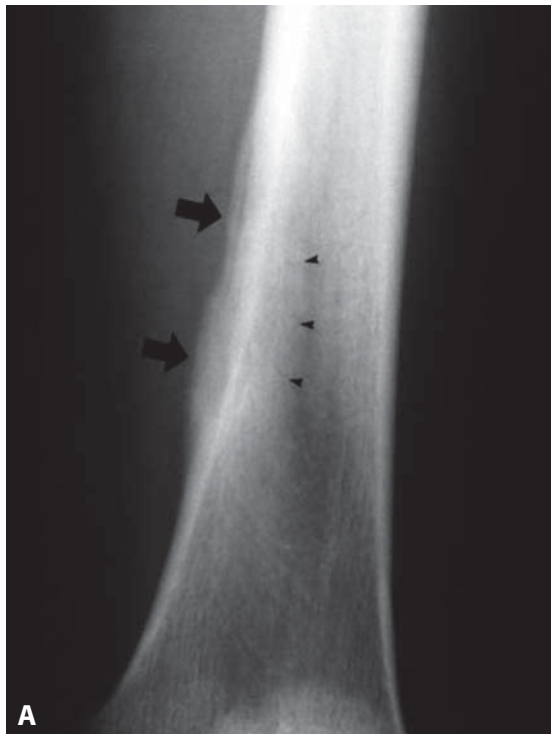

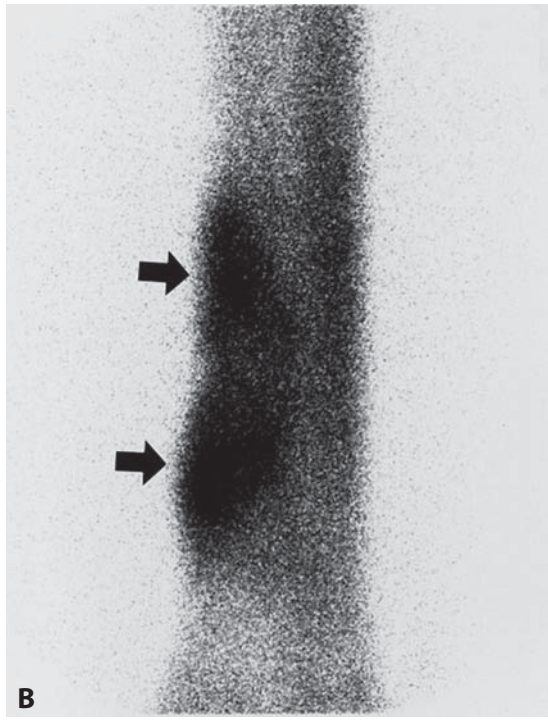

Fig. 17.32A, B Panosteal metastasis. **A** Anteroposterior radiograph of the left femoral shaft in a 47-year-old female with breast carcinoma shows diffuse thickening of the endosteum (*arrowheads*), periosteum (*arrows*) and cortex between. **B** Anterior pinhole scintigraph reveals increased tracer uptake in all bone layers (*arrows*)

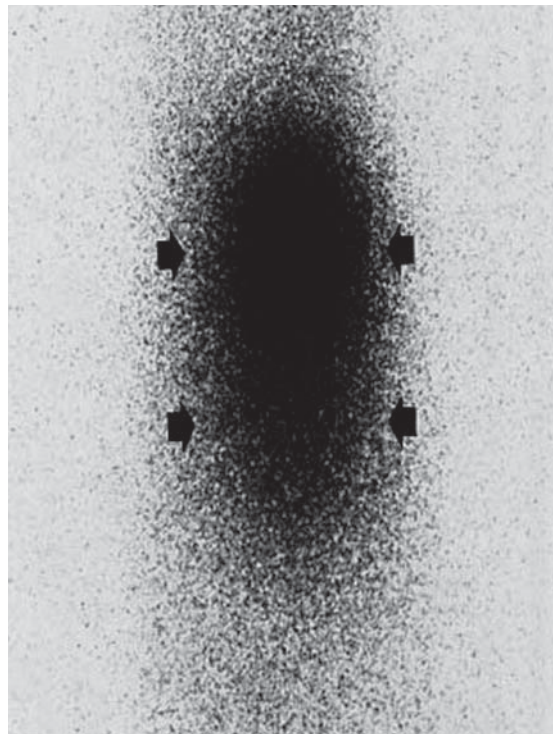

Fig. 17.33 Medullary metastasis. Anterior pinhole scintigraph of the right humeral shaft in a 64-year-old male with lung carcinoma shows fusiform tracer uptake within the medullary cavity (*arrows*)

In contrast to the absolute high prevalence of axial bone involvement, metastases are extremely rare in the bones of the hands and feet (Asthana et al. 2001; Bahk WJ et al. 2006) (Fig. 17.34) and uncommon in the patella (Fig. 17.35) and mandible (Fig. 17.11).

The last but not least important use of bone scintigraphy in skeletal metastases is intra- and posttherapeutic follow-up (Gabuniia at al. 1989; Cook and Fogelman 2001). Pinhole scanning is particularly useful in this situation since anatomy and pathology are appreciated in greater detail. This examination efficiently and reliably portrays, first, treatment-naive metastasis (Fig. 17.36A), the flare phenomenon (Fig. 17.36B), and, finally, the cured state (Fig. 17.36C) after adjuvant chemotherapy or external irradiation. The flare is a transient increase in the intensity of bone uptake during

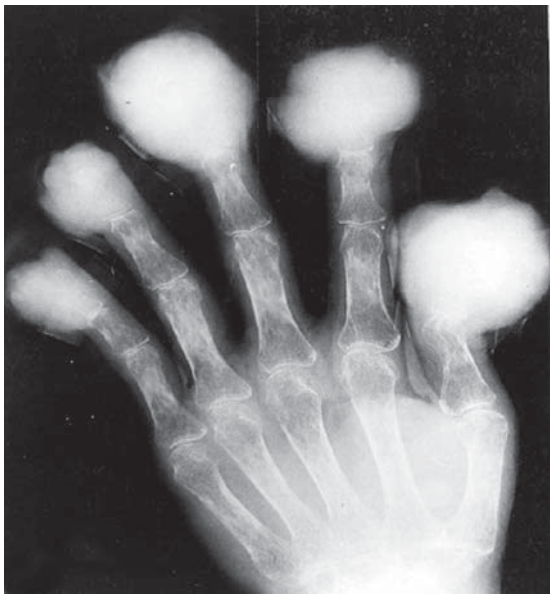

Fig. 17.34 Multiple acrometastases. Dorsopalmar radiograph of the right hand shows prominent bony clubbing of all fingertips due to osteoblastic metastases from gastric adenocarcinoma

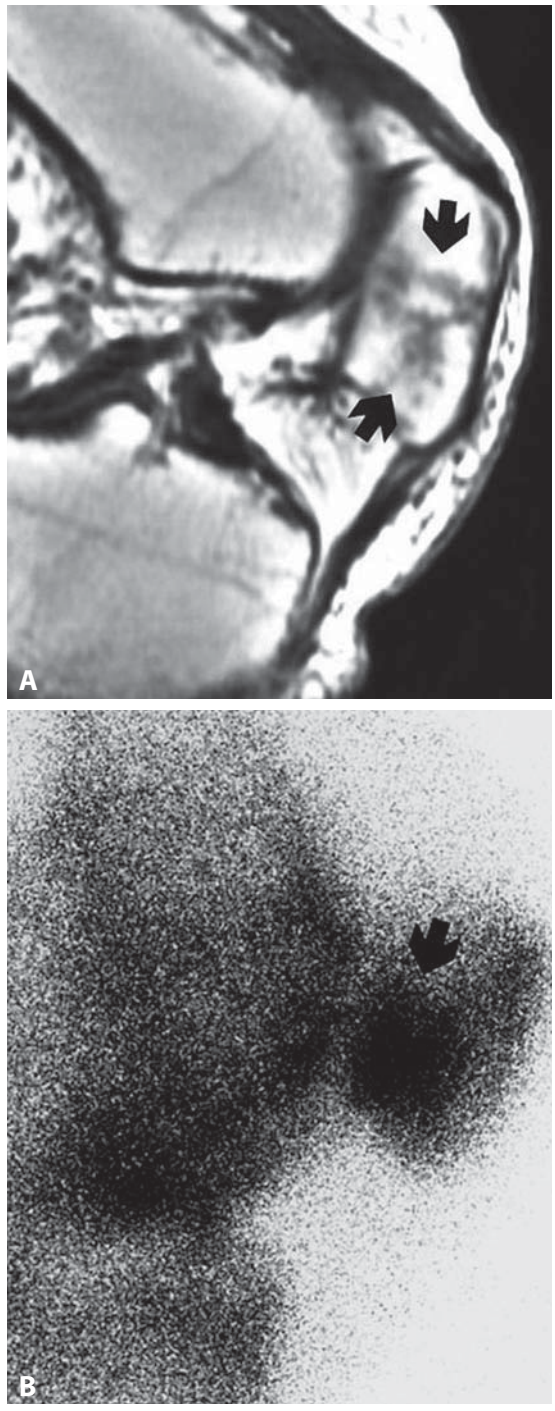

Fig. 17.35A, B Patellar metastasis. **A** Sagittal T1-weighted MRI of the right patella in a 57-year-old male with lung carcinoma shows irregular low signal in the lower half of the marrow space (*arrows*). **B** Lateral pinhole scan reveals concordant patchy uptake in the inferoposterior aspect of the patella (*arrow*)

treatment, usually chemotherapy, with subsequent recovery. One recent series, 24.4% of 33 patients who received chemotherapy for non-small-cell lung carcinoma showed the flare phenomenon (Lemieux et al. 2002).

17.1.1 Bone Marrow Scintigraphy in Metastasis

Cancer cells are carried to the bone marrow via the bloodstream and are anchored and implanted in the medullary sinusoidal arteries. Surviving tumor cells are facilitated to extravasate into the marrow space because blood flow is sluggish, the endothelium is loose, and the basement membrane is not present. Bone marrow metastases can occur without cortical involvement, for example, in breast carcinoma (Kamby et al. 1987). ^{99m}Tc-NCA95 bone-marrow scintigraphy can sensitively and accurately detect metastases, which are visualized as photopenic lesions (Fig. 17.37A). This finding sharply contrasts with the photodense (increased uptake) manifestation on ^{99m}Tc-MDP

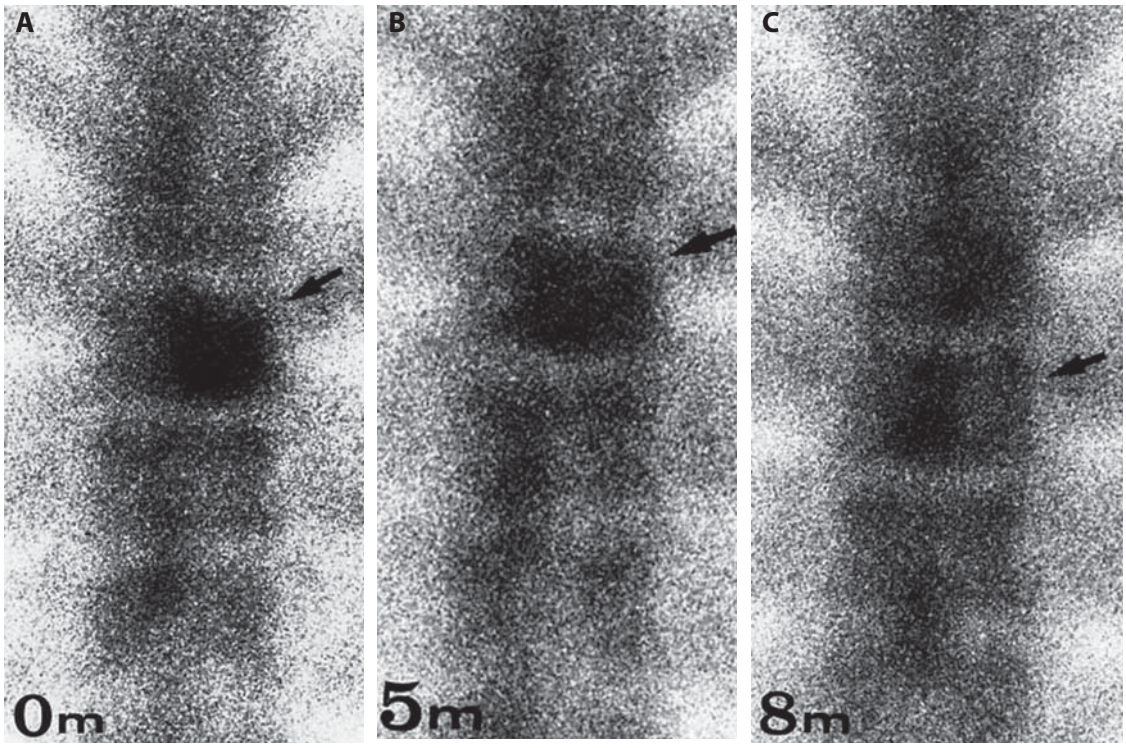

Fig. 17.36A–C Pre- and postadjuvant therapy evaluation of bone metastasis. **A** Initial pinhole scintigraph of the T7 vertebra in a 57-year-old female with breast carcinoma metastasis shows patchy uptake in therapy-naive metastasis (*arrow*). **B** First postadjuvant chemotherapy scan taken 5 months later shows "flare uptake" (*arrow*). **C** Second follow-up at 8 months shows no pathological tracer uptake (*arrow*)

scans (Fig. 17.37B). Approximately 90% of bone-marrow metastases are blood-borne, and, hence it is natural that bone-marrow metastases exist in the absence of affected bone (Fig. 17.38). The agents for bone marrow scanning are largely limited, including only ^{99m}Tc nanocolloid and ^{99m}Tc-labeled anti-nonspecific cross-reacting antigen (anti-NCA) 95.

Immunoscintigraphy has been shown to be a sensitive indicator of the presence and extent of malignant marrow infiltration (Reske et al. 1989; Duncker et al. 1990). It can distinguish malignancy from benignity in patients with an equivocal ^{99m}Tc-MDP bone scintigraphic change (Lee et al. 1995). The sensitivity and specificity were 100% and 79%, respectively. False-positives occur in degenerative arthritis of the spine, the marrow of which has been replaced with fat. If a marrow scan defect is found in concordance with a positive bone scan, radiography is mandatory to exclude benign conditions such as red marrow involution (Cooper et al. 1992), focal osteonecrosis (Haubold-Reuter et al. 1993), Paget's disease, and bone infarction (Yuasa et al. 1991).

Duncker et al. (1990) assessed the usefulness of immunoscintigraphy in patients with breast cancer suspected of having bone metastasis, finding marrow defects in 25 of 32 patients and bone invasion subsequently confirmed in 23 of 25 patients. ^{99m}Tc-MDP bone scintigraphy detected metastases in 17 of 32 patients, whereas anti-NCA95 antibody scan detected more metastatic sites in 12 of 17 patients. Other investigators have also reported that bone marrow scintigraphy is superior to bone scintigraphy in diagnosing metastases in patients with carcinomas of the lung, kidney, bladder, and prostate (Widding et al. 1990; Bourgeois et al. 1991) (Fig. 17.38). However, Bourgeois et al. found that the specificity of bone scan was 100% compared to 87% specificity for marrow scan.

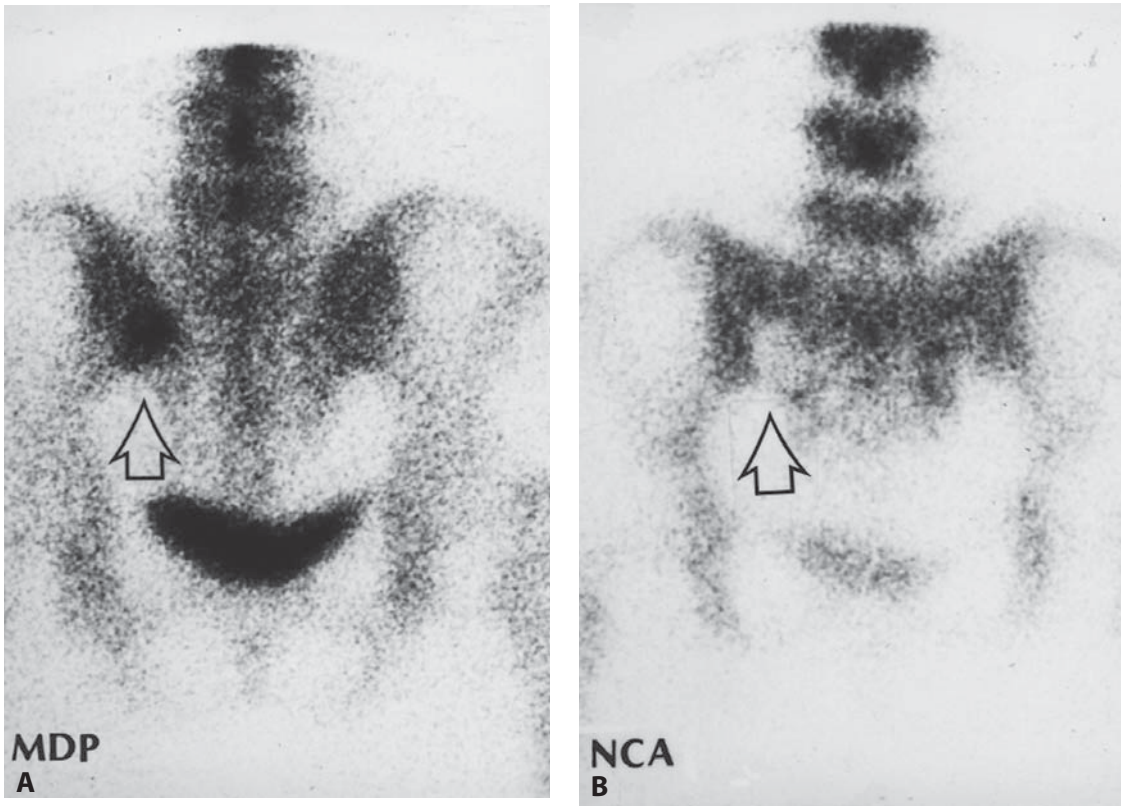

Fig. 17.37A, B Immunoscintigraphy of bone metastasis. **A** Posterior ^{99m}Tc-MDP bone scintigraph of the pelvis in a patient with metastasis from prostate carcinoma shows prominent tracer uptake in the left lower sacroiliac joint (*arrow*). **B** Posterior planar ^{99m}Tc-NCA95 immunoscintigraph reveals concordant photon defect (*open arrow*)

17.2 Primary Malignant Bone Tumors

Radiography is the single most efficient imaging method for primary bone tumors, both benign and malignant. Accordingly, bone scintigraphy was once not enthusiastically explored in primary bone tumors. However, with the popularization of refined gamma cameras, bone tumors have been subjected to extensive scintigraphic studies, leading to the accumulation of a volume of knowledge (Kirchner and Simon 1981; McLean and Murray 1984; Gilday et al. 1977). In addition, continued application of the pinhole technique to the diagnosis of bone tumors and tumorous conditions has theoretically and substantially contributed to widening of the horizon of ^{99m}Tc-MDP scanning in bone oncology (Baek et al. 1997; Bahk 1996, 1998; Bahk et al. 1995). This section describes the bone scintigraphic features of osteosarcoma, chondrosarcoma, Ewing's sarcoma, fibrosarcoma, and myelomas.

17.2.1 Osteosarcoma (Osteogenic Sarcoma)

Osteosarcoma is pathologically characterized by its ability to produce neoplastic bone in a fibrous stroma, hence osteogenic sarcoma. This is known as the most common variety of primary malignant bone tumor in the pediatric and adolescent age groups. Boys are affected slightly more frequently than girls. The most commonly affected bones are those of the knee with the proximal humerus the next most commonly affected. The location of tumor may be either central or parosteal in the metadiaphysis of the long bone with, not uncommonly, invasion of the adjacent soft tissue. Multiple primaries have been reported. Pathological fracture

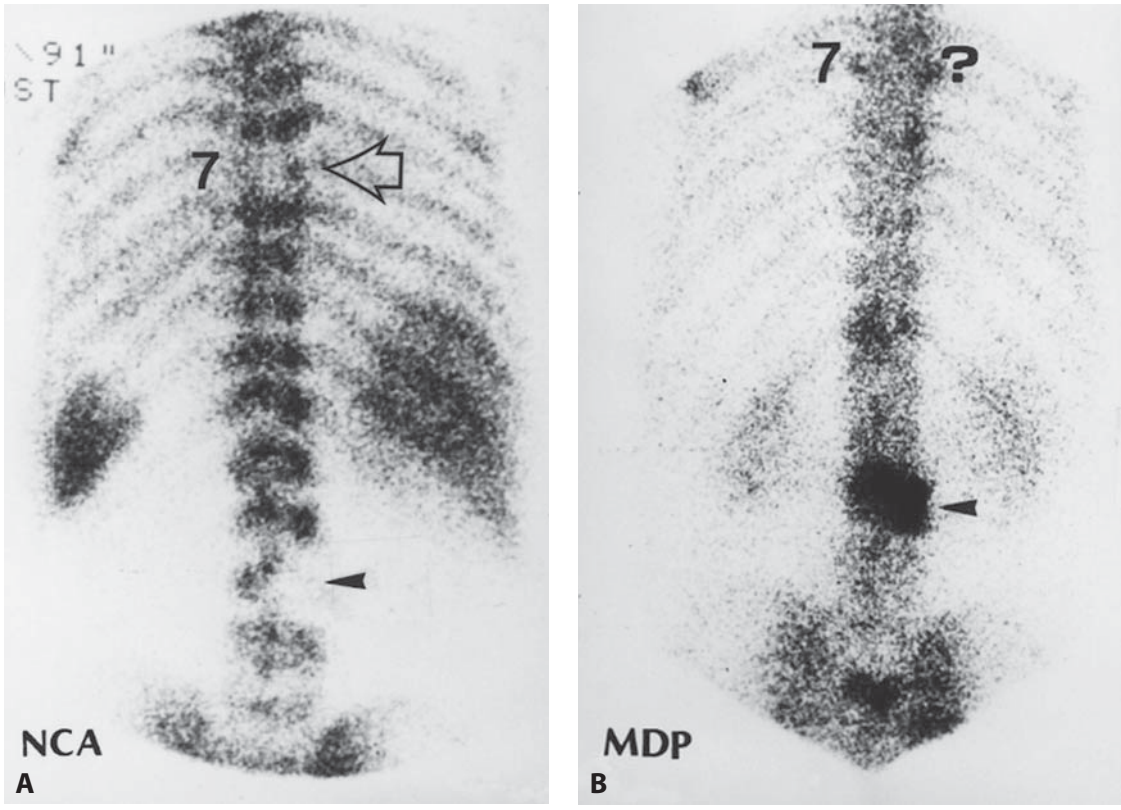

Fig. 17.38A, B Higher sensitivity of immunoscintigraphy in bone metastasis. **A** ^{99m}Tc-NCA95 immunoscintigraph of the spine with gastric cancer metastases shows photon defects in T7 and L3. **B** However, ^{99m}Tc-MDP bone scintigraph shows positive tracer uptake only in L3 (*arrow*) and no uptake in T7 (*?*)

is relatively common, deforming the affected bone. Zeifang and colleagues (2000) surgically treated 30 patients with pathological fracture out of 336 patients with primary malignant bone tumors, reflecting approximately a 9% frequency.

The essential radiographic features of osteosarcomas are osteosclerosis (Fig. 17.39A), osteolysis (Fig. 17.40A), and their combination (Fig. 17.41A). Spicular, sunburst-like, and corona-like bone formation that arises from the lesional bone and periosteum is pathognomonic, especially when the adjacent soft tissues are concomitantly invaded (Fig. 17.42A). Periosteal osteogenesis with elevation and rupture (Codman's triangle) is another important but not specific sign (Fig. 17.43A). Pathological fractures modify radiographic appearance, manifesting as fracture lines and fragmentation with or without dislocation within a tumor mass, which is the seat of osteolysis and hemorrhage and/or necrosis (Fig. 17.44A).

Contrast angiography provides valuable information on tumor vascularity and blush (Fig. 17.45). Unlike the more common varieties of osteosarcoma, the telangiectatic subtype radiographically presents as an osteolytic tumor strongly resembling aneurysmal bone cyst. Being high-grade osteosarcoma, this subtype produces minimal osteoid with a greater portion of tumor replaced by hemorrhage and/or necrosis (Fig. 17.46A, 17.47A). MRI is an excellent imaging method that can be used for in vivo tumor tissue characterization of the telangiectatic subtype of osteosarcoma (Murphey et al. 2003) (Fig. 17.47).

Scintigraphic manifestations vary according to the histological characteristics of the tumor. In general, the uniformly osteogenic or sclerotic type accumulates tracer extremely intensely

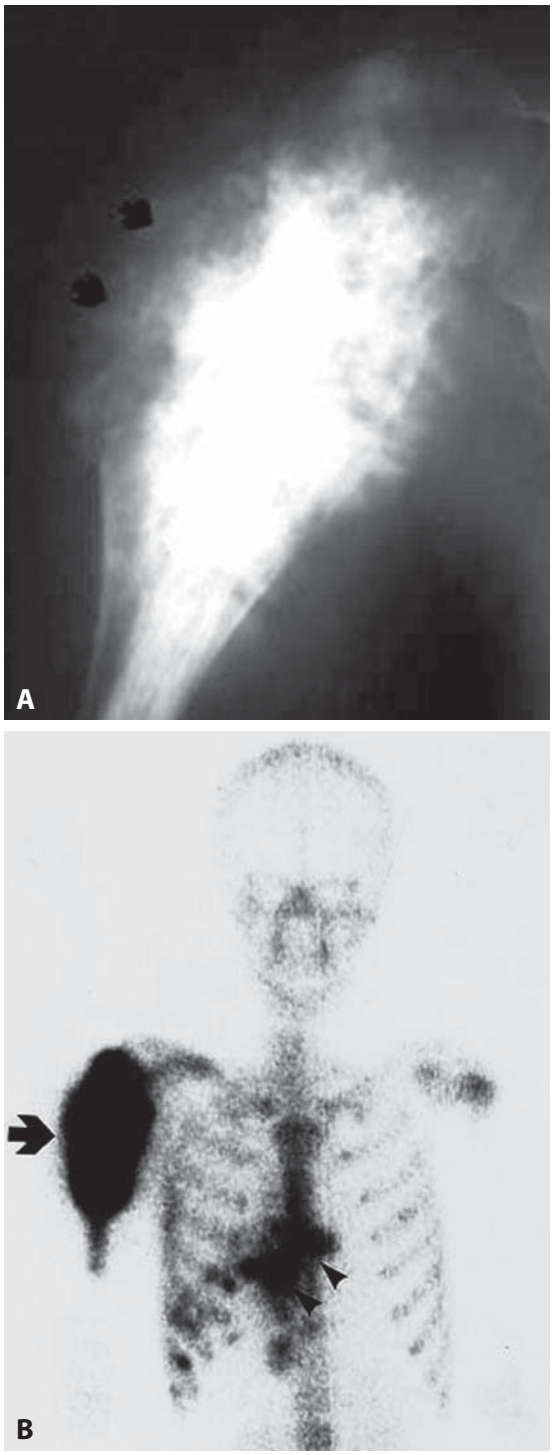

Fig. 17.39A, B Sclerotic osteosarcoma. **A** Anteroposterior radiograph of the right proximal humerus in a 12-year-old girl shows an Indian-club-shaped radiodense tumor with a shaggy contour (*arrow*). **B** Anterior bone scintigraph reveals intense tracer uptake in the tumor (*arrow*). The tracer uptake in the ribs and sternum are also due to metastasis (*arrowheads*)

(Fig. 17.39B) and the osteolytic type also accumulates tracer (Fig. 17.40B). The mixed type with intratumoral hemorrhage and/or necrosis presents as a mixture of photodense and photopenic areas (Fig. 17.41B). The main body of tumor within a long bone presented as a longitudinally oriented "hot" mass in both sclerotic and lytic types. The mass is fairly well demarcated on scintigraphs (Fig. 17.40B) but becomes distorted with patchy uptake when pathological fracture supervenes (Fig. 17.44C). Interestingly, the larger portion at the center of osteosarcoma with numerous fine tumor vessels and white blush is imaged as photopenia, and conversely the peripheral zone of tumor with lowered vascularity accumulates tracer rather intensely (Fig. 17.45). Fracture is usually indistinct on plain scintigraphs, and can be imaged as such only by pinhole scintigraphy (Fig. 17.47). Characteristically, soft-tissue invasion produces the scintigraphic "sunburst" sign (Figs. 17.41B and 17.42B). It is to be emphasized that magnification scanning is extremely helpful for the visualization and analysis of all these pathological changes in detail. Indeed, simple bone distortion and increased uptake seen on ordinary scintigraphs of an osteosarcoma can be resolved into the main bone change with intratumoral hemorrhage or necrosis and more importantly neoplastic osteogenesis in the periosteums and the adjacent soft tissues.

As is mentioned above, the telangiectatic osteosarcoma produces minimal osteoid tissues, ans is replaced by hemorrhage and necrosis. Scintigraphically, the tumor is presented as a large irregular photopenic lesion in the long bone metadiaphysis (Fig. 17.46B). Occasionally, pathological fracture and viable melted host bone or neoplastic osteoid may accumulate tracer visibly on pinhole scintigraphs (Fig. 17.47B).

17.2.2 Chondrosarcoma

The exact tissue origin of chondrosarcoma is obscure, but clearly the basic tissue is cartilage that is transformed into myxomatous, calcified, or even ossified tissue. The cell differentiation

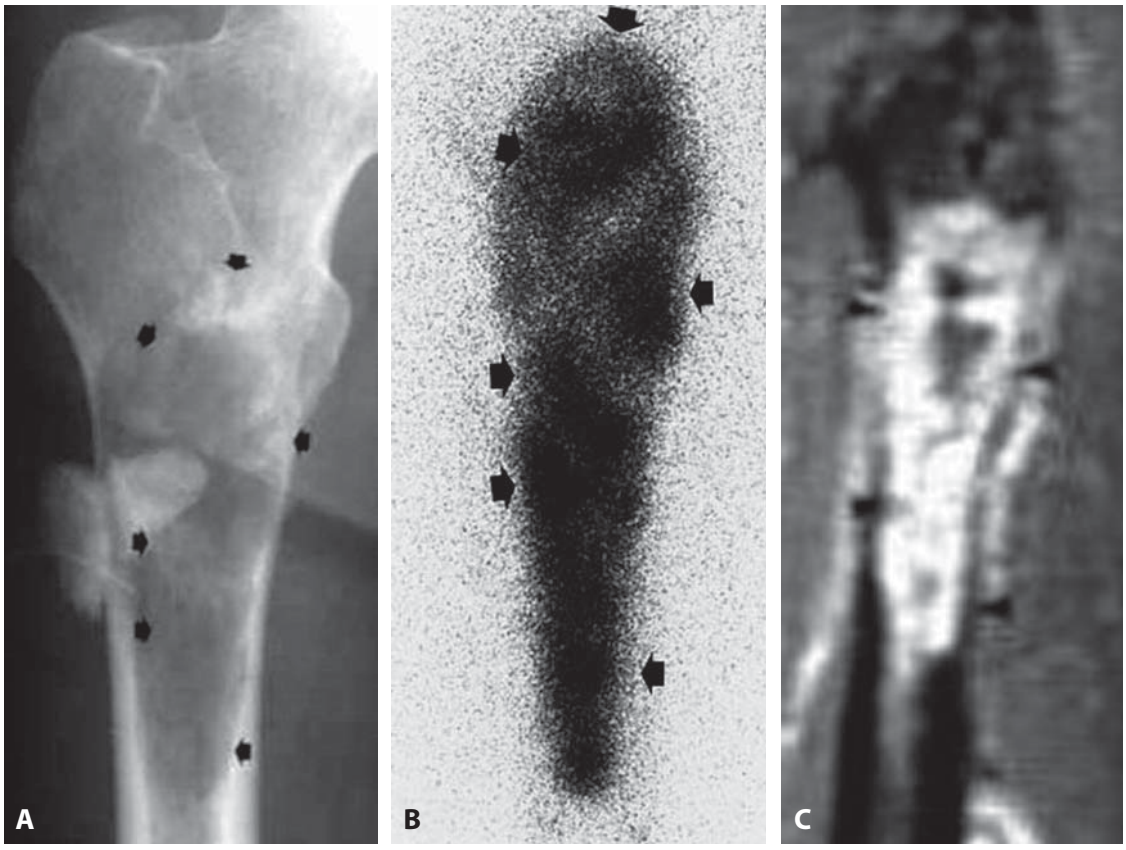

Fig. 17.40A–C Osteolytic osteosarcoma. **A** Anteroposterior radiograph of the right proximal femoral shaft in a 49-year-old male shows a large elongated concentric osteolytic tumor (*arrows*). The fingertip-like opaque shadow is exogenous material used as a stopper of a fenestration for biopsy. **B** Anterior bone scintigraph reveals intense tracer uptake in intramedullary tumor (*arrows*). **C** Gadolinium-enhanced T1-weighted MRI shows diffuse enhancement (*arrows*)

ranges from almost benign to highly malignant. The tumor is either primary (de novo) or transformed from a preexisting benign lesion such as osteochondroma, enchondroma, or exostoses. The incidence of primary chondrosarcoma ranges from 76% to 90%. This is a tumor of middle and old age (30–70 years) and is slightly more common in males than in females. As in osteosarcoma, the location is central, juxtacortical, or peripheral. The femur, the humerus, and the axial skeleton are involved in more than 75% of cases.

Radiographically, the primary central type of chondrosarcoma of the long bone manifests as a mixture of irregular mottled densities and lucencies with complete effacement of trabeculae, usually in the metaphysis. Demarcation may be fairly sharp or blurred. The tumor may permeate, penetrate, and break the cortex to form a bulging mass in the soft tissue (Fig. 17.48A). CT similarly shows the mixture of cartilage and mineralized component with cortical rupture and soft-tissue invasion with tumefaction (Fig. 17.48B). One case of chondrosarcoma in our file that was considered as the dedifferentiated type showed an irregular bone mass in the greater trochanter (Fig.17.49A). It was composed of osseous and cartilaginous elements with a melted crest and a pathological fracture.

Pinhole scintigraphic features of primary chondrosarcoma are the mixture of normal and slightly decreased uptake, cortical irregularity, bone deformation, and surrounding extended uptake (Fig. 17.48C). Comparison with radiographs reveals the tumoral area with irre-

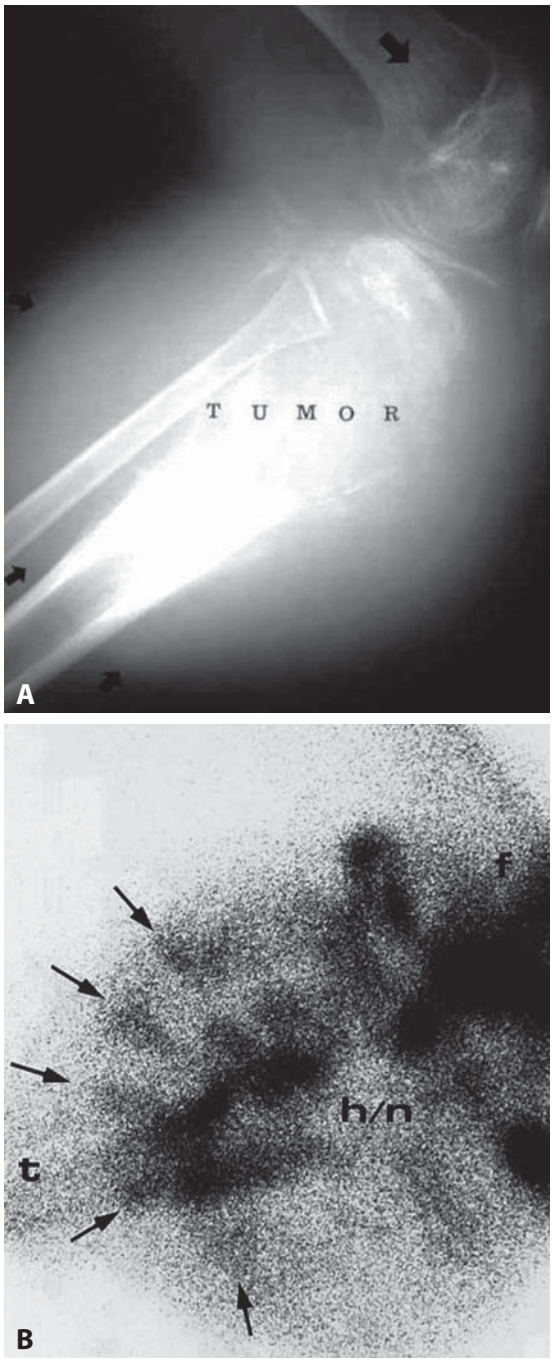

Fig. 17.41A, B Combined sclerotic and lytic osteosarcoma. **A** Lateral radiograph of the right proximal tibia in a 15-year-old boy shows a bizarre expansive tumor with sclerosis and lysis and soft-tissue invasion (*arrows*). **B** Lateral pinhole scintigraph reveals irregular areas of intense uptake mixed with photon defects (*arrows*) (*h/n* area of hemorrhage and necrosis as evidenced by MRI)

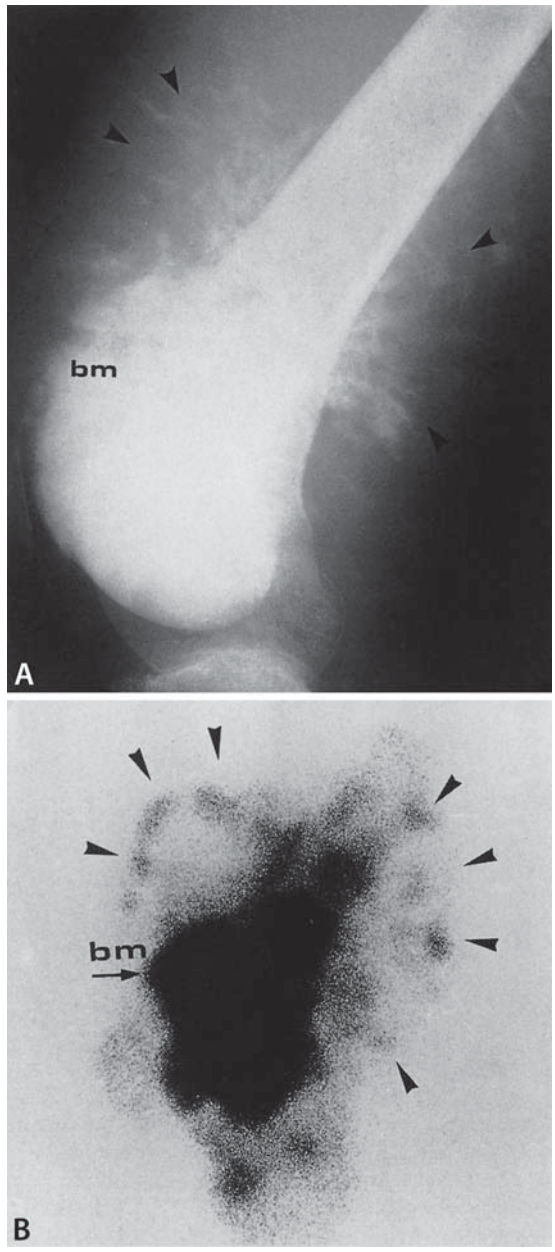

Fig. 17.42A, B Scintigraphic manifestation of the "sunburst" sign in osteogenic sarcoma. **A** Lateral radiograph of the right distal femur in a 21-year-old young man shows extensive neoplastic ossifications radiating into the muscles from a large sclerotic bone mass in the distal femur (*bm*). **B** Medial pinhole scan reveals bizarre linear and mottled tracer uptake radiating into the muscles (*arrowheads*) from the large tumor with extremely intense uptake in the distal femur (*bm*)

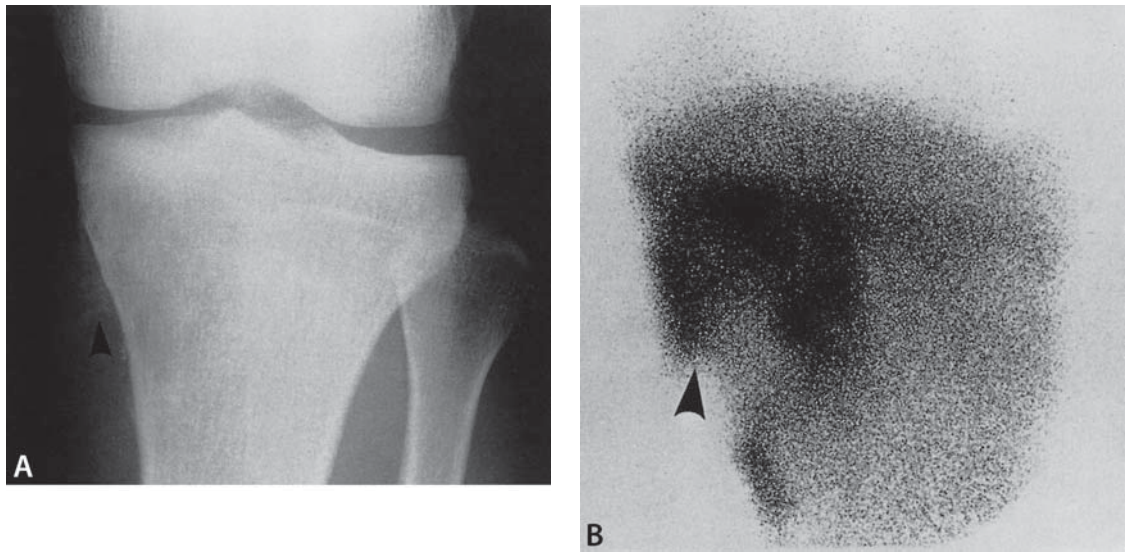

Fig. 17.43A, B Scintigraphic Codman's angle in osteogenic sarcoma. **A** Anteroposterior radiograph of the left knee in a 19-year-old young man reveals the classic, triangular periosteal elevation in the medial proximal tibial metaphysis (*arrowhead*) and osteolysis. **B** Anterior pinhole scan shows acutely angled, elevated periosteal uptake (*arrowhead*) and diffusely increased uptake in and around the destroyed bone

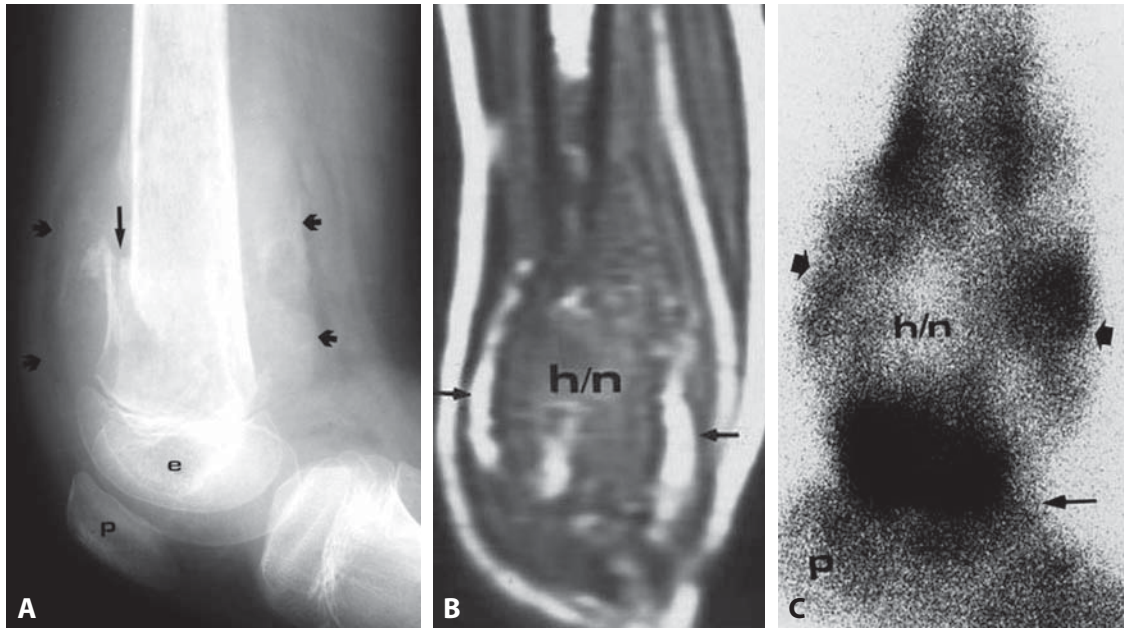

Fig. 17.44A–C Radiographic-MRI-scintigraphic correlation of osteosarcoma complicated with fracture. **A** Lateral radiograph of the left distal femur in a 13-year-old boy shows a mixture of sclerosis and lysis with soft-tissue invasion and tumefaction (*small arrows*). Note fracture line with dislocated fragments (*large arrow*) (*e* epiphysis, *p* patella). **B** Coronal T1-weighted MRI shows mixed signals of hemorrhage and necrosis within the main tumor (*h/n*). Rind-like bright and dark signals, respectively, denote fascial fat and ballooned cortex (*arrows*). **C** Anterior pinhole scan reveals a mixture of increased tracer uptake and photon defects in the main tumor (*h/n*) and surrounding nebulous uptake in expansive osteosarcoma (*small arrows*) (*large arrow* intense physeal and epiphyseal tracer uptake, *P* patella)

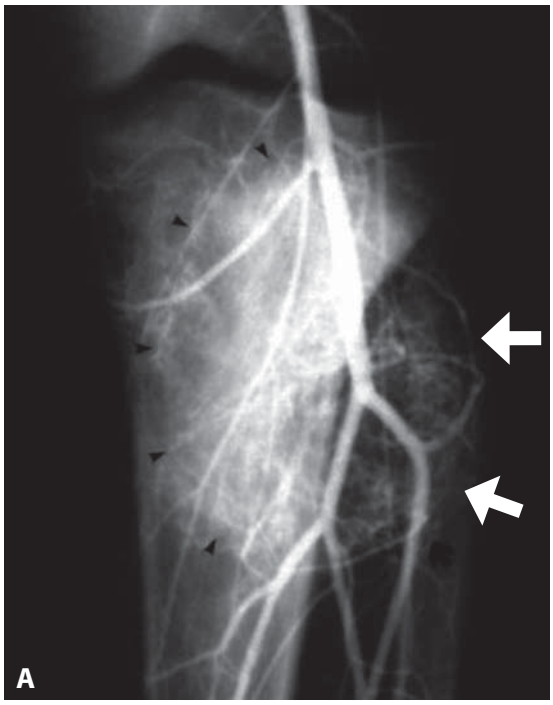

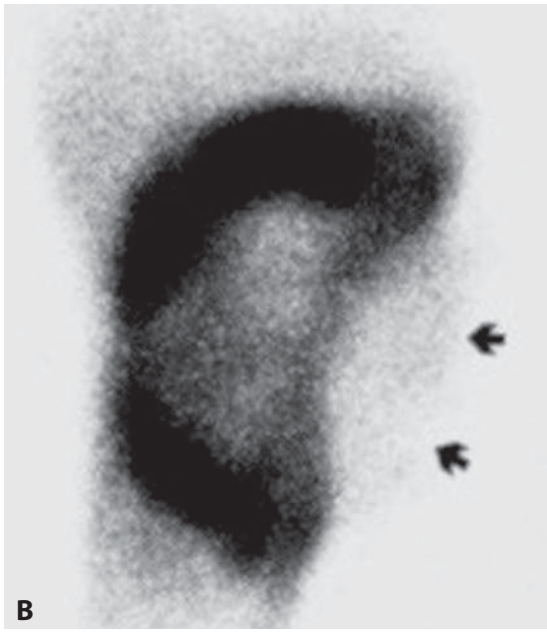

Fig. 17.45A, B Contrast angiography and pinhole scintigraphy in osteosarcoma. **A** Contrast arteriogram of the left proximal tibia with sclerotic tumor and soft-tissue invasion shows a fine meshwork of tumor vessels within the main tumor (*arrows*) and periphery (*arrowheads*). **B** Anterior pinhole scintigraph reveals subtle tracer uptake in the main tumor (*arrows*) and prominent reactive uptake in the periphery. The faintness of tumor uptake is presumably due to necrosis and neovascularization and prominent peripheral uptake due to reactive bone and neoplastic osteogenesis

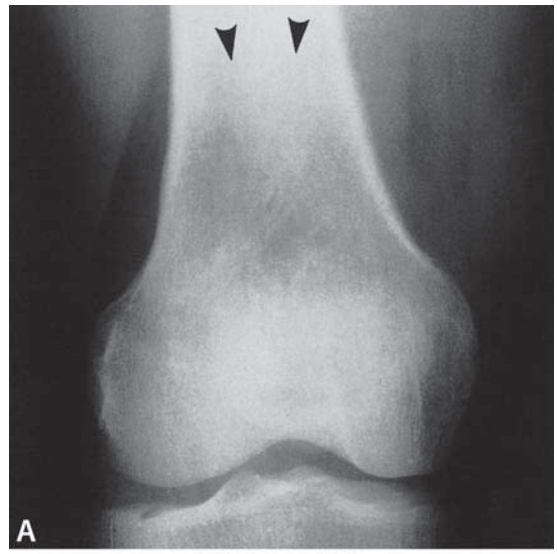

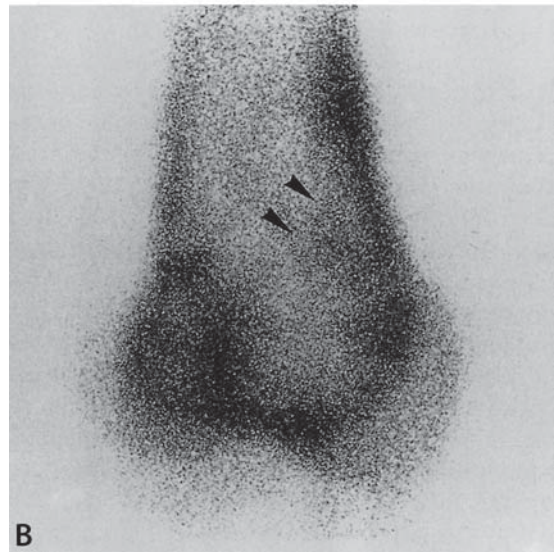

Fig. 17.46A, B Lucent and photopenic presentation of telangiectatic subtype of osteogenic sarcoma. **A** Anteroposterior radiograph of the right distal femur in a 33-year-old man reveals lysis with effaced trabeculae in the distal metaphysis (*arrowheads*). **B** Anterior pinhole scintigraph shows a large, well-demarcated, photopenic defect surrounded by a "hot" border. Mottled intratumoral tracer uptake is due to pathological fracture (*arrowheads*), which was proven by CT scan (not shown here)

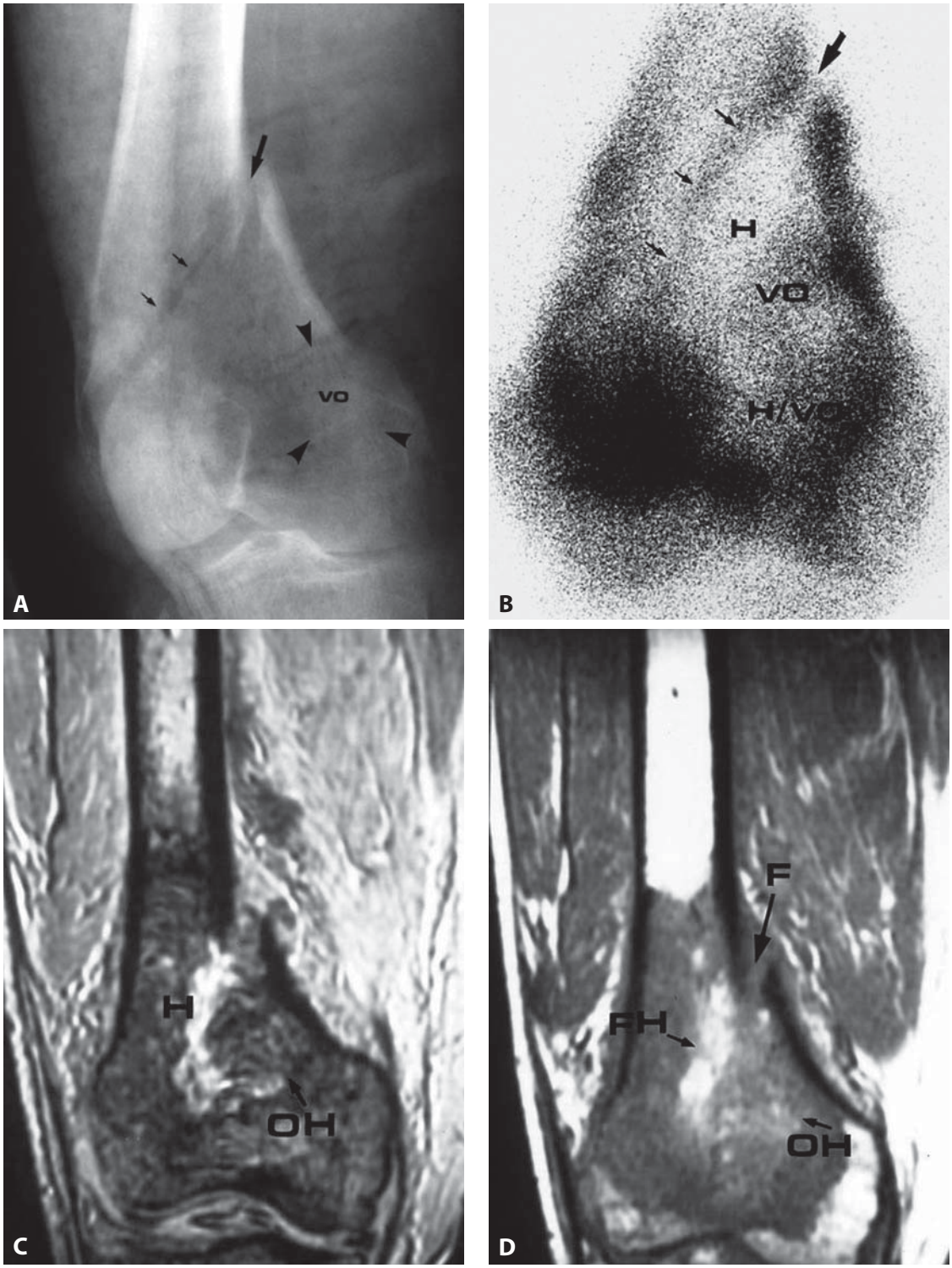

Fig. 17.47A–D Telangiectatic osteosarcoma. **A** Anteroposterior radiograph of the right distal femur in a 33-year-old male shows a large lytic lesion with fracture (*arrows*) and small island of visible osteoid (*VO*). **B** Anterior pinhole scintigraph reveals concordant photopenia in osteolysis and minimal uptake in visible osteoid (*VO*) (*H* hemorrhage, *H/VO* hemorrhage/osteoid). **C** Fat-suppression MRI demonstrates hemorrhage in the fracture site (*H*) and old hemorrhage (*OH*). **D** T1-weighted MRI reveals fresh hemorrhage (*FH*) in the fracture (*F*) and old intratumoral hemorrhage (*OH*)

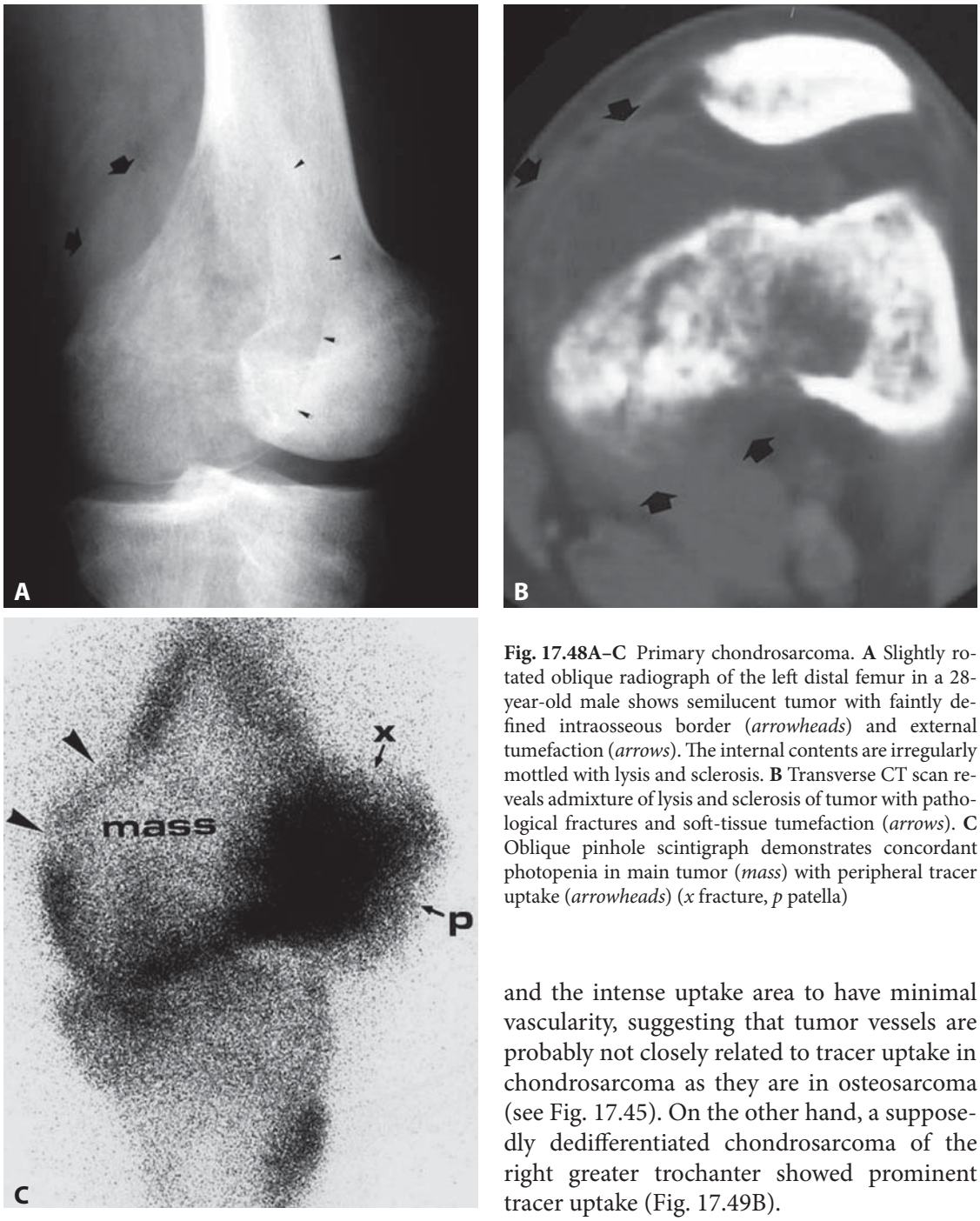

Fig. 17.48A–C Primary chondrosarcoma. **A** Slightly rotated oblique radiograph of the left distal femur in a 28-year-old male shows semilucent tumor with faintly defined intraosseous border (*arrowheads*) and external tumefaction (*arrows*). The internal contents are irregularly mottled with lysis and sclerosis. **B** Transverse CT scan reveals admixture of lysis and sclerosis of tumor with pathological fractures and soft-tissue tumefaction (*arrows*). **C** Oblique pinhole scintigraph demonstrates concordant photopenia in main tumor (*mass*) with peripheral tracer uptake (*arrowheads*) (*x* fracture, *p* patella)

gular uptake to correspond to semilucent tumor. CT discloses a hyperdense element of mineralized bone and hypodense elements of cartilage and necrosis (Fig. 17.48B). Contrast angiography in this case showed the low uptake area to contain numerous tumor vessels and the intense uptake area to have minimal vascularity, suggesting that tumor vessels are probably not closely related to tracer uptake in chondrosarcoma as they are in osteosarcoma (see Fig. 17.45). On the other hand, a supposedly dedifferentiated chondrosarcoma of the right greater trochanter showed prominent tracer uptake (Fig. 17.49B).

17.2.3 Ewing's Sarcoma

Ewing's sarcoma is a highly malignant tumor, consisting of small round cells of unknown tissue origin. The tumor predominantly affects children and young adults, with a strong predilection for males. No bones are immune, but the long bones of the lower extremity and pel-

vic bones are affected in 60% of patients. Not infrequently the spine and ribs are involved. The tumor tends to metastasize early to the bone and lung.

Radiographic features vary between patients, manifesting any of osteosclerosis, osteolysis, and mixed change and any combination of these. Bone condensation in the sclerotic type is intense, often with periosteal lamellation (Fig. 17.50A). The lamellation may be either single or multiple layered, giving rise to the "onion skin" sign if multilayering. Codman's triangle may be seen as in other malignant bone tumors. Osteolysis within the marrow space is permeative and poorly demarcated (Fig. 17.51A) and the mixed form shows a mixture of lysis and sclerosis (Fig. 17.51A). Occasional lesions of the irregular bones such as the pelvis and vertebrae may show ballooning (Fig. 17.52A). The ballooning may represent rapidly expanding osteolysis or "pseudoaneurysmal bone cyst".

Scintigraphic features also vary according to the tumor type. Basically, the osteosclerotic type accumulates tracer intensely (Fig. 17.50B) while the osteolytic type accumulates less tracer (Fig. 17.51B). Understandably, the tracer uptake in the mixed variant is irregular and heterogeneous (Fig. 17.51B). Nuclear angiography is ideal for detecting aneurysmal cystic change of Ewing's sarcoma or tumor hypervascularity (Fig. 17.52B). Bone scintigraphy has the additional diagnostic advantage of discovering regional and distant metastases in Ewing's sarcoma as in other malignancies.

17.2.4 Fibrosarcoma

Malignant fibrous tumors of bone include the primary and secondary fibrosarcomas and malignant fibrous histiocytoma that has been established as a distinctly independent entity. The primary form may originate from the medullary space, periosteums, or soft tissues, with secondary extension to bone. Pathologically, the tumor cells are spindle shaped, producing no bone, and the differentiation varies from low to highly malignant. This is a tumor of middle age, without gender predilection.

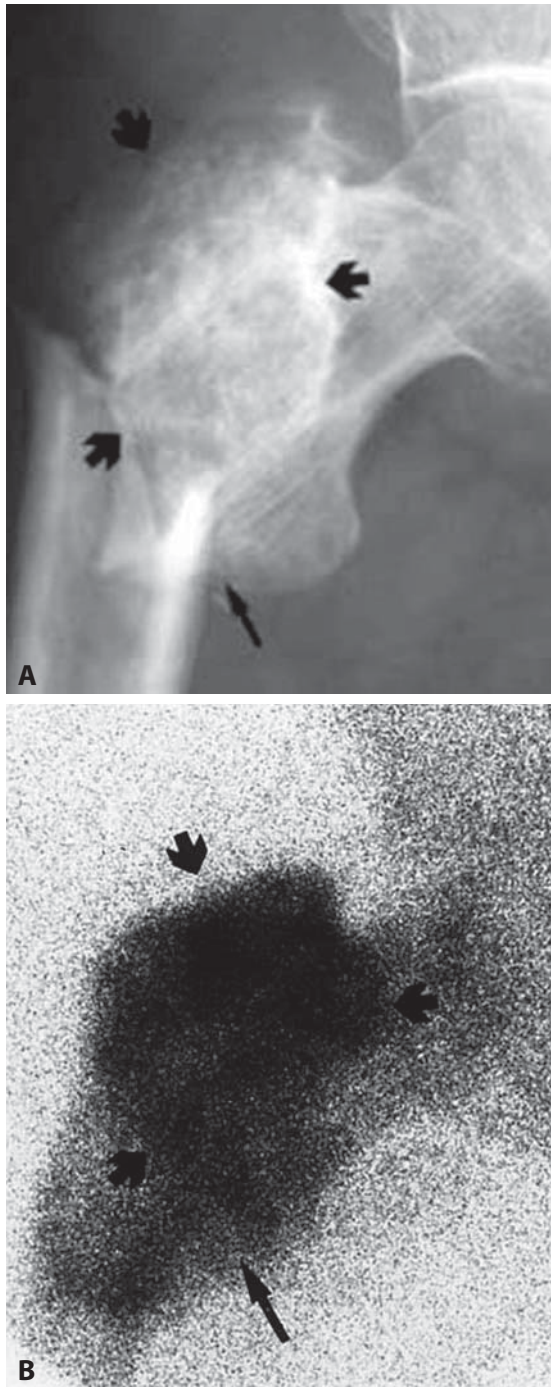

Fig. 17.49A, B Dedifferentiated chondrosarcoma. **A** Anteroposterior radiograph of the right proximal femur in a 67-year-old female shows an irregular bone tumor in the greater trochanter (*small arrows*). The trochanteric crest has melted and the subtrochanteric region shows fracture (*long arrow*). **B** Anterior pinhole scintigraph reveals square intense tracer uptake in the greater trochanteric tumor (*arrows*) with a sharp lower border formed by the fracture (*large arrow*)

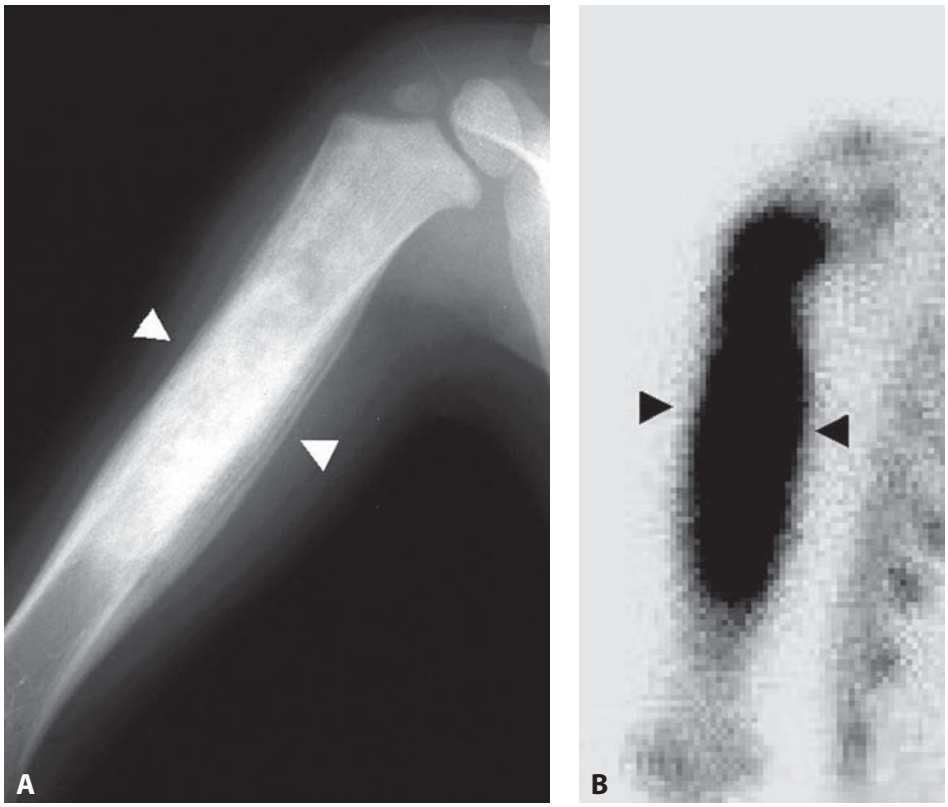

Fig. 17.50A, B Ewing's sarcoma. **A** Near lateral radiograph of the right humerus in a 5-year-old male child shows osteosclerosis with periosteal thickening (*arrowheads*). **B** Planar scintigraph reveals intense tracer uptake in sclerosing tumor (*arrowheads*)

Slightly more than 50% of cases are seen in the bones about the knee and in the humerus. Secondary fibrosarcomas are the result of malignant transformation of benign bone disorders such as Paget's bones, medullary bone infarcts, or irradiated bones.

The characteristic radiographic manifestation of fibrosarcomas of bone is large geographic bone destruction, the contour of which is poorly defined because reactive sclerosis is minimal or absent (Fig. 17.53A). Osteolysis in this tumor is permeative, and accordingly the border shows a moth-eaten appearance. Periosteal invasion is uncommon, but it may cause spiculation, lamellation, or even the Codman's triangle sign when present. Malignant fibrous histiocytoma also involves bone, forming a single large defect or multiple small defects located centrally or eccentrically in long-bone diaphyses. In occasional cases small lytic areas may coalesce (Capanna et al. 1984), and the tumor becomes expansive showing a bubbly appearance due to septum-like formations (Fig. 17.54).

Pinhole scintigraphy of primary fibrosarcoma shows a large ill-defined photon defect surrounded by an irregular rim of watershed or extended uptake (Fig. 17.53B). The photopenic manifestation of this tumor may be explained on the basis of that fibrous matrix is basically not osteogenic. The nonosteogeny of tumor along with the absence of significant reactive osteosclerosis may be a likely reason for poor scintigraphic demarcation. Infiltrating variants may present as patchy areas of intense tracer uptake intermingled with irregular photopenic areas. The intramedullary spread can be diagnosed by bone scan. The basic scan manifestations of malignant fibrous histiocytoma with bone destruction are essentially the same as those of osteolytic type primary fibrosarcoma

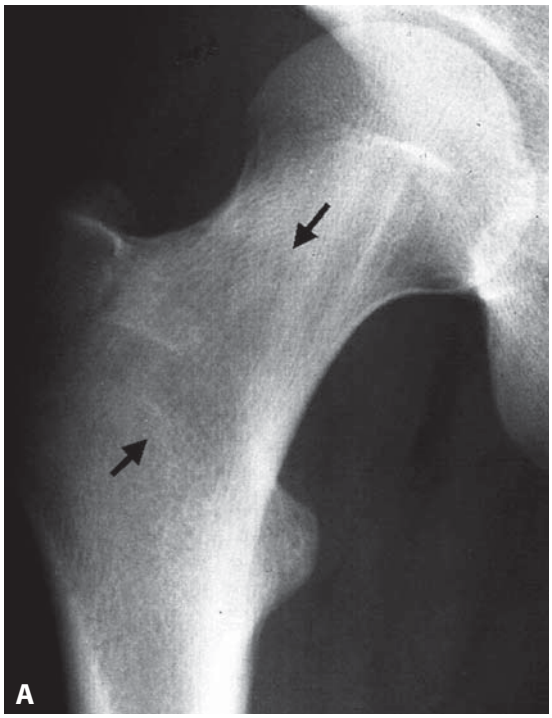

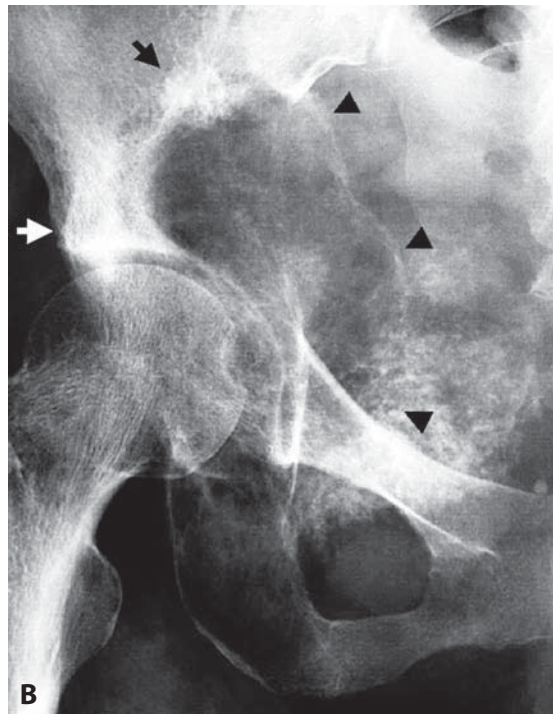

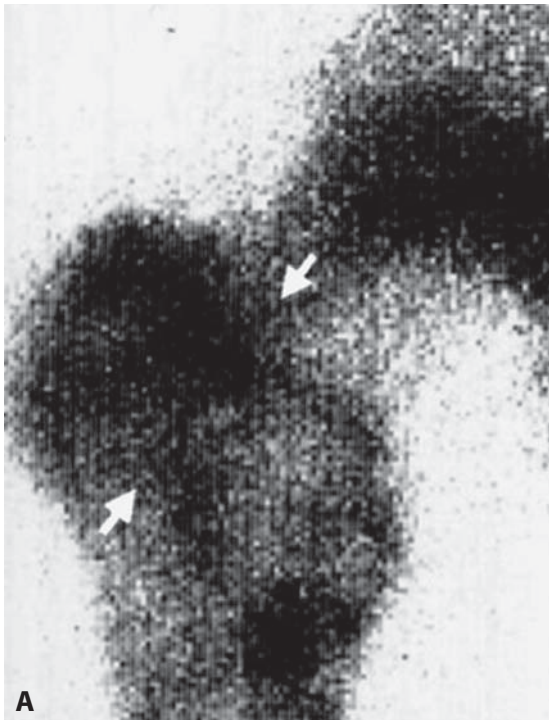

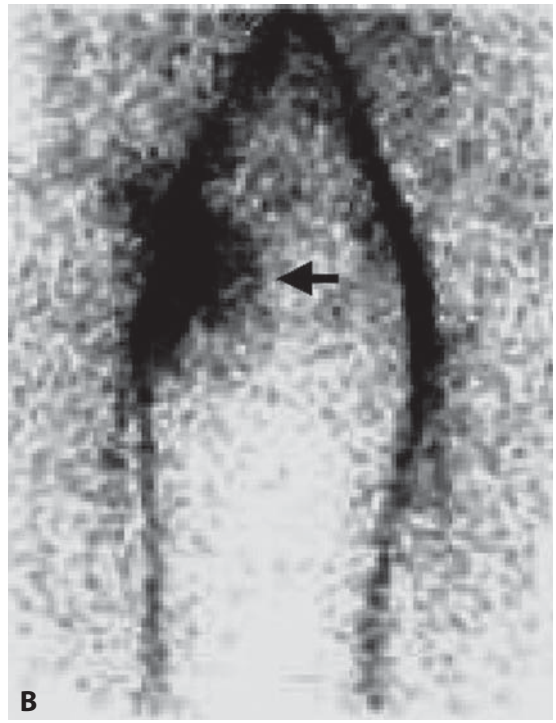

Fig. 17.51A, B Ewing's sarcoma. **A** Anteroposterior radiograph of the right proximal femur in a 17-year-old male shows a large ill-defined permeative osteolysis in the lower neck (*open arrow*) and sclerotic areas in the upper neck and trochanters (*arrows*). **B** Magnified anterior planar scintigraph reveals a concordant photon defect (*open arrow*) and patchy uptake (*solid arrows*)

Fig. 17.52A, B Ewing's sarcoma in the iliac bone. **A** Anteroposterior radiograph of the right pelvis in an adult shows a large irregular tumor with bone formation (*arrows*) and central ballooning osteolysis with rind (*arrowheads*). **B** Nuclear angiogram reveals prominent blood pool at the center of the tumor that corresponds to expansive lysis (*arrow*)

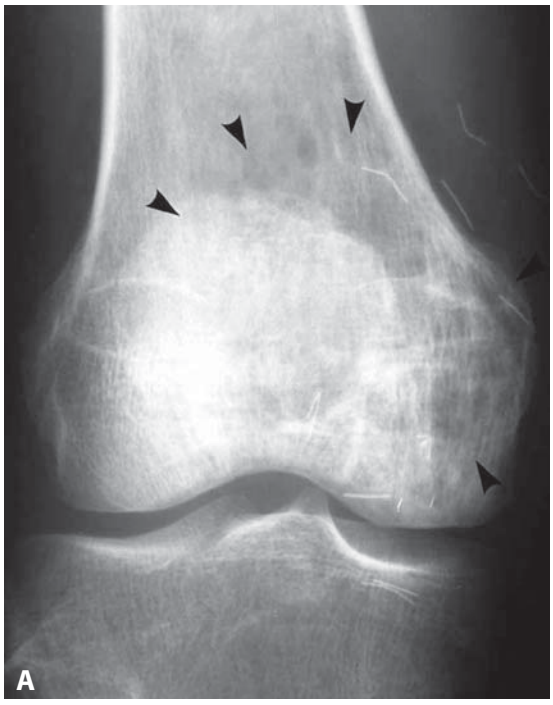

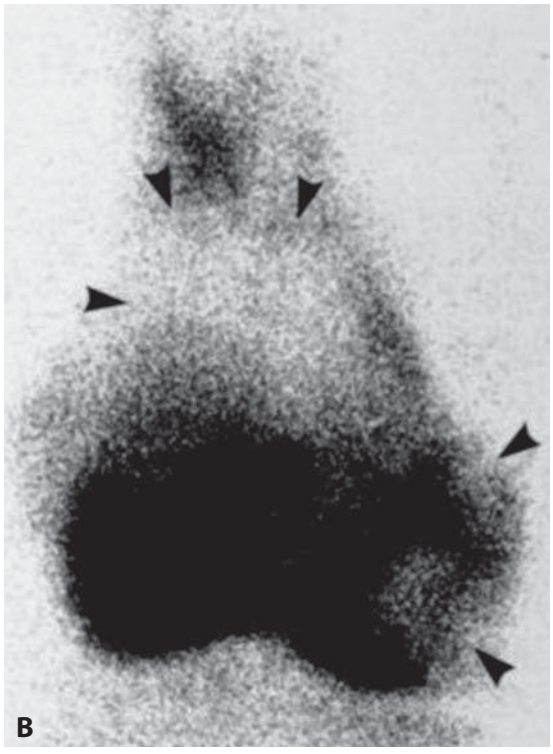

Fig. 17.53A, B Bone destruction in fibrosarcoma. **A** Anteroposterior radiograph of the right distal femur in a 36-year-old female shows large geographic bone destruction (*arrowheads*). **B** Anterior pinhole scan reveals a large photon defect in the main tumor (*upper three arrowheads*) with marginal tracer uptake in the reactive zone (*lower pair of arrowheads*)

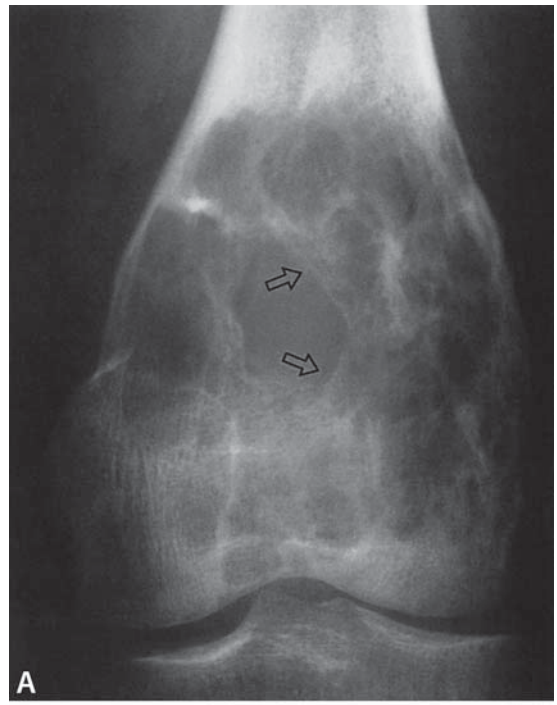

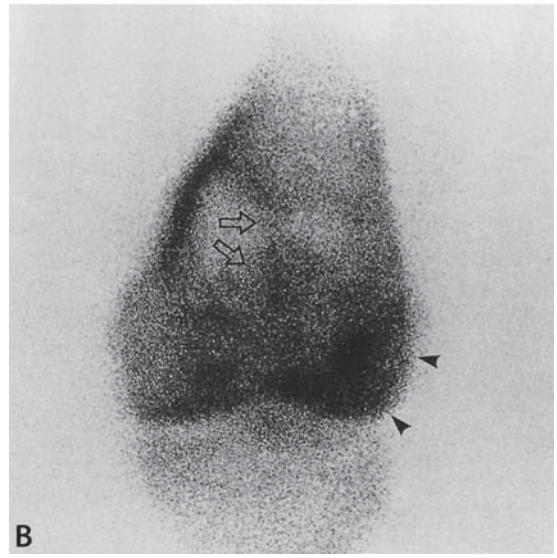

Fig. 17.54A, B Malignant fibrous histiocytoma. **A** Anteroposterior radiograph of the left distal femur in a 34-year-old man shows a large, expansile, lytic tumor involving centrally the metaphysis with multiple, irregular septations (*open arrows*). The cortices appear expanded, thinned, and scalloped but not ruptured. **B** Anterior pinhole scintigraph shows a large, expansile, photopenic mass with irregular septation (*open arrows*). The regional cortex shows increased tracer uptake medially where it is thinned and bulged. Patchy tracer uptake in the lateral condyle may represent extended uptake (*arrowheads*)

except for the expansiveness and multicystic appearance with septation (Fig. 17.54B). The latter finding has a strong resemblance to that in metastatic follicular thyroid carcinoma with septation (Fig. 17.21A).

17.2.5 Myeloma (Plasma Cell Myeloma)

Myeloma is characterized by neoplastic proliferation of abnormal plasma cells in the red bone marrow. Multiple myeloma is not a rare disease, accounting for 1% of all malignant tumors. This is primarily a disease of the elderly, but the range of incidence is wide, between 25% and 80%. One most recent population study performed in the South Thames area of the UK has shown the age-standardized rate of multiple myeloma to be 3.29 per 100,000 with the median age of those affected being 73 years (Phekoo et al. 2004). When first seen in the clinic the lesions are either multiple (more than 50%), generalized (15%), or solitary (25%). Solitary myeloma may eventually develop into multiple or generalized lesions. The axial skeleton including the skull, spine, pelvis, sternum, and shoulder bones, as well as the limb bones, are involved (Fig. 17.55). Symptoms include malaise, fatigability, skeletal pain, especially in the spine and rib cage, and bone deformity. The solitary form may well pass unnoticed and the generalized form may be disguised as simple osteoporosis. In either form, the first event that brings the patient to hospital may be pathological fractures. Protein electrophoresis may reveal an increase in the globulin fraction and immunoelectrophoresis can identify different types of globulin such as IgG, IgA, and rarely IgM.

The radiographic features include multiple or diffusely spread bone destructive changes or solitary lysis. Characteristically, lesions in the skull are well-defined and discrete, and give rise to a "punched-out" or "bubbly" appearance (Fig. 17.56). If generalized, however, the individual lesions imperceptibly blend into advanced senile osteoporosis (Fig. 17.57). Myelomatous bones are fragile and prone to pathological fracture, but the fractures are radiographically undetectable in most cases because of severe osteoporosis. An interesting radiographic sign of multiple myeloma is endosteal scalloping caused by the physical effect of proliferative plasma cells that are expansive (Fig. 17.58). With gradual increase in volume, myelomas in small bones such as the sternum and ribs may become expansive, eventually breaking the cortex (Fig. 17.59A). On occasion, such lesions are permeant and expansive, and induce a periosteal reaction (Fig. 17.60).

^{99m}Tc-MDP bone scintigraphy was once held to be of limited value since the plasma cells of myeloma do not accumulate tracer regar-

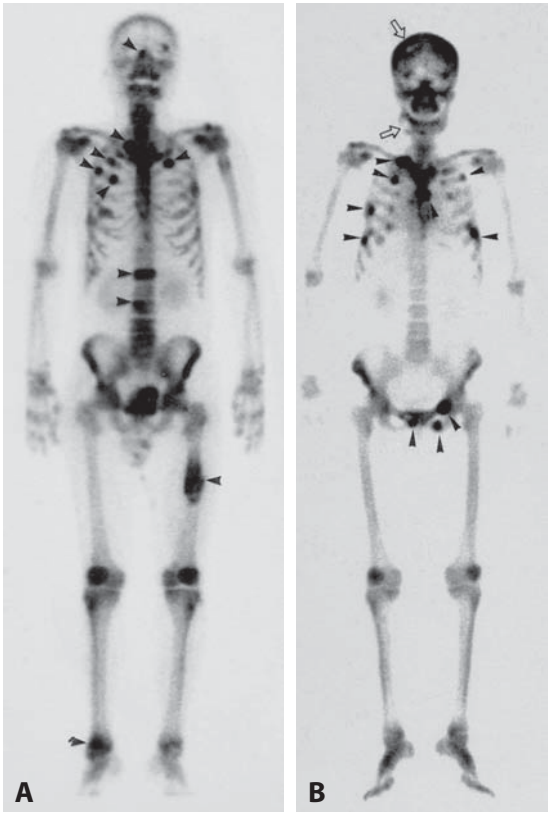

Fig. 17.55A, B Varied axial skeletal involvement in multiple myeloma in two different patients. **A** Anterior whole-body scintigraph in a 58-year-old man with multiple myeloma shows widely scattered spotty uptake in the nasal bone, ribs, spine, right femur, and left distal tibia (*arrowheads*). **B** Anterior whole-body scintigraph in a 56-year-old woman with multiple myeloma reveals involvement of the cranium, ribs, sternum, and pelvis (*arrowheads*). *Open arrow* in the skull denotes photopenic manifestation

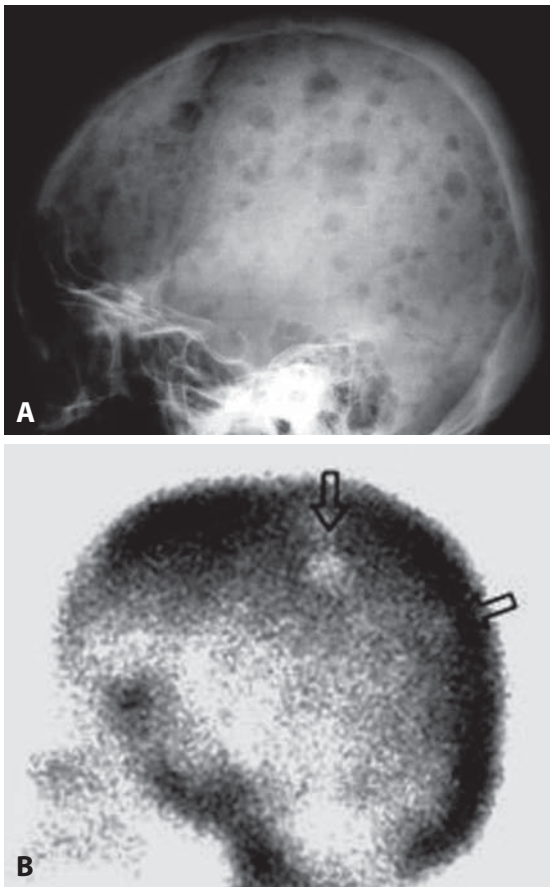

Fig. 17.56A, B Punched-out lysis in multiple myeloma. **A** Lateral radiograph of the skull in a 60-year-old female shows classic multiple punched out lesions. **B** Lateral pinhole scintigraph reveals many roundish photopenic areas (*open arrows*). Note that only large lesions are visualized. The planar scan did not reveal these lesions

dless of the disease type (Wahner et al. 1980; Waxman et al. 1981). However, the extended application of whole-body and pinhole scans to the diagnosis of myelomas have indicated that bone scintigraphy is not only useful but also even indispensable in certain clinical settings. The first and most important situation is probably pathological fractures that are common in myelomatosis. Radiographic diagnosis of such fractures is notably difficult and even harder when advanced myelomatosis is superimposed on severe porosis (Fig. 17.57). Fortunately, fractures intensely accumulate

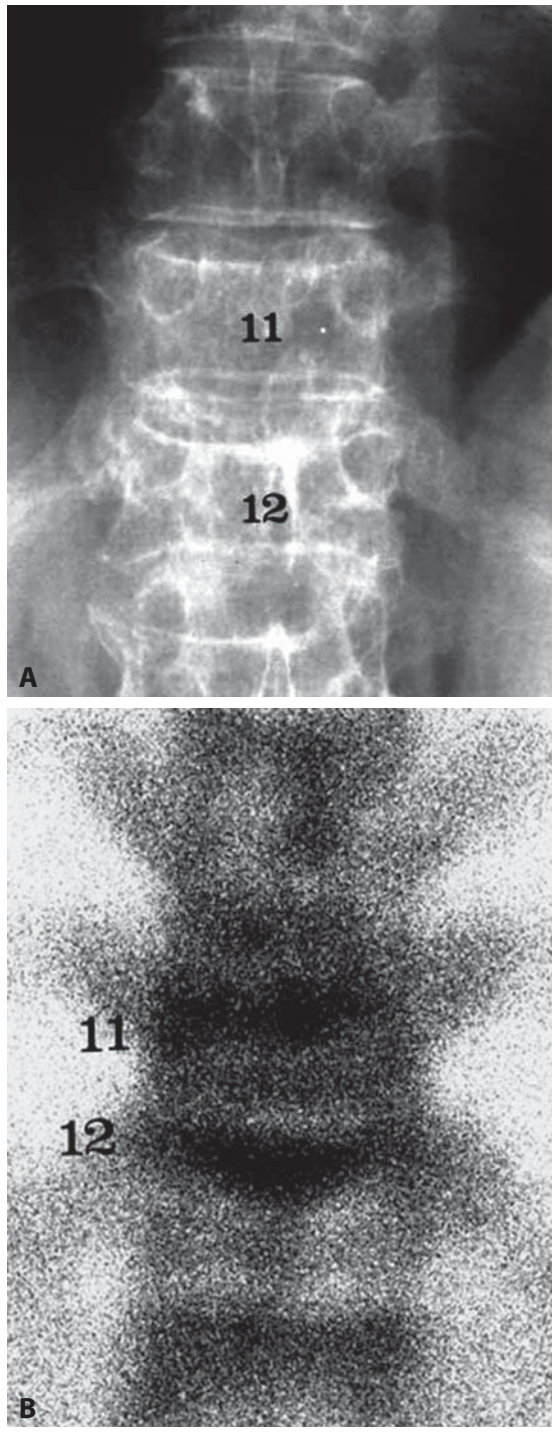

Fig. 17.57A, B Myelomatosis in porotic skeleton. **A** Anteroposterior radiograph of the lower thoracic spine with severe porosis shows blending of myeloma with porosis concealing fractures. **B** Posterior pinhole scan reveals diffusely increased bone uptake with prominent uptake in T11 and T12 upper endplates denoting compression fractures

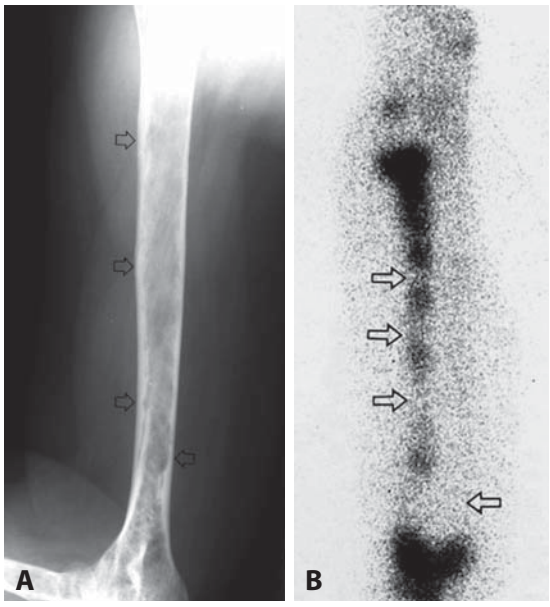

Fig. 17.58A, B Bone marrow scan of myelomatosis with endosteal scalloping. **A** Lateral radiograph of the right humerus in a 58-year-old female shows endosteal undulation (*open arrows*). **B** ^{99m}Tc-tin colloid scan reveals spotty photon defects due to myelomas that cause endosteal scalloping (*open arrows*)

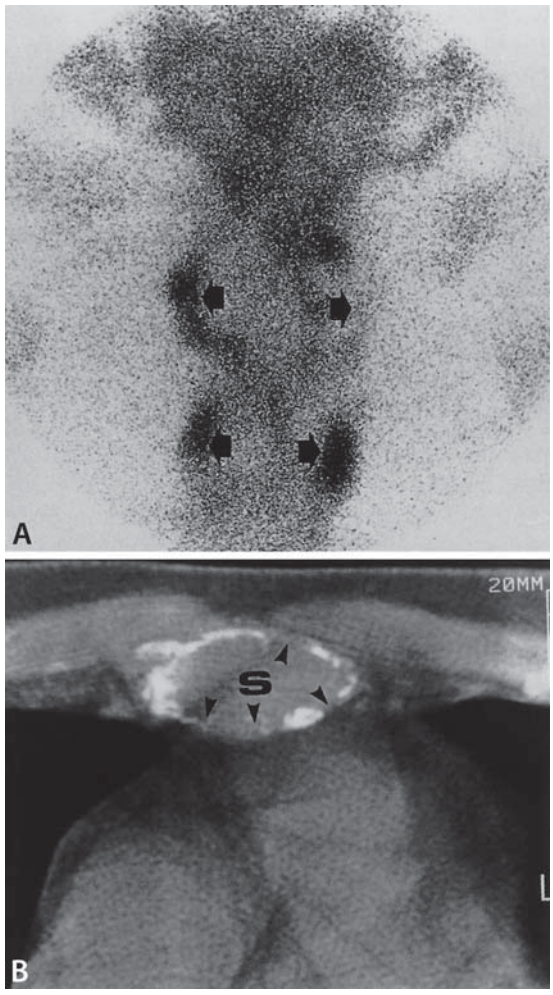

Fig. 17.59A, B Solitary plasmacytoma in the sternum. **A** Anterior pinhole scintigraph of the upper sternum shows expansile photopenic lesions in the upper two segments of the sternal body with bulging cortices that concentrate tracer intensely (*arrows*). The tracer uptake in the left lateral aspect of the uppermost lesion is decreased due to rupture. **B** Transverse CT scan of the first sternal segment(s) reveals broken egg-shell-like cortical rupture and expansile marrow (*arrowheads*)

tracer regardless of the porosis in host bones. The second advantageous situation is solitary myelomas in the long tubular bones and small bones such as the ribs and sternum (Fig. 17.59A). A sizeable lesion may be missed radiographically in these bones, but pinhole scintigraphy can reveal signs that strongly suggest or indicate the diagnosis. Myeloma in the sternum presents as an expansive photon defect visualized as broken eggshell-like uptake in the ruptured cortex (Fig. 17.59A). CT scan is an excellent alternative (Fig. 17.59B). Pinhole scintigraphy is far more informative in studying solitary myeloma in the long bones because it can distinguish permeative bone invasion from simple expansion (Fig. 17.60B). The tracer uptake in simple expansion or scalloping is negligible or very subtle at most, but that in actively invaded or ruptured cortex is obvious. The third advantage is scintigraphic detection of radiographically invisible myelomas, but this is rare.

On the other hand, ^{99m}Tc-tin colloid bone marrow scintigraphy is a useful adjunct to the diagnosis of myelomas (Feggi et al. 1988), and the myelomas, metastases, lymphoma, and leukemia that are rooted in the red bone marrow (Lentle et al. 1987). Bone marrow scanning using radiocolloids relies on the phagocytosis of reticuloendothelial cells. Accordingly, once bone marrow has been replaced with myeloma

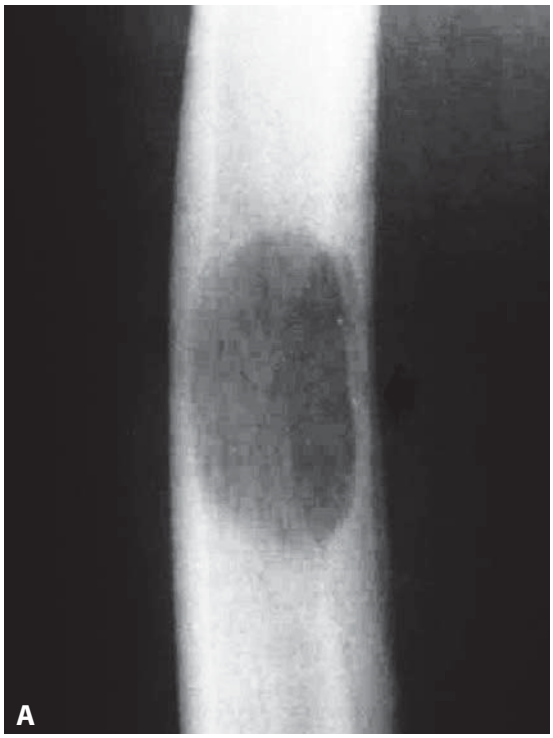

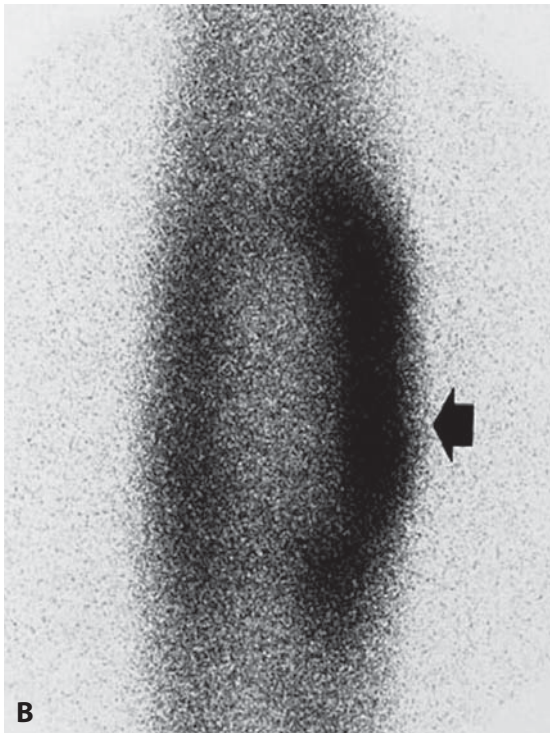

Fig. 17.60A, B Expansive myeloma with cortical invasion. **A** Anteroposterior radiograph of the right femur in a 62-year-old male shows a large ovoid lytic lesion in the marrow space with the invasion of local cortex and periosteum (*arrow*). **B** Anterior pinhole scintigraph reveals intense tracer uptake in the cortex (*arrow*)

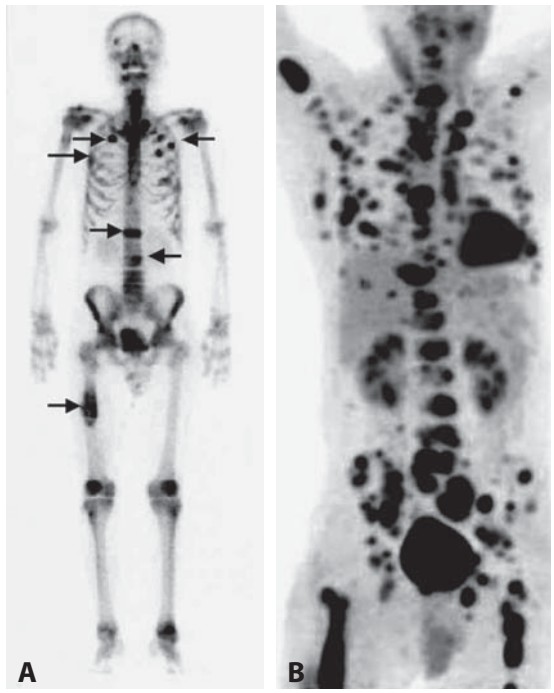

Fig. 17.61A, B ^{99m}Tc-MDP bone scintigraph and PET in multiple myeloma. **A** Anterior whole-body scan shows multiple spotty and mottled tracer uptake involving the skull, ribs, spine and right femur (*arrows*). **B** ^{18}F-FDG PET demonstrates multiple bone uptake. PET is far more revealing because myeloma cells directly accumulate FDG

cells they become photopenic on colloid scintigraphs (Fig. 17.58). ^{18}F-FDG PET is a useful adjunct to the diagnosis of multiple myeloma. The sensitivity and specificity in detecting multiple myeloma lesions have been reported to be 85% and 92%, respectively (Bredella et al. 2005). The superiority of ^{18}F-FDG PET is based on the fact that ^{18}F-FDG PET can directly visualize denatured plasma cells that avidly consume glucose while ^{99m}Tc-MDP bone scintigraphy can image indirect bone change that occurs secondarily (Fig. 17.61). In passing, it is worth mentioning that pinhole scintigraphy can conveniently and reliably evaluate and archive the results of adjuvant chemotherapy, external irradiation, or bone marrow replacement (Fig. 17.62).

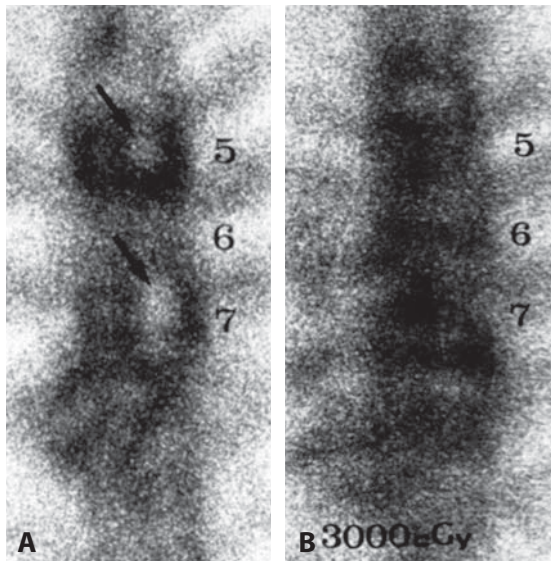

Fig. 17.62A, B Effect of irradiation effect on myelomas. **A** Preirradiation pinhole scan of the midthoracic spine in a 56-year-old female reveals tracer uptake with photon defects in the T5–T7 vertebrae. **B** Scan after irradiation (3000 cGy) reveals decreased tracer uptake with cure of the defects

17.3 Leukemias and Lymphomas

Leukemias and lymphomas respectively comprise myeloproliferative neoplasms and lymphoreticular tumors of the reticuloendothelial system. Clinically, leukemias are classified into the acute form and the chronic form. Acute leukemia affects both children and adults and chronic leukemia middle-aged adults. Lymphomas arise from the lymphocytic cells, reticulum cells, or primitive precursor cells, and they are pathologically classified as non-Hodgkin's lymphoma, Hodgkin's lymphoma, Burkitt's lymphoma, and mycosis fungoides.

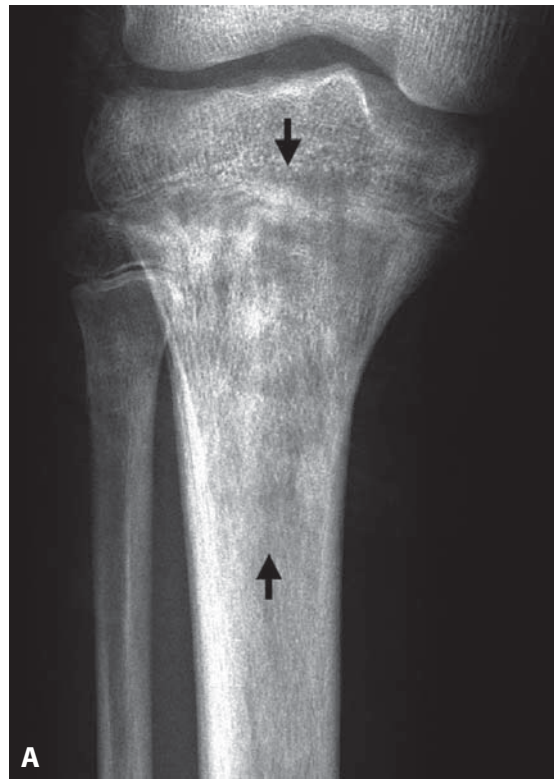

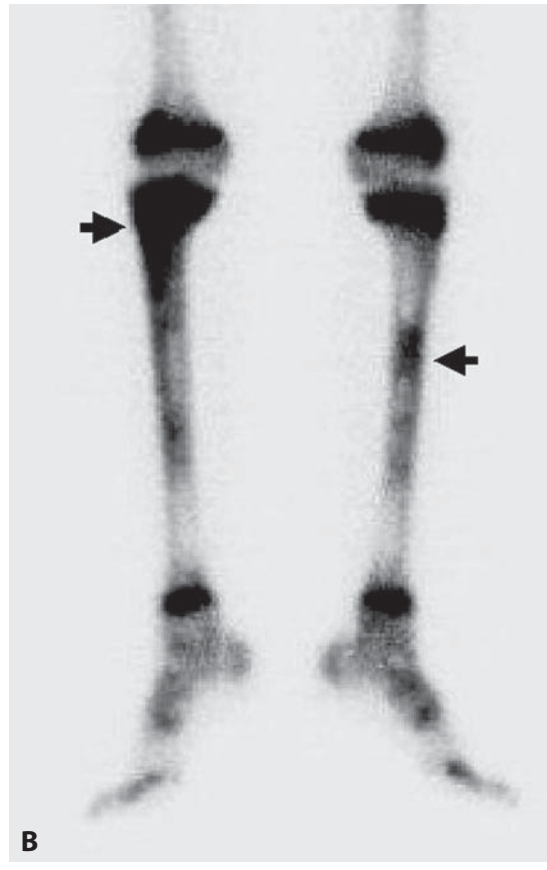

Fig. 17.63A, B Acute lymphocytic leukemia. **A** Anteroposterior radiograph of the right proximal tibia in a 16-year-old female shows a mixture of sclerosis and lysis due to leukemia in the metadiaphysis (*arrows*). **B** Planar bone scintigraph reveals intense tracer uptake in the right proximal tibial metadiaphysis and left tibial midshaft (*arrows*)

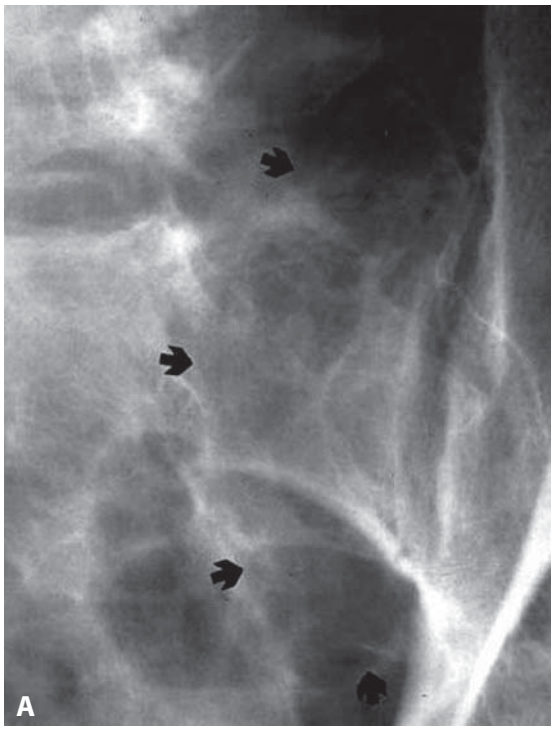

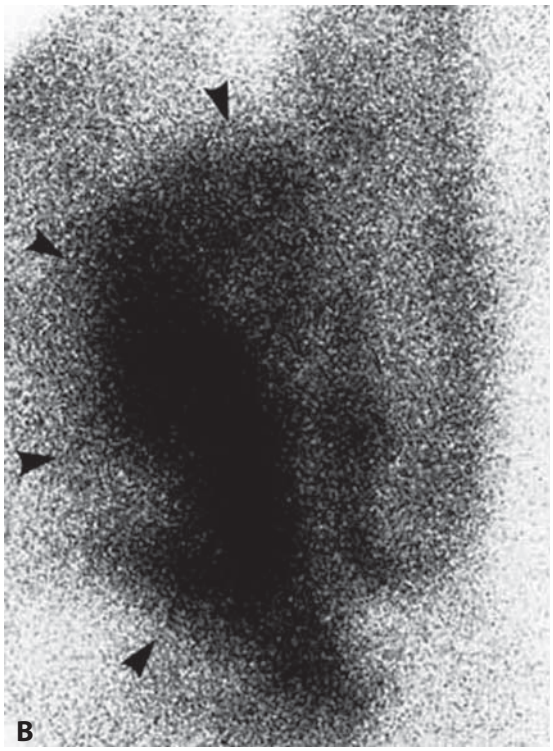

Fig. 17.64 Lymphoma in the sacrum. **A** Anteroposterior radiograph of the left half of the sacrum in a 47-year-old female shows a large geographic lysis delimited by the sacroiliac joint barrier (*arrows*). **B** Anterior pinhole scintigraph shows concordant tracer uptake (*arrowheads*)

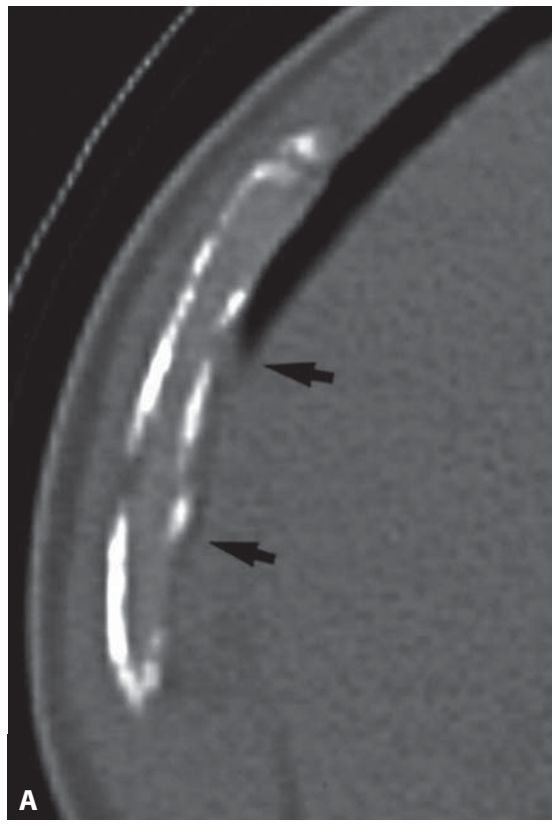

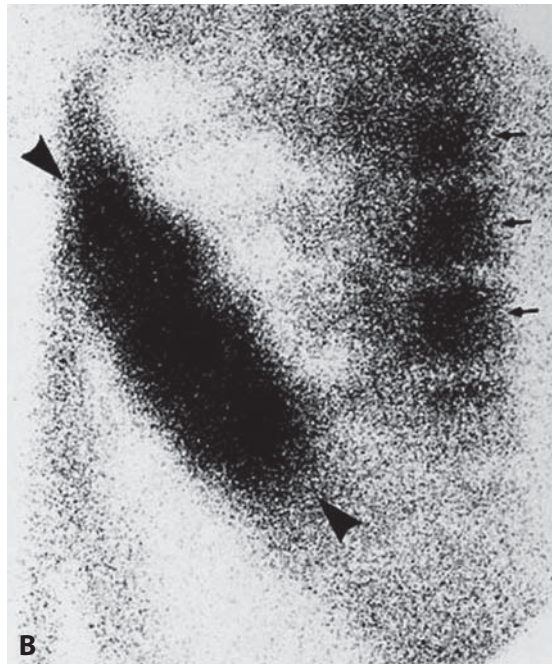

Fig. 17.65A, B Lymphoma in the rib. **A** Transverse CT of the right seventh rib in a 43-year-old male shows an expansive intramedullary lesion with cortical ruptures (*arrows*). **B** Pinhole scan reveals intense expansive tracer uptake (*arrowheads*). The uptake in the spine also represents lymphomatous involvement (*arrows*)

The radiographic changes of bone and bone marrow in acute leukemias are basically not dissimilar to those of multiple myeloma. Thus, radiographic features include diffuse osteopenia, irregular osteolysis and osteosclerosis, lucent metaphyseal band, and periosteal reaction (Fig. 17.63A). Chronic leukemia also manifests as osteopenia and occasional osteolysis that is discrete. On the other hand, lymphomas, both the non-Hodgkin's type and the Hodgkin's type, typically affect the axial bones including the skull, the facial bones, the spine, the pelvis, the ribs, and the femurs. The spread of lymphomas to bone occurs either directly from contiguous lymph nodes or through blood flow. Osteolysis is geographic in appearance with poorly defined borders in large flat or irregular bones such as the sacrum (Fig. 17.64A) or segmental with cortical rupture in small bones such as the ribs (Fig. 17.65A). Endosteal scalloping and periosteal or soft-tissue invasion may occasionally be seen as in myeloma.

^{99m}Tc-MDP bone scintigraphy of acute leukemia in children manifests as band-like uptake in the long bone metaphyses with small segmental uptake in the diaphyses (Fig. 17.63B). Generally, the scintigraphic features of lymphoma are similar to those of other osteolytic tumors (Fig. 17.64B). Tracer uptake becomes markedly intensified when the affected bone is fractured (Fig. 17.65B). Lymphocytic leukemia in adults characteristically accumulates tracer in scalloped endosteums of the long bones reflecting bone marrow involvement (Fig. 17.66).

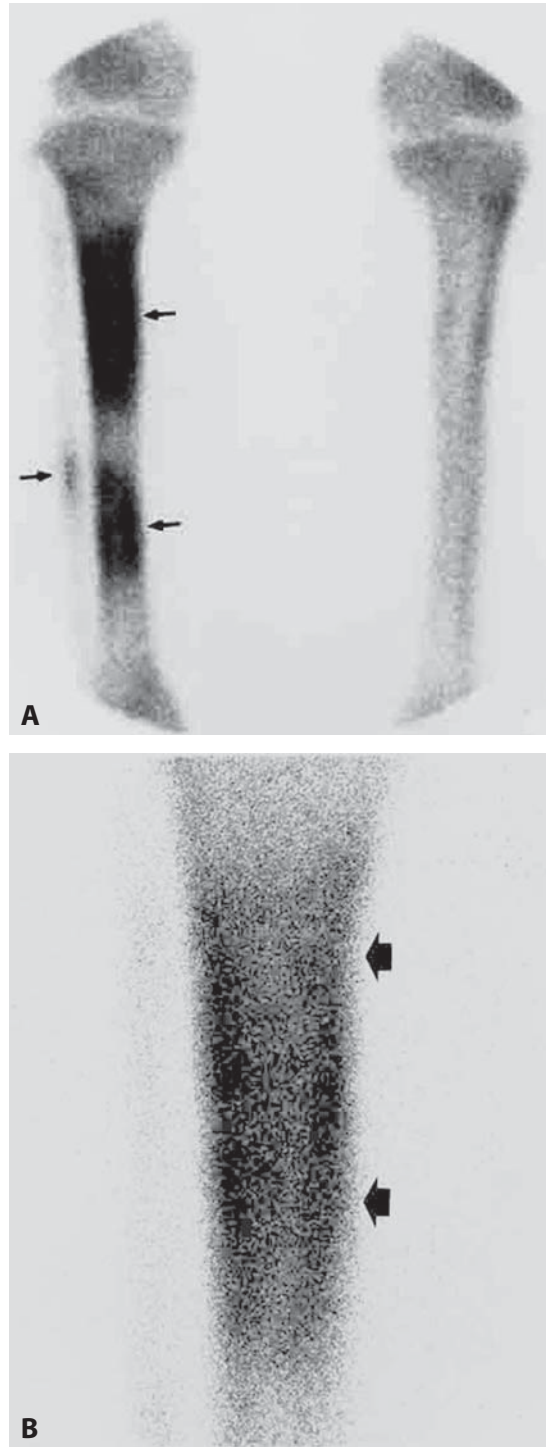

Fig. 17.66 Acute lymphocytic leukemia with endosteal involvement in an adult patient. A Anterior planar scintigraph of both legs in a 51-year-old female shows segmental tracer uptake in the upper and lower thirds of the right tibia (pair of arrows) and fibular mid-shaft (single arrow). B Anterior pinhole scintigraph localizes increased uptake to localize to endosteums (arrows)

17.4 Chordoma

Chordoma is a slow-growing, low-grade malignancy that arises from primitive notochordal mucoid intercellular material. The tumor is strongly inclined to involve both the caudal sacral region and the clivus near the sphenooccipital synchondrosis. The incidence ranges from 1% to 4% and is nearly twice as common

in men as in women, with the vast majority of cases occurring between the fourth and seventh decades of life. Sacrococcygeal lesions are more common in women than in men, whereas the spheno-occipital lesions have an equal sex distribution. Clinical manifestations relate to the location of the tumor. In the early stages the symptoms are mild and nonspecific. Sacrococcygeal invasion causes progressive perineal pain, constipation, urinary difficulties, and bleeding, whereas chordomas at the cranial base lead to increased intracranial pressure and compression of the adjacent structures causing headaches, blurred vision, memory loss, and emotional instability. When vertebrae are involved, tumors invade the spinal cord and nerve roots with pain, numbness, motor weakness, and paralysis.

Radiography shows an expansive, osteolytic mass with a lobular or geographic appearance. Typically, the tumors are located in the midline in the caudal sacrum or the skull base. Sacral chordoma produces an anteriorly protruding mass that contains irregular bony shards when seen on lateral radiographs. Rarely, the entire tumor mass may be located within the sacrum. Not infrequently, the sacral mass is overshaded by the intestinal contents and gas. A CT scan is ideal for revealing the lobular mass with osteolysis and irregular fragmentations (Fig. 17.67A).

Pinhole scintigraphy is valuable for the mapping of large, expansile, intraosseous photonic tumor, which is characteristically situated in the midline of the caudal sacrum. The tumor can be outlined by irregular, interconnected, spotty "hot" areas of reactive or destroyed bones around it (Fig. 17.67B).

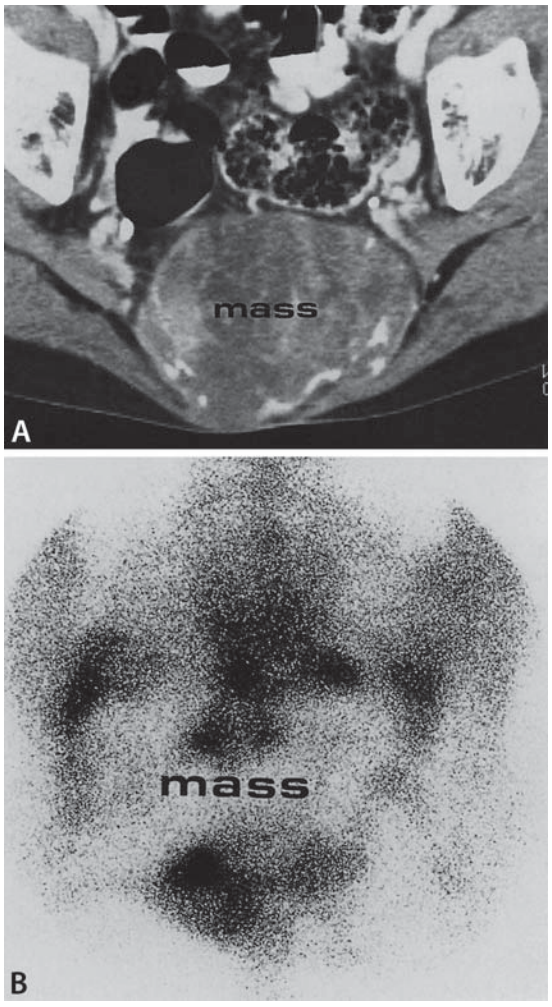

Fig. 17.67A, B Sacral chordoma with expansile mass. **A** Transverse CT scan of the lower sacrum in a 59-year-old woman with a large pelvic mass reveals an expansile tumor with irregularly broken cortices (*mass*). **B** Posterior pinhole scan of the sacrum shows a large, lobulated, photopenic mass (*mass*) surrounded by intense tracer uptake. The lateral borders appear photopenic due to rupture

17.5 Periosteal Leiomyosarcoma

Leiomyomas and leiomyosarcomas outside the uterus and gastrointestinal tract are extremely rare. Conklin et al. (1981) reported a case of leiomyoma that occurred in the tibia. Their case showed mild but diffusely increased tracer uptake. Recently, we came across a case of exophytic leiomyosarcoma arising from the subperiosteal layer of the juxtaspinal portion of the right ninth rib in a 40-year-old man (Fig. 17.68A, B). The tumor was photopenic with faint tracer uptake in the periphery where

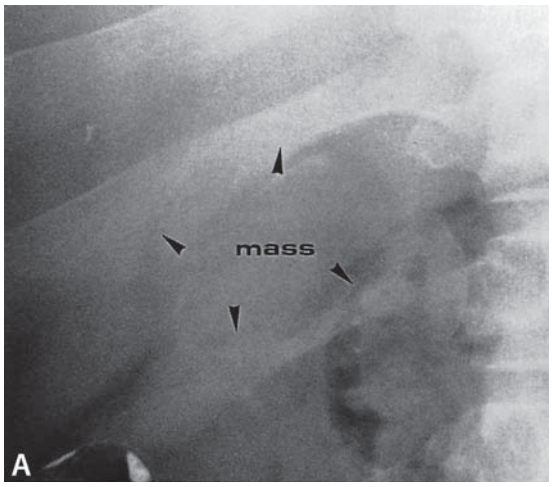

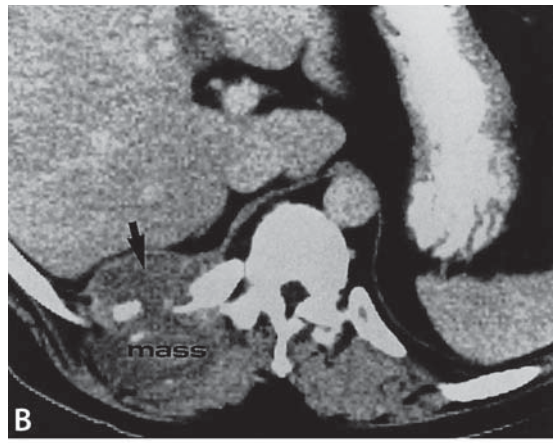

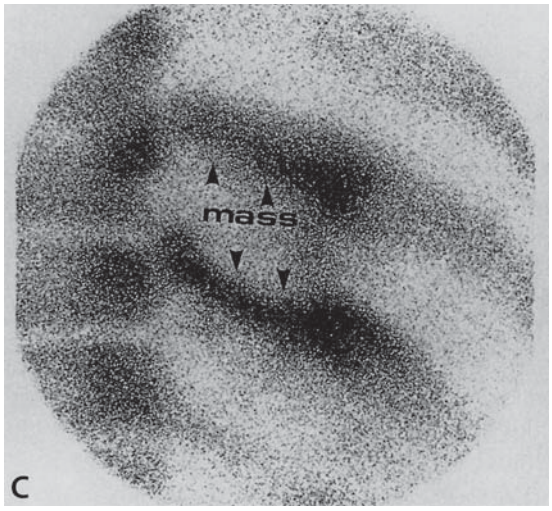

Fig. 17.68A–C Periosteal leiomyosarcoma with exophytic mass in the rib cage. **A** Anteroposterior radiograph of the right lower rib cage in 40-year-old man shows an ovoid, soft-tissue mass interposed between the two lowermost ribs near the spine (*mass*). The regional ribs are eroded (*arrowheads*). **B** Transverse CT scan demonstrates the tumor to be expansile and to consist of a soft-tissue mass (*mass*) with irregular rib destruction (*arrow*). **C** Posterior pinhole scintigraph shows moderate tracer uptake in the ribs that are eroded and compressed by the tumor interposed between them. The tumor itself is photopenic (*mass*)

a bone fragment was detached from the rib that was widely destroyed (Fig. 17.68C). Moderately intense uptake was noted in the host bone as well as the suprajacent rib that was compressed by the tumor. Histologically, the tumor was necrotic with hemorrhage.

References

Asthana S, Deo SV, Shukla NK, Raina V (2001) Carcinoma breast metastatic to the hand and the foot. Australas Radiol 45:380–382

Baek JH, Lee SY, Kim SH, et al (1997) Pinhole bone scintigraphic manifestation of fibrous dysplasia. Korean J Nucl Med 31:452–458

Bahk WJ, Rhee SK, Kang YK, et al (2006) Gastric cancer acrometastases to all digits of one hand following closed intramedullary nailing. Skeletal Radiol 35:529-532

Bahk YW (1996) Pinhole scanning in tumors and tumorous conditions of bone: a new imaging approach to skeletal radiology. J Orthop Sci 1:70–89

Bahk YW (1998) Pinhole scintigraphic diagnosis of bone tumors. J Korean Bone Joint Tumor Soc 4:1–12

Bahk YW, Kim OH, Chung SK (1987) Pinhole collimator scintigraphy in differential diagnosis of metastasis, fracture, and infections of the spine. J Nucl Med 28:447–451

Bahk YW, Park YH, Chung SK, Chi JG (1995) Bone pathological correlation of multimodality imaging in Paget's disease. J Nucl Med 36:1421–1426

Bourgeois P, Malarme M, Van Franck R, et al (1991) Bone marrow scintigraphy in prostatic carcinoma. Nucl Med Commun 12:35–45

Bredella MA, Sreinbach L, Caputo G, et al (2005) Value of FDG PET in the assessment of patients with multiple myeloma. AJR Am J Roentgenol 184:1199–1204

Capanna R, Bertoni F, Bacchini P, et al (1984) Malignant fibrous histiocytoma of bone. The experience at the Rizzoli Institute: report of 90 cases. Cancer 54:177–187

Citrin DL, McKillop JH (1978) Atlas of technetium bone scans. Saunders, Philadelphia

Coerkamp FG, Kroon HM (1988) Cortical bone metastases. Radiology 169:525–528

Conklin JJ, Camargo EE, Wagner H Jr (1981) Bone scan detection of peripheral periosteal leiomyoma. J Nucl Med 22:97

Cook GJ, Fogelman I (2001) The role of nuclear medicine in monitoring treatment in skeletal malignancy. Semin Nucl Med 31:206–211

Cooper M, Miles KA, Wraight EP, Dixon AK (1992) Degenerative disc disease in the lumbar spine: another cause for focally reduced activity on bone marrow scintigraphy. Skeletal Radiol 21:247–249

Deutch A, Resnick D (1980) Eccentric cortical metastases to the skeleton from bronchogenic carcinoma. Radiology 137:49–52

Duncker CM, Carrio I, Berna L, et al (1990) Radioimmune imaging of bone marrow in patients with suspected bone metastases from primary breast cancer. J Nucl Med 31:1450–1455

Feggi LM, Spanedda R, Scutellari PN, et al (1988) Bone marrow scintigraphy in multiple myeloma. A comparison with bone scintigraphy and skeletal radiology. Radiol Med (Torino) 76:311–315

Fleming WH, McIlraith ID, King R (1961) Photoscanning of bone lesions utilizing strontium 85. Radiology 77:635–636

Focacci C, Lattanzi R, Iadeluca ML, Campioni P (1998) Nuclear medicine in primary bone tumors. Eur J Radiol 27 [Suppl 1]:S123–131

Fogelman I, McKillop JH (1991) The bone scan in metastatic disease. In: Rubens RD, Fogelman I (eds) Bone metastases. Springer, Berlin Heidelberg New York

Gabuniia RI, Godin VP, Gristai AA, et al (1989) Scintigraphic evaluation of the efficacy of treatment of cancer of the breast with bone metastases. Med Radiol (Mosk) 34:49–53

Gilday DL, Ash JM, Reilly BJ (1977) Radionuclide skeletal survey for pediatric neoplasms. Radiology 123:399–406

Goodgold HM, Chen DCP, Majd M, et al (1984) Scintigraphic features of giant cell tumor. Clin Nucl Med 9:526–530

Greenspan A, Norman A (1988) Osteolytic cortical destruction: an unusual pattern of skeletal metastases. Skeletal Radiol 17:402–406

Haubold-Reuter BG, Duewell S, Schilcher BR, et al (1993) The value of bone scintigraphy, bone marrow scintigraphy and fast spin-echo magnetic resonance imaging in staging of patients with malignant solid tumours: a prospective study. Eur J Nucl Med 20:1063–1069

Hudson TM (1984) Scintigraphy of aneurysmal bone cysts. AJR Am J Roentgenol 142:761–765

Kamby C, Vejborg I, Daugaard S, et al (1987) Clinical and radiological characteristics of bone metastases in breast cancer. Cancer 60:2254–2261

Kim EE, Bledin AG, Gutierrez C (1983) Comparison of radionuclide images and radiographs for skeletal metastases from renal cell carcinoma. Oncology 40:284–286

Kim JY, Chung SK, Park YH, et al (1992) Pinhole bone scintigraphic appearances of osteoid osteoma. Korean J Nucl Med 26:160–163

Kim SH, Chung SK, Bahk YW (1993) Pinhole scintigraphic demonstration of trabeculated photopenic metastasis from follicular thyroid carcinoma: report of two cases. Korean J Nucl Med 27:305–308

Kirchner PT, Simon MA (1981) Radioisotopic evaluation of skeletal disease. J Bone Joint Surg Am 63:673–681

Lee KH, Chung J-K, Choi CW, et al (1995) Technetium-99m-labeled antigranulocytic antibody bone marrow scintigraphy. J Nucl Med 36:1800–1805

Lemieux J, Guimond J, Laberge F, et al (2002) The bone scan flare phenomenon in non-small-cell lung cancer. Clin Nucl Med 27:486–489

Lentle BC, Kotchen T, Catz Z, Penney HF (1987) Detecting bone marrow metastases at the time of examining the liver with radiocolloid. J Nucl Med 28:184–187

Levine E, De Smet AA, Neff JR, et al (1984) Scintigraphic evaluation of giant cell tumor of bone. AJR Am J Roentgenol 143:343–348

Lisbona R, Rosenthall L (1979) Role of radionuclide imaging in osteoid osteoma. AJR Am J Roentgenol 132:77–80

McKillop JH (1987) Bone scanning in metastatic disease. In: Fogelman I (ed) Bone scanning in clinical practice. Springer, Berlin Heidelberg New York

McLean RG, Murray IPC (1984) Scintigraphic patterns in certain primary malignant bone tumors. Clin Radiol 35:379–383

Murphey MD, wan Jaovisidha S, Temple HT, et al (2003) Telangiectatic osteosarcoma: radiographic-pathologic comparison. Radiology 229:545–553

Nadel HT, Rossleigh MA (1995) Tumor imaging. In: Treves ST (ed) Pediatric nuclear medicine, 2nd edn. Springer, Berlin Heidelberg New York, pp 496–527

Neumann RD, Kemp JD, Weiner RE (1995) Gallium-67 imaging for detection of malignant disease. In: Sandler MP, et al (eds) Diagnostic nuclear medicine, 3rd edn. Williams and Wilkins, Baltimore, pp 1243–1260

Phekoo KJ, Schey SA, Richards MA, et al (2004) A population study to define the incidence and survival of multiple myeloma in a National Health Service Region in UK. Br J Haematol 127:299–304

Pinkas L, Robinson D, Halpern N, et al (2001) ^{99m}Tc-MIBI scintigraphy in musculoskeletal tumors. J Nucl Med 42:33–37

Pistenma DA, McDougall IR, Kriss JP (1975) Screening for bone metastases. JAMA 255:46–50

Reske SN, Karstens JH, Gloeckner W, et al (1989) Radioimmunoimaging for diagnosis of bone marrow involvement in breast cancer and malignant lymphoma. Lancet 1(8633):299–301

Tanaka S, Matsumura Y, Tanaka M, et al (1991) Bone metastases in breast cancer and its risk factor – follow up study by bone scintigraphy. Kaku Igaku 28:1177–1180

Wahner HW, Kyle RA, Beabout JW (1980) Scintigraphic evaluation of the skeleton in multiple myelomas. Mayo Clin Proc 55:739–746

Waxman AD (1995) Thallium-201 and technetium-99m methoxyisobutyl isonitrile in nuclear oncology. In: Sandler MP, et al (eds) Diagnostic nuclear medicine, 3rd edn. Williams and Wilkins, Baltimore, pp 1261–1274

Waxman AD, Siensen JK, Levine AM, et al (1981) Radiographic and radionuclide imaging in multiple myeloma: the role of gallium scintigraphy. J Nucl Med 22:256–260

Widding A, Stilbo I, Hansen SW, et al (1990) Scintigraphy with nanocolloid Tc-99m in patients with small cell lung cancer, with special reference to bone marrow and hepatic metastases. Eur J Nucl Med 16:717–719

Yuasa K, Sugimura K, Okizuka AH, et al (1991) Bone infarction and fat island appearing as local defects in radionuclide bone marrow imaging. Kaku Igaku 28:91–96

Zeifang F, Sabo D, Ewerbeck V (2000) Pathological fractures in primary malignant bone tumors. Chirurg 71:1121–1125

18 Benign Tumors and Tumorous Conditions of Bone

Benign tumors originating from bone, cartilage, fibrous tissue, vessels, and unknown tissues are one of the most interesting objectives of pinhole scintigraphy. Such tumors include osteoma, osteoid osteoma, osteoblastoma, chondroma, enostosis, chondroblastoma, fibrous cortical defect and nonossifying fibroma, osteochondroma, primary bone cysts, giant cell tumor, and others. Another large group of bone diseases, in the diagnosis of which ^{99m}Tc-MDP scanning is beneficial, are tumorous conditions.

Technically, scintiscanning of benign bone tumors and tumorous conditions includes whole-body imaging followed by spot view and pinhole magnification. The examination may further include nuclear angiography as the clinical situation demands. Whole-body scintigraphy is ideal for (a) holistic portrayal of multiple lesions in polyostotic diseases such as enchondromatosis or Ollier's disease, familial exostosis, fibrous dysplasia, and histiocytosis X, (b) preoperative localization of the nidus in osteoid osteoma (Lisbona and Rosenthall 1979), and (c) assessment of lesional extent. In addition, individual pathological elements, such as fibrous and osseous components in fibrous dysplasia, can be semiqualitatively analyzed using pinhole scintigraphy (Baek et al. 1997).

Essential pathology, clinical sings, and radiographic and bone scintigraphic manifestations of these conditions are presented in this chapter. As mentioned in Chap. 17 the diagnostic use of gallium-67 citrate, thallium-201 chloride, and ^{99m}Tc-MIBI for skeletal tumors is not considered here since the uses of these radiopharmaceuticals are richly described in numerous articles and many textbooks (Nadel and Rossleigh 1995; Neumann et al. 1995; Waxman 1995; Focacci et al. 1998; Pinkas et al. 2001).

18.1 Benign Bone Tumors

18.1.2 Osteoma

Osteoma is a relatively rare, benign tumor that most typically involves the skull, especially the frontal and other paranasal sinuses, and extremely rarely the long and flat bones. Osteomas that involve the mandible, maxilla, temporal bone and maxillary sinus are termed by some workers "peripheral osteomas" (Woldenberg et al. 2005). Pathologically, the tumors consist of lamellar or woven lamellar bone in the form of either compact bone with Haversian systems or spongy bone, which is separated from host cancellous bone and is juxtacortical in location. Numerous annular cement lines are seen in the tumor periphery. The great majority of tumors are less than several centimeters in diameter and symptomless. Characteristically, the tumors do not invade adjacent bones. Rarely large osteomas may cause physical symptoms such as obstruction of the sinusal ostium. The great majority of osteomas are solitary, and rare multiple osteomas are almost always associated with Gardner's syndrome.

The radiographic features of compact osteomas are straightforward. They are characterized by a small, well-defined, round or ovoid ivory-like mass attached to the host bone cortex (Fig. 18.1A). In contrast, spongy osteoma

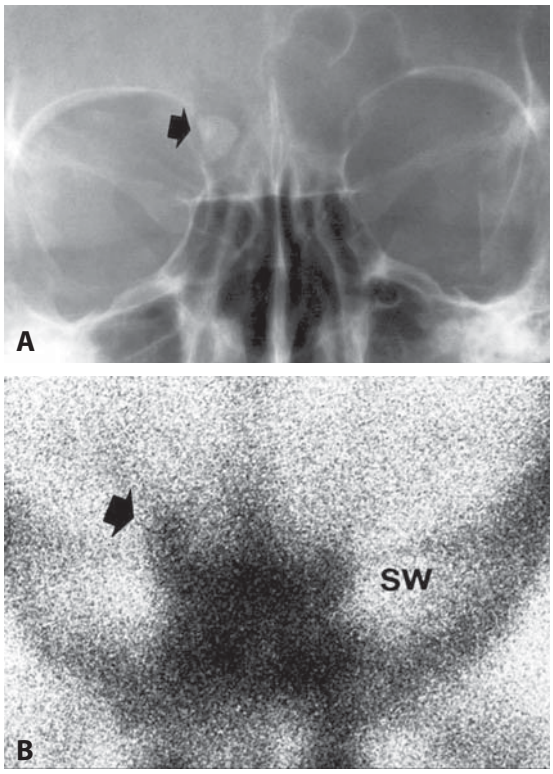

Fig. 18.1A, B Compact osteoma in the frontal sinus. **A** Posteroanterior radiograph of the skull in a 64-year-old woman shows a 10×8 mm dense bone tumor in the right frontal sinus (*arrow*). **B** Semi-Warers' view pinhole scan reveals tracer uptake in the tumor that is not clearly discernible from the background uptake (*arrow*)

presents as a round or ovoid semiopaque bony mass when radiographed en face (Fig. 18.2A) and as a mass that is centrally lucent and peripherally sclerotic in profile (Fig. 18.2B). The adjacent bones are intact. Mirra (1989) reports a giant osteoma that measured 6×6×4 cm. It involved the right iliac bone in a 61-year-old man (his Fig. 7.34 on page 181).

Pinhole scintigraphy reveals a well-defined round or ovoid tumor with increased tracer uptake. Interestingly, the uptake appears not so intense in compact osteoma (Fig. 18.1B) compared to that in spongy osteoma (Fig. 19.2B). Although cases are largely limited, it is tempting to assume that such a difference between the grades of tracer uptake in osteomas is probably related to the histological characteristics

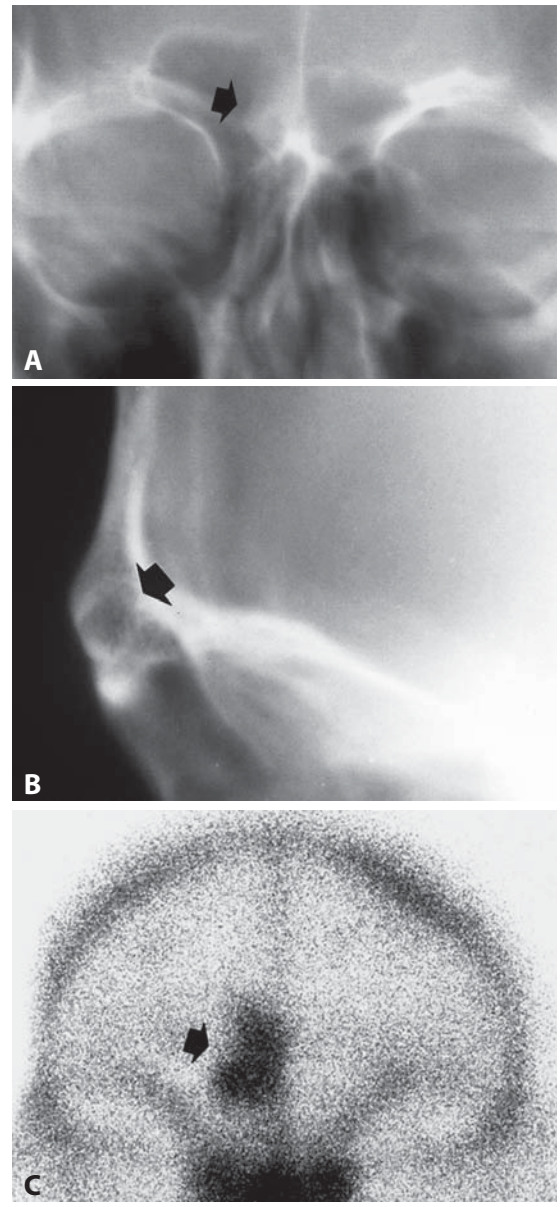

Fig. 18.2A–C Spongy osteoma in the frontal sinus. **A** Conventional coronal X-ray tomogram of the skull in a 37-year-old man shows a 20×10 mm ovoid, semiopaque bone tumor in the left frontal sinus arising from the midseptum (*arrow*). **B** Lateral radiograph reveals the ring-like tumor with radiolucent content (*arrow*). **C** Anterior pinhole scan reveals intense tracer uptake in the tumor (*arrow*)

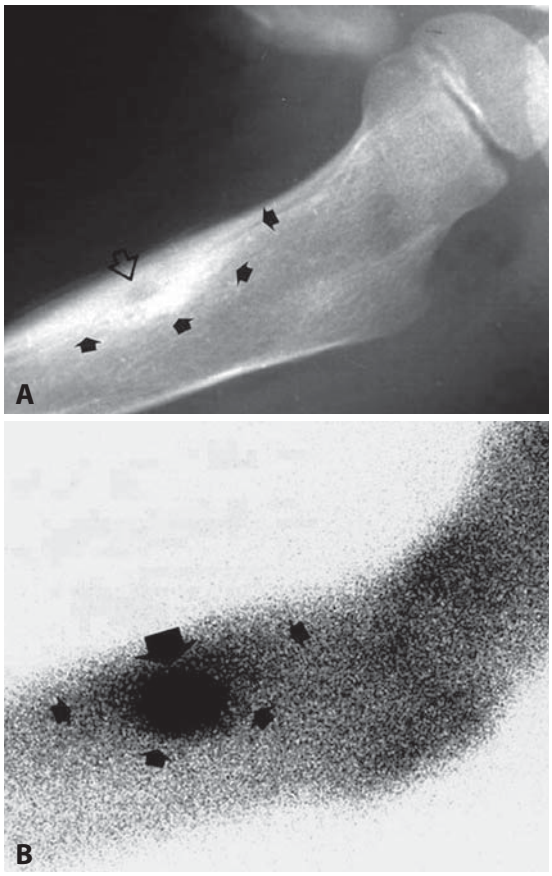

Fig. 18.3A, B Osteoid osteoma with central nidus. **A** Frog-leg view of the right femur in an 11-year-old boy with local pain shows diffuse bone thickening (*small arrows*) with a small ovoid lucent defect at the center (*open arrow*). **B** Pinhole scintigraph reveals a small ovoid area of intense tracer uptake (*large arrow*) surrounded by less intense uptake (*small arrows*)

of osteomas: more intense uptake in the spongy variant that is histologically and metabolically immature with active bone turnover than in the well-formed compact variant that is metabolically in a more or less inert state. Incidentally, in our series compact osteoma was found in a 64-year-old woman and spongy osteoma in a 37-year-old man.

18.1.3 Osteoid Osteoma

Osteoid osteoma is a benign, painful tumor innervated with nerve fibers (O'Connell et al. 1998). Pathologically, the tumor consists of a nidus that is framed with a thin fibrovascular rim and surrounded by diffuse reactive sclerosis of the host bone. The nidus, variously mineralized, is a meshwork of osteoid and woven bone with osteoclasts and dilated vessels. The tumor affects males two to three times more often than females in the second and third decades of life. Its prevalence is approximately 3% of all bone tumors, and osteoid osteoma accounted for 12.1% of all benign bone tumors in one Mayo Clinic series (Dahlin and Unni 1986a). More than 80% occur in the long bones and 10% in the spine.

Radiographically, the nidus presents as an ovoid or roundish lucent lesion within or near the cortex. It is less than 2 cm in size, and is characteristically surrounded by reactive sclerosis of various degrees. The nidus is typically located at the lesion center (Figs. 18.3A and 18.4A). The sclerosis may vary in grade ranging from marked to moderate. The radiographic appearance may be modified when the tumor is located in the periosteal or corticoperiosteal layer or in the irregular or small bones such as the vertebrae and tarsal bones.

The ^{99m}Tc-MDP bone scintigraphic features are characteristic. In particular pinhole scans show the "hotter spot within hot area" sign that is pathognomonic of osteoid osteoma (Figs. 18.3B and 18.4B). The central "hotter" area represents the osteoid nidus that is highly vascular and the surrounding "hot" area reactive osteosclerosis (Helms et al. 1984; Kim et al. 1992). Bone scanning is an invaluable means of accurate preoperative localization and subsequent surgical extirpation of the nidus especially in irregular bones (Sim et al. 1975).

18.1.4 Osteoblastoma

Osteoblastoma is a rare, benign tumor, which clinically and pathologically manifests in two different ways, conventional and aggressive. As is the case with osteoid osteoma, the neoplastic stroma of osteoblastoma is richly vascularized and produces osteoid and woven bone. The tumor is painful, occasionally with soft-tissue swelling and rarely with pathological fracture.

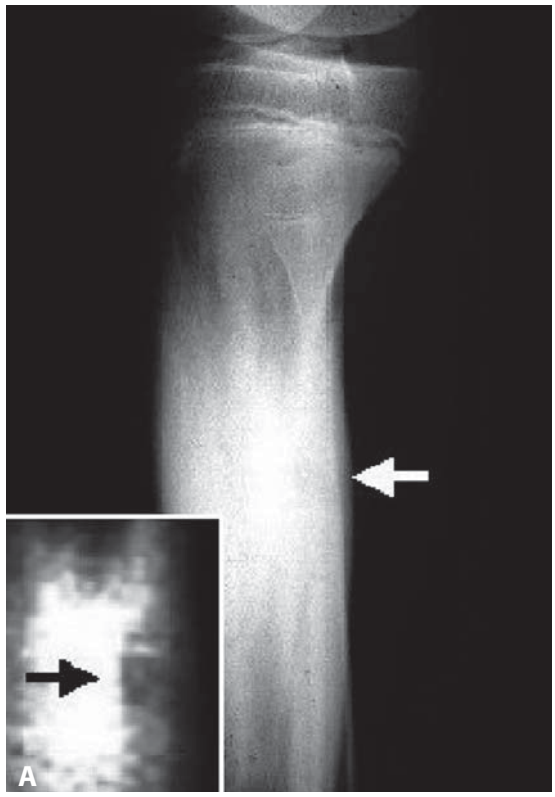

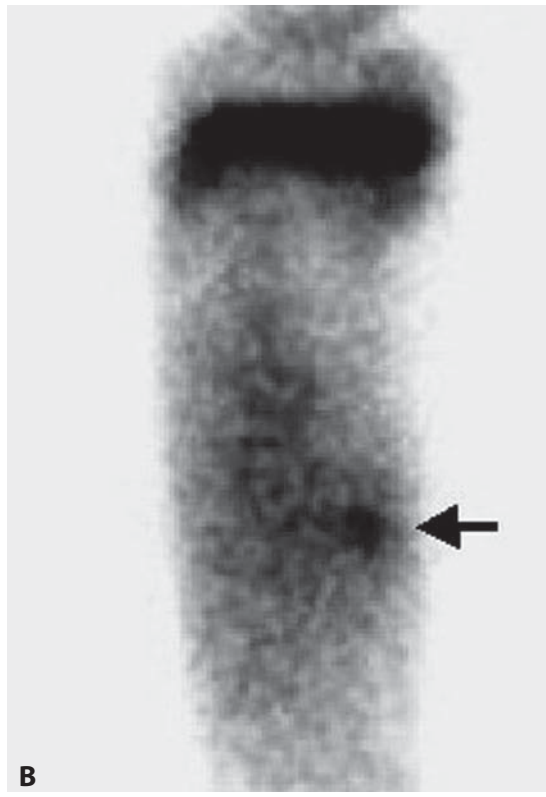

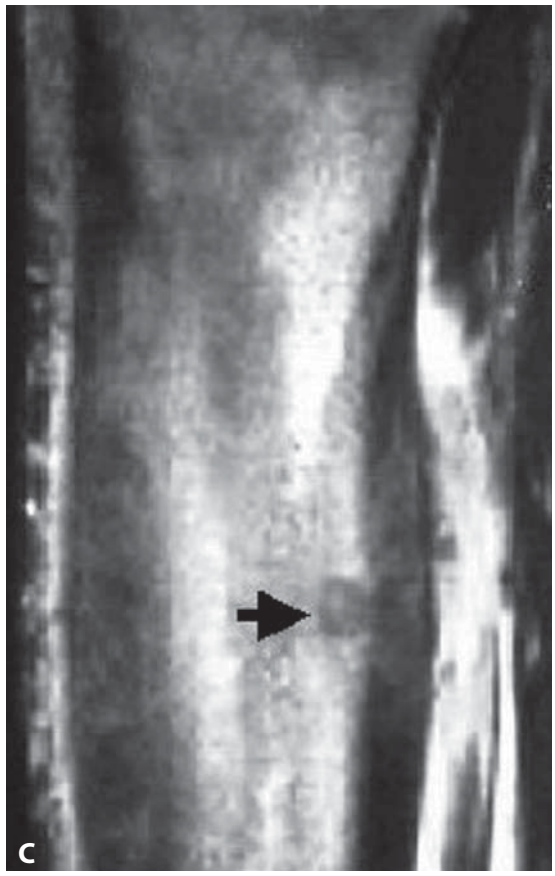

Fig. 18.4A–C Intracortical osteoid osteoma with dense sclerosis. A Lateral radiograph of the right tibial shaft in a 13-year-old boy with "morning" leg pain of 6 months duration shows diffuse sclerosis (arrow). Inset high-penetration radiograph portrays a small nidus (arrow). B Magnified 99mTc-MDP scintigraph shows typical spotty "hot" uptake in the nidus (arrow). C Proton density MRI shows a small nidus with central mineralization within the cortex (arrow)

Although no bones are immune, the spine and flat bones are most commonly affected. The size is usually not larger than 2 cm. Its prevalence is about 0.8% of all primary bone tumors, and about 80% of patients are younger than 30 years. Males are affected twice as frequently as females. Symptoms are not very specific. Pain is moderate and occasionally nocturnal and controllable by NSAIDs (Ferracini et al. 1998). The spinal involvement may cause muscle spasm, scoliosis, and neurological deficits.
The radiographic features include osteolysis or osteosclerosis, separately or combined, that is nonspecific in the majority of cases. The tumor may be expansive, thinning the overlying cor-

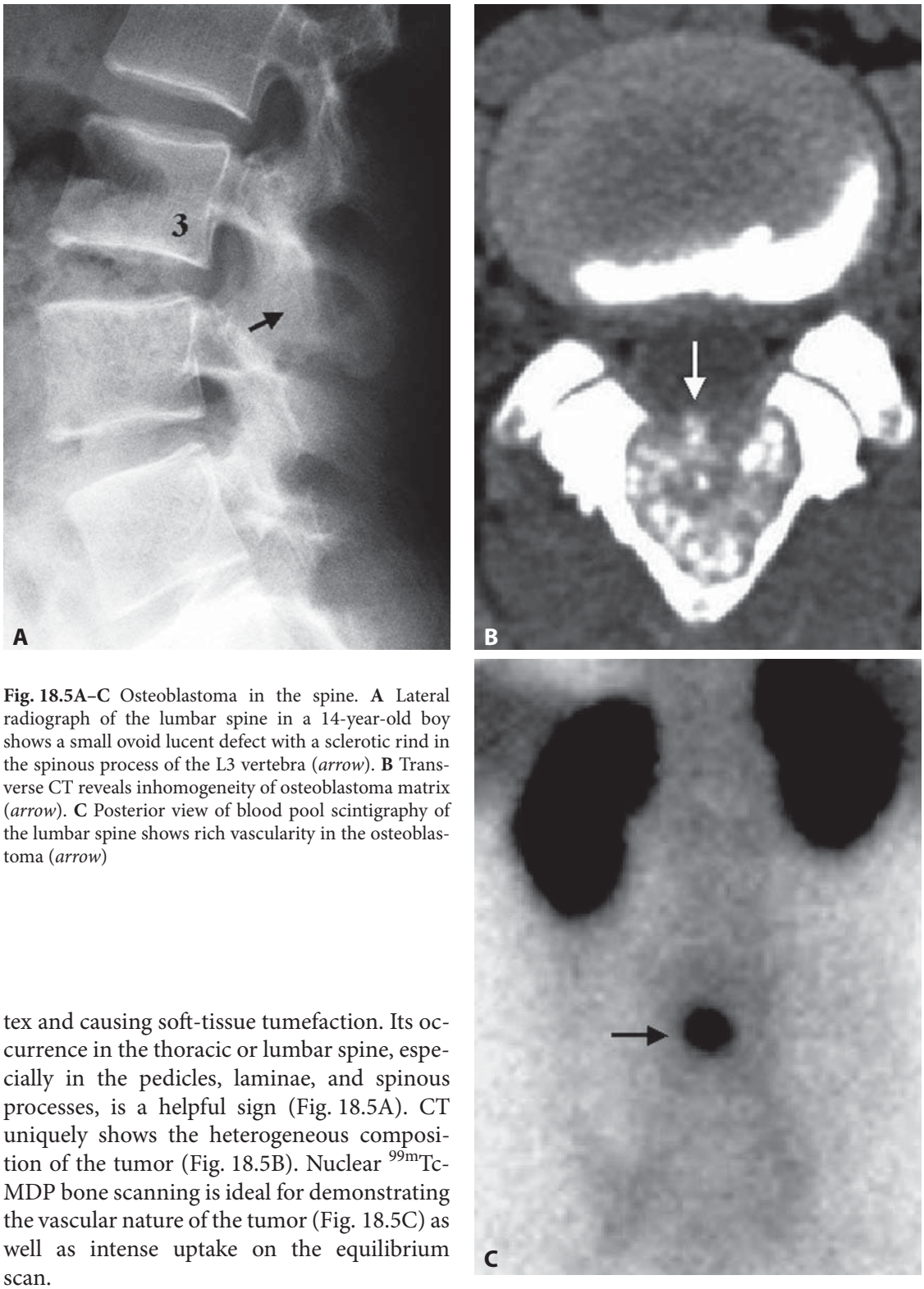

Fig. 18.5A–C Osteoblastoma in the spine. **A** Lateral radiograph of the lumbar spine in a 14-year-old boy shows a small ovoid lucent defect with a sclerotic rind in the spinous process of the L3 vertebra (*arrow*). **B** Transverse CT reveals inhomogeneity of osteoblastoma matrix (*arrow*). **C** Posterior view of blood pool scintigraphy of the lumbar spine shows rich vascularity in the osteoblastoma (*arrow*)

tex and causing soft-tissue tumefaction. Its occurrence in the thoracic or lumbar spine, especially in the pedicles, laminae, and spinous processes, is a helpful sign (Fig. 18.5A). CT uniquely shows the heterogeneous composition of the tumor (Fig. 18.5B). Nuclear ^{99m}Tc-MDP bone scanning is ideal for demonstrating the vascular nature of the tumor (Fig. 18.5C) as well as intense uptake on the equilibrium scan.

18.1.5 Enostosis (Compact Bone Island)

Enostosis is an innocuous, commonplace bone lesion of adults, being found in any bone with a predilection for the femur, pelvis, and ribs. Some consider this to be tumor-like condition and others a hamartoma. It has also been speculated to be congenital or developmental reflecting resorption failure during endochondral ossification (Greenspan 1995). Histologically, the lesion is composed of compact lamellar bone that is provided with haversian systems. The general incidence is unknown, but one radiographic study of 189 subjects showed an incidence of 1.1% in the pelvic bone. Both males and females are nearly equally affected. Lesions are ovoid, round, or oblong in shape and measure between 2 mm and 2 cm in diameter. Enostosis is known to change in size and may even spontaneously vanish. Its clinical implication is potential mimicry of metastasis and benign bone tumors. It is not a neoplastic entity, entirely differing from osteoma that involves almost exclusively the skull, especially the frontal and ethmoid sinuses. When an enostosis occurs in a vertebra it may give rise to an osteoma-like appearance, earning the nickname "endosteoma". Characteristically, the long axes of elongated enostoses in the long bones or pelvis are longitudinally orientated, and it is considered closely related to bone remodeling and tubulation. It is tempting to propose that the phenomenon be termed "*the longitudinal alignment sign*", which is most typically observed in slowly evolving benign tumors such as enchondromas and tumorous conditions such as nonossifying fibroma and familial multiple exostosis in growing bones (see sections 18.1.6 Enchondroma and 18.1.8 Fibrous Cortical Defect and Nonossifying Fibroma below). Occasionally, malignant bone diseases such as lymphoma, myeloma and metastasis and Hand-Schüller-Christian disease may present as longitudinally oriented osteolysis but they are typically ill-defined without rim or demarcation.

Radiography shows island-like, roundish, or oblong compact bone within cancellous bone, occasionally with partial plastering against the

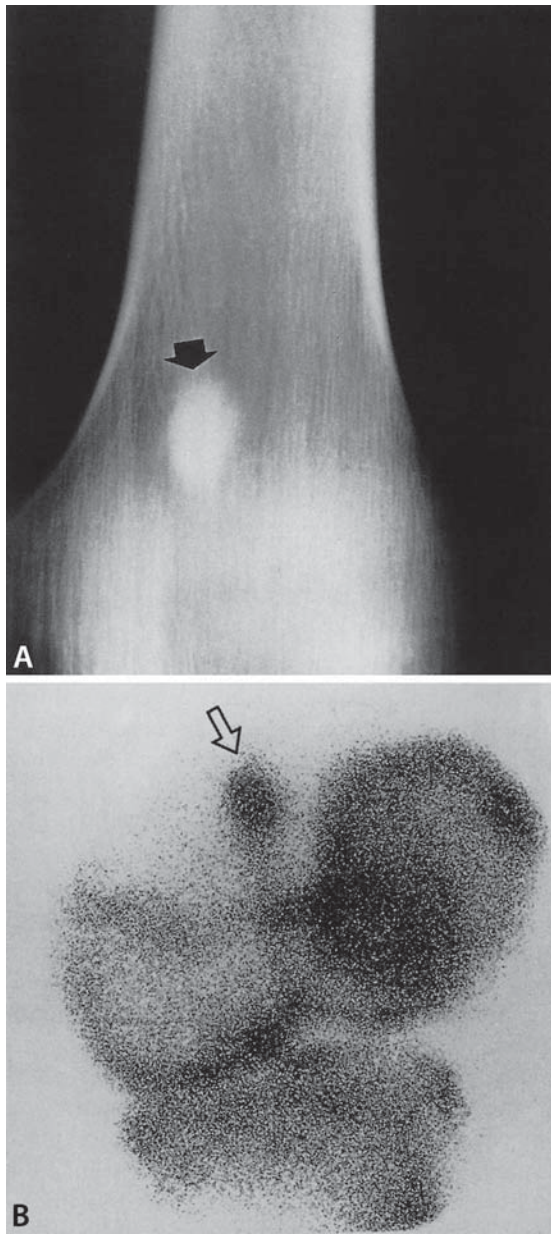

Fig. 18.6A, B Enostosis or compact bone island. **A** Anteroposterior conventional X-ray tomogram of the distal left femur in a 21-year-old young man reveals a large, bean-sized, compact bone within the marrow cavity (*arrow*). The lesion is longitudinally aligned and has a spicular contour. **B** Anterior pinhole scintigraph shows ovoid tracer uptake in the compact bone island (*open arrow*). The tracer intensity is similar to that of the other cortical bone. The lesion was asymptomatic

endosteum. The long axis typically aligns with that of the host bone trabeculae (Fig. 18.6A), and enostoses occasionally show emanations of thorny or spicular bones (Fig. 18.7A). Neither lysis nor sclerosis occurs in the adjacent bone, and the cortex is preserved. Enostoses in the vertebrae are usually ivory-dense, bordering but not invading the endplate (Fig. 18.8). Enostoses in the involutional stage are often not dense enough to arrive at an accurate diagnosis without the assistance of conventional X-ray tomography or CT (Fig. 18.6A).

Scintigraphically, enostoses accumulate tracer, the intensity of which varies according to size and age. About half of the enostoses studied by Hall et al. (1980) showed increased uptake. The high-resolution scintiscanner can detect more enostoses, and pinhole scanning diagnoses even more cases in far greater detail. Thus, pinhole scintigraphy of enostoses in long-bone metaphyses demonstrates elongated tracer uptake, the long axis of which is aligned with that of the host bone (Figs. 18.6B and 18.7B). The absence of tracer uptake in an osteoblastic bone lesion has been described as a sign of benignity, but this statement must be applied with caution after pinhole scintigraphic reassessment because the planar scan may fallaciously fail to detect tracer uptake. Occasionally an enostosis is first detected by pinhole scanning, and is only confirmed retrospectively by conventional tomography or CT (Fig. 18.6). The ivory-like enostosis of the vertebra is round or oblong abutting the cortex (Fig. 18.8C).

18.1.6 Enchondroma

Enchondroma, a benign tumor of the medullary cavity of the long bones, stems from and consists of lobules of mature hyaline cartilage. The great majority of these lesions are solitary, and 90% show discrete calcification in clusters or aggregations. The tumor is centrally located typically with longitudinal orientation of the long axis within the trabecular bone of the metaphysis or the diaphysis of the long bones of the hands, feet, and extremities. If subperiosteally located the tumor is referred to as periosteal chondroma. Enchondromatosis, or Ollier's

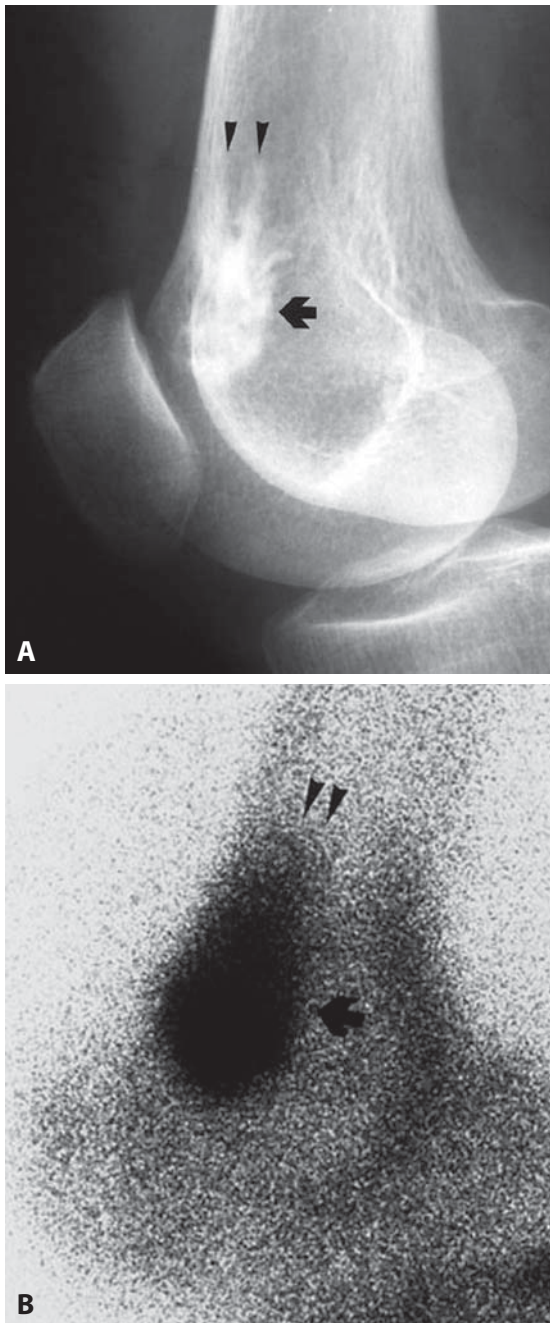

Fig. 18.7A, B Enostosis with thorny emanation. **A** Lateral radiograph of the right femur in a 65-year-old woman shows a 20×15 mm enostosis (*arrow*) with spicules emanating from its upper pole (*arrowheads*). The lesion was asymptomatic. **B** Lateral pinhole scintigraph reveals intense uptake in the main body of the enostosis (*arrow*) with less intense uptake in the spicules (*arrowheads*). The appearance of emanating spicules at the diaphyseal side of enostosis is considered to be related to bone remodeling or growth. A similar phenomenon occurs in enchondromas (see Figs. 18.8 and 18.9) and fibrous cortical defect (see Fig. 18.17)

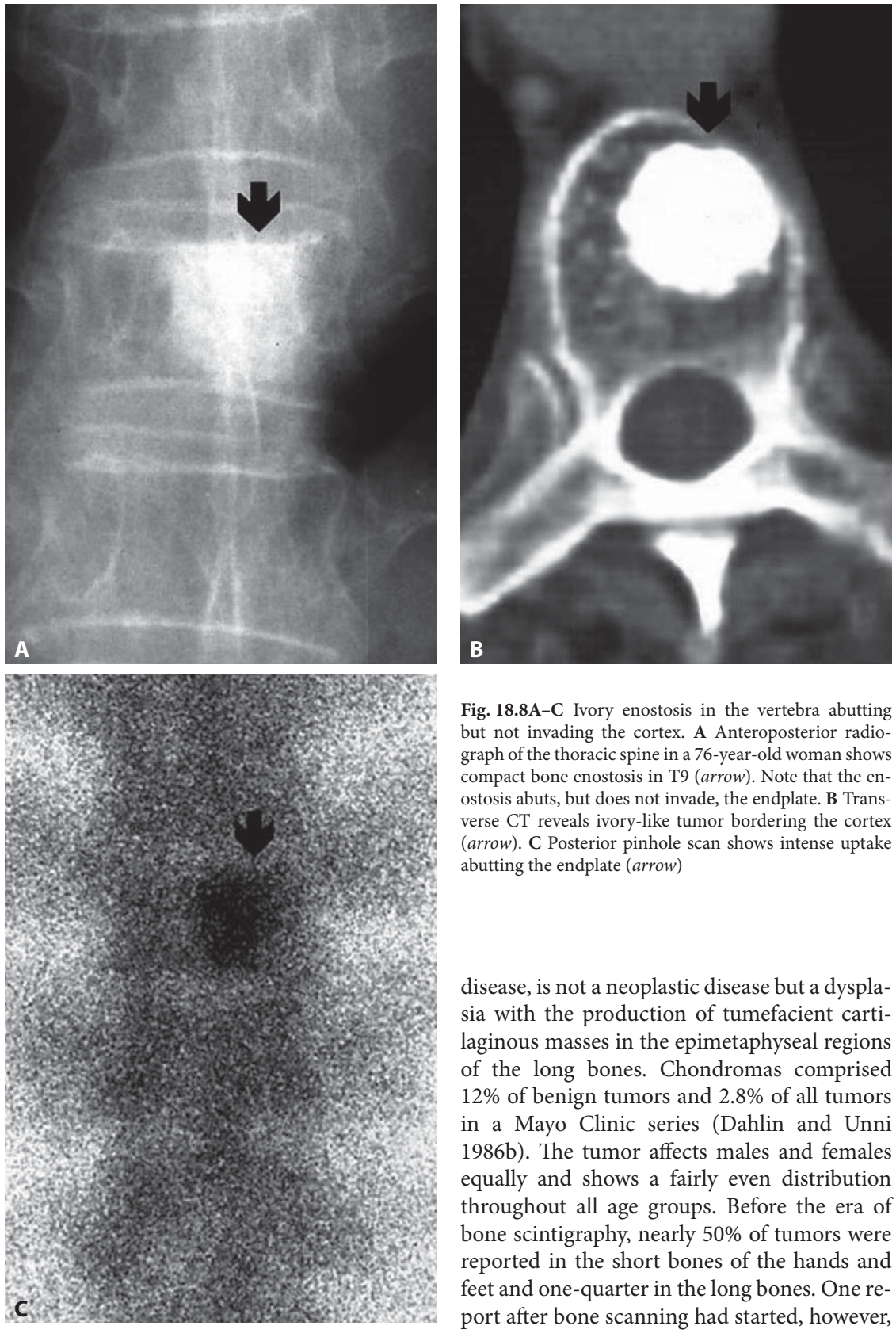

Fig. 18.8A–C Ivory enostosis in the vertebra abutting but not invading the cortex. **A** Anteroposterior radiograph of the thoracic spine in a 76-year-old woman shows compact bone enostosis in T9 (*arrow*). Note that the enostosis abuts, but does not invade, the endplate. **B** Transverse CT reveals ivory-like tumor bordering the cortex (*arrow*). **C** Posterior pinhole scan shows intense uptake abutting the endplate (*arrow*)

disease, is not a neoplastic disease but a dysplasia with the production of tumefacient cartilaginous masses in the epimetaphyseal regions of the long bones. Chondromas comprised 12% of benign tumors and 2.8% of all tumors in a Mayo Clinic series (Dahlin and Unni 1986b). The tumor affects males and females equally and shows a fairly even distribution throughout all age groups. Before the era of bone scintigraphy, nearly 50% of tumors were reported in the short bones of the hands and feet and one-quarter in the long bones. One report after bone scanning had started, however,

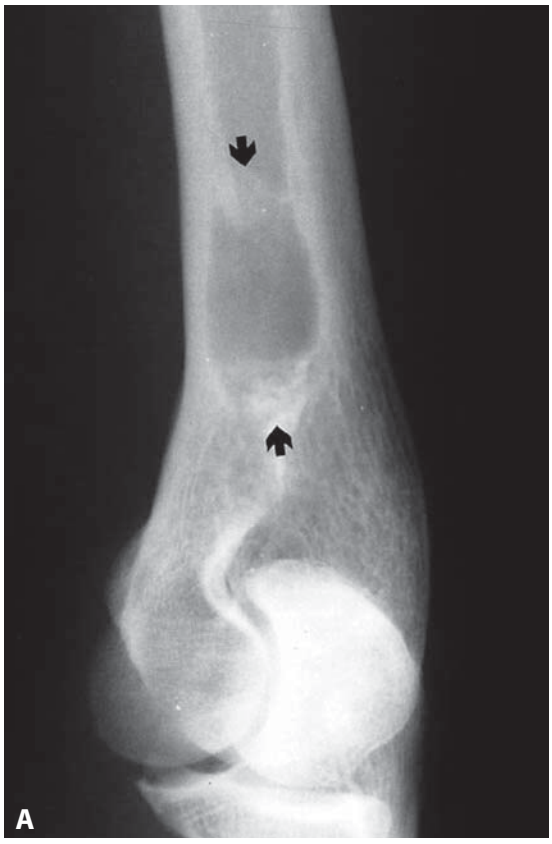

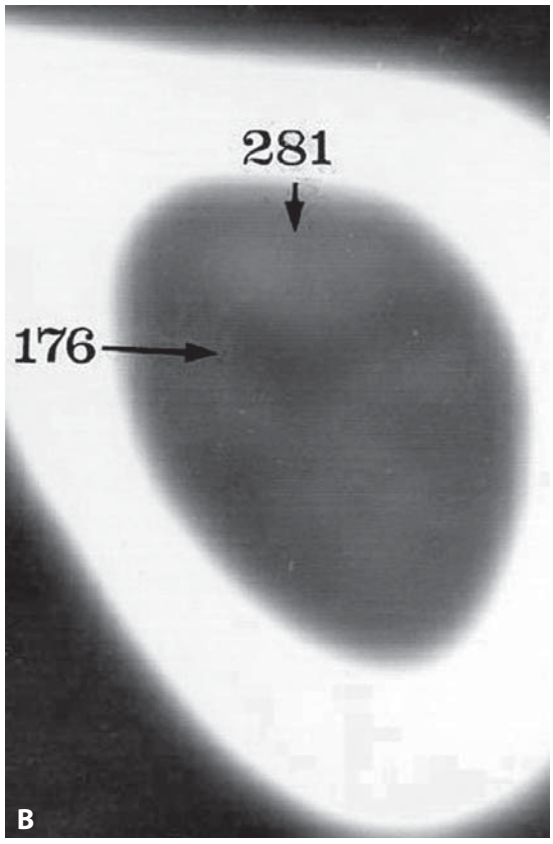

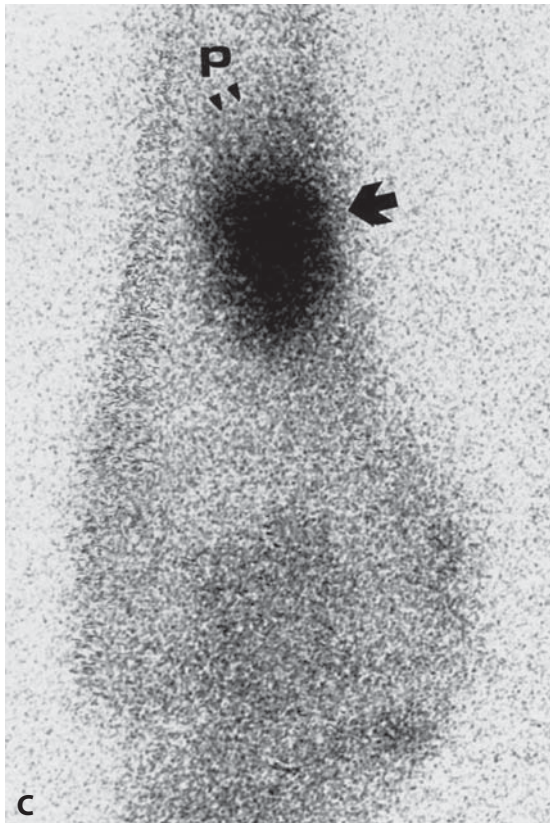

Fig. 18.9A–C Early enchondroma. **A** Oblique radiograph of the right distal humerus in a 45-year-old man shows a well-defined ovoid semilucent tumor in the medullary space with endosteal scalloping (*arrows*). Nebulosity is due to early mineralization. **B** CT demonstrates areas of early mineralization (HU 281) within the enchondroma against a cartilaginous matrix (HU 176). **C** Anterior pinhole scintigraph reveals concordant tracer uptake (*arrow*). Note the wider zone of penumbra in the diaphyseal aspect of the tumor uptake (*P*). The penumbra on the diaphyseal side of enchondromas appears analogous to the emanating spicules of enostosis (Fig. 18.6) and the leading cone-shaped mineralization of fibrous cortical defect (Fig. 18.17), all of which are related to bone remodeling

indicated a sharp decrease in the incidence in the short bones to less than 15%, contrasting with a dramatic increase in the incidence in the femur to about 40% (Mirra and Eckhardt 1989). Expansive enchondromas in the ribs and phalanges are called enchondroma protuberans. Benign enchondromas usually do not involve bones such as the ilium, which is the

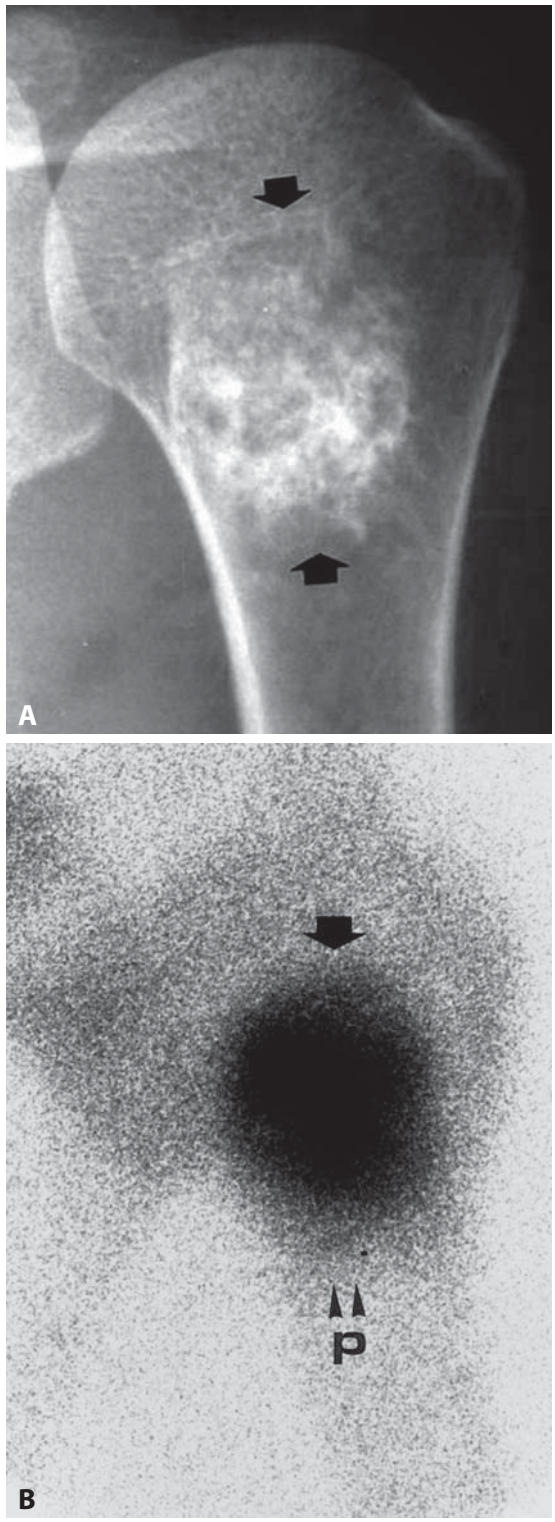

most common site of chondrosarcoma (Dahlin and Unni 1986b).

The radiographic features of solitary enchondroma vary according to disease stage. Early lesions manifest as seemingly expansive osteolysis with faint mineralization and characteristic endosteal scalloping (Fig. 18.9A). CT shows areas of incipient mineralization within a lucent tumor matrix (Fig. 18.9B). However, most enchondromas show distinct or obvious mineralization when first detected (Figs. 18.10A and 18.11A). The mineralization is mottled and clustered with various amounts of intermingled lucent cartilaginous components, and the tumor border is delineated only by an imaginary circle. It is our impression that the ratio of mineralization to nonmineralization in an enchondroma is probably related to the age of the tumor. Although observation was limited between two individuals, we noticed that an enchondroma in a 47-year-old patient contained fewer mineralized components (Fig. 18.10) than that in a 70-year-old patient (Fig. 18.11). As discussed below the extent and age of mineralization seemed to be closely related to the intensity of tracer uptake.

Additionally, peritumoral sclerosis or calcification appears to arise from the epiphyseal side of the tumor (Fig. 18.9A). It is in concordance with the observation that the mineralization in aged enchondromas is more complete in the epiphyseal and medial aspects of the tumor than in the diaphyseal and lateral aspects (Figs. 18.9A and 18.10A). These findings seem to suggest that the mineralization in en-

Fig. 18.10A, B Irregularly mineralized enchondroma. **A** Anteroposterior radiograph of the left proximal humerus in a 47-year-old woman shows an ovoid intramedullary tumor with mineralization (*arrows*). Peripheral tumor mineralization appears well-defined on the epiphyseal and medial sides (*lower arrow*) but irregularly spicular on the diaphyseal and lateral sides (*upper arrow*). This finding suggests that the tumoral ossification is first completed on the epiphyseal and medial sides. **B** Anterior pinhole scintigraph reveals concordant tracer uptake with a wider zone of penumbra in the diaphyseal aspect where bone remodeling or tumor repair is in progress (*P*)

chondromas starts from the epiphyseal side and lasts longer on the diaphyseal side. In supporting this suggestion the pinhole scan shows the penumbra, a reaction to neoplastic mineralization, to be greater on the diaphyseal side than on the epiphyseal and medial sides where mineralization has been completed.

Solitary enchondromas may often be disguised as plurifocal enchondromas when nonmineralized and mineralized parts of a lesion are counted separately. Conventional tomography, CT and pinhole scintigraphy are useful tools for identifying mineralized foci within an enchondroma (Fig. 18.12).

The basic bone scintigraphic finding is increased uptake, which is intramedullary in location in the long bone diaphysis or metadiaphysis (Figs. 18.9C, 18.10B and 18.11B). As in other tumors, pinhole scintigraphy provides unique information on the metabolic profile of the tumor tissue in different evolutional stages of an enchondroma (Fig. 18.12A, B). Theoretically, the cartilaginous tissues of burgeoning enchondromas should not accumulate tracer; only the denatured cartilage with mineralization would accumulate tracer. The cases shown in Figs. 18.9 and 18.12 exemplify the close relationship between mineralization and tracer uptake in enchondromas. In this context, it is worth emphasizing that not all radiolucent tumors are truly free of mineralization as shown in Fig. 18.9, and this is why many apparently lucent or faintly opaque enchondromas accumulate tracer so intensely. With progress of mineralization tracer uptake is further intensified (Fig. 18.10), and when mineralization gradually slows down and finally ceases tracer uptake decreases or normalizes (Fig. 18.11B). Interestingly, the correlation of scintigraphy and radiography shows that densely calcified enchondromas accumulate less tracer than those without calcification, and this finding is interpreted as reflecting the fact that calcification in enchondromas results from degeneration and poor vascularity (Dahlin and Unni 1986b) (Fig. 18.12). Intratumoral necrosis is another factor that may influence tracer uptake.

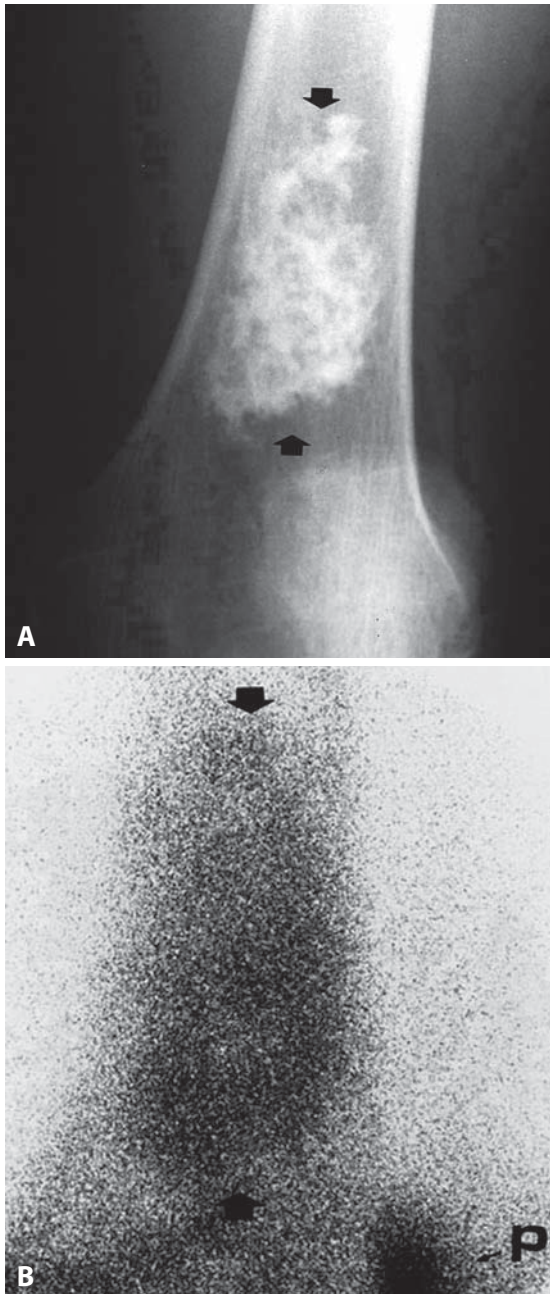

Fig. 18.11A, B Advanced mineralization in an aged enchondroma with a well-formed epiphyseal border. **A** Anteroposterior radiograph of the left distal femur in a 70-year-old woman with an asymptomatic enchondroma shows densely calcified tumor. Note that calcification is inhomogeneous with a well-formed border occurring in the epiphyseal aspect (*lower arrow*) and an irregular border on the opposite side (*upper arrow*). **B** Pinhole scintigraph reveals tracer uptake to be homogeneous (*arrows*) but the intensity is diffusely reduced compared to that of younger enchondromas with relatively less calcification (Fig. 18.9)

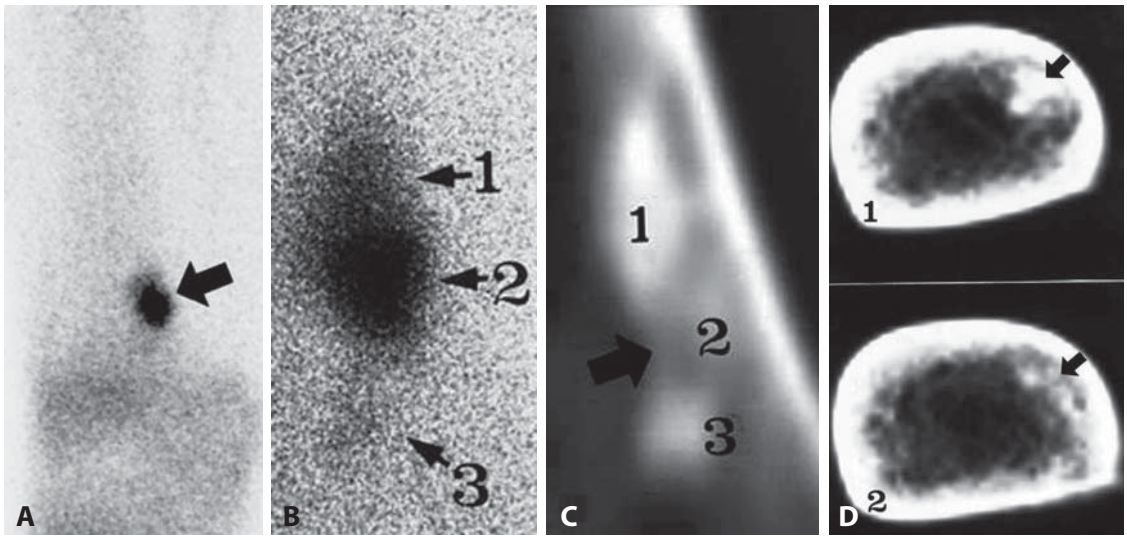

Fig. 18.12A–D Value of CT and bone scan in multiple enchondromas. **A** Planar spot scintigraph of the right femur in a 58-year-old man shows spotty uptake in the right distal femur. **B** Pinhole scintigraph reveals the lesion to consist of three well-defined areas of different tracer uptake (*1, 2, 3*). **C** Reconstructed CT scan demonstrates the three lesions to be mineralized to different degrees (*1, 2, 3*). **D** Transaxial CT slices show dense mineralization in the top lesion (*1, arrow*) and partial mineralization in the central lesion (*2, arrow*)

18.1.7 Chondroblastoma

Chondroblastoma is a rare bone tumor that almost exclusively originates from the physeal cartilage, and accounts for 1% of all primary bone tumors (McLeod and Beabout 1973). Histologically, the tumor consists of chondroblasts, chondroid tissue, and osteoclast-like giant cells resembling giant cell tumor or osteosarcoma, and 10 to 15% of tumors may be complicated by a secondary aneurysmal bone cyst. Boys are affected 1.7 times more commonly than girls and 75% occur in the first and second decades of life (Mirra and Eckhardt 1989). Most tumors measure less than 5 cm in size but the tumor may exceptionally attain a huge size. The long bones, including those about the knee and the proximal and distal humerus and the proximal femur, are involved in more than 70%. The greater trochanter and apophysis are also involved. Involvement of the ribs, ischium, ilium, talus, and calcaneus is rare and involvement of the skull, face, and wrist and hand is rarer still (Davila et al. 2004). The symptoms and signs are pain, bone swelling and disturbed joint motion when the tumor involves the juxta-articular bones.

Radiographically, chondroblastomas present as eccentric osteolysis in epiphysis (Fig. 18.13A) often with an open physeal line (Fig. 18.14A). Tumors are either defined sharply (Fig. 18.13A), poorly (Fig. 18.14A) or irregularly with a sclerotic border. The lesion may be concentric when it occurs in a carpal or tarsal bone (Fig. 18.15A). Mineralization, which is rarely extensive, has been reported in 30–50%. Occasionally the tumor erodes and bulges the endosteum and cortex eventually elevating and penetrating the cortex, and secondary aneurysmal bone cyst change is not uncommon (Fig. 18.15A). MRI is useful for tumor tissue characterization especially when aneurysmal bone cyst develops (Kaim et al. 2002). T1-weighted images reveal a rim of low signal surrounding tumor that is either homogeneously isointense (Fig. 18.13B) or low (Fig. 18.14B) or heterogeneous (Fig. 18.15B) and T2-weighted images show a mixture of various signals according to the constituents of the tumor matrix (Jee et al. 1999) (Figs. 18.13C and 18.14C). For example, chondroid (Fig. 18.13C and 18.14C) and aneurysmal bone cyst (Fig. 18.15C) seem to produce a high signal.

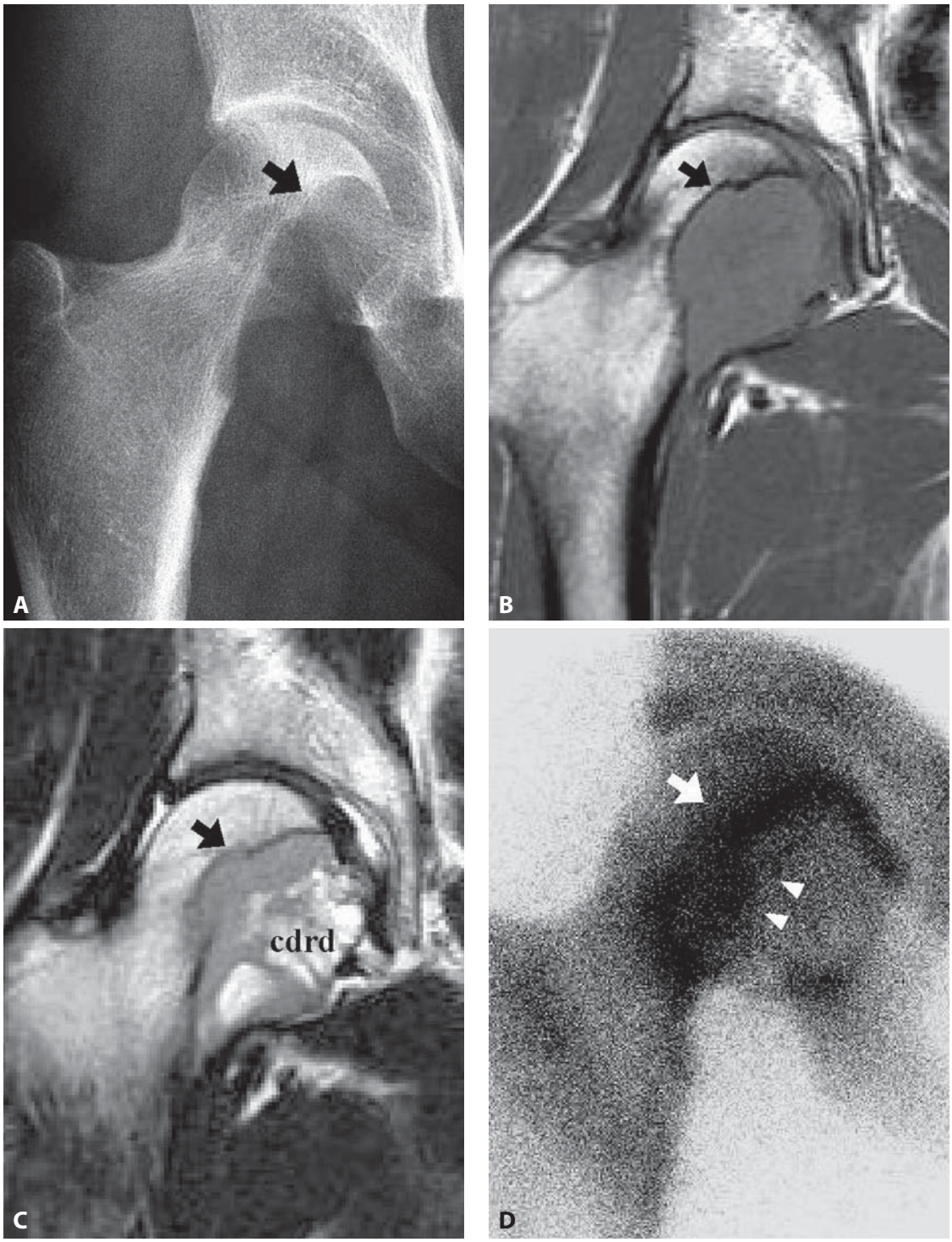

Fig. 18.13A–D Radiographic, MRI and pinhole scintigraphic correlation of chondroblastoma in the femoral head with well-defined, geographic osteolysis. **A** Anteroposterior radiograph of the right hip in a 27-year-old male shows an ovoid, radiolucent lesion with sharp, sclerotic rind (*arrow*). **B** Coronal T1-weighted MR image reveals low–intermediate signal in the bland tumor matrix with a low-signal rind (*arrow*). **C** Coronal T2-weighted MR image demonstrates high signal in chip-like chondroids (*cdrd*). **D** Anterior pinhole scintigraph shows tumor uptake to be isointense with an area of increased uptake in the mineralized zone (*arrowheads*) and sclerotic rind (*arrow*)

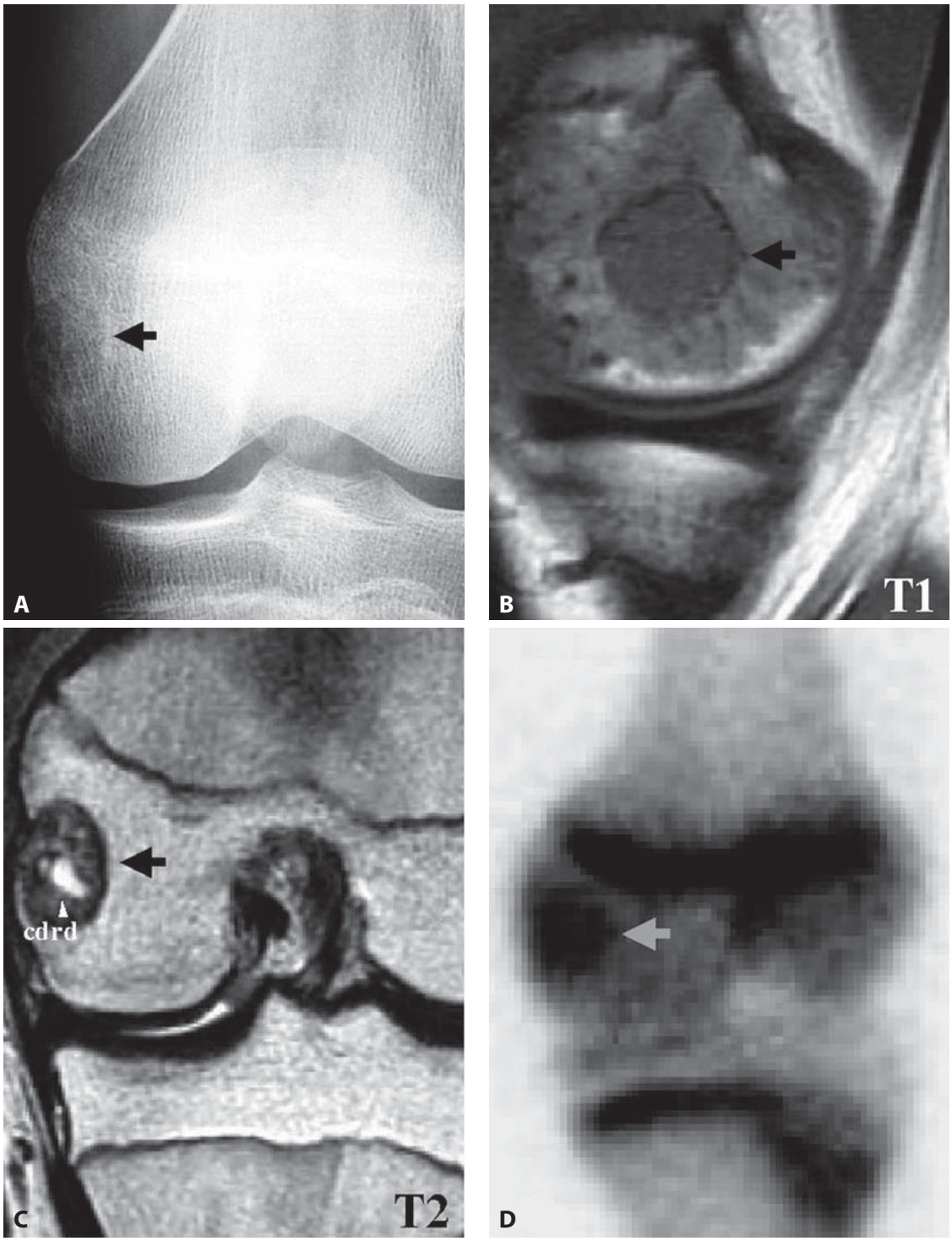

Fig. 18.14A–D Radiographic, MRI and planar scintigraphic correlation of poorly defined chondroblastoma in the distal femur. **A** Anteroposterior radiograph of the left distal femur in a 15-year-old boy shows faint eccentric tumor in the medial epiphysis (*arrow*). The proximal tibial physis is open. **B** Sagittal T1-weighted MR image reveals low–intermediate signal in the tumor matrix (*arrow*). The rind is sharply delineated with low signal. **C** Coronal T2-weighted MR image shows mixed signal in the matrix with high signal in chondroids (*cdrd*). Histology showed the chondroids to constitute about 40% of the tumor matrix. **D** Anterior planar scintigraph reveals intense tracer uptake (*arrow*)

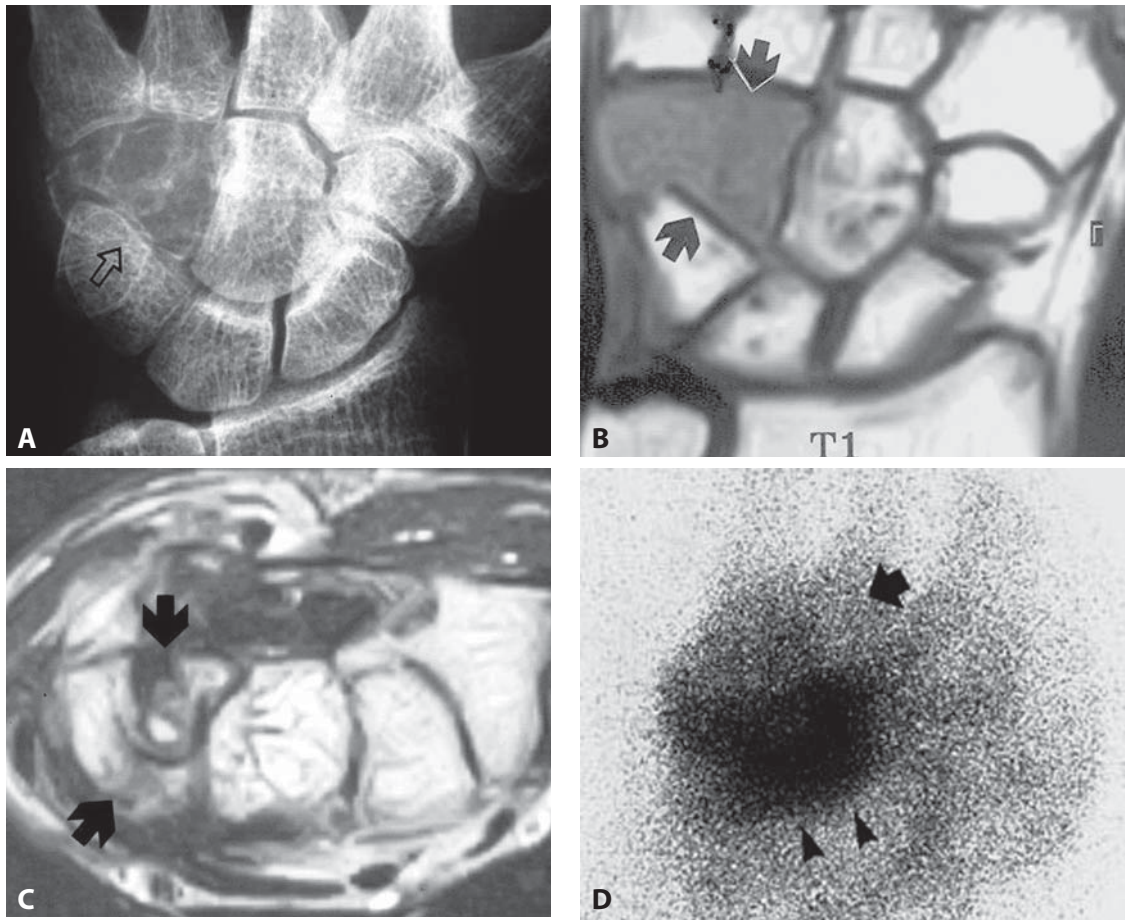

Fig. 18.15A–D Partially mineralized chondroblastoma in the carpal bone with pseudoseptation. **A** Dorsopalmar radiograph of the left wrist in a 39-year-old man shows radiolucent tumor with irregular septum-like mineralization in the hamate (*open arrow*). **B** Coronal T1-weighted MR image reveals low–intermediate signal in the bland tumor matrix in the outer zone and low signal in the mineralized matrix in the inner zone (*arrows*). **C** Transaxial T2-weighted MR image shows mixed signal in the tumor matrix (*lower arrow*) and low signal in the mineralized matrix (*upper arrow*). **D** Dorsal pinhole scintigraph reveals the tumor to consist of unchanged uptake in the bland tumor matrix (*arrow*) and high uptake in the mineralized matrix (*arrowheads*). Findings closely match in **B** and **D** but not in **C** and **D** due to the difference between projections

Three-phase bone scan reveals increased blood pool and bone uptake (Humphry et al. 1980). Tumor uptake is homogeneously intense on planar bone scans (Fig. 18.14D). However, the pinhole scan separates such homogeneous uptake into various components, as does MRI. Thus, uptake may be unchanged, increased or decreased (Figs. 18.13D and 18.15D). MRI correlation in our cases suggests that unchanged uptake is associated with a bland tumor matrix with or without chondroid (Fig. 18.13) and increased uptake with mineralization. Mineralized matrix on MRI shows low or isointense signal, and demonstrates increased or intermediate uptake (Figs. 18.13 and 18.15).

18.1.8 Fibrous Cortical Defect and Nonossifying Fibroma

These two conditions are closely interrelated, and, hence, have been described as evolutional forms of the same process (Jaffe 1958a; Mirra 1989a). Pathologically, lesions consist of fibrous tissue that is nonneoplastic and characterized

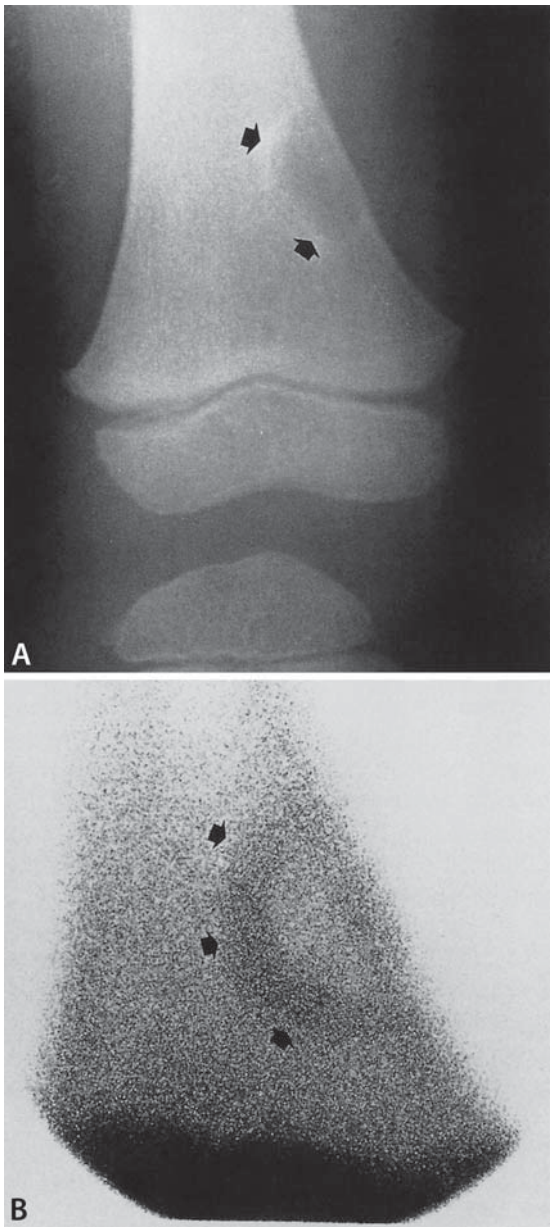

Fig. 18.16A, B Fibrous cortical defect. **A** Anteroposterior radiograph of the right distal femur in a 4-year-old boy shows a plum-sized lucency with a thin sclerotic rim in the medial aspect of the distal metaphysis. The defect is vertically aligned, abutting the cortex (*arrows*). **B** Anterior pinhole scintigraph shows a photopenic defect with a rim of very subtly increased tracer uptake (*arrows*). The thickness of the rim is obviously much greater than that of the radiographic rim, probably reflecting bone repair about the defect, although the lesion was clinically asymptomatic

by transient spindle-cell mesenchymal hyperplasia. Clinically, fibrous cortical defect is an ephemeral, asymptomatic and innocuous condition, mostly detected by chance in young children. The occurrence is solitary within the cortex of growing long bones. The vast majority of cases are slowly engulfed and replaced by reparative mineralization and imperceptibly blend into the host bone cortex as remodeling, tubulation and repair progress, and finally vanish during childhood and adolescence. However, a fraction of fibrous defects may proliferate and evolve into nonossifying fibromas within the medullary space.

Radiographically, fibrous cortical defect presents as a longitudinally stretched lucent defect surrounded by a thin sclerotic rim in the metaphyses of the long bones (Fig. 18.16A). The lesions are intra- or juxtacortical in location. With remodeling and tubulation or repair the rim slowly becomes obliterated from without and incorporated into the contiguous endosteum and cortex. At this time comet-like mineralization appears at the diaphyseal aspect of the radiolucent fibrous defect (Fig. 18.17A), and the "comet" appears to represent the rear of remodeling and tubulation that has a low MRI signal intensity (Fig. 18.17B). The mineralization is the extension of the endosteum and cortex, which also enshrouds the vanishing fibrous defect (Fig. 18.17A).

The comet-like repair mineralization at the diaphyseal side of the fibrous cortical defect seems to reflect the fact that the condition is influenced by the growth of the host bone. In this connection, it is of much interest that a similar change occurs in enostosis that emanates spicules from the diaphyseal border (Fig. 18.7) and also in enchondromas whose diaphyseal border is irregular with scintigraphic penumbra (Figs. 18.9 and 18.10), and that the change is related to remodeling and tubulation. Another significant feature common to the tumors and tumorous conditions in question is that their long axes are aligned with those of the host bones. As mentioned above, this finding may be termed the *longitudinal alignment sign*. A similar sign is also appreciated in nonossify-

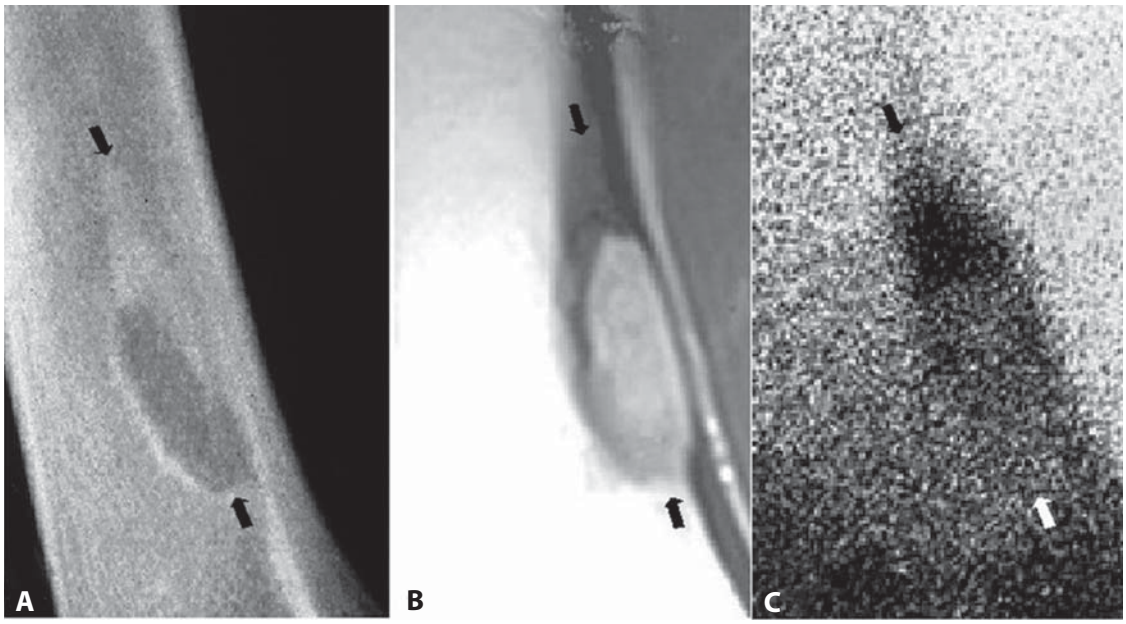

Fig. 18-17 A-C Fibrous cortical defect. **A** Lateral radiograph of the right distal femur in a 15-year-old girl shows a coaxially elongated lucent lesion surrounded by thin sclerotic rind in the juxtacortical zone of the metadiaphysis (arrow). Rind is partially incorporated into the contiguous endosteum, denoting repair in progress. Note comet-like mineralization at the rear or diaphyseal aspect (upper arrow). **B** T1-weighted coronal MRI reveals fibrous tissue with high signal intensity and repair mineralization with low signal intensity (upper arrow). **C** Anterior pinhole scintigraph reveals comet-like tracer uptake in repair mineralization in the rear (upper arrow) and low uptake in vanishing fibrous defect (lower arrow)

ing fibroma (Fig. 18.18), unicameral bone cysts in the long bones (Fig. 18.19) and flat bones (Fig. 18.24), and exostosis (Fig. 18.54), the evolution and involution of which are more or less intimately related with host bone growth. Cardinally, the sign may not appear in tumors or tumorous conditions of bone that are not related to bone development. It may also not occur in malignant bone tumors, the majority of which destroy the host bone in a short period of time not letting it to grow longitudinally with a sclerotic or preserved demarcation.

Nonossifying fibromas manifest as ovoid lucent lesions in the long bone metaphyses, whose border is defined by a sclerotic rim. The long axis of this tumor is also longitudinally oriented. In the late involutional stage it becomes mineralized and a smooth cortex develops to form an opaque tumor that is partially incorporated into the host bone cortex (Fig. 18.18A). Mirra (1989a) described a case of nonossifying fibroma with similar ossification in a 22-year-old woman (his Fig. 9.8A).

Ordinary scintigraphy is inappropriate for the study of many fibrous cortical defects because tracer uptake is usually low. Pinhole scintigraphy, however, can show even extremely subtle uptake that encircles a photopenic lesion that is contiguous with the cortex. Characteristically, tracer uptake is confined to the sclerotic periphery of the fibrous defect in the early phase (Fig. 18.16B) and gradually fills in the center during the involutional stage (Fig. 18.17C). With time, tracer uptake wanes at the metaphyseal aspect of the lesion where repair is finished but persists as polar uptake at the diaphyseal aspect where repair mineralization is still in progress (Fig. 18.17A, B). Tracer uptake in nonossifying fibromas in the late regressive stage with diffuse ossification is remarkably intense (Fig. 18.18B).

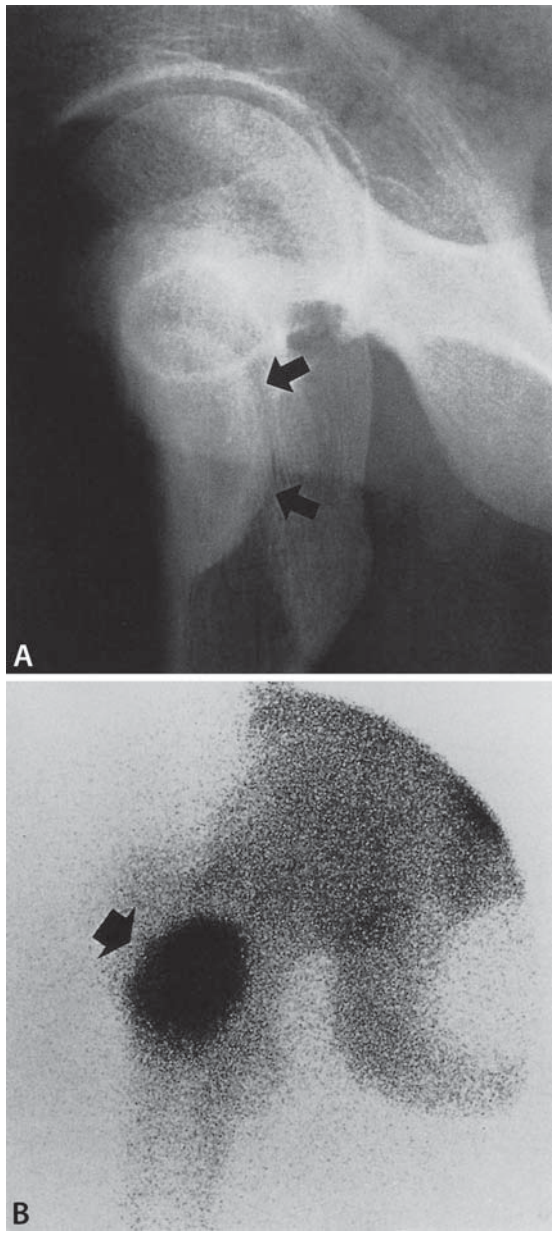

Fig. 18.18A, B Ossification in late regressive fibroma. **A** Lateral radiograph of the right proximal femur in a 24-year-old young man shows a small hen-egg sized, ossified tumor in the subtrochanteric region anteriorly, abutting the cortex (*arrows*). **B** Anterior pinhole scintigraph reveals homogeneous, intense tracer uptake in the tumor (*arrow*), reflecting ossification

Fibrous cortical defects may simulate simple bone cysts, but the intramedullary location of the former lesion is eccentric and the latter concentric (Fig. 18.19A). Nonossifying fibromas are also eccentric. It is to be noted that pinhole scintigraphy can diagnose simple bone cyst by delineating its fibrous wall. When mineralized nonossifying fibroma may resemble unicameral bone cyst with thickened wall; however, unlike mineralized fibroma, an uncomplicated bone cyst containing fluid is photopenic (Fig. 18.19B).

18.1.9 Osteochondroma (Exostosis)

Osteochondroma (exostosis) is a benign bony protuberance with a cartilaginous cap that originates from the cortex of the long bone metaphysis. The mechanism by which osteochondroma is formed was proposed hypothetically by Keith in 1920 (Keith 1920). He thought that the tumor results from the herniation of epiphyseal cartilage through a rent in the periosteal cuff of bone that surrounds the vacuolating zone of the epiphyseal cartilage, and D'Ambrosia and Ferguson (1968) experimentally substantiated the hypothesis. The tumor, formed from enchondral ossification of the cartilaginous cap, consists of ordinary cortex and medullary bone with either hematopoietic or fatty marrow. It is sessile or pedunculated in shape. When multiple the condition is called hereditary multiple exostoses, which has a great propensity to malignant transformation. The prevalence ranges from 20% to 35.8% of all benign tumors, and it is therefore one of the most common benign tumors. About 75% of solitary lesions occur before the age of 30 years. Symptoms are physical in nature, relating to the tumor size and location. Mechanical irritation, nerve compression, fracture, or malignant transformation cause pain, but the vast majority remain as a painless lump of long duration.

Radiographic features differ according to the tumor type: pedunculated, flat, or sessile. The first type is characterized by a bony protuberance with a cartilaginous cap (Figs. 18.20A and 18.21A), the second type by a flat excrescence with a saucer-like basin (Fig. 18.22A),

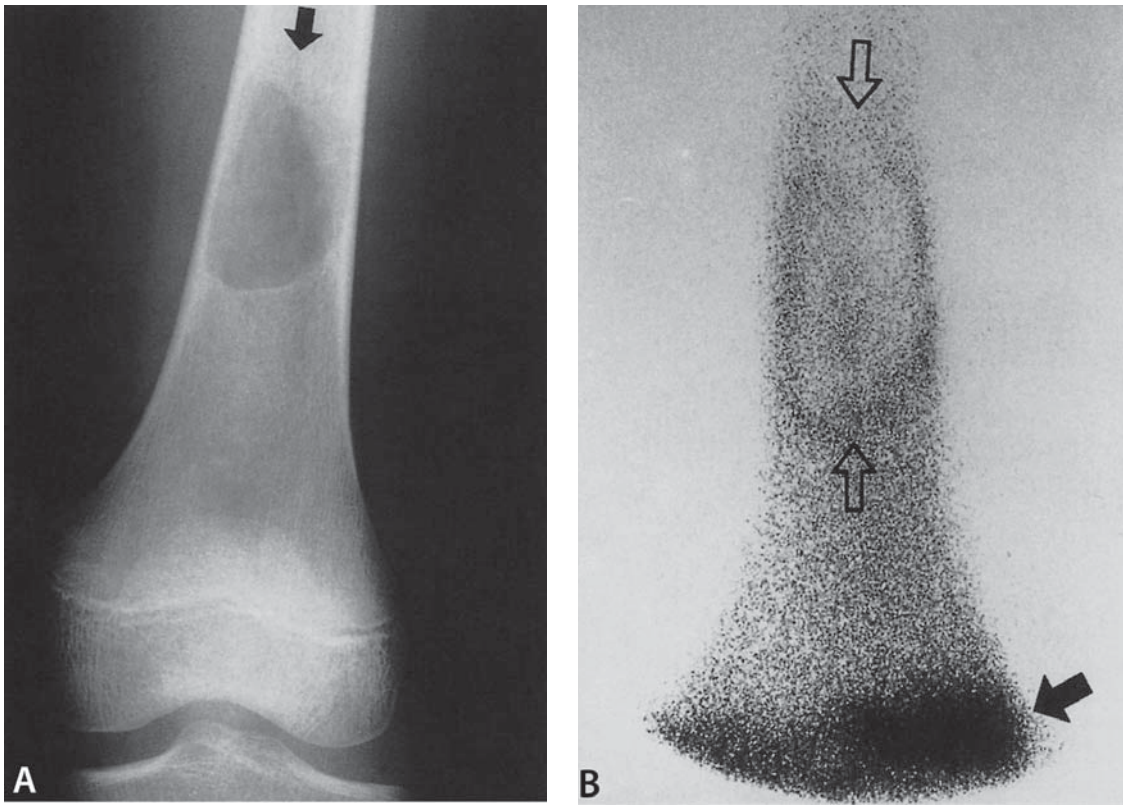

Fig. 18.19A, B Simple bone cyst. **A** Anteroposterior radiograph of the left distal femur in a 12-year-old boy with local pain shows a well-defined, vertically aligned, ovoid radiolucency with generally sharp demarcation (*arrow*). **B** Anterior pinhole scintigraph shows an elongated, ovoid photopenic defect with a "hot" rim in the distal femoral diaphysis (*open arrows*). Note intense physiological tracer accumulation in the distal femoral physis (*solid arrow*). The lesion was only suspicious on the ordinary planar image (not shown here)

and the third type by a mound-like elevation (Fig. 18.23A). The cartilaginous element of the tumor at the crest is radiographically invisible. Pedunculated osteochondromas extrude from the metaphyseal side of the epiphyseal plate, pointing to the diaphysis in the long bones.

Scintigraphically, only the bony portion accumulates tracer. In general, tracer uptake tends to be minimal when the tumor is small and old (Fig. 18.20B) and rather intense when the tumor is large and young (Fig. 18.21B). Particularly intense tracer uptake is observed at the bone–cartilage junction of osteochondromas where active enchondral ossification is taking place. The sessile variants accumulate tracer typically in the basin when saucerized (Fig. 18.22B) and at the summit when elevated (Fig. 18.23B).

18.1.10 Primary Bone Cysts

Cysts that originate primarily from the bone marrow include simple (unicameral or solitary) cysts and aneurysmal cysts. The former is a true cyst, containing clear serous fluid and a fibrous lining, whereas the latter consists of a multilocular cystic mass containing freely flowing blood and rarely an endothelial lining. The aneurysmal bone cyst is not a true cyst. It is a kind of arteriovenous malformation produced as a complication of some primary bone tumors or by trauma (Mirra 1989b). About 95% of simple bone cysts affect the metaphyseal side of the physeal plate in actively growing long bones. The absolute majority occur in the first and second decades of life, and boys are affected 2–2.5 times more often than girls. A report has indicated a prevalence of about 3% of all

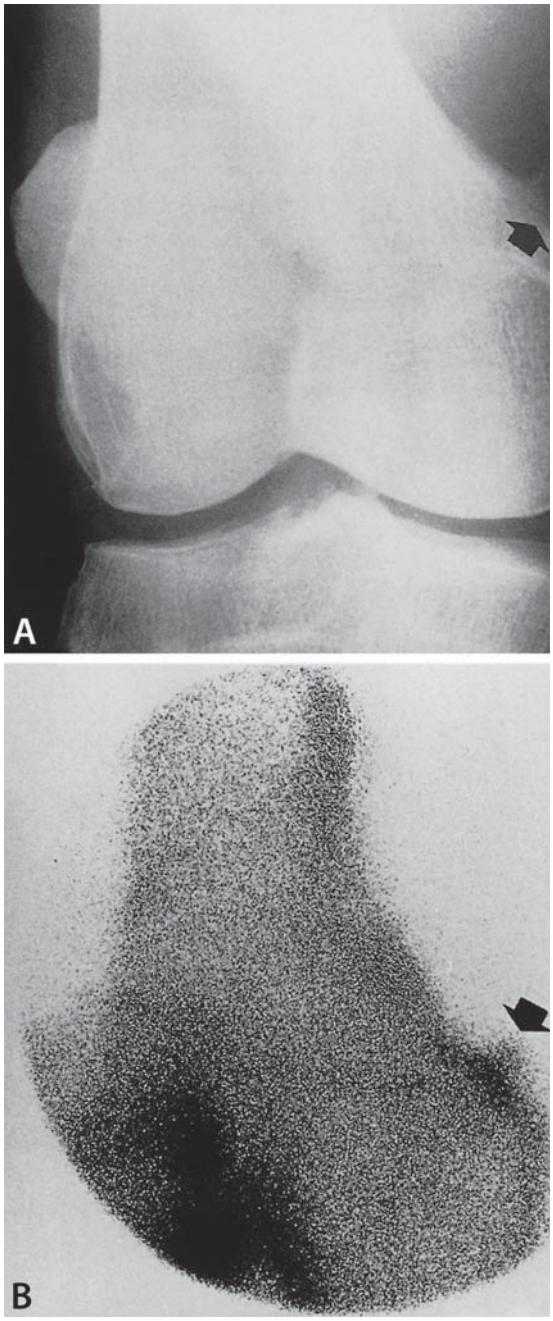

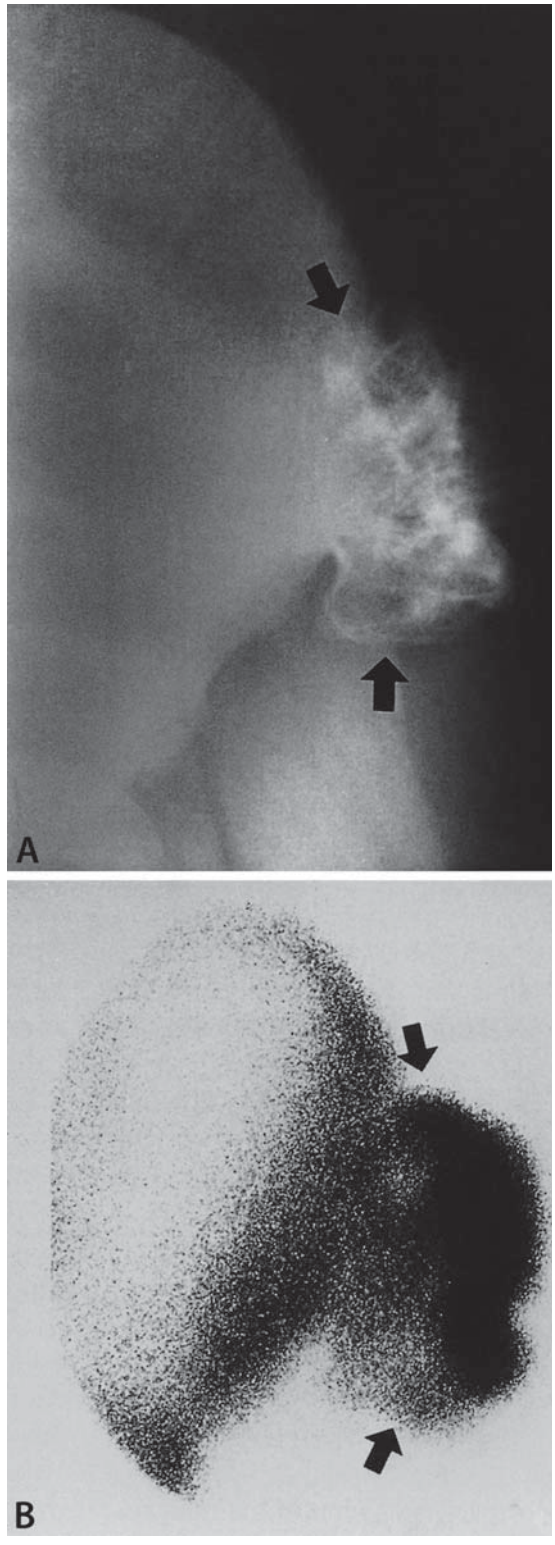

Fig. 18.20A, B Small exostosis in an old subject. **A** Anteroposterior radiograph of the right distal femur in a 69-year-old man reveals a small osseous projection arising from the medial aspect of the epimetaphysis (*arrow*). **B** Pinhole scintigraph indeed shows minimal tracer uptake in the small bony excrescence (*arrow*). The tumor was not seen on the ordinary spot scintigraph (not shown here)

◁ **Fig. 18.21A, B** Large exophytic osteochondroma in a young subject. **A** Anteroposterior radiograph of the left iliac bone in a 15-year-old boy with a hard lump in the left lower flank reveals an irregularly shaped bone tumor arising from the anterior superior iliac spine (*arrows*). The tumor crest is wavy in appearance and capped with cartilage that was confirmed by CT scan. **B** Anterior pinhole scan shows modestly increased tracer uptake in the tumor that is similar in intensity to that of the host bone. However, the tumor crest shows extremely intense uptake. The tumor was seen simply as a "hot" lesion on the ordinary scintigraph without differential uptake (not shown here)

biopsied bone tumors (Mirra 1989b). The proximal humerus and femur are involved in about 90% of cases, with occasional cases involving the pelvis and other bones of the limbs. With growth, the cyst gradually migrates toward the shaft.

Radiographically, unicameral bone cysts in infancy present as well-defined, slightly expansive, ovoid lucencies in the medullary space of the long bone metaphysis, which gradually migrate to the diaphysis with age (Fig. 18.19A). Most cysts show a thin sclerotic rim. The cysts in the flat bones also present as ovoid radiolucencies surrounded by a smooth sclerotic rim (Fig. 18.24A). Some cysts are septated. When the cystic fluid is dried and replaced by reparative osteofibrosis due to aging (Jaffe 1958b), fracture or bleeding, cysts may become organized and eventually faintly mineralized (Fig. 18.25A). Although rare, the "fallen fragment" sign is pathognomonic of simple bone cyst with chip fracture; the sign denotes a fracture fragment that moves around freely within the fluid-filled cystic cavity. If such a fragment is held undetached at the fracture site, it presents as a focal elevation of the bony wall (Fig. 18.24C).

Pinhole scintigraphy closely reflects the characteristic radiographic changes. Thus, cysts with fluid, blood and/or nonosseous tissue are indicated by ovoid or round hoop-like tracer uptake that surrounds photopenic content (Fig. 18.19B and 18.24B). On the other hand, aged bone cysts, whose fluid content has been replaced with reparative osteofibrosis, diffusely accumulate tracer, partially obliterating hoop-

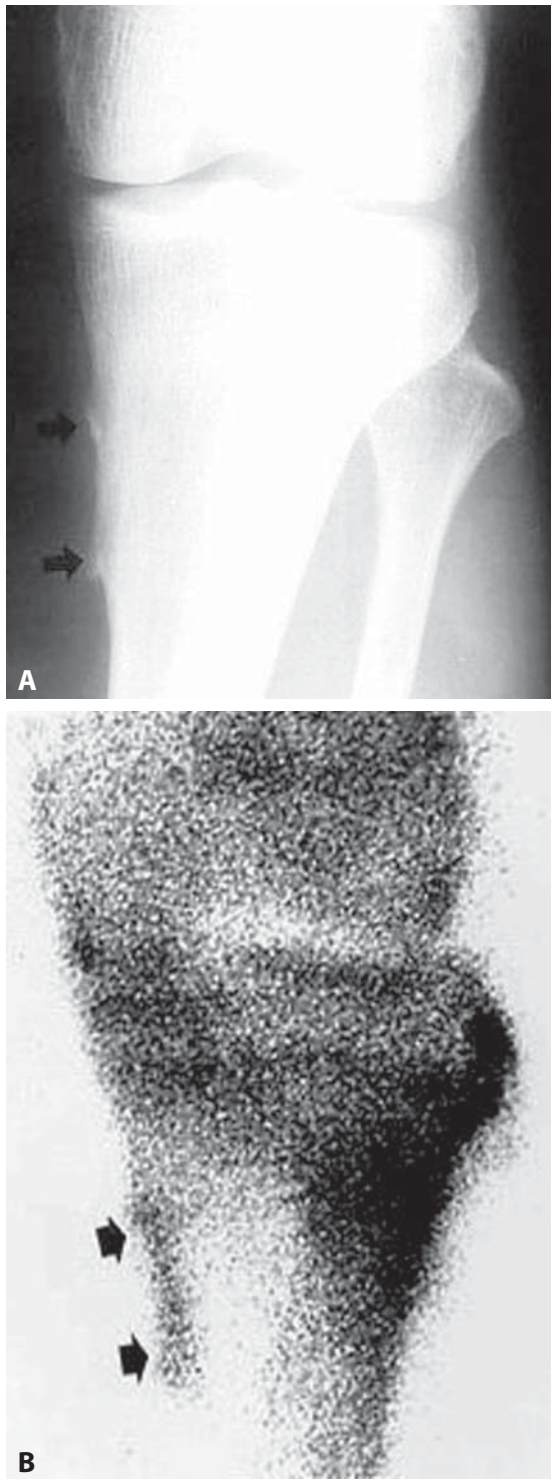

Fig. 18.22A, B Osteochondroma with a flat excrescence with a saucer-like basin. **A** Anteroposterior radiograph of the left proximal tibia shows a mild, flat elevation of the cortex at the medial aspect of the metadiaphysis (*arrows*). **B** Anterior magnified planar scintigraph reveals flat intracortical tracer uptake (*arrows*)

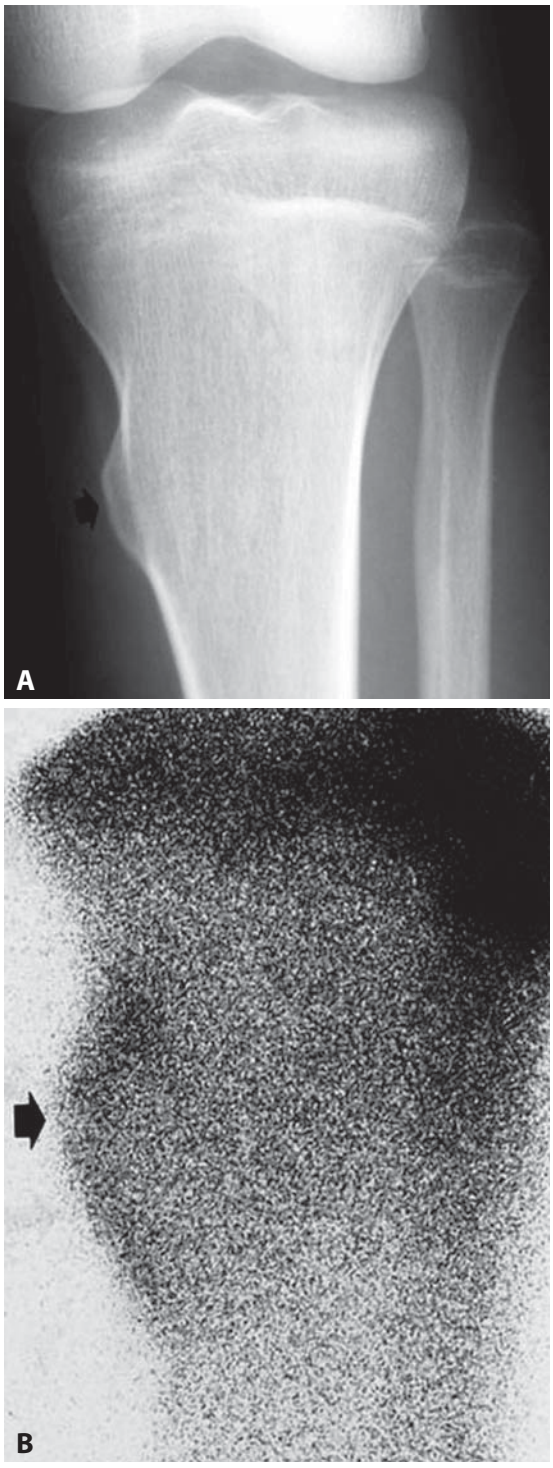

Fig. 18.23A, B Osteochondroma with a mound-like elevation without saucerization. **A** Anteroposterior radiograph of the left proximal tibia in a 16-year-old boy shows mild elevation of the cortex at the medial aspect of the metadiaphysis (*arrow*). **B** Anterior magnified planar scintigraph reveals subtle tracer uptake at the crest (*arrow*)

like uptake in the sclerotic wall with extended uptake in the adjacent bone (Fig. 18.25B). Understandably, the fallen fragment within a bone cyst is scintigraphically undetectable because of devascularization, but the fragment not fully detached from cyst wall may accumulate tracer (Fig. 18.24B). CT is most helpful in confirming undetached fractures in the cyst wall (Fig. 18.24C).

18.1.11 Aneurysmal Bone Cysts

Aneurysmal bone cyst is a spongy, multilocular, cystic lesion containing freely flowing blood or fluid. Manifesting rapid bone expansion with rather haphazard bone destruction, the lesion often mimics malignancy. The etiology is related to local trauma and hemodynamic change, and underlying diseases in the secondary type. Giant cell tumor, chondroblastoma, simple bone cyst, telangiectatic osteosarcoma, or other tumor are underlying in about one-third of cases. Some aneurysmal bone cysts are attended by prominent periosteal new bone formation while others are osteoblastic or filled with new bone (Hudson 1984). About 80% of patients are under 20 years of age. It is rare before the age of 5 years or after 50 years. Aneurysmal bone cysts affect virtually any bone, but about 70% of are found in the long bones and spine (Mirra 1989b). Unlike simple bone cysts, aneurysmal bone cysts involve the skull, mandible, maxilla, ribs, and patella. Swelling and pain are the main presenting symptoms in some 85% of patients.

The characteristic radiographic features include eccentric or concentric "blowout" or "bubbly" lysis in the long bone metaphyses (Fig. 18.26A), vertebrae, ribs (Fig. 18.27A), and other bones. Lesional borders are usually not sclerotic, and the overlying cortex is ballooned and extremely thinned but intact unless fractured (Fig. 18.28A). Periosteal thickening and lifting may result when the cystic change is aggressive and rapidly expansive. Occasionally, Codman's triangle is present. In the spine, lysis occurs in the vertebral body or the posterior structures, and when it affects the anterior portion of the rib, expansion is delimited by cartilage (Fig. 18.27A).

Scintigraphic manifestations include increased tracer uptake in the periphery of cysts with a central photon defect. Generally, tracer uptake is not so intense in aneurysmal bone cysts, and no correlation exists between the uptake pattern and histology (Hudson 1984). In occasional cases, pinhole scanning shows septation, reflecting the bubbly nature of aneurysmal bone cysts (Figs. 18.27B). Unlike sharply defined hoop-like uptake of simple bone cysts (Fig. 18.19B), the peripheral uptake in aneurysmal bone cysts is irregular. Small fractures in the ballooned wall of an aneurysmal bone cyst, not detected by radiography, can also be clearly indicated by spotty uptake (Fig. 18.28B).

18.1.12 Giant Cell Tumor

This is a common bone tumor of adults in the third or fourth decade of life; it comprises 5% of all bone tumors. Pathologically, the tumor is characterized by benign-looking osteoclast-like giant cells, connective tissue, and stromal cells. The tumor has a predilection for the long bone ends, and is eccentric in location. In more than 50% of cases the knee bones are affected, and the next most common sites are the distal end of the radius and the sacrum. The skull and the spine are rarely involved. In most series, women have been affected slightly more commonly than men. Symptoms and signs include pain, tenderness, swelling, and limited motion with occasional fractures.

The characteristic radiological features include localized osteolysis with trabeculation in

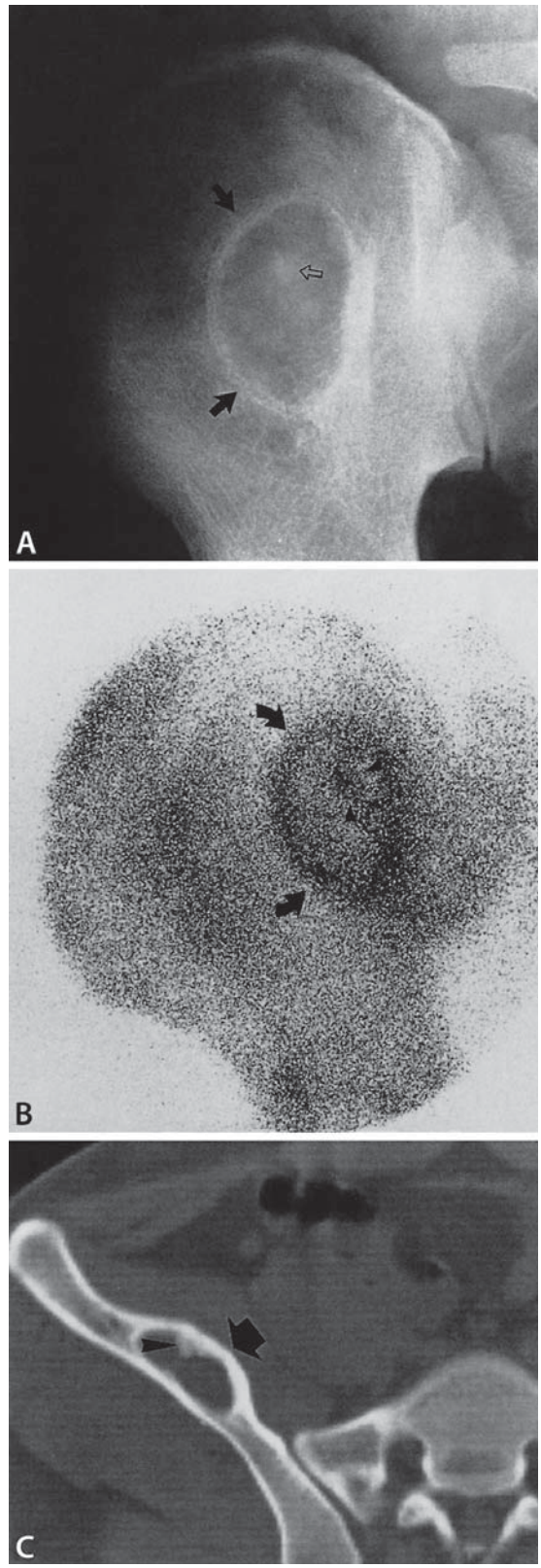

Fig. 18.24A–C Primary bone cyst in flat bone. **A** Anteroposterior radiograph of the right iliac bone in a 17-year-old young man shows a large, ovoid, vertically aligned, lucent lesion with sclerotic rim in the iliac fossa (*arrows*). A small island-like density is seen in the upper central aspect (*open arrow*). **B** Anterior pinhole scan shows a large, ovoid, photopenic defect with a "hot" rim in the iliac fossa (*arrows*). In addition, a small, separate, spotty uptake is noted in the upper central aspect of the defect (*arrowheads*). **C** Transverse CT scan demonstrates an expansile bone lesion with fluid density and bulging sclerotic cortex (*arrow*). A small, undetached fracture fragment is visualized in the anterior wall (*arrowhead*). The island-like density seen in the radiograph and scintigraph is most probably an incomplete fracture in the cyst wall

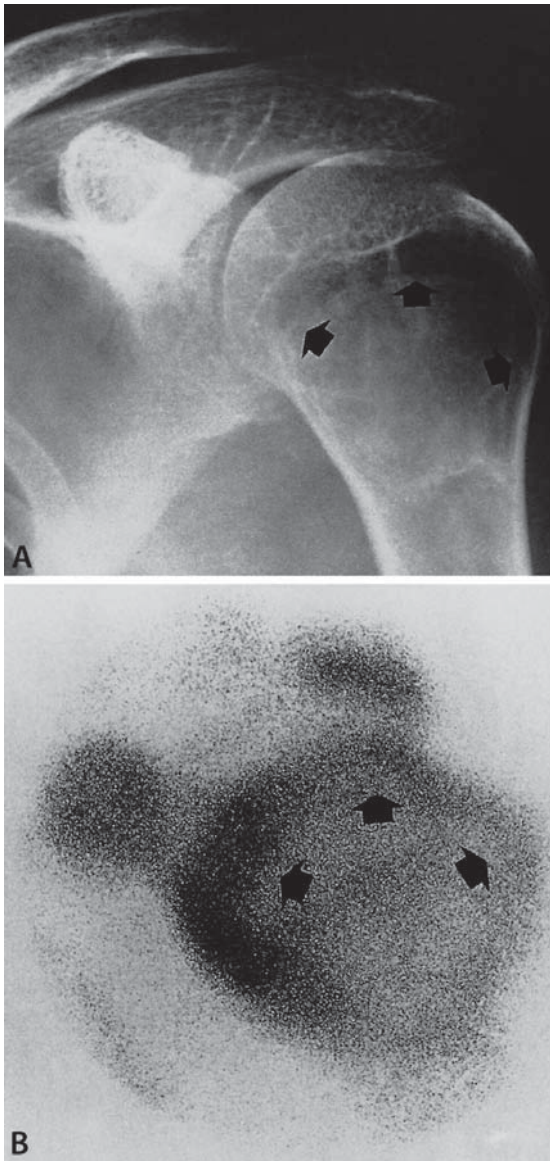

Fig. 18.25A, B Aged bone cyst with osteofibrosis. **A** Anteroposterior radiograph of the left shoulder in a 48-year-old man reveals a truncated, well-demarcated tumor located centrally in the proximal humeral metaphysis. The tumor is slightly calcified (*arrows*). **B** Anterior pinhole scintigraph shows the tumor to be essentially photopenic. The surrounding bone shows increased tracer uptake, probably extended tracer uptake (*arrows*). Note that the "hot" rim has disappeared

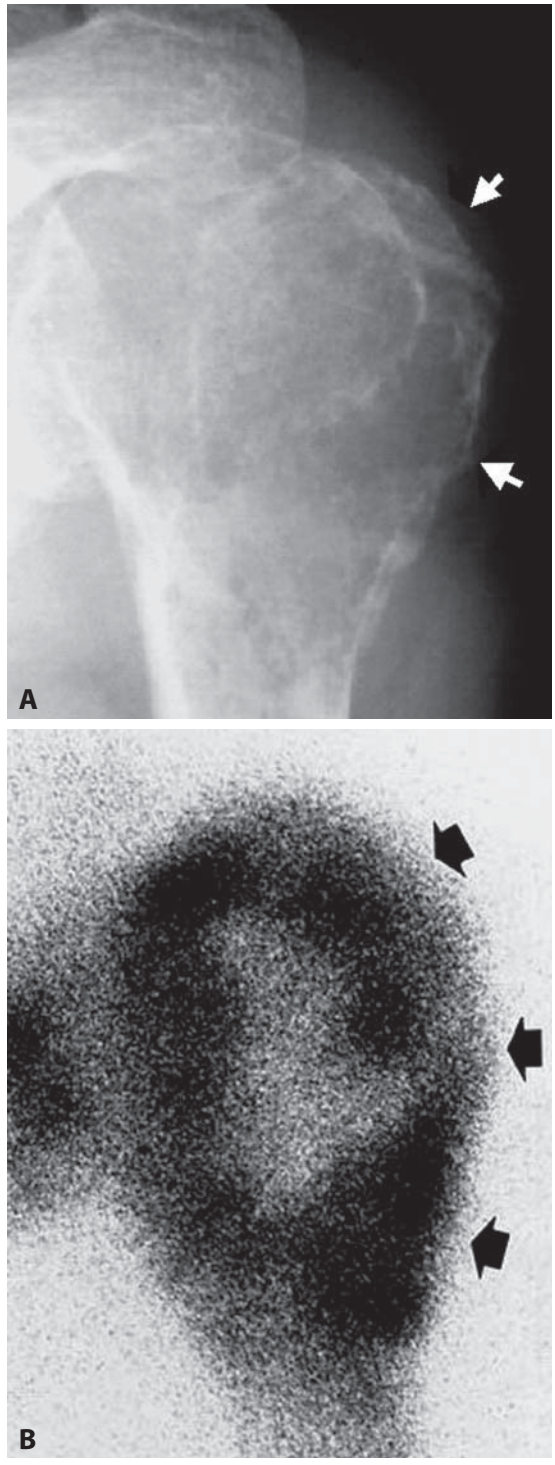

Fig. 18.26A, B Aneurysmal bone cyst of the humeral neck. **A** Anteroposterior radiograph of the left proximal humerus in a 67-year-old woman with cystic degeneration of a fibrous tumor shows ballooning of the lucent tumor with an extremely thin cortex (*arrows*). **B** Anterior pinhole scintigraph reveals prominent tracer uptake in the ballooned cyst wall with photopenic content (*arrows*)

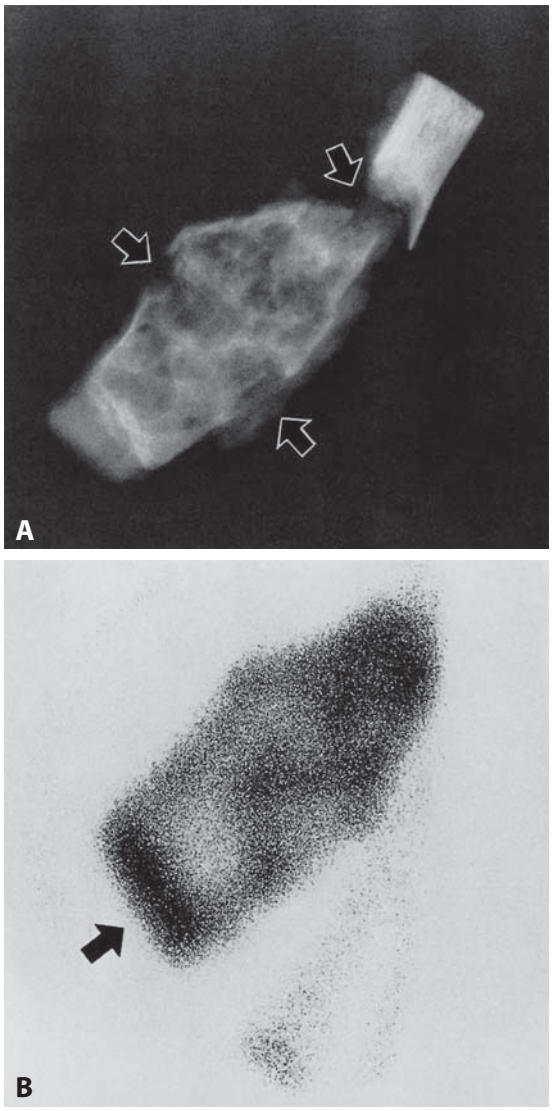

Fig. 18.27A, B Photon defects of secondary aneurysmal bone cyst. **A** Radiograph of the left seventh rib resected for cystic fibrous dysplasia with fracture in a 17-year-old male shows irregular lucent lesions with ballooning and rupture (*arrows*). **B** Anterior pinhole scintigraph reveals well-comparable photon defect of cysts (*arrows*)

the long bone epiphysis with metaphyseal extension after physeal fusion (Fig. 18.28A) and ballooning or lobulation in the flat and irregular bones such as the pelvis, the sacrum, and the skull (Fig. 18.29A). Lysis is geographic in appearance and confined within the host bone unless complicated by aneurysmal change. In some tumors the margins are permeated and ballooned with erosion of the overlying cortex. Cortical rupture is uncommon, but when present it is due to cystic change and trauma (Fig. 18.28C). Some giant cell tumors are modified with a cyst-like formation lined with fibrous connective tissue, which are likely to be related to hemorrhage (Mirra 1989d). MRI is unique for the delineation of the entire lesion as well as tissue characterization and cyst-like modification (Fig. 18.29B).

Bone scanning reveals ring-like or diffuse tracer uptake that is usually intense (Van Nostrand et al. 1986). Extended uptake around the tumor is a common phenomenon, rendering the true tumor margin difficult to define (Levine et al. 1984). Pinhole scintigraphy shows giant cell tumors as round, often lobular, photopenic masses with diffuse peripheral tracer uptake (Figs. 18.28B and 18.29C). When aneurysmal cystic change is present the tumor rapidly expands with spotty uptake in occasional pathological suptures (Fig. 18.28B).

18.1.13 Vertebral Hemangioma

Bone hemangioma is not a common disease. It affects any bones in the middle-aged population. Women are affected twice as commonly as men. Histologically, the lesions are composed of vascular channels of the cavernous, capillary or venous type. Many lesions are asymptomatic and detected by chance.

The radiographic features include osteopenia, trabecular coarsening, and cortical thinning with cystic or other types of lysis. Hemangioma in the vertebrae may show tiny bubbly shadows mixed with stippled bones. Although reduced in number the trabeculae become thickened clearly standing out against the lucent background of vascular channels. Characteristically, such trabeculae are vertically arranged giving rise to a corduroy appearance (Fig. 18.30A). The changes may extend to the transverse process and other parts of the vertebra. CT and MRI are indeed useful for the diagnosis of hemangioma. MRI reveals a high signal intensity on enhanced T1-weighted and proton density images with vertically aligned low signal intensities of thickened trabeculae (Fig. 18.30B).

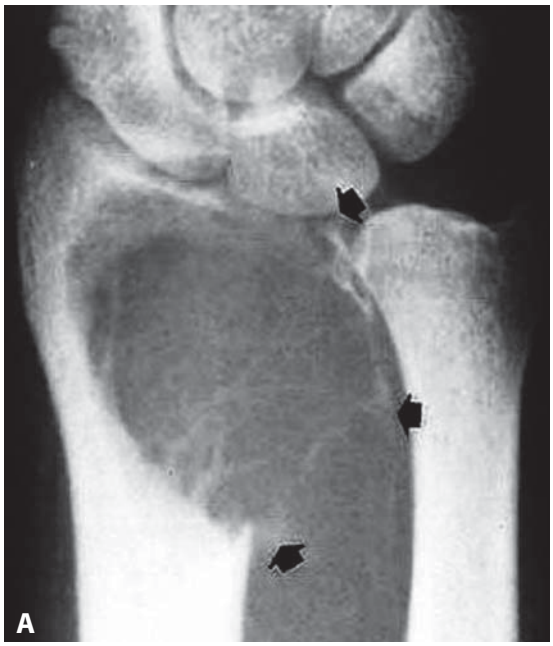

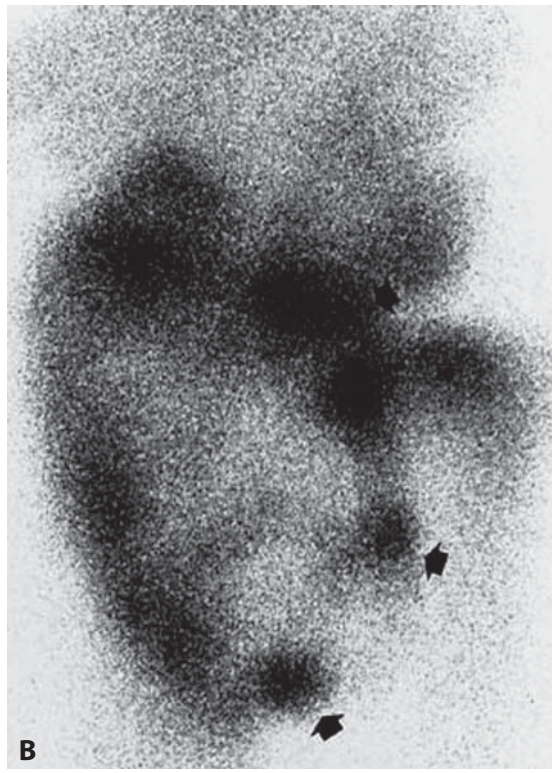

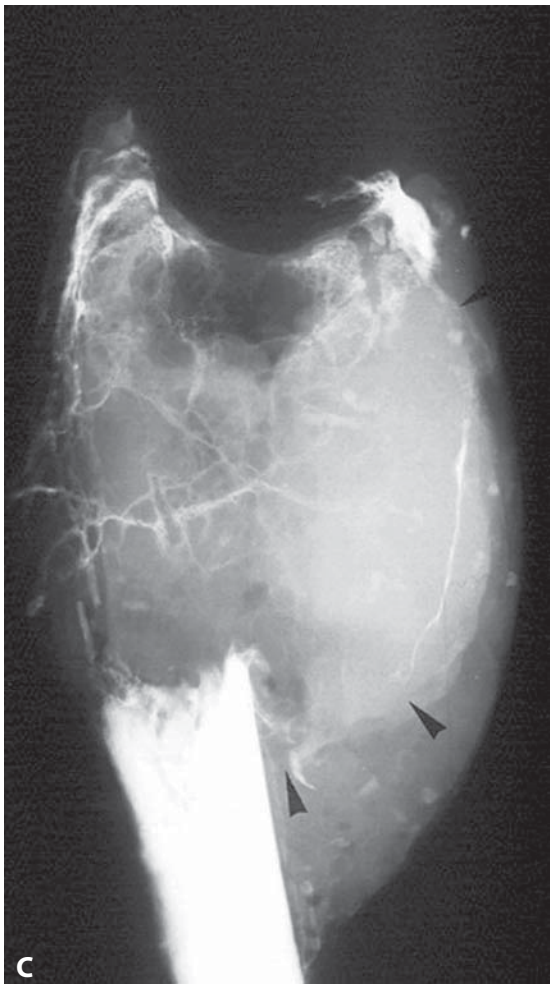

Fig. 18.28A–C Giant cell tumor with aneurysmal cyst change. **A** Dorsoventral radiograph of the right wrist in a 25-year-old man shows a large ballooning cyst with small suptures. **B** Anterior pinhole scintigraph reveals tracer uptake in the periphery of the ballooning cystic wall with spotty uptake in fractures (*arrows*). **C** Radiograph of resected tumor shows an expansive osteolytic tumor with stretched trabeculae and peripheral suptures (*arrowheads*)

Plain scintigraphy is usually not helpful, but the pinhole scan demonstrates a column of increased tracer uptake that is vertically oriented (Fig. 18.30C). This finding is considered to reflect the vertically aligned trabeculae that are thickened.

18.1.14 Periosteal Leiomyoma

Leiomyoma and its malignant counterpart, leiomyosarcoma, are extremely rare in bone. Conklin et al. (1981) reported a case of leiomyoma occurring in the tibia. The tumor showed diffuse, mild tracer uptake. A case of leiomyosarcoma arising from the rib is presented in Chapter 17 (Fig. 17.68).

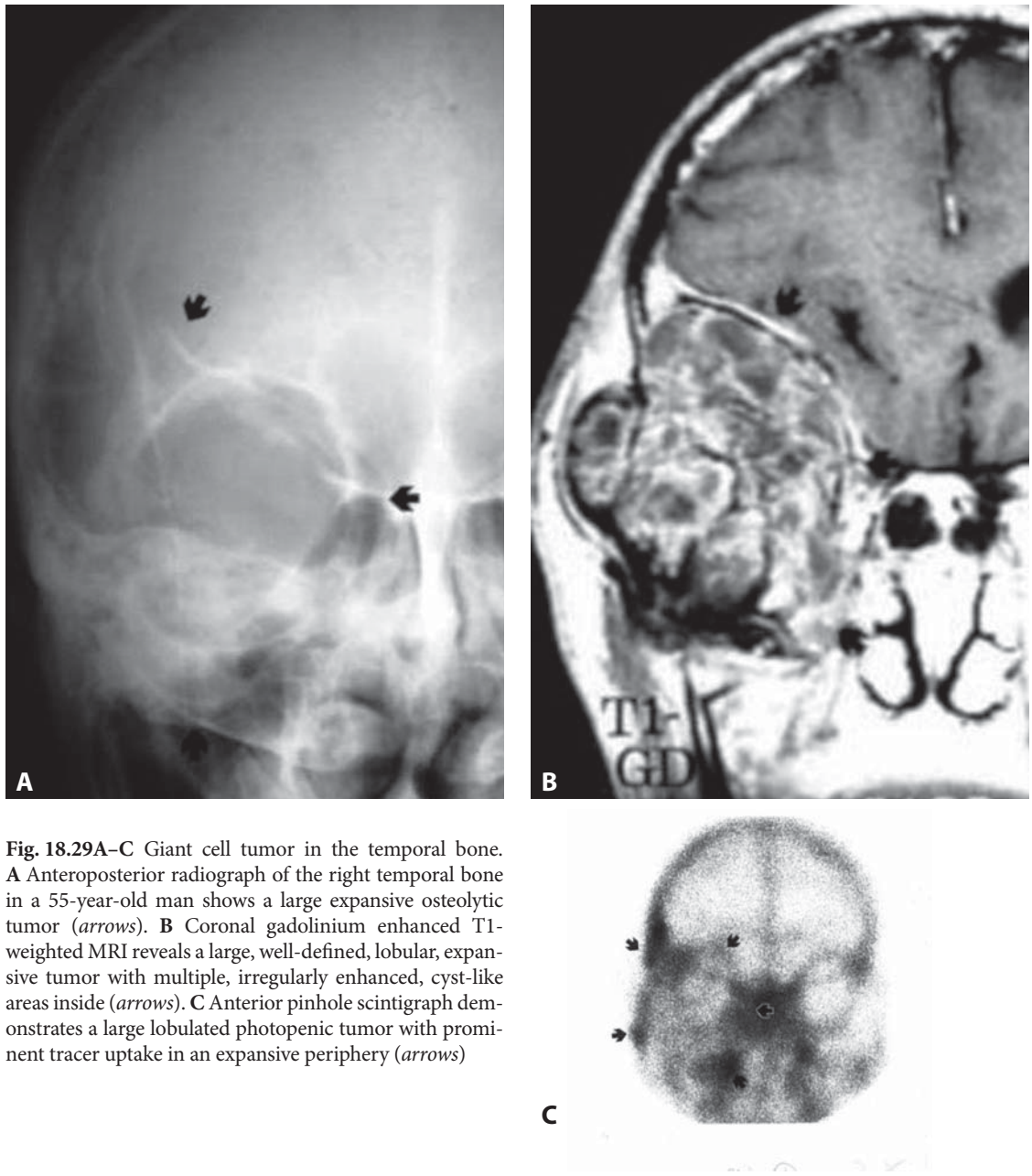

Fig. 18.29A–C Giant cell tumor in the temporal bone. **A** Anteroposterior radiograph of the right temporal bone in a 55-year-old man shows a large expansive osteolytic tumor (*arrows*). **B** Coronal gadolinium enhanced T1-weighted MRI reveals a large, well-defined, lobular, expansive tumor with multiple, irregularly enhanced, cyst-like areas inside (*arrows*). **C** Anterior pinhole scintigraph demonstrates a large lobulated photopenic tumor with prominent tracer uptake in an expansive periphery (*arrows*)

18.2 Tumorous Conditions of Bone

Tumorous conditions of bone are many. However, the present discussion is limited to some more common and scintigraphically important ones. They include fibrous dysplasia, juxtacortical fibromatosis, histiocytosis X, Paget's disease of bone, neurofibromatosis, Ollier's disease or osteochondromatosis, osteopoikilosis, and osteopetrosis.

18.2.1 Fibrous (or Fibro-osseous) Dysplasia

Fibrous dysplasia is an uncommon hamartomatous disease of bone related to developmental failure of bone forming mesenchyme. The etiology is obscure, and no hereditary trait has been established. Pathologically, the condition is characterized by metaplastic production of benign fibrous tissue stroma and spicules of woven bone formed therefrom; hence, fibro-osseous dysplasia. The bone spicules are C- or

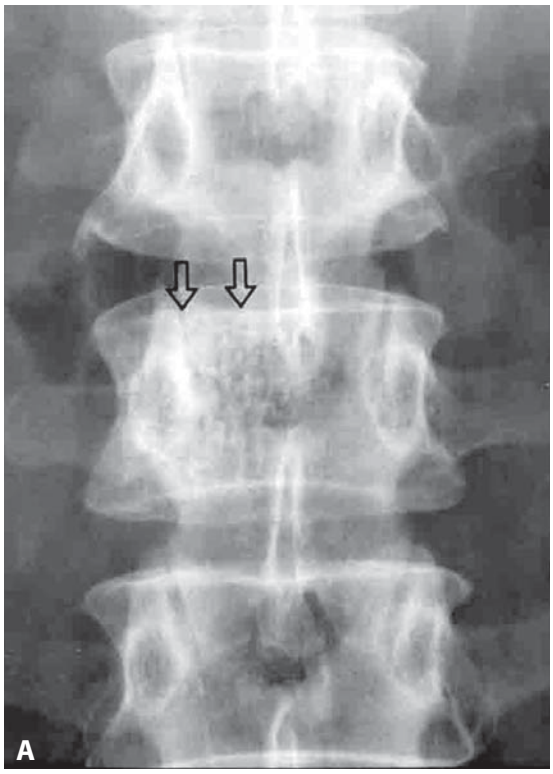

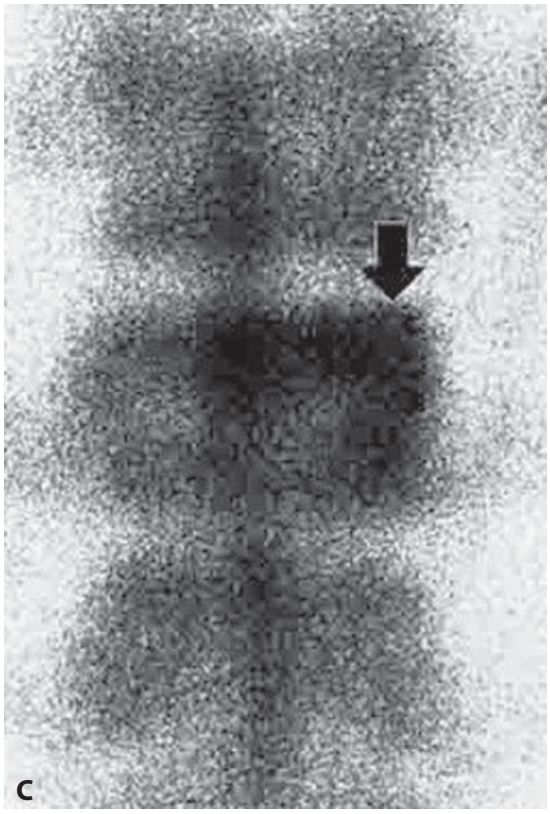

Fig. 18.30A–C Vertebral hemangioma. **A** Posteroanterior radiograph of the lumbar spine in a 60-year-old man shows small bubble-like lucent areas mixed with stippled bones in the right half of the L2 vertebral body (*open arrows*). **B** Proton-density sagittal MRI reveals high a signal intensity with vertical arranged corduroy-like low signal intensities (*arrow*). **C** Posterior pinhole scintigraph shows increased tracer uptake in the right half of the L2 vertebral body. Note the vertical orientation of the tracer uptake (*arrow*)

Y-shaped, curved, or straight and when intermingled they give rise to the "alphabet soup" appearance (Mirra and Gold 1989). The grade of ossification varies from site to site within the same lesion and from lesion to lesion in the same patient, making the proportion of the fibrous element to osseous element as well as radiographic and pinhole scan changes widely different. Microscopic cysts are common, and an ominous aneurysmal cyst has been reported. The disease may be either monostotic or polyostotic, with the former type being far

more frequent than the latter. The distribution of the polyostotic lesions can be bilateral, but a unilateral distribution is more typical. The incidence is less than 1% of primary bone tumors. About 85% of patients are under the age of 30 years. Unless local lesions are extensive or complicated by fracture, most monostotic lesions are asymptomatic and detected by chance. The polyostotic form can be grossly disfiguring. Fibrous dysplasia may occasionally be associated with sexual precocity and irregular café-au-lait pigmentation of the skin, which together comprise Albright's triad. No bone is immune, but the long bones, pelvis, ribs, and skull are most commonly affected.

Radiographic manifestations include an expansile ground glass-like and/or lucent bone defect with the obliteration of trabeculae, various amounts of ossification, and cyst formation (Figs. 18.31 and 18.32). The lesional margin is usually sclerotic. CT and MRI are useful for characterizing the various tissue components. The well-known shepherd's crook deformity of the proximal femur and the "candle flame" appearance of the long bones are characteristic signs. Pathological fracture is a common complication.

Whole-body bone scintigraphy can most efficiently detect polyostotic lesions (Fig. 18.33), and pinhole scintigraphy shows the characteristic features of the individual lesions (Fig. 18.31B). The tracer uptake in fibrous dysplasia is moderate to marked and just homogeneous on ordinary scans (Fitzer 1977; Büll et al. 1981). As anticipated, however, pinhole scintigraphy demonstrates that the texture of fibrous dysplasia is not plain but inhomogeneous and complex with photopenic and photodense elements, reflecting the complexity of the histology. In general, the fibrous and cystic lesions accumulate little or no tracer, whereas the osseous or mineralized foci intensely accumulate tracer (Fig. 18.31B). Understandably, pathological fractures accumulate tracer intensely (Fig. 18.32B).

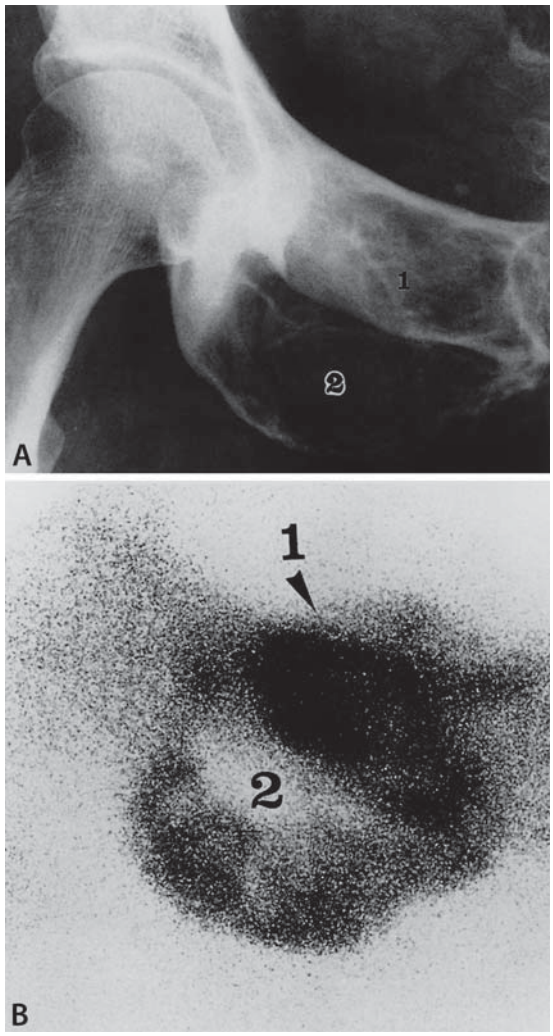

Fig. 18.31A, B Fibrous dysplasia. **A** Anteroposterior radiograph of the right ischiopubic ring in a 47-year-old woman shows large irregular lucencies with mesh-like trabecular bone in the superior pubic ramus (*1*) as well as cystic and ground-glass-like density in the inferior ischial ramus (*2*). The borders are sclerotic and the cortices expanded and thinned. **B** Anterior pinhole scintigraph shows very intense tracer uptake in the trabeculated, mesh-like superior pubic ramus (*1*) and an irregular photopenic defect in the cystic, lower ischial ramus (*2*)

18.2.2 Fibro-osseous Pseudotumor of the Digits

Fibro-osseous pseudotumor of the digits, or periostitis ossificans, is an injury-related disease of the periosteum not accompanied by bone fracture (Mirra 1989e). It has been described under various names such as parosteal

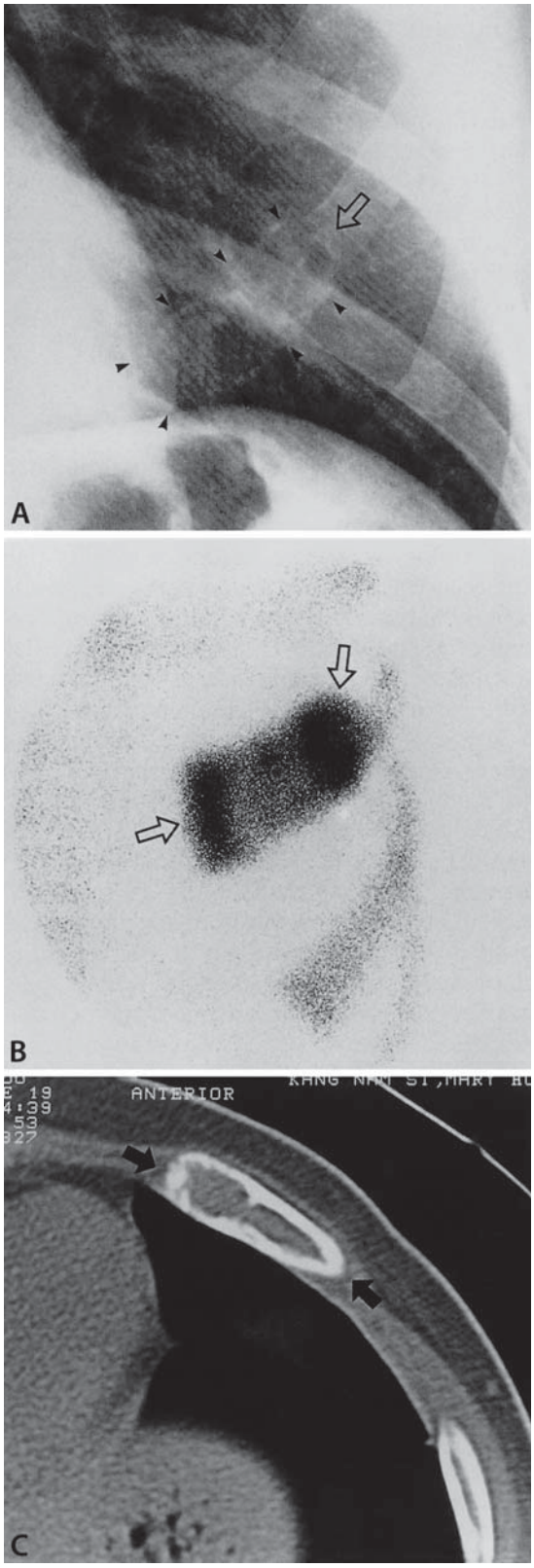

fasciitis and pseudomalignant tumor of the soft tissues. Clinically, the symptoms are characterized by localized, painful soft-tissue swelling, periosteal thickening and calcification. The fingers are affected far more frequently than the toes. In one series of 21 cases, 20 involved the fingers (Dupree and Enzinger 1986). The soft-tissue swelling or tumefaction may be prominent simulating malignancy and, hence, has earned the name of pseudomalignant osseous tumor of the soft tissues (Patel and Desai 1986). The rapidly growing variety may mimic extraskeletal osteosarcoma (Nishio et al. 2002). Women are predominantly affected. The pain in periostitis ossificans may be nocturnal and can be soothed by aspirin or NSAIDs as in osteoid osteoma.

Radiographically, the lesion is usually ill-defined with or without focal calcium deposits. In periostitis ossificans spotty calcification attached to the thickened periosteum may appear (Fig. 18.34A).

^{99m}Tc-MDP pinhole scanning reveals more intense tracer accumulation in the mineralized focus and less intense accumulation in the reactive change in the neighboring phalangeal bones (Fig. 18.34B).

18.2.3 Juxtacortical Fibromatosis (Desmoid Tumor of Soft Tissue)

Desmoid tumors arising from the extraosseous soft tissues and periosteums are rare. Desmoid tumors in contact with bone are termed juxtacortical or aggressive fibromatosis. The tumors

Fig. 18.32A–C Fracture in fibrous dysplasia. **A** Posteroanterior radiograph of the left chest reveals an irregular, expansile, lucent lesion in the anterior aspect of left rib 6 (*arrowheads*). A tiny cortical break is seen in the lateral border, representing a pathological fracture (*open arrow*). **B** Anterior pinhole scintigraph shows the lucent main lesion to concentrate tracer minimally and to be sided by very intense tracer uptake, especially in the lateral edge that is fractured (*vertical arrow*). The intense tracer uptake in the medial edge is in the costochondral junction (*horizontal arrow*). **C** CT scan delineates a more or less symmetrical, expansile, intramedullary lesion with a cortical break (*arrows*). The tumor tissue has a CT density equal to that of muscle

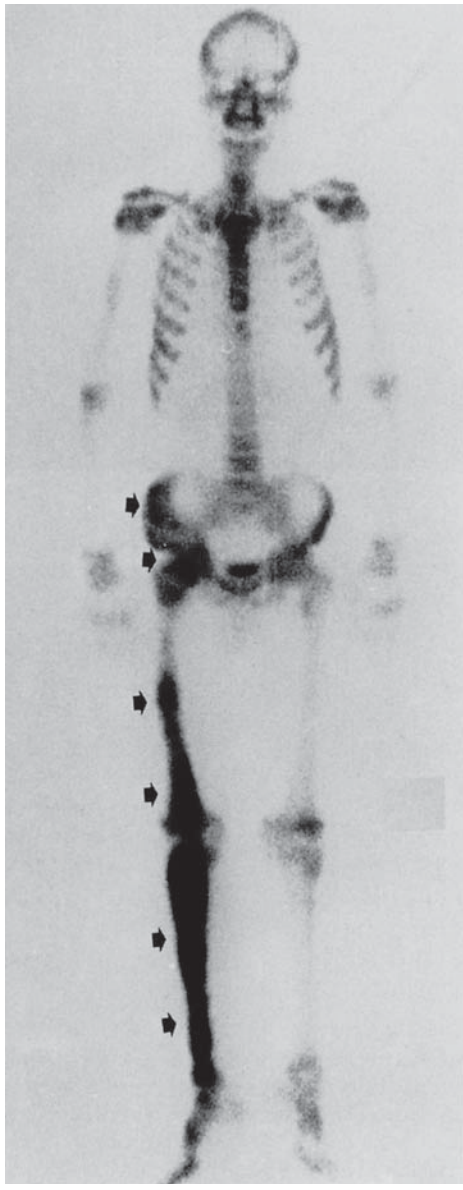

Fig. 18.33 Panoramic display of unilaterality and multiplicity of polyostotic fibrous dysplasia. Anterior whole-body scintigraph in a 55-year-old man demonstrates unilateral, polyostotic involvement of fibrous dysplasia in the pelvis, the femoral head, the distal femur, and the tibia on the right (*arrows*)

consist of collagen-producing fibroblasts with a high consistency. When located in a tight compartment between bones, for example the radius and ulna in the forearm, the lesion causes bowing and separation of the adjacent bones, with cortical scalloping and erosions. The tumors may be locally aggressive and prone to recur, but do not metastasize.

Radiographically, the tumors are not visible. But the presence of tumor can be suggested by indirect changes such as the bowing, separation, cortical thickening, scalloping, and erosions of the adjacent bones (Fig. 18.35A). The regional bones are atrophic and osteopenic. The cortex and subcortical bones are thickened and undulated with deep erosions. MRI is an excellent means to delineate the tumor and secondary bone and marrow changes.

Scintigraphically, this tumor does not concentrate tracer, but the erosions with reactive sclerosis, bowing, and widening of the adjacent bones are shown by pinhole scintigraphy, helping to diagnose the condition (Fig. 18.35B). Bony erosions are indicated by "hot" rims.

18.2.4 Histiocytosis X (Langerhans Cell Histiocytosis)

Histiocytoses include eosinophilic granuloma, Hand-Schüller-Christian disease, and Letterer-Siwe disease. Pathologically, these diseases are characterized by histiocyte proliferation in the lymphoreticular system. Histiocytosis X may involve any organ, and bone involvement is common. The clinical course is benign in the first two conditions, but grave in the last named. Eosinophilic granuloma and Hand-Schüller-Christian disease are amenable to simple curettage, a steroid regimen, or low-dose radiation. Histiocytoses are primarily diseases of the pediatric age group, with extended occurrence in young adults in the third decade of life. Letterer-Siwe disease affects infants in the first year of life, usually running a fatal course. The oldest patient affected with eosinophilic granuloma was aged 62 years (Mirra 1989c) and the oldest affected with Hand-Schüller-Christian was aged 61 years (Becelli et al. 2002). Boys are affected twice as commonly as girls. Approximately 70% of eosinophilic granulomas involve flat bones such as the skull, jaw, spine, pelvis, and ribs, and Hand-Schüller-Christian disease affects the skull in over 90% of patients. Letterer-Siwe disease is an acute lethal disease of infancy; it destroys the whole skeleton. The

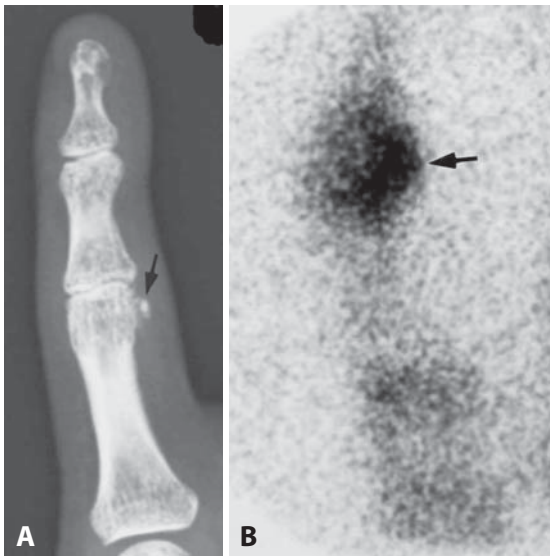

Fig. 18.34A, B Periostitis ossificans. **A** Dorsopalmar radiograph of the left fifth finger in a 31-year-old woman shows a small area of periosteal thickening with a tiny calcium deposit localized to the radial aspect of the head of the proximal phalanx (*arrow*). **B** Dorsal pinhole scan reveals a small avoid area of intense tracer uptake with less intense reactive uptake in the neighboring bones of the proximal phalangeal head and middle phalangeal base (*arrow*)

main change common to all these diseases is lysis with periosteal thickening and occasional cortical rupture or fracture.

As mentioned the basic radiographic feature of eosinophilic granuloma is osteolysis. The shape, contour, extent and expansion of the lesion may vary according to the chronicity and host bone anatomy. Thus, the lesions in the long bones are segmental, relatively well defined and concentric in the shaft (Fig. 18.36A) and those in the flat or irregular bones such as the pelvis and skull are typically geographic (Fig. 18.37A). The chronic lesions in the long bones may provoke bony proliferation, resulting in sclerosis or lamellation (Fig. 18.36A). Occasionally, cranial lesions may create a button-like sequestrum (Fig. 18.37A). The sequestrum can easily be confirmed by CT (Fig. 18.37B). Radiographically the ribs may be seen to have vanished due to total lysis, and vertebral involvement may produce vertebra plana. It is to be emphasized that the osteolytic

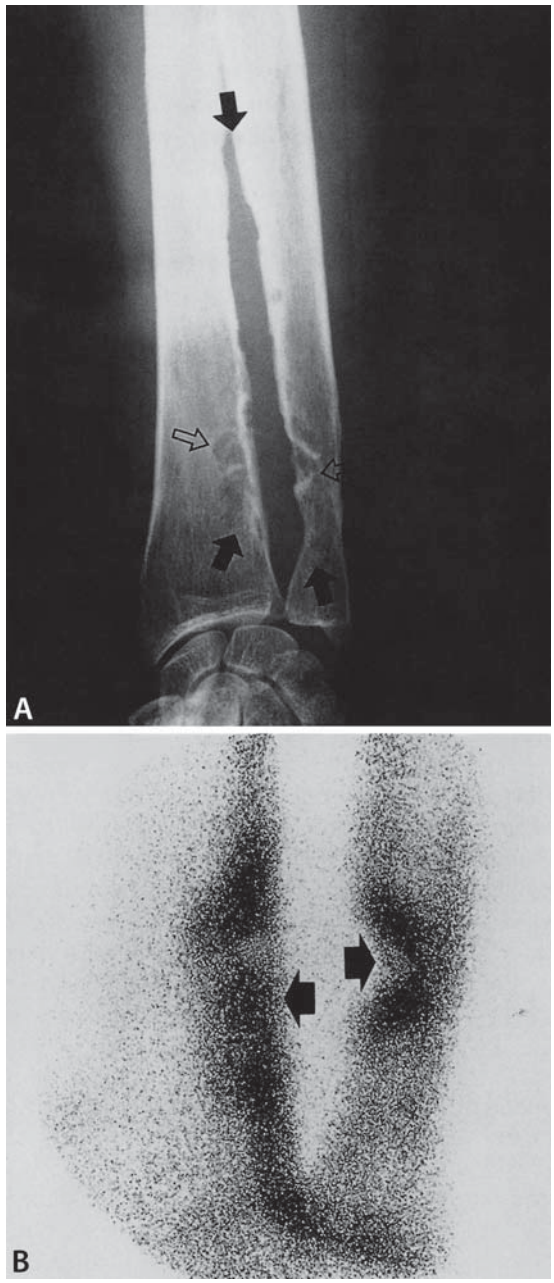

Fig. 18.35A, B Juxtacortical fibromatosis. **A** Dorsoventral radiograph of the right forearm with hard, beaded masses in a 61-year-old woman reveals irregular cortical thickening and scalloping with erosions as well as widening of the space between the distal radius and ulna (*between solid arrows*). Deeper erosions are noted in the distal aspect (*open arrows*). **B** Dorsal pinhole scan shows diffuse tracer uptake along the thickened and eroded cortices as well as the widened interosseous space. Observe that the deeper erosions do not concentrate tracer visibly (*arrows*)

lesions of Hand-Schüller-Christian disease are usually multifocal and geographic in appearance (Fig. 18.38A). CT is useful for accurate mapping of geographic lesions in irregular bones such as the sacrum and ilia (Fig. 18.38B).

Opinions regarding the usefulness of bone scintigraphy in histiocytosis are at variance, and bone scanning is generally considered less sensitive and specific than radiography (Parker et al. 1980; Crone-Munzebrock and Brassow 1983). However, the bones affected with eosinophilic granuloma or Hand-Schüller-Christian disease positively accumulate tracer (Westra et al. 1983; Azous et al. 2005). It is true that, like myeloma, histiocytosis X does not accumulate ^{99m}Tc-MDP by itself but can cause enough reaction in the contiguous endosteums and cortices to cause prominent tracer uptake that can suggest the diagnosis of histiocytosis X. Cortical uptake is intensified with the chronicity of the disease: The more chronic is the granuloma the more intense is the bone uptake (Figs. 18.39, 18.40 and 18.41B). In addition, high-resolution scintigraphy including pinhole scanning directly visualizes histiocytosis as a photopenic defect, enhancing the diagnostic sensitivity and specificity (Fig. 18.36B). Generally, bone tracer uptake in eosinophilic granulomas and Hand-Schüller-Christian disease is expansive and larger than the radiographic lesion probably due to the watershed uptake added to actual osseous invasion. Interestingly, we have observed doughnut-like tracer uptake in a case of cranial eosinophilic granuloma (Fig. 18.37C). It can be considered as the scintigraphic version of the "button sequestrum" of radiography and CT (Fig. 18.37A, B).

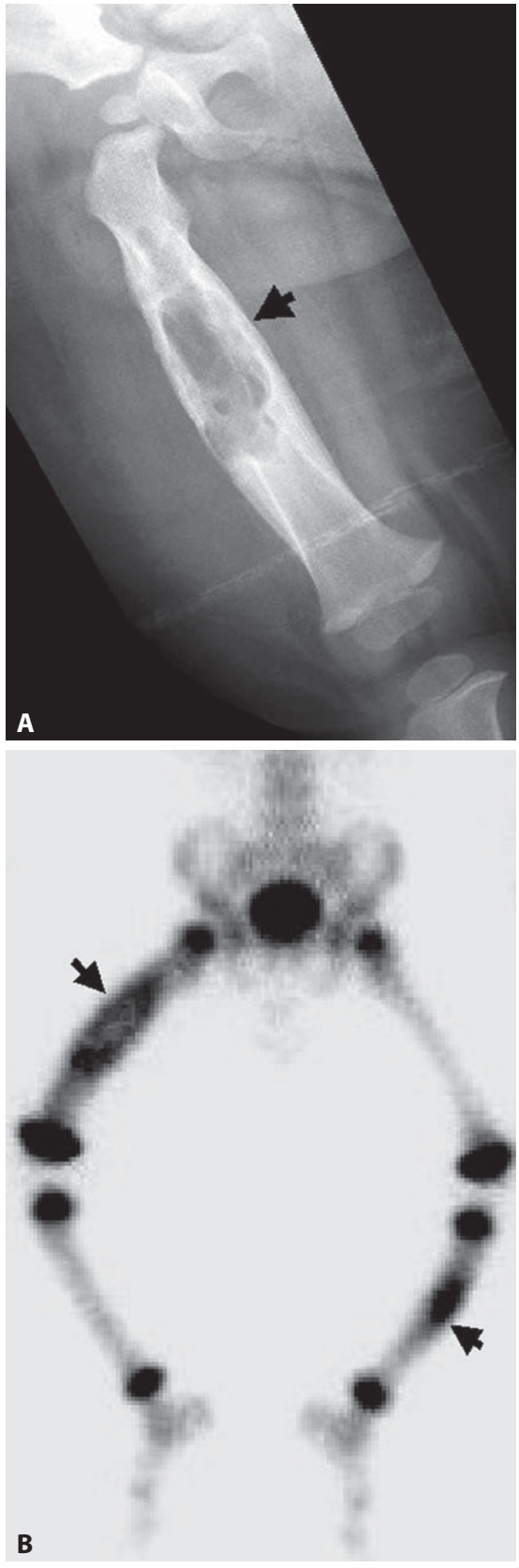

Fig. 18.36A, B Chronic eosinophilic granuloma in a long bone. **A** Anteroposterior radiograph of the right femur in a child shows an intramedullary lesion of chronic eosinophilic granuloma with expansive osteolysis, endosteal scalloping and cortical thickening (*arrow*). **B** Anterior planar scintigraph reveals a diffuse concentric intramedullary photon defect surrounded by cortical uptake (*upper arrow*). There is another focus in the contralateral tibial shaft (*lower arrow*)

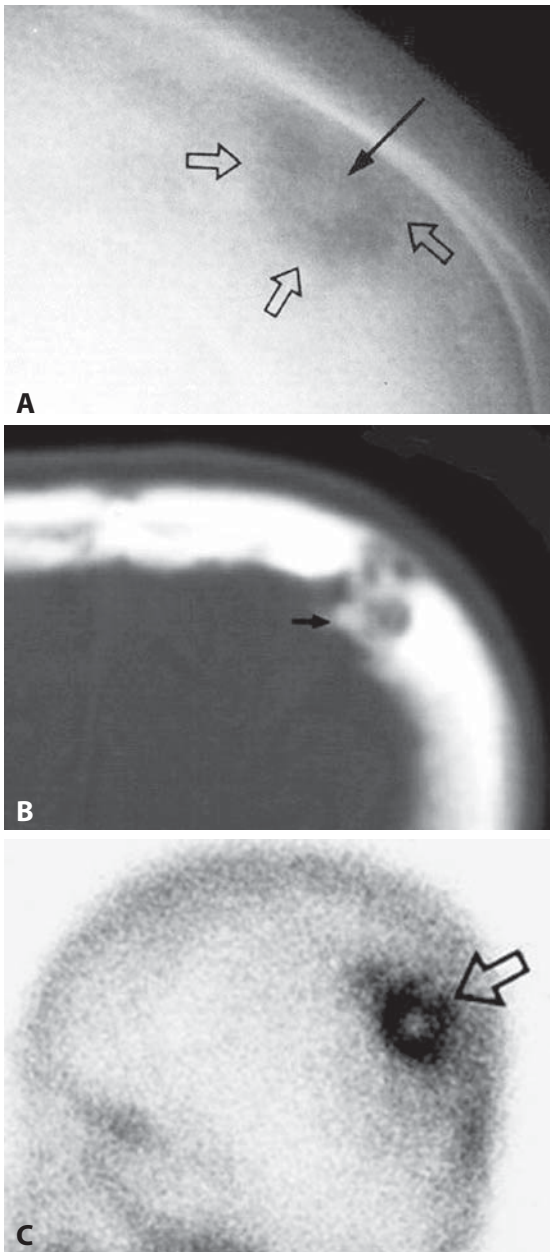

Fig. 18.37A–C Cranial eosinophilic granuloma with the "button sequestrum" sign. **A** Lateral radiograph of the skull in a 16-year-old boy shows ring-shaped osteolysis (*open arrows*) with a small island of sequestrum (*long arrow*) giving rise to a button-like appearance. **B** Transaxial CT scan reveals osteolysis involving the cranial bone with a small island of residual bone (*arrow*). **C** Lateral pinhole scintigraph demonstrates intense tracer uptake in the osteolysis and photon defect of sequestrum creating the scintigraphic "button sequestrum" sign (arrow)

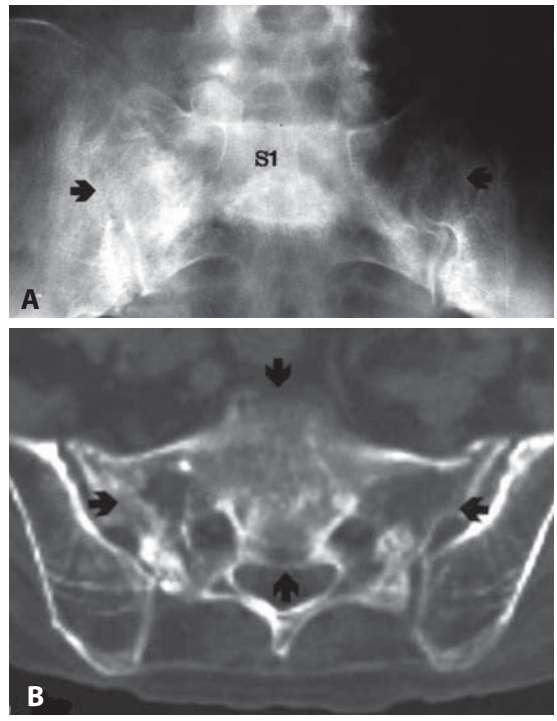

Fig. 18.38A, B Multiple geographic lesions with sclerosis in chronic Hand-Schüller-Christian disease. **A** Anteroposterior radiograph of the sacrum in a 58-year-old woman shows many geographic lesions with reactive sclerosis in the sacral wings and S1 vertebra (the same patient as in Fig. 18.41). **B** Transaxial CT more distinctly reveals geographic lesions (*arrows*). The central two arrows indicate S1 involvement with an irregular mixture of lysis and sclerosis

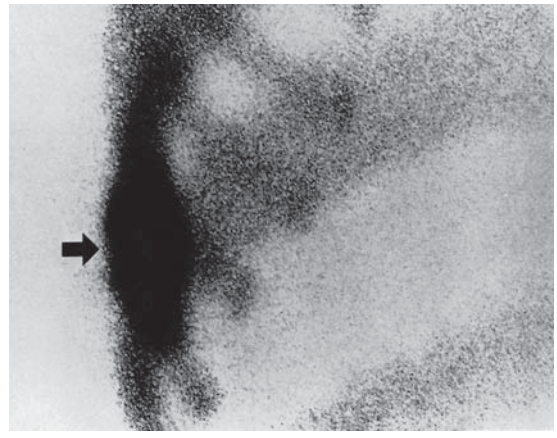

Fig. 18.39 Eosinophilic granuloma in the rib. Posterior oblique scintigraph of the axillary portion of right rib 7 shows expansile tracer uptake with relatively less intense uptake in the center (*arrow*)

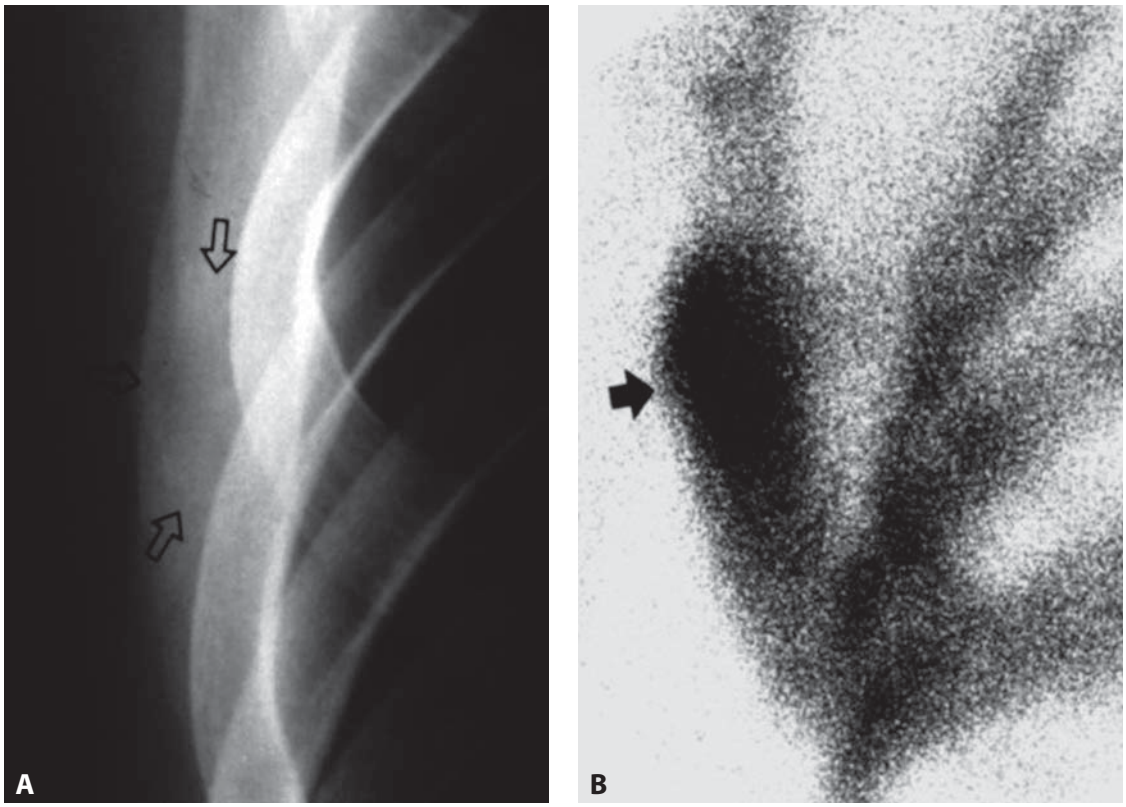

Fig. 18.40A, B Chronic eosinophilic granuloma in the scapula. **A** Tangential radiograph of the right scapula in a 33-year-old man shows osteolysis with reactive sclerosis in the lower lateral margin (*arrows*). **B** Anterior pinhole scintigraph reveals intense tracer uptake denoting chronic sclerotic reaction (*arrow*)

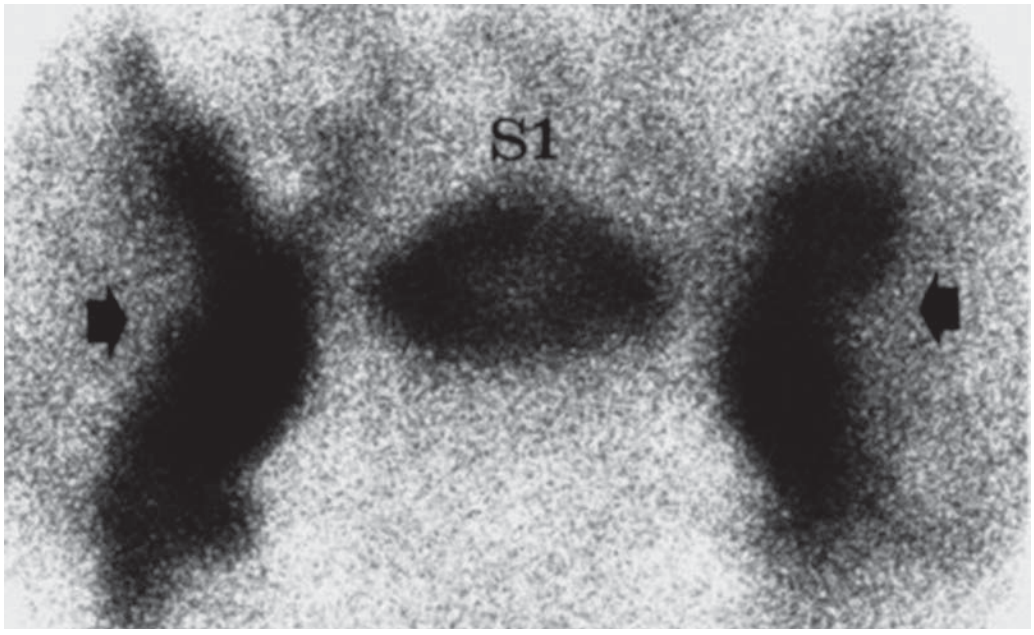

Fig. 18.41 Anterior pinhole scintigraph of the sacrum in a 58-year-old woman with Hand-Schüller-Christian disease shows prominent tracer uptake in the lateral parts and S1 vertebral body (the same patient as in Fig. 18.38)

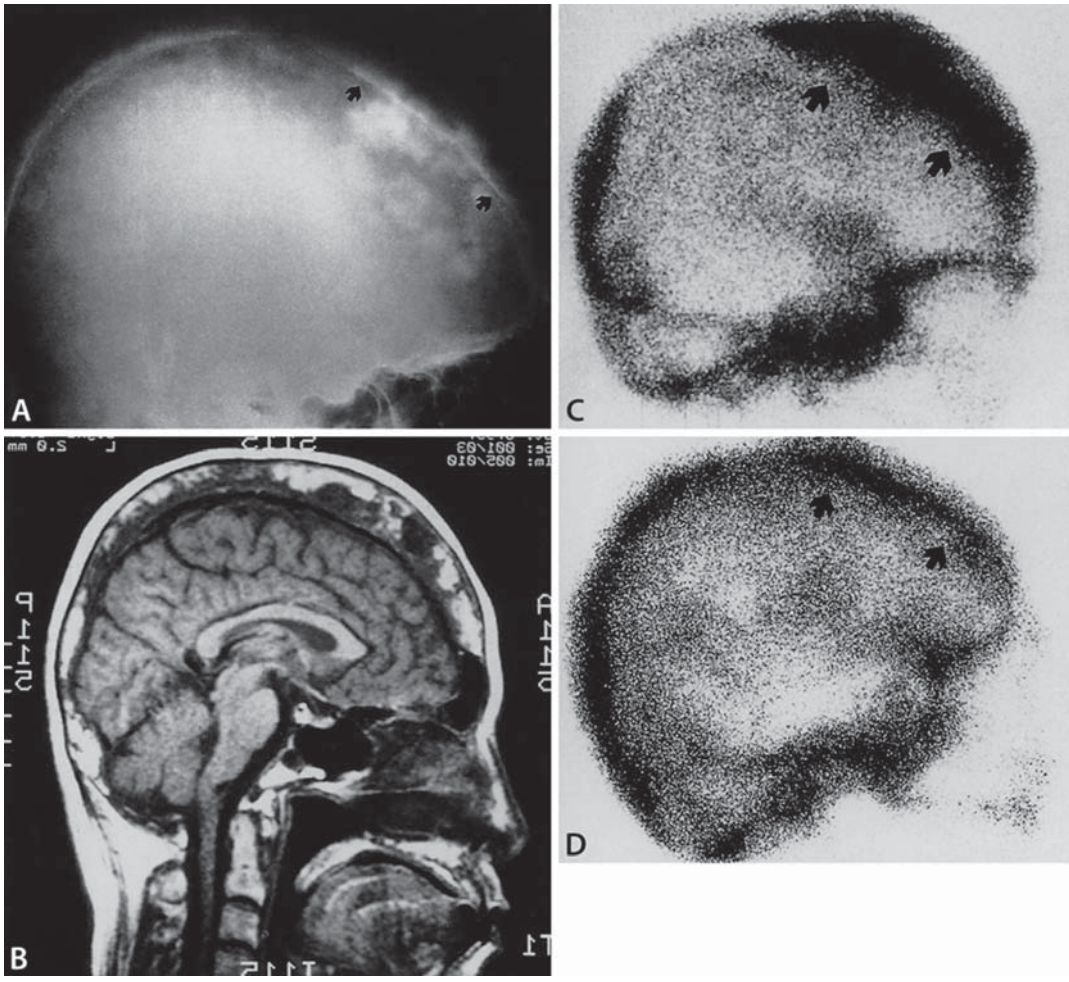

Fig. 18.42A–D Paget's disease. **A** Lateral radiograph of the skull in a 57-year-old woman with well-established Paget's disease shows the "cotton wool" sign with a widened diploic space in the frontal bone (*arrows*). **B** T1-weighted sagittal MRI reveals hyperintense diploic fat irregularly replaced by hypointense abnormal tissue. **C** Lateral pinhole scintigraph shows very intense tracer uptake in the frontal diploe where the most pronounced radiographic and MRI alterations are seen (*arrows*). **D** Follow-up lateral pinhole scintigraph 2 years later reveals the tracer uptake in the frontal bone to have become markedly reduced, having returned to a nearly normal state (*arrows*)

18.2.5 Paget's Disease of Bone (Osteitis Deformans)

Paget's bone disease is relatively common in Caucasians, but rare in Asians. The disease has been reported to be declining in the population in the United Kingdom and New Zealand. One recent study indicated that the prevalence of Paget's disease was about half that estimated 25 years ago (Doyle et al. 2002). This is a disease of middle age after 40 years, with an average age at onset between 50 and 55 years. Men are affected twice as frequently as women. The cause is not well understood, but one gene linked to Paget's disease and some other susceptibility loci as well as paramyxoviral gene products in pagetic osteoclasts have been identified (Roodman and Windle 2005). Numerous studies have indicated an autosomal dominant mode of inheritance. The common symptoms include local pain and tenderness with a skeletal deformation. Typically, however, these symptoms are disproportionately mild compared to pathological and radiographic changes that are occasionally ominous. Multiple bone involvement is the rule, but the monostotic

type is not rare, occurring in 10–35% of cases. Three disease phases are recognized: the osteolytic phase with active bone resorption, the osteoblastic phase with new bone formation, and the inactive phase. The osseous tissues produced in this disease are primitive and unorganized, without a haversian canal, and rich in vascularity.

Radiographic features include *porous sclerosis* (sclerolysis), trabecular thickening, bone enlargement, and encroachment on the marrow space. The disease affects any bone, and the most typical changes are observed in the skull, manifesting as the osteoporosis circumscripta sign and the "cotton-wool" sign: These signs respectively denote predominant lysis and overwhelming sclerosis (Fig. 18.42A). MRI may show the affected bones to be enlarged and expanded with a heterogeneous texture. In the cranium the changes occur in the diploic space, producing the "cotton-wool" sign, which consists of high and low intensities on T1-weighted images (Fig. 18.42B). The diploic space is expanded and the cranial tables, especially the inner one, become thickened, encroaching upon the brain below. The vertebrae, pelvis, femur, humerus, and ribs are common sites of involvement and the scapula, clavicle, and phalanges are less commonly involved. In the long bones the diaphyses and metaphyses are affected, showing pumice-bone-like porous sclerosis resulted from woven bone formation (Revel 1986) (Fig. 18.43A).

Pagetic vertebrae show three different patterns: (1) condensation in the endplates and lateral borders, the analogues to long-bone cortex, with a "picture frame" appearance (Fig. 18.44A), (2) generalized condensation with an "ivory"

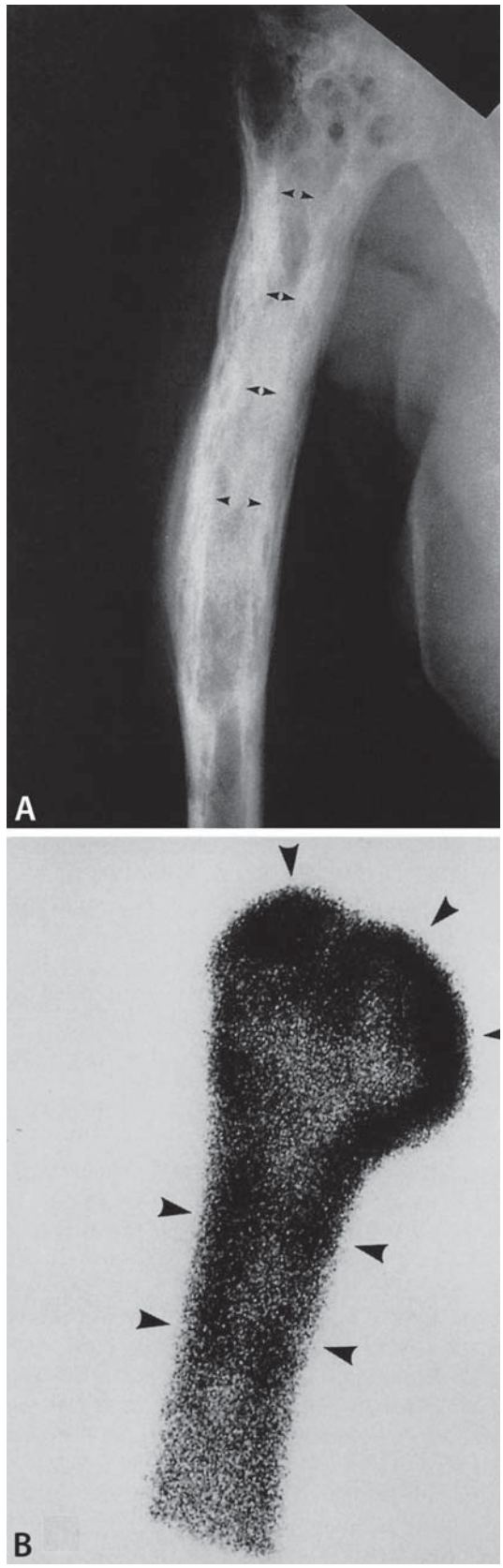

Fig. 18.43A, B Paget's disease in the long bones. **A** Anteroposterior radiograph of the right humerus in the same patient as shown in Fig. 18.42 reveals diffuse sclerosis with marrow space narrowing in the shaft except for the distal third (*arrowheads*). The humeral head and neck show irregular cortical thickening and coarsened trabeculae. **B** Anterior pinhole scintigraph shows tracer characteristically localized in the bone peripheries. The marrow space is encroached upon (*arrowheads*)

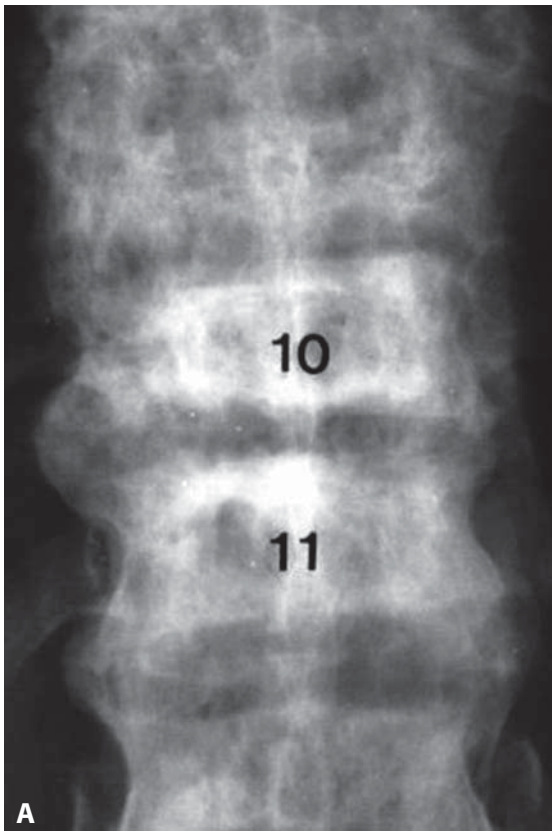

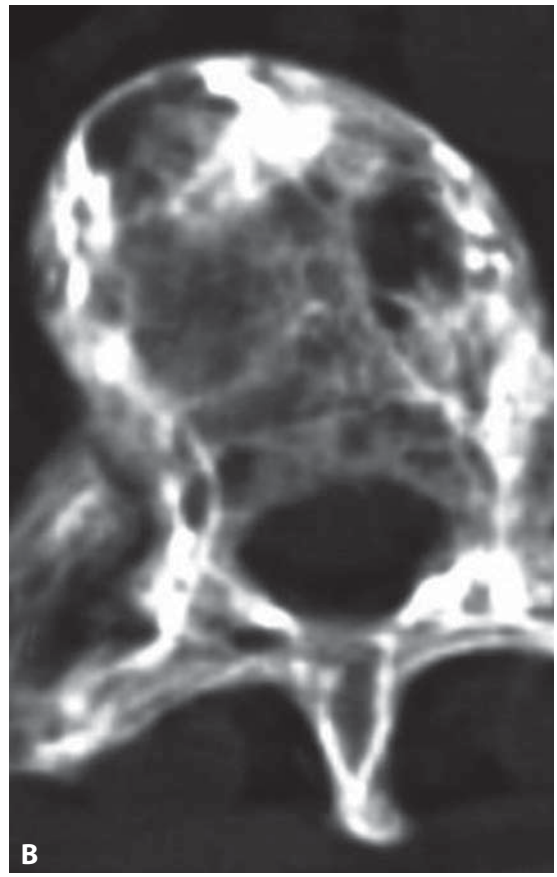

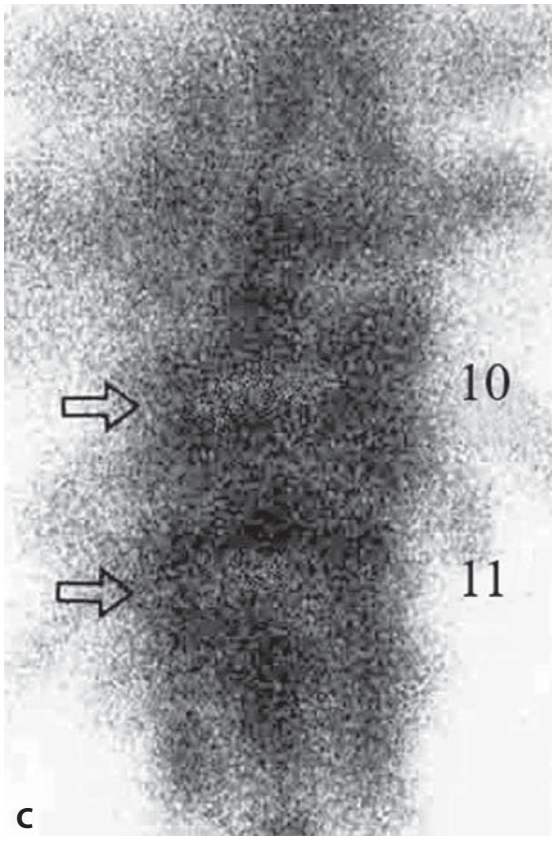

Fig. 18.44A–C Condensation of vertebral endplates and lateral borders in Paget's disease with a picture-frame appearance. **A** Anteroposterior radiograph of the lower thoracic spine in a 67-year-old man shows typical endplate and lateral border sclerosis of the T10 and T11 vertebral bodies. **B** Transaxial CT of the T10 vertebra reveals irregularly mixed lysis and sclerosis with a pumice-bone appearance. **C** Posterior pinhole scintigraph demonstrates increased tracer uptake in the endplates and lateral borders with photopenic interior giving rise to a picture-frame appearance (*open arrows*)

appearance (Fig. 18.45A), and (3) an intermediate pattern. In the "picture frame" type, CT may reveal pumice bone change (Fig. 18.44B). Pagetic sclerosis in the scapula more typically occurs in the margin and spine (Fig. 18.46A) and in the pelvis the cortices of the ischium, pubis, and ilium (Fig. 18.47A). When the sacrum is involved sclerosis brings the borders and foramina into relief (Fig. 18.48A).

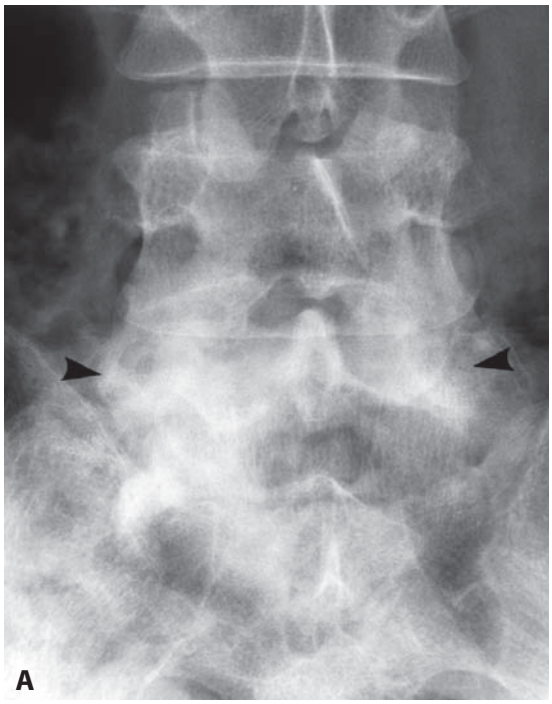

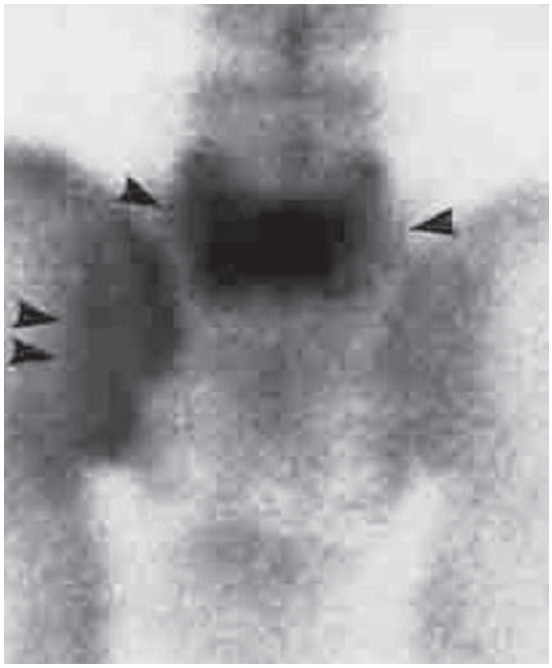

Fig. 18.45A, B Diffuse vertebral body condensation with ivory appearance. **A** Anteroposterior radiograph of the lower lumbosacral spine in a 60-year-old man shows diffuse condensation of the L5 vertebral body giving rise to a white ivory-like appearance (*arrowheads*). **B** Posterior pinhole scintigraph reveals diffuse tracer uptake in the L5 vertebral body with a black ivory appearance (*arrowheads*). Note the involvement of the right sacroiliac joint (*pair of arrowheads*). Right and left inverted on Print

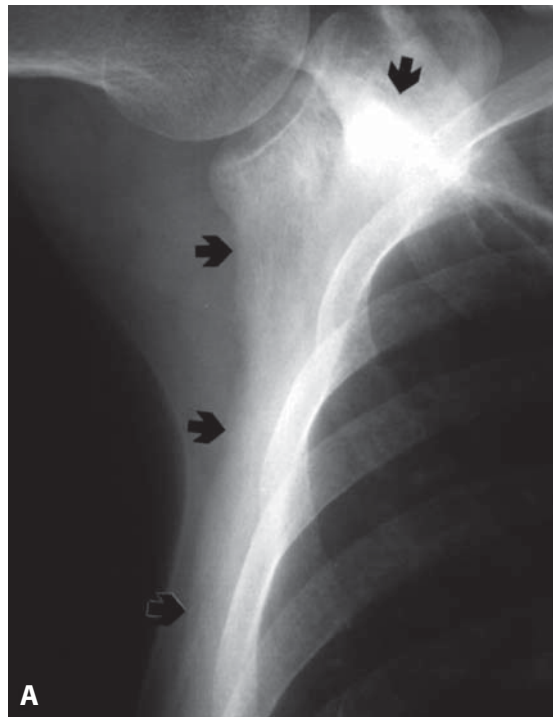

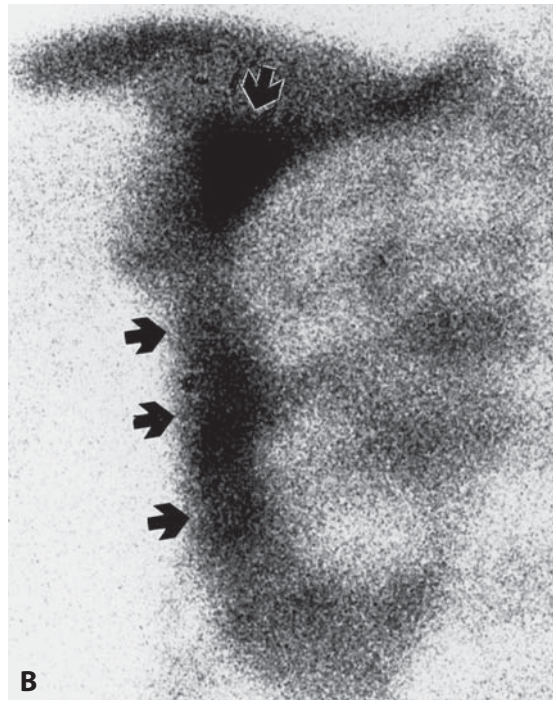

Fig. 18.46A, B Paget's disease of the scapula. **A** Anteroposterior radiograph of the left scapula in a 60-year-old man (same patient as in Fig. 18.45) shows diffuse sclerosis in the lateral margin (*three arrows*) and spine (*single arrow*). The radiograph is printed with the left side to the right to match the scintigraph. **B** Posterior pinhole scintigraph reveals diffuse tracer uptake in the lateral margin (*three arrows*) and spine (*single arrow*)

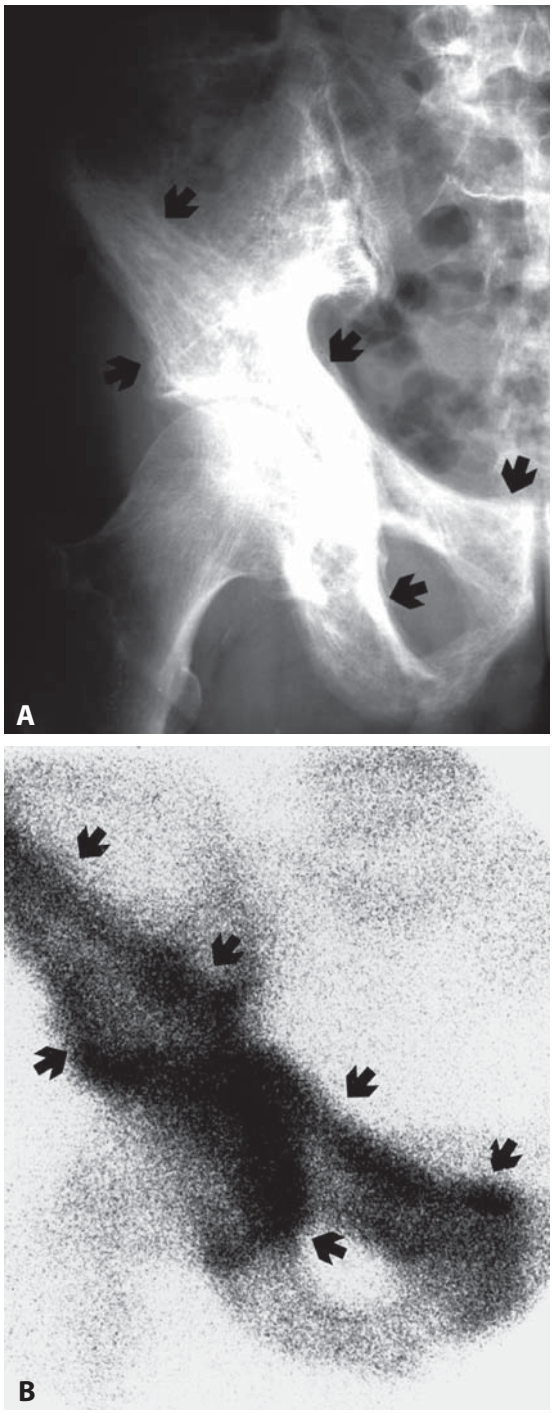

Fig. 18.47A, B Paget's disease of the pelvis. **A** Anteroposterior radiograph of the right hemipelvis in a 63-year-old man shows diffuse sclerotic Paget's disease change involving the ilium, ischium and pubis with cortical condensation (*arrows*). **B** Anterior pinhole scintigraph reveals prominent cortical tracer uptake in the ilium, ischium and pubis (*arrows*)

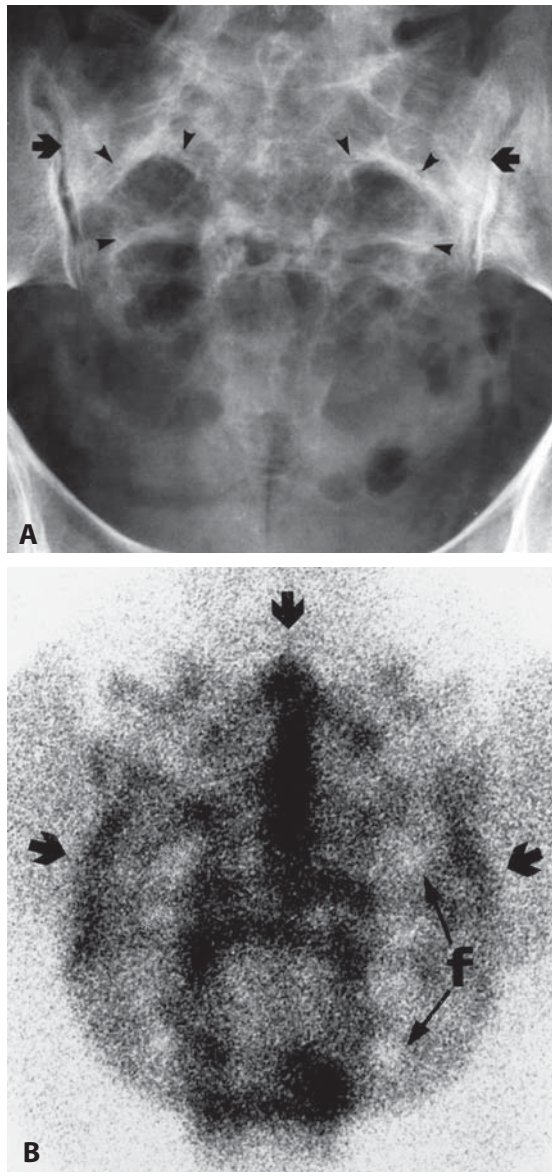

Fig. 18.48A, B Paget's disease of the sacrum. **A** Anteroposterior radiograph of the sacrum in a 59-year-old woman shows peculiar sclerosis in foraminal margins (*arrowheads*), crests, articular tubercles and sacral borders (*arrows*). **B** Posterior pinhole scintigraph similarly reveals tracer uptake in the foraminal margins (*f*), crests, articular tubercles and sacral borders (*arrows*) bringing the borders and foramina into relief

Whole-body bone scintigraphy is ideal for the detection and mapping of pagetic lesions since the great majority of cases are polyostotic (Fig. 18.49), and planar spot imaging is also useful for the study of individual lesions

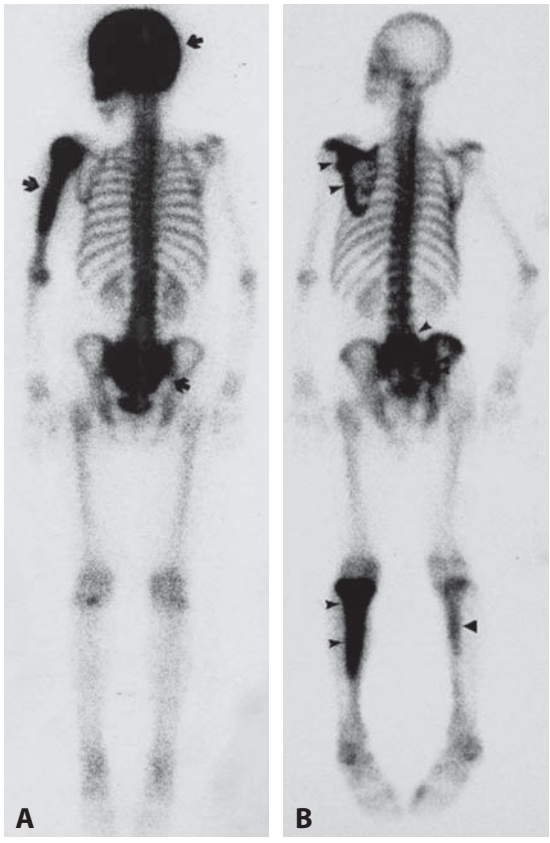

Fig. 18.49A, B Value of whole-body bone scintigraphy in Paget's disease. **A, B** Posterior whole-body scans in two different patients with polyostotic Paget's disease panoramically display involvement of the skull, left humerus, lumbar spine and sacrum (**A**, *arrows*) and involvement of the left scapula, lower lumbar spine, and both tibias (**B**, *arrowhead*)

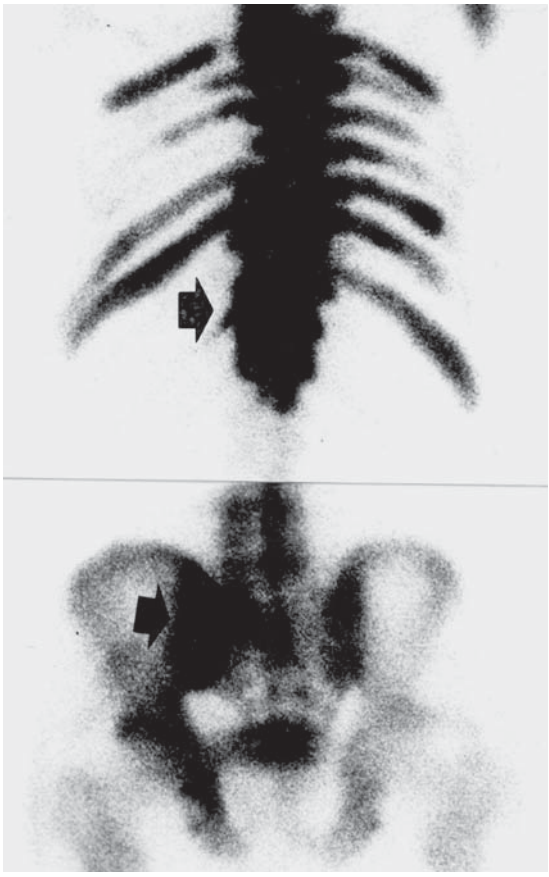

Fig. 18.50 Uses of planar spot scintigraphs in Paget's disease. *Top* Posterior spot scintigraph of the thoracic spine in a 67-year-old man shows very intense tracer uptake in the spine and ribs (*arrow*). Note that the tracer uptake is extreme so that it makes the affected bones appear pitch black. *Bottom* Posterior spot scintigraph of the pelvis reveals similar blackening of the left sacroiliac joint, midsacrum and left hip joint (*arrow*)

(Fig. 18.50). Generally, however, tracer uptake on planar scans is too intense so that the internal architectures and topography of the individual lesions are all effaced, although prominent uptake itself is an important clue to the diagnosis (Serafini 1976). Analytical information provided by pinhole scintigraphy is unique, and well comparable to that of radiography and pathology (Bahk et al. 1995). Thus, pinhole scintigraphy shows preferential tracer uptake in the cortices of the long bones (Fig. 18.43B) and flat bones (Fig. 18.46B) and the peripheries of the vertebrae (Fig. 18.44C) and irregular bones (Figs. 18.47 and 18.48). It is of interest to note that preferential uptake in the cranium peculiarly occurs in the diploic space that is expanded (Fig. 18.42C), whereas the receding outer and inner tables accumulate tracer only modestly, implying that the diploe is the main seat of pagetic change as indicated by MRI (Fig. 18.42B). Indeed, a triple correlation of radiography, MRI, and pinhole scanning indicates that the intense diploic uptake is in keeping with the advancing front of expansile porous sclerosis of the pagetic lesion, where bones are involved with brisk clastic and blastic activities (Fig. 18.42). In the late osteolytic phase tracer uptake becomes diminished (Fig. 18.42D). When the vertebrae are

affected two basically different patterns may be seen: one is the "picture frame" pattern (Fig. 18.44C) and the other is the "black ivory vertebra" pattern (Fig. 18.45B).

18.2.6 Neurofibromatosis (von Recklinghausen's Disease)

Neurofibromatosis is a fairly common, autosomal dominant, heredofamilial disorder of nonneoplastic nature (1 in 3,000 live births in Caucasians). The essential feature is hamartomatous tumefaction of neurogenous tissue with neatly bordered café-au-lait pigmentation of the skin. Clinical symptoms and signs include cutaneous pigmentations, subcutaneous tumors (fibroma molluscum), mental deficiency, exophthalmos, and abdominal visceral disorder. Multifocal skeletal changes may occur as a result of either direct erosion by intra- and extraosseous lesions or disturbed growth, during intrauterine or postnatal life. The long bones, the ribs, the skull, and the spine are most commonly affected. With the heralding appearance of freckle-like skin lesions in early life, other symptoms and signs begin to manifest themselves at any age during infancy and childhood. Scoliosis with or without kyphosis in the middle or lower thoracic vertebrae is an important diagnostic feature, occurring in about 60% of patients (Crawford and Bagamery 1986).

Radiographic features of skeletal involvement vary widely, with the spectrum ranging from a minor bone defect and deformity to bizarre disconfiguration. Commonly observed changes include bowing, atrophy, and pseudoarthrosis in the lower legs in infancy and hypoplasia, thinning or thickening, and crooking in later life. Periosteal thickening and subperiosteal hemorrhage are other important features. As mentioned above, middle and lower thoracic kyphosis is a very important feature.

The bone scintigraphic changes of neurofibromatosis may appear during infancy. They are subperiosteal hemorrhage (Abdel-Dayem and Papademetriou 1981) and pseudoarthrosis (Schaub and Hahn 1990). In both conditions, mild tracer uptake occurs in the lesional sites. A whole-body ^{99m}Tc-MDP bone scan in one of our patients with skin lesions demonstrated tracer uptake in the right fifth rib, T9-11 vertebrae with scoliosis, and sacral base (Fig. 18.51).

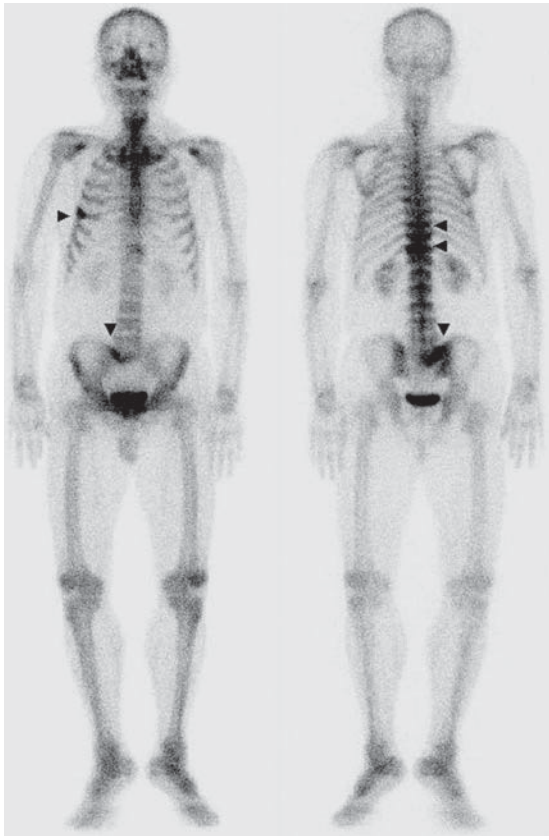

Fig. 18.51 Neurofibromatosis. Anterior (*left*) and posterior (*right*) whole-body scans in a 66-year-old man with longstanding skin lesions show tracer uptake in the right fifth rib, T9–T11 vertebrae with mild scoliosis, and the sacral base (*arrowheads*)

18.2.7 Enchondromatosis

Enchondromatosis including Ollier's disease and Maffucci's syndrome is a rare, nonhereditary, dysplastic condition characterized by the presence of multiple asymmetrically distributed intraosseous defects and subperiosteal deposition of cartilage. It interferes with skeletal growth, leading to shortening, slanting, and bending. As the prefix denotes the condition diffusely involves multiple bones formed by enchondral ossification, typically the long tu-

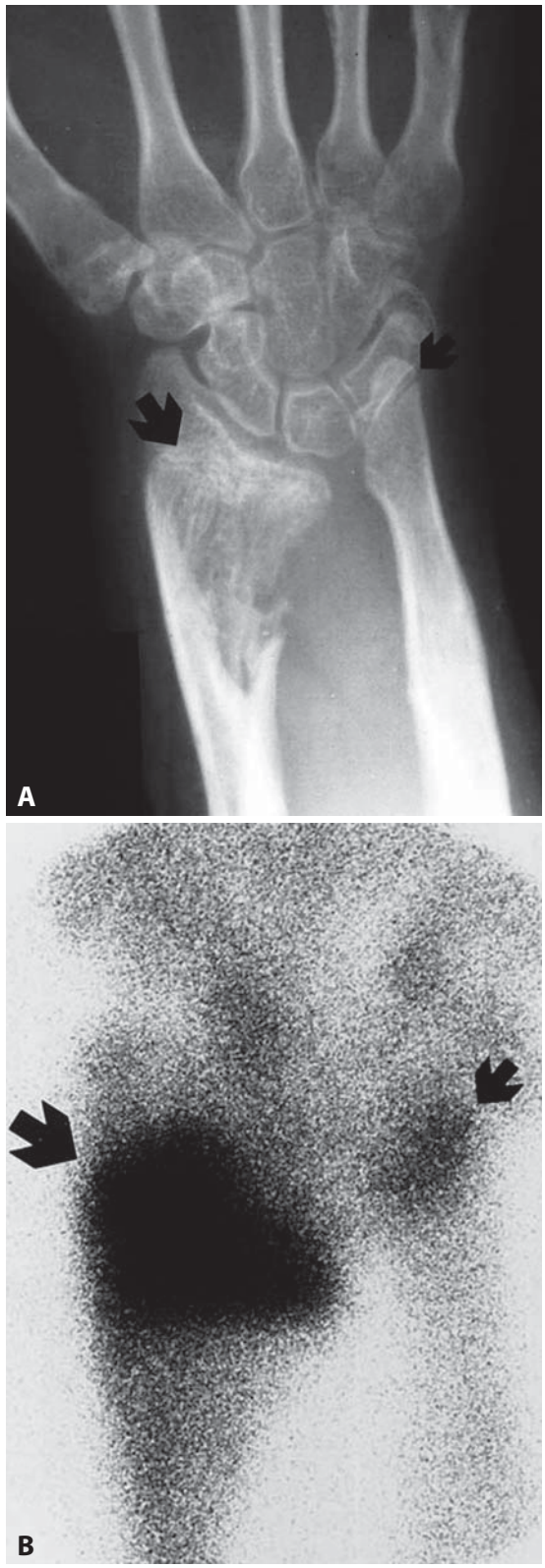

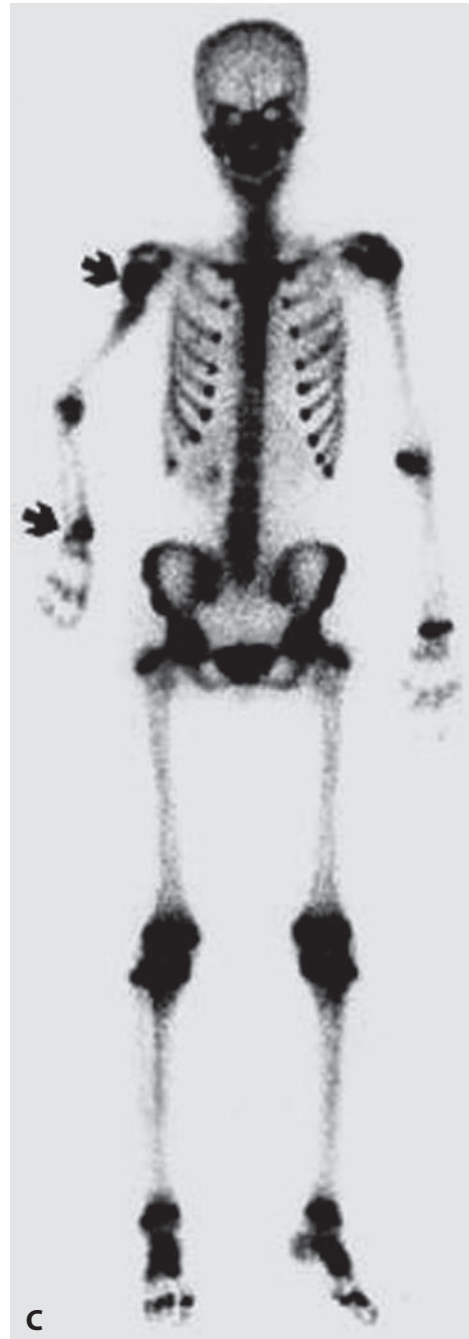

Fig. 18.52A–C Osteochondromatosis in the wrist. **A** Dorsopalmar radiograph of the right wrist in a 15-year-old girl shows longitudinally extending enchondromas in the distal radius and ulna with slanting, creating a V-shaped deformity (*arrows*). **B** Dorsal pinhole scintigraph reveals intense tracer uptake in enchondromas (*arrows*). Note that tracer uptake is confined to lesional tissue sparing the epiphyseal end. **C** Anterior whole-body scan panoramically displays multiple foci in the right upper extremity bones (*arrows*)

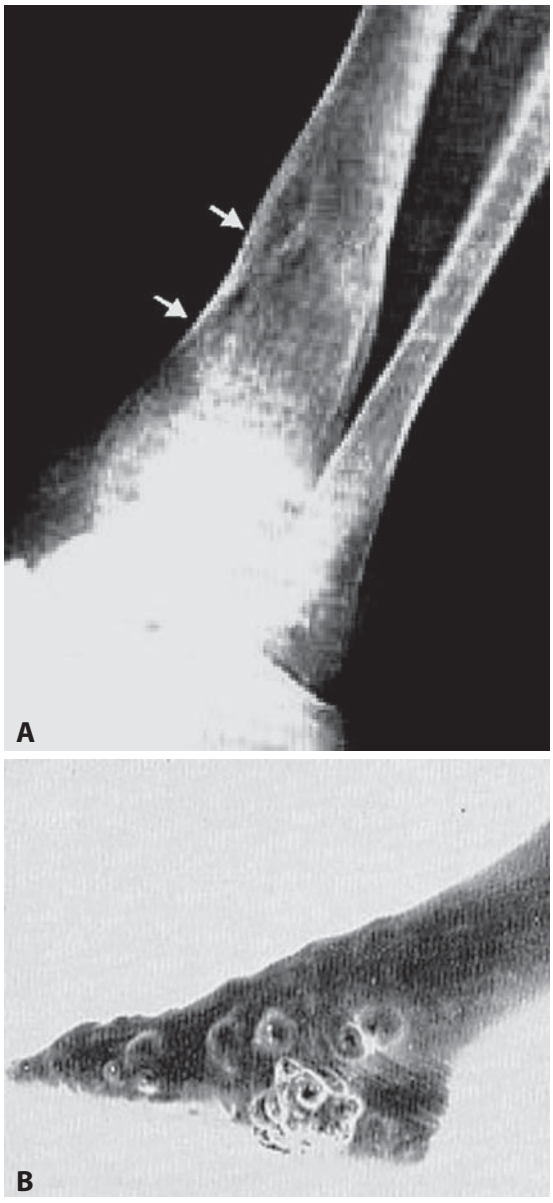

Fig. 18.53A, B Osteochondroma in Maffucci's syndrome. **A** Oblique radiograph of the right ankle in a 13-year-old girl shows enchondromas in the distal tibia (*arrows*). The metaphysis appears widened due to disturbed tubulation and remodeling. **B** Lateral photograph reveals multiple grapefruit-like tumors of hemangioma

bular bones. In Ollier's disease multiple enchondromas are mainly or exclusively on one side of the body. In some patients, the lesions are discrete and two or three in number. Maffucci's syndrome is a condition, in which multiple enchondromas occur in association with cavernous hemangiomas. Symptoms and signs usually appear in the first or second decade of life, comprising palpable bony masses and deformity. When lesions are scanty they may pass unnoticed. Males are affected twice as frequently as females.

The characteristic radiographic features include multiple, streaky, radiolucent bone defects with various amounts of calcification. Defects are longitudinally stretched in the long bones. Diseased limbs are asymmetrically dwarfed. When the long bones such as the radius and ulna are affected, slanting of the bone end may occur owing to partial arrest of ossification (Fig. 18.52A). Simultaneous involvement of the radius and ulna may result in Madelung's deformity. The other sequelae include limb length discrepancy and subluxation or dislocation. On the other hand, Maffucci's syndrome manifests as enchondroma along with soft tissue hemangiomatosis that can be easily confirmed by direct injection of contrast medium (Bahk 1964) (Fig. 18.53).

Whole-body ^{99m}Tc-MDP bone scintigraphy panoramically shows increased tracer uptake in enchondromas irregularly distributed in the long bones. The lesions are located predominantly or exclusively on one side of the body (Fig. 18.52). The whole-body scan also visualizes skeletal deformity and shortening. On the other hand, it is of interest that pinhole scintigraphy shows specific accumulation of tracer in the dysplastic osteochondral tissues in the dwarfed centroulnar aspect of the distal radial metadiaphysis and the centroradial aspect of the distal ulnar metadiaphysis, but not in the epiphyses (Fig. 18.52C). Thus, Madelung's slanting deformity in enchondromatosis appears to be closely related to the eccentric localization of dwarfing dysplasias in the distal radius and ulna.

18.2.8 Hereditary Multiple Exostoses

Hereditary multiple exostoses are autosomal dominant bone disorders characterized by the formation of multiple osteochondromas in the long-bone metadiaphyses and flat or irregular bone edges on both sides of the body. Their

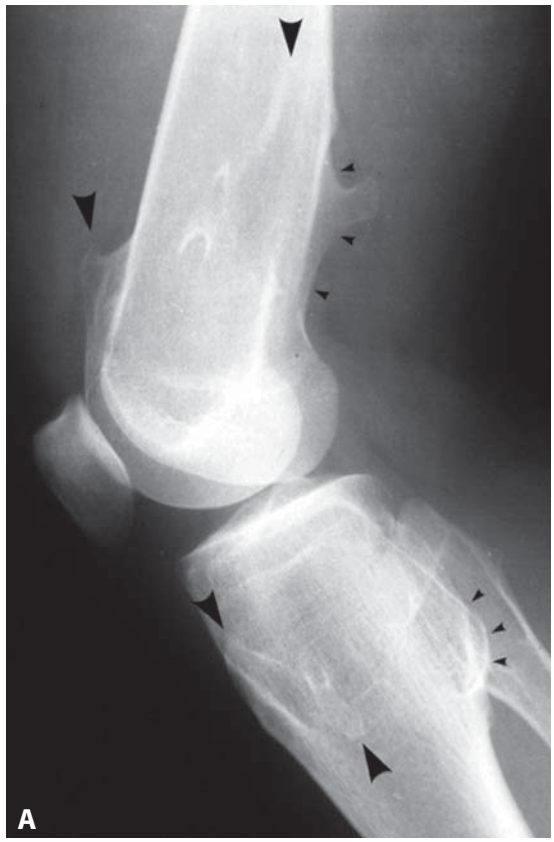

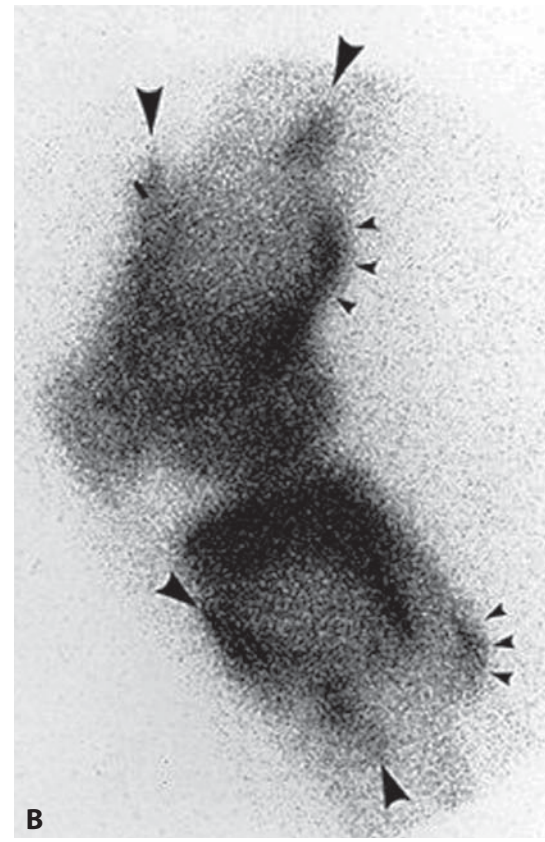

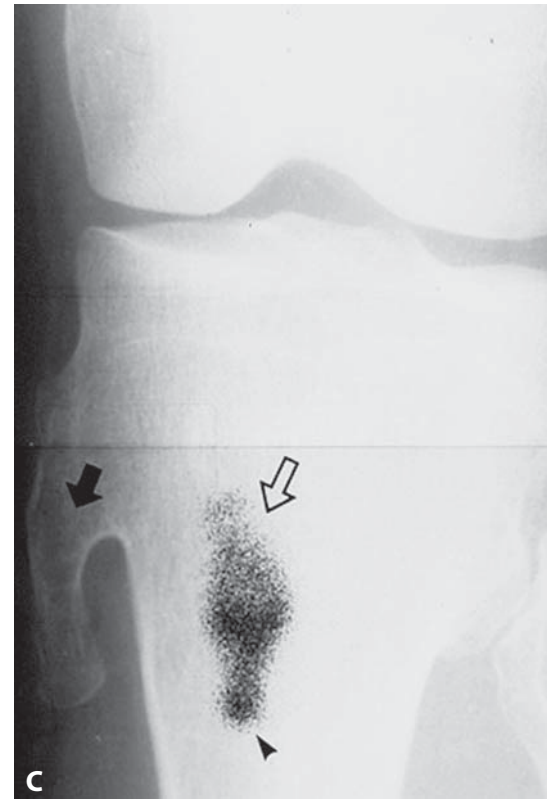

Fig. 18.54A–C Hereditary multiple exostosis. **A** Lateral radiograph of the right knee in a 22-year-old nun shows many coat-hanger-type bony outgrowths arising from the metaphyses of the distal femur and proximal tibia (*arrowheads*). Note typical longitudinal stretching of outgrowths with their tips pointing towards the diaphysis. **B** Lateral pinhole scintigraph reveals increased tracer uptake at the tips reflecting physiological activity (*arrowheads*). **C** Anteroposterior radiograph shows the largest symptomatic osteochondroma involving the medial metaphyseal cortex of the proximal tibia that was resected to relieve severe pain (*solid arrow*). *Inset* is a preoperative pinhole scan of the resected osteochondroma (*open arrow*). Higher tracer uptake is seen in the diaphyseal half of the lesion that has been irritated by habitual kneeling (*arrowhead*). Note longitudinal stretching of the outgrowths with their tips pointing towards the diaphysis

prevalence has been reported to vary widely from 1/50,000 in Western countries (Rambeloarisoa et al. 2002) to 19.4% in children and 9.5% in adults in a study of an isolated community in Manitoba (Black et al. 1993). Genetically, the disorder is heterozygous consisting of three chromosomal foci of the EXT1 gene

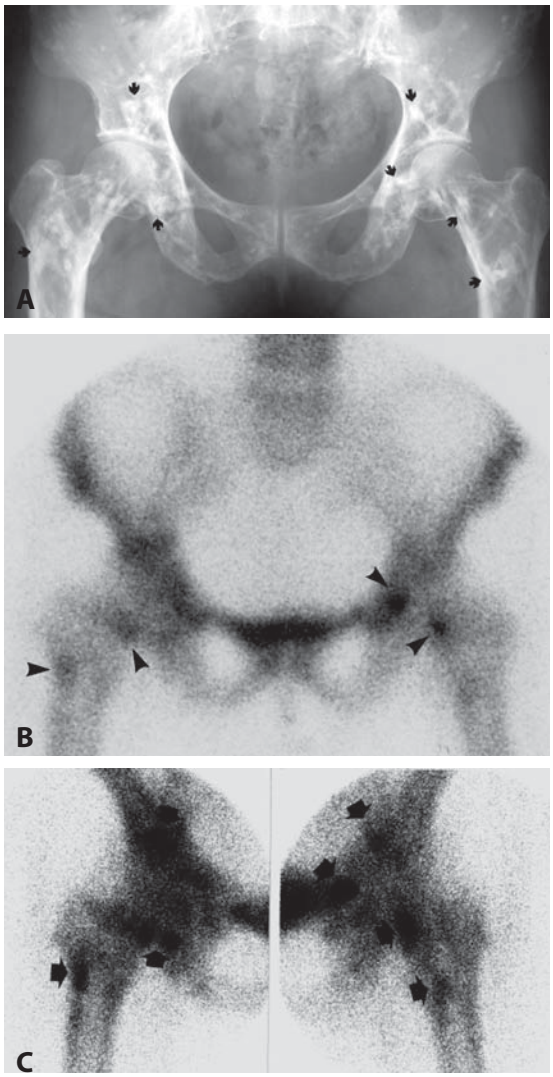

Fig. 18.55A–C Osteopoikilosis. **A** Anteroposterior radiograph of the pelvis and hips in a 67-year-old woman shows innumerable small island-like compact bones (*arrows*). Most lesions are discrete and some are confluent. The host bones are normal. Osteopoikilosis was an incidental finding in this patient. **B** Anterior planar bone scan reveals few barely discernible lesions (*arrowheads*). **C** Anterior pinhole scan reveals multiple lesions with distinct tracer uptake

on chromosome 8q23-q24, EXT2 on 11p11-p13, and EXT3 on 19p (Shi et al. 2002; Pierz et al. 2002). Lesions are typically multiple or even numerous. Hard lumps can be palpated as early as in early childhood in the bones of the knees, shoulders, scapulas and iliac crests that are externally well-exposed. Secondary deformity or shortening of the affected bones is common, and clinically the exostotic tumors with more or less pointed tips may irritate or injure the adjacent nerves or vessels, causing discomfort, pain, and even vascular damage, although this is rare. Malignant transformation has been reported with the risk ranging from 1–2% for the solitary type (Lichtenstein 1972; Garrison et al. 1982) to 10–25% for the multiple type (Ochsner 1978). As mentioned above, this condition is a model example of benign bone diseases that manifest the *longitudinal alignment sign*.

The characteristic radiographic features include coat-hanger-like bony outgrowths arising from the metaphyses of the long bones with their tips pointing towards the diaphyses (Fig. 18.54A). Most osteochondromas in the scapulas and the pelvis are mushroom-shaped with a cartilaginous cap (Fig. 18.21A). When malignant transformation occurs the contour, especially the summit, becomes enlarged and roughened.

^{99m}Tc-MDP bone scanning has been used for the diagnosis of this condition (Epstein and Levin 1978). Scintigraphically, individual osteochondromas are shown as coat-hanger-like bony outgrowths, typically arising from the long bone metaphyses with the tips pointing towards the diaphyses (Fig. 18.54B). The intensity of uptake varies according to the size and age of the tumors: the younger and larger the tumor the more intense is the tracer uptake and vice versa (Figs. 18.20 and 18.21). Thus, bone scanning provides useful metabolic information on each tumor, helping to distinguish actively changing tumor from inert tumor. Tracer uptake may become suddenly increased with a rapidly enlarging mass if malignant transformation supervenes.

18.2.9 Osteopoikilosis

Osteopoikilosis, an autosomal dominant disorder, has been sporadically reported (Benli et al 1992). The individual lesions, indistinguishable from solitary enostoses or bone islands, are round or ovoid in shape and measure from a few millimeters to a few centimeters in size.

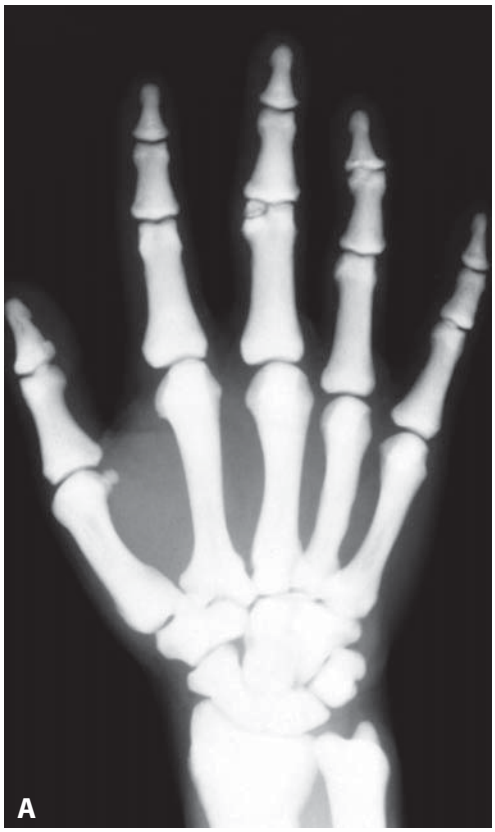

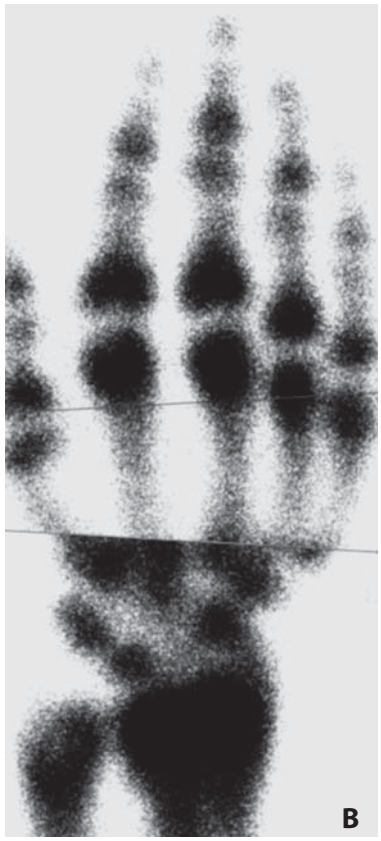

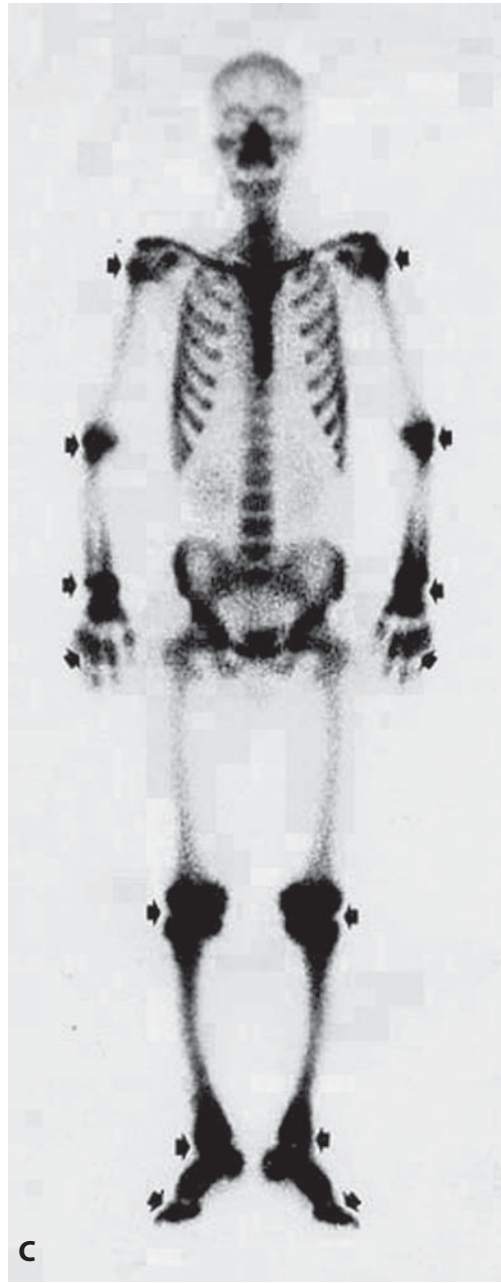

Fig. 18.56A–C Osteopetrosis of the hand (the same patient as shown in Fig. 18.57). **A** Dorsopalmar radiograph of the right hand in a 36-year-old woman shows marked osteosclerosis totally obliterating the trabeculae and cortex with the creation of the classic "chalky bone" sign. **B** Dorsal pinhole scan reveals intense tracer uptake in the bones of the entire hand, producing a "black chalky bone" appearance, the scintigraphic version of radiographic "white chalky bone" sign. **C** Anterior whole-body bone scan shows generally increased skeletal uptake with particularly prominent uptake in the long bone metaepiphysis (*arrows*)

The foci are composed of lamellar osseous tissue provided with a haversian system, being scattered within the spongiosa of the long bone metaphyses and the pelvis. Histologically, the lesions contain all bone cells including the osteoblasts, osteoclasts, and osteocytes, and yet no residual cartilage matrix can be found. On this basis, it has been suggested that the small compact bones in osteopoikilosis are probably not formed through endochondral ossification (Resnick and Niwayama 1988). Relationship has been indicated to exist between this disorder and other osteosclerotic bone disorders, osteopathia striata and melorheostosis. Combined with nevi, osteopoikilosis comprises Buschke-Ollendorf syndrome.

The characteristic radiographic features include the demonstration of multiple or often numerous small spotty compact bones within the cancellous bones of the femurs and pelvis (Fig. 18.55A) and other long bones. The individual lesions may be discrete or confluent. When viewed tangentially the foci are seen to be plastered to the endosteal surface. The host bones are normal.

Bone scintigraphy was once used negatively, identifying the lesions not by positive uptake but indirectly suggesting the diagnosis by noting the absence of uptake (Whyte et al. 1978). Modern gamma cameras are able to detect ^{99m}Tc-MDP uptake in osteopoikilosis (Mungovan et al. 1994). However, the sensitivity of planar scintigraphy is still low compared to that of pinhole scanning (Fig. 18.55B, C). Interestingly, pinhole magnification can provide additional information on the metabolic profile of each lesion when the lesions measure 1 cm or more. Thus, the younger foci with active osteogenesis accumulate tracer, but the older ones do not. This information may serve as a discriminant between benign osteopoikilosis and metastases.

18.2.10 Osteopetrosis

Osteopetrosis, a genetic disease of osteoclast failure, is characterized by diffuse bone sclerosis with the obliteration of marrow, compromising hematopoiesis. Histologically, the disorder is caused by the failure of bone resorption with the persistence of mineralized cartilage, which prevents normal replacement by mature bone. This condition is classified into at least four different types according to genetic traits: the autosomal recessive lethal type, the intermediate recessive type, the autosomal dominant type (Albers-Schönberg disease), and the recessive type with tubular acidosis. Of these, the intermediate recessive type is mild and Albers-Schönberg disease is also relatively mild, and may pass unnoticed until pathological fracture occurs.

The characteristic radiographic changes include generalized osteosclerosis of the skeleton, both tubular and flat bones, with obliteration of the cortex, giving rise to a "marble bone" or "chalky bone" appearance (Fig. 18.56A). In the vertebrae all the parts including the posterior structure, spinous processes, and transverse processes are densely petrified with peculiar accentuation of the endplates (Fig. 18.57A).

Pinhole scintigraphy shows generally increased tracer uptake with particularly intense uptake in the epimetaphyses of the long bones (Fig. 18.56B). The findings appear to reflect the fact that ossification and tubulation and modeling are continuously attempted in the epimetaphyses. A similar phenomenon is observed in the spine, whose endplates, which are analogous to the epimetaphyses of the long bones, accumulate tracer intensely giving rise to an anvil-like appearance on the anterior scan (Fig. 18.57B, C). Whole-body ^{99m}Tc-MDP bone scintigraphy is ideal for displaying and archiving systemic involvement of the condition (Fig. 18.56C).

References

Abdel-Dayem HM, Papademetriou T (1981) Subperiosteal hemorrhage in neurofibromatosis: appearance in scintigraphy. Clin Nucl Med 6:272

Azous EM, Saigal G, Rodriguez MM, et al (2005) Langerhans' cell histiocytosis: pathology, imaging and treatment of skeletal involvement. Pediatr Radiol 35:103–115

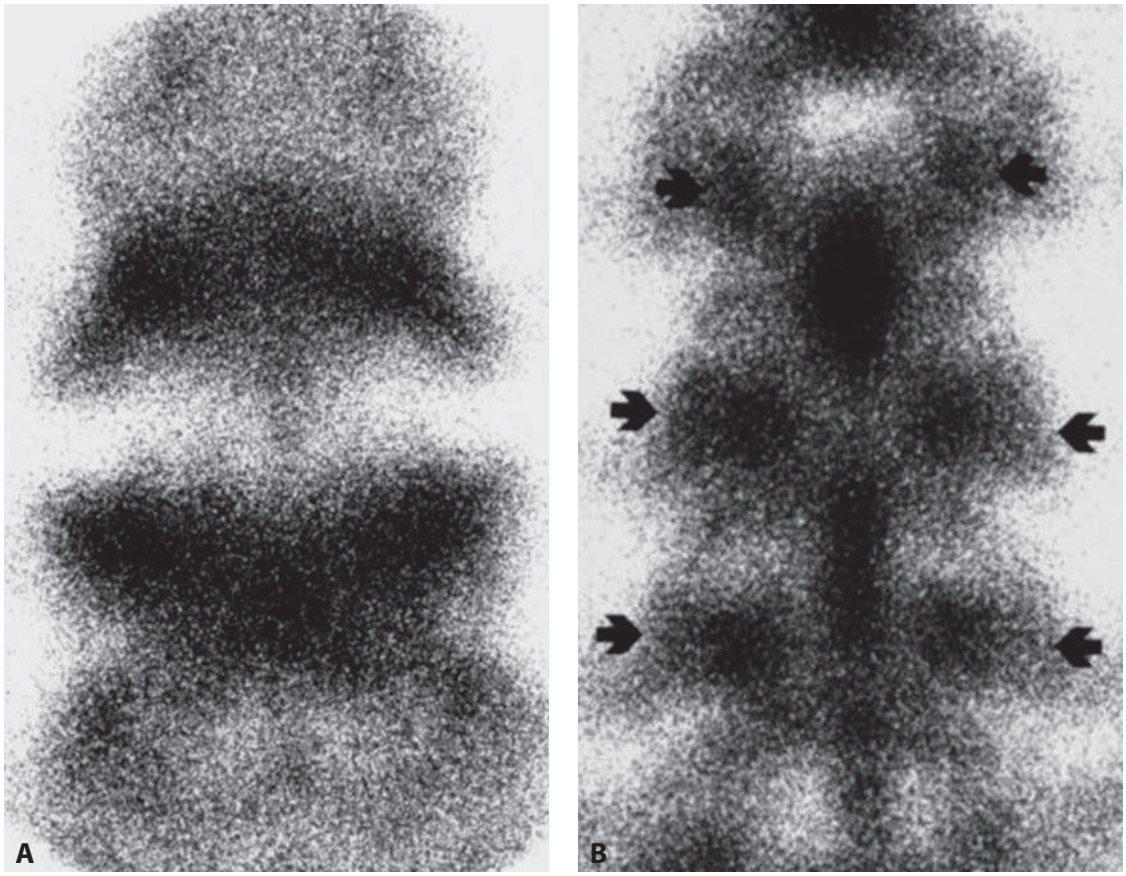

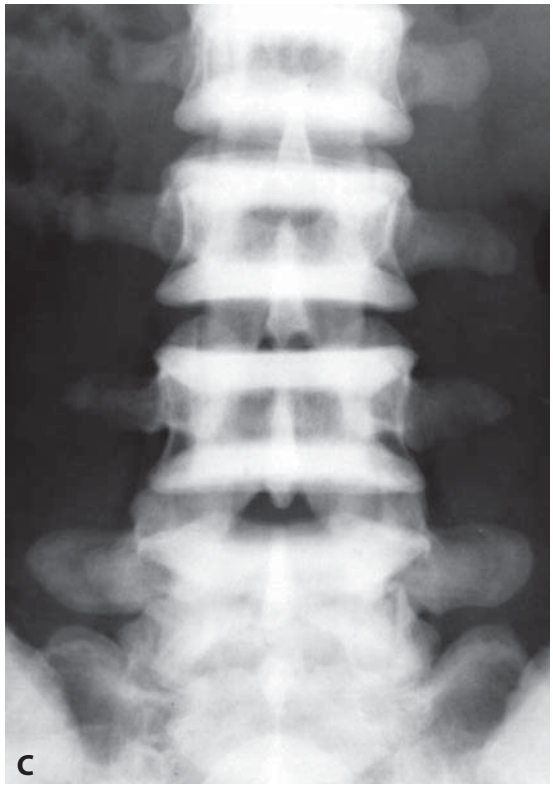

Fig. 18.57A–C Osteopetrosis of the spine (the same patient as shown in Fig. 18.56). **A** Anterior pinhole scintigraph of the lumbar spine shows peculiar anvil-like tracer uptake in the vertebral endplates. **B** Posterior pinhole scan reveals prominent tracer uptake in the vertebrae including the bodies, pedicles and transverse processes (*arrows*) and the spinous processes in the midline. **C** Posteroanterior radiograph demonstrates generalized osteosclerosis involving the bodies, endplates, pedicles, transverse processes and spinous processes. There is particularly prominent sclerosis in the endplates, which are analogous to long-bone epimetaphyses

Baek JH, Lee SY, Kim SH, et al (1997) Pinhole bone scintigraphic manifestation of fibrous dysplasia. Korean J Nucl Med 31:452–458

Bahk YW (1964) Dyschondroplasia with hemangiomata (Maffucci's syndrome). Radiology 82:407–410

Bahk YW, Park YH, Chung SK, Chi JG (1995) Bone pathological correlation of multimodality imaging in Paget's disease. J Nucl Med 36:1421–1426

Becelli R, Carboni A, Gianni C, Alterio A, Renzi G (2002) A rare condition of Hand-Schuller-Christian disease. J Craniofac Surg 13:759–761

Benli IT, Akalin S, Boysan E, et al (1992) Epidemiological, clinical and radiological aspects of osteopoikilosis. J Bone Joint Surg Br 74:504–506

Black B, Dooley J, Pyper A, Reed M (1993) Multiple hereditary exostoses. An epidemiologic study of an isolated community in Manitoba. Clin Orthop Relat Res 287:212–217

Büll U, Keyl W, Meister P, et al (1981) Wertigkeit der 'Region-of-interest'-Technik in der skelettszintigraphischen Diagnostik primärer Knochentumoren. Radiologe 21:46–51

Conklin JJ, Camargo EE, Wagner H Jr (1981) Bone scan detection of peripheral periosteal leiomyoma. J Nucl Med 22:97

Crawford AH Jr, Bagamery N (1986) Osseous manifestations of neurofibromatosis in childhood. J Pediatr Orthop 6:72–88

Crone-Munzebrock W, Brassow F (1983) A comparison of radiographic and bone scan findings in histiocytosis X. Skeletal Radiol 9:170–173

D'Ambrosia R, Ferguson AB Jr (1968) The formation of osteochondroma by epiphyseal cartilage transplantation. Clin Orthop Relat Res 61:103–115

Dahlin DC, Unni KK (eds) (1986a) Osteoid osteoma. In: Bone tumors. 4th edn. Thomas, Springfield

Dahlin DC, Unni KK (eds) (1986b) Chondroma. In: Bone tumors, 4th edn. Thomas, Springfield

Davila JA, Amrami KK, Sundaram M, et al (2004) Chondroblastoma of the hands and feet. Skeletal Radiol 33:582–587

Doyle T, Gunn J, Anderson G, et al (2002) Paget's disease in New Zealand: evidence for declining prevalence. Bone 31:616–619

Dupree WB, Enzinger FM (1986) Fibro-osseous pseudotumor of the digits. Cancer 58:2103–2109

Epstein DA, Levin EJ (1978) Bone scintigraphy in hereditary multiple exostoses. AJR Am J Roentgenol 130:331–333

Fitzer PM (1977) Radionuclide angiography – brain and bone imaging in craniofacial dysplasia (CFD): case report. J Nucl Med 18:709–712

Ferracini R, Zorzan A, Mauro PP, Masse G, Masterson EL (1998) Acetabular osteoblastoma: description of a case. Chir Organi Mov 83:413–417

Focacci C, Lattanzi R, Iadeluca ML, Campioni P (1998) Nuclear medicine in primary bone tumors. Eur J Radiol 27 [Suppl 1]:S123–131

Garrison RC, Unni KK, MeLeod RA, et al (1982) Chondrosarcoma arising in osteochondroma. Cancer 49:1890–1897

Greenspan A (1995) Bone island (enostosis): current concept – a review. Skeletal Radiol 24:111–115

Hall FM, Goldberg RP, Davies JAK, et al (1980) Scintigraphic assessment of bone islands. Radiology 135:737–742

Helms CA, Hattner RS, Vogler JB III (1984) Radionuclide skeletal survey for pediatric neoplasms. Radiology 151:779–785

Hudson TM (1984) Scintigraphy of aneurysmal bone cysts. AJR Am J Roentgenol 142:761–765

Humphry A, Gilday DL, Brown RG (1980) Bone scintigraphy in chondroblastoma. Radiology 137:497–499

Jaffe HL (ed) (1958a) Fibrous cortical defect and non-ossifying fibroma. In: Tumors and tumorous conditions of the bones and joints. Lea & Febiger, Philadelphia, pp 76–91

Jaffe HL (ed) (1958b) Solitary bone cyst. In: Tumors and tumorous conditions of the bones and joints. Lea & Febiger, Philadelphia, pp 63–75

Jee WH, Park YK, McCauley TR, et al (1999) Chondroblastoma: MR characteristics with pathologic correlation. J Comput Tomogr 23:721–726

Kaim AH, Hugli R, Bonel HM, Jundt G (2002) Chondroblastoma and clear cell chondrosarcoma: radiological and MRI characteristics with histopathological correlation. Skeletal Radiol 31:88–95

Keith A (1920) Studies on the anatomical changes which accompany certain growth disorders of the human body. I. The nature of the structural alterations in the disorder known as multiple exostosis. J Anat 54:101–115

Kim JY, Chung SK, Park YH, et al (1992) Pinhole bone scintigraphic appearances of osteoid osteoma. Korean J Nucl Med 26:160–163

Levine E, De Smet AA, Neff JR, et al (1984) Scintigraphic evaluation of giant cell tumor of bone. AJR Am J Roentgenol 143:343–348

Lichtenstein L (1972) Osteocartilaginous exostosis In: Bone tumors, 4rh edn. Mosby, Saint Louis, pp 17–28

Lisbona R, Rosenthall L (1979) Role of radionuclide imaging in osteoid osteoma. AJR Am J Roentgenol 132:77–80

McLeod RA, Beabout JW (1973) The roentgenographic features of chondroblastoma. AJR Am J Roentgenol 118:646–471

Mirra JM (1989a) Fibrohistiocytic tumors of intramedullary origin. In: Mirra JM (ed) Bone tumors. Lea & Febiger, Philadelphia, pp 692–719

Mirra JM (1989b) Aneurysmal bone cyst. In: Mirra JM (ed) Bone tumors. Lea & Febiger, Philadelphia, pp 1267–1331

Mirra JM (1989c) Eosinophilic granuloma. In: Mirra JM (ed) Bone tumors. Lea & Febiger, Philadelphia, pp 1023–1045

Mirra JM (1989d) Giant cell tumors. In: Mirra JM (ed) Bone tumors. Lea & Febiger, Philadelphia, p 958 (Fig. 13.17)

Mirra JM (1989e) Periostitis ossificans. In: Mirra JM (ed) Bone tumors. Lea & Febiger, Philadelphia, pp 1589–1605

Mirra JM, Eckhardt JJ (1989) Enchondroma versus chondrosarcoma. In: Mirra JM (ed) Bone tumors. Lea & Febiger, Philadelphia, pp 476–531

Mirra JM, Gold RH (1989) Fibrous dysplasia. In: Mirra JM (ed) Bone tumors. Lea & Febiger, Philadelphia, pp 191–226

Mungovan JA, Tung GA, Lambiase RE, et al (1994) Tc-^{99m} MDP uptake in osteopoikilosis. Clin Nucl Med 19:6–8

Nadel HT, Rossleigh MA (1995) Tumor imaging. In: Treves ST (ed) Pediatric nuclear medicine, 2nd edn. Springer, Berlin Heidelberg New York, pp 496–527

Neumann RD, Kemp JD, Weiner RE (1995) Gallium-67 imaging for detection of malignant disease. In: Sandler MP, et al (eds) Diagnostic nuclear medicine, 3rd edn. Williams and Wilkins, Baltimore, pp 1243–1260

Nishio J, Iwasaki H, Soejima O, et al (2002) Rapidly growing fibro-osseous pseudotumor of the digits mimicking extraskeletal osteosarcoma. J Orthop Sci 7:410–413

Ochsner PE (1978) Multiple cartilaginous exostoses and neoplastic degeneration: review of the literature. Z Orthop Ihre Grenzgeb 116:369–378

O'Connell JX, Nanthakumar SS; Nielsen GP, Rosenberg AE (1998) Osteoid osteoma: the uniquely innervated bone tumor. Mod Pathol 11:175–180

Parker BR, Pinckney L, Etcubanas E (1980) Relative efficacy of radiographic and radionuclide bone surveys in the detection of the skeletal lesions of histiocytosis X. Radiology 134:377–380

Patel MR, Desai SS (1986) Pseudomalignant osseous tumor of soft tissue: a case report and review of the literature. J Hand Surg [Am] 11:66–70

Pierz KA, Stieber JR, Kusumi K, Dromans JP (2002) Hereditary multiple exostoses: one center's experience and review of etiology. Clin Orthop Relat Res 401:49–59

Pinkas L, Robinson D, Halpern N, et al (2001) ^{99m}Tc-MIBI scintigraphy in musculoskeletal tumors. J Nucl Med 42:33–37

Rambeloarisoa J, el Guedj M, Legeai-Mallet L, et al (2002) Hereditary multiple exostoses after 40 years of development: a case report. Rev Med Interne 23:657–664

Resnick D, Niwayama G (1988) Enostosis, hyperostosis, and periostitis. In: Resnick D, Niwayama G (eds) Diagnosis of bone and joint disorders, 2nd ed. Saunders, Philadelphia, pp 4073–4139

Revel PA (1986) Paget's disease of bone. In: Pathology of bone. Springer, Berlin Heidelberg New York, pp 147–167

Roodman GD, Windle JJ (2005) Paget disease of bone. J Clin Invest 115:200–208

Schaub T, Hahn K (1990) Fibröse Dysplasie. In: Brussatis F, Hahn K (eds) Nuklearmedizin in der Orthopädie. Springer, Berlin Heidelberg New York

Serafini AN (1976) Paget's disease of the bone. Semin Nucl Med 6:47–58

Shi YR, Wu JY, Hsu YA, et al (2002) Mutation screening of the EXT genes in patients with hereditary multiple exostoses in Taiwan. Genet Test 6:237–243

Sim FH, Dahlin DC, Beabout JW (1975) Osteoid osteoma: diagnostic problems. J Bone Joint Surg Am 63:154–159

Van Nostrand D, Madewell JE, NcNiesh LM, et al (1986) Radionuclide bone scanning in giant cell tumor. J Nucl Med 27:329–338

Waxman AD (1995) Thallium-201 and technetium-99m methoxyisobutyl isonitrile in nuclear oncology. In: Sandler MP, et al (eds) Diagnostic nuclear medicine, 3rd edn. Williams and Wilkins, Baltimore, pp 1261–1274

Westra SJ, van Woerden H, Postma A, et al (1983) Radionuclide bone scintigraphy in patients with histiocytosis X. Eur J Nucl Med 8:303–306

Whyte MP, Murphy WA, Siegel BA (1978) ^{99m}Tc-pyrophosphate bone imaging in osteopoikilosis, osteopathia astriata, and melorheostosis. Radiology 127:439–443

Woldenberg Y, Nash M, Bodner L (2005) Peripheral osteoma of the maxillofacial region. Diagnosis and management: a study of 14 cases. Med Oral Patol Oral Cir Bucal 10 [Suppl 2]:E139–142

19 Soft-tissue Tumors and Tumor-like Conditions

Soft-tissue tumors are defined as neoplasms derived from nonepithelial extraskeletal tissue of the body excluding the reticuloendothelial system, neuroglial cells, and supporting tissue of various parenchymal organs (Enzinger and Weiss 1983). Representative soft tissues from which neoplasms commonly arise are the muscles, fat, skin, blood and lymph vessels, lymph nodes, and nerve fibers. A survey of 1331 consecutive cases of benign soft-tissue tumors showed lipoma to be the most common, accounting for nearly half of the entire series, and fibrocystic tumors and hemangioma were relatively common (Myhre-Jensen 1981). Among sarcomas, liposarcoma ranked first, and fibrosarcoma, rhabdomyosarcoma, unclassified sarcomas, leiomyosarcoma, and synovial sarcoma followed in descreasing order. The prevalence rate of sarcoma was estimated to be approximately 1% of all malignant tumors, and the benign to malignant mesenchymal tumor ratio was 100:1 in a hostpial population (Enzinger and Weiss 1983).

On the other hand, relatively common tumorous conditions of soft tissue are fibromatoses, neurofibromatosis (von Recklingausen's disease), hemangiomatosis, lymphangiomatosis, and synovial chondromatosis. Infective lymphadenitis and local or diffuse soft-tissue edema due to venous congestion in the lower limbs may clinically present as tumor-like conditions.

Radiographic manifestations of soft tissue tumors largely depend on tissue characteristics. Basically, fat tissue tumors present as radiolucent lesions surrounded by muscles or bordered by bone, whereas tumors derived from nonfat tissues such as muscle, fibrous tissue, and vessels present as water or higher density masses. Radiodensities of soft-tissue tumors are also influenced by tumor volume and tumor cell density or cellularity. Most sarcomas with predominantly stromal proliferation are radiodense, especially when the mass is voluminous (Fig. 19.1). Generally, the border of tumors is well defined or easy to recognize when discrete and poorly defined when invasive. The neighboring bone may be directly invaded by sarcoma (Fig. 19.2) and deformed or eroded by longstanding benign tumors if they are large and hard. Synovial sarcoma (Fig. 19.3) and skin cancer (Fig. 19.4) similarly penetrate or destroy contiguous bone.

Hemangiomas are occasionally detected by noting phleboliths (Murphy et al. 1995) (Fig. 19.5), and synovial osteochondromatosis by mineralized loose bodies within the confinement of the synovial sac (Fig. 19.6). The radiographic and ^{99m}Tc-MDP bone scintigraphic features of common tumor-like diseases of the soft tissue are presented in their respective sections in Chapter 18. They include juxtacortical fibromatosis (Fig. 18.35), neurofibromatosis (Fig. 18.51), and hemangiomatosis in Maffucci's syndrome (Fig. 18.53). It is to be emphasized that tissue characterization of soft-tissue tumors can be more efficiently achieved using CT, MRI, and sonography.

^{99m}Tc-MDP bone scintigraphy of soft-tissue tumors may reveal increased tracer uptake of various intensities ranging from subtle to marked. On the whole, however, soft-tissue tumors tend to accumulate tracer less than modestly so that they are more properly appreciated using pinhole scintigraphy (Figs. 19.1, 19.2, 19.5 and 19.6). The tumor uptake is homogeneous (Fig. 19.1B) and matches well the radiographic

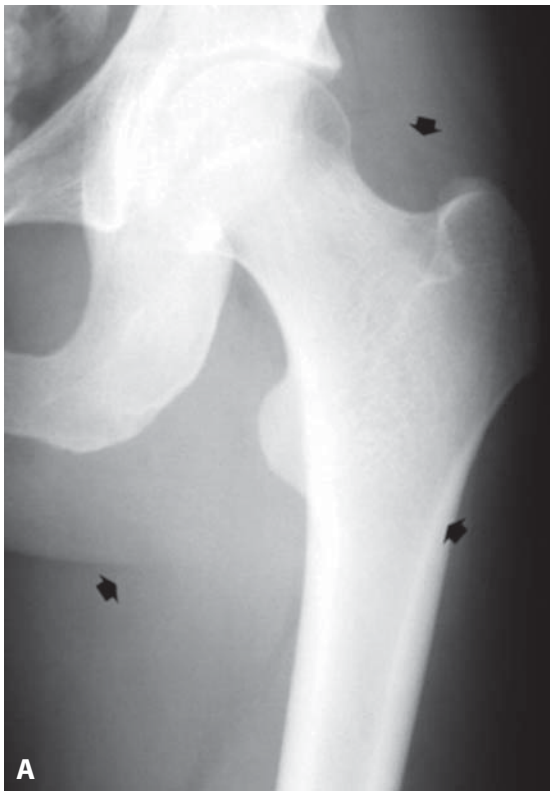

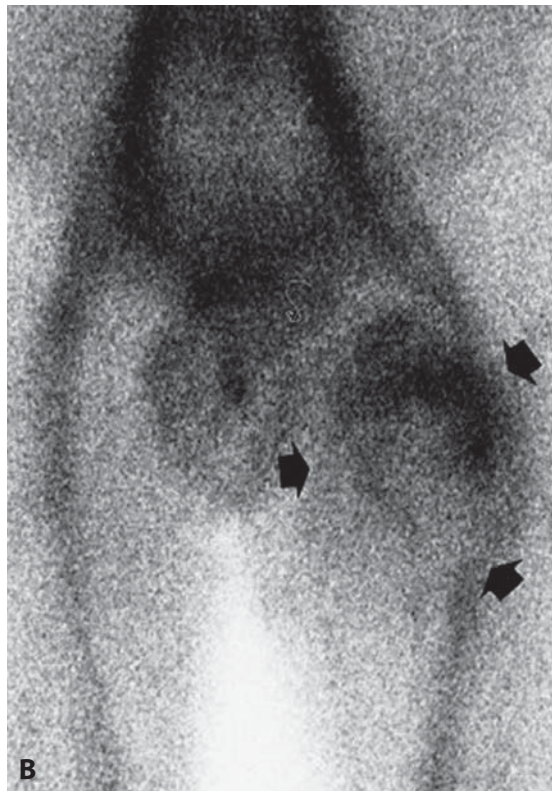

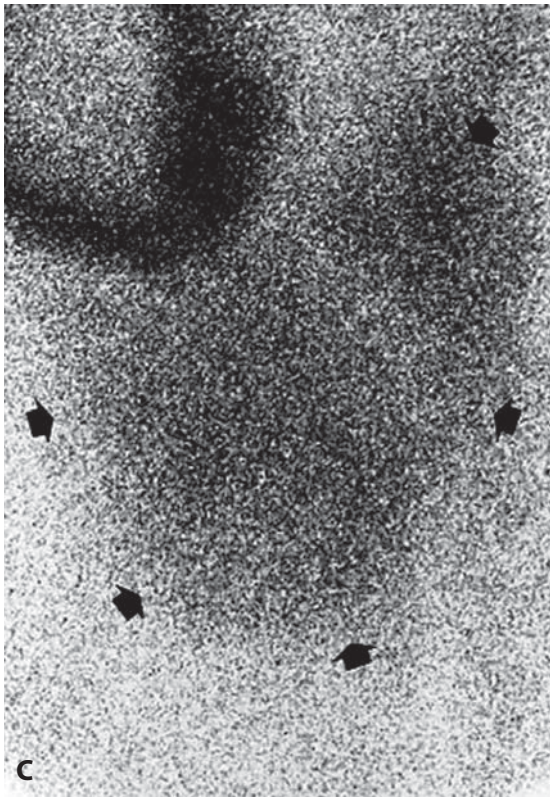

Fig. 19.1A–C Rhabdomyosarcoma in the thigh. **A** Anteroposterior radiograph of the left hip in a 27-year-old man shows a large poorly defined soft-tissue mass (*arrows*). Local bones are intact. **B** Nuclear angiogram reveals generalized tracer staining of the mass (*arrows*) with more intense uptake in the upper part (*uppermost arrow*). **C** Pinhole scintigraph shows better delineation of the mass with differential uptake in the upper part (*uppermost arrow*)

mass (Fig. 19.2B). Hypovascular tumors accumulate tracer poorly, and intratumoral hemorrhage or necrosis is indicated by photon defect (Fig. 19.2B). Scintigraphically, local bone invasion by soft-tissue malignancy seems to react in a different manner according to the type of tumor. For example, synovial sarcoma induces a prominent bone reaction with intense uptake (Fig. 19.3), whereas skin cancers directly invade contiguous bones, causing osteolysis with photon defect surrounded by prominent reactive uptake (Fig. 19.4B). Caverous hemangio-

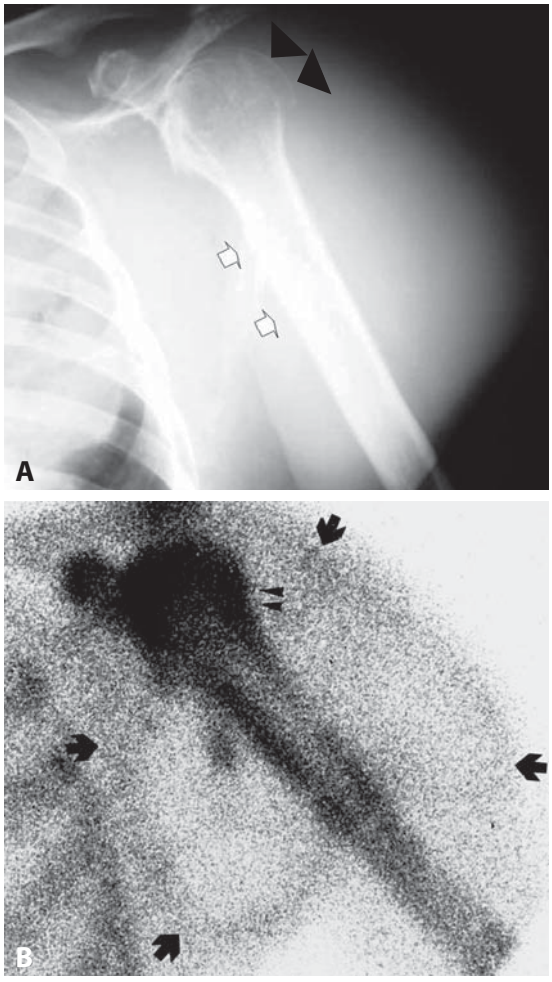

Fig. 19.2A, B Spindle cell sarcoma in the upper arm. **A** Anteroposterior radiograph of the left proximal upper arm in a 56-year-old man shows a huge bilobular soft-tissue tumor surrounding the humerus. Osteolysis is present in the head and neck (*arrowheads*) and the cortex buried within tumor (*open arrows*). **B** Anterior pinhole scintigraph reveals faint but significant tracer uptake in the bilobular tumor periphery (*arrows*). Note that the destroyed humeral head and neck and intratumoral cortex intensely accumulate tracer (*arrowheads*)

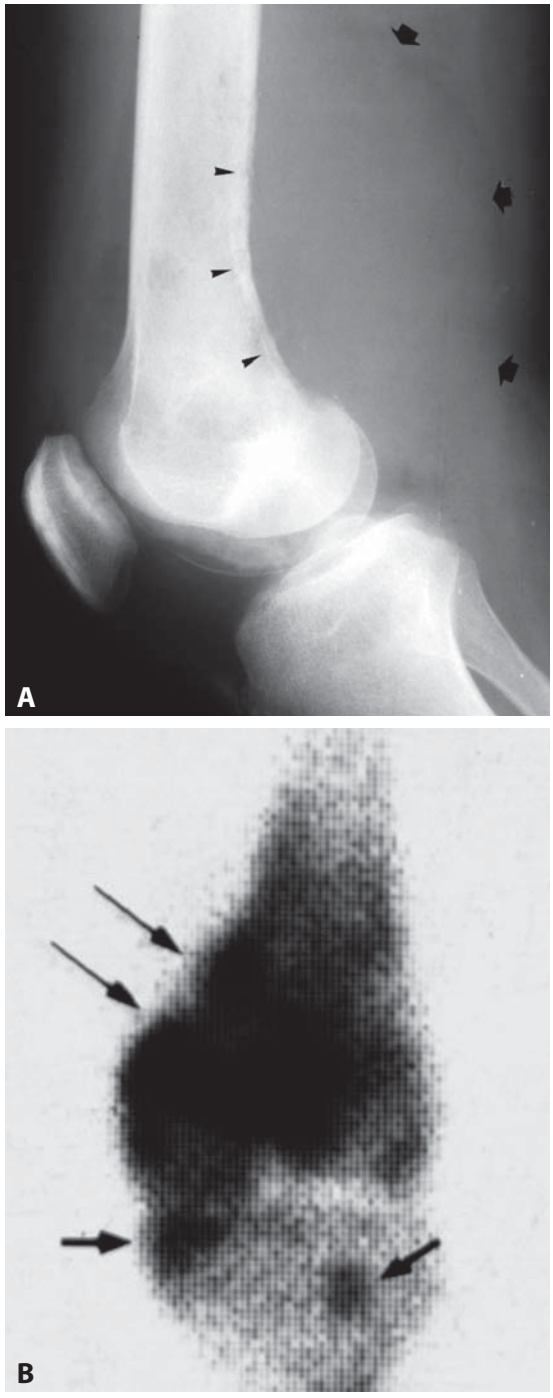

Fig. 19.3A, B Synovial sarcoma. **A** Lateral radiograph of the left knee in a 25-year-old man shows a large ovoid soft-tisse tumor in the posterior aspect of the distal femur (*arrows*) with local cortical resorption (*arrowheads*). **B** Anterior planar scintigraph reveals increased tracer uptake in the medial and posterior aspects of the distal femur and knee joint (*large arrows*). Note that there are small spotty areas of increased tracer uptake overlying the tibial head reflecting below knee extension (*small arrows*)

ma can be diagnosed by noting tracer uptake in the area in which phleboliths are shown on plain radiographs (Fig. 19.5). Hemangiomatous uptake is usually extremely subtle, and can be detected only by pinhole scintigraphy.

The mechanism involved in soft-tissue uptake of ^{99m}Tc-MDP remains unclear, except in

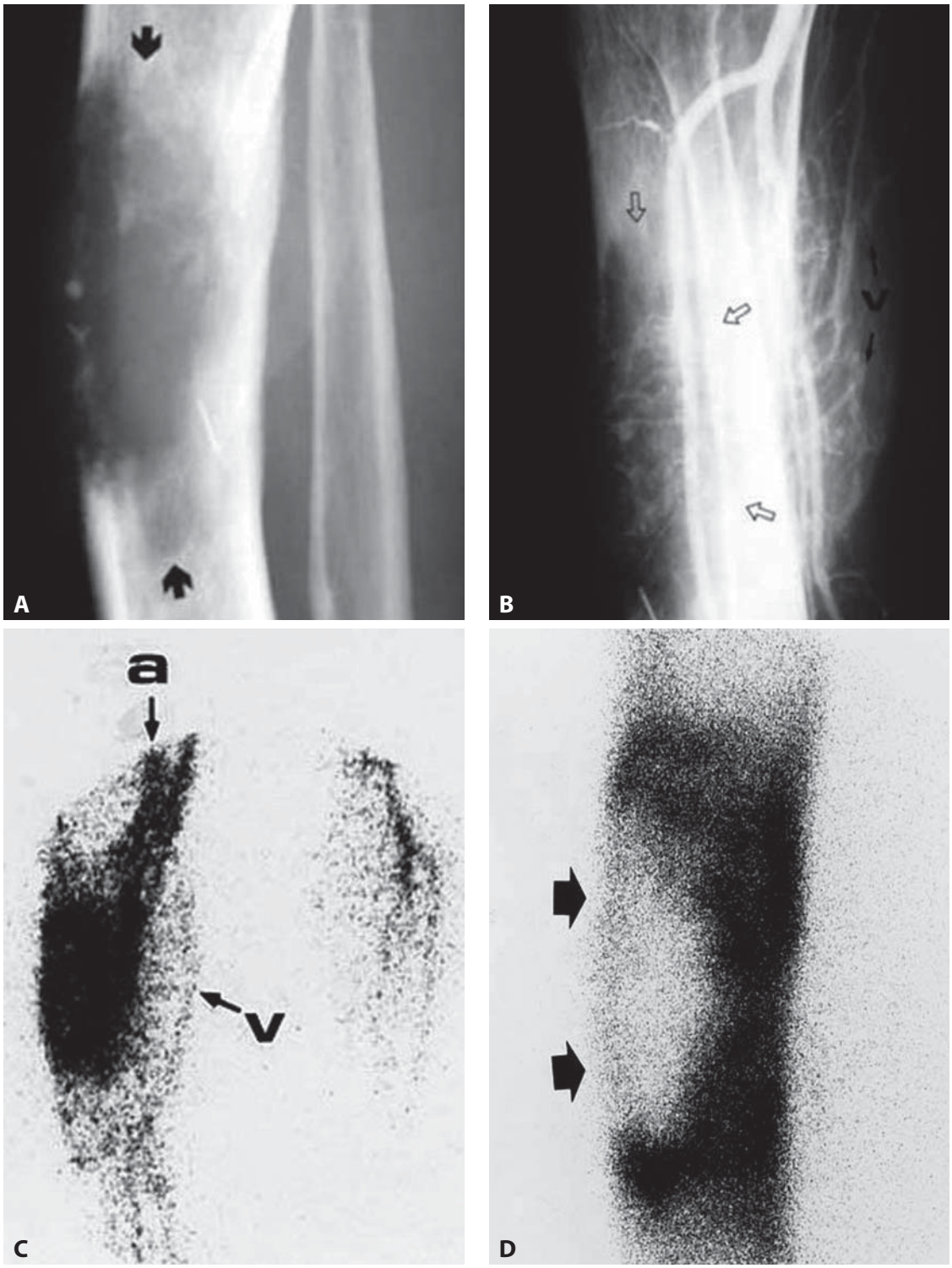

Fig. 19.4A–D Contiguous bone invasion of skin cancer. **A** Anteroposterior radiograph of the left leg in a 69-year-old man with longstanding skin carcinoma shows a large ovoid area of geographic lysis in the tibial shaft (*arrows*). **B** Contrast angiogram shows neovascularization (*arrows*) and arteriovenous shunts *(v)*. **C** Nuclear angiogram demonstratres close concordance of the findings of neovascularization and arteriovenous shunts (*a, v*). **D** Anterior pinhole scintigraph shows the area with neovascularization to be photopenic (*arrows*) and extremely intense uptake in peritumoral bone. A similar phenomenon occurs in osteosacroma (see Fig. 17.45)

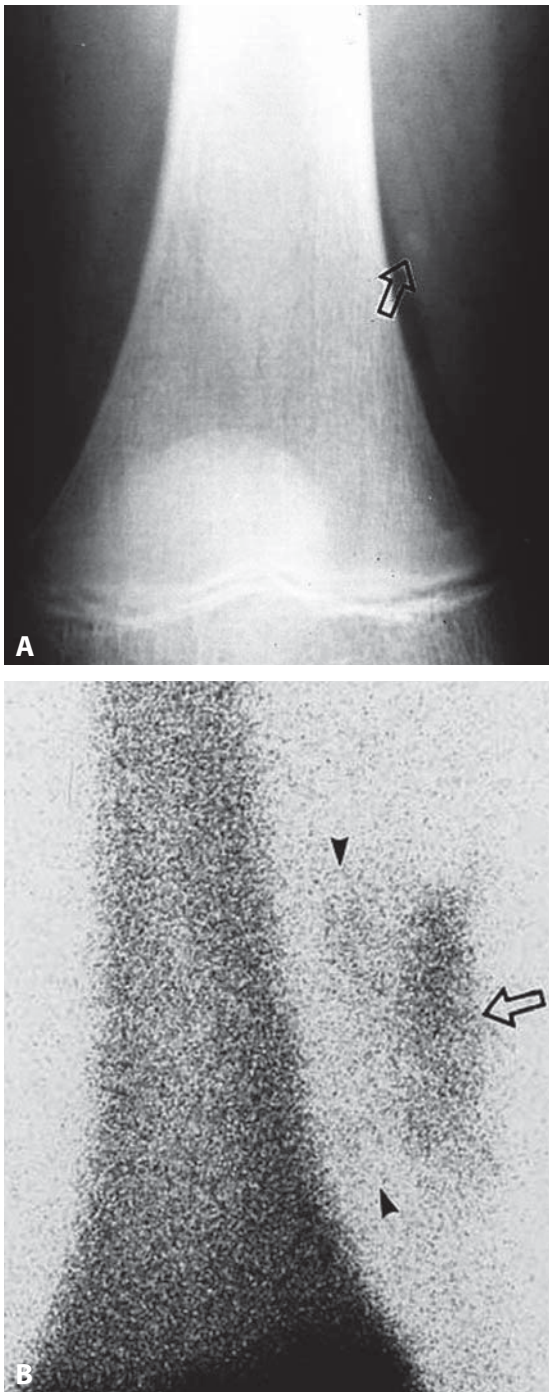

Fig. 19.5A, B Deep-seated small cavernous hemangioma. **A** Anteroposterior radiograph of the left lower thigh in an 11-year-old boy shows a small phlebolith within the deep muscle layer (*open arrow*). **B** Anterior pinhole scintigraph reveals significantly increased tracer uptake in the lateral compartment of hemangioma (*open arrow*). In contrast the medial compartment with a phlebolith accumulates tracer faintly suggesting fibrous replacement (*arrowheads*)

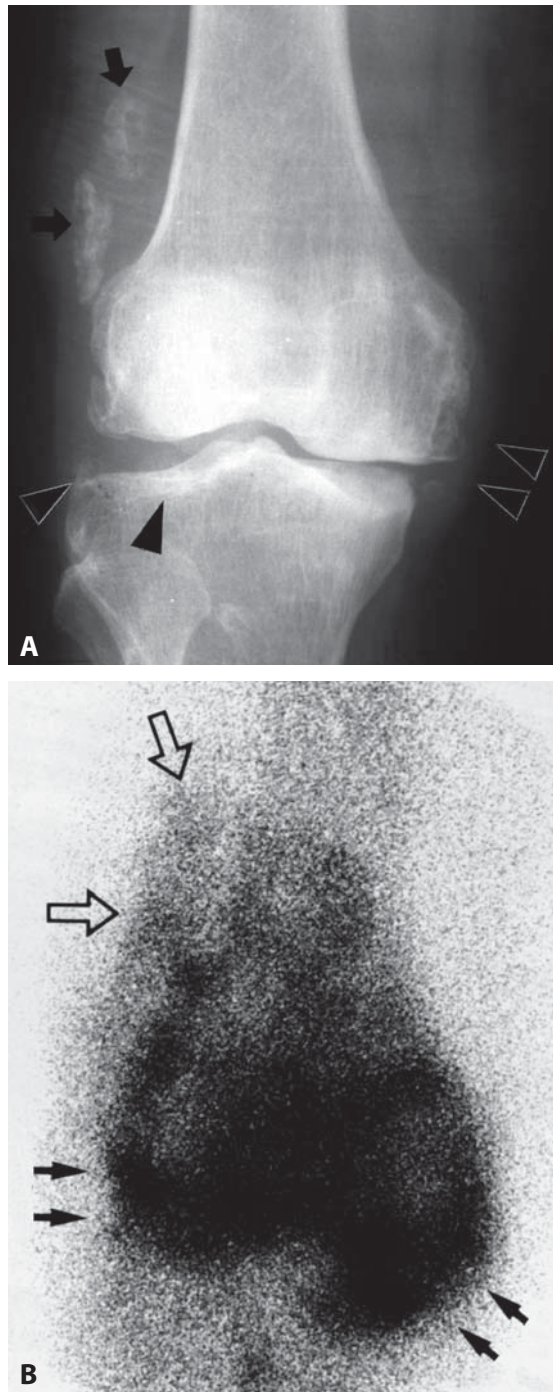

Fig. 19.6A, B Synovial osteochondromatosis in the knee joint. **A** Anteroposterior radiograph of the right knee in a 67-year-old woman shows multiple mineralized loose bodies in the knee joint (*arrowheads*) and within the confinement of the suprapatellar bursa (*arrows*). **B** Anterior pinhole scintigraph reveals intense tracer uptake in the osteochondromas and synovial lining (*solid arrows*). Lesions in the suprapatellar bursa are also well visualized (*open arrows*)

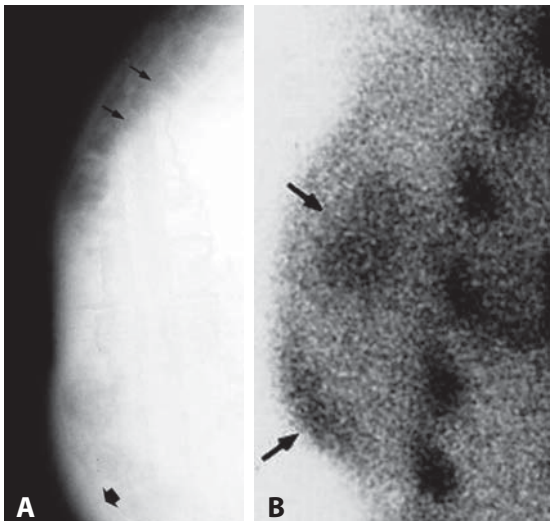

Fig. 19.7A, B Carcinoma buried in a large, dense breast. **A** Mediolateral radiograph of the right breast in a 43-year-old woman shows dense dysplastic fibrous tissue with localized skin thickenng in the lower part (*single arrow*) and supicious aberration in the upper portion (*pair of arrows*). **B** Mediolateral planar scintigraph reveals two patchy areas of increased tracer uptake in double-focus carcinoma (*arrows*)

hemangiomas and mineralization in myositis ossificans. The tracer uptake in hemangiomas is self-explanatory and heterotopic ossification in myostitis occurs in the same way as the ossification in normal living bones. Increased blood flow, calcification, and histological damage are recognized as important factors in ^{99m}Tc phosphate uptake by soft tissue. In dying

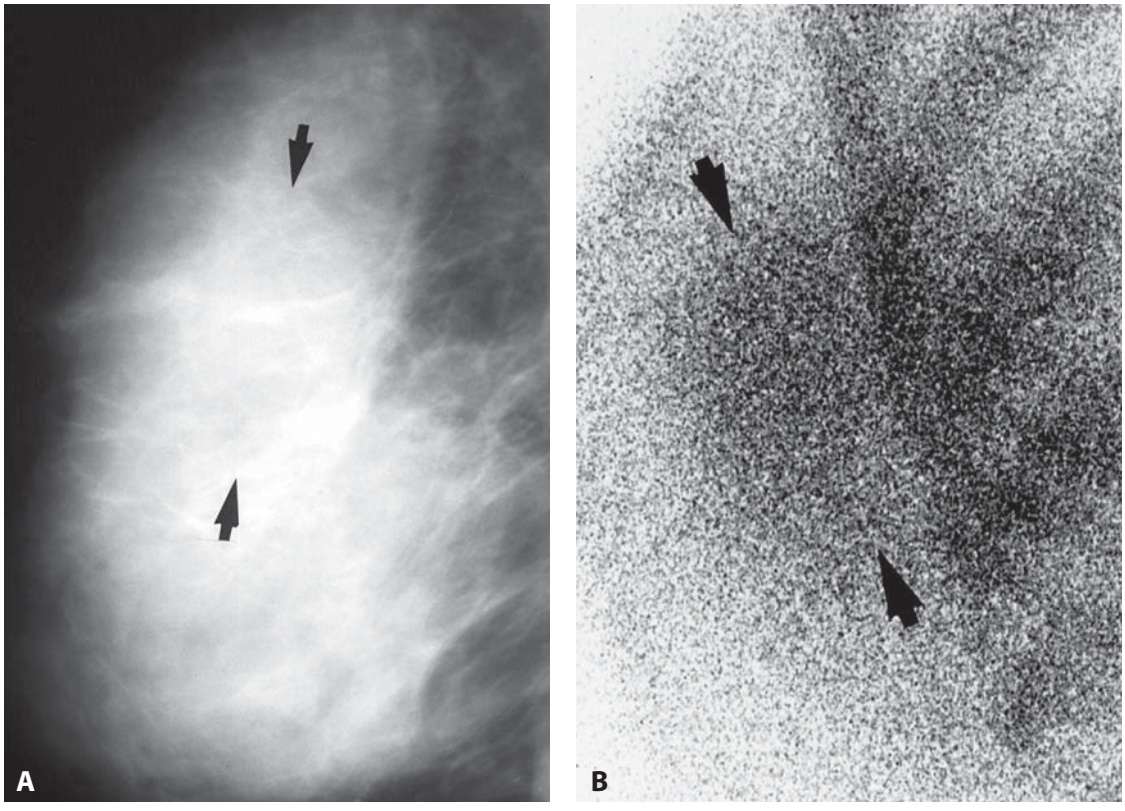

Fig. 19.8A, B Dysplasia of the breast. **A** Mediolateral radiograph of the left breast in a 44-year-old woman with a painless, palpable mass in the deep central zone shows dense dysplastic tissue without any defined tumor (*between arrows*). **B** Mediolateral pinhole scintigraph reveals a large, symmetrical, ovoid area of minimally increased tracer uptake in the deep central region (*arrows*)

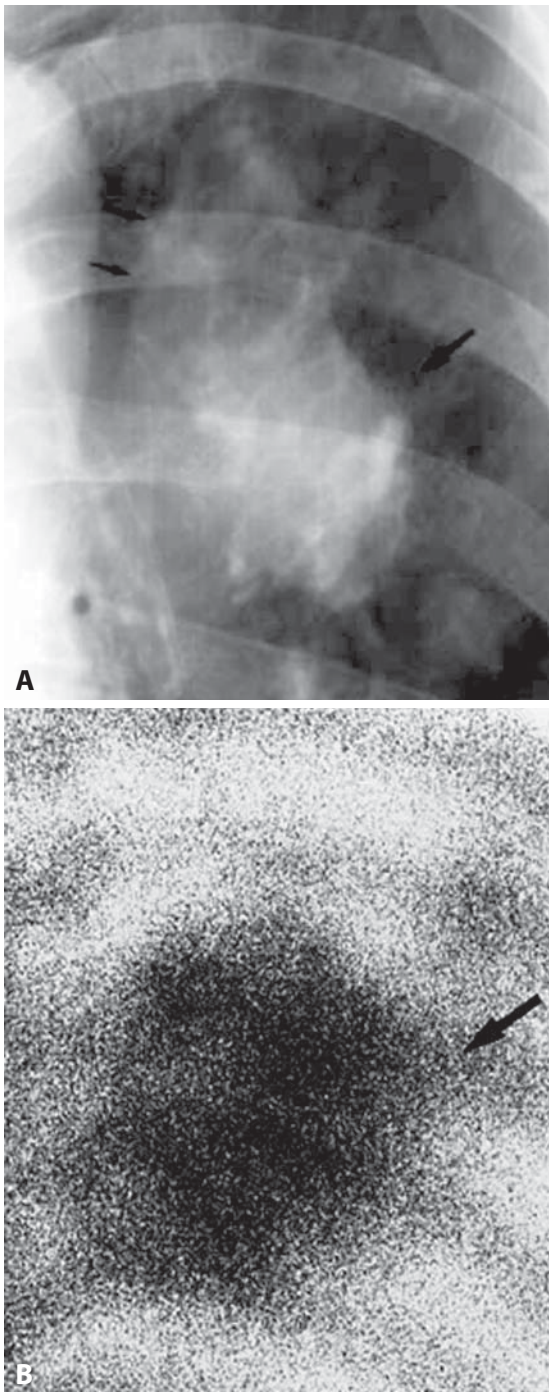

Fig. 19.9A, B Bronchogenic carcinoma with ^{99m}Tc-MDP uptake. **A** Posteroanterior radiograph of the left lung in a 53-year-old man shows a large roundish tumor mass in the hilum (*single arrow*). It is attached with a broad fan-shaped density with a fading tail at the top (*pair of arrows*). **B** Anterior pinhole scintigraph reveals moderate tracer uptake in the tumor proper but not in the attachment. The latter is probably not a neoplastic lesion but associated with lung consolidation due to atelectasis

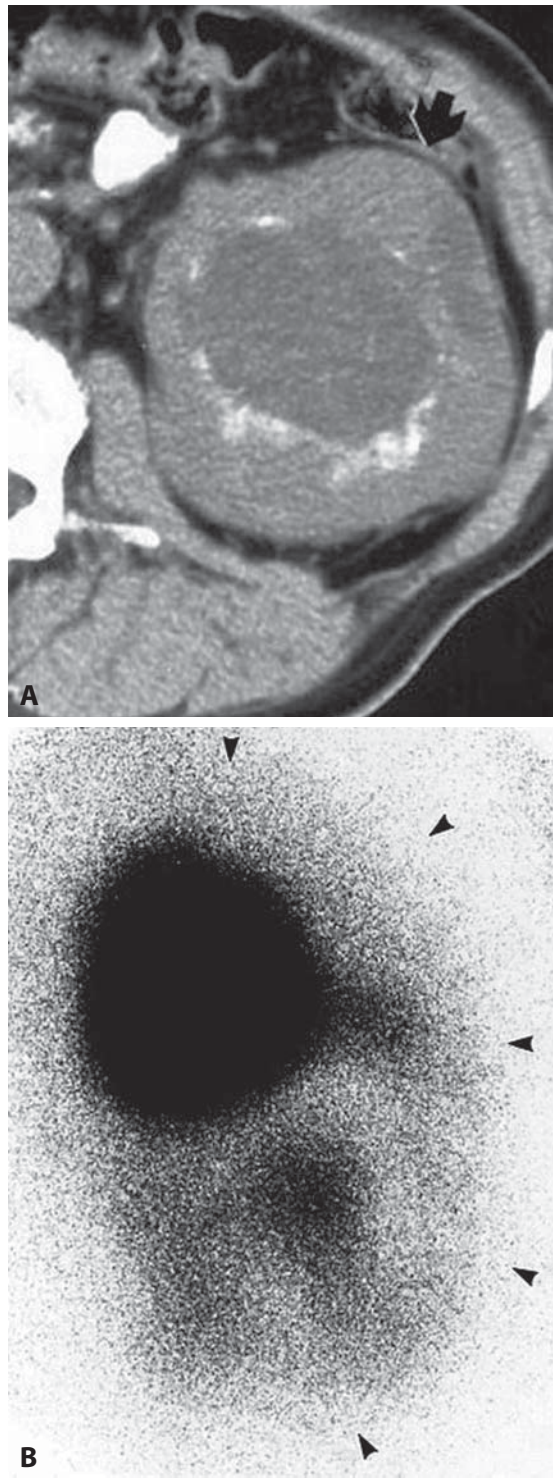

Fig. 19.10A, B Calcified renal cell carcinoma. **A** Transaxial CT of the left kidney in a 57-year-old man shows a large, roundish, low-density tumor with a calcified rim in the intermediary zone (*arrow*). **B** Posterior pinhole scintigraph reveals a sharply demarcated, round tumor with intense tracer uptake within the kidney (*arrowheads*)

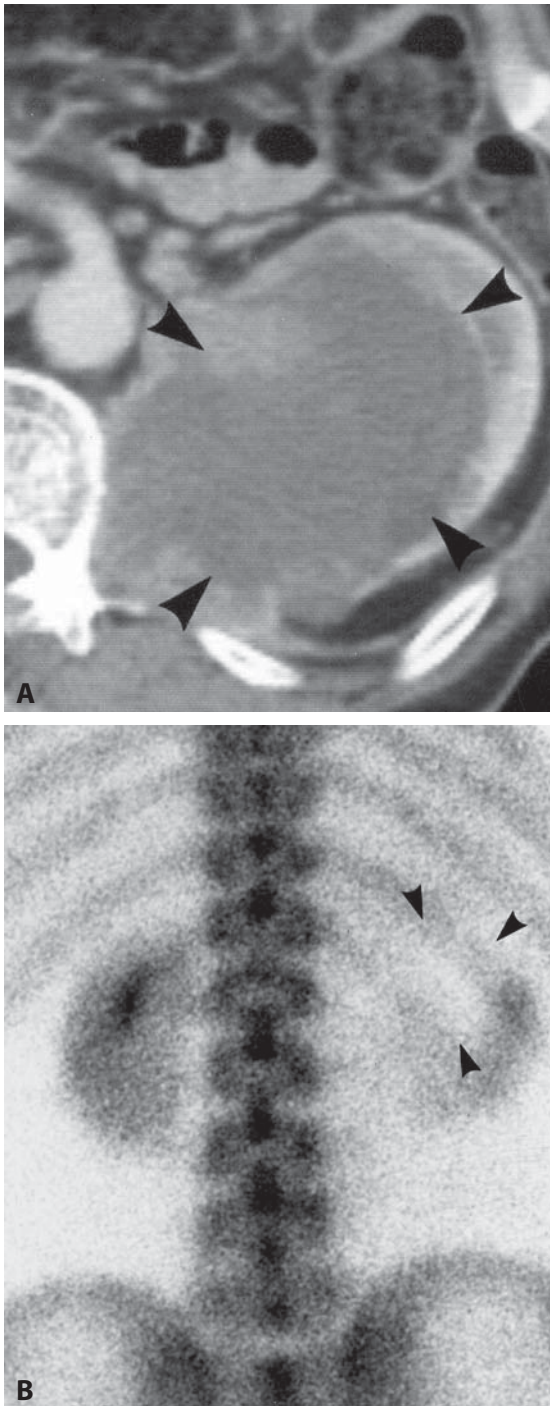

Fig. 19.11A, B Necrotized renal cell carcinoma. **A** Contrast-enhanced transaxial CT image of the left kidney in a 67-year-old man shows a large, sharply defined, ovoid, low-density tumor surrounded by compressed renal parenchyma (*arrowheads*). **B** Posterior planar bone scintigraph reveals a large photopenic tumor (*arrowheads*)

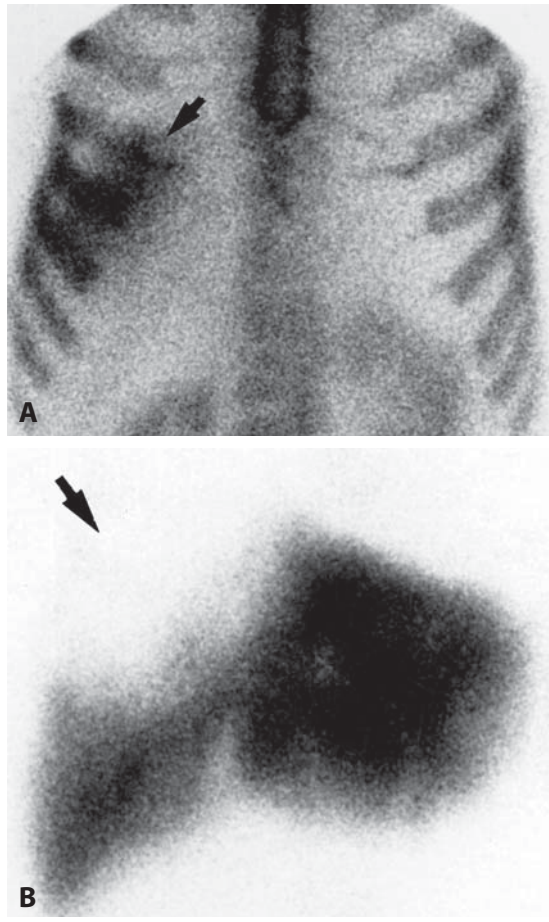

Fig. 19.12A, B ^{99m}Tc-MDP uptake by liver metastasis. **A** Anterior bone scintigraph of the upper abdomen in a 62-year-old man with liver metastasis of pancreatic carcinoma shows increased tracer uptake in the hepatic dome (*arrow*). **B** Anterior ^{99m}Tc-phytate hepatoscan reveals a large, well-defined, ovoid photon defect (*arrow*)

or dead myocytes of muscle, high titers of intracellular calcium and phosphate anions may exceed the solubility product value of calcium phosphate, leading to the formation of amorphous calcium phosphate that may subsequently be transformed into hydroxyapatite (Wahner and Dewanjee 1981). It has also been confirmed that ^{99m}Tc phosphate uptake in the soft tissues is proportional to the tissue calcium content (Silberstein et al. 1975).

Certain soft-tissue tumors, especially primary carcinomas and benign tumors with

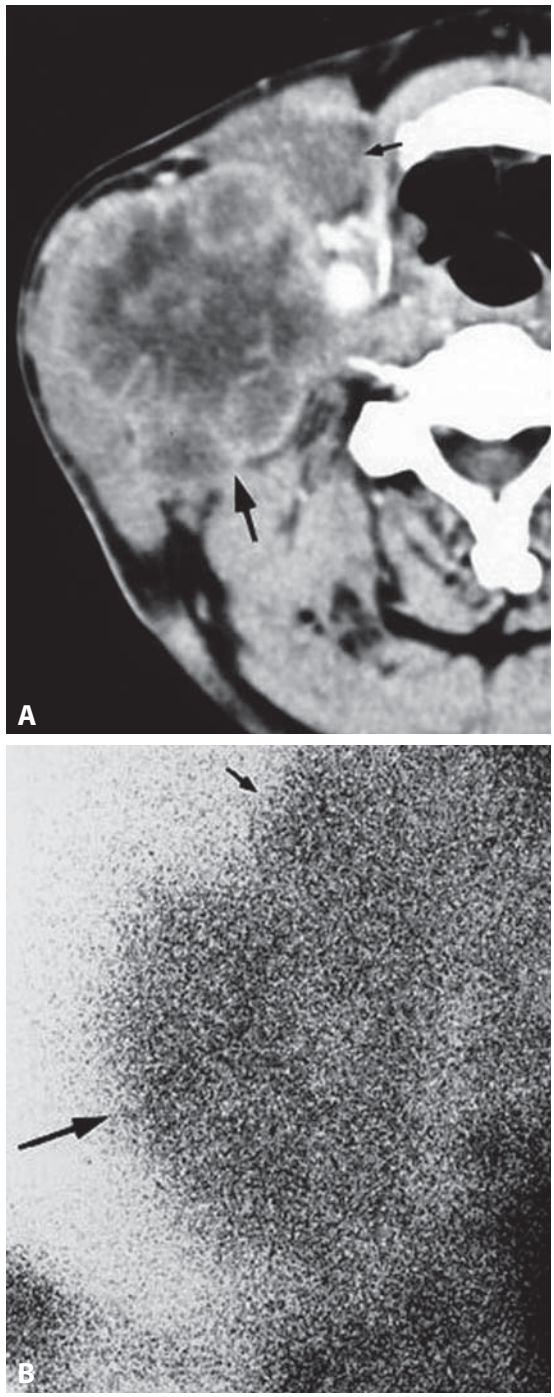

Fig. 19.13A, B Lymph node metatasis of malignant tumor. **A** Contrast enhanced CT of right lateral neck in a 54-year-old man with necrotic metastasis of poorly differentiated carcinoma of unknown primary shows an irregularly enlarged lymph node with central low density area (*large arrow*) and a small daughter nodule (*small arrow*). **B** Anterior pinhole bone scintigraph reveals moderately increased tracer uptake in both the main nodule (*large arrow*) and the daughter nodule (*small arrow*)

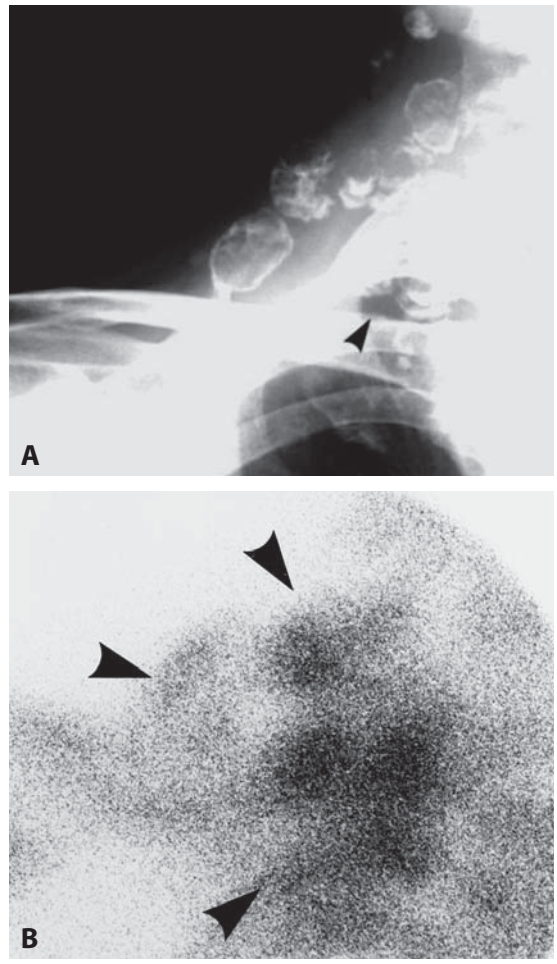

Fig. 19.14A, B Tuberculous lymphadenitis. **A** Anteroposterior radiograph of the right supraclavicular fossa in a 53-year-old woman shows mamy calcified lymph nodes (*arrowheads*). **B** Anterior pinhole scintigraph reveals multiple round areas of increased tracer uptake in the calcified lymph nodes (*arrowheads*)

microscopic or macroscopic calcification, may show considerable ^{99m}Tc-MDP uptake, facilitating diagnosis. Such tumors include breast cancer (Pickhardt and McDermott 1997; Piccolo et al. 1997), bronchogenic carcinoma (McKenna et al. 2004), pulmonary hamartoma (Burke and Rubens 1993), hepatoblastoma (Cory et al. 1987), hepatoma (Desai et al. 1983), renal cell carcinoma (Shih et al. 1986), uterine leiomyoma (Teixeira et al. 2000), urinary bladder carcinoma (Rohren 2001), and ovarian

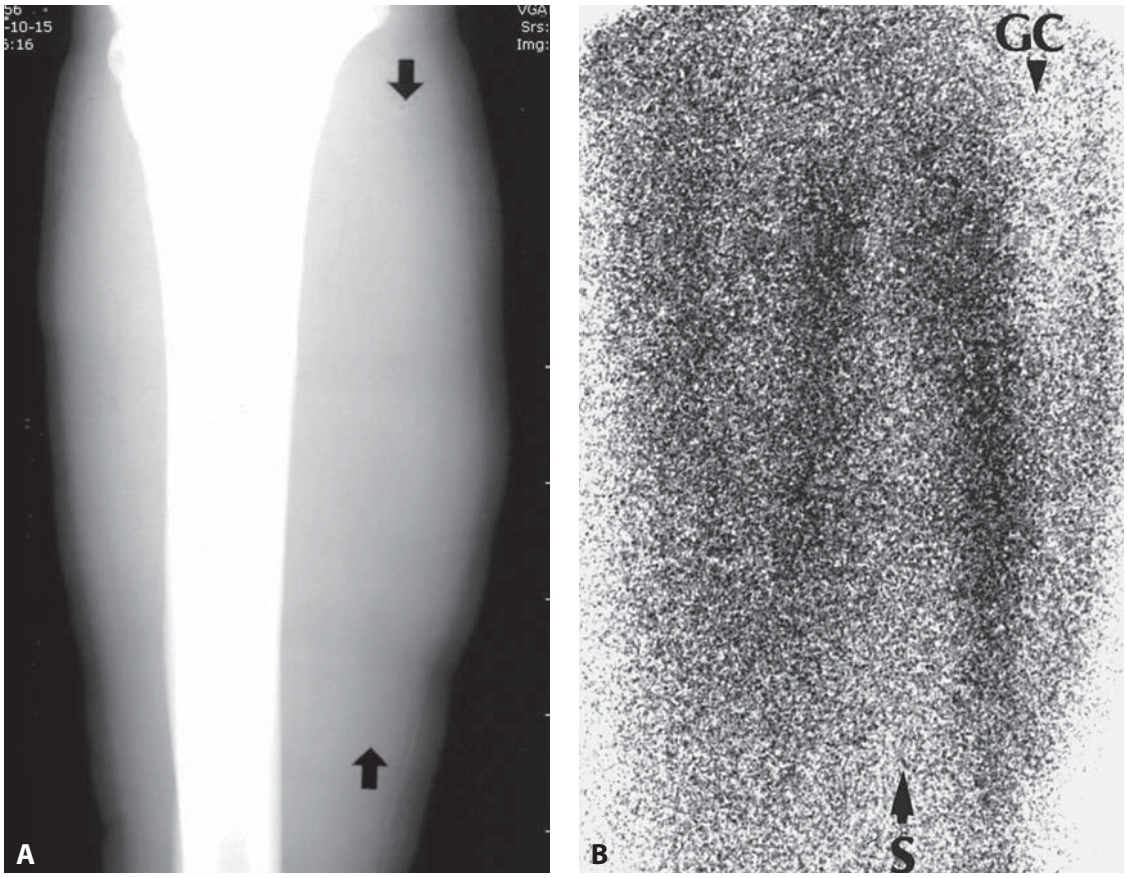

Fig. 19.15A, B Diffuse congestive soft-tisse swelling. **A** Anteroposterior radiograph of the right leg in a 47-year-old man with venous congestion due to massive cirrhotic ascites shows diffuse soft-tissue swelling (*arrows*). **B** Anterior pinhole bone scintigraph reveals longitudinal stripe-like uptake in the fascial planes against diffuse less intense background uptake in subcutaneous areolar tissues. Note that muscles do not significantly accumulate tracer (*GC* gastrocnemius muscle, *S* soleus muscle)

cancer (Beres et al. 1991). In addition, thyroid carcinomas (Montes et al. 1999) and orthotopic (Riedy and Adler 2000) and retrosternal goiters (Garty et al. 1984) and lymph node, and soft-tissue metastases have also been reported to accumulate ^{99m}Tc-MDP.

Our experience indicates that ^{99m}Tc MDP pinhole scintigraphy is useful for diagnosing and characterizing tumors of the breast, particularly when tumors are buried in a large, dense breast (Fig. 19.7). Dysplasia of the breast can also be visualized, but tracer uptake is comparatively low (Fig. 19.8). Certain bronchogenic carcinomas intensely accumulate ^{99m}Tc-MDP so that bone scintigraphy may be used even as a primary diagnostic procedure. Actually, the bone scan perfomed for tumor staging in one of our patients with lung carcinoma incidentally demonstrated prominent tracer uptake (Fig. 19.9). Calcified renal cell carcinomas also intensely accumulate bone tracer (Fig. 19.10), contrasting with the fact that ordnary renal cell carcinomas do not take up tracer (Shih et al. 1986) (Fig. 19.11). The ^{99m}Tc-MDP uptake by hepatoblastoma (Cory et al. 1987) and hepatocellular carcinoma is well known (Desai et al. 1983). In addition, the visualization of hepatic metastases on ^{99m}Tc-MDP bone scan is not rare (Romyn et al. 1987). In a 62-year-old man we observed pancreatic head carcinoma metastasized to the right hepatic lobe to accumulate ^{99m}Tc-MDP on bone scan (Fig. 19.12).

Another important group of malignant soft-tissue tumors comprises metastases to lymph

nodes (Fig. 19.13) and soft tissue. ^{99m}Tc-MDP bone scintigraphy can be advantageously used for the simultaneous diagnosis of not only primary tumors originating from soft tissues and parenchymal organs but also their metastases to the bones (Fig. 17.2), lymph nodes, and muscles (Figs. 17.41 and 17.42).

Miscellaneous conditions that simulate tumors include tuberculous lymphadenitis (Fig. 19.14) and soft tissue edema that causes localized or diffuse soft-tissue swelling. It is interesting that pinhole scintigraphy demonstrates that the diffuse soft-tisse swelling due to venous congestion in the lower limb typically occurs in the fascial planes and subcutaneous tissue but not within the muscles (Anvar et al. 2000) (Fig. 19.15).

References

Anvar MD, Khiabani HZ, Nesland JM, et al (2000) Vascular and stromal features in the skin of the lower limb in patients with chronic limb ischemia (CLI) and oedema. Eur J Vasc Endovasc Surg 20:125–131

Beres RA, Patel N, Krasnow AZ, et al (1991) Concentration of Tc-99m MDP in ovarian carcinoma and its soft tissue metastases. Clin Nucl Med 16:550–552

Burke W, Rubens MB (1993) Uptake of technetium-99m methylene diphosphonate by a pulmonary hamartoma/mesenchymoma. Br J Radiol 66:74–76

Cory DA, Siddiqui AR, Cohen MD (1987) Uptake of technetium 99m MDP by hepatoblastoma. Eur J Nucl Med 12:546–547

Desai AG, Schaffer B, Park CH (1983) Accumulation of bone-scanning agents in hepatoma. Radiology 149:292

Enzinger FM, Weiss SW (1983) General considerations. In: Soft tissue tumors. Mosby, St. Louis, pp 1–13

Garty I, Rosen G, Risescu J (1984) Extraosseous ^{99m}Tc-MDP uptake in mediastinal thyroid goiter: two case reports. Eur J Nucl Med 9:521–524

McKenna D, Igbal A, O'Keeffe D (2004) Tc-99m methylene diphosphonate uptake in a primary lung cancer. Clin Nucl Med 29:723–724

Montes TC, Munoz C, Rivero JI, et al (1999) Uptake of Tc-99m sestamibi and Tc-99m MDP in anaplastic carcinoma of the thyroid (nondiagnostic CT and ultrasound scans). Clin Nucl Med 24:355–356

Murphy MD, Fairbairn KJ, Parman LM, et al (1995) From the archives of the AFIP. Musculoskeletal angiomatous lesions: radiographic-pathology correlation. Radiographics 15:893–917

Myhre-Jensen O (1981) A consecutive 7-year series of 1331 benign tissue tumours. Clinicopathologic data. Comparison with sarcomas. Acta Orthop Scand 52:287–293

Piccolo S, Lastoria S, Muto P, et al (1997) Scintimammography with ^{99m}Tc-MDP in the detection of primary breast cancer. Q J Nucl Med 41:225–230

Pickhardt PJ, McDermott M (1997) Intense uptake of technetium-99m-MDP in primary breast adenocarcinoma with sarcomatoid metaplasia. J Nucl Med 38:528–530

Riedy G, Adler L (2000) Tc-99m MDP thyroid uptake in a patient with a large nontoxic goiter. Clin Nucl Med 25:929–930

Rohren EM (2001) Tc-99m MDP uptake in a calcified bladder tumor. Clin Nucl Med 26:58–59

Romyn AM, Bushnell DL, Freeman ML, Kaplan E (1987) Visualization of metastatic liver disease on technetium-99m bone scintigraphy. Clin Nucl Med 12:264–267

Shih WJ, Deland FH, Domstad PA, Purcell M (1986) Ring-like uptake pattern of a skeletal imaging agent in a huge renal cell carcinoma. Clin Nucl Med 11:319–321

Silberstein EB, Francis MD, Tofe AJ, Slough CL (1975) Distribution of ^{99m}Tc-Sn diphosphonate and free ^{99m}Tc-pertechnetate in selected hard and soft tissues. J Nucl Med 16:58–61

Teixeira AB, Etchebehere CS, Calvalho, et al (2000) Tc-99k MDP uptake in uterine leiomyoma. Clin Nucl Med 25:484

Wahner HW, Dewanjee MK (1981) Drug-induced modulation of Tc-99m pyrophosphate tissue distribution: what is involved? J Nucl Med 22:555–559

20 Otorhinological Disorders

This chapter describes ^{99m}Tc-MDP pinhole scanning manifestations of inflammation, infections, granulomas, and malignant tumors of the paranasal sinuses, nasal cavity, nasopharynx, and mastoid. The other otorhinological diseases of scintigraphic interest such as fibrous dysplasia, Paget's disease, and giant cell tumor are discussed in detail in their respective chapters. Most recently, ^{18}F-FDG PET has become increasingly used for the diagnosis, staging and restaging, and monitoring of treatments of malignant tumors of the nose, pharynx, and throat with promising results (Yen et al 2005; Rivera et al. 2005). Traumatology is not included in this discussion since it is primarily the objective of radiography, CT, and MRI.

The paranasal sinuses consist of two paired (maxillary sinuses and ethmoid cells) and two unpaired (frontal and sphenoid sinuses) air spaces lined with the mucoperiosteal membrane in the midline and paramedian planes of the face and skull base. The nasal cavity is located between the maxillary sinuses and the ethmoid cells, below the frontal sinus, and in front of the sphenoid sinus, and contains three paired turbinates with interposed meati and a midline bony septum.

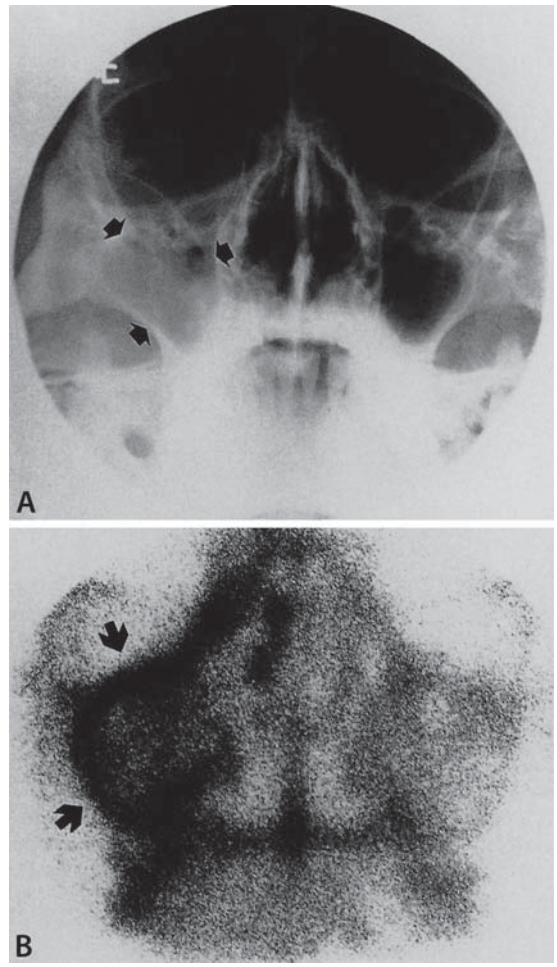

Fig. 20.1A, B Maxillary sinusitis. **A** Waters' view radiogaph of the maxillary sinuses in a 39-year-old woman shows marked clouding of the entire right maxillary sinus (*arrows*). **B** Tilted anterior pinhole scintigraph shows diffusely increased tracer uptake in the entire sinus with the most intense uptake in the wall. Note that the involvement is diffuse and generalized (*arrows*)

20.1 Rhinosinusitis and Mucocele

Rhinosinusitis or paranasal sinusitis is the inflammation of mucosal lining of the paranasal sinuses. It is a ubiquitous infective disease that is usually associated with allergic rhinitis or a viral infection of the upper respiratory tract,

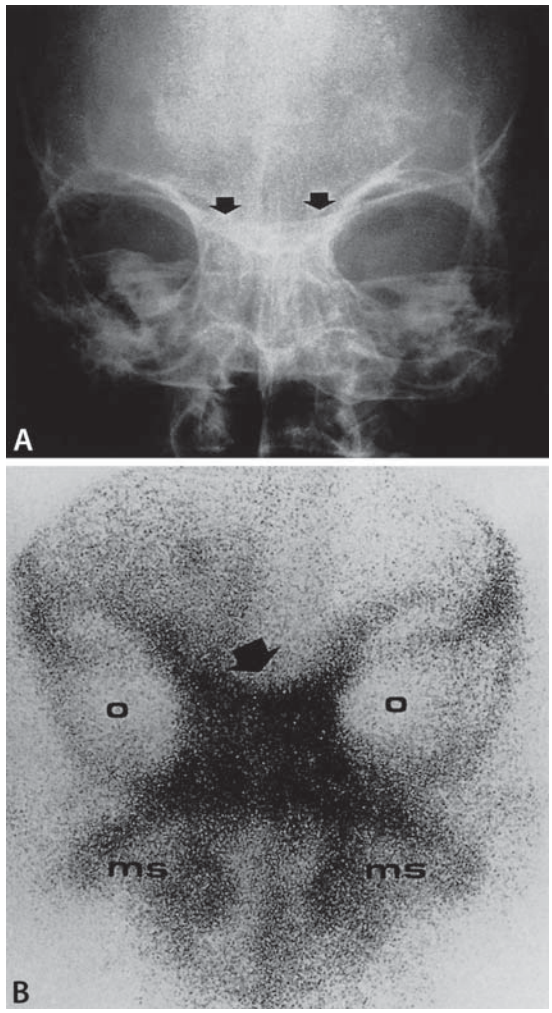

Fig. 20.2A, B Ethmoid sinusitis. **A** Posteroanterior radiograph of the skull reveals complete opacification of the ethmoid sinuses located between the orbits (*arrows*). **B** Anterior pinhole scintigraph shows intense tracer uptake in the entire ethmoid sinuses (*arrow*) located between the orbits (*o*). Compare with the clearly aerated maxillary sinuses (*ms*). The relative smallness of the orbits and maxillary sinuses is due to the diminishing effect in the periphery of the field of view

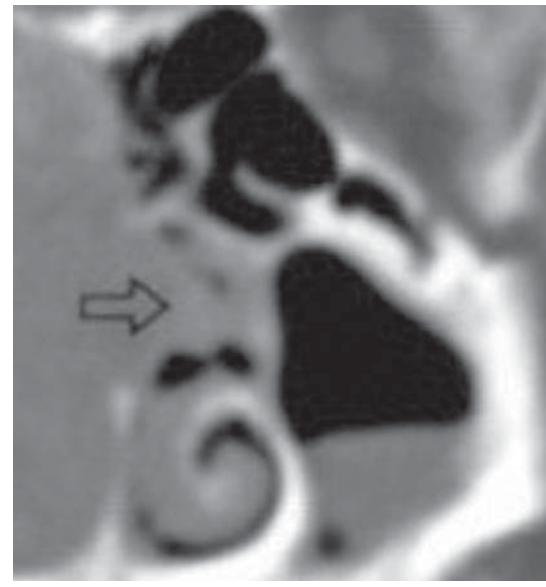

Fig. 20.3 Upright CT scan of acute sinusitis secondary to nasal carcinoma (the same patient as in Fig. 20.11). Coronal CT scan of the left antrum in a 71-year-old woman shows air-fluid level. Note that thers is no significant mucoperiosteal thickening in this acute sinusitis (*open arrow*)

and classified into the acute, subacute, or chronic from. The acute form manifests mucosal swelling, congestion, and hyperemia with effusion or pus and the chronic form mucoperiosteal thickening. The most common infective agents are *Streptococcus pneumoniae* and *Haemophilus influenzae* (Evans et al. 1975). Allergic fungal sinusitis is a variant of chronic sinusitis.

With the blockage of the sinusal ostia by edema, trauma, surgery, or tumor the effusion becomes chronically retained and results in mucocele formation (Evans 1981). The mucocele is a chronic, inflammatory lesion with cyst formation lined with the low columnar or pseudostratified epithelium. It chronically stimulates and erodes the mucoperiosteum, and slowly balloons the bony wall of the sinus, causing sclerosis. The frontal sinus is most commonly involved, followed by the ethmoid, maxillary, and sphenoidal sinuses (Zeifer 2001).

The radiographic manifestations of sinusitis are characterized by complete or partial opacification of the sinus (Figs. 20.1A and 20.2A). Not infrequently, the effusion or pus in acute sinusitis may be interfaced with air forming an air-fluid level on upright radiographs or CT (Fig. 20.3). In chronic sinusitis the mucoperiosteal membrane becomes diffusely thickened (Fig. 20.4). Being expansive in nature mucoceles diffusely obliterate the sinusal space with bony wall sclerosis and ballooning of various

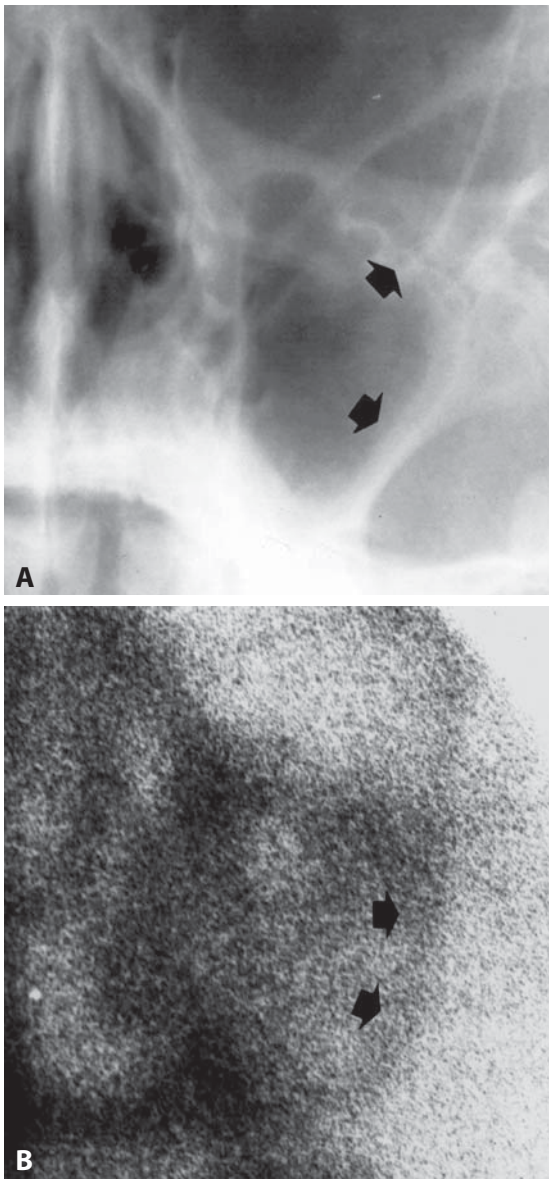

Fig. 20.4A, B Chronic sinusitis. **A** Waters' view radiograph of the left maxillary sinus in a 39-year-old woman with chronic sinusitis shows mucoperiosteal thickening in the superolateral wall of the left antrum (*arrow*). **B** Waters' view pinhole scan reveals concordant increased tracer uptake in the thickened mucoperiosteum (*arrows*)

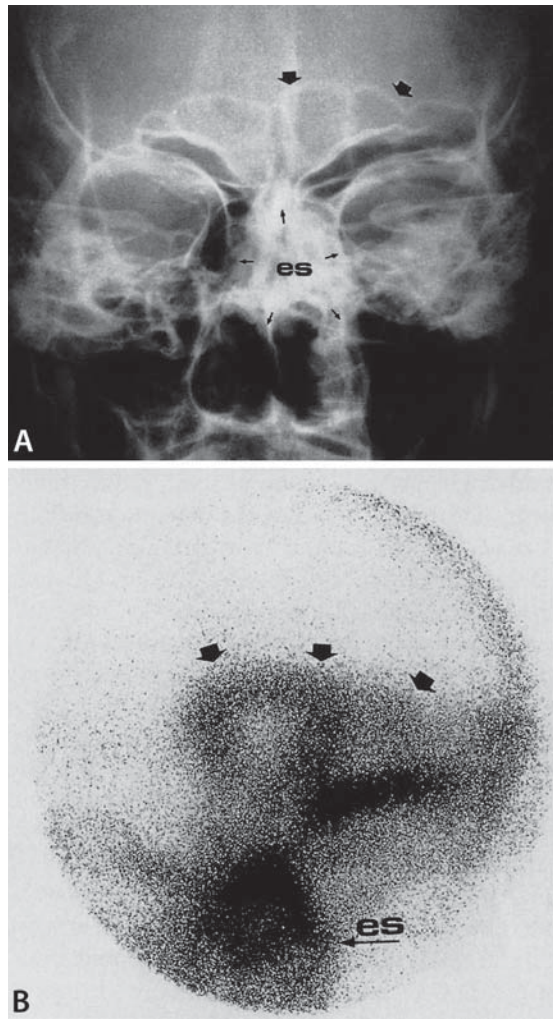

Fig. 20.5A, B Obstructive frontal sinusitis with mucus accumulation. **A** Posteroanterior radiograph of the skull shows diffuse clouding of the frontal sinus with suspicious blurring of the thickened sinus wall in the left half (*arrows*) as well as an obstructing mass in the ipsilateral ethmoid sinus (*es*). **B** Anterior pinhole scintigraph shows intense tracer uptake only in the wall of the left frontal sinus (*thick arrows*). The right half of the sinus is uninvolved. The patterns of tracer uptake in the two halves of the frontal sinus are distinctly different, but the radiographic finding is ambiguous. Observe the intense tracer uptake in the obstructing ethmoidal sinus tumor (*es*)

degrees according to the duration of the disease Pinhole scintigraphy of acute maxillary sinusitis shows annular uptake in the mucoperiosteal membrane of the entire sinusal wall (Fig. 20.1B). Such annular uptake in sinusitis is in contrast with focal uptake in malignant midline reticulosis (Fig. 20.7) and carcinoma (Fig. 20.8B). When sinusitis affects the ethmoidal sinus whole sinusal cells accumulate tracer, totally obliterating the sinus (Fig. 20.2B). The tracer uptake in chronic sinusitis with mucoperiosteal thickening tends to be mild and less intense

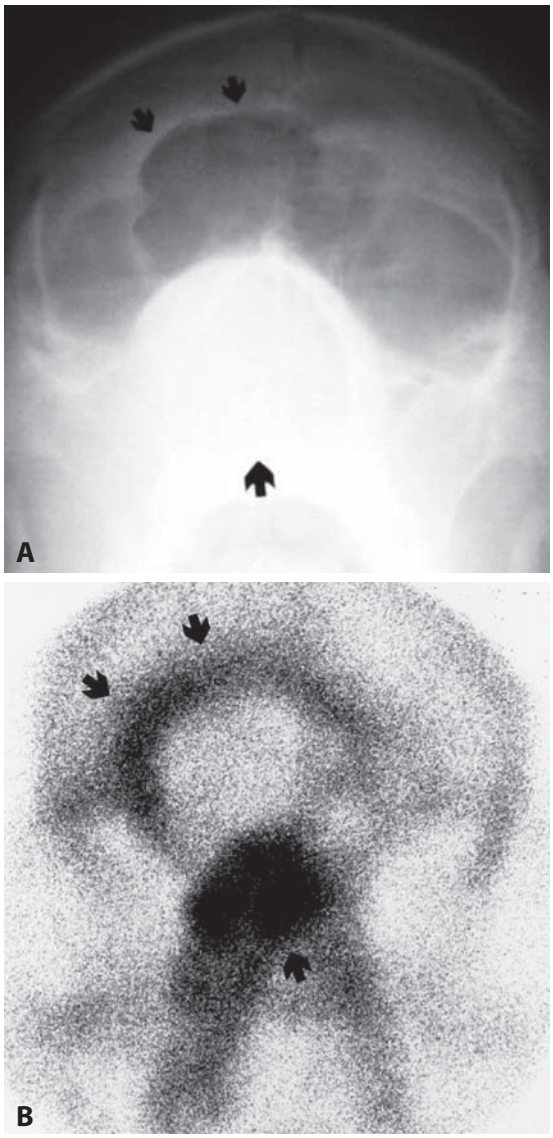

Fig. 20.6A, B Mucocele in the frontal sinus. **A** Waters' view radiograph of the face in a 21-year-old man with frontal sinus mucocele secondary to nasal Ewing's tumor shows ballooning of the frontal sinus with reactive wall thickening (*arrows*). The mass in the nose represents Ewing's tumor (*single arrow*). **B** Pinhole scintigraph reveals dilatation of the frontal sinus with reactive tracer uptake in the wall (*arrows*). Note the tracer uptake localized to the Ewing's tumor (*single arrow*)

than in acute sinusitis (Fig. 20.4B). In mucoceles the ballooned sinusal walls intensely accumulate tracer, giving rise to a cumulus-like appearance (Figs. 20.5B and 20.6B).

20.2 Granulomatous and Similar Diseases

Granulomas of the nasal cavity and paranasal sinuses comprise another important disease group diagnosed by ^{99m}Tc-MDP scaintigraphy. Tuberculosis, syphilis, sarcoidosis, malignant midline reticulosis, midline granuloma, and Wegener's granulomatosis belong to this group. A clinical feature common to all these diseases is that pathological changes start from the nasal cavity, subsequently spreading to the paranasal sinuses and perinasal structures including the palate. In the beginning the process takes the form of simple mucoperiosteal thickening and nodularity and slowly progresses to invade, destroy, and eventually mutilate the perinasal structures.

The radiographic features include soft-tissue mass, nasal obstruction, sinus clouding, and destruction of the nasal and perinasal bones (Fig. 20.7A). Pinhole scintigraphically, granulomas do not accumulate tracer, but invaded bones of the nasal turbinate, septum, wall, and maxillary sinusal wall accumulate tracer (Fig. 20.7B). The spread of disease to other sinuses and perinasal bones is also indicated by increased uptake in the specific sites.

20.3 Maxillary Sinus Carcinoma

Carcinomas of the sinonasal cavities are uncommon with a prevalence of less than 1% of all malignancies. Squamous cell carcinoma is most common with adenocarcinoma being the next most common (Weymuller 1993). Plain radiography, CT, and MRI are standard diagnostic methods. Pinhole bone scintigraphy is also a valuable tool for studying local bone invasion and distant skeletal metastases. It is technically simple and economically not burdensome.^{18}F-FDG PET has been increasingly used in recent years for the same purposes.

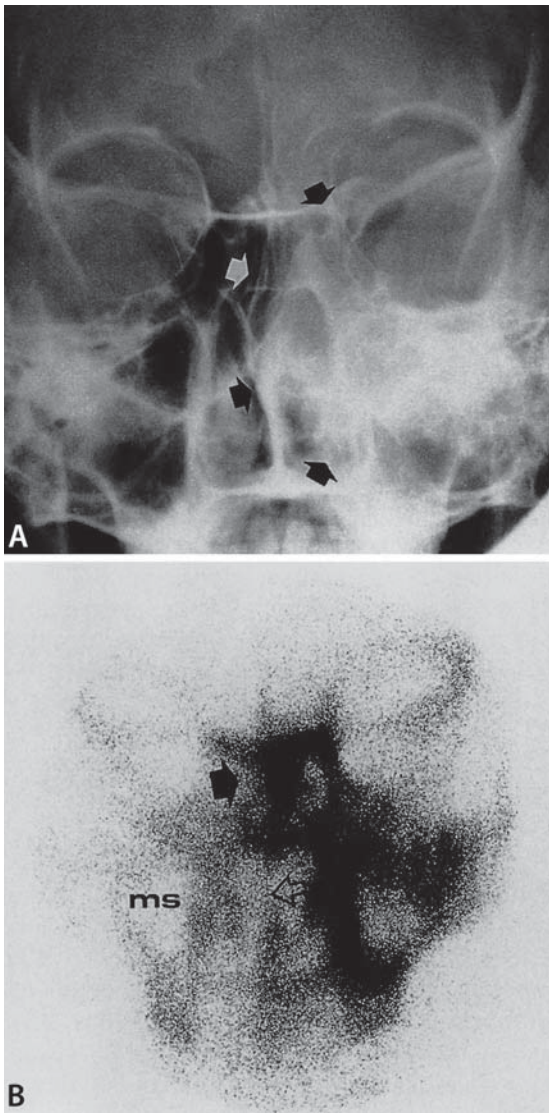

Fig. 20.7A, B Malignant midline reticulosis. **A** Waters' view radiograph in a 27-year-old woman with a nasal tumor reveals a soft-tissue mass in the left nasal cavity with diffuse clouding of the ipsilateral maxillary and ethmoid sinuses and septal bulging (*arrows*). The right maxillary sinus is clearly aerated. **B** Anterior pinhole scan shows extremely intense tracer uptake diffusely in the ipsilateral maxillary and ethmoid sinus walls (*solid arrow*), denoting a wide spread to the mucoperiosteums. In addition, a small photopenic defect (*open arrow*) is seen in the perforated midseptum (*ms denote maxillary sinus*)

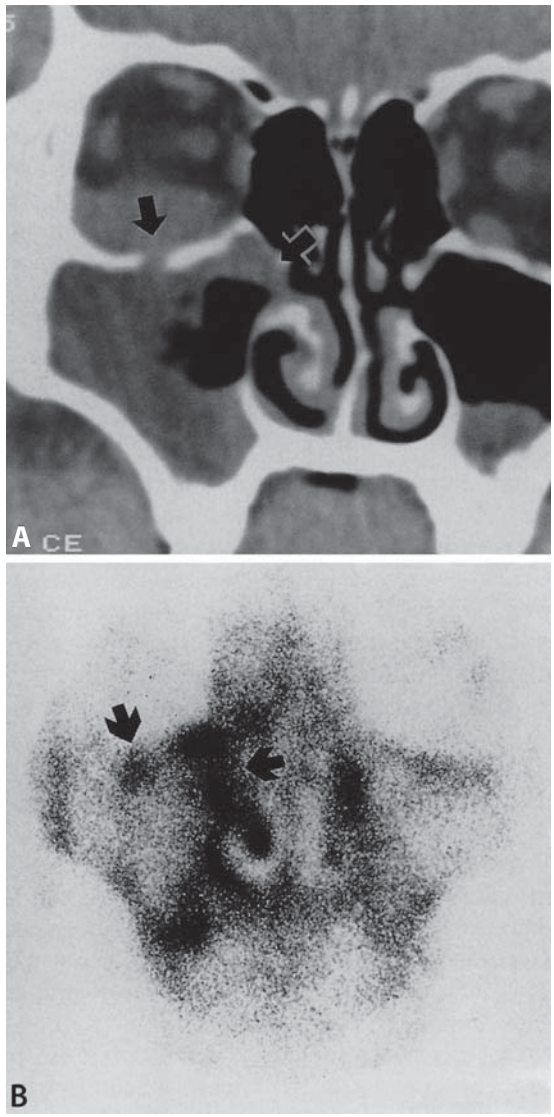

Fig. 20.8A, B Maxillary sinus carcinoma. **A** Coronal CT scan of the right maxillary sinus shows clouding of the antral cavity with perforations in the upper medial wall and the central aspect of the roof (*arrows*). The inferior nasal turbinate appears thickened. **B** Anterior pinhole scintigraph of the right maxillary sinus shows intense tracer uptake in the medial wall including the inferior turbinate (*horizontal arrow*) and another area of spotty uptake in the roof at the site of perforation (*vertical arrow*). Unlike the generalized involvement in sinusitis, the wall involvement in maxillary sinus cancer is characteristically eccentric and partial

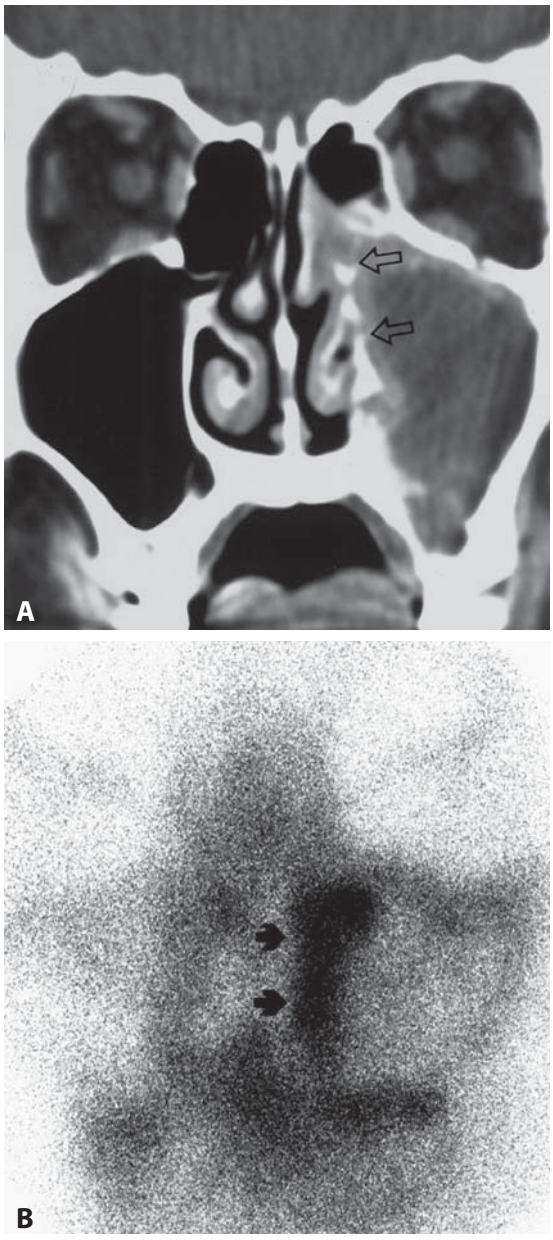

Fig. 20.9A, B Sectional or focal involvement of sinus wall in carcinoma. **A** Coronal CT of the maxillary sinus in a 39-year-old woman shows irregular perforation of the medial bony wall of the left antrum (*open arrows*). Diseased sinus cavity is diffusaely clouded due to effusion. **B** Waters' view pinhole scan reveals tracer uptake in the destroyed medial wall (*arrows*)

The radiographic changes include local bone erosion and destruction and clouding of the sinus, most commonly the maxillary sinus. Extension of carcinoma to the neighboring sinuses and nasal cavity as well as bones is the natural course of the disease. Accordingly, it is difficult to radiographically distinguish carcinomatous changes in the paransal sinus from simple sinusitis. It is also not easy to analytically observe carcinomatous changes in detail because of clouding and complexity of topography. Fortunately, however, pinhole bone scanning shows two basically different features, greatly helping distinguish sinusitis from carcinoma. Thus, the tracer uptake is simply diffuse in acute or subacute sinusitis (Fig. 20.1A) and focal or sectional in uncomplicated carcinomas (Figs. 20.8 and 20.9). In the natural course of tumors the nasal cavity, orbit, and ethmoidal sinuses are contiguously invaded (Fig. 20.10A). It is to be mentioned that the tracer uptake in cancer-bearing sinusal walls does not necessarily indicate neoplastic invasion, but may also reflect nonspecific reaction or the watershed phenomenon. Cancer penetrations of the antral wall are seen not as a photon defect but as intense uptake when they are not large enough. As is well known, carcinomatous tissues do not accmulate bone scan agent except when mineralized. However, cancer cells avidly accumulate ^{18}F-FDG so that they can be directly identified by PET (Fig. 20.10C).

20.4 Malignant Tumors of the Nasal Cavity

Malignant tumors of the nasal cavity or endonasal malignancies are uncommon, accounting for less than 1% of all malignancies and about 3% of upper respiratory tract cancers (Carrau and Myers 2001). Two recent studies on histopathological prevalence showed squamous cell (epidermoid) carcinoma to represent 26–39% and lymphoma 26% with septal involvement in 48% (Kharoubi 2005; Euteneuer et al. 2005). The tumors were staged T4 in 52% of cases when the initial diagnosis was made (Euteneuer et al. 2005). We have experience of a case of Ewing's tumor originating from the nasal

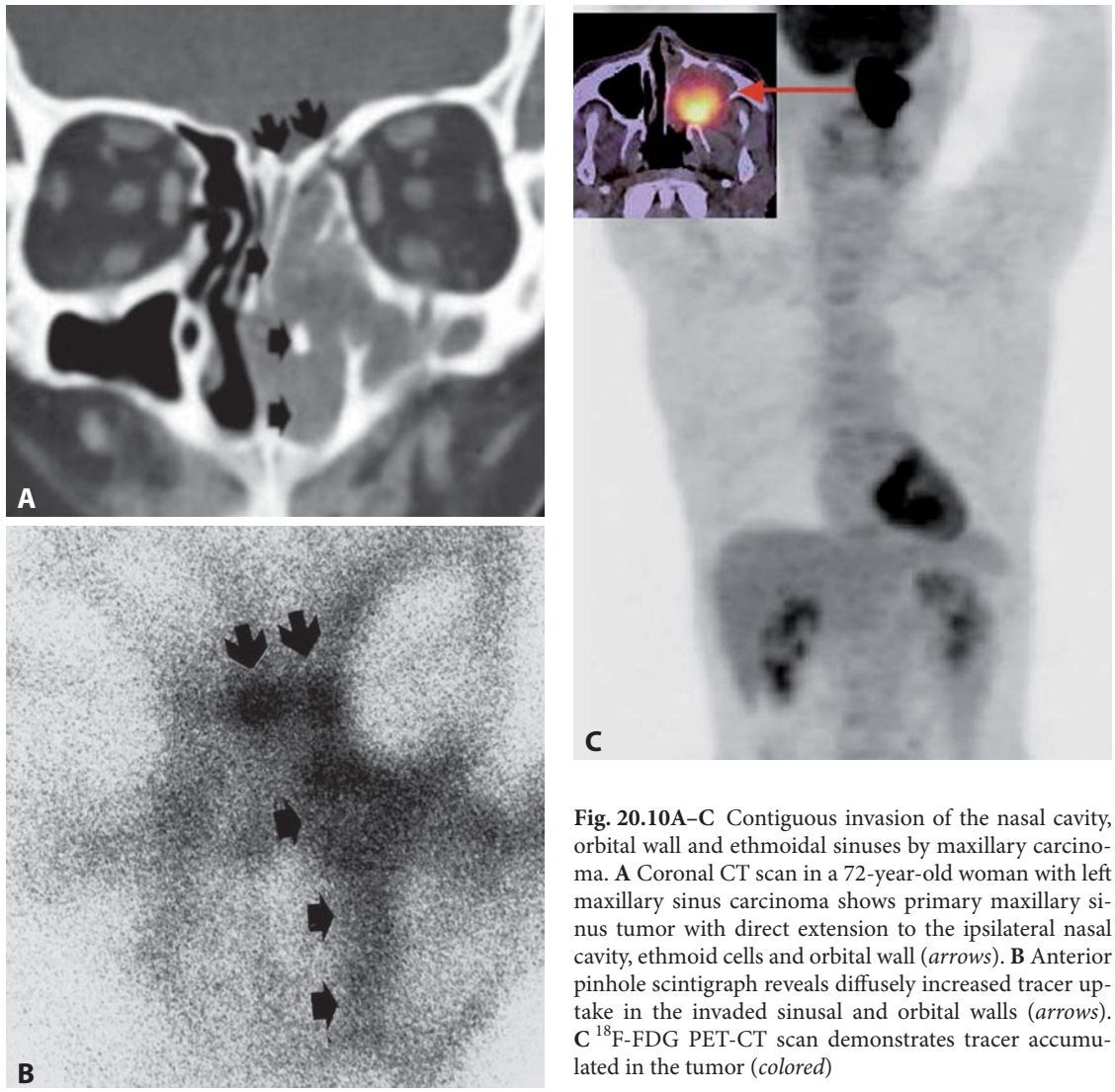

Fig. 20.10A–C Contiguous invasion of the nasal cavity, orbital wall and ethmoidal sinuses by maxillary carcinoma. **A** Coronal CT scan in a 72-year-old woman with left maxillary sinus carcinoma shows primary maxillary sinus tumor with direct extension to the ipsilateral nasal cavity, ethmoid cells and orbital wall (*arrows*). **B** Anterior pinhole scintigraph reveals diffusely increased tracer uptake in the invaded sinusal and orbital walls (*arrows*). **C** ^{18}F-FDG PET-CT scan demonstrates tracer accumulated in the tumor (*colored*)

septum, causing nasal obstruction and frontal sinus mucocele (Fig. 20.6)

Radiography shows an expansive soft-tissue mass filling the nasal cavity with invasion of the nasal septum, turbinates, and sinusal walls of the neighboring maxillary and ethmoid sinuses. More than half of nasal carcinomas are in an advanced stage with sinusal involvement when first radiographed. CT is ideal for assessing all these changes in greater detail (Fig. 20.11A). When tumor obstructs the nasal cavity along with the sinusal ostium a mucocele may be created in the paranasal sinuses, especially in the frontal and ethoidal sinuses (Fig. 20.6A).

Pinhole scanning is an ideal tool for the diagnosis of invasion of the nasal septum, turbinates, and sinusal wall. To be specific, permeated bones or small osteolysis are indicated by intense uptake and penetrated or destroyed bones manifest as photon defects when they are large enough (Fig. 20.11B). As is well known, most cancers do not accumulate ^{99m}Tc-MDP, but avidly accumulate ^{18}F-FDG so that they are distinctly visualized on PET (Fig. 20.12). Mucoceles produced by nasal obstruction manifest as a ballooned sinus with intense peripheral uptake (Fig. 20.6B).

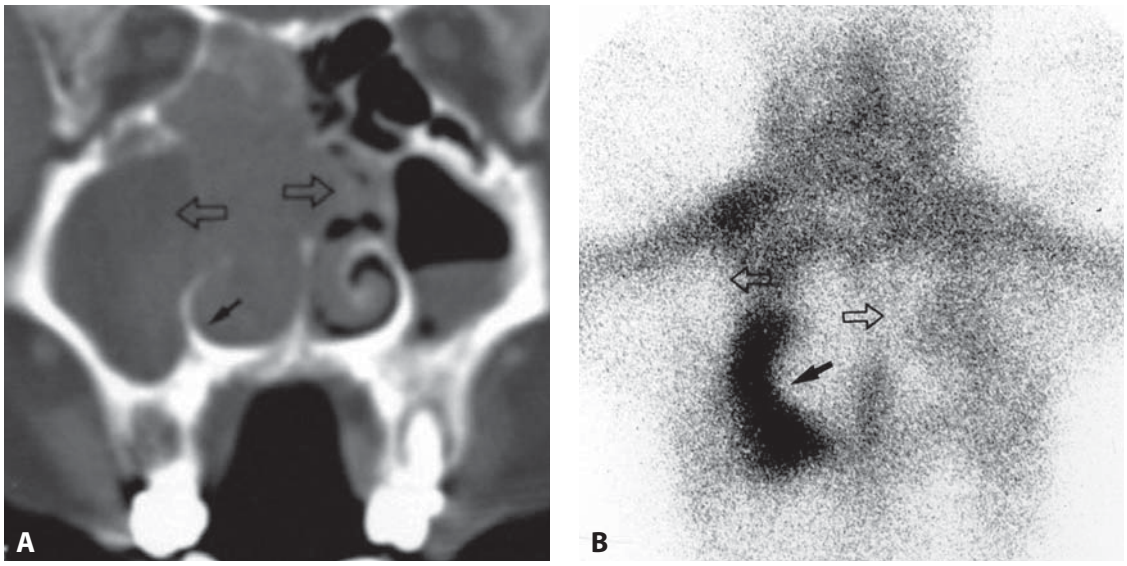

Fig. 20.11A, B Value of CT in the diagnosis of nasosinusal tumor (the same patient as in Fig. 20.3). **A** Coronal CT scan of the nasosinusal system in a 71-year-old woman with squamous cell carcinoma of the right nasal cavity shows tumor extension to the adjacent structures including the nasal septum (*right open arrow*) and the medial maxillary sinusal wall (*left open arrow*). Note resisting bone in the lower nasal compartment (*solid arrow*). **B** Anterior pinhole scan reveals unimpressive tracer uptake in destroyed bones (*open arrows*) with contrasting intense uptake in resisting bone (*solid arrow*)

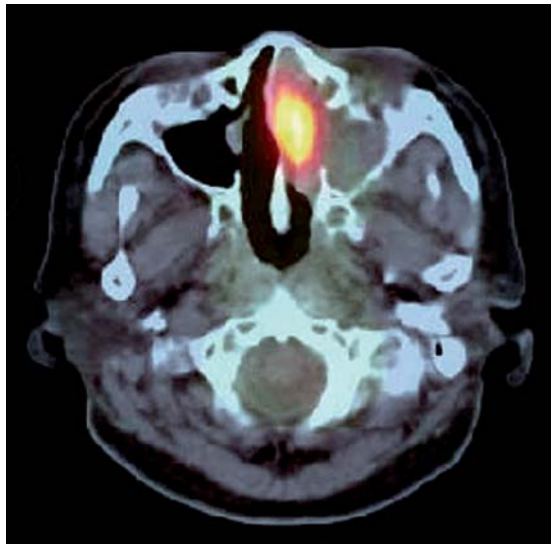

Fig. 20.12 ^{18}F-FDG PET-CT scan in maxillary carcinoma. Transaxial CT scan of the left maxillary sinus in a 70-year-old man shows positive uptake in carcinoma (*colored*)

20.5 Nasopharyngeal Carcinoma

Nasopharyngeal carcinoma is relatively rare in most parts of the world, with prevalence of 0.25% of all cancers in North America. It is, however, one of the most common and important malignant tumors in China, particularly in Kwantung Province and in Taiwan where it accounts for approximately 18% of all cancers (Hsu et al. 1982).

On the whole, plain radiography of nasopharyngeal tumors is not as informative as that of the paranasal or nasal cavity tumors, but CT and MRI are very helpful in diagnosing, staging, and radiaton treatment planning, intensity-modulated radiotherapy in particular (Manavis et al. 2005).

^{99m}Tc-MDP bone scintigraphy is useful for the diagnosis of local bone invasion and distant metastases. Planar bone scans may show increased tracer uptake at the tumor site but without anatomical detail. Pinhole scanning is

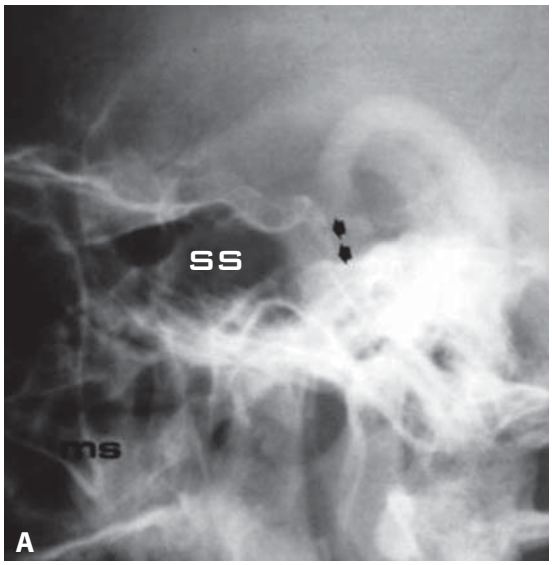

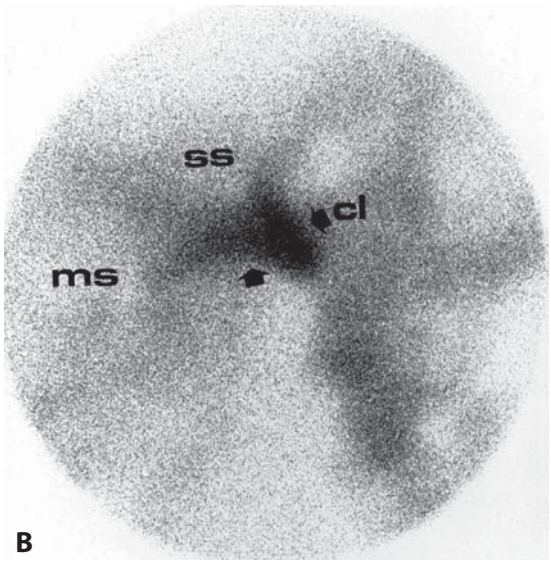

Fig. 20.13A, B Contiguous spread of nasopharyngeal carcinoma to the clivus. **A** Lateral radiograph of the pharynx in a 50-year-old man shows nonspecific focal sclerosis in the clivus (*arrows*) (*ss* sphenoid sinus, *ms* maxillary sinus). **B** Lateral pinhole scintigraph reveals intense tracer uptale localized to the clivus (*cl*) denoting osteoblastic metastasis of pharyngeal carcinoma (*arrow*)

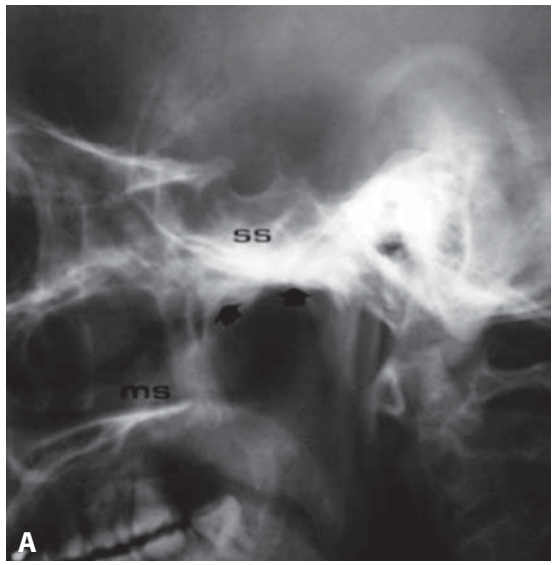

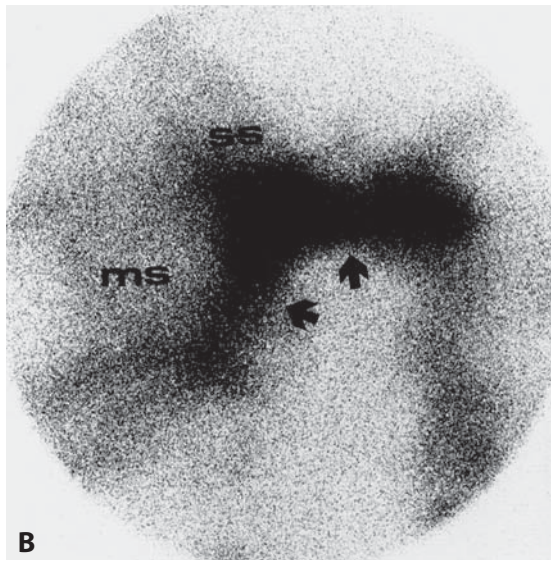

Fig. 20.14A, B Extended spread of nasopahryngeal carcinoma to the middle norma basalis. **A** Lateral radiograph of the pharynx in a 61-year-old man shows diffuse sclerosis in the nasopharyngeal bones including the sphenoid sinus floor (*ss*) and the posterior maxillary sinus wall (*ms*). **B** Lateral pinhole scintigraph reveals diffusely increased tracer uptake in the middle norma basalis including the sphenoid sinus floor (*ss*) and maxillary sinus wall (*ms*)

an efficient means of assessing osseous invasion in the middle part of the norma basalis of the skull. It can sensitively and three-dimensionally detect contiguous spread to the sphenoidal sinus, clivus, pterygoid plates, and posterior walls of the maxillary sinuses as well as the basioccipital bones. For more accurate observation of the topography of the skull base, a lateral scintigraph is recommended since it can visualize two easily indentifiable anatomical landmarks: the posterior maxillary sinus wall in front and the foramen magnum behind at

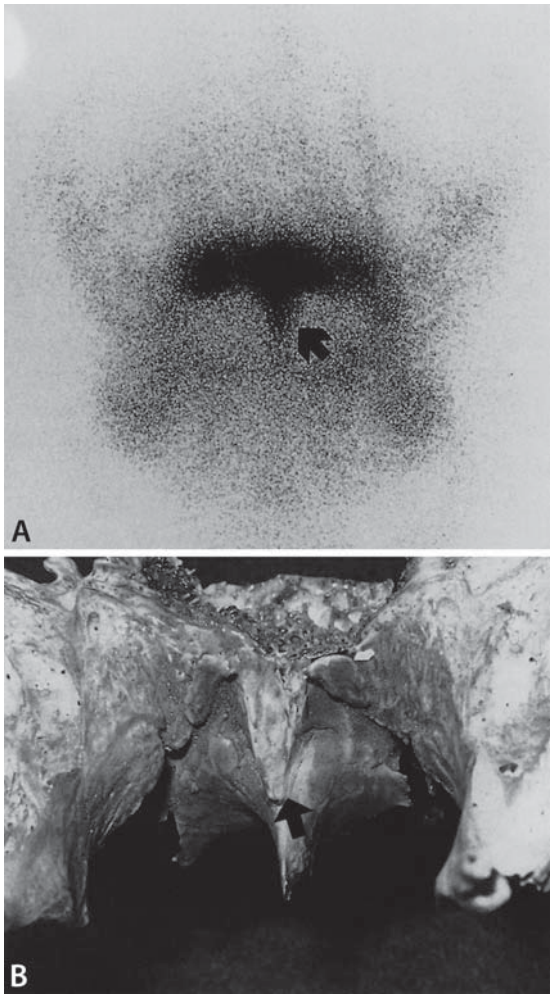

Fig. 20.15A, B Local invasion of the sphenoid sinus floor and the rostrum in nasopharyngeal cancer. **A** Posterior pinhole scintigraph of the sphenoid bone in a 52-year-old man with known nasopharyngeal carcinoma operated on 2 years previously shows increased tracer uptake in the floor of the sphenoid sinus, including the rostrum (*arrow*). **B** Photograph of the posterior aspect of the bony choana shows the characteristic appearance and location of the rostrum (*arrow*) in relation to the pterygoid plates, vomer, and nasal turbinates

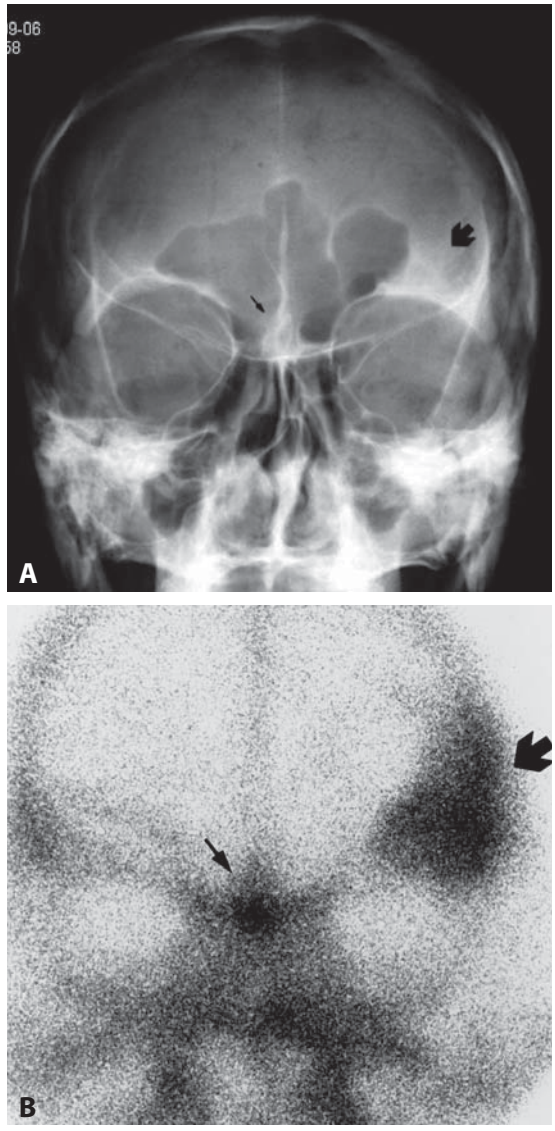

Fig. 20.16A, B Distant metastasis of nasopharyngeal carcinoma to the frontal bone. **A** Posteroanterior radiograph of the skull in a 56-year-old man with nasopharyngeal carcinoma shows localized sclerosis in the pharyngeal tubercle (*small arrow*) and diffuse sclerosis in the left frontal bone (*large arrow*), respectively denoting primary and metastatic carcinoma. **B** Anterior pinhole scintigraph reveals concordant tracer uptake localized to the tubercle (*small arrow*) and the left frontal bone (*large arrow*). The lesion in the tubercle was retrospectively diagnosed after pinhole scintigaphy

the end of the inferior extension of the clivus. Figure 20.13 clearly demonstrates the invasion of the clivus by nasopharyngeal carcinoma and the anterior border of the foramen magnum. With further spread of nasopahryngeal carcinoma the lateral view may show diffused tracer uptake in the skull base with extension anteriorly to the posterior vomerine border, the pterygoid plates, and the sphenoidal sinus floor, and posteriorly to the anterior border of the foramen magnum (Fig. 20.14). On the other hand, contiguous spread of tumor to the mid-

line and paramedian structures such as the sphenoid sinus floor, rostrum, vomer, and pterygoid plates are most advantageously visualized on posterior or anterior scintigraphy (Fig. 20.15).

High sensitivity and usefulness of bone scintigraphy have been emphasized in the diagnosis of skull base invasion by nasopharyngeal carcinoma (Saeed et al. 2001). These authors found ^{99m}Tc-MDP bone SPECT to be superior to planar bone scanning, plain radiography, or even CT. As shown by our series pinhole scintigraphy not only sensitively detects local bone invasion but also accurately depicts the anatomical site and extent of contiguous invasion (Figs. 20.13 and 20.14). Furthermore, bone scanning is indeed helpful for the diagnosis of distant skeletal metastasis, which is not uncommon (Fig. 20.16). One study by Sundram et al. (1990) showed prevalence of distant bone metastases in the first diagnosed group to be 23% and in the follow-up group 59%. A high prevalence of distant metastases from nasopharyngeal cancer was repeatedly emphasized in a more recent review (Chiesa and De Paoli 2001). Metastases occur in the spine, ribs, pelvis, and lower limb in descending order of frequency (Sundram et al. 1990). The higher specificity and sensitivity of ^{18}F FDG PET in the diagnosis of primary nasopharynageal carcinomas and local or distant metastases deserve emphasis (Fig. 20.17).

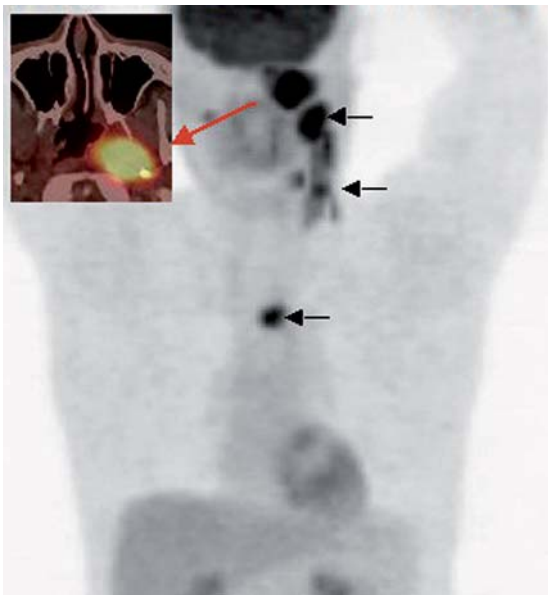

Fig. 20.17 ^{18}F-FDG PET-CT of nasopharyngeal carcinoma with lymph node metastases. Anterior PET-CT scan of the neck and chest in a 53-year-old man shows primary carcinoma in the left oropharynx (*ned arrow*) with multiple lymph node metasatases (*arrows*). *Inset* Close-up scan reveals accurate topography with positive FDG uptake in the carcinoma (*colored*)

20.6 Inflammatory Diseases of the Mastoidal Bones

The mastoidal bones along with the petrous ridge and the tympanic portion of the temporal bone and the temporomandibular joints are interesting objectives of pinhole scintigraphy. Once familiarized with normal pinhole scintigraphic anatomy, deviations from the norm can readily be recognized as such, permitting the diagnosis of mastoiditis, petrositis, and otitis media as well as cholesteatoma. Scintigraphically, these inflammatory diseases manifest as increased tracer uptake in the specific anatomical sites, and cholesteatomas produce photon defects when they are sufficiently large.

Mastoiditis usually starts by mucosal inflammation, so-called catarrh, as an extension of a middle ear infection. The most common offenders are beta-hemolytic streptococci and pneumococci, and in infants *Haemophilus influenzae*. Unchecked, the infection further spreads to the petrous bone, causing petrositis (Chole 1993). Occasionally, keratinizing squamous epithelium may evolve from chronic inflammatory foci in the external ear, gradually creep into the mastoid antrum via the tympanic cavity and epitympanum, and grow to form secondary cholesteatomas (Chole 1993). Intractable infections in the middle and external ears are often attended by destruction of the external auditory meatus and inflammation in the adjoining temporomandibular joint.

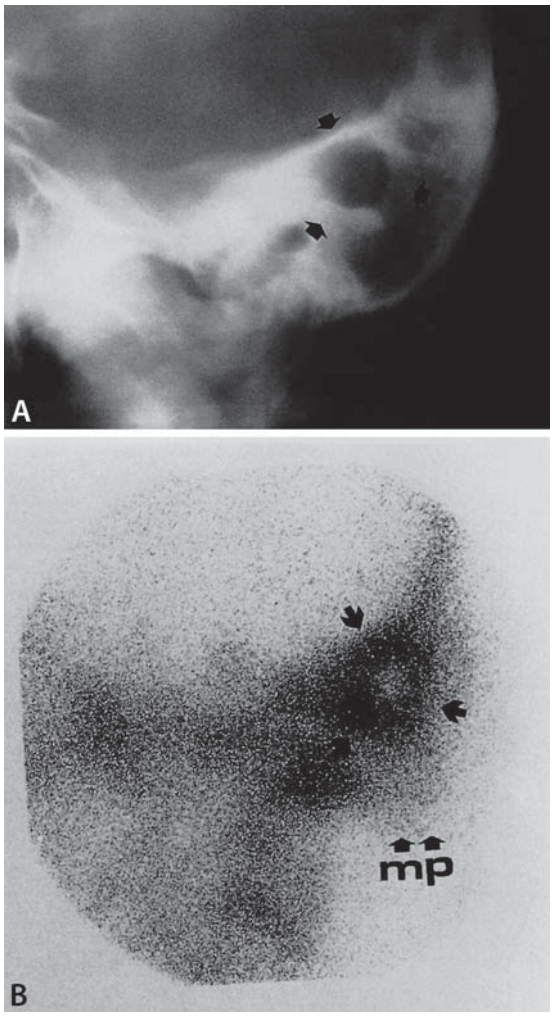

Fig. 20.18A, B Scintigraphic demonstration of secondary cholesteatoma. **A** Stenvers' view conventional X-ray tomograph of the left mastoid in a 36-year-old man with longstanding mastoiditis reveals a well-demarcated, roundish bone defect in the mastoid antrum surrounded by diffuse sclerosis (*arrows*). **B** Stenver' view pinhole scintigraph of the left mastoid shows a small photopenic defect surrounded by intense tracer uptake (*arrows*). The mastoid tip is faintly indicated (*mp*)

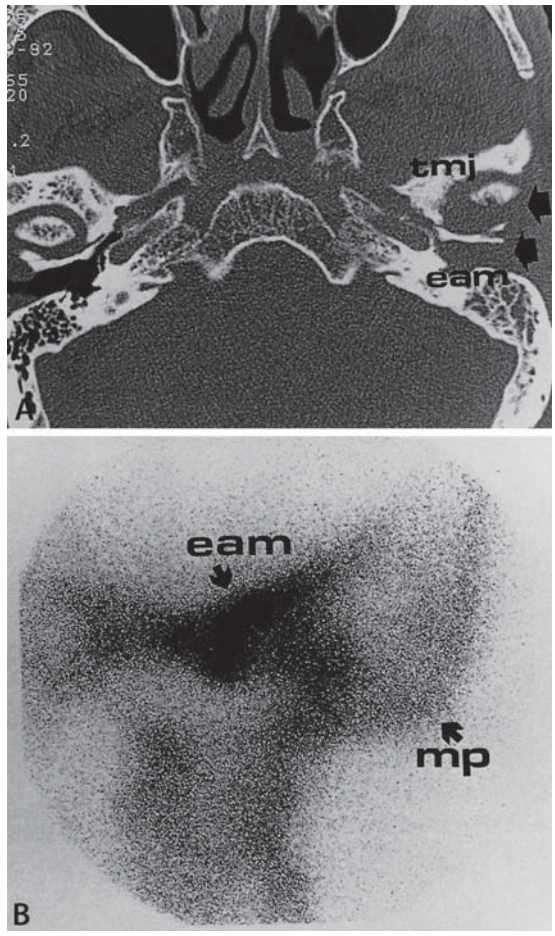

Fig. 20.19A, B Temporomandibular joint involvement in malignant otitis. **A** Axial CT scan through the temporomandibular joints in a 79-year-old man with an intractable left otitis shows marked bone resorption in the left temporomandibular joint (*tmj*) and osteolysis in the external auditory meatus (*eam*). **B** Stenver' pinhole scan shows extremely intense tracer uptake in the destroyed external auditory meatus (*eam*) and temporomandibular joint. The mastoid process is faintly indicated (*mp*)

Radiographic features of mastoiditis include the thickening of the air cell septi and clouding of the mastoidal and petrous bones in the acute and subacute stages, and osteosclerosis in the chronic recurrent form. Cholesteatomas present as photon defects, the demarcation of which may be sharp or poor according to lesion size and degree of perifocal sclerosis. Conventional tomography or CT is the method of choice for the investigation of cholesteatomas and associated mastoiditis (Fig. 20.18A). Tomography is also useful for the diagnosis of malignant otitis with sympathetic involvement of the temporomandibular joint (Fig. 20.19A).

Pinhole scintigraphy shows intense uptake in the infected mastoid bone. As is the case

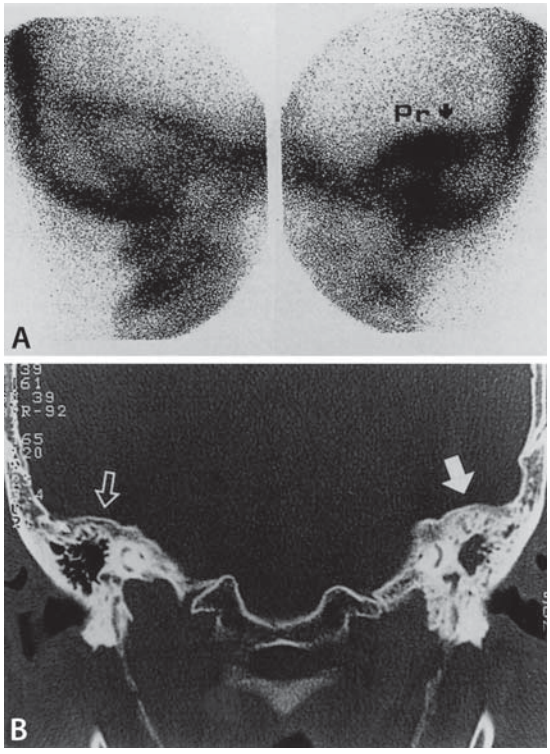

Fig. 20.20A, B Petrositis. **A** Stenvers' view pinhole scan of both mastoids in a 66-year-old woman with chronic mastoiditis shows intense tracer uptake localized in the petrous ridge (*Pr*) of the left mastoid, which also concentrates tracer diffusely. Compare with the contralateral normal mastoid. **B** Coronal CT scan shows diffuse obliteration of air cells with sclerotic trabeculae and a small cholesteatoma (1 cm in diameter) beneath the sclerotic left petrous ridge (*solid arrow*). The air cells in the right mastoid are normally aerated (*open arrow*). Radiography revealed sclerosis in the left antral region without specific indication of petrositis (not shown here). Observe that small cholesteatoma cannot be visualized by pinhole scintigraphy

with radiography, Stenvers' view scintigraphy is indispensable for efficient study of mastoiditis and cholesteatoma (Fig. 20.18B). At the moment, ^{99m}Tc-MDP pinhole bone scanning is the sole means available for assessing the metabolic state of mastoiditis. When the petrous bone is involved, an area of increased tracer uptake specifically appears in the petrous ridge (Fig. 20.20). Indeed, pinhole bone scintigraphy can sensitively indicate the spread of mastoiditis to the petrous ridge. Intractable otitis with auditory meatal destruction and related inflammation in the adjacent temporomandibular joint can also be sensitively diagnosed (Fig. 20.19B). On the other hand, cholesteatomas create photon defects surrounded by intense uptake if the lesions are encapsulated and larger than 1 cm in size (Fig. 20.18B). However, smaller or invasive cholesteatomas are not visualized, but merely show increased uptake in the antral region.

References

Carrau RL, Myers EN (2001) Neoplasms of the nose and paranasal sinuses. In: Bailey BJ et al. (eds) Head and neck surgery—Otolaryngology, 3rd edn. Philadelphia: Lippincott Williams & Wilkins, pp 1247–1265

Chiesa F, De Paoli F (2001) Distant metastases from nasopharyngeal cancer. J Otorhinolaryngol Relat Soec 63:214–216

Chole RA (1993) Chronic otitis media, mastoiditis, and petrositis. In: Cummings CW et al (eds) Otolaryngology – Head and neck surgery, 2nd edn. St. Louis: Mosby-Year Book

Euteneuer S, Sudhoff H, Bernal-Sprekelsen M, et al (2005) Malignomas of the nasal cavity and the paranasal sinuses: clinical characteristics, therapy and prognosis of different tumor types. Laryngorhinootologie 83:33–39

Evans C (1981) Etiology and treatment of frontoethmoidal mucocele. J Laryngol Otol 95:361–375

Evans FO, Sydnor JB, Moore WEC, et al (1975) Sinusitis of maxillary antrum. N Engl J Med 293:735–739

Hsu MM, Huang SC, Lynn TC, et al (1982) The survival of patients with nasopharyngeal carcinoma. Otolaryngol Head Neck Surg 90:2890295

Kharoubi S (2005) Malignant tumors of nasal fossae: anatomicoclinical study and a new classification: study on 21 cases. Cancer Radiother 9:187–195

Manavis J, Sivridis L, Koukourakis MI (2005) Nasopharyngeal carcioma: the impact of CT-scan and of MRI on staging, radiotherapy treatment planning, and outcome of the disease. Clin Imaging 29:128–133

Rivera S, Leryer C, Busson P, Maignon P (2005) Nasopharyngeal carcinomas: from biology to clinic. Cancer Radiother 9:55–68

Saeed S, Haq S, Sohaib M, Khan AN (2001) Skull base involvement by a nasopharyngeal carcinoma shown by Tc-99m MDP SPECT but not by comupted tomography. Clin Nucl Med 26:930–932

Sundram FX, Chua ET, Goh AS, et al (1990) Bone scintigraphy in nasopharyngeal carcinoma. Clin Radiol 42:166–169

Weymuller EA Jr (1993) Malignant neoplasm. In: Cummings CW et al (eds) Otolaryngology – head and neck surgery, 2nd edn. Mosby-Year Book, St. Louis

Yen TC, Chang JT, Ng SH, et al (2005) The value of 18F-FDG PET in the detection of stage M0 carcinoma of the nasopharynx. J Nucl Med 46:405–410

Zeifer BA (2001) Sinus imaging. In: Bailey BJ et al. (eds) Head and neck surgery—Otolaryngology, 3rd edn. Philadelphia: Lippincott Williams & Wilkins, pp. 329–343

21 PET-CT in Bone and Joint Diseases

Sung-Hoon Kim and Yong-Whee Bahk

Except for acute trauma such as fracture, contusion or sprain, and physical injury such as electric or thermal burn or freezing, the damage to cells in disease starts at the molecular or chemical level followed by anatomical response. Accordingly, a truly early diagnosis of a disease requires an appropriate means to detect preanatomical change, and PET is a modality that meets this requirement.

PET, the latest high technology nuclear imaging modality, has been shown to be a potent tool for the imaging of early metabolic change and simultaneous quantitative assessment of the change, and is widely used in many economically developed countries. Its indications include the diagnosis, staging and restaging, therapy planning, assessment of therapeutic effects, recurrence monitoring, and prognostication of neoplastic conditions and inflammations. Until recently, PET suffered from a crucial inherent problem of inaccuracy in localizing detected lesions because of suboptimal anatomical information. The problem, however, has been successfully overcome by hybridizing PET with CT. In addition, the production and distribution of special radiopharmaceuticals have also become tremendously improved so that they are now available without major difficulty in everyday practice.

Cancer cells metabolize increased amounts of glucose and produce increased amounts of lactase via glycolysis (Warburg 1931). Adopting this principle, PET utilizes ^{18}F-fluoro-2-deoxy-d-glucose (fluorodeoxyglucose, FDG), an analogue of glucose, for the imaging of cancer cells that consume more glucose than ordinary cells. Like glucose, FDG is transported into cells by glucose transporter proteins and phosphorylated by hexokinase to FDG-6-phosphate. FDG-6-phosphate, however, is not further metabolized and long retained within cells. Multiple factors affect the level of intracellular FDG with the raised level of expression of glucose transporter proteins being one of the main factors. Compared to normal cells, cancer cells exhibit increased hexokinase (glucose phosphorylating enzyme) expression and decreased expression of glucose-6-phosphate (Nelson et al. 1996; Smith 2000). FDG is not tumor-specific. It is to be noted that due to the elevated glycolytic activity, inflammatory cells, neutrophils, and activated macrophages also avidly accumulate FDG, resulting in high FDG uptake in inflammation and infection.

In the 1960s, fluorine-18 (^{18}F) was first used as fluoride for the gamma camera imaging of bone. Soon thereafter ^{18}F-fluoride's physical characteristics were found not to be suitable for bone scanning, and ^{18}F-fluoride was replaced by ^{99m}Tc-MDP that has ideal physical and biological characteristics (Blau et al. 1962). Like ^{99m}Tc-MDP, bone uptake of ^{18}F-fluoride depends on local blood flow and osteoblastic activity. ^{18}F-fluoride is preferentially accumulated at active bone remodeling sites, and forms fluoroapatite by exchanging with the hydroxyl group in hydroxyapatite crystals (Blau et al. 1972; Cook 2002). This is still fondly used for ^{18}F-fluoride PET for the diagnosis of bone metastases.

21.1 Tumors

21.1.2 Primary Tumors of Bone and Soft Tissue

^{18}F-FDG PET can be used for various primary tumors of bones and soft tissues. Although the true impact on oncology is yet to be assessed, PET has already been shown to be useful for the clinical study of some bone and soft-tissue tumors. A large series of PET studies performed in 202 patients with sarcomas, benign tumors, and tumorous conditions showed a sensitivity of 93%, a specificity of 66.7%, and an accuracy of 81.7% (Schulte et al. 2000). These cases included 70 high-grade sarcomas, 21 low-grade sarcomas, 40 benign tumors, 47

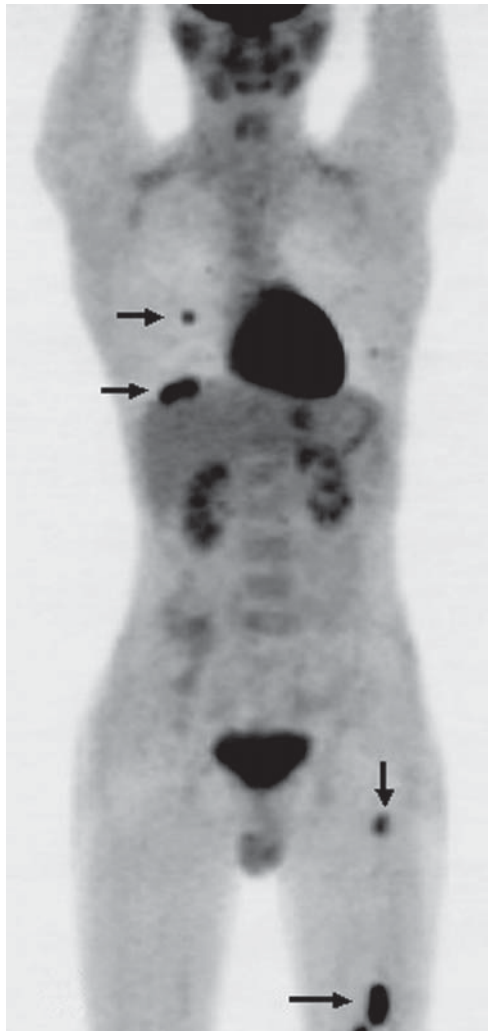

Fig. 21.1 Simultaneous diagnosis of primary osteosarcoma and regional and distant metastases. Anterior whole-body PET-CT in a 16-year-old boy shows focal FDG uptake in primary osteosarcoma in the left distal femur (*bottom arrow*) with a small regional skip lesion in the proximal femur (*single small arrow*) and in metastases in the right lower lung (*two arrows*)

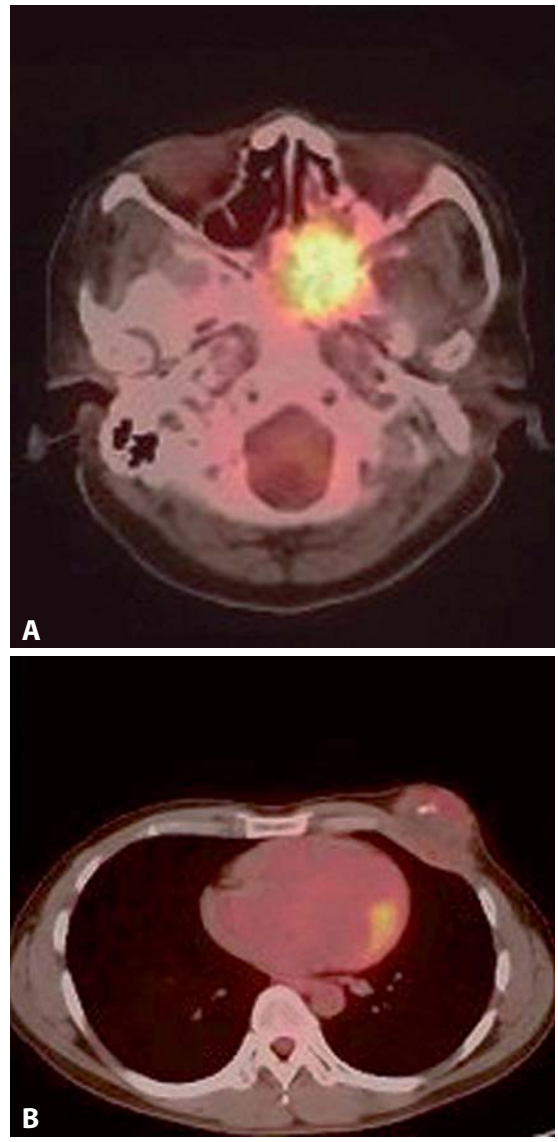

Fig. 21.2A, B Chondrosarcoma. **A** PET-CT of the skull base in a 62-year-old woman shows an area of bone destruction with intense FDG uptake in the left nasal cavity. **B** PET-CT of the chest in a 61-year-old man reveals a bulging ovoid soft-tissue mass and small calcification with weak FDG uptake in the left sixth rib

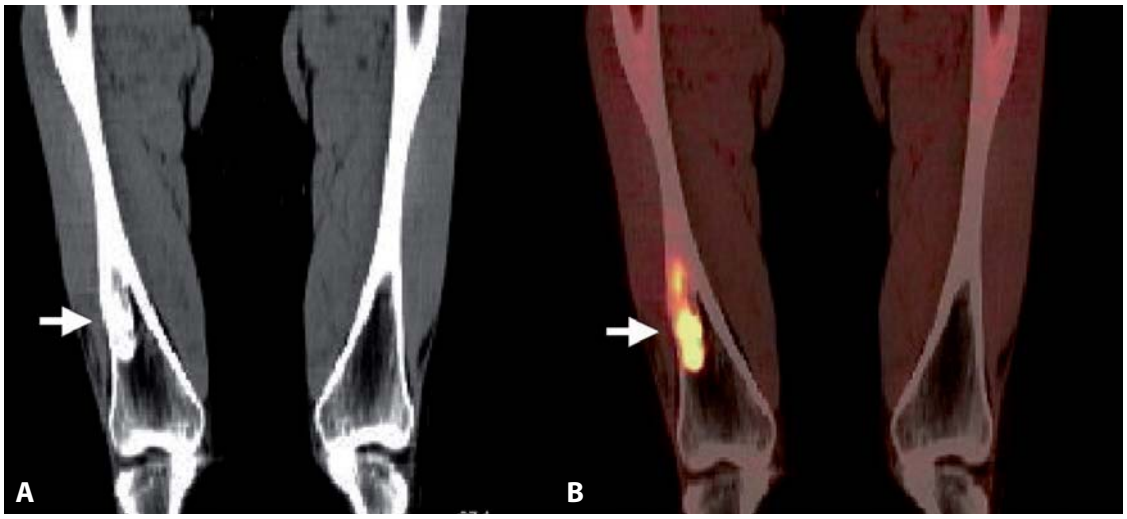

Fig. 21.3A, B Fibrous dysplasia simulating malignant tumor. **A** Coronal CT of the right femur in a 38-year-old woman shows a small intramedullary sausage-like bone and fibrous tissue attached to the endosteum (*arrow*). **B** Anterior PET-CT reveals prominent FDG uptake in the fibro-osseous lesion, simulating malignant tumor (*arrow*)

tumor-like lesions, and others. High-grade sarcomas were correctly diagnosed but the result with low-grade sarcomas was disappointing. More recent data on FDG uptake and tumor grade similarly reveals a significant difference between low-grade and high-grade chondrosarcomas, but not between benign cartilage tumors and grade 1 chondrosarcomas (Lee et al. 2004). Foo et al. (2004) also investigated biological activities of benign cartilaginous tumors and chondrosarcomas of various grades. We have so far carried out ^{18}F-FDG PET in osteosarcoma (Fig. 21.1), chondrosarcoma (Fig. 21.2), Ewing's sarcoma, multiple myeloma (Fig. 17.61), and plasmacytoma.

FDG is known to intensely accumulate not only in malignant tumors but also in some benign conditions, especially histiocytic and giant-cell containing lesions (Aoki et al. 2001). Indeed, significant uptake occurs in giant-cell tumor, fibrous dysplasia, and hematogenous osteomyelitis, all of which are benign (Fig. 21.3). Fortunately, this critical drawback of the inability of PET to distinguish between benign and malignant conditions can partially be overcome by obtaining delayed scans. Most highly malignant tumors may not reach peak activity until 4 hours, whereas the radioactivity of benign lesions plateaus as early as at 30 minutes (Lodge et al. 1999).

FDG uptake becomes decreased in tumor necrosis induced by adjuvant therapy (Schulte et al. 1999). Conversely, the uptake is increased in reactive fibrous tissue, impeding the distinction of complete from partial response to chemotherapy (Jones et al. 1996). In the evaluation of local tumor recurrence in amputated stumps, *diffuse* FDG uptake in the stump may normally be observed up to 18 months after surgery, but *focal* FDG without clinical evidence of benign complication should alert one to the possibility of recurrence (Hain et al. 1999) (Fig. 21.4).

In a review on ^{18}F-FDG PET imaging in osteosarcoma, Brenner et al. (2003) stated that it is rather premature to draw any definitive conclusion as to the advantages or limitations of FDG PET in the study of osteosarcoma because the amount of study is insufficient. And yet they pointed out that PET is beneficial in the following situations: (a) selection of ideal biopsy sites in a large heterogeneous tumor (Fig. 21.5), (b) outcome prediction of adjuvant chemotherapies, (c) distinguishing postoperative change from residual tumor or local recurrence, and (d) detection of distant metastasis (Fig. 21.6). In chondrosarcomas the

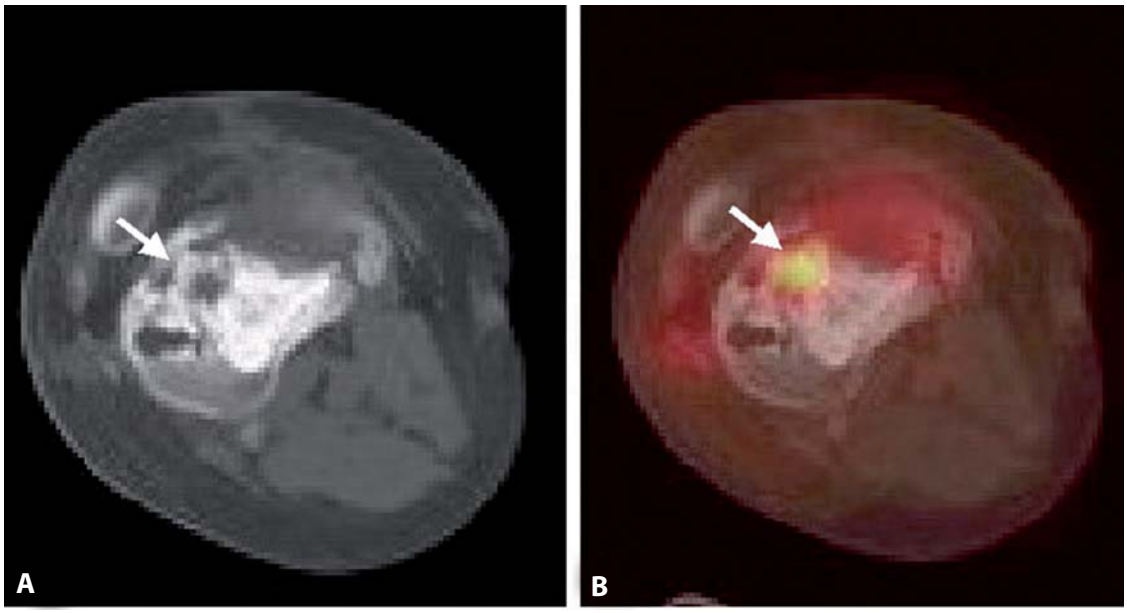

Fig. 21.4A, B Local recurrence of osteosarcoma. **A** Transverse CT scan of the right distal femur in a 21-year-old man shows a mixture of irregular sclerosis and lysis in previously irradiated tumor (*arrow*). **B** Transverse PET-CT reveals a roundish area of prominent FDG uptake denoting local recurrence (*arrow*)

combined use of histopathological tumor grade and the standardized uptake value (SUV) significantly enhances the predictability of clinical course, allowing the identification of patients at high risk of local recurrence or metastasis (Brenner et al. 2004).

In bone lymphomas, which characteristically invade the marrow, FDG PET has been shown to be more sensitive than ^{99m}Tc-MDP bone scanning and, hence, to more accurately identify the biopsy site, leading to improved tumor staging (Moog et al. 1998) (Fig. 21.7).

Regarding the usefulness of FDG PET in soft-tissue tumors, a prospective study carried out by Lucas et al. (1999) has indicated that PET helps make more accurate grading (Fig. 21.8). Indeed, in primary soft-tissue sarcomas, SUVs have been shown to be well correlated with tumor grade, with a sensitivity of 91% and a specificity 88% (Schwarzbach et al. 2000) (Fig. 21.9). They concluded that PET can complement preoperative radiographic study of soft-tissue sarcomas and that it is a potent diagnostic tool for local recurrences of high- and intermediate-grade sarcomas such as spindle cell sarcoma (Fig. 21.10). Most recently, Even-Sapir et al. (2004) conducted a comparative study on the efficacy of ^{18}F-fluoride PET and PET-CT in malignant skeletal disease, and concluded that the anatomical data provided by low-dose CT of a PET-CT scanner obviates the need for a full-dose diagnostic CT scan for correlation purposes.

21.1.3 Metastatic Bone Tumor

For the investigation of metastatic bone tumor ^{18}F-FDG PET, ^{18}F-NaF PET and ^{99m}Tc-MDP bone scintigraphy reinforced with either the pinhole technique or SPECT are used. Each of these modalities has merits and drawbacks, and the first two methods have been shown to be more sensitive and specific but costly (Hetzel et al. 2003). Regarding the application and usefulness of pinhole scintigraphy in the diagnosis of metastatic bone tumors, a full account is given in Chapter 17.

Bone uptake of ^{18}F-NaF and ^{99m}Tc-MDP is known to specifically occur at the site of active bone formation and is closely dependent on local blood flow. Actually, ^{18}F-NaF preferentially accumulates at the site of active bone remodeling or neoplastic osteogenesis to form fluoro-

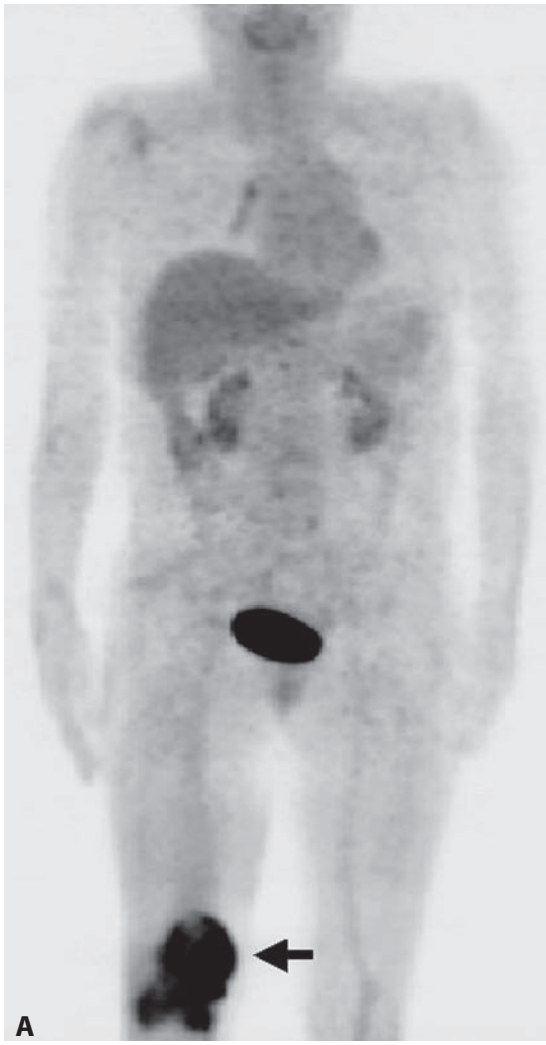

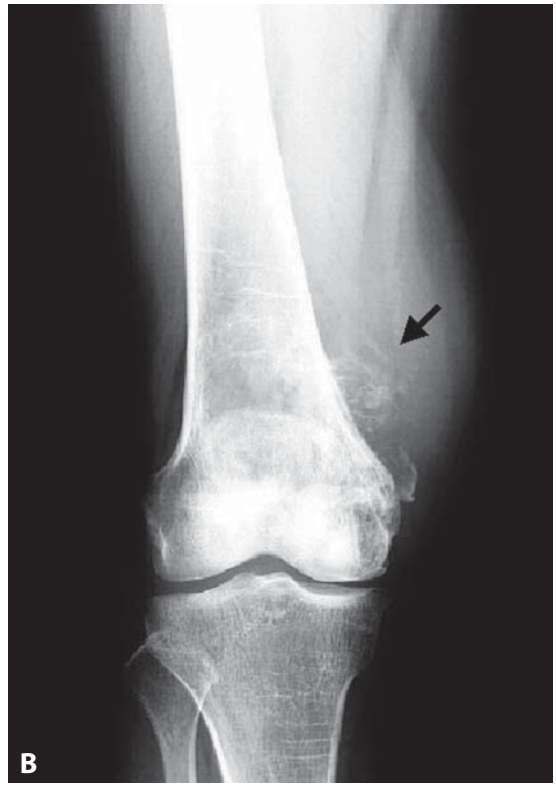

Fig. 21.5A, B High-grade osteosarcoma demonstrating intense FDG uptake. **A** Anterior whole-body FDG-PET in a 63-year-old woman shows a localized, expansive, roundish FDG uptake in the right medial femoral condyle (*arrow*). No skip bone or distant metastasis is noted. **B** Anteroposterior radiograph reveals a poorly defined expansive tumor with invasion of the adjacent soft tissue (*arrow*). Note neoplastic osteogenesis

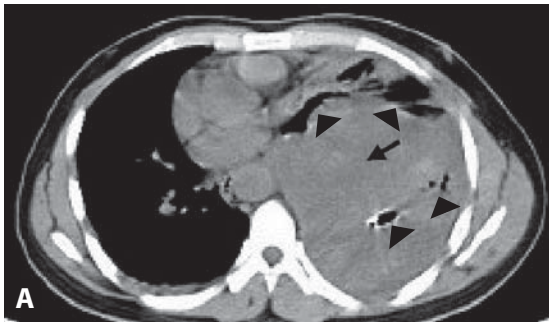

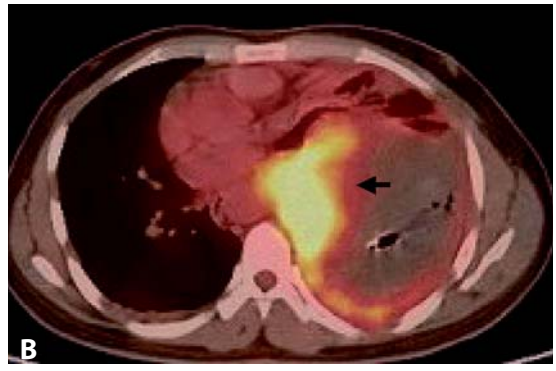

Fig. 21.6A, B Pleuropulmonary metastases of osteosarcoma. **A** Transverse CT scan of the lower chest in a 42-year-old man shows a large lobulated mass in the left lower lung (*arrow*). The tumor engulfs lower lung bronchi (*lower arrowheads*) and displaces upper lung bronchi away from it (*upper arrowheads*). **B** PET-CT reveals FDG uptake only in the medial aspect of the tumor in the mediastinal pleural metastasis (*arrow*) and not in pulmonary metastasis

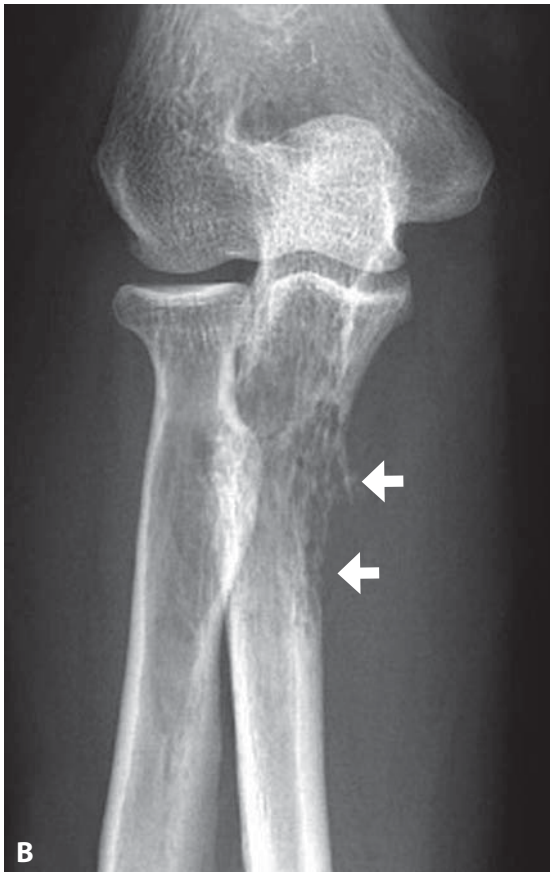

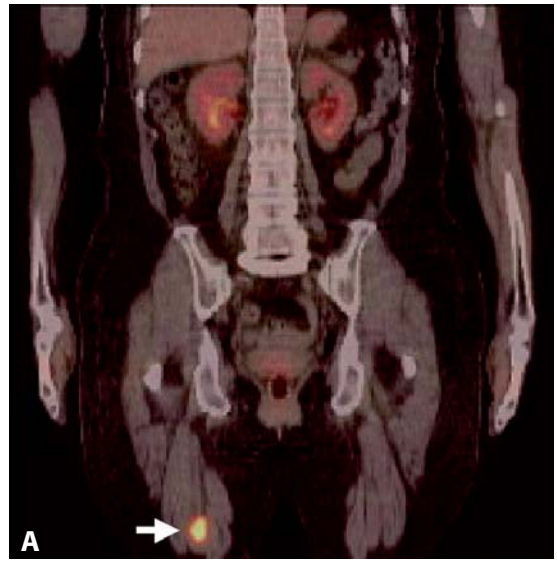

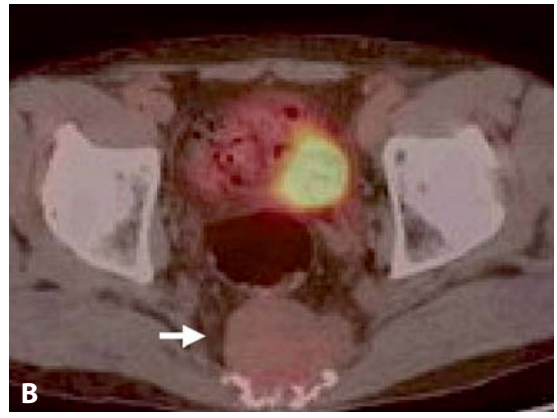

Fig. 21.8A, B FDG uptake correlates with tumor grade in soft-tissue tumors. **A** Posterior whole-body PET-CT in a 52-year-old woman with high-grade clear-cell sarcoma shows a small area of intense FDG uptake in the posterior aspect of the right mid-thigh (*arrow*). **B** Transverse FDG PET-CT of the pelvis in a 61-year-old man with low-grade sacral chordoma shows a large ovoid hypodense mass in the presacral space with faint FDG uptake (*arrow*)

◁ **Fig. 21.7A, B** Bone lymphoma. **A** Anterior PET-CT of the right ulna in a 47-year-old woman shows an ovoid lesion with intense FDG uptake in the proximal shaft. **B** Anteroposterior radiograph reveals eccentric melting-ice osteolysis in the proximal part of the ulnar shaft (*arrows*). Note high concordance of the two examinations

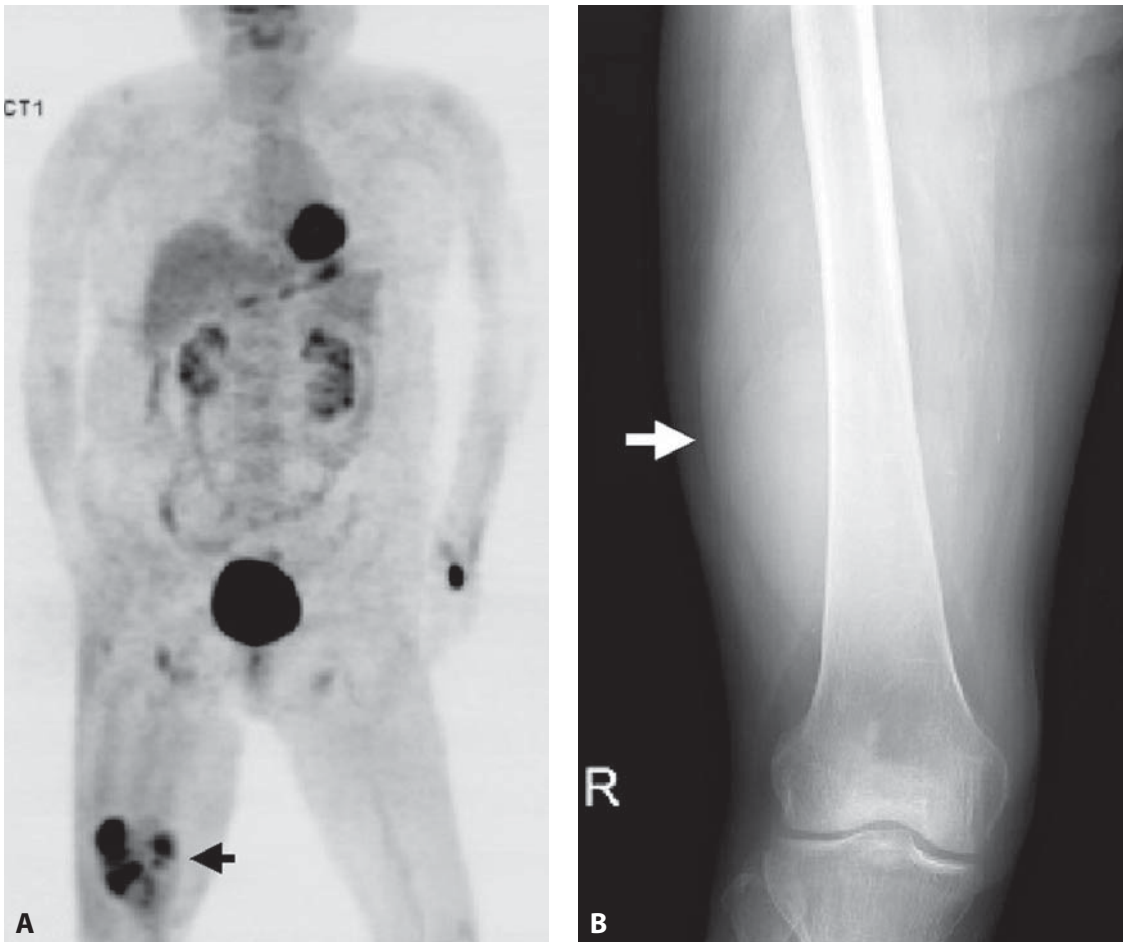

Fig. 21.9A, B High-grade dedifferentiated liposarcoma with intense FDG uptake. **A** Whole-body PET in a 73-year-old woman shows intense tracer uptake sharply localized to FDG-avid solid component of liposarcoma in the posterior aspect of right thigh (*large arrow*). Note that soft-tissue tumor with fat component does not accumulate FDG. **B** Anteroposterior radiograph of the right thigh reveals a large soft-tissue mass in the lower thigh without bony change (*arrow*)

apatite by exchanging with the hydroxyl groups of the hydroxyapatite crystals. Unlike these bone-seeking agents, however, ^{18}F-FDG directly accumulates in tumor cells. In addition, ^{18}F-FDG PET has several distinct advantages over ^{99m}Tc-MDP bone scanning. First, PET can be started 1 hour after FDG injection while MDP bone scintigraphy takes 3 hours. Second, spatial resolution and contrast are better. Third, sectional images are regularly obtained. Fourth, quantification is much easier, and, last but most important as already mentioned, PET directly visualizes tumor because tumor cells ingest FDG. It is to be mentioned, however, that FDG PET has two important drawbacks. One is bone marrow hyperplasia induced by adjuvant chemotherapy or the administration of granulocyte-colony stimulation factor. The hyperplasia of red bone marrow thus induced intensely accumulates FDG simulating metastasis (Sugawara et al. 1998a) (Fig. 21.11). The other is strong FDG uptake in normal brain, which prevents the detection of skull metastasis.

Comparison of the diagnostic efficacy of ^{18}F-NaF PET and planar ^{99m}Tc-MDP scan in bone tumor including metastases has shown that the former procedure detects twice as much benign and malignant bone lesions than the latter. The accuracy of differential diagnosis

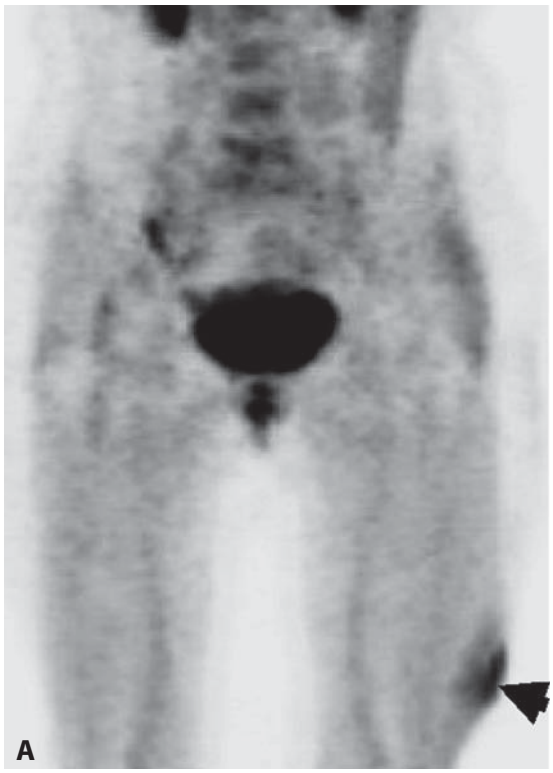

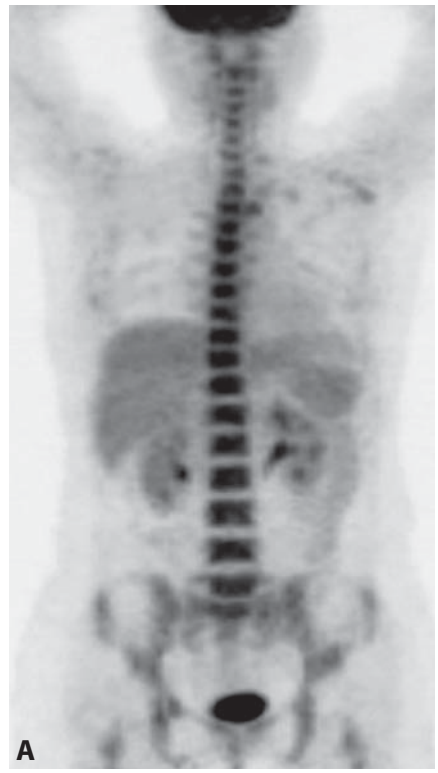

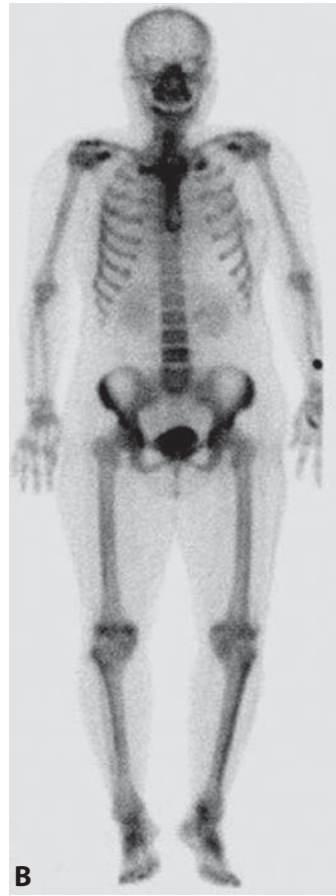

Fig. 21.10A, B Local recurrence of spindle cell sarcoma. **A** Whole-body PET-CT in a 52-year-old woman shows a long segmental FDG uptake in the anterolateral aspect of the vastus lateralis muscle of the left thigh (*arrow*). **B** Transverse PET-CT reveals high FDG uptake in the tumor recurrence (*arrow*)

of benign and malignant lesions is 97% for ^{18}F-NaF PET and 80.5% for planar ^{99m}Tc-MDP scans, and fluoride PET has been shown to be particularly useful for the study of spinal lesions (Schirrmeister et al. 1999).

FDG PET has been shown to be superior to ^{99m}Tc-MDP scanning in investigating metastases of almost all types of cancers (Yang et al. 2002). Assessed on a patient-by-patient basis, FDG PET has demonstrated a sensitivity similar to that of ^{99m}Tc-MDP scanning, but the specificity was much higher, 98% versus 61% (Bury et al 1998). The higher accuracy is considered to be due to the fact that FDG PET can detect metastases in the bone marrow that are not detectable by bone scanning (Cook 2002). In general osteolytic metastases are more sensitively detected by FDG PET (Fig. 21.12), whereas osteoblastic lesions are better visualized on ^{99m}Tc-MDP scans (Fig. 21.13). Increased FDG uptake in osteolytic metastases is related to vascular deprivation and hypoxia (Clavo et al. 1995; Hiraga et al. 2000) and low FDG uptake in osteoblastic metastases to low tumor cellularity. Actually, studies have indicated that the sensitivity of FDG PET for osteoblastic metastases from breast cancer and prostate cancer is lower than that of bone scintigraphy (Moon et al. 1998; Cook et al. 1998; Shreve et al. 1996; Yeh et al. 1996). It has also been reported that the sensitivity of FDG PET for bone metastasis is 90%, which is higher than 82% for MRI and 71% for ^{99m}Tc-MDP bone scanning (Daldrup-Link et al. 2001), and our own experience has confirmed this (Fig. 21.14). It is worthy of emphasis that, in addition to its superior sensitivity, FDG PET can detect lymph node and soft-tissue involvement.

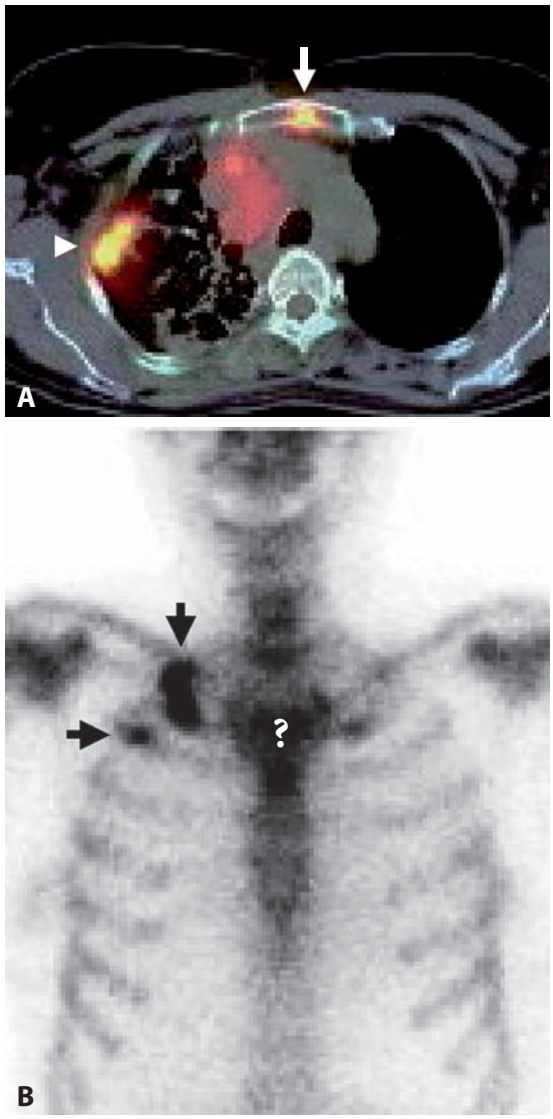

Fig. 21.12A, B ^{18}F-PET can detect osteolytic metastases before ^{99m}Tc-MDP bone scan. **A** PET-CT of the chest in a 52-year-old woman with lung carcinoma shows a small focus of FDG uptake in the manubrium sterni (*arrow*) and long cancer (*arrowheads*). **B** Initial anterior bone scintigraph shows no definite tracer uptake in the sternum (*?*). Note that the right first and second ribs accumulate MDP (*arrows*)

◁ **Fig. 21.11A, B** Marrow hyperplasia developed immediately after granulocyte-colony stimulating factor injection simulating diffuse bone metastasis. **A** Anterior whole-body PET-CT in a 53-year-old woman shows diffusely increased FDG uptake in the bone marrow of the entire spine, pelvis and femurs. **B** Anterior whole-body ^{99m}Tc-MDP bone scintigraph reveals no abnormal uptake

21.1.3.1 ^{18}F-FDG PET-CT Assessment of Therapeutic Response

^{18}F-FDG PET can be used beneficially for predicting responses to and eventual outcome of hormonal or adjuvant therapy of cancer. Indeed, FDG PET can provide reliable visual and

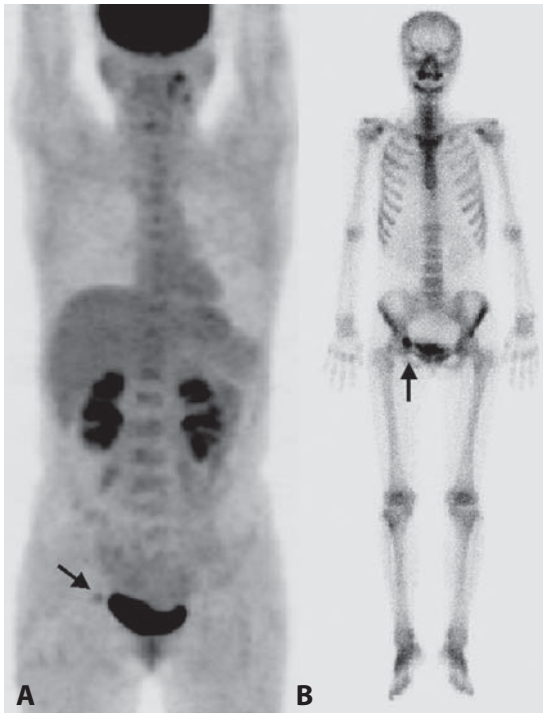

Fig. 21.13A, B Weak ^{18}F-FDG uptake in osteoblastic metastasis. **A** Anterior whole-body FDG PET-CT in a 47-year-old women with an osteoblastic metastasis to the right ischium shows very faint FDG uptake (*arrow*). **B** Anterior whole-body ^{99m}Tc-MDP bone scintigraph reveals prominent tracer uptake (*arrow*)

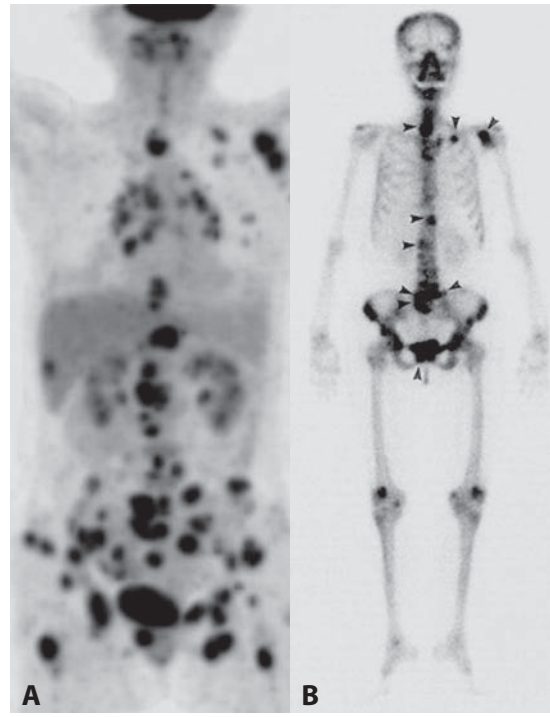

Fig. 21.14A, B High detectability of metastases by ^{18}F-FDG PET. **A** Anterior whole-body PET-CT in a 65-year-old woman with breast cancer shows innumerable lesions not only in the skeleton but also in the lymph nodes. **B** Anterior ^{99m}Tc-MDP whole-body bone scan reveals sparingly spread metastases that are limited to the bone (*arrowheads*)

objective quantitative data in terms of the SUV for a rapid and accurate evaluation of response to chemotherapy, helping establish the best treatment plan and often alleviating confusion as well. Mortimer et al. (2001) performed FDG PET before and 1 week after tamoxifen administration in breast cancer patients with bone metastases, and found that the FDG PET uptake pattern after tamoxifen is an important predictor of therapeutic response (Fig. 21.15). Assisted by CT anatomy, PET-CT can sensitively and specifically diagnose bone metastases as well as soft-tissue invasion, making the procedure essential for optimal treatment planning. In particular PET-CT is useful in the evaluation of spinal metastases (Mester et al. 2004).

21.1.3.2 Flare phenomenon

The flare phenomenon is a reaction related to new bone formation and increased blood flow following adjuvant chemotherapy or irradiation. In contrast to the previously held view, flare is the rule rather than the exception if treatment is successful. Indeed, Rossleigh et al. (1984) observed it to occur in 10 of 27 patients with breast carcinoma, and Coleman et al. (1988) saw flare in as many as 12 of 16 patients receiving systemic therapy for bone metastases from breast cancer. The phenomenon can also be induced by local irradiation. It is transitory in nature, occurring within 6 months of the initiation of systemic therapy or external irradiation. If flare is not born in mind, it may interfere with proper evaluation of therapeutic effects.

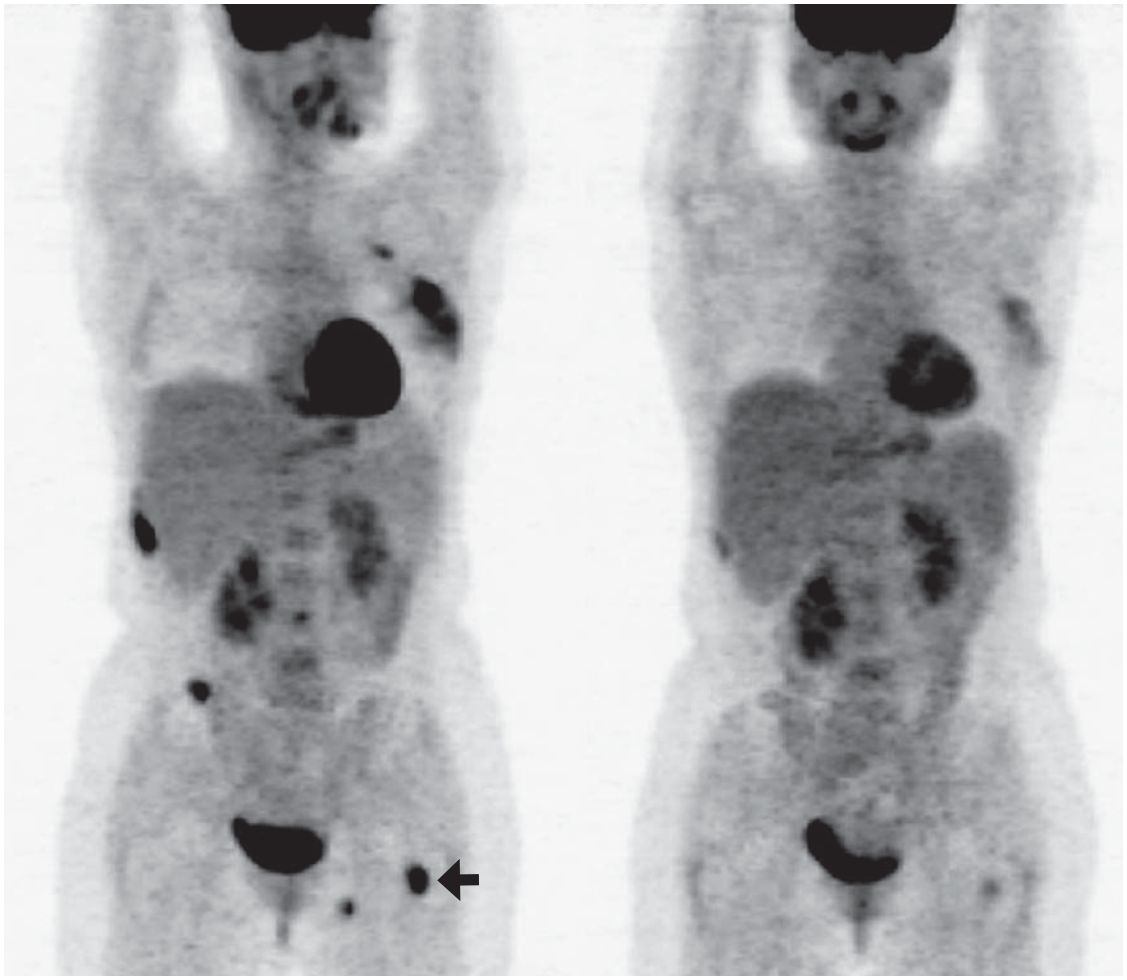

Fig. 21.15 ^{18}F-FDG PET-CT evaluation of chemotherapy response. *Left* Anterior whole-body PET-CT in a 33-year-old woman with breast carcinoma shows widely spread FDG uptake in metastases involving the left rib cage, right lower rib, right ilium, and left femur (*arrow*). *Right* After chemotherapy (3 months on Adriamycin + Taxotere) PET-CT reveals nearly complete resolution of metastases

21.2 Infectious Diseases

The fact that FDG avidly accumulates at the sites of infection or inflammation is one of the major reasons for false-positive results when the procedure is applied to tumor diagnosis. Interestingly, however, the same fact becomes an advantage when judiciously used for the study of infectious diseases. Evidence indicates that cells exhibit increased expression of glucose transporters when activated by inflammation (Chakrabarti et al. 1994; Gamelli et al. 1996). Glucose metabolism and FDG uptake in inflammatory cells are more complicated than in malignant cells (Alavi and Zhuang 2003). For example, numerous cytokines and growth factors, the levels of which are often elevated during infection, dramatically affect glucose uptake by inflammatory cells (Lang et al. 1992; Yao et al. 1995). Thus, FDG PET can more accurately detect infections than leukocyte scans, gallium scans, and MRI. In particular, FDG PET seems to have an incremental value in assessing chronic osteomyelitis, fever of unknown origin, and HIV infection (de Winter et al. 2002).

When bony architecture has been altered by previous trauma, surgery, or adjacent soft-tis-

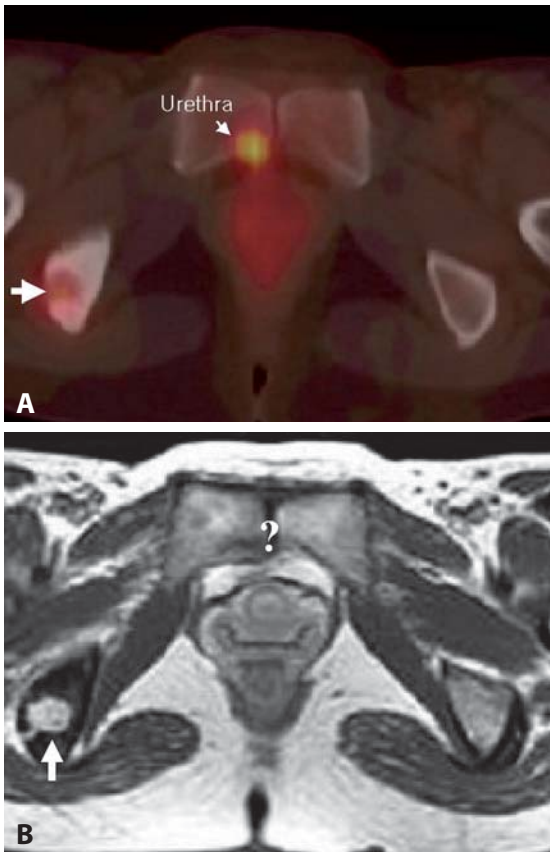

Fig. 21.16A, B Chronic active osteomyelitis detected by ^{18}F-FDG PET-CT. **A** PET-CT of the pelvis in a 24-year-old woman shows localized FDG uptake in the sclerotic right ischial tuberosity (*arrow*). Prominent spotty uptake overlapping the right pubis is in the urethra that is mismatched. **B** T2-weighted MRI reveals a small round infective focus with high signal intensity in the right ischial tuberosity (*arrow*)

sue infection, it is extremely difficult to diagnose osteomyelitis and to distinguish bone infection from soft-tissue infection by nonsurgical methods (Kolindou et al. 1996). PET, however, can sensitively pinpoint infective or inflammatory foci undisturbed by anatomical changes because FDG accumulates not in bone but in activated macrophages. Another important advantage is that SUVs are instantly obtainable so that on the one hand it can help differentiate between acute and chronic infection and on the other hand discriminate malignant from benign conditions. A number of articles have appeared attesting to the value of FDG PET in bone infections. Stumpe et al. (2000) found FDG PET to be highly sensitive for the diagnosis of acute and subacute osteomyelitis, and clinical studies conducted by Guhlmann et al. (1998) and Zhuang et al. (2000) have demonstrated FDG PET sensitivity of 95–100% and specificity of 85.7–95%. In addition, one more recent paper reports the sensitivity, specificity, and accuracy of FDG PET in suspected chronic musculoskeletal infection of the peripheral bones to be 100%, 86%, and 93%, respectively (de Winter et al. 2001) (Fig. 21.16). FDG PET is useful for the study of infections in the axial bones as well, the operated spine in particular. Indeed, FDG PET achieved 100% sensitivity and 90% specificity in 33 patients with suspected spinal osteomyelitis (de Winter et al. 2001). The latest study by the same group on spinal infection in patients with a history of previous spinal surgery yielded an overall accuracy of 86% with a negative predictive value of 100% (de Winter et al. 2003). In addition, the diagnostic efficacy of PET in low-grade spondylitis with adjacent soft-tissue infection and advanced bone degeneration has been reported to be superior to that of MRI, ^{67}Ga citrate scan, or ^{99m}Tc-MDP bone scintigraphy (Gratz et al. 2002). According to de Winter et al. (2001), FDG PET and labeled leukocyte scans are equally accurate in peripheral skeletal infection, but PET is definitely more accurate in axial skeletal infection. Nevertheless, since the positive predictive value is lower than the negative predictive value, caution must be exercised in interpreting a positive FDG PET (Alavi and Zhuang 2003).

According to Einhorn (1998), the healing of a bone lesion includes an inflammatory phase attended by a highly activated state of cell metabolism and glucose consumption. Experimental studies have shown that ^{18}F-FDG uptake similarly increases in bacterial infection (Sugawara et al. 1999) and aseptic inflammatory processes (Yamada et al. 1995). In an animal study using rabbit tibiae by Koort et al. (2004),

uncomplicated healing of bone damage produced by sterile operation was associated with a transient increase in FDG uptake at 3 weeks, which returned nearly to normal by 6 weeks. In contrast, localized osteomyelitis continuously caused intense FDG uptake at both 3 and 6 weeks without significant interval change. Compared to ^{99m}Tc-MDP bone scintigraphy FDG PET more efficiently distinguishes chronic osteomyelitis from healing bone reaction (Sugawara et al. 1998b; de Winter et al. 2000). However, an interval of 3 to 6 months should be allowed before follow-up PET to minimize the risk of false-positive findings during the initial stages of postsurgical or posttraumatic bone healing (de Winter et al. 2002).

Controversy exists about the usefulness of FDG PET in differentiating infections from loosening of arthroplasties. Zhuang et al. (2001) analyzed 74 prostheses with suspicious infection in 62 patients, and found FDG PET to be useful for detecting infections in lower limb arthroplasties and more accurate for the diagnosis of infections in hip prostheses than in knee prostheses. On the other hand, Stumpe et al. (2004) observed that FDG PET is more specific but less sensitive than conventional radiography in the diagnosis of prosthetic infection. Enhanced anatomy of PET-CT permits precise localization of osteomyelitis, greatly helping distinguish bone infection from soft-tissue infection. For example, FDG PET-CT can accurately separate osteomyelitis from soft-tissue infection in diabetic feet (Keidar et al. 2005).

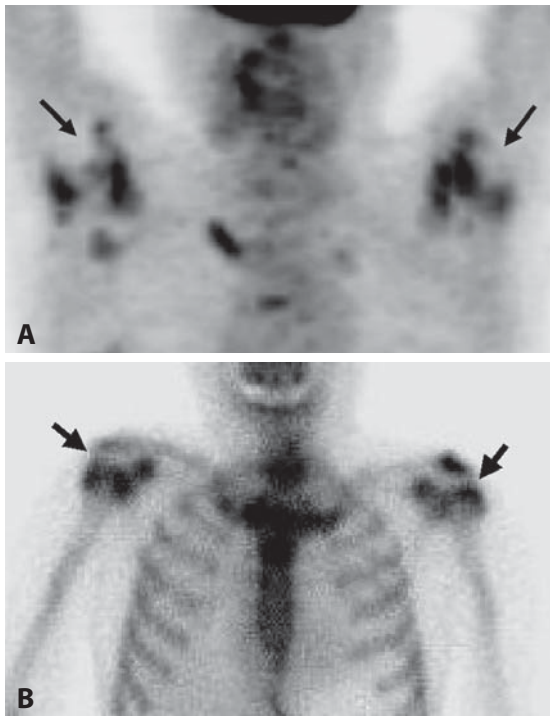

Fig 21.17A, B ^{18}F-FDG uptake in rheumatoid arthritis of the shoulder joints. **A** Anterior PET in a 64-year-old woman shows FDG uptake in the shoulder joints (arrows). **B** ^{99m}Tc-MDP bone scintigram reveals increased tracer uptake in the acromioclavicular and glenohumeral joints (*arrows*)

21.3 Rheumatoid Arthritis

FDG PET has been shown to be able to provide imaging information on molecular and metabolic change in synovitis and pannus of rheumatoid arthritis as activated macrophages and inflammatory tissue avidly accumulate FDG. Experiments suggested that tumor necrosis factor-α (TNF-α) enhances glucose entry into macrophages, regulating glucose transport and metabolism in fibroblasts (Gamelli et al. 1996; Cornelius et al. 1990). The mechanism involved in the action of TNF-α is considered to be operative in chronic synovial inflammation, backing up the rationale for FDG PET assessment of metabolic activity in rheumatoid arthritis (Feldmann and Naini 2001; Beckers et al. 2004). According to these authors FDG accumulates in inflamed synovia, and SUV measurements positively correlate with metabolic activity of diseased joints. These authors cautiously pointed out that the separation of synovitis from tenosynovitis by PET is extremely difficult in the wrist and metacarpophalangeal joints, the most common and typical sites of

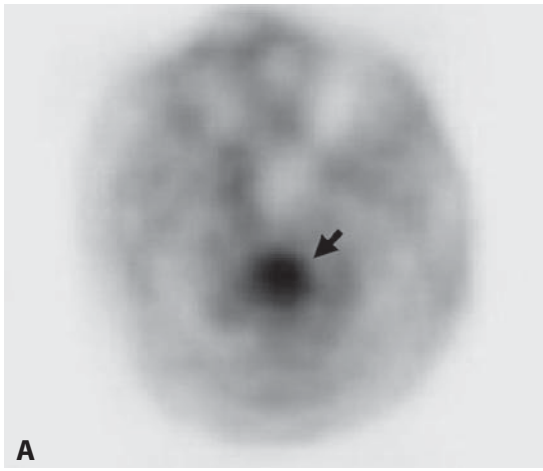

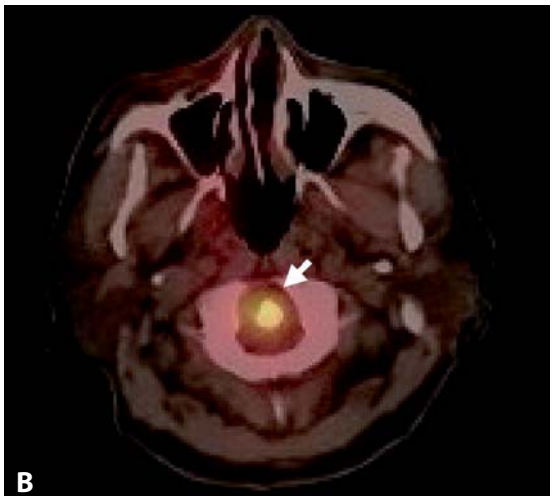

Fig. 21.18A, B FDG uptake in rheumatoid arthritis of the atlantoaxial joint. **A** Transverse PET image shows increased FDG uptake in the skull base (*arrow*). **B** PET-CT precisely localizes the FDG uptake to the atlantoaxial joint (*arrow*)

rheumatoid arthritis, simply because PET cannot provide accurate anatomical information. Such an anatomy-related drawback has largely been solved by the introduction of high-technology PET-CT (Fig. 21.17). Indeed, the level of resolution of CT hybridized with PET is such that now PET-CT can detect FDG accumulated in small and anatomically complex bones with inflammation, for example the rheumatoid odontoid process at the skull base (Fig. 21.18).

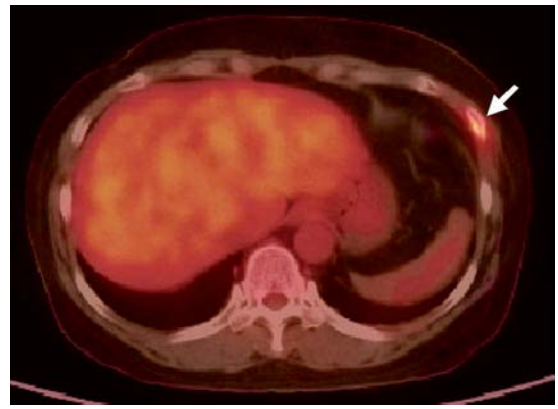

Fig. 21.19 FDG uptake in acute fracture site. Transverse PET-CT of the middle chest in a 57-year-old woman shows a small focal FDG uptake in a fracture of a left rib (*arrow*)

21.4 Fractures

Nuclear physicians are frequently confronted with the difficult task of differentiating primary or metastatic tumors from fracture since inflammatory cells also migrate to acute fracture sites, leading to high FDG uptake (Fig. 21.19). Generally, however, the fractures of traumatic or osteoporotic origin tend to accumulate less FDG than malignant tumors or infections (Kato et al. 2003; Schmitz et al. 2002). Characteristically, FDG uptake in fractures gradually diminishes and disappears after 3 months if not complicated by an infection (Zhuang et al. 2003).

References

Alavi A, Zhuang H (2003) PET imaging in infectious diseases. In: Valk PE, Bailey DL, Townsend DW, Maisey MN (eds) Positron emission tomography: basic science and clinical practice, 1st edn. Springer, London

Aoki J, Watanabe H, Shinozaki T, et al (2001) FDG PET of primary benign and malignant bone tumors: standardized uptake value in 52 lesions. Radiology 219:774–777

Beckers C, Ribbens C, André B, et al (2004) Assessment of disease activity in rheumatoid arthritis with ^{18}F-FDG PET. J Nucl Med 45:956–964

Blau M, Nagler W, Bender MA (1962) Fluorine-18: a new isotope for bone scanning. J Nucl Med 3:332–334

Brenner W, Bohuslavizki KH, Eary JF (2003) PET imaging of osteosarcoma. J Nucl Med 44:930–942

Brenner W, Conrad EU, Eary JF (2004) FDG PET imaging for grading and prediction of outcome in chondrosarcoma patients. Eur J Nucl Med Mol Imaging 31:189–195

Bury T, Baretto A, Daenen F, et al (1998) Fluorine–18 deoxyglucose positron emission tomography for the detection of bone metastases in patients with non-samll cell lung cancer. Eur J Nucl Med 25:1244:-1247

Chakrabarti R, Jung CY, Lee TP, et al (1994) Changes in glucose-transport and transporter isoforms during the activation of human peripheral blood lymphocytes by phytohemagglutinin. J Immunol 152:2660–2668

Chung JK, Kim YK, Yoon JK, et al (1999) Diagnostic usefulness of F-18 FDG whole body PET in detection of bony metastases compared to Tc-^{99m} MDP bone scan. J Nucl Med 40:96P

Clavo AC, Brown RS, Wahl RL (1995) Fluorodeoxyglucose uptake in human cancer cell lines is increased by hypoxia. J Nucl Med 36:1625–1632

Coleman RE, Mashiter G, Whitaker KB, et al (1988) Bone scan flare predicts successful systemic therapy for bone metastases. J Nucl Med 29:1354–1359

Cook GJ (2002) Skeletal and soft tissue. In: Wahl RL, Buchanan JW (eds) Principles and practice of positron emission tomography, 1st edn. Lippincott Williams & Wilkins, Philadelphia

Cook GJ, Houston S, Rubens R, Maisey MN, et al (1998) Detection of bone metastases in breast cancer by ^{18}FDG PET: differing metabolic activity in osteoblastic and osteolytic lesions. J Clin Oncol 16:3375–3379

Cornelius P, Marlowe M, Pekala PH (1990) Regulation of glucose transport by tumor necrosis factor-α in cultured murine 3T3-L1 fibroblasts. J Trauma 30:S15–S20

Daldrup-Link H, Franzius C, Link TM, et al (2001) Whole-body MR imaging for detection of bone metastases in children and young adults: comparison with skeletal scintigraphy and FDG PET. AJR Am J Roentgenol 177:229–236

de Winter F, Van de Wiele C, Vogelaers D, et al (2000) FDG PET is highly accurate in the diagnosis of chronic osteomyelitis in the central skeleton (abstract). J Nucl Med 41:57

de Winter F, van de Wiele C, Vogelaers D, et al (2001) Fluorine-18 fluorodeoxyglucose-positron emission tomography: a highly accurate imaging modality for the diagnosis of chronic musculoskeletal infections. J Bone Joint Surg Am 83:651–660

de Winter F, Vogelaers D, Gemmel F, et al (2002) Promising role of 18-F-fluoro-d-deoxyglucose positron emission tomography in clinical infectious diseases. Eur J Clin Microbiol Infect Dis 21:247–257

de Winter F, Gemmel F, Van de Wiele C, et al (2003) 18-fluorine fluorodeoxyglucose positron emission tomography for the diagnosis of infection in the postoperative spine. Spine 28:1314–1319

Einhorn TA (1998) The cell and molecular biology of fracture healing. Clin Orthop 355:S7–S21

Even-Sapir E, Metser U, Flusser G, et al (2004) Assessment of malignant skeletal disease: initial experience with ^{18}F-fluoride PET/CT and comparison between ^{18}F-fluoride PET and ^{18}F-fluoride PET/CT. J Nucl Med 45:272–278

Feldmann M, Naini RN (2001) Anti-TNFa therapy of rheumatoid arthritis: what have we learned? Annu Rev Immunol 19:163–196

Foo SS, Ramdave S, Berlangieri SU, Scott AM (2004) Detection of occult bone metastases of lung cancer with fluorine-18 fluorodeoxyglucose positron emission tomography. Australas Radiol 48:214–216

Gamelli RL, Liu H, He LK, et al (1996) Augmentations of glucose uptake and glucose transporter-1 in macrophages following thermal injury and sepsis in mice. J Leukoc Biol 59:639–647

Gratz S, Dorner J, Fischer U, et al (2002) ^{18}F-FDG hybrid PET in patients with suspected spondylitis. Eur J Nucl Med 29:516–524

Guhlmann A, Brecht-Krauss D, Suger G, et al (1998) Fluorine-18-FDG PET and technetium-99m antigranulocyte antibody scintigraphy in chronic osteomyelitis. J Nucl Med 39:2145–2152

Hain SF, O'Doherty MJ, Lucas JD, et al (1999) Fluorodeoxyglucose PET in the evaluation of amputations for soft tissue sarcoma. Nucl Med Commun 20:845–848

Hetzel M, Arslandermir C, Konig HH, et al (2003) F-18 NaF PET for detection of bone metastases in lung cancer: accuracy, cost-effectiveness, and impact on patient management. J Bone Miner Res 18:2206–2214

Hiraga T, Mundy GR, Yoneda T (2000) Bone metastases-morphology. In: Rubins RD, Mundy GR (eds) Cancer and the skeleton. Martin Dunitz, London

Jones DN, McCowage GB, Sostman HD, et al (1996) Monitoring of neoaduvant therapy response of soft-tissue and musculoskeletal sarcoma using fluorine-18-FDG PET. J Nucl Med 37:1438–1444

Kato E, Aoki J, Endo K (2003) Utility of FDG-PET in differential diagnosis of benign and malignant fractures in acute to subacute phase. Ann Nucl Med 17:41–46

Keidar Z, Militianu D, Melamed E, et al (2005) The diabetic foot: initial experience with ^{18}F-FDG PET/CT. J Nucl Med 46:444–449

Kolindou A, Liu Y, Ozker K, et al (1996) In-111 WBC imaging of osteomyelitis in patients with underlying bone scan abnormalities. Clin Nucl Med 21:183–191

Koort JK, Mäkinen TJ, Knuuti J, et al (2004) Comparative 18F-FDG PET of experimental Staphylococcus aureus osteomyelitis and normal bone healing. J Nucl Med 45:1406–1411

Lang CH, Bagby GJ, Dobrescu C, et al (1992) Modulation of glucose metabolic response to endotoxin by granulocyte colony-stimulating factor. Am J Physiol 263: R1122–R1129

Lee FY, Yu J, Chang SS, et al (2004) Diagnostic value and limitations of fluorine-18 fluorodeoxyglucose positron emission tomography for cartilaginous tumors of bone. J Bone Joint Surg Am 86:2677–2685

Lodge MA, Lucas JD, Marsden PK, et al (1999) A PET study of ^{18}FDG uptake in soft tissue masses. Eur J Nucl Med 26:22–30

Lucas JD, O'Doherty MJ, Cronin BF, et al (1999) Prospective evaluation of soft tissue masses and sarcomas using fluorodeoxyglucose positron emission tomography. Br J Surg 86:550–556

Mester U, Lerman H, Blank A, et al (2004) Malignant involvement of the spine: assessment by ^{18}F-FDG PET/CT. J Nucl Med 45:279–284

Moog F, Bangerter M, Kotzerke J, et al (1998) 18-F-fluorodeoxyglucose-positron emission tomography as a new approach to detect lymphomatous bone marrow. J Clin Oncol 16:603–609

Moon DH, Maddahi J, Siverman DH, et al (1998) Accuracy of whole-body fluorine-18-FDG PET for the detection of recurrent or metastatic breast carcinoma. J Nucl Med 39:431–435

Mortimer JE, Dehdashti F, Siegel BA, et al (2001) Metabolic flare: indicator of hormone responsiveness in advanced breast cancer. J Clin Oncol 19:2797–2803

Nelson CA, Wang JQ, Leav I, et al (1996) The interaction among glucose transport, hexokinase, and glucose-6-phosphatase with respect to ^{3}H-2-deoxyglucose retention in murine tumor models. Nucl Med Biol 23:533–541

Rossleigh MA, Lovegrove FT, Reynolds PM, et al (1984) Assessment of response to therapy of bone metastases in breast cancer. Aust N Z J Med 14:19–22

Schirrmeister H, Guhlmann A, Kotzerke J, et al (1999) Sensitivity in detecting osseous lesions depends on anatomic localization: planar bone scintigraphy versus ^{18}F PET. J Nucl Med 40:1623–1629

Schmitz A, Risse JH, Textor J, et al (2002) FDG-PET findings of vertebral compression fractures in osteoporosis: preliminary results. Osteoporos Int 13:755–761

Schulte M, Brecht-Krauss D, Werner M, et al (1999) Evaluation of neoadjuvant therapy response of osteogenic sarcoma using FDG PET. J Nucl Med 40:1637–1643

Schulte M, Brecht-Krauss D, Heymer B, et al (2000) Grading of tumors and tumorlike lesions of bone: evaluation by FDG PET. J Nucl Med 41:1695–1701

Schwarzbach MHM, Dimitrakopoulou-Strauss A, Willeke F, et al (2000) Clinical value of [^{18}F] fluorodeoxyglucose positron emission tomography imaging in soft tissue sarcomas. Ann Surg 231:380–386

Shreve PD, Grossman HB, Gross MD, et al (1996) Metastatic prostatic cancer: initial findings of PET with 2-deoxy-2-[F-18]fluoro-D-glucose. Radiology 199:751–756

Smith TAD (2000) Mammalian hexokinases and their abnormal expression in cancer. Br J Biomed Sci 57:170–178

Stumpe KD, Dazzi H, Schaffner A, et al (2000) Infection imaging using whole-body FDG-PET. Eur J Nucl Med 27:822–832

Stumpe KD, Notzli HP, Zanetti M, et al (2004) FDG PET for differentiation of infection and aseptic loosening in total hip replacements: comparison with conventional radiography and three-phase bone scintigraphy. Radiology 231:333–341

Sugawara Y, Fisher SJ, Zasadny KR, et al (1998a) Preclinical and clinical studies of bone marrow uptake of fluorine-18-fluorodeoxyglucose with or without granulocyte colony-stimulating factor during chemotherapy. J Clin Oncol 16:173–180

Sugawara Y, Braun DK, Kison PV, et al (1998b) Rapid detection of human infections with fluorine-18 fluorodeoxyglucose and positron emission tomography: preliminary results. Eur J Nucl Med 25:1238–1243

Sugawara Y, Gutowski TD, Fisher SJ, et al (1999) Uptake of positron emission tomography tracers in experimental bacterial infections: a comparative biodistribution study of radiolabeled FDG, thymidine, L-methionine, ^{67}Ga-citrate, and ^{125}I-HSA. Eur J Nucl Med 26:333–341

Warburg O (1931) The mechanism of tumors. Richard Smith, New York, pp 129–169

Yamada S, Kubota K, Kubota R, et al (1995) High accumulation of fluorine-18-fluorodeoxyglucose in turpentine-induced inflammatory tissue. J Nucl Med 36:1301–1306

Yang SN, Liang JA, Lin FJ, et al (2002) Comparing whole body ^{18}F-2-deoxyglucose positron emission tomography and technetium-99m methylene diphosphonate bone scan to detect bone metastases in patients with breast cancer. J Cancer Res Clin Oncol 128:325–328

Yao WJ, Hoh CK, Hawkins RA, et al (1995) Quantitative PET imaging of bone marrow glucose metabolic response to hematopoietic cytokines. J Nucl Med 36:794–799

Yeh SD, Imbriaco M, Larson SM, et al (1996) Detection of bony metastases of androgen-independent prostate cancer by PET-FDG. Nucl Med Biol 23:693–697

Zhuang H, Duarte PS, Pourdehnad M, et al (2000) Exclusion of chronic osteomyelitis with F-18 fluorodeoxyglucose positron emission tomographic imaging. Clin Nucl Med 25:281–284

Zhuang H, Duarte PS, Pourdehnad M, et al (2001) The promising role of ^{18}F-FDG PET in detecting infected lower limb prosthesis implants. J Nucl Med 42:44–48

Zhuang H, Sam JW, Chacko TK, et al (2003) Rapid normalization of osseous FDG uptake following traumatic or surgical fractures. Eur J Nucl Med 30:1096–1103

22 A Genetic Consideration of Skeletal Disorders

Yong-Whee Bahk and Soo-Kyo Chung

The human skeleton has the unique function of calcium storage and liberation in addition to locomotion and hematopoiesis, and acting as the body framework. Under the complex homeostatic regulation of calcitonin and parathormone as well as the influence of auxiliary hormones and vitamin D, living bones are ceaselessly engaged with deposition and removal of calcium salts in the form of bone production and resorption, which are mediated by the activities of osteoblasts and osteoclasts, respectively. Basically, skeletal diseases are reflected first as quantitative changes in osseous calcium salts and serum calcium levels. The mobilization of calcium salts from and excessive deposition on bone in bone disorders, both nongenetic and genetic, may result in demineralization or decalcification and osteosclerosis, respectively. Then, with the advance of disease, pathological and anatomical skeletal changes may follow manifesting in the form of osteopenia, osteoporosis, osteolysis, sclerosis, eburnation, bone defect, growth disturbance, and deformity, either singly or in combination. Thus, in order to ideally detect bone disorders at an early stage, the calcium metabolic profile of bone must be obtained by an appropriate means before anatomical change takes place.

Methodologically, bone scintigraphy that uses ^{99m}Tc-MDP, a representative calcium salt analog, is suitable for this purpose because it can simultaneously provide information on both the metabolism and anatomy of normal and diseased bones (Fig. 22.1A, B). It is also a potent tool for the study of muscular, enthetic, and subcutaneous soft-tissue disorders and various parenchymal organ tumors (Chapter 19). Primary bone infections and infected fractures, prostheses, and operative wounds can specifically be detected by ^{111}In- or ^{99m}Tc-labeled white blood cells. One recent clinical study has confirmed the accuracy of ^{111}In-leukocyte scintigraphy in the diagnosis of posttraumatic and postoperative cranial and spinal infections (Medina et al. 2000). In an endeavor to substitute costly ^{111}In with economical ^{99m}Tc, leukocytes labeled with hexamethyl-propylene amine oxime (HMPAO) have been introduced. The image quality of the ^{99m}Tc-HMPAO leukocyte scan is acceptable (Fig. 22.2). ^{67}Ga citrate is another useful agent for both bone infections and tumors (Fig. 22.3). On the other hand, the bone marrow can be imaged using ^{99m}Tc nanocolloid and ^{99m}Tc-labeled anti-NCA95 antibody (Fig. 22.4).

For a genetic consideration and categorical description of ^{99m}Tc-MDP bone scan manifestations it seems appropriate to classify skeletal disorders into two major groups. The first group is designated to include the skeletal disorders that are associated with genetic imbalance or heredity and the second group the disorders that are inflammatory, infective, traumatic, degenerative, and neoplastic in nature without a known association with genome problem so far. The disorders in the first group, far fewer in occurrence than the second group, are related to autosomal or sex chromosomal imbalance or mutations. Well-known autosomal and sex chromosomal disorders include Turner's syndrome, Klinefelter's syndrome, and trisomy defects, and the other major genetic disorder groups are mucopolysaccharidoses and osteochondrodysplasias. The diseases of the former group are known to be caused by genetically determined deficiencies of lysoso-

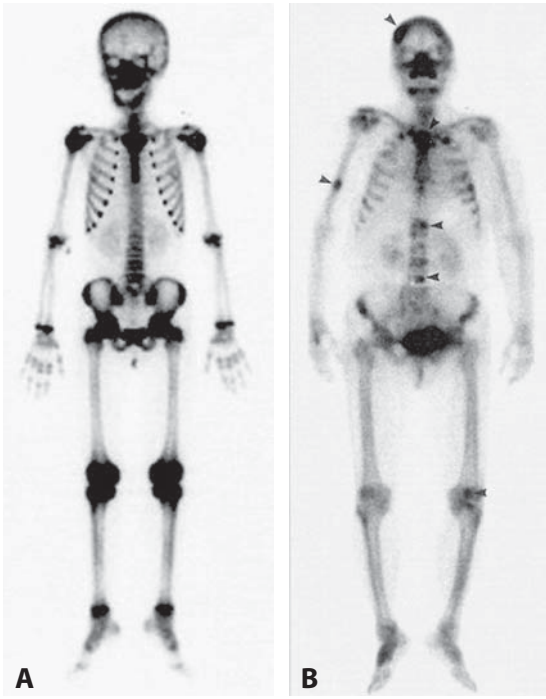

Fig. 22.1A, B ^{99m}Tc-MDP bone scan of normal developing skeleton and senile porotic skeleton with metastases. **A** Anterior whole-body scan in an 11-year-old girl shows normal bones with characteristic high tracer uptake in the actively growing long bone epiphyses. **B** Anterior whole-body scan in a 63-year-old woman with diffuse porosis reveals generalized low skeletal uptake. Disseminated hot areas are due to metastases (*arrowheads*)

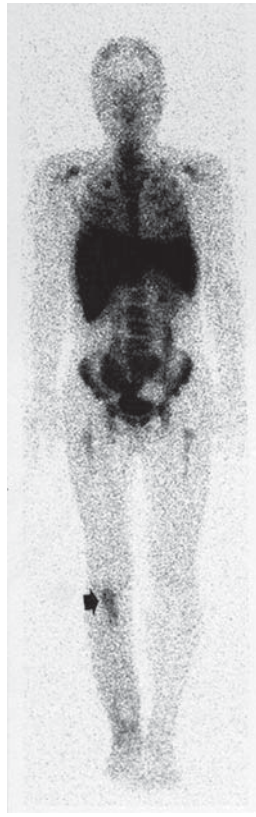

Fig. 22.2 Anterior whole-body ^{99m}Tc-HMPAO-leukocyte scintigraph in a 31-year-old man with chronic osteomyelitis shows focal tracer uptake in the right proximal tibial metaphysis (*arrow*)

mal enzymes that degrade mucopolysaccharides (McAlister and Herman 1995), and clinically include Hurler's disease, Hunter's syndrome and Morquio's disease. On the other hand, the latter group embraces Marfan's syndrome, Paget's disease (Roodman and Windle 2005), neurofibromatosis, familial multiple exostosis (Pierz et al. 2002; Shi et al. 2002), osteopoikilosis (Benli et al. 1992; Bonde and Vielfreund 2001), osteopetrosis (Taranta et al. 2003), and osteogenesis imperfecta (Goldman 1995), and many others.

Certain skeletal disorders are due to the action of several different genes and are accordingly referred to as polygenic disorders. Osteoarthritis and rheumatoid arthritis (Wordsworth 1995), ankylosing spondylitis (Fong 2000), Reiter's syndrome, and osteoporosis (Peacock et al. 2002; Cohen-Solal and de Vernejoul 2004) belong to this category. Spondyloarthropathies including ankylosing spondylitis and Reiter's syndrome can be established by antigen tests, the HLA-B27 antigen assay in particular (Morris et al. 1974; Kahn 1988), and they constitute excellent indications for ^{99m}Tc-MDP bone scan (Kim et al. 1999).

With widespread use of antigen tests and gene typing, an increasing number of bone diseases have become recognized as having genetic backgrounds. Diffuse idiopathic skeletal hyperostosis (Shapiro et al. 1976), reactive arthritis (Leirisalo et al. 1982), slipped capital fe-

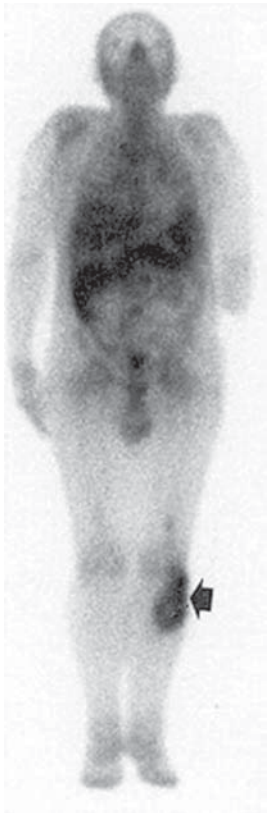

Fig. 22.3 Anterior whole-body ^{67}Ga citrate scintigraph in a 76-year-old man shows intense tracer uptake with a small photon defect in the left proximal tibial metadiaphysis (*arrow*)

moral epiphysis (Mullaji et al. 1993), and hydroxyapatite crystal deposition disease (Pinals and Short 1965; McCarty and Gatter 1966; Amor et al. 1977) are examples of gene-related disorders.

The second, yet by far larger category, is simple pathological entities that have no known cause-and-effect relationship with genetic abnormality. Disorders in this category include infections, inflammatory disorders, osteochondroses, avascular osteonecrosis, trauma, sports injuries, most metabolic and nutritional disorders, and most tumors and tumorous conditions of bone. Clinically, these disorders constitute major indications for ^{99m}Tc-MDP bone scanning.

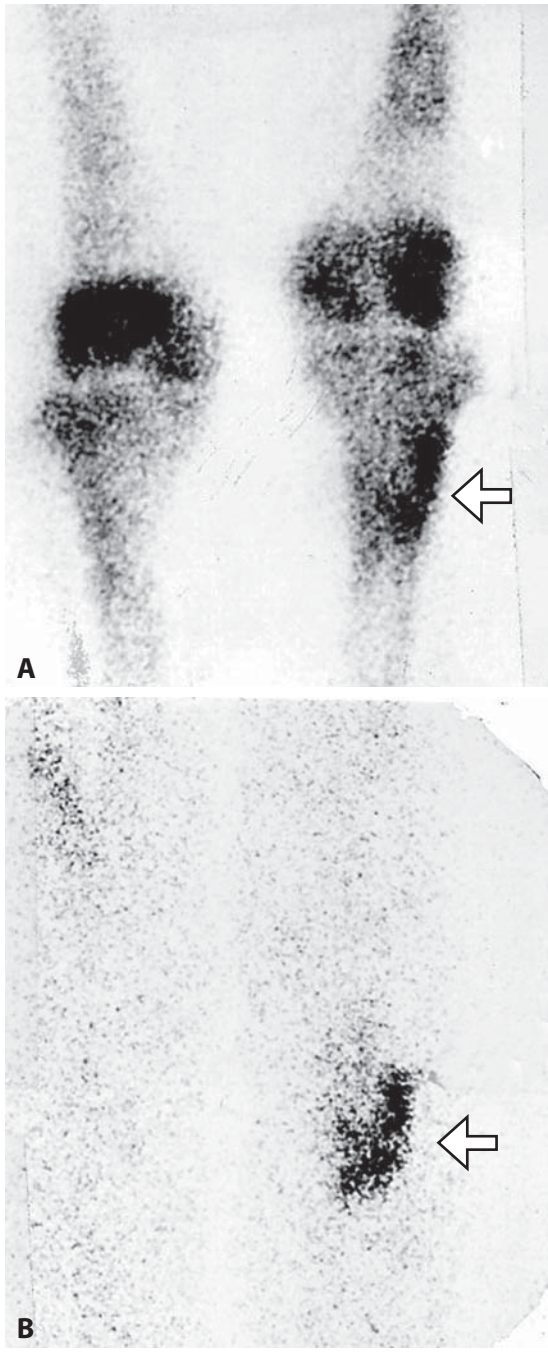

Fig. 22.4A, B Bone scan and marrow scan in acute osteomyelitis. **A** Anterior planar ^{99m}Tc-MDP bone scan of both knees shows increased uptake in the left proximal tibial metaphysis (*open arrow*). **B** ^{99m}Tc-NCS95 bone marrow scan reveals selective tracer uptake in infective focus (*open arrow*)

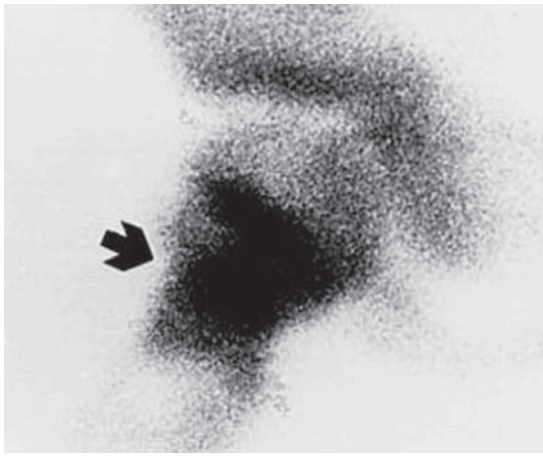

Fig. 22.5 Anterior pinhole ^{99m}Tc-MDP bone scintigraph of the right hip shows characteristic metaphyseal localization of acute osteomyelitis (*arrow*)

Fig. 22.6 Transverse, sagittal and coronal SPECT images of the right knee show increased tracer uptake in the medial tibial plateau and the lateral femoral and tibial condyles indicating degenerative arthritis (*arrows*). The image contrast is enhanced but resolution remains suboptimal

22.1 Essential Bioanatomy of the Musculoskeletal System

The musculoskeletal system consists of bones, joints, and muscles and musculotendinous units. Bone is involved in complex biomechanical, metabolic, and endocrine activities like the brain, heart, and tumors. As mentioned above, bone tissues are produced, maintained, and eliminated by the ceaseless osteoblastic and osteoclastic activity. The principal roles played by these cells are to maintain bone integrity and body calcium homeostasis by balancing the ratio of production and resorption of collagenous matrices and governing the mineralization process. Collagen production is common to various connective tissues, but mineralization is unique to bone cells. Skeletal muscles are rich in actin and myosin whose interactions effect contraction (Williams et al. 1989). They are composed of a large number of muscle fibers (specialized cells). Muscle fibers, individually invested by the endomysium, are grouped into fascicles enveloped in successive connective tissue sheaths. Variable numbers of fascicles form a skeletal muscle ensheathed by the epimysium. Tendon is a specialized connective tissue that on one side unites to the muscle belly forming the musculotendinous unit and on the other side attaches to the periosteum, the fibrous capsule of the joint, or directly to bone.

22.2 ^{99m}Tc-MDP Bone Scintigraphic Techniques

The scintigraphic techniques used for the imaging the musculoskeletal system include planar whole-body scintigraphy (Fig. 22.1), planar spot scintigraphy, planar pinhole scintigraphy (Fig. 22.5), planar SPECT (Fig. 22.6), pinhole SPECT (Fig. 22.7), and nuclear angiography (Fig. 22.8).

22.3 ^{99m}Tc-MDP Bone Scintigraphy in Autosomal and Polygenic Bone Disorders

With the extended uses of the pinhole magnification technique ^{99m}Tc-MDP bone scan is increasingly applied to the diagnosis of some autosomal and polygenic bone disorders. So far no specific role in the narrow genuine sense of

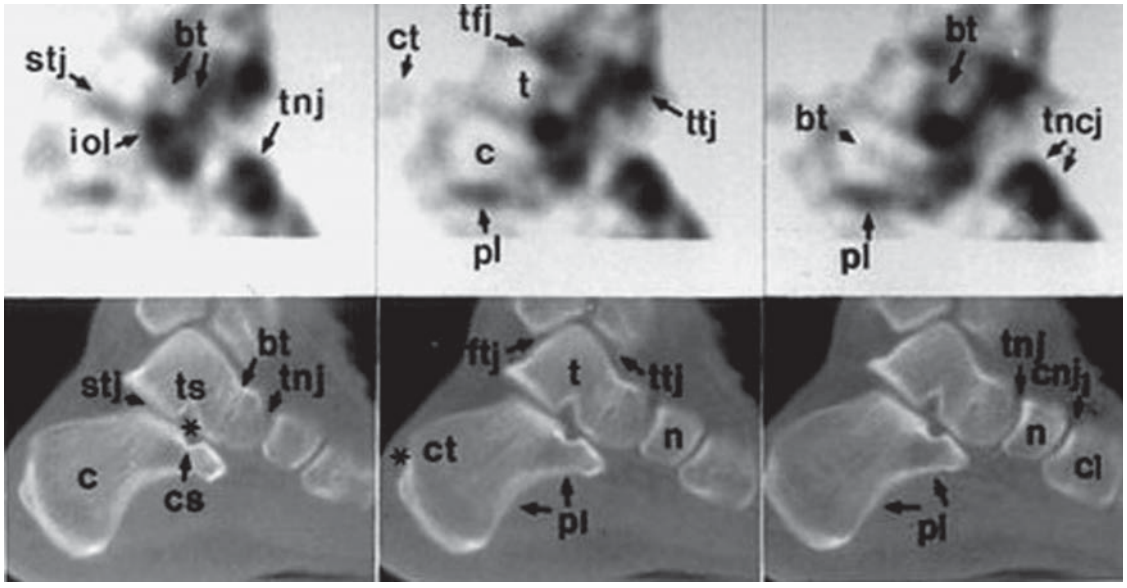

Fig. 22.7 Lateral pinhole SPECT (*upper panel*) and CT (*lower panel*) of a normal adult ankle shows many anatomical landmarks: the subtalar joint (*stj*), bone trabeculae (*bt*), interosseous ligament (*iol*), talonavicular joint (*tnj*), tibiofibular joint (*tfj*), talus (*t*), calcaneal tuberosity (*ct*), calcaneus (*c*), plantar ligament insertion (*pl*), talonavicular joint (*tnj*), tarsal sinus (*ts*), navicular (*n*) and others

genetic medicine is played by bone scintigraphy, and such a role would not be a reality in the future since by nature bone scanning is not an appropriate modality for use in research in the realm of gene or gene-based disease mechanisms. This section describes scintigraphic manifestations of the more common genetically determined skeletal disorders in the frame of macroscopic imaging diagnosis. There is a more or less full account elsewhere in this book of each bone and joint disorder presented in this section.

22.3.1 Autosomal Skeletal Disorders

Representative autosomal skeletal disorders are osteochondrodysplasias and dysostoses. From a long list of these disorders, we could perform ^{99m}Tc-MDP bone scanning in Albers-Schönberg's osteopetrosis and familial multiple exostosis. Other skeletal disorders with an autosomal trait of scintigraphic interest are neurofibromatosis and osteopoikilosis. Most recently, Paget's bone disease has also been added to the list of gene-linked disorders (Roodman and Windle 2005).

22.3.1.1 Albers-Schönberg's Disease

Albers-Schönberg's disease, one of four types of osteopetrosis, is a benign autosomal dominant disorder. It is also referred to as the "marble" bone disease, and pathologically characterized by the persistence of primary spongiosa that has failed to be eliminated by resorption during remodeling. Radiographic features include diffuse sclerosis, defective tubulation, and metaphyseal clubbing. It is asymptomatic and usually found by chance due to fracture. Whole-body scanning is useful for panoramic display of systemic involvement with peculiar tracer uptake in the long-bone metaphyses (Fig. 18.56). The pinhole scan shows intense tracer uptake in clubbed tubular bone ends and flared vertebral endplates (Fig. 18.57).

22.3.1.2 Hereditary Multiple Exostoses

Hereditary multiple exostoses, also synonymously called multiple cartilaginous exostoses or diaphyseal aclasia, are a benign autosomal dominant disease of dysplastic nature with an estimated prevalence of 1 in 50,000 in Western countries (Rambeloarisoa et al. 2002). One

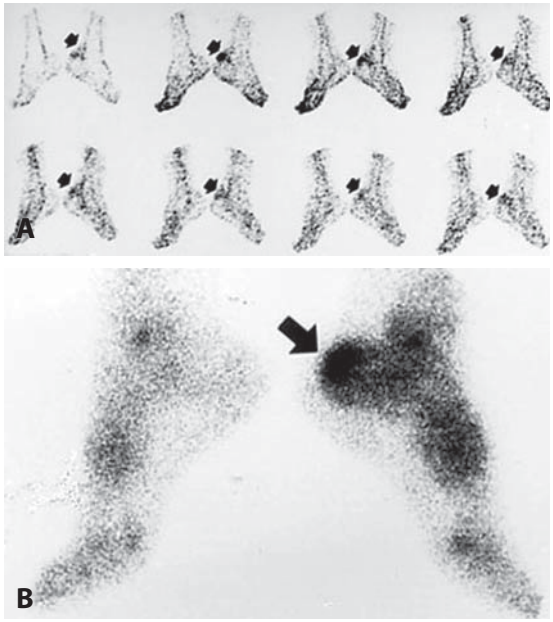

Fig. 22.8A–C Scintiangiography in retrocalcaneal infective osteitis. **A** Arterial phase scan shows increased blood flow in infective focus (*arrows*). **B** Blood-pool scan reveals increased staining (*arrow*). **C** Equilibrium phase scan demonstrates prominent bone uptake (*arrow*)

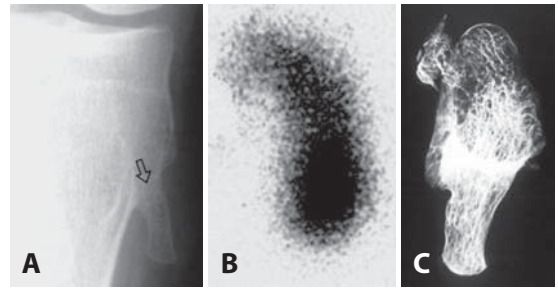

Fig. 22.9A–C Exostosis (the same patient as in Fig. 18.54). **A** Anteroposterior radiograph of the right knee in a 22-year-old woman shows a coat-hanger-like bony outgrowth arising from the medial metaphysis of the proximal tibia (*arrow*). **B** Pinhole scintigraph reveals increased tracer uptake at the tip that was painful. **C** Radiograph of surgical specimen shows reactive sclerosis in the tip

epidemiological study performed in Manitoba revealed a higher incidence of 19.4% in children and 9.5% in adults (Black et al. 1993). This condition is ascribed to the excessive production of spongiosa, resulting in cartilage-capped osteochondromas that typically arise from the metadiaphyseal aspect of the physis (Rubin 1964). Clinically, exostoses present as painless lumps around the knees and elbows usually in boys. Symptoms are produced when the mass mechanically compresses or irritates a surrounding vessel, nerve or tendon (Fig. 22.9A). Malignant transformation, which occurs in about 2% of the solitary type and 10–25% of the multiple type (Ochsner 1978; Dahlin and Unni 1986), is an important complication. Whole-body scintigraphy is used for panoramic mapping of multiple bony outgrowths and pinhole scintigraphy for molecular information that is expressed by increased tracer uptake in the mechanically stimulated portion of exostoses (Fig. 22.9B, C).

22.3.2 Polygenic Skeletal Disorders

Polygenic skeletal disorders are caused by the action of several different genes. Rheumatoid arthritis, ankylosing spondylitis, and Reiter's syndrome belong to them. These disorders can be assessed by antigen typing, HLA-B27 antigen in particular, and are excellent indications for bone scintigraphic study.

22.3.2.1 Rheumatoid Arthritis

Rheumatoid arthritis is probably the most common inflammatory disorder of synovial joints. It is a disorder of scintigraphic interest whose diagnosis can be established by high-titer rheumatoid factor and positive histocompatibility HLA-B27 or HLA-DR4 antigen. Women are affected two to three times more often than men. It may affect any synovial joints with a strong proclivity to small joints in the hands, wrists, and feet. Involvement is characteristically polyarticular and symmetrical on both sides of the body. Early pathological changes include synovial congestion, edema, and exudation. Hyperemia and disuse cause prominent osteopenia in the periarticular bones. Pannus formation and granulation follow eroding and destroying articular cartilages and bones with resultant joint-space narrowing and consequential deformity. Whole-body

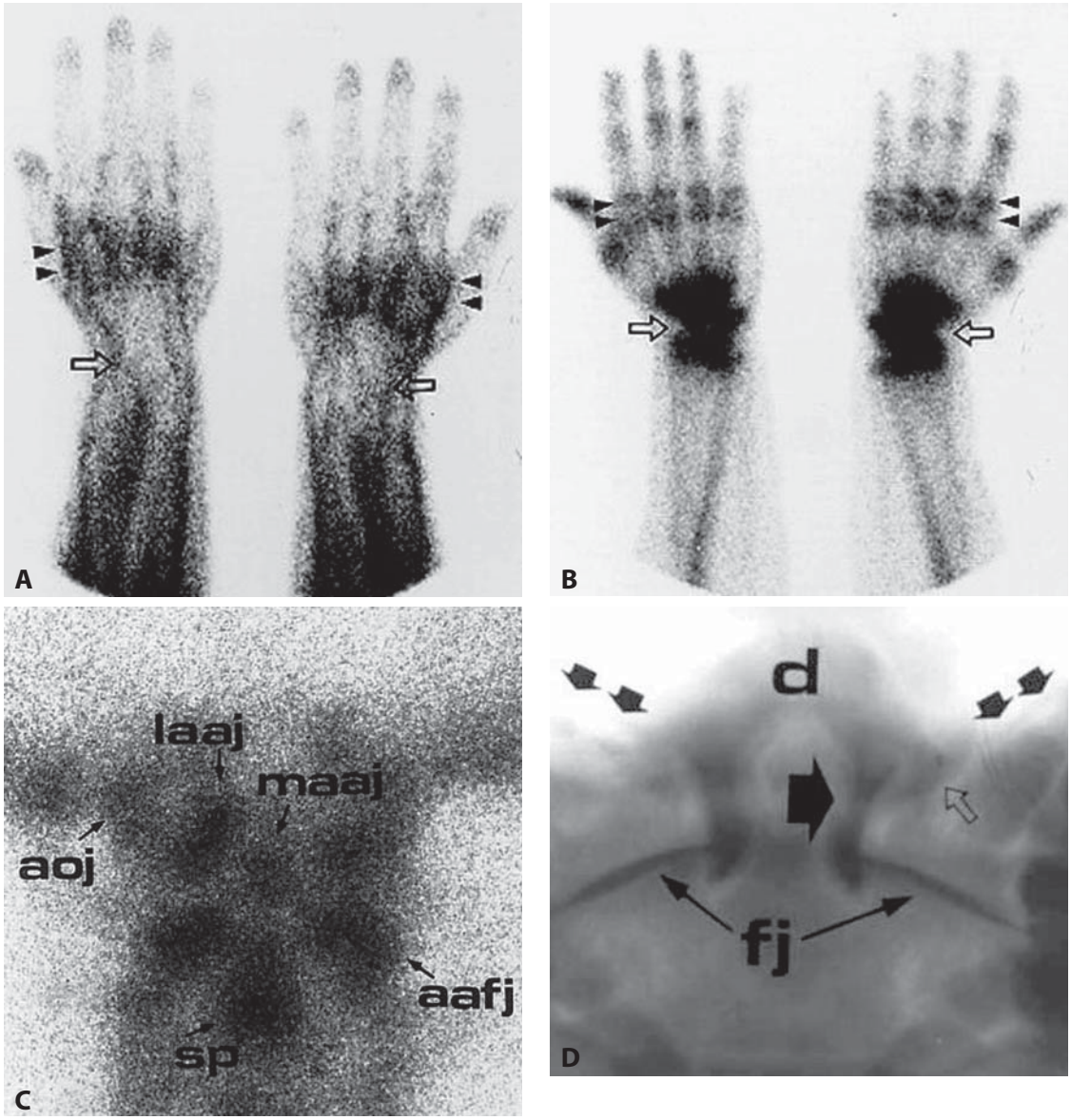

Fig. 22.10A–D Usefulness of ^{99m}Tc-MDP bone scintigraphy in acute rheumatoid arthritis. **A** Dorsopalmar nuclear angiogram of the wrists and fingers in a 37-year-old woman shows increased vascularity in the wrists (*open arrows*) and the carpometacarpal and metacarpophalangeal joints (*arrowheads*). **B** Equilibrium phase scintigraph reveals increased tracer uptake in the wrists (*open arrows*) and the carpometacarpal and metacarpophalangeal joints (*arrowheads*). **C** Anterior pinhole scintigraph of the skull base with rheumatoid arthritis in another patient reveals well-defined patchy tracer uptake in the atlantooccipital joint (*aoj*), lateral atlantoaxial joint (*laaj*), median atlantoaxial joint (*maaj*) and dense, atlantoaxial facet joint (*aafj*) and C1 spinous process (*sp*). **D** Conventional X-ray tomogram identifies the dense (*d*), atlantoaxial joint (*large arrow*), focal erosion (*open arrow*), atlantooccipital joints (*pairs of arrows*), and facet joints (*fj*)

scintigraphy is ideal for the diagnosis and archiving of symmetrical, polyarticular disease (Fig. 10.2) and scintiangiography provides dynamic information on lesional vascularity that reflects disease activity (Fig. 22.10A, B). Thus, angiography reveals increased vascularity in the acute phase with synovitis and normal return in remission. On the other hand, pinhole scanning is indeed useful for showing both morphological and metabolic changes, especially in complex anatomical sites such as the skull base where the atlantooccipital and atlantoaxial joints are involved (Fig. 22.10C, D). In

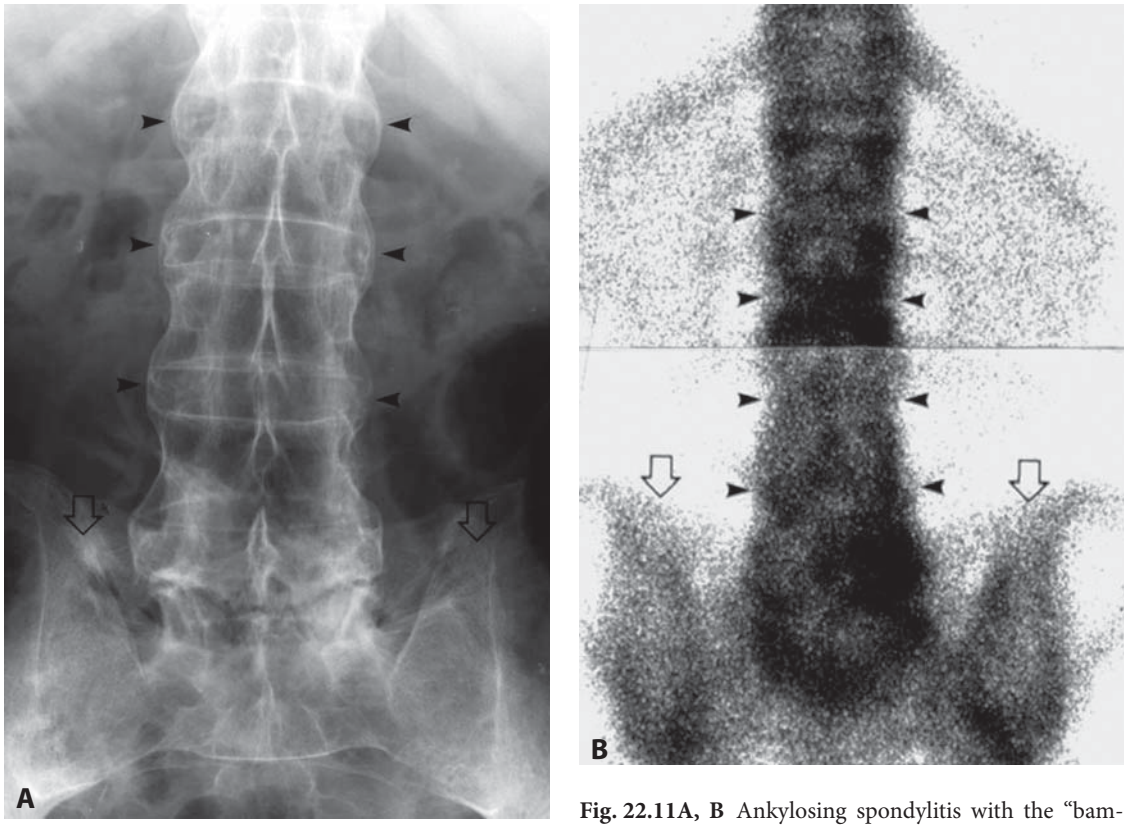

Fig. 22.11A, B Ankylosing spondylitis with the "bamboo spine" sign. **A** Anteroposterior radiograph of the lumbar spine in a 63-year-old man shows diffusely obliterated spine, disk spaces, and facet joints due to ligamental mineralization (*arrowheads*). Note sacroiliac joint involvement (*open arrows*). **B** Posterior pinhole scintigraph reveals diffuse obliteration of the spine, disk spaces and joints giving rise to the scintigraphic "bamboo spine" sign (*arrowheads*)

addition, pinhole SPECT can visualize characteristic synovial alteration in rheumatoid arthritis (Bahk et al. 1998) (Fig. 2.10).

22.3.2.2 Ankylosing Spondylitis

Ankylosing spondylitis and Reiter's syndrome are seronegative spondyloarthropathies of genetic and scintigraphic interest. Both conditions show a close association with HLA-B27 antigen. Thus, more than 90% of patients with ankylosing spondylitis possess HLA-B27 antigen, and HLA-DR4 has also been shown to be related to the clinical signs of this disorder (Kahn 1988).

Ankylosing spondylitis is a nonspecific inflammatory disease. It typically starts from the sacroiliac joints, and slowly extends to the diskovertebral, apophyseal, costovertebral, and neurocentral joints of the thoracic, lumbar, sacral, and cervical spine in that order. In the late stage, the annulus fibrosus, the anterior longitudinal ligament, and the interspinous ligaments become ossified producing the characteristic "bamboo spine" sign (Fig. 22.11A). The whole-body scan displays increased tracer uptake in the sacroiliac joints and the ossified ligaments and syndesmophytes of the thoracolumbar spine, obliterating the disk spaces and facet joints (Fig. 22.11B). Tracer uptake is considerably increased in the early and intermediate florid stages, but becomes reduced in the late ossifying stage when the disease is metabolically quiescent.

22.3.2.3 Reiter's Syndrome

Reiter's syndrome is another genetic spondyloarthropathy of bone scintigraphic interest. As in ankylosing spondylitis prevalence of positive HLA-B27 test is very high. A frequency of

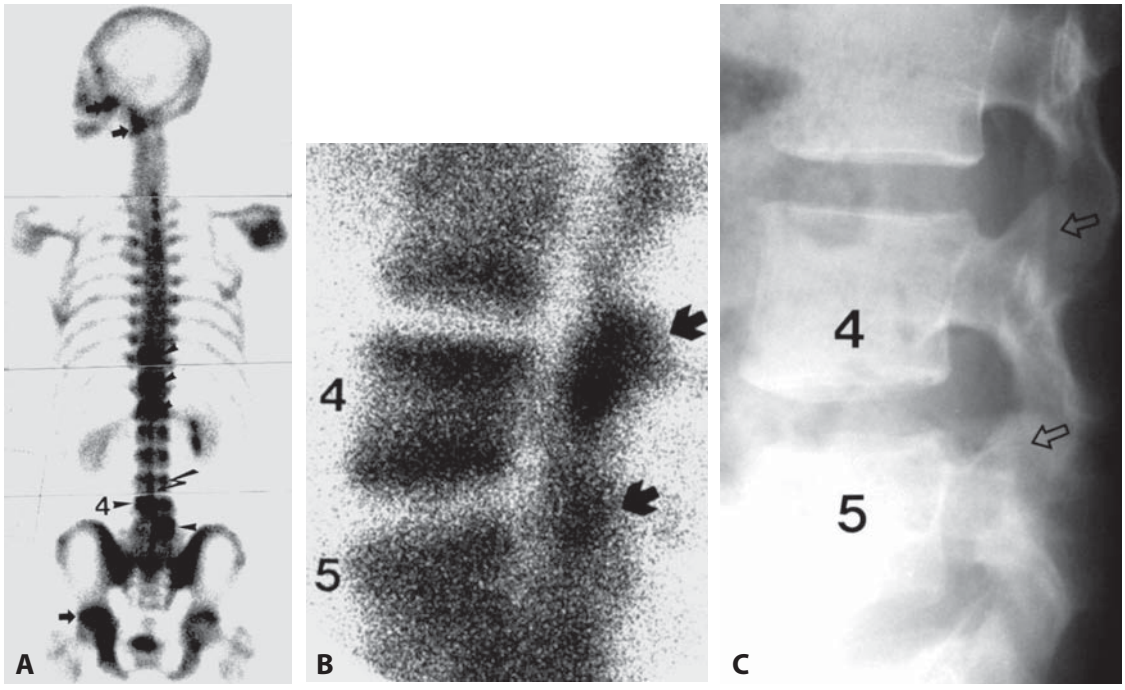

Fig. 22.12A–C Scintigraphic manifestations of Reiter's syndrome. **A** Posterior planar scan of the axial skeleton in a 23-year-old man shows tracer uptake in the temporomandibular joint (*uppermost arrow)*, atlantoaxial joint (*second arrow*), thoracolumbar and lower lumbar spine (*arrowheads*), and left hip (*bottom arrow*). The involvement is asymmetrical and pauciarticular. **B** Lateral pinhole scintigraph of the lumbar spine in another patient with early Reiter's syndrome shows increased tracer uptake in L3–4 and L4–5 facet joints (*arrows*). **C** Lateral radiograph reveals blurring and obliteration of the affected facet joints (*open arrows*)

96% has been reported (Morris et al. 1974). The presence of HLA-B27 antigen predisposes to Reiter's syndrome after exposure to an infectious agent and clinical expression may be markedly influenced by genetic factors. The disease mechanism is yet not established but possible interaction between several different infective organisms and a specific genetic background is being seriously considered. Clinically, the syndrome consists of the triad of urethritis, arthritis, and conjunctivitis. Enthesopathy is a prominent feature (Groshar et al. 1997; Kim et al. 1999). Radiographic changes include tendinitis, fasciitis, sausage digit, and paravertebral enthesitis, manifesting either singly or in combination. Osteophytosis is a common finding in the late stage. The whole-body scan is useful for understanding the skeletal involvement. Unlike in rheumatoid arthritis, joint involvement in Reiter's syndrome is asymmetrical and pauciarticular (Fig. 22.12A). ^{99m}Tc-MDP bone scan sensitively detects enthesopathy in the absence of radiographic alterations in 14.1% of patients (Kim et al. 1999). Pinhole scanning markedly raises the sensitivity and specificity of the diagnosis of Reiter's syndrome (Fig. 22.12B, C).

22.4 Other HLA-associated Skeletal Disorders

Other HLA-associated skeletal disorders of scintigraphic interest include reactive arthritis, diffuse idiopathic skeletal hyperostosis or DISH (Forestier's disease), slipped capital femoral epiphysis, and calcific periarthritis (hydroxyapatite crystal deposition disease).

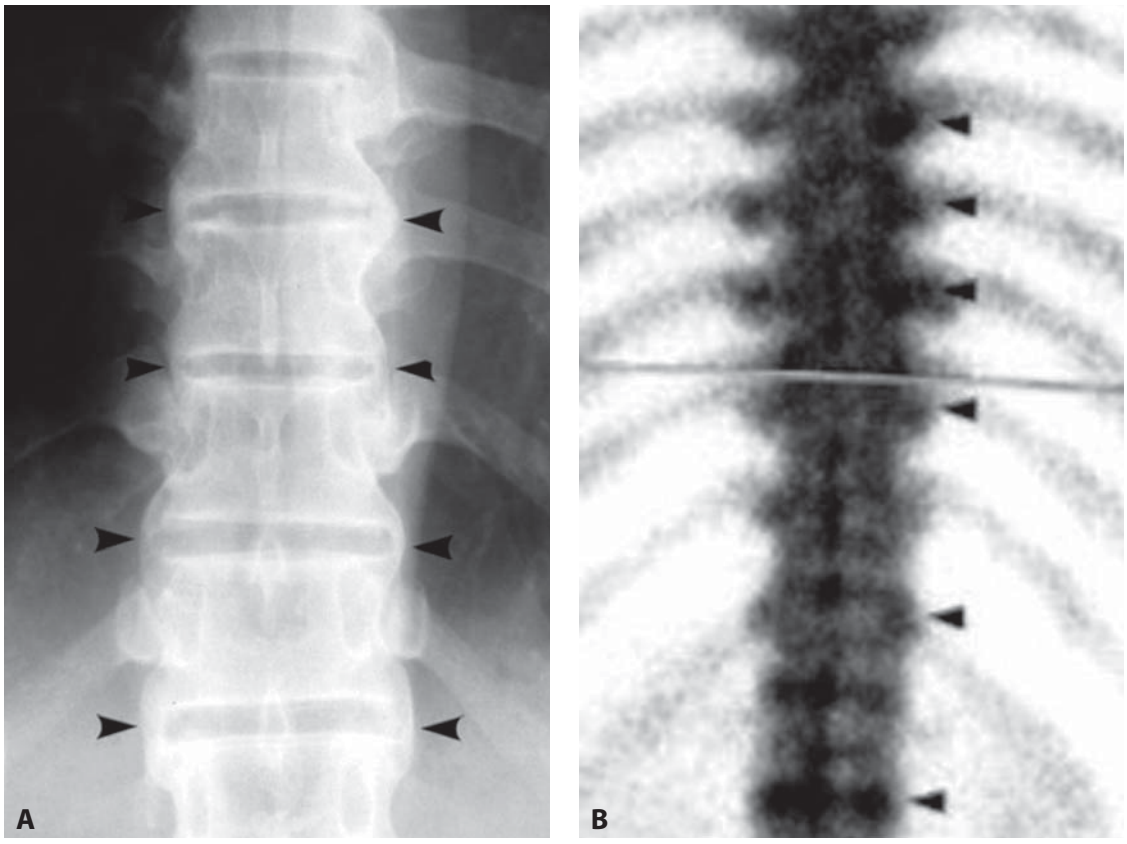

Fig. 22.13A, B Diffuse idiopathic skeletal hyperostosis. **A** Anteroposterior radiograph of the thoracolumbar spine in a 29-year-old man shows diffuse ossification of the longitudinal ligament with bumpy hyperostosis in more than five contiguous vertebrae (*arrowheads*). **B** Posterior pinhole scan reveals increased tracer uptake in the ossified ligament with bumpy elevation (*arrowheads*)

22.4.1 Reactive Arthritis

Reactive arthritis is a well-known rheumatic disorder that is initiated or triggered by a variety of infective agents without direct joint contamination. Sacroiliitis in ankylosing spondylitis and Reiter's syndrome are classic examples of reactive arthritis. According to Leirisalo et al. (1982), the sacroiliitis in Reiter's syndrome is more common in those with positive HLA-B27 antigen. The ^{99m}Tc-MDP scan shows intense uptake in the sacroiliac joints, characteristically in the synovial compartments.

22.4.2 Diffuse Idiopathic Skeletal Hyperostosis (Forestier's Disease)

Diffuse idiopathic skeletal hyperostosis is a disorder characterized by the ossification of the anterior longitudinal ligament with raised hyperostosis localized to the anterolateral aspects of the vertebral body–intervertebral disk junctions in the thoracolumbar and cervical spine (Fig. 22.13A). HLA-B27 antigen is positive in 34% of patients (Shapiro et al. 1976). Radiographically, the disk spaces appear blurred, but well-preserved. Bone scintigraphy shows diffusely increased tracer uptake in the anterolateral aspects of several contiguous vertebrae (Fig. 22.13B). The intervertebral disk spaces are obliterated due to increased tracer uptake with bulging lateral borders. Occasionally, the costovertebral and apophyseal joints as well as the spinous processes, to which interspinous ligaments are attached, also accumulate tracer. Such a scan finding of ours is at variance with the classic description that the apophyseal joints are not affected. Quite similarly to ankylosing

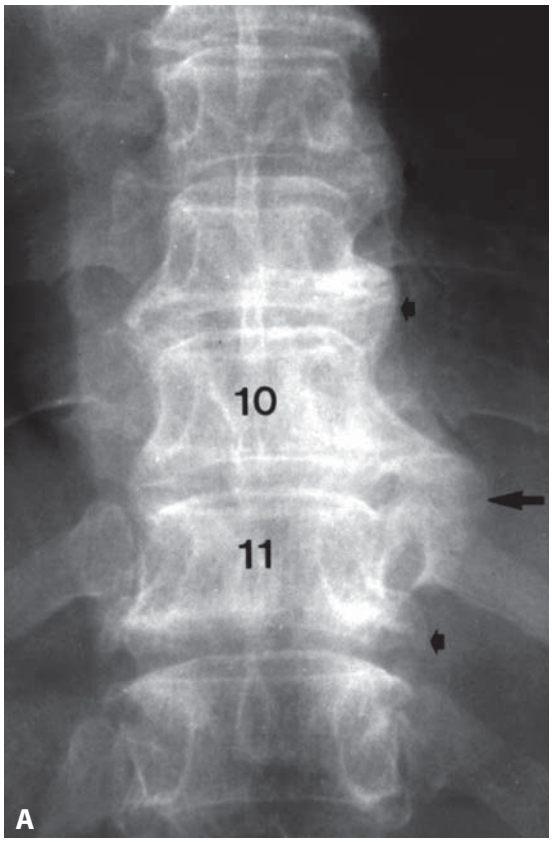

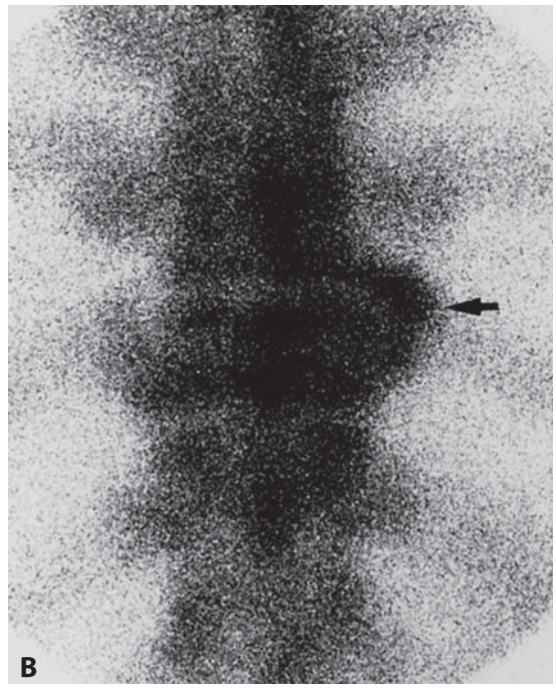

Fig. 22.14A, B Aged hyperostosis without increased tracer uptake. **A** Anteroposterior radiograph of the thoracolumbar spine shows bumpy hyperostosis (*small arrows*). Note especially prominent hypertrophy at the level of the T10–11 disk space on the left (*large arrow*). It was a painful lesion. **B** Posterior pinhole scintigraph reveals no increased tracer uptake in bumpy elevations except in the painful one at the level of the T10–11 disk space (*arrow*)

spondylitis, tracer uptake is prominent in the early stage of the disease, whereas it is reduced in the late stage when hyperostosis becomes ossified and metabolically inert (Fig. 22.14).

22.4.3 Slipped Capital Femoral Epiphysis

Slipped capital femoral epiphysis is the medioposterior spillage of the capital epiphysis of the femur in children and adolescents. Slippage typically involves the zone of hypertrophic chondrocytes of an actively developing physeal plate. Trauma, excessive physical activity, growth spurt, and obesity are suggested as contributory factors. This condition has been associated with relatively high prevalence of genetic markers. Indeed, one study by Mullaji et al. (1993) showed that HLA-B27 antigen was positive in 20% of patients with this disorder. The characteristic bone scintigraphic features include intense tracer uptake in the flattened capital femoral epiphysis with mild photopenia in its base and lateroanterior buckling of the metaphysis (Fig. 13.10).

22.4.4 Calcific Periarthritis (Hydroxyapatite Crystal Deposition Disease)

Calcific periarthritis is a painful and often disabling disorder that is precipitated by acute and chronic trauma. Calcific periarthritis consists of tendinitis and bursitis, and is characterized by hydroxyapatite crystal deposition in the degenerated tendinous or ligamentous tissue and bursa. The shoulder, hand, wrist, pelvis and hip, knee, and ankle are the favorite sites with the shoulder being most commonly affected. Pinals and Short (1965) related multiple calcific periarthritis to a fundamental defect in connective tissue. Amor et al. (1977) have proposed a genetic predisposition on the basis of high prevalence of HLA-A2 (66%) and HLA-Bw (34%) in this disorder. Radiography can

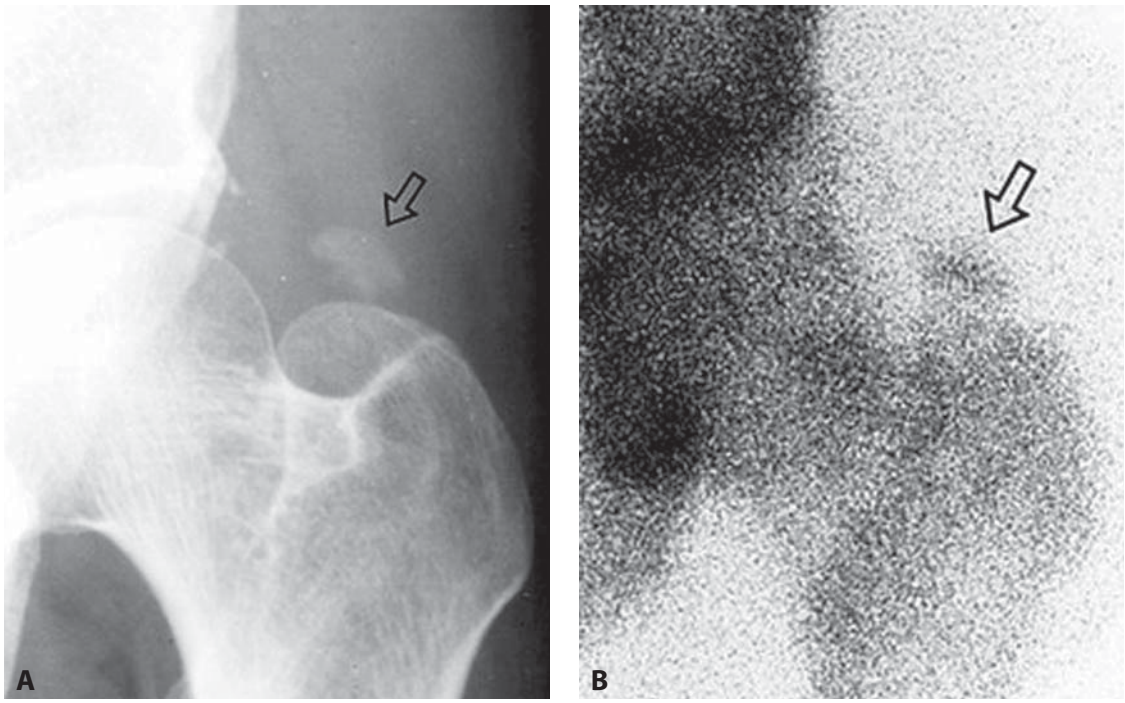

Fig. 22.15A, B Calcific bursitis. **A** Anteroposterior radiograph of the left hip in a 46-year-old woman shows a bean-shaped calcium deposit in the trochanteric bursa (*open arrow*). The lesion was painful. **B** Anterior pinhole scintigraph reveals tracer accumulation in this calcific bursitis (*open arrow*)

sensitively detect calcification in and around a joint. Ordinary bone scintigraphy is not so informative, but pinhole scintigraphy can detect subtle tracer uptake in calcified lesions, leading to the diagnosis of tendinitis or bursitis (Fig. 22.15). A distinctive advantage of ^{99m}Tc-MDP bone scan is that it shows the metabolic profile of such calcification. Indeed, tracer positively accumulates in painful calcifications but not in quiescent ones.

22.5 Non-genetic Skeletal Disorders

Non-genetic skeletal disorders are neither heritable nor linked with any known genetic imbalance. Infections, vascular disorders, aseptic necrosis, trauma, recreational and sports injuries, nutritional disorders, most tumors and tumor-like conditions, and many other disorders belong to this category, and they are described in detail in their respective chapters.

References

Amor B, Cherot A, Delbarre, et al (1977) Hydroxyapatite rheumatism and HLA markers. J Rheumatol Suppl 3:101–104

Bahk YW, Chung SK, Park YH, et al (1998) Pinhole SPECT imaging in normal and morbid ankles. J Nucl Med 39:130–139

Benli IT, Akalin S, Boysan E, et al (1992) Epidemiological, clinical and radiological aspects of osteopoikilosis. J Bone Joint Surg Br 74:504–506

Black B, Dooley J, Pyper A, Reed M (1993) Multiple hereditary exostoses. An epidemiologic study of an isolated community in Manitoba. Clin Orthop Rel Res 287:212–217

Bonde CT, Vielfreund L (2001) Buschke-Ollendorff syndrome. Connective tissue nevi in osteopoikilosis. Ugeskr Laeger 8:170–171

Cohen-Solal M, de Vernejoul MC (2004) Genetics of osteoporosis. Rev Med Interne 25 [Suppl 5]:S526–530

Dahlin DC, Unni KK (1986) Chondroma. In: (eds) Bone tumors, 4th edn. Thomas, Springfield

Fong KY (2000) The genetics of spondyloarthropathies. Ann Acad Med Singapore 29:370–375

Goldman AB (1995) Heritable diseases of connective tissue, epiphyseal dysplasia, and related conditions. In: Resnick D, Niwayama K (eds) Diagnosis of bone and joint disorders, 3rd edn. Saunders, Philadelphia

Groshar D, Rosenbaum M, Rosner I (1997) Enthesopathies, inflammatory spondyloenthesopathies and bone scintigraphy. J Nucl Med 38:2003–2005

Kahn MA (1988) Ankylosing spondylitis and heterogeneity of HLA-B27. Semin Arthritis Rheum 18:134–141

Kim SH, Chung SK, Bahk YW, et al (1999) Whole-body and pinhole bone scintigraphic manifestations of Reiter's syndrome: distribution patterns and early and characteristic signs. Eur J Nucl Med 26:163–170

Leirisalo M, Skylv G, Kousa M, et al (1982) Followup study on patients with Reiter's disease and reactive arthritis, with special reference to HLA-B27. Arthritis Rheum 25:249– 259

McAlister WH, Herman TE (1995) Osteochondrodysplasias, dysostoses, chromosomal aberrations, mucopolysaccharidoses, and mucolipidoses. In: Resnick D, Niwayama G (eds) Diagnosis of bone and joint disorders, 3rd edn. Philadelphia, Saunders

McCarty DJ, Gatter RA (1966) Recurrent acute inflammation associated with focal apatite crystal deposition. Arthritis Rheum 9:804–819

Medina M, Viglietti AL, Gozzeli L, et al (2000) Indium-111 labelled white blood cell scintigraphy in cranial and spinal septic lesions. Eur J Nucl Med 27:1473–1480

Morris R, Metzger AL, Bluestone R, et al (1974) HL-A W27 – A clue to the diagnosis and pathogenesis of Reiter's syndrome. New Engl J Med 290:554–556

Mullaji AB, Emery RJH, Joysey VC, et al (1993) HLA and slipped capital femoral epiphysis. J Orthop Rheumatol 6:167–169

Ochsner PE (1978) Multiple cartilaginous exostoses and neoplastic degeneration: review of the literature. Z Orthop Ihre Grenzgeb 116:369–378

Peacock M, Turner CH, Econs MJ, Foroud T (2002) Genetics of osteoporosis. Endocr Rev 23:303–326

Pierz KA, Stieber JR, Kusumi K, Dormans JP (2002) Hereditary multiple exostoses: one center's experience and review of etiology. Clin Orthop Relat Res 401:49–59

Pinals RS, Short CL (1965) Calcific periarthritis involving multiple sites. Arthritis Rheum 8:462

Rambeloarisoa J, el Guedj M, Legeai-Mallet L, et al (2002) Hereditary multiple exostoses after 40 years of development: a case report. Rev Med Interne 23:657–664

Roodman GD, Windle JJ (2005) Paget disease of bone. J Clin Invest 115:200–208

Rubin (1964) Dynamic classification of bone dysplasias. Year Book Medical Publishers, Chicago

Shapiro RF, Utsinger PD, Wiesner KB, et al (1976) The association of HL-A B27 with Forestier's disease (vertebral ankylosing hyperostosis). J Rheumatol 3:4–8

Shi YR, Wu JY, Hsu YA, et al (2002) Mutation screening of the EXT genes in patients with hereditary multiple exostoses in Taiwan. Genet Test 6:237–243

Taranta A, Migliaccio S, Recchia I, et al (2003) Genotype-phenotype relationship in human ATP6i-dependent autosomal recessive osteopetrosis. Am J Pathol 162:57–68

Williams PL, Warwick R, Dyson M, Bannister LA (1989) Gray's anatomy, 37th edn. Churchill Livingstone, Edinburgh

Wordsworth P (1995) Genes and arthritis. Br Med Bull 51:249–266

Appendix: Basic Physics of Pinhole Scintigraphy

Tae Suk Suh and Yong-Whee Bahk

A.1 Factors Affecting Scintigraphic Imaging

This appendix presents a basic description of pinhole scintigraphy, including: the effects of pinhole collimator on the parameters important for detecting lesions, such as spatial resolution and sensitivity, the quantitative parameters for measuring spatial resolution and sensitivity, and the general principles of factors affecting scan image formation.

The final image of scintigraphy is the result of a collective effect of complex processes which are affected by a number of factors. These include (a) radionuclide, (b) radioactivity, (c) collimator design, (d) scintillation detector, (e) electronic devices, (f) image display and recording devices, (g) image data processing, (h) movement of patient, and (i) artifacts. Each of these factors singly or in combination can alter the spatial resolution, object contrast, and sensitivity, which in turn influence lesion detectability of a scintigraphic system.

A.1.1 Radionuclides

The choice of a radionuclide for scintigraphic imaging is based on the rule that, in addition to a strong avidity for the organ or tissue under study, the radiation dose delivered to the patient should be kept as low as possible and the count density as high as possible to enhance lesion detectability. To optimize such contradicting demands, the half-life of a radionuclide must be just so short that the designed test can be terminated within a reasonable period of time, which is nevertheless compatible with the biological phenomenon under investigation. To maximize the detection function of the instrumentation, radionuclides should have high photon yields to provide high count rates. It is also desirable that a radionuclide emit a monochromatic gamma ray, with the energy ranging between 110 and 160 keV. Photons having energies less than 110 keV are known to have a high photopeak efficiency within NaI(Tl) crystals but exhibit a poor intrinsic spatial resolution performance due to their poor statistics of localization. On the other hand, photons having energies greater than 160 keV suffer from a low count density due to low photopeak efficiencies of detection in a thin crystal, but nevertheless exhibit an increased intrinsic spatial resolution performance because of high energy deposit within the crystals. On the basis of these desiderata, ^{99m}Tc with a half-life of 6 hours and a monochromatic gamma ray of 140 keV is an ideal radionuclide for scintigraphy. Furthermore, ^{99m}Tc can easily label bone-seeking radiopharmaceuticals such as methylene diphosphonate, pyrophosphate, and polyphosphates, making it readily acceptable for skeletal imaging in clinical practice.

A.1.2 Radioactivity

The amount of radioactivity administered to a patient has a decisive effect on image formation. To achieve a statistically adequate count density within a short scan time, a higher activity is required to provide a high count rate. There are two limiting factors for increasing

the amount of radioactivity: the radiation from and the toxicity of the radiolabeled agents. The radiation delivered to the body varies with the decay characteristics of the radionuclide. For example, ^{131}I delivers a high radiation dose to the subject through bichromatic gamma and beta emissions, but, being a pure gamma emitter, ^{99m}Tc delivers a much lower dose. The biological half-life of an imaging agent also has an important effect on both the magnitude and distribution pattern of the radiation dose within the body. It is well known that the longer the biological half-life, the greater is the absorbed radiation dose.

Since the amount administered in a given clinical study is in the order of milligrams or less, and clinical trials are under extremely strict control, toxicity may impose no major problem as far as the radiopharmaceuticals currently in use are concerned. For the optimum image quality, the impurities or contaminants of a radiopharmaceutical are to be maintained at the lowest possible level since they increase radiation dose without contributing to image quality.

A.1.3 Collimator Design

The primary aim of the collimator in a scintillation camera system is to direct the gamma rays emitted from a selected location of the body or a target to the scintillation detector in a specially desired manner. In practice, four different types of collimators are in use: the pinhole collimator and the parallel hole, converging, and diverging multihole collimators. The size of the image formed in the detector is a function of the characteristics of the collimator and the detector-face-to-object distance. When the thickness of the collimator wall or hole septa is insufficient, significant penetration of the collimator material by gamma photons can occur even at the relatively low energy level of 140 keV of ^{99m}Tc. The usual design to reduce penetration to an acceptable level is to increase the thickness of the wall or hole septa. This, however, inevitably detracts from the collimator efficiency due to reduction in the area seen by the detector. The selection of a particular type of collimator is dictated fundamentally by the size of the organ and the specific energy to be imaged. When the organ or tissue is small, such as the thyroid gland or a bone and joint, a pinhole collimator details pathological findings in enlarged display mode with greatly enhanced resolution. On the other hand, for a larger organ or body system such as the cardiopulmonary, hepatorenal, and skeletal systems, a multihole collimator should be utilized to obtain the total system image with appropriate quality in terms of count density and resolution within a reasonably short period of time. The collimators have a decisive effect on the formation of scan images. It is of paramount importance carefully to choose the optimum trade-off conditions between spatial resolution and scan efficiency.

A.1.4 Scintillation Detector

Most scintigraphic devices employ a sodium iodide crystal activated with thallium [NaI(Tl)] as the detector medium. Since sodium iodide has both a high Z number of iodine ($Z=53$) and a high density of NaI(Tl) material (3.53 g/cm^3), it can provide a high detection efficiency through the enhanced photoelectric effect. Diameter (D) and thickness (t) are two key factors that directly govern the detectability of gamma rays within crystal (Fig. A1). Thus, an increase in crystal diameter is followed by an increase in the count rates and object areas imaged.

An important parameter of a scintillation crystal is the photopeak detection efficiency. It is defined as the probability that a gamma ray traversing a channel of the collimator is totally absorbed by the crystal, resulting in the production of a photopeak pulse. In essence, the photopeak detection efficiency depends on photon energy and crystal thickness, and is also associated with the sensitivity of the imaging device to register the count rate. It has been shown that the photopeak detection efficiency increases with increasing crystal thickness for all photon energies, but that for a given crystal thickness it decreases with increasing gamma ray energy.

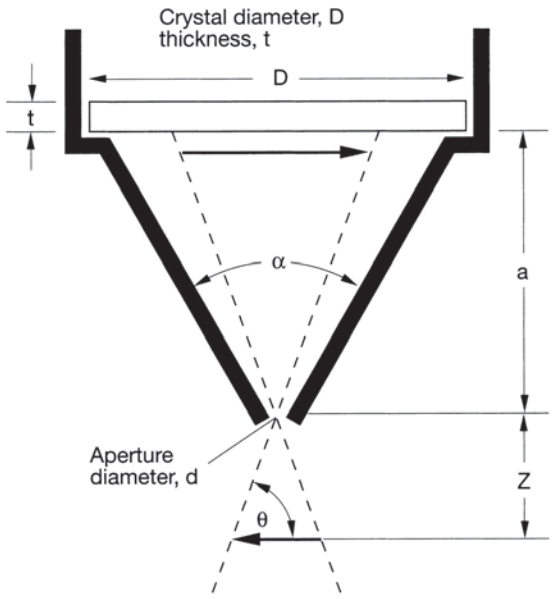

Fig. A1 Schematic diagram showing the set of parameters used in describing resolution and sensitivity of the pinhole collimator. *D, t* detector (crystal) diameter and thickness, respectively; *a, Z* aperture-to-detector distance and aperture-to-object distance, respectively; *d, d_e* physical and effective aperture diameter; *α, θ* acceptance angle and oblique angle between source plane and gamma ray path

A.1.5 Electronic Devices

The electronic devices that compose a gamma camera system include the photomultiplier tube, preamplifier, linear amplifier, pulse-height analyzer, multichannel analyzer, scaler/timer, and rate meter.

Photomultiplier Tube The light produced by scintillation in crystal is too small in amount and too weak in intensity for the human eye to perceive or for an imaging device to display without amplification. In principle, the photomultiplier tube is a light-sensitive device which converts light into measurable electronic pulses. The photomultiplier tube consists of a photocathode, a series of dynodes, and an anode sealed in a vacuum glass cylinder. When the photocathode is hit by light photons in crystal, electrons of low energy (0.1–1 eV) are produced through photoelectric interaction. The photoelectrons are then multiplied by acceleration through a series of dynode actions, resulting in the generation of an electric pulse at the anode.

Preamplifier Since the electric pulses arriving at the anode are still feeble, it is necessary to amplify them at least to the order of several volts prior to further processing. Such anode outputs of a photomultiplier tube, however, cannot be fed into an amplifier because there is a significant difference between the output impedance of the photomultiplier tube and the input impedance of the amplifier, and to solve this impedance mismatch the preamplifier has been created.

Linear Amplifier The linear amplifier is a specially designed, integrated circuit which amplifies the electric pulses arriving from a preamplifier and processes them for analysis. The magnitude of the amplification can be adjusted by gain control.

Pulse-Height Analyzer The setting of the pulse-height analyzer, an electric version of an X-ray grid, is one of the most critical parameters in detecting lesions. The collimators of gamma cameras are so designed as to allow only those photons traveling in a direction defined by the collimator holes to reach the crystal. A collimator, however, cannot distinguish the original unscattered photons from scattered photons on the basis of their energy. It is well known that the scattered photons detected within the crystal tend to degrade the image quality because they do not originate directly from within the field of view of the detector or target organ. The scattered photons, having lost a part of their energy through the Compton effect, enter the crystal with reduced energy compared to the primary photons. Consequently, the former can be discriminated from the latter by means of pulse-height analyzer. The pulse-height analyzer permits only those photons whose pulse amplitudes fall within a certain preselected energy range (energy win-

dow) to be recorded as actual counts. The fraction of the counts presented to the analyzer is called pulse-height analyzer efficiency, an important parameter of count rate. When the lower level of the energy window is raised, the scattered photons with reduced energy level are eliminated, improving the spatial resolution. This process, however, is achieved at the inevitable expense of counts detected and, hence decreased sensitivity. When the lower level of the energy window is scaled down, the reverse takes place.

A.1.6 Image Display and Recording Devices

Most scintillation cameras utilize a cathode-ray tube as a means of image display. The cathode-ray tube is a highly evacuated glass tube containing five basic components: an electron gun, a focusing electrode, horizontal deflection plates, vertical deflection plates, and a phosphor screen. Of these, the phosphor of the display screen of cathode-ray tube directly effects the image contrast. There are two major sorts of phosphor, ^{31}P and ^{11}P. Their relative luminescence differs. The image from ^{11}P appears superior because of its high contrast. However, the superiority is attained at the expense of a loss of informational content of the image. High contrast is the result of a background erasing effect from before the time the information signals were recorded.

Gamma cameras use either Polaroid film or 35- or 70-mm transparencies for image recording. Conveniently, the Polaroid film requires no developer or fixer, but it has the significant drawback of a limited gray scale and inferior contrast. Although photographic processing is necessary, 35- or 70-mm transparency films provide much higher contrast and a sufficient number of gray scales. The latest image recording system, known as multiformat, is capable of displaying various size and number of scan images in a single sheet of radiographic film. The quality of the multiformat display has been shown to be indeed satisfactory with sharp definition of individual pixels and uniformity of their size.

To maximize image quality two photographic requirements must be met. One is careful matching of film type to the presenting imaging requirements, and the other is accurate focusing of the display dots. Regarding the film type, it has been shown empirically that high-contrast film is best suited for portraying a hot lesion, whereas a low-contrast film is preferred for recording a cold lesion or blood flow pattern.

A.1.7 Image Data Processing

There are a number of image data processing techniques by which the quality of the final image obtained from the initial image can be improved. The latest method utilizes computers. The application of computers to image formation requires the collection of image data on a disk or a magnetic tape linked with an imaging device. The capacity of the computer used in gamma camera system is determined by the number of matrices or memory sizes. Each element of the image matrix, called a pixel, contains certain number of counts and is digitized in X–Y positions. The digitized images provide the user with information with which the digitized data can be postprocessed without destroying the original image data. Methodologically, the image data processing techniques include data interpolation, data smoothing, background erasing, contrast enhancement, digital filtering, and color mapping.

A.1.8 Movement of Patient

It is obvious that the patient's movement during scanning has deleterious effects on lesion display. For example, movement during the imaging of a hot lesion tends to increase the apparent size of the lesion with unsharp contour, while motion during the imaging of a cold or small hot lesion may result in total omission of the lesion. It is therefore critical to eliminate all unnecessary movements. This can be accomplished simply by asking the cooperation of the patient, by the use of immobilizing devices or mild sedation, or by employing a computer-assisted composite imaging technique that aligns and superimposes centroids

to produce motion-free images. As an alternative, the motion effect can be held to a minimum by increasing the count density by maximizing the amount of radioactivity administered. Shortening of scan time is still another means, but of course this lessens image quality due to low count density.

A.1.9 Artifacts

Any artifact can affect the final image. The two most common causes of artifacts are radiation contamination of the patient's skin, clothing, collimator, and detector, and the false cold areas created by metallic ornaments, coins in the pocket, zippers, and hooks. In practice, nearly all artifacts can be recognized as such if one is familiar with their characteristic appearance and, when necessary, by obtaining different views which may show whether or not the tracer uptake in question moves with patient or detector.

A.2 Effects of Pinhole Collimator Design

As described in the general introduction, a number of factors are involved in scan image formation. This section discusses the effects of pinhole collimator design on lesion-detecting parameters such as spatial resolution and sensitivity, along with comments on quantitative parameters for measuring spatial resolution and sensitivity.

The selection of a particular type of collimator is made primarily on the basis of the size or area of the organ to be imaged, and on the degree of detail desired in the anatomy. Thus, when a target area is not too large, and scintigraphy of higher resolution and greater detail is desired, the pinhole collimator is the collimator of choice. One major disadvantage of using the pinhole collimator is the low sensitivity due to reduced count rates. However, optimization of the two mutually contradictory factors of high resolution and low sensitivity can be achieved by choosing an appropriate aperture diameter.

A pinhole collimator is a cone-shaped lead shield which tapers into a small aperture perforated at the center of the tip at a distance (a) from the detector face (Fig. A1). The geometry of the pinhole creates an inverted image of the target organ in crystal from the photons traveling through a small aperture. The pinhole collimator design is based on an aperture diameter (d), acceptance angle (α), collimator length (a), and pinhole material. Any change in pinhole collimator design can affect lesion detectability by altering the spatial resolution and sensitivity. Both spatial resolution and sensitivity are also affected by the energy of the radionuclide used. The effective diameter of the pinhole decides the actual collimator efficiency since gamma rays penetrate thin edges of the aperture. With distance, pinhole imaging suffers from rapidly changing field of view size, resolution, and sensitivity. Pinhole scintigraphy produces images with a high resolution but a limited field of view. Theoretically, the exact relationship between pinhole collimator parameters and resolution and sensitivity can be established only with much difficulty, and it is beyond the scope of this book to make an attempt to derive the mathematical formulae related to this complex problem. However, since it is essential for comprehension of the relationship between collimator design parameters and lesion detecting parameters such as resolution and sensitivity, a brief discussion seems warranted. Below, a simple mathematical form is derived to represent the dependence of resolution and sensitivity on a given pinhole collimator design.

A.2.1 Spatial Resolution

Spatial resolution is one of the two most important indicator parameters of gamma camera performance. It denotes the ability to accurately determine the original location of gamma rays within the source area. According to Brownell (1959), the geometrical spatial resolution can be defined as the distance between the two point sources that produces touching

image circles in the crystal detector. The geometric spatial resolution R_C of a pinhole collimator is given by:

$$R_c = \frac{(a+Z)}{a} d_e \quad (1)$$

where a and Z are the aperture-to-detector distance and aperture-to-object distance, respectively, d and d_e are the physical and effective aperture diameter, respectively (Fig. A1). A mathematical expression for the path length of the general ray through the pinhole collimator is necessary in deriving analytical formulae for the effective area. Figure A2 is a cross-section in a plane including the common axis of crystal and collimator. Ray I, normally incident, has a path length of:

$$T_1 = 2\left(b - b_0\right) \cot \alpha / 2 \quad (2)$$

where b, b_0, and α denote an arbitrary distance from the central axis of the pinhole, the physical radius, and the acceptance angle, respectively. The effective area A of the pinhole for normally incident rays may be written as:

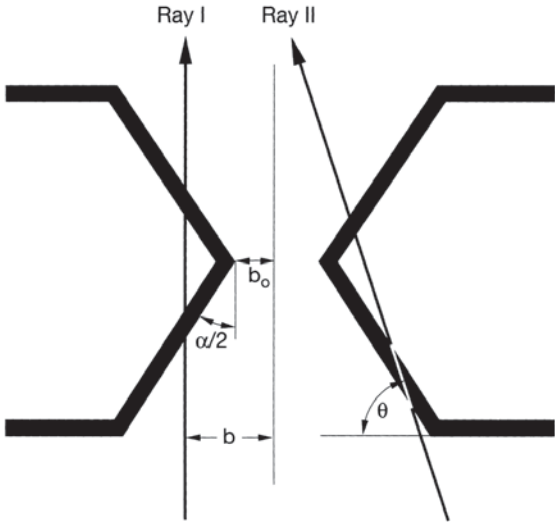

Fig. A2 Schematic diagram showing section in a plane passing through the common axis of crystal and collimator. *Ray I* and *Ray II* are normally incident with an angle of incidence θ at radius b; b_o physical radius of pinhole aperture; $\alpha/2$ half value of acceptance angle

$$A = 2\pi \int_0^\infty b e^{-\mu T(b)} \delta b \quad (3)$$

where $e^{-lT(b)}$ represents the attenuation factor for rays at radius b. Using mathematical integration, the equation yields:

$$A = \pi b_0^2 + 2\pi \int_{b_0}^\infty b e^{-2\mu(b - b_0)\cot \alpha/2} \delta b \quad (4)$$

$$= \pi \left[b_0^2 + \frac{1 + 2\mu b_0 \cot\alpha/2}{2\mu^2 \cot 2\alpha/2} \right] \quad (5)$$

in which the bracketed term may be identified as b^2. The effective diameter de is given by:

$$d_e = \left[d \left(d + 2\mu^{-1} \tan\alpha/2 \right) \right]^{1/2} \quad (6)$$

where α is the angle shown in Fig. A1 and represents the acceptance angle between the collimator walls. and l^{-1} is the mean free path of gamma rays in the collimator material. The expression for ray II in the general situation becomes complicated since the radial symmetry of the integral is lost. A more detailed description for the expression for the general path length is given by Paix (1967). The overall system resolution R_0 consists of the collimator spatial resolution R_C, intrinsic resolution R_i, and scatter spatial resolution R_S:

$$R_0 = \sqrt{R_c^2 + \{(Z/a)R_i\}^2 + R_s^2} \quad (7)$$

where Z/a is the magnification factor associated with a collimator of length (a) and an aperture-to-object distance (Z; Fig. A1). The system resolution improves when Z is smaller because the resulting magnification factor reduces the effective contribution to intrinsic resolution R_i. It is to be noted that the scatter spatial resolution R_S can be minimized by the use of a scatter reduction technique such as asymmetrical energy window setting or preferential weighting of the energy spectrum.

A.2.2 Sensitivity

Sensitivity is the parameter of the scintillation camera which refers to its ability to efficiently convert a source of incident gamma rays of

known activity to a recorded count and to locate data for imaging. The sensitivity (*S*) is given by: (number of gamma rays displayed on the screen)/(total number of gamma rays emitted from the source). Theoretically, the count rate of the gamma camera with various factors of the imaging device which convert the gamma rays emitted from a point source into recorded counts can be estimated by:

$$S_c = G\tau\phi\sigma e^{-\mu z} \tag{8}$$

where s is the photopeak efficiency, the pulse height analyzer efficiency, r the activity distribution of the source, e^{-lz} attenuation factor, and G the geometric efficiency of the collimator. The geometric efficiency is defined as the fraction of the gamma rays emitted by the subject that pass through the aperture. The geometric efficiency of a pinhole collimator for all points on the plane at a distance Z below the pinhole shown in Fig. A1 is given by:

$$G = \frac{\pi\left(d_e/2\right)\left(d_e/2\right)\sin\Theta}{4\pi\left(Z\mathrm{cosec}\Theta\right)^2} \tag{9}$$

$$G = \frac{d_e^2 \sin^3\Theta}{16Z^2} \tag{10}$$

where de and Z are as defined in the spatial resolution expression (Eq. 1), and θ is the angle shown in Fig. A1. The geometric efficiency and spatial resolution of a pinhole collimator deteriorate as the aperture-to-source distance increases. For a given field size, a pinhole collimator designed with a large acceptance angle (α) ensures the best sensitivity and resolution. Nevertheless, if α is too large, the working distance from source to collimator becomes inconveniently small, thus excessively losing the resolution and sensitivity at the edge of the field. It has been shown that an acceptance angle of 70° is a well-balanced compromise for most clinical purposes. It should be recognized from Eqs. 1 and 10 that the geometric efficiency is not constant throughout the plane at a fixed distance from the aperture, and that both sensitivity and resolution decline with an increase in distance from the aperture.

A.2.3 Measurement of Spatial Resolution

Two parameters, full width at half maximum (FWHM) and modulation transfer function (MTF), have been used to measure the resolution of an imaging device. Bar phantoms or hand-made phantoms are also used for a semiquantitative assessment of resolution.

Full Width at Half Maximum The response of an imaging device to a line source of radioactivity across the field of view of a collimator is a line-spread function (LSF). In practice, LSF measurements are made with a long thin plastic catheter filled with a radioactive solution. The technique for gamma camera LSF measurements involves collecting and storing digitized data from the line source using a gamma camera system with an interfaced computer. FWHM is the width of the curve at 50% of the maximum value that represents quantitative information gained from LSF measurements. The value approximates the geometric radius of resolution of the collimator (*R*). It must be stressed, however, that FWHM reflects the response of the device in air only. LSF and FWHM measurements are tedious to perform and do not reflect clinical situations.

Modulation Transfer Function The most complete characterization of the resolution of an imaging device is given by the MTF, while enabling one to measure spatial resolution performance in a scatter medium. To understand MTF fully, a knowledge of Fourier analysis is essential. The basic concept is based on the theory that all images can be resolved into a spectrum of spatial frequencies by means of Fourier analysis. MTF for a given spatial frequency is defined as the ratio of the image contrast to the object contrast. When the spatial resolution is ideal, the image and object contrast are the same, and the resulting MTF is unity. When image contrast is 0, MTF is 0. A detailed description of MTF is beyond the scope of this book, and readers are referred to the excellent papers by Gregg (1968) and Rossman and Lubberts (1966). MTF of an imaging device is difficult to measure directly, but com-

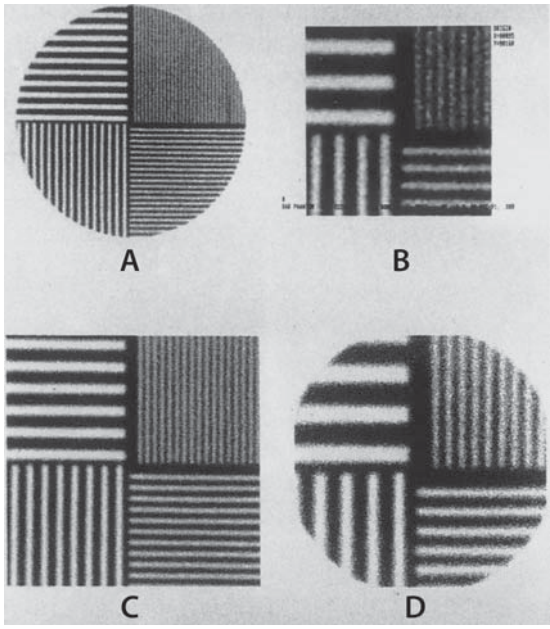

Fig. A3A–D A 90° quadrant, parallel lead-bar phantom used for the measurement of spatial resolution of scintillation camera. **A–D** Results of various magnification techniques using bar phantom: **A** reference scintigraph from 140 keV LEAP parallel hole collimator; **B** blow-up zoom scintigraph; **C** geometric magnification scintigraph; **D** pinhole magnification scintigraph

putation from the line spread function of a gamma camera can be utilized for MTF measurements.

Phantom Measurement Since the measurement of the two quantitative indices of spatial resolution, FWHM and MTF, is time consuming, clinically a semiquantitative evaluation using a 90-quadrant bar phantom is preferred. The phantom consists of four sets of parallel lead bars arranged in four quadrants of a lucite holder as shown in Fig. A3. The spacing and width of the lead bars vary in each quadrant, but they are the same within the same quadrant. The smallest spacing seen on the test scan image can be used as an indicator of spatial resolution of the gamma camera system. For more accurate estimation, a very narrowly spaced multiple hole phantom can be used.

A.2.4 Measurement of Sensitivity

For measuring the sensitivity of an imaging device three parameters are used: point sensitivity, line sensitivity, and plane sensitivity.

Point Sensitivity This parameter is defined as the fraction of gamma rays detected per unit time for a point source of radioactivity. In a gamma camera, the point sensitivity is more or less constant in the field of view of the collimator while in a rectilinear scanner it varies from point to point.

Line Sensitivity This parameter is defined as the fraction of gamma rays detected per unit time per unit length of a long line source of uniform radioactivity. The count profile of a line source is known as the line-spread function. Line-spread function is primarily used in the calculation of FWHM and MTF to evaluate spatial resolution.

Plane Sensitivity This parameter is defined as the fraction of gamma rays detected per unit time per unit area of a large plane source of uniform radioactivity. This parameter is commonly used to compare the sensitivities of two imaging devices. Plane sensitivity can be easily measured, and it does not vary with the distance of the plane source from the collimator providing the area of the plane source is maintained larger than the field of view of the collimator at that distance.

A.3 Technical Factors of Pinhole Scintigraphy

A.3.1 Pinhole Magnification

Theoretically it is possible to relate any point that appears on the cathode-ray tube screen to a point on a source plane at a known distance below the pinhole aperture, and this denotes the highest resolution. In clinical practice, high resolution images of various magnifications can be obtained using a pinhole collimator. The

resolution of a pinhole collimator (R_C) in the object plane is given by Eq. 1 (Fig. A1). The overall system resolution in the object plane includes the magnification factor [(a/*Z*)], where a and Z represent aperture-to-detector distance and aperture-to-object distance, respectively, as given by Eq. 7. Clearly, when a is smaller than Z, the magnification factor becomes reduced with a resultant decrease in the effective contribution of intrinsic resolution to the overall system resolution and vice versa. Since a is fixed for a given pinhole collimator attached to each gamma camera system Z remains the only variable factor, and it must be adjusted according to the size or area of the target under study for optimum imaging. As indicated by Eqs. 1 and 7, magnification can be made greater by reducing Z with a resultant improvement of the overall system resolution, the summation of both collimator resolution and its contribution to intrinsic resolution. The equations also indicate that the sensitivity of a pinhole collimator can be enhanced by increasing magnification, and this can be achieved simply by reducing the aperture-to-object distance, Z. However, the field of view size diminishes acutely as the aperture-to-object distance lessens. Thus, it appears that the improvement of spatial resolution and collimator efficiency by magnification is achieved only at the expense of the size of the field of view. Other important points shown by Eq. 10 are that the collimator efficiency is not homogeneous throughout the plane at a fixed distance from the aperture, and that resolution and sensitivity become degraded in the periphery.

Figure A3 presents the results of wvarious magnification techniques using a bar phantom. Figure A3A illustrates a reference scintigraph obtained using 140 keV low-energy all-purpose (LEAP) parallel hole collimator, and Fig. A3B and C are scintigraphs obtained using two different magnification techniques with the same parallel hole collimator, the former by the blow-up zoom technique and the latter by simple geometric magnification. The first blow-up method magnifies the original image data through interpolation of the surrounding pixel data to produce a new pixel value assigned between them. In consequence, notwithstanding the apparent magnification of the image by a factor of, for example, 2 as in this situation, the image quality becomes degraded without a true improvement of resolution. With the second method, the image magnification is achieved by the analog change in the gain of digitally controlled amplifiers for displacement signals. Since, in this method, the pixel size itself is not changed with magnification option, the resolution remains the same as in the reference method. On the other hand, as illustrated in Fig. A3D, an image magnification with true improvement of resolution can be achieved by the use of a pinhole collimator. It is visually obvious that the resolution of pinhole magnification is actual and far better than that of other magnification methods. It is to be mentioned that, because of acute change in the field of view size with distance, pinhole scintigraphy suffers from a miniaturizing distortion of the images of the structures that lie at a distance from the target center. In order to minimize such distortion the crystal diameter (*D*) should be made as minimal as possible for a given value of the crystal-to-aperture distance (*a*; Fig. A1). In practice, however, such image distortion seriously matters only when the evaluation of size is critical, an extremely rare clinical case as far as scintigraphy is concerned. Rather the miniaturizing distortion can be beneficial as the minification of the structures out of interest contributes to close up the structures of interest in the foreground.

A.3.2 Acquisition Time for Various Aperture Sizes

The change in pinhole size provides a simple means of altering the resolution and sensitivity of a gamma camera system. The basic relationship between pinhole size and resolution or sensitivity is discussed above, and resolution and sensitivity are inversely related to one other. The major concern in this section is the acquisition time required for an appropriate number of counts to accumulate to image a given object using pinhole collimators of vari-

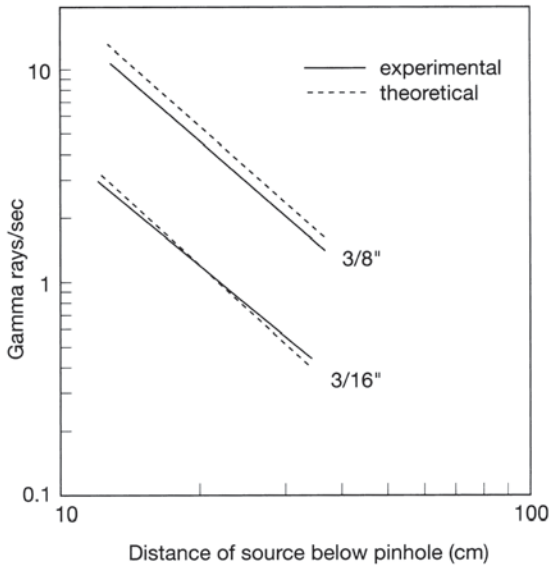

Fig. A4 Overall sensitivity of gamma camera (in air) for a point source of ^{131}I (3.5 μCi). *Abscissa* distance of a source below pinhole for two different diameters of pinhole; *ordinate* number of gamma rays displayed on screen per second. *Solid line* experimental graph; *dotted line* theoretical graph (redrawn from Mallard et al. 1963)

ous aperture sizes. According to theoretical estimation of the sensitivity given by Eqs. 8 and 10, the sensitivity in terms of counts per unit time is proportional to the square of effective pinhole aperture size. The sensitivity for two pinhole apertures using 3.5 μCi of ^{131}I as a source is shown in Fig. A4 (Mallard et al. 1963). From these curves it can be seen that the sensitivity increases by a factor of about 3.6±0.5 as the size of the pinhole aperture changes from 3/16 to 3/8 in, and the value is in reasonably good accord with 2^2, or 4, which would be expected from Eq. 10. The difference between the theoretically predicted and measured values can be accounted for by the difference between the physical and effective diameters of the pinhole. Tables A1 and A2 give the acquisition times needed to accumulate 10 k-counts for various aperture sizes for a thyroid phantom and a hip joint.

Table A1 Time (s) required for 10 k-counts from a thyroid phantom

Aperture-to-source distance (cm)	Aperture (mm)			
	2	3	4	6
2	27.80	12.74	6.68	3.21
4	34.99	17.20	8.92	4.30
8	72.94	35.61	19.04	9.30

Activity, 500 μCi for thyroid phantom.

Table A2 Time (s) required for 10 k-counts: hip joint

Aperture-to-source distance (cm)	Aperture (mm)			
	2	3	4	6
2	108.49	67.85	35.62	17.35
4	130.30	74.71	39.18	19.11
8	148.56	88.98	49.62	22.95

A.3.3 Acquisition Time for Various Aperture-to-Object Distances

As with resolution, the sensitivity of the pinhole collimator is also enhanced with a decrease in the aperture-to-object distance. Furthermore, both the spatial resolution and collimator efficiency improve as the aperture-to-object distance lessens. Plotted in Fig. A4 are the sensitivity versus aperture-to-object distance from a point source for various aperture sizes. It is to noted that the pinhole efficiency is reduced in an inverse square manner with increasing aperture-to-object distance (Z), as would be expected from Eq. 10. Tables A1 and A2 give the acquisition times for 10 k-counts to accumulate at various aperture-to-object distances using various aperture sizes for a thyroid phantom and a hip joint, respectively, and the same data are plotted in Fig. A5.

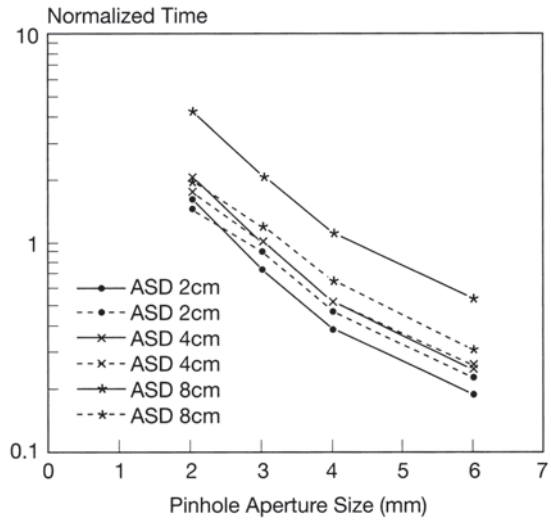

Fig. A5 Acquisition time required for 10 k-counts for various aperture-to-source distances (2, 4, 8 cm) using various aperture sizes (2, 3, 4, 6 mm) in a thyroid phantom (s) and the hip joint in a normal subject (s). The time is normalized at an aperture-to-source distance of 4 cm and an aperture size of 3 mm with the thyroid phantom. This combination of distance and aperture size is commonly used in daily clinical examinations

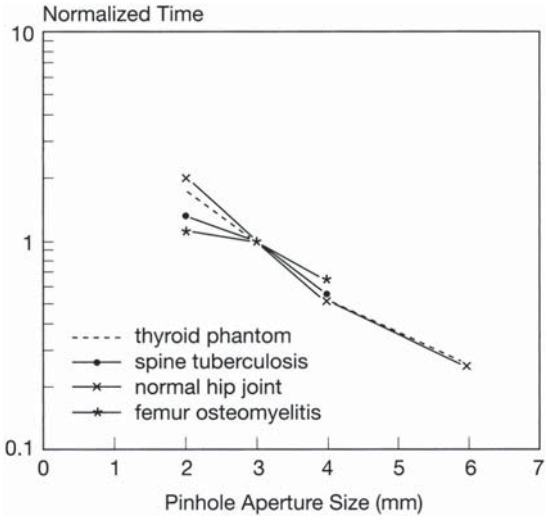

Fig. A6 Acquisition time required for 10 k counts at a fixed aperture-to-object distance (4 cm) for various pinhole aperture sizes (2, 3, 4, 6 mm) in spinal tuberculosis, osteomyelitis of the femur, a normal hip joint, and a thyroid phantom. The time is normalized at a pinhole aperture-to-object distance of 4 cm and an aperture size of 3 mm with the thyroid phantom

The acquisition times required for 10 k-counts to accumulate using pinhole collimators with various aperture sizes in a normal hip joint, spinal tuberculosis, and chronic osteomyelitis of the femur at a fixed aperture-to-object distance of 4 cm are plotted in Fig. A6.

References

Brownell GL (1959) Medical radioisotope scanning. IAEA, Vienna

Gregg EC (1968) Modulation transfer function, information capacity and performance criteria of scintiscans. J Nucl Med 9:116–127

Mallard JR, Inst FP, Myers MJ (1963) The performance of a gamma camera for the visualization of radioactive isotopes in vivo. Phys Med Biol 8:165–182

Paix D (1967) Pinhole imaging of gamma rays. Phys Med Biol 12:489–500

Rossman K, Lubberts G (1966) Some characteristics of the line spread-function and modulation transfer function of medical radiographic films and screen-film systems. Radiology 86:235–241

Subject Index

C

D

E

F

G

H

I

J

K

L

M

N

O

P

R

S

T

U

V

W